IntechOpen

Ferroelectrics
Characterization and Modeling

Edited by Mickaël Lallart

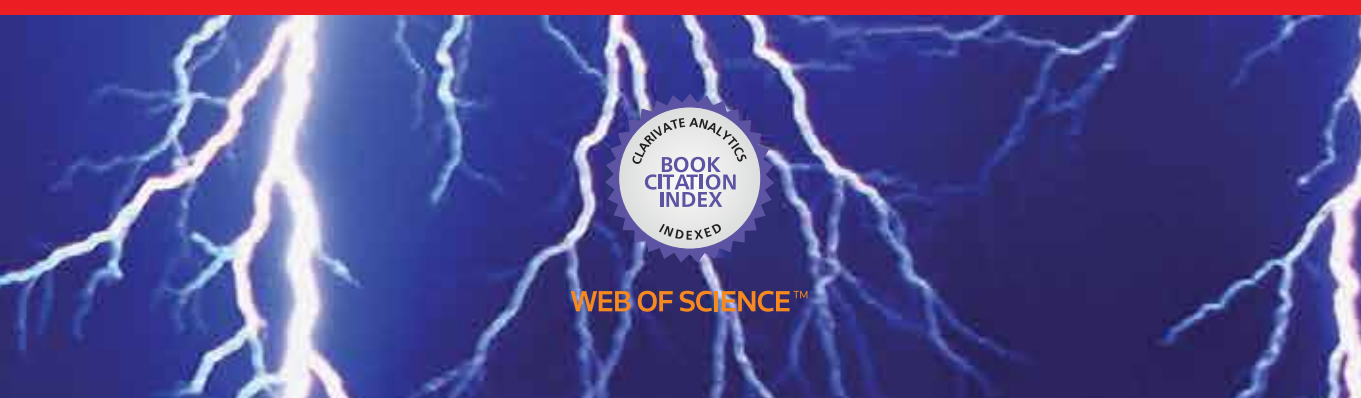

FERROELECTRICS - CHARACTERIZATION AND MODELING

Edited by **Mickaël Lallart**

Ferroelectrics - Characterization and Modeling
http://dx.doi.org/10.5772/946
Edited by Mickaël Lallart

Contributors

Vid Bobnar, Marko Hrovat, Janez Holc, Marija Kosec, Duo Liu, Yawei Li, Zhigao Hu, Junhao Chu, Krystyna Holderna-Natkaniec, Sining Yun, Khian-Hooi Chew, Lye Hock Ong, Makoto Iwata, Hamit Yurtseven, Emel Kilit, Josep Canet-Ferrer, Juan Martinez-Pastor, Yuriy Poplavko, Vitaliy Molchanov, Yuriy Prokopenko, Victor Kazmirenko, Jingzhong Xiao, Steffen Trimper, Thomas Bose, Abdelowahed HAJJAJI, yahia Boughaleb, Daniel Jean Guyomar, Yonghai Chen, Caihong Jia, Xianglin Liu, Shaoyan Yang, Zhanguo Wang, Kaoru Miura, Funakubo Hiroshi, Morioka Hitoshi, Ehara Yoshitaka, Chentir Mohamed-Tahar, Saito Keisuke, Yokoyama Shintaro, Oikawa Takahiro, Anastasia Muliana, Kaltenbacher, Barbara Kaltenbacher, Rashed Adnan Islam, Shashank Priya, Emre Erdem, Ruediger-A. Eichel, Yutaka Aikawa, Jeffrey F. Webb, DORIN DADARLAT, ABDELHAK HADJ SAHRAOUI, STEPHANE LONGUEMART, Sergio Koval, Jorge Lasave, Ricardo Migoni, Naresh Dalal, Jorge Kohanoff, Ho-Kei Chan, Vytautas Samulionis, Juras Banys, Andrius Dziaugys, Wolfgang Kleemann, Vladimir Shvartsman, Yulian Vysochanskii, Jan Macutkevic, Jan Dec, Seweryn Miga, Naik

Notice

First published in Croatia, 2011 by INTECH d.o.o.
eBook (PDF) Published by IN TECH d.o.o.
Place and year of publication of eBook (PDF): Rijeka, 2019. IntechOpen is the global imprint of IN TECH d.o.o.
Printed in Croatia

Legal deposit, Croatia: National and University Library in Zagreb

Additional hard and PDF copies can be obtained from orders@intechopen.com

Ferroelectrics - Characterization and Modeling
Edited by Mickaël Lallart

p. cm.

ISBN 978-953-307-455-9

eBook (PDF) ISBN 978-953-51-4455-7

Meet the editor

Mickaël Lallart graduated from Institut National des Sciences Appliquées de Lyon (INSA Lyon), Lyon, France, in electrical engineering in 2006, and received his Ph.D. in electronics, electrotechnics, and automatics from the same university in 2008, where he worked for the Laboratoire de Génie Electrique et Ferroélectricité (LGEF). After working as a post-doctoral fellow in the Center for Intelligent Material Systems and Structures (CIMSS) in Virginia Tech, Blacksburg, VA, USA in 2009, Dr. Lallart has been hired as an Associate Professor in the Laboratoire de Génie Electrique et Ferroélectricité. His current field of interest focuses on electroactive materials and their applications, vibration damping, energy harvesting and Structural Health Monitoring, as well as autonomous, self-powered wireless systems.

Contents

Preface XIII

Part 1 Characterization: Structural Aspects 1

Chapter 1 **Structural Studies in Perovskite Ferroelectric Crystals Based on Synchrotron Radiation Analysis Techniques 3**
Jingzhong Xiao

Chapter 2 **Near-Field Scanning Optical Microscopy Applied to the Study of Ferroelectric Materials 23**
Josep Canet-Ferrer and Juan P. Martínez-Pastor

Chapter 3 **Internal Dynamics of the Ferroelectric $(C_3N_2H_5)_5Bi_2Cl_{11}$ Studied by ^1H NMR and IINS Methods 41**
Krystyna Hołderna-Natkaniec, Ryszard Jakubas and Ireneusz Natkaniec

Chapter 4 **Structure – Property Relationships of Near-Eutectic $BaTiO_3 – CoFe_2O_4$ Magnetoelectric Composites 61**
Rashed Adnan Islam, Mirza Bichurin and Shashank Priya

Chapter 5 **Impact of Defect Structure on 'Bulk' and Nano-Scale Ferroelectrics 79**
Emre Erdem and Rüdiger-A. Eichel

Chapter 6 **Microstructural Defects in Ferroelectrics and Their Scientific Implications 97**
Duo Liu

Part 2 Characterization: Electrical Response 115

Chapter 7 **All-Ceramic Percolative Composites with a Colossal Dielectric Response 117**
Vid Bobnar, Marko Hrovat, Janez Holc and Marija Kosec

Chapter 8 **Electrical Processes in Polycrystalline $BiFeO_3$ Film 135**
Yawei Li, Zhigao Hu and Junhao Chu

Chapter 9 **Phase Transitions in Layered Semiconductor - Ferroelectrics 153**
Andrius Dziaugys, Juras Banys, Vytautas Samulionis, Jan Macutkevic, Yulian Vysochanskii, Vladimir Shvartsman and Wolfgang Kleemann

Chapter 10 **Non-Linear Dielectric Response of Ferroelectrics, Relaxors and Dipolar Glasses 181**
Seweryn Miga, Jan Dec and Wolfgang Kleemann

Chapter 11 **Ferroelectrics Study at Microwaves 203**
Yuriy Poplavko, Yuriy Prokopenko, Vitaliy Molchanov and Victor Kazmirenko

Part 3 Characterization: Multiphysic Analysis 227

Chapter 12 **Changes of Crystal Structure and Electrical Properties with Film Thickness and Zr/(Zr+Ti) Ratio for Epitaxial $Pb(Zr,Ti)O_3$ Films Grown on $(100)_c SrRuO_3//(100)SrTiO_3$ Substrates by Metalorganic Chemical Vapor Deposition 229**
Mohamed-Tahar Chentir, Hitoshi Morioka, Yoshitaka Ehara, Keisuke Saito, Shintaro Yokoyama, Takahiro Oikawa and Hiroshi Funakubo

Chapter 13 **Double Hysteresis Loop in $BaTiO_3$-Based Ferroelectric Ceramics 245**
Sining Yun

Chapter 14 **The Ferroelectric Dependent Magnetoelectricity in Composites 265**
L. R. Naik and B. K. Bammannavar

Chapter 15 **Characterization of Ferroelectric Materials by Photopyroelectric Method 281**
Dadarlat Dorin, Longuemart Stéphane and Hadj Sahraoui Abdelhak

Chapter 16 **Valence Band Offsets of $ZnO/SrTiO_3$, $ZnO/BaTiO_3$, $InN/SrTiO_3$, and $InN/BaTiO_3$ Heterojunctions Measured by X-Ray Photoelectron Spectroscopy 305**
Caihong Jia, Yonghai Chen, Xianglin Liu, Shaoyan Yang and Zhanguo Wang

Part 4 Modeling: Phenomenological Analysis 325

Chapter 17 **Self-Consistent Anharmonic Theory and Its Application to $BaTiO_3$ Crystal 327**
Yutaka Aikawa

Chapter 18 **Switching Properties of Finite-Sized Ferroelectrics 349**
L.-H. Ong and K.-H. Chew

Chapter 19 **Intrinsic Interface Coupling in Ferroelectric Heterostructures and Superlattices 373**
K.-H. Chew, L.-H. Ong and M. Iwata

Chapter 20 **First-Principles Study of ABO_3: Role of the *B*–O Coulomb Repulsions for Ferroelectricity and Piezoelectricity 395**
Kaoru Miura

Chapter 21 ***Ab Initio* Studies of H-Bonded Systems: The Cases of Ferroelectric KH_2PO_4 and Antiferroelectric $NH_4H_2PO_4$ 411**
S. Koval, J. Lasave, R. L. Migoni, J. Kohanoff and N. S. Dalal

Chapter 22 **Temperature Dependence of the Dielectric Constant Calculated Using a Mean Field Model Close to the Smectic A - Isotropic Liquid Transition 437**
H. Yurtseven and E. Kilit

Chapter 23 **Mesoscopic Modeling of Ferroelectric and Multiferroic Systems 449**
Thomas Bose and Steffen Trimper

Chapter 24 **A General Conductivity Expression for Space-Charge-Limited Conduction in Ferroelectrics and Other Solid Dielectrics 467**
Ho-Kei Chan

Part 5 Modeling: Nonlinearities 491

Chapter 25 **Nonlinearity and Scaling Behavior in a Ferroelectric Materials 493**
Abdelowahed Hajjaji, Mohamed Rguiti, Daniel Guyomar, Yahia Boughaleb and Christan Courtois

Chapter 26 **Harmonic Generation in Nanoscale Ferroelectric Films 513**
Jeffrey F. Webb

Chapter 27 **Nonlinear Hysteretic Response of Piezoelectric Ceramics 537**
Amir Sohrabi and Anastasia Muliana

Chapter 28 **Modeling and Numerical Simulation of Ferroelectric Material Behavior Using Hysteresis Operators 561**
Manfred Kaltenbacher and Barbara Kaltenbacher

Preface

Ferroelectricity has been one of the most used and studied phenomena in both scientific and industrial communities. Properties of ferroelectrics materials make them particularly suitable for a wide range of applications, ranging from sensors and actuators to optical or memory devices. Since the discovery of ferroelectricity in Rochelle Salt (which used to be used since 1665) in 1921 by J. Valasek, numerous applications using such an effect have been developed. First employed in large majority in sonars in the middle of the 20th century, ferroelectric materials have been able to be adapted to more and more systems in our daily life (ultrasound or thermal imaging, accelerometers, gyroscopes, filters…), and promising breakthrough applications are still under development (non-volatile memory, optical devices…), making ferroelectrics one of tomorrow's most important materials.

The purpose of this collection is to present an up-to-date view of ferroelectricity and its applications, and is divided into four books:

- *Material Aspects*, describing ways to select and process materials to make them ferroelectric.
- *Physical Effects*, aiming at explaining the underlying mechanisms in ferroelectric materials and effects that arise from their particular properties.
- *Characterization and Modeling*, giving an overview of how to quantify the mechanisms of ferroelectric materials (both in microscopic and macroscopic approaches) and to predict their performance.
- *Applications*, showing breakthrough use of ferroelectrics.

Authors of each chapter have been selected according to their scientific work and their contributions to the community, ensuring high-quality contents.

The present volume aims at exposing characterization methods and their application to assess the performance of ferroelectric materials, as well as presenting innovative approaches for modeling the behavior of such devices.

The book is decomposed into five sections, including structural and microstructural characterization (chapters 1 to 6), electrical characterization (chapters 7 to 11), multiphysic characterization (chapters 12 to 16), phenomenological approaches for modeling the

behavior of ferroelectric materials (chapters 17 to 24), and nonlinear modeling (chapters 25 to 28).

I sincerely hope you will find this book as enjoyable to read as it was to edit, and that it will help your research and/or give new ideas in the wide field of ferroelectric materials.

Finally, I would like to take the opportunity of writing this preface to thank all the authors for their high quality contributions, as well as the InTech publishing team (and especially the publishing process manager, Ms. Silvia Vlase) for their outstanding support.

June 2011

Dr. Mickaël Lallart
INSA Lyon, Villeurbanne
France

Part 1

Characterization: Structural Aspects

1

Structural Studies in Perovskite Ferroelectric Crystals Based on Synchrotron Radiation Analysis Techniques

Jingzhong Xiao[1,2]
[1]*CEMDRX, Department of Physics, University of Coimbra, Coimbra,*
[2]*International Centre for Materials Physics,*
Chinese Academy of Sciences, Shenyang,
[1]*Portugal*
[2]*China*

1. Introduction

Perovskite oxide materials, having the general formula ABO_3, form the backbone of the ferroelectrics industry. These materials have come into widespread use in applications that range in sophistication from medical ultrasound and underwater sonar systems, relatively mundane devices to novel applications in active and passive damping systems for sporting goods and automobiles [1-3]. Recent developments in regard to relaxor-based single crystal piezoelectrics, such as $Pb(Zn_{1/3}Nb_{2/3})O_3$–$PbTiO_3$ (PZNT), $Pb(Fe_{1/2}Nb_{1/2})O_3$–$PbTiO_3$ (PFNT) and $Pb(Mg_{1/3}Nb_{2/3})O_3$–$PbTiO_3$ (PMNT) have shown superior performance compared to the conventional $Pb(Zr,Ti)O_3$ (PZT) ceramics[4, 5]. Particularly, their ultrahigh piezoelectric and electromechanical coupling factors in the <001> direction can reach to d_{33}>2000pC/N and $k_{33}\approx$94%, which have attracted tremendous interests and still make these materials very hot.

However, the origin and structural nature of their ultrahigh performances remains one inquisitive but obscure subject of recent scientific interest.To better understand the structural nature of the outstanding properties, it is very important for investigating the ferroelectric domain structure in these materials. In ferroelectrics, according to the electrical and mechanical compatibility conditions, domain structures of 180° and non-180° will form with respect to crystal symmetry. There is a closely relationship between the domain structure and the crystal symmetry. Through the observation on ferroelectric domain configurations, the crystal structures can be confirmed. Ferroelectric domains are homogenous regions within ferroelectric materials in which polarizations lie along one direction, that influence the piezoelectric and ferroelectric properties of the materials for utilization in memory devices, micro-electromechanical systems, etc. Understanding the role of domain structure on properties relies on microscopy methods that can inspect the domain configuration and reveal the evolution or the dynamic behaviour of domain structure.

It is also well known that the key to solve this issue of exploring the origin of the excellent properties is to reveal the peculiar complex perovskite crystal structures in these materials. Through study in structure behavior under high-pressure and local structure at atomic level will be helpful for better understanding this problem.

2. Synchrotron radiation X-ray structure investigation on ferroelectric crystals

$Pb(Zn_{1/3}Nb_{2/3})O_3$-$PbTiO_3$ (PZNT) and $Pb(Fe_{1/2}Nb_{/1/2})O_3$–$PbTiO_3$ (PFNT) crystal are model ABO_3-type relaxor ferroelectric materials (or ferroelectrics), which demonstrates excellent performance in the filed of dielectrics, piezoelectrics, and electrostriction, etc. To explore the common issues of structural nature and the relationship between structure and performance of ultrahigh-performance in these materials, in this chapter, the novel X-ray analysis techniques based on synchrotron radiation light, such as synchrotron radiation X-Ray topography, high-pressurein situ synchrotron radiation energy dispersive diffraction, and XAFS method, are utilized to investigate the domain configuration, structure and their evolution behavior induced by temperature changes and external field.

2.1 Application of white beam synchrotron radiation X-ray topography for in-situ study of ferroelectric domain structures

Ferroelectric domains can be observed by various imaging techniques such as optical microscopy, scanning electron microscopy (SEM), transmission electron microscopy (TEM), X-ray imaging, and etc. Imaging is normally associated with lenses. Unlike visible light or electrons, however, efficient lenses are not available for hard X-rays, essentially because they interact weakly with matter. Comparatively as an X-ray imaging method, X-ray topography plays a vital role in providing a better understanding of ferroelectric domain structure.[6] X-rays are more penetrating than photons and electrons, and the advent of synchrotron radiation with good collimation, a continuous spectrum (white beam) and high intensity has given X-ray topography additional powers. The diffraction image contrast in X-ray topographs can be accessed from variations in atomic interplanar spacings or interference effects between X-ray and domain boundaries so that domain structure can be directly observed (with a micrometer resolution). Especially, via a white beam synchrotron radiation X-ray diffraction topography technique (WBSRT), one can study the dynamic behaviour of domain structure and phase evolution in ferroelectric crystals respectively induced by the changes of sample temperature, applied electric field, and other parameter changes.
In this chapter, a brief introduction to principles for studying ferroelectric domain structure by X-ray diffraction imaging techniques is provided. The methods and devices for in-situ studying domain evolution by WBSR are delineated. Several experimental results on dynamic behavior of domain structure and induced phase transition in ferroelectric crystals accessed at beam line 4W1A of the Beijing Synchrotron Radiation Laboratory (BSRL) are introduced.

2.1.1 Principle of synchrotron radiation X-ray topography

a. X-ray topography approach

X-ray diffraction topography is an imaging technique based on Bragg diffraction. In the last decades, X-ray diffraction topography to characterize crystals for the microelectronics industry were developed and completely renewed by the modern synchrotron radiation sources. [6]
Its images (topographs) record the intensity profile of a beam of X-rays diffracted by a crystal. A topograph thus represents a two-dimensional spatial intensity mapping of reflected X-rays, i.e. the spatial fine structure of a Bragg spot. This intensity mapping reflects the distribution of scattering power inside the crystal; topographs therefore reveal the

irregularities in a non-ideal crystal lattice. The basic working principle of diffraction topography is as follows: An incident, spatially extended X-ray beam impinges on a sample, as shown in Fig.1. The beam may be either monochromatic, or polychromatic (i.e. be composed of a mixture of wavelengths (white beam topography)). Furthermore, the incident beam may be either parallel, consisting only of rays propagating all along nearly the same direction, or divergent/convergent, containing several more strongly different directions of propagation.

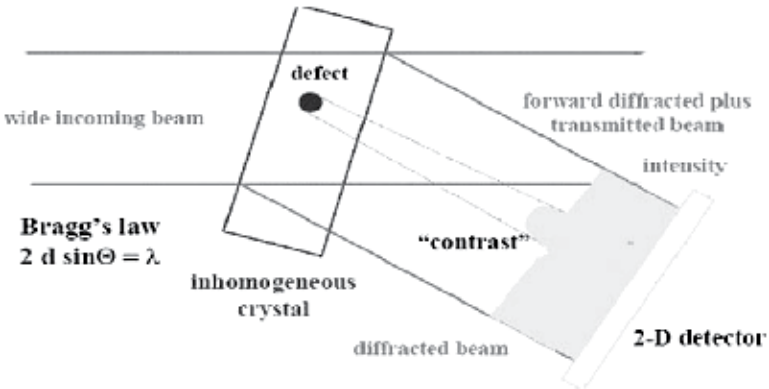

Fig. 1. The scheme of basic principle of diffraction topography.

A homogeneous sample (with a regular crystal lattice) would yield a homogeneous intensity distribution in the topograph (a "flat" image). Intensity modulations (topographic contrast) arise from irregularities in the crystal lattice, originating from various kinds of defects such as cracks, surface scratches, dislocations, grain boundaries, domain walls, etc. Theoretical descriptions of contrast formation in X-ray topography are largely based on the dynamical theory of diffraction. This framework is helpful in the description of many aspects of topographic image formation: entrance of an X-ray wave-field into a crystal, propagation of the wave-field inside the crystal, interaction of wave-field with crystal defects, altering of wave-field propagation by local lattice strains, diffraction, multiple scattering, absorption. Theoretical calculations, and in particular numerical simulations by computer based on this theory, are thus a valuable tool for the interpretation of topographic images. Contrast formation in white beam topography is based on the differences in the X-ray beam intensity diffracted from a distorted region around the defect compared with the intensity diffracted from the perfect crystal region. The image of this distorted region corresponds to an increased intensity (direct image) in the low absorption case.

To conduct a topographic experiment, three groups of instruments are required: an x-ray source, potentially including appropriate x-ray optics; a sample stage with sample manipulator (diffractometer); and a two-dimensionally resolving detector (most often X-ray film or camera). The x-ray beam used for topography is generated by an x-ray source, typically either a laboratory x-ray tube (fixed or rotating) or a synchrotron source. The latter offers advantages due to its higher beam intensity, lower divergence, and its continuous wavelength spectrum. The topography technique combinning with a synchrotron source, is well adapted to in-situ experiments, where the material, in an adequate sample environment device, is imaged while an external parameter (temperature, electrical field, and etc) is changed.

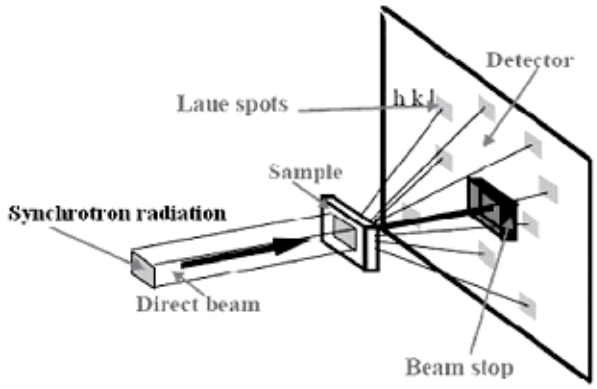

Fig. 2. Experimental arrangement for synchrotron radiation white beam Laue topography.

b. White beam X-ray topography

A simple way to understand the creation of X-ray topographic images is to consider a Laue photograph (Fig. 2). A polychromatic (white) X-ray beam, containing X-ray energies from about 6 keV to 50 keV (X-ray wavelengths from approximately 2 Å to 0.25 Å), impinges on a crystal. [6] The beam is diffracted in many directions, creating Laue spots. The positions of the diffraction spots appear according to the Bragg equation:

$$E = \frac{hc}{2d\sin\theta_B}, \text{ or } \lambda = 2d\sin\theta_B \tag{1}$$

where E is the incident X-ray energy (and λ is the incident wavelength) selected by crystal planes with spacing d, h is Planck's constant, c is the speed of light, and θ_B is the Bragg angle. Each spot contains uniform intensity if the crystal is perfect.

If, however, the crystal is strained, streaks appear instead of spots due to variations in lattice spacing. In fact, each Laue spot contains a spatial distribution of diffracted intensity attributable to the presence of defects in the crystal. This distributed intensity is difficult to see because Laue spots are typically the same size as the X-ray beam pinhole, and the incident X-ray beam is divergent, but each tiny Laue spot is actually an X-ray topograph. At synchrotron radiation facilities, a collimated white X-ray beam can be used to illuminate a sample crystal, and spots with the much larger cross section of the synchrotron X-ray beam are recorded. The resulting data are an array of Laue spots, as shown in Fig. 2, each of which is an X-ray topograph arising from a different set of atomic planes.

c. Ferroelectric domain characterizations

The existence of antiparallel 180° domains is one of the fundamental properties of ferroelectrics and direct observation of these domains is invaluable to the understanding of the polarization reversal mechanism of ferroelectric structures. Among the techniques of visualizing antiparallel domains, conventional x-ray topography is an important and efficient method although its application is limited by the only available characteristic radiations. However, this limitation is easily overcome by the white-beam synchrotron radiation topography (WBSRT). A unique aspect of WBSRT is the opportunity it affords to select out of the continuous spectrum any intended wavelengths to activate strong anomalous scattering. And, with the WBSRT, it is possible for several diffraction images

with anomalous dispersion effect to be activated simultaneously so that the contrast reversal of 180° domains can be directly observed.[7-9] The natural collimation and high intensity of the radiation also make the real-time observation of domain dynamics feasible. As shown in Fig.3, when working with a coherent x-ray beam, and if the phases of the structure factors are different, the 180° ferroelectric domains can be revealed.
Considering the mechanical and electrical compatibility conditions, allowed domains in ferroelectrics are the 180o or non-180o ones with the different planes as the domain walls.[8, 9] The extinction condition for a domain wall is:

$$\Delta P \bullet g = 0 \tag{2}$$

where g is the reciprocal vector of the diffracting plane, $\Delta P = P_1 - P_2$ is the difference of the polarization vectors across the domain wall. Non-180° domain structure is illustrated in Fig.4.

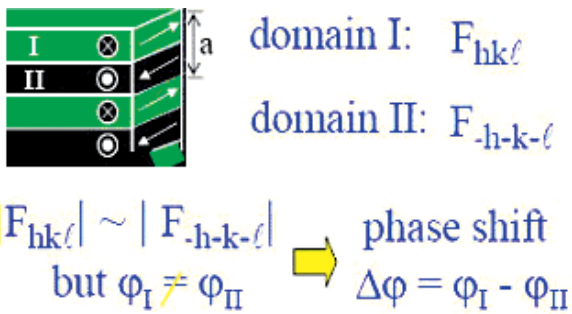

Fig. 3. (Colour on the web only) Scheme of 180° domain.

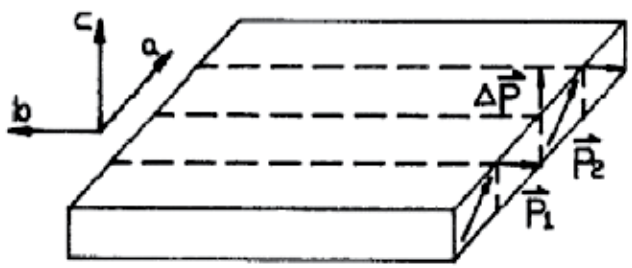

Fig. 4. Scheme of non-180° domain.

2.1.2 In-situ topography measurements

White beam synchrotron radiation topography not only overcomes the drawback of long exposure time for the conventional x-ray topography, but also extends the scope of topography study. The excellent collimation and high intensity of the synchrotron radiation makes the possibility of enlarging the distance between the light source and sample, to improve the image resolution and enlarge the distance between the sample and the detector. These allow ones able to install the samples inside large environmental chambers with changes of temperature, electric field, or other parameters, to carry out the in-situ topography studies. [10]

a. High temperature condition

A high-temperature chamber was used for in situ topography study. The cylindrical furnace in use was made of pure graphite. Two beryllium windows were used for incident and outgoing x-rays. Two thermocouples attached close to the specimen were used to monitor and control the temperature. A digital control power supply can ramp the electric current smoothly when starting to heat. The temperature control system is based on the Eurotherm controller (model 818) and solid state relay (SSR). By using PID control and time proportion method, the temperature stability is about 0.05°C when holding and 0.1°C when ramping. The on-line PC can set and monitor the temperature via RS-232 interface. A sketch of this chamber is shown in Fig. 5.

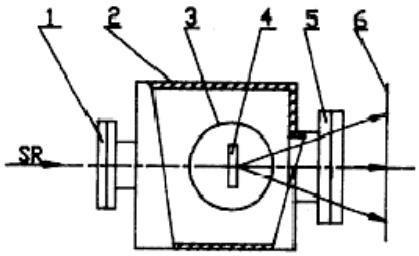

Fig. 5. Sketch of the high temperature sample chamber: 1-entrance Be window; 2-water cooling environment chamber; 3-furnace; 4-specimen; 5-exit Be window; 6-film.

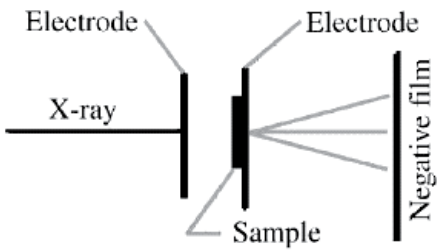

Fig. 6. The experimental arrangement for applying electric field.

b. DC electric field

The change of the ferroelectric domain structure due to the applied DC field can also be observed by white beam synchrotron radiation topography. Fig. 6 is the experimental arrangement of applying the DC field. The distance between the two electrodes was 4 mm and the applied DC voltage ranged from 0 to 4400 V. The samples can be installed on the surface of plastic plates. The DC electrical field can be applied on two Al electrodes covering on the surface of two X-ray transparent organic materials.

2.1.3 In-situ topography study in ferroelectric crystals

The in-situ experiments are performed at Beijing Synchrotron Radiation Facility (BSRF). The x-ray topography station and attached 4W1A beamline are part of the BSRF. The 4W1A is a 45m long white/monochromatic wiggler beamline. When the BEPC is operated at the

energy of 2.2 GeV and the magnetic field of the wiggler at 1.8T. The topography station situated at the end of the beamline 4W1A is mainly used for the study of the perfection of single crystals, high resolution multi-crystal diffraction and x-ray standing wave research. The main equipment of the station consists of a white radiation topography camera, three environmental sample chambers, an x-ray video imaging system and a four crystal monochromatic camera.

The white radiation topography camera and three environmental sample chambers are used for the dynamic topographic experiments with change of temperature, stress, electric field or other parameters. The white radiation camera has five axes to rotate the specimen to any orientation with the incident beam and to rotate the detector to collect the any diffracted beam.

a. Domain and temperature-induced phase transformation in 0.92Pb $(Zn_{1/3}Nb_{2/3})O_3$–0.08$PbTiO_3$ crystals

The aim of this present work is to investigate temperature-dependence phase evolution in 0.92Pb $(Zn_{1/3}Nb_{2/3})O_3$–0.08$PbTiO_3$ (PZN–8% PT) crystals, by employing a real time white-beam synchrotron X-ray radiation topography method (WBSRT). By combining this technique with other complementary structural experiments, a novel picture of low symmetry phase transformation and phase coexistence is suggested.

PZN–8% PT single crystals used in this experiment were grown by the PbO flux method. A plate perpendicular to [001] axis is cut and well polished to approximately 200 μm in thickness. Real time observation is performed at the topography station at the 4W1A beam line of Beijing Synchrotron Radiation Laboratory (BSRL). The storage ring is 2.2 GeV with beam current varied from 50 mA to 90 mA. A cylindrical furnace with coiled heating elements arranged axially around the sample space is used for in situ topography investigation. After carefully mounted the samples on the hot-stage, we heat them at a slow rate of 0.5 ^oC/min, observe and record the dynamic topography images by photo films. Through the topography images obtained by this method, we can clearly observe the ferroelectric domain configurations and their evolution as a function of temperature in PZN–8% PT crystals.[11]

Fig. 7 shows a series of synchrotron radiation topography images with (112) reflection of the (001) crystal plate taken at different temperatures. From Fig. 7 (a) to (i), we find that the domain structures are very complex. They can be categorized into three kinds of domains and addressed as A, B, and C, as shown in Fig. 7 (j).

The A domain walls, which are at approximately 45^o to the [100] axis, can be obviously observed at room temperature. These domain walls are considered to be the 71^o (or 109^o) ones in rhombohedral PZN–PT crystals, and can be clearly observed before heating the sample to 132 ^{o}C. With increasing temperature from 75 ^{o}C to 131 ^{o}C, as shown in Fig. 7 (b)–(c), the B domain laminates become progressively obvious and coexist with the A domains. On the other hand, these domain laminates are along the [010] axis, which can be classified into 90 ^{o} tetragonal domain walls. At the point of 131 ^{o}C, the tetragonal domains become most clear. With heating the sample to above 132 ^{o}C, as shown in Fig. 7 (d), we find that the rhombohedral 71 ^{o} (or 109 ^{o}) domain walls (A laminates) become vague, and the image background becomes brighter than before. However, the tetragonal domain walls are still clear. This phenomenon shows that the phase transition from rhombohedral to tetragonal phase (R–T transition) starts at 75 ^{o}C, and the tetragonal domains grow gradually.

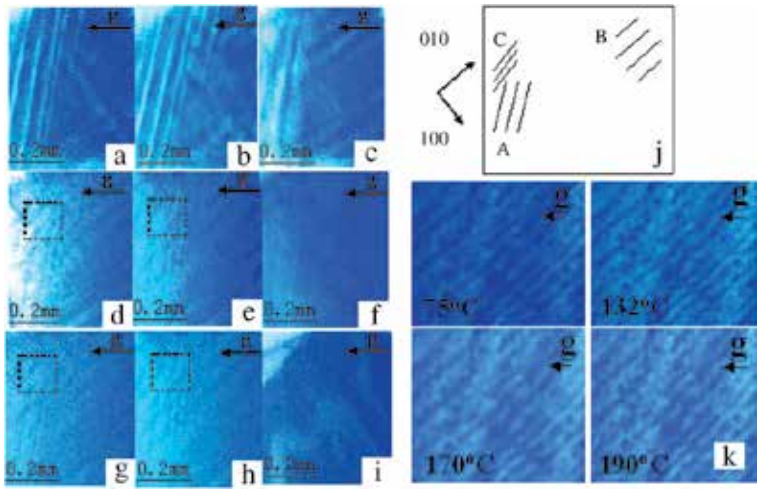

Fig. 7. (Colour on the web only) Images of the in situ synchrotron radiation topography in PZN–8% PT crystals, the x-rays incident direction to the crystal is [001], the diffraction vector is g = (112): (a) room temperature (20 °C); (b) heating to 75 °C; (c) heating to 131 °C; (d) heating to 132 °C; (e) heating to 190 °C; (f) heating to 262 °C; (g) cooling to 190 °C; (h) cooling to 75 °C; (i) cooling to room temperature; (j) Schematic picture for presenting the ferroelectric domain configurations in the topography images of PZN–8% PT crystals; (k) enlarged images of C domain walls from 75 °C to 190 °C.

Most particularly, a set of unique domain walls (C domain walls) appear at this temperature, which is quite different from the A and B domains. This kind of domain walls is shown in Fig.7 (k), through the enlarged images taken from 75 °C to 190 °C. As the figures show, the C domain laminates deviate from the (010) direction at 15 °–20 °. According to the knowledge of domains orientation in crystals with different symmetry and X-ray diffraction extinction relations, as formula (2) shows, these laminates can be considered to be neither rhombohedral nor tetragonal domain structures, but a new monoclinic phase domain structure.

With further heating of the system to about 132 °C, we find this domain structure is very stable and coexists with B tetragonal domains. Upon further heating to above Tc (170 °C), the monoclinic C domain structure also remains. This case shows that a monoclinic phase not only appears in the process of ferroelectric–ferroelectric phase transformation, but also coexists with the cubic phase well above TC . With the temperature elevating to about 262 °C, we find nearly all the ferroelectric domains disappear, as shown in Fig. 7 (f).

Whilst cooling the sample from 262 °C to 75 °C, the monoclinic domains (C laminates), as well as the tetragonal domains (B laminates), are found to reappear, whereas the rhombohedral domains (A laminates) cannot be recovered by cooling to room temperature. During the crystal growth, a rapid cooling process was employed for quick crystallization and to avoid the generation of a pyrochlore phase, which results in a strain field in the crystal. The rhombohedral A domains are expected to be induced by this kind of strain field and preserved at room temperature. Thus A domains do not reappear after the crystals are re-cooled from 260 °C to room temperature with a slow cooling rate, since this cooling process possibly releases the crystal strain field. However, the monoclinic phase was not generated by the strain field induced during the crystal growth, since the particular C domains as well as B domains can be recovered at 75 °C by slow cooling.

Generally, with the sample temperature reaches to the Curie temperature, there occurs a ferroelectric-paraelectric phase transition in conventional ferroelectrics, which results in the disappearance of the domain structure. However in relaxor ferroelectrics, as shown in Fig. 8 the domain structure can be observed clearly on (111) face of PZN-8%PT crystal when the sample temperature is much higher than the Curie temperature. This phenomenon can be induced by the micro-polarization-region in relaxor crystals.
Through in situ synchrotron radiation topography under various temperatures, the complex configuration and dynamic evolution of ferroelectric domains in ferroelectric crystals are obtained. It is expected that the present results will encourage more research interest in exploring the origin of the ultra-high piezoelectric and electrostriction properties in ferroelectrics and other advanced materials.

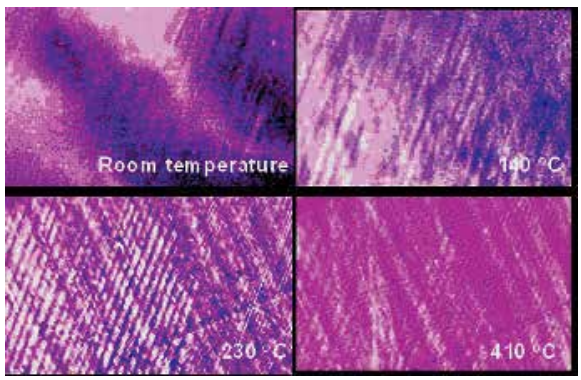

Fig. 8. (Colour on the web only) The temperature induced evolution of the domain structure on (111) face of PZN-8%PT crystal, observed by in situ synchrotron radiation topography.

b. Electrical field induced domain structure

The $Gd_2(MoO_4)_3$ (GMO) crystals were grown by the induction-heated CZ technique. The (0 0 1) crystal pieces of 10 – 15mm diameter were cut and polished into 2.0 or 0.5mm in thickness. The transparent pieces were using to study the DC electric field induced domain structure by transmission X-ray topography at beam line 4W1A of the Beijing Synchrotron Radiation Laboratory (BSRL) The change of the domain structure due to the applied DC field was also observed. Fig. 6 is the experimental arrangement of applying the DC field. The distance between the two electrodes was 4mm and the applied DC field ranged from 0 to 4400 V.

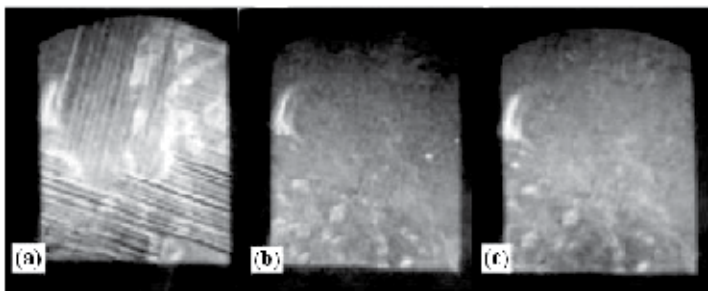

Fig. 9. The domain structure of GMO varies with the applied DC field.

Fig. 9 is a set of series topographs when an applied DC field was added on the GMO crystal piece. Fig. 9 (a) and (b) are the results obtained when the applied voltage was 600 and 700 V, respectively, and the domain structure did disappear. Fig. 9 (c) was the result when the voltage was lowered to zero. From these photographs, we concluded that the multidomain could be transformed to single domain by applying a DC field and that the single domain could be kept even if the applied DC field was taken away. This experimental result shows us that it is possible to make a periodically poled GMO crystal, despite the presence of ferroelectric and ferroelastic domains in the unpoled GMO crystal. From these results, we concluded that the ferroelectric and ferroelastic multidomains could be transformed to a single domain by the applied DC field, and the single domain could be kept even if the applied DC field was taken away.[12]

2.2 High-pressure structural behavior in PZN-PT relaxor ferroelectrics

The ideal structure of ABO_3-type perovskite can be described as a network of corner-linked octahedra, as shown in Fig.10. With *B* cations at the centre of the octahedra and *A* cations in the space (coordination 12) between the AO_{12} and BO_6 polyhedra. As its *B* cation comprised by Zn^{2+}, Nb^{5+}, and Ti^{4+} ions, as well as the *A* cation comprised by Pb^{2+} ion, PZNT deviates from the ideal perovskite by cation displacements or a rotation (or tilting) of BO_6 octahedra. The possible ''off-centering'' of the *B* cations makes the crystal structure more complex than that of the ideal ABO_3-type perovskites and reasonably influence the properties. Previously, approaches towards the understanding of the relaxor ferroelectrics were focused on the structural evolution induced by the changes of chemical composition, electrical field or temperature environment.[13-14] Virtually, these above variables induce phase transitions by mainly playing a role of causing displacement of the cation and anion and rotation of BO_6 octahedra in perovskite.

Nevertheless, directly compressing the materials can also induce similar results that will provide a new ken and approach to investigate the complex structure in the ferroelectrics and other functional materials. It is pointed out that the effect of pressure is a ''cleaner'' variable, since it acts only on interatomic interactions.[15] Compared to other parameters, as an extreme variable, high-pressure is of the unique importance in elucidating ferroelectrics, for the unique structural change is susceptible to pressure. Studying the structural changes and compressive behaviors under high-pressure condition is able to facilitate the understanding for structural nature of the high-performances in relaxor ferroelectrics or other novel functional materials under normal state. Thus, recently, the high-pressure structural investigations in relaxor ferroelectrics had become very popular.[16,17] For instance, Kreisel, et al performed a high-pressure investigation by Ramman spectroscopy of $Pb(Mg_{1/3}Nb_{2/3})O_3$ (PMN), and had obtained the unusual pressure-dependent Ramman relaxor-specific spectra and phase change. By combining the external parameter high pressure with x-ray diffuse scattering method, a pressure-induced suppression of the diffuse scattering in PMN was indicated. Their observed pressure-induced suppression of diffusesed scattering above 5GPa is also a general feature in relaxors at high pressure.[18] In this present work, we performed a high-pressure synchrotron radiation energy-dispersive x-ray diffraction (EDXD) investigation on 0.92PZN-0.08PT ferroelectrics, to study the compressive behavior of the materials under high-pressure condition.

Fig. 10. Illustration of ideal ABO_3-type perovskite structure, which can be described as a network of corner-linked octahedral.

2.2.1 High-pressure synchrotron radiation energy-dispersive x-ray diffraction (EDXD)

The high-pressure X-ray diffraction patterns employed an energy-dispersive method and were recorded on the wiggler beam line (4W2) of the Beijing Synchrotron Radiation Laboratory (BSRL).[19] A WA66B-type diamond anvil cell (DAC) was driven by an accurately adjustable gear-worm-level system. The 0.92PZN-0.08PT powders and pressure calibrating materials (Platinum powder) were loaded into the sample chamber of a T301 stainless steel gasket. A mixture of methanol/ ethanol 4:1 was used as the pressure medium. Pressure was determined from (111), and (220) peaks of Pt along with its respective equation of state. The *d*-values of the specimens can be obtained according to the energy dispersion equation:

$$E \cdot d = \frac{0.619927}{\sin\theta}(keV \cdot nm) \tag{3}$$

The polychromatic X-ray beam was collimated to a 40×30 μm sized spot with the storage ring operating at 2.2 G eV. The diffracted beam was collected between 5 and 35 k eV and the diffraction 2θ angle between the direct beam and the detector was set at about 15.9552 °. The experiment setup is shown in Fig. 11. The pressure-induced crystallographic behavior was studied up to 40.73GPa at room temperature in 22 steps during the pressure-increasing process, and the evolution of high-pressure EDXD patterns is obtained.

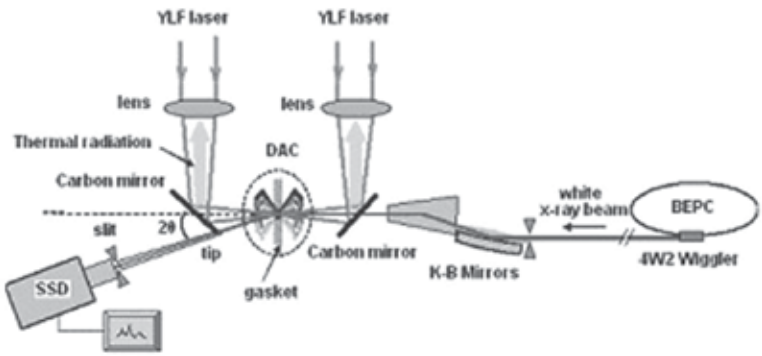

Fig. 11. The setup of high-pressure X-ray energy-dispersive diffraction experiment.

2.2.2 High-pressure compressive behavior in PZNT-PT crystals

Fig.12 shows the selected EDXD patterns of 0.92PZN-0.08PT sample under different pressures, from which the peaks of (110), (111), (200), (210), and (211) indexed in terms of rhombohedral structure can be observed. The strong peaks of (111) and (200) of Pt, whose photonic energy is 19.72keV and 22.77keV respectively, will also be clearly observed. Apart from these diffraction lines, several fluorescence peaks of Pb and Nb are emerged in the low-energy side of the curve.

With increasing pressures from the ambient pressure (0 GPa), the (110) and (200) peak become broader, the intensity of (210) and (211) peaks start to decrease from 5.17GPa. On further increasing pressure, the intensity of (210) and (211) peaks become weaker from 21.34GPa, and the (210) peak vanishes at the pressure of 28.38 G Pa. at about 40.73GPa, these two peaks seem to be vanished. The abrupt changes of the EDXD patterns indicates that the phase transitions can possibly be induced by applying pressures, and the estimated transition pressure point is at about 5.17GPa and 28.38GPa, respectively.

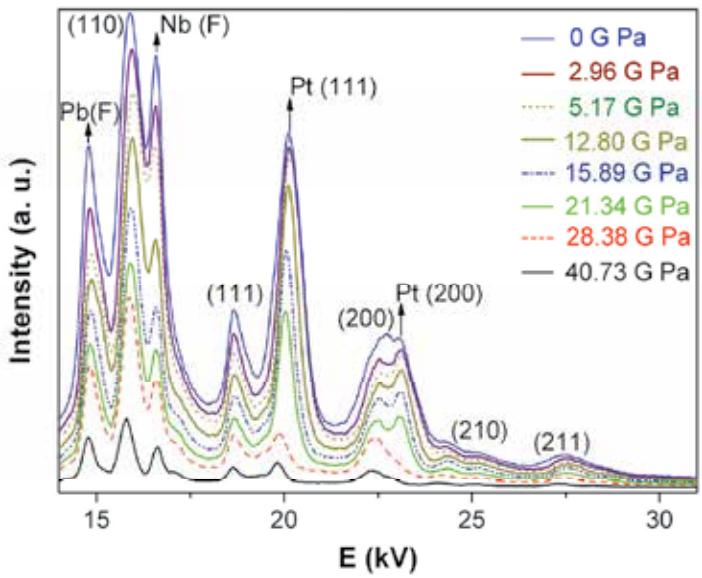

Fig. 12. (Colour on the web only)The EDXD curves of PZNT sample under different pressures, the maximum pressure applied here is 40.73 G Pa. Pb (F) and Nb (F) indicate the fluorescence peaks of Pb and Nb emerged in the low-energy side.

In order to better understand the pressure-induced phase transition and compressive behavior of 0.92PZN-0.08PT, we calculated the structure parameters such as interplanar spacing value (d-value) evolving under various pressures according to experiment results and equation (1), as shown in Fig.13. It is noticed that, as a function of pressure, the d-value decreasing issues of different peaks of (110), (200), and (211) are greatly different, reveals that the compressibility of structural parameters is anisotropic. To investigate the compression behavior of the sample in different pressures, we divided the $d_{(110)}$ vs. pressure curve into several zones. It shows the decreasing rate of $d_{(110)}$ spacing in different pressure zones is different, i.e., the decreasing rate of the zones of *A*, *C*, *E*, and *G* are not identical, which should demonstrate that the change of compressibility is also nonlinear.

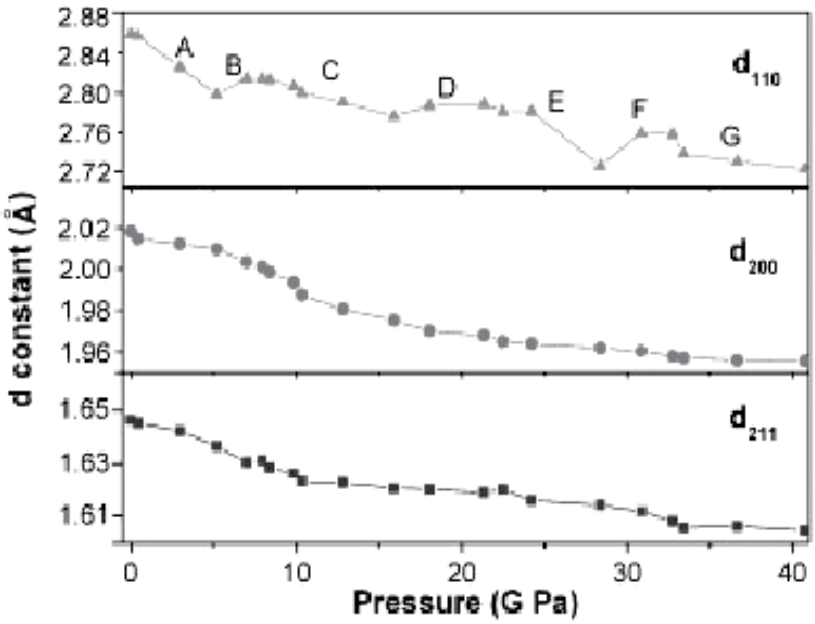

Fig. 13. The curves of d-spacing parameters of different diffraction peaks under various pressures. Top part: $d_{(110)}$ vs. pressure; Middle part: $d_{(200)}$ vs. pressure; and Bottom part: $d_{(211)}$ vs. pressure.

The abrupt changes appeared in *B*, *D*, and *F* zones of the curve, which are corresponding to the three pressure ranges of about 5.17-7.5GPa, 15.2GPa-21.4GPa, and 30.3-34.5GPa, respectively, showing several kinky ranges.[20] We name this phenomenon as "multi-kinky" pressure behavior. This behavior is considered not to be induced by the measurement errors according to the error analysis. Generally, the energy resolution of the detector in EDXD experiment is a key parameter to determine diffraction peak position. In the present experiment, Si (Li) detector is adopted and its energy resolution is estimated to be about 170 e V, from which the measuring error of diffraction peak position may be calculated to be less than 3 eV, corresponding to a relative measuring error of structural parameter of $(\Delta d/d) \approx 10^{-4}$. But for instance, in Fig.13a, the calculated $(\Delta d/d)$ of the (110) face in kinky ranges is estimated to be at the order of 10^{-2}. Therefore, the abnormal change of *d*-spacing under high-pressure should be intimately related to the structural characteristics of ABO_3 compounds. Particularly, in *B* and *D* zones, the $d_{(110)}$ value firstly increases and then decreases with the applied pressures, which seems to show a abnormal compressive behavior. While in *F* zone, the $d_{(110)}$ value decreases with the increased pressure. This behavior can be ascribed to the abruptly changed strain induced by structural transformation from phase *E* to the phase *G*. The *B*, *D*, and *F* zones can also be considered as the areas for phase-coexistence, or transformation regions.[21] The d-spacing vs. pressure curves of (200) and (211) peaks also exhibit multi-kinky changes and nonlinear compressive behavior. Therefore, it is estimated that this multi-kinky behavior is indicative of pressure-induced multi-phase transition and phase coexistence occurs in 0.92PZN-0.08PT crystals. The accurate pressure-induced lattice changes extracted from the high-pressure EDXD experiments will be published elsewhere.

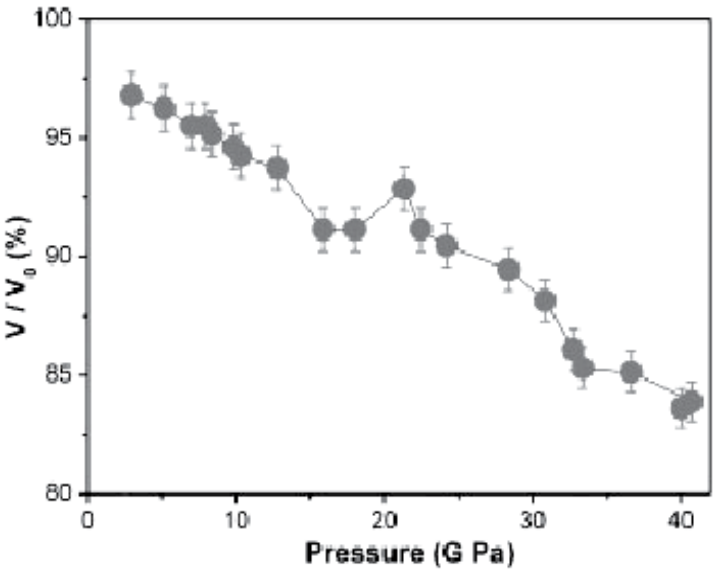

Fig. 14. The curves of the relative volume V/V_0 vs. pressure curve of 0.92PZN-0.08PT sample.

Fig.14 shows the relative volume V/V_0 vs. pressure curve of 0.92PZN-0.08PT, from which can be seen that the volume of the unit cell changes with the increasing pressure. Similar to the curve of $d_{(110)}$ vs. pressure, this curve can also demonstrate interesting multi- kinky compressive behavior. We roughly fit the experimental data to Birch-Murnaghan (BM) equation and get the equation of state (EOS) of 0.92PZN-0.08PT as following:

$$P = \frac{3}{2}B_0\left[\left(\frac{V}{V_0}\right)^{-\frac{7}{3}} - \left(\frac{V}{V_0}\right)^{-\frac{5}{3}}\right] * \left\{1 - \frac{3}{4}\left(4 - B_0^1\right) \times \left[\left(\frac{V}{V_0}\right)^{-\frac{2}{3}} - 1\right]\right\} \quad (4)$$

the bulk modulus B_0 and its first-order derivative B_0^1 for 0.92PZN-0.08PT system are obtained as B_0 = 267±15GPa, B_0^1 = 4.

As shown in Fig.13 and Fig.14, the structure parameters (d and V) display several abrupt changes around several crossover pressures (or during several pressure ranges), which are the suggestive of the anomalous phase transitions and multi-kinky compressive behavior of 0.92PZN-0.08PT crystals under high-pressure condition. It is speculated that this kinky behavior of the structural parameters of 0.92PZN-0.08PT could also be a more general feature in ABO_3-type perovskite oxides. For instance, some similar anomalous behaviors had also been presented in $BaTiO_3$ and $PbTiO_3$.[20] Through the calculations using a first-principles approach based on density-functional theory, an enormous tetragonal strain can be induced in these two simple perovskites by application of a negative hydrostatic pressure. Their structural parameters such as cell volume and atomic displacements were found to display a kinky behavior suggestive of proximity to a phase transition. Comparatively, in the present work, a multi-kinky compressive behavior in 0.92PZN-0.08PT which is more complex than single kinky behavior appeared in $BaTiO_3$ and $PbTiO_3$ was obtained. In a way, the different compressive behavior between 0.92PZN-0.08PT and the

simple peroveskites may be ascribed to the chemical composition variation. The *B* cation of $BaTiO_3$ and $PbTiO_3$ is only comprised by Ti^{4+} ion, while that of 0.92PZN-0.08PT is comprised by Zn^{2+}, Nb^{5+}, and Ti^{4+} ions, which makes the structure of 0.92PZN-0.08PT more complex than that of $BaTiO_3$ and $PbTiO_3$.

The unique nonlinear behavior in 0.92PZN-0.08PT can also be explained in terms of the relative compressibilities of the octahedral (BO_6 polyhedral) and dodecahedral (AO_{12} polyhedral) cation sites in the perovskites structure, or of the compressibilities of the *A*-O and *B*-O bonds, as shown in Fig.10. It is clearly that the relative compressibilities of the AO_{12} and BO_6 sites must play an important role in determining whether the perovskite structure becomes more or less distorted with increasing pressure.[22] From the curves of cell volume or d-spacing Vs pressure, we found that the bulk compressibilities in 0.92PZN-0.08PT varying with applying pressures. Since 0.92PZN-0.08PT is of perovskite structure comprised by AO_{12} and BO_6 polyhedra, we think the evolution of the bulk compressibilities in it can also be ascribed to the relative compressibilities of the AO_{12} and BO_6.

The so-called polyhedral approach is based on the observation that the identification of cation–oxygen polyhedra, M_xO_y, not only simplifies the description of complex crystal structures, but also allows a better understanding of physical properties for materials containing similar polyhedra.[23,24] Considering the influence of the bond length and the anion/cation charge of a given polyhedron on the compressibility, the empirical expression for the compressibility of a given polyhedron were derived:

$$K_{poly} = \frac{4}{3}\frac{d^3}{S^2 Z_0 Z_a} GPa^{-1} \tag{5}$$

Z_a is the anion charge, Z_0 the cation charge, d the bond length in Å and S^2 an ionicity scaling factor equal to 1/2 for oxygen-based polyhedra. The extension of this approach is to assume that the compressibility of complex crystals with linked polyhedra can be derived when κ_{poly} for each polyhedron is known. Based on the consideration of the influence of cation–anion distances and angles between polyhedra (polyhedra tilting), J. Kresiel et al proposed a simple model to deduce the bulk compressibility, κ_{bulk}, from the compressibility of each constituent polyhedron:

$$K_{bulk} = \sum_i x_i \frac{V_i}{V_0} k_i^{poly} \tag{6}$$

where the index i refers to a given type of cation–anion polyhedron and x_i is the concentration on a crystallographic site. V_i and V_0 are the volumes of a given polyhedron and the unit cell, as described by

$$\sum_i \left(x_i \frac{V_i}{V_0} \right) = 1 \tag{7}$$

Since in PZN-PT crystal, the AO_{12} polyhedron is PbO_{12} dodecahedra and the BO_6 polyhedra is comprised by Zn-O group, Nb-O group, and Ti- O group. The equation (6) was modified to estimate the compressive behavior of 0.92PZN-0.08PT as following:

$$K_{PZNT} = \frac{V_{PbO12}}{V_{PZNT}} + x\frac{V_{ZnO6}}{V_{PZNT}} + y\frac{V_{NbO6}}{V_{PZNT}} + z\frac{V_{TiO6}}{V_{PZNT}} \tag{8}$$

where x, y, z implies the concentration of Pb^{2+}, Zn^{2+}, Nb^{5+}, and Ti^{4+} ions, respectively. Due to these cations being chemically very different, it is believed that the compessibilities of these MO_6 polyhedra will be different on applying various pressures, which influence the total compressibilities in 0.92PZN-0.08PT crystals. Therefore, although this high-pressure diffraction technique only allow the determination of the mean bond distance, d, averaged over the entire crystal for each distinct polyhedron, the modified model can be considered as an approach to explain the compressive behavior and the change of compressibilities of 0.92PZN-0.08PT crystal under high-pressure conditions.

Therefore, through the method of high pressure synchrotron radiation energy-dispersive x-ray diffraction, the abnormal compressive behavior in 0.92PZN-0.08PT under high-pressure have been observed, which is considered to be intimately related to the structural characteristics of 0.92PZN-0.08PT crystals. The high-pressure compressive behavior reflects and uncovers abundant structural information under extreme conditions, which is helpful to intrigue significant interests in exploring the structural nature and chemical (or physical) origin of ultrahigh performance in relaxor ferroelecric materials and other functional materials.

2.3 XAFS study in relaxor ferroelectrics

Relaxor ferroelectrics are a class of ferroelectrics that have a diffuse, frequency-dependent permittivity maximum, with a relaxation spectrum much broader than the Debye type. But these features do not provide a direct link to the key structural element that is essential for relaxor ferroelectrics. A common, crucial element in all Pb containing relaxors, Pb(B′, B′′)O3, is a size mismatch between the ferroelectrically active B′′ cations and the ferroelectrically inactive B′ cations. The data of extended X-ray absorption fine structure (EXAFS) based on synchrotron radiation can provide local structural evidence in indicating the structural origin of the anomanous properties in relaxors.

2.3.1 Synchrotron radiation XAFS approach

X-ray absorption fine structure (XAFS) refers to the details of how x-rays are absorbed by an atom at energies near and above the core-level binding energies of that atom, as shown in Fig.15. Specifically, XAFS is the modulation of an atom's x-ray absorption probability due to the chemical and physical state of the atom. XAFS spectra are especially sensitive to the formal oxidation state, coordination chemistry, and the distances, coordination number and species of the atoms immediately surrounding the selected element. Because of this dependence, XAFS provides a practical and simple way to determine the chemical state and local atomic structure for a selected atomic species. XAFS can be used in a variety of systems and bulk physical environment.

X-ray absorption measurements are relatively straightforward, provided one has an intense and energy-tunable source of x-rays, such as a synchrotron radiation source. Many experimental techniques and sample conditions are available for XAFS, including such possibilities as very fast measurements of high spatial resolution. Since the characteristics of synchrotron sources and experimental station dictate what energy ranges, beam sizes, and intensities are available, this often puts practical experimental limits on the XAFS measurements that can be done even if there are few inherent limits on XAFS. The x-ray absorption spectrum is typically divided into two regimes: x-ray absorption near-edge spectroscopy (XANES) and extended x-ray absorption fine-structure spectroscopy (EXAFS).

Though the two have the same physical origin, this distinction is convenient for the interpretation. XANES is strongly sensitive to formal oxidation state and coordination chemistry (e.g., octahedral, tetrahedral coordination) of the absorbing atom, while the EXAFS is used to determine the distances, coordination number, and species of the neighbors of the absorbing atom.

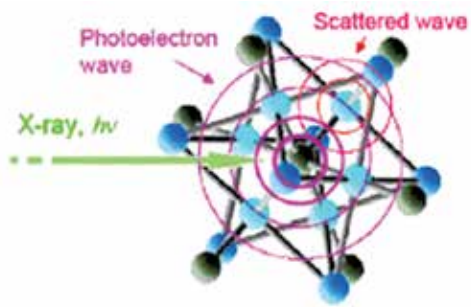

Fig. 15. (Colour on the web only) Illumination of XAFS measurements.

2.3.2 XAFS study in $Pb(Fe_{1/2}Nb_{1/2})_{1-x}Ti_xO_3$ (PFNT) relaxor crystals

Lead iron niobate $Pb(Fe_{1/2}Nb_{1/2})O_3$ (PFN) has been studied of great interest recently because of its multiferroic and relaxor ferroelectric properties. $Pb(Fe_{1/2}Nb_{1/2})_{1-x}Ti_xO_3$ (PFNT) is a modified material which has been also studied extensively in recent years. PFNT undergoes a rhombohedral-tetragonal phase transition with the increase of Ti concentration.[25] Recent study reveals that the morphotropic phase boundary (MPB) is in the range $0.06 < x < 0.08$.[26] The PFNT ceramics (x=0.13) shows a diffuse phase transition at 398 K.[27] The (001)-cut PFNT (x=0.48) single crystal undergoes a tetragonal-cubic phase transition at 518 K, but no Curie temperature was detected below 570 K in the (001)-cut PFNT (x=0.06) crystal.[28,29]

We investigated the dielectric properties of PFNT single crystals below room temperature.[30] The EXAFS results provided a clear picture of the local structure of iron ions in PFNT, and the pre-edge XAFS suggests that the observed dielectric anomaly is induced by the hopping conductivity between Fe^{2+} and Fe^{3+}. we report the low temperature (90~300 K) dielectric properties of the (100)-cut PFNT single crystals. Two dielectric anomaly induced by different mechanisms were observed in the low Ti-doped sample, while only one was detected in the high Ti-doped sample. The mechanism of the dielectric anomalies were discussed based on the microstructures investigated by X ray absorption fine structure (XAFS) results.

High quality PFNT single crystals (x=0.07, named sample A; x=0.48, named sample B) were fabricated without any impure phase. Both samples were cut with surface parallel to (100) plane. Pre-edge and extended x ray absorption fine structure (EXAFS) data were collected at the beamline 13B of Photo Factory, National High Energy Institute of Japan at room temperature. To measure the dielectric properties, aluminium electrodes were evaporated on both sides of the samples.[30]

From activation energy consideration, it seems that the A-site doping can change the activation energy values but the B-site doping can not. Considering the different B-site doping of our two samples, though the crystal structures are very different, they have the close activation energy values.[30] Fig.16 (a) shows the background-subtracted pre-edge XAFS spectra at Fe K-edge for both samples, with tree peaks (named A, B and C).

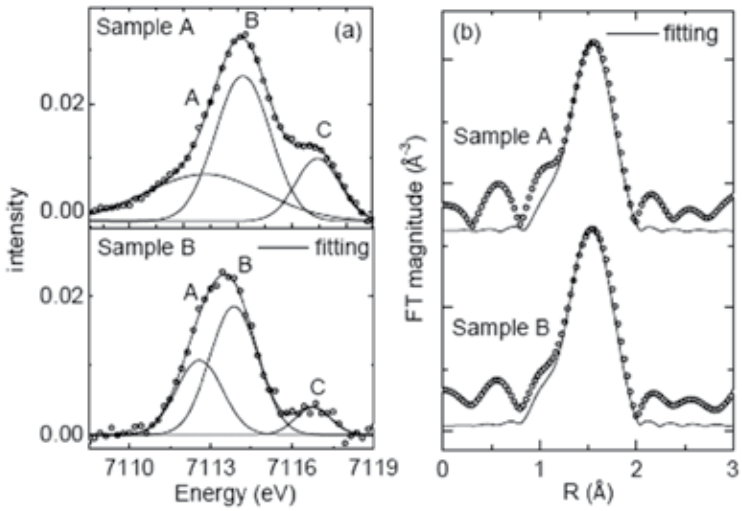

Fig. 16. (a) Pre-edge absorption spectra of Fe K edge, symbols are experiment data, and lines arefitting results by Gaussian function; (b) Fourier transform of Fe K edge (first coordinate shell), symbols are experiment data, and lines are fitting results

The experiment data is fit perfectly using three Gaussian functions. The positions of the three peaks are determined to be 7112.8, 7114.2 and 7116.9 eV for sample A, and 7112.6, 7113.9 and 7116.8 eV for sample B, respectively. All the three peaks of sample B are slightly lower energy shifted than sample A, approximately 0.1~0.3 eV. This might be due to their different crystal structures. Peak B is located around 7114 eV, which is close to the value reported for ferric compounds. The separation between peak A and peak B corresponds to the typical separation of the order of 1.4 eV that has been reported for Fe2+ and Fe3+, therefore, Fe2+ ions exist in our crystals.[30] The pre-edge XAFS suggests that the first anomaly is induced by the hopping conductivity between Fe2+ and Fe3+. The local structure of iron ions is studied by EXAFS at Fe K-edge. Fig.16(b) shows the Fourier transform of the Fe K-edge spectra for both samples. The first coordinate shell (Fe-O) is well separated and analysised, and the structure parameters are listed in Table I.

x	N	R	σ^2 (10^{-3})	E_0	R factor (%)
0.07	5.4±0.2	2.011±0.003	6	-5.5±0.5	1.1
0.48	5.7±0.1	2.007±0.005	6	-8.2±0.8	2.3

Table 1. (Colour on the web only) Parameters of the first coordinate shell of Fe K edge: N is coordinate number, R is the distance of Fe-O, σ 2 is Debye-Waller factor, E0 is energy shift, and R is relative error.

The coordinate number of both samples is smaller than 6, implying that there are oxygen vacancies in our crystals. Moreover, the sample A has a smaller coordinate number than the sample B, indicating the higher oxygen vacancy concentration of sample A than sample B, which can be also confirmed by the impedance spectra (not shown here) that sample A has much smaller resistance than sample B. The distance of Fe-O for both samples is very close.

It is worth noticing that the two samples have the close Debye-Waller (DW) factor value, implying that the local environment of iron ions in sample A is similar to that in sample B. Based on the EXAFS results, we conclude that the B-site doping hardly changes the local structure of iron ions. Thus, the electrons might need the similar energy to overcome the potential barrier to hop between Fe2+ and Fe3+, leading to the close activation energy value. On the other hand, we assume that for the A-site doping, the local structure of iron ions might be distorted significantly, and then results in the different activation energy values.

3. Conclusion

The principles for studying ferroelectric domain structure by white beam synchrotron radiation X-ray diffraction topography (WBSRT)has been introduced, and several results on dynamic behavior of domain structure and phase transition in several ferroelectric crystals induced by temperature and DC electric field had been introduced. Due to its simple principle and accessible setup, WBSRT has become a unique method to characterize ferroelectric materials. WBSRT offers an elegant solution to observe ferroelectric domain structures, to study the dynamic domain behavior and in-situ phase evolution induced by the changes of temperature, electric field, or other parameters, along with other structural study techniques it is possible to give insight into various phenomena occuring in ferroic materials. Through the method of high pressure synchrotron radiation energy-dispersive x-ray diffraction, the abnormal compressive behavior in 0.92PZN-0.08PT under high-pressure have been observed, which is considered to be intimately related to the structural characteristics of 0.92PZN-0.08PT crystals. The high-pressure compressive behavior reflects and uncovers abundant structural information under extreme conditions. The XAFS did a good job to give us a clear picture of the localized state hopping conductivity, and the similar local environment of iron ions is the origin of the close activation energy of the samples. All these will be helpful to intrigue significant interests in exploring the structural nature and chemical (or physical) origin of ultrahigh performance in relaxor ferroelecric materials and other functional materials.

4. Acknowledgment

The support of this work by the National Natural Science Foundation of China (No. 10401004), China Postdoctoral Science Foundation (No. 20040350122), and Portugal FCT project of PTDC/FIS/116146/2009 is grateful acknowledged.

5. References

[1] Eitel. R. E, Novel piezoelectric ceramics:development of high temperature, high performance piezoelectric on the basis of structure, Thesis in Department of Materials Science and Engineering, The Pennsylvania State University, 2003.

[2] Yoshikawa. S, Bogue. A, Degon. B, Commercial Application of Passive and Active piezoelectric Vibration Control, Proceedings of the *11th IEEE International Symposium on Applications of Ferroelectrics*, (eds. E. Colla, D. Damjanovic & N. Setter) Montreux, Switzerland, 1998; 29:3-4.

[3] Jaffe. B, Cook.R, Jaffe. H, *Piezoelectric Ceramics,* Academic Press, New York, (1971).

[4] Park. S. E., Shrout. T.R., J. Appl. Phys., 1997; 82: 1804.

[5] Dong. M., Ye. Z. G, J. Crystal Growth, 2000; 209: 81.
[6] David. R., Gabrielle. G., X-ray topography, NIST Recommended Practice Guide, Special publication 960-10.
[7] Huang. X, Jiang. S, Zeng. W, Hu. X, Feng. D, Appl. Phys. Lett., 1995; 66:2649.
[8] Zhao. J, Yang. P, Jiang. S, Appl. Phys. Lett., 1991; 59:1952.
[9] Cloetens. P, Boller. E, Ludwig. W, Baruchel. J, europhysics news, 2010; March:46.
[10] Jiang. J, Zhao. J, Tian. Y, Instr. and Meth., 1993; 366: 354.
[11] Xiao. J, Zhang. X, Zhu.P, Huang. W, Yuan. Q, Solid State Communication, 2008; 148: 109.
[12] Yuan. Q, Zhao. C, Luo. W, Yin. X, Journal of Crystal Growth, 2001; 233:717.
[13] Fujishiro, K.; Vlokh, R.; Kiat, J.; Dkhil, B.; Yamashita, Y. *Jpn. J. Appl. Phys.* 1998, *37*, 5246-5248.
[14] Xiao, J.; Tian, Y.; Huang, W.; Hang, Y.; Yin, S. *Phys. Lett. A*. 2002, *300*, 456-460.
[15] Paszkowicz, W. *Nuclear Instruments and Method in Physics Research B*.2002, *198*, 142-182.
[16] Kreisel, J.; Bouvier, P.; Naglione, M.; Dkhil, S. A. *Phys. Rev. B*. 2004, *69*, 090104.
[17] Kreisel, J.; Dkhil, B.; Bouvier, P.; Kiat, J. *Phys. Rev. B*. 2002, *65*, 172101.
[18] Janolin, P. E.; Dkhil, B.; Bouvier, P.; Kreisel, J.; Thomas, P. A. *Phys. Rev. B*. 2006, *73*, 094128.
[19] Liu, J.; Li, Y. *Phys.: Condens. Matter*. 2002, *14*, 10505-10509.
[20] Tinite, S.; Rabe, K.; Vanderbilt, D. *Phys. Rev. B*. 2003, *68*, 144105.
[21] Bellaiche, L.; Kunc, K.; Besson, J. *Phys. Re. B*. 1996, *54*, 8945-8959.
[22] Zhao, J.; Ross, N.; Angel, R. *Acta Crystallographica Section B*. 2004, *60*, 263-271.
[23] Hazen, R. *Rev. Mineral*. 1985, *14*, 317-346.
[24] Kreisel, J.; Glazer, A. *J. Phys.: Condens. Matter*. 2000, *12*, 9689-9698.
[25] V.V.S.S. Sai Sunder, and A. M. Umarji, Material Research Bulletin, 30, 427-434, (1995)
[26] S. P. Singh, A. K. Singh, and D. Pandey, J. Phys.: Condense Matter 19, 036217, (2007)
[27] S. P. Singh, A. K. Singh, and D. Pandey, Ferroelectrics, 324, 49 (2005)
[28] C.-S. Tu, C. T. Tseng, R. R. Chien, V. Hugo Schmidt, and C.-M. Hsieh, J Appl. Phys. 104,054106 (2008)
[29] Jie Wang, X. G. Tang, H. L. W. Chan, C. L. Choy, and Haosu Luo, Appl. Phys. Lett. 86, 152907,(2005)
[30] Kui Liu, Xinyi Zhang, Shiqiang Wei, Jingzhong Xiao, Dielectric anomalies induced by different mechanisms in Pb(Fe1/2Nb1/2)1-xTixO3 single crystals, arXiv:0810.1346(October 2008).
[31] Emiel Hensen, Qingjun Zhu, Pang-Hung Liu, Kuei-Jung Chao, and Rutger van Santen, Journal of Catalysis 226, 466–470 (2004)

2

Near-Field Scanning Optical Microscopy Applied to the Study of Ferroelectric Materials

Josep Canet-Ferrer and Juan P. Martínez-Pastor
Institut de Ciència dels Materials de la Universitat de València. I(CM)UV
Spain

1. Introduction

During the last century, the spatial resolution of the optical microscope reached its theoretical limit which is given by diffraction of light and hence close to its wavelength (Abbe, 1882). As a result, several techniques like electron microscopy, tunnel effect or Scanning Probe Microscopy (SPM), were proposed as alternatives to improve spatial resolution. Despite several optical techniques are beating the diffraction limit (Hell & Stelzer, 1992; Harke et al., 2008) in general optical microscopy resolution is considerably limited at the fast growing field of Nanotechnology. In fact, the optimization of electro-optical devices sometimes requires the study of material properties below the nanometre scale. For that purpose, the resolution of the Transmission Electron Microscope (TEM) is the highest one being able to observe the atomic structure (and composition) of a vast number of compounds. The inconveniences of this powerful technique are related with the preparation of the material under study since the sample thickness must be reduced to 100 nm. Alternatively, the Scanning Electron Microscope (SEM) is often used for structural characterization when atomic resolution is not mandatory. The SEM is a valuable tool for imaging metallic or semiconductor samples, but it results less useful for characterizing dielectric materials. For this reason, Atomic Force Microscopy (AFM) could be considered the best option for studying ferroelectric surfaces. Other than morphology, the measurement of physical magnitudes can be also performed by means of the AFM (Asenjo et al., 2006; Cefali et al., 2003; Kwak et al., 2000), which leads to another important advantage with respect to electron microscopes. In fact, most of the experiments previously performed in different fields of Material Science have been revisited at the nanometer scale by means of advanced SPM techniques. Given the great variety of them, in this chapter we focus our attention in the Near-field Optical Scanning Microscope (NSOM), because of during last years it has been revealed as a powerful technique for studying ferroelectric domains and domain walls in a non-invasive way, (Eng & Gutherodt, 2000; Lamela et al., 2007, 2009; Lifante et al., 2008).

The AFM can be considered the simplest but also the most versatile scanning probe instrument, since most of the SPMs are developed on the basis of an AFM, as described in Section 2. The NSOM is one of these rather recent techniques, which allows the microscope user to study optical features and correlate with the topography that is being registered

simultaneously. Thanks to this fact, NSOM has been successfully used to characterize domain walls between inverted poled ferroelectric domains, to define the refractive index profiles of metal diffused channel waveguides or in order to identify solid phases embedded into ferroelectric layers (Canet-Ferrer et al., 2006a, 2006b, 2007, 2008). For a better understanding of the NSOM images, in Section 3 it is proposed a theoretical approach to explain some near-field effects typically observed on ferroelectric materials. Our formalism is based in the angular spectra decomposition of the near-field, which is considered to propagate into an effective dielectric constant media. Thanks to the magnitude of the optical contrast and geometry of the domain walls, using such a simple formalism we can obtain semi-quantitative information of the refractive index profile in ferroelectric materials. In section 4 we will show the experimental NSOM possibilities by means of the characterization of a well known ferroelectric surface: the potassium niobate (KNO). Finally, the experimental results are semi-quantitatively explained by means of the formalism described in section 3.

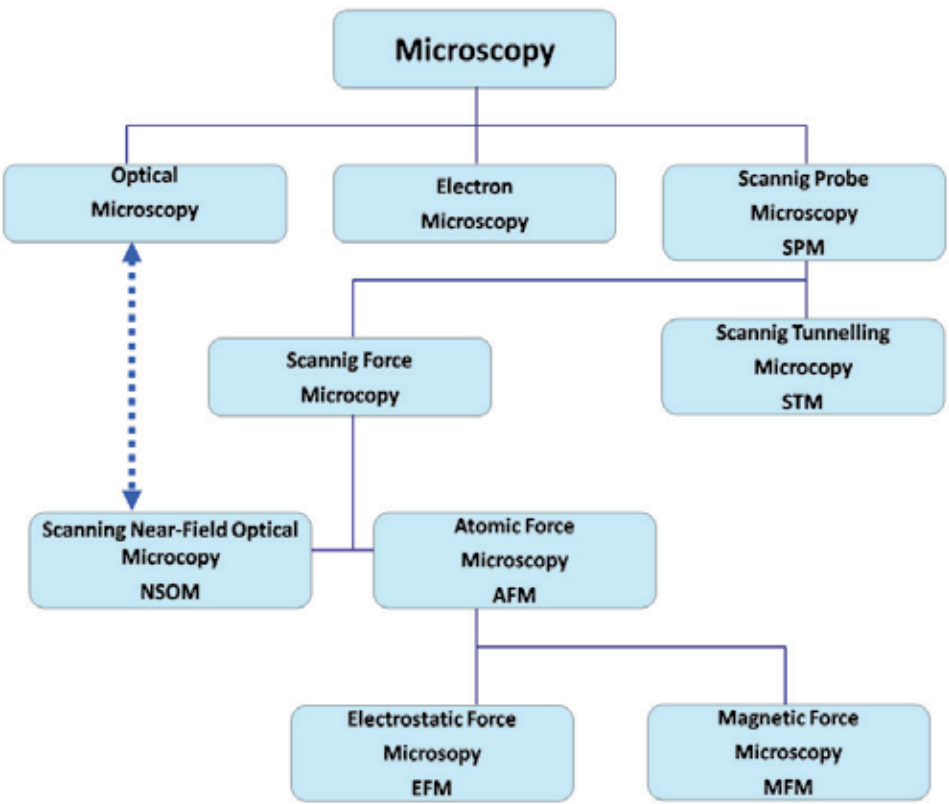

Fig. 1. Summary of the classification of new microscopes. The Scanning Probe Microscopy can be divided in tunnel and force-probe microscopes. The AFM is the most simple of the last ones but it is also the base of a vast number of advanced force microscopy techniques. The NSOM can be considered as a force-probe microscope being the main differences with the AFM related with the feedback system.

2. Experimental details of the AFM

This section consists of a brief introduction to the AFM technique followed by the description of the commercial electronics used by experimental set-up in this work. As a peculiarity, we can mention that the SPM techniques were proposed many years ago, but they could not be developed until the 80s because of such techniques required positioning systems of great precision. Nowadays, thanks to existence of piezoelectric positioners and scanners, the tip-sample distance can be controlled with a precision in the order of the Angstrom. As a result, the AFM resolution is limited by other effects different from relative tip-sample motion precision.

2.1 The AFM

The basis of the AFM is the control of the local interaction between the microscope probe and the material surface. The probe, usually a silicon nano-tip, is located at the end of a micro-cantilever. To obtain images of the sample topography, the distance between the tip and the sample is kept constant by an electric feedback loop. The AFM working principle varies depending on the operation mode. In the case of ferroelectric surfaces the most used method is the "non-contact mode" due to the fact that such mode allows the simultaneous measurement of electrostatic interactions (Eng et al., 1998, 1999). Working in non-contact mode, an external oscillation is induced to the cantilever by means of a mechanical actuator. In our commercial AFM (*Nanotec Electronica S.L.*) a Schäffer-Kirchoff® laser is mounted in the tip holder for monitoring the cantilever motion. The laser beam (<3mW at 659 nm wavelength) is aligned in order to be focused in the cantilever (see Fig. 2a) impinging the reflected light in a four-quadrant photodetector (Fig. 2b). In this way, the cantilever oscillation can be determined by comparison between the signals measured in the four diodes of the detector. If the frequency of the external excitation is close to the resonant frequency of the cantilever (i.e. 14-300 kHz), the oscillation amplitude generates an analogical signal that can be measured using lock-in techniques (synchronous amplification). Far away of the sample surface, the dynamics of the cantilever-tip system can be approached to a forced (driven) harmonic oscillator. But if the probe is located close to the sample (in the range of 10-25 nm), the tip is exposed to the surface interaction and the harmonic oscillator is damped by *van der Waals* forces. Since the damping force is determined by the position of the tip with respect to the sample, the oscillation amplitude also depends on such distance. For this reason, the feedback control maintains the oscillation amplitude in order to keep constant the tip-sample distance during the scan. Therefore, as the feedback correction consists in a displacement of the tip along the Z-axis, the sample roughness is reproduced by the tip motion which is monitored to obtain AFM topography images.

Nowadays, the AFM tip fabrication process has received much attention in order to obtain an enhancement of the microscope resolution, due to the fact that the tip size and shape determine the interaction forces. In addition, the tip can suffer other modifications like cobalt coating for MFM probes or doping for local current measurements. In this sense, several AFM advanced techniques can be performed using the appropriate tip in order to obtain electrostatic or magnetic information of the surface with an important resolution enhancement. We describe below the modifications introduced in our commercial AFM (electronics) for obtaining optical information of the sample surface.

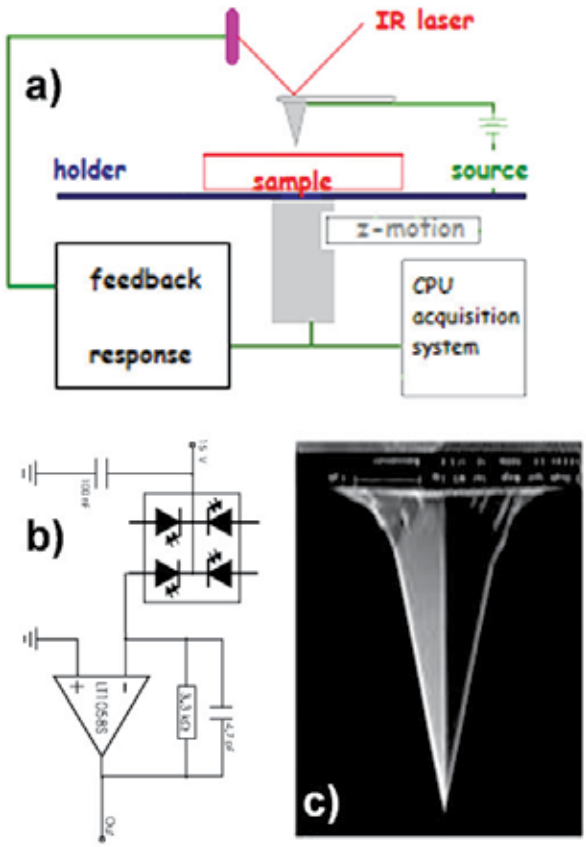

Fig. 2. (a) AFM scheme. (b) four-quadrant photodetector. (c) Standard Silicon probe (PointProbePlus, *Nanosensors*^{TM}).

2.2 The NSOM

The NSOM is a SPM technique whose resolution is limited by the probe parameters and which allows the microscope user to obtain the optical and the topography information simultaneously (Kawata, Ohtsu & Irie, 2000; Paeleser & Moyer, 1996). This fact makes NSOM a valuable tool in the study of materials at the nanometer scale by refractive index contrast, surface backscattering or light collection at local level.

Our NSOM is based on a tuning-fork sensor head, whose setup (Fig. 3a) is similar to that of a commercial AFM working in dynamic mode, but in this case, the standard silicon probe is replaced by a tip shaped optical fibre (Fig. 3b). The probe is mounted on a tuning pitch-fork quartz sensor (AttoNSOM-III from *Attocube Systems AG*), which is driven at one of its mechanical resonances, parallel to the sample surface Fig. 3c. In a similar way than at AFM, this vibration is kept constant by the AFM feedback electronics in order to maintain the tip-sample distance. The tuning fork sensor is controlled with the feedback electronics and data acquisition system used in our commercial AFM (Dulcinea from *Nanotec S.L.*). Simply the AFM tapping motion is substituted by the shear force oscillation of the tuning-fork quartz. Our NSOM is used in illumination configuration under a constant gap mode (Figure 3a) in order to obtain transmission images, by measuring the transmitted light using an extended

silicon photodetector located on the sample holder. For this purpose, the excitation light (laser diode) is delivered through a 2x2 fibre beam splitter using one of the coupler inputs (I1). One of the beam splitter outputs (O1) is connected to the fibre probe while the other output (O2) can be used to control the excitation power. Finally, the light reflected at the sample surface is guided to another photodetector thought the remaining beam splitter input (I2). The electrical signals (reflection and transmission) produced by both photodetectors are coupled to a low noise trans-impedance pre-amplifier and processed by the AFM image acquisition system (i.e. a digital sample processor). Even in previous works, the comparison of transmission and reflection images has been determinant for the understanding of the experimental results; in ferroelectric materials we are going to focus our attention on transmission images exciting the sample with 660nm wavelength.

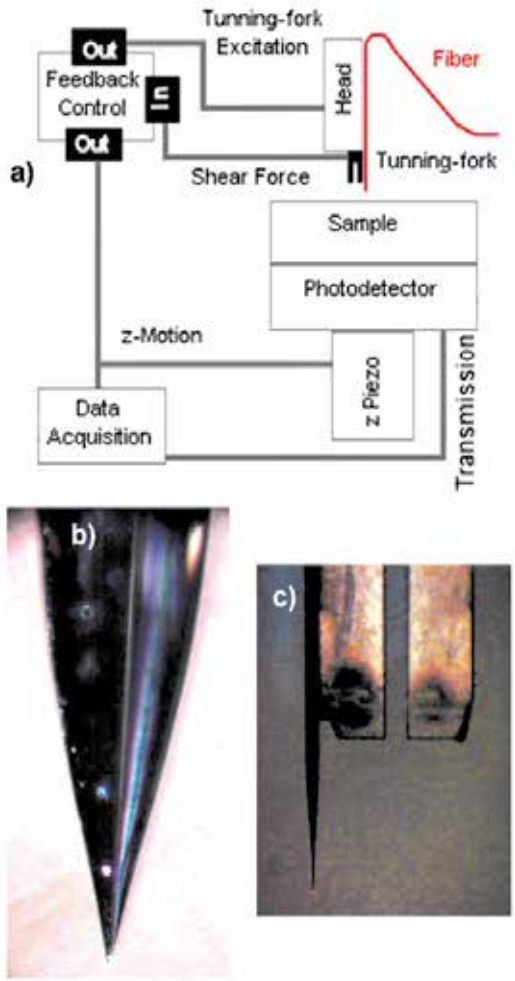

Fig. 3. (a) NSOM illumination scheme, pictured taken from (Canet-Ferrer et al., 2007). (b) NSOM probe prepared in our lab: aluminium coated tip. (c) The NSOM probe mounted on one of the arms of a tuning fork.

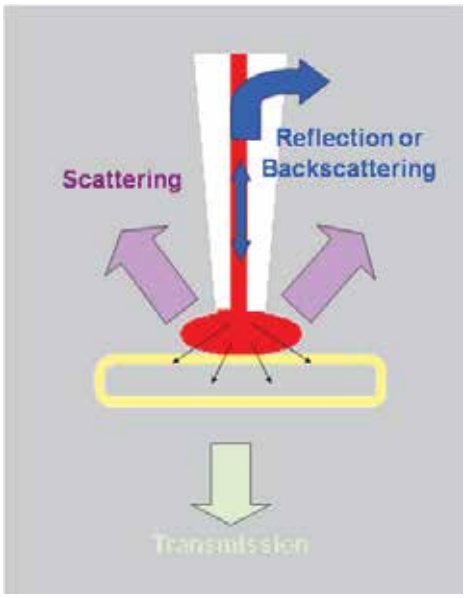

Fig. 4. Different kinds of near-field optical signals. All of them could be measured in illumination configuration.

3 Theoretical approach

3.1 2D model for NSOM optical transmission

Optical images acquired by NSOM can be treated by means of theoretical calculations in order to extract all the information they contain, but unfortunately, there is not a friendly analytical expression to describe transmitted signal under near-field conditions through a sample whose surface usually exhibits a random roughness. In this sense, the task of reproducing a refractive index profile of surface and sub-surface objects from optical transmission contrasts requires a great calculation effort to obtain accurate results. In addition, the surface characteristics of ferroelectric materials present other difficulties to perform quantitative analysis of the optical contrasts since some parameters are not exactly known, as the density of doping atoms, diffusion mechanism or strain maps. Fortunately, sometimes it is enough discriminating the domain structure for achieving valuable information for the optimization of the material applications. In this sense, NSOM transmission images can be easily interpreted if we take the next considerations in a 2D-model: (i) the sample is considered a flat surface composed by two different layers whose thicknesses would depend on the sample characteristics; (ii) an effective refractive index is considered at the upper-layer depending on the tip position (i.e. at each pixel of the image), while the second layer present an homogeneous refractive index; and (iii) the electromagnetic field distribution in the plane of the probe aperture is approached to a Gaussian spatial distribution with a standard deviation $\sigma \sim 80$ nm (i.e., approximately the tip aperture diameter), as illustrated in Fig. 5(a). Taking into account these considerations the light transmission contrasts can be simulated as follows.

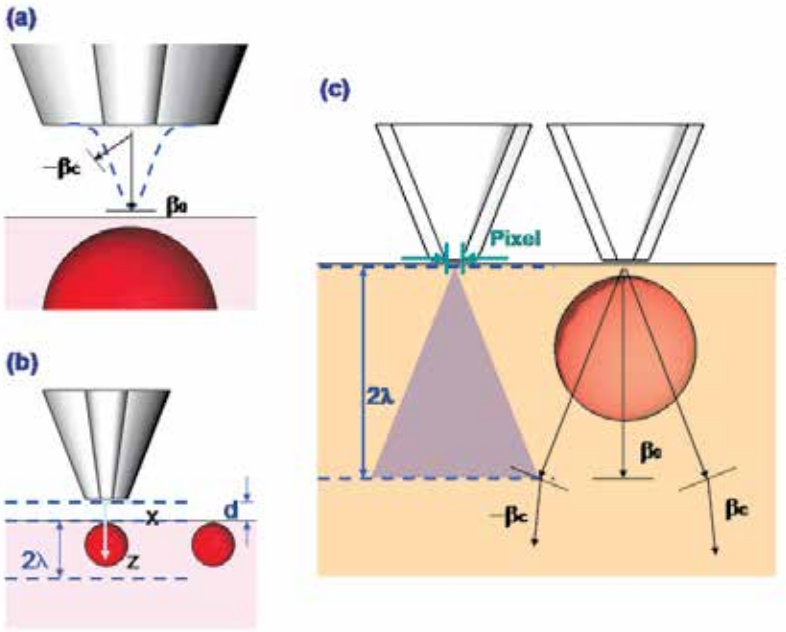

Fig. 5. (a) Near-field probe close to the feedback range. The optical intensity on the aperture plane is approached to a Gaussian field distribution. (b) Scheme of the main interfaces considered in our 2D simulation. Working at constant gap mode the tip is maintained at a distance, d, of a few nanometers. The upper layer is considered as a flat film (2λ thickness) with an average refractive index, $n_{eff}(x, y)$, which depends on the position. Below the channel upper-layer (at a far-field distance), we find the homogeneous media (the pictures are not at a correct scale in all dimensions). (c) 2D representation of the near-field probe (80 nm) in feedback range close to a scatter object larger than the wavelength. The relative position of the propagating light cone and the sphere immersed in the upper layer depends on their optical convolution. Therefore, a different effective refractive index n_{eff} is expected for each pixel of the NSOM tip scan. Figure taken from (Canet-Ferrer et al., 2008).

Firstly, the electromagnetic field distribution coming from the optical probe is decomposed into its angular spectrum.

$$E(x, z=0) = \sum_{\beta=-\pi/2}^{\beta=\pi/2} c^{(\beta)} e^{k_x x} \tag{1}$$

The excitation light is developed into a linear combination of plane-waves simplifying the calculations since the transmission for each component can be treated separately (Nieto-Vesperinas, 2006). Such decomposition consists of a 2D-Fourier transform of the propagating and evanescent plane waves:

$$c^{(\beta)} = \sigma\sqrt{2\pi}\int e^{\frac{-1}{2}\left(\frac{x}{\sigma}\right)^2} e^{-k_x x} dx \tag{2}$$

where k_x is the projection of the wavenumber along the X axis and $\beta = k_z$ is the wavenumber corresponding to the propagation direction, see Fig. 5a. First, the plane-waves propagate in free space from the tip to the sample surface (i.e. a typical air gap of 10 nm under feedback conditions, represented by the distance "d" in Fig. 5b). At this point, reflection at the surface (and later at rest of interfaces) is considered according to condition (i) and beneath it, the plane-wave components propagate through an inhomogeneous medium (the sample upper-layer). As an approach, the light transmission can be calculated by an effective medium approximation (condition ii), due to the variations in the refractive index during the light propagation. The transmission of each plane-wave at the sample surface is determined through the boundary conditions of Maxwell equations between two dielectric media (Hecht E. & Zajac, 1997):

$$T_{eff}^{(\beta)} = [t_{eff}^{(\beta)}]^2 = \left| \frac{E_{eff}^{(\beta)}(x, z = d)}{E_i^{(\beta)}(x, z = d)} \right|^2 \tag{3}$$

Let notice that, if a suitable reference plane is chosen for the angular spectrum decomposition, the transmission for each incident plane wave, $E_i(\beta)$, would correspond to the Fresnel coefficient at the incidence angle

$$\theta_i = \text{Arcsin}(kx / n_{air}\, k_0) \tag{4}$$

which is related with the β-wavenumber by

$$\beta_i^2 = n_{air}\, k_0^2 - k_x^2 \tag{5}$$

while the angle of the transmitted wave can be directly obtained from the Snell's law (Hecht E. & Zajac, 1997)

$$\theta_{eff} = Arc\sin\left[\frac{n_{air}}{n_{eff}} \sin\theta_i \right] \tag{6}$$

Once the light traverses the upper-layer it suffers a second reflection (and refraction) at the interface with the homogeneous refractive index material. Expressions like (3)-(6) can be deduced again to determine the transmission coefficients through the second layer, but, in this case, the incidence angle corresponds to the inclination of waves in the effective media (θ_{eff}),

$$T_{sl}^{(\beta)} = [t_{sl}^{(\beta)}]^2 = \left| \frac{E_{sl}^{(\beta)}(x, z = d + 2\lambda)}{E_{eff}^{(\beta)}(x, z = d + 2\lambda)} \right|^2 \tag{7}$$

Before reaching the photodetector in transmission configuration, the light arrives at the substrate-air interface which introduces a last transmission coefficient:

$$T_{air}^{(\beta)} = [t_{air}^{(\beta)}]^2 = \left| \frac{E_{air}^{(\beta)}(x, z)}{E_{sl}^{(\beta)}(x, z)} \right|^2 \tag{8}$$

Notice that in this interface the plane-waves arriving with an incidence angle larger than the critical one for total internal reflection (θ_{tir}) will not contribute to the optical signal. At the same time, the finite dimensions of the detector must be also taken into account since the numerical aperture (NA) of the photodiode could also introduce another limiting angle. Having both facts into account, it is defined the cut-off wave-number, β_c = NA k_0, like the maximum wave-vector of the propagated light, which is equivalent to a maximum receiving angle θ_c by the relation $\beta_c^2 = n_i\ k_0(1-\sin 2\theta_{cut})$ (Hecht B. et al., 1998), limited by either the detector or total internal reflections. As a result, the expression for the light arriving to the detector can be written as:

$$T = \sum_{-\beta_c}^{\beta_c} T_{air}^{(\beta)} T_{sl}^{(\beta)} T_{eff}^{(\beta)} \left| c^{(\beta)} \right|^2 \tag{9}$$

It is worth noting that during the wave-front propagation the Gaussian beam coming from the NSOM suffer a great divergence. Therefore, if the upper-layer is extended beyond the near-field (e.g., upper-layer up to 2λ thick) the electromagnetic field distribution at the interface with the second layer is considerably extended. In these conditions the second layer can be considered as a homogeneous media with a constant refractive index, satisfying condition (ii). On one hand, the precision estimating the values for the thickness of layers are not critical for the semi-quantitative discussion aimed in this work since such parameter mainly affects the phase of the propagating fields. Nevertheless, it is necessary to point out that the real thickness of each layer must be had into account in certain cases, like in very thin films (thickness << λ) or stratified media (with possible optical resonances) for which multiple reflections are expected to contribute significantly to the transmitted field. In those cases, it is recommended to calculate the transmission coefficients having into account the phase component (Chilwell & Hodgkinson, 1984; Yeh, Yariv & Hong, 1977). On the other hand, samples which consist of a photonic device (like waveguides, beam splitters, optical filters, amplifiers, etc) would requires the decomposition of the sample profile in multiple layers with the aim to distinguish between the different interfaces delimiting the device geometry. For instance, in Ref. (Canet-Ferrer et al., 2008) we simulated the refractive index contrast produced by solid phases present on the surface of a channel waveguide in lithium niobate. In that case, the presence of the waveguide was considered by introducing an additional layer.

3.2 Effective media approach

It is necessary to point out that according to condition (ii) the effective refractive index is going to depend on the upper-layer local composition. Therefore, a different refractive index must be considered at each measuring point (at each pixel of the transmission image). Figure 2(c) illustrates how the local refractive index could be estimated in a general case. It is based on the effective medium theory (EMT), which during last years has been successfully applied to ferroelectric materials (Sherman et al., 2006). The effective dielectric constant ε_{eff} (and therefore the refractive index) for a N-dimensional material (in our case we limit the model to N=2) comprising inclusions of other material with permittivity ε′ and a filling factor p with respect to the host medium (in our case the upper-layer) with a permittivity ε_{up} is given by (Bruggeman, 1935):

$$\varepsilon_{eff} = \frac{1}{2(D-1)}\{(Dp-1)\varepsilon' + (D-1-Dp)\varepsilon_{up} + \sqrt{[(Dp-1)\varepsilon' + (D-1-Dp)\varepsilon_{up}]^2 + 4(D-1)\varepsilon'\varepsilon_{up}}\} \quad (10)$$

At each pixel we consider the area corresponding to the light cone cross-section limited by the detector and, consequently, the filling factor is determined with respect to such area, as indicated in figure 2c (i.e. the isosceles triangle determined by β_c). As a result, the estimation of the refractive index when scanning the surface of the upper layer by the NSOM tip is based on the convolution between the propagating light cone and the objects producing optical contrast. Assuming that both the hidden object and the host matrix are homogeneous, the effective refractive index profile becomes proportional to the spatial convolution along the scan direction of the cone of light and the scatter depicted in Fig. 5c. Therefore the optical contrast can be directly interpreted by means of geometrical considerations (Canet-Ferrer et al., 2008). Unfortunately, dielectric profile usually presents a Gaussian shape at the ferroelectric domain walls and consequently the effective dielectric constant cannot be determined by means of Eq. 10. In that case the refractive index at the upper layer pixels must be evaluated by means of

$$\varepsilon_{eff} = \frac{\int_S \varepsilon(x,z)dxdy}{\int_S dxdy} \quad (11)$$

Where ε(x,z) represents the dielectric constant as a function of the position and S is the surface defined by the light cone. Eq. 11 can be easily evaluated for the scanning situation depicted in Fig. 6. But in this case the index profile is not a bivaluated function; therefore the effective refractive index and the optical contrast would not be directly related by the respective spatial convolution. Having this fact into account, in the next section we are going to propose and alternative way to extract information from transmission images.

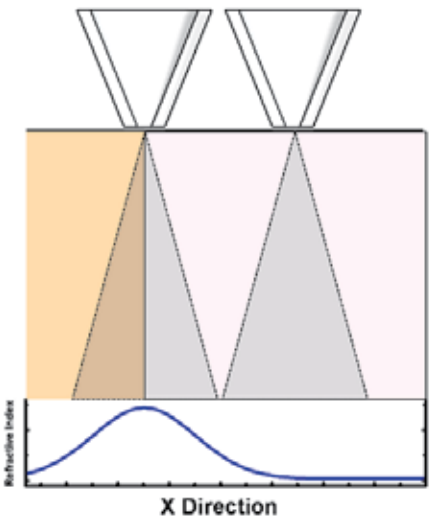

Fig. 6. At the top, it is depicted the NSOM tip in two different points: i) the domain wall and ii) the center of a wide ferroelectic domain. It is also marked the evaluation area as shadowed triangles. At the bottom, the refractive index profile is represented.

4. Characterization of the domain walls in potassium niobate.

In this section we are going to study the refractive index profile induced by ferroelectric domains in a potassium niobate ($KNbO_3$) bulk sample performed by means of NSOM. The potassium niobate $KNbO_3$ (KNO) belongs to the group of perovskite-type ferroelectric materials, like the Barium Titanate. At room temperature, the KNO has an orthorhombic crystal structure with space group Amm_2 and presents natural periodic ferroelectric domains with 180^o spontaneous polarization (Topolov, 2003). Extensive theoretical and experimental studies have been performed on this material since the discovery of its ferroelectricity (Matthias, 1949), due to its outstanding electro-optical, non-linear optical and photorefractive properties (Duan et al., 2001; King-Smith & Vanderbilt, 1994 ; Postnikov et al., 1993; Zonik et al., 1993). In the last decade, the KNO has received much attention due to the relation existing between the piezoelectric properties and the domain structures. However, many of these properties are not well understood at the nanometer scale. From the technological point of view some ferroelectric crystals, as KNO, form natural periodic and quasi-periodic domain structures. The motion of such domain wall plays a key role in the macroscopic response. For this reason, a variety of experimental techniques such as polarizing optical microscopy, anomalous dispersion of X-rays, Atomic Force Microscopy (AFM), Scanning Electron Microscopy (SEM) and Transmission Electron Microscopy (TEM), have been used to study the electrostatic properties of the KNO domains (Bluhm, Schwarz & Wiesendanger, 1998; Luthi et al., 1993; Yang et al., 1999). From the different techniques employed in the domain structure characterization, the Electrostatic Force Microscopy (EFM) and Piezoelectric Force Microscopy (PFM) have been turned into useful practices (Labardi, Likodimos & Allegrini, 2000), since such techniques are based in the electrostatic interaction between the AFM tip and the surface polarization. But unfortunately both methods present important limitations working with bulk materials due the huge external electric field required for inducing the mentioned interaction. As an alternative, the NSOM has been used to demonstrate how the optical characterization of the ferroelectric domains is able to offer useful information even working with bulk materials.

The advantage of our NSOM consists of the possibility of acquiring the images with nanometric resolution, containing the optical information and the topographical features, simultaneously. In the present sample, our probes reached a resolution better than 100 nm on the lateral directions and around 1-3 nm in height (in topography). About the optical images, it can be distinguished two main components contributing to the near-field signal: i) surface scattering and ii) evanescent waves transformed in propagating waves in the presence of a refractive index enhancement (Wang & Siqueiros, 1999). In the first case, the scattering is more important as the light source is closer to the surface; thus scattered waves mainly contain information about the interaction of the tip with the surface roughness. On the other hand, information of the local refractive index (effective refractive index estimated by means of Eq. 11 for the upper layer) is manly contained in the evanescent waves arriving to the detector. Depending on the ratio between both contributions the transmission signal could contain topographical features merged with the optical contrasts (Hecht et al., 1997).

In a previous work the scattering contribution was demonstrated to be considerably reduced by using a visible light source as excitation (Canet-Ferrer et al., 2007). In addition, the topography contribution can be even negligible in KNO due to the huge refractive index

contrast in this material. For example, Fig. 7 shows two NSOM images (topography and transmission) acquired simultaneously. The topography image (Fig. 7a) shows a certain roughness forming elongated structures with a depth of around 5-7 nm (Fig. 7b) that we attribute to the sample polishing process. In contrast, the transmission image (Fig. 7c) is mainly composed by wider optical modulations (Fig. 7d) orientated on a different direction (with respect to surface features), and thus the optical contrasts cannot be correlated with topography details. For a better comparison, the profiles extracted from Figs. 7a and 7c (marked with a grey line) are depicted in Figs. 7b and 7d. It can be changes in the transmitted light larger than 30-35 mV over an average absolute value for the transmission intensity around 2 V. Assuming that the observed optical modulations are produced by the refractive index contrast at the domain walls, the resulting optical contrast would be in the order of predictions and measurements in pervoskite-type materials (Otto et al., 2004; Chaib, Otto & Eng, 2002a; Chaib et al., 2002b).

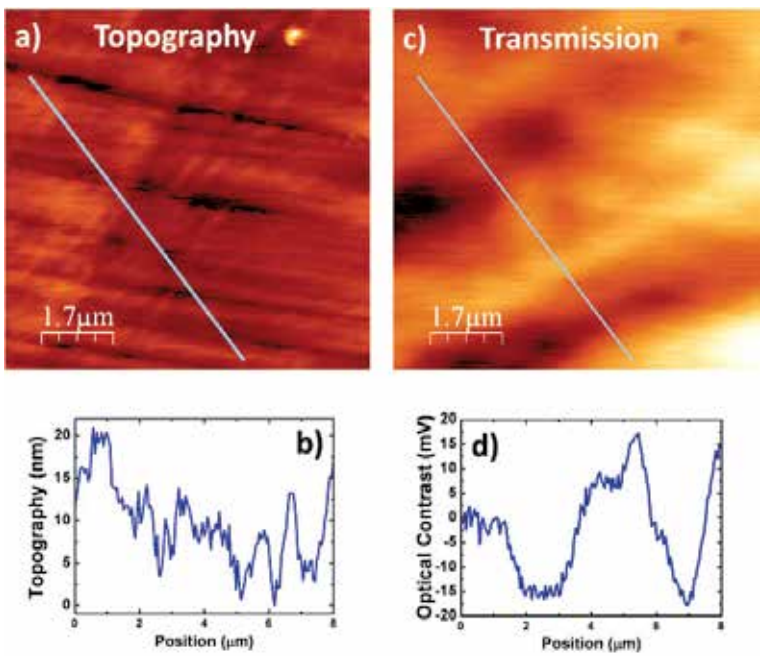

Fig. 7. Topography image (a) and profile along the blue line (b) of a KNO surface. Idem for transmission image in (c) and (d).

The next step consists of deducing a relation between the measured optical contrast and the refractive index. On the one hand, close to the domain wall the effective dielectric constant at the upper-layer is better estimated by means of Eq. 11. On the other hand, the relation between the optical contrast and the effective refractive index is rather complicate. For this reason, it would be more helpful to establish simple relations between the refractive index and the transmission of plane waves composing the Gaussian excitation beam. For example, the optical contrast ($\Delta T^{(0)}$) produced by the normal incidence component ($\beta=0$) as a function of the refractive index change in different points of the upper layer (Δn) can be expressed as follows:

$$\frac{\Delta T^{(0)}}{T^{(0)}} = -\frac{(n-1)}{n+1}\frac{\Delta n}{n} \tag{12}$$

being $T^{(0)}$ the transmittance of the mentioned plane wave and n the refractive index of the material at the point of incidence. However, not all the plane waves in the angle range defined by $[-\beta_c, \beta_c]$ will contribute to the optical contrast with the same intensity. In fact, almost 85% of the electromagnetic field intensity is contained at the low inclination waves, being the normal incidence ($\beta=0$) the main amplitude component. In order to illustrate this fact, in Fig. 8 it is shown the transmittance of a material (with refractive index 2.2 at the second layer) as a function of the upper-layer effective refractive index. The calculation is performed by considering that transmitted light is measured through an extended detector (high NA), which means that β_c is limited by θ_{tir}. Calculated curves stand for the entire Gaussian excitation field (red line) and for only the contribution of normal incidence plane wave (blue line). As above suggested, the transmittance of the electromagnetic field distribution is noticeably influenced by the normal incidence component. It is also worth mentioning that the transmittance change can be approximated by a linear behaviour for relatively small index contrast, being the slope of both curves quite similar in such case. Consequently, even if the approximation of a point-like light source by a planar wave could seem rough, very close values of $(\Delta T/\Delta n)$ are expected in both cases.

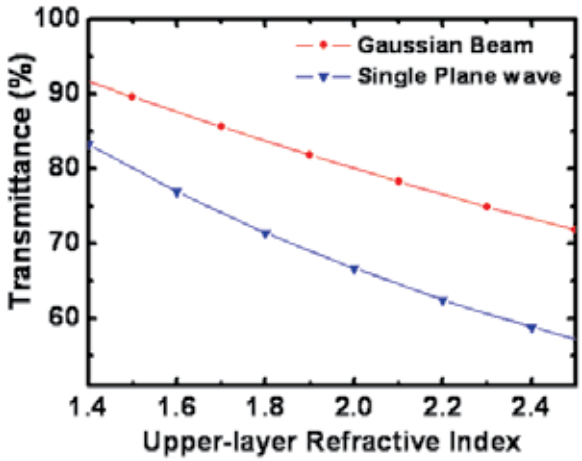

Fig. 8. Transmittance calculated the entire Gaussian beam (red line) and its normal incidence component (blue line) through a two layer sample as a function of the upper-layer effective refractive index. The thickness of each layer is selected according to the real KNO sample dimensions: 2λ for the upper-layer, 1mm for the second layer.

Thanks to this fact, transmission images can be converted into refractive index images by means of a simple expression:

$$\frac{\Delta T}{T} \cong \frac{\Delta T^{(0)}}{T^{(0)}} = -\frac{(n-1)}{n+1}\frac{\Delta n}{n} \tag{13}$$

where now T is the averaged optical signal of a transmission image and ΔT is the experimental optical contrast between two different pixels. The details of the calculation (normalization, numerical aperture effects, tip-sample distances, etc) and its limitations (related with the domain size) are out of the scope of the present work. However, Eq. 13 represents a very simple and semi-quantitative expression to account for local refractive index contrasts in a given material, applicable if the component β=0 dominates the transmittance. As an example, Fig. 9a shows a transmission image acquired under similar conditions to Fig. 7b, but in another zone of the sample. From Fig. 9a we generate the corresponding refractive index image (Fig. 9b) by applying Eq. 13. We can associate optical variations of around 14 mV (with respect to an average background signal of 2V) with refractive index contrasts of around 3% (with respect to the KNO bulk refractive index n_{sl}= 2.2) by comparing a given profile line in both images (Figs. 9c and 9d). Quantitatively, such a contrast is large as compared to reported values in other ferroelectric materials (Canet-Ferrer et al., 2006; Lamela et al., 2009; Han et al., 2009). On the other hand, it is in agreement with respect to the theoretical predictions in Ref. (Chaib et al., 2002b).

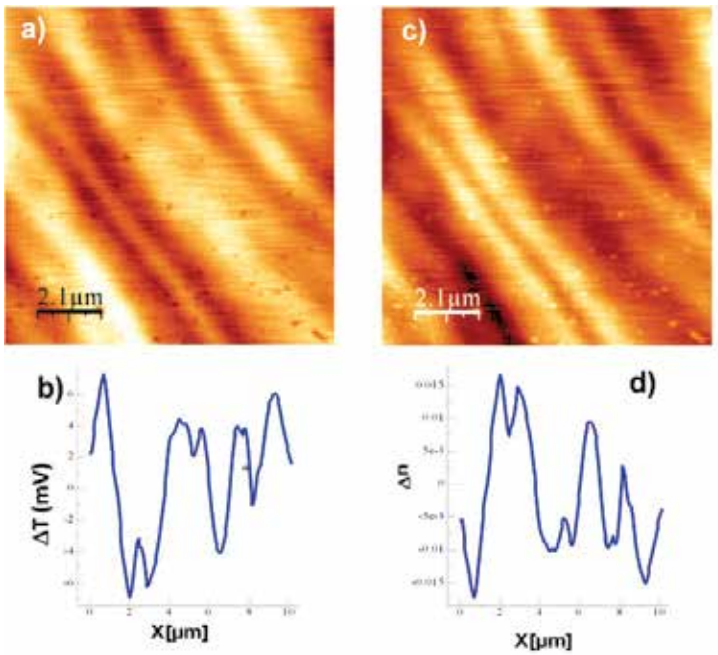

Fig. 9. Transmission (a) and the corresponding refractive index contrast image (c) of the KNO surface. They are accompanied by the corresponding profiles (b) and (d), respectively.

Finally the refractive index images can be used for studying the periodicity and width of the domains by means of averaging the profiles extracted from many images. After comparing several zones of the sample surface, it is observed certain dependence of the optical contrast on the domain width. The results are plotted in Fig. 10a like a scatter cloud where, despite the dispersion in the experimental data, it is observed a clear tendency to increase the refractive index contrast with the size of the domains. A priori this result could seem contradictory, since it is supposed that the larger domains could easily relax the strain at the

interfaces. In fact, Chaib et al. calculated the refractive index contrast for different domain sizes and showing how such contrast become smaller for walls belonging larger domains, contrary to our observations. Consequently we can conclude there is another effect related with the domain size influencing the optical contrast measurement. This effect could be explained attending to the expected refractive index profiles at the domain walls (Fig. 6). For this purpose, the refractive index images have been fitted to Gaussians profiles, one for each domain wall. As a result we can conclude that in our sample the domain walls are not separated enough to observe a fully developed refractive index contrast, as illustrated in Fig. 10b. At the top panel two separated domain walls (red horizontal line) leads to a maximum optical contrast (blue vertical arrow). At the bottom panel of Fig. 10b, the measured contrast (and width) is highly reduced when the domain walls get closer. The optical contrasts are thus underestimated in this case as previously reported (Han et al., 2009).

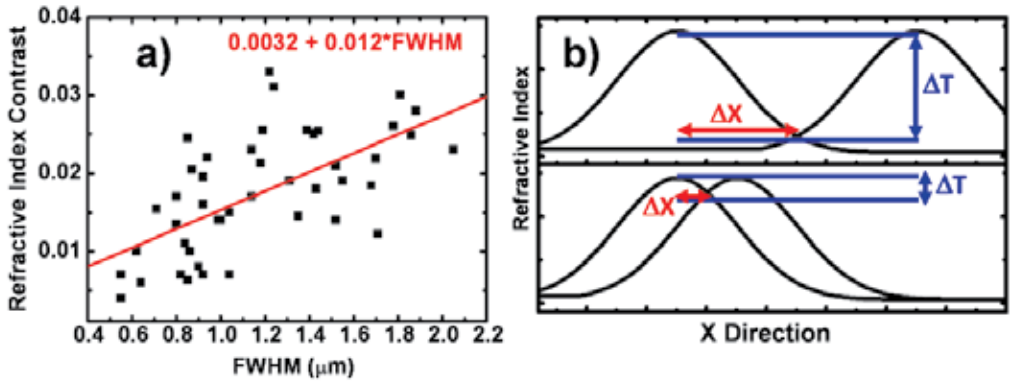

Fig. 10. (a) Optical contrast as a function of the domain size; (b) effect of proximity between the domain walls on the optical contrast.

5. Conclusions

The AFM main properties have been described with the aim to approach the reader to the SPM microscopes. The characteristics of a commercial AFM electronics have been specified since it is the basis of our NSOM. The NSOM illumination configuration has been described in order to study ferroelectric materials. Even if EFM and PFM are the most used techniques to observe electrostatic effects in ferroelectric thin films, NSOM characterization can offer information on the refractive index changes at the domain structure. In the near-field images we observe a clear optical contrast at the domain walls which an average value is around 2% in transmission. These contrasts appear with negligible effect of the topographic features and presenting certain dependence on the separation between domain walls. Thanks to the refractive index contrast images, the average separation between domain walls is found to be around 1.5 μm. Finally, it is worth noting the fact that NSOM imaging provides the possibility of characterizing bulk samples, which are inaccessible by EFM or PFM, without a special preparation of the surface (chemical selective etching, for example), as done to observe periodic domain structures by standard optical microscopy.

6. Acknowledgements

The main author, J. C.-F., thanks the Spanish MCI for his FPI grant BES-2006-12300.

7. References

Abbe E (1882) J. Roy. Micr. Soc. 3 300.

Asenjo A, Jaafar M, Navas D & Vazquez M (2006). *Quantitative magnetic force microscopy analysis of the magnetization process in nanowire arrays.* J. Appl. Phys. 100 023909.

Bluhm H, Schwarz UD & Wiesendanger R, (1998). *Origin of the ferroelectric domain constrast observed in lateral force microscopy.* Phys. Rev. B, 57, 161.

Bruggeman DAG, (1935). "*Berechnung verschiedener physikalischer Konstanten von heterogenen Substanzen*", Ann. Phys. 24 636.

Canet-Ferrer J, Martin-Carron L, Martinez-Pastor J, Valdes JL, (2006). *Scanning probe microscopy applied to the study of domains and domain walls in a ferroelectric $KNbO_3$ crystal.* Bol. Soc. Esp. Ceram y Vidrio, 45, 218.

Canet-Ferrer J, Martin-Carron L, Martinez-Pastor J, Valdes JL, Martínez-Pastor, Carvajal JJ & Diaz F, (2006). *Near-field optical and atomic force microscopy studies of a $RbTiOPO_4$ single crystal with ferroelectric domains.* Bol. Soc. Esp. Ceram y Vidrio, 45, 223.

Canet-Ferrer J, Martin-Carron L, Martinez-Pastor J, Valdes JL, Peña A, Carvajal JJ & Diaz F, (2007). *Scanning prope microscopies applied to the study of the domain wall in a ferroelectric crystal.* J. Microsc. 226, 133.

Canet-Ferrer J, Martinez-Pastor J, Cantelar E, Jaque F, Lamela J, Cussó F & Lifante G (2008). *Near-field scanning optical microscopy to study nanometric structural details of $LiNbO_3$ Zn-diffused channel waveguides,* J. Appl. Phys. 104, 094313.

Cefali E, Patane S, Guciardi PG, Labardi M & Alegrini M (2003). *A versatile multipurpose scanning probe microscope.* J. Microsc. 210 262.

Chaib H, Otto T & Eng LM, *Theoretical study of ferroelectric and optical properties in the 180º ferroelectric domain wall of tetragonal $BaTiO_3$.* Phys. Stat. Sol., 233, 250.

Chaib H, Schlaphof F, Otto T & Eng LM (2002). *Electrical and Optical Properties in 180º Ferroelectric Domain Wall of Tetragonal $KNbO_3$.* Ferroelectrics 291, 143.

Chilwell J &Hodgkinson I, (1984). *Thin-films field transfer matrix-theory of planar multilayer waveguides and reflection from prism-loades waveguides.* J. Opt. Soc. Am. A, 1, 742.

Duan C, Mei WN, Liu J & Hardy JR, (2001). *First-principles study on the optical properties of $KNbO_3$.* J. Phys. : Condens. Matter. 13, 8189.

Eng LM, Guntherodt HJ, Rosenman G Skliar A Oron M, Katz M & Eger D (1998). *Nondestructive imaging and characterization of ferroelectric domains in peridodically poled crystals.* J. Appl. Phys. 83, 5973.

Eng LM (1999). *Nanoscale domain engineering and characterization of ferroelectric domains.* Nanotechnology, 10, 405.

Eng LM & Gutherodt HJ, (2000). *Scanning force microscopy and near-field scanning optical microscopy of ferroelectric and ferroelastic domain walls.* Ferroelectrics, 236 35.

Han TPJ, Jaque F, Lamela J, Jaque D, Lifante G, Cusso F & Kamiskii AA (2009). *Effect of the ferroelectric domain walls in the scanning near field optical microscopy response of*

periodically poled $Ba_2NaNb_5O_{15}$ and $LiNbO_3$ crystals. J. Phys.: Condens. Matter. 21, 042201.

Hecht B, Bielefeldt H, Novotny L, Heinzelmann H & Pohl DW, (1997). *Facts and artefacts in near-field optical microscopy.* J. Appl. Phys. 81, 2492.

Hecht B, Bielefeldt H, Novotny L, Heinzelmann H & Pohl DW, (1998). *Influence of detection optics on near-field optical imaging,* J. Appl. Phys. 84 5873.

Hecht E & Zajac A (1997). *Optics,* ISBN 978-0805385663-5, 3rd ed., Addison Wesley, Reading, M A, Boston.

Hell S & Stelzer E.H.K. (1992). *Properties of a 4Pi confocal fluorescence microscope.* J. Opt. Soc. Am. A, 9 2159.

Harke B, Keller J, Ullal C.K. Westphal V Schoenle & Hell S (2008). *Resolution scaling in STED microscopy.* Optics Express, 16 4154.

Kawata S, Ohtsu M & Irie M (2000). *Nano-Optics,* ISBN 3-540-41829-6, Springer-Verlag. Berlin/Heidelberg.

King-Smith RD & Vanderbilt D, (1994). *First-principles investigation of ferroelectricity in perovskite compounds.* Phys. Rev B, 49, 5828.

Kwak KJ, Hosokawa T, Yamamoto N, Muramatsu H & Fufihira M (2000). *Near-field fluorescence imaging and simultaneous observation of the surface potential.* J. Microsc. 202 413.

Labardi M, Likodimos V, Allegrini M, (2000). *Force-microscopy contrast mechanisms in ferroelectric domain imaging.* Phys. Rev. B, 61, 14390.

Lamela J, Jaque F, Cantelar E, Jaque D, Kaminskii AA & Lifante G, (2007). *BPM simulation of SNOM measurements of waveguide arrays induced by periodically poles BMM crystals.* Optical and quantum electronics, 39 10.

Lamela J, Sanz-Garcia JA, Cantelar E, Lifante G, Cusso F, Jaque F, Canet-Ferrer J & Martinez-Pastor J (2009). *SNOM study of ferroelectric domains in doped $LiNbO_3$ crystals.* Physics Procedia: 2008 Interantional conference on luminescence and optical spectroscopy of condensed matter, 2, 479.

Lifante G. Lamela J, Cantelar E, Jaque D, Cusso F Zhu SN & Jaque F, (2008). *Periodic ferroelectric domain structures characterization by Scanning Near Field Optical Microscopy.* Ferroelectrics, 363 187.

Luthi R, Haefke H, Meyer KP, Meyer E, Howald L & Guntherodt HJ, (1993). *Surface & domain structures of ferroelectric crystals studies with scanning force microscopy*, J. Appl. Phys. 74, 7471.

Matthias BT, (1949). *New ferroelectric crystals*. Phys. Rev., 75, 1771.

Nieto-Vesperinas M, (2006). *Scattering and diffraction in physical optics,* 978-9812563408-7, (2dn ed.)World Scientific, Singapore

Otto T, Grafström S, Chaib H & Eng LM (2004). *Probing the nanoscale electro-optical properties in ferroelectrics.* Appl. Phys. Lett. 84, 1168.

Paeleser MA & Moyer PJ. (1996). *Near-field optics : Theory, instrumentation and applications,* ISBN 978-0471043119, (1st Ed) John Wiley&Sons inc., USA.

Postnikov AV, Neumann T, Borstel G & Methfessel M, (1993). *Ferroelectric structure of $KNbO_3$ and $KTaO_3$ from first-principles calculations.* Phys. Rev. B, 48, 5910.

Sherman VO, Tagantsev AK, Setter N, Iddles D & Price T, (2006). *Ferroelectric-dielectric tunable composites,* J. Appl. Phys. 99 074104.

Topolov VY, (2003). *Domain wall displacements and piezoelectric activity of $KNbO_3$ single crystals.* J. Phys. : Condens. Matter., 15, 561.

Wang S, Siqueiros JM, (1999). *Influence of the sample-probe coupling on the resolution of transmitted rear-field optical image.* Opt. Lasers Eng. 31, 517.

Yang TJ, Gopalan V, Swart PJ & Mohideen U, (1998). *Direct observation of pinning and bowing of a single ferroelectric domains wall.* Phys. Rev. Lett., 82, 4106.

Yeh P, Yariv A & Hong CS, (1977). *Electromagnetic propagation in periodic stratified media. I. General Theory.* J. Opt. Soc. Am., 67, 423.

Zgonik M, Schlesser R, Biaggio I, Voit E, Tscherry J & Gunter P, (1993). *Materials constants of $KNbO_3$ relevant for electro-and-acousto-optics.* J. Appl. Phys., 74, 1287.

3

Internal Dynamics of the Ferroelectric $(C_3N_2H_5)_5Bi_2Cl_{11}$ Studied by ^1H NMR and IINS Methods

Krystyna Hołderna-Natkaniec[1],
Ryszard Jakubas[2] and Ireneusz Natkaniec[3,1]
[1]*Department of Physics Adam Mickiewicz University, Poznań,*
[2]*Faculty of Chemistry, University of Wroclaw, Wroclaw,*
[3]*Joint Institute for Nuclear Research, Dubna,*
[1,2]*Poland*
[3]*Russian Federation*

1. Intoduction

Ferroelectric properties of materials of the general formula $R_aM_bX_{(3b+a)}$ (R-organic cation, M=Sb, Bi, X=Cl, Br, I) have been studied during the last twenty years (Gagor, 2011; Sobczyk, 1997; Piecha, 2005; Jakubas, 2005). The family of halogenobismuthates (III) and halogenoantimonates (III) is characterized by a rich diversity of the anionic forms. It has been shown that ferroelectricity is restricted to compounds characterized by two types of the anionic substructure: two-dimensional anionic layers $(M_2X_9^{3-})_\infty$ and discrete bioctahedral units $Bi_2X_{11}^{5-}$. Especially, the latter type compounds evoke much interest because all connections crystallizing with the $R_5M_2X_{11}$ composition, reported to date, were found to exhibit ferroelectric properties. Within this subclass there are known three imidazolium ferroelectrics which appeared to be isomorphous in their paraelectric phase.
One of these compounds, namely imidazolium undecachlorodibismuthate III of chemical formula $(C_3N_2H_5)_5Bi_2Cl_{11}$ (abbreviated as ICB) undergoes the following sequence of phase transitions (Sobczyk, 1997; Piecha, 2005; Jakubas, 2005) :

$$P\bar{4}n2 \xrightarrow{360K} P2_1/n \ (\text{I}\rightarrow\text{II}),\ P2_1/n \xrightarrow{166K} P2_1 \ (\text{II}\rightarrow\text{III}).$$

Phase III exhibits the ferroelectric properties. The $Bi_2Cl_{11}^{-5}$ anion consists of two octahedrons joined by their top ligands with the bridging chlorine atom Cl(5) placed at the inversion centre. In the paraelectric phase two of five cations are ordered. The remaining three cations (nonequivalent) are disordered being distributed over two positions (two –site model). In the ferroelectric phase these cations become more and more ordered with decreasing of temperature and below 100 K they are fully ordered.
The aim of our study was to check if the distortion of the crystal structure taking place through the ferroelectric-paraelectric phase transition in $[(C_3N_2H_5)_5Bi_2Cl_{11}]$ is accompanied by a change in a molecular dynamics of the imidazolium cation. The methods suitable for this purpose were the inelastic incoherent neutron scattering and ^1H NMR.

In the inelastic incoherent neutron scattering (IINS) spectra the intensity of selected bands depends on the number of scattering centres, amplitude of vibrations of atoms and cross-section for neutron scattering. The cross-section for neutron scattering on protons σ^{inc} is 82 barn and brings a dominant effect, while σ^{inc} for C, N, Bi and Cl nuclei is 5.5, 11.5, 9.1, 21.8 barns, respectively. Therefore the vibration modes induced by motion of hydrogen atoms give intense bands in the IINS spectrum. Consequently, the IINS spectroscopy is a nice tool to observe dynamics of protons (Lovesey,1984; Dianoux, 2003). To discuss the internal dynamics of protons of imidazolium the ^{1}H NMR study was undertaken. The analysis of ^{1}H NMR absorption signal by the continuous wave method gives insight into the slow internal motions of frequencies of several kHz [Abragam,1961].

2. Experiment

Inelastic incoherent neutron scattering measurements (IINS) for $(C_3H_5N_2)_5Bi_2Cl_{11}$ were performed using the inverted geometry spectrometer NERA at the high flux pulsed reactor IBR-2, JINR in Dubna, Russia (flnp.jinr.ru/134; Natkaniec,1994). The upper limit of energy transfer in the spectra analysed was set at 1700 cm^{-1} (~211 meV), because according to the scattering low, the band intensity and the spectrometer resolving power decrease with increasing energy transfer (Lovesey, 1984). The IINS spectra were recorded at several temperatures on heating the sample in the range from 20 K to 300 K ($\Delta T = \pm 1$ deg). They were detected by 15 crystalline detectors arranged to collect scattering at different angles from the range 20 - 160°, at every 10°, and recorded for the incident neutrons wavelengths ranging from 0.1 to 7Å. Final spectra were obtained by summation of those taken at different angles, normalization to the monitor count and subtraction of the background from sample holder and the cryostat. Then, the averaging over the whole Brillouin zone was performed. The density of states function $G_{cal}(\nu)$ was calculated according to the following formula for double differential scattering cross-section σ of neutrons on protons in the sample (Lovesey,1984):

$$\frac{d^2\sigma}{d\Omega dE} = \frac{\overrightarrow{k_F}}{\overrightarrow{k_I}} \sum_p b_{inc,p}^2 \frac{\exp\left(-2W_p\left(\vec{Q},\nu\right)\right)}{\left(1\text{-}\exp\left(-\frac{h\nu}{2k_BT}\right)\right)} \times G(\upsilon) \tag{1}$$

where k_F and k_I are the wave vectors of incident and scattered neutrons, respectively, b_{inc} - the incoherent scattering length, $\exp(-2W_p(Q,\upsilon))$ is the Debye-Waller factor. The neutron momentum transfer vector $Q = k_F - k_I$ scans many Brillouin zones in the sample studied. The effect of neutron scattering on protons was dominant (Lovesey,1984; Dianoux, 2003).

The density functional theory calculations were performed for the following reference systems: isolated resonance hybrid of imidazole (Im), isolated imidazolium cation $(Im)^+$ with the Becke-style hybrid B3LYP functional (Becke's three-parameter exchange correlation functional in combination with the Lee-Yang-Parr functional) (Becke, 1988, 1992, 1993; Lee, 1988), while the calculations for a cluster $(Im)^+Cl^-$ and $BiCl_3(IMD)_3^+$ were performed with B3LYP functional with the LanL2Dz basis set [Zhanpelsov, 1998; Niclasc, 1995) both using the Gaussian'03 program (Frish, 2003). The output (without scaling) was used to calculate the IINS spectra with the programme a-Climax (Ramirez-Cuesta, 2004)

which was used for modelling of the neutron scattering function S(Q, ν) at a TOSCA spectrometer. The intensities in the spectrum of single phonon neutron scattering calculated by the a-CLIMAX are expressed as the δ function. Then, taking into regard the different geometry of TOSCA (www.isis.stfc.ac.uk) and NERA [flnp.jinr.ru/134; Natkaniec, 1993) spectrometers, the phonon densities of the state function $G_{cal}(\nu)$ were calculated at the Γ point approximation. To enable a comparison of the quantum chemical calculations with the experimental data, the δ function of the phonon density of states (frequency and intensity of the subsequent bands) was convoluted with the spectrometer resolving power using the program RESOL (Kazimirov, 2003). In the IINS vibrational spectra the optical selection rules are not valid and all transitions were observed. This property of the IINS spectra permits testing internal structure by the calculations of the normal modes in the low frequency vibrational spectra.
The QC calculations were performed also by the semi-empirical PM3 method [Steward, 1989; 1991, 2004; Khavryutchenko, 1990) for the same systems. This method is reliable for organic chemistry and nitro-compounds. It is attractive for the computation of vibrational mode wavenumbers because of its low computational cost.
The ^1H NMR measurements were carried out on a powdered sample of ICB on a lab-made spectrometer operating in the double modulation system at a frequency of 22.6 MHz varying in the range up to 200 kHz, at permanent magnetic field (F^{19} NMR stabilization) in the temperature range from 140 to 380 K.

3. Results

Fig.1 presents the scattering intensity I(λ) versus incoming neutron wavelength in ICB at 20, 90, 140, 180 and 294 K. The spectrum recorded at 20 K, in the range of the incident neutron wavelengths from 0.5 to 1.3 Å, shows the bands assigned to internal vibrations well separated from the branch of lattice vibrations appearing in the range from 1.3 to 3.8 Å. The presence of the lattice vibration bands at 2.2, 2.6, 2.75, 3.34 Å suggests ordering of the crystal structure at low temperatures. On heating, above the phase transition at 166 K, the bands of $G_{exp}(\nu)$ spectra get broadened. The branch of the lattice vibrations is separated from the internal vibration modes up to room temperature. The intensity of the peak corresponding to the elastic neutron scattering occurring at the incident neutron wavelength of 4.5 Å decreases on heating the sample.
No contribution of the quasi-elastic neutron scattering QENS to the IINS spectrum of ICB was observed within the FWMH of the elastic line of 5.6 cm^{-1}, in the range from 20 to 294 K, so the frequencies of stochastic motions of protons were different than 10^{-12} Hz. The IINS spectra were converted into the amplitude-weighted spectrum of the phonon density of states, $G_{exp}(\nu)$, presented in Fig. 2. The phonon density of state spectra $G_{exp}(\nu)$ calculated in the single-phonon scattering approximation show bands of different widths at different temperatures. From the form of the low temperature lattice branch of the $G_{exp}(\nu)$ analysed at low energy transfer, one may conclude on the ordering or disordering of the structure.
The $G_{exp}(\nu)$ spectrum of the crystal under study recorded at 20 K shows strong bands of normal internal vibrations at the energy transfer of 628, 765, 817, 877, 974 , 1115, 1204 cm^{-1}. On heating this band gets broadened and its intensity decreases. The $G_{exp}(\nu)$ spectra taken at 140 K and 180 K show intensive bands at 635, 758, 810, 852, 928, 1027 cm^{-1} and 675, 795, 870, 912, 954, 1001, 1051, 1147 cm^{-1}, respectively. The broadening of the bands significantly

increases above 90 K. At room temperature the spectrum gets smeared, but the energy gap between the branch of the lattice modes and that of internal vibrations is well seen.

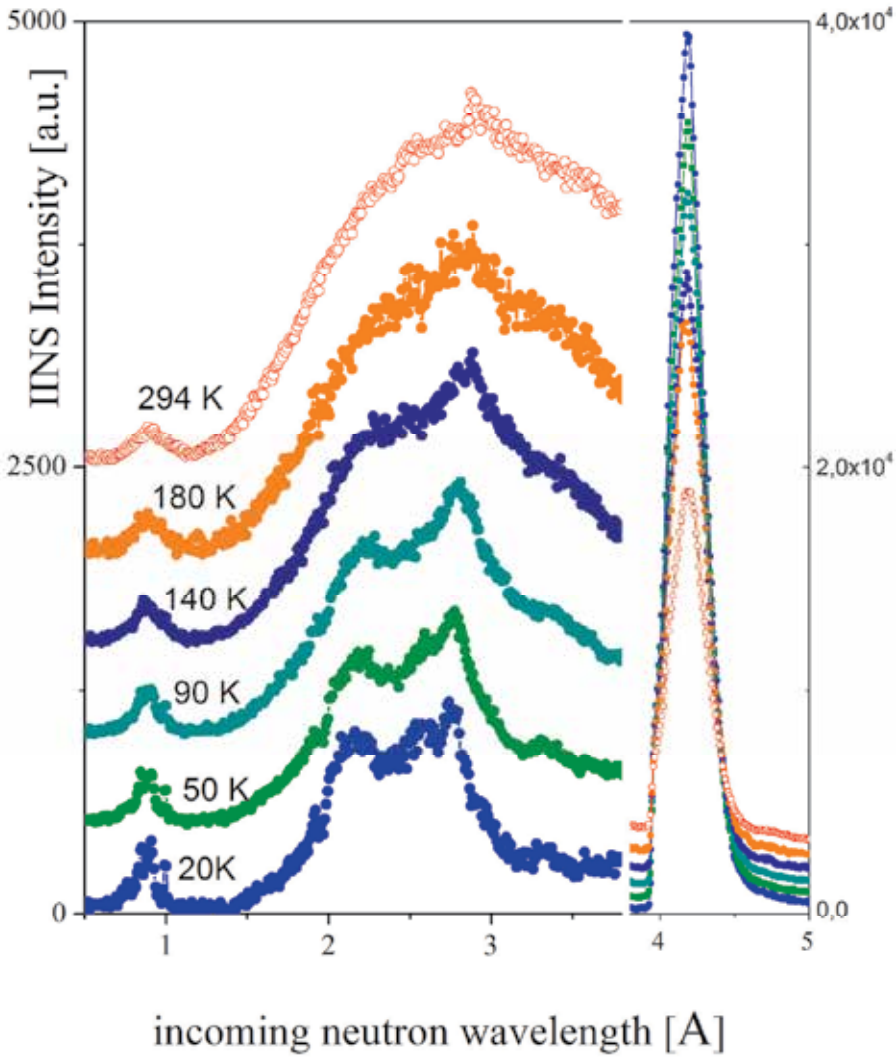

Fig. 1. The scattering intensity of the IINS spectra of imidazolium undecachlorodibismuthate (III) *versus* incoming neutron wave lengths measured at different temperatures (Holderna-Natkaniec, 2008).

The low frequency region of the experimental G(ν) (up to 30 cm^{-1}) can be described by the square function of the energy transfer, as shown in Fig. 2a. This indicates the Debye-like behaviour of the G(ν) function and ordering of the system. At room temperature a linear character of the low frequency dependence G(ν) was observed (Fig.2b), the crystal structure of the compound under investigations is partially disordered (cationic sublayer).

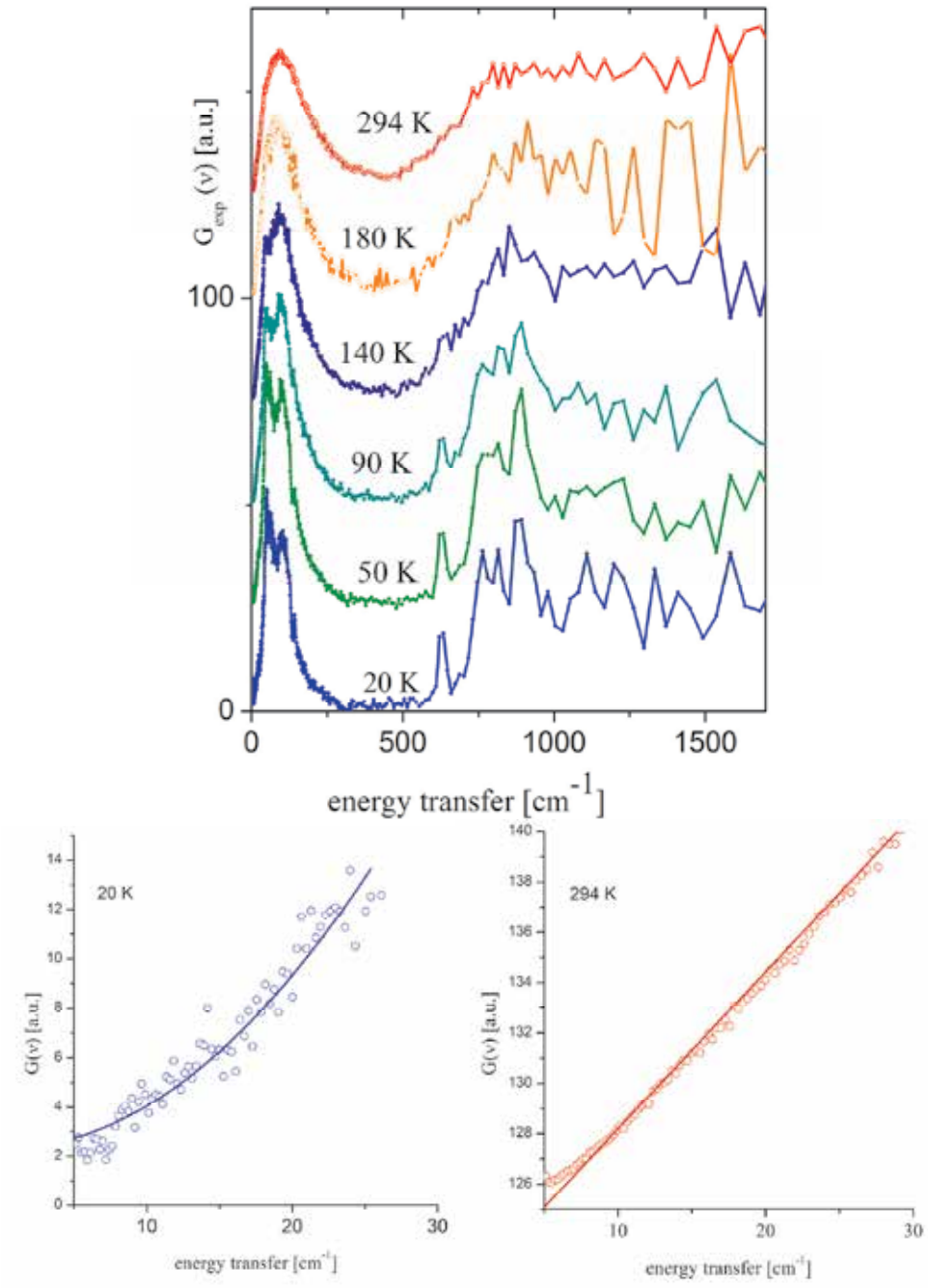

(a) (b)

Fig. 2. Spectra of imidazolium undecachlorodibismuthate (III) converted on single phonon scattering approximation to the generalized density of vibrational states G(υ) (Holderna-Natkaniec, 2006).
Low frequency region of generalized density of state at 20 K(fig.2a) and 294 K (fig.2b).

4. Discussion

Calculations of the vibrational spectra require the molecular structure and the force field constants to be known**.** In order to analyse the low-temperature spectrum of ICB the structures of isolated molecule of diamagnetic Im, $(Im)^+$, Im^+Cl^- system and the connection of imidazolium cations with the halogenobismuthate(III) anion were optimised. The force field was determined as a derivative of the total energy of the molecule over the atoms' displacements. Fig. 3 presents the structure of an isolated imidazolium cation and the notation assumed. Table 1 collects the bond lengths and angles between the bonds determined on the basis of X-ray diffraction at 150 K by S. Martinez-Carrera, (1966) and from the neutron diffraction data by B.M. Craven, R.K. McMullan, J.D. Bell, H.C. Freeman, (Craven et al., 1977) given at 150 K for imidazole (*abbreviation* Im) and for the sample of ICB studied at room temperature (Jakubas, 2005) together with the structure optimisation data (Holderna-Natkaniec,2006). On the basis of the X-ray and neutron diffraction data (Piecha et al., 2007; Zhang et al., 2005; Adams et al.,2008; Levasseur et.al., 1991; Zhang et al., 2005; Valle&Ettorare ,1997) it can be concluded that imidazolium cation actually does not have the mm2 symmetry. However, the five-membered ring of imidazole skeleton is planar, but the hydrogen atoms lay more than 0.16 Å out-of-plane of the heterocyclic ring system, while both nitrogen atoms are linked to hydrogen atoms. Similarly as the other heterocyclic ring systems, imidazole can be represented as a resonance hybrid.

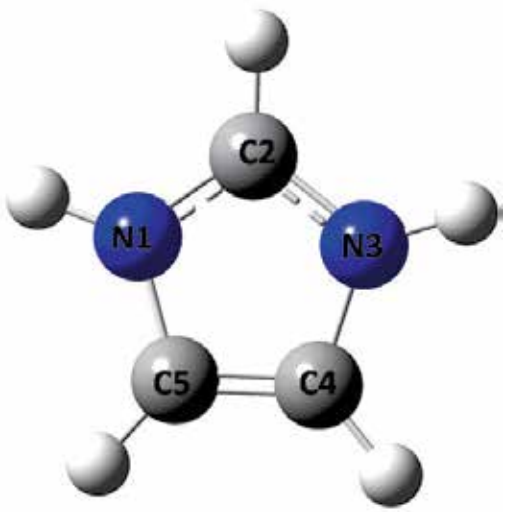

Fig. 3. Skeleton of imidazole with the atom numbering system.

The quality of the agreement of the experimental data X_{exper} (Jakubas, 2005; Craven,1977) with the values predicted by quantum mechanical calculations $X_{predicted}$ can be expressed by the root mean square deviation determined as:

$$RMS = \sqrt{\frac{\sum \left(x_{cal} - x_{\exp} \right)^2}{n}} \,. \tag{2}$$

Only the structure of the ordered (Im) skeleton (Jakubas, 2005) was used for comparison with the other data collected in Table 1, as the hydrogen positions determined by X-Ray diffraction are charged with too much error because of low electron density clouds of hydrogen atom. The lowest *RMS* value for bond length and angles is 0.0011 Å and 2.80°, respectively. Consequently, the B3LYP/LanL2Dz method leads to the geometric parameters of imidazole structure close to the experimental data.

Property /bond length [A]	$(Im)_5Bi_2Cl_{11}$ X-ray [RT] (Jakubas, 2005)				$(Im)^o$ B3LYP/ 6-311G*	$(Im)^+$ B3LYP/ 6-311G*	$(Im)^+$ LanL2Dz	$(Im^+)_3$ $BiCl_6$ LanL2Dz		
N1-C2	**1.269**	*1.241*	*1.256*	*1.258*	1.2156	1.349_3	1.2156	1.2156	1.2502	1.2158
C2-N3	**1.216**	*1.265*	*1.276*	*1.333*	1.2690	1.326_3	1.2590	1.2690	1.2759	1.2650
N3-C4	**1.352**	*1.365*	*1.329*	*1.368*	1.3433	1.377_7	1.3432	1.3432	1.3290	1.3432
C4-C5	**1.241**	*1.328*	*1.298*	*1.238*	1.2413	1.358_0	1.2413	1.2412	1.2977	1.2412
C5-N1	**1.343**	*1.374*	*1.338*	*1.354*	1.3525	1.369_0	1.3524	1.3524	1.3380	1.3526
N1-H	0.819	*1.153*	*1.052*	*1.172*	1.0715	1.047_0	1.0000	1.000	1.000	1.000
N2-H		*1.044*	*1.017*	*0.840*		0.999_9	1.0000	1.000	1.000	1.000
C2-H	1.108	*1.118*	*1.078*	*0.866*	1.1091	1.0822	1.0900	1.091	1.090	1.0899
C4-H	1.033	*1.020*	*1.119*	*0.851*	1.0933	0.9583	1.0900	1.090	1.0899	1.0900
C5-H	1.003	*0.946*	*0.957*	*1.046*	1.0334	1.0307	1.009	1.0899	1.090	1.0900
Angles [deg]										
C5 N1 C2	**107.5_9**	*110.03*	*108.04*	*111.95*	108.59	107.26	108.59	108.59	108.04	109.59
N1 C2 N3	**109.41**	*106.31*	*110.00*	*103.05*	109.50	111.26	109.40	109.40	110.99	109.40
C2 N3 C4	**107.80**	*97.69*	*106.76*	*111.17*	107.79	105.38	107.79	107.79	106.75	107.79
N3 C4 C5	**106.64**	*100.36*	*107.37*	*104.74*	106.55	109.77	106.53	106.53	107.87	106.54
C4 C5 N1	**107.37**	*108.35*	*106.93*	*109.03*	107.37	109.77	107.37	107.37	106.33	107.37
C5 N1 H	**119.60**	*125.3*	*121.22*	*116.10*	122.44	133.31		125.70	125.97	125.70
N1 C2 H	**121.02**	*122.15*	*116.29*	*115.29*	125.72	110.44		125.29	124.50	125.29
C5 C4 H	**128.94**	*120.36*	*141.30*	*147.02*	131.97	133.21		126.73	107.87	126.73
N1 C5 H	**122.90**	*121.39*	*120.05*	*110.30*	128.25	117.38		126.31	126.83	126.31
RMS (l)					0.0011	0.0067	0.0009	0.0011	0.0015	0.0015
RMS(∠)					2.75	6.44		2.84	2.85	2.84

Table 1. Comparison of observed and calculated geometry of imidazole. (in bold - the parameters of ordered structure).

Fig.4 presents the low-temperature spectra of the phonon density of states $G_{exp}(\nu)$ for ICB compared with the spectra calculated by DFT and semi-empirical methods for the systems discussed, in the energy transfer range up to 1700 cm^{-1}. Harmonic vibrational wavenumbers of normal modes computed for the reference systems and those corresponding to the experimental of ICB are listed in Table 2. It can be seen that the agreement is remarkable, showing that the DFT/LanL2Dz performed for a simple system built of imidazolium cation and $BiCl_6$ anion has accurately modelled the system, while the region of internal modes is well described by DFT/B3LYP/6-311G** performed for isolated imidazolium cation. The frequencies are unscaled.

As shown Fig.4, the internal vibration of anion mainly influence the phonon density of state spectrum in the lattice branch region (below 400 cm^{-1}).

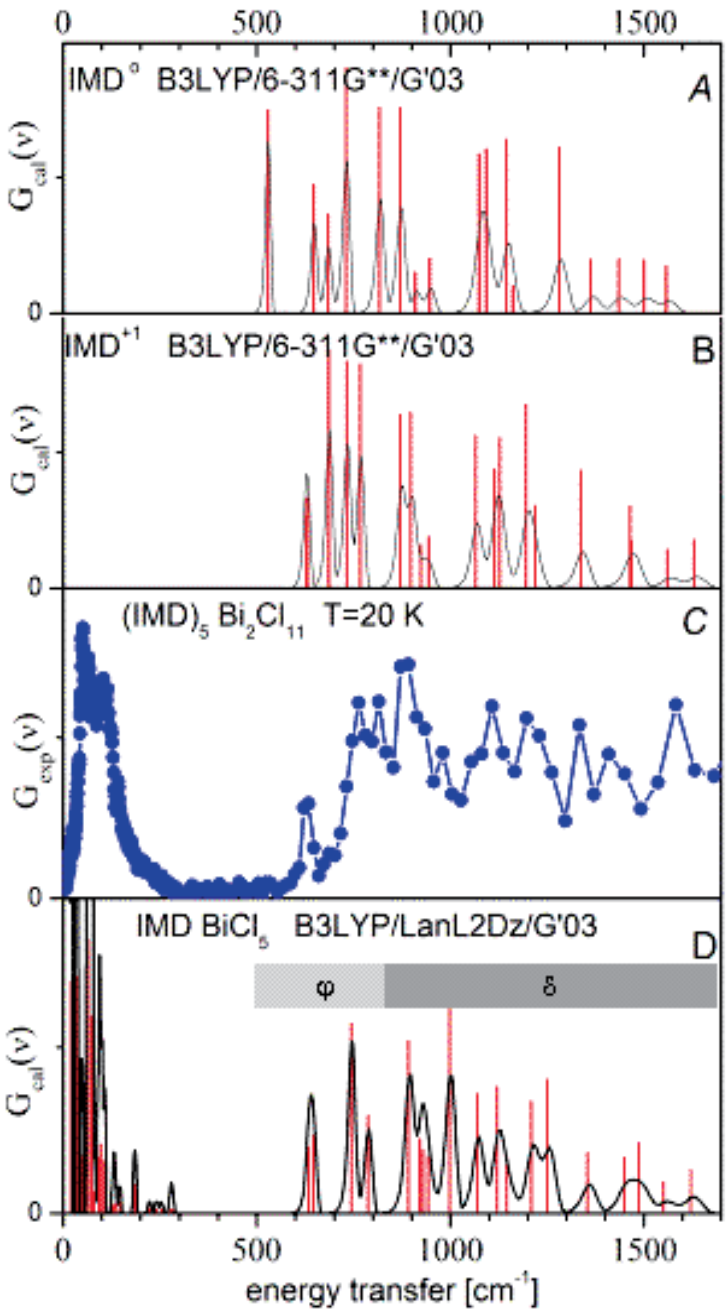

Fig. 4. Comparison of the low temperature phonon density of state spectra of imidazolium undecachlorodibismuthate (III) (C) with the ones calculated in the isolated molecule approximation by the Density Functional Theory method B3LYP with 6-311G** and LanL2Dz basis sets for the following systems: (Im) (A) , $(Im)^+$ (B), $(Im)_3 BiCl_6$ (D), respectively (below energy transfer 800 cm^{-1} in Holderna-Natkaniec, 2008).

IINS IBC 20K [cm^{-1}]	IR IBC 10K [cm^{-1}]	Raman IBC 290K [cm^{-1}]	IINS (Im) [21] 20 K [cm^{-1}]	Im^0 DFT [cm^{-1}]	assignment	(Im^+) DFT [cm^{-1}]	assignment	$(Im^+)Cl$ DFT [cm^{-1}]	assignment	ImCl PM3 [cm^{-1}]	Assignment and PED (Potential Energy Distribution) in %	$(Im^+)BiCl_6$ DFT [cm^{-1}]	$(Im_3)BiCl_3$ DFT [cm^{-1}]	assignment
48.6								49	δ[C4-N3-H] δ [C2-N3-H]			20 34 47	25, 28,35 41,46 52,58	δ[NH…Cl] δ[Cl-Bi-Cl]
62.5								78	δ[N3H Cl]	176	δ[C4-N3-H] 48 δ[C2-N3-H] 47	64, 72, 79, 91, 96	61,67 70,73 75,78 82,94	ρ[N N] δ[Cl-Bi-Cl]
104.1 142.3	165	111 117 219 233 261						294	λ[N3H Cl]	273	υ[N3 Cl] 71 υ[Cl6 H] 16	105,128 129,131, 133,145, 184,223, 240,252, 276,279, 281,	100,106 110,117 119,126 159,162 174,175 184,198 204,213 232,281	δ[N…N] υ[N…N] υ[N3 Cl] δ[Cl-Bi-Cl]
628.0±5	619	618	623	529	χ[N1-C5]	626	χ [C4-C5] χ [N1-C5] χ [C2-N1]					634.	632, 639	λ [N1-H Cl]
628.0±5	623		623			629	ρ[C4-N3-C2] ρ[C5-N1-C2]	631	ρ[C4-N3-C2] χ [C4-N3] χ [N3-C2] χ [C4-C5]	314	ρ[C4-N3-C2] 78 χ[C4-N3] 6 χ[N3-C2] 6 χ[C4-C5] 5	645.	640, 642, 651, 660	χ[C4-C5]A
685±7.			661	646	ρ[C4-N3-C2] ρ[C5-N1-C2]	688	ρ[C5-N1-C2] ρ[C4-N3-C2]	652	ρ[C4-N3-C2]	730	χ[C4-C5]34 χ[N1-C5] 28 χ[C2-N1]19			
736±5	753		743	683	ρ[C5-N1-C2] ρ[C4-N3-C2]	734	χ[C4-C5] ρ[C4-N3-C2] χ[N3-C4] χ[C2-N1	703	ρ[C4-N3-C2] ρ[C5-N1-C2]			744.	723 781	ρ[C4-N3-C2]
765.5±5	764			730		764	χ[C4-C5] ρ[N1-C2-N3]	783	χ[C4-C5] ρ[C4-N3-C2] ρ[C5-N1-C2]	779	ρ[C4-N3-C2] 21 χ[C4-C5]15 χ[C2-N1]15 χ[N3-C2] 15 χ[C4-N3]11	787.	782 790 849	χ [C4-C5] ρ[C2-N3] χ [N3-C4] χ [C2-N1]
790±7				817						877	δ[C2-N1-C5] 28 δ[C4-C5-N1]21 δ[N3-C2-N1] 16	891.	889	λ[N3-H Cl6] 49.% λ[N3-H..Cl6] 22.%
817.6±5			834			858	χ[C4-C5] ρ[N1-C2-N3]	852	λ[N3-H...Cl6] δ[C2-N3-C4] δ[N3-C2-N1]	893	λ[N3-H Cl6] 49 λ[N1-H..Cl6] 22 δ[C4-N3-H] 9 ρ[C4-N3-C2] 8 δ[C2-N3-H] 7	921.	898 905 915	λ[N1-H Cl6] ρ[C5-N1-C2] ρ[C4-N3-C2]
887.8±7	872			870	ρ[C4-N3-C2]	890	ρ[N3-C4-C5] ρ[C4-C5-N1]	871	λ[N3-H...Cl6] λ[N3-H...Cl6] λ[N3-H...Cl6] ρ[C4-N3-C2]	921	λ[N3-H Cl6] 18 δ[C4-N3-C2] 18 δ[C5-C4-N3] 17 δ[C2-N3-H] 9 δ[N3-C2-N1] 8	928.	922 923 929	λ[N3-H Cl6] δ[C5-C4-N3] δ[C5-C4-N3] δ[N3-C2-N1]
903±10	902	904	908	909	δ[C4-N3-C2] δ[C5-C4-N3]	919	δ[C4-N3-C2] δ[C5-C4-N3]	913	ρ[C4-C5-N1] λ[N3-H...Cl6] ρ[C4-N3-C2]	925	λ[N3-H...Cl6] 42 λ[N3-H...Cl6] 23 ρ[C4-N3-C2] 13 δ[C4-N3-H] 5	942.	933 941	λ[N3-H..Cl6] δ[N2-N3-C4] δ[N3-C2-N1]
931±9	922		935 938	946	δ[N1-C2-H] δ[N3-C2-H] δ[H-C4-N3]	938	δ[N1-C2-H] δ[N3-C2-H] δ[H-C4-N3]	942	δ[N1-C2-H] δ[N3-C2-H] δ[H-C4-N3]	1022	ρ[C4-C5-N1] 24 λ[N3-H...Cl6] 20 ρ[C4-N3-C2] 17 ρ[C5-C4-H] 11 ρ[C2-N1-H] 6		944 945 957	λ[N1-H-Cl6] δ[N1-C2-H] δ[C2-N3-H]

IINS IBC 20K [cm^{-1}]	IR IBC 10K [cm^{-1}]	Raman IBC 290K [cm^{-1}]	IINS (Im) [21] 20 K [cm^{-1}]	Im^0 DFT [cm^{-1}]	assignment	(Im^+) DFT [cm^{-1}]	assignment	$(Im^+)Cl$ DFT [cm^{-1}]	assignment	ImCl PM3 [cm^{-1}]	Assignment and PED (Potential Energy Distribution) in %	$(Im^+)BiCl_6$ DFT [cm^{-1}]	$(Im_3)BiCl_3$ DFT [cm^{-1}]	assignment
974.2±17			961					1062	δ[N1-C2-H] δ[N3-C2-H] δ[H-C4-N3] δ[C5-C4-H]	1038	λ[N3-H...Cl6] 20 δ[N1-C2-H]- 22 δ[N3-C2-H] 21 δ[H-C4-N3] 16 δ[C5-C4-H] 13	998	986 999 1032	λ[N3-H..Cl6] ρ[C2-N3-H] ρ[N3-C4-H]
1059±17	1039							1084	ρ[C2-N3-H] ρ[N3-C4-H]	1075	δ[C5-C4-H] 23 δ[H-C4-N3] 23 δ[C4-C5-H] 14 δ[N1-C5-H] 13			
1065±17	1043 1046 1049 1084	1041 1087	1061	1074	ρ[C2-N3-H] ρ[N3-C4-H]	1070	δ[C4-N3-C2] δ[C5-C4-N3]	1108	δ[C5-C4-H] ρ[H-C4-N3]	1089	ρ[C2-N1-H] 51 ρ[C5-C4-H] 11 ρ[C2-N1] 8 ρ[N1-C5] 7	1069	1041 1066 1074	ρ[N3-C2-N1] δ[C4-C5-H] δ[N1-C5-H]
1115±17	1089 1109	1108	1098	1092		1120	δ[C5-C4-H] δ[H-C4-N3] δ[C4-C5-H]	1137	ρ[C5-C4-H]	1116	ρ[N3-C2-N1] 56 ρ[C4-C5-N1] 14 ρ[C4-N3-C2] 10 ρ[C5-C4-H] 6	1121	1078 1113 1119	δ[N1-C2-H δ[C2-N3-H]
	1156 1161 1189	1171 1190	1141	1145	δ[H-N1-C4] δH-N1-C2] δ[H-N3-C2] δ[H-N3-C4]	1134	δ[C5-C4-H] δ[H-C4-N3]	1169	δ[N1-C5-H] δ[N1-C2-H] δ[N3-C2-H]	1135	ρ[C5-C4-H] 15 δ[N1-C5-H] 12 δ[N1-C2-H]11 ρ[C4-C5-N1] 11 δ[N3-C2-H] 10	1146.	1121 1149 1150	δ[C2-N3-H] δ[N1-C5-H]
1204±20			1186	1161	δ[H-C-N] δ[H-C-C]	1199.	δ[N1-C5-H] δ[N3-C2-H] δ[N1-C2-H]	1231	δ[C-N3-H] δ[N3-C-H]	1140	ρ[C5-C4-H] 34 ρ[N3-C2-N1] 14 ρ[C4-C5-N1] 10 δ[N1-C5-H] 7 δ[C4-C5-H] 6	1209.	1156 1207 1215	δ[N1-C5-H] δ[N1-C2-H] δ[N3-C2-H]
1235±20	1302		1265	1281	δ[N1-C2-N3] δ[N1-C2-H] δ[N3-C2-H]	1221	δ[H-N1-C4] δ[H-N1-C2] δ[H-N3-C2] δ [H-N3-C4]	1333.	δ[N1-C5-H] δ[C2-N3-H...Cl]	1246	δ[C4-C5-N1] 3 δ[C2-N1-H] 31	1250.	1234 1236 1249 1270	δ[C4-C5-N1] δ[C2-N1-H]
	1306			1363	δ[C4=C5-H] υ [C4-N3]	1343	δ[H-C-N] δ[H-C-C]	1397.	δ[C2-N3-H...Cl]	1369	υ [C4-N3] 32 υ [C5-N1] 28	1354	1347 1357 1357	δ[N1-C5-H] δ[N3-C4-H]
		1438		1434	υ [N1-C5] υ [N1-C2] υ [N3-C2]	1471	δ[N1-C2-H] δ[N3-C2-H] υ [N1-C5] υ [C4-N3]	1435	υ [N1-C2] υ [N3-C2]	1519	υ [N1-C2] 41 υ [N3-C2]9 δ[C4=C5-H] 7		1445 1449 1474	υ [N1-C5] υ [N1-C2]
								1460	υ [N1-C5]	1562	υ [N1-C2] 30 υ [N3-C4] 27 δ[N3-C2-H] 20		1475 1480 1484	υ [N1-C5]
	1527 1576			1500	υ [C4=C5] υ [N1-C2]	1560	υ [N1-C2] υ [N3-C2]	1523	υ [N1-C2] υ [N3-C2]	1632	υ [N3-C2] 49 υ [C4=C5] 18		1554 1556 1557	υ [N1-C2]
	1581	1579		1558	υ [C4=C5]	1629	υ [C4=C5]	1593	υ [C4=C5]	1694	υ [C4=C5] 51 υ [N3-C2] 16		1597 1614 1624	υ [C4=C5]

Used notation : χ– torsional out-of-plane, ρ out-of plane, δ deformational –in-plane, ν -stretching

Table 2. The frequencies and assignment of the observed bands of normal modes calculated for different clusters, modeling interactions in ICB

The normal modes of diamagnetic imidazole were calculated in the isolated molecule approximation by B3LYP/6-311G**. They were predicted at 529, 646, 683 and 730 cm^{-1} as torsional puckering and close to 800 cm^{-1} are separated from deformational in-plane modes, as shown Fig.4A. For the isolated imidazolium cation $(Im)^+$ they have been calculated by B3LYP/6-311G** at 626, 629.7, 688.0, 734 and 764 cm^{-1} (Fig.4B). The B3LYP/LanL2Dz calculations made for the Im^+Cl^- system predicted the lowest intra-molecular torsional out-of-plane modes assigned to ρ[C4-N3-C2], χ[C2-N3], χ[C3-N3] at 631, 652, 703 cm^{-1} and to ρ[C4-N3-C2], ρ[C5-N1-C2] at 765 and 811 cm^{-1}, respectively (Table 2). As follows from the calculations performed for $[(Im)_3\ BiCl_6]$ by B3LYP/LanL3Dz, the torsional out-of-plane modes appear in the energy transfer region from 640.9 to 890.0 cm^{-1} (Fig.4D). According to PM3 results, they are at 730 and 779 cm^{-1}. Also in the IINS spectrum of polycrystalline imidazolium recorded at 20 K [24] the bands assigned to the out-of-plane vibrations are at 623, 661, 743 cm^{-1}. In the experimental neutron vibration spectra of ICB taken at 20 K the lowest intra-molecular modes appear at (628 ± 5) (asymmetric in the low frequency part), (651 ± 5), (685 ± 5), (736 ± 5), (765 ± 5) and (817 ± 8) cm^{-1}. Moreover, the FT IR spectra of ICB taken in KBr (Piecha et al., 2009) show two modes (at 619 and 623 cm^{-1} at 10 K, as split on cooling from modes recorded at 620 cm^{-1} at 166K), and next subsequently at 753 and 764, 782 cm^{-1}. The calculated and experimental frequencies are close, then the influence of external interactions on these modes is rather weak.

The other bands observed in the experimental spectra are at (888 ± 8) and (931 ± 10), (974 ± 10), (1059 ± 17) cm^{-1}. Also the low temperature G(ν) spectra of polycrystalline imidazole (Loeffen, et al.,1995) show bands at 909, 935, 961, 1061 cm^{-1} assigned to the deformational in-plane modes predicted for the isolated diamagnetic molecule (Im) by B3LYP/6-311G** methods to be at 870, 909, 946, 1074 cm^{-1}, while for the cation of imidazole $(Im)^+$ the B3LYP/6-311G** calculations give their positions at 890, 919, 938, 1071 cm^{-1}. These modes can be assigned mainly to the deformational in-plane δ[C-N1-C], δ[C-N2-H]. According to the B3LYP/LanL2Dz calculations for the Im^+Cl^- system**,** they are predicted at 871, 913, 942, 1062 cm^{-1}, while the PM3 calculations give their positions at 893, 921, 925, 1038 cm^{-1}. The calculations performed for $(Im)_3BiCl_5$ by the B3LYP/LanL2Dz method predicted the positions of the deformational in-plane modes in the region from 905 to 1032 cm^{-1}.

The observed evolution in this part of the $G_{exp}(\nu)$ spectra (887, 974) cm^{-1} may be assigned to the dynamics of hydrogen bond. In the $G_{exp}(\nu)$ spectra taken of the compound under study in the ferroelectric phase, the above mentioned bands appear at nearly the same energy transfer values; their intensity is reduced because of thermal motions.

The $G_{exp}(\nu)$ spectrum recorded in paraelectric state, at 180 K, shows bands at 632, 816 and 862 cm^{-1} (Fig. 2) which may be assigned to normal modes of almost free (Im) group in the structure of the compound studied. The calculated phonon density of states spectrum $G_{cal}(\nu)$ of diamagnetic imidazolium for the structure under optimisation, determined at 150 K by the neutron elastic scattering method (Craven et al., 1977), gives the bands assigned to normal modes at 646, 816, 870 cm^{-1}. Hence, one may conclude that in the paraelectric phase the (Im) groups are almost free in the crystal structure of the compound studied.

4.2 H…B interaction

In the crystal structure of ICB the N-H…Cl interactions are involved. Fig.5 presents schematically the shorter hydrogen bridge bond system lying nearly along the (010) axis. The distances between H…Cl atoms of the N-H…Cl bridge, forming the zigzag chain, are 2.327, 2.648 Å, respectively [Jakubas, et al., 2005]**.** These hydrogen bonds are weak.

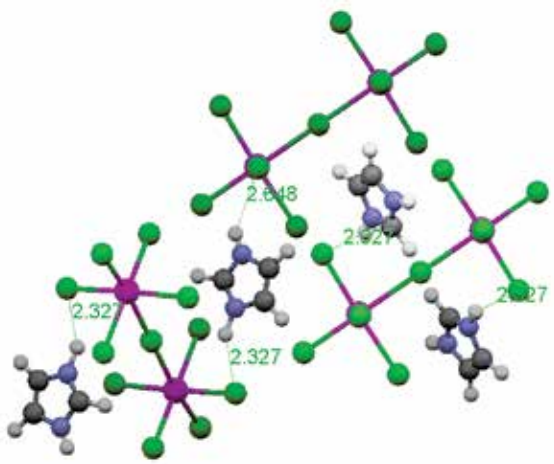

Fig. 5. Systems of the shortest hydrogen bridge bonds N-H…Cl of the sample studied.

The characteristic hydrogen bond vibration modes for normal hydrogen bonds can be assigned subsequently as (Jeffrey, 1997) :

- bending (λ),
- stretching N…H (ν), both in the lattice branch as well as the out-of-plane bending,
- out-of-plane (ρ) when hydrogen atom undergoes vibrations perpendicular to the axis of the hydrogen bridge bond N-H…Cl,
- deformational in-plane (δ), in the region corresponding to the internal modes.

The stretching ν[N-H] is not manifested in the IINS spectrum, because of low resolution power of the spectrometers at energy transfer close to 3000 cm^{-1} (according to the scattering law the resolution of the IINS spectra decreases with increasing energy transfer) and therefore this mode is studied by IR spectroscopy. Fig. 6 presents schematically, using arrows, the characteristic displacement of atoms forming hydrogen bridge bond on the example of the simplest system Im+-Cl^-.

Analysis of the effect of hydrogen bond on the internal dynamics should also include the bending and stretching modes in the lattice branch and the stretching vibrations ν [N-H]; in agreement with the DFT calculations performed for the Im^+Cl^- and $(Im)_3BiCl_6$ systems, the bands predicted to appear at 49 and 294 cm^{-1} should be assigned to λ[NH...Cl] and ν[N-H...Cl] vibrations, respectively; the former bring information on the changes along the chain of hydrogen bonds.

The DFT calculations predict the N-H…X out-of-plane bending modes ρ (hydrogen vibrations - perpendicular to the imidazolium plane) at 1084 cm^{-1}. The N-H...Cl in-plane bend mode was predicted for simple system at 1231 cm^{-1}. For $(Im)_3BiCl_5$ the modes are calculated by DFT method at lower frequencies (~ 1032, and 1213 cm^{-1}), respectively. Both nitrogen atoms of imidazolium pentagon are involved in the hydrogen bridge N-H…X. Analysis of the phonon density of state spectra taken at different temperatures shows that in the paraelectric phase the band at (890 ± 10) cm^{-1} and (1204 ± 20), (1235 ± 20) cm^{-1} recorded in the ferroelectric state was weaker.

In the crystals structure of ICB the hydrogen bridge bonds interactions between neighbouring imidazolium group also take place. The neutron vibrational spectra of solid imidazole (Loeffen, 1995) show the low frequency bands at 623, 661, 743 cm^{-1}. The data are close to energy transfer values obtained for ICB at 20 K, as was given in Table 2.

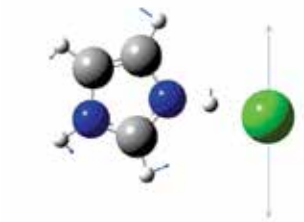

Hydrogen bond bend, 49 cm^{-1}

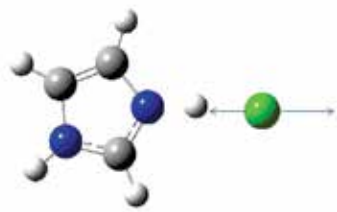

Hydrogen bond stretch, 294 cm^{-1}

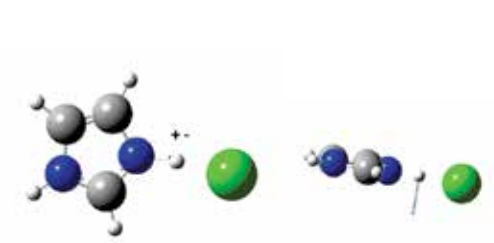

Hydrogen bond out of plane bend, 1084 cm^{-1}

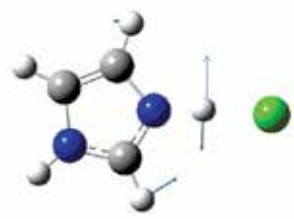

Hydrogen bond in plane bend, 1231 cm^{-1}

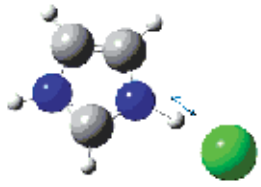

N-H stretch, 3676 cm^{-1}

Fig. 6. Hydrogen bond vibration modes for N-H…Cl.

4.3 ^1H NMR

Internal dynamics of imidazolium cations was studied by different ^1H NMR techniques (Abragam, 1983). The first derivative of the absorption line recorded by the continuous wave method at selected temperatures is presented in Fig.7. In the H NMR spectra at 220K one may distinguished two components of the line, characterised by the slope line widths dH' and dH". The line width of the broad component changes slightly and its intensity decreases on heating. Finally, the broad component of ^1H NMR line ($\delta H=9.5 * 10^{-4}T$) disappeared at about T=290 K. It means that above 290 K imidazolium cations undergo fast reorientation. In the temperature range (227 - 293) K the ratio of areas of particular components of the NMR spectrum, disregarding the narrowest line, is 2/3, which is in agreement with the X-Ray data (Jakubas et al, 2005).

This suggests different mobilities of imidazolium cations of ICB at the room temperature. Three imidazolium cations seem to be more mobile than the other two. The three disordered imidazolium cations occupy positions at the centre of inversion and are distributed between two positions (180^0 reorientation model) within the pentagonal ring. Above room temperature they are indistinguishable because all of them are orientationally disordered, which has also been indicated by the calorimetric studies (Przeslawski et al., 2007, Piecha et al.,2007).

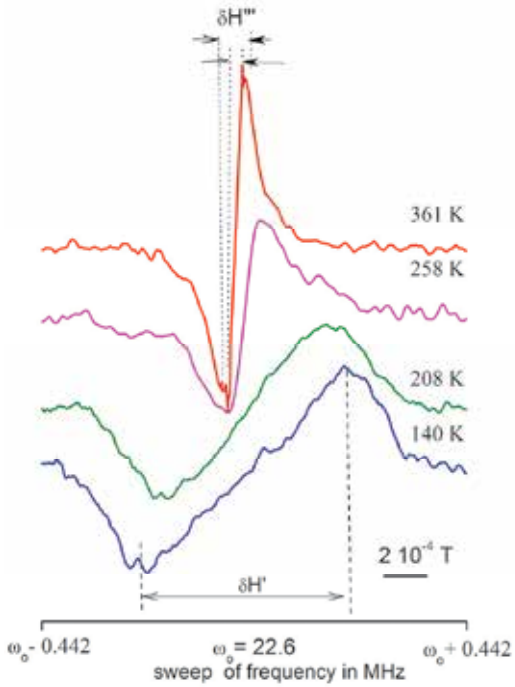

Fig. 7. First derivative of ^{1}H NMR absorption at different temperature

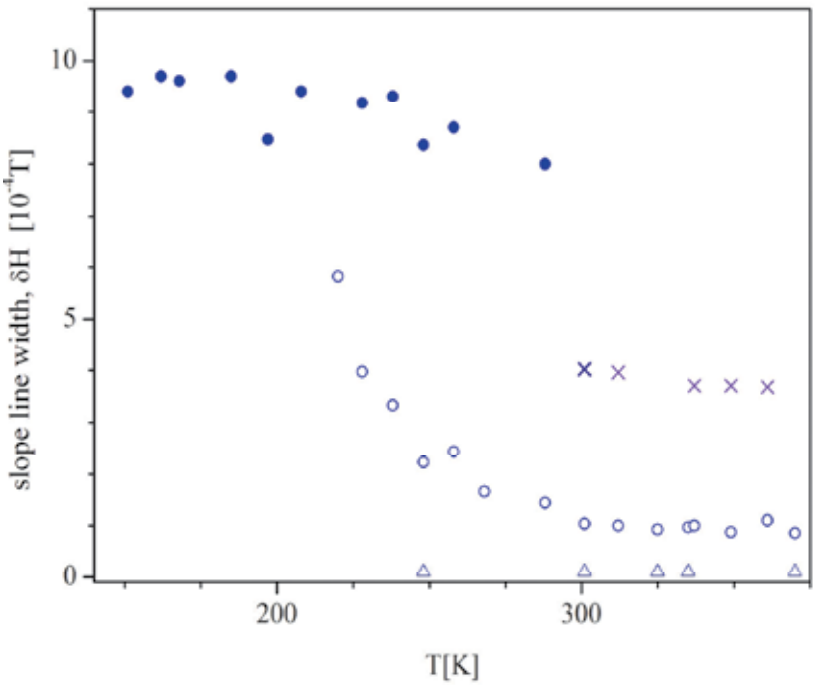

Fig. 8. Temperature dependence of ^{1}H NMR slope line width of ICB.

The two narrow components of NMR spectrum with slope line widths of 3 10^{-4}T and 0.1* 10^{-4}T were also observed on heating from 227 K to 375 K. As two of the five hydrogens of imidazolium cation were bonded to nitrogens (denoted as N1 and N3 in Fig.3) they were involved also in hydrogen bridge bonds N-H…N network. These protons perform translational diffusion which explains the appearance of the component of the smallest slope line width (0.1 10^{-4} T). The component of the δH=3 10^{-4} T can be assigned to the dynamics of the other three hydrogen atoms of the imidazole ring. It means that the imidazolium cation does not undergo diffusion process in the bulk of the crystal studied.
Fig. 9 presents the temperature dependence of the second moment M_2 of the ^{1}H NMR line. No change in M_2 of ^{1}H NMR lines was found below 166K. When temperature was increased above the phase transition point, the value of ^{1}H M_2 decreased from 8.5·10^{-8} T^2 at 166 K approaching 1.2·10^{-8} T^2 at room temperature.
The second moment value for the rigid lattice was determined from the van Vleck formula (vanVleck,1948):

$$M_2 = \frac{3}{5}\gamma_H^2 \hbar^2 I(I+1)\frac{1}{N}\sum_{j,k}^{N} r_{H-H}^{-6} + \frac{4}{15}\gamma_S^2 \hbar^2 S(S+1)\frac{1}{N}\sum_{j,k}^{N} r_{H-S}^{-6}, \quad (3)$$

where I - the resonant spin, S - the nonresonant spins, γ_H – the gyromagnetic ratio of resonant spin, γ_S – the gyromagnetic ratio of nonresonant spins, $r_{j,k}$ – internuclear distance in whole sample, N - number of resonant spin in the molecule.

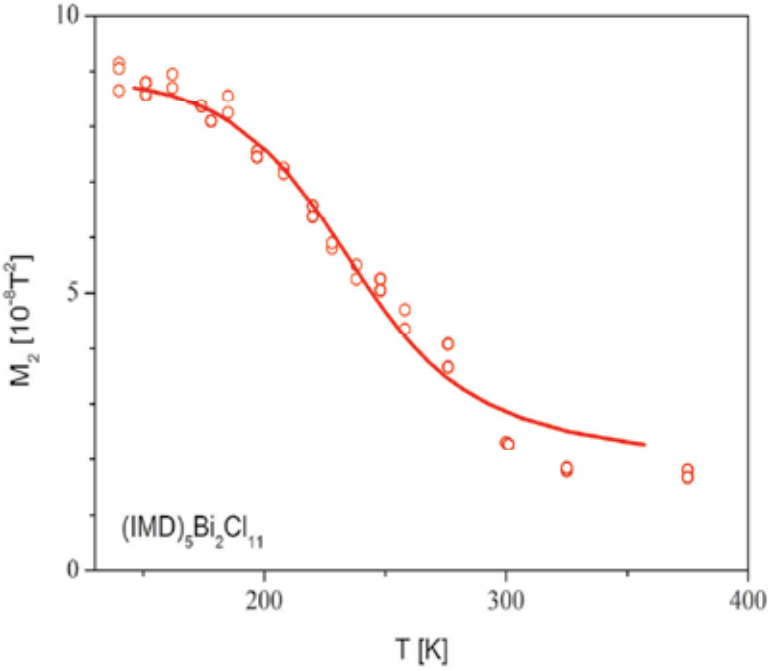

Fig. 9. Temperature dependence of second moment of ^{1}H NMR line of imidazolium undecachlorodibismuthate (III)
(Holderna-Natkaniec, 2008).

The second moment of the ^{1}H NMR line was calculated taking into account the homo- H-H and hetero-nucleus H-N interactions. Given the structural parameters from the diffraction study [Jakubas, et al., 2005; Martinez-Carrera, 1996; Craven et al., 1997; Piecha et at., 2007, 2009; Bujak & Zaleski ,2003;) and assuming that all N-H bond are not coplanar with the imidazole skeleton, we find M_2^{rigid} as 10.7 $\cdot 10^{-8}$ T^2, as a sum of 5.3 and 3.7 (in 10^{-8} T^2) from H-H, and H-N intramolecular interactions, respectively, whereas the inter-imidazole contribution to ^{1}H M_2 takes the value of 1.7 $\cdot 10^{-8}$ T^2. When the inter-nucleus vector $r_{j,k}$ undergoes reorientation around the distinguished axis a, and $\gamma_{j,k}$ is the angle between them, the second moment decreases from the rigid lattice value M_2^{rigid} according to the formula (Slichter,1980):

$$M_2^{rot} = M_2^{rigid}\left(\frac{3\cos^2\gamma_{j,k}-1}{2}\right)^2 . \quad (4)$$

The imidazolium is considered to perform reorientations around the following axes:

- the axis in the plane of the pentagon and parallel to the N1-N3 direction (the axis of minimum value of the moment of inertia),
- the axis in the plane of the pentagon, perpendicular to the N1-N3 direction, passing through C2 and the middle of the C4-C5 bond,
- the axis perpendicular to the plane of the five-membered imidazole ring, for which the moment of inertia is the highest.

The proton jump in N-H…Cl bridges is the reason why M_2 value changes to 10.55 10^{-8} T^2. The effect of the anisotropic reorientations of imidazolium cation about the mentioned above two-fold symmetry axes on the M_2 reduces its value to 9.5 and 8.5 $\cdot 10^{-8}$ T^2, respectively. The reorientation around the nearly five-fold symmetry axis caused a reduction of M_2 to 2.1 $\cdot 10^{-8}$ T^2, which is close to the M_2 value observed at room temperature. The diffusion process in the bulk of the crystal is a reason that second moment value decreased on heating above room temperature.

The temperature dependence of the second moment of NMR line is described by the formula (Gutowsky, 1950):

$$(\delta H)^2 = B^2 + (C^2 - B^2)\, 2/\pi \,\mathrm{arctg}\,(\alpha\gamma\delta H / 2\pi\nu_c), \quad (5)$$

where δH^2 - the second moment of NMR line at temperature T (when $\delta H \sim \nu_c$), B^2, C^2 - the NMR second moment determined for the high- and low-temperature plateau, for $\mathrm{sqrt}(C^2) << \nu_c$ or $\mathrm{sqrt}(B^2) >> \nu_c$, respectively, α - a constant of the order of 1, γ- the gyromagnetic factor of a resonant nucleus, ν_c - the frequency of intramolecular reorientations described by the Arrhenius dependence: $\nu_c = \nu_o \cdot \exp(-E_a/RT)$. The activation energy of the imidazolium cation reorientation in ICB was close to 12.3 kJ/mol.

The calculated values of the second moment indicate that below the ferroelectric phase transition the imidazolium cations are ordered, while above the transition temperature to the paraelectric phase the onset of the cation reorientation with a frequency of an order of several kHz takes place.

In order to describe the form of the ^{1}H NMR absorption line the ratio of its fourth and second moments was determined versus temperature, as shown in Fig.8c. On heating above 200 K a considerable increase in the M_4/M_2 ratio is observed, as the shape of the ^{1}H NMR signal changes from a Gauss to Lorentz one. Moreover, on heating from 200 K (ICB is an insulator) to 300 K the electrical conductivity increases (Zdanowska-Fraczek et al., (2009), Munch et al.,(2001)). At 300 the imidazolium cation are disordered and the line is narrow.

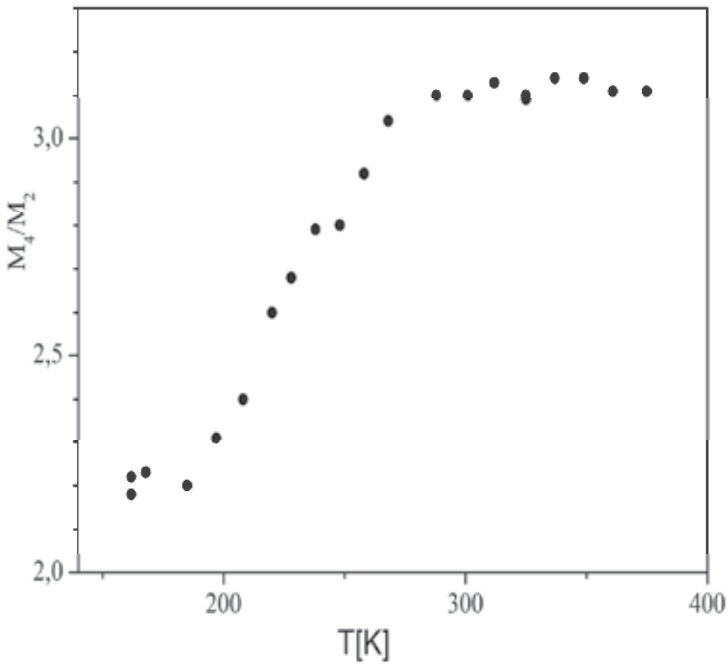

Fig. 8. c. The ratio of fourth and second moment of the ^1H NMR line at different temperatures (Zdanowska-Fraczek et al., (2009)).

The temperature dependence of the spin-lattice relaxation time of $(Im)_5Bi_2Cl_{11}$ is shown in [22]. On heating from the ferroelectric to the paraelectric phase, the relaxation time continuously decreases from 176 s at 87 K to 2.4 s at 166 K. In the paraelectric phase the decrease in the relaxation time is reasonably smaller, and T_1 is equal to 1.1 s at 345 K. Above the next phase transition temperature at 366 K, T_1 increases, and at 389 K it is 6.7 s. Unfortunately, the local minimums of the function describing the relaxation rate versus reciprocal temperature were obtained at temperatures of both phase transitions. Therefore we can estimate only the activation energy for the pentagon (Im) cation reorientation when $\omega\tau_c >> 1$, i.e. from the right branch of the experimental results of T_1 versus reciprocal temperature in semi-logarithmic scale. It is close to 12 kJ/mol, as was obtained from the temperature dependence of the second moment of the ^1H NMR line.

5. Conclusions

Results of IINS, ^1H NMR and QC calculations obtained for the imidazolium undecachlorodibismuthate (III) studied in temperature range from 20 K to 290 K permit proposing the assignment of subsequent bands in their vibrational spectrum. As an attempt to explain the differences in vibrational spectra of imidazolium cation and the sample studied, especially in the range 760 - 1700 cm^{-1}, the results were discussed *versus* the data of quantum chemical calculations performed for different reference systems to get insight into the vibrational spectrum of the molecule studied and also to conclude about the molecular structure. The importance of hydrogen bonds formation in the ferroelectric phase was shown.

Analysis of the temperature dependence of ^{1}H NMR line width and the second moment of NMR line give a unique possibility to conclude about the onset of reorientation of imidazolium cations close to the phase transition at 166 K accompanied by proton diffusion at higher temperatures. On heating the changes in the ^{1}H NMR and IINS spectra can be interpreted as the onset of proton jump in N-H...Cl hydrogen bond, reorientation of imidazole ring around the pseudo-five-fold symmetry axis and diffusion process in the crystal. The activation energy of this cation's reorientation was estimated as 12.3 kJ/mol.

6. Acknowledgment

The QC calculation were performed under the grant at PSCC in Poznan.

7. References

Gągor, A.; Piecha, A.; Jakubas, R.; Miniewicz,A.; (2011). Crystal structure and characterization of a novel acentric imidazolium analog [$C_3N_2H_5^+$][Br^-], *Chemical Physics Letter*s, Vol.503, (2011), pp.134-138 (*and references cited therein*).

Sobczyk , L.; Jakubas ,R.; Zaleski , J.; (1997). Self-Assembly of Sb(III) and Bi(III) Halo-Coordinated Octahedra in Salts of Organic Cations. Structure, P roperties and Phase Transitions, *Polish Journal of Chemistry,* Vol. 71, (1997), pp. 265 -300, (and references cited therein).

Piecha , A.; Bator , G.; Jakubas, R.; (2005). Critical slowing down of low-frequency dielectric relaxation in ferroelectric $(C_3N_2H_5)_5Bi_2Cl_{11}$, *Journal of Physics: Condensed Matter.* Vol.17, (2005), pp. L411-L417.

Jakubas, R.; Piecha, A.; Pietraszko, A.; Bator, G.; (2005). Structure and ferroelectric properties of $[C_3N_2H_5]_5Bi_2Cl_{11}$, *Physical Review*, Vol B 72, (2005), pp. 104107.1- 8. DOI: 10.1103/PhysRevB.72.104107.

Lovesey, S.W., *Theory of Neutron Scattering from Condensed Matter*, Clarendon Press, Oxford 1984. Oxford University Press 2006, ISBN 0-19-852029-8.

Dianoux, A.J.; Lander, E,; (Eds), *Neutron data Booklet*, ILL Neutrons for Sciences, Grenoble, 2003. ISBN:0-9704143-7-4.

Abragam, A.; *The Principles of Nuclear Magnetism*, Oxford University Press, Oxford, 1983. ISBN 13:9780198520146.ISBN10:10-19-852014-X

www.isis.stfc.ac.uk/instruments/tosca

www.jinr.ru, http:/flnp.jinr.ru/134

Natkaniec, I.; Bragin, S. I.; Brankowski, J.; Mayer, J.;(1993). Inverted geometry spectrometer NERA, *Proceedings of the ICANS XII Meeting*, Abington, 1993, vol. I, 1994, RAL Report, 94-025, I, pp.89-94. Rutherford Appleton Laboratory, Abingdon, Oxfordshire, UK, May 24-28, 1993.

Becke, D.A., (1988). Density-functional exchange-energy approximation with correct asymptotic behavior, *Physical Review* Vol. A 38, (1988), pp.3098-3100; (1992) Density-functional thermochemistry. II. The effect of the Perdew-Wang generalized-gradient correlation correction , *Journal of Chemical Physics* , Vol.97, No.12, (1988), pp. 9173-9177; (1993) Density-functional thermochemistry. III. The role of exact exchange, *The Journal of Chemical Physics,* Vol.98,No.7, (1993), pp. 5648-5652.

Lee, C.; Yang, W.; Parr, R. G.; (1988). *Development of the Colle-Salvetti correlation-energy formula into a functional of the electron density*, Physical Review, *Vol. B 37, (1988), pp. 785-789.*

Zhanpeisov, N.; Matsuoka, M.; Yamashite, H.; Anpo, M.; (1998). Cluster Quantum Chemical *ab Initio* Study on the Interaction of NO Molecules with Highly Dispersed Titanium Oxides Incorporated into Silicalite and Zeolites, (1998). *Journal of Physical Chemistry*, Vol.B102, (1998), pp. 6915-6920.

Niclasc, N.; Dolg, M.; Stoll, H.; Preuss, H.;; (1995). Ab initio energy-adjusted pseudopotentials for the noble gases Ne through Xe: Calculation of atomic dipole and quadrupole polarizabilities. *Journal of Chemical Physics*, Vol. 102, No. 22, (1995), pp. 8942-8953.

Gaussian 03, Revision C.02, Frisch, M. J.; Trucks, G. W.; Schlegel, H. B.; Scuseria, G. E.; Robb, M. A.; Cheeseman, J. R.; Montgomery, Jr., J. A.; Vreven, T.; Kudin, K. N.; Burant, J. C.; Millam, J. M.; Iyengar, S. S.; Tomasi, J.; Barone, V.; Mennucci, B.; Cossi, M.; Scalmani, G.; Rega, N.; Petersson, G. A.; Nakatsuji, H.; Hada, M.; Ehara, M.; Toyota, K.; Fukuda, R.; Hasegawa, J.; Ishida, M.; Nakajima, T.; Honda, Y.; Kitao, O.; Nakai, H.; Klene, M.; Li, X.; Knox, J. E.; Hratchian, H. P.; Cross, J. B.; Bakken, V.; Adamo, C.; Jaramillo, J.; Gomperts, R.; Stratmann, R. E.; Yazyev, O.; Austin, A. J.; Cammi, R.; Pomelli, C.; Ochterski, J. W.; Ayala, P. Y.; Morokuma, K.; Voth, G. A.; Salvador, P.; Dannenberg, J. J.; Zakrzewski, V. G.; Dapprich, S.; Daniels, A. D.; Strain, M. C.; Farkas, O.; Malick, D. K.; Rabuck, A. D.; Raghavachari, K.; Foresman, J. B.; Ortiz, J. V.; Cui, Q.; Baboul, A. G.; Clifford, S.; Cioslowski, J.; Stefanov, B. B.; Liu, G.; Liashenko, A.; Piskorz, P.; Komaromi, I.; Martin, R. L.; Fox, D. J.; Keith, T.; Al-Laham, M. A.; Peng, C. Y.; Nanayakkara, A.; Challacombe, M.; Gill, P. M. W.; Johnson, B.; Chen, W.; Wong, M. W.; Gonzalez, C.; and Pople, J. A.; Gaussian, Inc., Wallingford CT, 2004.

Ramirez-Cuesta,A.J.J; (2004) CLIMAX 4.0.1, the new version of the software for analyzing and interpreting INS spectra *Computer Physics Communication*. 157 (2004), 226-238.

http://www.ccdc.cam.ac.uk

Kazimirov, W. J.; I. Natkaniec, I.; *Programme for Calculation of the Resolution Function of NERA-PR and KDSOG-M Inelastic Neutron Scattering Inverse Geometry Spectrometers*, Preprint P14-2003-48 JINR, Dubna, 2003.

Stewart,J. J .P.; Optimization of parameters of semiempirical methods.I Methods; *Journal of Computational chemistry*. Vol.10, (1989), 209-220.; Optimization of parameters for semiempirical methods, II Applications , *Journal of Computational chemistry*. Vol.10, (1989) pp. 221-264; (1991), Optimization of parameters for semiempirical methods. III Extension of PM3 to Be, Mg, Zn, Ga, Ge, As, Se, Cd, In, Sn, Sb, Te, Hg, Tl, Pb, and Bi (pp. 320–341). *Journal of Computational chemistry*. 12, (1991), pp. 320-341., Optimization of parameters for semiempirical methods IV: extension of MNDO, AM1, and PM3 to more main group elements *Journal of Molecular Modeling Vol.* 10, (2004),pp. 155-164,DOI-10.1007/3 00894-004-0183-2..

Khavryutchenko, V. D.; *COSPECO Complex Program for Vibrational Spectroscopy*, Instytiute of Surface Chemistry Ukrainian Academy of Sciences, Kiev, 1990.

Martinez-Carrera, S.; (1996). The crystal structure of imidazole at -150°C, Acta Crystallographica. Vol.20 (1966) 783-789 . doi:10.1107/S0365110X66001853

Craven, B.M.; McMullan, R.K.; Bell, J.D.; Freeman, H.C.; The crystal structure of imidazole by neutron diffraction at 20°C and -150°C, *Acta Crystallographica*. Vol. B33 (1977) 2585-2589. doi:10.1107/S0567740877008954

Holderna-Natkaniec, K.; Natkaniec, I.; Jakubas, R.; Nowak, D.; Medycki, W.; Internal dynamics of $(C_3N_2H_5)_5Bi_2Cl_{11}$ studied by IINS, ^1H NMR and QC methods, *Journal of Molecular Structure*. Vol. 891 (2008) 143-150.

Wang, Y-T.; Tang, G-M.; Wan, W-Z.; (2006). Naphthalene-2,7-diol-imidazole, *Acta Crystallographica*, Vol. E62, (2006), pp. o-3396-o3397.

Piecha, R. Jakubas, , A. Pietraszko; Baran, J.; (2007). Structural characterization and spectroscopic properties of imidazolium chlorobismuthate(III): $[C_3H_5N_2]_6[Bi_4Cl_{18}]$, *Journal of molecular structures* , Vol. 844-845, (2007), pp. 132-139.

Bujak, M.; Zaleski, J.; (2003). Structure of chloroantomonates(III) with imidazolium cation $(C_3H_5N_2)SbCl_4$ and $(C_3H_5N_2)_2SbCl_5$ *Journal of Molecular structures*, Vol. 647 (2003). pp.121-128.

Zhang H.; Fang,L.; Dronskowski,D.; Krauze,K,; Yuan,R.; (2005). Bis(imidazolium)hexachlorostrontate(IV), *Acta Crystallographica*, Vol.E61, (2005), m541-m542.

Valle, G.; Ettorore, R.; (1991). Bis(imidazolium)tetrachloropalladium, *Zietschrift fur Kristallographie*, Vol.212, (1997), pp. 166-168.

Levasseur, G.; Beauchanyp, A. L.;(1991). Structure of imidazolium hexachlorotantalate (V), *Acta Crystallographica*, Vol. C47, (1991), pp.547-550.

Adams, Ch.; Kurawa, M. A.; Lusi, M.; Orpen, A. G.; (2008). Solid State synthesis of coordination compounds from basic metal salts, *Crystals Engineering Communications*,Vol.10 (2008) pp.1790-1795

Piecha, A.; Kinzhybalo, K.; Slepokura, K.; Jakubas, R.; (2007). Structural characterization, thermal and electrical properties of imidazolium bromoantimonate (III)$(C_3H_5N_2)_3Sb_2Br_9$, *Journal of Solid State Chemistry*, Vol. 180, (2007), pp. 264-275.

Loeffen P. W.; Pettifer, R. F.; Fillaux, F.; Kearley, G.J.; (1995). Vibrational force field of solid imidazole from inelastic neutron scattering. *Journal of Chemical Physics*. Vol. 103, (1995) pp.8444-8455.

Piecha, A.; Jakubas, R.; Bator, G.; Baran, J. (2009). Infrared investigations of the order–disorder ferroelectric phase transitions in imidazolium halogenobismuthates (III) and halogenoantimonates (III): $(C_3N_2H_5)_5Bi_2Cl_{11}$, $(C_3N_2H_5)_5Bi_2Br_{11}$and $(C_3N_2H_5)_5Sb_2Br_{11}$, *Vibrational spectroscopy* Vol. 51.No. 2, (2009) ,pp.226-237.

Jeffrey, G.A.; An Introduction to Hydrogen Bonding, New York, Oxford, 1997.

Przeslawski, J.; Kosturek, B.; Dacko, S.; Jakubas, R.; (2007). Thermal and optical properties of the ferroelectric $(C_3N_2H_5)_5Bi_2Cl_{11}$ crystal , *Solid State Communications*.Vol.142, (2007), 713-717.

Slichter, C.P.; *Principles of magnetic resonance*, Springer Verlag, Berlin, Heidelberg, New York 1980.

Van Vleck, J. H.; The dipolar broadening of magnetic resonance lines in crystals, *Physical. Review*. Vol.74, (1948), pp.1168-1183.

Gutowsky, H. S.; Pake, G. E.; Nuclear Magnetism in Studies of Molecular Structure and Rotation in Solids: Ammonium Salts, *Journal of Chemical Physics. Vol.* 18, (1950), 162-163.

Zdanowska-Fraczek, M.; Holderna-Natkaniec, K.; Fraczek, Z. J.; Jakubas, R.; Molecular dynamics and electrical conductivity of $(C_3N_2H_5)_5Bi_2Cl_{11}$, *Solid State Ionic*s , Vol. 180, No. 1, (2009), pp. 9-12.

Munch, W.; Kreuer K. D.; Silvestri, W.; Maier, J.; Seifert, G.;The diffusion mechanism of an excess proton in imidazole molecule chains: first results of an ab initio molecular dynamics study, *Solid State Ionic*, Vol.145, No.1-4, (2001) , pp. 437-443.

4

Structure – Property Relationships of Near-Eutectic $BaTiO_3$ – $CoFe_2O_4$ Magnetoelectric Composites

Rashed Adnan Islam[1], Mirza Bichurin[2] and Shashank Priya[3]
[1]*Philips Lumileds Lighting Co, 370 W. Trimble Rd, San Jose CA,*
[2]*Inst. of Electron. & Inf. Syst., Novgorod State Univ., Veliky Novgorod,*
[3]*Materials Science and Engineering, Virginia Tech, Blacksburg, VA 24061,*
[1,3]*USA*
[2]*Russia*

1. Introduction

Magnetoelectric (ME) materials become magnetized when placed in an electric field, and conversely electrically polarized when placed in a magnetic field. Dielectric polarization of a material under magnetic field, or an induced magnetization under an electric field, requires the simultaneous presence of long-range ordering of magnetic moments and electric dipoles (Suchtelen, 1972; Smolensky, 1958; Astrov, 1968; Fiebig 2005). Said materials offer potential for new generations of sensor, filter, and field-tunable microwave dielectric devices (Bichurin, 2002). Unfortunately to date, the ME exchange in single phase materials has been found to be quite small (Dzyaloshinskii, 1959; Astrov, 1960). However, quite large effects are found in composites of piezoelectric and magnetostrictive phases, both of the particle-particle and laminate (Ryu, 2002a, 2002b) types. In these composites, enhanced ME exchange is the result of an elastic-coupling mediated across the piezoelectric-magnetostrictive interfacial area. The original work on ME composites concerned particle-particle composites and was performed at the Philips Laboratories. These ME composites were prepared by unidirectional solidification of an eutectic composition of the quinary system Fe-Co-Ti-Ba-O (O'dell, 1965; Boomgaard, 1976). The eutectic composition was reported to consist of 38 mol% $CoFe_2O_4$. Unidirectional solidification helps in the decomposition of the eutectic liquid (L) into alternate layers of the constituent phases: piezoelectric perovskite (P) and piezomagnetic spinel (S) phases, i.e., $L \rightarrow P + S$. Their results showed ME voltage coefficients as high as dE/dH=50mV/cm•Oe (Boomgaard, 1974; Van Run 1974). Subsequent work on eutectic compositions of $BaTiO_3$-$CoFe_2O_4$ (BTO–CFO) prepared by unidirectional solidification have reported a ME coefficient of 130 mV/cm•Oe (Boomgaard, 1978). Unfortunately, unidirectional solidification has several disadvantages such as (i) limitation on the choice of compositions and material systems, (ii) difficulty in critical control over the composition when one of the components is a gas (i.e., oxygen), and (iii) processing temperature and time. However these limitations could be alleviated by synthesizing ME composites using a conventional ceramic processing route.

Recently, giant ME effect has been reported in laminate composites of piezoelectric and magnetostrictive materials (Ryu, 2003a; Ryu, 2003b; Dong, 2003a; Dong 2003b). The magnetoelectric laminate composite were fabricated in sandwich structure, embedding piezoelectric PMN-PT single crystal between magnetostrictive Terfenol-D alloys. This material exhibited the ME coefficient of 10.30 V/cm.Oe, which is ~80 times higher than that previously reported in either naturally occurring magnetoelectrics or Artificially-Designed Composites (ADC). Even though the ME coefficient is considerably higher, these materials have certain disadvantages as compared with the artificially-designed composites, such as eutectic composition of $BaTiO_3$-$CoFe_2O_4$. Laminated magnetoelectrics are very attractive from the fabrication point of view however suffer from several other drawbacks such as high cost for single crystal, difficult to miniaturize, decay of epoxy bonding and complicated sensing circuits. Again all these laminated composites use lead based product which is a highly toxic element and it is better to eliminate this toxic element and introduce lead-free compositions in magnetoelectric composites.

For bulk magnetoelectric composite higher ME coefficient implies higher elastic coupling between the magnetic and piezoelectric phases (Prellier, 2005). The elastic coupling can be maximized by having coherent response from the magnetostrictive phase under dc bias, so that the stress on the piezoelectric lattice across the grains is in phase with each other. For this purpose, a coherent interface between piezoelectric and magnetostrictive phase is very important. A coherent interface can transfer the strain very efficiently from magnetostrictive to the piezoelectric phase. An artificial interface can also be created by fabricating a co-fired bilayer composite. Previously, we have demonstrated $BaTiO_3$ – $(Ni_{0.8}Zn_{0.2})Fe_2O_4$ bilayer composite having a coherent interface and exhibiting high magnetoelectric sensitivity (Islam, 2006).

In this chapter, high-resolution scanning electron microscopy (SEM) investigation of the product microstructure of BTO–CFO polycrystalline solution that underwent eutectic decomposition has been carried out to compare the interface microstructure with that of co-fired bilayer composites. The interfacial microstructure of said composite was examined, revealing an elemental distribution and grain mismatching between BTO rich grains and a BTO-CFO matrix. Further, we report the magnetoelectric properties of near eutectic compositions. The focus in this study is on quantifying the interface effect rather than magnitude of the magnetoelectric coefficient.

2. Experimental

2.1 Powder preparation and sintering

Reagent-grade powders of $BaCO_3$, TiO_2, $CoCO_3$ and Fe_2O_3, were obtained from Alfa Aesar, Co. MA. USA. Stoichiometric ratios of the powders were mixed according to formulation $BaTiO_3$ (BTO) and $CoFe_2O_4$ (CFO) and ball milled separately for 24 hours with alcohol and YSZ grinding media (5mm diameter, Tosoh Co. Tokyo, Japan). After drying at 80^{o}C the powders were calcined. BTO powders were calcined at 900^{o}C for 3 hours and CFO powders were calcined at 1000^{o}C for 5 hours in separate alumina crucibles. After calcination the powders were crushed and sieved using a sieve of US mesh # 270. After that X-ray diffraction pattern of all different powders (BTO and CFO) were taken to check the formation of single phase perovskite (for BTO) or spinel (for CFO) using Siemens Krystalloflex 810 D500 x-ray diffractometer. Next, 30 and 35 mole% CFO powders were

mixed stoichiometrically with BTO powders. All the powders were mixed using alcohol and grinding media in a polyethylene jar and ball milled for 36 hours. The slurries were dried at 80°C, crushed and sieved with a stainless steel sieve of US mesh #170. The powders were then pressed to pellets of size 12.7x 1.5 mm^2 in a hardened steel die using a hydraulic press under a pressure of 15 MPa. For the bilayer composite, first BTO powders were pressed under 5 MPa pressure and the CFO powders were added on top of BTO powders. These powders were pressed together under 15 MPa pressure. Then the pellets were sealed in a vacuum bag and pressed isostatically in a laboratory cold isostatic press (CIP) under a pressure of 207 MPa. Pressureless sintering of composites was performed in air using a Lindberg BlueM furnace at 1250°C for 5 hours. Bilayer composite was sintered at 1200°C under the same condition. After firing the overall bilayer composite thickness was approximately 1.5 mm with ~1 mm thickness of the CFO and ~0.5 mm thickness of the BTO layer. The diameters of these fired samples were in the range of 10.4 – 10.6 mm.

2.2 Characterization

Microstructural analysis of the sintered samples was conducted by Zeiss Leo Smart SEM using the polished and thermal etched samples. In order to perform magnetoelectric and dielectric measurements, an Ag/Pd electrode was applied on the samples and fired at 850°C for 1 hour. The magnetic properties of the powder and sintered samples were measured by an alternating gradient force magnetometer (AGFM) at room temperature. The magnetoelectric coefficient (dE/dH) was measured by an A.C. magnetic field at 1 kHz and 1 Oe amplitude (H). The AC magnetic field was generated by a Helmholtz coil powered by Agilent 3320 function generator. The output voltage generated from the composite was measured by using a SRS DSP lock- in amplifier (model SR 830). The magnetoelectric coefficient (mV / cm.Oe) was calculated by dividing the measured output voltage by the applied AC magnetic field and the thickness of sample in cm. The sample was kept inside a Helmholtz coil, placed between two big solenoid coils and powered by KEPCO DC power supply. For frequency dependent magnetoelectric coefficient measurement, the Helmholtz coil was powered by the HP 4194 network analyzer (0.5 Oe AC field) and the voltage gain was measured on the secondary terminal. For this measurement, a DC bias of 200 Oe was used using a pair of Sm-Co magnet placed on top and bottom of the sample holder. This set-up produced constant 200 Oe DC bias as measured by the magnetometer. During the frequency dependent measurement, our system was limited to applied DC bias of 200 Oe.

3. Results and discussion

3.1 Structural characterization

Figure 1 (a) shows the X-ray diffraction patterns of calcined BTO and CFO powders. No other phase in addition to perovskite and spinel was detected. The approximate lattice parameter of BTO calculated from the XRD pattern was a = 3.994 Å and c = 4.05 Å where the tetragonality c/a is 1.014. The lattice parameter of CFO powder was calculated to be 8.337Å. Figure 1 (b) shows the composite diffraction pattern of BTO – 30 CFO and BTO – 35 CFO. Only perovskite and spinel peaks were observed in the diffraction pattern. Perovskite peaks are marked as P and spinel peaks are marked as S and the corresponding (hkl) indices are also noted in this figure. It can be seen in this figure that as the percentage of CFO increases, the intensity of perovskite peaks (e.g. P – (101) peak) decreases and the intensity of spinel peak (S – (311)) increases.

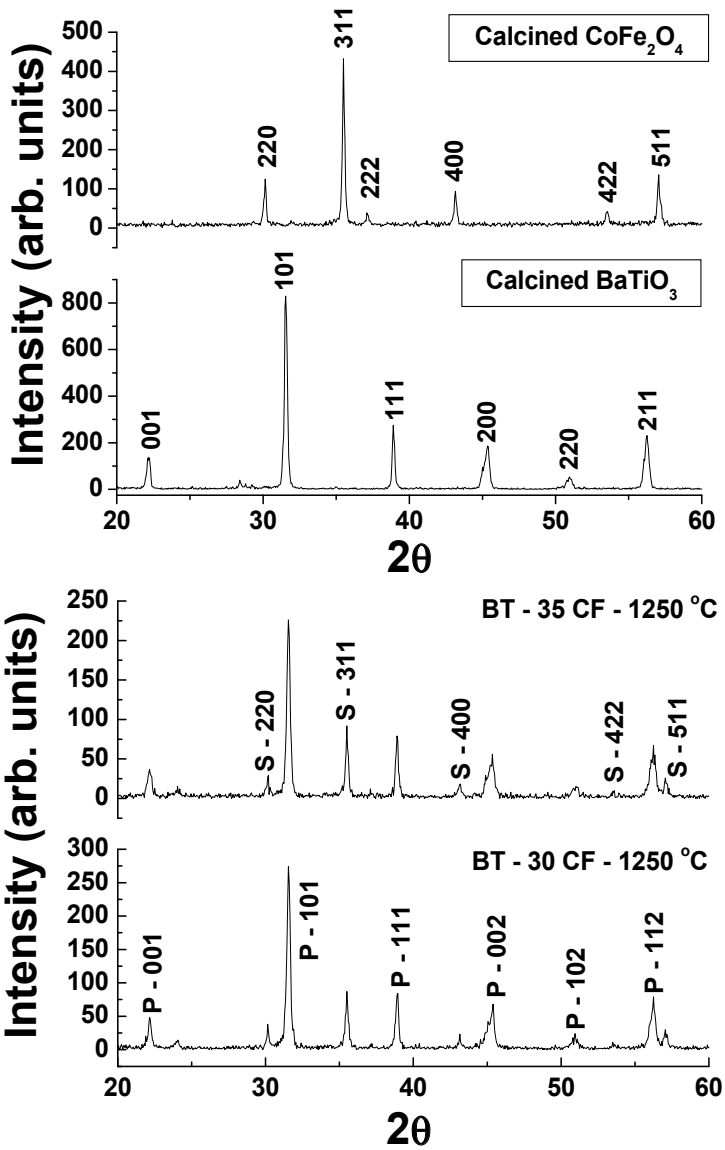

Fig. 1. (a) XRD patterns of calcined BTO and CFO powder and (b) XRD patterns of BT – 30 CF and BT – 35 CF magnetoelectric composite, sintered at 1250°C.

Figure 2 shows the SEM microstructure at low magnification (500X) for (a) BTO–30CFO, and (b) BTO–35CFO. The images reveal island-like structures comprised of multiple grains in a eutectic matrix, as marked in the images. EDS demonstrated that these multi-grain islands were BTO-rich, relative to the matrix that was constituted of a BTO-CFO solution. These microstructural features resemble those of hypo- and/or hyper-eutectic alloys in metallic systems. Some needle-shaped features, as indicated by arrows in Fig. 2 (b), were observed for BTO–35CFO, which were determined to be BTO-rich by EDS. In addition, clear interfaces were observed between the BTO-rich regions and the CFO-rich matrix.

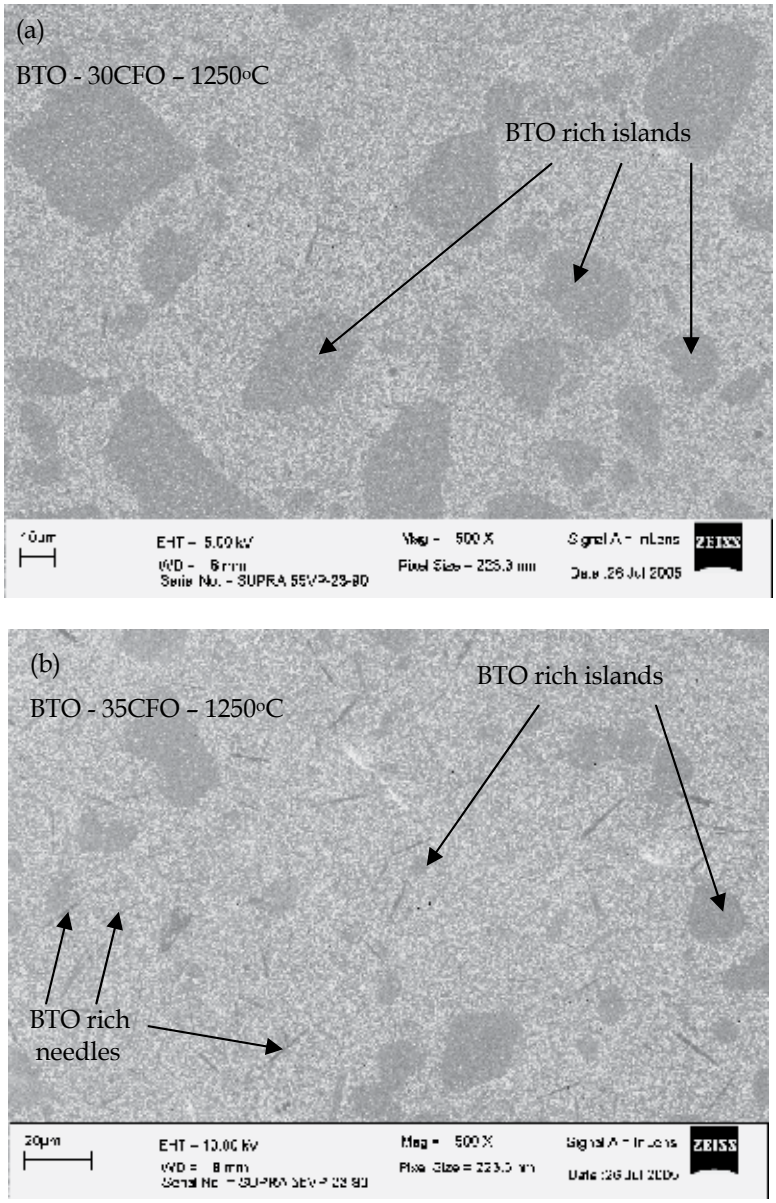

Fig. 2. SEM micrograph of BTO – CFO composites sintered at 1250°C, (Magnification: 500 X). (a). BTO – 30 CFO and (b) BT – 35CFO.

Figure 3(a) is a higher-resolution image showing the grain structure in the vicinity of an interfacial region between the BTO-rich islands and the CFO-rich matrix. A clear boundary between the strained BTO–CFO (i.e., matrix) and BTO-rich (i.e., multi-grain islands) phases is distinguishable, as indicated by dashed line. The deformation of the matrix can be seen by the formation of twin-bands, which reduces the excess strain imposed by the inclusions. Figure 2 also shows magnified (10^5X) images of the microstructure taken from (b) a BTO-rich island, and (c) the CFO-rich matrix. It can be seen that the grain sizes of both regions are

quite small: the average grain size in the BTO-rich islands was ~150nm and that of the CFO-rich matrix region was ~215nm. Due to the formation of $BaTiO_3$ – $CoFe_2O_4$, grain size increased as more $CoFe_2O_4$ and $BaTiO_3$ forms the matrix. Again in the matrix due to the lattice mismatch between $CoFe_2O_4$ (~8.337 Å) and $BaTiO_3$ (a = 3.994 Å and c = 4.05 Å) grain, it is possible to develop stress concentration inside the piezoelectric grain, and the result is presence of twin boundaries, cleavage, strain fields, absence of nanosized domain near the interface and large piezoelectric domain width observed in the matrix. On the other hand the $BaTiO_3$ rich phase has a uniform grain size, lower stress concentration and presence of piezoelectric domains.

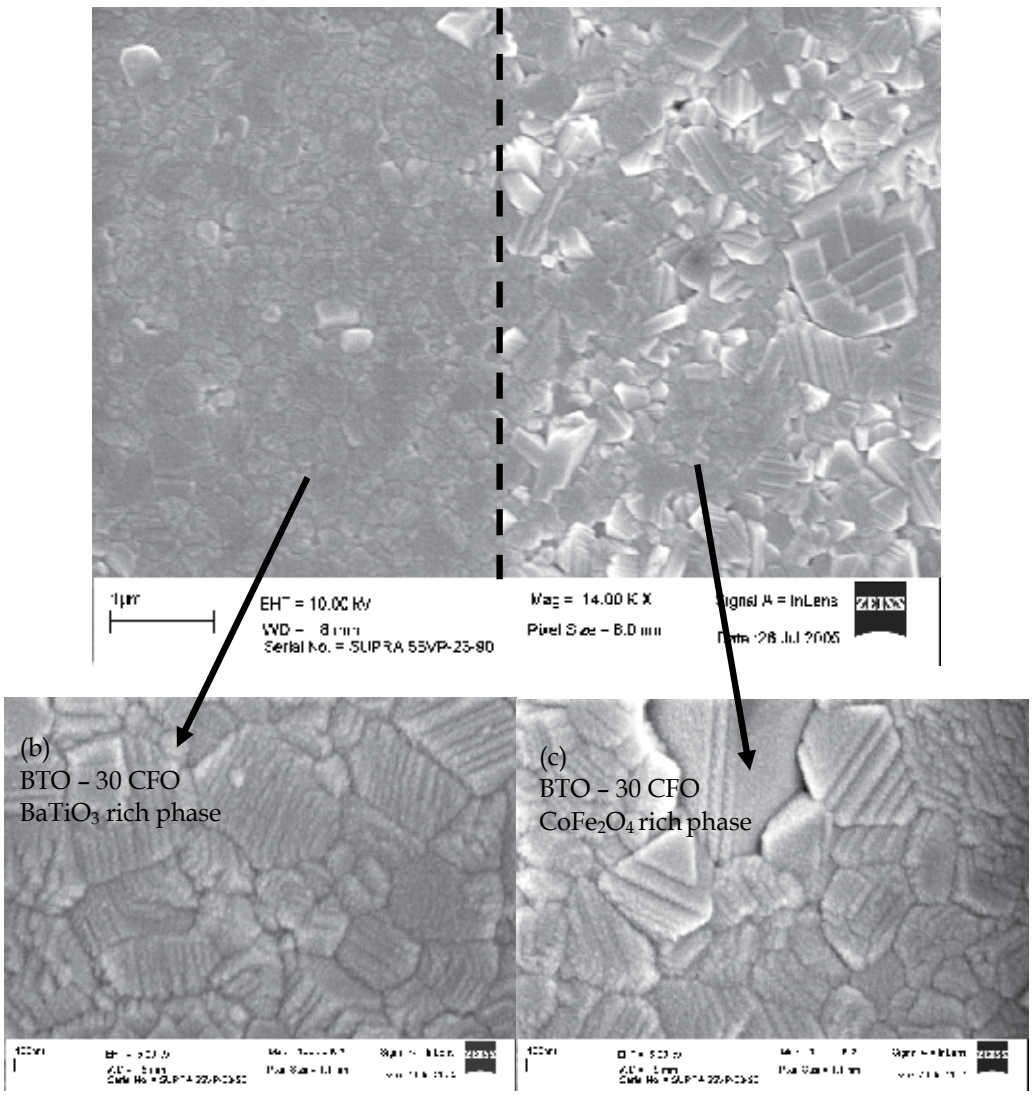

Fig. 3. Magnified SEM image of BTO – CFO magnetoelectric composites at the interface between the BT-rich region and the matrix. (a) interfacial region, (b) grain structure in the BT rich phase (100 kX) and (c) grain structure in the matrix (100 kX).

(a)
BT – 30 CF

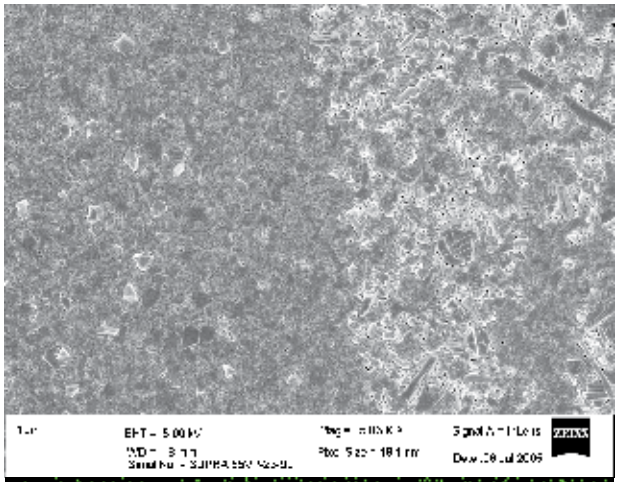

(b)
Co Map

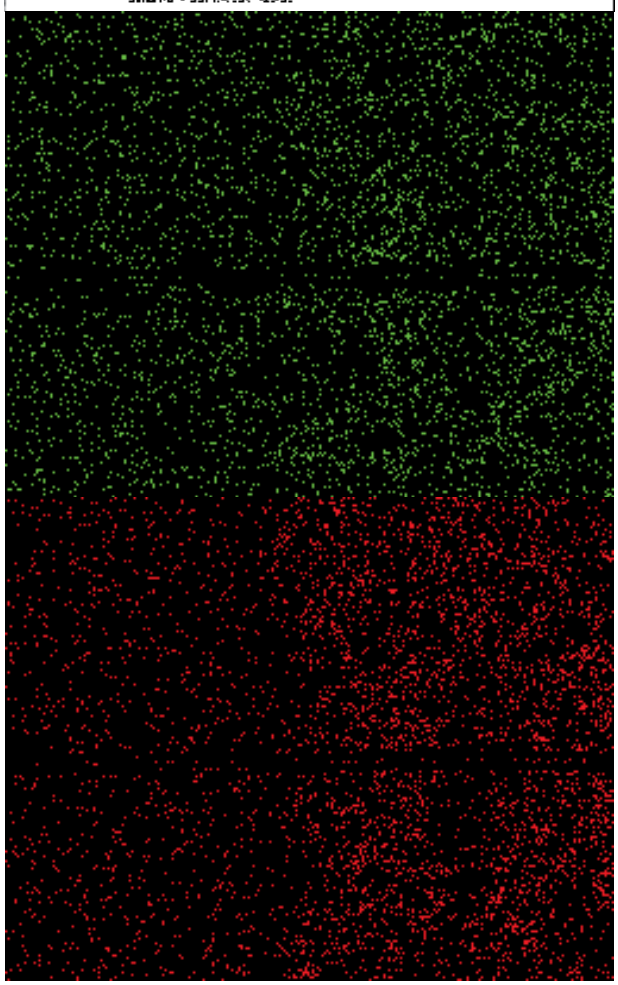

(c)
Fe Map

Fig. 4. Interface microstructure of 0.7 $BaTiO_3$ – 0.3 $CoFe_2O_4$. (a) SEM micrograph, (b) Co distribution and (c) Fe distribution.

Recently, Echigoya et al. have studied the interfacial structure of unidirectional solidified BTO–CFO eutectics, grown by a floating zone method (Echigoya, 2000). Two types of morphologies were found for different growth conditions, and based on HRTEM images the following orientation relationships between phases were identified (a) for hcp $BaTiO_3$: (111)CFO//(00.1)BTO and (110)CFO//(11.0)BTO; and (b) for tetra/cubic $BaTiO_3$: (001)CFO//(001)BTO and (100)CFO//(100) BTO. The results of Fig. 2 show that the polycrystalline ceramics also exhibit high degree of coherency across the interface, evidencing continuous grain growth. X-ray mapping of Co and Fe were done at the interface using Zeiss Leo Smart SEM and it is clearly noticed from the Figure 4 that Co and Fe is rich on the right side of the interface. In the $BaTiO_3$ rich phase, there is a uniform distribution of Co and Fe inside the piezoelectric matrix. EDX elemental analysis shows that, in the $BaTiO_3$ rich phase the atomic percentage of Co and Fe is around 10% and 7% whereas in the matrix, the atomic percentage of Co and Fe raised to 17.76% and 34.73%. These results are consistent with that expected if the BTO-rich regions constitute a hypo-eutectic phase, prior to eutectic decomposition.

Figure 5(a) and (b) shows the bright field TEM images of the sintered BTO – 30 CFO samples. The sintered samples were found to consist of high defect structures such as twin boundaries, cleavage, strain fields etc. in the BTO - CFO matrix which develop to accommodate the mismatch in the BTO and CFO lattices, as CFO lattice parameter is more than double the lattice parameter of BTO lattice. These types of structure usually show larger width domain patterns, characteristic of 90° domains and the intergranular heterogeneity in domain width is observed. The observed defects are in line with the SEM images. A finer scale domain structure, which usually has striation like morphology and periodically spaced, is almost absent in this structure which means that the structure is in a stressed condition. These finer domains appear when the stress is relieved from the structure.

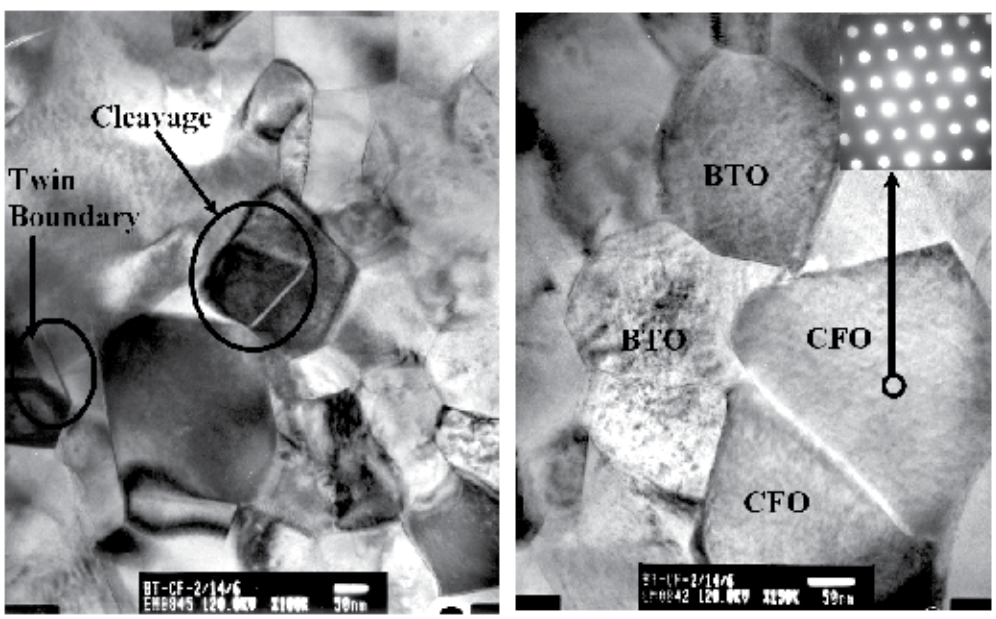

Fig. 5. TEM images of BT – 30 CF composite

Figure 6 shows the interface microstructure of BTO – 33.5 CFO co-fired bilayer composites. A very coherent interface is formed by sintering these two phases together. On the CFO side, an indication of the liquid phase sintering at the interface which may be due to the lower sintering temperature of CFO has been observed. This may be advantageous for accommodating the stress at the interface created in the CFO regions under ac magnetic field. Far from interface, the microstructure observed is single phase on either side.

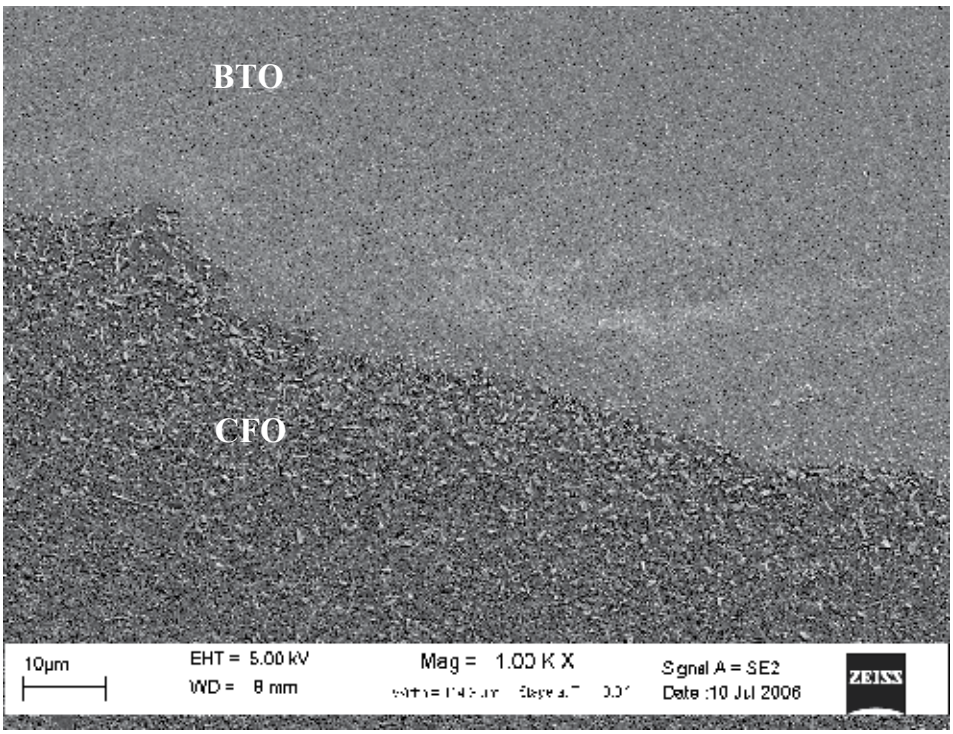

Fig. 6. SEM micrograph of the BTO-CFO bilayer composite.

3.2 Dielectric and ferroelectric characterization

Figure 7 shows the ferroelectric (polarization vs. electric field) and strain (% strain vs. electrical field) of BTO – 33.5 CFO cofired bilayer composite. The polarization of 35 $\mu C/cm^2$ and strain of about 0.14% was recorded at 4.5 kV/mm. Compared to the bilayer composite, the ferroelectric response for the sintered particulate composite was very weak due to the lower resistivity, which clearly indicates the problem in obtaining the larger ME coupling. Interface diffusion and ferrite connectivity reduces the resistivity and hence the decreases the ferroelectric response. Figure 8 (a) to (f) shows the temperature dependence of the dielectric constant and dielectric loss for BT – 30 CFO, BT – 35 CFO and BTO – 33.5 CFO bilayer composites at different frequencies. For bulk (BTO – 30 CFO and BTO – 35 CFO) composites, the maximum in the dielectric constant was found at 145^{o}C. At 100 Hz frequency, however no peaks were observed in the dielectric loss factor at that temperature as shown in Figure 8 (b) and (d). The sharp increase in the dielectric loss factor was observed for both the compositions at the high temperatures which are related to the space charge effect. A completely different behavior was found when the dielectric

constant and dielectric loss of BTO -33.5 CFO bilayer composite have been plotted in terms of temperature (Figure 8 (e) and (f)). Very sharp peak in dielectric constant was found at around 125 ^{o}C for all of the frequencies (except 100 kHz). This signifies the pure $BaTiO_3$ behavior. Again peaks were observed for dielectric loss at 125 ^{o}C for higher frequencies (10 and 100 KHz). In general BTO - 33.5 CFO bilayer composites found to be a lossy material where the dielectric loss was found to be around 0.4 at 1 kHz and room temperature.

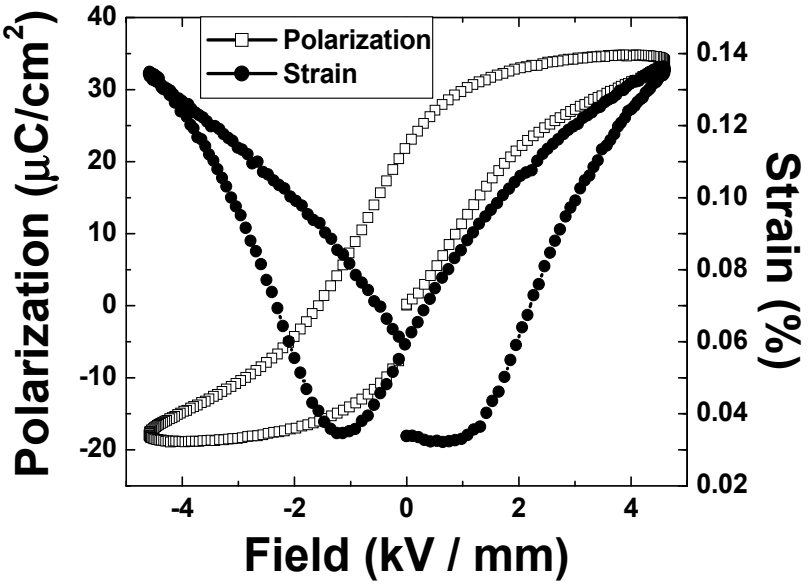

Fig. 7. Ferroelectric properties, polarization and strain as a function of electric field.

3.3 Ferromagnetic and magnetoelectric characterization

Figure 9 shows the magnetic properties for sintered BT – 30 CFO, BT – 35CFO and BTO – 33.5 CFO cofired bilayer composite. The co-fired bilayer composite shows higher saturation (0.881 emu) magnetization and slightly higher coercive field (973.33 Oe) than BTO – CFO bulk composite. BTO – 35 CFO shows saturation magnetization of 0.881 emu and coercivity of 973.33 Oe as indicated in Table 1. This is due to the contribution of pure CFO phase. Bilayer composite also shows better remnant magnetization than the bulk. Figure 10 (a) shows the variation of magnetoelectric coefficient as a function of dc bias. The bulk composites show the maxima at 1500 Oe with a ME coefficient of 2.2 mV/cm. Oe for BTO – 35 CFO. But for the bilayer composite it reaches a maximum value of 3.9 mV/cm.Oe and then saturates. The measurement has been taken in condition where the applied magnetic field is perpendicular to the sample surface. Figure 10 (b) shows the frequency dependent magnetoelectric coefficient. At around 430 kHz all the samples show giant magnetoelectric coefficient. BTO – 33.5 CFO bilayer composite exhibits ME coefficient around 3.6 V/cm.Oe and the BTO – 35 CFO bulk composite reaches around 0.95 V/cm. Oe. This is a very high magnetoelectric coefficient for BTO – CFO composite at resonance frequency, which is higher than the recent reported value of 2540 mV/cm.Oe at 160 KHz and 270 Oe DC bias for BTO – 20 CFO composite (Ren, 2005).

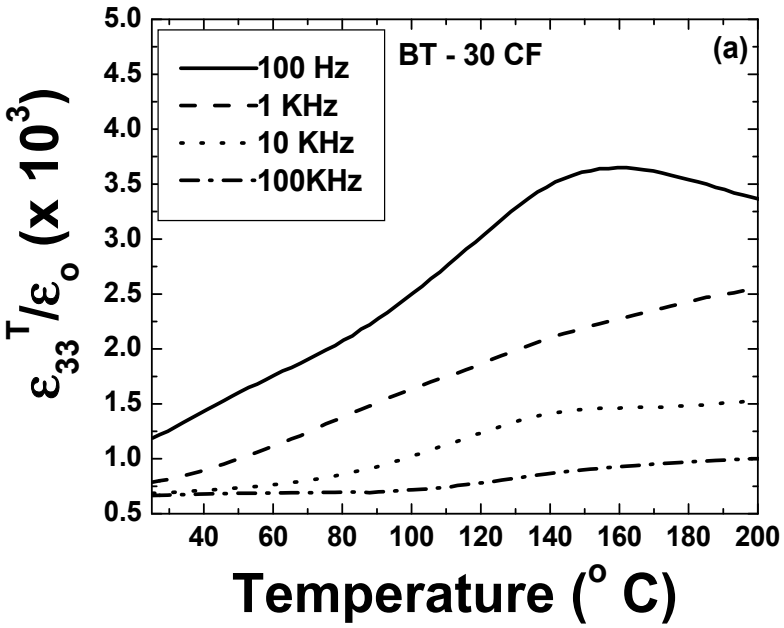
BT - 30 CF
(a)
100 Hz
1 KHz
10 KHz
100KHz
$\varepsilon_{33}^T/\varepsilon_o$ (x 10^3)
Temperature (^{o} C)

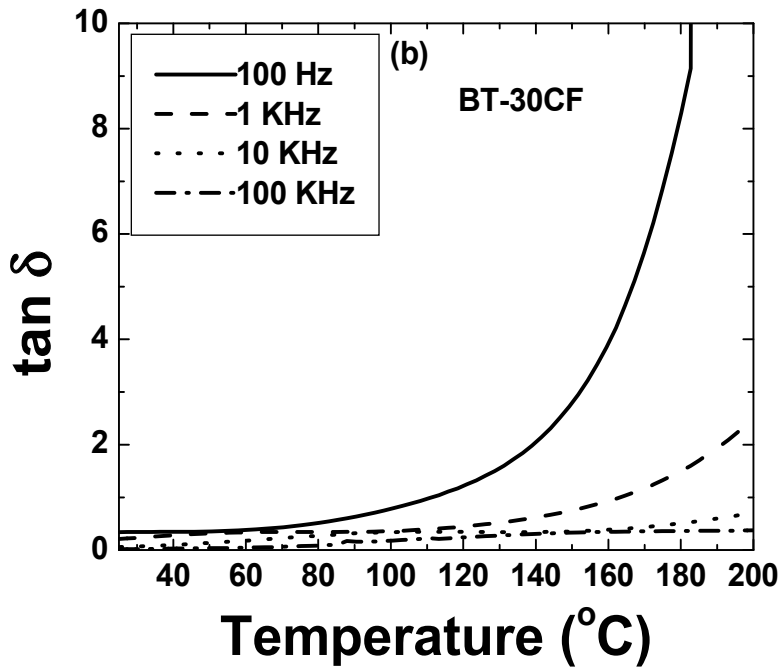
(b)
BT-30CF
100 Hz
1 KHz
10 KHz
100 KHz
tan δ
Temperature (^{o}C)

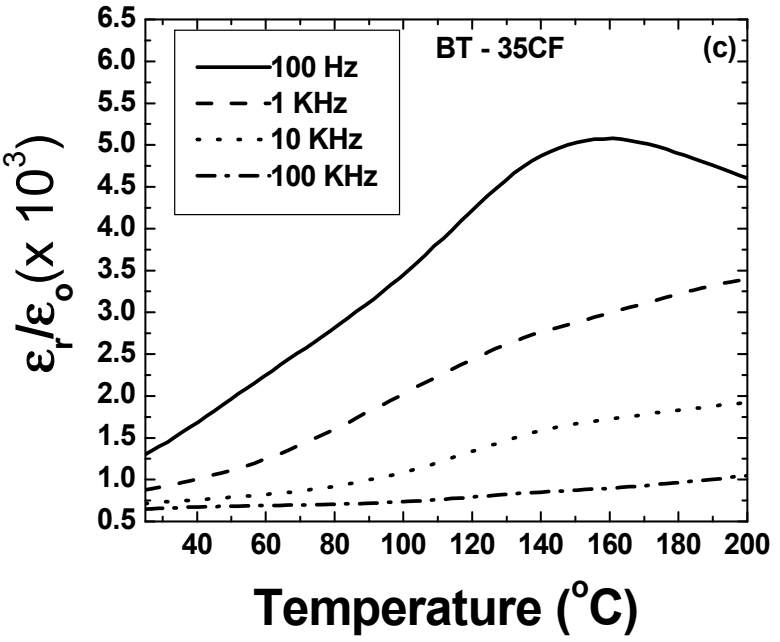
BT - 35CF
(c)
100 Hz
1 KHz
10 KHz
100 KHz
$\varepsilon_r/\varepsilon_o$(x 10^3)
Temperature (^{o}C)

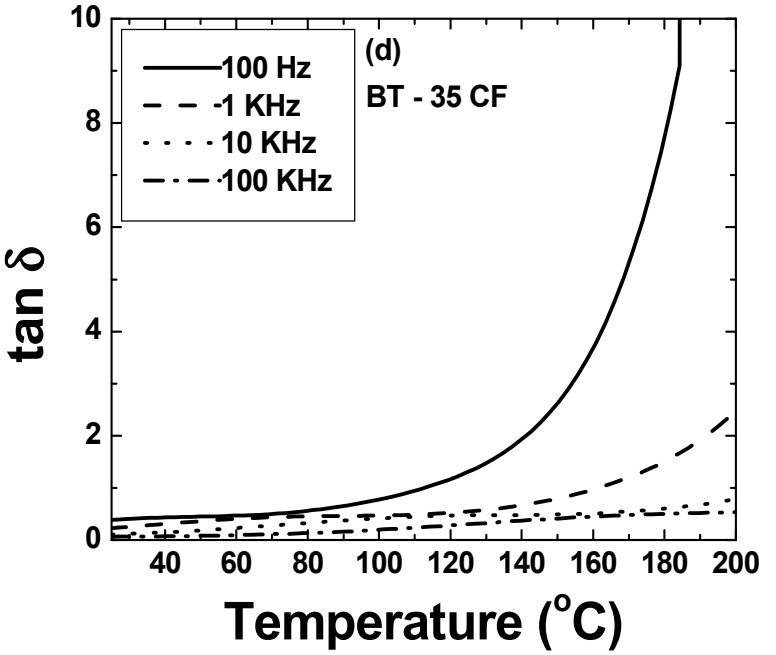
(d)
BT - 35 CF
100 Hz
1 KHz
10 KHz
100 KHz
tan δ
Temperature (^{o}C)

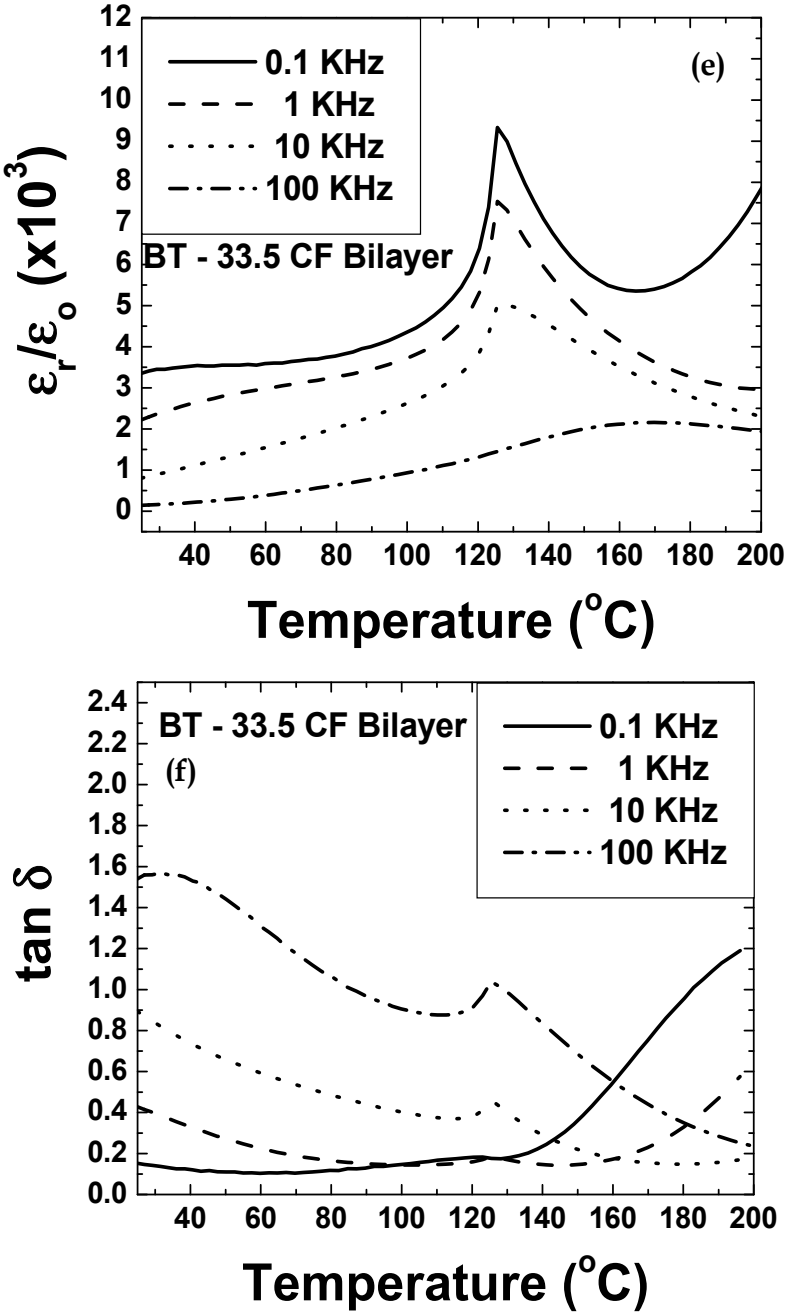

Fig. 8. Dielectric properties of BTO – CFO composites, (a) temperature dependent dielectric constant for BTO – 30 CFO, (b) temperature dependent dielectric loss for BTO – 30 CFO, (c) temperature dependent dielectric constant for BTO – 35 CFO, (d) temperature dependent dielectric loss for BTO – 35 CFO, (e) temperature dependent dielectric constant for BTO – 33.5 CFO and (f) temperature dependent loss constant for BTO – 33.5 CFO.

Analysis of low frequency ME effect in the layered CFO-BTO structures (Fig.10 (a)) can be conducted based on the equation for the longitudinal ME coefficient (Bichurin, 2003):

$$\alpha_{E,33}=\frac{E_3}{H_3}=2\frac{\mu_0 kv(1-v)\,{}^{p}d_{31}\,{}^{m}q_{31}}{\{2\,{}^{p}d_{31}^2(1-v)+{}^{p}\varepsilon_{33}[({}^{p}s_{11}+{}^{p}s_{12})(v-1)-v({}^{m}s_{11}+{}^{m}s_{12})]\}}\times$$
$$\times\frac{[({}^{p}s_{11}+{}^{p}s_{12})(v-1)-kv({}^{m}s_{11}+{}^{m}s_{12})]}{\{[\mu_0(v-1)-{}^{m}\mu_{33}v][kv({}^{m}s_{12}+{}^{m}s_{11})-({}^{p}s_{11}+{}^{p}s_{12})(v-1)]+2\,{}^{m}q_{31}^2kv^2\}}$$

The equation presented above allows for the determination of the longitudinal ME coefficient as function of volume fractions, physical parameters of phases and elastic-elastic interfacial coupling parameter k. From comparison of theory and data the importance of an interfacial coupling parameter between phases can be inferred. This interphase interfacial connection parameter was shown to be weak for CFO–BTO. In our case k is about 0.1. Estimation of ME effect in the EMR range (Fig.10(b)) has been performed using the above equation (Bichurin, 2003). Because of inconveniences in the analytical expressions for effective parameters of bulk CFO-BTO composites, computer calculations of the dependence of effective parameters on the relative piezoelectric phase volume in ME composite have been performed. Calculations of longitudinal ME coefficient have also been performed for electric and magnetic fields applied for bulk composites using the material parameters in (Harshe, 1993; Bichurin, 2010). The obtained values of the ME voltage coefficient coincide with previously published data. As follows from the comparison of obtained results, the ME voltage coefficient was approximately 20% greater than that calculated from the experimental data using the model. This is explained by the fact that the internal (local) magnetic field in the ferrite component is considerably different than that of the externally applied magnetic field.

	BTO – 30 CFO	**BTO – 35 CFO**	**BTO -33.5 CFO**
Coercivity (Oe)	646.77	677.49	973.3
Saturation magnetization (emu/ 100 gm)	0.557	0.702	0.881
Remnant magnetization (emu/ 100 gm)	0.246	0.279	0.345

Table 1. Magnetic Properties of BTO – CFO Composites

This question of 'why the elastic interaction in system with uniform distribution of two phases and coherent interfaces between the phases is weak' needs addressing. Our results indicate that the reasons for weak response may not be related to elastic-coupling between phases, but rather to the magnetic flux distribution within the matrix. Compared to the results of Philips Research Lab, the 1 kHz values reported here are quite low, which can be attributed to the process difference, polycrystalline matrix, nanograin structure and twin formation. In our research we used conventional sintering method compared to the unidirectional solidification of Philips Laboratory. In unidirectional solidification process, a significant amount of time is allowed to melt the components under desired atmosphere and then solidify with heat transfer confined along one direction. This results in the consolidation of the ferrite into dendrite structure, which hinders the distribution of the ferrite phases. Also the longer time helps the grain growth and unidirectional solidification

results in preferential texture. All these contributes to the larger ME coefficient. In our process smaller grain size (150 – 215 nm) results in lower ME coefficient and also the well dispersed ferrite particle reduces the resistivity of the overall bulk composite system. Grain size has significant effect on the magnitude of ME coefficient. Our previous results show that as the piezoelectric grain size drops below 200 nm, the ME coefficient drops rapidly (Islam, 2008). Finally in conventional sintering the grains are in random orientations and defects (such as twin boundaries, cleavage) in the structures are notable, all of which hinder the piezoelectric properties. The ME coefficient was notably higher for the bilayer, than for the eutectic composites. This comparison shows that coherent interfaces between composites of similar composition is not by any means the factor controlling the magnitude of the ME coefficient. Rather, continuity of flux lines is equally important for the expression of the ME product tensor property between phases.

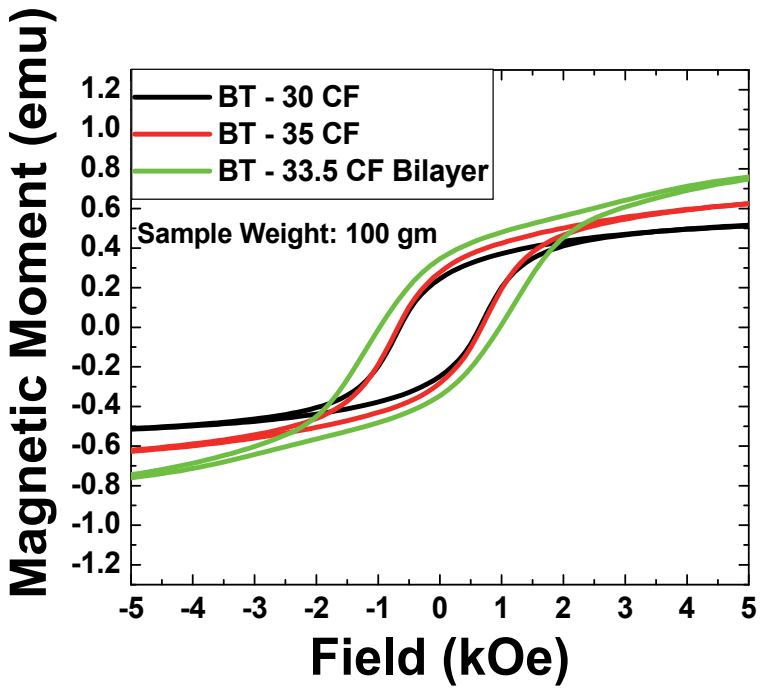

Fig. 9. Ferromagnetic Hysteresis loop of sintered BTO – 30 CFO, BTO – 35 CFO and BTO – 33.5 CFO bilayer magnetoelectric composites.

4. Conclusion

A microstructural investigation of $BaTiO_3$–$CoFe_2O_4$ polycrystalline solutions for compositions close to the eutectic point has been investigated along with dielectric, ferromagnetic and magnetoelectric behavior. Multi-grain BTO-rich islands were found in a CFO-rich matrix. Analysis of the interfacial regions revealed that the two phases have a high degree of coherency, enabling continuous grain growth. Also the bilayer type composite structure shows better performance as it shows very high magnetoelectric coefficient (3.6 V/cm. Oe) at high frequency (434 KHz).

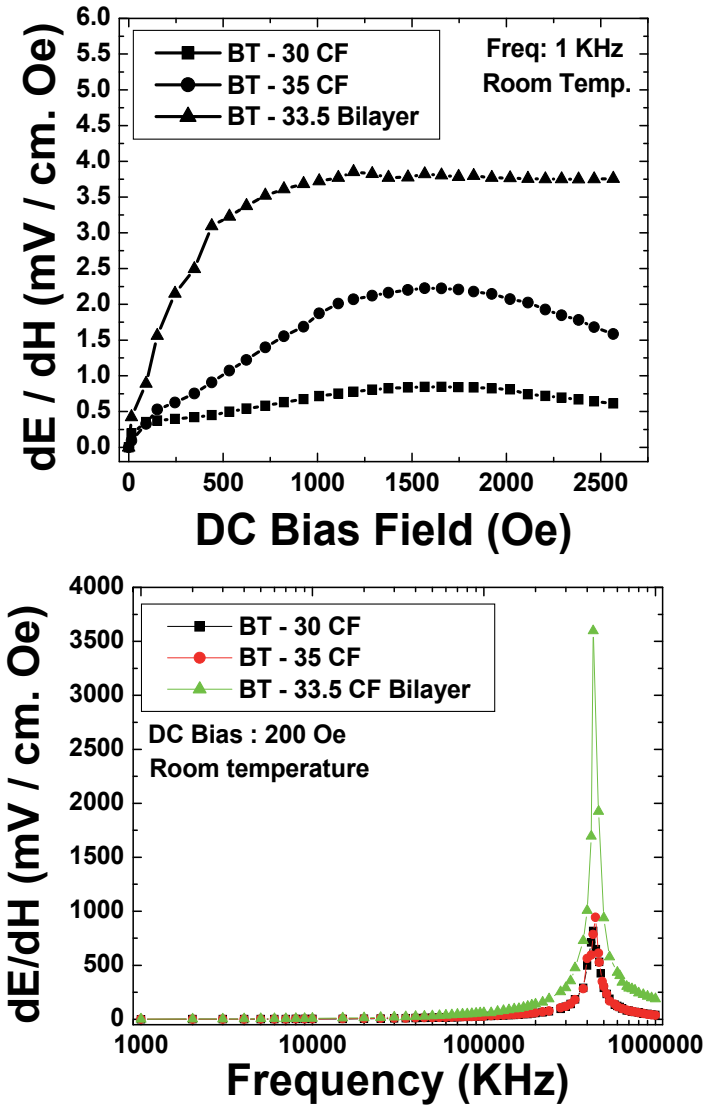

Fig. 10. Magnetoelectric Coefficient of different BTO – CFO composites as a function of (a) DC bias and (b) frequency.

5. Acknowledgement

The authors gratefully acknowledge the support from National Science Foundation INAMM program.

6. References

Astrov, DN. Al'shin, BI. Zhorin, RV. and Drobyshev, LA. (1968). *Sov. Phys. – JETP 28.* pp. 1123.

Astrov DN. (1960). *Sov. Phys. – JETP*, 11, pp. 708.

Bichurin, MI, Petrov, VM, Petrov, RV. et. al. (2002). Magnetoelectric microwave devices. *Ferroelectrics*, 280, 211.

Bichurin MI, Petrov VM, Srinivasan G. (2003) Theory of low-frequency magnetoelectric coupling in magnetostrictive-piezoelectric bilayers. *Phys. Rev.*, B68, pp. 054402.

Bichurin MI, Filippov DA, Petrov VM et al. (2003) Resonance magnetoelectric effects in layered magnetostrictive-piezoelectric composites *Phys.Rev*. B68, pp. 132408.

Bichurin MI, Petrov VM, Averkin SV, Filippov AV. (2010) Electromechanical resonance in magnetoelectric layered structures. *Physics of the Solid State*, 52, pp. 2116-2122.

Boomgaard JVD, Van Run AMJG and Suchtelen JV. (1976). Magnetoelectricity in Piezoelectric – Magnetostrictive Composite. *Ferroelectrics.* 10. pp. 295-298.

Boomgaard JVD and Born RAJ. (1978). A Sintered Magnetoelectric Composite Material $BaTiO_3$- Ni (Co, Mn) Fe_2O_4. J.Mater.Sci. 13. pp. 1538-1548.

Boomgaard JVD, Terrell DR, Born RAJ et. al. (1974) An insitu grown Eutectic Magnetoelectric Composite Material: Part I: Composition and Unidirectional Solidification. *J.Mater.Sci.* 9. pp. 1705-1709.

Dong S, Li J, and Viehland, D. (2003). Ultrahigh Magnetic Field Sensitivity in Laminates of Terfenol-D and $Pb(Mg_{1/3}Nb_{2/3})O_3$-$PbTiO_3$. *Appl. Phys. Lett.*; 83 [11]. pp. 2265-2267.

Dong S, Li J, and Viehland D (2003). Giant Magnetoelectric Effect in Laminate Composite. IEEE Trans. Ultrason. Ferroelec. Freq. Ctrl., 50 [10], pp. 1236-1239.

Dzyaloshinskii, IE. (1959). On the magneto-electrical effects in antiferromagnets. *Sov. Phys. JETP.* 10. pp. 628–629.

Echigoya J, Hayashi S and Obi Y. (2000) Directional solidification and interface structure of $BaTiO_3$-$CoFe_2O_4$ eutectic, *J. Mater. Sci.*, 35, pp 5587.

Feibig, M. (2005). Revival of Magnetoelectric Effect. *J.Phys. D: Appl. Phys.;* 38, pp. R123-R152.

Harshe G, Dougherty JP, Newnham RE. (1993). Theoretical modeling of multilayer magnetoelectric composites, *Int. J. Appl. Electromagn. Mater.,* 4, pp. 161.

Islam RA and Priya S. (2006). Magnetoelectric properties of the lead--free cofired $BaTiO_3$-$Ni_{0.8}Zn_{0.2}Fe_2O_4$ bilayer composite. *Appl. Phys. Lett,* 89, 152911.

Islam RA and Priya S. (2008), Effect of piezoelectric grain size on magnetoelectric coefficient of $Pb(Zr_{0.52}Ti_{0.48})O_3$-$Ni_{0.8}Zn_{0.2}Fe_2O_4$ particulate composites *J. of Mater. Sci.,* 43 (10), pp. 3560.

O'dell TH. (1965). Magnetoelectrics – A New Class of Materials. *Electronics and Power*. 11. pp. 266-268.

Prellier W, Singh MP and Murugavel P. (2005). The single-phase multiferroic oxides: from bulk to thin film *J. Phys: Condensed Matter.,* 17, R803.

Ren SQ, Weng LQ, Song SH et. al. (2005) $BaTiO_3$/$CoFe_2O_4$ particulate composites with large high frequency magnetoelectric response *J. Mater. Sci.* 40, pp. 4375.

Ryu J, Priya S and Uchino K. (2002). Magnetoelectric Effect in Composites of Magnetostrictive and Piezoelectric Materials. *J. Electroceram*. 8, pp. 107- 119.

Ryu J, Priya S, Uchino K, Viehland D et. al. (2002). High Magnetoelectric Properties in $0.68Pb(Mg_{1/3}Nb_{2/3})O_3$-$0.32PbTiO_3$ Single Crystal and Terfenol-D Laminate Composite. *J. Korean Ceram. Soc.* 39. pp. 813-817.

Ryu, J, Priya, S, Carazo, AV et. al. (2001). Effect of the Magnetostrictive Layer on Magnetoelectric Properties in Lead Zirconate Titanate/Terfenol-D Laminate Composites, J. of Amer. Ceram. Soc. 84 (12). pp. 2905 – 2908.

Ryu J, Carazo AV, Uchino K, et. al. Piezoelectric and Magnetoelectric Properties of Lead Zirconate Titanate/Ni-Ferrite Particulate Composites. *J. of Mater. Sci.* 7 (1). pp. 17 – 24.

Smolensky, G. and Ioffe, VA. (1958). *Colloque International du Magnetisme*; Communication No. 71.

Suchtelen, JV. (1972). Product Properties: A New Application of Composite Materials. *Philips Research Report*, 27, pp. 28 – 37.

Van Run AMJG, Terrell DR, and Scholing JH. (1974) An insitu grown Eutectic Magnetoelectric Composite Material.

Magnetoelectric Composite Material. Part II: Physical Properties. *J.Mater.Sci.* 9. pp 1710 - 1714.

5

Impact of Defect Structure on 'Bulk' and Nano-Scale Ferroelectrics

Emre Erdem and Rüdiger-A. Eichel
Institut für Physikalische Chemie I, Universität Freiburg, Albertstr. 21, D-79104 Freiburg Germany

1. Introduction

Ferroelectric materials offer a wide range of dedicated physical properties such as high dielectric constant, spontaneous polarisation, pyroelectric and piezoelectric effects which can be applied in thin-film non-volatile memories or 'bulk' actuators, multi-layer capacitors, thermal sensors and transducers (1–3). In that respect, desired materials properties for specific applications may be tailored by controlling the defect structure by means of aliovalent doping, rendering so-termed *'hard'* or *'soft'* piezoelectric materials (4–6).
Another important impact on ferroelectric properties results from the confined size in nano-scale architectures (7). At the nanometer scale physical and chemical properties are expected to differ markedly from those of the 'bulk' material. Owing to a *size-driven phase transition*, a critical particle size exists below which ferroelectricity does no longer occur (8).
In this chapter, we will first outline the nature of the *size-driven* para-to-ferroelectric phase transition, as well as the concepts of *defect chemistry*. On that basis, the interplay between confined size at the nano-regime and the development of defect structure will be characterized. The here studied ferroelectric lead titanate nano-powders may be considered as a model system for more complex ferroelectric nano architectures (1; 2). Furthermore, the results discussed here may be transferred to large extent to other important perovskite oxides with divalent A- and tetravalent B-site, such as $BaTiO_3$ or Pb[Zr,Ti]O_3 (PZT). The defect chemistry of ferroelectric perovskite oxides with monovalent A- and pentavalent B-site, such as the [K,Na]NbO_3 (KNN) solid solution system, however has shown some important deviations from the defect structure characterized for PZT compounds (9; 10).

2. Synthesis of perovskite oxide nano-powders

Many different strategies have been employed in recent years to synthesize ferroelectric nano-powders. These include hydrothermal (11), alkoxide (12), co-precipitation (13) and sol-gel (14) techniques. The main drawback associated with the above-mentioned routes is the agglomeration of particles, which prevents the synthesis of ultra-fine nano-powders. This problem may be overcome by two alternative methods – the *combined polymerization and pyrolysis* (CPP) technique (15; 16) and the *high-energy ball milling* (HEBM) cold mechanical alloying (17; 18). In particular, both methods provide the opportunity to homogeneously incorporate aliovalent transition-metal or rare-earth dopants with concentrations ranging between $10^{-2} - 10^{0}$ mol%.

2.1 Combined polymerization and pyrolysis

The CPP-route starts from a monomeric metallo-organic precursor through combined solid-state polymerisation and pyrolysis (15; 16). Adjustment of various mean particle sizes is obtained by choosing appropriate calcination temperatures. A remarkable optimization of the CPP route is obtained by applying special tempering conditions, e.g. oxidative atmosphere or quenching into a non-equilibrium state. With this technique, ultrafine $PbTiO_3$ powders down to 5 nm mean grain size result (15). CPP based nano-particles are characterized by a comparatively high reaction homogeneity, particularly in the polymerization step. The particle sizes may further by decreased by subsequently applying to high energy ball milling. Recent results of the CPP technique include the synthesis of nano-scale $BaTiO_3$ (19) and $PbTiO_3$ powders (15; 16) with mean particle sizes ranging from 150 nm down to 5 nm.

The corresponding results from differential thermogravimetric analysis (DTA) (weight loss, blue line) and differential scanning calorimetry (DSC) (thermal change) of the CPP precursor are given in figure 1(a). The TGA results show exothermic changes in specific temperatures (assigned in figure 1(a)) of the precursor due to the CPP formation reactions, as well as evaporation of various volatiles and phase changes of the crystal. The CPP of $PbTiO_3$ is initialized around 510 K and peaking at 530 K coupled by the polymerization of $-C = C-$ double bonds in the methyacrylate part of the ligand from the precursor (15). The pyrolysis of the hydrocarbons occurs at 554 K and is followed by formation of $PbTiO_3$ ($T_{max} = 554$ K) while release of carbon and other volatiles processed. The deconvolution of the two main overlapping peaks between $740 - 770$ K corresponds to the complete combustion and evaporation of amorphous organic residues (753 K). The ferro-to-paraelectric phase transition occurs at the Curie temperature for $PbTiO_3$ (763 K). Further heating of the sample gives rise to mass losses due to PbO evaporization.

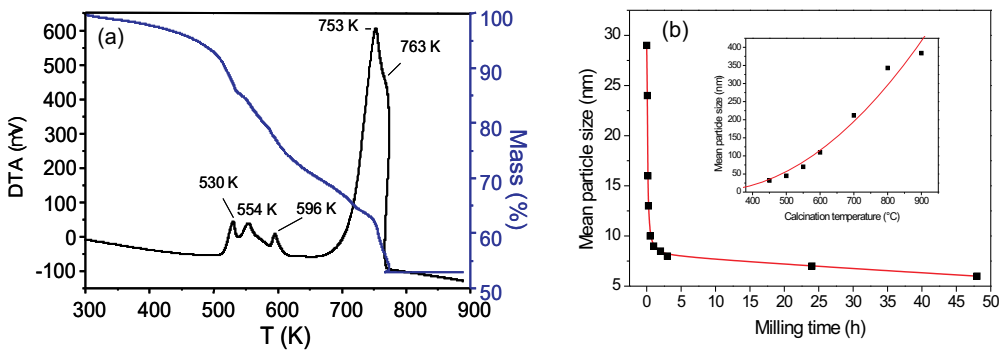

Fig. 1. (a) - differential thermogravimetric analysis (weight loss) and differential scanning calorimetry (thermal change) of the precursor. (b) - mean particle size as function of calcination temperature. The inset shows the variation in mean particle size as function of different ball-milling times.

As function of calcination temperature, the mean particle size of the nano-powders can be controlled, as shown in figure 1(b). The corresponding mechanism is the following: (*i*) a low calcination temperatures gives the smallest particle size and increasing the temperature gives much larger patrticle size, (*ii*) applying additionally high-energy ball milling to the smallest particles obtained after calcination, even smaller particle sizes result (see inset in figure 1(b)). Moreover, this method allows to introduce dopants by resolving the corresponding metal

ions into the solution. In addition it is observed that after calcination the solid-state solution exhibits a rate of homogeneous.
A special advantageous feature of the CPP-preparation route is its ability to introduce small amounts of dopant ions, such as Cr^{3+}, Mn^{2+}, Fe^{3+}, Cu^{2+} or Gd^{3+} for instance, by just adding the corresponding metal acetates to the monomeric precursor.
Although the CPP-route offers a flexible preparation technique to obtain different mean particle sizes as function of appropriate calcination temperature and atmosphere, the particle-size distribution typically is rather broad. In addition to that, nano-particles below 20 nm proved being largely amorphous. These problems can be circumvented by performing ball milling subsequent to the CPP-route. The most important advantages of CPP-route are its excellent control over particle size, shape and morphology (phase purity) by adjusting the calcination temperature.

2.2 High-energy ball milling

An alternative strategy to synthesize nano-grained ferroelectric compounds is the use of cold mechanical alloying by means of high-energy ball milling. Varying mean grain sized can be obtained by different milling times. The here presented HEBM nano-powders were obtained for milling times in an interval between milling times 1 and 50 h at a speed of 300 rpm and a ball-to-powder weight ratio of 10:1.
The advantage over the above mentioned CPP-route, which requires a calcination step at an elevated temperature to convert the precursor into the ferroelectric phase, is that this technique virtually is performed at ambient temperature. Furthermore, there is no need of high-purity inorganic or organometallic chemicals for the starting materials, thus offering an inexpensive processing route and additionally overcoming problems associated with high sensitivity to moisture which typically requires special precaution and handling.
An advantage in common concerning the use of ferroelectric nano-powders as compared to the standard high-temperature mixed-oxide solid-state reaction techniques is that dense ceramics may be obtained at considerably lower sintering temperatures owing to the inherent high rate of homogeneity of the synthesized nano-powders. This argument particularly is relevant for the synthesis of lead-containing ferroelectric compounds, such that the loss of PbO at high temperatures can be markedly reduced.

3. Size-driven para-to-ferroelectric phase transition

The most prominent impact of lead titanate nano-powders is that a *size-driven phase transition* from the ferroelectric to the paraelectric state can be observed below a critical mean particle size at ambient temperature. In the following section, we briefly outline the theoretical foundations describing the size-driven phase transition by means of the Landau-Ginzburg theory, as well as summarize experimental results monitoring the phase transition on various length scales.

3.1 Landau-Ginzburg theoretical description of the size-driven phase transition

The phenomenological *Landau-Ginzburg theory* (LGT) furnishes a systematic basis to discuss the phase transition properties of bulk ferroelectrics (20–22). In recent years several attempts were made to extend the LGT to nanolayers (23–25) and nanoparticles (26–31). Starting from the total free energy of a infinite-size and homogeneous ferroelectric, the latter two gradient and surface terms were added for a finite-size ferroelectric particle

$$F = \int_V dV \left[\frac{1}{2} A'(T - T_C) P^2 + \frac{1}{4} B' P^4 + \frac{1}{6} C' P^6 + \frac{1}{2} D' (\nabla P)^2 \right] + \frac{D'}{2\delta} \int_S dS \; P^2 \qquad (1)$$

Obviously, the gradient and surface terms are only of relevance in an outer shell. They comprise the surface field contribution in the formation of the polarisation gradient. The effect of the surface on the polarisation is taken into account through the concept of the extrapolation length d (24; 26; 27). In solving the pertinent *Euler-Lagrange* equation for minimising the free energy, the polarisation is obtained considering the boundary condition according to the extrapolation length conception.
The size dependence of the polarization and the Curie temperature of ferroelectric particles with a first-order transition were studied in the previous study (8) where different polarization quantities refer to (i) polarisation at the particle centre (ii) average polarization of the particle (iii) polarization at the particles outer boundary, and (iv) polarisation difference between particle centre and border.
Because of the electrostrictive coupling between lattice strain and polarization in perovskite-type ABO_3 systems, the deformation of the tetragonal unit cell depends on the polarization, and particularly the tetragonality $(\frac{c}{a} - 1)$ is proportional to the square of P_s (32). As a result, the variation of P_s involves a change of the c/a-ratio near the nano-particle surface. For $PbTiO_3$ nano-particles, the LGT predicts a critical size of $d_{\text{crit}}^{\text{LGT}} = 4.2$ nm (26), whereas the hitherto experimentally estimated critical size amounts to $d_{\text{crit}}^{\text{exp}} = 12.6$ nm (33). This discrepancy for controversial values of d_{crit} can be attributed to the polarization gradient, a nano-crystalline surface layer and the depolarization effect. The effect of a depolarization field (E_d) and a space-charge layer on the Curie temperature T_C shift was comprised within a finite-size multi-domain model of a cubic ferroelectric particle (34). On the other hand, a phenomenological theory of the size-dependent dielectric susceptibility (28) was based on spherical ferroelectric particles, thereby unfortunately disregarding the surface energy which plays a decisive role in the physics of nano-materials. Finally a model was proposed (30) which gives due consideration to the depolarisation field E_d and also includes the surface and domain-wall energies.
However, a homogeneous comprehensive theory was not yet elaborated so far, and existing models yield rather scattering d_{crit} values. Nevertheless, very recent Landau phenomenological theory calculations for confined ferroelectric nanoparticles are very good agreement with experimental results (35).

3.2 X-ray diffraction

The size-driven phase transition can be directly monitored by considering the corresponding XRD patterns of the nano-powders as function of mean grain size. In figure 2 the XRD patterns of nano-powders obtained by CPP and HEBM are compared to each other.
All observed reflexes can be explained by the perovskite structure. For the 'bulk' $PbTiO_3$ component, the corresponding reflexes are indexed. In figure 2(a) the XRD patterns for the nano-powders obtained from CPP are shown. All nano-powders exhibit Bragg reflexes characteristic for the $PbTiO_3$ crystal structure. With decreasing mean particle size, the (001) and (100) reflexes that belong to the crystalline lattice constants, a and c, approach each other. This indicates the corresponding size-driven ferro-to-paraelectric phase transition from tetragonal to cubic crystal symmetry. Furthermore, for the nano-scale particles, the reflexes are considerably broadened, which hinders further structural refinement.
Figure 2(b) compares the XRD patterns for nano-powders obtained by HEBM for varying milling times. The determined c/a-ratio of the $PbTiO_3$ powders decreases from 85 to 20 nm, when varying the milling time from 30 to 50 h.

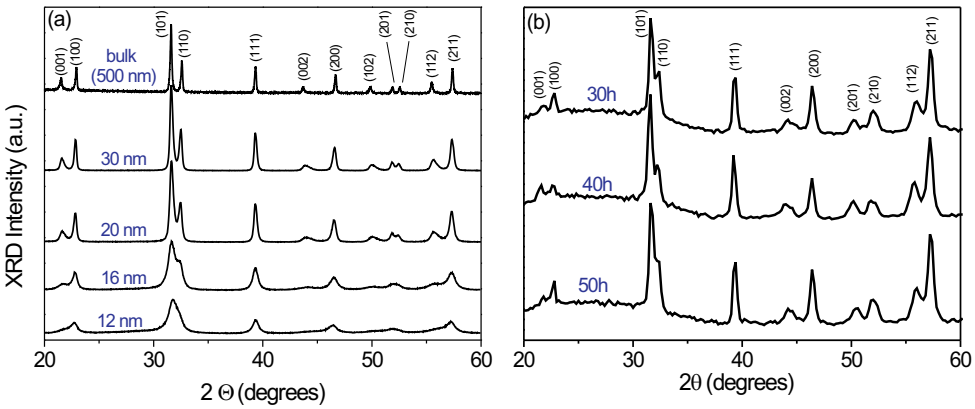

Fig. 2. XRD patterns lead titanate nano-powders as function of mean grain size. (a) - $PbTiO_3$ nano-powders as synthesized by the CPP-route for varying calcination temperatures. (b) - $PbTiO_3$ nano-powders as synthesized by HEBM for varying milling times.

3.3 Raman spectroscopy

A microscopic description of the ferroelectric behavior requires the consideration of lattice dynamics by means of the *soft-mode theory*. Accordingly, in the ferroelectric phase the $PbTiO_3$ cations are displaced from the centre of the anion lattice, resulting in an inner electric field with a permanent electric moment and a spontaneous polarization. Contrary, in the paraelectric phase $PbTiO_3$ has cubic symmetry and can be polarized along any of the three equivalent 4^{th}-order axes. Upon the transition to the tetragonal symmetry, one direction is chosen as the crystallographic *c*-axis and is associated with a characteristic lattice vibrational mode, either acoustic or optical. In the paraelectric phase all ions move collectively with the same phase, whereas in the ferroelectric phase anions and cations move independently of each other with opposite phases. Both modes can be of longitudinal or transversal type and their frequency depends on temperature. When a ferroelectric phase transition takes place, the transversal optical mode exhibits an instability and its frequency decreases towards zero, i.e. it 'softens'. At T_C the mode is 'frozen' and the mode frequency reaches zero. This enables a rise of a non-zero order parameter and lowers the crystal symmetry. Such a vibrational mode is called '*soft mode*'. In case of nano-particles it is aimed that softening occurs not by temperature but by reduction of lattice parameters, hence particle size.

Correspondingly, Raman spectroscopy can be employed to study the occurrence of soft mode as function of mean grain-size. The corresponding Raman-spectra are depicted in figure 3. In figure 3(a) the Raman spectra as function of mean particle size are shown, where the corresponding phonon modes are assigned according to 'bulk' $PbTiO_3$ (36).

Assuming a strong correlation between the crystalline unit-cell dimensions (*a*, *c*) and the longitudinal optical (LO) and transversal optical (TO) phonon modes, with decreasing mean particle size, the LO modes shift to higher wave numbers whereas the TO modes are shifted to lower wave numbers. More importantly, the soft-mode becomes weaker for small particle sizes and finally disappears below a critical particle diameter, d_{crit}, indicating the transition from a ferroelectric to a paraelectric nano-powder. This observation may be explained by considering that for nano-sized compounds the quotient between number of atoms at the

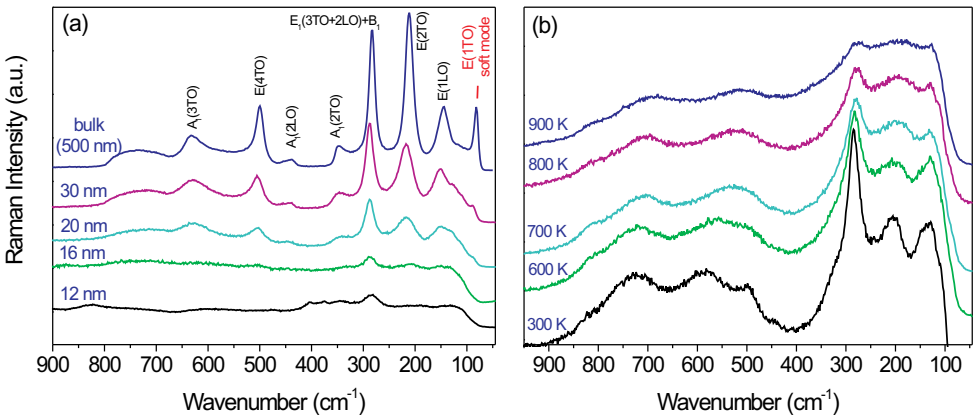

Fig. 3. Raman spectra of $PbTiO_3$. (a) - Raman spectra as function of mean grain size. (b) - Raman spectra as function of temperature.

surface and atoms in the bulk markedly increases. Accordingly, short-range forces become more dominant as compared to long range forces. As a consequence, a *size-driven phase transition* occurs, such that the Curie temperature for bulk $PbTiO_3$, $T_C = 766$ K is reduced to a value below ambient temperature.
This size-driven phase transition is compared to a temperature-induced phase transition for a specimen of 16 nm mean grain size (cf. (figure 3(b)). By increasing the measuring temperature similar Raman lines occur as observed fo a 'bulk' sample. However, above 700 K the Raman lines start to disappear. This is around 60 K lower than the value of bulk T_C, indicating a reduction in the value of T_C at 16 nm mean grain size.

3.4 X-ray Absorption Near Edge Structure

The size dependent X-ray Absorption Near Edge Structure (XANES) of $PbTiO_3$ gives significant information about the nature of phase transitions. We find that we can quantitatively relate the local structure of several Ti perovskites with the pre-edge and post-edge peaks in their XANES spectra. Here, the size effect on Ti *K*- edge and Pb *L*3-edge XANES spectra is investigated. In order to characterize the local structure of the $PbTiO_3$ nano-powders, XANES at Ti *K*-edge and Pb *L*3-edge was compared to the 'bulk' compounds. The corresponding XANES-spectra are shown in figure 4. The pre-edge features (labeled as **A** and **B** in figure 4) are atrributed to quadrupolar transitions of t_{2g}-type orbitals situated in the absorption Ti-atom (37). The transition **A** is caused by hybridization of $p-$ and d-symmetry states at the Ti-atom under the influence of the neighboring oxygen atoms that takes place if the inversion symmetry is broken relative to the absorbing atom position (37). The pre-edge feature **B** is refered to the Ti 1*s*-electron transition to the unoccupied 3*d*-states of the neighbouring Ti-atoms and the transition occurs if there are 4*d*-atoms in the neighbourhood of the absorbing Ti-atom (37; 38).
The transitions labeled **C**, **D**, **E**, **F** and **G** at energies above the absorption edge are related to electronic transitions and to the atomic structure of second and third-nearest neighbours of Ti within distances up to 1.0 nm (37; 38). The pre-edge features labeled as **C**, **E** and **F** in the spectrum for the bulk ferroelectric do not appear in the spectrum for the nano-structured sample.

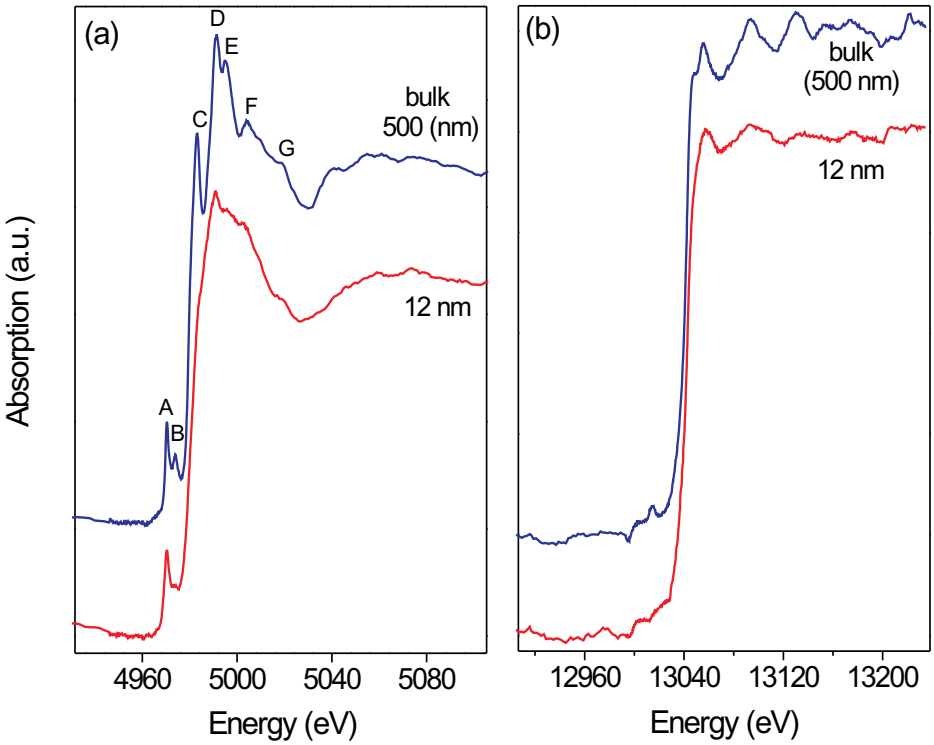

Fig. 4. X-ray Absorption Near Edge Structure spectra of 'bulk' and nano-scale $PbTiO_3$ powders. (a) - Ti *K*-edge. (b) - Pb L_3-edge.

It is noteworthy to say that the experimental results that we obtained are in very good agreement with the simulation of XANES spectra given in literature (37). Pb *L*3-edge XANES spectrum showed in Figure 4 the absorption features after the edge are related to the internal transitions between the 2p and the empty d states in Pb^{2+} ions (37).
Overall, as compared with the 'bulk' sample (500 nm), the 12 nm sample yields broadened spectral features, concerning pre-edge structures (**A**-**D**) and the post-edge (**E**-**G**) structures. Clearly, if the mean particle size falls below a critical value (ca. 6 nm), any translational symmetry is largely removed and the idea of persistent tetragonal structural units no longer stays. Changing of symmetry translates into more diffuse scattering pathways and results in the smearing of Ti *K*- edge XANES features, indicating structural transition from tetragonal phase to cubic phase, in other words a transition from ferroelectric-to-paraelectric phase.

3.5 EPR-spectroscopy

In order to monitor the size-driven phase transition on an atomic level, electron paramagnetic resonance (EPR) spectroscopy has been applied. As a paramagnetic probe ion Cr^{3+} has been incorporated into the $PbTiO_3$ lattice (15). In that respect, Cr^{3+} is a very suitable probe ion, because ionic size is very close to that of Ti^{4+} and furthermore, trivalent Cr^{3+} is a high-spin

ion ($S = \frac{3}{2}$) which sensitively probes subtle structural changes by means of its quadrupole fine-structure interaction.
The corresponding EPR spectra for Cr^{3+}-doped $PbTiO_3$ nano-powders are illustrated in figure 5(a) for varying mean particle sizes, as compared to a bulk Cr^{3+}:$PbTiO_3$ compound measured at varying temperature (cf. figure 5(b)).
First, the *size-driven phase transition* of Cr^{3+}:$PbTiO_3$ nano-powders is considered (figure 5(b,d)). For nano-powders of mean grain-size above a critical value ($d > d_{\mathrm{crit}}$), the EPR spectra are characteristic of a central transition and satellite transitions. This situation points to an axial site symmetry at the Cr^{3+}-site, indicating tetragonal symmetry of the Cr^{3+}:$PbTiO_3$ nano-powders. Upon reduced mean grain size, the splitting of the satellite resonances monotonically reduces, until a single resonance emerges at $d \leq d_{\mathrm{crit}}$. This situation only occurs if the fine-structure interaction vanishes, which is valid only for cubic symmetry. The corresponding size-driven phase transition is illustrated by exploiting the variation of the axial fine-structure parameters D as function of mean grain size (cf. figure 5(d)).
As comparison, in figure 5(a,c), the *temperature-induced phase transition* of bulk Cr^{3+}:$PbTiO_3$ is shown. A similar behavior for the splitting of satellite resonances for temperatures below T_C is observed, where the single-line situation characteristic for the paraelectric state is observed for temperatures above the Curie temperature, $T \geq T_C = 765$ K.
Both phase transitions show a first-order character (8; 15).

3.6 Core-Shell structural model for nano-scale ferroelectrics

As a structure model of the spherical nanoparticles to give a comprehensive explanation for the size effect, the so-called *core-shell model* is proposed to show that the surface shell with a cubic structure covers the particle core with a tetragonal structure. In ferroelectric nanoparticles the core-shell model is in close relation with the particles size distribution. The spherical nanoparticle consists of two main parts: the core which is tetragonal (or ferroelectric) and the shell which is cubic (or paraelectric). The shell consists of an extremely distorted surface layer which partly is amorphous, partly a so-termed 'dead layer' and partly an extreme non-symetric crystal structure whereas the core consist of particles which are still tetragonal particles. The formation of core-shell structure has been demonstrated previously very successfully for ZnO nanoparticles (39; 40) where 8 nm core was embedded inside a 1 nm thick shell. Here, with the aid of analytical spectroscopic techniques our results also support the concept of core-shell model of ferroelectric nanoparticles where the nanoparticle consists of ferroelectric tetragonal-core and an outer tetragonal-to-cubic gradient-shell. When going to ultrafine particle size, outer gradient-shell effects increasingly dominates the tetragonal-core contributions, thus readily explaining the size driven tetragonal-to-cubic phase transition. The same effect has been already observed by NMR and EPR for Mn^{2+}:$BaTiO_3$ (8) and Cr^{3+}:$PbTiO_3$ (16).
The mean particle sizes were determined from X-ray diffraction, based on the single-line method. The details of the method were given in our previous study on nano-sized $PbTiO_3$ powders. The size distributions after milling are not Gaussian or Lorentzian, they rather resemble to log-normal functions.

4. Defect chemistry of ferroelectric nano-powders

To formally describe defects, such as lattice vacancies for instance, and dopant ions in the solid state, the *Kröger-Vink* notation is commonly used (41). In the framework of this notation, ions with lower valence than the one they replace (*acceptors*) are designated by a bar (A'_B) and ions with higher valence (*donors*) by a dot ($D^{\bullet}_B$). With that respect, the number of bars or dots

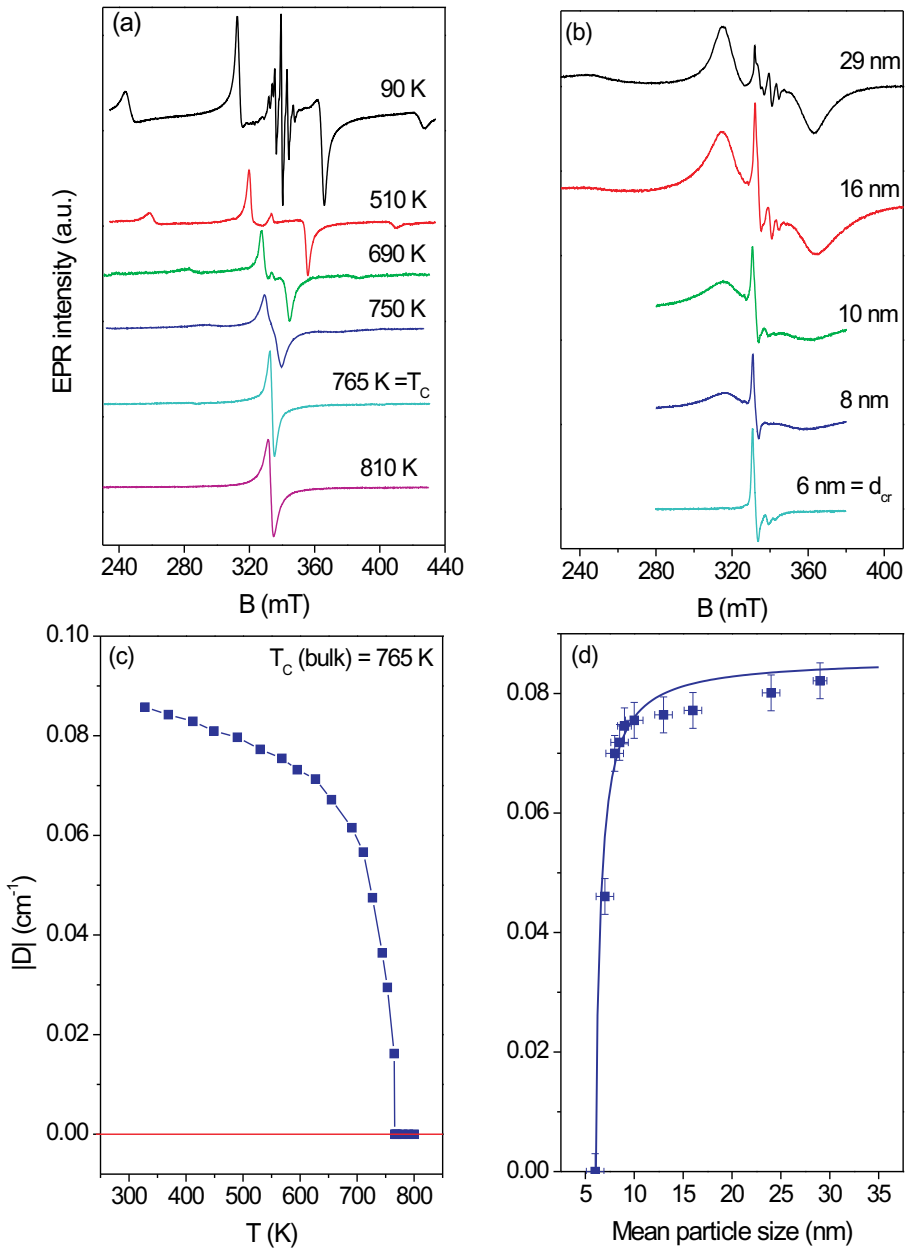

Fig. 5. (a,b) - X-band EPR spectra of Cr^{3+}-doped $PbTiO_3$. (a) - temperature dependent EPR spectra of bulk Cr^{3+}:$PbTiO_3$. (b) - size-dependent EPR spectra of Cr^{3+}:$PbTiO_3$ nano-powders measured at ambient temperature. (c,d) - phase transition monitored via the axial fine-structure parameter *D*.

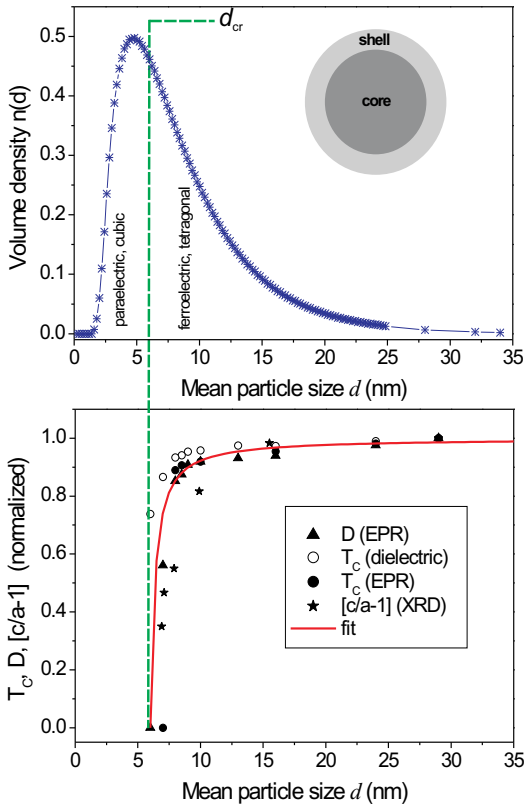

Fig. 6. The log-normal distributuion of particle sizes (top) and the drastic reduction of physical parameters by reducing the size below 10 nm (below).

designates the relative charge mismatch. The subscript defines the lattice site at which the considered defect is incorporated. In case the valence of both ions is equal, the superscript is a cross ($B_B^{\times}$). Interstitials are defined by an i as subscript, lattice vacancies - such as oxygen vacancies for instance – are given by $V_O^{\bullet\bullet}$ and electronic charge carriers by e'. The validity of the Kröger-Vink notation is, however, restricted to *dilute* defects that do not interact with each other.

For the here considered oxide perovskite ferroelectrics, the most relevant defects are *cation vacancies* (lead vacancies, V''_{Pb}), *anion vacancies* (oxygen vacancies, $V_O^{\bullet\bullet}$), *acceptor*-type ions with a lower positive charge than the ion they replace (e.g. Fe^{3+} for Ti^{4+}, Fe'_{Ti}), or *donor*-type ions with a higher positive charge than the ion they replace (e.g. Gd^{3+} for Pb^{2+}, $Gd^{\bullet}_{Pb}$).

With respect to the reaction of incorporation for Fe_2O_3 and Gd_2O_3 into $PbTiO_3$, the standard oxide reaction scheme for the synthesis of lead titanate is considered

$$PbO + TiO_2 \longrightarrow Pb_{Pb}^{\times} + Ti_{Ti}^{\times} + 3O_O^{\times} \tag{2}$$

With respect to the doping with Fe_2O_3, the oxide of the acceptor contains less oxygen per cation (Fe_2O_3) than the binary oxide of the host cation it replaces (TiO_2). Accordingly, the substitution of an acceptor oxide for the host oxide results in the introduction of an equivalent number of oxygen vacancies according to the *incorporation reaction*

$$Fe_2O_3 \xrightarrow{2TiO_2} 2Fe'_{Ti} + 3O_O^{\times} + V_O^{\bullet\bullet} \tag{3}$$

Additional to the oxygen vacancies generated by means of acceptor doping, a second source for the existence of oxygen vacancies peculiar to lead-containing materials consists in the loss of the volatile PbO component during high-temperature treatment (42) owing to the *defect equilibrium*

$$Pb_{Pb}^{\times} + O_O^{\times} \rightleftharpoons PbO(g) + V''_{Pb} + V_O^{\bullet\bullet} \tag{4}$$

creating *Schottky*-defect pairs.

An important issue for ferroelectric compounds are the diffusion properties of the above introduced defects. In that respect, the $V_O^{\bullet\bullet}$ will be rather mobile down to ambient temperature, because there are always nearest-neighbor oxygen sites in the perovskite structure with which the $V_O^{\bullet\bullet}$ may exchange their position. On the other hand, the V''_{Pb} and Fe'_{Ti} have no nearest-neighbor cation sites, for which reason they are rather immobile and their diffusion may only be observed at considerably higher temperatures (generally above about 1000 °C). Consequently, only the $V_O^{\bullet\bullet}$ contribute to the ionic conductivity of perovskite compounds at moderate temperatures.

In the so-termed *extrinsic regime*, where the concentration of defects is above a limit in which the defects may be regarded as *isolated*, the interaction of oppositely charged defects, such as negatively-charged acceptor dopants and positively charged oxygen vacancies, becomes important. Correspondingly, the ionic conductivity of the involved defects can be significantly reduced owing to the formation of defect complexes

$$Fe'_{Ti} + V_O^{\bullet\bullet} \rightleftharpoons (Fe'_{Ti} - V_O^{\bullet\bullet})^{\bullet} \tag{5}$$

where application of the law of mass action results in the following mass-action constant (43)

$$K_{Fe} = \frac{[(Fe'_{Ti} - V_O^{\bullet\bullet})^{\bullet}]}{[Fe'_{Ti}][V_O^{\bullet\bullet}]} \tag{6}$$

Generally, the magnitude of K is strongly dependent on the host system. Whereas for Fe^{3+}-doped $SrTiO_3$ at most half of the Fe^{3+} but all of the $V_O^{\bullet\bullet}$ are bound in defect complexes (43–45), for Fe^{3+}:$PbTiO_3$ exclusively $(Fe'_{Ti} - V_O^{\bullet\bullet})^{\bullet}$ defect complexes are formed and no 'free' Fe'_{Ti} could be observed for temperatures below 300 K (46). With this regard, Fe^{3+}:$BaTiO_3$ represents an intermediate situation (47–50), such that $K_{Fe:SrTiO_3} \leq K_{Fe:BaTiO_3} \leq K_{Fe:PbTiO_3}$ is valid.

Vice-versa, a donor-type dopant may reduce the concentration of oxygen vacancies in the lattice. This is owing to the reason that the oxide of a donor (Gd_2O_3) contains more oxygen per cation than the binary host oxide it replaces (PbO). Correspondingly, the excess oxygen serves to reduce the concentration of oxygen vacancies according to the following incorporation reaction

$$Gd_2O_3 + V_O^{\bullet\bullet} \xrightarrow{2PbO} 2Gd_{Pb}^{\bullet} + 3O_O^{\times} \tag{7}$$

For high donor-dopant concentration the oxygen vacancy concentration may thus be reduced to a very small amount characteristic of intrinsic ionic disorder. Alternatively, the donor

doping enhances the concentration of cation vacancies according to

$$Gd_2O_3 \overset{2PbTiO_3}{\longrightarrow} 2Gd^{\bullet}_{Pb} + 3O^{\times}_{O} + V''_{Pb} \tag{8}$$

Contrary to the situation for acceptor-doping, for donor-doped $PbTiO_3$ compounds there is no formation of defect complexes between the donor ion and cation vacancies, such that the corresponding lattice defects ($Gd^{\bullet}_{Pb}$, V''_{Pb}) rather exist as 'isolated' centers (51).
A question that is still controversially discussed is the defect chemistry of co-doped compounds. These materials are simultaneously doped by an acceptor and a donor dopant, such as (Gd^{3+},Fe^{3+}):$PbTiO_3$ for instance. Two competing mechanisms for charge compensation are then conceivable; either the lattice vacancies generated by the two dopants cancel each other, or the defects formed add together. In the former scenario the amount of $V^{\bullet\bullet}_{O}$ would be considerably reduced by the donor doping and as consequence also the concentration of $(Fe'_{Ti} - V^{\bullet\bullet}_{O})^{\bullet}$ defect complexes should be decreased. Alternatively, the latter mechanism describes a situation where even in 'soft' co-doped compounds $(Fe'_{Ti} - V^{\bullet\bullet}_{O})^{\bullet}$ are present.

4.1 Defect-structure of acceptor-doped $PbTiO_3$ studied by EPR

The *'method-of-choice'* for the characterization of defect structure is provided by EPR spectroscopy (5; 52). The information content obtained from the analysis of the EPR spectra is twofold. First, it can be distinguished between 'isolated' Fe'_{Ti} functional centers and centers that have formed a $(Fe'_{Ti} - V^{\bullet\bullet}_{O})^{\bullet}$ defect complex for reasons of charge compensation. Second, the site symmetry at the Fe^{3+}-site is obtained, for which reason in case of a $(Fe'_{Ti} - V^{\bullet\bullet}_{O})^{\bullet}$ defect dipole, its orientation with respect to the orientation of the spontaneous polarization, P_S, in the $PbTiO_3$ nano-powders may be deduced (53). Correspondingly, the defect dipoles may be oriented either parallel $(Fe'_{Ti} - V^{\bullet\bullet}_{O})^{\bullet}_{\parallel}$ or perpendicular $(Fe'_{Ti} - V^{\bullet\bullet}_{O})^{\bullet}_{\perp}$ with respect to the orientation of P_S. In case of an 'isolated' Fe'_{Ti} center, an isotropic EPR line accounts for a cubic and paraelectric $PbTiO_3$ phase.
The corresponding EPR spectra for the obtained Fe^{3+}-modified $PbTiO_3$ nano-powders with varying mean grain size are given in figure 7. For comparison, also the EPR spectrum of a 'bulk' sample with mean grain size of about 500 nm is depicted (top). The spectrum consists of a dominant low-field peak at $\approx$ 100 mT characteristic for the existence of $(Fe'_{Ti} - V^{\bullet\bullet}_{O})^{\bullet}_{\parallel}$ defect complexes (54). As function of decreasing mean grain size, additional peaks occur in the EPR spectra, which may be explained by the following scenario: For nano-sized samples an increasing contribution arises from the surface of the nano-grains. According to a *core-shell model* (55; 56), this surface has cubic $PbTiO_3$ structure and thus is paraelectric. In cubic crystal symmetry, the advantage in energy of formation of an $(Fe'_{Ti} - V^{\bullet\bullet}_{O})^{\bullet}$ defect associate over the 'isolated' defects (Fe'_{Ti}, $V^{\bullet\bullet}_{O}$) (46) vanishes. Consequently, the observation of an isotropic EPR at $g = 2.002$ (figure 7(a), bottom) accounts for the existence of an isolated Fe'_{Ti} center in a paraelectric surface region. The third resonance at $\approx$ 150 mT is characteristic for a $(Fe'_{Ti} - V^{\bullet\bullet}_{O})^{\bullet}$ defect complex of rhombic site symmetry at the site of the Fe^{3+} functional center. Its origin may be twofold: First, it may be a $(Fe'_{Ti} - V^{\bullet\bullet}_{O})^{\bullet}_{\perp}$ defect dipole, oriented perpendicular to the direction of spontaneous polarization. Second, it may be a $(Fe'_{Ti} - V^{\bullet\bullet}_{O})^{\bullet}$ defect complex in a distorted crystal symmetry. Both scenarios agree with the existence of a distorted interface layer in the nano-crystals between the ferroelectric core and the paraelectric surface.
Schematically, the corresponding 'core-shell structure' is illustrated in figure 8. At the ferroelectric core of the $PbTiO_3$ nano-particles, $(Fe'_{Ti} - V^{\bullet\bullet}_{O})^{\bullet}_{\parallel}$ defect dipoles are formed that

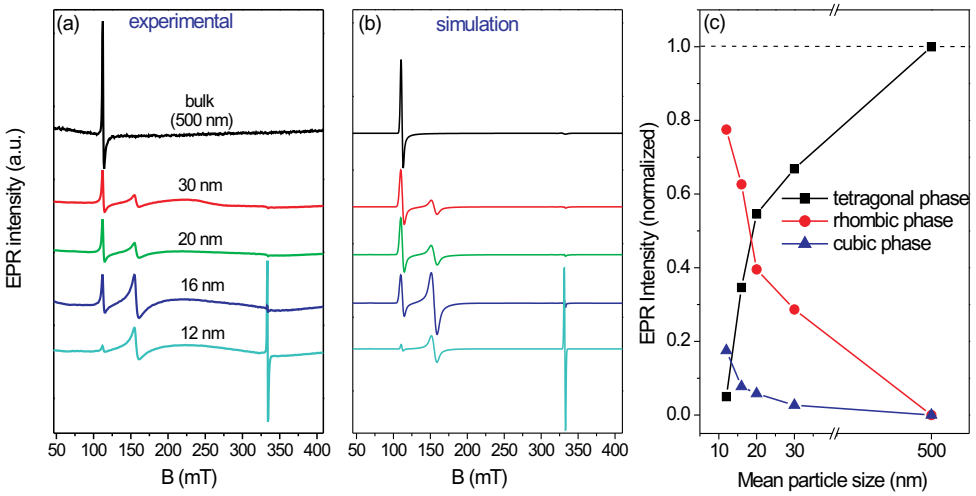

Fig. 7. (a,b) - X-band (9.4 GHz) EPR spectra of Fe^{3+}-doped $PbTiO_3$ nano-powders as function of mean grain size (indicated above the spectra). (a) - experimental spectra. (b) - numerical spectrum simulation. (c) - quantitative analysis of site symmetry as function of mean grain size, indicating the change in defect structure when approaching the nano-regime.

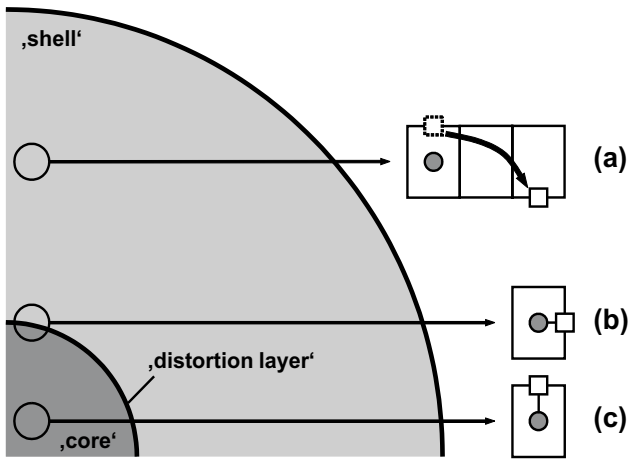

Fig. 8. Schematical illustration of the '*core-shell structure*' for Fe^{3+}-doped $PbTiO_3$ ferroelectric nano-particles. (a) - 'isolated' Fe'_{Ti} and $V_O^{\bullet\bullet}$ defects at the paraelectric surface. (b) - $(Fe'_{Ti} - V_O^{\bullet\bullet})^{\bullet}$ defect complexes of rhombic site symmetry at interface layer. (c) - $(Fe'_{Ti} - V_O^{\bullet\bullet})^{\bullet}_{\|}$ defect dipoles at the ferroelectric core. The corresponding unit cells are illustrated by rectangles, the Fe^{3+}-functional centers by a gray circle and the oxygen vacancies by open squares.

are aligned along the direction of spontaneous polarization. In contrast, at the paraelectric surface 'isolated' Fe'_{Ti} and $V_O^{\bullet\bullet}$ defects exist. This particularly impacts the ionic conductivity at the surface of $PbTiO_3$ nano-grains because the $V_O^{\bullet\bullet}$ act as ionic charge carriers when not

bound to $(Fe'_{Ti} - V_O^{\bullet\bullet})^{\bullet}$ defect complexes. In between ferroelectric core and the paraelectric surface region a distorted interface layer exists, which explains the existence of $(Fe'_{Ti} - V_O^{\bullet\bullet})^{\bullet}$ defect complexes of rhombic site symmetry.
Quantitatively, the amount of the three above mentioned defects is analyzed as function of the determined site symmetry as depicted in figure 7(c). Obviously, a marked *size-driven* change in defect structure is observed when comparing 'bulk' and nano-scale ferroelectrics.

4.2 Defect-structure of donor-doped $PbTiO_3$ studied by EPR

In contrast to the Fe^{3+} functional center in $PbTiO_3$ that is incorporated at the Ti-site and acts as an acceptor, the Gd^{3+}-center substitutes for Pb^{2+} at the A-site and hence acts as a donor. Furthermore, charge compensation is performed through the formation of lead vacancies in distant coordination spheres, such that no defect complexes are formed (51).
The corresponding X-band (9.4 GHz) and Q-band (34.1 GHz) EPR spectra of Gd^{3+}-doped $PbTiO_3$ nano-powders as compared to a 'bulk' compound are shown in figure 9. The nano-powders were obtained by HEBM for 10 h and subsequent calcination at various temperatures, yielding mean grain sizes in an interval between 50 and 500 nm.
The main result of the EPR-analysis is that the Gd^{3+} fine-structure interaction is only slightly reduced for decreasing mean grain size of the Gd^{3+}:$PbTiO_3$ nano-powders. Considerably more pronounced is an increased line-broadening owing to fine-structure strain. Adopting the above mentioned core-shell model also for the Gd^{3+}-doped $PbTiO_3$ nano-grains, the enhanced fine-structure strain can be rationalized by a superposition of EPR-resonances from Gd^{3+} functional center at the tetragonal core, the cubic shell and at the rhombic interface layer.
Considering the obtained EPR linewidths ΔB_{pp} for the two systems of nano-powders studied, a marked variation between the CPP-prepared Fe^{3+}-doped $PbTiO_3$ and the HEBM-obtained Gd^{3+}-doped $PbTiO_3$ nano-powders is observed. Whereas for the CPP-synthesis route almost no variation in ΔB_{pp} between the 'bulk' and the nano-scale materials can be determined, the HEBM-prepared nano-powders show a pronounced increase in ΔB_{pp}. This observation may be mainly traced back to the different distributions of grain size. Whereas the CPP-route provides nano-powders with log-normal distribution in grain size (15; 56), HEBM involves locally high temperature during the milling that increases the particle size and because comparatively long milling periods typically are required, the corresponding distribution in grain size is considerably larger (17; 18).

4.3 Defect chemistry of acceptor- and donor-doped nano-scale ferroelectrics

For 'bulk' $PbTiO_3$ compounds it is well established that the Fe^{3+} functional center acts as an acceptor and forms $(Fe'_{Ti} - V_O^{\bullet\bullet})^{\bullet}$ defect complexes for partial charge compensation (46; 57). According to the EPR results, each Fe^{3+} functional center is over-compensated by one oxygen vacancy. In order to obtain overall charge neutrality, exact charge compensation of two $(Fe'_{Ti} - V_O^{\bullet\bullet})^{\bullet}$ defect complexes is accomplished by one additional lead vacancy. Accordingly, the following defect equilibrium describes the 'bulk' situation in Fe^{3+}-doped $PbTiO_3$

$$2[V''_{Pb}] \approx [(Fe'_{Ti} - V_O^{\bullet\bullet})^{\bullet}] \tag{9}$$

The striking observation is that even though the Fe^{3+}-doping renders *'hard'* piezoelectric compounds, the $(Fe'_{Ti} - V_O^{\bullet\bullet})^{\bullet}$ defect dipole is positively charged for which reason it acts as a donor center in the equation for charge compensation.
The defect equilibrium, however, is drastically changed for Fe^{3+}-doped $PbTiO_3$ nano-powders where the Fe^{3+} functional centers rather exist as 'isolated' Fe'_{Ti}-centers that

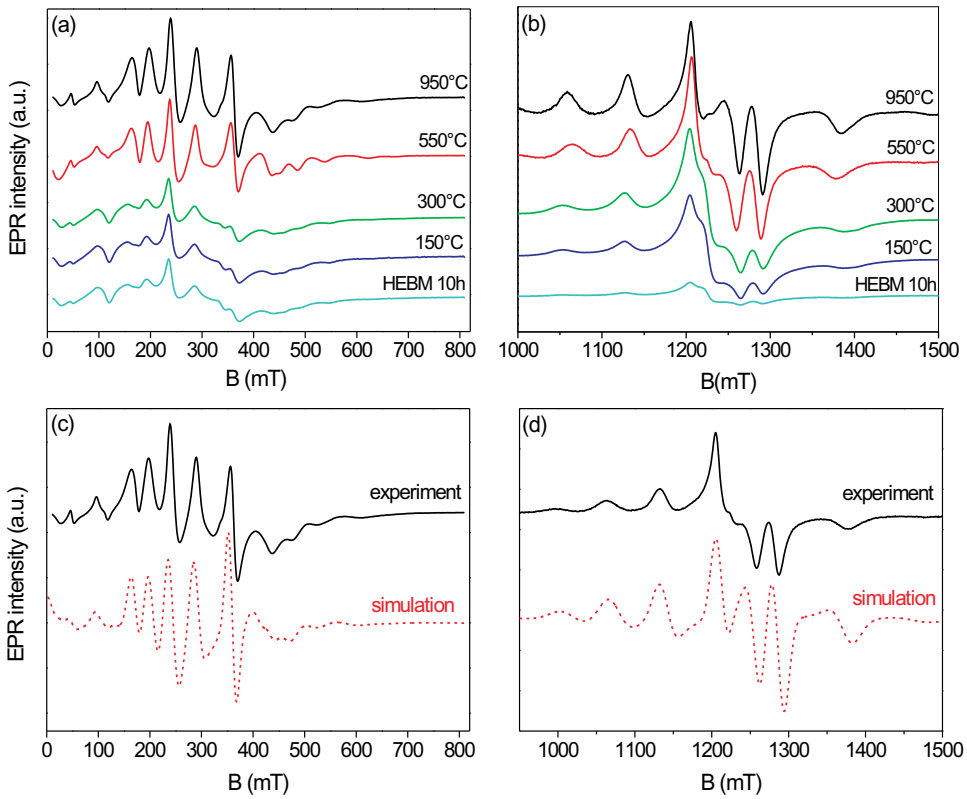

Fig. 9. (a,b) EPR spectra of Gd^{3+}-doped $PbTiO_3$ nano-powders as function of mean grain size after high-energy ball-milling for 10 h and subsequent calcination at various temperatures. (a,c) - X-band (9.4 GHz) EPR spectra. (b,d) - Q-band (34.1 GHz) EPR spectra. (c,d) - numerical spectrum simulations.

do not form $(Fe'_{Ti} - V_O^{\bullet\bullet})^{\bullet}$ defect complexes. For this reason, the defect equilibrium defined for the 'bulk' Fe^{3+}:$PbTiO_3$ compounds in equation (9), is modified to

$$[Fe'_{Ti}] \approx 2[V_O^{\bullet\bullet}] \tag{10}$$

Now the Fe'_{Ti} acts as an acceptor and the concentration of *mobile* oxygen vacancies is considerably enhanced because in the nano-regime the concentration of $(Fe'_{Ti} - V_O^{\bullet\bullet})^{\bullet}$ defect complexes is considerably decreased or even vanishes in the paraelectric state. This provides a means to explain the increased (ionic) conductivity often reported for nano-sized ferroelectric compounds (58). On the other hand, owing to the absence of $(Fe'_{Ti} - V_O^{\bullet\bullet})^{\bullet}$ defect dipoles, the '*hardening*' effect is expected to decrease for nano-sized materials. Furthermore, the defect equilibrium described in equation (10) necessitates no formation of V''_{Pb} for overall charge neutrality, as is required for 'bulk' compounds described in equation (9).
Contrary to the situation for 'hard' Fe^{3+}-doped $PbTiO_3$, for the 'soft' Gd^{3+}-doped $PbTiO_3$ compound there is no association of defect complexes that impacts the charge neutrality

condition. The donor-type $Gd^{\bullet}_{Pb}$-center necessitates a reduced concentration of oxygen vacancies but increased concentration of lead vacancies results according to

$$2[V''_{Pb}] \approx 2[V^{\bullet\bullet}_{O}] + [Gd^{\bullet}_{Pb}] \tag{11}$$

Here, no pronounced impact of the nano-regime on the defect structure is observed. Correspondingly, the defect-chemical mechanisms established for 'soft' ferroelectric compounds can be directly transferred to nano-scale ferroelectrics.

5. Conclusion

In summary, two main results emerge when studying nano-scale ferroelectrics. First, a *size-driven phase transition* occurs below a critical grain size and second, this ferro-to-paraelectric phase transition is accompanied by a pronounced *size-driven change in defect chemistry*.

Concerning the *size-driven phase transition*, the structural properties of spherical nano-particles can be explained by a *core-shell model*. According to this model, the nano-grains consist of a surface shell with a cubic structure that covers the particle core with a tetragonal structure. The nano-particles accordingly possess a ferroelectric core and an outer tetragonal-to-cubic gradient-shell. When going below an ultra-fine particle size, the outer gradient-shell effects increasingly dominates the tetragonal-core contributions, thus explaining the size driven tetragonal-to-cubic phase transition.

With respect to the *size-driven change in defect chemistry* of ferroelectric perovskite oxides, it has to be distinguished between acceptor- and donor-doped compounds. The defect complexes that exist in 'bulk' acceptor-doped materials vanish in the nano-regime, such that the 'hardening' effect is considerably decreased, whereas the ionic conductivity is increased. On the other hand, the defect-chemical mechanisms established for 'soft' ferroelectric compounds can be directly transferred to nano-scale ferroelectrics.

Finally, two effective methods have been introduced for the synthesis of ferroelectric nanoparticles. Both have advantages and drawbacks which can be summarized as follows: The Combined Pyrolysis and Polymerization (CPP) involves a precursor with subsequent calcinations that controls the particle size. This method easily allows incorporation of dopant ions in the form of metal acetylacetonates. With the need of this indirect technique, mean grain sizes down to about 10 nm can be reached. However, there is the possibility of agglomeration during calcinations, which may cause considerable size-distribution broadening. On the other hand, High Energy Ball Milling (HEBM) works without the need of wet chemistry (precursor) and subsequent high-temperature treatment (calcination). The particle size is controlled via the milling time through a mechanical alloying process. As starting material the corresponding metal oxides (also for doping) are used. This direct technique provides small particle sizes below 10 nm. However, high mechanical strain may cause large grain-size distributions.

6. Acknowledgements

We are very grateful for fruitful discussions and experimental support from many colleagues, particularly to Dr. Peter Jakes (Universität Freiburg), Prof. Mehmet Somer (Koc University Istanbul), Dr. S.K.S. Parashar (KIIT University India), Prof. Donald M. Smyth (Lehigh), Prof. Rolf Böttcher (University of Leipzig), Dr. H.-J. Gläsel, Dr. Hartmann (IOM Leipzig) Dr. A. Bartasyte (CNRS-INP Grenoble-Minatec), Prof. H. Rumpf (Universität Bonn), and Prof. J.

Banys (University of Vilnius). Financially, this research has been supported by the DFG center of excellence 595.

7. References

[1] Scott, J. F. (2000). *Ferroelectric Memories*, Springer, Berlin.
[2] Waser, R. (2005). *Nanoelectronics and Information Technology*, Wiley.
[3] Setter, N. (2002). *Piezoelectric Materials in Devices*, Swiss Federal Institute of Technology, Lausanne.
[4] Smyth, D. M. (2000). *The Defect Chemistry of Metal Oxides*, Oxford University Press, New York.
[5] Eichel, R.-A. (2008). *J. Am. Ceram. Soc.*, Vol. 91, 691.
[6] Morozov, M.I.; Damjanovic, D. (2010). *J. Appl. Phys.*, Vol. 107, 034106.
[7] Rüdiger, A.; Schneller, T.; Roelofs, A.; Tiedke, S.; Schmitz, T.; Waser, R. (2005). *Appl. Phys. A*, Vol. 80, 1247.
[8] Böttcher, R.; Klimm, C.; Michel, D.; Semmelhack, H. C.; Völkel, G.; Gläsel, H. J.; Hartmann, E. (2000). *Phys. Rev. B*, Vol. 62, 2085.
[9] Eichel, R.-A.; Erünal, E,; Drahus, M.D.; Smyth, D.M.; van Tol, J.; Acker, J.; Kungl, H.; Hoffmann, M.J. (2009). *Phys. Chem. Chem. Phys.*, Vol. 11, 8698.
[10] Erünal, E.; Eichel, R.-A.; Körbel, S.; Elsässer, C.; Acker, J.; Kungl, H.; Hoffmann, M.J. (2010). *Funct. Mat. Lett.* Vol. 3, 19.
[11] Hu, Y. M.; Gu, H. S.; Chen, W. P.; Wang Y. (2010). *Mater. Chem. Phys.*, Vol. 121, 10.
[12] Fukui, T. (1998). *J. Sol-Gel Sci. Tech.*, Vol. 11, 31.
[13] Zorel, H. E.; Ribeiro, C. A.; Crespi, M. S. (2001). *J. Mater. Sci. Lett.*, Vol. 20, 621.
[14] Selbach, S. M.; Wang, G.; Einarsrud,M.-A.; Grande, T. (2007). *J. Amer. Cer. Soc.*, Vol. 90, 2649.
[15] Erdem, E; Böttcher, R.; Semmelhack, H.-C.; Gläsel, H.-J.; Hartmann, E.; Hirsch, D. (2003). *J. Mater. Sci.*, Vol. 38, 3211.
[16] Erdem, E; Kiraz, K.; Somer, M.; Eichel, R.-A. (2010). *J. Eur. Ceram. Soc.*, Vol. 30, 289.
[17] Parashar, S. K. S.; Choudhary, R. N. P.; Murty, B. S. (2003). *J. Appl. Phys.*, Vol. 94, 6091.
[18] Parashar, S. K. S.; Choudhary, R. N. P.; Murty, B. S. (2004). *Mat. Sci. Eng. B*, Vol. 110, 58.
[19] Gläsel, H. J.; Hartmann, E.; Hirsch, D.; Böttcher, R.; Klimm, C.; Michel, D.; Semmelhack, H. C.; Hormes, J.; Rumpf, H. (1999). *J. Mater. Sci.*, Vol. 34, 2319.
[20] Lines, M. E.; Glas, A. M. (2001). *Principles and Applications of Ferroelectrics and Related Materials*, Oxford, Great Britain.
[21] Xu, Y. (1991). *Ferroelectric Materials and Their Applications*, North Holland, Amsterdam.
[22] Strukov, B. A.; Levanyuk, A. P. (1998). *Ferroelectric Phenomena in Crystals: Physical Foundations*, Springer, Berlin.
[23] Kretschmer, R.; Binder, K. (1979). *Phys. Rev. B*, Vol. 20, 1065.
[24] Tilley, D. R.; Zeks, B. (1984). *Sol. Stat. Commun.*, Vol. 49, 823.
[25] Glinchuk, M. D.; Eliseev, E. A.; Stephanovich, V. A. (2002). *Physica B-Condens. Matter*, Vol. 322, 356.
[26] Zhong, W. L.; Wang, Y. G.; Zhang, P. L.; Qu, B. D. (1994). *Phys. Rev. B*, Vol. 50, 698.
[27] Wang, C. L.; Smith, S. R. P. (1995). *J. Phys. Condens. Matter*, Vol. 7, 7163.
[28] Rychetsky, I; Hudak, O (1997). *J. Phys. Condens. Matter*, Vol. 9, 4955.
[29] Sheshadri, K.; Lahiri, R.; Ayyub, P.; Bhattacharya, S. (1999). *J. Phys. Condens. Matter*, Vol. 11, 2459.
[30] Glinchuk, M. D.; Morozovskaya, A. N. (2003). *phys. statu. solidi B*, Vol. 238, 81.
[31] Glinchuk, M. D.; Bykov, P. I. (2004). *J. Phys. Condens. Matter*, Vol. 16, 6779.

[32] Devonshire, A. F. (1949). *Philosophical Magazine*, Vol. 40, 1040.
[33] Ishikawa, K.; Yoshikawa, K.; Okada, N. (1988). *Phys. Rev. B*, Vol. 37, 5852.
[34] Shih, W. Y.; Shih, W. H.; Aksay, I. A. (1994). *Phys. Rev. B*, Vol. 50, 15575.
[35] Morozovska, A. N.; Glinchuk, M. D; Eliseev, E. A. (2007). *Phys. Rev. B*, Vol. 76, 014102.
[36] Burns, G.; Scott, B. A. (1973). *Phys. Rev. B*, Vol. 7, 3088.
[37] Mesquita, A.; Michalowicz, A.; Mastelaro, V. R. (2009). *Journal of Physics: Conference Series*, Vol. 190, 012081.
[38] Vedrinskii, R. V.; Kraizman, V. L.; Novakovich, A. A.; Demekhin, P. V.; Urazhdin, S. V. (1998). *J. Phys. Condens. Mat.* Vol. 10, 9561.
[39] Schneider, J. J.; Hoffmann, R. C.; Engstler, J.; Dilfer, S.; Klyszcz, A.; Erdem, E; Jakes, P.; Eichel, R.-A. (2009). *J. Mater. Chem.*, Vol. 19, 1449.
[40] Schneider, J. J.; Hoffmann, R. C.; Engstler, J.; Erdem, E; Jakes, P.; Eichel, R.-A.; Bauermann, L.-P.; Bill, J. (2010). *Chem. Mater.*, Vol. 22, 2203.
[41] Kröger, F.A.; Vink, H. J.(1956). In: *Solid State Physics*, Seitz, F.; Turnbull, D. (Ed.), Vol. 3, 273.
[42] Holman, R. L.; Fulrath, R. M. (1973). *J. Appl. Phys.*, Vol. 44, 5227.
[43] Merkle, R.; Maier, J. (2003). *Phys. Chem. Chem. Phys.*, Vol. 5, 2297.
[44] Kirkpatrick, E. S.; Müller, K. A.; Rubins, R. S. (1964). *Phys. Rev.*, Vol. 135, A86.
[45] Waldkirch, T. von; Müller, K. A.; Berlinger, W. (1972). *Phys. Rev. B*, Vol. 5, 4324.
[46] Meštrić, H.; Eichel, R.-A., Kloss, T.; Dinse, K.-P.; Laubach, So.; Laubach, St.; Schmidt, P.C. (2005). *Phys. Rev. B*, Vol. 71, 134109.
[47] Siegel, E.; Müller, K. A. (1979). *Phys. Rev. B*, Vol. 20, 3587.
[48] Possenriede, E.; Schirmer, O. F.; Donnerberg, H. J.; Godefroy, G.; Maillard, A. (1989). *Ferroelectrics*, Vol. 92, 245.
[49] Kornienko, S.M.; Bykov, I. P.; Glinchuk, M. D.; Laguta, V. V.; Belous, A. G.; Yastrabik, L. (1999). *Phys. Solid State*, Vol. 41, 1688.
[50] Böttcher, R.; Langhammer, H. T.; Müller, T.; Abicht, H. P. (2008). *J. Phys. Condens. Matter*, Vol. 20, 505209.
[51] Eichel, R.-A.; Meštrić, H.; Kungl, H.; Hoffmann, M. J. *Appl. Phys. Lett.*, Vol. 92, 122506.
[52] Eichel, R.-A. (2007). *J. Electroceramics*, Vol. 19, 9.
[53] Erdem, E.; Eichel, R.-A.; Kungl, H.; Hoffmann, M. J.; Ozarowski, A.; van Tol, H.; Brunel, L. C. (2007). *Phys. Script.*, Vol. T129, 12.
[54] Meštrić, H.; Eichel, R.-A.; Dinse, K.-P.; Ozarowski, A.; van Tol, J.; Brunel, L. C. (2004). *J. Appl. Phys.*, Vol. 96, 7440.
[55] Aoyagi, S.; Kuroiwa, Y.; Sawada, A.; Kawaji, H.; Atake, T. (1973). *J. Thermal Analy. Calor.*, Vol. 81, 627.
[56] Erdem, E; Semmelhack, H.-C.; Böttcher, R.; Rumpf, H.; Banys, J.; Matthes, A.; Gläsel, H.-J.; Hirsch, D.; Hartmann, E. (2006). *J. Phys. Condens. Matter*, Vol. 18, 3861.
[57] Erdem, E.; Drahus, M. D.; Eichel, R.-A.; Kungl, H.; Hoffmann, M. J.; Ozarowski, A.; van Tol, H.; Brunel, L. C. (2008). *Funct. Mat. Lett.*, Vol. 1, 7.
[58] Guo, X.; Pithan, C.; Ohly, C.; Jia, C. L.; Dornseiffer, J.; Haegel, F. H.; Waser R. (2005). *Appl. Phys. Lett.* Vol. 86, 082110.

6

Microstructural Defects in Ferroelectrics and Their Scientific Implications

Duo Liu
State Key Laboratory of Crystal Materials,
Shandong University, Jinan, Shandong,
P. R. China

1. Introduction

Properties of materials are closely linked to their defect structure. Numerous studies have proved that the existence of a small amount of microstructural defects can dramatically change the way of materials behaving in response to external fields. Based on these, various kinds of functional devices have been developed, which have changed the daily life of human beings. Currently, the most important application of defects in industry is probably semiconductor devices intentionally doped with foreign atoms to realize desirable band structures to tune the behaviors of electrons. Defects are also intentionally introduced into metals and insulators to achieve better performances.

Similarly, defects in ferroelectric materials are also extremely important. As a subject that has been investigated for decades, it has been proved that defects and the associated stress and electrical fields could change ferroelectric behaviors such as polarization reversal, domain kinetics, phase transition temperatures, and ferroelectric fatigue. Up to date, numerous studies have been devoted to understanding oxygen vacancies, dislocations, domain walls, voids, and microcracks in ferroelectrics. Actually, almost all aspects of ferroelectric properties are defect-sensitive. For example, doped PZTs could either be "soft" or "hard" with variable coercive fields. Oxygen vacancies play a determinant role on the fatigue process of ferroelectric oxides. Dislocations may hinder the motion of ferroelectric domain walls.

Recent interests on the design and fabrication of nanodevices stem from the distinct and fascinating properties of nanostructured materials. Among those, ferroelectric nanostructures are of particular interests due to their high sensitivity, coupled and ultrafast responses to external inputs [1]. With the decrease of the size of ferroelectric component down to nanoscale, a major topic in modern ferroelectrics is to understand the effects of defects and their evolution [2]. Defects will change optical, mechanical, electrical and electromechanical behaviors of ferroelectrics [3, 4]. However current understanding is limited to bulk and thin film ferroelectrics and is still not sufficiently enough to describe their behaviors at nanoscale. In view of the urgent requirement to integrate ferroelectric components into microdevices and enhanced size-dependent piezoelectricity for nanosized ferroelectric heterostructure, [5] it becomes essential to explore the role of defects in nanoscale ferroelectrics.

In this Chapter, the author will first discuss the effects associated with different types of defects in $BaTiO_3$, a model ferroelectric, from the point of views of the classical ferroelectric Landau-Ginsberg-Devonshire (LGD) theory. The author will then present some recent progresses made on this area. Among those include 1) critical size for dislocation in $BaTiO_3$ nanocube, 2) (111) twined $BaTiO_3$ microcrystallites and the photochromic effects.

2. Thermodynamic description of ferroelectrics

Most important phenomena associated with hysteretic, polarization, domain wall, and phase transition behaviors in ferroelectrics can be described by using the thermodynamic Landau-Ginzburg-Devonshire (LGD) theory. The LGD theory has been demonstrated to be the most powerful tool to understand ferroelectric behaviors especially when the materials are under the influence of external fields (electrical, temperature, and stress) [6, 7].

Most ferroelectric materials undergo a structural phase transition from a high temperature non-ferroelectric paraelectric phase into a low temperature ferroelectric phase of a lower crystal symmetry. The phase transition temperature is usually called the Curie temperature. In most cases, the dielectric constant above the Curie temperature obeys the Curie-Weiss law.

The change of internal energy, dU, of a ferroelectric material subjected to a small strain dx, electric displacement dD_i, and entropy dS can be expressed by

$$dU = TdS + X_{ij}dx_{ij} + E_i dD_i \tag{1}$$

where T is the temperature of the thermodynamic system. Since most piezoelectric systems are subjected to stress, electric field and temperature variations, it is convenient to express the free energy into the form of the Gibbs energy

$$dG = -SdT - x_{ij}dX_{ij} - D_i dE_i \tag{2}$$

According to the Taylor expansion around a certain equilibrium state, $G_0(T)$, the Gibbs free energy can be expanded in terms of the independent variables T, X and D

$$\begin{aligned} G = G_0(T) &+ \left(\frac{\partial G}{\partial T}\right)\Delta T + \left(\frac{\partial G}{\partial X_{ij}}\right)X_{ij} + \left(\frac{\partial G}{\partial D_i}\right)D_i + \frac{1}{2}\left(\frac{\partial^2 G}{\partial T^2}\right)\Delta T^2 \\ &+ \frac{1}{2}\left(\frac{\partial^2 G}{\partial X_{ij}\partial X_{kl}}\right)X_{ij}X_{kl} + \frac{1}{2}\left(\frac{\partial^2 G}{\partial D_i \partial D_j}\right)D_i D_j + \frac{1}{2}\left(\frac{\partial^2 G}{\partial T \partial X_{ij}}\right)\Delta T X_{ij} \\ &+ \frac{1}{2}\left(\frac{\partial^2 G}{\partial T \partial D_j}\right)\Delta T D_j + \frac{1}{2}\left(\frac{\partial^2 G}{\partial X_{ii}\partial D_k}\right)X_{ij}D_k + \cdots\cdots \end{aligned} \tag{3}$$

This phenomenological theory treats the material in question as a continuum without regard to local microstructure variations [8]. Although the treatment itself does not provide physical insight on the origin of ferroelectricity, it has been demonstrated as the most powerful tool for the explanation of some ferroelectric phenomena such as Curie-Weiss relation, the order of phase transition and abnormal electromechanical behaviors [9]. Equation (3) can be rewritten as [10]:

$$\begin{aligned}\Delta G &= a_1(P_1^2+P_2^2+P_3^2)+a_{11}(P_1^4+P_2^4+P_3^4)+a_{12}(P_1^2P_2^2+P_2^2P_3^3+P_1^2P_3^2)\\ &+a_{111}(P_1^6+P_2^6+P_3^6)+a_{112}[P_1^4(P_2^2+P_3^2)+P_2^4(P_1^2+P_3^2)+P_3^4(P_2^2+P_1^2)]\\ &+a_{123}P_1^2P_2^2P_3^2-\frac{1}{2}s_{11}(X_1^2+X_2^2+X_3^2)-s_{12}(X_1X_2+X_2X_3+X_1X_3)\\ &-\frac{1}{2}s_{44}(X_4^2+X_5^2+X_6^2)-Q_{11}(X_1P_1^2+X_2P_2^2+X_3P_3^2)\\ &-Q_{12}[X_1(P_2^2+P_3^2)+X_2(P_1^2+P_3^2)+X_3(P_2^2+P_1^2)]\\ &-Q_{44}(X_4P_2P_3+X_4P_2P_3+X_6P_2P_1)\end{aligned} \tag{4}$$

where the coefficients, a_1, a_2, and a_3 can be identified from equation (4) and s and Q are known as the elastic compliance and the electrostrictive coefficient, respectively.
For a ferroelectric perovskite, equation (4) can be further simplified if the crystal structure and the corresponding polarization are taken into consideration. The polarization for cubic, tetragonal, orthorhombic and rhombohedral ferroelectrics is listed in Table 1, where 1, 2, and 3 denotes the a-, b-, and c- axis in a unit cell.

Cubic	$P_1^2=P_2^2=P_3^2=0$
Tetragonal	$P_1^2=P_2^2=0,\ P_3^2\neq 0$
Orthorhombic	$P_1^2=P_2^2\neq 0,\ P_3^2=0$
Rhombohedral	$P_1^2=P_2^2=P_3^2\neq 0$

Table 1. The polarization for cubic, tetragonal, orthorhombic, and rhombohedral structures.

Thus, considering the tetragonal ferroelectric system in the absence of external electrical field and without temperature change, the electric displacement, D, equals to the polarization in the direction parallel to the c- axis. The free energy can then be further simplified as

$$G=G_0(T)+\frac{1}{2}a_1P^2+\frac{1}{4}a_2P^4+\frac{1}{6}a_3P^6+\frac{1}{2}sX^2+QXP^2+\cdots\cdots \tag{5}$$

where $a_1=\beta\ (T-T_c)$ with β a positive constant, T_c is the Curie temperature for second-order phase transitions or the Curie-Weiss temperature ($\neq$ the Curie temperature) for first-order phase transition.

3. Point defects

Point defects occur in crystal lattice where an atom is missing or replaced by an foreign atom. Point defects include vacancies, self-interstitial atoms, impurity atoms, substitutional atoms. It has been long realized even the concentration of point defects in solid is considered to be very low, they can still have dramatic influence on materials properties [11,12]:

- Vacancies and interstitial atoms will alternate the transportation of electrons and atoms within the lattice.
- Point defects create defect levels within the band gap, resulting in different optical properties. Typical examples include F centers in ionic crystals such as NaCl and CaF_2. Crystals with F centers may exhibit different colors due to enhanced absorption at visible range (400 – 700 nm).

The most important point defect in ferroelectric perovskites is oxygen vacancies. Perovskite-related structures exhibit a large diversity in properties ranging from insulating to metallic to superconductivity, magneto-resistivity, ferroelectricity, and ionic conductivity. Owing to this wide range of properties, these oxides are used in a great variety of applications. For example, $(Ba,Sr)TiO_3$ and $Pb(Zr,Ti)O_3$ are high-dielectric constant materials being considered for dynamic and nonvolatile random access memories, $Pb(Zr,Ti)O_3$ is high piezoelectric constant material being used for actuators and transducers, and $LaMnO_3$ and $(La,Sr)CoO_3$ are being used as electrode materials in solid oxide fuel cells. Oxygen vacancies in perovskites are particularly of interests due partly to the loosely packed oxygen octahedra that lead to high mobility of oxygen vacancies. In perovskite ferroelectrics, a lot of works have been conducted to understand the behaviors of oxygen vacancies under the influence of external fields, such as electrical, stress and thermal fields, sometimes as a function of temperatures [13]. Oxygen vacancies play an essential role on ferroelectric fatigue during the operation of a ferroelectric component subjected to continuous load of electrical or stress fields, though many other factors such as microcracks [14], spatial charges [21], electrodes[15], surfaces and interfaces[16], voids, grain boundaries [21] may also lead to ferroelectric fatigue. The accumulation of oxygen vacancies in the electrode/ferroelectric interface has been confirmed by experimental studies. This oxygen deficient interface region could either screen external electrical field [24,17] or pin domain walls [18], both of which will reduce the polarizability of the ferroelectric thin films. Although ferroelectric fatigue induced by the accumulation of oxygen vacancies is considered to be permanent, thermal or UV treatment in oxygen rich environment can sometimes partially recover the switchability. Another option is to use conductive oxide electrode materials such as LSCO or YBCO which can serve as sinks for oxygen vacancies and prevent their accumulation at the electrode/film interface [19,20].

Recently, efforts have been made on hydrothermal synthesis of $BaTiO_3$ nanoparticles of various sizes to understand the ferroelectric size effect by using $BaCl_2$ and TiO_2 as the starting materials. [21,22]. The growth of $BaTiO_3$ nanoparticles is commonly believed to follow a two step reaction mechanism: 1) the formation of Ti-O matrix, 2) the diffusive incorporation of Ba^{2+} cations. The second step is believed to the rate determinant process. Due to the presence of H_2O, OH^- groups are always present in hydrothermal $BaTiO_3$. As a result, some studies have been performed to understand OH- effects on ferroelectricity. D. Hennings et al reported that a reduction of hydroxyl groups in $BaTiO_3$ nanoparticles promotes cubic-to-tetragonal phase transition [23]. Similar results had also been obtained by other studies on $BaTiO_3$ particles with sizes varying from 20 nm to 100 nm [24,25]. These experimental observations imply that point defects and possibly the associated electrical fields can lead to structural phase transition, as suggested by the soft-mode theory.

Currently, point defects in ferroelectrics are mostly studied by optical methods such as FT-IR spectroscopy or Raman spectroscopy. For $BaTiO_3$, the stretching vibration of lattice OH-groups occurs at 3462.5-3509.5cm^{-1}, characterized by a sharp absorption peak [26]. In contrast, surface OH- groups are characterized by a broad absorption peak located at 3000-3600 cm^{-1} [44,27] due to the uncertain chemical environment on surface region. Raman spectroscopy is also a powerful tool to understand the size effect of ferroelectrics, which is quite sensitive to local variation of lattice structure. S. Wada et al. reported that OH- groups in $BaTiO_3$ correspond to an 810 cm^{-1} Raman shift [28]. As point defects can create extra

electron levels in the band gap, photoluminescent spectroscopy had also been utilized to study the band structure of $BaTiO_3$, which is frequently conducted at low temperatures. Some other techniques such as HRTEM [29] and AFM [30] have also been used to study point defects.

4. Dislocations in ferroelectrics

The LGD theory predicts that dislocations in a ferroelectric will change the local ferroelectric behaviors around them. Considering a perovskite ferroelectric single domain with a tetragonal structure, the coordinate system is defined as x//[100], y//[010], and z//[001] with the spontaneous polarization, P_3, parallel to the z axis and $P_1=P_2=0$. The variation of piezoelectric coefficients induced by a {100} edge dislocation can be found with a method derived from combination of the Landau-Devonshire free energy equation [10] and dislocation theory [31]. As previous works suggest [32], the elastic Gibbs free energy around an edge dislocation can be modified as

$$G[P,T,\sigma_{ij}(x,y)] = G_0 + a_1^* P^2 + a_{11}P^4 + a_{111}P^6 + \frac{1}{2}s_{11}(\sigma_{11}^2 + \sigma_{22}^2 \\ \sigma_{33}^2) + s_{12}(\sigma_{11}\sigma_{22} + \sigma_{11}\sigma_{33} + \sigma_{22}\sigma_{33}) + \frac{1}{2}s_{44}\sigma_{12}^2 + E_{core} \tag{6}$$

with

$$a_1^*[T,\sigma_{ij}(x,y)] = a_1 - [Q_{11}\sigma_{33} + Q_{12}(\sigma_{11} + \sigma_{22})] \tag{7}$$

where G_0 is the free energy in the paraelectric state, a_1, a_{11} and a_{111} are the dielectric stiffness constants at constant stress, σ_{ij} is the internal stress field generated by an edge dislocation, P is the spontaneous polarization parallel to the polar axis, s_{ij} is the elastic compliance at constant polarization, E_{core} is the dislocation core energy and Q_{ij} represents the electrostriction coefficients. The stress field generated by an edge dislocation is well documented in the literature and is known as

$$\sigma_{11} = -\frac{\mu b}{2\pi(1-\nu)}\frac{y(3x^2+y^2)}{(x^2+y^2)^2},\ \sigma_{22} = \frac{\mu b}{2\pi(1-\nu)}\frac{y(x^2-y^2)}{(x^2+y^2)^2}$$

$$\sigma_{33} = \nu(\sigma_{11}+\sigma_{22}),\ \sigma_{12} = \frac{\mu b}{2\pi(1-\nu)}\frac{x(x^2-y^2)}{(x^2+y^2)^2} \tag{8}$$

$$\sigma_{13} = \sigma_{23} = 0$$

where μ is the shear modulus, b is the Burgers vector and ν is Poisson's ratio. A schematic plot of the stress field surrounding an edge dislocation is given in Fig. 1a.

The variation of the spontaneous polarization associated with the stress field due to an edge dislocation is then found by minimizing the modified Landau-Devonshire equation with respect to polarization $\left[\left(\partial G \diagup \partial P\right) = 0\right]$. Upon rearrangement, this gives [7]

$$P^2[T,\sigma_{ij}(x,y)] = \frac{-a_{11} + \sqrt{(a_{11}^2 - 3a_1^*[T,\sigma_{ij}(x,y)]a_{111})}}{3a_{111}} \tag{9}$$

Once the polarization is known for a given position, the piezoelectric coefficient, d_{33}, can be calculated by using [2]

$$d_{33} = 2\varepsilon_{33}Q_{11}P \tag{10}$$

where d_{33} is the piezoelectric coefficient along the polar axis.

Elastic Constants		Piezoelectric Coefficients	
C_{11} (GPa)	275	T (K)	298
C_{12} (GPa)	179	$a_1\left(VmC^{-1}\right)$	$3.34\times10^5(T-381)$
C_{13} (GPa)	152	$a_{11}\left(Vm^5C^{-3}\right)$	$4.69\times10^6\left(T-393\right)-2.02\times10^8$
C_{33} (GPa)	165	$a_{111}\left(Vm^9C^{-5}\right)$	$-5.52\times10^7\left(T-393\right)+2.76\times10^9$
C_{44} (GPa)	54	$Q_{11}\left(m^4C^{-2}\right)$	0.11
C_{66} (GPa)	113	$Q_{12}\left(m^4C^{-2}\right)$	–0.045

Table 2. Elastic and piezoelectric properties required for theoretical calculations for barium titanate single crystals.

The elastic compliance, dielectric stiffness constants and electrostriction coefficients used in the calculation were found for $BaTiO_3$ from other works [33,34]. The resulting d_{33} contour around the dislocation core is plotted and shown in Fig. 1b, where some singular points resulted from the infinite stress at the dislocation core are discarded. It is clearly seen that the piezoelectric coefficient d_{33} deviate from the standard value (86.2 pm/V at 293 K), due to the presence of the stress field. The area dominated by transverse compressive stresses exhibits an enhanced piezoelectric response while the area dominated by tensile stresses shows reduced effects. Note that the influence of stress field shows asymmetric effects on the piezoelectric coefficients due to the combination of equations (7) and (9). This simple calculation also suggests that the area significantly influenced by an edge dislocation could easily reach tens of nanometers as a result of the dislocation long-range stress field. In addition, dislocation stress field will also change the local properties of its surrounding area, like chemical reactivity, electron band structure, absorption of molecules and so on. However, stress field solely sometimes is not sufficient to describe all effects; a fully understanding of dislocation effects on ferroelectricity requires in-depth knowledge on electrical fields induced by the charged core area, which is currently not fully addressed in literature.

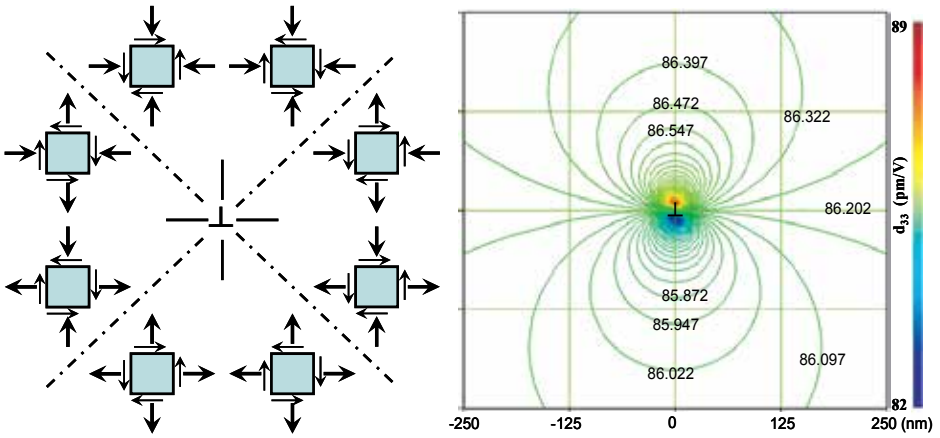

Fig. 1. The schematic representation of the stress field around an edge dislocation (a) and the resulting piezoelectric coefficient contour (b) calculated from the Landau-Devenshire theory.

Recently, many studies have been performed to understand dislocation effects on ferroelectricity. M. W. Chu et al. [35] found that misfit dislocations between PZT islands and $SrTiO_3$ substrate (height: 4nm, width: 8 nm) can lead to polarization instability, as confirmed by HRTEM and PFM tests. C. L. Jia et al [36] found that the elastic stress field of a dislocation in $SrTiO_3$/PZT/$SrTiO_3$ multilayered structures, even if it is located in regions far from the ferroelectric material, can have a determinant effect on ferroelectricity. A decrease of local spontaneous polarization of 48% was obtained by calculation. C. M. Landis et al. [37] found by non-linear finite element method (FEM) simulation that the stress field of dislocations can pin domain wall motions. L. Q. Chen et al [38] found by phase field simulations that misfit dislocations will alternate ferroelectric hysteresis. D. Liu et al performed nano indentation tests on individual 90^o and 180^o domains on $BaTiO_3$ single crystal and found that in an area free of dislocations the nucleation of dislocations induced by an indenter with tip radius of several tens of nanometers will be accompanied by the formation of ferroelectric domains of complex domain patterns, as confirmed by PFM tests. Recently, dislocation effects had been extended to other areas. For example, a theoretical work even predicted that dislocations may induce multiferroic behaviors in ordinary ferroelectrics [39]. In a recent study, the Author's group found that there exists a critical size below which dislocations in barium titanate ($BaTiO_3$), a model ferroelectric, nanocubes can not exist. While studying the etching behaviors of $BaTiO_3$ nanocubes with a narrow size distribution by hydrothermal method, it was confirmed that the etching behaviors of $BaTiO_3$ nanocubes are size dependent; that is, larger nanocubes are more likely to be etched with nanosized cavities formed on their habit facets. In contrast, smaller nanocubes undergo the conventional Ostwald dissolution process. A dislocation assisted etching mechanism is proposed to account for this interesting observation. This finding is in agreement with the classical description of dislocations in nanoscale, as described theoretically [40].

5. Dislocation size effect

The author's group reported an interesting observation on BaTiO3 nanocubes synthesized through a modified hydrothermal method. Detailed analysis is provided as follows. The

experimental procedure is relatively simple. First a small amount of NaOH:KOH mixture was placed into a Teflon-lined autoclave. After the addition of $BaCl_2$ and TiO_2 (anatase), the autoclave was sealed and heated at 200°C for 48 hours. After reaction, the product was collected by filtering and washing thoroughly with deionized water and diluted HCl acid. The reaction is as follows:

$$2NaOH + TiO_2 + BaCl_2 \rightarrow BaTiO_3 + 2NaCl + H_2O \quad (11)$$

The free Gibbs energy of the formation of $BaTiO_3$ at 200°C was calculated. The enthalpy of formation is

$$\Delta H = 2\Delta H_{NaCl} + \Delta H_{H2O} + \Delta H_{BaTiO3} - (2\Delta H_{NaOH} + \Delta H_{BaCl2} + \Delta H_{TiO2})$$

$$= -2 \times 411.2 - 285.830 - 1659.8 - (- 2\times425.6 - 855.0 - 944.0) = -117.83 \text{ KJ} \cdot \text{mol}^{-1}$$

The entropy of formation is

$$\Delta S = 2S_{NaCl} + S_{H2O} + S_{BaTiO3} - (2S_{NaOH} + \Delta S_{BaCl2} + S_{TiO2})$$

$$= 2\times72.1 + 69.95 + 108.0 - (2 \times 64.4 + 123.67 + 50.62) = 19.06 \text{ J}^{o}\text{C} \cdot \text{mol}^{-1}$$

Then the free Gibbs energy of formation at reaction temperature 200°C is

$$\Delta G = \Delta H - T\,\Delta S$$

$$= - 117.83 - 19.06\times473/1000 = -126.845 \text{ KJ} \cdot \text{mol}^{-1}$$

It can be seen that the formation of $BaTiO_3$ proceed easily at 200 °C. Our experiments had shown that $BaTiO_3$ nanocubes can be formed at temperatures as low as 180°C, as shown in Fig. 2, much lower than the temperature required by conventional solid-state reactions. All the diffraction peaks can be indexed to tetragonal $BaTiO_3$ (P4mm, JCPD 81-2203).

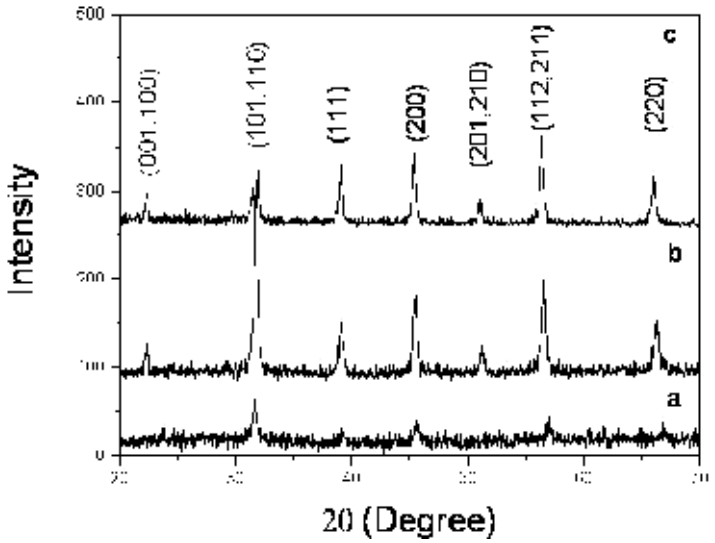

Fig. 2. XRD patterns of $BaTiO_3$ nanocubes synthesized at a) 180°C , b) 200°C and c) 220°C.

After the synthesis of $BaTiO_3$ nanocubes, we also studied their etching behaviors in hydrothermal environment. The etching process of $BaTiO_3$ nanocubes was carried out in diluted HCl solution (1M). The $BaTiO_3$ nanocubes were first mixed with HCl solution and then the mixture was treated in hydrothermal environment at 120°C for 2.5 hours. The reaction time and temperature had been optimized in consideration that over reaction may lead to the formation of TiO_2, as shown in Fig. 3 and Fig. 4.

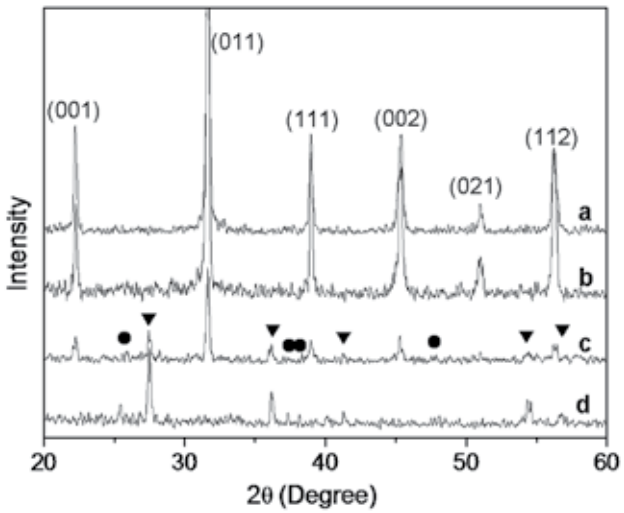

Fig. 3. XRD patterns of the final products after hydrothermal treatment at 120°C for various time: a) 30 min, b) 40 min, c) 50 min, d) 60 min. The ▼ and ● marks correspond to rutile and anatase TiO_2, respecitively.

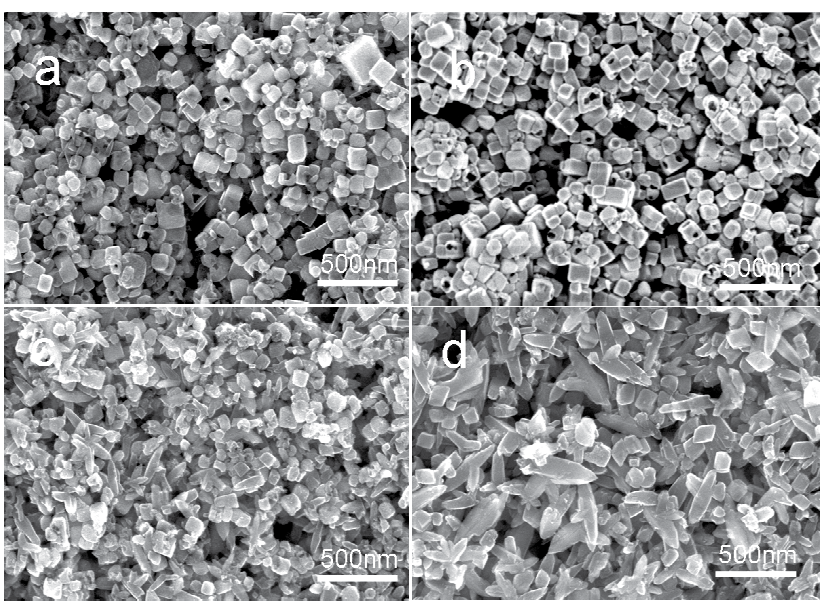

Fig. 4. SEM images of the final products after hydrothermal treatment at 120°C for a) 30 min, b) 40 min, c) 50 min, and d) 60 min.

Fig. 5a shows a typical SEM image obtained on the as-synthesized product. It can be seen that all nanoparticles exhibit a cubic morphology with sizes of ~ 30-100 nm. FTIR analysis reveals that the $BaTiO_3$ nanocubes contain a very small amount of lattice OH- groups, considerably less than $BaTiO_3$ nanoparticles synthesized by regular hydrothermal method. Fig. 5b shows a typical SEM image of the etched product, which reveals particle sizes smaller than that of the as-synthesized product (Fig. 5a). Besides, it is also interesting to note the fact that small cavities are formed on some nanocubes.

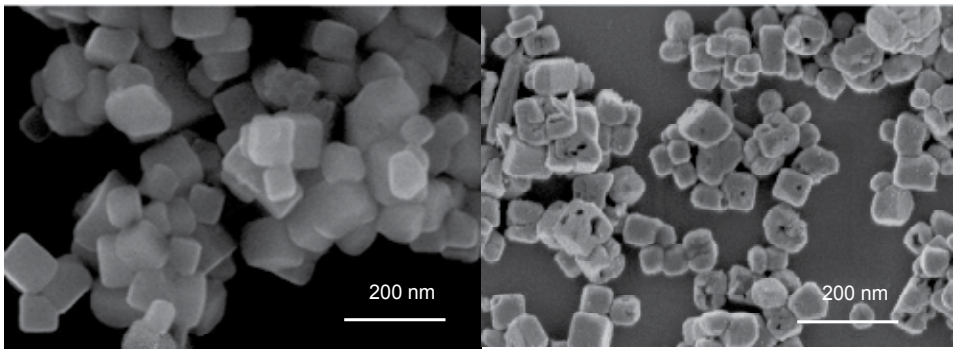

(a) (b)

Fig. 5. SEM image of BaTiO3 nanocubes before (a) and after (b) hydrothermal etching. (Copyright 2008 @ American Chemical Society.)

A statistical analysis reveals that these cavities only present on nanocubes greater than ~60 nm. Fig. 5 shows SEM images of nanocubes of different sizes obtained under the same experimental conditions. It can be clearly seen that nanocubes smaller than ~60 nm remain intact, while cavities are selectively formed on those greater than ~60 nm. The etching process was initiated on the surface and can penetrate all the way through a nanocube. In most case, there is only one etch pit in one nanocube while occasionally there are two or three etch pits observed.

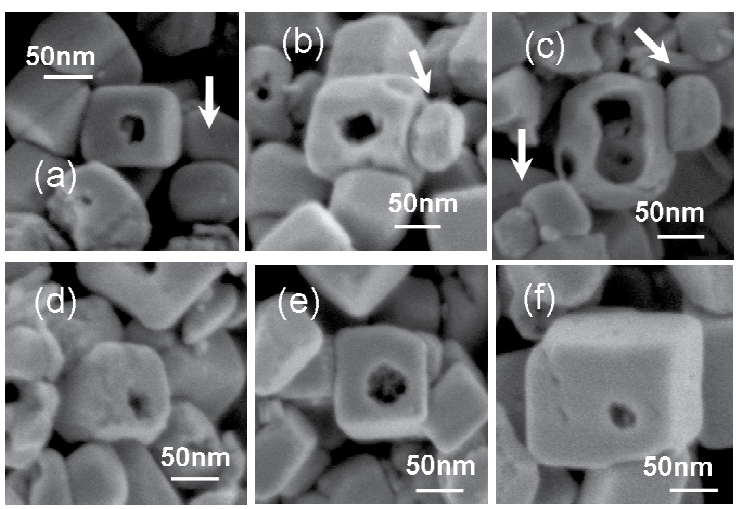

Fig. 6. SEM images of $BaTiO_3$ nanocubes after hydrothermal etching.

All the observation seems to be in controversy to the Ostwald dissolution mechanism, which predicts that small particles will dissolve first during a chemical reaction. However, our experiments reveal that smaller $BaTiO_3$ nanocubes show a better chance to remain intact though their corners and edges seem to have dissolved. The dissolution of corners and edges could be understood based on the Gibbs-Thompson relation. The Gibbs-Thompson relation suggests that, for a small particle, its corners and edges have enhanced chemical reactivity and their dissolutions are energetically favored. The Gibbs-Thompson relation also implies that smaller nanocubes have higher dissolubility and should dissolve first in compensation of the growth of larger ones.

Fig. 7a shows a typical HRTEM image taken on a $BaTiO_3$ nanocube with length of ~ 15 nm. It is evident that the nanocube is enclosed by (100) and (110) habit facets due to their high chemical stabilities [41]. Fig. 7b shows the fast Fourier transformation (FFT) image of Fig. 7a, which shows that the nanocube contains cubic lattices with lattice parameters of ~ 0.4 nm, suggesting that the nanocube is in cubic non-ferroelectric phase, in agreement with many previous studies. A careful examination of the lattice on the enlarged FFT filter image (Figure 7c) shows that the nanocube exhibit perfect lattice without dislocation or stacking faults. However, on the surface region, defective layers with distinct structures were formed due possibly to the presence of non-stoichiometric Ti-O layer as a result of Ba^{2+} dissolution in acid [42,43]. As suggested by previous studies, the formation of $BaTiO_3$ in base contains two steps, namely the precipitation of Ti-O networks and the incorporation of Ba^{2+}. Similarly, the dissolution of $BaTiO_3$ in acid contains outward diffusion of Ba^{2+} followed by phase transition of Ti-O network into TiO_2. As the Ti-O surface layers prevent Ba^{2+} from dissolution out of the Ti-O matrix, it can be expected that the dissolution rate of $BaTiO_3$ will be slowed down as the reaction proceeds. It is also possible that at certain stage of the reaction the particles may contain a $BaTiO_3$ core surrounded by a TiO_2 shell.

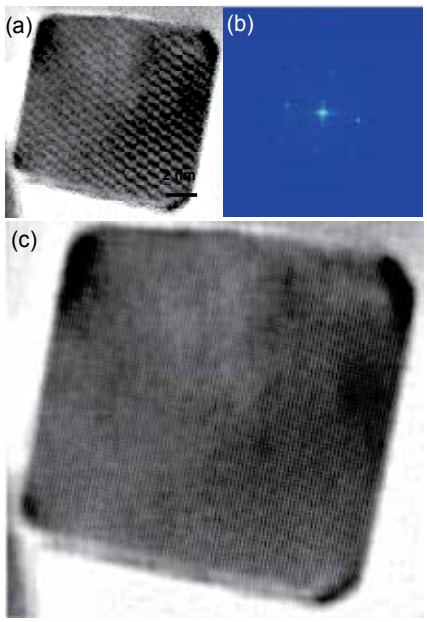

Fig. 7. HRTEM image taken on a BaTiO3 nanocube (a), the corresponding FFT pattern (b), and filtered image (c).

In contrast, the existence of dislocation inside a nanoparticle will dramatically change the way of the dissolution of nanoparticles. As dislocated regions are highly strained, regions with dislocations usually exhibit enhanced chemical reactivity. Preferential removal of atoms in the dislocation core area has been extensively observed on various materials such as metals, semiconductors and insulators. Although point defects such as the aforementioned oxygen vacancies and hydroxyl groups may also increase local etching rate, unlike extended defects, their effect is limited in a very small region and, even if there is any, should be observable on all nanocubes of various sizes no matter they are greater or smaller than 60 nm.

This observation also implies that there exists a critical size for dislocation to present inside $BaTiO_3$ nanocubes, and possibly all other nanoparticles. To understand this, we need to look into more details about the elastic theory of dislocation in nanoparticles. A literature review reveals that the classical elastic theory indeed predicts a characteristic length below which dislocation can not exist within an isolated nanoparticle [44, 45]. It was suggested that dislocations would be driven out of the crystal spontaneously when the size of the crystal is less than a characteristic length given by [46,47]

$$A_c \cong 2Gb/\sigma_p \tag{12}$$

where G is the shear modulus, b is the Burgers vector of the dislocation, and σ_p is the Peierls stress given by [48]

$$\sigma_p = \frac{3\sqrt{3}}{2}\frac{a(1-\upsilon)}{Gb}\tau_{\max}^2 \tag{13}$$

where G is the shear modulus of the material, a the lattice parameter, υ the Poisson's ratio, and τ_{max} the ideal shear strength.

For $BaTiO_3$, the average shear modulus is estimated to be 55 GPa with a method introduced by Watt and Peselnick [49], Burgers vector $b = a[110]/2$=0.28 nm, and the ideal shear strength of 5.5 GPa, as determined by nanoindentation test [50]. Bu substituting the data into equation (13), A_c for spherical $BaTiO_3$ nanoparticles is estimated to be ~22 nm. The calculated value is smaller than that determined experimentally due to a combination of the following factors: (1) the assumption of spherical shape used in the original model may not be fully transferrable to cubic shaped nanoparticles; (2) the elastic anisotropy of $BaTiO_3$ means that an average shear modulus may not be sufficiently accurate; (3) the presence of the Ti-O surface layers may also lead to alternate the case from the model; (4) possibly the most important, ferroelectric size effects could also play a role. In fact, all these possibilities lie on the fact that the elastic properties of $BaTiO_3$ nanocubes could deviate from the bulk values. As a result, we performed first principle *ab-initio* calculation on $BaTiO_3$ with the CASTEP module of Materials Studio in the assumption of the nanocubes having a cubic lattice structure. The calculated elastic modulus are C_{11}= 284.9 GPa, C_{12}= 110.8 GPa, C_{44} (shear modulus, G)= 116.2 GPa. The computed C_{12} and C_{44} agree well with experimental values, while C_{11} is ~10% greater than the experimental value [51]. Inserting C_{44} to Equation (13) yields a characteristic length of 46.5 nm, which is much closer to the observed critical length. This calculation suggests that ferroelectric size effect has to be considered while describing the etching behaviors of $BaTiO_3$ nanocubes. As discussed above, this critical size

effect is expected to be observed in other nanostructured materials. This had recently been demonstrated in gallium nitride (GaN) [52].

6. (111) twins in $BaTiO_3$

The origin of ferroelectricity can be attributed to extrinsic contribution associated with ferroelectric domain wall and intrinsic contribution from lattice distortion [10]. The extrinsic contributions to ferroelectric properties are dominated by: (a) the population of domains, and (b) the mobility of domain walls. In real ferroelectric materials, additional considerations arise owing to the presence of the crystal surfaces and imperfections. In a perfect crystal without imperfections or space charges, ρ is equal to zero. However, the free charge density is different from the perfect crystal at the surface region or in the neighborhood of defects, which alternatively results in the formation of a charge layer. This charge layer may introduce a depolarization field in the nearby regions. When a ferroelectric crystal is cooled from a paraelectric phase to a ferroelectric phase in the absence of applied fields, different crystal regions may take one of these polarization directions such that the total depolarization energy can be minimized. Each volume of uniform polarization is referred to as a ferroelectric domain, and is bounded by domain walls are referred to as domain walls.

There are two types of domain boundaries for a tetragonal perovskite, the polar axes of which are perpendicular or antiparallel with respect to each other. The walls which separate domains with oppositely orientated polarization are defined as 180° domain walls and those which separate domains with perpendicular polarization are called 90° domain walls. Unlike its ferromagnetic counterpart, a perovskite ferroelectric possesses a domain wall width in the order of a few unit cells. Since the length of c- axis of a perovskite tetragonal structure, c_T, is slightly different from that of the a- axis, a_T, the polarization vectors on each side of a 90° domain wall form an angle slightly smaller than 90°. The angle can be calculated by

$$\alpha = 2 \times \tan^{-1}(c_T / a_T) \tag{14}$$

For $BaTiO_3$, taking c_T = 4.04 Å and a_T = 3.99Å, one obtains 90.7°, as illustrated in Fig. 8.

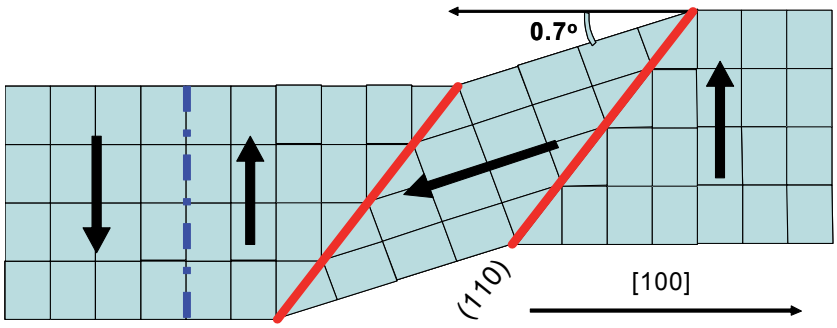

Fig. 8. Schematic illustration of the 180° and 90° domain walls in $BaTiO_3$.

Besides regular 90° and 180° twin walls, $BaTiO_3$ crystallites containing (111) twins have also been reported. (111) twinned $BaTiO_3$ was first observed in single crystals grown via

the Remeika method [53] and in bulk ceramics [54] in 1950s. Existing evidences suggest that the formation of (111) twins in ceramics are closely related to the exaggerated growth of the hexagonal $BaTiO_3$ phases on the twin plane which involved oxygen octahedra sharing the face [55]. It has also been suggested that (111) twins can lead to the exaggerated growth of $BaTiO_3$ grains in ceramics following a twin-plane re-entrant edges (TPREs) mechanism [56,57] since the decreasing of activation energy of nucleation on the TPREs.

We recently reported the controlled synthesis of $BaTiO_3$ microcrystallites through a two-step synthesis approach [58,59]. The synthesis method is quite similar to the synthesis of BaTiO3 nanocubes, except that the starting anatase TiO_2 powders were first treated in autoclave for 5 hours. Then, $BaCl_2$ and water were added into the autoclave, followed by heat treatment at 180°C for different period of time up to 20 days. It is found that the pretreated TiO_2 is essential for the synthesis of penetrated $BaTiO_3$. The crystallites exhibit penetrated morphologies and contain multiple (111) twins, originated from amorphous TiO_2 clusters.

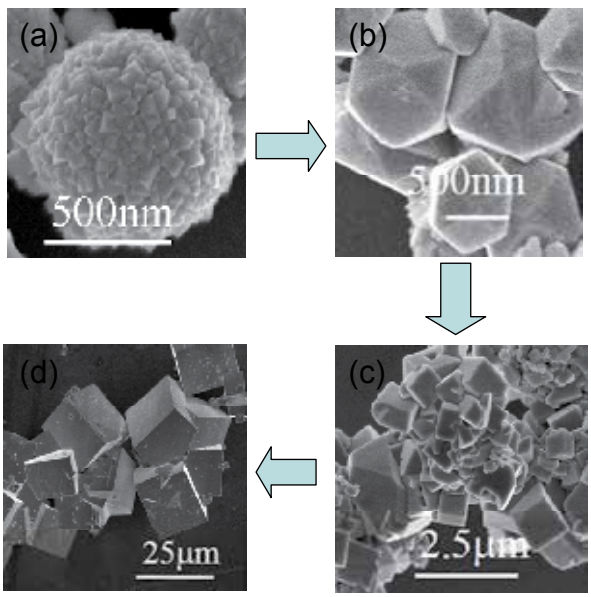

Fig. 9. SEM images of penetrated $BaTiO_3$ microcrystallite obtained at different synthesis stages. (Copyright 2010 @ Royal Society of Chemistry).

Figure 10a shows the photograph of (111) twined $BaTiO_3$ nanoparticles before and after UV irradiation. The UV-vis absorption spectra reveal the presence of defect energy levels after UV irradiation. The color of the powders changes from pale yellow to dark brown after UV irradiation. Oxygen vacancies create additional energy levels within the forbidden energy gap of titanates, usually 0.2-0.3 eV below the conduction band edge [60,61].Figure 10c shows the XPS spectra of Ti-2*p* electrons before and after UV irradiation. A careful curve fitting shows that a shoulder peak appears at position ~ 1.3 eV lower than that of Ti^{4+} cations, suggesting the presence of Ti^{3+} cations [62]. The mechanism for the formation of Ti^{3+} cations is discussed as follows. As the valence band of $BaTiO_3$ is dominated by O-2*p* orbits, whereas the conduction band is the Ti-3*d* orbits [17], electrons of O-2*p* orbits can be excited by UV

photons to the Ti-*3d* orbits, resulting in the formation of gaseous oxygen and leaving behind oxygen vacancies inside the microcrystallites. The excited electrons are either trapped by Ti^{4+} to form Ti^{3+} centers or are trapped by oxygen vacancies to form F-centers, both of which could have strong absorption at visible region, resulting in the observed photochromic effect. However, it is still unclear why the photochromic effect can hardly be observed on regular $BaTiO_3$ nanocubes without (111) twins. It seems that the (111) twin walls may also have a role during the process described above. Previous HRTEM investigations had revealed that the (111) twin walls are composed of $Ba\text{-}O_{3\text{-}x}\text{-}[V_O]_x$ instead of $Ba\text{-}O_3$ plane to balance the charge of adjacent Ti^{4+} ions [63].

Fig. 11 shows the magnetization (M) versus applied magnetic field (H) curves measured at room temperature before and after the UV irradiation. The green sample presents very weak ferromagnetism with saturation magnetization of ~ 7×10^{-5} emu/g. The saturation magnetization for the UV irradiated $BaTiO_3$ crystallites is substantially enhanced and becomes ~ 6.7×10^{-4} emu/g, due to the increase of oxygen vacancies caused by UV photons. However, the coercive field does not change and remains to be ~ 305 Oe. The inset of Fig. 11 is the *M-H* curve of the sintered bulk sample. The sintered bulk sample is diamagnetic. This behavior is similar to other nanosized oxides particles due to the magnetic origin of defects.

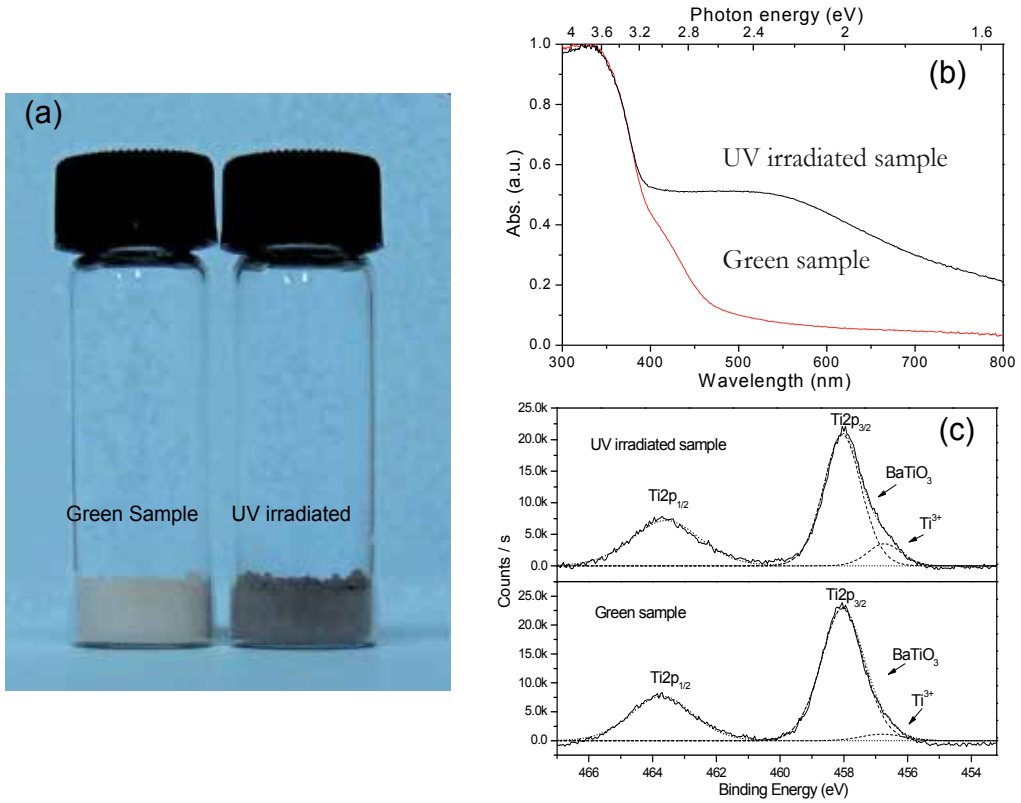

Fig. 10. Photographs of (111) twinned BaTiO3 nanoparticles (a), the corresponding UV-vis absorption spectra (b) and XPS spectra (c) before and after UV irradiation reveal photochromic effect. (Copyright 2010 @ American Chemical Society).

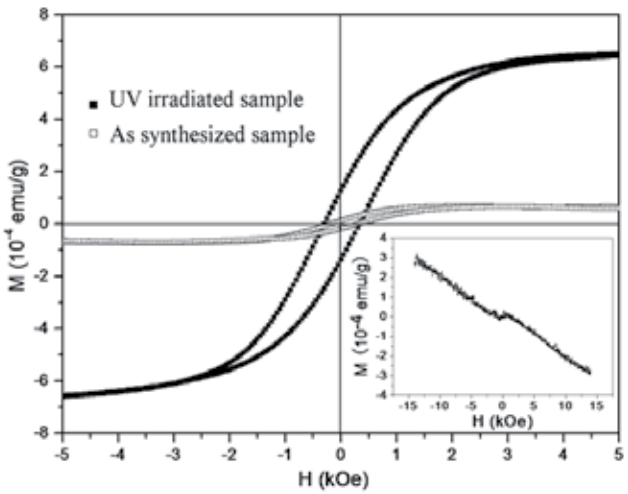

Fig. 11. Room-temperature M-H curves of the UV-irradiated $BaTiO_3$ sample and the as-synthesized sample. The inset is the M-H curve of the sintered bulk sample. (Copyright 2010 @ American Chemical Society).

7. Conclusions

Insightful understanding and careful control of defect structures in ferroelectric does not only provide an efficient tool for tuning ferroelectric properties, but also open a window for exploring novel properties of ferroelectric materials, previously believed impossible or negligible. We expect that there will be more investigations conducted on this area not only from the viewpoint of ferroelectrics but also with cautious consideration of their technical implications.

Acknowledgement. The authors would thank National Science Foundation of China (NSFC) through grant # 50702031, # 51021062 and # 60974117, the Excellent Young Investigators Award Foundation of Shandong Province (Grant No. BS2009CL021), SRF for ROCS, State Education Ministry, National Basic Research Program of China (973 Program) through grant # 2009CB930503) for financial support.

8. References

[1] Scott, J. F. *Science.* 2007, 315, 954-959.
[2] Damjanovic, D. *Rep. Prog. Phys.* 1998, 61, 1267-1324.
[3] Gopalan, V.; Dierolf, V. ; Scrymgeour, D. A.;*Annu. Rev. Mater. Res.,* 2007**,** 37, 449.
[4] Scrymgeour, D. A. ; Gopalan, V. ; *Phys. Rev. B*, 2005, 72, 24103.
[5] Majdoub, M. S; Sharma, P.; Cagin, T. *Phys. Rev. B.* 2008, 77, 125424-1-125424-9.
[6] Devonshire, A.F.; *Philosophical Magazine*, 1949, 40, 1040.
[7] Devonshire, A.F.; *Philosophical Magazine,* 1951**,** 42, 1065.
[8] Lines M.E.; Glass, A.M.; Principles and applications of ferroelectrics and related materials [Oxford University Press, New York, 1977].
[9] Abplanalp, M.; Fousek, J.; Gunter, P.; *Phys. Rev. Lett.*, 2001**,** 86, 5799.
[10] Haun, M.J.; Furman, E.; Jang, S.J.; Mckinstry, H.A.; Cross, L.E.; *J. Appl. Phys.*, 1987**,** 62, 3331.

[11] Agullo-Lopez, F.; Catlow, C. R. A.; Townsend, P.; *Point Defects in Materials*, 1988, Academic Press, London.
[12] Stoneham, A. M. ; *Theory of Defects in Solids*, 1976, Clarendon Press, Oxford.
[13] Waser, R. ; Smyth, D. M.; *Ferroelectric Thin Films: Synthesis and Basic Properties*, ed. C. A. P. Araujo, J. F. Scott, 1996, pp. 47–92, GW Taylor, Singapore: Gordon & Breach.
[14] Jiang, Q. Y. ; Subbarao, E. C ; Cross, L. E.; *J. Appl. Phys.*, 1994, 75, 7433.
[15] Jiang, Q. Y. ; Subbarao, E. C. ; Cross, L. E. ; *Ferroelectrics*, 1994, 154, 119.
[16] Jiang, Q. Y. ; Cao, W. ; Cross, L. E. ; *J. Am. Ceram. Soc.*, 1994, 77, 211.
[17] Duiker, H. M. ; Beale, P. D. ; Scott, J. F. ; Paz de Araujo, C. A. ; Melnick, B. M. ; Cuchiaro, J. D. ; McMillan, L. D. ; *J. Appl. Phys.*, 1990, 68, 5783.
[18] Scott, J. F. ; Dawber, M. ; *Appl. Phys. Lett.*, 2000, 76, 3801.
[19] Ramesh, R. ; Gilchrist, H. ; Sands, T. ; Keramidas, V. G. ; Hakenaasen, R.; *Appl. Phys. Lett.*, 1993, 63, 3592.
[20] Ramesh, R. ; Lee, J. ; Sands, T. ; Keramidas, V. G. ; Auciello, O. ;*Appl. Phys. Lett.*, 1994, 64, 2511.
[21] Chen, H. J. ; Chen, Y. W. ; *Ind. Eng. Chem. Res.*, 2003, 42, 473.
[22] Dutta, P. K. ; Asiaie, R.; Akbar, S. A. ; Zhu, W. ; *Chem. Mater.*, 1994, 6, 1542.
[23] Hennings, D.; Schreinemacher, S. ; *J. Euro. Ceram. Soc.*, 1992, 9, 41.
[24] Wada, S. ; Suzuki, T. ; Noma, T. ;*Jpn. J. Appl. Phys.*, 1995, 34, 5368.
[25] Wada, S. ; Suzuki, T. ; Noma, T. ; *J. Ceram. Soc. Jpn.*, 1996, 104, 383.
[26] Kapphan, S.; Weber, G.; *Ferroelectrics*, 1981, 37, 673.
[27] Wada, S.; Suzuki, T. ; Noma, T. ; *J. Ceram. Soc. Jpn.*, 1995, 103, 1220.
[28] Noma, T. ; Wada, S. ; Yano, M. ; Suzuki, T.; *J. Appl. Phys.*, 1996, 80, 5223.
[29] Jia, C. L. ; Lentzen, M. ; Urban, K. ;*Science*, 2003, 299, 870.
[30] Namai, Y.; Matsuoka, O.; *J. Phys. Chem. B*, 2005, 109, 23948.
[31] Hirth J.P.; Lothe, J.; *Theory of dislocations* [Wiley, New York, ed. 2nd, 1982].
[32] Alpay, S.P.; Misirlioglu, I.B.; Nagarajan, V.; Ramesh, R.; *Appl. Phys. Lett.*, 2004, 85, 2044.
[33] Berlincourt D.; Jaffe, H.; *Phys. Rev.*, 1958, 111, 143.
[34] Bell, A.J.; *J. Appl. Phys.*, 2001, 89, 3907.
[35] Chu, M. W.; Szafraniak, I.; Scholz, R.; Harnagea, C.; Hesse, D.; Alexe, M. ; Gosele, U.; *Nat. Mater.*, 2004, 3, 87.
[36] Jia, C. L.; Mi, S. B.; Urban, K.; Vrejoiu, I.; Alexe, M.; Hesse, D.; *Phys. Rev. Lett.*, 2009, 102, 117601.
[37] Kontsos, A. ; Landis, C. M. ; *Int.J.Solids Struct.*, 2009, 46, 1491.
[38] Li, Y. L. ; Hu, S. Y. ; Choudhury, S.; Baskes, M. I.; Saxena, A.; Lookman, T. ; Jia, Q. X. ; Schlom, D. G.; Chen, L. Q. ; *J. Appl. Phys.*, 2008, 104, 104110.
[39] Betouras, J. J. ; Giovannetti, G. ; J. V. D. Brink, *Phys. Rev. Lett.*, 2007, 98, 257602.
[40] Qin, S.; Liu, D. ; Liu, H. ; Zuo, Z.; *J. Phys. Chem. C*, 2008, 112, 17171.
[41] Eglitis, R.; Borstel, I. G.; Heifets, E.; Piskunov, S.; Kotomin, E. *J. Electroceram.*, 2006, 16, 289-292.
[42] Clark, I. J. ; Takeuchi, T. ; Ohtori, N. ; Sinclair, D. C. *J. Mater. Chem.*, 1999, 9, 83-91.
[43] Blanco-Lopez, M. C. ; Rand, B. ; Riley, F. L. *J. Eur. Ceram. Soc.* 1997, 17, 281-287.
[44] Siegel, R. W. *Annu. Rev. Mater. Sci.* 1991, 21, 559-578.
[45] Madhukar, A.; Lu, S. Y.; Konker, A.; Ho, M.; Hughes, S. M.; Alivisatos, A. P. *Nano Lett.* 2005, 5, 479-482.
[46] Narayan, J. *J. Appl. Phys.* 2006, 100, 034309[1]-034309[5].
[47] Gryaznov, V. G.; Polonsky, I. A.; Romanov, A. E.; Trusov L. I. *Phys. Rev. B*. 1991, 44, 42-46.
[48] Joos, B.; Duesbery, M. S. *Phys. Rev. Lett.* 1997, 78, 266-269.
[49] Watt, J. P.; Peselnick, L. *J. Appl. Phys.* 1980, 51, 1525-1531.

[50] Liu, D.; Chelf, M.; White, K. W. *Acta Mater*. 2006, 54, 4525-4531.
[51] K.-H. Hellwege, Ed., Landolt-Bornstein: Numerical Data and Functional Relationships in Science and Technology, New Series, Group III, vols. 11 and 18, Berlin: Springer-Verlag, 1979 and 1984.
[52] Colby, B.; Liang, Z.; Wildeson, I.H.; Ewoldt, D.H., Sands, T.D.; Garca, R. E.; Stach, E. A.; *Nano Lett.,* 2010, 10, 1568–1573
[53] Remeika, J. P.; Jackson, W. M. J. Am. Chem. Soc. 1954, 76, 940–941
[54] Tennery, V. J.; Anderson, F. R. *J. Appl. Phys*. 1959, *29*, 755–758.
[55] Recnik, A.;. Kolar, D. *J. Am. Ceram. Soc*. 1996, *79*, 1015–1018.
[56] Hu, K. A.; Hiremath, B. V.; Newnham, R. E. *Phase. Transit*. 1986, *6*, 153–164.
[57] Lee, H. Y.; Kim, J. S. *J. Am. Ceram. Soc*. 2002, *85*, 977–980.
[58] Qin, S; Liu, D.; Zheng, F; Zuo, Z.; Liu H; Xu, X; *CrystEngComm*, 2010, 12, 3003
[59] Qin, S; Liu, D.; Sang, Y.; Zuo, Z.; Zhang, X.; Zheng, F; Liu H; Xu, X; *J. Phys. Chem. Lett.* 2010, 1, 238.
[60] Cronemeyer, D. C. *Phys. Rev*. 1959, *113*, 1222.
[61] Berglund, C. N.; Braun, H. J. *Phys. Rev*. 1967, *164*, 790.
[62] Paik, U.; Yeo, J. G.; Lee, M. H.; Hackley, V. A.; Jung, Y. G. *Mater. Res. Bull*. 2002, *37*, 1623.
[63] Renik, A.; Bruley, J.; Mader, W.; Kolar, D.; Rühle, M.; *Philosophical Magazine Part B* , 1994, 70, 1021-1034.

Part 2

Characterization: Electrical Response

7

All-Ceramic Percolative Composites with a Colossal Dielectric Response

Vid Bobnar, Marko Hrovat, Janez Holc and Marija Kosec
Jožef Stefan Institute, Jamova 39, SI-1000, Ljubljana
Slovenia

1. Introduction

Dielectric materials, which are used to control and store charges and electric energy, play a key role in modern electronics and electric power systems. As commercial and consumer requirements for compact and low cost electronic and electrical power systems as well as for very high energy capacitive storage systems grow substantially, the development of high dielectric constant materials has become one of the major scientific and technology issues (Reynolds & Buchanan, 2004; Scott, 2007). High dielectric constant materials are highly desirable for use, not only as capacitor dielectrics, but also in a broad range of advanced electromechanical applications, such as actuators, sonars, and, particularly, as high-frequency transducers (Zhang et al., 2002). The input electric energy that can be converted into the strain energy is namely directly proportional to the square of the electric field and to the dielectric constant of the electroactive material. Thus, by increasing the dielectric constant the required electromechanical response, i.e., strain can be induced under a much reduced electric field.

Extremely large dielectric constants are expected only for ferroelectrics in a very narrow temperature range close to the paraelectric-to-ferroelectric phase transition or for systems with hopping charge carriers yielding dielectric constant that diverges towards low frequencies. High-capacitance ceramic capacitors are therefore mostly made of very thin layers of ceramic material (usually a ferroelectric) placed between conductive plates. The most important part of the market in passive devices is, at present, made up of multilayer ceramic capacitors (MLCCs), comprising alternating thin layers of conductor (inner electrodes) and ceramic (Takeshima et al., 1997), which turns out to be the most efficient geometry for attaining high-density charge storage. A similar geometrical approach can also intuitively explain the dielectric response of a percolative composite – a composite comprising a conductive filler embedded in a dielectric matrix. The fact that the effective dielectric constant of the mixture is much larger than the dielectric constants of the individual constituents is due to the fact that close to the percolation point (the volume fraction when the conductive admixture forms a continuous network and, consequently, the system begins to conduct electricity) there are many conducting particles which are isolated by very thin dielectric/ferroelectric layers. A comparison between configurations of a MLCC and a percolative composite is presented in Fig. 1. Unfortunately, the percolative

approach in developing high dielectric constant materials has up to now very often been handicapped by the impossibility of preparing homogeneous metal–insulator composites with metal concentrations very close to the percolation threshold.

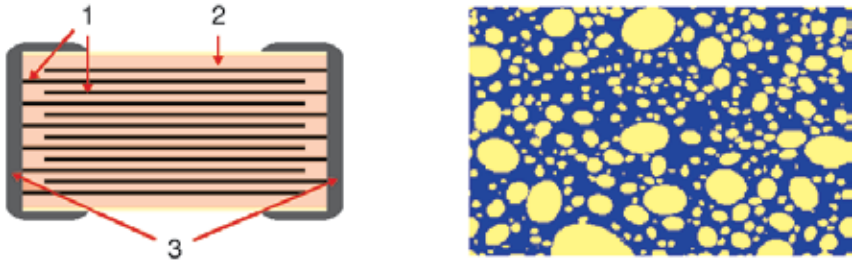

Fig. 1. Schematic configuration of a multilayer ceramic capacitor (MLCC) (left; 1-metallic electrodes, 2-thin layers of dielectric/ferroelectric ceramics, 3-metallic contacts) and a percolative composite (right; yellow and blue regions represent conductive and dielectric/ferroelectric material, respectively).

Exceptionally high dielectric constants which were obtained by making use of the conductive percolative phenomenon in ceramic composites made of perovskite ruthenium-based conductive ceramics and perovskite ferroelectric ceramics, are reported in this chapter. The potential of these all-ceramic percolative composites for use as high dielectric constant materials in various applications is demonstrated: Due to a homogeneous distribution of conductive ceramic grains within the ferroelectric ceramic matrix, the dielectric response of the lead-based $Pb(Zr,Ti)O_3$–$Pb_2Ru_2O_{6.5}$ and $0.65Pb(Mg_{1/3}Nb_{2/3})O_3$-$0.35PbTiO_3$–$Pb_2Ru_2O_{6.5}$ as well as of the lead-free $(K,Na)NbO_3$–RuO_2 systems namely follows the predictions of the percolation theory. Thus, values of the dielectric constant are near the percolation threshold for two orders of magnitude higher than in the pure matrix ferroelectric ceramics.

2. Percolative composites

The theory of percolation was initially developed to describe several abrupt transitions commonly found in transport phenomena. Based on this model, a general theory was built that explains a physical process in which a macroscopic magnitude is strongly modified as a result of small microscopic changes in connectivity (Feng et al., 1987). One such process is the anomalous behavior of a metal-insulator composite near its percolation threshold, which is characterized by an abrupt discontinuity in the real part of the electrical conductivity (Bergman & Imry, 1977; Kirkpatrick, 1973). An excellent review for the system consisting of randomly distributed metallic and dielectric regions is given in the paper of Efros and Shklovskii (Efros & Shklovskii, 1976): It is shown that the static dielectric constant diverges at the percolation threshold – at the volume fraction of metallic regions (p) where the insulator-to-metal transition occurs, i.e., the static effective electrical conductivity σ of such a heterogeneous system undergoes a transition from

$$\sigma = \sigma_{matrix} [(p_c-p)/p_c]^{-q} , \quad (1)$$

which is valid below the percolation threshold p_c, into

$$\sigma = \sigma_{metal}\,[(p-p_c)/p_c]^t \ , \tag{2}$$

which holds true for $p>p_c$. σ_{matrix} and σ_{metal} are conductivities of the dielectric and metallic phases, respectively (of course $h=\sigma_{matrix}/\sigma_{metal}<<1$). This behavior is depicted in Fig. 2, which also reveals that a smooth transition from Eq. (1) to Eq. (2) occurs in some small interval Δ near the percolation point.

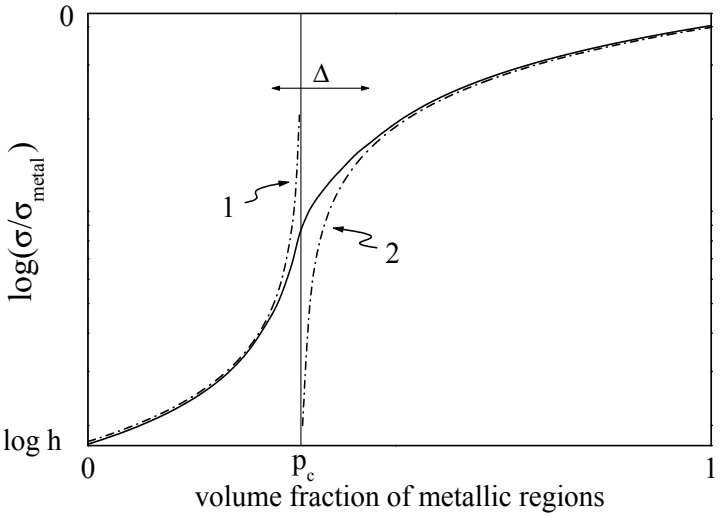

Fig. 2. The theoretical dependence of the effective electrical conductivity σ (solid line) for a system consisting of randomly distributed metallic and dielectric regions. A smooth transition between behaviors described by Eqs. (1) and (2) (dash-dotted lines) occurs in small interval Δ near the percolation point p_c (vertical line).

Very high dielectric constants can thus be achieved in metal-insulator composites close to the percolation point. However, up to now mainly organic percolative composites (Dang et al., 2003; Huang et al., 2004; Xu & Wong, 2005) and inorganic composites comprising metal particles dispersed in a dielectric matrix (Deepa et al., 2007; Grannan et al., 1981; Li et al., 2001; Yoshida, 1990) have been developed. In organic percolative composites values of the dielectric constant as high as 7000 were obtained (Huang & Zhang, 2004). As the dielectric constant of a polymer is typically less than 100, i.e., far below the values of inorganic ferroelectrics, which reach several thousands, it is not surprising that the dielectric constant in percolative composites with an inorganic matrix can reach values as high as 80000 (Pecharroman et al., 2001).

2.1 All-ceramic percolative composites

Composites of ferroelectric ceramics and conductive ceramic particles can offer a major advantage in the development of high dielectric constant materials, as percolative systems comprising ceramics and metal particles are relatively sensitive to processing. The latter can be sintered in air only if a noble metal is used; however, if the conductive component is based on a non-noble metal, the system has to be fired in a neutral or reducing atmosphere. Such a procedure can negatively influence the electrical properties of ferroelectric ceramics, which are, due to the relatively high dielectric constant, very suitable for the matrix in a

percolative system. For example, insulating ferroelectric $BaTiO_3$ or $Pb(Zr,Ti)O_3$ systems can become semiconducting as a result of reduction (Raymond & Smyth, 1996). The combination of insulating and conducting ceramics is thus inherently better than the combination of oxide ceramics and metallic particles, as the all-oxide ceramic systems can be sintered in air. On the other hand, all-ceramic systems could suffer from reactions between both constituents during high-temperature sintering, resulting in new compounds or solid solutions with undesirable characteristics. The compatibility between the chosen ceramic matrix and the conductive ceramics must therefore be carefully evaluated.

3. Processing and structural analysis

3.1 Synthesis of all-ceramic percolative composites

3.1.1 $Pb(Zr,Ti)O_3$–$Pb_2Ru_2O_{6.5}$ system

$Pb(Zr,Ti)O_3$–$Pb_2Ru_2O_{6.5}$ all-ceramic percolative system was made from $PbZr_{0.53}Ti_{0.47}O_3$ (PZT) and $Pb_2Ru_2O_{6.5}$ powders. These two systems have been chosen as $Pb_2Ru_2O_{6.5}$ is a very good electrical conductor, having the resistivity of 270×10^{-8} Ωm (Pierce et al., 1982), and as investigations of the phase equilibrium in the Pb–Zr–Ti–Ru–O system showed that PZT is compatible with $Pb_2Ru_2O_{6.5}$ at least up to 1000°C (Hrovat et al., 2001). PZT powder with a 6 mol.% excess of PbO was prepared by mechanochemical synthesis (Kuščer et al., 2006) from high-purity PbO, ZrO_2, and TiO_2. The excess lead oxide was added to compensate for its evaporation during the synthesis. $Pb_2Ru_2O_{6.5}$ powder was prepared by solid-state synthesis from PbO and RuO_2 by repeated firing with intermediate grinding (three times) at 850°C. Prereactered PZT and $Pb_2Ru_2O_{6.5}$ powders were mixed, pressed into pellets and fired on platinum foils at 850°C for 15 min.

3.1.2 $0.65Pb(Mg_{1/3}Nb_{2/3})O_3$-$0.35PbTiO_3$–$Pb_2Ru_2O_{6.5}$ system

Although values of the dielectric constant as high as 40000 were detected in the PZT-$Pb_2Ru_2O_{6.5}$ composite (Bobnar et al., 2008), a further challenge was to find another ceramic system, with much higher dielectric constant as those of PZT if possible, which would also be compatible with the $Pb_2Ru_2O_{6.5}$ system. $0.65Pb(Mg_{1/3}Nb_{2/3})O_3$-$0.35PbTiO_3$ (PMN-35PT) perovskite ferroelectric, which has a very high dielectric constant as this composition is close to the morphotropic phase boundary (Priya et al., 2002), was found to be such a system, and, consequently, in the developed PMN-35PT–$Pb_2Ru_2O_{6.5}$ composite values of the dielectric constant higher than 10^5 were detected (Bobnar et al., 2009a). Similarly to the PZT, PMN-35PT powder was prepared by mechanochemical synthesis (Kuščer et al., 2007). A mixture of PbO, MgO, TiO_2, and Nb_2O_5 in the molar ratio corresponding to the stoichiometry of 0.65PMN–0.35PT with 2 mol % of the PbO excess was high-energy milled in a planetary mill for 64 hours. A total of 200 g of powder was placed in the vial. Finally, prereactered PMN-35PT and $Pb_2Ru_2O_{6.5}$ powders were mixed, pressed into pellets and fired on platinum foils at 1000°C for 4 hours.

3.1.3 Lead-free $K_{0.5}Na_{0.5}NbO_3$–RuO_2 composite

As lead represents a possible ecological hazard, a great deal of current materials research is oriented toward environmentally friendly lead-free materials. Thus, $K_{0.5}Na_{0.5}NbO_3$–RuO_2 (KNN-RuO_2) lead-free percolative composite has also been developed (Bobnar et al., 2009b): RuO_2 is a very good electrical conductor with the resistivity of 40×10^{-8} Ωm (van Loan, 1972)

and it has been found that there is no reaction between KNN and RuO_2 at temperatures even higher than 1000°C. $K_{0.5}Na_{0.5}NbO_3$ powder was prepared by solid-state synthesis from K_2CO_3, Na_2CO_3, and Nb_2O_5. A total of 2 wt.% of potassium-sodium germanate was added to lower the sintering-temperature of KNN. The powder mixtures were homogenized, calcined at 900°C for 4 hours and milled to yield submicron-sized powders. KNN and RuO_2 powders were then mixed in acetone in a ball mill. The powders were pressed into pellets and fired on platinum foils at 1000°C for 2 hours.

3.2 Characterization methods

The phase composition of the PZT, PMN-35PT, KNN, and $Pb_2Ru_2O_{6.5}$ powders was checked by X-ray powder diffraction using a Philips PW 1710 X-ray diffractometer with Cu Kα radiation. The X-ray spectra were measured from $2\Theta=20^o$ to $2\Theta=70^o$.

Fired PZT–$Pb_2Ru_2O_{6.5}$, PMN-35PT–$Pb_2Ru_2O_{6.5}$, and KNN–RuO_2 samples were characterized using X-ray powder diffraction. A JEOL 5800 scanning electron microscope (SEM) equipped with a link ISIS 300 energy-dispersive X-ray analyzer (EDS) was used for the overall microstructural and compositional analyses. The samples prepared for the SEM were mounted in epoxy in a cross-sectional orientation and then polished using standard metallographic techniques. Prior to analysis in the SEM, the samples were coated with carbon to provide electrical conductivity and avoid charging effects. The microstructures of the polished samples were studied using back-scattered electron imaging and compositional contrast to distinguish between the phases that differ in density (average atomic number Z).

3.3 Structural properties

Microstructures and X-ray spectra of developed all-ceramic percolative composites are shown in Fig. 3. The microstructure of the PZT–$Pb_2Ru_2O_{6.5}$ composite with 15 vol.% of $Pb_2Ru_2O_{6.5}$ consists of small, light-grey inclusions ($Pb_2Ru_2O_{6.5}$) in a dark-grey matrix (sintered PZT). The small black spots are pores. PMN-35PT–$Pb_2Ru_2O_{6.5}$ microstructure (also the sample with 15 vol. % of $Pb_2Ru_2O_{6.5}$) consists of small, light-grey $Pb_2Ru_2O_{6.5}$ inclusions, a dark-grey PMN-PT matrix, and a few pores. The microstructure of the lead-free KNN–RuO_2 sample with 15 vol.% of RuO_2 reveals that the grey KNN matrix consists of cubic-shaped grains, while the light-grey inclusions are RuO_2 grains.

In each of the three composites the conductive filler is uniformly distributed throughout the matrix. The EDS microanalysis did not detect any solid solubility in developed composites, which confirms the results obtained with X-ray analyses: Only the peaks of the initial compounds are present in the fired samples and, furthermore, no shifts in the peaks' positions were observed (for comparison, the X-ray spectra of individual PZT, KNN, and $Pb_2Ru_2O_{6.5}$ constituents are included in Fig. 3). The results therefore indicate that (i) PZT and $Pb_2Ru_2O_{6.5}$, (ii) PMN-35PT and $Pb_2Ru_2O_{6.5}$, as well as (iii) KNN and RuO_2 are compatible at the firing temperatures.

Structural analysis thus revealed a demanded structure of composites – there is no reaction and no solid solubility between constituents and the conductive filler is uniformly distributed throughout the matrix. Consequently, the dielectric response of the developed PZT–$Pb_2Ru_2O_{6.5}$, PMN-35PT–$Pb_2Ru_2O_{6.5}$, and KNN-RuO_2 composites should follow the predictions of the percolation theory.

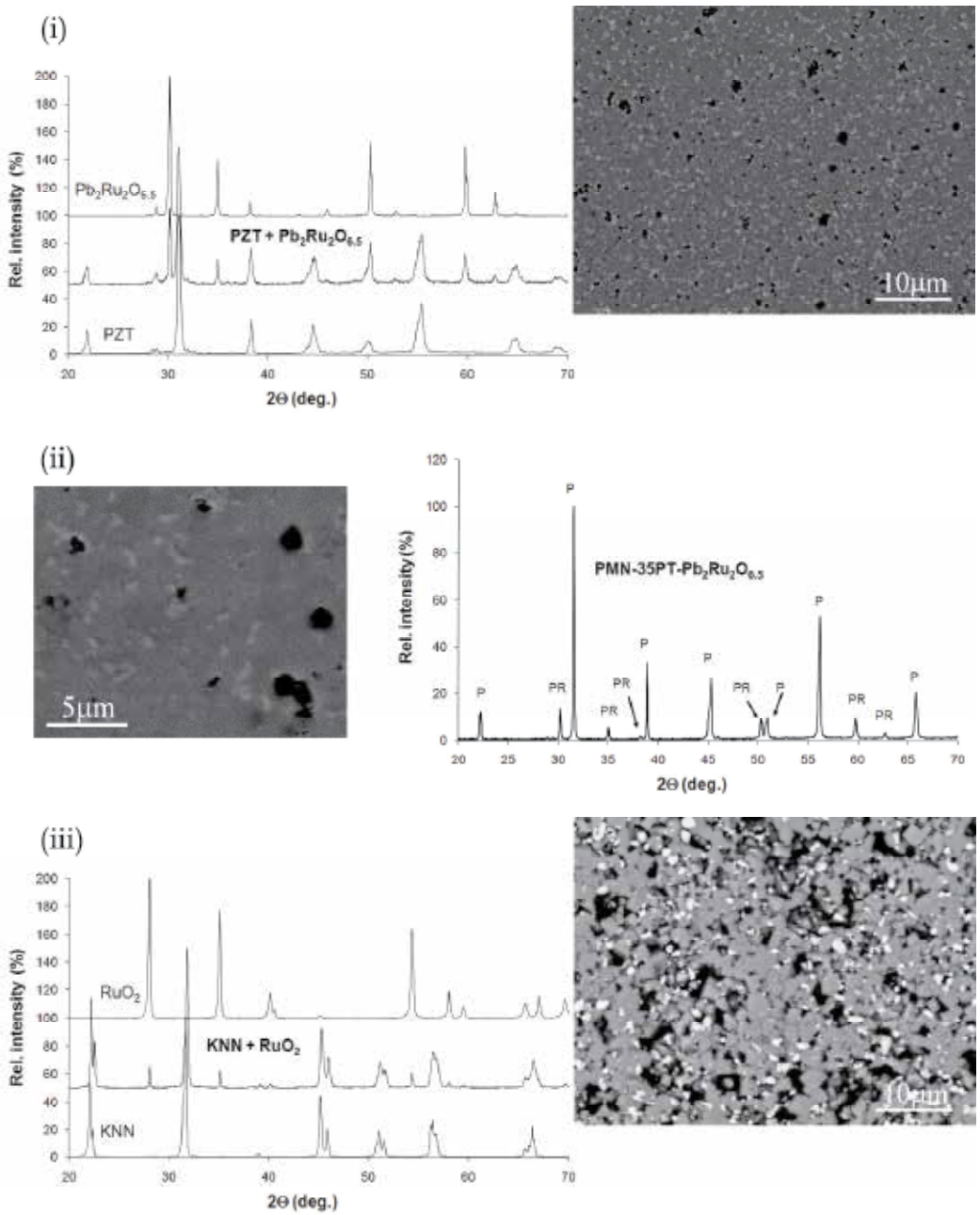

Fig. 3. Microstructures and X-ray spectra of developed all-ceramic percolative composites: (i) PZT–$Pb_2Ru_2O_{6.5}$ with 15 vol. % of $Pb_2Ru_2O_{6.5}$; (ii) PMN-35PT–$Pb_2Ru_2O_{6.5}$ with 15 vol. % of $Pb_2Ru_2O_{6.5}$; (iii) KNN–RuO_2 with 15 vol. % of RuO_2. For comparison, the X-ray spectra of individual PZT, KNN, and $Pb_2Ru_2O_{6.5}$ constituents are included in (i) and (iii), while in the PMN-35PT–$Pb_2Ru_2O_{6.5}$ X-ray spectrum peaks of the PMN-35PT and $Pb_2Ru_2O_{6.5}$ are denoted with P and PR, respectively.

4. Dielectric response of composites

Samples of 5–6 mm in diameter with sputtered gold electrodes on both surfaces were used for dielectric characterization. The complex dielectric constant $\varepsilon^*(\nu,T)=\varepsilon'-i\varepsilon''$ was measured as a function of the frequency (ν; 20 Hz to 1 MHz) and temperature (T; heating and cooling rates of $\pm 0.5°Cmin^{-1}$) using an HP4284A precision LCR meter. The amplitude of the probing ac electric signal, applied to samples with a thickness of ≈300 μm, was 1 V. The temperature was stabilized using a lock-in bridge technique with a Pt100 resistor as a thermometer. The real part of the complex ac-conductivity $\sigma^*(\nu,T)=\sigma'+i\sigma''$ was calculated via $\sigma'=2\pi\nu\varepsilon_0\varepsilon''$ with ε_0 being the permittivity of free space.

4.1 Qualitative description of the frequency spectra

The frequency dependence of the room-temperature dielectric constant ε' and conductivity σ' in PZT–$Pb_2Ru_2O_{6.5}$ samples with different $Pb_2Ru_2O_{6.5}$ volume concentrations is shown in Fig. 4. There exist several mixing formulae, or even different approaches, which predict or describe the dielectric response of a two-component heterogeneous system. For example, a detected behavior of the electrical conductivity – at higher frequencies σ' increases, while at lower frequencies values tend toward the dc-conductivity plateau – could easily be modeled by an equivalent circuit composed of two RC circuits connected in serial. The resistivity of the low-frequency plateau is then R_1+R_2, while at higher frequencies the conductivity follows a ν^2 law if $R_2>>R_1$ (Efros & Shklovskii, 1976), as is, evidently, the case in a percolative composite (then the value of the low-frequency plateau is just the resistivity of the matrix). However, although a crossover from the plateau to the ν^2 dependence has in fact been observed in the $Al_6Si_2O_{13}$-molybdenum composite (Pecharroman & Moya, 2000), the $\sigma'(\nu)$ increase here is much weaker. This is not surprising, as for granular systems, rather than modeling the spectra by various equivalent circuits with frequency-independent elements, more physically transparent models are needed in order to adequately describe their effective dielectric response.

The complex electrical conductivity of different metal-insulator composites can often be described by the two exponent phenomenological percolation equation – an excellent review of this method is given in (Chiteme et al., 2007). The equation is also known as the general effective medium equation. In fact, by using the effective medium approach (EMA – assuming that the probing field is homogeneous within the individual particles) it has been derived that the ac conductivity in a random system follows a ν^s behavior with $s<1$ (Springett, 1973), as has in fact been detected in our composites. In the limit of EMA also a rather general approach has been formulated (Petzelt & Rychetsky, 2005), which states that for any two-component composite with sharp particle boundaries the dielectric response can be composed of two additive parts. One part describes the sum of the original bulk responses weighted by the relative volumes, while the second part describes the localized particles affected by the depolarization field depending on particle shape and its surroundings. Within this approach, the spherical shape of inclusions leads to a percolation threshold of 1/3 (Rychetsky et al., 1999), thus a more general particle form and topology would be needed to describe smaller threshold, as is frequently observed (also in our case, as will be shown in the next subsection). However, the detected dielectric response of all developed composites (see PZT–$Pb_2Ru_2O_{6.5}$ in Fig. 4, PMN-PT–$Pb_2Ru_2O_{6.5}$ in Fig. 5, and KNN-RuO_2 in Fig. 6) can be qualitatively understood:

At lower frequencies the conductivity of the $Pb_2Ru_2O_{6.5}$ or RuO_2 inclusions is effectively blocked, while at sufficiently high frequencies their higher conductivity is revealed since most of the charge carriers have no time to feel the blocking boundaries. The effective ac-conductivity σ' therefore increases with frequency (and would increase up to the high-frequency plateau corresponding to the value of the $Pb_2Ru_2O_{6.5}$ or RuO_2 conductivity). As even for an inhomogeneous system the Kramers-Kronig relations must be satisfied, the increasing σ' contribute to the static dielectric constant via a strong dielectric relaxation. In systems with the composition very close to the percolation threshold (the PZT–$Pb_2Ru_2O_{6.5}$ composite with 17 vol. % of $Pb_2Ru_2O_{6.5}$ in Fig. 4 and the lead-free KNN-RuO_2 composite with 20 vol. % of RuO_2 in Fig. 6), ac-conductivity is almost frequency-independent in the entire experimental range. Considering the Kramers-Kronig relations, we may conclude that here the strong conductivity dispersion shifts below 10 Hz, as, on the other hand, the dielectric constant in these samples strongly increases at lower frequencies.

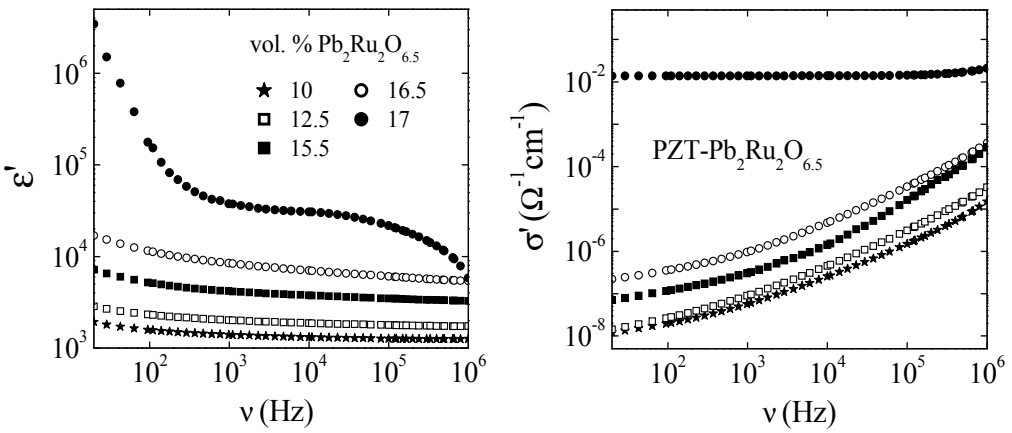

Fig. 4. Frequency dependence of the real parts of the complex dielectric constant ε' and conductivity σ' measured at room temperature for PZT–$Pb_2Ru_2O_{6.5}$ samples with different volume concentrations of $Pb_2Ru_2O_{6.5}$.

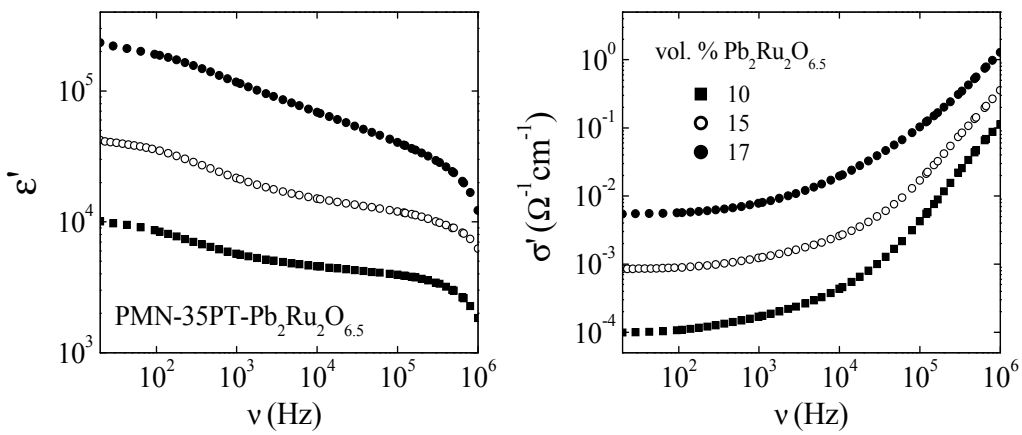

Fig. 5. Room-temperature dielectric constant and conductivity as a function of the frequency for PMN-35PT–$Pb_2Ru_2O_{6.5}$ samples with different $Pb_2Ru_2O_{6.5}$ volume concentrations.

In contrast to both lead-based systems, the experimental condition plays an important role in the KNN-RuO_2 composite, as being emphasized in Fig. 6. Here, the main frames show the frequency dependence of ε' and σ' in samples with different RuO_2 volume concentration, measured at room temperature under vacuum. While the evaluation of data on increasing RuO_2 content is very similar to that in the PZT–$Pb_2Ru_2O_{6.5}$ and PMN-35PT–$Pb_2Ru_2O_{6.5}$ systems, the low-pressure condition is very important. The inset namely clearly reveals that ε', measured in air, additionally strongly increases at lower frequencies. Most probably this is due to the conductivity contribution of water in the pores – in the KNN-RuO_2 these are much larger than in the lead-based composites (see Fig. 3). This is further endorsed by the fact that data taken under atmospheric pressure but with highly-hygroscopic silica-gel placed in the sample cell are almost identical to those detected under vacuum. Thus, all results, hereupon presented for the KNN-RuO_2 system, were obtained under vacuum, while the pressure condition did not play any role in denser lead-based PZT–$Pb_2Ru_2O_{6.5}$ and PMN-35PT–$Pb_2Ru_2O_{6.5}$ systems.

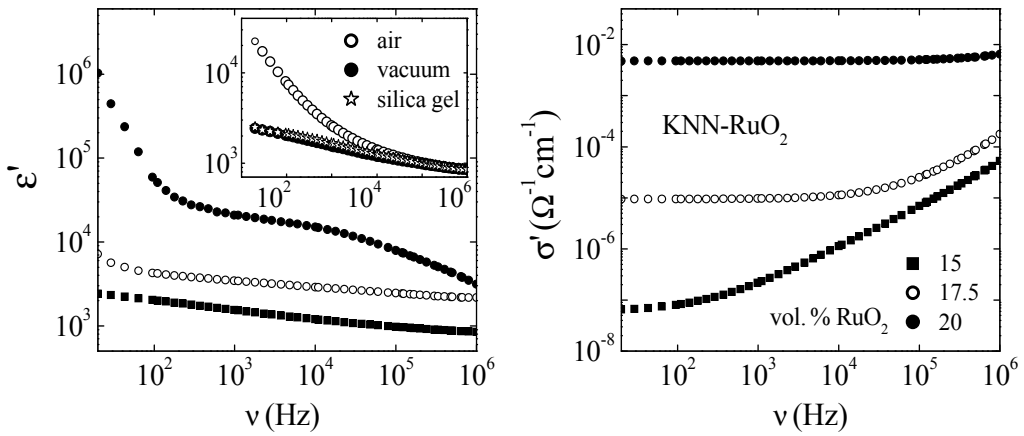

Fig. 6. Frequency dependence of ε' and σ' measured under vacuum at room temperature in KNN–RuO_2 samples with different volume concentrations of RuO_2. The inset shows data obtained in the sample with 15 vol. % of RuO_2 after three different treatment procedures.

4.2 Evolution of the dielectric constant vs. the conductive filler volume concentration

Values of the real part of the complex dielectric constant evidently strongly increase with higher conductive filler volume concentration (see ε'(ν) spectra for samples with different compositions in Figs. 4 to 6). This dependence is clearly depicted in Figs. 7 and 8, which show the evolution of ε' (measured at room temperature at the frequency of 1 kHz) in all developed all-ceramic percolative composites versus the conductive filler volume content. The solid line represents the fit of the experimental data to an expression derived from general percolation theories (Bergman & Imry, 1977; Efros & Shklovskii, 1976)

$$\varepsilon' = \varepsilon_m [(p_c - p)/p_c]^{-q}, \quad (3)$$

which has been, up to now, successfully applied to several organic and inorganic percolative composites (Huang et al., 2004; Pecharroman et al., 2001; Song et al., 1986). Here, ε_m is the

real part of the complex dielectric constant of the insulator matrix, p is the volume concentration of the conductive admixture, p_c is the percolation threshold for the conduction (unambiguously defined in the ideal composite with the zero conductivity of the matrix via $\sigma_{dc}=0$ for $p<p_c$), and q is the critical exponent. Several values for the percolation critical exponents and the threshold value have been proposed on the basis of theoretical derivations (Bergman & Imry, 1977; Efros & Shklovskii, 1976; Feng et al., 1987) or numerical calculations (Straley, 1977; Webman et al., 1975). While standard percolation theories on three-dimensional lattices assume $q\approx0.9$ and $p_c\approx0.16$ (Kirkpatrick, 1973), rather different values (usually a much higher p_c) have been experimentally detected in various percolative systems, which can be explained in terms of the continuous percolation theory (Feng et al., 1987). Here, the fit of the PZT–$Pb_2Ru_2O_{6.5}$ data yields $q=0.723\pm0.004$ and $p_c=0.171\pm0.001$. It is interesting that almost identical value of q has been detected in the samples consisting of small Ag particles, randomly embedded in a non-conducting KCL host (Grannan et al., 1981) and also predicted by numerical calculations performed on a cubic lattice of resistors with two possible values of resistance (Straley, 1977). The fit of the KNN–RuO_2 data yields $q=1.05\pm0.04$ ($q=1$ is obtained in the framework of the effective medium approach regardless of the space dimensionality (Efros & Shklovskii, 1976)) and $p_c=0.205\pm0.004$, and the fit of the PMN-35PT–$Pb_2Ru_2O_{6.5}$ data yields $q=0.89\pm0.04$ and $p_c=0.174\pm0.003$. However, the most important fact is that exact fits of ε' in Figs. 7 and 8 further confirms the perfect outgrowth of the PZT–$Pb_2Ru_2O_{6.5}$, PMN-35PT–$Pb_2Ru_2O_{6.5}$, and KNN–RuO_2 composites, with the dielectric constant near the percolation threshold being for two orders of magnitude higher than in the pure matrix (PZT, PMN-35PT, or KNN) ferroelectric ceramics – this hold true also for the PMN-35PT–$Pb_2Ru_2O_{6.5}$ and KNN–RuO_2 composites, where a significant fraction of porosity, which can clearly be seen in Fig. 3 (and is many times observed in KNN-based ceramic composites (Sun et al., 2008)) undoubtedly alters the dielectric response, i.e., decreases the dielectric constant.

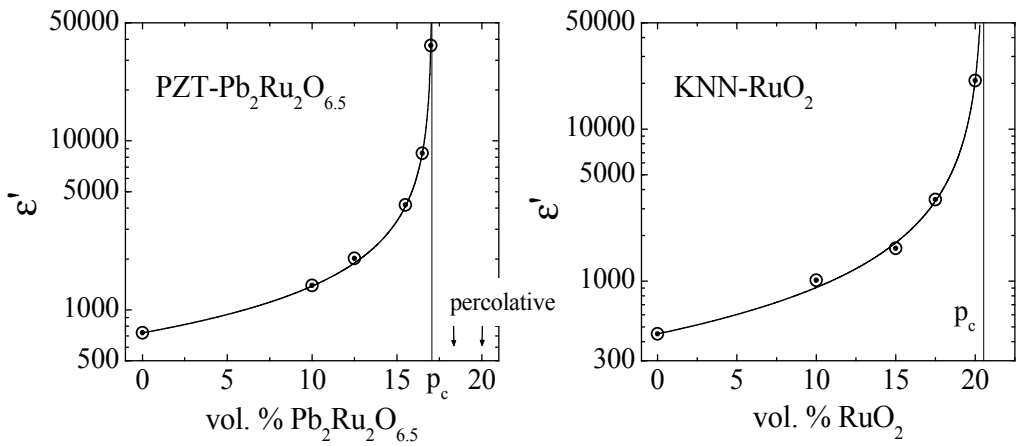

Fig. 7. The real part of the complex dielectric constant of the PZT–$Pb_2Ru_2O_{6.5}$ and KNN–RuO_2 composites vs. the conductive filler volume content, measured at room temperature at the frequency of 1 kHz. Solid lines represent fits of the experimental data to Eq. (3), while vertical lines indicate the percolation threshold p_c. Arrows indicate two percolative, i.e., electrically conductive PZT–$Pb_2Ru_2O_{6.5}$ samples – their ε' values cannot be determined.

It should once again be stressed out that the effective conductivity, similar as the effective dielectric constant (Eq. (3)), exhibits a critical behavior in the vicinity of p_c (see Eqs. (1) and (2)), while at the percolation point σ' undergoes an abrupt discontinuity. Such a behavior is clearly depicted in Fig. 8 for the PMN-35PT–$Pb_2Ru_2O_{6.5}$ system. Consequently, the dielectric loss factor tanδ=ε''/ε' becomes extremely high near p_c (see Fig. 9). Thus, percolative samples with compositions near the percolation threshold are by default not suitable for applications where the dielectric loss factor should be small. However, the electrical conductivity in samples with lower conductive filler concentration, where dielectric constant is still much

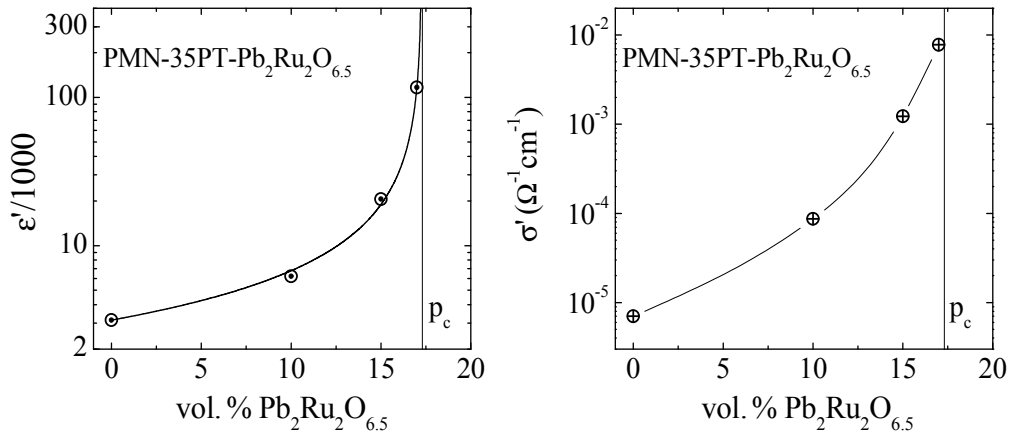

Fig. 8. Evolution of the dielectric constant and the dependence of the electrical conductivity on the $Pb_2Ru_2O_{6.5}$ volume content in PMN-35PT–$Pb_2Ru_2O_{6.5}$ samples at room temperature at the frequency of 1 kHz. The solid line through the ε' experimental data is the fit to Eq. (3). The solid line through the σ' data is a guide to the eye, while vertical lines in both graphs denote the percolation threshold.

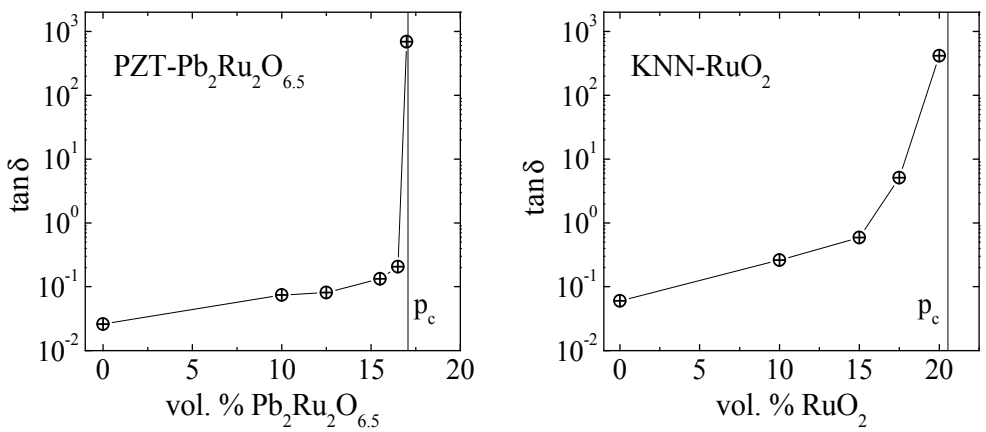

Fig. 9. Dependence of the dielectric loss factor tanδ=ε''/ε' on the conductive filler volume concentration in the PZT–$Pb_2Ru_2O_{6.5}$ and KNN–RuO_2 all-ceramic percolative composites. Solid lines are guides to the eye.

higher than in the pure matrix ceramic system, are supposedly acceptable for applications – for example, PZT–$Pb_2Ru_2O_{6.5}$ samples with p<0.165 (see Figs. 7 and 9), where tanδ<0.1, while dielectric constant still reaches values above 5000.

4.3 Temperature stability of the response

The temperature dependence of the dielectric constant ε' and ac electrical conductivity σ', measured at various frequencies in the PZT–$Pb_2Ru_2O_{6.5}$ sample (10 vol. % of $Pb_2Ru_2O_{6.5}$), is shown in Fig. 10 for the temperature interval of -125°C–125°C. Although above room temperature, due to the increasing conductivity, ε' at lower frequencies strongly increases, the detected dependences are rather smooth around room temperature. Similar conclusion applies for the KNN–RuO_2 system – ε'(T) detected at two frequencies in the sample with 15 vol. % of RuO_2 is shown in the inset to Fig. 10.

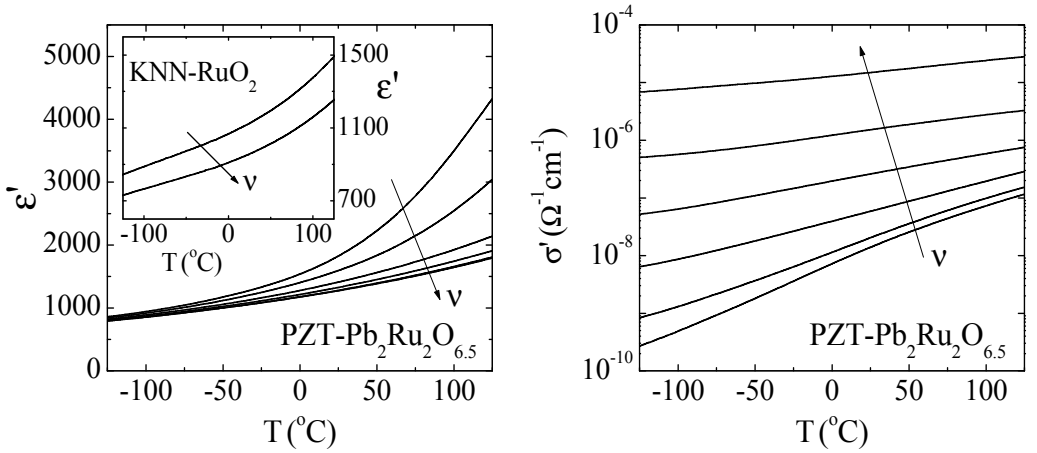

Fig. 10. Temperature dependence of the dielectric constant and ac electrical conductivity, measured at several frequencies (30 Hz, 100 Hz, 1 kHz, 10 kHz, 100 kHz, 1 MHz, order indicated by arrows) in the PZT–$Pb_2Ru_2O_{6.5}$ sample with 10 vol. % of $Pb_2Ru_2O_{6.5}$. The inset shows ε' measured as a function of the temperature at two frequencies (100 kHz, 1 MHz) in the KNN–RuO_2 sample with 15 vol. % of RuO_2.

While temperatures of the paraelectric-to-ferroelectric phase transition in the PZT and KNN systems are much above the highest measured temperature (≈370°C in the PZT and ≈420°C in the KNN), this phase transition, taking place in the matrix, dominates the temperature dependence of the PMN-35PT–$Pb_2Ru_2O_{6.5}$ composite in the measured temperature range. Fig. 11 shows the temperature dependence of the dielectric constant and ac electrical conductivity, detected at various frequencies in the PMN-35PT–$Pb_2Ru_2O_{6.5}$ sample with 15 vol. % of $Pb_2Ru_2O_{6.5}$. The paraelectric-to-ferroelectric phase transition in the pure PMN-PT system of this composition takes place at T_c≈165°C (Colla et al., 1998), but, as can be seen in Fig. 11, becomes slightly diffusive in a heterogeneous composite system – the ε'(T) and σ'(T) maxima are frequency dependent here and at temperatures lower than T_c. We may, however, as in the case of PZT–$Pb_2Ru_2O_{6.5}$ and KNN–RuO_2 systems, still conclude that at higher frequencies the temperature dependence is relatively smooth in the range around room temperature, i.e., in the temperature range most interesting for eventual applications.

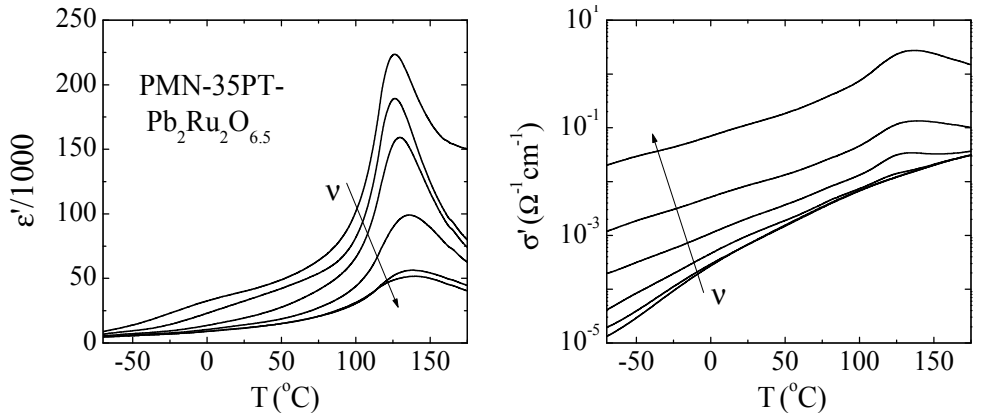

Fig. 11. Temperature dependence of the dielectric constant and ac electrical conductivity, detected at various frequencies (20 Hz, 100 Hz, 1 kHz, 10 kHz, 100 kHz, 1 MHz, order indicated by arrows) in the PMN-35PT–$Pb_2Ru_2O_{6.5}$ sample with 15 vol. % of $Pb_2Ru_2O_{6.5}$.

4.4 Feasibility of electric-field poling

As stated in the introduction, high dielectric constant materials are highly desirable for use not only as capacitor dielectrics but also in a broad range of advanced electromechanical applications, where mainly their piezoelectric response is employed.

The piezoelectric effect is the linear electromechanical interaction between the mechanical and the electrical state in crystalline materials with no inversion symmetry. It is a reversible process: materials that exhibit the direct piezoelectric effect – the internal generation of electrical charge resulting from an applied mechanical force, also exhibit the reverse effect – the internal generation of a mechanical force resulting from an applied electrical field.

The electrical and mechanical behavior of the material is generally described by the strain-charge coupled equations:

$$\{S\}=[s^E]\{T\}+[d^t]\{E\}, \tag{4}$$

$$\{D\}=[d]\{T\}+[\varepsilon^T]\{E\}. \tag{5}$$

Here, {S} and {T} are strain and stress vectors, respectively, while {D} and {E} represent vectors of the electric displacement and electric field. [ε] and [s] are dielectric constant and compliance tensors, while [d] is the direct piezoelectric effect tensor and [d^t] is the converse piezoelectric effect tensor. The superscript E indicates a zero or constant electric field, the superscript T indicates a zero or constant stress field, and the superscript t stands for transposition of a matrix.

For a material of the 4mm – case of poled tetragonal piezoelectric ceramics (Jaffe et al., 1971) – and of the 6mm crystal class, Eqs. (4) and (5) simplify in the case of zero stress field into

$$\begin{bmatrix} S_1 \\ S_2 \\ S_3 \\ S_4 \\ S_5 \\ S_6 \end{bmatrix} = \begin{bmatrix} 0 & 0 & d_{31} \\ 0 & 0 & d_{32} \\ 0 & 0 & d_{33} \\ 0 & d_{24} & 0 \\ d_{15} & 0 & 0 \\ 0 & 0 & 0 \end{bmatrix} \begin{bmatrix} E_1 \\ E_2 \\ E_3 \end{bmatrix}; \quad \begin{bmatrix} D_1 \\ D_2 \\ D_3 \end{bmatrix} = \begin{bmatrix} \varepsilon_{11} & 0 & 0 \\ 0 & \varepsilon_{22} & 0 \\ 0 & 0 & \varepsilon_{33} \end{bmatrix} \begin{bmatrix} E_1 \\ E_2 \\ E_3 \end{bmatrix} \tag{6}$$

using the Nye notation, in which elastic constants and elastic moduli are labeled by replacing the pairs of letters xx, yy, zz, yz, zx, and xy by the number 1, 2, 3, 4, 5, and 6, respectively. This means that the external electric field generates electric displacement, i.e., electric polarization, and strain through the converse piezoelectric effect.

However, ceramic materials are multicrystalline structures made up of large numbers of randomly orientated crystal grains. The random orientation of the grains results in a net cancelation of the piezoelectric effect. Thus, the ceramic material must be poled – a dc bias electric field is applied (usually the fired ceramic piece is cooled through the Curie point under the influence of the field) which aligns the ferroelectric domains, resulting in a net piezoelectric effect.

As the electrical conductivity of percolative composites strongly increases on approaching the percolation threshold, the feasibility of poling the PZT- $Pb_2Ru_2O_{6.5}$ samples has been checked. PZT- $Pb_2Ru_2O_{6.5}$ system has been chosen as its electrical conductivity is much lower than in the PMN-35PT–$Pb_2Ru_2O_{6.5}$ system or in the KNN–RuO_2 samples which are not treated under vacuum. After poling the PZT-$Pb_2Ru_2O_{6.5}$ samples with a high dc bias electric field, the piezoelectric coefficient d_{33} (strain in the direction of the applied measuring field) has been measured using a small ac voltage. It should be noted that, while various piezoelectric coefficients are usually determined and thus the indication is absolutely necessary, the dielectric constant is almost without exception determined in the direction of the applied field, i.e., ε' without indices in fact denotes the dielectric constant ε_{33}.

Results of piezoelectric characterization are shown in Fig. 12. While in samples, which are very close to the percolation threshold, the breakdown electric field is below 5 kV/cm, samples with lower $Pb_2Ru_2O_{6.5}$ content can be poled with the dc bias electric fields higher than 30 kV/cm. It is thus once again revealed that percolative samples with compositions near the percolation threshold are not very suitable for applications, while samples with lower conductive filler concentration, where dielectric constant is still much higher than in the pure ceramic matrix, are very promising for use as high dielectric constant materials.

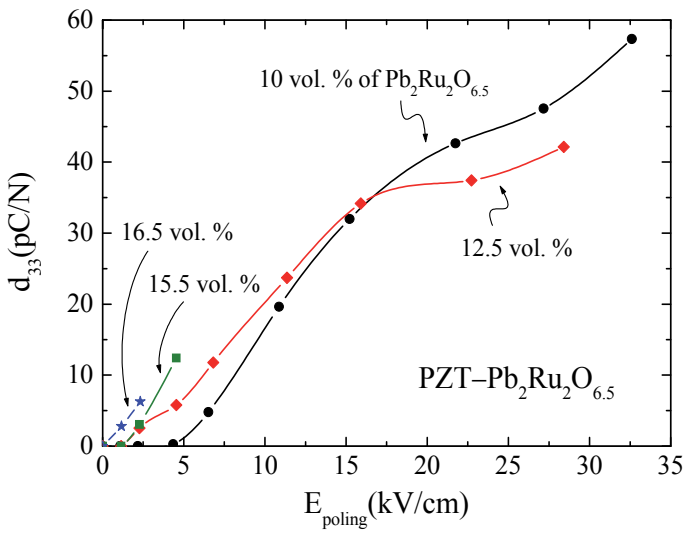

Fig. 12. Piezoelectric coefficient d_{33} in various PZT-$Pb_2Ru_2O_{6.5}$ samples, measured with small ac voltage, after poling the sample with a high dc bias electric field (E_{poling}).

5. Conclusion

Development of all-ceramic percolative composites
i. PZT-$Pb_2Ru_2O_{6.5}$
ii. PMN-35PT–$Pb_2Ru_2O_{6.5}$ and
iii. KNN–RuO_2
based on the perovskite ferroelectric and ruthenium-based conductive ceramics is reported in this chapter. The structural analysis revealed that there were no chemical reactions between the constituents during processing, which resulted in a perfect structure of composites – conductive ceramic grains are uniformly distributed throughout the ferroelectric ceramic matrix. Thus, in the lead-based PZT-$Pb_2Ru_2O_{6.5}$ and PMN-35PT–$Pb_2Ru_2O_{6.5}$ and in the lead-free KNN–RuO_2 systems the dielectric response in fact follows the predictions of the percolation theory. As a result, the dielectric constant strongly increases on the conductive filler increasing content, reaching values near the percolation threshold that are for two orders of magnitude higher than in the pure matrix ceramics. Furthermore, the determined critical exponents and percolation points agree reasonably with the theoretically predicted values. The frequency- and temperature-dependent dielectric response of all developed systems is also presented and discussed.
Finally, not only structural and dielectric results, i.e., a successful synthesis of lead-based and lead-free percolative systems exhibiting a stable giant dielectric response, but also electromechanical properties demonstrate the potential of all-ceramic percolative composites for use as high-dielectric-constant materials in various applications.

6. Acknowledgment

This work was supported by the Slovenian Research Agency under project J1-9534 and program P2-0105-0106/05 and under European project 6. FP NMP3-CT-2005-515757. We thank to Prof. Horst Beige from the Martin-Luther University in Halle, Germany, for kindly making the experimental facility for the electromechanical characterization of the PZT–$Pb_2Ru_2O_{6.5}$ system accessible and to Dr. Ralf Steinhausen for help with these measurements.

7. References

Bergman, D. J. & Imry, Y. (1977). Critical behavior of the complex dielectric constant near the percolation threshold of a heterogeneous material. *Physical Review Letters*, Vol. 39, Iss. 19, Nov. 1977, pp. 1222-1225, ISSN 0031-9007.

Bobnar, V.; Hrovat, M.; Holc, J. & Kosec, M. (2008). Giant dielectric response in Pb(Zr,Ti)O_3–$Pb_2Ru_2O_{6.5}$ all-ceramic percolative composite. *Applied Physics Letters*, Vol. 92, Iss. 18, May 2008, 182911 3pp., ISSN 0003-6951.

Bobnar, V.; Hrovat, M.; Holc, J.; Filipič, C.; Levstik, A. & Kosec, M. (2009a). Colossal dielectric response in all-ceramic percolative composite 0.65Pb($Mg_{1/3}Nb_{2/3}$)O_3-0.35$PbTiO_3$-$Pb_2Ru_2O_{6.5}$. *Journal of Applied Physics*, Vol. 105, Iss. 3, Feb. 2009, 034108 5pp., ISSN 0021-8979.

Bobnar, V.; Hrovat, M.; Holc, J. & Kosec, M. (2009b). All-ceramic lead-free percolative composite with a colossal dielectric response. *Journal of the European Ceramic Society*, Vol. 29, Iss. 4, Mar. 2009, pp. 725-729, ISSN 0955-2219.

Chiteme, C.; McLachlan, D. S. & Sauti, G. (2007). ac and dc percolative conductivity of magnetite-cellulose acetate composites. *Physical Review B*, Vol. 75, Iss. 9, Mar. 2007, 094202 13pp., ISSN 1098-0121.

Colla, E. V.; Yushin, N. K. & Viehland, D. (1998). Dielectric properties of $(PMN)_{(1-x)}(PT)_x$ single crystals for various electrical and thermal histories. *Journal of Applied Physics*, Vol. 83, Iss. 6, Mar. 1998, pp. 3298-3304, ISSN 0021-8979.

Dang, Z.-M.; Lin, Y.-H. & Nan, C.-W. (2003). Novel ferroelectric polymer composites with high dielectric constants. *Advanced Materials*, Vol. 15, Iss. 19, Oct. 2003, pp. 1625-1629, ISSN 0935-9648.

Deepa, K. S.; Sebastian, M. T. & James, J. (2007). Effect of interparticle distance and interfacial area on the properties of insulator-conductor composites. *Applied Physics Letters*, Vol. 91, Iss. 20, Nov. 2007, 202904 3pp., ISSN 0003-6951.

Efros, A. L. & Shklovskii, B. I. (1976). Critical behaviour of conductivity and dielectric constant near the metal-non-metal transition threshold. *Physica Status Solidi (b)*, Vol. 76, Iss. 2, Aug. 1976, pp. 475-485, ISSN 0370-1972.

Feng, S.; Halperin, B. I. & Sen, P. N. (1987). Transport properties of continuum systems near the percolation threshold. *Physical Review B*, Vol. 35, Iss. 1, Jan. 1987, pp. 197-214, ISSN 1098-0121.

Grannan, D. M.; Garland, J. C. & Tanner, D. B. (1981). Critical behavior of the dielectric constant of a random composite near the percolation threshold. *Physical Review Letters*, Vol. 46, Iss. 5, Feb. 1981, pp. 375-378, ISSN 0031-9007.

Hrovat, M.; Benčan, A.; Holc, J. & Kosec, M. (2001). Subsolidus phase equilibria in the RuO_2–TiO_2–ZrO_2 system. *Journal of Materials Science Letters*, Vol. 20, Iss. 22, Nov. 2001, pp. 2005-2008, ISSN 0261-8028.

Huang, C. & Zhang, Q. M. (2004). Enhanced dielectric and electromechanical responses in high dielectric constant all-polymer percolative composites. *Advanced Functional Materials*, Vol. 14, Iss. 5, May 2004, pp. 501-506, ISSN 1616-301X.

Huang, C.; Zhang, Q. M.; deBotton, G. & Bhattacharya, K. (2004) All-organic dielectric-percolative three-component composite materials with high electromechanical response. *Applied Physics Letters*, Vol. 84, Iss. 22, May 2004, pp. 4391-4393, ISSN 0003-6951.

Jaffe, B.; Cook, W. R. & Jaffe, H. (1971). *Piezoelectric Ceramics,* Academic Press, New York, ISBN 0-12-379550-89.

Kirkpatrick, S. (1973). Percolation and conduction. *Reviews of Modern Physics*, Vol. 45, Iss. 4, Oct. 1973, pp. 574-588, ISSN 0034-6861.

Kuščer, D.; Holc, J.; Kosec, M. & Meden, A. (2006). Mechano-synthesis of lead–magnesium–niobate ceramics. *Journal of the American Ceramic Society*, Vol. 89, Iss. 10, Oct. 2006, pp. 3081-3088, ISSN 1551-2916.

Kuščer, D.; Holc, J. & Kosec, M. (2007). Formation of $0.65Pb(Mg_{1/3}Nb_{2/3})O_3$–$0.35PbTiO_3$ using a high-energy milling process. *Journal of the American Ceramic Society*, Vol. 90, Iss. 1, Jan. 2007, pp. 29-35, ISSN 1551-2916.

Li, J.-F.; Takagi, K.; Terakubo, N. & Watanabe, R. (2001). Electrical and mechanical properties of piezoelectric ceramic/metal composites in the $Pb(Zr,Ti)O_3$/Pt system. *Applied Physics Letters*, Vol. 79, Iss. 15, Oct. 2001, pp. 2441-2443, ISSN 0003-6951.

Pecharroman, C. & Moya, J. S. (2000). Experimental evidence of a giant capacitance in insulator-conductor composites at the percolation threshold. *Advanced Materials*, Vol. 12, Iss. 4, Feb. 2000, pp. 294-297, ISSN 0935-9648.

Pecharroman, C.; Esteban-Betegon, F.; Bartolome, J. F.; Lopez-Esteban, S. & Moya, J. S. (2001). New percolative $BaTiO_3$-Ni composites with a high and frequency-independent dielectric constant ($\varepsilon_r \approx 80000$). *Advanced Materials*, Vol. 13, Iss. 20, Oct. 2001, pp. 1541-1544, ISSN 0935-9648.

Petzelt, J. & Rychetsky, I. (2005). Effective dielectric function in high-permittivity ceramics and films. *Ferroelectrics*, Vol. 316, 2005, pp. 89-95, ISSN 0015-0193.

Pierce, J. W.; Kuty, D. W. & Larry, J. L. (1982). The chemistry and stability of ruthenium-based resistors. *Solid State Technology*, Vol. 25, Iss. 10, Oct. 1982, pp. 85-93, ISSN 0038-1101.

Priya, S.; Viehland, D. & Uchino, K. (2002). Importance of structural irregularity on dielectric loss in $(1–x)Pb(Mg_{1/3}Nb_{2/3})O_3–(x)PbTiO_3$ crystals. *Applied Physics Letters*, Vol. 80, Iss. 22, Jun. 2002, pp. 4217-4219, ISSN 0003-6951.

Raymond, M. V. & Smyth, D. M. (1996). Defects and charge transport in perovskite ferroelectrics. *Journal of Physics and Chemistry of Solids*, Vol. 57, Iss. 10, Oct. 1996, pp. 1507-1511, ISSN 0022-3697.

Reynolds, T. G. III & Buchanan, R. C. (2004). Ceramic capacitor materials. In: *Ceramic Materials for Electronics*, Editor Buchanan, R. C., pp. 141-206, Marcel Dekker, ISBN 0-8247-4028-9, New York.

Rychetsky, I.; Hudak, O. & Petzelt, J. (1999). Dielectric properties of microcomposite ferroelectrics. *Phase Transitions*, Vol. 67, Iss. 4, 1999, pp. 725-739, ISSN 0141-1594.

Scott, J. F. (2007). Applications of modern ferroelectrics. *Science*, Vol. 315, Iss. 5814, Feb. 2007, pp. 954-959, ISSN 0036-8075.

Song, Y.; Noh, T. W.; Lee, S.-I. & Gaines, J. R. (1986). Experimental study of the three-dimensional ac conductivity and dielectric constant of a conductor-insulator composite near the percolation threshold. *Physical Review B*, Vol. 33, Iss. 2, Jan. 1986, pp. 904-908, ISSN 1098-0121.

Springett, B. E. (1973). Effective-medium theory for the ac behavior of a random system. *Physical Review Letters*, Vol. 31, No. 24, Dec. 1973, pp. 1463-1465, ISSN 0031-9007.

Straley, J. P. (1977). Critical exponents for the conductivity of random resistor lattices. *Physical Review B*, Vol. 15, Iss. 12, Jun. 1977, pp. 5733-5737, ISSN 1098-0121.

Sun, X.; Chen, J.; Yu, R.; Xing, X.; Qiao, L. & Liu, G. (2008). $BiFeO_3$-doped $(Na_{0.5}K_{0.5})NbO_3$ lead-free piezoelectric ceramics. *Science and Technology of Advanced Materials*. Vol. 9, Iss. 2, Jun. 2008, 025004 4 pp., ISSN 1468-6996.

Takeshima, Y.; Shiratsuyu, K.; Takagi, H. & Sakabe, H. Y. (1997). Preparation and dielectric properties of the multilayer capacitor with $(Ba,Sr)TiO_3$ thin layers by metalorganic chemical vapour deposition. *Japanese Journal of Applied Physics*, Vol. 36, No. 9B, Sep. 1997, pp. 5870-5873, ISSN 0021-4922.

van Loan, P. R. (1972). Conductive ternary oxides of ruthenium, and their use in thick film resistor glazes. *American Ceramic Society Bulletin*, Vol. 51, No. 3, Mar. 1972, pp. 231-233, ISSN 0002-7812.

Webman, I.; Jortner, J. & Cohen, M. H. (1975). Numerical simulation of electrical conductivity in microscopically inhomogeneous materials. *Physical Review B*, Vol. 11, Iss. 8, Apr. 1975, pp. 2885-2892, ISSN 1098-0121.

Xu, J. & Wong, C. P. (2005). Low-loss percolative dielectric composite. *Applied Physics Letters*, Vol. 87, Iss. 8, Aug. 2005, 082907 3pp., ISSN 0003-6951.

Yoshida, K. (1990). Percolative conduction in a composite system of metal and ceramics. *Journal of the Physical Society of Japan*, Vol. 59, No. 11, Nov. 1990, pp. 4087-4095, ISSN 0031-9015.

Zhang, Q. M.; Li, H.; Poh, M.; Xia, F.; Cheng, Z.-Y.; Xu, H. & Huang, C. (2002). An all-organic composite actuator material with a high dielectric constant. *Nature*, Vol. 419, Issue 6904, Sep. 2002, pp. 284-287, ISSN 0028-0836.

8

Electrical Processes in Polycrystalline $BiFeO_3$ Film

Yawei Li[1], Zhigao Hu[1] and Junhao Chu[1,2]
[1]*Key Laboratory of Polar Materials and Devices, Ministry of Education, Department of Electronic Engineering, East China Normal University, Shanghai*
[2]*National Laboratory for Infrared Physics, Shanghai Institute of Technical Physics, Chinese Academy of Sciences, Shanghai*
People's Republic China

1. Introduction

As an oxide with perovskite structure, Bismuth ferrite ($BiFeO_3$, BFO) has been studied from 1970s (Teague, et al. 1970; Kaczmarek, et al. 1975). The structure and magnetic properties of BFO were confirmed before 1970s. As reported, the crystal structure of BFO is perovskite with rhombohedral distortion and the space group is R3c. BFO is G-type antiferromagnetic. It was controversial about whether BFO was ferroelectrics until the hysteresis loop of single crystal BFO was measured in 1970 (Teague, et al. 1970). According to Teague's results, the single crystal BFO was anisotropy. The remnant polarizations (P_r) along the (100) and (111) direction were 3.5μC/cm² and 6.1μC/cm² at the temperature of liquid nitrogen, respectively. However, because of the higher leakage current in the bulk BFO, it was difficult to measure the ferroelectric properties of BFO at room temperature. The problem of higher leakage blocks not only the studies of the electrical properties of BFO, but also the application of BFO in electrical devices. In 2003, the epitaxial BFO films with higher electrical resistivity and higher remnant polarization was fabricated by pulsed laser deposition (PLD) method (J. Wang, 2003). The value of P_r of the epitaxial BFO films is about 50μC/cm². This value is larger than that of the traditional ferroelectrics such as $Pb(Zr,Ti)O_3$ (PZT), $BaTiO_3$ (BTO). If the BFO film with larger P_r can be used in ferroelectric memory (FeRAM), the size of the storage cell can be reduced and the storage density can be increased (Maruyama, 2007). More studies on BFO films are carried out (Eerenstein, 2005; Zavaliche, 2005; Singh, 2007; Hauser, 2008; Liu, 2008; Yang, 2008). Even though the leakage mechanism in epitaxial BFO film has been studied (Pabst, 2007), the higher leakage current is still an obstacle for the study and application of polycrystalline BFO films. Compared to the epitaxial BFO films grown on perovskite structure substrate, the applications of polycrystalline BFO on silicon wafer are broader in the field of microelectronic devices. In this chapter, polycrystalline BFO films are fabricated by different physical and chemical methods on buffered silicon and perovskite structure substrate. The structural and electrical properties of these polycrystalline BFO films are investigated.

2. Experiments

Considering the universality of our conclusion for different polycrystalline BFO films, the samples studied in this work are fabricated by two different methods, PLD and chemical solution deposition (CSD) methods. The former is a typical physical method of film deposition. The later is a chemical method. At the same time, different materials are used as substrate. For the samples prepared by PLD, n-type silicon covered by a layer of (La,Sr)CoO_3 (LSCO) is used as substrate. The layer of LSCO acts as bufferlayer for the growth of BFO and bottom electrode for the electrical measurement. For the samples prepared by CSD, the single crystal $SrTiO_3$ (STO) covered by $LaNiO_3$ (LNO) is used as substrate.

2.1 The fabrications of BFO films by PLD method

For the preparation of polycrystalline BFO films by PLD method, single-side polished silicon wafer is used as substrate. Before the deposition of BFO film, a layer of LSCO is deposited on the surface of silicon wafer by PLD. The component of the LSCO target is $(La_{0.5}Sr_{0.5})CoO_3$. The component of BFO target is $Bi_{1.05}FeO_3$. The excess bismuth is used to compensate the evaporation of bismuth at higher temperature during the growth of BFO films. The depositions of LSCO and BFO are carried out in a vacuum chamber with background pressure lower than 10^{-4} Pa. A KrF excimer laser with the wavelength of 248 nm is used for the deposition. During the deposition of LSCO layer, the oxygen pressure in the chamber is about 25 Pa. The temperature of the silicon wafer is 650°C (Li, 2009). Details about the deposition conditions are listed in table 1. The deposition of LSCO layer is carried out for 20 minutes. After the deposition, the oxygen pressure in the chamber increased to 50 Pa and maintained for 30 min. The thickness of the LSCO layer is about 200 nm obtained from the scanning electronic microscope.

Target	LSCO	BFO
Frequency of pulse	5Hz	3Hz
Oxygen pressure	25Pa	3Pa
Substrate temperature	650°C	700°C
Deposition time	20min	90min
Holding temperature	650°C	495°C
Holding oxygen pressure	50 Pa	3Pa/1.01×10^5 Pa
Holding time	30min	30min

Table 1. The deposition conditions of LSCO and BFO films grown on silicon wafer by PLD method.

The oxygen pressure in the chamber during the deposition of the polycrystalline BFO films is 3 Pa. the temperature of the substrate is kept at 700°C. Details about the deposition conditions of BFO films are also listed in table 1. The deposition of BFO films is carried out for 90 minutes. After the deposition, the BFO films are cooled to 495°C slowly and held for 30 min in a certain oxygen pressure. In order to study the effect of oxygen vacancies, two kinds of BFO films are fabricated by PLD. For the BFO film containing less vacancy of oxygen, the oxygen pressure in the chamber is 1.01×10^5 Pa when the sample is held at 495°C for 30min. For the sample containing more vacancy of oxygen, the oxygen pressure in the chamber is just 3 Pa when the sample is kept at 495°C for 30min (Li, 2008).

2.2 The fabrications of BFO films by CSD method

Regarding the preparation of polycrystalline BFO films by CSD method, single crystal STO is used as substrate. A layer of LNO is fabricated on the surface of STO before the preparation of BFO films. The layer of LNO is also fabricated by CSD method and is used as bottom electrode. Both STO and LNO are perovskite structure and smaller crystal constant than BFO. Therefore, the substrate and the LNO layer can induce the growth of BFO films. The fabrication of LNO layer by CSD method is same to the way has been reported in literature (Meng, 2001). For the synthesizing of LNO precursor, lanthanum nitrate and nickel acetate are used as starting materials. The mixture of acetic acid and water are used as solvent. Lanthanum nitrate and nickel acetate with a stoichiometric molar ratio of 1:1 are dissolved in the solvent. The concentration of the precursor is 0.3mol/L. For the preparation of the LNO layer, the LNO precursor is spin-coated on STO substrate at 3000rpm for 20 s. the wet film is dried at 180^{o}C for 300s in a rapid thermal process furnace. Then the dried film is calcined at 380^{o}C for 300s for the organic compound pyrolyzing. Finally, the amorphous film is annealed at 650^{o}C for 300s for crystallization. The cycle of coating and thermal process are repeated six times to obtain LNO layer with expected thickness.

In regard to the synthesizing of BFO precursor, bismuth nitrate and nickel acetate are used as starting materials. Acetic acid is used as solvent (Li, 2005). The fabrication of BFO film is also contained two steps, spin-coating precursor on LNO covered STO substrate and rapid thermal process in furnace. The precursor is spin-coated at 4000rpm for 20 s. The film is dried at 180^{o}C for 240s, pyrolyzed at 350^{o}C for 240s, and annealed at 600^{o}C for 240s. Two kinds of BFO films with different electrical resistivity are fabricated.

2.3 The crystalline and electrical characterizations

The crystallinity of BFO, LSCO, and LNO films is characterized by x-ray diffraction (XRD) using Cu Kα as radiation source (D/MAX-2550V, Rigaku Co.). During the XRD measurement, the continuous θ-2θ scanning mode with the interval of 0.02^o is used. All XRD characterizations are carried out at room temperature. For the electrical measurement, platinum is used as top electrode. Platinum dots with the diameter of 2×10^{-2}cm are sputtered onto the surface of the polycrystalline BFO films using a shadow mask. The ferroelectric properties are measured using a ferroelectric test system (Permier II, Radiant Technologies, Inc.). During the measurement, the frequency of the alternating current (ac) signal is 1 kHz. Two triangle waves with different polarity are used as the applied voltage. Before each measurement of hysteresis loop, a pre-polar voltage is applied on the film. The dielectric properties of the polycrystalline BFO films are measured using an impedance analyzer (Hewlett-Packard 4194A). The voltage of the small ac signal is 0.05V. The frequency dependence of the permittivity and dielectric loss is measured in the frequency range from 100 Hz to 1 MHz. The voltage dependence of the permittivity is measured at 1 MHz. The leakage current behaviour of the polycrystalline BFO films under dc voltage bias is measured using an electrometer (Keithley 6517A). Besides the electrical measurements carried out at room temperature, the temperature dependence permittivity and leakage current measurements are carried out at different temperatue and the temperature is controlled with an accuracy of ±0.5K using a variable temperature micro-probe stage (K-20, MMR technologies, Inc.).

3. Crystalline structures

Because the impurity has great effects on the electrical properties of the BFO films, it is important that the studied polycrystalline BFO films do not contain any impurity or parasitical phase. The structure of the polycrystalline BFO films fabricated by PLD and CSD on different substrates is investigated firstly.

3.1 The crystalline structure of BFO films fabricated by PLD method

Figure 1 shows the XRD curves of the polycrystalline BFO films grown on LSCO covered silicon substrate and thermal treated at different oxygen pressure. The XRD curve of LSCO film grown on silicon wafer by PLD method is also exhibited in the figure. The indexes of each diffractive peak are labelled in the figure. The indexes of pseudo-cubic structure are used for BFO films.

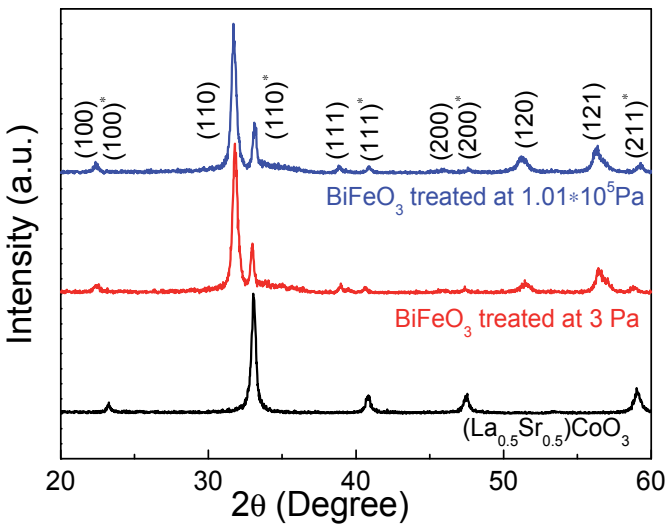

Fig. 1. The XRD patterns of $(La_{0.5}Sr_{0.5})CoO_3$ film and $BiFeO_3$ films fabricated by PLD method and thermal treated at different oxygen pressure. The labels contained a star (*) indicate the diffractive peaks of LSCO. The indexes of pseudo-cubic structure are used to label the diffractive peaks of BFO films.

There is no any trace of impure phase in the XRD curves of the polycrystalline BFO films thermal treated at 1.01×10^5 Pa or 3 Pa. Neither LSCO nor BFO films exhibit (100) preferential orientation even the (100) silicon wafer is used as substrate. The position of the diffractive peak does not show perceptible shift for the two kinds of BFO films thermal treated at different oxygen pressure. It indicates that the thermal process at different oxygen pressure does not affect the crystalline structure of the polycrystalline BFO films. The pseudo-cubic crystal constant calculated from the XRD curve is about 3.96Å. This value is close to the value of bulk BFO (JCPDS: 74-2016). Therefore, even the crystal constant of LSCO is smaller than that of BFO, the mismatch between BFO and LSCO has no effect on the crystalline structure of the polycrystalline BFO films. Moreover, the full width at half maximum (FWHM) of the diffractive peak has no obvious variety. It indicates that the size of the crystal grain in the two kinds of BFO films is not influenced by the difference of the thermal process.

3.2 The crystalline structure of BFO films fabricated by PLD method

Figure 2 shows the XRD curve of polycrystalline BFO film grown on LNO covered (100)STO substrate. The position and relative intensity of the diffractive peak for bulk BFO is also exhibited in the figure. The data of the bulk BFO comes from JCPDS and is used to discuss the difference between the polycrystalline film and bulk.

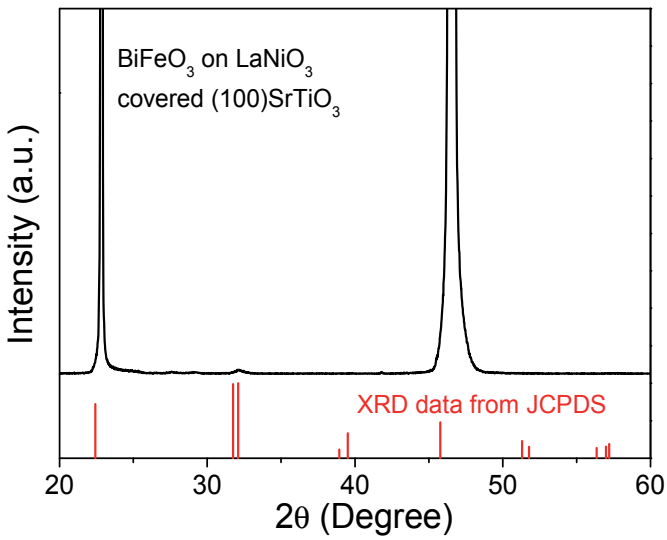

Fig. 2. The XRD patterns of $BiFeO_3$ films grown on $LaNiO_3$ covered (100)$SrTiO_3$ substrate by chemical solution deposition. The data of bulk $BiFeO_3$ (JCPDS: 74-2016) is also displayed in this figure using short straight line. The height of the straight line represents the relative intensity of the diffractive peak.

Compared with the BFO films grown on LSCO covered (100) silicon substrate by PLD method, the BFO film grown on LNO covered (100) STO substrate exhibits highly (100) preferential orientation. It can be ascribed to the inducement from the substrate with perovskite structure and smaller mismatch between BFO, LNO and STO. The existence of (110) and (104) diffractive peaks indicate that the BFO film is not epitaxial monocrystalline film but polycrystalline film. Compared with the XRD data of BFO bulk, the diffractive peaks shift towards higher angle. This means that the out-of-plane crystal constant of the BFO film is smaller than that of BFO bulk.

4. Electrical properties of polycrystalline BFO films

Ferroelectric hysteresis, dielectric response and leakage behaviour are the primary electrical characterization of ferroelectric films. Most of these electrical performances are related to the temperature. In this section, the electrical properties of polycrystalline BFO films fabricated by different methods are studied at different temperature.

4.1 Dielectric response of polycrystalline BFO films

The frequency dependence of capacitance and loss tangent of polycrystalline BFO films fabricated by PLD and CSD methods are shown in figure 3 and figure 4, respectively.

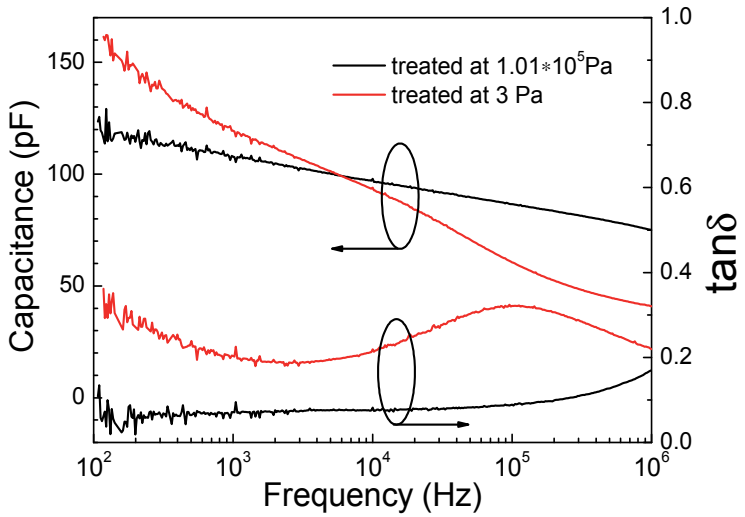

Fig. 3. The frequency dependence of capacitance and loss tangent of BFO films prepared by PLD method and thermal treated at 1.01×10^5 Pa (black) or 3 Pa (red).

The capacitance of BFO film treated at 1.01×10^5 Pa decreases approximatively linearly with the frequency increasing. The value of loss tangent keeps about 0.08 at the frequency range between 100 Hz and 100 kHz, and rises to about 0.17 when the frequency achieves to 1 MHz. the capacitance of the BFO film treated at 3 Pa decreases faster than that of the film treated at 1.01×10^5 Pa. The loss tangent of the film treated at 3 Pa is larger than that of the film treated at 1.01×10^5 Pa. The loss tangent increases with the frequency decreasing in the frequency range between 100 Hz and 1 kHz. The increase of loss tangent at lower frequency range suggests that the dc leakage current is higher in this BFO film. In addition, there is a broad relaxation peak near 10^5 Hz in the loss tangent curve.

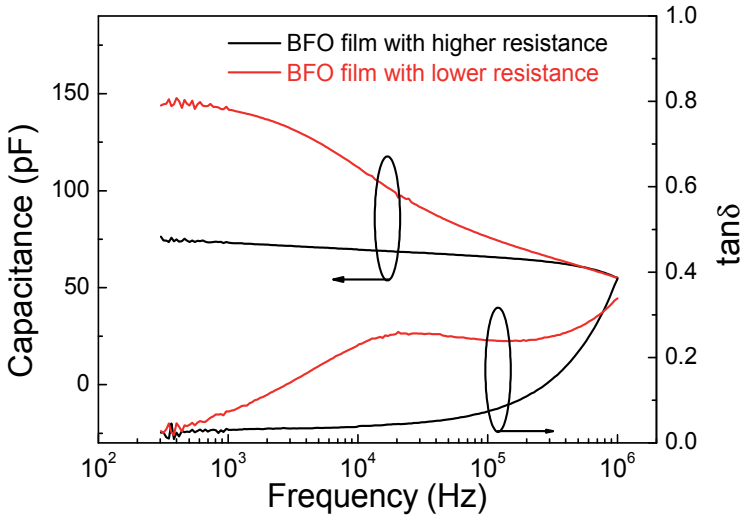

Fig. 4. The frequency dependence of capacitance and loss tangent of BFO films prepared by CSD method.

Similar phenomena can be observed from the frequency dependence of capacitance and loss tangent of BFO films fabricated by CSD method, as shown in fig. 4. The frequency dependence of capacitance and loss tangent of BFO film with higher resistivity is similar to the results of the BFO film prepared by PLD method and thermal treated at 1.01×10^5 Pa. The capacitance of the BFO film with lower resistivity decreases faster than that of the BFO films with higher resistivity, and an obvious relaxation peak can be observed from the frequency dependence of loss tangent. Similar results have also been reported in pure and lanthanum-substituted BFO film (Singh et al., 2007). According to Singh's result, the leakage current in BFO films can be depressed greatly by substituting part bismuth using lanthanum. The frequency dependence of relative dielectric constant of pure BFO film varies distinctly compared with that of the lanthanum-substituted BFO film. A broad relaxation peak exists in the frequency dependence of loss tangent of the pure BFO film but can not be observed in the frequency dependence of loss tangent of the lanthanum-substituted BFO film. All of these results suggest that the evident variety of permittivity and the broad relaxation peak in the frequency dependence of loss tangent are relative to the higher leakage current in the polycrystalline BFO films. Because that the BFO films fabricated by PLD method and thermal treated at different oxygen pressure, the density of the vacancy of oxygen is different. The results of BFO films fabricated by PLD method also confirm that the dielectric relaxation in the BFO films with lower electrical resistivity is relevant to the defect of oxygen.

Dielectric relaxation process related to the vacancy of oxygen usually follows the Debye-type law. This kind of process can be represented by the empirical expression established by Cole and Cole (Cole & Cole, 1941)

$$\varepsilon^*_{cole} = \varepsilon_\infty + \frac{\varepsilon_s - \varepsilon_\infty}{1 + (i\omega\tau)^{1-\alpha}} \tag{1}$$

Where ε^*_{cole} is the complex dielectric constant, ε_s is the static dielectric constant, ε_∞ is the dielectric constant at high frequency, τ is relaxation time and ω is the circular frequency. α is a parameter which is used to describe the distribution of relaxation time. The value of α is between 0 and 1. When α equals to 0, the equation (1) is simplified to Debye model, which has a certain relaxation. Besides the dielectric relaxation related to oxygen vacancies, there are some other factors which have contributions to the dielectric response in the polycrystalline BFO films with lower electrical resistivity. These factors exist also in the BFO films with higher electrical resistivity. The dielectric response of these factors does not display the Debye-type relaxation and can be represented by universal dielectric response (UDR) model. In this model, the real part and imaginary part of complex dielectric constant can be described respectively as (Lunkenhjeimer et al.,2002; Tselev et al., 2004)

$$\begin{aligned} \varepsilon_{rT} &= \frac{1}{\varepsilon_0}\sigma_0 \tan\left(\frac{\pi}{2}s\right)\omega^{s-1} \\ \varepsilon''_T &= \frac{\sigma_{dc}}{\omega\varepsilon_0} + \frac{\sigma_0}{\varepsilon_0}\omega^{s-1} \end{aligned} \tag{2}$$

where ε_{rT} and ε''_T are the real part and imaginary part of complex dielectric constant. σ_{dc} is the dc electric conductivity, which is induced by the leakage current. σ_0 is a pre-power term

and *s* is a parameter with the value between 0 and 1. Considering the dielectric response related to the oxygen vacancies and all the other dielectric response processes, the frequency dependence of complex dielectric constant of the BFO films with lower electrical resistivity should following a model which is constituted by Cole-Cole's model and UDR model. The expression of the model is

$$\varepsilon^* = \varepsilon^*_{cole} + \varepsilon^*_T \tag{3}$$

where ε^* is the complex dielectric constant of polycrystalline BFO films with lower electrical resistivity, ε^*_{cole} and ε^*_T are the complex dielectric constant contributed by the relaxation processes related to oxygen vacancies and the dielectric response process following UDR model respectively. For the polycrystalline BFO film fabricated by PLD method and thermal treated at 3 Pa, the measured circular frequency dependence of complex dielectric constant and fitting results according to equation (3) is shown in fig. 5 (Li, 2008). The values of some parameters in the model are listed in table 2.

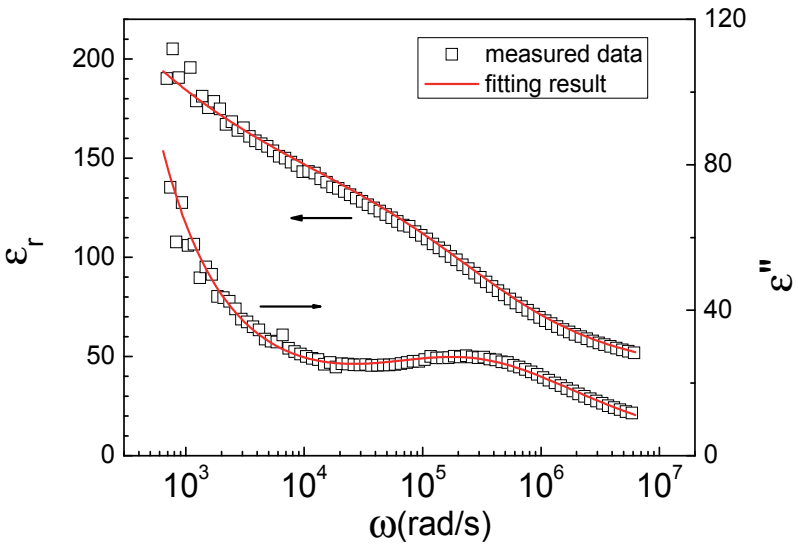

Fig. 5. The measured circular frequency dependence of complex dielectric constant and the fitting results for the polycrystalline BFO films fabricated by PLD method and thermal treated at 3 Pa.

According to the fitting results, the electrical resistivity of the polycrystalline BFO film fabricated by PLD and thermal treated at 3 Pa is less than the orders of magnitude $10^9\Omega\cdot$cm. This result coincides with the published work (Eerenstein, 2005). The lower electrical resistivity means higher leakage current in the films, which obstructs the measurement of ferroelectric properties of polycrystalline BFO films.

τ (s)	σ_{dc} ($\Omega^{-1}\cdot cm^{-1}$)	σ_0 ($\Omega^{-1}\cdot cm^{-1}$)	α	s
3.35×10^{-6}	2.61×10^{-9}	2.02×10^{-11}	0.60	0.72

Table 2. Values of some parameters used in the Debye and UDR combinatorial model.

Besides the relaxation process related to defect of oxygen, the interfacial polarization which occurs between the ferroelectric film and the electrode has significant impact on the measured dielectric response. Liu *et al.* have reported their results on the interfacial polarization between BFO films and the electrode (Liu, 2008). If there is the dielectric response induced by the interfacial polarization, the measured frequency dependence of capacitance will change significantly when different dc bias voltage applied on the samples (Zhang, 2005; Liu, 2008). The frequency dependence of capacitance of the polycrystalline BFO film fabricated by PLD and thermal treated at 3 Pa is measured under dc bias voltage between 0 and 3V. The results are shown in Fig. 6. In contrast to the results reported by Liu *et al.* (Liu, 2008), the curves of the frequency dependence of capacitance measured under different dc bias voltage almost overlap for our sample. A small difference between the curves can be observed from the enlarged plot. The difference dues to the nature of ferroelectrics that dielectric constant changes with the applied dc voltage. It is indicated that the dielectric response contributed by interfacial polarization between the BFO film and electrode can be ignored in our sample.

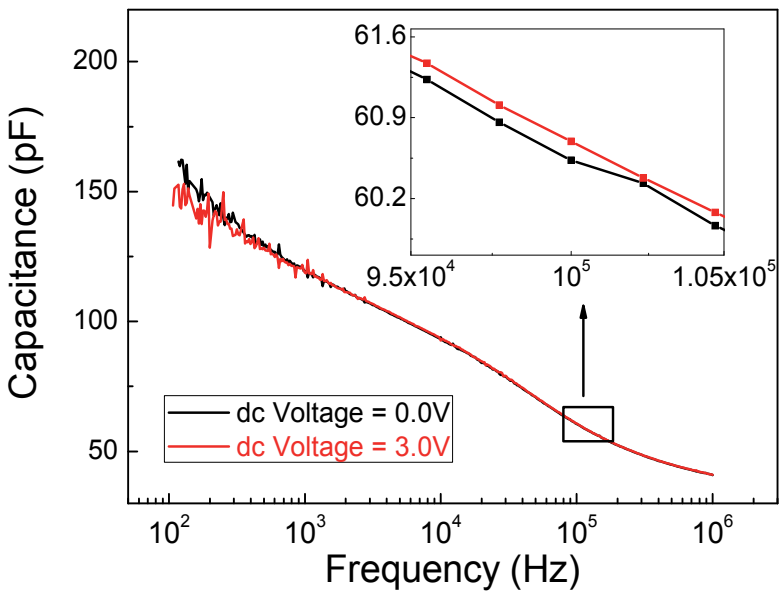

Fig. 6. The frequency dependence of capacitance of the polycrystalline BFO films fabricated by PLD method and thermal treated at 3 Pa measured at different dc bias voltage (0V and 3V). The inset figure exhibits the enlarged parts of the curves nearby 100 kHz.

Now, it is confirmed that the Debye-type relaxation process in polycrystalline BFO films with lower electrical resistivity is related to oxygen vacancies. More research is needed to investigate how the oxygen vacancies work. The dielectric relaxation process related to oxygen defects in the polycrystalline BFO films fabricated by CSD method with lower electrical resistivity is studied at different temperature.

Figure 7 display the temperature dependence of capacitance and loss tangent of polycrystalline BFO film with lower electric resistivity prepared by CSD method in the temperature range between 230K and 430K. The results are measured at different frequency. The capacitance decreases with the increase of the measuring frequency at a certain temperature. This result is consistent with the frequency dependence of capacitance of polycrystalline BFO films prepared by PLD method. A broad peak can be observed in the temperature dependence of loss tangent. The peak position shifts to higher temperature with the increase of the measuring frequency.

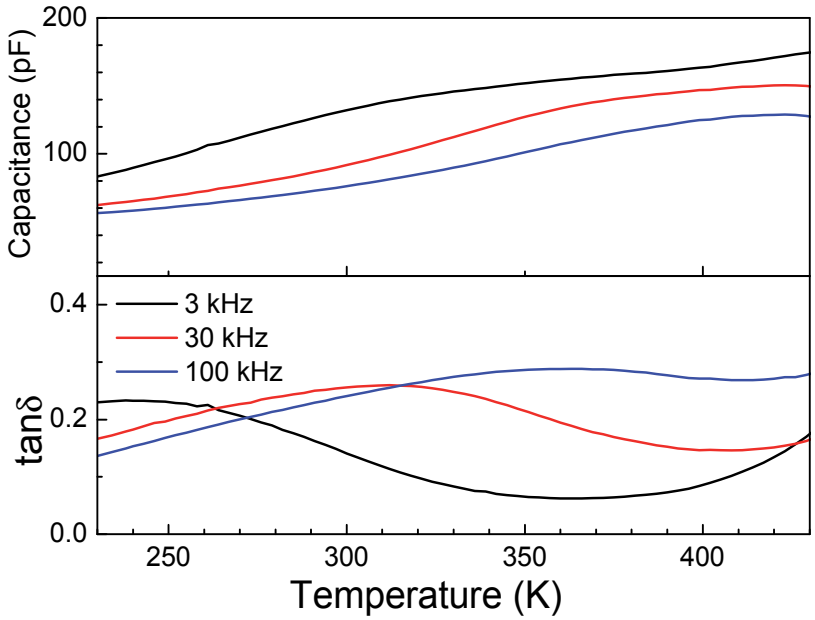

Fig. 7. The temperature dependence of capacitance and loss tangent of the polycrystalline BFO films fabricated by CSD method.

The temperature corresponds to the maximum of loss tangent at a certain measuring frequency is denoted as T_m. The value of T_m increases with the increase of the measuring frequency. The relationship between the logarithm of frequency and the reciprocal of T_m is plotted in Fig. 8 Inset. The relationship between the logarithm of measuring frequency and the reciprocal of T_m is nearly linear. It is suggested that the relationship between the measuring frequency and T_m following the Arrehenius law, which can be expressed as (Samara, 2003)

$$f = f_0 \exp\left(-\frac{E}{k_B T_m}\right) \tag{4}$$

Where f_0 is the pre-exponential term and E is the activation energy for the relaxation process, k_B is the Boltzmann's constant.

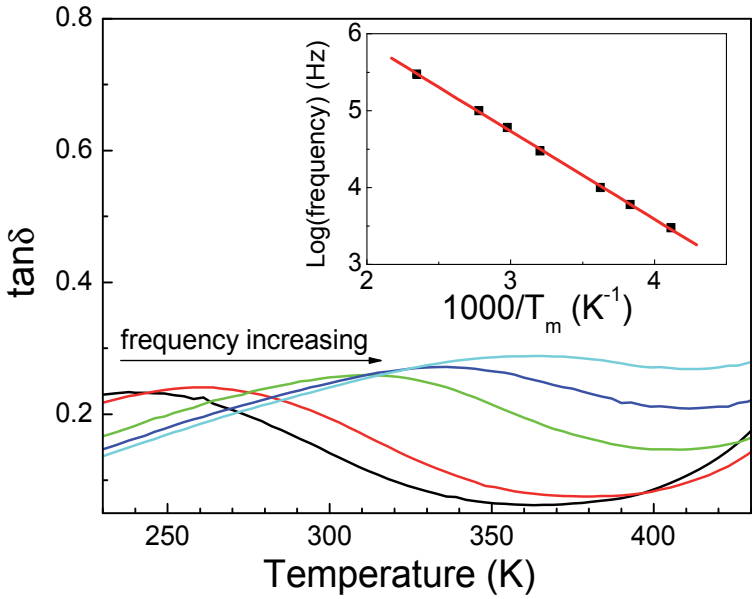

Fig. 8. The temperature dependence of loss tangent of the polycrystalline BFO films fabricated by CSD method. The value of T_m increases with increase of the measuring frequency. The Inset displays the relationship between the measuring frequency and the reciprocal of T_m. The straight line is linear fitting for the experimental data.

According to the result of linear fitting, the activation energy for the relaxation process related to oxygen vacancies is about 230 meV. As reported, the activation energy for dipolar relaxation in ferroelectrics is about 100~400meV (Samara, 2003). Therefore, the relaxation process with the activation energy of 230 meV in our samples may be a kind of dipolar relaxation process related to oxygen vacancies. Besides the vacancy of oxygen, another primary defect is Fe^{2+} (Palkar, 2002; Yun, 2003; Y. P. Wang, 2004). Therefore, it is suggested that the dipolar which induced this relaxation process is composed by vacancy of oxygen and Fe^{2+} (Vo-Fe^{2+}). It should be pointed out that the transfer of polaron in ferroelectrics also has the dielectric response similar to what has been observed above. But the activation energy for transfer of polaron is lower than the value calculated from our samples in the order of magnitude (Bidault, 1995). Therefore, the possible contribution from the transfer of polaron is excluded.

4.2 Ferroelectric and leakage behaviors of polycrystalline BFO films

As mentioned above, the higher leakage current in polycrystalline BFO films is related to the presence of a large number of oxygen vacancies. For the BFO film with higher electrical resistivity prepared by CSD method, the ferroelectric properties can be measured at lower temperature. The hysteresis loops and voltage dependence of capacitance of the sample measured at 70K are shown in Fig. 9.

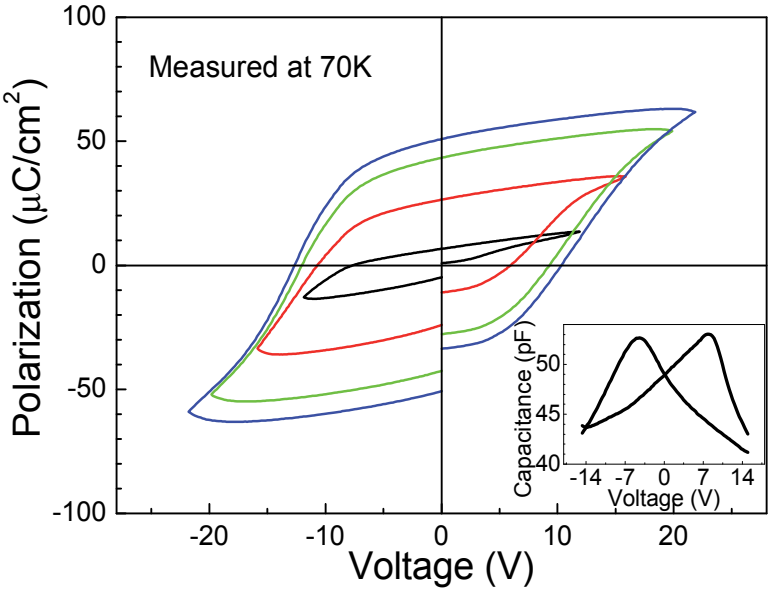

Fig. 9. The hysteresis loops under different applied voltages for the polycrystalline BFO film fabricated by CSD method. The inset displays the voltage dependence of the capacitance. Both ferroelectric hysteresis and the voltage dependence of the capacitance are measured at 70 K.

As shown in Fig. 9, the hysteresis loop exhibits the trend of saturation when the applied voltage is higher than 16V. The difference between the sample under positive bias and negative bias may be induced by the different top and bottom electrodes. Correspondingly, the voltage dependence of capacitance also shows an asymmetric butterfly-shape curve. According to the definition (Park, 2000)

$$tunability = (C_{\max} - C_{\min}) / C_{\max} \tag{5}$$

where C_{max} and C_{min} are the maximum and minimum of the capacitance under different applied voltage, the tunability of capacitance for the polycrystalline BFO film prepared by CSD method is about 22% at 70K.

However, when the temperature increases, the leakage current rises rapidly. The leakage current is so high that the film is breakdown before saturation under an applied voltage at room temperature. The measurements on the ferroelectric properties are impossible for this BFO film. Therefore, it is useful to study the leakage behaviour and the relationship between the leakage current and temperature.

The conductance of the polycrystalline BFO film prepared by CSD method is measured under different voltage at the temperature range between 80K and 350K. The results are exhibited in Fig. 10 (Sun, 2006).

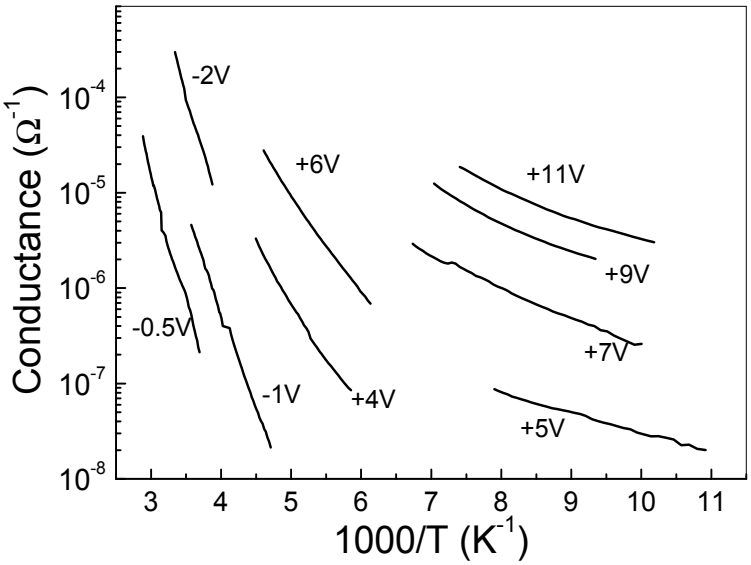

Fig. 10. The temperature dependence of conductance under different applied voltage of BFO film prepared by CSD method. The labels nearby each lines is the voltage applied on the film. (Sun, 2006)

In the semi-log plot, the relationship between the conductance and the reciprocal of temperature is approximately linear. This relationship follows the Poole-Frenkel (PF) emission (Pabst, 2007; Yang, 2008), which can be expressed as

$$\sigma_{PF} = c\exp\left[-\frac{1}{k_B T}\left(E_I - \sqrt{\frac{q^3 V}{\pi\varepsilon_0\varepsilon_r d}}\right)\right] \tag{6}$$

where c is a constant and E_I is the trap ionization energy which is related to the hopping of charge carrier. V is the voltage applied on the BFO film and d is the thickness of the BFO film. According to Pabst's report, the PF emission is the dominant transport mechanism in epitaxial BFO films (Pabst, 2007). Therefore, it is reasonable that PF emission is also one of the dominant leakage mechanisms in polycrystalline BFO film. However, there is an obvious difference between the experimental results of epitaxial and polycrystalline films. For epitaxial BFO films, the slope of the line *log(σ)* vs. *1000/T* varies linearly with the applied voltage (Pabst, 2007). But the slope of the lines in Fig. 10 has great difference. The lines can be divided into two groups according to their slope. According to equation (6), the relationship between the slope and the square root of the applied voltage can be expressed as

$$slope = \frac{1}{k_B}\sqrt{\frac{q^3 V}{\pi\varepsilon_0\varepsilon_r d}} - \frac{1}{k_B}E_I = c'\sqrt{V} - \frac{E_I}{k_B} \tag{7}$$

The coefficient c' is related to the dielectric constant ε_r. Regarding the data measured under higher applied voltage, the result is close to the epitaxial BFO film. However, for the data measured under lower applied voltage, the derived dielectric constant is one order of magnitude smaller than the reported value. In order to study the origin of the difference under different voltages, conductive tip atomic force microscopy (CAFM) is used.

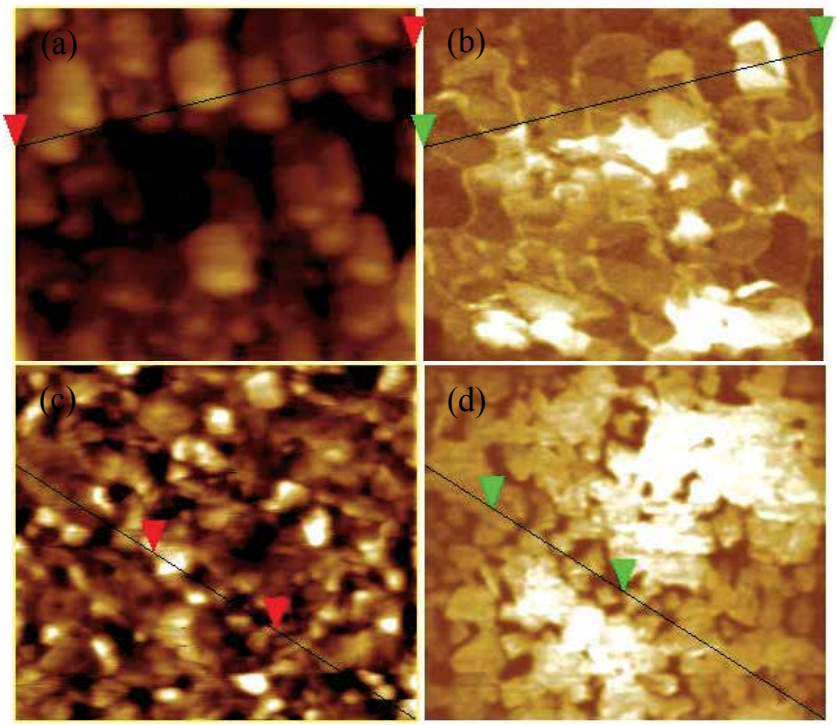

Fig. 11. The images of conductive tip atomic force microscopy (Area 1μm×1μm). (a) Surface morphology of the BFO film under 2.5 V voltage; (b) Current mapping of the BFO film under 2.5V voltage; (c) Surface morphology of the BFO film under 4.5 V voltage; (d) Current mapping of the BFO film under 4.5V voltage (Sun, 2006).

Figure 11 displays the CAFM images with different voltages applied on the tip. When the applied voltage is 2.5V, the area of grain boundary is highlight in fig. 11(b). This means that the leakage current flows along the grain boundary. When the applied voltage rises to 4.5V, all the grain is highlight. This means the current flows primarily through the whole grains. Comparing to the results of the leakage measurements, it is inferred that there is a region with lower dielectric constant at the grain boundary area. This region is the transfer access for leakage current when the voltage applied on the samples is smaller (Sun, 2006).

4.3 Ferroelectrics of polycrystalline BFO films on buffered silicon wafer

Compared to the BFO films grown on STO substrate, BFO films grown on silicon wafer has broader application prospects once the leakage problem is resolved. Figure 12 exhibits the ferroelectric hysteresis of the polycrystalline BFO films grown on LNO buffer silicon wafer.

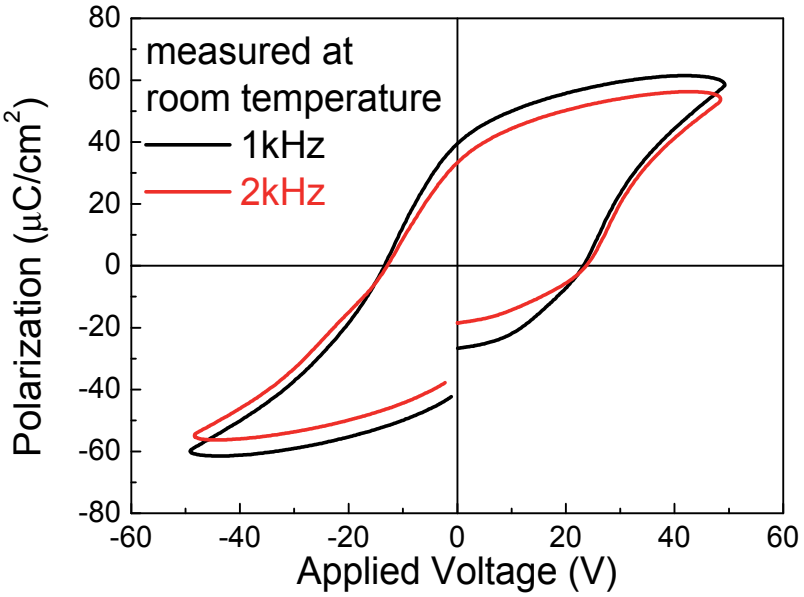

Fig. 12. The ferroelectric hysteresis of the polycrystalline BFO films grown on LNO buffer silicon wafer.

The layer of BFO is grown by PLD method and the buffer layer/bottom electrode LNO is fabricated by CSD method. The measurements are carried out at room temperature. Compared to the LSCO buffer layer fabricated by PLD, LNO layer fabricated by CSD is a more suitable buffer layer for the growth of high quality polycrystalline BFO films. Compared to the epitaxial BFO films on buffered-STO substrate, the value of Pr of polycrystalline BFO films is smaller. But the value is still larger than that of PZT and BTO films. Therefore, it is useful for the substitution of PZT in FeRAM.

5. Conclusion

In summary, the polycrystalline BFO films are fabricated on buffered silicon wafer and STO substrates. The electrical processes in the polycrystalline BFO films are investigated. The existence of a large number of oxygen vacancies not only increases the leakage current in BFO films, but also influence the dielectric response of the polycrystalline BFO films. The dielectric response is contributed in the form of dipolar combined by oxygen vacancy and Fe^{2+}. For the polycrystalline BFO films do not contain many oxygen vacancies, the Poole-Frenkel emission is the dominant transport mechanism when the polycrystalline BFO film. A region with lower dielectric constant exists at the grain boundary in polycrystalline BFO films. This region is the primary leakage access when the polycrystalline BFO film is under lower applied voltage. These results have significance for the researches on the applications of film in microelectronic devices.

6. Acknowledgments

One of the authors (Y. W. Li) thanks Prof. J. L. Sun for the useful discussion. This work was financially supported by Natural Science Foundation of China (Grant Nos. 60906046 and 11074076), Major State Basic Research Development Program of China (Grant Nos. 2007CB924901 and 2011CB922200), Projects of Science and Technology Commission of Shanghai Municipality (Grant Nos. 10DJ1400201, 10SG28, 10ZR1409800, and 09ZZ42), the Innovation Research Project of East China Normal University, and the Program for Professor of Special Appointment (Eastern Scholar) at Shanghai Institutions of Higher Learning.

7. References

Bidault O. ; Maglione M. ; Actis M. ; Kchikech M. (1995). Polaronic relaxation in perovskites. *Phys. Rev. B* 52, 4191. ISSN : 0163-1829.

Cole K. S. ; Cole R. H. (1941). Dispersion and absorption in dielectrics. *J. Chem. Phys.*, 9, 341. ISSN : 0021-9606.

Eerenstein W. ; Morrison F. D. ; Dho J. ; Blamire M. G. ; Scott J. F. ; Mathur N. D. (2005). Comment on "Epitaxial $BiFeO_3$ multiferroic thin film heterostructures". *Science*, 307, 1203a. ISSN : 0036-8075.

Hauser A. J. ; Zhang J. ; Mier L. ; Ricciardo R. A. ; Woodward P. M. ; Gustafson T. L. ; Brillson L. J. ; Yang F. Y. (2008). Characterization of electronic structure and defect states of thin epitaxial $BiFeO_3$ films by UV-visible absorption and cathodoluminescence spectroscopies. *Appl. Phys. Lett.*, 92, 222901. ISSN : 0003-6951.

Kaczmarek W., Pajak Z. & Polomska M.(1975). Differential thermal analysis of phase transitions in $(Bi_{1-x}La_x)FeO_3$ solid solution. *Solid. State. Comm.*, 17, 807. ISSN : 0038-1098.

Li Y. W. ; Sun J. L. ; Chen J. ; Meng X. J. ; Chu J. H. (2005). Preparation and characterization of $BiFeO_3$ thin films grown on $LaNiO_3$-coated $SrTiO_3$ substrate by chemical solution deposition. *J. Cryst. Growth*, 285, 595. ISSN : 0022-0248.

Li Y. W. ; Hu Z. G. ; Yue F. Y. ; Yang P. X. ; Qian Y. N. ; Cheng W. J. ; Ma X. M. ; Chu J. H. (2008). Oxygen-vacancy-related dielectric relaxation in $BiFeO_3$ films grown by pulsed laser deposition. *J. Phys. D : Appl. Phys.*, 41, 215403. ISSN : 0022-3727.

Li Y. W. ; Hu Z. G. ; Yue F. Y. ; Zhou W. Z. ; Yang P. X. ; Chu J. H. (2009). Effects of deposition temperature and post-annealing on structure and electrical properites in $(La_{0.5}Sr_{0.5})CoO_3$ films grown on silicon substrate. *Appl. Phys. A*, 95, 721. ISSN : 0947-8396.

Liu G. Z. ; Wang C. ; Wang C. C. ; Qiu J . ; He M. ; Xing J. ; Jin K. J. ; Lu H. B. ; Yang G. Z. (2008). Effects of interfical polarization on the dielectric properties of $BiFeO_3$ thin film capacitors. *Appl. Phys. Lett.*, 92,122903. ISSN : 0003-6951.

Lunkenheimer P. ; Bobnar V. ; Pronin A. V. ; Ritus A. I. ; Volkov A. A. ; Loidl A. (2002). Origin of apparent colossal dielectric constants. *Phys. Rev. B* 66, 052105. ISSN : 0163-1829.

Maruyama K. ; Kondo M. ; Singh S. K. ; Ishiwara H. (2007). New ferroelectric material for enbedded FRAM LSIs. *FUJITSU Sci. Tech. J.* , 43, 502. ISSN : 0016-2523.

Meng X. J. ; Sun J. L. ; Yu J. ; Ye H. J. ; Guo S. L. ; Chu J. H. (2001). Preparation of highly (100)-oriented metallic $LaNiO_3$ films on Si substrates by a modified metalorganic decomposition technique. *Appl. Surf. Sci.*, 171, 68. ISSN : 0169-4332.

Pabst G. W. ; Martin L. W. ; Chu Y. H . ; Ramesh. R. (2007). Leakage mechanisms in $BiFeO_3$. *Appl. Phys. Lett.*, 90, 072902. ISSN : 0003-6951.

Palkar V. R. ; John J. ; Pinto R. (2002). Observation of saturated polarization and dielectric anomaly in magnetoelectric $BiFeO_3$ thin films. *Appl. Phys. Lett.*, 80, 1628. ISSN : 0003-6951.

Park B. H. ; Gim Y. ; Fan Y . ; Jia Q. X. ; Lu P. (2000). High nonlinearity of $Ba_{0.6}Sr_{0.4}TiO_3$ films heteroepitaxially grown on MgO substrates. *Appl. Phys. Lett.*, 77, 2587. ISSN : 0003-6951.

Samara G. A. (2003). The relaxational properties of compositionally disordered ABO_3 perovskites. *J. Phys : Condens. Matter*, 15, R367. ISSN : 0953-8984.

Singh S. K. ; Maruyama K. ; Ishiwara H. (2007). The influence of La-substitution on the micro-structure and ferroelectric properties of chemical-solution-deposited $BiFeO_3$ thin films. *J. Phys. D : Appl. Phys.*, 40, 2705. ISSN : 0022-3727.

Sun J. L. ; Li Y. W. ; Li T. X. ; Lin T. ; Chen J. ; Meng X. J. ; Chu J. H. (2006). The leakage current in $BiFeO_3$ films derived by chemical solution deposition. *Ferroelectrics*, 345, 83. ISSN : 0015-0193.

Teague J. R.; Gerson R. & James W. J. (1970). Dielectric hysteresis in single crystal $BiFeO_3$. *Solid. State. Comm.*, 8, 1073. ISSN : 0038-1098.

Tselev A. ; Brooks C. M. ; Anlage S. M. ; Zheng H. M. ; Salamanca-Riba L. ; Ramesh R. ; Subramanian M. A. (2004). Evidence for power-law frequency dependence of intrinsic dielectric response in the $CaCu_3Ti_4O_{12}$. *Phys. Rev. B* 70, 144101. ISSN : 0163-1829.

Yang H. ; Wang H. Zou G. F. ; Jain M. ; Suvorova N. A. ; Feldmann D. M. ; Dowden P. C. ; DePaula R. F. ; MacManus-Driscoll J. L. ; Taylor A. J. ; Jia Q. X. (2008). Leakage mechanisms of self-assembled $(BiFeO_3)_{0.5}$:$(Sm_2O_3)_{0.5}$ nanocomposite films. *Appl. Phys. Lett.*, 93, 142904. ISSN : 0003-6951.

Wang J. ; Neaton J. B. ; Zheng H. ; Nagarajan V. ; Ogale S. B. ; Liu B. ; Viehland D. ; Vaithyanathan V. ; Schlom D. G. ; Waghmare U.V. ; Spaldin N. A. ; Rabe K. M. ; Wutting M. ; Ramesh R. (2003). Epitaxial $BiFeO_3$ multiferroic thin film heterstructures. *Science*, 299,1719. ISSN : 0036-8075.

Wang Y. P. ; Zhou L. ; Zhang M. F. ; Che X. Y. ; Liu J. M. ; Liu Z. G. (2004). Room-temperature saturated ferroelectric polarization in $BiFeO_3$ ceramics synthesized by rapid liquid phase sintering. *Appl. Phys. Lett.*, 84, 1731. ISSN : 0003-6951.

Yun K. Y. ; Noda M. ; Okuyama M. (2003). Prominent ferroelectricity of $BiFeO_3$ thin films prepared by pulsed-laser deposition. *Appl. Phys. Lett.*, 83, 3981. ISSN : 0003-6951.

Zavaliche, F. ; Shafer P. ; Ramesh R. ; Cruz M. P. ; Das R. R. ; Kim D. M. ; Eom C. B. (2005). Polarization switching in epitaxial $BiFeO_3$ films. *Appl. Phys. Lett.*, 87, 252902. ISSN : 0003-6951.

Zhang L. (2005). Electrode and grain-boundary effects on the conductivity of $CaCu_3Ti_4O_{12}$. *Appl. Phys. Lett.*, 87, 022907. ISSN : 0003-6951.

9

Phase Transitions in Layered Semiconductor - Ferroelectrics

Andrius Dziaugys[1], Juras Banys[1], Vytautas Samulionis[1], Jan Macutkevic[2], Yulian Vysochanskii[3], Vladimir Shvartsman[4] and Wolfgang Kleemann[5]
[1]*Department of Radiophysics, Faculty of Physics, Vilnius University, 2600 Vilnius*
[2]*Center for Physical Sciences and Technology, A. Gostauto 11, 2600 Vilnius*
[3]*Institute of Solid State Physics and Chemistry, Uzhgorod University, Uzhgorod 88000*
[4]*Institute for Materials Science, Duisburg-Essen University, 45141 Essen*
[5]*Faculty of physics, Duisburg-Essen University, 47048 Duisburg*
[1,2]*Lithuania*
[3]*Ukraine*
[4,5]*Germany*

1. Introduction

$CuInP_2S_6$ crystals represent an unusual example of an anticollinear uncompensated two-sublattice ferroelectric system (Maisonneuve et al., 1997). They exhibit a first-order phase transition of the order–disorder type from the paraelectric to the ferrielectric phase (T_c = 315 K). The symmetry reduction at the phase transition (C2/c to Cc) occurs due to the ordering in the copper sublattice and the displacement of cations from the centrosymmetric positions in the indium sublattice. X-ray investigations have shown that Cu ion can occupy three types of positions (Maisonneuve et al., 1997). The ordering of the Cu ions (hopping between Cu^1u and Cu^1d positions) in the double minimum potential is the reason for the phase transition dynamics in $CuInP_2S_6$. In (Maisonneuve et al., 1997) it was suggested that a coupling between P_2S_6 deformation modes and Cu^+ vibrations enable the copper ion hopping motions that lead to the onset of ionic conductivity in this material at higher temperatures. At low temperatures a dipolar glass phase appears in $CuInP_2S_6$ weakly doped with antiferroelectric $CuCrP_2S_6$ or ferroelectric $CuInP_2Se_6$ (Macutkevic et al., 2008).
The copper chromium thiophosphate $CuCrP_2S_6$ crystallizes in a layered two-dimensional structure of the $Cu^IM^{III}P_2S_6$ (M = Cr, In) type described above (Maisonneuve et al., 1995). It is formed by double sheets of sulfur atoms sandwiching the metal cations and P–P groups which occupy the octahedral voids defined by the sulfur atoms. At room temperature the crystal structure has a space group of C2/c (Colombet et al., 1982). At 64 K, the Cu positions are confined to those of an antiferroelectric order where the crystal structure has the space group of Pc (Maisonneuve et al., 1995). Thus, the mechanism of the dielectric transition is likely to involve hopping of the copper ions among two or more positions. Two phase transitions have been observed at 155 K and 190 K by dielectric measurement and differential scanning calorimetry (DSC). The crystal is antiferroelectric below 155 K and paraelectric above 190 K. For the intermediate phase between 155 and 190 K, a quasi-

antipolar structure has been proposed. Solid solutions $CuCr_{1-x}In_xP_2S_6$, $x > 0$, are therefore expected to reveal disordered dipolar glass phases as a consequence of randomness and frustration as confirmed recently (Maior et al., 2008).

Similar signatures of disorder might also be expected for the magnetic ground state of $CuCr_{1-x}In_xP_2S_6$, where magnetic Cr^{3+} ions are randomly replaced by diamagnetic In^{3+} ions in the antiferromagnetic (AF) compound $CuCrP_2S_6$ with a Néel temperature $T_N \approx 32$ K (Colombet et al., 1982). Owing to its competing ferromagnetic (FM) intralayer and AF interlayer exchange interactions (Colombet et al., 1982), randomness and frustration might eventually give rise to spin glass phases in $CuCr_{1-x}In_xP_2S_6$, $x > 0$, similarly as in the related AF compound $Fe_{1-x}Mg_xCl_2$ (Bertrand et al., 1982; Mattsson et al., 1996). The possible coexistence of this spin glass phase with the dipolar glassy one (Maior et al., 2008) is another timely motivation to study $CuCr_{1-x}In_xP_2S_6$. Indeed, '*multiglass*' behavior was recently discovered in the dilute magnetic perovskite $Sr_{0.98}Mn_{0.02}TiO_3$ (Shvartsman et al., 2008), paving the way to a new class of materials, '*disordered multiferroics*' (Kleemann et al., 2009).

The above mentioned comparison of the two families of dilute antiferromagnets $CuCrP_2S_6$:In and $FeCl_2$:Mg is not fortuitous. Originally, a strong structural analogy had been noticed between the lamellar compounds FeX_2 (X = Cl or Br) and transition metal (M) thio-phosphate phases, MPS_3, such as $FePS_3$ (Colombet et al., 1982). Both families are characterized by van der Waals gaps between their crystalline slabs and their ability to act as intercalation host material. The analogy becomes formally apparent when using the notations $Fe_2P_2S_6$ or – stressing the occurrence of P_2 pairs – $[Fe_{2/3}(P_2)_{1/3}]S_2$ (Klingen et al., 1973), and substituting $(Fe^{2+})_2$ by (Cu^+Cr^{3+}). This transcription discloses, however, that in contrast to the FeX_2 compounds even the undoped $CuCrP_2S_6$ is a 'dilute magnet' from the beginning (*i.e.* in the absence of non-magnetic In^{3+}), since it always hosts two diamagnetic cation sublattices occupied by Cu and P ions. This 'extra' dilution must be taken into account for understanding the magnetic and magnetoelectric properties discussed below.

This manuscript includes broad band spectroscopy, SQUID and piezoelectric measurement techniques, which helped to complement the list of already known properties of the investigated crystals and reveal new features such as dipole glass behaviour, magneto-electric coupling, and piezoelectric response. This crystal family is very interesting for various transducers because of the quite broad temperature region (285 to 330 K) for the phase transition.

2. Broad band dielectric spectroscopy of layered crystals

2.1 Ferrielectric phase transition in $CuInP_2S_6$, $Ag_{0.1}Cu_{0.9}InP_2S_6$ and $CuIn_{1+\delta}P_2S_6$ crystals

Results of the broadband dielectric measurements of $Ag_{0.1}Cu_{0.9}InP_2S_6$ are presented in Fig. 1. At low frequencies the dielectric losses increase with increasing temperature mainly due to the high ionic conductivity. The real part of the dielectric permittivity at 1 MHz already corresponds to the static one, because at that frequency ε'' is already much smaller than ε' (A. Dziaugys et al., 2010). It was found, that impurity of Ag ions, or addition of extra In ions drastically changes the ferrielectric phase transition temperature (static dielectric permittivity maximum temperature) (Table 1).

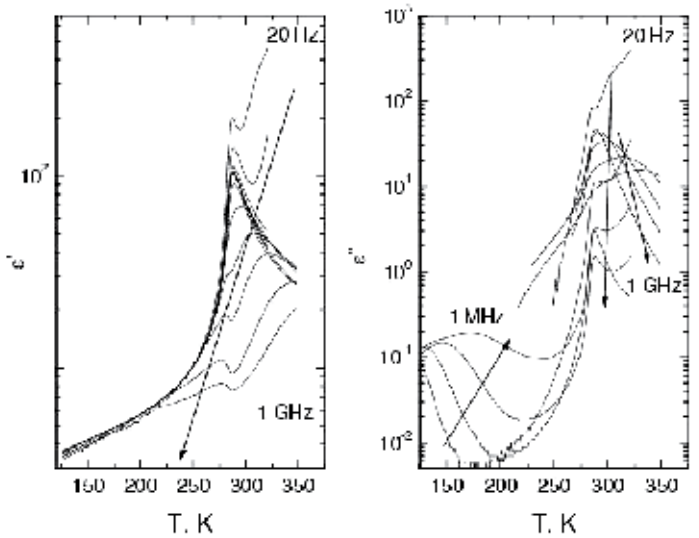

Fig. 1. Temperature dependence of the complex dielectric permittivity of $Ag_{0.1}Cu_{0.9}InP_2S_6$.

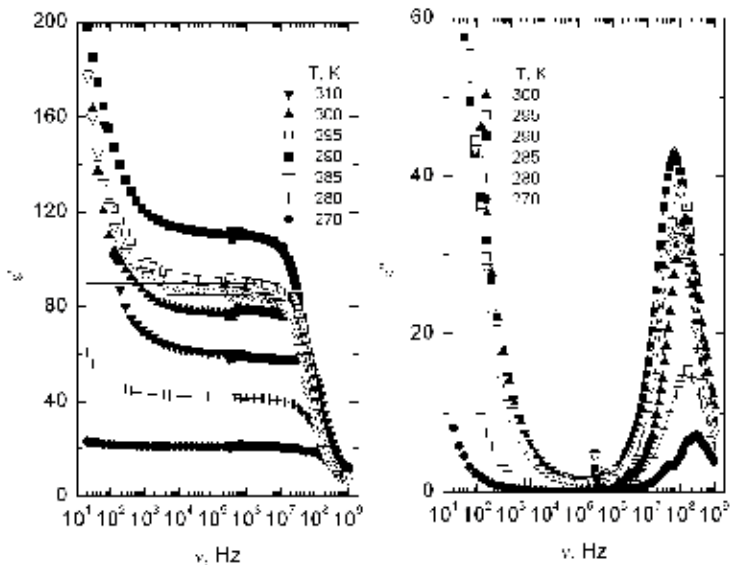

Fig. 2. Frequency dependence of complex dielectric permittivity of $Ag_{0.1}Cu_{0.9}InP_2S_6$ crystals measured at different temperatures. Solid lines are best fits according to *Eq.* (1).

Crystal	Phase transition temperature, K
$CuInP_2S_6$	313 (A. Dziaugys et al. 2010)
$CuIn_{1+\delta}P_2S_6$	330 (A. Dziaugys et al. 2011)
$Ag_{0.1}Cu_{0.9}InP_2S_6$	285 (A. Dziaugys et al. 2010)

Table 1. Phase transition temperatures got from the dielectric measurements.

The nature of such phase transition, similar to the pure $CuInP_2S_6$, is ferrielectric - ordering in the copper sublattice and displacement of cations from the centrosymmetric positions in the indium sublattice. The ferrielectric dispersion in the vicinity of T_c begins at about 10 MHz for $Ag_{0.1}Cu_{0.9}InP_2S_6$ and ranges up to the GHz region (Fig. 2). The characteristic minimum of ε' appears above 100 MHz at T = 285 K for $Ag_{0.1}Cu_{0.9}InP_2S_6$ and 500 MHz at T = 330 K for $CuIn_{1+\delta}P_2S_6$ indicating a critical slowing down typical of the order–disorder ferroelectric phase transitions (Grigas, 1996). The frequency plot of the complex permittivity at different temperatures (Fig. 2) was fitted with the Cole–Cole formula:

$$\varepsilon^*(\omega) = \varepsilon_\infty + \frac{\Delta\varepsilon}{1+(i\omega\tau)^\alpha}, \tag{1}$$

where $\Delta\varepsilon$ represents the dielectric strength of the relaxation, τ is the mean Cole–Cole relaxation time, ε_∞ represents the contribution of all polar phonons and electronic polarization to the dielectric permittivity and a is the Cole–Cole relaxation time distribution parameter. *Eq.* (1) reduces to the Debye formula if $\alpha = 0$. The obtained parameters are presented in Fig. 3. At higher temperatures the α parameter is very small and indicates Debye type dielectric dispersion.

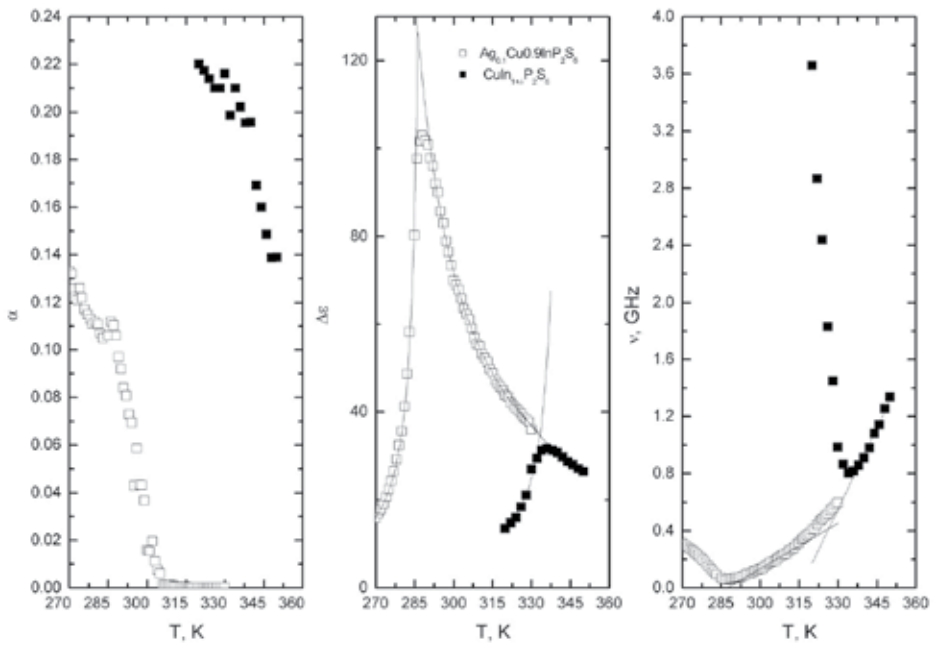

Fig. 3. Cole–Cole parameters of $Ag_{0.1}Cu_{0.9}InP_2S_6$ and $CuIn_{1+\delta}P_2S_6$ crystals.

On cooling the α parameter increases up to 0.133 for $Ag_{0.1}Cu_{0.9}InP_2S_6$ and 0.22 for $CuIn_{1+\delta}P_2S_6$ substantially below ferrielectric phase transition temperature T_c. The distribution of the relaxation times is much broader in the ferrielectric phase than in the paraelectric one. The temperature dependence of the dielectric strength $\Delta\varepsilon$ was fitted with the Curie–Weiss law:

$$\Delta\varepsilon = \frac{C_{p,f}}{\left|T - T_{Cp,Cf}\right|}, \tag{2}$$

where $C_{p,f}$ is the Curie–Weiss constant and $T_{Cp,Cf}$ is the Curie–Weiss temperature obtained from the fitting correspondingly in the paraelectric and ferrielectric phases. The ratios C_p/C_f = 7.8 (6.45 for $CuIn_{1+\delta}P_2S_6$), $C_p/T_{Cp} \approx 10$ (for both crystals) and mismatch T_{Cf}–T_{Cp} = 20 K (62 K for $CuIn_{1+\delta}P_2S_6$), show the first-order "order–disorder" ferroelectric phase transition. The temperature dependence of the mean Cole–Cole relaxation time τ in the paraelectric phase was fitted with the classical law (Grigas, 1996):

$$\tau = \tau_0 e^{U/kT} \frac{C_p}{T - T_{Cp}}, \tag{3}$$

where τ_0 is the relaxation time as $T \to \infty$ and the exponential factor describes deviations from phenomenological Landau theory close to the phase transition temperature, which appears due to critical fluctuations. The parameters obtained for $Ag_{0.1}Cu_{0.9}InP_2S_6$ are τ_0=8.1×10^{-16} s, U/k = 2980 K (0.26 eV).

2.2 Ferrielectric and dipolar glass phase coexistence in $CuInP_2S_6$ and $Ag_{0.1}Cu_{0.9}InP_2S_6$ crystals

At temperatures below 175 K dielectric dispersion effects can be observed at low frequencies for pure $CuInP_2S_6$ (Fig. 4). A similar dielectric dispersion also occurs in $Ag_{0.1}Cu_{0.9}InP_2S_6$ and in $CuIn_{1+\delta}P_2S_6$ at low temperatures. Such dielectric dispersion is typical of dipolar glasses (Figs. 4 and 5) (Macutkevic et al. 2008).

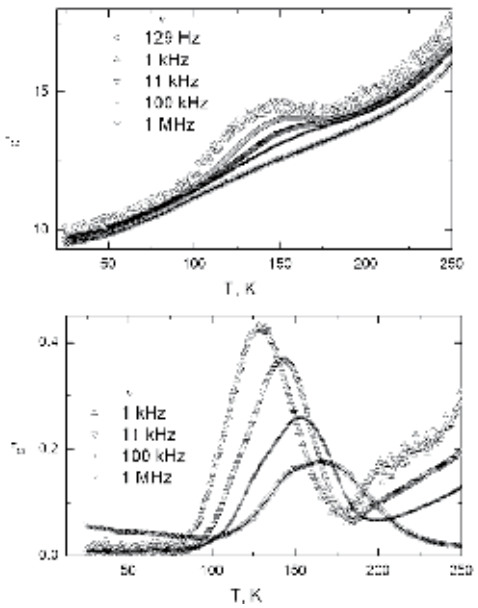

Fig. 4. Temperature dependence of the complex dielectric permittivity of $CuInP_2S_6$ crystals. Low temperature region.

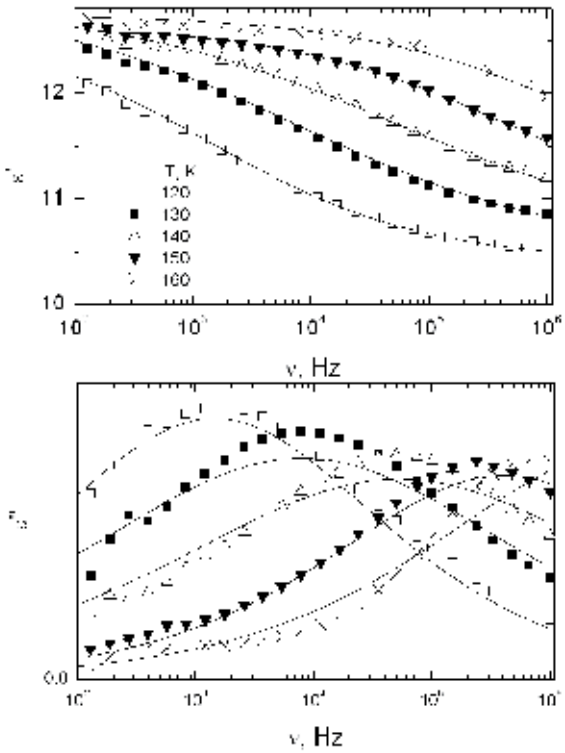

Fig. 5. Frequency dependence of the complex dielectric permittivity of $CuInP_2S_6$ crystals measured at different low temperatures. Solid lines are best fits to *Eq.* (1).

From dielectric spectra for $CuInP_2S_6$ and $Ag_{0.1}Cu_{0.9}InP_2S_6$ the Cole–Cole parameters were calculated. Very high and almost temperature independent value of the distribution of relaxation times α indicates a very wide distribution of relaxation times. The mean relaxation time increases on cooling according to the Vogel–Fulcher law:

$$\tau = \tau_0 \exp \frac{E_f}{k(T - T_0)} \tag{4}$$

where E_f is the activation energy and T_0 the freezing temperature. Obtained parameters are presented in (Dziaugys et al., 2010; Dziaugys et al., 2011). The freezing temperature is higher for $Ag_{0.1}Cu_{0.9}InP_2S_6$ as compared to $CuInP_2S_6$ and $CuIn_{1+\delta}P_2S_6$. What is the nature of dipole glass phase in pure $CuInP_2S_6$? First of all we must admit that the freezing occurs mainly in the copper sublattice, since the ferroelectric interaction exists only for copper ions in $CuInP_2S_6$. Secondly, in the dipole glass phase disorder should exist in the copper sublattice and competitive (ferroelectric and antiferroelectric) interactions occur between copper ions or (and) between copper ions and lattice. Competitive interactions can also occur between copper and indium ions. The static disorder in the copper sublattice was observed by X-ray investigations mainly at higher temperatures (Maisonneuve et al., 1997). This disorder is just random distribution of copper ions between more than the three positions (Cu^1, Cu^2, Cu^3). However, this is only a static picture of disorder in $CuInP_2S_6$. The dielectric spectroscopy

reveals that the dynamic disorder in $CuInP_2S_6$ does not vanish in the ferroelectric phase. The dynamic disorder is hopping of Cu ions between several possible static occupation positions. This hopping freezes at very low temperatures. The $CuInP_2S_6$ is a ferroelectric (ferrielectric) for which a dipole glass phase at low temperatures is observed even in the (nominally) pure crystal. Therefore $CuInP_2S_6$ with small amount of additions, independent from physical properties of the additions (ferroelectric, antiferroelectric or nonferroelectric) should exhibit the same phase diagram – the ferrielectric phase transition at higher temperatures and the freezing into a dipole glass phase at lower temperatures.

2.3 Phase transitions in antiferroelectric $CuCrP_2S_6$ and $CuIn_{0.1}Cr_{0.9}P_2S_6$ crystals

The antiferroelectric phase transition in $CuCrP_2S_6$ and $CuIn_{0.1}Cr_{0.9}P_2S_6$ is accompanied by a step-like dielectric anomaly (Fig. 6). The width of the step is approximately 5K for $CuCrP_2S_6$ and 20 K for $CuIn_{0.1}Cr_{0.9}P_2S_6$ Taking the temperature, corresponding to the peak point of the step as the temperature of phase transition, it was found that $T_c \approx 170$ K for $CuCrP_2S_6$ and 167 K for $CuIn_{0.1}Cr_{0.9}P_2S_6$.

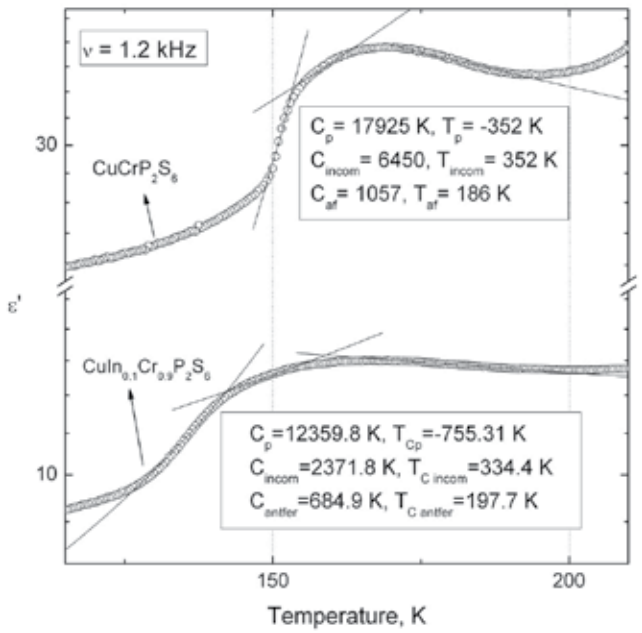

Fig. 6. Temperature dependence of the real part of the dielectric permittivity of a) $CuIn_{0.1}Cr_{0.9}P_2S_6$ and b) $CuInCrP_2S_6$. Solid lines are fitted according to the Curie – Weiss law.

While analyzing the sample from low temperatures, ε' rises slowly between 30 K and 125 K for $CuIn_{0.1}Cr_{0.9}P_2S_6$ and 150 K for $CuCrP_2S_6$, after which it increases abruptly and then smoothly, while at 167 K for $CuIn_{0.1}Cr_{0.9}P_2S_6$ and 170 K for $CuCrP_2S_6$ it starts decreasing. As we can see the ε' maximum is no so well pronounced as in $CuInP_2S_6$ (Banys et al., 2004), therefore such property is typical of antiferroelectrics (Kittel, 1951). The T width of this dielectric anomaly and the slope changes just below 167 K ($CuIn_{0.1}Cr_{0.9}P_2S_6$) and 170 K ($CuCrP_2S_6$) agree with the hypothesis of a slowly evolving short-range dipole order. Knowing that the copper dipole configuration is antipolar at T<150 K, we infer from the

relatively continuous decrease of ε' at 125 K ($CuIn_{0.1}Cr_{0.9}P_2S_6$) and 150 K ($CuInCrP_2S_6$) that the intermediate phase is quasi–antipolar (or incommensurate). It was found that $\varepsilon'(T)$ follows a Curie –Weiss law, *Eq.* (2). The ratio of $C_p/C_{af} >> 2$ indicates a first order phase transition to take place in both crystals.

2.4 Inhomogeneous ferrielectrics

The temperature dependence of the real and imaginary parts of the complex dielectric permittivity ε^* at various frequencies ν of $CuCr_{0.3}In_{0.7}P_2S_6$ crystals are presented in Fig. 7. We can see three different regions of dielectric dispersion. At temperatures T > 220 K and frequencies ν < 1 MHz the dielectric dispersion is mainly caused by the high conductivity, similarly as in pure $CuCrP_2S_6$ and $CuInP_2S_6$ crystals. The dielectric dispersion caused by the relaxation soft mode is observed in the vicinity of the ferroelectric phase transition temperature $T_c \approx 256$ K for $CuCr_{0.3}In_{0.7}P_2S_6$ and $T_c \approx 247$ K for $CuCr_{0.2}In_{0.8}P_2S_6$ and at higher frequencies (ν > 1 MHz). The dispersion at low temperatures (T < 170 K) is characteristic of the freezing into the dipole glass state. It is likely that substitutions in the chromium sublattice give rise to a more complex potential relief in which the copper ions move. As a consequence a part of the copper ions does not participate in the cooperative dynamics involved in the ferroelectric ordering. The dependence of the dielectric permittivity on frequency has been fitted with the Cole-Cole formula. The parameter $\Delta\varepsilon$ in the vicinity of the ferroelectric phase transition temperature follows the Curie-Weiss law, *Eq.* 2. To find out its order we have calculated the Curie-Weiss constants in the paraelectric and ferroelectric phases, respectively: $C_p \approx 4940$ K and $C_f \approx 2580$ K. From the ratio of these constants (1.92) it is clear that crystal with x = 0.7 undergoes a second-order phase transition. The ratio $C_{p,f}/T_C$ is in the order 10, therefore the observed phase transition is mainly of the "order-disorder" type (Grigas, 1996). The Cole-Cole mean relaxation time τ increases with decreasing temperature, according to the Vogel-Fulcher law. No anomaly of the relaxation time is

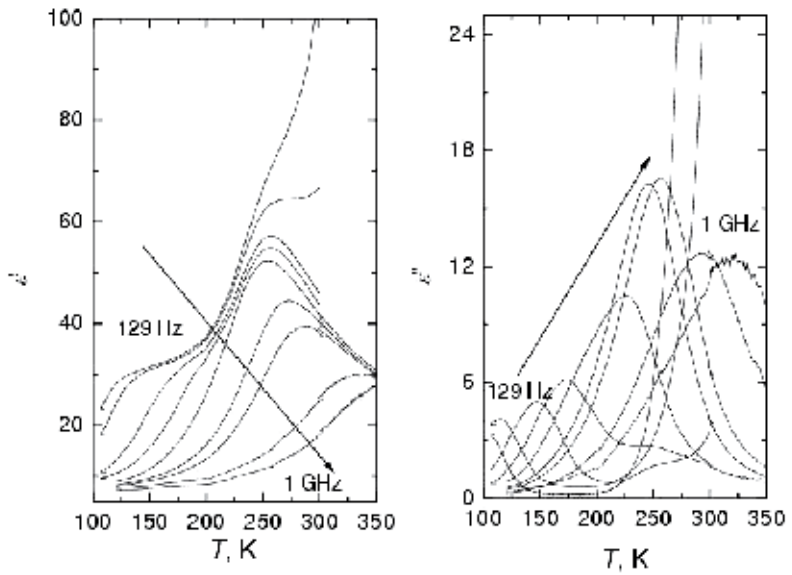

Fig. 7. Temperature dependence of the complex dielectric permittivity of $CuCr_{0.3}$ $In_{0.7}CrP_2S_6$

observed in the vicinity of the ferroelectric phase transition. In order to get information that is more precise about the relaxation-time distribution function, a special approach has been developed. A detailed description can be found in (Banys et al., 2002). We assume that the complex dielectric spectrum $\varepsilon^*(\nu)$ can be represented as a superposition of independent individual Debye-type relaxation processes (Schafer et al., 1996; Kim et al., 2000; Pelster et al., 1998)

$$\varepsilon^*(\nu) = \varepsilon_\infty + \Delta\varepsilon \int_{-\infty}^{\infty} \frac{f(\tau) d\lg\tau}{1 + i\omega\tau}. \tag{4}$$

The distributions of relaxation times of the investigated ferrielectric $CuCr_{0.3}In_{0.7}P_2S_6$ are presented in Fig. 8. One can recognize that the relaxation-time distribution function significantly broadens at low temperatures, as it is typical for dipole glasses. Let us consider the copper ions moving in asymmetric double well potentials. The movement consists of fast oscillations in one of the minima with occasional thermally activated jumps between the minima. The jump probability is governed by the Boltzmann probability of overcoming the potential barrier between the minima. The relaxation time in such a system is given by:

$$\tau = \tau_0 \frac{\exp[E_b / k_B(T - T_0)]}{2\cosh(A / 2k_B T)}. \tag{5}$$

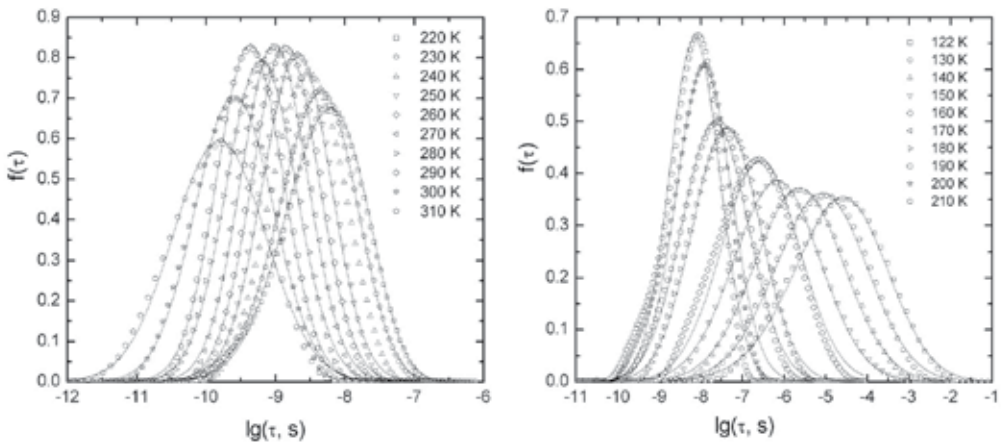

Fig. 8. Distribution of relaxation times of mixed ferroelectric $Cu(In_{0.7}Cr_{0.3})P_2S_6$ obtained from dielectric spectra (points). The solid lines are best fits according to *Eq.* (4).

The parameter A accounts for the asymmetry of the local potential produced by the mean-field influence of all the other dipoles. Thus, the local polarization of copper ions is

$$p = \tanh(A / 2k_B T) \tag{6}$$

and the distribution function $\varpi(p)$ of the local polarizations:

$$\varpi(p) = \frac{2k_B T}{\sqrt{2\pi}\sigma_A(1 - p^2)} \exp\left[-\frac{(a\tanh[p] - a\tanh[\bar{p}])^2}{2\sigma_A(2k_B T)^2} \right]. \tag{7}$$

We further consider that the asymmetry A and the potential barrier E_b of the local potential are randomly distributed around their mean values A_0 and E_{b0} according to a Gaussian law resulting in the distribution functions:

$$f(E_b) = \frac{1}{\sqrt{2\pi}\sigma_{Eb}} \exp\left(-\frac{(E_b - E_{b0})^2}{2\sigma_{Eb}^2}\right) \tag{8}$$

with

$$f(A) = \frac{1}{\sqrt{2\pi}\sigma_A} \exp\left(-\frac{(A - A_0)^2}{2\sigma_A^2}\right), \tag{9}$$

where σ_{Eb} and σ_A are the standard deviations of E_b and A, respectively, from their mean values. Fits with the experimentally obtained relaxation-time distributions were performed and the results are presented in Fig. 8 as solid lines. Knowing the average asymmetry A and the standard deviation of asymmetry σ_A we have calculated the distributions of local polarization $w(p)$ (Fig. 9).

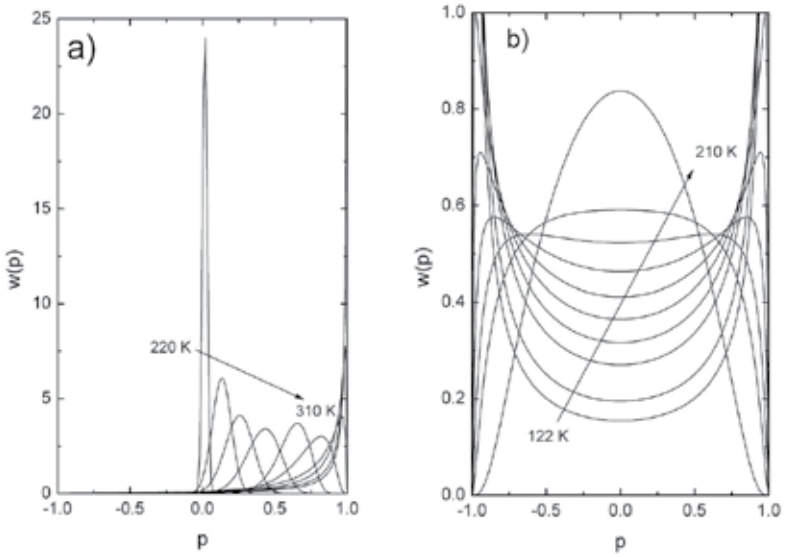

Fig. 9. Distribution of local polarizations $w(p)$ of a $CuCr_{0.3}In_{0.7}P_2S_6$ crystal: at several temperatures.

A broad distribution of local polarization is observed in both investigated ferrielectrics are typical for inhomogeneous ferroelectrics. It indicates that not all copper ions are ordered in the ferrielectric phase. This fact was confirmed also by X ray investigations of pure $CuInP_2S_6$. By further cooling non-ordered copper ions form a glassy phase and finally become frozen. Knowing the distribution function $w(p)$, both the average (macroscopic) polarization

$$\overline{p} = \int_{-1}^{1} p w(p) dp \tag{10}$$

and the Edwards-Anderson glass order parameter

$$q_{EA} = \int_{-1}^{1} p^2 w(p) dp \tag{11}$$

can be calculated (Fig. 10). The temperature behavior of the average polarization is typical for the second-order ferroelectric phase transition.

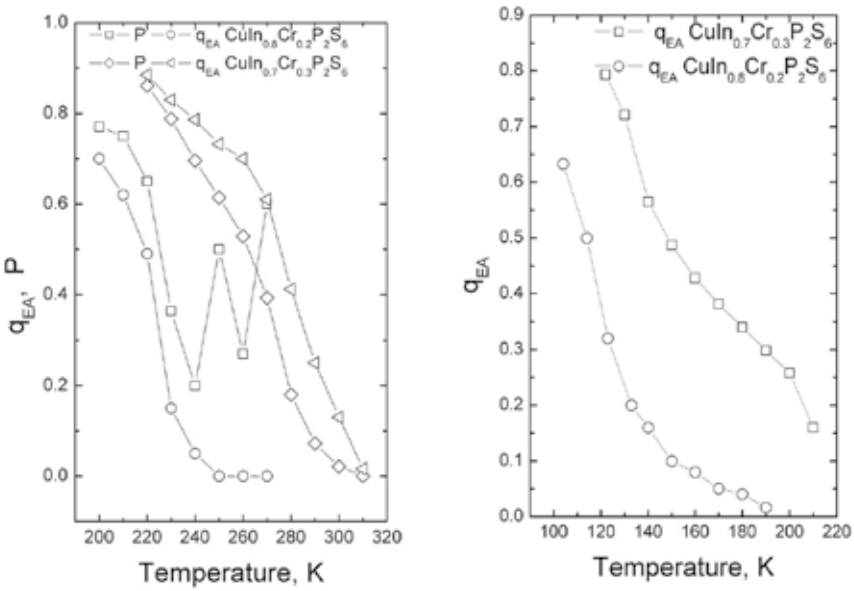

Fig. 10. Temperature dependence of the spontaneous polarization P and the Edwards-Anderson parameter q_{EA} of mixed $CuCr_{0.2}In_{0.8}P_2S_6$ and $CuCr_{0.3}In_{0.7}P_2S_6$ crystals.

2.5 Dipole glass state in mixed $CuCr_{1-x}In_xP_2S_6$ crystal

The temperature dependence of the dielectric properties in the $CuCr_{1-x}In_xP_2S_6$ mixed crystals with x = 0.5 is presented in Fig. 11. The shoulder-like $\varepsilon'(T)$ anomaly shifts toward higher temperatures with increasing frequency. The dielectric relaxation is also expressed in the dielectric losses. The dielectric dispersion at low temperatures (T < 170 K) is typical of dipole glasses. At higher temperatures the dielectric dispersion is clearly symmetric and observed only at higher frequencies. On cooling it strongly passes to lower frequencies and becomes more asymmetric. The dielectric dispersion is described with the Cole-Cole formula. The Cole-Cole mean relaxation time τ increases with decreasing temperature, according to the Vogel-Fulcher law, the parameters of which are noticed in Table 2.

	$CuIn_{0.5}Cr_{0.5}P_2S_6$	$CuIn_{0.4}Cr_{0.6}P_2S_6$
T_0, K	23	20
E/k, K (eV)	1554 (0.134)	1575 (0.136)
τ_0, s	$7.67 \cdot 10^{-13}$	$4.7 \cdot 10^{-13}$

Table 2. Parameters of the Vogel–Fulcher law.

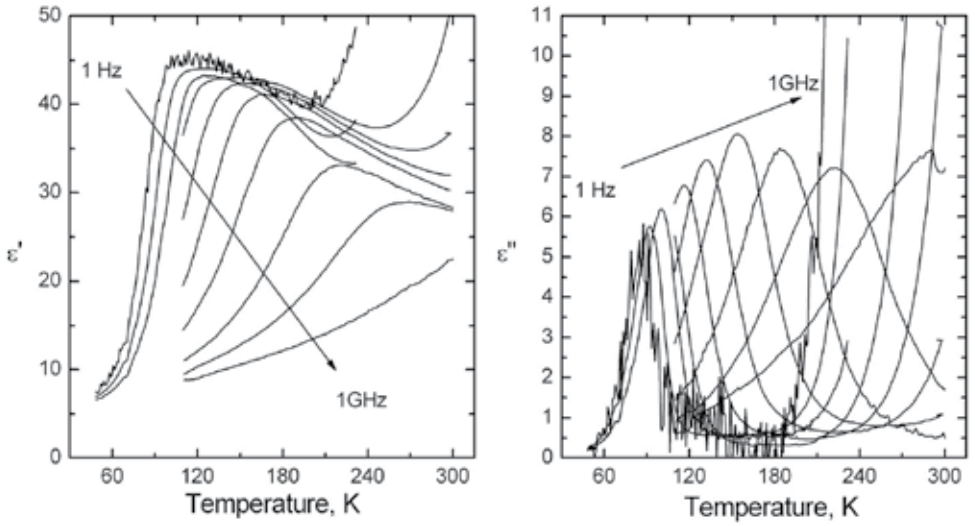

Fig. 11. Temperature dependence of the complex dielectric permittivity of $CuIn_{0.5}Cr_{0.5}CrP_2S_6$

Broad and very asymmetric distributions of relaxation times are observed in both investigated dipolar glasses (Fig. 12). To get more insight into the nature of such distributions, they are fitted by the double well potential model described above.

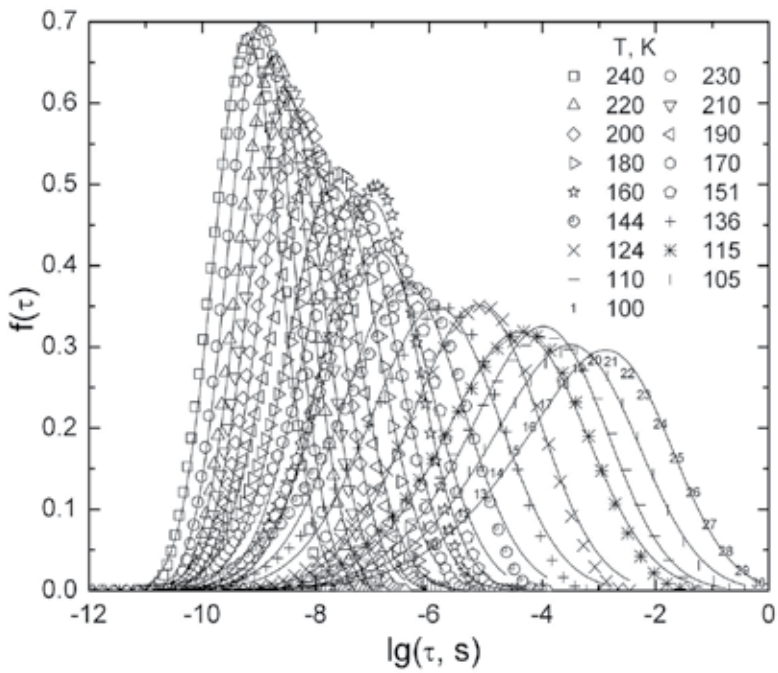

Fig. 12. Distribution of relaxation times of ferroelectric $CuCr_{0.5}In_{0.5}P_2S_6$

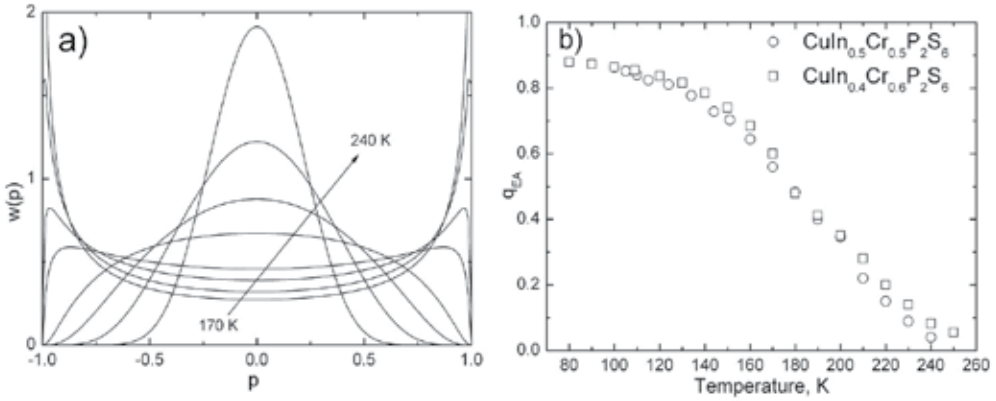

Fig. 13. a) Distribution of local polarizations $w(p)$ of $CuCr_{0.5}In_{0.5}P_2S_6$ at several temperatures. b) Temperature dependence of the Edwards-Anderson parameter of mixed $CuCr_{0.5}In_{0.5}P_2S_6$ and $CuCr_{0.6}In_{0.4}P_2S_6$ crystals.

From the double well potential parameters the local polarization distribution has been calculated (Fig. 13). The temperature behavior of the local polarization distribution is very similar to that of other dipole glasses like RADP or BP/BPI (Banys et al., 1994). The order parameter is an almost linear function of the temperature and does not indicate any anomaly.

2.6 Phase diagram of the mixed $CuIn_xCr_{1-x}P_2S_6$ crystals

The phase diagram of $CuCr_{1-x}In_xP_2S_6$ mixed crystals obtained from our dielectric results is shown in Fig. 14. Ferroelectric ordering coexisting with a dipole glass phase in $CuCr_{1-x}In_xP_2S_6$ is present for $0.7 \leq x$. On the other side of the phase diagram for $x \leq 0.9$ the antiferroelectric phase transition occurs. At decreasing concentration x the antiferroelectric phase transition temperature increases. In the intermediate concentration range for $0.4 \leq x \leq 0.6$, dipolar glass phases are observed.

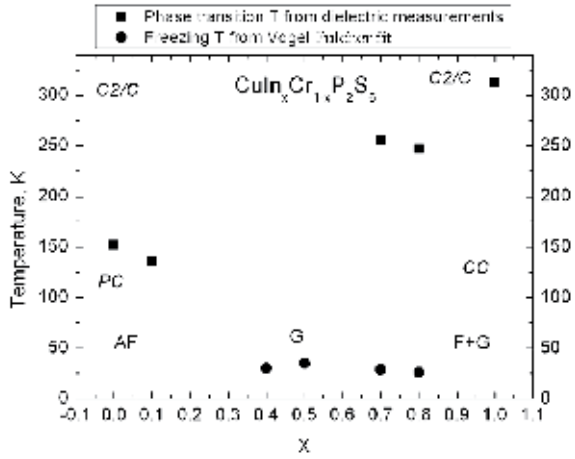

Fig. 14. Phase diagram of $CuCr_{1-x}In_xP_2S_6$ crystals. AF – antiferroelectric phase; G – glass phase; F+G – ferroelectric + glass phase.

3. Magnetic properties of $CuCr_{1-x}In_xP_2S_6$ single crystals

3.1 Experimental procedure

Single crystals of $CuCr_{1-x}In_xP_2S_6$, with x = 0, 0.1, 0.2, 0.4, 0.5, and 0.8 were grown by the Bridgman method and investigated as thin as-cleft rectangular platelets with typical dimensions 4×4×0.1 mm^3. The long edges define the *ab*-plane and the short one the *c*-axis of the monoclinic crystals (Colombet et al., 1982). While the magnetic easy axis of the x = 0 compound lies in the *ab*-plane (Colombet et al., 1982), the spontaneous electric polarization of the x = 1 compound lies perpendicular to it (Maisonneuve et al., 1997).

Magnetic measurements were performed using a SQUID magnetometer (Quantum Design MPMS-5S) at temperatures from 5 to 300 K and magnetic fields up to 5 T. For magneto-electric measurements we used a modified SQUID *ac* susceptometer (Borisov et al., 2007), which measures the first harmonic of the *ac* magnetic moment induced by an external *ac* electric field. To address higher order ME effects, additional *dc* electric and/or magnetic bias fields are applied (Shvartsman et al., 2008).

3.2 Temperature dependence of the magnetization

The temperature (T) dependence of the magnetization (M) measured on $CuCr_{1-x}In_xP_2S_6$ samples with x = 0, 0.1, 0.2, 0.4, 0.5 and 0.8 in a magnetic field of $\mu_0 H$ = 0.1 T applied perpendicularly to the *ab*-plane are shown in Fig. 15a within 5 ≤ T ≤ 150 K. Cusp-like AF anomalies are observed for x = 0, 0.1, and 0.2, at T_N ≈ 32, 29, and 23 K, respectively, as displayed in Fig. 15. While Curie-Weiss-type hyperbolic behavior, $M \propto (T - \Theta)^{-1}$, dominates above the cusp temperatures (Colombet et al., 1982), near constant values of M are found as $T \rightarrow 0$. They remind of the susceptibility of a uniaxial antiferromagnet perpendicularly to its easy axis, $\chi_\perp \approx const.$, thus confirming its assertion for $CuCrP_2S_6$ (Colombet et al., 1982).

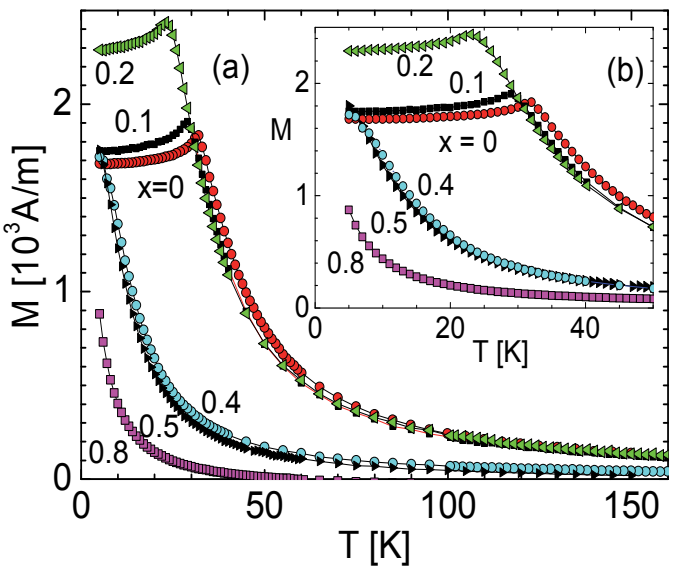

Fig. 15. Magnetization M *vs.* temperature T obtained for $CuCr_{1-x}In_xP_2S_6$ with x = 0, 0.1, 0.2, 0.4, 0.5, and 0.8 in $\mu_0 H$ = 0.1 T applied parallel to the *c* axis before (a) and after correction for the diamagnetic underground (b; see text).

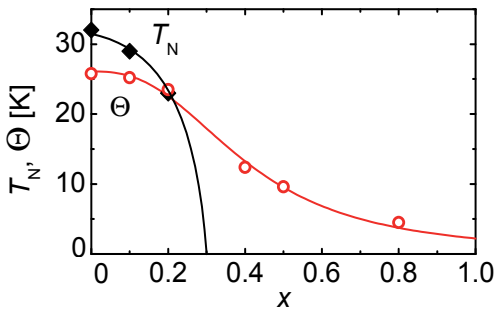

Fig. 16. Néel and Curie temperatures, T_N and Θ, *vs.* In^{3+} concentration x, derived from Fig. 15 (M) and Fig. 17 ($1/M$), and fitted by parabolic and logistic decay curves (solid lines), respectively.

At higher In^{3+} contents, $x \geq 0.4$, no AF cusps appear any more and the monotonic increase of M on cooling extends to the lowest temperatures, $T \approx 5$ K. Obviously the Cr^{3+} concentration falls short of the percolation threshold of the exchange interaction paths between the Cr^{3+} spins, which probably occurs at $x \approx 0.3$.

A peculiarity is observed at the highest In^{3+} concentration, $x = 0.8$ (Fig. 15a). The magnetization assumes negative values as $T > 60$ K. This is probably a consequence of the diamagnetism of the In^{3+} sublattice, the constant negative magnetization of which becomes dominant at elevated temperatures. For an adequate evaluation of the Cr^{3+} driven magnetism we correct the total magnetic moments for the diamagnetic background via the function

$$M = \frac{C}{T - \Theta} + D \,. \tag{12}$$

This model function accounts for pure Curie-Weiss behavior with the constant C at sufficiently high temperature and for the corresponding diamagnetic background D at all compositions. Table 3 presents the best-fit parameters obtained in individual temperature ranges yielding highest coefficients of determination, R^2. As can be seen, all of them exceed 0.999, hence, excellently confirming the suitability of *Eq.* (12). The monotonically decreasing magnitudes of the negative background values $D \approx -53$, -31, and -5 A/m for $x = 0.8$, 0.5, and 0.4, respectively, reflect the increasing ratio of paramagnetic Cr^{3+} *vs.* diamagnetic In^{3+} ions. We notice that weak negative background contributions, $D \approx -17$ A/m, persist also for the lower concentrations, $x = 0.2$, 0.1 and 0. Presumably the diamagnetism is here dominated by the other diamagnetic unit cell components, *viz.* S_6 and P_2.

x	Θ [K]	C [10^3A/(m·K)]	D [A/m]	best-fitting range	R^2
0	25.8±0.2	20.72±0.22	-28.7±2.2	T ≥ 50 K	0.9999
0.1	25.2±0.2	18.16±0.16	-16.4±0.9	T ≥ 45 K	0.9994
0.2	23.5±0.2	19.53±0.13	-16.6±1.0	T ≥ 45 K	0.9997
0.4	12.4±0.2	6.56±0.06	-4.5±0.4	T ≥ 34 K	0.9998
0.5	9.6±0.3	6.99±0.10	-31.4±0.4	T ≥ 29 K	0.9994
0.8	4.5±0.1	3.19±0.02	-54.6±0.3	T ≥ 21 K	0.9998

Table 3. Best-fit parameters of the data in Fig. 15 to *Eq.* (12).

Remarkably, the positive, *i.e.* FM Curie-Weiss temperatures, $26 > \Theta > 23$ K, for $0 \le x \le 0.2$ decrease only by 8%, while the decrease of T_N is about 28% (Fig. 16). This indicates that the two-dimensional (2D) FM interaction within the *ab* layers remains intact, while the interplanar AF coupling becomes strongly disordered and, hence, weakened such that T_N decreases markedly. It is noticed that our careful data treatment revises the previously reported near equality, $\Theta \approx T_N \approx 32$ K for $x = 0$ (Colombet et al., 1982). Indeed, the secondary interplanar exchange constant, $J_{inter}/k_B = -1$K, whose magnitude is not small compared to the FM one, $J_{intra}/k_B = 2.6$ K (Colombet et al., 1982), is expected to drive the crossover from 2D FM to 3D AF 'critical' behavior far above the potential FM ordering temperature, Θ.

As can be seen from Table 3 and from the intercepts with the T axis of the corrected $1/M$ *vs.* T plots in Fig. 17, the Curie-Weiss temperatures attain positive values, $\Theta > 0$, also for high concentrations, $0.4 \le x \le 0.8$. This indicates that the prevailing exchange interaction remains FM as in the concentrated antiferromagnet, $x = 0$ (Colombet et al., 1982). However, severe departures from the straight line behavior at low temperatures, $T < 30$ K, indicate that competing AF interactions favour disordered magnetism rather than pure paramagnetic behavior. Nevertheless, as will be shown in Fig. 19 for the $x = 0.5$ compound, glassy freezing with non-ergodic behavior (Mydosh, 1995) is not perceptible, since the magnetization data are virtually indistinguishable in zero-field cooling/field heating (ZFC-FH) and subsequent field cooling (FC) runs, respectively.

The concentration dependences of the characteristic temperatures, T_N and Θ, in Fig. 16 confirm that the system $CuCr_{1-x}In_xP_2S_6$ ceases to become globally AF at low T for dilutions $x > 0.3$, but continues to show preponderant FM interactions even as $x \to 1$. The tentative percolation limit for the occurrence of AF long-range order as extrapolated in Fig. 16 is reached at $x_p \approx 0.3$. This is much lower than the corresponding value of $Fe_{1-x}Mg_xCl_2$, $x_p \approx 0.5$ (Bertrand et al., 1984). Also at difference from this classic dilute antiferromagnet we find a stronger than linear decrease of T_N with x. This is probably a consequence of the dilute magnetic occupancy of the cation sites in the $CuCrP_2S_6$ lattice (Colombet et al., 1982), which breaks intraplanar percolation at lower x than in the densely packed Fe^{2+} sublattice of $FeCl_2$ (Bertrand et al., 1984).

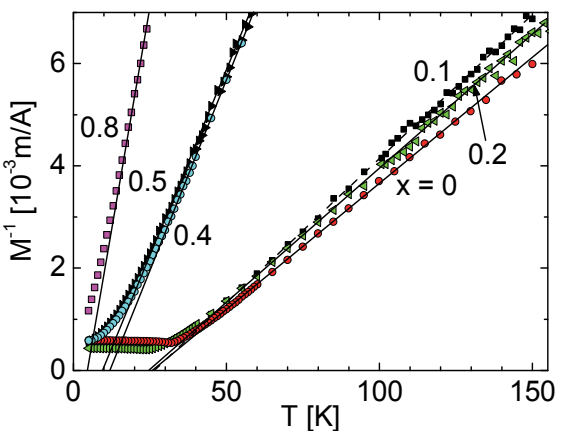

Fig. 17. Inverse magnetization M^{-1} corrected for diamagnetic background, *Eq.* (12), *vs.* T taken from Fig. 15 (inset). The straight lines are best-fitted to corrected Curie-Weiss behavior, *Eq.* (12), within individual temperature ranges (Table 3). Their abscissa intercepts denote Curie temperatures, Θ (Table 3).

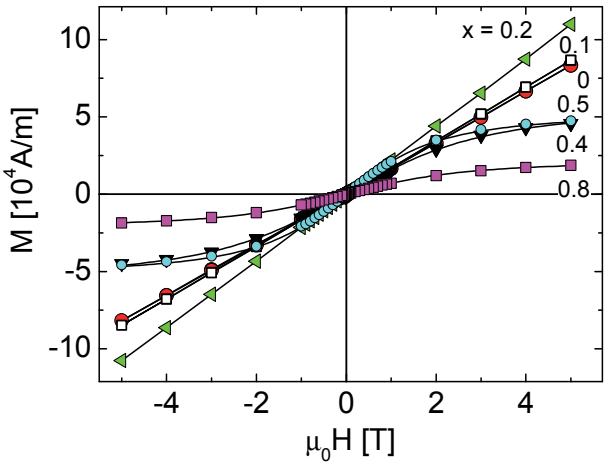

Fig. 18. Out-of-plane magnetization of $CuCr_{1-x}In_xP_2S$ with $0 \le x \le 0.8$ recorded at $T = 5$ K in magnetic fields $|\mu_0 H| \le 5$ T. The straight solid lines are compatible with $x = 0$, 0.1, and 0.2, while Langevin-type solid lines, *Eq.* (14) and Table 4, deliver best-fits for $x = 0.4$, 0.5, and 0.8.

A sigmoid logistic curve describes the decay of the Curie temperature in Fig. 16,

$$\Theta = \frac{\Theta_0}{1 + (x/x_0)^p}, \tag{13}$$

with best-fit parameters $\Theta_0 = 26.1$, $x_0 = 0.405$ and $p = 2.63$. It characterizes the decay of the magnetic long-range order into 2D FM islands, which rapidly accelerates for $x > x_0 \approx x_p \approx 0.3$, but sustains the basically FM coupling up to $x \to 1$.

3.3 Field dependence of the magnetization

The magnetic field dependence of the magnetization of the $CuCr_{1-x}In_xP_2S$ compounds yields additional insight into their magnetic order. Fig. 18 shows FC out-of-plane magnetization curves of samples with $0 \le x \le 0.8$ taken at $T = 5$ K in fields -5 T $\le \mu_0 H \le 5$ T. Corrections for diamagnetic contributions as discussed above have been employed. For low dilutions, $0 \le x \le 0.2$, non-hysteretic straight lines are observed as expected for the AF regime (see Fig. 15) below the critical field towards paramagnetic saturation. Powder and single crystal data on the $x = 0$ compound are corroborated except for any clear signature of a spin-flop anomaly, which was reported to provide a slight change of slope at $\mu_0 H_{SF} \approx 0.18$ T (Colombet et al., 1982). This would, indeed, be typical of the easy *c*-axis magnetization of near-Heisenberg antiferromagnets like $CuCrP_2S$, where the magnetization components are expected to rotate jump-like into the *ab*-plane at $\mu_0 H_{SF}$. This phenomenon was thoroughly investigated on the related lamellar MPS_3-type antiferromagnet, $MnPS_3$ albeit at fairly high fields, $\mu_0 H_{SF} \approx 4.8$ T (Goossens et al., 2000), which is lowered to 0.07 T for diamagnetically diluted $Mn_{0.55}Zn_{0.45}PS_3$ (Mulders et al., 2002).

In the highly dilute regime, $0.4 \le x \le 0.8$, the magnetization curves show saturation tendencies, which are most pronounced for $x = 0.5$, where spin-glass freezing might be expected as reported *e.g.* for $Fe_{1-x}Mg_xCl_2$ (Bertrand et al., 1984). However, no indication of hysteresis is visible in the data. They turn out to excellently fit Langevin-type functions,

$$M(H) = M_0\left[\coth(y) - 1/y\right], \tag{14}$$

where $y = (m\mu_0 H)/(k_B T)$ with the 'paramagnetic' moment m and the Boltzmann constant k_B. Fig. 18 shows the functions as solid lines, while Table 4 summarizes the best-fit results.

x	M_0	m	$N = M_0/m$
0.4	65.7 kA/m	5.6×10^{-23} Am² = 6.1μ_B	1.2 nm^{-3}
0.5	59.6 kA/m	8.5×10^{-23} Am² = 9.2μ_B	0.7 nm^{-3}
0.8	24.7 kA/m	6.86×10^{-23} Am² = 7.4μ_B	0.4 nm^{-3}

Table 4. Best-fit parameters of data in Fig. 18 to *Eq.* (14).

While the saturation magnetization M_0 and the moment density N scale reasonably well with the Cr^{3+} concentration, 1-x, the 'paramagnetic' moments exceed the atomic one, $m(Cr^{3+})$ = 4.08 μ_B (Colombet et al., 1982) by factors up to 2.5. This is a consequence of the FM interactions between nearest-neighbor moments. They become apparent at low T and are related to the observed deviations from the Curie-Weiss behavior (Fig. 17). However, these small '*superparamagnetic*' clusters are obviously not subject to blocking down to the lowest temperatures as evidenced from the ergodicity of the susceptibility curves shown in Fig. 15.

3.4 Anisotropy of magnetization and susceptibility

The cluster structure delivers the key to another surprising discovery, namely a strong anisotropy of the magnetization shown for the x = 0.5 compound in Fig. 19. Both the isothermal field dependences $M(H)$ at T = 5 K (Fig. 19a) and the temperature dependences $M(T)$ shown for $\mu_0 H$ = 0.1 T (Fig. 19b) split up under different sample orientations. Noticeable enhancements by up to 40% are found when rotating the field from parallel to perpendicular to the c-axis. At T = 5 K we observe $M_\perp \approx 70$ and 2.5 kA/m *vs.* $M_\parallel \approx 50$ and 1.8 kA/m at $\mu_0 H$ = 5 and 0.1 T, respectively (Fig. 19a and b).

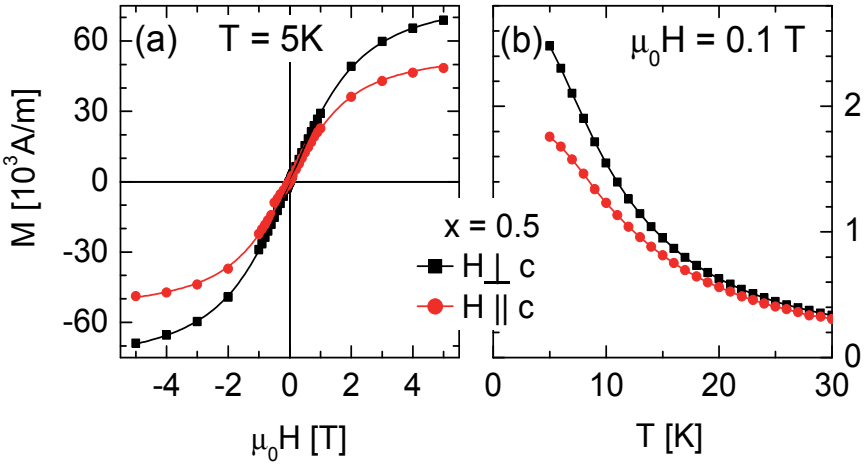

Fig. 19. Magnetization M of $CuCr_{0.5}In_{0.5}P_2S_6$ measured parallel (red circles) and perpendicularly (black squares) to the c axis (a) *vs.* $\mu_0 H$ at T = 5 K (best-fitted by Langevin-type solid lines) and (b) *vs.* T at $\mu_0 H$ = 0.1T (interpolated by solid lines).

At first sight this effect might just be due to different internal fields, $H^{int} = H - NM$, where N is the geometrical demagnetization coefficient. Indeed, from our thin sample geometry, 3×4×0.03 mm^3, with $N_\parallel \approx 1$ and $N_\perp << 1$ one anticipates $H_\parallel{}^{int} < H_\perp{}^{int}$, hence, $M_\parallel < M_\perp$. However, the demagnetizing fields, $N_\perp M_\perp \approx 0$ and $N_\parallel M_\parallel \approx 50$ and 1.8 kA/m, are no larger than 2% of the applied fields, H = 4 MA/m and 80 kA/m, respectively. These corrections are, hence, more than one order of magnitude too small as to explain the observed splittings. Since the anisotropy occurs in a paramagnetic phase, we can also not argue with AF anisotropy, which predicts $\chi_\perp > \chi_\parallel$ at low T (Blundell, 2001). We should rather consider the intrinsic magnetic anisotropy of the above mentioned 'superparamagnetic' clusters in the layered $CuCrP_2S_6$ structure. Their planar structure stems from large FM in-plane correlation lengths, while the AF out-of-plane correlations are virtually absent. This enables the magnetic dipolar interaction to support in-plane FM and out-of-plane AF alignment in $H_\perp$, while this spontaneous ordering is weakened in $H_\parallel$. However, the dipolar anisotropy cannot explain the considerable difference in the magnetizations at saturation, $M_0\parallel$=58.5 kA/m and $M_0{}^\perp$ = 84.2 kA/m, as fitted to the curves in Fig. 19a. This strongly hints at a mechanism involving the total moment of the Cr^{3+} ions, which are subject to orbital momentum transfer to the spin-only $^4A_2(d^3)$ ground state. Indeed, in the axial crystal field zero-field splitting of the $^4A_2(d^3)$ ground state of Cr^{3+} is expected, which admixes the $^4T_{2g}$ excited state via spin-orbit interaction (Carlin, 1985). The magnetic moment then varies under different field directions as the gyrotropic tensor components, $g_\perp$ and $g_\parallel$, while the susceptibilities follow $g_\perp{}^2$ and $g_\parallel{}^2$, respectively. However, since $g_\perp$ = 1.991 and $g_\parallel$ = 1.988 (Colombet et al., 1982) the single-ion anisotropies of both M and χ are again mere 2% effects, unable to explain the experimentally found anisotropies.

Since single ion properties are not able to solve this puzzle, the way out of must be hidden in the collective nature of the 'superparamagnetic' Cr^{3+} clusters. In view of their intrinsic exchange coupling we propose them to form 'molecular magnets' with a high spin ground states accompanied by large magnetic anisotropy (Bogani & Wernsdörfer, 2008) such as observed on the AF molecular ring molecule Cr_8 (Gatteschi et al., 2006). The moderately enhanced magnetic moments obtained from Langevin-type fits (Table 4) very likely refer to mesoscopic 'superantiferromagnetic' clusters (Néel, 1961) rather than to small 'superparamagnetic' ones. More experiments, in particular on time-dependent relaxation of the magnetization involving quantum tunneling at low T, are needed to verify this hypothesis.

It will be interesting to study the concentration dependence of this anisotropy in more detail, in particular at the percolation threshold to the AF phase. Very probably the observation of the converse behavior in the AF phase, $\chi_\perp < \chi_\parallel$ (Colombet et al., 1982), is crucially related to the onset of AF correlations. In this situation the anisotropy will be modified by the spin-flop reaction of the spins to $H_\parallel$, where $\chi_\parallel$ jumps up to the large $\chi_\perp$ and both spin components rotate synchronously into the field direction.

3.5 Magnetoelectric coupling

Magnetic and electric field-induced components of the magnetization, $\boldsymbol{M} = \boldsymbol{m}/V$,

$$\mu_0 M_i = -\partial F / \partial H_i = \mu_0 \mu_{ij} H_j + \alpha_{ij} E_j + \beta_{ijk} E_j H_k + \frac{\gamma_{ijk}}{2} E_j E_k + \delta_{ijkl} H_j E_k E_l \,, \qquad (15)$$

related to the respective free energy under Einstein summation (Shvartsman et al., 2008)

$$F(\mathbf{E},\mathbf{H}) = F_0 - \frac{1}{2}\varepsilon_0\varepsilon_{ij}E_iE_j - \frac{1}{2}\mu_0\mu_{ij}H_iH_j - \alpha_{ij}H_iE_j - \frac{\beta_{ijk}}{2}H_iE_jH_k - \frac{\gamma_{ijk}}{2}H_iE_jE_k - \frac{\delta_{ijkl}}{2}H_iH_jE_kE_l \quad (16)$$

were measured using an adapted SQUID susceptometry (Borisov et al., 2007). Applying external electric and magnetic *ac* and *dc* fields along the monoclinic [001] direction, $E = E_{ac}\cos\omega t + E_{dc}$ and H_{dc}, the real part of the first harmonic *ac* magnetic moment at a frequency $f = \omega/2\pi = 1$ Hz,

$$m'_{ME} = (a_{33}E_{ac} + \beta_{333}E_{ac}H_{dc} + \gamma_{333}E_{ac}E_{dc} + 2\delta_{3333}E_{ac}E_{dc}H_{dc})(V/\mu_o), \quad (17)$$

provides all relevant magnetoelectric (ME) coupling coefficients a_{ij}, β_{ijk}, γ_{ijk}, and δ_{ijkl} under suitable measurement strategies.

First of all, we have tested *linear* ME coupling by measuring m_{ME}' on the weakly dilute AF compound $CuCr_{0.8}In_{0.2}P_2S_6$ (see Fig. 15 and 16) at $T < T_N$ as a function of E_{ac} alone. The resulting data (not shown) turned out to oscillate around zero within errors, hence, $\alpha \approx 0$ ($\pm$ 10^{-12} s/m). This is disappointing, since the (average) monoclinic space group C2/m (Colombet et al., 1982) is expected to reveal the linear ME effect similarly as in $MnPS_3$ (Ressouche et al., 2010). We did, however, not yet explore non-diagonal couplings, which are probably more favorable than collinear field configurations.

More encouraging results were found in testing higher order ME coupling as found, *e. g.*, in the disordered multiferroics $Sr_{0.98}Mn_{0.02}TiO_3$ (Shvartsman et al., 2008) and $PbFe_{0.5}Nb_{0.5}O_3$ (Kleemann et al., 2010). Fig. 20 shows the magnetic moment m_{ME}' resulting from the weakly dilute AF compound $CuCr_{80}In_{20}P_2S_6$ after ME cooling to below T_N in three applied fields, E_{ac}, E_{dc}, and (a) at variant H_{dc} with constant $T = 10$ K, or (b) at variant T and constant $\mu_0H_{dc} = 2$ T.

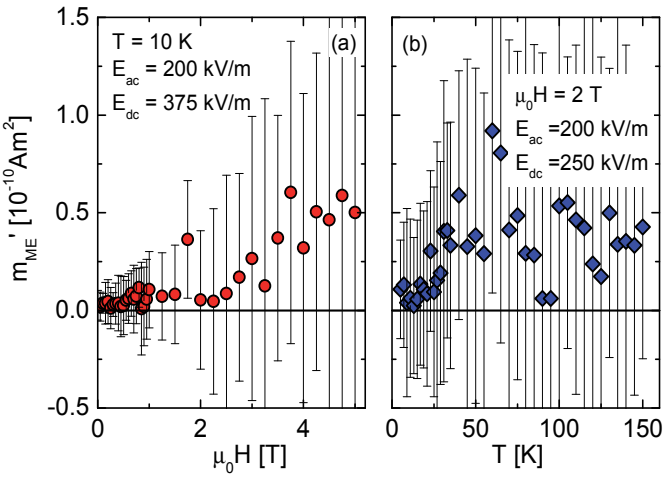

Fig. 20. Magnetoelectric moment m_{ME}' of $CuCr_{0.8}In_{0.2}P_2S_6$ excited by E_{ac}= 200 kV/m at $f = 1$ Hz in constant fields E_{dc} and H_{dc} and measured parallel to the c axis (a) *vs.* μ_0H at $T = 5$ K and (b) *vs.* T at $\mu_0H = 2$ T.

We notice that very small, but always positive signals appear, although their large error limits oscillate around $m_{ME}' = 0$. That is why we dismiss a finite value of the second-order magneto-bielectric coefficient γ_{333}, which should give rise to a finite ordinate intercept at $H = 0$ in Fig. 20a according to *Eq.* (17). However, the clear upward trend of $\langle m_{ME}' \rangle$ with increasing magnetic field makes us believe in a finite *biquadratic* coupling coefficient. The average slope in Fig. 20a suggests $\delta_{3333} = \mu_o \Delta m_{ME}' / (2V \Delta H_{dc} E_{ac} \Delta E_{dc}) \approx 4.4 \times 10^{-25}$ sm/VA. This value is more than one to two orders of magnitude smaller than those measured in $Sr_{0.98}Mn_{0.02}TiO_3$ (Shvartsman et al., 2008) and $PbFe_{0.5}Nb_{0.5}O_3$ (Kleemann et al., 2010), $\delta_{3333} \approx -9.0 \times 10^{-24}$ and 2.2×10^{-22} sm/VA, respectively. Even smaller, virtually vanishing values are found for the more dilute paramagnetic compounds such as $CuCr_{0.5}In_{0.5}P_2S_6$ (not shown). The temperature dependence of m_{ME}' in Fig. 20b shows an abrupt increase of noise above $T_N = 23$ K. This hints at disorder and loss of ME response in the paramagnetic phase.

3.6 Summary

The dilute antiferromagnets $CuCr_{1-x}In_xP_2S_6$ reflect the lamellar structure of the parent compositions in many respects. First, the distribution of the magnetic Cr^{3+} ions is dilute from the beginning because of their site sharing with Cu and (P_2) ions in the basal *ab* planes. This explains the relatively low Néel temperatures (< 30 K) and the rapid loss of magnetic percolation when diluting with In^{3+} ions ($x_c \approx 0.3$). Second, at $x > x_c$ the AF transition is destroyed and local clusters of exchange-coupled Cr^{3+} ions mirror the layered structure by their nearly compensated total moments. Deviations of the magnetization from Curie-Weiss behavior at low T and strong anisotropy remind of super-AF clusters with quasi-molecular magnetic properties. Third, only weak third order ME activity was observed, despite favorable symmetry conditions and occurrence of two kinds of ferroic ordering for $x < x_c$, ferrielectric at $T < 100$ K and AF at $T < 30$ K. Presumably inappropriate experimental conditions have been met and call for repetition. In particular, careful preparation of ME single domains by orthogonal field-cooling and measurements under non-diagonal coupling conditions should be pursued.

4. Piezoelectric and ultrasonic investigations of phase transitions in layered ferroelectrics of $CuInP_2S_6$ family

Ultrasonic investigations were performed by automatic computer controlled pulse-echo method and the main results are presented in papers (Samulionis et al., 2007; Samulionis et al., 2009a; Samulionis et al., 2009b). Usually in $CuInP_2S_6$ family crystals ultrasonic measurements were carried out using longitudinal mode in direction of polar c-axis across layers. The pulse-echo ultrasonic method allows investigating piezoelectric and ferroelectric properties of layered crystals (Samulionis et al., 2009a). This method can be used for the indication of ferroelectric phase transitions. The main feature of ultrasonic method is to detect piezoelectric signal by a thin plate of material under investigation. We present two examples of piezoelectric and ultrasonic behavior in the $CuInP_2S_6$ family crystals, viz. $Ag_{0.1}Cu_{0.9}InP_2S_6$ and the nonstoichiometric compound $CuIn_{1+\delta}P_2S_6$. The first crystal is interesting, because it shows tricritical behavior, the other is interesting for applications, because when changing the stoichiometry the phase transition temperature can be increased. For the layered crystal $Ag_{0.1}Cu_{0.9}InP_2S_6$, which is not far from pure $CuInP_2S_6$ in the phase diagram, we present the temperature dependence of the piezoelectric signal when

a short ultrasonic pulse of 10 MHz frequency is applied (Fig. 20). At room temperature no signal is detected, showing that the crystal is not piezoelectric. When cooling down a signal of 10 MHz is observed at about 285 K. It increases with decreasing temperature. Obviously piezoelectricity is emerging.

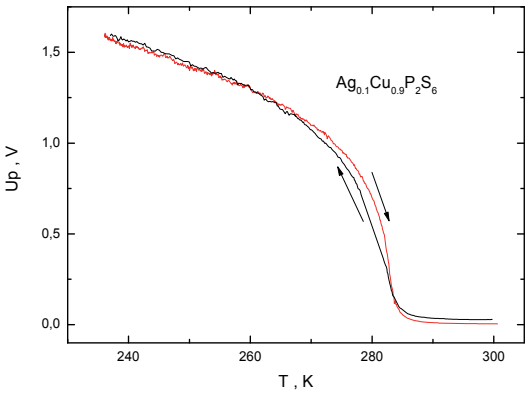

Fig. 21. Temperature dependences of ultrasonically detected piezoelectric signal in an $Ag_{0.1}Cu_{0.9}InP_2S_6$ crystal. Temperature variations are shown by arrows.

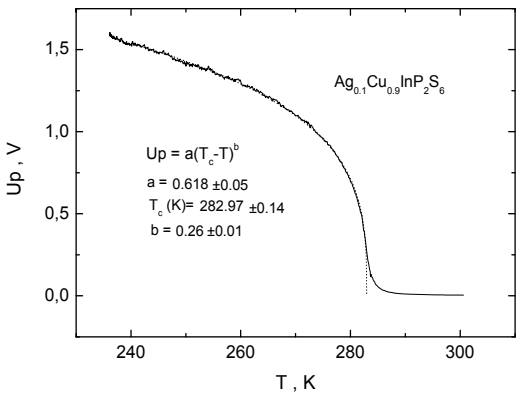

Fig. 22. Temperature dependences of the amplitude of piezoelectric signal and the least squares fit to *Eq.* (18), showing that the phase transition is close to the tricritical one.

The absence of temperature hysteresis shows that the phase transition near $T_c = 283$ K is close to second-order. In order to describe the temperature dependence of the amplitude of the ultrasonically detected signal we applied a least squares fit using the equation:

$$U_p = A(T_c - T)^{\beta} \tag{18}$$

In our case the piezoelectric coefficient g_{33} appears in the piezoelectric equations. The tensor relation of the piezoelectric coefficients implies that $\boldsymbol{g} = \mathbf{d}\ \boldsymbol{\varepsilon}_t^{-1}$. According to (Strukov & Levanyuk, 1995) the piezoelectric coefficient d in a piezoelectric crystal varies as $d \propto \eta_0/(T_c\text{-}T)$. Assuming that the dielectric permittivity $\boldsymbol{\varepsilon}_t$ can be approximated by a Curie

law it turns out that the amplitude of our ultrasonically detected signal varies with temperature in the same manner as the order parameter η_0. Hence, according to the fit in Fig. 22 the critical exponent of the order parameter (polarization) is close to the tricritical value of 0.25.

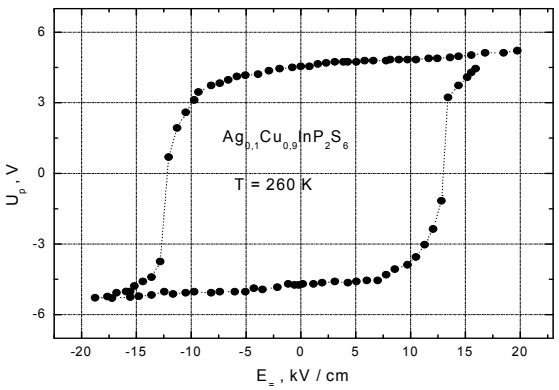

Fig. 23. dc field dependence of the piezoelectric signal amplitude in a $Ag_{0.1}Cu_{0.9}InP_2S_6$ crystal

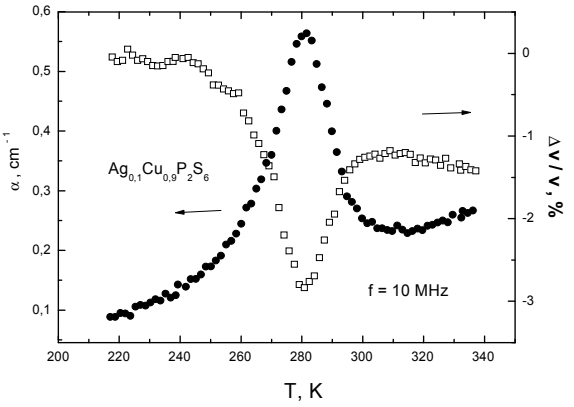

Fig. 24. Temperature dependences of the longitudinal ultrasonic attenuation and velocity in a $Ag_{0.1}Cu_{0.9}InP_2S_6$ crystal along the *c*-axis

In the low temperature phase hysteresis-like dependencies of the piezoelectric signal amplitude on dc electric field with a coercive field of about 12 kV/cm were obtained (Fig. 23). Thus the existence of the ferroelectric phase transition was established for $Ag_{0.1}Cu_{0.9}InP_2S_6$ crystal. The existence of the phase transition was confirmed by both ultrasonic attenuation and velocity measurements. Since the layered samples were thin, for reliable ultrasonic measurements the samples were prepared as stacks from 8-10 plates glued in such way that the longitudinal ultrasound can propagate across layers. At the phase transition clear ultrasonic anomalies were observed (Fig. 24). The anomalies were similar to those which were described in pure $CuInP_2S_6$ crystals and explained by the

interaction of the elastic wave with polarization (Valevicius et al., 1994a; Valevicius et al., 1994b). In this case the relaxation time increases upon approaching T_c according to Landau theory (Landau & Khalatnikov, 1954) and an ultrasonic attenuation peak with downwards velocity step can be observed. The increase of velocity in the ferroelectric phase can be attributed to the contribution of the fourth order term in the Landau free energy expansion. In this case the velocity changes are proportional to the squared order parameter. Also the influence of polarization fluctuations must be considered especially in the paraelectric phase.

Obviously the increase of the phase transition temperature is a desirable trend for applications. Therefore, it is interesting to compare the temperature dependences of ultrasonically detected electric signals arising in thin pure $CuInP_2S_6$, $Ag_{0.1}Cu_{0.9}InP_2S_6$ and indium rich $CuInP_2S_6$, where *c*-cut plates are employed as detecting ultrasonic transducers. Exciting 10 MHz lithium niobate transducers were attached to one end of a quartz buffer, while the plates under investigation were glued to other end. Fig. 24 shows the temperature dependences of ultrasonically detected piezoelectric signals in thin plates of these layered crystals. For better comparison the amplitudes of ultrasonically detected piezoelectric signals are shown in arbitrary units. It can be seen, that the phase transition temperatures strongly differ for these three crystals. The highest phase transition temperature was observed in nonstoichiometric $CuInP_2S_6$ crystals grown with slight addition of In i.e. $CuIn_{1+\delta}P_2S_6$ compound, where δ = 0.1 - 0.15. The phase transition temperature for an indium rich crystal is about 330 K. At this temperature also the critical ultrasonic attenuation and velocity anomalies were observed similar to those of pure $CuInP_2S$ crystals.

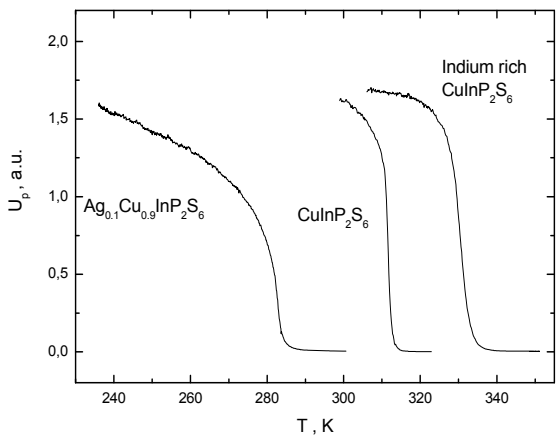

Fig. 25. The temperature dependences of ultrasonic signals detected by c-cut plates of $CuInP_2S_6$, $Ag_{0.1}Cu_{0.9}InP_2S_6$ and indium rich $CuInP_2S_6$ crystals.

Absence of piezoelectric signals above the phase transition shows that the paraelecric phases are centrosymetric. But at higher temperature piezoelectricity induced by an external *dc* field due to electrostriction was observed in $CuIn_{1+\delta}P_2S_6$ crystalline plates. In this case a large electromechanical coupling (K = 20 – 30 %) was observed in *dc* fields of order 30 kV/cm. It is necessary to note that the polarisation of the sample in a *dc* field in the field cooling regime strongly increases the piezosensitivity. In these $CuIn_{1+\delta}P_2S_6$ crystals at room temperature an

electromechanical coupling constant as high as > 50 % was obtained after appropriate poling, what is important for applications.

5. Conclusions

It was determined from dielectric permittivity measurements of layered $CuInP_2S_6$, $Ag_{0.1}Cu_{0.9}InP_2S_6$ and $CuIn_{1+\delta}P_2S_6$ crystals in a wide frequency range (20 Hz to 3 GHz) that:

1. A first-order phase transition of order – disorder type is observed in a $CuInP_2S_6$ crystal doped with Ag (10%) or In (10%) at the temperatures 330 K and 285 K respectively. The type of phase transition is the same as in pure $CuInP_2S_6$ crystal.
2. The frequency dependence of dielectric permittivity at low temperatures is similar to that of a dipole glass phase. Coexistence of ferroelectric and dipole glass phases or of nonergodic relaxor and dipole glass phase can be observed because of the disorder in the copper sublattice created by dopants.

Low frequency (20 Hz – 1 MHz) and temperature (25 K and 300 K) dielectric permittivity measurements of $CuCrP_2S_6$ and $CuIn_{0.1}Cr_{0.9}P_2S_6$ crystals have shown that:

1. The phase transition temperature shifts to lower temperatures doping $CuCrP_2S_6$ with 10 % of indium and the phase transition type is of first-order as in pure $CuCrP_2S_6$.

Layered $CuIn_xCr_{1-x}P_2S_6$ mixed crystals have been studied by measuring the complex dielectric permittivity along the polar axis at frequencies 10^{-5} Hz - 3 GHz and temperatures 25 K – 350 K Dielectric studies of mixed layered $CuIn_xCr_{1-x}P_2S_6$ crystals with competing ferroelectric and antiferroelectric interaction reveal the following results:

1. A dipole glass state is observed in the intermediate concentration range $0.4 \le x \le 0.5$ and ferroelectric or antiferroelectric phase transition disappear.
2. Long range ferroelectric order coexists with the glassy state at $0.7 \le x \le 1$.
3. A phase transition into the antiferroelectric phase occurs at $0 \le x \le 0.1$, but here no glass-like relaxation behavior is observed.
4. The distribution functions of relaxation times of the mixed crystals calculated from the experimental dielectric spectra at different temperatures have been fitted with the asymmetric double potential well model. We calculated the local polarization distributions and temperature dependence of macroscopic polarization and Edwards – Anderson order parameter, which shows a second-order phase transition.

Solid solutions of $CuCr_{1-x}In_xP_2S_6$ reveal interesting magnetic properties, which are strongly related to their layered crystal structure:

1. Diamagnetic dilution with In^{3+} of the antiferromagnetic $x = 0$ compound experiences a low percolation threshold, $x_p \approx 0.3$, toward 'superparamagnetic' disorder without tendencies of blocking or forming spin glass.
2. At low temperatures the 'superparamagnetic' clusters in $x > 0.3$ compounds reveal strong magnetic anisotropy, which suggests them to behave like 'molecular magnets'.

Crystals of the layered $CuInP_2S_6$ family have large piezoelectric sensitivity in their low temperature phases. They can be used as ultrasonic transducers for medical diagnostic applications, because the PT temperature for indium rich $CuInP_2S_6$ crystals can be elevated up to 330 K.

6. Acknowledgment

Thanks are due to P. Borisov, University of Liverpool, for help with the magnetic and magneto-electric measurements.

7. References

Banys, J., Klimm, C., Völkel, G., Bauch, H. & Klöpperpieper, A. (1994). Proton-glass behavior in a solid solution of (betaine phosphate)0.15 (betaine phosphite)0.85, *Phys. Rev. B.*, Vol. 50, p. 16751 – 16753

Banys, J., Lapinskas, S., Kajokas, A., Matulis, A., Klimm, C., Völkel, G. & Klöpperpieper, A. (2002). Dynamic dielectric susceptibility of the betaine phosphate (0.15) betaine phosphite (0.85) dipolar glass *Phys. Rev. B*, Vol. 66, pp. 144113

Banys, J., Macutkevic, J., Samulionis, V., Brilingas, A. & Vysochanskii, Yu. (2004). Dielectric and ultrasonic investigation in $CuInP_2S_6$ crystals, *Phase Transitions*, Vol. 77, pp. 345 - 358

Bertrand, D., Bensamka, F., Fert, A. R., Gélard, F., Redoulès, J. P. & Legrand, S. (1984). Phase diagram and high-temperature behaviour in dilute system $Fe_xMg_{1-x}Cl_2$, J. *Phys. C: Solid State Phys.*, Vol. 17, pp. 1725 – 1734

Bertrand, D., Fert, A. R., Schmidt, M. C., Bensamka, F. & Legrand, S. (1982). Observation of a spin glass-like behaviour in dilute system $Fe_{1-x}Mg_xCl_2$, *J. Phys. C: Solid State Phys.*, Vol. 15, pp. L883 – L888

Blundell, S. (2001). *Magnetism in Condensed Matter* (1st edition), Oxford Univ. Press, ISBN 019850591, Oxford

Blundell, S. (2007). Molecular magnets, *Contemp. Phys.*, Vol. 48, pp. 275 - 290

Bogani, L. & Wernsdörfer, W. (2008). Molecular spintronics using single-molecule magnets, *Nat. Mater.*, Vol. 7, pp. 179 – 186

Borisov, P., Hochstrat, A., Shvartsman, V.V. & Kleemann, W. (2007). Superconducting quantum interference device setup for magnetoelectric measurements, *Rev. Sci. Instrum.* Vol. 78, pp. 106105-1 -106105-3

Cajipe, V. B., Ravez, J., Maisonneuve, V,. Simon, A., Payen, C., Von Der Muhll, R. & Fischer, J. E. (1996). Copper ordering in lamellar $CuMP_2S_6$ (M = Cr, In): transition to an antiferroelectric or ferroelectric phase, *Ferroelectrics* 185, pp.135 - 138

Carlin, R.L. (1984). In: *Magneto-structural correlations in exchange-coupled systems*, *NATO ASI Series,* Willett, R.D., Gatteschi, D., Kahn, O. (Eds.),Vol. 140, pp. 127-155. Reidel, ISBN: 978-90-277-1876-1, Dordrecht

Colombet, P., Leblanc, A., Danot, M. & Rouxel, J. (1982). Structural aspects and magnetic properties of the lamellar compound $Cu_{0.50}Cr_{0.50}P_2S_6$, *J. Sol. State Chem.* Vol. 41, 174

Dziaugys, A., Banys, J., Macutkevic, J., Sobiestianskas, R., Vysochanskii, Yu. (2010). Dipolar glass phase in ferrielectrics: $CuInP_2S_6$ and $Ag_{0.1}Cu_{0.9}InP_2S_6$ crystals, *Phys. Stat. Sol. (a)*, Vol. 8, pp. 1960 - 1967

Dziaugys, A., Banys, J. & Vysochanskii, Y. (2011). Broadband dielectric investigations of indium rich $CuInP_2S_6$ layered crystals, *Z. Kristallogr.*, Vol. 226, pp.171-176.

Gatteschi, D., Sessoli, R. & Villain, J. (2006). *Molecular Nanomagnets,* Oxford University Press, ISBN 0198567537, Oxford

Goossens, D. J., Struder, A. J., Kennedy, S. J. & Hicks, T. J. (2000). The impact of magnetic dilution on magnetic order in $MnPS_3$, *Phys.: Condens. Matter*, Vol. 12, pp. 4233 - 4242

Grigas, J. (1996). *Microwave dielectric spectroscopy of ferroelectrics and related materials*, Gordon & Breach Science Publishers, Amsterdam

Kim, B., Kim, J. & Jang, H. (2000). Relaxation time distribution of deuterated dipole glass, *Ferroelectrics,* Vol. 240, pp. 249

Kittel, C. (1951), Theory of antiferroelectric crystals, *Phys. Rev.* Vol. 82, pp. 729-732

Kleemann, W., Bedanta, S., Borisov, P., Shvartsman, V. V., Miga, S., Dec, J., Tkach, A. & Vilarinho, P. M. (2009). Multiglass order and magnetoelectricity in Mn^{2+} doped incipient ferroelectrics, *Eur. Phys. J. B*, Vol. 71, pp. 407 - 410

Kleemann, W., Shvartsman, V. V., Borisov, P. & Kania, A. (2010). Coexistence of antiferromagnetic and spin cluster glass order in the magnetoelectric relaxor multiferroic $PbFe_{0.5}Nb_{0.5}O_3$, *Phys. Rev. Lett.*, Vol. 105, pp. 257202-1 -257202-4

Klingen, W., Eulenberger, G. & Hahn, H. (1973). Über die Kristallstrukturen von FeP_2Se_6 und $Fe_2P_2S_6$, *Z. Anorg. Allg. Chem.*, Vol. 401, pp. 97 - 112

Landau, L. & Khalatnikov, I., (1954). About anomalous sound attenuation near the phase transition of second-order (in Russian), *Sov. Phys. (Doklady)*, Vol. 96, pp. 459- 466

Macutkevic, J., Banys, J., Grigalaitis, R. & Vysochanskii, Y. (2008). Asymmetric phase diagram of mixed $CuInP_2(S_xSe_{1-x})_6$ crystals, *Phys.Rev. B*, Vol. 78, pp. 06410-1 - 06410-3

Maior, M. M., Motria, S. F., Gurzan, M. I., Pritz, I. P. & Vysochanskii, Yu. M. (2008). Dipole glassy state in layered mixed crystals of $Cu(In,Cr)P_2(S,Se)_6$ system, *Ferroelectrics*, Vol. 376, pp. 9 - 16

Maisonneuve, V., Evain, M., Payen, C., Cajipe, V. B. & Molinie, P. (1995). Room-temperature crystal structure of the layered phase $Cu^{I}In^{III}P_2S_6$, *J. Alloys Compd.*, Vol. 218, pp.157-164

Maisonneuve, V., Cajipe, V. B., Simon, A., Von Der Muhll, R. & Ravez, J. (1997). Ferrielectric ordering in lamellar $CuInP_2S_6$, *Phys. Rev. B*, Vol. 56, pp. 10860 - 10868

Mattsson, J., Kushauer, J., Bertrand, D., Ferré, J., Meyer, P., Pommier, J. & Kleemann, W. (1996). Phase diagram and mixed phase dynamics of the dilute Ising antiferromagnet $Fe_{1-x}Mg_xCl_2$, $0.7 \leq x < 1$. *J. Magn. Magn. Mat.*, Vol. 152, pp. 129 - 138

Mulders, A. M., Klaasse, J. C. P. , Goossens, D. J., Chadwick, J. & Hicks, T. J. (2002). High-field magnetization in the diluted quasi-two-dimensional Heisenberg antiferromagnet $Mn_{1-x}Zn_xPS_3$, *J. Phys.: Condens. Matter*, Vol. 14, pp. 8697

Mydosh, J. A. (1993). Spin glasses - an experimental introduction (first edition), Taylor & Francis, ISBN 0748400389, Oxford

Néel, L. (1961). Superparamagnétisme des grains très fins antiferromagnétiques, *Acad. Sci. Paris, C. R.*, Vol. 252, 4075 – 4080

Pelster, R., Kruse, T., Krauthäuser, H.G., Nimtz, G. & Pissis P. (1998). Analysis of 2-Dimensional Energy and Relaxation Time Distributions from Temperature-Dependent Broadband Dielectric Spectroscopy, *Phys. Rev. B*, Vol. 57, pp. 8763 - 8766

Ressouche, E., Loire, M., Simonet, V., Ballou, R., Stunault, A. & Wildes, A. (2010). Magnetoelectric $MnPS_3$ as a candidate for ferrotoroidicity, *Phys. Rev. B,* Vol. 82, pp. 100408(R)-1 - 100408(R)-4

Samulionis, V., Banys, J. & Vysochanskii, Y. (2009a). Piezoelectric and elastic properties of layered materials of $Cu(In,Cr)P_2(S,Se)_6$ system, *J. Electroceram.*, Vol. 22, pp. 192-197

Samulionis, V., Banys, J. & Vysochanskii, Y. (2009b). Linear and nonlinear elastic properties of $CuInP_2S_6$ layered crystals under polarization reversal, *Ferroelectrics*, Vol. 379, pp. 293-300

Samulionis, V., Banys, J. & Vysochanskii, Y. (2007). Piezoelectric and Ultrasonic Studies of Mixed $CuInP_2(S_XSe_{1-X})_6$ Layered Crystals *Ferroelectrics*, Vol. 351, pp. 88-95

Schafer, H., Sternin, H. E., Stannarius, R., Arndt, M. & Kremer, F. (1996), Novel Approach to the Analysis of Broadband Dielectric Spectra, *Phys. Rev. Lett.*, Vol. 76, pp. 2177-2180.

Shvartsman, V. V., Bedanta, S., Borisov, P., Kleemann, W., Tkach, A. & Vilarinho, P. M. (2008). (Sr,Mn)TiO_3 - a magnetoelectric multiglass, *Phys. Rev. Lett.*, Vol. 101, pp. 165704-1 - 165704-4

Simon, A., Ravez, J., Maisonneuve, V., Payen, C. & Cajipe, V. B. (1994). Paraelectric-ferroelectric transition in the lamellar thiophosphate $CuInP_2S_6$. *Chem. Mater.*, Vol. 6, pp. 1575 - 1580

Strukov, B. A. & Levanyuk, A. (1995). *Ferroelectric phenomena in crystals* (in Russian), Nauka-Fizmatlit, Moscow, p.117.

Valevicius, V., Samulionis, V. & Banys, J. (1994). Ultrasonic dispersion in the phase transition region of ferroelectric materials, *J. Alloys Compd.*, Vol. 211/212, pp. 369-373

Valevicius, V., Samulionis, V., Banys, J., Grigas, J. & Yagi, T. (1994). Ultrasonic study of ferroelectric phase transition in DDSP, *Ferroelectrics*, Vol. 156, pp. 365-370

Vysochanskii, Yu. M., Stepanovich, V. A., Molnar, A. A., Cajipe, V. B. & Bourdon, X. (1998). Raman spectroscopy study of the ferrielectric-paraelectric transition in layered $CuInP_2S_6$, *Phys. Rev. B.*, Vol. 58, pp. 9119 - 9124

10

Non-Linear Dielectric Response of Ferroelectrics, Relaxors and Dipolar Glasses

Seweryn Miga[1], Jan Dec[1] and Wolfgang Kleemann[2]
[1]*Institute of Materials Science, University of Silesia, Katowice*
[2]*Angewandte Physik, Universität Duisburg-Essen, Duisburg*
[1]*Poland*
[2]*Germany*

1. Introduction

The dielectric response of dielectrics with respect to temperature, pressure, frequency and amplitude of the probing electric field is an essential issue in dielectric physics (Jonscher, 1983). This concerns both normal dielectrics and those specified as ferro- or antiferroelectrics (Lines & Glass, 1977). This basic phenomenon of dielectric materials has been extensively studied in the literature both experimentally and theoretically, however, mainly restricting to the linear dielectric response where a linear relationship between polarization, P, and external electric field, E,

$$P = \varepsilon_0 \chi_1 E, \tag{1}$$

is fulfilled. Here ε_0 and χ_1 stand for the electric permittivity of the free space (dielectric constant) and the linear electric susceptibility of a given dielectric material, respectively. In the framework of this approach the analysis of the dielectric relaxation is possible via the Debye model (including the Cole-Cole equation and related formulae in case of multidispersive behavior) and the relaxation rate can often be described by an Arrhenius relation (Jonscher, 1983; Lines & Glass, 1977; Debye, 1929; von Hippel, 1954; Böttcher, 1973; Kremer & Schönhals, 2003) or by an activated dynamic scaling law (Fisher, 1986; Kleemann et al., 2002) which in the particular case of the exponent $\theta\nu = 1$ converts into the well known Vogel-Fulcher-Tammann relation (Jonscher, 1983; Kremer & Schönhals, 2003). More complex distribution functions of relaxation-times are used as well (Jonscher, 1983; Böttcher, 1973; Kremer & Schönhals, 2003).
At higher electric fields *Eq.* (1) becomes violated and the relation between polarization and electric field is better represented by a power series of E,

$$P = \varepsilon_0 \left(\chi_1 E + \chi_2 E^2 + \chi_3 E^3 + \chi_4 E^4 + \chi_5 E^5 + ...\right), \tag{2}$$

which contains higher order terms with respect to the external electric field, where χ_i with $i > 1$ are the non-linear susceptibilities: second-order, third-order and so on (Böttcher, 1973). These non-linear components are referred to as hypersusceptibilities and the non-linear contribution to the polarization response is designated as the hyperpolarization (Jonscher,

1983). While the higher-order susceptibilities contain a wealth of important information (Wei & Yao, 2006a; Wei & Yao, 2006b), the hyperpolarization has nevertheless been less studied due to obstacles like (i) the difficulty of the respective dielectric measurements, because the nonlinear signal is usually some orders of magnitude smaller than the linear response, and (ii) lack of an appropriate theory to deal with dielectric spectra as a function of the electric field (Chen & Zhi, 2004).

In order to overcome the technological challenge we have constructed a fully automatized *ac* susceptometer for simultaneous measurements of the phase resolved complex linear and complex non-linear *ac* susceptibilities of lossy and dispersive dielectric materials (Miga, Dec & Kleemann, 2007). It allows measurements over a wide range of experimental variables, such as *ac* amplitudes up to 40 V, frequencies from 10^{-2} to 10^{3} Hz, and temperatures from 100 K to 600 K utilizing only current/voltage and analogue/digital converters and a computer. In contrast to the commonly used analysis of the charge accumulated on a standard capacitor in series with the sample our method is based on the analysis of the current flowing directly through the sample. Absence of any capacitive voltage dividers in the measurement circuit eliminates uncontrolled phase shifts. That is why the instrument provides high quality nonlinear susceptibility data and in particular appears as a very convenient tool for discrimination between continuous and discontinuous phase transitions when determining the sign of the real part of the third order dielectric susceptibility.

We have applied this new instrument to various basic ferroelectric scenarios, such as the classic first- and second-order ferroelectric transitions of barium titanate ($BaTiO_3$) (Miga & Dec, 2008), triglycine sulphate (TGS) (Miga & Dec, 2008) and lead germanate ($Pb_5Ge_3O_{11}$) (Miga & Dec, 2008), the double anomalous second-order transitions of Rochelle salt (Miga et al., 2010a), the smeared transition of the classic relaxor ferroelectrics lead magno-niobate ($PbMg_{1/3}Nb_{2/3}O_3$, PMN) (Dec et al., 2008) and strontium-barium niobate ($Sr_{0.61}Ba_{0.39}Nb_2O_6$, SBN61) (Miga & Dec, 2008), the dipolar glassy and ferroelectric transitions of Li^+-doped potassium tantalate ($K_{1-x}Li_xTaO_3$, KLT) with x = 0.005, 0.011 and 0.063 (Dec et al., 2010; Miga et al., 2010b).

2. Theoretical background of nonlinear dielectric response

Dielectric properties of materials are usually investigated via linear dielectric response. In this case a linear relationship, *Eq.* (1), between polarization, P, and external electric field, E, is fulfilled. At higher field intensities, the polarization may be a non-linear function of the electric field strength. For not too high electric field strength, one can present the polarization as the power series expansion in the variable E, *Eq.* (2). For symmetry reasons the second-order dielectric susceptibility is nonzero only for macroscopically noncentrosymmetric systems.

Let us consider the Landau-Ginzburg-Devonshire (LGD) theory of ferroelectric phase transitions (PT) (Ginzburg, 1945; Devonshire, 1949). According to this theory the free energy density G of a ferroelectric material within its paraelectric phase is represented as a power series expansion with respect to the polarization P,

$$G(E,P,T) = -EP + G_0 + \frac{1}{2}A(T-T_0)P^2 + \frac{1}{4}BP^4 + \frac{1}{6}CP^6 + \cdots \tag{3}$$

where G_0 stands for the free energy at $P = 0$, A and T_0 are constants. B and C are usually smooth functions of temperature (Fujimoto, 2003). In the ferroelectric phase the polarization P, yields the spontaneous one, P_s, as an order parameter. The sign of B determines the kind of the PT. For positive B a continuous (second-order) PT occurs. On the other hand, for negative B a discontinuous (first-order) PT appears. Let us first consider a continuous PT to occur at $T_0 = T_c$. In this case one can drop the last term in *Eq.* (3) without loss of generality. Thermodynamic equilibrium requires fulfilment of the condition

$$\frac{\partial G}{\partial P} = 0 = -E + A(T - T_c)P + BP^3 . \tag{4}$$

This relationship between E and P denotes the electric equation of state. After successive differentiation of this equation with respect to P one obtains the following susceptibilities (Ikeda et al., 1987):

$$\chi_1 = \frac{1}{\varepsilon_0[A(T - T_c) + 3BP^2]} \tag{5}$$

$$\chi_2 = -3\varepsilon_0^2 BP\chi_1^3 \tag{6}$$

$$\chi_3 = -(1 - 18\varepsilon_0 BP^2\chi_1)\varepsilon_0^3 B\chi_1^4 . \tag{7}$$

The second-order susceptibility is proportional to the polarization P, therefore it changes sign when the polarization changes direction. Additionally χ_2 vanishes when the polarization of the sample vanishes. That is why χ_2 is a sensitive probe of the net polarization, but it is unsuitable for determination of the PT order. In contrast to χ_2 the odd order susceptibilities χ_1 and χ_3 depend on the square of the polarization, which makes them insensitive to the orientation of the polarization. Moreover, χ_1 and χ_3 do not vanish, even if the polarization is equal to zero. For classic ferroelectrics on heating the spontaneous polarization P_s vanishes at the PT point and is zero within the paraelectric phase, where *Eq.* (7) simplifies to

$$\chi_3 = -\varepsilon_0^3 B\chi_1^4 . \tag{8}$$

Due to positive B, χ_3 is negative above a continuous PT point. Within the ferroelectric phase P=P_s and $P_S^2 = (A / B)(T_c - T)$, hence,

$$\chi_3 = 8\varepsilon_0^3 B\chi_1^4 . \tag{9}$$

Within the ferroelectric phase χ_3 has a positive sign. Thus the LDG theory predicts a change of sign of χ_3 at a continuous PT. The scaling theory (Stanley, 1971) predicts that B scales as B=$B_0|\tau|^{\gamma-2\beta}$, where $\tau = (T - T_c) / T_c$. $\gamma$and $\beta$are critical exponents of the linear susceptibility and of the order parameter, respectively. For the Landau universality class, where γ- 2β= 0 (*i. e.* γ= 1, β= ½) one expects a temperature independent value of B within the paraelectric phase.

A similar calculation for a discontinuous PTs, where $B < 0$ and $C > 0$, yields $\chi_3 > 0$ at all temperatures, in particular also above PT (Ikeda et al., 1987). Fortunately from an

experimental point of view χ_3 is given by this same equation (8) within paraelectric phase independent of the ferroelectric PT order. The sign of χ_3 is a sensitive probe for discrimination between continuous and discontinuous ferroelectric PTs.

In all known ferroelectrics the paraelectric phase is located above the stability range of the ferroelectric one. However, sodium potassium tartrate tetrahydrate (Rochelle salt, RS) (Valasek, 1920, 1921) apart from a classic high temperature paraelectric phase has an additional, unusual one located below the ferroelectric phase. Both PTs, between the paraelectric phases and the ferroelectric one have continuous character. In order to predict the sign of χ_3 within the low-temperature paraelectric phase one can refer to the theory of Mitsui (Mitsui, 1958). Within this theory the electric equation of state for RS is similar to *Eq.* (4) with a positive coefficient of the cubic term, P^3. Therefore a negative sign of χ_3 is expected within low-temperature paraelectric phase (Miga et al., 2010a).

Another class of dielectrics are relaxor ferroelectrics. They are usually considered as structurally disordered polar materials, which are characterized by the occurrence of polar nanoregions (PNRs) of variant size below the so-called *Burns* temperature, T_d (Burns & Dacol, 1983) far above the ferroelectric Curie temperature, T_c. In contrast to conventional ferroelectrics, relaxors do not exhibit any spontaneous macroscopic symmetry breaking. In addition they are characterized by a large, broad and frequency-dependent peak in the temperature dependence of dielectric susceptibility. According to the spherical random-bond-random-field (SRBRF) model (Pirc & Blinc, 1999) the dipole moments of individual nanopolar clusters interact via a spin-glass-type random exchange coupling, and are subject to quenched random local electric fields. The model Hamiltonian of such a system is formally written as

$$H = -\frac{1}{2}\sum_{ij} J_{ij}\vec{S}_i \cdot \vec{S}_j - \sum_i \vec{h}_i \cdot \vec{S}_i - g\vec{E} \cdot \sum_i \vec{S}_i \,, \tag{10}$$

where J_{ij} are glass-like random intercluster couplings or bonds, $\vec{h}_i$ and $\vec{E}$ random local and uniform external electric fields, respectively. In the dynamic approximation it is assumed that PNRs reorient by means of stochastic flips described by a relaxation time τ. This model yields negative χ_3 with two extremes observed at the freezing temperature, T_f, and at the peak temperature of χ_1, T_m.

The measured values of χ_1 and χ_3 can be used for calculating the so-called scaled non-linear susceptibility, a_3, which is given by (Pirc & Blinc, 1999)

$$a_3 = -\frac{1}{\varepsilon_0^3}\frac{\chi_3}{\chi_1^4} \,. \tag{11}$$

Within the paraelectric phase of classic ferroelectrics a_3 is equal to the nonlinearity coefficient B, *cf. Eq*s. (8) and (11). For ferroelectics displaying a continuous PT, $a_3 = -8B$ within ferroelectric phase. The SRBRF model yields negative χ_3 and positive a_3 with two extremes observed at the freezing temperature, T_f, and at the peak temperature of χ_1, T_m. It should be noticed that systems like dipolar glasses a_3 are also expected to exhibit a critical singularity at T_f, where $\chi_3 \propto (T - T_f)^{-\gamma}$ with the mean field exponent $\gamma = 1$ (Pirc et al., 1994).

A schematic comparison of predictions of the above theories is presented in Fig. 1.

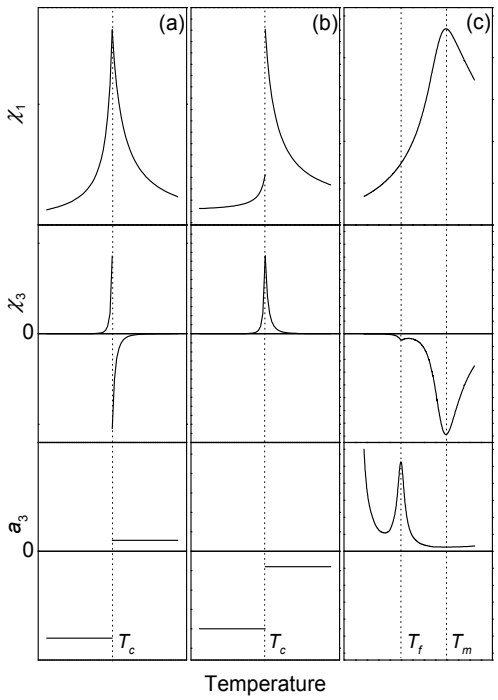

Fig. 1. Schematic presentation of linear and nonlinear responses of classic ferroelectrics with (a) continuous PTs, (b) discontinuous PTs, and (c) relaxor ferroelectrics (see text).

3. Methods of measurement of nonlinear dielectric response

Nonlinear dielectric response can be measured using two different kinds of experimental methods. The first one is based on the investigation of the *ac* linear dielectric susceptibility as a function of a *dc* bias field. A schematic presentation of this method is shown in Fig. 2a. One applies to the sample a weak probing *ac* electric field with fixed amplitude (that warrants a linear response) and a superimposed variable *dc* bias field, E_B. The bias field amplitude may reach values up to $5.5 \cdot 10^7$ Vm^{-1} (Leont'ev et al., 2003). In barium titanate a strong *dc* field induces the PT between paraelectric and ferroelectric phases (Wang et al., 2006). By changing the value of the *dc* electric field the local slope of the polarization curve is probed in many points. For such a kind of experiment one can use commercially available LRC meters or impedance analyzers, *e.g.* Agilent E4980A or Solartron 1260. The electric field dependence of the linear susceptibility of ferroelectrics displaying continuous PT fulfils the following relations (Mierzwa et al., 1998):

$$\frac{1}{\chi^3(E)} + \frac{3}{\chi^2(E)\chi(0)} - \frac{4}{\chi^3(0)} = 27\varepsilon_0^3 BE^2 \tag{12}$$

for the paraelectric phase and

$$\frac{1}{\chi^3(E)} - \frac{3}{2\chi^2(E)\chi(0)} + \frac{1}{2\chi^3(0)} = 27\varepsilon_0^3 BE^2 \tag{13}$$

for the ferroelectric one. $\chi(E)$ and $\chi(0)$ are the susceptibilities for bias, E, and zero electric field, respectively. By use of *Eq*s. (12) and (13) one can calculate the nonlinearity coefficient B. Its knowledge allows us to calculate the third-order nonlinear susceptibility χ_3. Unfortunately, the above described method has at least one restriction when investigating the nonlinear dielectric response. Namely, during so-called field heating/cooling runs, unwanted poling and remnant polarization of the investigated sample can evolve under a high bias field.

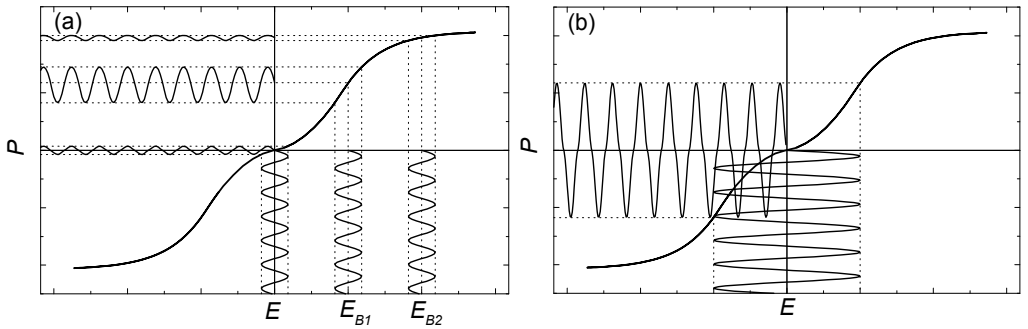

Fig. 2. Presentation of methods of measurement of nonlinear dielectric response using (a) a weak probing *ac* electric field with fixed amplitude and a superimposed variable *dc* bias field, and (b) an enhanced *ac* field. The effects are exaggerated for visualisation.

The second kind of method is free from this restriction. A schematic presentation of this method is shown in Fig. 2b. During the experiment the sample is exposed to an *ac* probing field with sufficiently large amplitude. Consequently, under this condition the temperature dependences of the linear and nonlinear susceptibilities are determined under zero *dc* field in heating and cooling runs. That is why the nonlinear susceptibility detected this way can be referred to as a dynamic nonlinear susceptibility related to *ac* dielectric nonlinearity. Usually the amplitude of this field is much smaller than the bias field strength used in the above described experiment. As a result of the nonlinear $P(E)$ dependence, the output no longer remains harmonic. The distorted signal may be subjected to Fourier analysis revealing all harmonic components in the polarization response. This is the main idea of our nonlinear *ac* susceptometer (Miga et al., 2007). Using harmonics of displacement current density j_i one can calculate the linear and nonlinear dielectric susceptibilities χ_i as follows:

$$
\begin{aligned}
\chi_1 &= \frac{1}{\varepsilon_0\omega} E_0^{-1} \left(j_1 + j_3 + j_5 + j_7\right) - 1, \\
\chi_2 &= \frac{1}{\varepsilon_0\omega} E_0^{-2} \left(j_2 + 2j_4 - 3j_6\right), \\
\chi_3 &= \frac{1}{\varepsilon_0\omega} E_0^{-3} \left(-\frac{4}{3} j_3 - 4j_5 - 8j_7\right), \\
\chi_4 &= \frac{1}{\varepsilon_0\omega} E_0^{-4} \left(-2j_4 + 8j_6\right), \\
\chi_5 &= \frac{1}{\varepsilon_0\omega} E_0^{-5} \left(\frac{16}{5} j_5 + 16j_7\right)
\end{aligned}
\tag{14}
$$

where ω and E_0 are the angular frequency and the amplitude of the applied electric field respectively. In *Eq*. 14 the terms up to seventh order are involved, hence, susceptibilities up to the fifth order can be regarded as reliable even for strongly nonlinear materials. Neglecting harmonics higher than the order of a considered susceptibility may lead to artificial effects. The next important point is the simultaneous measurement of all displacement current components, which considerably improves the accuracy of the measured susceptibilities (Bobnar et al., 2000). In case that the phase shifts of the displacement current harmonics are known it is possible to calculate the real, χ_i', and imaginary, χ_i'', parts of all susceptibilities. This is impossible, when measurements are done with a *dc* bias electric field. It should be noted that up to now commercial instruments for the dynamic measurement of complex nonlinear dielectric susceptibilities are unavailable.

4. Experimental results

4.1 Ferroelectrics displaying continuous PTs

Triglycine sulphate, $(NH_2CH_2COOH)_3{\cdot}H_2SO_4$ (TGS) is a model ferroelectric displaying a continuous PT. Sodium potassium tartrate tetrahydrate (Rochelle salt, RS), $NaKC_4H_4O_6{\cdot}4H_2O$, and lead germanate, $Pb_5Ge_3O_{11}$ (LGO) exhibit continuous PTs, as well. Despite the quite different structures of the crystals and different mechanisms of their PTs, a negative sign of the real part of the third-order nonlinear susceptibility is expected in their paraelectric phases. Fig. 3 shows the temperature dependences of the real parts of the linear, the third order nonlinear dielectric susceptibilities, and the scaled susceptibility, a_3. The linear susceptibility of a TGS crystal (Fig. 3a) obeys a Curie-Weiss law within the paraelectric phase very well with a critical exponent γ =1.000±0.006. According to predictions of the phenomenological theory of ferroelectric PT, χ_3' changes its sign at the PT point (Fig. 3b).

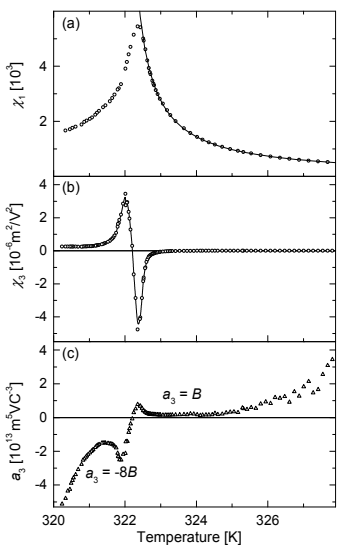

Fig. 3. Temperature dependences of the real parts of the linear (a) and third order non-linear (b) susceptibilities and a_3 coefficient (c) of TGS. The amplitude of the probing *ac* electric field was 5kVm^{-1}.

While below T_c the third-order susceptibility has positive values, it is negative above T_c. As was mentioned earlier such change in the sign of χ_3' is one of the primary features of the continuous ferroelectric PT. The scaled non-linear susceptibility has been evaluated using *Eq.* (11). The measured values of χ_1' and χ_3' were used for calculations. The temperature dependence of a_3 of TGS crystal is shown in Fig. 3c. Within the paraelectric phase a_3 is equal to B and has a positive value. This is an attribute of the continuous PT. Moreover, a_3 is practically temperature independent within the temperature range of $T_c + 0.2\ \mathrm{K} < T < T_c + 2\ \mathrm{K}$ above the PT point. This behaviour is consistent with predictions of the scaling theory and confirms that TGS belongs to the Landau universality class. Weak temperature dependence of a_3 and $1/|T\text{-}T_c|$ dependence of χ_1' leads to a $1/|T\text{-}T_c|^4$ anomaly of χ_3' (see *Eq.* 11). Therefore the temperature dependence of χ_3' is much sharper than that of χ_1'. Consequently, χ_3' rapidly vanishes in the surrounding of the PT. An increase of a_3 as observed within the paraelectric phase close to T_c is probably due to crystal defects. A similar effect was reported for a γ-ray damaged TGS crystal (Cach, 1988). Then within the ferroelectric phase a_3 changes slowly due to the contribution of the domain walls to the resultant dielectric response. In the ferroelectric state the measured values of the linear and non-linear susceptibilities, which were used for calculation, involved the responses not only from the ''pure'' ferroelectric system but also from the domain walls, which were forced to move under the probing electric field.

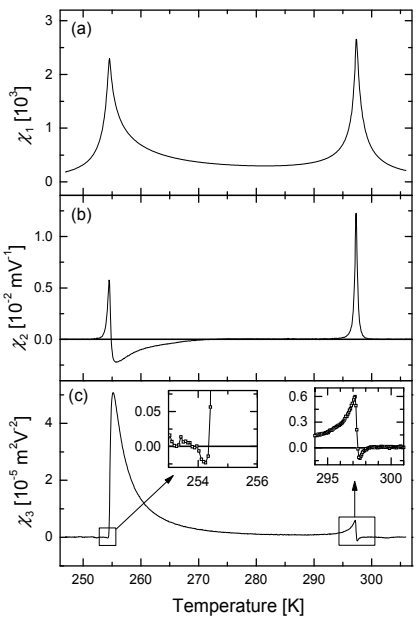

Fig. 4. Temperature dependences of the real parts of the linear (a), the second (b) and the third (c) order nonlinear susceptibilities of Rochelle salt. The amplitude of the probing *ac* electric field was 500 Vm^{-1}.

Fig. 4 shows the temperature dependences of the linear, the second, and the third-order nonlinear susceptibilities of Rochelle salt. The temperature dependences of χ_1' and χ_3' are, close to the high temperature ferroelectric-paraelectric PT (≈ 297.4 K), qualitatively similar to

those of the TGS crystal. As was mentioned earlier, RS displays an additional low temperature PT. This transition between the ferroelectric and the low temperature paraelectric phase appears at about 254.5 K. At this PT χ_3' changes its sign as compared to the high temperature PT (Fig. 4c). As a result of the inverse order of phases, χ_3' is negative below and positive above the low temperature PT. In this way the third-order nonlinear susceptibility is negative in both paraelectric phases close to PT points. Fig. 4b shows the temperature dependence of the second-order nonlinear susceptibility. The sign of this susceptibility depends on the net polarization orientation. Therefore it can be changed by polarization of the sample in the opposite direction. The simplest way to change the sign of χ_2' is a change of the wires connecting the sample to the measuring setup. So, in contrast to sign of the χ_3', the sign of the second order nonlinear susceptibility is not very important. In the case of χ_2' most important is its nonzero value and the observed change of sign of this susceptibility at 273 K. This hints at a modification of the domain structure within the ferroelectric phase. The next change of sign at the low temperature PT point is originating from different sources of the net polarization above and below this point. Above 254.5 K this polarization comes from the uncompensated ferroelectric domain structure, whereas within the low-temperature paraelectric phase it originates merely from charges screening the spontaneous polarization within the ferroelectric phase.

Lead germanate (LGO) displays all peculiarities of a continuous ferroelectric PT (see Fig. 5 a, c, e) (Miga et al., 2006). However, a small amount of barium dopant changes this scenario (Miga et al., 2008). Ba^{2+} ions replacing the host Pb^{2+} influence the dielectric properties. 2% of barium dopant causes a decrease of the linear susceptibility, broadening of the temperature dependence of χ_1', and a decrease of the PT temperature. Despite all these changes the temperature dependences of χ_1' for pure and barium doped LGO are qualitatively similar. A completely different situation occurs, when one inspects the nonlinear dielectric response. Small amounts of barium dopants radically change the temperature dependence of the third-order nonlinear susceptibility (Fig.5 b). Similarly to linear one the anomaly of the third-order nonlinear susceptibility shifts towards lower temperature and decreases. The most important difference is the lacking change of sign of χ_3'. In contrast to pure LGO for barium doped LGO the third-order nonlinear susceptibility is positive in the whole temperature range. Therefore one of the main signatures of classic continuous ferroelectric PTs is absent. Due to the positive value of χ_3' the scaled nonlinear susceptibility is negative in the whole temperature range (Fig. 5d). No change of a_3 is observed. This example shows the high sensitivity of the nonlinear dielectric response to the character of the PT. In the discussed case a change of character of the PT is due to the presence of barium induced polar nanoregions (PNRs). The occurrence of PNRs results in weak relaxor properties of barium doped LGO.

4.2 Ferroelectrics displaying discontinuous PT

Barium titanate, $BaTiO_3$ (BT), is a model ferroelectric displaying three discontinuous ferroelectric PTs (von Hippel, 1950). Two of them appear – at rising temperatures - between rhombohedral, orthorhombic and tetragonal ferroelectric phases at about 200 K and 280 K respectively. The final discontinuous PT appears between the ferroelectric tetragonal and the cubic paraelectric phase at about 400 K. Fig. 6 shows the temperature dependences of the real parts of the linear (a) and third-order nonlinear (b) susceptibilities, and the a_3 coefficient (c) of a BT crystal in the vicinity of the ferroelectric-paraelectric PT. The amplitude of a probing *ac* electric field was equal to 7.5 kVm^{-1}.

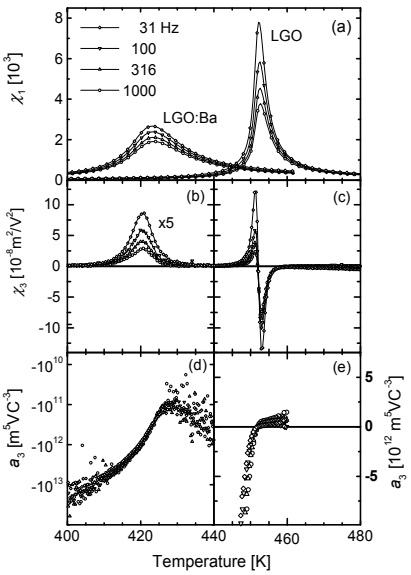

Fig. 5. Temperature dependences of the real part of the linear dielectric susceptibility (a) for LGO:Ba 2% and LGO, real part of third-order nonlinear dielectric susceptibility for (b) LGO: Ba 2% and (c) LGO, and scaled nonlinear susceptibility a_3 for (d) LGO:Ba 2%, and (e) LGO crystals. The amplitude of the probing *ac* electric field was 15 kVm^{-1}.

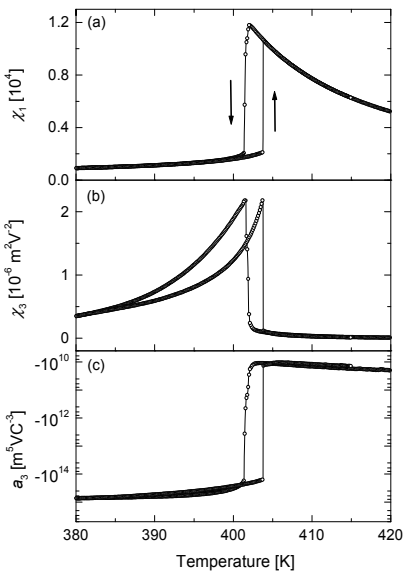

Fig. 6. Temperature dependences of the real parts of the linear (a) and third order non-linear (b) susceptibilities and of the a_3 coefficient (c) of a $BaTiO_3$ crystal. The amplitude of the probing *ac* electric field was 7.5kVm^{-1}.

Temperature hysteresis is one of the typical features of discontinuous PT. Therefore for viewing this phenomenon Fig. 6 presents results for cooling and heating runs. The third-

order nonlinear susceptibility is positive, both within the ferroelectric and the paraelectric phases (Fig. 6b). Just below T_c a rapid decrease of the third-order dielectric susceptibility is observed. For that reason, the value of χ_3' is much smaller within the paraelectric phase than in the ferroelectric one, yet it is still positive. The positive sign of χ_3' as detected in BT is consistent with predictions of the phenomenological theory of discontinuous ferroelectric PTs. Unlike the scaled nonlinear susceptibilities of crystals displaying a continuous PT, a_3 of $BaTiO_3$ is negative in the whole investigated temperature range (Fig. 6c). However, similarly to TGS (Fig. 3) or RS (Fig. 4) a jump-like change of a_3 occurs at the PT. Within the paraelectric phase a_3 is equal to B (see section 4.1) and displays weak temperature dependence. Wang *et al.* (Wang et al., 2007) proposed incorporation of higher order terms (up to the eighth power) in the Landau potential for the temperature independence of the experimentally obtained B coefficient. This proposition was given for analyzing the data collected with a bias field up to 1500 kV/m. Fig. 6 shows data collected for a two hundred times smaller electric field, for which terms at such high order are not important. They cannot explain the temperature dependence of the nonlinearity coefficient B. Hence, although the nonlinear properties of $BaTiO_3$ have been investigated already for six decades, the question of the temperature dependence of the nonlinearity parameter B is still open.

4.3 Relaxor ferroelectrics

The classic relaxor ferroelectric lead magno-niobate ($PbMg_{1/3}Nb_{2/3}O_3$, PMN) (Smolenskii et al., 1960) displays an average cubic structure in the whole temperature range (Bonneau et al., 1991). No spontaneous macroscopic symmetry breaking is observed in this relaxor. On the other hand and in contrast to PMN, the relaxor strontium-barium niobate $Sr_{0.61}Ba_{0.39}Nb_2O_6$ (SBN61) spontaneously undergoes a structural phase transition. On cooling the vanishing of a mirror plane leads to a lowering of the tetragonal symmetry from 4/*mmm* to 4*mm* at a temperature of about 348 K (Oliver et al., 1988).

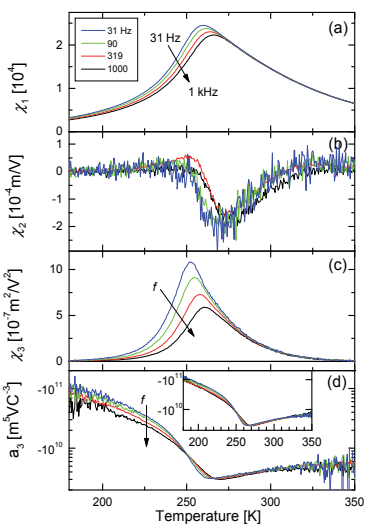

Fig. 7. Temperature dependences of χ_1' (a), χ_2' (b), χ_3' (c) and a_3 (d) of a PMN crystal measured at f = 31, 100, 319, and 1000 Hz. A probing *ac* electric field with an amplitude of 12 kV/m was applied along the [100] direction.

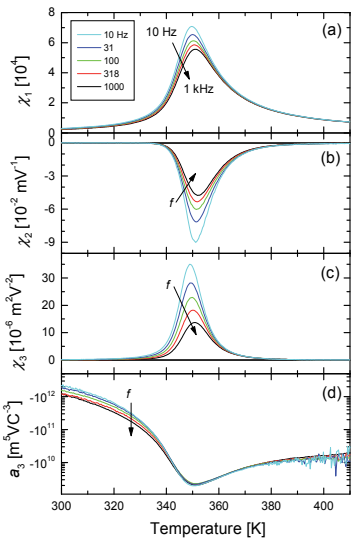

Fig. 8. Temperature dependences of χ_1' (a), χ_2' (b), χ_3' (c) and a_3 (d) of a SBN61 crystal measured at f = 10, 31, 100, 318, and 1000 Hz. A probing *ac* electric field with an amplitude of 7.5 kV/m was applied along the [001] direction.

Fig. 7 presents the temperature dependences of the real parts of the linear, χ_1' (a), second-order, χ_2' (b), and third-order, χ_3' (c), dielectric susceptibilities and of the scaled nonlinear susceptibility a_3 (d) of the PMN single crystal recorded along [100] direction (Dec et al., 2008). The linear susceptibility displays features of a relaxor i.e. a large, broad and frequency-dependent peak in the temperature dependence. Nonzero χ_2' as presented in Fig. 7b is an indicator of net polarization of the crystal. The presence of this polarization was independently confirmed by measurements of thermo-stimulated pyroelectric current of an unpoled sample. Integration of this current indicates an approximate value of the average polarization as low as 3×10^{-5} C/m^2. This polarization is much smaller than the spontaneous polarization of ferroelectrics, but is well detectable. The observed pyroelectric response and nonzero χ_2' hints at an incomplete averaging to zero of the total polarization of the PNR subsystem. Fig. 7c shows the temperature dependence of the third-order nonlinear susceptibility. In contrast to the predictions of the SRBRF model, χ_3' is positive in the whole temperature range. The positive sign of χ_3' may result from a term $18\varepsilon_0 BP^2\chi_1$ exceeding unity in *Eq*. 7. Positive sign of χ_3' results in a negative sign of a_3. Consequently the sign of a_3 differs from that predicted by the SRBRF model. Having in mind that corrections due to the fifth harmonic contribution produce large noise at temperatures below 210 K and above 310 K (Fig. 7d, main panel), less noisy a_3 data calculated only from first and third harmonics are presented in the inset to Fig. 7d. Since both χ_1' and χ_3' do not display any anomalies in the vicinity of the freezing temperature T_f ≈ 220 K, also a_3 does not exhibit any maximum in contrast to SRBRF model predictions. It continues to increase monotonically by almost two orders of magnitude when decreasing the temperature from 260 to 180 K. This result is independent of the number of harmonics used for experimental data analysis. It is worth stressing that despite the remarkable

dispersion of χ_1' and χ_3', the scaled susceptibility a_3 does not display any sizable frequency dependence, even around the temperatures of the susceptibility peaks. It may, hence, be considered as a static quantity (Glazounov & Tagantsev, 2000). According to our result the dispersion of a_3 is even weaker than reported previously (Glazounov & Tagantsev, 2000).

Fig. 8 shows results of measurements of the linear and nonlinear dielectric response of SBN61 crystal (Miga & Dec, 2008). The probing electric *ac* field was applied along [001], which is the direction of the polar axis below T_c. The peak temperatures of the linear susceptibility (Fig. 8a) are a few degrees above the temperature of the structural phase transition. Fig. 8b presents the temperature dependence of the second-order susceptibility. Similarly to results obtained on PMN this susceptibility is non-vanishing. However, the values of χ_2' of SBN61 are almost two orders of magnitude larger than those measured on PMN. Therefore χ_2' is detectable even forty degrees above T_c. Analysis of the thermo-stimulated current indicates a net polarization of a nominally unpoled SBN61 crystal equal to 5×10^{-2} C/m^2. The higher value of this polarization (in comparison with PMN) results in higher values of χ_2'. Fig. 8c shows the temperature dependence of χ_3'. This susceptibility is positive within both the ferroelectric and the paraelectric phase. Again, the sign of χ_3' disagrees with predictions of the SRBRF model. As was discussed above, the positive sign of χ_3' presumably originates from the presence of net polarization (detected by χ_2', see Fig. 8b). The disagreeing sign of χ_3' leads to a disagreement of the sign of a_3 as well (Fig. 8d). The scaled nonlinear susceptibility shows an anomaly related to the phase transition, but it does not exhibit any additional peak as predicted by the SRBRF model.

The results obtained for both relaxor ferroelectrics are qualitatively similar. Therefore, they are independent of the presence or absence of a structural phase transition and macroscopic symmetry breaking. As discussed in Section 2 the dielectric properties of relaxors are mainly determined by PNRs, which were detected in both of the above relaxors. Unfortunately, the early version of the SRBRF model (Pirc et al., 1994) predicts a negative sign of the third-order nonlinear dielectric susceptibility, which is not confirmed in experiments. Consequently the sign of the scaled nonlinear susceptibility a_3 is incorrect as well. Very probably this unexpected result is due to the fact that the PNRs primary do not flip under the *ac* electric field, but merely change their shape and shift their centers of gravity in the sense of a breathing mode (Kleemann et al., 2011).

4.4 Dipolar glasses

4.4.1 Orientational glasses

The formation of dipolar glasses in incipient ferroelectrics with perovskite structure, ABO_3, such as $SrTiO_3$ and $KTaO_3$, by *A*-site substitution with small cations at low concentrations has been a fruitful topic since more than 20 years (Vugmeister & Glinchuk, 1990). For a long time probably the best-known example has been the impurity system $K_{1-x}Li_xTaO_3$ (KLT for short) with $x << 1$, whose complex polar behavior is known to be due to the interaction of the (nearly) softened transverse-optic mode of the host-lattice and the impurity dynamics (Höchli et al., 1990). Fig. 9 shows the structure model of *A*-site substituted Li^+ viewing the nearest neighbor environment in the $KTaO_3$ lattice from two different perspectives. At very low concentrations, $x \approx 0.01$, it reveals signatures of glasslike behavior (Höchli, 1982; Wickenhöfer et al., 1991), while a ferroelectric ground state with inherent domain structure is encountered at higher concentrations, $x \geq 0.022$ (Kleemann et al., 1987).

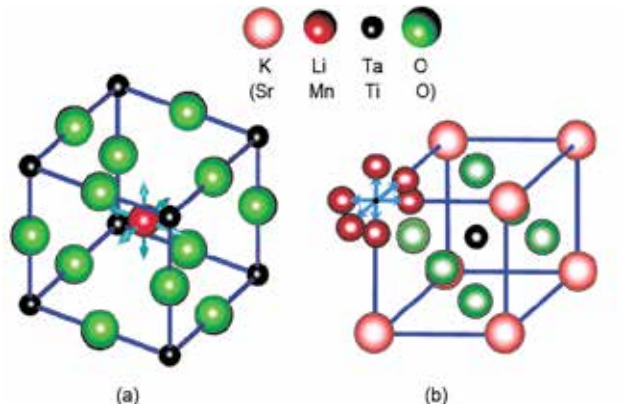

Fig. 9. Displacement vectors (blue arrows) of an off-center Li^+ (Mn^{2+}) ion in *A*-site doped $KTaO_3$ ($SrTiO_3$) viewed (a) from the center of 12 surrounding oxygen ions and (b) from the corner of the elementary cell.

Only recently a similar system has been discovered with qualitatively new properties. The impurity system $Sr_{1-x}Mn_xTiO_3$ (SMnT for short; Fig. 9) reveals very similar dipolar glassy properties, but the additional magnetic degrees of freedom of the Mn^{2+} dopant enable simultaneously a spin glass state (Shvartsman et al., 2008). This unique 'multiglass' situation has paved the way to a new materials class: 'disordered multiferroics' (Kleemann et al., 2008).
In addition to conventional tests of the glass transition, *e. g.* by verifying the divergence of the polar relaxation times, the behavior of the nonlinear susceptibility is believed to similarly decisive. As was first acknowledged in spin glass physics (Binder & Young, 1986), but later on also in the field of orientational glasses (Binder & Reger, 1992), criticality at the glass temperature, T_g, is expected to give rise to a divergence of the third-order nonlinear susceptibility, $\chi_3' \propto \partial^3 P / \partial E^3$, where the polarization P denotes the homogeneous order parameter. Recent experimental attempts will be reported below.

4.4.2 Orientational glass $K_{0.989}Li_{0.011}TaO_3$

The experiments on KLT were performed on a Czochralski grown single crystal sample with x = 0.011 with dimensions 3×2×0.5 mm^3 and (100) surfaces (Kleemann et al., 1987). Dipolar relaxation was studied as a function of temperature T via measurements of the complex dielectric susceptibility, $\chi = \chi' - i\chi''$ vs. T, by use of different experimental methods adapted to different frequency ranges, $10^{-3} \le f \le 10^6$ Hz. They included a Solartron 1260 impedance analyzer with 1296 dielectric interface (Fig. 10a and b) and a digital lock-in analyzer (Wickenhöfer et al., 1991) (Fig. 10c) for linear, and a homemade computer-controlled digital susceptometer (Miga et al., 2007) for non-linear dielectric susceptibility data (Fig. 11) at high precision under relatively low excitation voltages.
Fig. 10a and b show dielectric susceptibility data, $\chi'(T)$ and $\chi''(T)$, for frequencies $10^{-3} < f < 10^6$ Hz, which reveal various signatures of glassy behaviour. The peak of $\chi'(T)$ in Fig. 10a converges toward a finite glass temperature, $T_m \rightarrow T_g$ = (33.6 ± 0.1) K (Wickenhöfer et al., 1991) following critical dynamics with a power law $\tau = 1/(2\pi f) = \tau_0 \varepsilon^{-z\nu}$, where $\varepsilon = (T_m / T_g - 1) > 0$ is the reduced temperature and $z\nu = 6.6 \pm 0.2$ is the dynamical critical exponent. Essentially the same (static) glass temperature, T_g = (33.5±1.5) K, emerges for the

'largest' relaxation time τ_m as defined by the condition $\chi''(f_{\min},T) = 0.05\chi''_{\max}(T)$ from frequency spectra of the loss function $\chi''(f)$ in Fig. 10c (Kleemann et al., 2011). In this figure it is clearly seen, how the center of gravity of the loss spectrum shifts to very low frequencies and its width broadens toward very long relaxation times, $\tau_m \to \infty$, as $T \to T_g$.

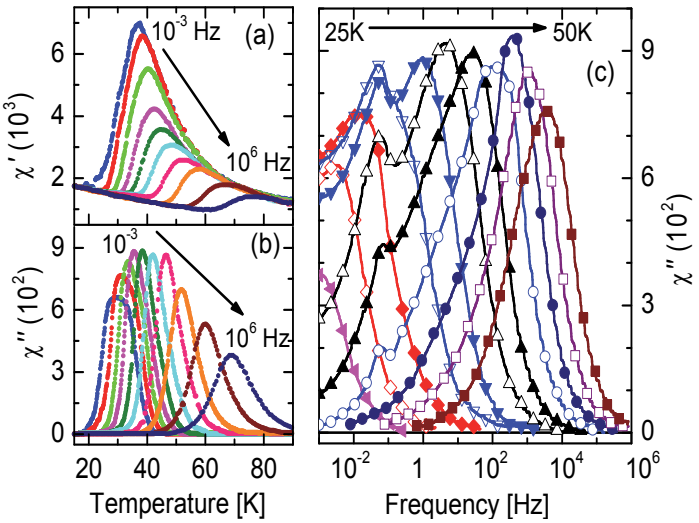

Fig. 10. Dielectric susceptibility, $\chi'(T)$ (a), $\chi''(T)$ (b), and $\chi''(f)$ (c) of $K_{0.989}Li_{0.011}TaO_3$ measured at frequencies $10^{-3} < f < 10^6$ Hz and temperatures $10 < T < 90$ K. Decades of f and steps of $\Delta T = 2.5$ K are parameters in (a, b) and (c), respectively.

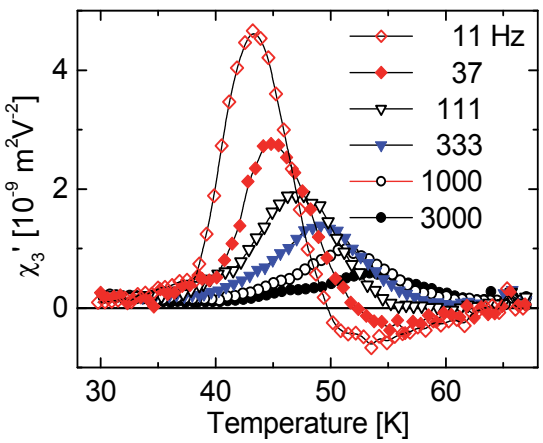

Fig. 11. Nonlinear susceptibility $\chi_3'(T)$ of $K_{0.989}Li_{0.011}TaO_3$ measured at frequencies $11 < f < 3000$ Hz.

A complementary test of glassy criticality refers to the third-order nonlinear susceptibility, $\chi_3' \propto \partial^3 P / \partial E^3$. It fulfils the expectation of a divergence at T_g (Binder & Reger, 1992) only partially. Fig. 11 shows χ_3' *vs.* T for frequencies 11 Hz ≤ f ≤ 3 kHz on cooling with

dT/dt = -0.2K/min under an *ac* field amplitude E_0 = 45 kV/m and by analyzing the emerging signal up to the fifth harmonic (Kleemann et al., 2011). While χ'_3 drops below zero on the high-T edge at low frequencies, all signals are dominated by positive low-T peaks. This unexpected result is very probably due to the fact that the dipolar glass KLT is only insufficiently modeled by a pseudospin system in full analogy to an Ising spin glass (Binder & Reger, 1992). Actually we deal with a frustrated system of nanoclusters (Vugmeister & Glinchuk, 1990), which are subject to complex dipolar interactions and underlie internal dynamical degrees of freedom. As a consequence the nanodipolar clusters do not primarily flip under the external electric *ac* field, but merely change their shape and shift their centers of gravity in the sense of a breathing mode. Obviously this action becomes more effective the lower the temperature (*i.e.* the higher the lattice permittivity) and the lower the frequency. Thus the expected negative divergence is replaced by a positive peak nearly coinciding with that of the linear susceptibility, χ'_1 (Fig. 10a).

4.4.3 Multiglass $Sr_{0.98}Mn_{0.02}TiO_3$

The experiments on $Sr_{0.98}Mn_{0.02}TiO_3$ were performed on a ceramic sample prepared by a mixed oxide technology (Tkach et al., 2005). Preponderant incorporation of Mn^{2+} onto *A*-sites of the perovskite structure (Fig. 9) was confirmed by energy dispersive X-ray spectra (Tkach et al., 2006), Mn^{2+} ESR analysis (Laguta et al., 2007), and EXAFS spectroscopy (Lebedev et al., 2009; Levin et al., 2010). Fig. 12 shows the components of the complex dielectric susceptibility $\chi = \chi' - i\chi''$ recorded at frequencies $10^{-3} \le f \le 10^6$ Hz and temperatures $10 \le T \le 100$ K as $\chi'(T)$ (a) and $\chi''(f)$ (c). The broad and strongly frequency dependent peaks of both components are related to the dynamics of polar clusters created by off-center displacements of Mn^{2+} cations (Tkach et al., 2007). The position of the peak temperatures T_m in Fig. 12a is well described by a power law of the respective frequency, $f(T_m) \propto (T_m / T_g - 1)^{z\nu}$, which is a typical manifestation of glassy critical behavior (Shvartsman et al., 2008). Best fits of the experimental data yield the glass temperature T_g = 38.3 ± 0.3 K (Fig. 12b) and the dynamical critical exponent, $z\nu$ = 8.5 ± 0.2, which compares well with that of spin glasses (Jönsson, 2004). Obviously the dynamics of the polar clusters becomes frozen at T_g, where the relaxation time $\tau = 1/(2\pi f)$ diverges on a percolating network. This defines a PT from the disordered super-paraelectric to a cluster glass state. Similarities with superspin glass characteristics (Jönsson, 2004) are obvious. As described elsewhere (Shvartsman et al., 2008, Kleemann et al., 2009) this freezing process initiates also the transition of the Mn^{2+} spin moments into a spin glass state, which is magneto-electrically coupled to the dipolar glass state.

Another striking indicator of the dipolar glass state is the memory effect, which arises after isothermally annealing the sample below T_g. Fig. 12b shows an example of 'burning a hole' with depth $\Delta\chi'(T_w) = \chi'_{\text{wait}} - \chi'_{\text{ref}}(T_w) \approx -6$ at the wait temperature T_w = 32.5 K after waiting for $t_w \approx 10.5$ h (arrow). It signifies the asymptotic approach to the 'stiff' glassy ground state at T_w, which has the lowest susceptibility with respect to an external homogeneous field. Since the structure of the glassy ground state varies as a function of the temperature, the system is 'rejuvenating' at temperatures sufficiently far from T_w (Jönsson, 2004), hence, localizing the 'burnt hole' around T_w. This contrasts with the global decrease expected for an ordinarily relaxing metastable system.

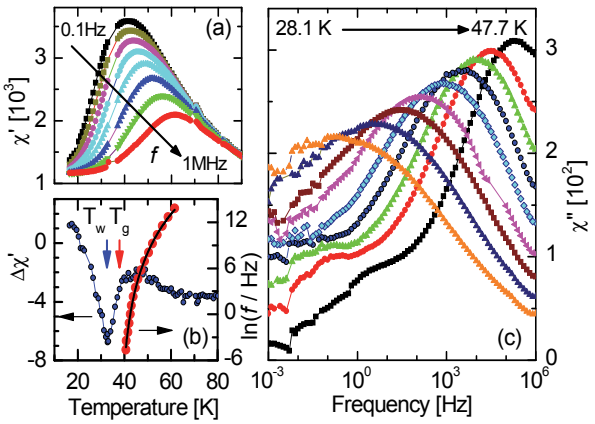

Fig. 12. (a) $\chi'(T)$ of $Sr_{0.98}Mn_{0.02}TiO_3$ recorded at E_{ac}= 60 V/m and frequencies $f = 10^{-1}$, 10^0, 10^1, 10^2, 10^3, 10^4, 10^5, and $0.4 \cdot 10^6$ Hz. (b) Frequency (f) dependence of the peak temperature (T_m) of $\chi'(T)$ taken from (a), plotted as ln(f/Hz) vs. T_m, and fitted by a critical power law (solid line), and difference curve $\Delta\chi' = \chi'_{wait} - \chi'_{ref}$ *vs.* T obtained at f = 10 Hz and E_{ac}= 60 V/m upon heating after zero-field cooling from 80 K and waiting for 10.5 h at T_w = 32.5 K (χ'_{wait}) or without waiting (χ'_{ref}), respectively. T_g and T_w are marked by arrows. (c) $\chi''(f)$ as measured at frequencies $10^{-3} \le f \le 10^6$ Hz and temperatures $28.1 \le T \le 47.7$ K in 2.2 K steps.

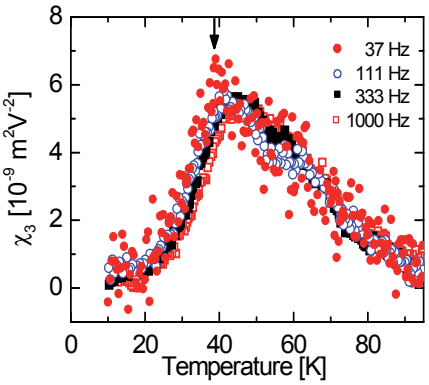

Fig. 13. Temperature dependence of the third-order nonlinear dielectric susceptibility of $Sr_{0.98}Mn_{0.02}TiO_3$ measured at f = 37, 111, 333 and 1000 Hz. The dipolar glass freezing temperature $T_g \approx 38$ K is indicated by a vertical arrow.

The glass transition may also be judged from spectra χ'' *vs.* log f (Shvartsman et al., 2008) similarly as shown for $K_{0.989}Li_{0.011}TaO_3$ (Fig. 10c). Since $\chi''(f)$ measures the distribution function of relaxation times, its extension over more than nine decades of frequencies clearly signifies the glassy nature of the system. At low frequencies, $f < 10^{-1}$ Hz, the low-f branch of $\chi''(T)$ is observed to gradually lift up and to become horizontal at $T < 38.9$ K. This suggests it to extend with finite amplitude to $f_{min} \to 0$, hence, $\tau_{max} \to \infty$ for the percolating glass cluster. Maybe the ultimate proof of the very existence of a generic dipolar glass is given by the dynamic nonlinear susceptibility $\chi_3 = (\partial^3 P / \partial E^3) / (6\varepsilon_0)$ (Miga et al., 2007) in Fig. 13. This

seems to indicate a divergence as $T \to T_g$ and $f \to 0$ as predicted by theory (Binder & Reger, 1992), but has rarely been evidenced on orientational glasses (Hemberger et al., 1996). At the lowest frequency, f = 37 Hz, a fairly sharp peak is encountered, whose high-T branch might be considered as a critical hyperbola. Excess noise, however, prevents from seriously fitting a critical exponent, which should be close to $\gamma = 1$ as found previously (Hemberger et al., 1996). However, since the nonlinear susceptibility is modified by non-diverging ferroic (*viz.* ferroelectric) correlations due to progressive cluster formation on cooling, we cannot expect rigorous proportionality to the 'spin' glass susceptibility (Binder & Reger, 1992). Very probably the expected divergence is damped out similarly as in the case of KLT (Fig. 11).

5. Conclusion

In subsections 4.1 – 4.4 we presented different groups of polar materials separately and compared qualitatively their dielectric properties with predictions of suitable theories. It is likewise interesting to compare quantitatively different materials. The scaled nonlinear susceptibility, a_3, is defined independently of the kind of material and its symmetry. This quantity is a measure of the nonlinearity of the investigated object. For an adequate comparison we have chosen values of a_3 within centrosymmetric phases of different materials close to their temperatures of phase transition or of peak positions of the linear susceptibility, respectively. Fig. 14 shows thus collected values of a_3. In view of the very large differences between the different a_3 values a logarithmic scale is used. Consequently, only the magnitude values, $|a_3|$, are presented. The highest $|a_3|$ was found for Rochelle salt, RS. Lower nonlinearity appears in sequence in the ferroelectric crystals TGS, LGO, BT, barium doped LGO, multiglass $Sr_{0.98}Mn_{0.02}TiO_3$, orientational glass $K_{0.989}Li_{0.011}TaO_3$ and relaxor ferroelectrics PMN and SBN 61. Obviously, classic ferroelectrics undergoing continuous PT are characterized by high nonlinearity, while structural disorder and presence of PNRs diminish the nonlinearity. Consequently relaxor ferroeletrics are characterized by the smallest values of a_3. In other words, displacive ferroelectrics exhibiting soft-mode softening are most affected by nonlinearity, while typical order-disorder systems do not obtain their ferroelectricity primarily from the nonlinear interionic potential. The mechanism of their phase transition rather reflects the statistics of local hopping modes, in particular when being accompanied by quenched random fields as in relaxor ferroelectrics (Westphal et al., 1992; Kleemann et al., 2002), but probably also in partial order-disorder systems like $BaTiO_3$ (Zalar et al., 2003).

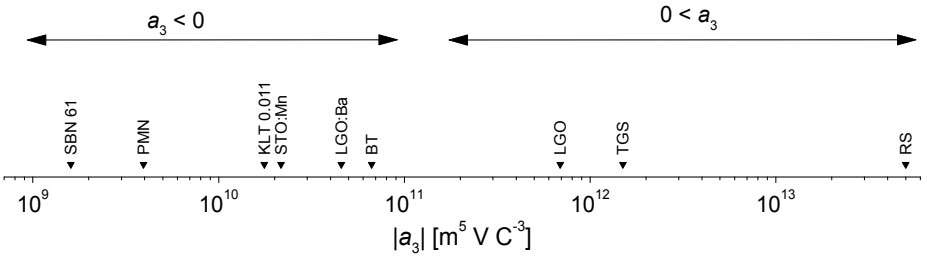

Fig. 14. Absolute values of the scaled nonlinear susceptibility, $|a_3|$, within centrosymmetric phases close to temperatures of phase transitions (for classic ferroelectrics) or peak positions of the linear susceptibility at low-f (for relaxor ferroelectrics and glasses).

The comparison of nonlinear dielectric response of various kinds of polar materials presented in this chapter gives evidence that such kind of measurement is a very sensitive tool for determination of the nature of ferroelectrics. Particularly useful for this purpose are the third-order dielectric susceptibility and the scaled non-linear susceptibility, a_3. In our opinion, the second-order dielectric susceptibility is less significant, since it is more characteristic of the sample state than of a particular group of ferroelectrics. If anything, this susceptibility contains information about the distinct polar state of the sample. This information may be used for checking the presence of a center of inversion. The nonlinear dielectric response of classic ferroelectric crystals displaying continuous or discontinuous phase transition stays in a good agreement with predictions of the thermodynamic theory of ferroelectric phase transition. Predictions of the scaling theory for TGS crystal are also successfully verified experimentally. The situation is much more complex in disordered systems like ferroelectric relaxors or dipolar glasses. Respective theories properly explaining the observed features have still to be developed and tested via dynamic nonlinear dielectric response.

6. Acknowledgment

The authors are grateful to D. Rytz, A. Tkach, and P.M. Vilarinho for providing samples. WK thanks the Foundation for Polish Science (FNP), Warsaw, for an Alexander von Humboldt Honorary research grant.

7. References

Binder, K. & Reger, J. D. (1992). Theory of orientational glasses: models, concepts, simulations, *Adv. Phys.*, Vol. 41, pp. 547 – 627

Binder, K. & Young, A. P. (1986). Spin glasses: Experimental facts, theoretical concepts, and open questions, *Rev. Mod. Phys.*, Vol. 58, pp. 801 – 976

Bobnar, V., Kutnjak, Z., Pirc, R., Blinc, R., & Levstik, A. (2000). Crossover from glassy to inhomogeneous-ferroelectric nonlinear dielectric response in relaxor ferroelectrics, *Phys. Rev. Lett.*, Vol. 84, pp. 5892 – 5895

Bonneau, P., Garnier, P., Calvarin, G., Husson, E., Gavarri, J. R., Hewat, A. W. & Morell, A. (1991). X-ray and neutron diffraction studies of the diffuse phase transition in $PbMg_{1/3}Nb_{2/3}O_3$ ceramics, *J. Solid State Chem.*, Vol. 91, pp. 350-361

Böttcher, C. J. F. (1973). *Theory of Electric Polarization*, Elsevier, Amsterdam, Oxford, New York

Burns, G. & Dacol, F. H. (1983). Crystalline ferroelectrics with glassy polarization behavior, *Phys. Rev. B*, Vol. 28, pp. 2527 - 2530

Cach, R. (1988). Time changes of the internal bias field in γ-damaged TGS crystal, *Acta Univ. Wrat.* LIII, Vol. 1084, pp. 125 - 133

Chen, A. & Zhi, Y. (2004). DC electric-field dependence of the dielectric constant in polar dielectrics: "multi-polarization-mechanism" model, *Phys. Rev. B*, Vol. 69, p. 174109-1 - 174109-8

Debye, P. (1929). *Polar Molecules*, The Chemical Catalog Company, Inc., New York

Dec, J., Miga, S., Kleemann, W. & Dkhil, B. (2008). Nonlinear dielectric properties of PMN relaxor crystals within Ginzburg-Landau-Devonshire approximation, *Ferroelectrics*, Vol. 363, p. 141 – 149

Dec, J., Miga, S., Trybuła, Z., Kaszyńska, K. & Kleemann, W. (2010). Dynamics of Li^+ dipoles at very low concentration in quantum paraelectric potassium tantalate, *J. Appl. Phys.*, Vol. 107, p. 094102-1 – 094102-8

Devonshire, A. F. (1949). Theory of barium titanate, Part I, *Phil. Mag.*, Vol. 40, pp. 1040 - 1063

Fisher, D. S (1986). Scaling and critical slowing down in random-field Ising systems, *Phys. Rev. Lett.*, Vol. 56, p. 416 – 419

Fujimoto, M. (2003). *The physics of structural phase transitions* (2nd ed.), Springer-Verlag, Berlin, Heidelberg, New York

Ginzburg, V. L. (1945). On the dielectric properties of ferroelectric (Seignetteelectric) crystals and barium titanate, *Zh. Exp. Theor. Phys.*, Vol. 15, pp. 739 - 749

Glazounov, A. E. & Tagantsev, A. K. (2000). Phenomenological model of dynamic nonlinear response of relaxor ferroelectrics, *Phys. Rev. Lett.* vol. 85, pp. 2192-2195

Hemberger, J., Ries, H., Loidl, A. & Böhmer, R. (1996). Static freezing transition at a finite temperature in a quasi-one-dimensional deuteron glass, *Phys. Rev. Lett.*, Vol. 76, pp. 2330 – 2333

Höchli, U. T. (1982). Dynamics of freezing electric dipoles, *Phys. Rev. Lett.*, Vol. 48, pp. 1494 – 1497

Höchli, U. T., Knorr, K. & Loidl, A. (1990). Orientational glasses, *Advan. Phys.*, Vol. 39, pp. 405 – 615

Ikeda, S., Kominami, H., Koyama, K. & Wada, Y. (1987). Nonlinear dielectric constant and ferroelectric-to-paraelectric phase transition in copolymers of vinylidene fluoride and trifluoroethylene, *J. Appl. Phys.*, Vol. 62, pp. 3339 – 3342

Jönsson, P.E. (2004). Superparamagnetism and spin-glass dynamics of interacting magnetic nanoparticle systems, *Adv. Chem. Phys.*, Vol. 128, pp. 191 – 248

Jonscher A. K. (1983). *Dielectric Relaxation in Solids*, Chelsea Dielectrics, London

Kleemann, W., Kütz, S. & Rytz, D. (1987). Cluster glass and domain state properties of $KTaO_3$:Li, *Europhys. Lett.* , Vol. 4, pp. 239 – 245

Kleemann W., Dec J., Lehnen P., Blinc R., Zalar B., and Pankrath R. (2002). Uniaxial relaxor ferroelectrics: the ferroic random-field Ising model materialized at last, *Europhys. Lett.*, Vol. 57, pp. 14 – 19

Kleemann, W., Shvartsman, V.V., Bedanta, S., Borisov, P., Tkach, A. & Vilarinho, P. M. (2008). (Sr,Mn)TiO_3 – a magnetoelectrically coupled multiglass, *J. Phys.: Condens. Matter,* Vol. 20, pp. 434216-1 – 434216-6

Kleemann, W., Bedanta, S., Borisov, P., Shvartsman, V. V., Miga, S., Dec, J., Tkach, A. & Vilarinho, P.M. (2009). Multiglass order and magnetoelectricity in Mn^{2+} doped incipient ferroelectrics, *Eur. Phys. J. B*, Vol. 71, pp. 407 – 410

Kleemann, W., Dec, J., Miga, S. & Rytz, D. (2011). Polar states of the impurity system $KTaO_3$:Li, *Z. Kristallogr.* Vol. 226, pp. 145 - 149

Kremer, F. & Schönhals, A. (Eds.). (2003). *Broadband Dielectric Spectroscopy*, Springer-Verlag, Berlin, Heidelberg, New York

Laguta, V. V., Kondakova, I. V., Bykov, I. P, Glinchuk, M. D., Tkach, A., Vilarinho, P. M. & Jastrabik, L. (2007). Electron spin resonance investigation of Mn^{2+} ions and their dynamics in Mn-doped $SrTiO_3$, *Phys. Rev. B*, Vol. 76, pp. 054104-1 - 054104-6

Lebedev, A. I., Sluchinskaja, I. A., Erko, A. & Kozlovskii, A. F. (2009). Direct evidence for off-centering of Mn impurity in $SrTiO_3$, *JETP-Lett.*, Vol. 89, pp. 457 - 467

Leont'ev, I. N., Leiderman, A., Topolov, V. Yu. & Fesenko, O. E. (2003). Nonlinear properties of barium titanate in the electric field range $0 \le E \le 5.5\times10^7$ V/m, *Phys. Solid State*, Vol. 45, pp. 1128-1130

Levin, I., Krayzman, V., Woicik, J. C., Tkach, A. & Vilarinho, P. M. (2010). X-ray absorption fine structure studies of Mn coordination in doped perovskite $SrTiO_3$, *Appl. Phys. Lett*., Vol. 96, pp. 052904-1 – 052904-3

Lines, M. E. & Glass, A. M. (1977). *Principles and Applications of Ferroelectrics and Related Materials*, Oxford University Press, London

Mierzwa, W., Fugiel, B. & Ćwikiel, K. (1998). The equation-of-state of triglycine sulphate (TGS) ferroelectric for both phases near the critical point, *J. Phys.: Condens. Matter*, Vol. 10, pp. 8881 - 8892

Miga, S., Dec, J., Molak, A. & Koralewski, M. (2006). Temperature dependence of nonlinear susceptibilities near ferroelectric phase transition of a lead germanate single crystal, *J. Appl. Phys*., Vol. 99, pp. 124107-1 - 124107-6

Miga, S., Dec, J. & Kleemann, W. (2007). Computer-controlled susceptometer for investigating the linear and non-linear dielectric response, *Rev. Sci. Instrum*., Vol. 78, pp. 033902-1 - 033902-7

Miga, S. & Dec, J. (2008). Non-linear dielectric response of ferroelectric and relaxor materials, *Ferroelectrics*, Vol. 367, p. 223 – 228

Miga, S., Dec, J., Molak, A. & Koralewski, M. (2008). Barium doping-induced polar nanoregions in lead germanate single crystal, *Phase Trans*., Vol. 81, pp. 1133 –1140

Miga, S., Czapla, Z., Kleemann, W. & Dec, J. (2010a). Non-linear dielectric response in the vicinity of the 'inverse melting' point of Rochelle salt, *Ferroelectrics*, Vol. 400, p. 76–80

Miga, S., Kleemann, W. & Dec J. (2010b). Non-linear dielectric susceptibility near to the field-induced ferroelectric phase transition of $K_{0.937}Li_{0.063}TaO_3$, *Ferroelectrics*, Vol. 400, p. 35 – 40

Mitsui, T. (1958). Theory of the ferroelectric effect in Rochelle salt, *Phys. Rev*., Vol. 111, pp. 1259 – 1267

Oliver, J. R., Neurgaonkar, R. R. & Cross, L. E. (1988). A thermodynamic phenomenology for ferroelectric tungsten bronze $Sr_{0.6}Ba_{0.4}Nb_2O_6$ (SBN:60), *J. Appl. Phys*., Vol.64, pp. 37-47

Pirc, R., Tadić, B. & Blinc, R. (1994). Nonlinear susceptibility of orientational glasses, *Physica B*, Vol. 193, pp. 109 - 115

Pirc, R. & Blinc, R. (1999). Spherical random-bond-random-field model of relaxor ferroelectrics, *Phys. Rev. B*, Vol. 60, pp. 13470 - 13478

Shvartsman, V. V., Bedanta, S., Borisov, P., Kleemann, W., Tkach, A. & Vilarinho, P. (2008). $(Sr,Mn)TiO_3$ – a magnetoelectric multiglass, *Phys. Rev. Lett*., Vol. 101, pp. 165704-1 – 165704-4

Smolenskii, G. A., Isupov, V. A., Agranovskaya, A. I. & Popov, S . N. (1960). Ferroelectrics with diffuse phase transition (in Russian), *Sov. Phys. -Solid State*, Vol. 2, pp. 2906-2918

Stanley, H. E. (1971). *Introduction to Phase Transitions and Critical Phenomena*, Clarendon, Oxford

Tkach, A., Vilarinho, P. M. & Kholkin, A. L. (2005). Structure-microstructure-dielectric tunability relationship in Mn-doped strontium titanate ceramics, *Acta Mater*., Vol. 53, pp. 5061- 5069

Tkach, A., Vilarinho, P. M. & Kholkin, A. L. (2006). Dependence of dielectric properties of manganese-doped strontium titanate ceramics on sintering atmosphere, *Acta Mater*., Vol. 54, pp. 5385 - 5391

Tkach, A., Vilarinho, P. M. & Kholkin, A. L. (2007). Non-linear dc electric-field dependence of the dielectric permittivity and cluster polarization of $Sr_{1-x}Mn_xTiO_3$ ceramics, *J. Appl. Phys.* , Vol. 101, pp. 084110-1 - 084110-9

Valasek, J. (1920). Piezoelectric and allied phenomena in Rochelle salt, *Phys. Rev*., Vol. 15, pp. 537 - 538

Valasek, J. (1921). Piezo-electric and allied phenomena in Rochelle salt, *Phys. Rev*., Vol. 17, pp. 475 - 481

von Hippel, A. (1950). Ferroelectricity, domain structure, and phase transitions of barium titanate, *Rev. Mod. Phys*., Vol. 22, pp. 222 - 237

von Hippel, A. (1954). *Dielectrics and Waves*, Wiley, New York

Vugmeister, B. E. & Glinchuk, M. D. (1990). Dipole glass and ferroelectricity in random-site electric dipole systems, *Rev. Mod. Phys*., Vol. 62, pp. 993 – 1026

Wang, Y. L., Tagantsev, A. K., Damjanovic, D. & Setter, N. (2006). Anharmonicity of $BaTiO_3$ single crystals, *Phys. Rev. B*, Vol. 73, pp. 132103-1 - 132103-4

Wang, Y. L., Tagantsev, A. K., Damjanovic, D., Setter, N., Yarmarkin, V. K., Sokolov, A. I. & Lukyanchuk, I. A. (2007). Landau thermodynamic potential for $BaTiO_3$, *J. Appl. Phys*., Vol. 101, pp. 104115-1 - 104115-9

Wei, X. & Yao, X. (2006a). Reversible dielectric nonlinearity and mechanism of electrical tunability for ferroelectric ceramics, *Int. J. Mod. Phys. B*, Vol. 20, p. 2977 - 2998

Wei, X. & Yao, X. (2006b). Analysis on dielectric response of polar nanoregions in paraelectric phase of relaxor ferroelectrics, *J. Appl. Phys*., Vol. 100, p. 064319-1 – 064319-6

Westphal, V., Kleemann, W. & Glinchuk, M. (1992). Diffuse phase transitions and random field-induced domain states of the "relaxor" ferroelectric $PbMg_{1/3}Nb_{2/3}O_3$, *Phys. Rev. Lett*., Vol. 68, pp. 847 - 950

Wickenhöfer, F., Kleemann, W. & Rytz, D. (1991). Dipolar freezing of glassy $K_{1-x}Li_xTaO_3$, x = 0.011, *Ferroelectrics*, Vol. 124, pp. 237 – 242

Zalar, B., Laguta, V. V. & Blinc, R. (2003). NMR evidence for the coexistence of order-disorder and displacive components in barium titanate, *Phys. Rev. Lett*., Vol.90, pp. 037601-1 - 037601-4

11

Ferroelectrics Study at Microwaves

Yuriy Poplavko, Yuriy Prokopenko,
Vitaliy Molchanov and Victor Kazmirenko
National Technical University "Kiev Polytechnic Institute"
Ukraine

1. Introduction

Dielectric materials are of interest for various fields of microwave engineering. They are widely investigated for numerous applications in electronic components such as dielectric resonators, dielectric substrates, decoupling capacitors, absorbent materials, phase shifters, etc. Electric polarization and loss of dielectric materials are important topics of solid state physics as well. Understanding their nature requires accurate measurement of main dielectric characteristics. Ferroelectrics constitute important class of dielectric materials. Microwave study of ferroelectrics is required not only because of their applications, but also because important physical properties of theses materials, such as phase transitions, are observed at microwave frequencies. Furthermore, most of ferroelectrics have polydomain structure and domain walls resonant (or relaxation) frequency is located in the microwave range. Lattice dynamics theory also predicts strong anomalies in ferroelectric properties just at microwaves. That is why microwave study can support the investigation of many fundamental characteristics of ferroelectrics.

Dielectric properties of materials are observed in their interaction with electromagnetic field. Fundamental ability of dielectric materials to increase stored charge of the capacitor was used for years and still used to measure permittivity and loss at relatively low frequencies, up to about 1 MHz (Gevorgian & Kollberg, 2001). At microwaves studied material is usually placed inside transmission line, such as coaxial or rectangular waveguide, or resonant cavity and its influence onto wave propagation conditions is used to estimate specimen's properties. Distinct feature of ferroelectric and related materials is their high dielectric constant ($\varepsilon = 10^2 - 10^4$) and sometimes large dielectric loss ($\tan\delta = 0.01 - 1$). High loss could make resonant curve too fuzzy or dissipate most part incident electromagnetic energy, so reflected or transmitted part becomes hard to register. Also because of high permittivity most part of incident energy may just reflect from sample's surface. So generally conventional methods of dielectrics study may not work well, and special approaches required.

Another problem is ferroelectric films investigation. Non-linear ferroelectric films are perspective for monolithic microwave integrated circuits (MMIC) where they are applied as linear and nonlinear capacitors (Vendik, 1979), microwave tunable resonant filters (Vendik et al., 1999), integrated microwave phase shifter (Erker et al., 2000), etc. Proper design of these devices requires reliable evidence of film microwave dielectric constant and loss tangent. Ferroelectric solid solution $(Ba,Sr)TiO_3$ (BST) is the most studied material for

possible microwave applications. Lucky for microwave applications, BST film dielectric constant in comparison with bulk ceramics decreases about 10 times (ε_{film} ~ 400 – 1000) that is important for device matching. Temperature dependence of ε_{film} becomes slick that provides device thermal stability (Vendik, 1979), and loss remains within reasonable limits: tanδ ~ 0.01 – 0.05 (Vendik et al., 1999). Accurate and reliable measurement of ferroelectric films dielectric properties is an actual problem not only of electronic industry but for material science as well. Film-to-bulk ability comparison is an interesting problem in physics of ferroelectrics. Properties transformation in thin film could be either favourable or an adverse factor for electronic devices. Ferroelectric materials are highly sensitive to any influence. While deposited thin film must adapt itself to the substrate that has quite different thermal and mechanical properties. Most of widely used techniques require deposition of electrodes system to form interdigital capacitor or planar waveguide. That introduces additional influence and natural film's properties remain unknown.
Therefore, accurate and reliable measuring of dielectric constant and loss factor of bulk and thin film ferroelectrics and related materials remains an actual problem of material science as well as electronic industry.

2. Bulk ferroelectrics study

At present time, microwave study of dielectrics with ε of about 2 – 100 and low loss is well developed. Some of theses techniques can be applied to study materials with higher permittivity. Approximate classification of most widely used methods for large-ε materials microwave study is shown in Fig. 1.

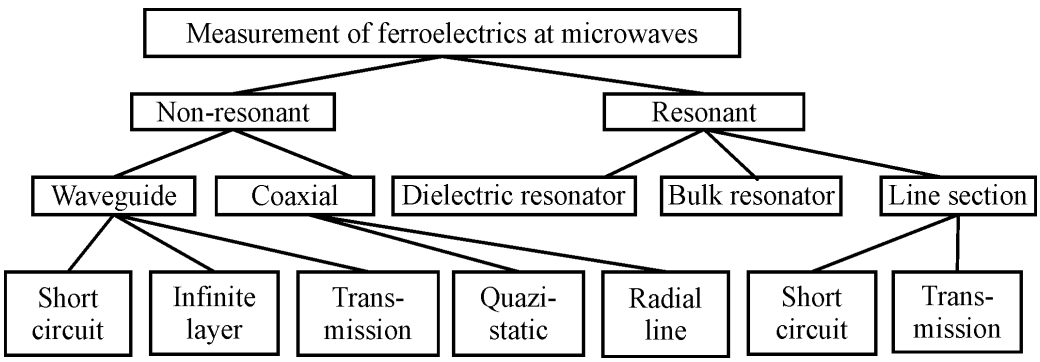

Fig. 1. Microwave methods for ferroelectrics study

Because of high dielectric constant, microwave measuring of ferroelectrics is quite unconventional. The major problem of high-ε dielectric microwave study is a poor interaction of electromagnetic wave with studied specimen. Because of significant difference in the wave impedance, most part of electromagnetic energy reflects from air-dielectric boundary and can not penetrate the specimen. That is why, short-circuited waveguide method exhibit lack of sensitivity. If the loss of dielectric is also big, the sample of a few millimetres length looks like "endless". For the same reason, in the transmission experiment, only a small part of electromagnetic energy passes through the sample to output that is not sufficient for network analyzer accurate operation. Opened microwave systems such as resonators or microstrip line suffer from approximations.

One of the most used methods utilizes measurement cell in the form of coaxial line section. Studied specimen is located in the discontinuity of central line. Electric field within the specimen is almost uniform only for materials with relatively low permittivity. This is quazistatic approximation that makes calculation formulas simpler. If quazistatic conditions could not be met, then radial line has to be studied without approximations. For the high ε materials coaxial method has limitations. Firstly, samples in form of thin disk have to be machined with high precision in a form of disk or cylinder. Secondly, many ferroelectric materials have anisotropic properties, so electric field distribution in the coaxial line is not suitable. This work indicates that a rectangular waveguide can be improved for ferroelectrics study at microwaves.

2.1 Improved waveguide method of ferroelectrics measurements

The obvious solution to improve accuracy of measurement is to reinforce interaction of electromagnetic field with the material under study. One of possible ways is to use dielectric transformer that decreases reflection. For microwave study, high-ε samples are placed in the cross-section of rectangular waveguide together with dielectric transformers, as shown in Fig. 2.

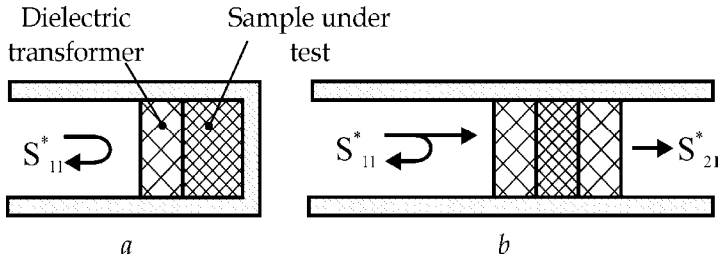

Fig. 2. Measurement scheme: *a*) short-circuit line method, *b*) transmission/reflection method

A quarter-wave dielectric transformer with $\varepsilon_{trans} = \sqrt{\varepsilon_{sample}}$ can provide a perfect matching, but at one certain frequency only. In this case, the simple formulas for dielectric constant and loss calculations can be drawn. However, mentioned requirement is difficult to implement. Foremost, studied material dielectric constant is unknown *a priori* while transformer with a suitable dielectric constant is also rarely available. Secondly, the critical limitation is method validity for only one fixed frequency, for which transformer length is equal precisely to quarter of the wavelength. Moreover, the calculation formulas derived with the assumption of quarter wave length transformers lose their accuracy, as last requirement is not perfectly met.

Insertion of dielectric transformers still may improve matching of studied specimen with air filled part of waveguide, though its length and/or permittivity do not deliver perfectly quarter wave length at the frequency of measurement. Dielectric transformers with ε_{trans} = 2 – 10 of around quarter-wave thickness are most suitable for this purpose. Influence of transformers must be accurately accounted in calculations.

2.2 Method description

The air filled section of waveguide, the transformer, and the studied sample are represented by normalized transmission matrices $\tilde{\mathbf{T}}$, which are the functions of lengths and

electromagnetic properties of neighbour areas. Applying boundary conditions normalized transmission matrix for the basic mode can be expressed as:

$$\tilde{\mathbf{T}}_i = \sqrt{\frac{\mu_{i-1}}{\mu_i}} \cdot \begin{bmatrix} \frac{\gamma_i + \gamma_{i-1}}{2\sqrt{\gamma_{i-1}\gamma_i}} e^{-j\dot{\gamma}_i d} & \frac{\gamma_i - \gamma_{i-1}}{2\sqrt{\gamma_{i-1}\gamma_i}} e^{-j\dot{\gamma}_i d} \\ \frac{\gamma_i - \gamma_{i-1}}{2\sqrt{\gamma_{i-1}\gamma_i}} e^{j\dot{\gamma}_i d} & \frac{\gamma_i + \gamma_{i-1}}{2\sqrt{\gamma_{i-1}\gamma_i}} e^{j\dot{\gamma}_i d} \end{bmatrix}, \quad (1)$$

where μ_i is permeability of i-th medium; γ_i is propagation constant in i-th medium; d is the length of i-th medium. Transmission matrix of whole network can be obtained by the multiplication of each area transmission matrices:

$$[\tilde{\mathbf{T}}] = \tilde{\mathbf{T}}_n \cdot \tilde{\mathbf{T}}_{n-1} \cdot \ldots \cdot \tilde{\mathbf{T}}_1 . \quad (2)$$

The order of multiplying here is such, that matrix of the first medium on the wave's way appears rightmost. Then, for the convenience, the network transmission matrices can be converted into scattering matrices whose parameters are measured directly.

In case of non-magnetic materials scattering equations, derived from (2), can be solved for every given frequency. However, this point-by-point technique is strongly affected by accidental errors and individual initiations of high-order modes. To reduce influence of these errors in modern techniques vector network analyzer is used to record frequency dependence of scattering parameters (Baker-Jarvis, 1990). Special data processing procedure, which is resistive to the individual errors, such as nonlinear least-squares curve fitting should be used:

$$\min_{(\varepsilon', \varepsilon'')} \sum_n \sigma_n \left(S_n^{meas} - S(f_n, \varepsilon', \varepsilon'') \right)^2 . \quad (3)$$

Here σ_n is the weight function; S_n^{meas} is measured S-parameter at frequency f_n; $S(f_n, \varepsilon', \varepsilon'')$ is calculated value of scattering parameter at the same frequency, assuming tested material to have parameters ε' and ε''. Real and imaginary parts of scattering parameters are separated numerically and treated as an independent, i.e. the fitting is applied to both real and imaginary parts.

Proper choice of weight is important for correct data processing. Among possible ways, there are weighted derivatives, and the modulus of reflection or transmission coefficients. These methods emphasize the influence of points near the minimum values of the reflection or transmission, which just exactly have the highest sensitivity to properties of studied material.

The choice between short-circuited line or transmission/ reflection methods depends on which method has better sensitivity, and should be applied individually.

2.3 Examples of measurements

Three common and easily available materials were used for experimental study. Samples were prepared in the rectangular shape that is adjusted to *X*-band waveguide cross section. Side edges of samples for all experiments were covered by silver paste. Summary on measured values is presented in Table 1.

Material	Reflection		Transmission	
	ε	tanδ	ε	tanδ
TiO_2	96	0.01	95	0.01
$SrTiO_3$	290	0.02	270	0.017
$BaTiO_3$	590	0.3		

Table 1. Summary on several studied ferroelectric materials

Measured data and processing curves are illustrated in Fig. 3, 4. In reflection experiment minima of S_{11} are deep enough to perform their reliable measurement, so numerical model coincides well with experimentally acquired points. For transmission experiment total amount of energy passed trough sample is relatively low, but there are distinct maxima of transmission, which also are registered reliably.

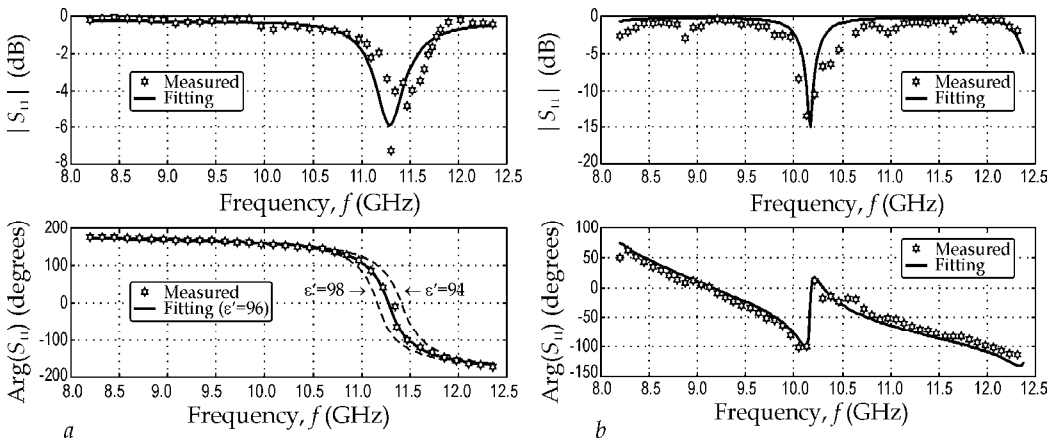

Fig. 3. Measured data and processing for reflection experiments: TiO_2, ε = 96, thickness 2.03 mm (*a*); $SrTiO_3$ of 3.89 mm thickness with 6.56 mm teflon transformer (*b*)

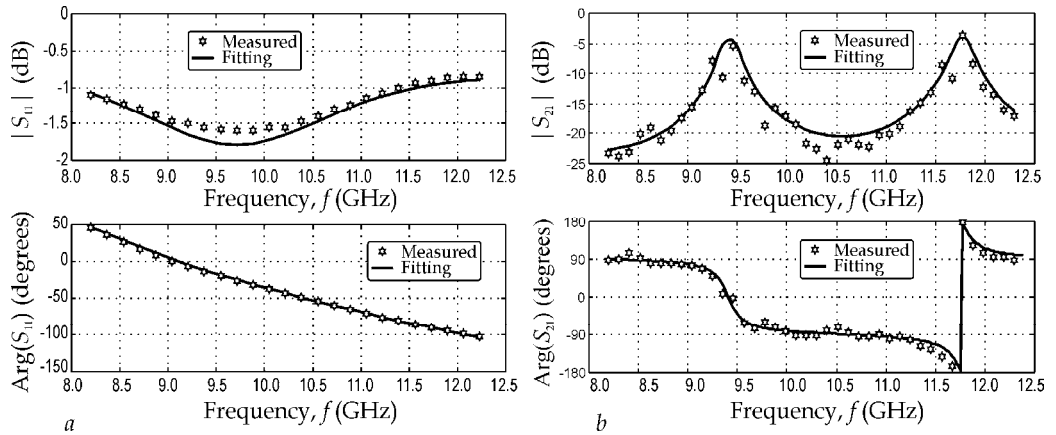

Fig. 4. Measured data and processing for: 1.51mm $BaTiO_3$ with 6.56 mm teflon transformer (*a*), reflection experiment; 3.89 mm $SrTiO_3$, transmission experiment (*b*)

$BaTiO_3$ is very lossy material with high permittivity. In reflection experiment, Fig. 4, there is fuzzy minimum of S_{11}, so calculation of permittivity with resonant techniques is inaccurate. Change in reflection coefficient across whole X-band is about 0.5 dB, so loss determination by resonant technique might be inaccurate too. Our calculations using fitting procedure (3) show good agreement with other studies in literature.

2.4 Order-disorder type ferroelectrics at microwaves

There are two main frequency intervals of dielectric permittivity dispersion: domain walls relaxation in the polar phase and dipole relations in all phases. Rochelle Salt is typical example of this behaviour, Fig. 5. Here and after ε_1, ε_2, ε_3 are diagonal components of permittivity tensor.

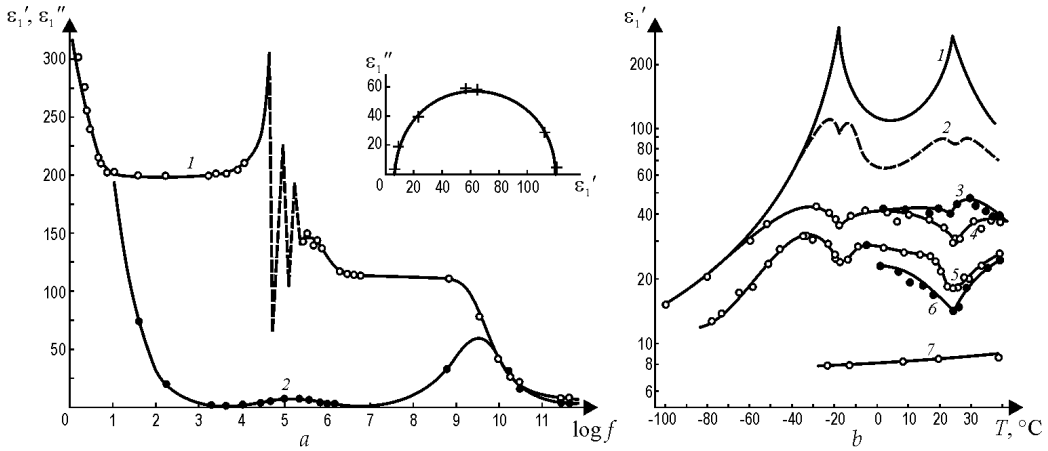

Fig. 5. Rochelle Salt microwave study: ε'_1 and ε''_1 frequency dependence at 18° C (*a*); ε'_1 temperature dependence at frequencies (in GHz): *1* – 0.8; *2* – 5.1; *3* – 8.4; *4* – 10.2; *5* – 20.5; *6* – 27; *7* – 250 (*b*)

Sharp maxima of at $\varepsilon'_1(f)$ in the frequency interval of 10^4 – 10^5 Hz mean piezoelectric resonances that is accompanied by a fluent ε′-decrease near 10^6 Hz, Fig. 5, *a*. The last is domain relaxation that follows electromechanical resonances. In the microwaves Rochelle Salt ε'_1 dispersion with ε''_1 broad maximum characterizes dipole relaxation that can be described by Debye equation

$$\varepsilon^*(\omega) = \varepsilon_\infty + \frac{\varepsilon(0) - \varepsilon(\infty)}{1 + i\omega\tau}, \tag{4}$$

where τ is relaxation time, ε(∞) is infrared and optical input to ε_1 why ε(0) is dielectric permittivity before microwave dispersion started.

Microwave dispersion in the Rochelle Salt is observed in all phases (in the paraelectric phase above 24°C, in the ferroelectric phase between –18° – +24°C, and in the antiferroelectric phase below –18°C, Fig. 5, *b*. To describe ε*(ω,T) dependence in all these phases using eq. (1) one need substitute in the paraelectric phase $\tau = \tau_0/(T - \theta)$ and $\varepsilon(0) - \varepsilon(\infty) = C/(T - \theta)$. Experiment shows that in paraelectric phase C = 1700 K, θ = 291 K and $\tau_0 = 3.2 \cdot 10^{-10}$ s/K. By the analogy this calculations can be done in all phases of Rochelle Salt.

Figure 6 shows main results of microwave study of TGS (another well known order-disorder type ferroelectric). Dipole relaxation in the polar phase demonstrates $\varepsilon'_2(f)$ decrease between 10 and 300 GHz with $\varepsilon''_2(f)$ maximum near 100 GHz, Fig. 6, *a*. Note, that 1 cm^{-1} corresponds to f = 30 GHz.

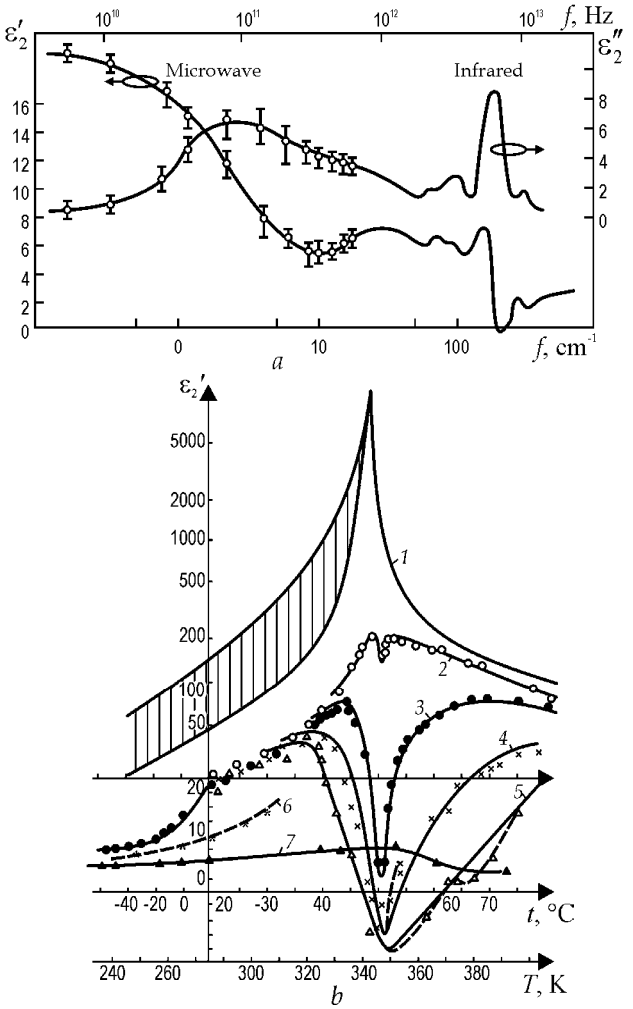

Fig. 6. TGS crystals microwave study: ε'_2 and ε''_2 frequency dependence at 300 K (*a*); ε'_2 temperature dependence at frequencies: *1* – 1 KHz, *2* – GHz, *3* – 16 GHz, *4* – 26 GHz, *5* – 37 GHz , *6* – 80 GHz, *7*– 250 GHz (*b*)

In contrast to Rochelle Salt, TGS is not piezoelectric in the paraelectric phase. In the Curie point $\varepsilon'_2(T)$ at microwaves demonstrates minimum. The family of $\varepsilon^*_2(f,T)$ characteristics can be well described by the modified Debye equation

$$\varepsilon^*(\omega,T) = \varepsilon_{IR} + \frac{C}{T-\theta+i\omega\tau_0} \tag{5}$$

where ε_{IR} is the infrared input to permittivity. In a paraelectric phase TGS crystal microwave properties can be described by the parameters C = 3200 K, θ = 321 K and $\tau_0 = 2 \cdot 10^{-10}$ sec/K. Microwave properties of the DKDP $\varepsilon^*_3(f, T)$ dependences that is characterized by the heavy deuteron relaxation looks very similar to TGS and Rochelle Salt crystals, Fig. 7, *a*. However, in the KDP crystals protons dynamics makes dielectric dispersion spectra similar to displace ferroelectric, Fig. 7, *b*.

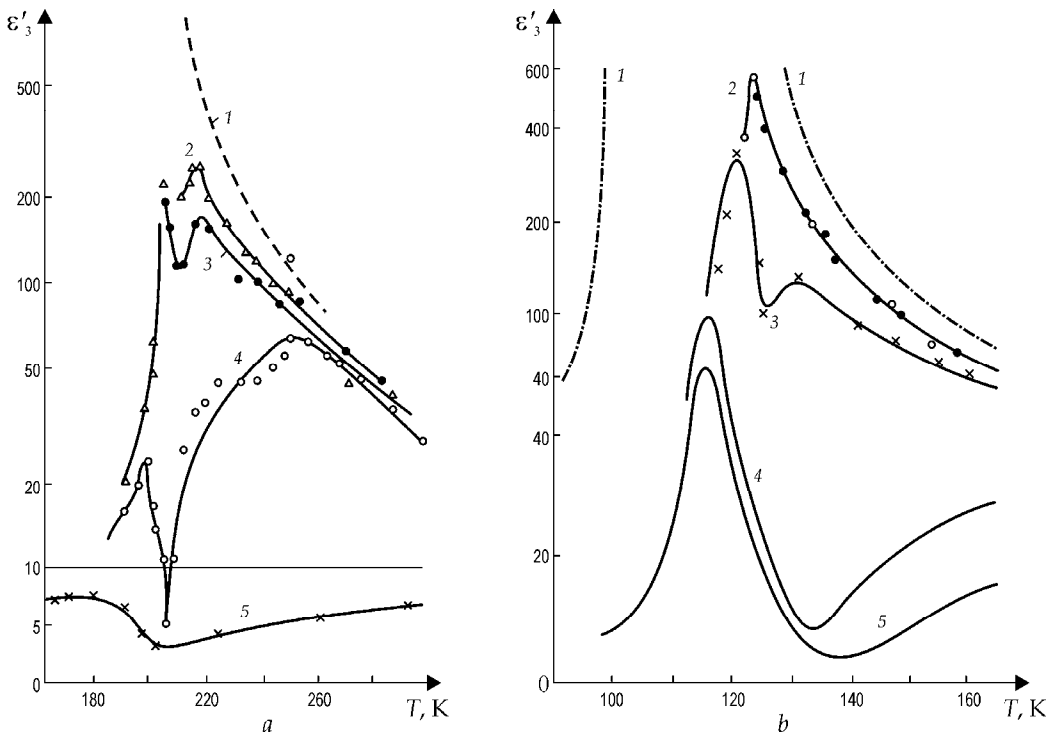

Fig. 7. Microwave dielectric dispersion in ferroelectrics of KDP type: KD_2PO_4 $\varepsilon'_3(T)$ at frequencies: 1 – 0.3 GHz; *2* – 8.6 GHz ; *3* – 9.7 GHz ; 4 – 26 GHz; 5 – 250 GHz (*a*); KH_2PO_4 $\varepsilon'_3(T)$ at frequencies: *1* – 1 kHz, *2* –9.4 GHz; *3* – 80 GHz , *4* –200 GHz; *5* –340 GHz (*b*)

2.5 Ferroelectrics of displace type at microwaves

In the ferroelectric phase the ε-dispersion at microwaves depends on domain walls vibration. That is why in the single-domain crystal practically no decrease in ε at microwaves is observed, as it is shown in Fig. 8, *a* with the example of $LiNbO_3$ crystal. Resonant change in ε_3 and ε_1 at megahertz frequencies means only piezoelectric resonances while far infrared ε-maxima are obliged to the lattice vibrations.

However, in the multidomain crystals dielectric dispersion at microwaves results in ε-decrease that is accompanied by tanδ maximum near frequency 9 GHz, shown in Fig. 8, *b* for multidomain $LiTaO_3$ crystal (there are also many piezoelectric resonances in the megahertz area).

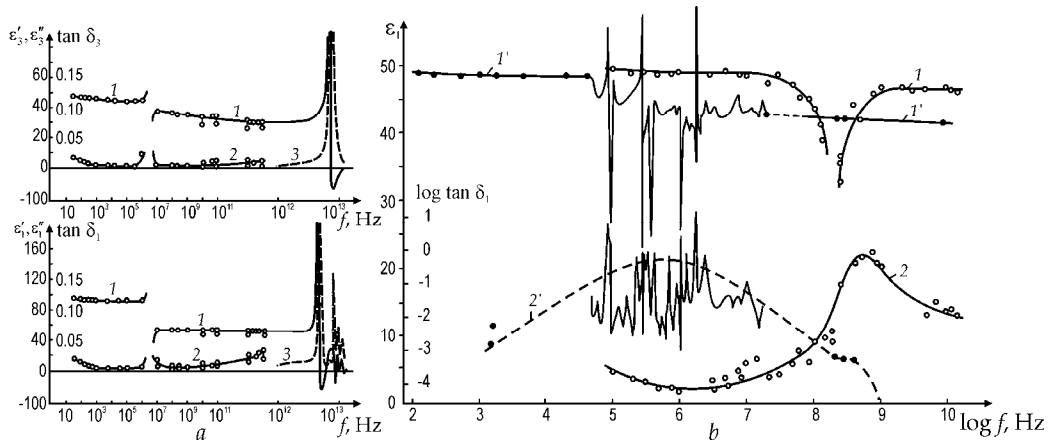

Fig. 8. Dielectric spectrums of ferroelectric crystals at 300 K: single domain $LiNbO_3$ ε_3 and $\tan\delta_3$, ε_1 and $\tan\delta_1$ (*a*); $LiTaO_3$: *1* - ε_1, *2* – $\tan\delta_1$ single domain; *1* – ε_1, *2* – $\tan\delta_1$ for multidomain crystal (*b*)

Polycrystalline ferroelectrics have obviously multidomain structure and, as a result, show microwave ε-dispersion, as it is shown in Fig. 9 for $PbTiO_3$ and $BaTiO_3$ (ε″ maximum is observed near frequency of 9 GHz while ε′ decreases in two times). More "soft" ceramics $Ba(Ti,Sn)O_3$ demonstrate microwave dispersion at lower but microwave frequencies: broad ε″ maximum is seen at 1 GHz.

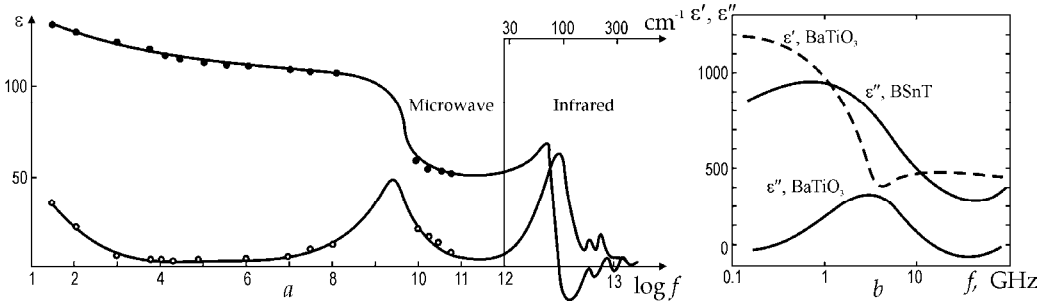

Fig. 9. Ferroelectric permittivity frequency dependence at 300 K: $PbTiO_3$ ceramics 1 - ε′ and 2 - ε″ (*a*); ceramics $BaTiO_3$ and $Ba(Ti,Sn)O_3$ = BSnT microwave study (*b*)

Microwave properties of displace type ferroelectrics in the paraelectric phase depends on soft lattice vibration mode. That is why Lorentz oscillator model is a basic model to describe ε* frequency dependence:

$$\varepsilon^*(\omega) = \varepsilon_\infty + \frac{\varepsilon(0) - \varepsilon(\infty)}{1 + (\omega/\omega_{TO})^2 + i\Gamma\,\omega/\omega_{TO}}. \tag{6}$$

In this equation let assume $\varepsilon(0) - \varepsilon(\infty) = C/(T-\theta)$ and soft mode critical frequency dependence on temperature is $\omega_{TO} = A\sqrt{T-\theta}$. Relative damping factor is $\Gamma = \gamma/\omega_{TO}$, as a result:

$$\varepsilon'(\omega,T)-\varepsilon_\infty = CA^2\frac{A^2(T-\theta)-\omega^2}{\left[A^2(T-\theta)-\omega^2\right]^2+\gamma^2\omega^2};$$

$$\varepsilon''(\omega,T)-\varepsilon_\infty = CA^2\frac{\gamma\omega}{\left[A^2(T-\theta)-\omega^2\right]^2+\gamma^2\omega^2}; \qquad (7)$$

$$\operatorname{tg}\delta \approx \frac{\gamma\omega}{A^2(T-\theta)},$$

where A is Cochran coefficient, C is Curie-Weiss constant, γ is damping coefficient. From ε and tanδ temperature dependences at various frequencies, as for instance Fig. 10, *a*, soft mode temperature dependence can be calculated, Fig. 10, *b*. Main lattice dynamics parameters of studied ferroelectrics are shown in Table 2.

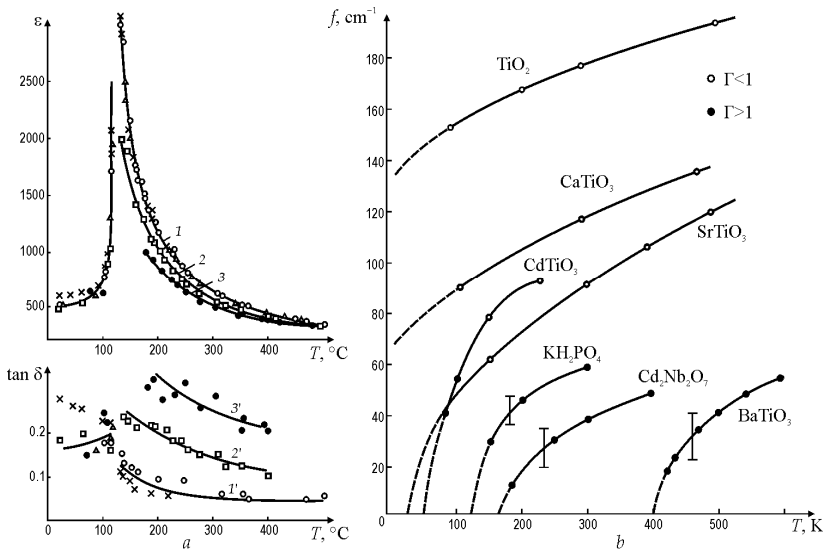

Fig.10. Paraelectrics at microwaves: $BaTiO_3$ ε (*1, 2, 3*) and tanδ (*1′, 2′, 3′*) temperature dependence at different frequencies: *1* – 9.4–37 GHz; *2* – 46 GHz; *3* – 76 GHz (*a*); soft modes frequency dependence for various paraelectrics obtained by microwave and far infrared experiments (*b*)

Material	P_c, μQ/cm²	$T_к$, K	θ, K	$C\cdot10^{-4}$, K	A/2π, GHz · $K^{-1/2}$
$CaTiO_3$	–	–	– 90	4.5	170
$SrTiO_3$	–	–	35	8.4	180
$BaTiO_3$	30	400	388	12	75
$PbTiO_3$	80	780	730	15	90
$KNbO_3$	30	685	625	18	95
$LiNbO_3$	70	1500	–	–	–

Table 2. Lattice parameters of some ferroelectric materials

3. Ferroelectric films investigation

3.1 Various methods comparison

Most of existing studies of ferroelectric films (22 published experiments listed in the review by Gevorgian & Kollberg, 2001) are drawn with the use of electrodes. For instance, the opposite-electrodes method is employed to study the system Pt/BST/Pt (Banieki et al., 1998). However, in most cases, ferroelectric film is studied between planar electrodes applied to the opened surface of the film. In that case, film parameters can be extracted from the impedance of interdigital planar capacitor as well as from the coplanar phase shifter study. Nevertheless, in all mentioned methods, the "natural film" microwave ε and tanδ remain unknown, because a complex system of "electrode-film-electrode" is investigated. Nevertheless, the data related to the "natural film" as well as to film components properties and substrates properties are important: their frequency and temperature characteristics are shown in Fig. 11.

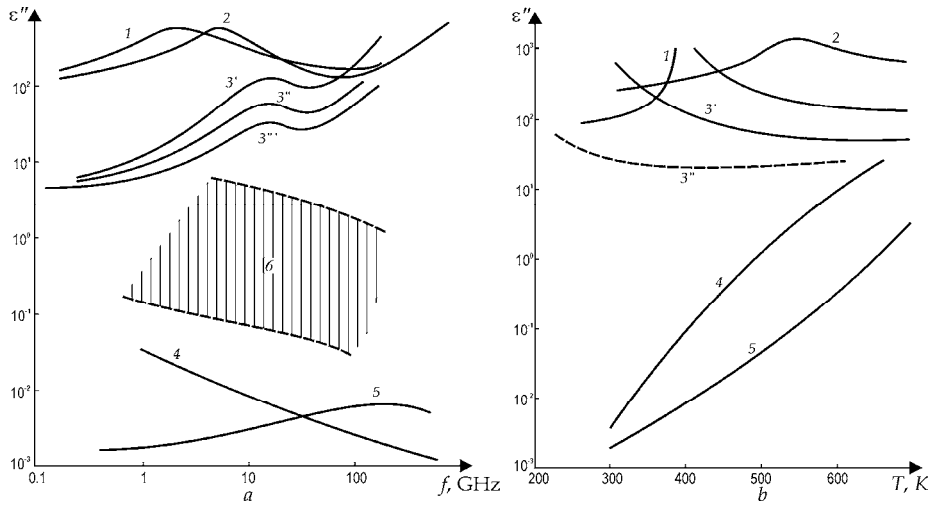

Fig. 11. Films, ceramics and crystals characterization at microwaves; ε″frequency dependence at 300 K: *1* – $BaTiO_3$ ceramics; *2* – PbTi,ZrO_3 ceramics; *3′*– BST (Ba,$SrTiO_3$) ceramics; *3″*– BST film 15 μm, 3‴ – BST film 2 μm, *4* – Si crystal, *5* – GaAs crystal; 6 – mixed oxides of BaO, TiO_2, PbO, SrO before film synthesis (*a*); ε″ temperature dependence at 80 GHz: *1* – $BaTiO_3$ ceramics; *2* –PbTi,ZrO_3 ceramics, *3′*– BST ceramics, *3″*– BST film 15 μm, *4* – Si crystal, *5* – GaAs crystal (*b*)

It is necessary to note that dielectric constant calculation from the planar capacitance is approximate while microwave loss cannot be even estimated. Point is that metallic electrodes strongly affect onto measured ε_{film} value (and especially onto film's tanδ) through the mechanical stress and skin effect in electrodes. Moreover, as a rule, dielectric parameters of film with interdigital electrodes are usually obtained at low frequency (of about 1 MHz); however, next this information is applied to microwave device elaboration. In the mass production small portion of the substrate could be sacrificed for test electrodes area. However, in laboratory study, single film gets unusable after electrodes deposition. So the electrodeless techniques are very important. A comparison of different methods of ferroelectric film study at microwaves is shown in Fig. 12.

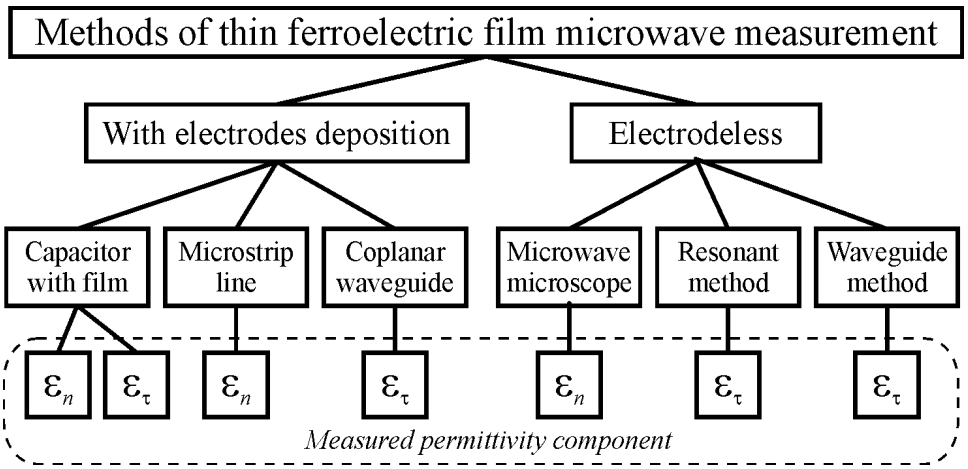

Fig. 12. Microwave methods for ferroelectric films study

Thin ferroelectric film is usually deposited onto dielectric substrate. Practically used films have thickness of 0.1–1 mm. Thermal expansion coefficient and lattice parameter of the substrate are different from those of thin film. Thus, film suffers from mechanical stress. This stress changes films properties comparing to the properties of bulk ferroelectric. Dielectric constant and loss could be decreased by order of magnitude. On the other hand, directional mechanical stress contributes to the anisotropy of film's parameters. So methods of films study must not only register film's response, but consider anisotropy as well.
Because of high dielectric constant and loss microwave testing of ferroelectrics is quite complex. In thin film study a question becomes even more complicated by film small thickness. This work presents waveguide method, suitable for thin films study.

3.2 Waveguide method description

Common technique for dielectric material measuring in the waveguide usually relies on complex scattering parameters measurement of waveguide section which cross section is filled with studied material. That technique can be easily adapted for measurement of the layered structures where properties of one layer are unknown.
However, this approach faces irresolvable difficulties with thin films. Simple estimation shows that X-band waveguide being entirely baffled with film of 1 μm thickness that has $\varepsilon = 1000$ and $\tan\delta = 0.05$ has phase perturbation of only about 0.4°, and brings attenuation of about -0.002 dB. These quantities are obviously out of equipment resolution capabilities. That is why, the goal is to arrange the interaction of film with electromagnetic field in such a way that brings recognizable response.
In proposed method, film-on-substrate specimen is centrally situated along the waveguide (Fig. 13). It is known that electric field intensity is highest in centre of waveguide so highest possible interaction of film with the electric field is provided.
Dielectric constant and loss can be found by solving scattering equations at one certain frequency. However, the accuracy of one-point technique is strongly affected by the accidental error (Baker-Jarvis, 1990). Proposed method accuracy is improved by the recording of complete frequency dependence of scattering parameters using contemporary vector network analyzer. Similarly to the method for bulk samples study, gathered experimental data then processed utilizing nonlinear least squares curve fitting technique (3).

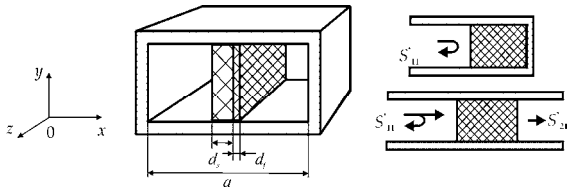

Fig. 13. Schematic representation of experiment

For the *S*-parameters calculations, electromagnetic field problem can be solved utilizing longitudinal wave representation (Egorov, 1967), (Balanis, 1989). Applying boundary conditions on media boundaries yields a complex nonlinear equation with respect to complex propagation constant:

$$\begin{aligned}
&\beta_s \tan\left(\beta_s \frac{a}{2} - \varphi_s\right) = \beta_f \tan\left(\beta_f \frac{a}{2} - \varphi_f\right);\\
&\varphi_s = \beta_s\left(\frac{a}{2} - d_s\right) + \operatorname{atan}\left[\frac{\beta}{\beta_s}\cot\left(\beta\left(\frac{a}{2} - d_s\right)\right)\right];\\
&\varphi_f = \beta_f\left(\frac{a}{2} + d_f\right) + \operatorname{atan}\left[\frac{\beta}{\beta_f}\cot\left(\beta\left(\frac{a}{2} + d_f\right)\right)\right],
\end{aligned} \tag{8}$$

where $\beta = \sqrt{k^2 - \gamma^2}$, $\beta_s = \sqrt{\varepsilon_s k^2 - \gamma^2}$, $\beta_f = \sqrt{\varepsilon_f k^2 - \gamma^2}$ are transverse wave numbers in the air, substrate and film media respectively, d_s is substrate thickness, d_f is film thickness, a is width of wide wall of waveguide, γ is propagation constant, k is free space wave number. In this equation, the position of film-substrate boundary assumed to be exactly at the middle of waveguide, however known displacement can be taken in account.

3.3 Experimental result

Described measurement technique was utilized for study of BST thin films. The film of about 1 μm thickness was deposited onto 0.5mm MgO substrate in a pulsed laser ablation setup. Special measurement cell was elaborated to provide reliable contact of specimen under test with waveguide walls, Fig. 14. Automatic network analyzer was calibrated with

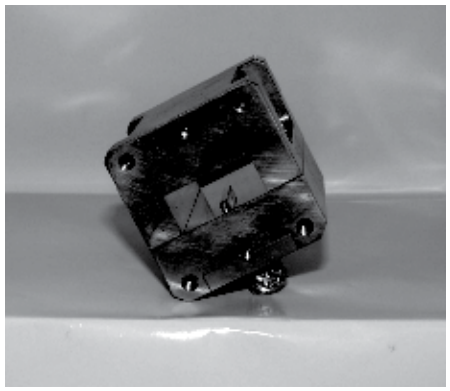

Fig. 14. Waveguide measurement cell for thin films study

appropriate X-band calibration kit. Then two reference measurements were performed. First one is a measurement of empty cell. It makes possible to determine cell's electrical length more precisely. Second one is the measuring of substrate alone. This stage is required to determine the actual loss of the "substrate-in-waveguide" system because only on this background film properties will be recognized.
Numerous experiments with the same samples show reliable repeatability of experiments. Fig. 15 illustrates an example of measured data fitting for MgO substrate and 0.84μm thick BST film.

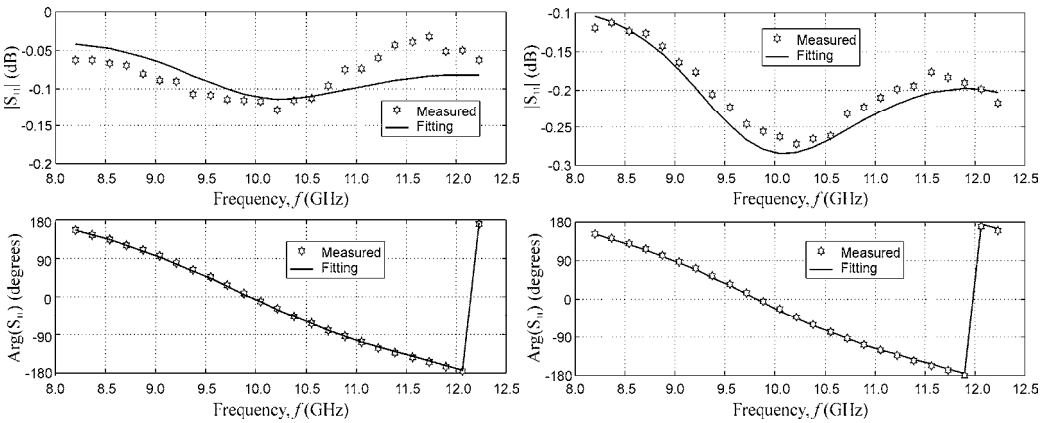

Fig. 15. Measured data and calculation for: 0.5 mm thickness MgO substrate (*a*), 0.84 μm BST film on 0.5 mm thickness MgO substrate. Specimen dimensions are 22 × 10 mm (*b*)

Average value of substrate permittivity is ε' = 9.9, tanδ = $3 \cdot 10^{-4}$. As to the film fitting to the calculation exhibits good agreement and yields ε = 450, tanδ = 0.05. Both reflection of shorted waveguide with sample and transmission in the 2-port system can be used, however the first method is preferable because of higher sensitivity.
Presented technique of thin ferroelectric film examination can be applied also for study of relatively thick (10μm and more) films that have non-ferroelectric nature. The method can be successfully used, for example, to study semiconductor films deposited onto dielectric subtract when traditional metering technique brakes down.

3.4 Uncertainty of non-resonant waveguide method for thin films measurement

Ideal contact of studied specimen with waveguide walls is hard to achieve and there small air gaps on the interface. These gaps may degrade accuracy substantially. Though some estimations consider 2.5-7 μm gap acceptable (Champlin & Glover, 1966), this value is too general and hard to verify. So it is desirable to enforce interface contact as much as possible.
Though films permittivity and loss are estimated using least squares curve fitting technique (3), let's begin uncertainty estimation with single point accuracy. Parameters of studied film are derived from indirect measurements. They contain uncertainties of dimensions measurements, scattering parameters magnitude and phase uncertainties, and rounding errors of processing procedure. In waveguide experiment magnitude and phase of reflection coefficient are measured directly (real and imaginary part to be precise, but that does not change further explanations). Their simulation values depend on sample's physical dimensions, permittivity and loss:

$$\dot{S} = \dot{S}\left(\varepsilon_f, \tan\delta_f, \varepsilon_s, \tan\delta_s, L, d_f, d_s\right), \tag{9}$$

where $\varepsilon_f, \tan\delta_f$ is permittivity and loss of studied film, $\varepsilon_s, \tan\delta_s$ is permittivity and loss of the substrate, L is sample's length, d_f, d_s is film and substrate thickness respectively. This equation is implicit function, which relates mentioned parameters.

Due to low loss substrate effective loss of measurement cell is low. In such conditions permittivity is mainly found by phase measurement, whereas loss is found from magnitude measurements (Janezic & Jargon, 1999). Large difference in sensitivities allows separate analysis of permittivity and loss uncertainties.

Sensitivities of calculated values of film's permittivity and loss to uncertainties of directly measured values can be estimated using rules of implicit function differentiation. Then for every given frequency permittivity and loss uncertainty can be expressed as:

$$\begin{aligned}
\Delta\varepsilon_f &= \frac{1}{\dfrac{\partial\angle S_{11}}{\partial\varepsilon_f}}\sqrt{\left(\frac{\partial\angle S_{11}}{\partial L}\Delta L\right)^2 + \left(\frac{\partial\angle S_{11}}{\partial d_f}\Delta d_f\right)^2 + \left(\Delta\angle S_{11}\right)^2 + \left(\frac{\partial\angle S_{11}}{\partial\varepsilon_s}\Delta\varepsilon_s\right)^2}; \\
\Delta\tan\delta_f &= \frac{1}{\dfrac{\partial|S_{11}|}{\partial\tan\delta_f}}\sqrt{\left(\frac{\partial|S_{11}|}{\partial L}\Delta L\right)^2 + \left(\frac{\partial|S_{11}|}{\partial d_f}\Delta d_f\right)^2 + \left(\Delta|S_{11}|\right)^2 + \left(\frac{\partial|S_{11}|}{\partial\tan\delta_s}\Delta\tan\delta_s\right)^2},
\end{aligned} \tag{10}$$

where ΔL uncertainty of length measurement, Δd_f is uncertainty of film thickness measurement, $\Delta|S_{11}|$ is uncertainty of magnitude of scattering parameter, $\Delta\angle S$ is uncertainty of phase of scattering parameter, $\Delta\varepsilon_s$ and $\Delta\tan\delta_s$ is uncertainty of substrate's parameters. Listed uncertainties are related to instrument uncertainties. Uncertainty of substrate thickness measurement is usually much smaller, than listed values, so it is omitted for the sake of clarity, though might be accounted exactly same way. Listed uncertainties were estimated numerically for the following conditions: frequency 10 GHz, film's thickness 1 μm, film's permittivity ε = 500, loss tanδ = 0.05, sample length 20 mm, substrate thickness 0.5 mm, permittivity ε = 9.9, loss tanδ = 10^{-4}, their values presented in Table 3. Table 4 presents summary on instrument uncertainties.

$\frac{\partial\angle S_{11}}{\partial\varepsilon_f}, \deg$	$\frac{\partial\angle S_{11}}{\partial L}, \frac{\deg}{m}$	$\frac{\partial\angle S_{11}}{\partial d_f}, \frac{\deg}{m}$	$\frac{\partial\angle S_{11}}{\partial\varepsilon_s}, \deg$
0.04	35000	$2.2\cdot10^7$	22
$\frac{\partial\lvert S_{11}\rvert}{\partial L}, \frac{dB}{m}$	$\frac{\partial\lvert S_{11}\rvert}{\partial d_f}, \frac{dB}{m}$	$\frac{\partial\lvert S_{11}\rvert}{\partial\tan\delta_s}, dB$	$\frac{\partial\lvert S_{11}\rvert}{\partial\tan\delta_f}, dB$
30	1700	0.02	4.23

Table 3. Sensitivities to uncertainties of directly measured values

Parameter	Value	Note
ΔL	10 μm	Micrometre screw
Δd_f	10 nm	Reflectometer
$\Delta\varepsilon_s$	0.1	1%
$\Delta\tan\delta_s$	10^{-4}	10%
$\Delta\lvert S_{11}\rvert$	0.02	HP 8510C
$\Delta\angle S_{11}$	2°	HP 8510C

Table 4. Instrument uncertainties

For the film under consideration uncertainty of permittivity measurement $\Delta\varepsilon/\varepsilon$ is about 14%, while uncertainty of loss measurement $\Delta\tan\delta_f/\tan\delta$ is about 93%. For the film with loss $\tan\delta = 0.1$ loss uncertainty will be 47%.
If method applied for film study in production process, i.e. the same substrate used in all measurements, then uncertainty of substrate permittivity and loss could be eliminated and permittivity uncertainty improves to about 10%.
These values present worst case estimation of single point measurement. Uncertainty of final parameters is reduced by least squares processing. With 50 point equally distributed along measurement frequency range sensitivity to uncertainty of scattering parameter determination can be reduced by order of magnitude to

$$\frac{\partial\varepsilon_f}{\partial\angle S_{11}} = 3\frac{1}{\deg}; \qquad \frac{\partial\tan\delta_f}{\partial|S_{11}|} = 0.15.$$

Then averaged uncertainty of film's permittivity reduces to 2% and loss to 10%.

3.5 Coplanar line method

In actual devices a system of electrodes is deposited on the surface of ferroelectric film. Geometry of the electrodes depends on film permittivity. At the same time metal electrodes can modify film permittivity and loss. Therefore it would be desirable to perform measurement directly in the device with deposited electrodes.
One of the most usable electrode system forms a coplanar line, Fig.16. Measurement of permittivity and loss of ferroelectric film integrated in coplanar line is discussed below.

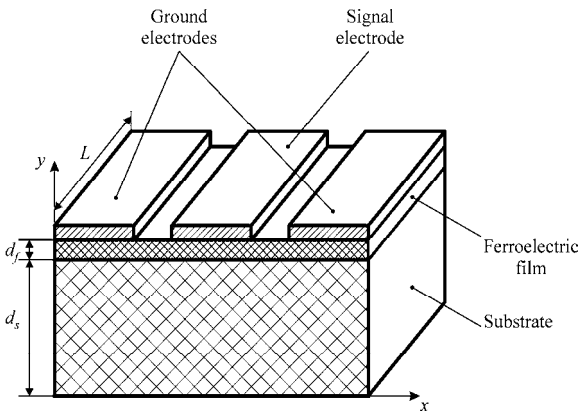

Fig. 16. Coplanar line on substrate with deposited ferroelectric film

Electromagnetic field problem for the structure given in Fig.16 was solved by finite element method. Electromagnetic field of quasi TEM mode was described in terms of vector and scalar potential applying the Lorenz gauge. As a result the problem was reduced to partial differential equation for scalar potential φ :

$$\nabla\left(\varepsilon(y)\nabla\varphi\right)+\varepsilon^2(y)k^2\varphi=0\,, \tag{11}$$

where $\varepsilon(y)$ is distribution of dielectric permittivity along the y – axis. Characteristic impedance Z and effective permittivity ε_{ef} of coplanar line can be found from solution of equation (11) by formulas:

$$\begin{aligned} Z &= Z_0\frac{V^2}{\sum\limits_{i=1}^{N}\sqrt{\varepsilon_i}\iint\limits_{S_i}\left(\left(\frac{\partial\varphi}{\partial x}\right)^2+\left(\frac{\partial\varphi}{\partial y}\right)^2\right)dxdy}; \\ \varepsilon_{ef} &= \frac{\sum\limits_{i=1}^{N}\left(\varepsilon_i\iint\limits_{S_i}\left(\left(\frac{\partial\varphi}{\partial x}\right)^2+\left(\frac{\partial\varphi}{\partial y}\right)^2\right)dxdy\right)}{\iint\limits_{S}\left(\left(\frac{\partial\varphi_1}{\partial x}\right)^2+\left(\frac{\partial\varphi_1}{\partial y}\right)^2\right)dxdy}, \end{aligned} \tag{12}$$

where $Z_0\approx 120\pi\ \Omega$ is the characteristic impedance of free space, V is the electrode voltage, N is the quantity of domains with different permittivities, ε_i is the permittivity of the i -th domain, S_i is the cross-section are of the i -th domain, φ_1 is the solution of the equation (11) for the case if $\varepsilon_i=1, i=\overline{1,N}$.

Dependences of characteristic impedance and effective permittivity of coplanar line deposited on the ferroelectric film and low permittivity dielectric wafer versus permittivity of ferroelectric film and its thickness are shown in Fig.17.

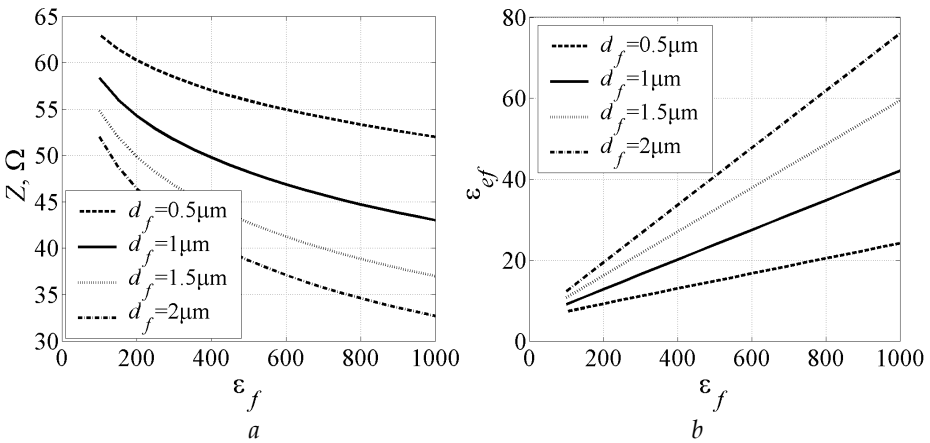

Fig. 17. Characteristic impedance (a) and effective permittivity (b) of coplanar line versus permittivity and thickness of ferroelectric film deposited on substrate with permittivity equal to 10

Measurement cell for study of permittivity and loss tangent of ferroelectric film is shown in Fig.18. Two-port measurement of frequency dependences of scattering parameters was performed by vector network analyzer.

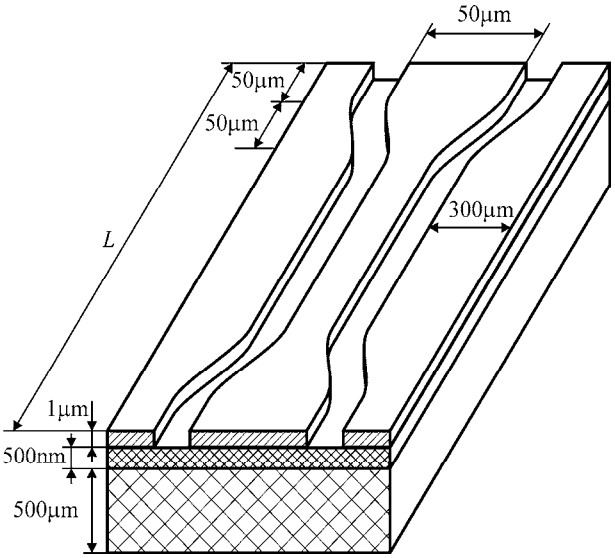

Fig. 18. Coplanar line measurement cell

Scattering matrix of coplanar line section with the length equal to L connected to ports with characteristic impedance Z_1 can be calculated from formulas:

$$S_{11} = j\frac{\left(Z^2 - Z_1^2\right)\sin\left(\gamma L\right)}{2ZZ_1\cos\left(\gamma L\right) + j\left(Z^2 + Z_1^2\right)\sin\left(\gamma L\right)}, \tag{13}$$

$$S_{21} = \frac{2ZZ_1}{2ZZ_1\cos\left(\gamma L\right) + j\left(Z^2 + Z_1^2\right)\sin\left(\gamma L\right)}, \tag{14}$$

where $\gamma = \dfrac{2\pi f\sqrt{\varepsilon_{ef}}}{c}$ is the propagation constant in the coplanar line.

Measured frequency dependences of scattering matrix parameters were approximated by formulas (13) and (14) by least square method:

$$\min_{\left(\varepsilon_f,\,\tan\delta_f\right)} \sum_n \sigma_n \left(S_n^{meas} - S\left(f_n, \varepsilon_f, \tan\delta_f\right)\right)^2, \tag{15}$$

where $S\left(f_n, \varepsilon_f, \tan\delta_f\right)$ is calculated value of scattering parameter at the frequency f_n assuming tested film to have permittivity ε_f and loss tangent $\tan\delta_f$.

Fig.19 demonstrates measured and calculated after solving of approximation problem (15) the frequency dependences of scattering matrix parameters for the structure presented in Fig.18.

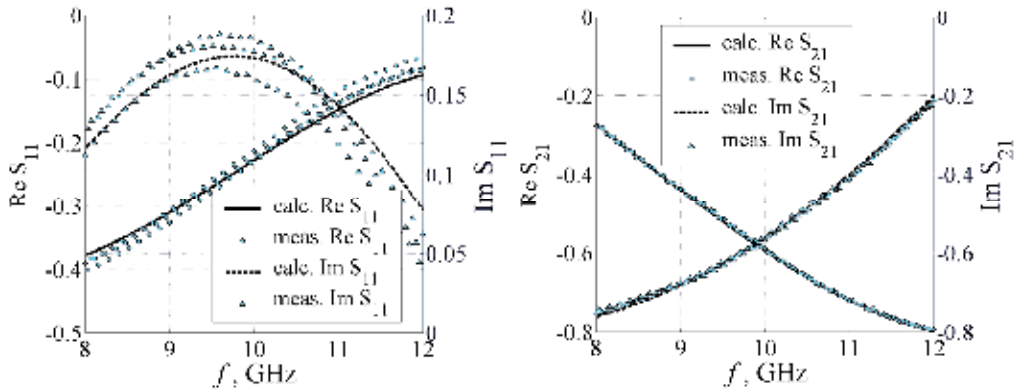

a b

Fig. 19. Measured and calculated frequency dependences of scattering matrix parameters S_{11} (a) and S_{21} for the structure shown in Fig. 18

Relative uncertainty of film permittivity measurement can be defined as uncertainty of implicit measurement:

$$\delta\varepsilon_f = \frac{1}{\left|\Theta^S_{\varepsilon_f}\right|}\sqrt{(\delta \mathrm{S})^2 + \left(\Theta^S_{d_f}\delta d_f\right)^2 + \left(\Theta^S_L \delta L\right)^2 + \left(\Theta^S_h \delta h\right)^2 + \left(\Theta^S_{\varepsilon_s}\delta\varepsilon_s\right)^2} \tag{16}$$

where $\Theta^\alpha_\beta = \frac{\beta}{\alpha}\frac{\partial\alpha}{\partial\beta}$ is the sensitivity of the parameter α to alteration of the parameter β, $\delta\beta$ is the relative uncertainty of the parameter β measurement, S is the measured parameter of scattering matrix, ε_s is the permittivity of substrate, h is the substrate thickness.

Analysis of the formula (16) predicts that uncertainty of film thickness measurement makes the main contribution in measurement uncertainty of film permittivity. Estimation prediction of film permittivity measurement uncertainty is about 10% if uncertainty of film thickness measurement is about 10 nm for the film thickness about 500 nm and its permittivity around 200. The uncertainty rises up while either film thickness or its permittivity decreases.

Uncertainty of film loss tangent measurement is larger than uncertainty of permittivity measurement because of smaller value of the sensitivity of scattering matrix parameters to alteration of film loss tangent $\Theta^S_{\tan\delta_f}$. Estimation predicts the uncertainty of film loss tangent measurement around 30% for the film thickness about 500 nm and its permittivity around 200.

Described technique was verified during measurement of ferroelectric films deposited by sol-gel method on semi-insulated silicon substrate. Some results of the verification are presented in table 5.

Ferroelectric film composition	Annealing temperature, °C	Film thickness, μm	Permittivity
$Pb(Ti,Zr)O_3$	700	0.35	90±15
$Pb(Ti,Zr)O_3$	800	0.35	120±15
$(Ba,Sr)TiO_3$	650	0.2	125±30
$(Ba,Sr)TiO_3$	750	0.2	250±40

Table 5. Results of investigation of ferroelectric films deposited on semi-insulated silicon substrate by sol-gel method

3.6 Resonator method description

Thin ferroelectric films can also be studied using composite dielectric resonator (CDR) method. Simple equations for effective permittivity and loss, based on parallel layers model, in case of significant difference in layers thickness, which is a case for thin films, give inadequate results. Thus, electromagnetic problem for "film-on-substrate" composite dielectric resonator should be solved without approximations.

To calculate resonant frequencies of the CDR one may solve electromagnetic problem for the configuration, depicted in Fig. 20. Square shaped CDR of length L and thickness d_s is made from material with ε_s and placed inside waveguide with $a \times b$ cross-section parallel to its narrow wall. Waveguide is filled with ε_a. Dielectric film of thickness d_f and permittivity ε_f is deposited onto resonator surface. The problem is solved using partial domains method.

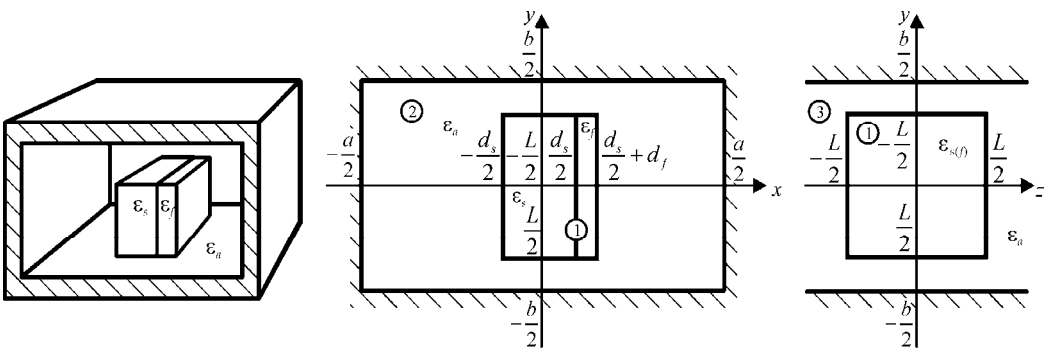

Fig. 20. Square shape CDR with film inside of rectangular waveguide

In every domain 1 and 2 electromagnetic field may be expressed using x-components of electrical $\Gamma^e = (\Gamma^e,0,0)$ and magnetic $\Gamma^m = (\Gamma^m,0,0)$ Hertz vectors. To do that electromagnetic field in every domain is presented as series of eigen functions:

$$\Gamma_i^{e(m)} = \sum_{j=0}^{\infty} A_{ij}^{e(m)} \Phi_{ij}^{e(m)}(x,y) Z_{ij}^{e(m)}(z), \tag{17}$$

where i is number of partial domain, $A_{ij}^{e(m)}$ series coefficients to be found, $\Phi_{ij}^{e(m)}(x,y)$ is eigen function number j of partial domain number i,, $Z_{ij}^{e(m)}(z)$ is solution of Helmholtz equation in every domain.

Using equality requirement for tangential components of the field in $|z|=\frac{L}{2}$ planes the problem can be reduced to the set of homogenous Fredholm's integral equations of the I kind relative to distribution of magnetic and electric Hertz vectors $\Psi^e(x,y)$, $\Psi^m(x,y)$:

$$\iint_S \left(G_n^e(x,x',y,y')\Psi^e(x,y)+G_n^m(x,x',y,y')\Psi^m(x,y)\right)dxdy=0, \quad n=1,2, \tag{18}$$

where S is waveguide cross-section. Integral equations kernels $G_n^e(x,x',y,y')$, $G_n^m(x,x',y,y')$ can be expressed with eigen functions of areas $\Phi_{ij}^{e(m)}(x,y)$, $Z_{ij}^{e(m)}(z)$ and their derivatives. Integral equation can be solved using the method of moments, so finally electromagnetic problem reduces to nonlinear eigen values problem. These eigen values are the resonant frequencies of studied system.

Basic mode oscillations can be excited as in waveguide, so in resonator itself. However, in matched waveguide section there are no parasitic oscillations, which are natural to standalone resonator.

CDR's made of Al_2O_3 (ε =9.6), $BaTi_4O_9$, and $DyScO_3$, $SmScO_3$, LSAT with ε = 26.3, 25.1, 22.7 respectively were simulated and studied experimentally. CDR dimensions ratio was in the range d/L = 0.2…0.01. Results summary is presented in Fig. 21.

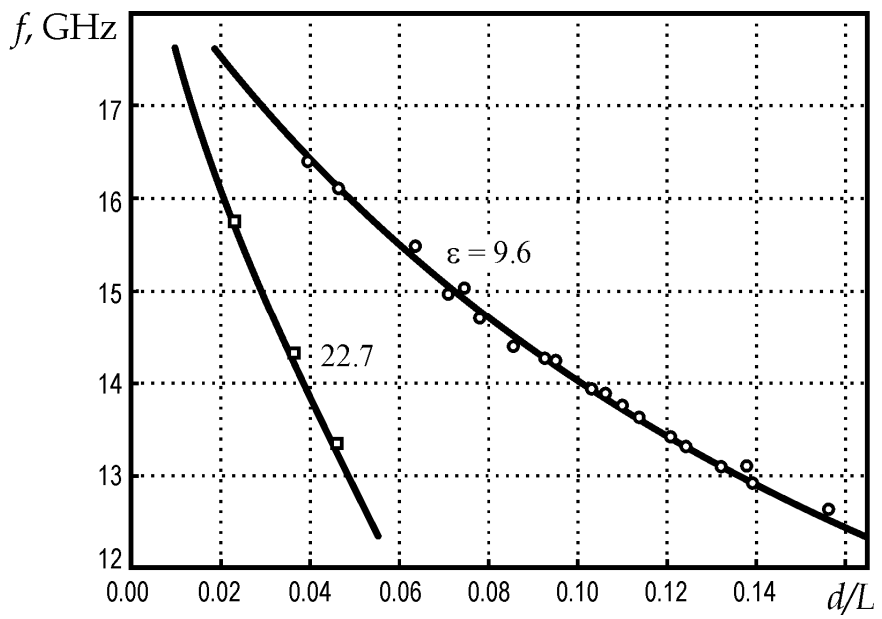

Fig. 21. Simulated and measured dependencies of CDR resonant frequency for small dimensions ratio (d/L) with ε_s = 9.6, 22.7, 26.3

Because all measurements are held relative resonant frequency of resonator without film, uncertainty depends mainly on dimensions uncertainty. Resonant frequency shift for CDR with film depends on film's thickness, Fig. 22. Frequency range, where this method is applicable, depends on CDR's resonant frequencies, which in turn depend on dimensions and substrate permittivity.

To reduce measurement uncertainty the resonator thickness d_s should be rather small. However it leads to increasing of resonator length L which would be greater than narrow wall width. In this case the resonator should be placed by such a way that ferroelectric film surface would be almost parallel to wide wall of waveguide with some angle shift to satisfy resonator excitation condition.

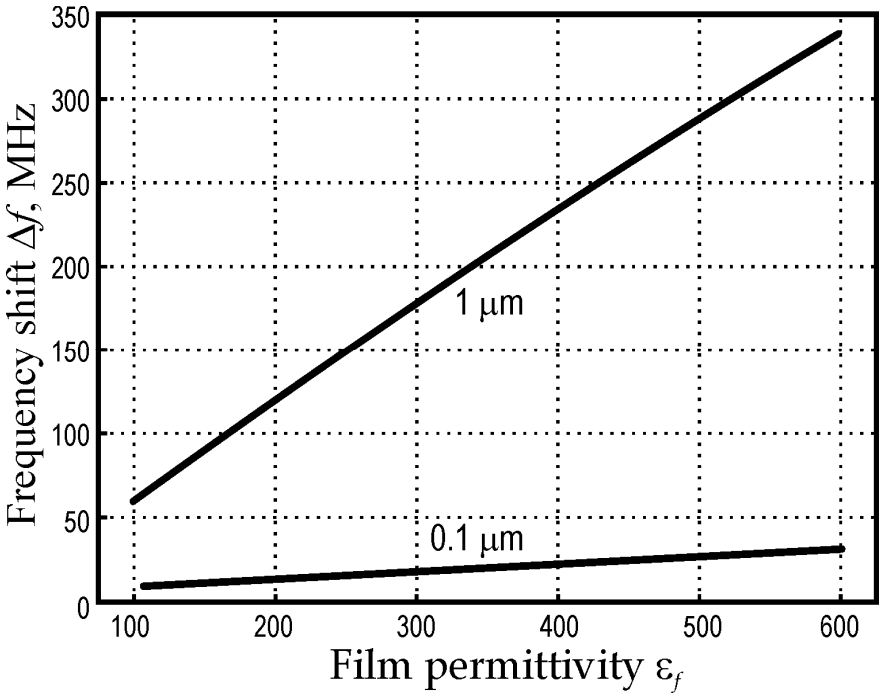

Fig. 22. Resonant frequency shift for 1 μm and 0.1 μm films on 0.1 mm thick substrate with ε = 26

4. Conclusion

Electrodeless methods for bulk and thin film ferroelectric materials study presented. In non-resonant methods partial filling of waveguide cross-section may be applied for rare and expensive materials study. Permittivity and loss of studied specimen are determined by solving scattering equations for waveguide section with studied specimen against measured scattering parameters. The choice for transmission or reflection method depends on sensitivity of scattering matrix to change of ε and tanδ of studied specimen. Study of scattering parameters frequency dependency and subsequent their approximation with appropriate measurement cell models allows to increase measurement accuracy and reduce susceptibility to random error.

To measure ε and tanδ of thin films studied specimen may be located lengthwise inside of rectangular waveguide. This allows better interaction of thin film with electromagnetic field.
For the system with metal electrodes deposited on the surface of ferroelectric film the coplanar line technique may be applied. This method can be extended for other electrode layouts.
Another option for thin films study might be use of resonant techniques. To increase sensitivity to film's properties thin composite resonator required. However, to tune it to required frequency composite resonator should have larger dimensions, thus irregular waveguide might be required. Otherwise sample should be oriented with large tilt angle, almost normal to waveguide's wide wall.

5. References

Baker-Jarvis J. (1990). Transmission/reflection and short-circuit line permittivity measurements, *NIST Technical Note 1341*, Jul. 1990

Baker-Jarvis, J. Geyer, R. G. & Domich, P. D. (1992). A nonlinear least-squares solution with causality constraints applied to transmission line permittivity and permeability determination. *IEEE Trans. on Instr. and Meas.,* Vol: 41, Issue: 5, Oct. 1992, pp. 646 – 652.

Balanis, C. A. (1989). *Advanced Engineering Electromagnetics*, Wiley, 1989, pp. 394–409, ISBN 0-471-62194-3

Banieki, J. D.; Laibowitz, R. R.; Shaw, T. M.; Duncombe, P. R. & Neumayer, D. A. (1998). Dielectric relaxation of Ba0.7Sr0.3TiO3 films from 1 MHz to 20 GHz, *Applied Phys. Lett.*, vol. 72, pp. 498-500, 1998

Champlin, K. S. & Glover, G. H. (1966). Gap effect in measurements of large permittivity. *IEEE Trans. Microwave Theory Tech.*, 1966, vol. 14, pp. 397-398

Egorov, Y. V. (1967). *Partially filled rectangular waveguides*, Soviet radio, Moscow, 1967, pp. 19–72 (in Russian).

Erker, E. G.; Nagra, A. S.; Liu, Yu; Periaswami, P.; Taylor, T. R.; Speck, J. & York, R.A. (2000). Monolitic Ka-band phase shifter using voltage tunable BaStTiO3 parallel plate capacitors. *IEEE Microwave and Guided Wave Letters*, vol. 10, # 1, January 2000, pp. 7-12

Gevorgian, S. S. & Kollberg, E.L. (2001). Do we really need ferroelectrics in paraelectric phase only in electrically controlled microwave devices? *IEEE Trans. Microwave Theory Tech.*, vol. 49, #11, Nov. 2001, pp.2117-2123

Janezic, M. D. & Jargon, J. A. (1999). Complex permittivity determination from propagation constant measurements. *IEEE Microwave and Guided Wave Letters*. Vol. 9, Issue 2, Feb. 1999, P. 76 – 78

Lanagan, M. T.; Kim, J. H.; Dube, D. C.; Jang, S. J. & Newnham, R. E. (1988). A Microwave Dielectric Measurement Technique for High Permittivity Materials, *Ferroelectrics*, Vol. 82, 1988, pp. 91-97

Vendik, O. G. (Ed.). (1979). *Ferroelectrics at Microwaves*, Soviet Radio, Moscow, Russia (in Russian)

Vendik, O. G.; Vendik, I. B. & Samoilova, T. B. (1999). Nonlinearity of superconducting transmission line and microstrip resonator. *IEEE Trans. Microwave Theory Tech.*, vol. 45, #2, Feb. 1999, pp. 173-178

Part 3

Characterization: Multiphysic Analysis

12

Changes of Crystal Structure and Electrical Properties with Film Thickness and Zr/(Zr+Ti) Ratio for Epitaxial $Pb(Zr,Ti)O_3$ Films Grown on $(100)_cSrRuO_3//(100)SrTiO_3$ Substrates by Metalorganic Chemical Vapor Deposition

Mohamed-Tahar Chentir[1], Hitoshi Morioka[1,2],
Yoshitaka Ehara[1], Keisuke Saito[2], Shintaro Yokoyama[1],
Takahiro Oikawa[1] and Hiroshi Funakubo[1]
[1]*Tokyo Institute of Technology, Department of Innovative and Engineered Materials, Interdisciplinary Graduate School of Science and Engineering*
[2]*Application Laboratory, Bruker AXS*
Japan

1. Introduction

Lead zirconium titanate, $Pb(Zr,Ti)O_3$ [PZT], have been intensively studied for various ferroelectric applications, and have a renewal interest due to their promising application for microelectromechanical systems (MEMS) because of their outstanding ferroelectric and piezoelectric properties. Remanent polarization (P_r) is the not only most fundamental parameter but also the practical importance for real applications to achieve high density devices. Spontaneous polarization (P_S) is the expected maximum P_r value of the materials that depend on the composition, orientation and the crystallinity of $Pb(Zr,Ti)O_3$. Thus, in an academic point of view, lots of efforts have been made to investigate P_S value. However, PZT crystals with single domain are hard to be obtained, inducing a lack of direct characterization of P_S values using PZT single crystal. This situation is due to $c/a/c/a$ polydomain structure of PZT, where a domain and c domain are respective (100) and (001) oriented domains. This domain structure is the result of relaxation process of stress induced under the growth process of PZT.

To achieve this purpose, we switch our idea from growth of the bulky single crystal to epitaxial films with polar axis orientation. In addition, a comprehensive and systematic characterization of ferroelectric properties of PZT films with different volume fraction of polar-axis-oriented domain is investigated.

This chapter investigates the thickness and Zr/(Zr+Ti) ratio dependencies of domain structure and ferroelectric properties, and correlates physical properties, namely lattice

parameters and the volume fractions of the domains, as well as the electrical properties such as P_r and P_S.

2. Experimental

PZT thin films were grown on $(100)_c SrRuO_3//(100)SrTiO_3$ substrates at 540°C by pulsed-metal organic chemical vapor deposition (MOCVD) from $Pb(C_{11}H_{19}O_2)_2$ - $Zr(O{\cdot}t\text{-}C_4H_9)_4$ - $Ti(O{\cdot}i\text{-}C_3H_7)_4$ - O_2 system (Nagashima et al., 2001). Epitaxial $(100)_c SrRuO_3$ thin films used for bottom electrode layers were grown on $(100)SrTiO_3$ substrates by MOCVD (Okuda et al., 2000). The Zr/(Zr+Ti) ratio and the film thickness of PZT films were controlled by the input gas concentration of the source gases and the deposition time, respectively. In this work, we studied PZT films having thickness ranging from 50 to 250 nm.

The orientation of the deposited films was analyzed by high-resolution X-Ray Diffraction (XRD) using a four-axis diffractometer (PANalytical X'Pert MRD). The high-resolution XRD reciprocal space mapping (HRXRD-RSM) was also employed for more detail analysis of crystal structure (orientation, in-plane and out-of-plane lattice parameters, and the internal axial angle) and estimating the relative volume fraction of the *c*-domain in tetragonal phase (Saito et al., 2003a).

Electron-beam deposition was used to deposit 100 μmϕ Pt top electrodes for the electrical property characterization of PZT films. The polarization – electric-field (*P* - *E*) hysteresis loops of the as-deposited films were measured at 20 Hz by the ferroelectric tester using pulsed rectangular wave (Radiant Technologies RT6000HVS and TOYO Corporation FCE-1).

3. Results and discussion

In this section, we demonstrate, first of all, film thickness dependency of the crystal structure of PZT films. We show that polar-axis-oriented films were obtained at very thin films region. Then, we detail the Zr/(Zr+Ti) ratio dependency of the domain structure. For this purpose, we will compare crystal structure evolution as a function of the Zr/(Zr+Ti) ratio at two thicknesses, 50 and 250 nm. This comparative study aims to emphasis the role of the Zr/(Zr+Ti) ratio in PZT film as well as the thickness dependency, discussed in first instance.

Finally, we will cross check the up mentioned results by monitoring the evolution of electrical properties versus thickness and the Zr/(Zr+Ti) ratio in the films. We will synthesis these data by identifying the linear relationship between the square of spontaneous polarization (P_s^2) and tetragonal distortion (1-*c*/*a*).

Nevertheless, prior to proceeding to this characterization, it is important to check the epitaxial relationship between the bottom electrode and PZT films.

Indeed, it must be kept in mind that the framework of this study is the fundamental understanding of the impact of crystal structure change on the electrical properties, and polycrystalline films might induce measurement artefacts. The epitaxial growth of PZT films on $(100)SrRuO_3//(100)SrTiO_3$ substrates was ascertained by High Resolution Transmittance Electron Microscopy (HRTEM) as presented on Fig. 1(a).

Indeed, Fig. 1(a) shows a cross-sectional TEM image of 50 nm thick PZT(35/65) film. It presents smooth interfaces. Fig. 1(b) reveals atomically sharp interface between PZT and

$SrRuO_3$ bottom electrode. Moreover, this latter figure shows clearly a coherent epitaxial relationship at PZT/$SrRuO_3$ interface.

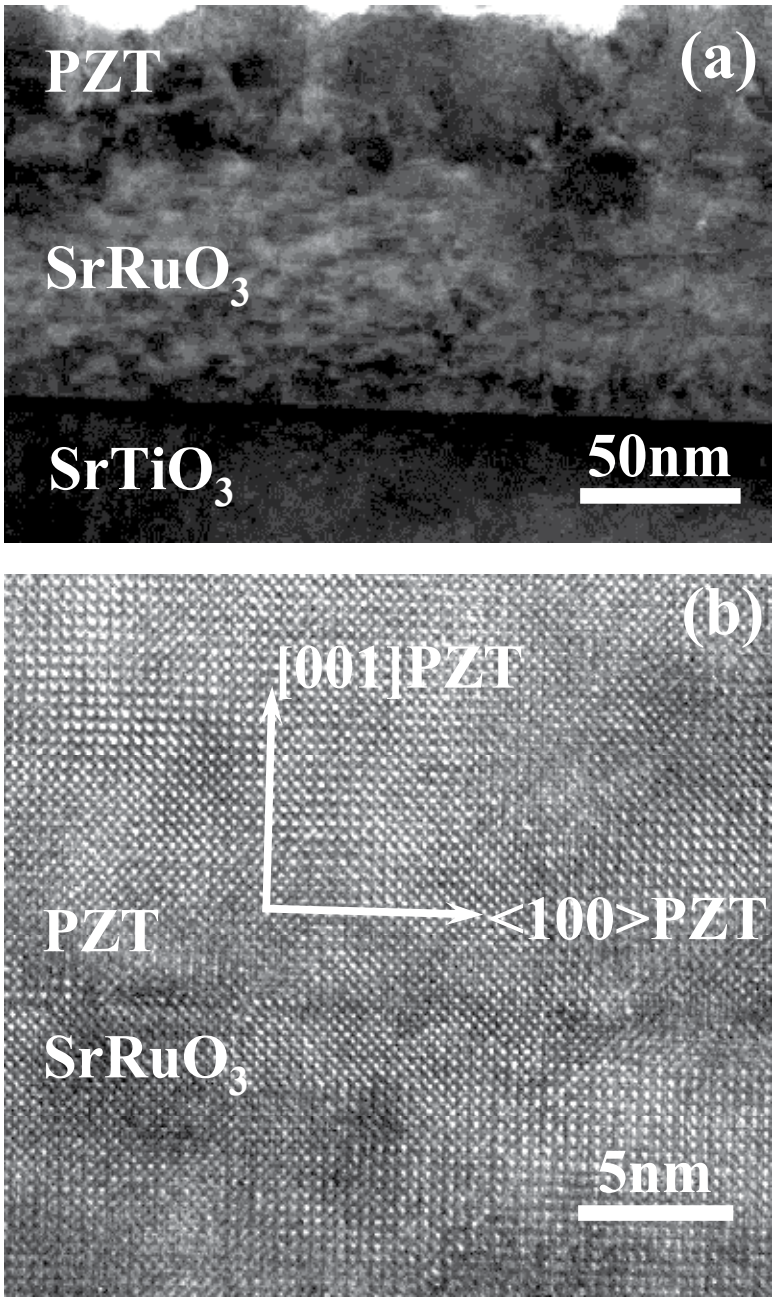

Fig. 1. Cross sectional TEM imaging of PZT(35/65)/$SrRuO_3$/$SrTiO_3$ (a). HRTEM of PZT-$SrRuO_3$ interface reveals a coherent epitaxial growth of PZT on $SrRuO_3$ bottom electrode (b).

3.1 Evolution of domain structure versus film thickness

For this part of our investigation, we chose to characterize PZT films with the Zr/(Zr+Ti) ratio of 0.35 that have a tetragonal symmetry. Fig. 2 presents XRD plots for the 2θ angle range of $2\theta = 40$ - 50°. On this figure we notice that PZT *200* peak decreases with decreasingly film thickness. This phenomenon might have two possibilities: one is the change of the tilting angle against the surface normal direction. The other is the change of domain structure from the mixed domain structure of *a* and *c* domains to fully *c*-domain oriented film with decreasing film thickness.

Hence, using XRD-RSM technique (Fig. 3), we could monitor *c*-domain volume fraction $[V_c = V_{(001)}/(V_{(100)}+V_{(001)})]$ as a function of film thickness as shown in Fig. 4. On this figure, we notice that films having thicknesses under around 75 nm, are perfect polar axis-oriented films. Over this threshold, *c*-domain volume fraction decreases almost linearly with increasing thickness up to 230 nm..

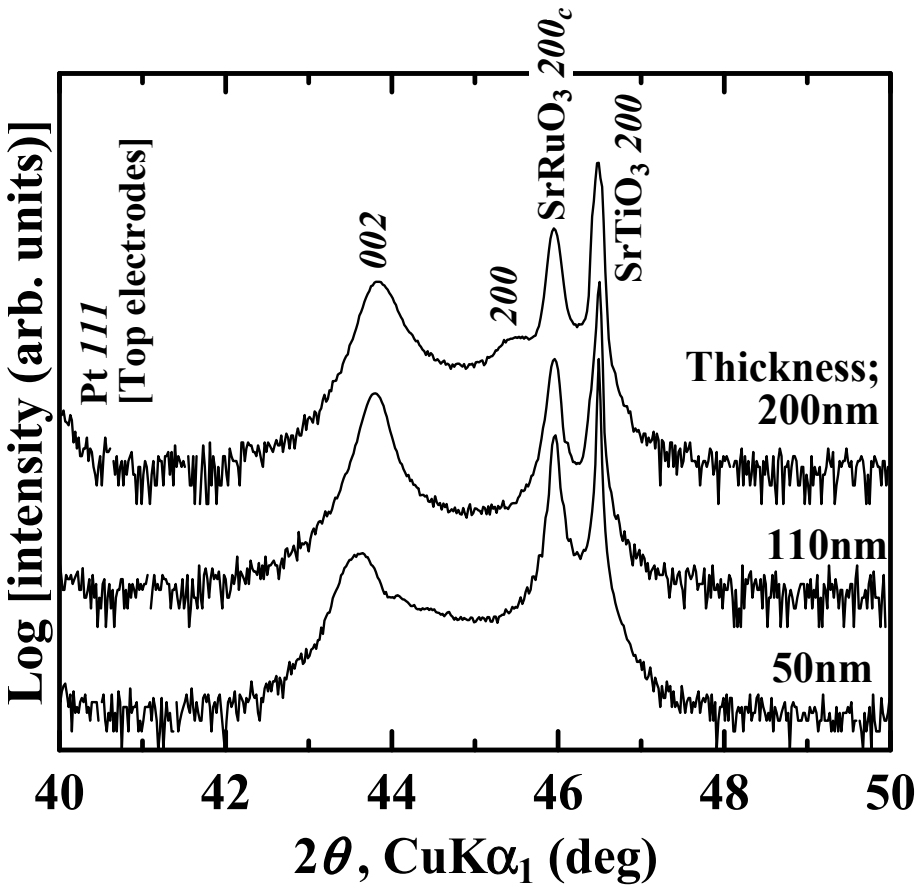

Fig. 2. XRD plots of PZT(35/65) films having thicknesses ranging from 50 to 200 nm. As film thickness increases, PZT *200* peak appears indicating the coexistence of *a*-domain with *c*-domains.

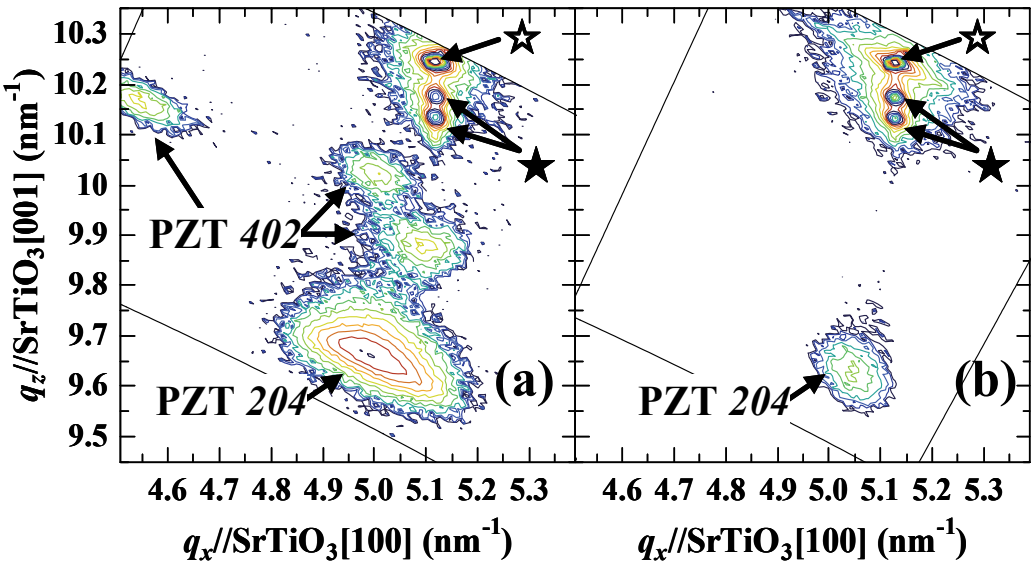

Fig. 3. XRD-RSM of PZT(35/65) films having thicknesses of (a) 250 nm and (b) 50 nm. SrTiO_3 *204* spot (☆) and splitted sport of SrRuO_3 *204* (★) are also illustrated.

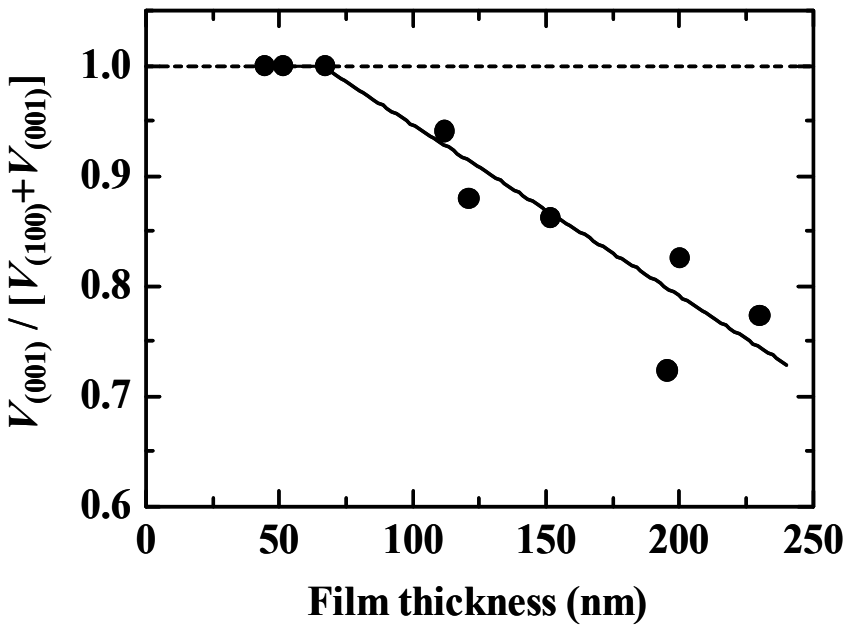

Fig. 4. Evolution of *c*-domain volume fraction [V_c=$V_{(001)}$/($V_{(100)}$+$V_{(001)}$)] as a function of PZT thickness in the case of PZT(35/65) films.

Finally, we checked strain condition when film thickness decrease in the case of PZT(35/65) material. For this purpose, we calculated the both in-plan ($a_{//}$ and $c_{//}$) and out-of-plan ($a_{\perp}$ and $c_{\perp}$) lattice parameters as a function of PZT film thickness (Fig. 5). On this figure, we also indicate $SrTiO_3$ lattice parameter (a= 0.3905 nm) as well as unstrained PZT(35/65) lattice parameters extracted from powder data (a = 0.398 nm and c = 0.413 nm) (Shirane & Suzuki, 1952). It is interesting to notice that in-plan and out-of-plan lattice parameters are almost constant regardless of the film thickness range studied in this work, demonstrating almost relaxed unit cells due to the large lattice mismatch between $Pb(Zr_{0.35}Ti_{0.65})O_3$ films and $SrTiO_3$ substrates.

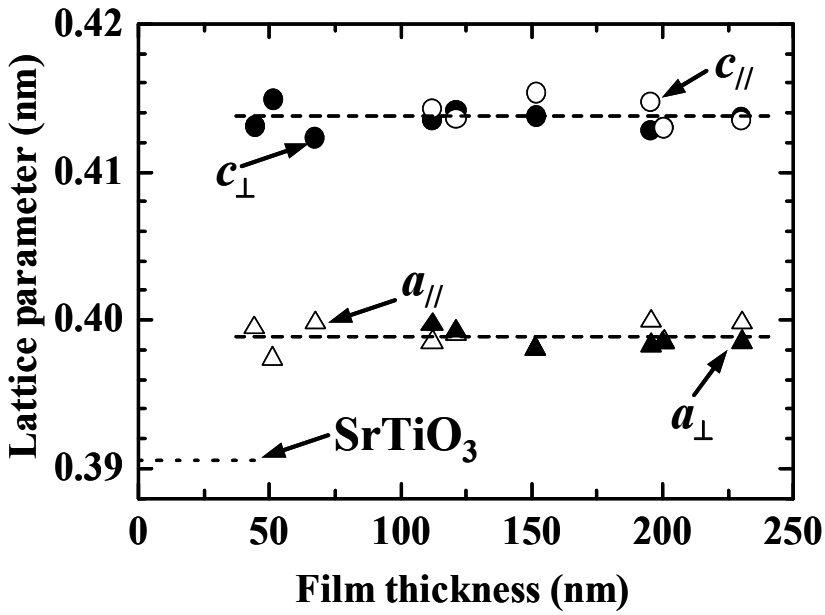

Fig. 5. In-plane and out-of-plane lattice parameters as function of film thickness in the case of $Pb(Zr_{0.35}Ti_{0.65})O_3$ films.

3.2 Domain structure evolution versus film composition

Fig. 6 presents X-ray diffraction diagrams of PZT films having 50 and 250 nm in thickness with various Zr/(Zr+Ti) ratio. All films are found to have (100) and/or (001) orientations regardless of the film thickness and Zr/(Zr+Ti) ratio. Epitaxial relationship of (001)/(100)PZT //(100)$_c$$SrRuO_3$//(100) $SrTiO_3$ was ascertained by XRD pole figure measurement for all films.
Figures 7(a) - (f) summarize a- and c-axes lattice parameters, tetragonality (c/a ratio) and the internal angles (α), and the unit cell volume as a function of the Zr/(Zr+Ti) ratio for 50 and 250 nm-thick PZT films. Reported data by Shirane et al. for PZT powder are also presented on these figures (Shirane & Suzuki, 1952).
As shown in Fig. 7, our experimental data are in good agreement with reported data of powders. However, an intermediate region can easily be observed in the 250 nm thick sample. This region could be related to the coexistence of both tetragonal and rhombohedral phases (Morioka et al. 2004a), suggesting a strain relaxation mechanism at this thickness (Morioka et al. 2004b).

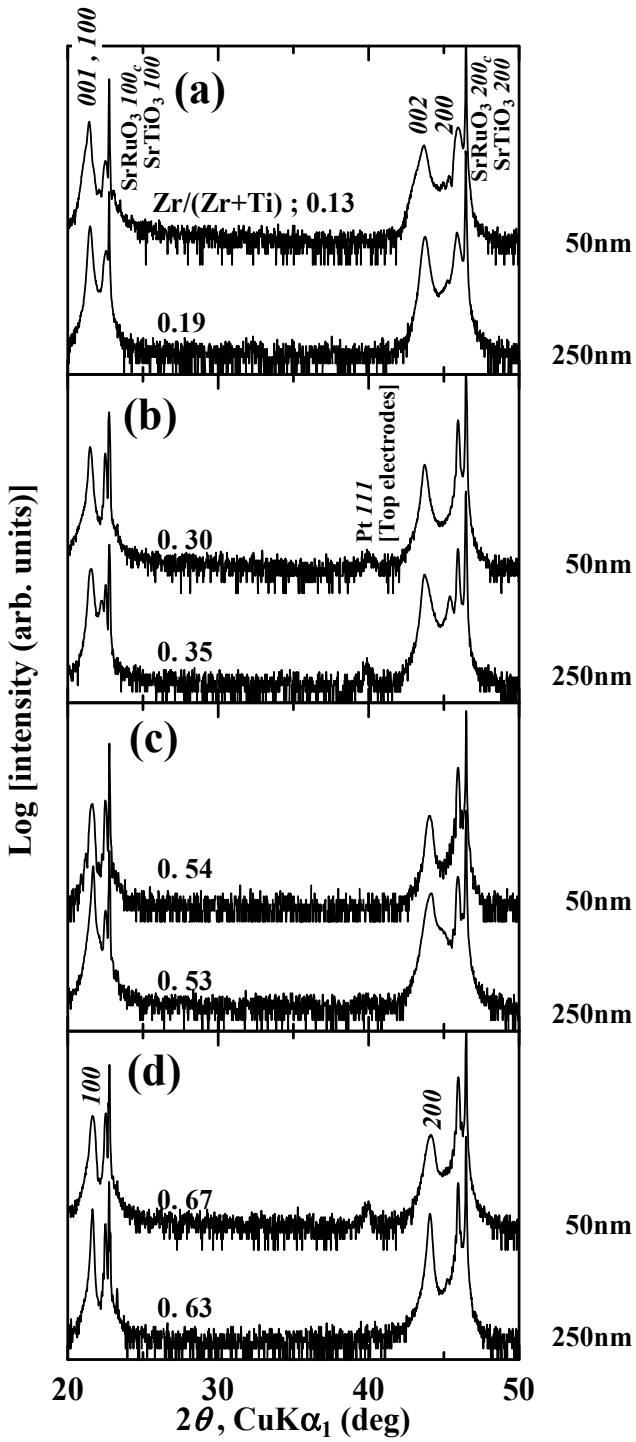

Fig. 6. XRD ω-2θ diagrams of PZT films having 50 and 250 nm in thickness and different Zr/(Zr+Ti) ratio: from small Zr/(Zr+Ti) ratio (a) to large Zr/(Zr+Ti) ratio (d).

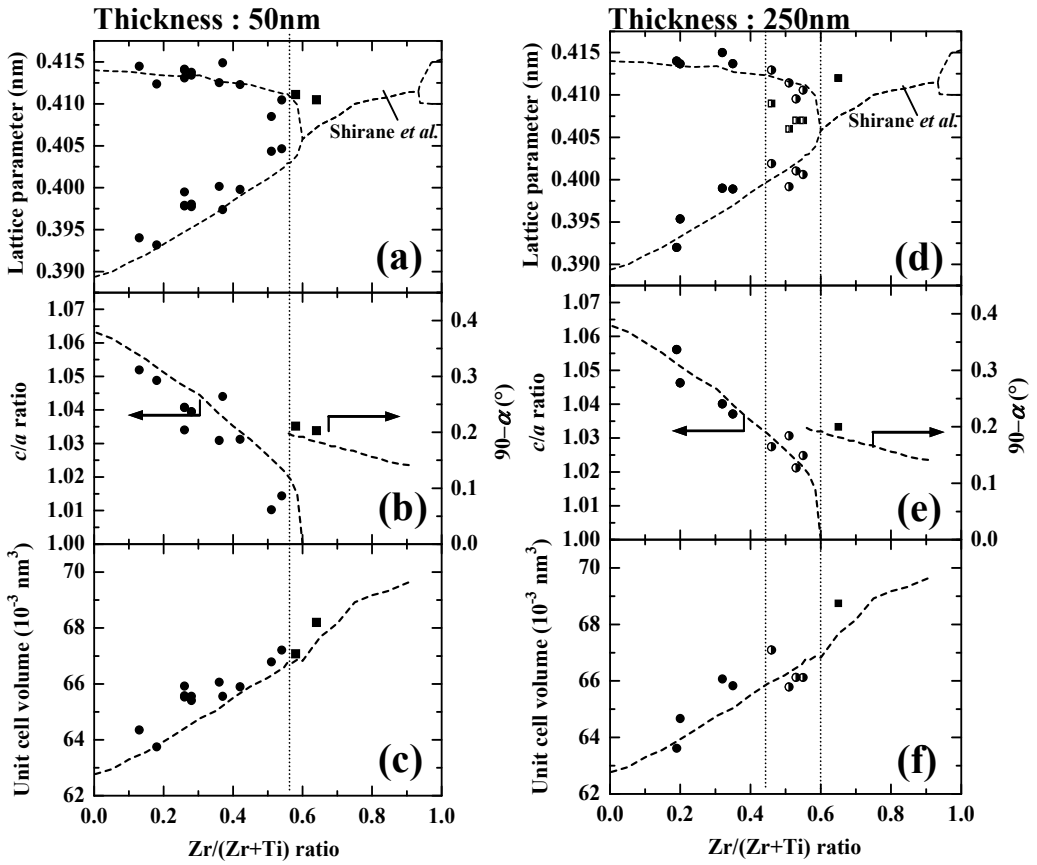

Fig. 7. Lattice parameters (a, d), tetragonality, c/a ratio, and the internal angles and (b, e), and unit cell volume (c, f) as a function of Zr/(Zr+Ti) ratio for (a)-(c) 50 and (d)-(f) 250 nm thick films. Dashed lines are powder data reported by Shirane et al (Shirane & Suzuki, 1952).

The c-domain relative volume fractions, V_c, are shown in Fig. 8 as a function of the Zr/(Zr+Ti) ratio. These values are obtained from HRXRD-RSM characterization reported elsewhere (Morioka et al. 2004a).

On this figure we notice that the 50 nm thick Films are fully polar axis-oriented films, (001) orientation, regardless of the Zr/(Zr+Ti) ratio up to 54% (Fig. 8(a)). On the other hand, V_c decreased with increasing PZT film thickness. Indeed, we notice for the 250 nm thick films (Fig. 8(b)) that V_c is about 70% up to Zr/(Zr+Ti) = 0.45. In the intermediate region, V_c fluctuates between 55 and 75% due to the experimental errors induced by the tetragonal and rhombohedral duplicated peaks (Saito et al., 2003b). This result is totally coherent with our previous results showing the domain structure simplification with decreasing PZT film thickness. The structure domain simplification from coexisting *a*- and *c*-domains to fully polar axis orientation is supported by the compressive stress appearing at very thin deposited films (Morioka et al., 2003; Morioka et al., 2009). This compressive stress is induced by the lattice misfit stress and thermal stress due to the mismatches of lattice parameters and thermal expansion coefficients between PZT films and $SrTiO_3$ substrates, respectively.

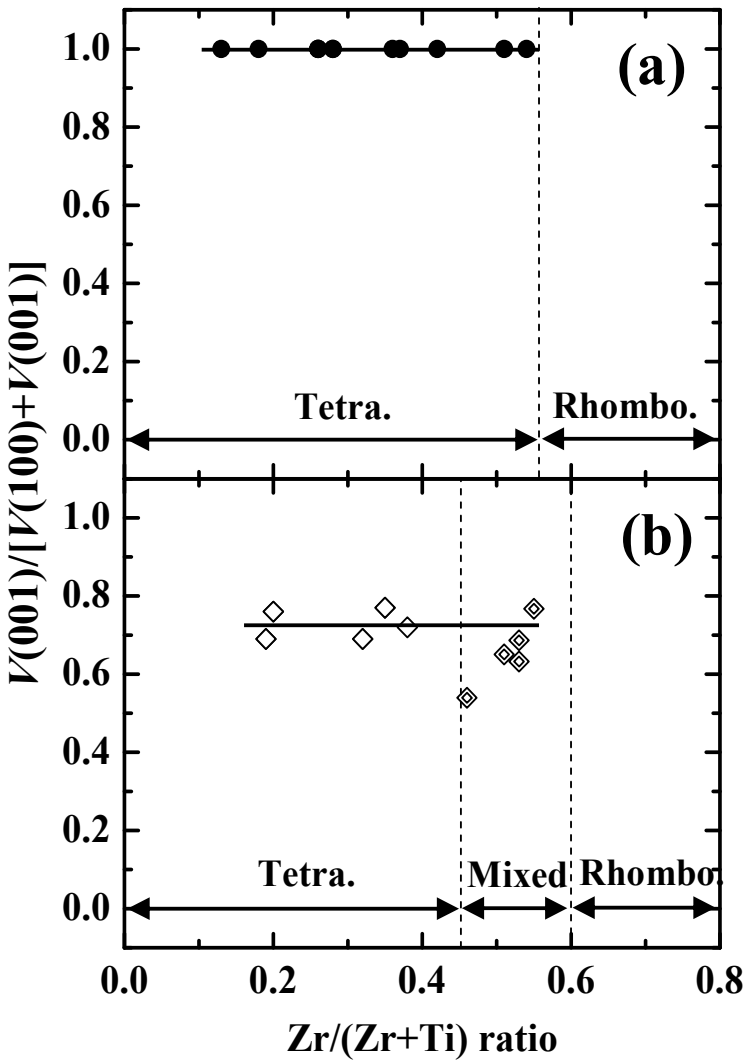

Fig. 8. c-domain volume fraction, V_c, measured from HRXRD-RSM data (Morioka et al. 2004a) for (a) 50 and (b) 250 nm thick PZT films.

3.3 Electrical characterization

Fig. 9 shows the leakage current density as a function of applied electric field for 50 and 250 nm thick PZT films with various Zr/(Zr+Ti) ratio. We notice that PZT thickness and Zr/(Zr+Ti) ratio influences leakage current density. Indeed, below 20% of Zr/(Zr+Ti) ratio, the 250 nm thick films show higher current density than 50 nm thick sample [see Fig. 9(a)]. Increasing Zr/(Zr+Ti) ratio in films lead to a decrease of the leakage current density level in the 250 nm thick PZT films from above 10^{-3} A/cm² to 10^{-6} A/cm² at an electric field of 100 kV/cm for Zr/(Zr+Ti) ratio ranging from 0.19 and 0.63 respectively.

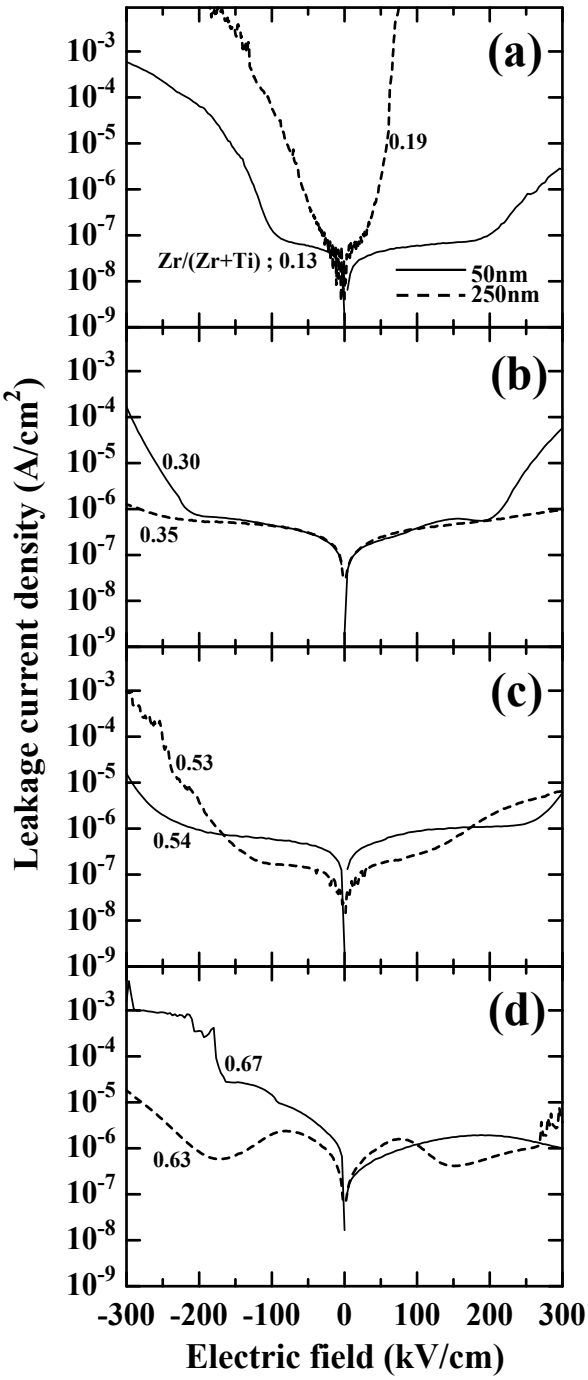

Fig. 9. Leakage current density as a function of electric filed for 50 nm thick (plain line) and 250 nm thick (dotted line) PZT thin films with different Zr/(Zr+Ti) ratio: from small Zr/(Zr+Ti) ratio (a) to large Zr/(Zr+Ti) ratio (d).

On the other hand, the 50 nm thick PZT film show a relatively low leakage current level oscillating between 10^{-7} and 10^{-5} A/cm² at an electric field of 100 kV/cm, independently from the Zr/(Zr+Ti) ratio. These results are coherent with reported data (Shiosaki, 1995; Oikawa et al., 2002). Indeed, it has been shown that PZT films with low Zr/(Zr+Ti) ratio present typically larger leakage current density compared to that of films with large Zr/(Zr+Ti) ratio (Shiosaki, 1995). While it has been revealed (Oikawa et al., 2002) that Sr and/or Ru diffusion into PZT might create a conductive path, which is in good agreement with our results because a longer deposition time could induce a large amount of Sr and/or Ru diffusion into the bottom electrode.

Fig. 10 summarizes the polarization - electric field (*P* - *E*) relationships for films with various Zr/(Zr+Ti) ratio and film thickness.

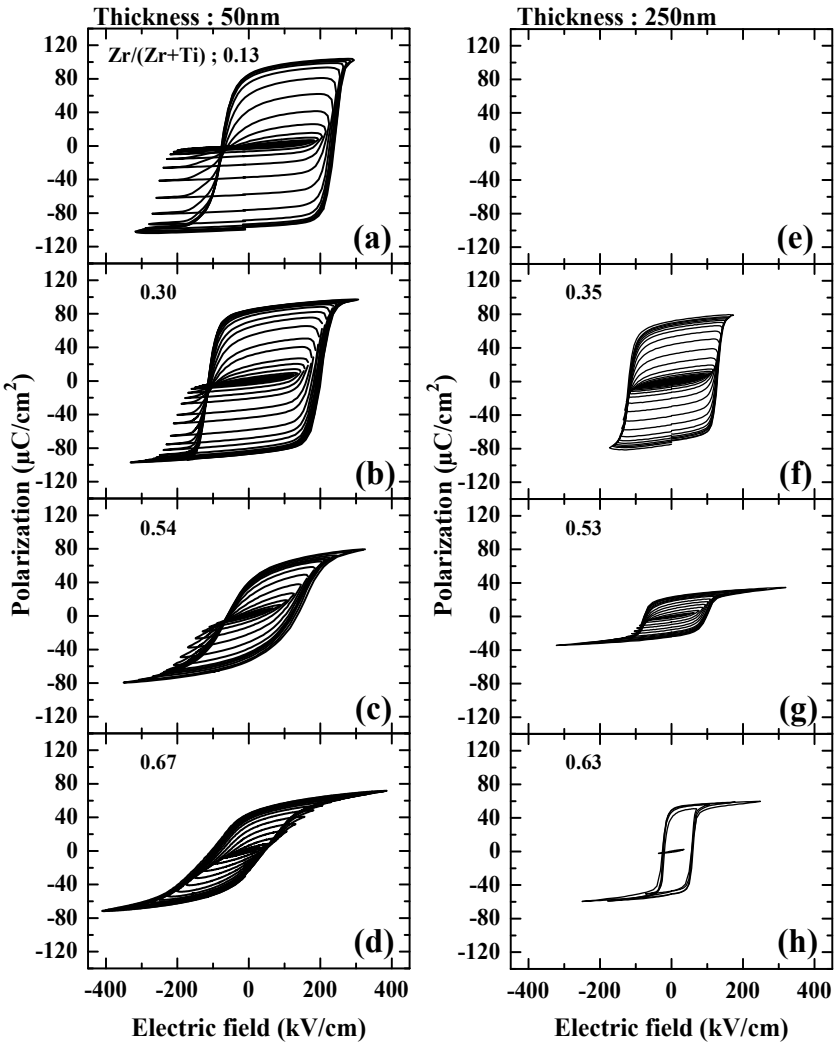

Fig. 10 Polarization - electric field (*P* - *E*) relationships for films with various Zr/(Zr+Ti) ratio and film thickness. from 50 nm thick films [(a)-(d)] and 250 nm thick films [(e) - (h)].

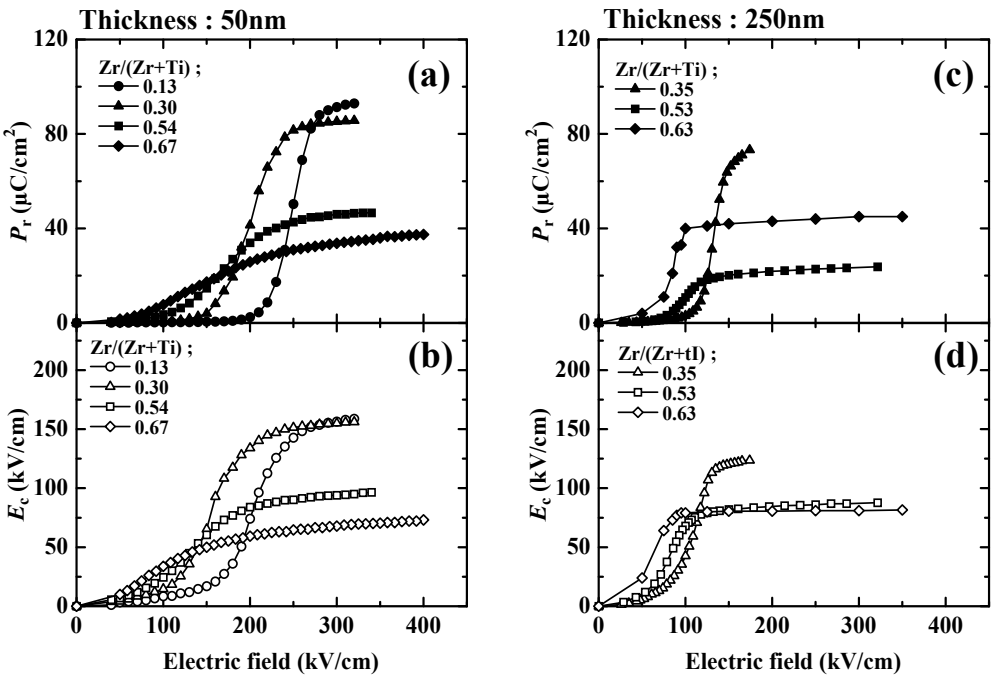

Fig. 11. Saturation properties of P_r and E_c values against the maximum applied electric filed for 50 nm [(a), (b)] and 250nm [(c), (d)] PZT films having various Zr/(Zr+Ti) ratio content.

Notice that the 250 nm thick film with Zr/(Zr+Ti)=0.19 showed high leakage current level that cannot display *P* - *E* hysterisis loops from the PZT films [Fig. 9(a)]. However, others showed *P* - *E* hysteresis loops originated to the ferroelectricity. Good saturation properties of *Pr* and the coercive field (*Ec*) against the maximum electric filed are confirmed for both of 50 nm and 250 nm thick films.

We notice on these figures that fully polar axis oriented [(001)-oriented] films with 50 nm in thickness exhibit larger P_r values than 250 nm PZT films with the coexistence of (100) and (001) orientations. This result is coherent if we consider the difference in the relative volume fraction of the *c*-domain in the latter samples. However, the differences in domain structure between the two thickness of the present samples remains and issue to fix for a good comparative analysis.

To get insight into this issue, we calculated the spontaneous polarization (P_{sat}) from P_r/V_c, calibrated P_r value by the *c*-domain volume fraction, V_c, assuming that the 90° *a*-domain do not switch under an external electric field. The results are summarized in Fig. 12.

On this figure, P_r values extracted from 50 nm-thick films are presented with closed diamonds, while open diamonds represents P_r values of 250 nm-thick films. By way of comparison, we included on Fig. 12, reported data for the 100% *c*-axis-oriented $Pb(Zr_{0.5}Ti_{0.5})O_3$ film by Ishida et al. (square plot) (Ishida et al., 2002) and also theoretical calculated data of P_{sat} against the Zr/(Zr+Ti) ratio reported by Haun et al. (dashed line) (Haune et al., 1989).

We notice that the estimated P_{sat} value in the present study is larger than reported data. However, our results have the same trend as predicted by theoretical calculations.

A good explanation of this latter result might be given by getting insight into the relationship linking tetragonality (c/a) to spontaneous polarization (P_{sat}).

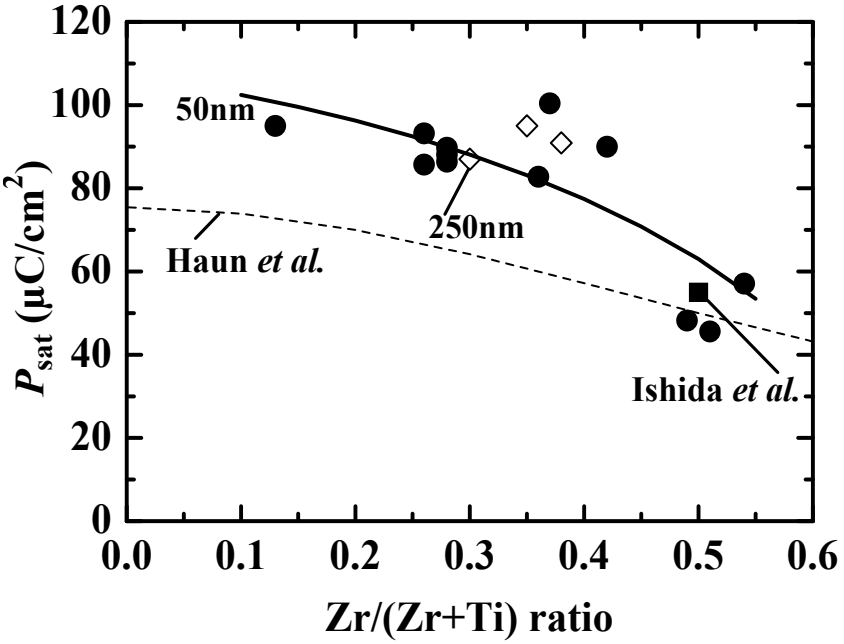

Fig. 12. Estimated P_{sat} as a function of Zr/(Zr+Ti) ratio in films.

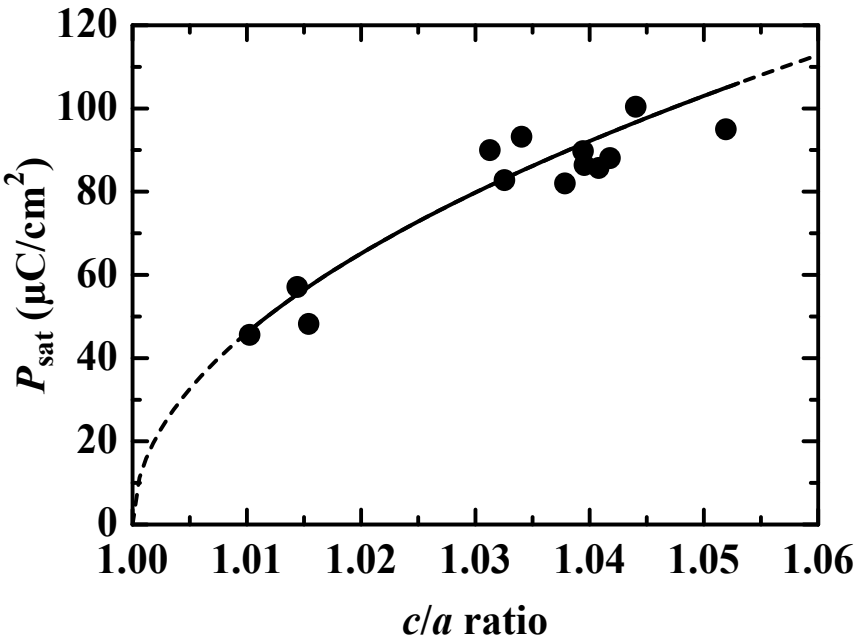

Fig. 13. Relationship between P_{sat} and the c/a ratio of PZT films.

Indeed, the unit cell distortion inducing P_{sat} might be related to cell parameters by the following equation (Joan & Shirane, 1992):

$$Q \cdot P_{sat}^{\ 2} = \frac{c}{a} - 1 \tag{1}$$

where, Q represents the apparent electrostrictive coefficient.
To highlight this relationship, we gathered data presented on Figures 7(b) and (e) and Fig. 12 on the same chart, as shown in Fig. 13:
Our data seem to be in agreement with the quadratic form presented in equation (1) linking P_{sat} to unit cell tetragonality, c/a ratio. In a previous article we could emphasis that our estimated electrostrictive coefficient, Q, is $Q = 0.049$ m^4/C^2
We also characterized the relative dielectric constant (ε_r) versus Zr/(Zr+Ti) ratio as well as thickness dependency. These results are presented on Fig. 14. On this figure, we notice that both thicknesses considered in this study respect the same ε_r tendency with regards to Zr content. Indeed, ε_r increases with increasing Zr/(Zr+Ti) ratio.

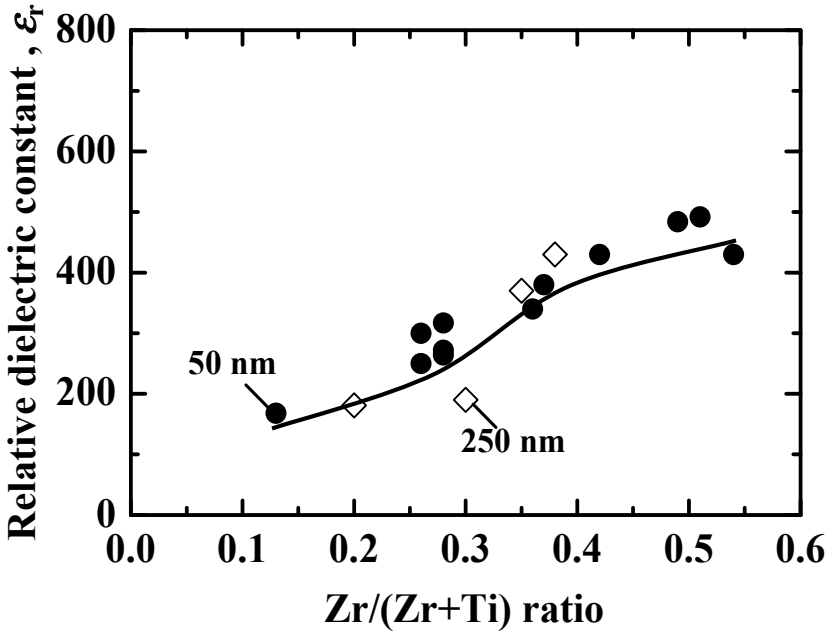

Fig. 14. Evolution of ε_r measured at 1 kHz as function of Zr/(Zr+Ti) ratio for 50 nm (●) and 250 nm (◇) thick films.

On the other hand, we noticed that squareness in P - E hysteresis loops defined by the P_r/P_{sat} ratio, is also influenced by the Zr/(Zr+Ti) ratio of the films regardless of V_c in the film. [see Fig. 15 (a)]. Indeed, as it can be observed on this figure, both 50 nm and 250 nm thick films present the same decreasing trend when Zr/(Zr+Ti) ratio increases. This result is in a good agreement with results presented on Fig. 14 since ε_r can be extracted from the saturated branch of P - E hysteresis loops.

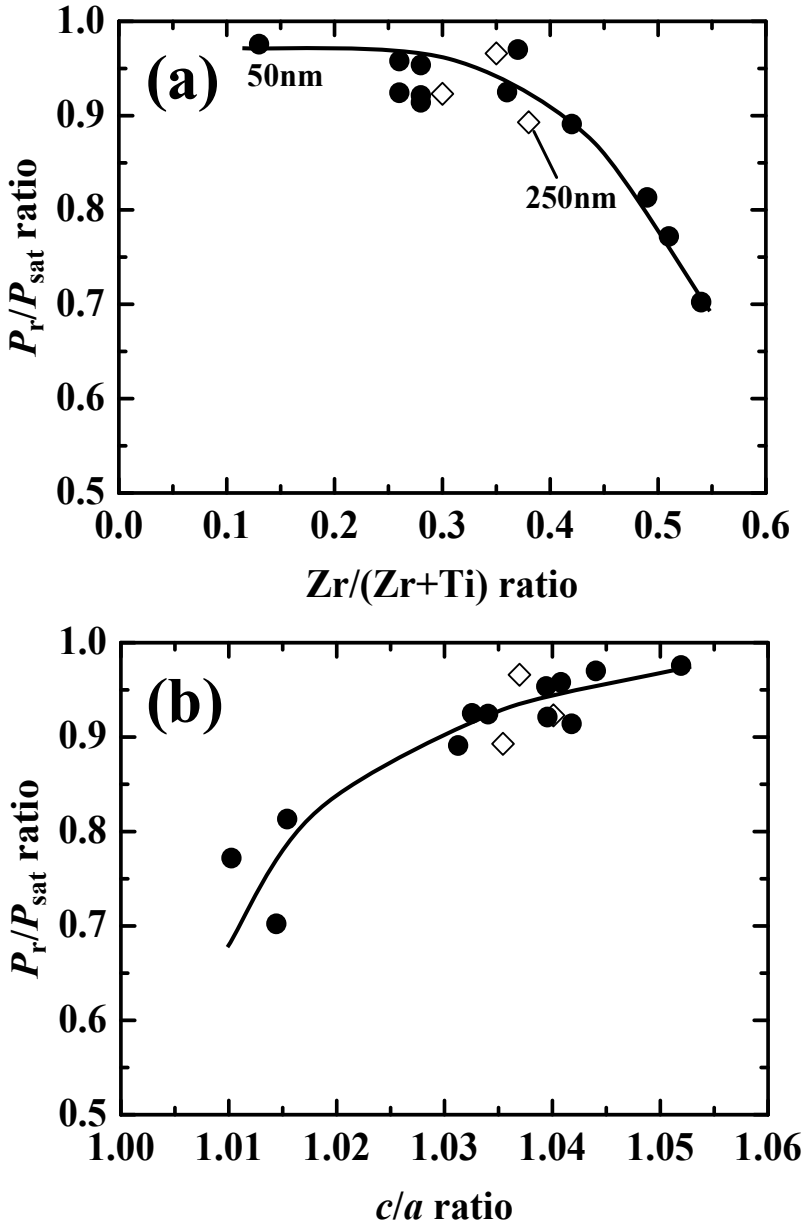

Fig. 15. Evolution of P_r/P_{sat} ratio as function of Zr/(Zr+Ti) ratio (a) and c/a ratio (b)

4. Summary

Epitaxial PZT thin films were grown at 540°C on $SrRuO_3$-coated (001) $SrTiO_3$ substrates by pulsed MOCVD. To characterize the impacts of the Zr/(Zr+Ti) ratio and the film thickness on the volume fraction of *c*-domain, 50 nm and 250 nm thick films have been grown with different Zr/(Zr+Ti) ratio ranging from 0.1 to 0.7.

HRXRD characterization showed that 50 nm thick films present a fully polar-axis oriented tetragonal films regardless of Zr/(Zr+Ti) up to 0.54, while 250 nm thick films are tetragonal single phase for the films with the Zr/(Zr+Ti) ratio smaller than 0.45, then, coexistence of tetragonal and rhombohedral phase from Zr/(Zr+Ti)=0.45 to 0.6. Appearing of two symmetry coexistence is related to the stress relaxation process occurring at relatively thick film.

Concerning electrical properties, 50-nm-thick PZT films with fully polar-axis orientation present larger P_r and P_{sat} values than thicker films. On the other hand, we investigated the impact of Zr/(Zr+Ti) ratio on the ferroelectricity of PZT films, showing the linear relationship between P_{sat}^2 and the c/a ratio of the films.

5. Acknowledgement

This work was partially supported by Grants-in-Aid from the Ministry of Education, Culture, Sports, Science and Technology, Japan for the Elements Science and Technology Project (21360316 and 20047004)"

6. References

K. Nagashima, M. Aratani, and H. Funakubo, J. Appl. Phys. 89, 4517 (2001).
N. Okuda, K. Saito, and H. Funakubo, Jpn. J. Appl. Phys., Part 1 39, 572 (2000).
K. Saito, T. Kurosawa, T. Akai, T. Oikawa, and H. Funakubo, J. Appl. Phys. 93, 545 (2003).
G. Shirane and K. Suzuki, J. Phys. Soc. Jpn. 7, 333 (1952).
H. Morioka, S. Yokoyama, T. Oikawa, K. Saito and H. Funakubo. Mat. Res. Soc. Symp. Proc. 784, C6.2.1 (2004)
H. Morioka, S. Yokoyama, T. Oikawa and H. Funakubo Appl. Phys. Lett. 85, 3516 (2004).
K. Saito, T. Kurosawa, T. Akai, S. Yokoyama, H. Morioka, T. Oikawa, and H. Funakubo, Mater. Res. Soc. Symp. Proc. 748, U13.4 (2003).
H. Morioka, G. Asano, T. Oikawa, H. Funakubo, and K. Saito, Appl. Phys. Lett. 82, 4761 (2003).
H. Morioka, K. Saito, S. Yokoyama, T. Oikawa, T. Kurosawa, and H. Funakubo, J. Mater. Sci. 44, 5318 (2009)
T. Shiosaki, Science Forum, Japan (1995)
T. Oikawa, K. Takahashi, J. Ishida, Y. Ichikawa, T. Ochiai, K. Saito, A. Sawabe and H. Funakubo, Int. Ferro. 46, 55 (2002)
J. Ishida, T. Yamada, A. Sawabe, K. Okuwada, and K. Saito, Appl. Phys. Lett. 80, 467 (2002)
M. J. Haun, Z. Q. Zhuang, E. Furman, S. J. Jang, and L. E. Cross, J. Am. Ceram. Soc. 72, 1140 (1989)
F. Jona and G. Shirane, Ferroelectric Crystal, 145, Dover, New York, (1992).

13

Double Hysteresis Loop in $BaTiO_3$-Based Ferroelectric Ceramics

Sining Yun
School of Material Science and Engineering,
Xi'an University of Architecture and Technology, Xi'an, Shaanxi,
China

1. Introduction

In 1951, the notion of anti-ferroelectricity based on the phenomenological theory was firstly proposed by C. Kittel (Kittel, 1951), and who predicted exist of the anti-ferroelectric materials and its some intrinsic characteristics. Subsequently, a double hysteresis (**P–E**) loop and a ferroelectric-antiferroelectric (FE-AFE) phase transition were observed in $PbZrO_3$ (Shirane et al., 1951, 1952) and Pb(Zr, Ti)O_3 (Sawaguchi, 1953) ceramics with a perovskite structure. Since then, the double hysteresis loop, one important macroscopic effect, has been regarded as a typical characteristic of antiferroelectric materials. This kinds of antiferroelectric behavior is also observed in Pb(Zr, Sn, Ti)O_3 and Pb(La, Zr, Sn, Ti)O_3 ceramics (Berlincourt, 1963, 1964; Biggers & Schulze, 1974; Gttrttritja et al., 1980; Shebanov et al., 1994).

Interestingly, the double hysteresis loops have been observed in $BaTiO_3$ (Merz, 1953), $BaTiO_3$-based (Ren, 2004; Zhang & Ren, 2005, 2006; Liu et al., 2006), $(Na_{0.5}Bi_{0.5})TiO_3$-based (Takenaka, 1991; Sakata & Masuda, 1974; Tu et al., 1994; Sakata et al., 1992), (Ba, Sr)TiO_3 (Zhang et al., 2004), $KNbO_3$ (Feng & Ren, 2007, 2008), $BiFeO_3$ (Yuen et al., 2007) and other lead-based perovskite ceramics such as Pb$(Yb_{0.5}Ta_{0.5})O_3$ (Yasuda & Konda, 1993), Pb$(Fe_{2/3}W_{1/3})O_3$-Pb$(Co_{1/2}W_{1/2})O_3$ (Uchino & Nomura, 1978), Pb$(Sc_{0.5}Ta_{0.5})O_3$ (Chu et al., 1993) and Pb$(Co_{1/2}W_{1/2})O_3$ (Hachiga et al., 1985) over the past decades. However, the observed double hysteresis loops have different physical origins.

For the physical origins of the double ***P-E*** loops observation in the perovskite structure materials, they can be generally classified into several groups below: (1) the double ***P-E*** loops result from antiferroelectric components. i.e., the observed double ***P-E*** loops in $PbZrO_3$ and Pb(Zr, Ti)O_3 ceramics. (2) the double ***P-E*** loops result from an electric field-induced antiferroelectric-to-ferroelectric phase transition as shown observed in Pb(La, Zr, Sn, Ti)O_3 ceramics. (3) two successive paraelectric-antiferroelectric-ferroelectric (***PE-AFE-FE***) phase transitions is often observed in highly ordered perovskite lead-based and lead-free complex compounds, and the double ***P-E*** loops are expected to accompany this phase transition. Such case often occur in Pb$(Yb_{0.5}Ta_{0.5})O_3$, Pb$(Fe_{2/3}W_{1/3})O_3$-Pb$(Co_{1/2}W_{1/2})O_3$, Pb$(Sc_{0.5}Ta_{0.5})O_3$ and Pb$(Co_{1/2}W_{1/2})O_3$ and $(Na_{0.5}Bi_{0.5})TiO_3$-based ceramics. (4) an aging effect far below Curie temperature (T_c) can induce the double ***P-E*** loops observation in many kind different compositional ceramics such as acctor-doped $BaTiO_3$ ceramics, Mn-

doped (Ba, Sr)TiO_3 ceramics, $KNbO_3$-based ceramics and $BiFeO_3$ ceramics. The aging-induced double ***P-E*** loops has been the highlights based on the high-quality publications and their cited times. (5) for the observed double ***P-E*** loops in $BaTiO_3$ crystals at the Curie point, its origin can not attributed to any one group mentioned above. The $BaTiO_3$ crystals go from a paraelectric to a ferroelectric state, while (Pb, Ba)ZrO_3 ceramics go from an antiferroelectric to a ferroelectric state when an electric field is applied. It is generally believed that the Curie point of the $BaTiO_3$ crystal shifts to higher temperature when a dc bias field is applied. The more detailed discussion about the origin of the double ***P-E*** loops in the $BaTiO_3$ crystal can consult the previous literatures titled "A theory of double hysteresis for ferroelectric crystals" (Srivastava, 2006).

After a brief review of the physical origin of double hysteresis loops in different perovskite structure ($A^+B^{5+}O_3$, $A^{2+}B^{4+}O_3$, $AA'BO_3$, $ABB'O_3$, etc) ceramic materials, this chapter begins with aging effect, namely a gradual change in physical properties with time. This is followed by discussions of the aging-induced double hysteresis loops in Bi doped (Ba, Ca)TiO_3 and Bi doped (Ba, Sr, Ca)TiO_3 ferroelectric ceramics. Some emphasis will be on the roles of acceptor-doping and donor-doping in understanding the physics of these materials.

2. Experimental procedures

2.1 Ceramics synthesis

A conventional solid reaction route was employed to synthesize ceramics samples. Reagent grade $BaCO_3$ (99.8%), Bi_2O_3 (99.8%), $SrCO_3$ (99.8%), $CaCO_3$ (99.8%) and TiO_2 (98%) as the raw materials were weighed according to the compositions $(Ba_{1-x}Ca_x)_{1-1.5y}Bi_yTiO_3$ (Bi-BCT, x =0.10, 0.20 and 0.30, y=0.05) and $(Ba_{1-x}Ca_{x/2}Sr_{x/2})_{1-1.5y}Bi_yTiO_3$ (Bi-BCST, x=0.10, 0.20 and 0.40, y=0 and 0.05). $(Ba_{0.925}Bi_{0.05})(Ti_{0.90}Ca_{0.10})O_3$ (designated hereafter Bi-BTC) was prepared to compare the effect of Ca substitution at the Ti sites of Bi-BCT. After ball-milled in alcohol for 6 h using agate balls in a planetary mill, the slurry was dried, and then calcined at 1100 ^{o}C for 4-5h. The calcined powder was ball milled and dried again to obtain homogeneous powder. Pellets of 10 mm in diameter and ~1 mm thick were pressed using 5 % PVA binder. Slow heating at 500 ^{o}C for 3-4h burned out the binder. The samples were sintered at 1240 ^{o}C -1300^{o}C in air for 3 h, with heating rates of 200^{o}C/h. The samples were cooled with the furnace.

2.2 Characterizations

The phase structures of the ceramics at different temperature were checked by the X-ray powder diffraction (XRD, D/Max2200 RZGAKV: Rigaku Inc.D, Japan) on an automated Rigaku D/max 2400 X-ray diffractometer with rotating anode using CuK_α radiation. The microstructures were examined by a scanning electron microscopy (SEM, Quanta 200 FEG System: FEI Co., USA) with X-ray energy dispersive spectroscopy (EDS) for chemical analysis. Raman scattering investigation was performed at room temperature by using an ALMEGA dispersive Raman spectrometer (ALMEGA, Therm Nicolet, Madison,WI).

2.3 Property measurements

After polishing, the dimensions were measured before silver electrodes were deposited on the pellets, then the specimens were fired at 810 ^{o}C for 10 mins. Dielectric properties at

frequencies ranging from 0.1kHz to 100 kHz were measured with an Agilent 4284A LCR meter, as samples were heated at a rate of 2 °C/min from negative 80 to positive 200 °C. Hysteresis loops were measured in a wide temperature range using a computer-controlled, modified Sawyer-Tower circuit at frequency of 1 Hz. Current-field relation was measured on an automatic ferroelectric test system of aixACT TF-ANALY2ER2000. Applied electric field signal is triangular, and a period time is a second.

3. Results and discussion

3.1 Structural analysis

It has been reported that the solubility limit of Bi is around 5 at. % in $BaTiO_3$ (Zhou et al., 1999), and around 10 at. % in $(Ba_{0.2}Sr_{0.8})TiO_3$ (Zhou et al., 2000), respectively. Moreover, 5 at. % of Bi doping can be fully incorporated into the perovskite lattice of $Ba_{1-x}Sr_xTiO_3$ ($x < 0.80$) (Zhou et al., 2001). It is then possible to assume that 5 at. % of Bi doping can be fully incorporated into the perovskite lattice of $(Ba_{1-x}Ca_x)TiO_3$ (Bi-BCT, x=0.10, 0.20 and 0.30) and $(Ba_{1-x}Ca_{x/2}Sr_{x/2})TiO_3$ (Bi-BSCT, x=0.10, 0.20 and 0.40). XRD analysis confirmed this assumption. Fig. 1 show the XRD patterns of 5 at. % of Bi doped $(Ba_{1-x}Ca_x)TiO_3$ ceramics. The XRD patterns of all the compositions showed mainly a single perovskite phase.

The structural evolution of Bi-doped BCST ceramics samples from x=0.10 to 0.40 is shown in Fig. 2. The XRD results of 5 at. % Bi-doped BCST are consistent with those of $(Ba_{1-x}Sr_x)_{1-1.5y}Bi_yTiO_3$ (Zhou et al., 2001) and Bi-BCT, showing that they are a single phase. The crystalline symmetry of Bi-doped BCST ceramics is a rhombohedral for x=0.40. However, it tends appreciably towards the tetragonal for x=0.20. The rhombohedral phase is illustrated by the increased splitting between the (021) and (003) peaks in two-theta near 39° while the tetragonal phase is illustrated by the increased splitting between the (002) and (200) peaks in two-theta near 45°. There are splits in the peaks observed at two-theta of about 39° and 45°, respectively, as shown in Fig.3, indicating the coexistence of the tetragonal and rhombohedral phases of Bi-BCST for x=0.10 and that of Bi-BCT for x=0.10 and 0.20.

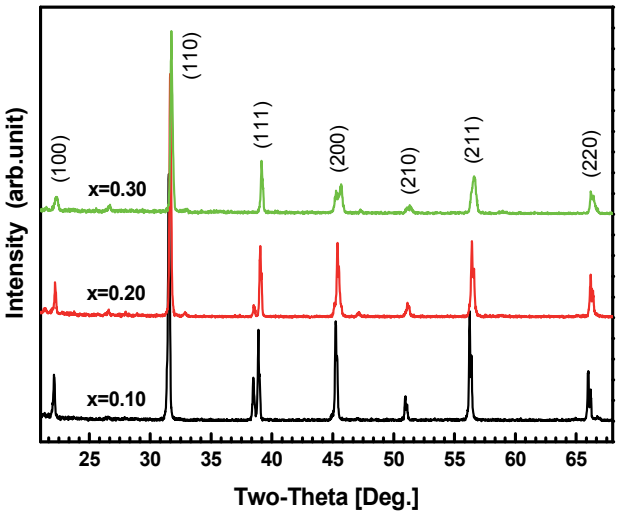

Fig. 1. XRD patterns of Bi-BCT ceramics with different compositions (x=0.10, 0.20 and 0.30, y=0.05).

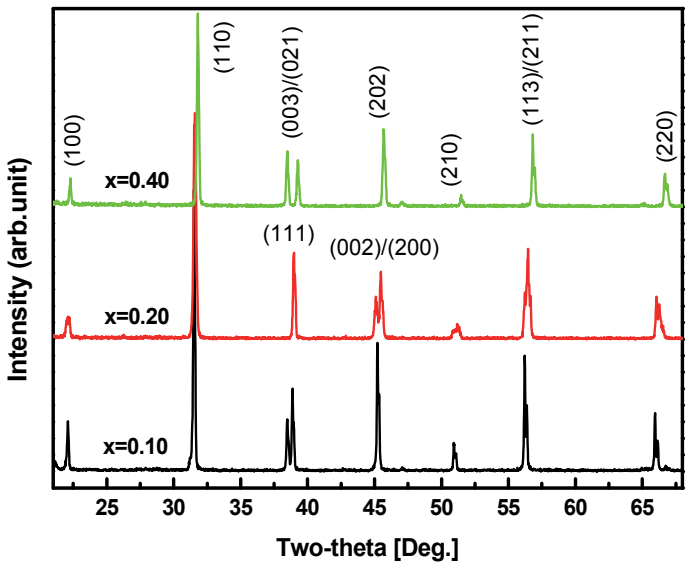

Fig. 2. XRD patterns of Bi-BSCT ceramics with different compositions (x=0.10, 0.20 and 0.40, y=0.05).

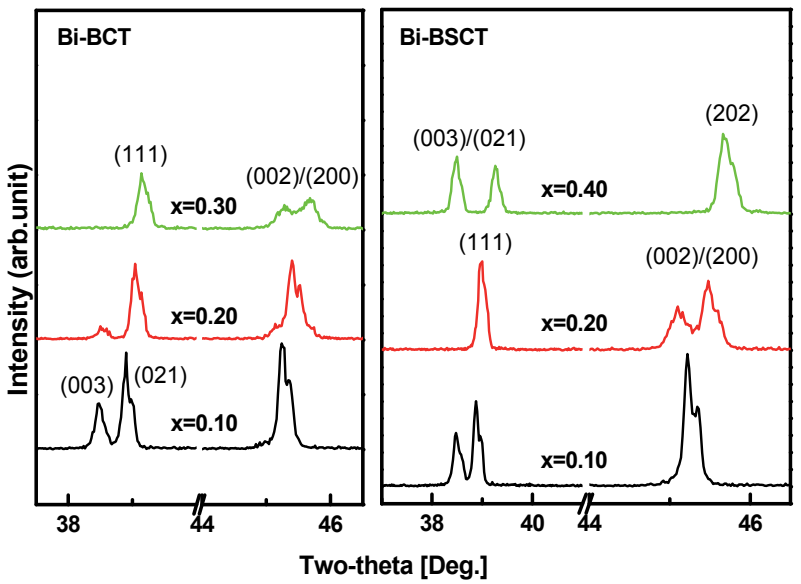

Fig. 3. Enlarged XRD patterns of Bi-BCT and Bi-BSCT(y=0.05) ceramics with different compositions with two-theta value ranging from 37.5° to 46.5°.

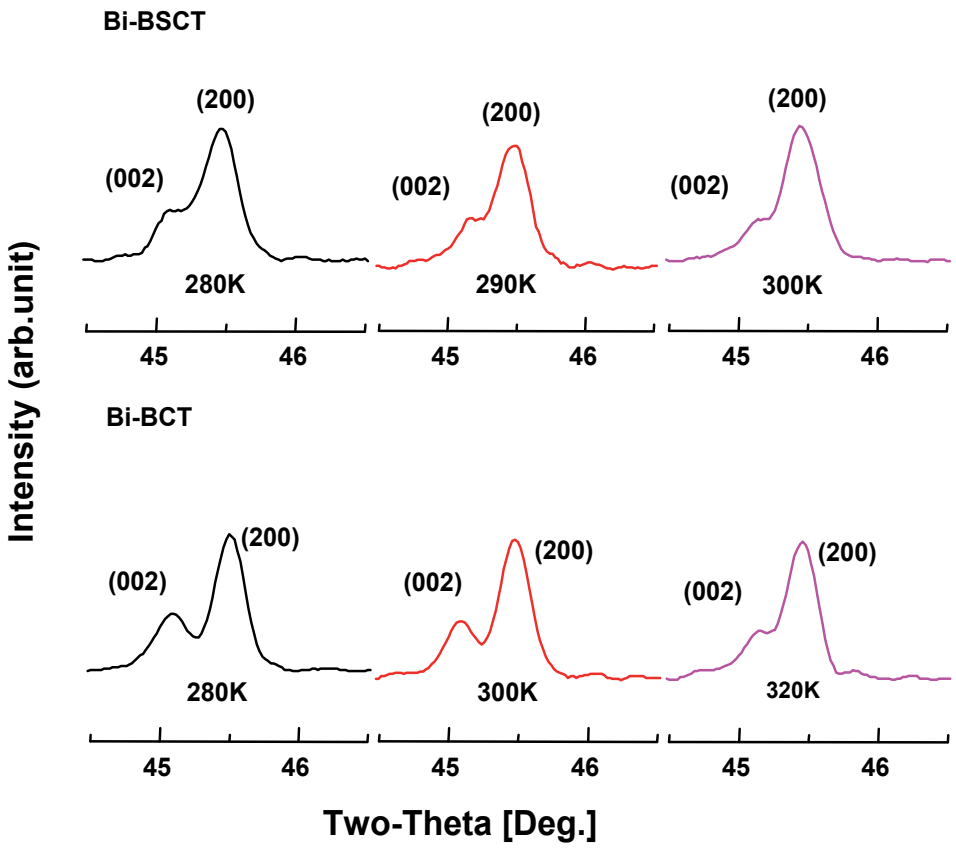

Fig. 4. Changes in the (002)/(200) reflection of XRD patterns of Bi-BCT and Bi-BSCT (x=0.10, y=0.05) ceramics with different temperatures.

To check the crystal symmetry, X-ray powder diffraction (XRD) at different temperatures was performed for Bi-BCT and Bi-BSCT (x=0.10, y=0.05). Fig. 4 shows the form of one of the structure sensitive maxima in the XRD patterns. It is found from the changes in the (002)/(200) refection with temperature that Bi-BCT ceramics have a tetragonal structure throughout the whole temperature range from 280 K up to 320 K while Bi-BSCT ceramics have a tetragonal structure throughout the whole temperature range from 280 K up to 300 K.

3.2 Ferroelectric properties

Fig. 5 and Fig. 6 show the plots of polarization ***P*** vs electrical field ***E*** (***P-E***) at elevate temperature for Bi-BCT and Bi-BCST (x=0.10 and 0.20, y=0.05), respectively. A well-behaved hysteresis loop can be observed at 280 K for Bi-BCT (x=0.10 and 0.20). When the temperature was increased, the double hysteresis loop, typical of antiferroelectric materials, was observed at 300 K for Bi-BCT and at 280 K for Bi-BSCT, with a nearly linear ***P-E*** relationship at the mid-part of the hysteresis loop. With further increased temperature, hysteresis could not be detected, the ***P-E*** loops were slim and showed dielectric quasilinearity over a wide electric field range.

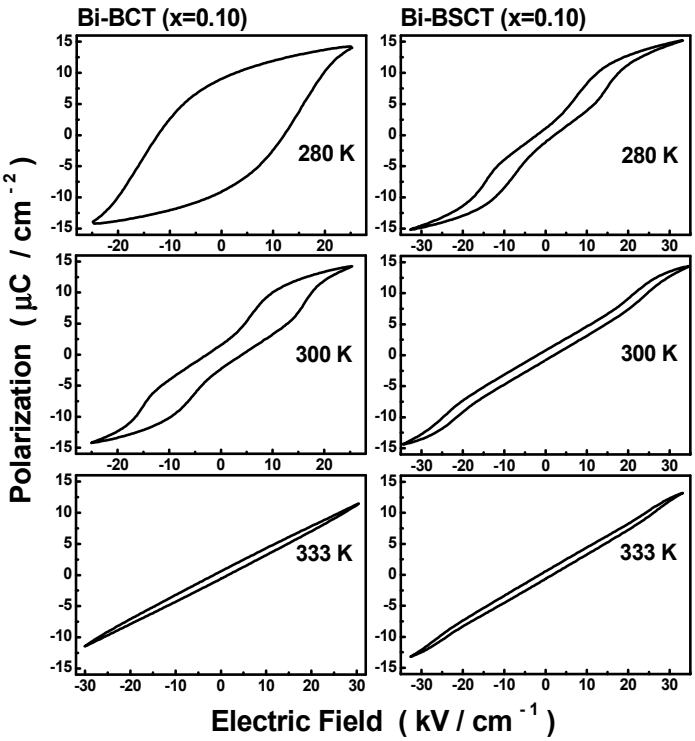

Fig. 5. The electrical field (**E)** dependence of polarization (**P)** at elevated temperature measured at 1 Hz for Bi-BCT and Bi-BSCT (x=0.10,y=0.05).

Note that a remarkable double-like ***P-E*** loop is not observed for Bi-BCT (x=0.30). However, the ***E*** dependence of ***P*** and current density (***J***) **(J-E)** relationships have shown that four remarkable ***J*** peaks are observed for Bi-BCT (x=0.30), indecating of the existence of double-like ***P-E*** loop for x=0.30 in Bi-BCT. Talking about that the present chapter foucses on the double ***P-E*** loops in Bi-BCT and Bi-BSCT ceramics, the related data for **J-E** relationship are not shown here.

The ***P-E*** loops transform from the normal hysteresis loop to an interesting double-like hysteresis loop, and then to the nearly linear one with increasing temperature. These characteristics obtained from the loops at elevated temperature suggest that different ferroelectric behaviors have occurred in Bi-BCT. It seems that two successive paraelectric-antiferroelectric-ferroelectric (***PE-AFE-FE***) phase transitions exist in Bi-BCT ceramics. By contrast, this similar transform from the normal to the double to the quasilinear can not be detected in Bi-BSCT ceramics. Polarization data at a lower temperature could not be obtained for Bi-BSCT ceramics due to the limitation of the present measuring equipment. However, one can assume that an ferroelectric–antiferroelectric transformation occurs at a lower temperature (temperature is less than 280 K) for Bi-doped BCST ceramics. This assumption needs to be confirmed experimentally. The appropriate research is now being carried out.

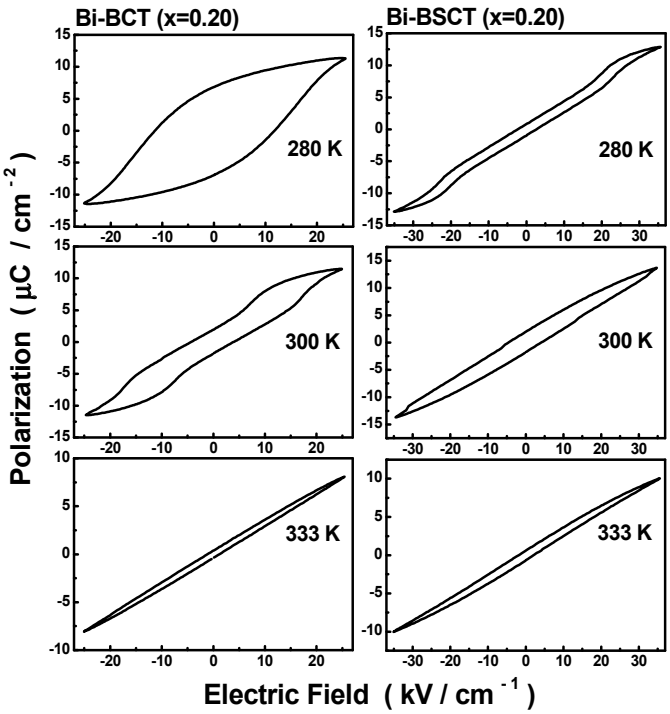

Fig. 6. The electrical field (**E)** dependence of polarization (**P)** at elevated temperature measured at 1 Hz for Bi-BCT and Bi-BSCT (x=0.20,y=0.05).

A linear dielectric response is observed for Bi-BCT and Bi-BSCT, that is, the ***P-E*** relationship is close to linear, unlike that for normal ferroelectrics and lead-based relaxors. The quasi-linear ***P-E*** relationship looks somewhat similar to that taken on the antiferroelectric sample. In this case, the linear ***P-E*** dependence is typical for antiferroelectric materials. In order to demonstrate that dielectric quasi-linearity in a certain electric field range is a typical antiferroelectric behavior or not, a complete investigation including the electric field-induced and temperature-induced structure phase transition has been performed in our previous literatures.

3.3 Dielectric properites

The temperature dependence of the dielectric constant and the dielectric loss of Bi-BCT and Bi-BSCT ceramics for different frequencies are shown in Fig. 7(A)-(D). The dielectric constant has a broad maximum at a temperature of the peak dielectric constant (T_m). T_m increases with increasing frequency. For example, T_m is equal to 341 K at 1 kHz and 347 K at 1 MHz for Bi-BCT (x=0.10), respectively. With decreasing temperature, the value of dielectric loss increases rapidly around the temperature of the dielectric loss. With increasing frequencies, the peak dielectric constant decreases and T_m shifts to high temperature. Such change trends of the dielectric constant and the dielectric loss with the frequencies and the temperatures is a type of dielectric relaxation behavior, which has been reported in detail in the solid state physics text book.

The possible mechanism for the relaxor behavior observation in Bi-doped $SrTiO_3$ (Ang et al., 1998), Bi-doped $Ba_{1-x}Sr_xTiO_3$ (Zhou et al., 2001), Ca-doped $SrTiO_3$ (Bednorz & Müller, 1984) and Li-doped $KTaO_3$ (Toulouse et al., 1994) has been discussed in detail in the previous publications. A widely accepted viewpoint is that the dielectric relaxation behavior in these systems was due to a random electric field induced ferroelectric domain state. According to their viewpoint, the Bi^{3+} ions which substitute for A-site ions in BCT and BCST ceramics can also be located at off-center positions and A-site vacancies may also appear to compensate for the charge misfit arising from the A-site ions substituted by Bi^{3+} ions. A random electric field formed by off-center Bi^{3+} ions and Bi^{3+}–V''_A dipoles would then suppress the ferroelectricity of BCT and BCST and result in the relaxor behavior observed for Bi-doped BCT and BCST. If Ca^{2+} ions can locate at B-sites like Ti^{4+} ions, to balance the charge misfit, a next-neighbor oxygen can be vacant, and form a Ca^{2+}–V_O neutral center. Such Ca^{2+}–V_O centers form dipoles and thus set up local electric fields, which suppress the ferroelectricity of BCT and BCST and result in the relaxor behavior observed in BCT and BCST.

In most cases of ferroelectric phase transition, where the new ordered phase originates from structural changes, there will be a peak in the dielectric spectrum but not all peculiarities or peaks correspond to a structural phase transition. For example, All classical relaxors, such as $Pb(Mg_{1/3}Nb_{2/3})O_3$ (PMN) and low x (1-x)$Pb(Mg_{1/3}Nb_{2/3})O_3$-x$PbTiO_3$ (Bokov & Ye, 2006), show the dielectric peaks but do not undergo the ferroelectric (or antiferroelectric) phase transition. Therefore, the dielectric peak may only indicate the possible phase transition. If the ***FE-AFE-PE*** transition has occurred in Bi-BCT, there will be two corresponding dielectric peak in the dielectric spectrum. However, the dielectric spectrum of Bi-BCT and Bi-BSCT show only one peak at temperature ranging from 190 K to 428 K as seen in Fig.7.

On the other hand, there is no direct indication of the appearance of antiferroelectric components in $(Ba,Ca)TiO_3$ (Han et al., 1987; Zhuang, et al., 1987; Mitsui & Westphal, 1961; Baskara & Chang, 2003). Therefore, the aging-induced effect should be responsible for the double ferroelectric hysteresis observation in Bi-BCT and Bi-BSCT ceramics.

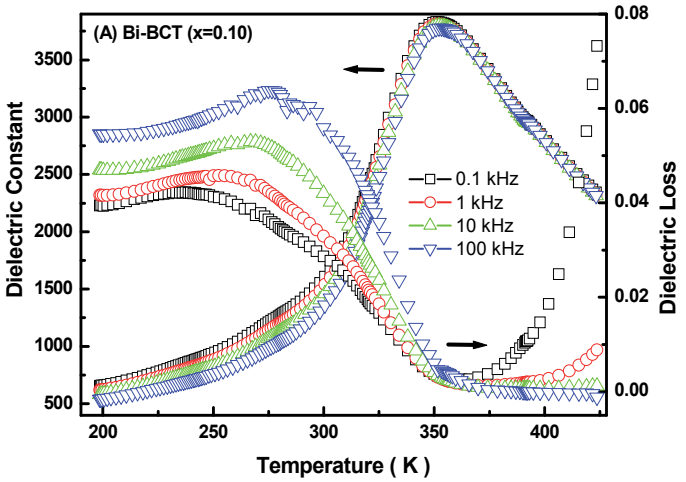

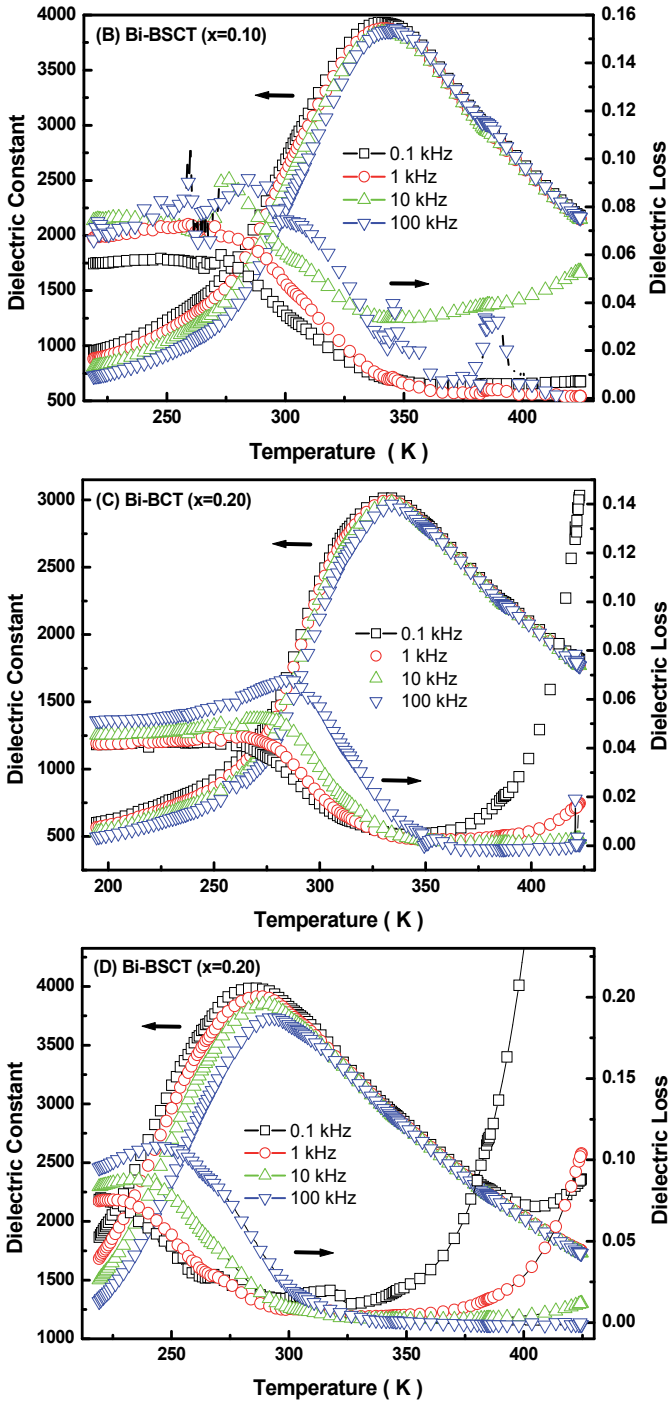

Fig. 7. Temperature dependence of the dielectric constant and the dielectric loss of Bi-BCT and Bi-BSCT for x=0.10 ((A) and (B)), x=0.20 ((C) and (D)) and y=0.05 at 0.1, 1, 10, 100 kHz (for dielectric constant, from top to bottom, for dielectric loss, from bottom to top).

3.4 Ferroelectric aging effect

The interesting aging-induced double ***P-E*** hysteresis loop was also reported in various ferroelectric systems. Many mechanisms such as the grain boundary effect (Karl & Hardtl, 1978), the domain-wall pinning effect (Postnikov et al, 1970), the volume effect (Lambeck & Jonker, 1986) and symmetry-conforming short range ordering (SC-SRO) mechanism of point defects (Ren, 2004; Zhang & Ren, 2005, 2006; Liu et al., 2006) have been proposed to explain this phenomenon. Although all these models seem to be able to provide a self-consistent explanation of the double hysteresis loop in aged ferroelectric crystals, the grain boundary effect cannot explain the perfect double ***P-E*** loop exists in the aged single-crystal sample, the domain-wall pinning effect cannot explain the restoration of the initial multidomain state from a single-domain state because there would be no domain wall to be dragged back, and the volume effect is based on a key assumption that there exist dipolar defects and they follow spontaneous polarization after aging (Zhang & Ren, 2005, 2006). Compared all these models, SC-SRO mechanism, which also is a volume effect, provides a microscopic explanation for the origin of aging, and it involves no assumption. The conformation of the defect dipole with spontaneous polarization naturally comes from the symmetry-conforming property of the defects. Generally, all these models agree that defects play a decisive role in the aging induced phenomena. However, they differ much in the driving force for defect migration.

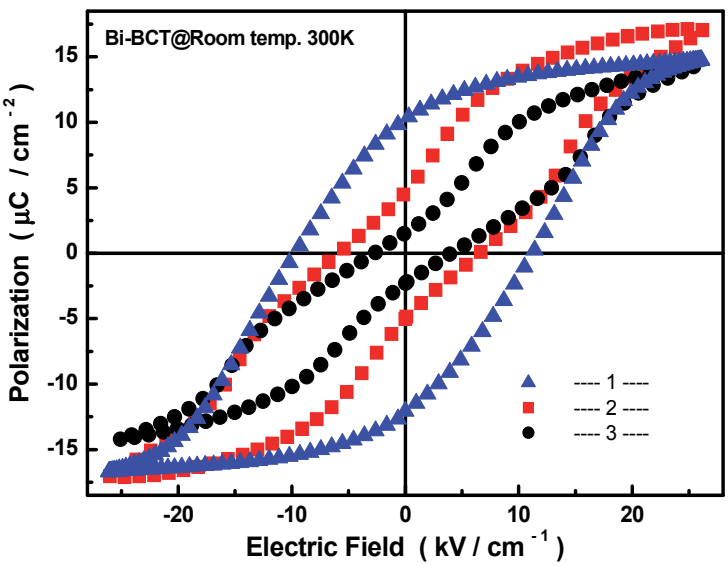

Fig. 8. Hysteresis loops for fresh and aged Bi-BCT (x=0.10) ceramic samples at room temperature of 300 K. (1—Fresh or deaged ; 2—A shorter period of aging; 3—A longer period of aging).

To check further whether there is a diffusional aging effect, the samples were "de-aged" by holding them at 470 K for 1 h, followed by a quick cooling to room temperature above Curie temperature. The room temperature hysteresis loops were measured simultaneously. Fig. 8 shows the experimental results of the hysteresis loops for the Bi-BCT in de-aged (fresh) and

aged state, respectively. The de-aged sample shows a normal hysteresis loop, but all the aged samples show interesting double hysteresis loops. The change from the single ***P-E*** loops in the de-aged sample to the double ***P-E*** loops in the aged sample should exclude antiferroelectric components and any electric field-induced ***PE-FE*** phase transition near Curie temperature. It indicates that the aging effect must be responsible for the double ***P-E*** loops observed in Bi-BCT.

3.5 Raman analysis

The aging effect in acceptor-doped ferroelectrics is generally considered to be due to the migration of oxygen vacancies (which are highly mobile) during aging (Ren, 2004; Zhang & Ren, 2005, 2006; Liu et al., 2006; Zhang et al., 2004; Feng & Ren, 2007, 2008). However, the O^{2-} vacancies in our Bi-BCT and Bi-BSCT samples were not formed artificially by substitution of lower-valence ions for Ti ions on the B-sites. To understand the aging effect in Bi-BCT, we need to analyze its defect structure. For Bi doped BCT and BSCT with the ABO_3 pervoskite structure [$(Ba_{0.90}Ca_{0.10})_{0.925}Bi_{0.05}TiO_3$ and $(Ba_{0.90}Sr_{0.05}Ca_{0.05})_{0.925}Bi_{0.05}TiO_3$], there are two possible vacancies: first, the Bi^{3+} ions substituted for A-site divalent ions (Ba^{2+}, Sr^{2+} or/and Ca^{2+}) in BCT and BSCT can be located at off-center positions of the A-site, so that A-site vacancies are formed to compensate the charge imbalance arising from the substitution, and second, that Ca^{2+} ions substitute for Ti^{4+} ions in BCT, and cause the formation of O^{2-} vacancies to balance the charge misfit. The previous experimental results from equilibrium electric conductivity (Han et al., 1987), scanning electric microscopy (Zhuang, et al., 1987), neutron diffraction (Krishna et al, 1993) and Raman and dielectric spectroscopies (Zhuang, et al., 1987; Chang & Yu, 2000; Park et al., 1993), have given evidence that a small amount of Ca^{2+} ions can substitute for Ti^{4+} ion causing the formation of O^{2-} vacancies to balance the charge misfit, although the ionic radius and chemical valence of the Ca^{2+} ions is very different from those of the Ti^{4+} ions. 4 mol% Ca^{2+} ions were found to have substituted for the Ti^{4+} ions even when the molar ratio of (Ba+Ca)/Ti was 1 for the starting materials used by Krishna et al. in their studies of $Ba_{0.88}Ca_{0.12}TiO_3$ samples prepared by the solid-state reaction technique. Following the above-mentioned suggestion, it seems that substitution of the Ca^{2+} ions for the Ti^{4+} ions had occurred in the Bi-BCT and Bi-BSCT ceramics prepared by the solid-state reaction technique.

Since aging is controlled by the migration of mobile oxygen vacancies, an experimental study of the formation of O^{2-} vacancies in Bi-BCT by Raman scattering at room temperature was performed with the results shown in Fig. 9. (Ba0.925Bi0.05)(Ti0.90Ca0.10)O2.90 (Bi-BTC) ceramics were prepared in order to compare the effect of Ca substitution at the Ti sites of Bi-BCT. In single crystal and ceramic samples of $BaTiO_3$, almost the same Raman bands, such as those at 165 cm^{-1} [A(TO)], 173 cm^{-1} (mixed modes), 266 cm^{-1} [A(TO)], 306 cm^{-1} [E(TO)], 470 cm^{-1} [E(T)+A(L)], 516 cm^{-1} [A(T)] and 712 cm^{-1} [A(LO)+E(LO)], were observed (Burns, 1974; Begg et al., 1996). Very similar results were also observed in $(Ba_{1-x}Ca_x)TiO_3$ and $BaTi_{1-y}Ca_yO_3$ ceramics (Chang & Yu, 2000). For A-site substitution, with increasing x, the Raman bands related to the phonon vibration of the Ba-O bonds shift to higher frequency (512 and 719 cm^{-1} for x = 0.005, 521 and 730 cm^{-1} for x = 0.20) while the Raman bands caused by the phonon vibration of the Ti-O bonds shift to lower frequency (259 and 306 cm^{-1} for x = 0.005, 248 and 298 cm^{-1} for x = 0.20). For B-site substitution, Ba-O bonds are closely related to the formation of the 517 and 718 cm^{-1} bands, and Ti-O bonds are closely related to the formation of the 257

and 307 cm^{-1} bands in $BaTi_{1-y}Ca_yO_3$. Fig.9 shows the bands 299, 520 and 723 cm^{-1} were independent of the formation of Ca_{Ba} and Ca_{Ti} in Bi-BCT and Bi-BTC. From these results we can conclude that Ba-O bonds are closely related to the formation of the 520 and 723 cm^{-1} bands, and Ti-O bonds to the formation of the 262 and 299 cm^{-1} bands. We also find the development of a weak new Raman band at 827cm^{-1} for Bi-BTC and Bi-BCT (see Fig. 9). Almost the same Raman bands (832 cm^{-1}) have been observed in $Ba(Ti_{0.985}Ca_{0.005}Nb_{0.01})O_3$ and $BaTi_{1-y}Ca_yO_3$ (y=0.005 and 0.015) ceramics (Chang & Yu, 2000). This higher frequency Raman band has resulted from the formation of Ca_{Ti} defects. That is, Ca^{2+} ion substitution for B-site Ti^{4+} ions has occurred in Bi-BCT, and O^{2-} vacancies have formed to compensate for the charge imbalance. The present results give critical evidence for the formation of O^{2-} vacancies.

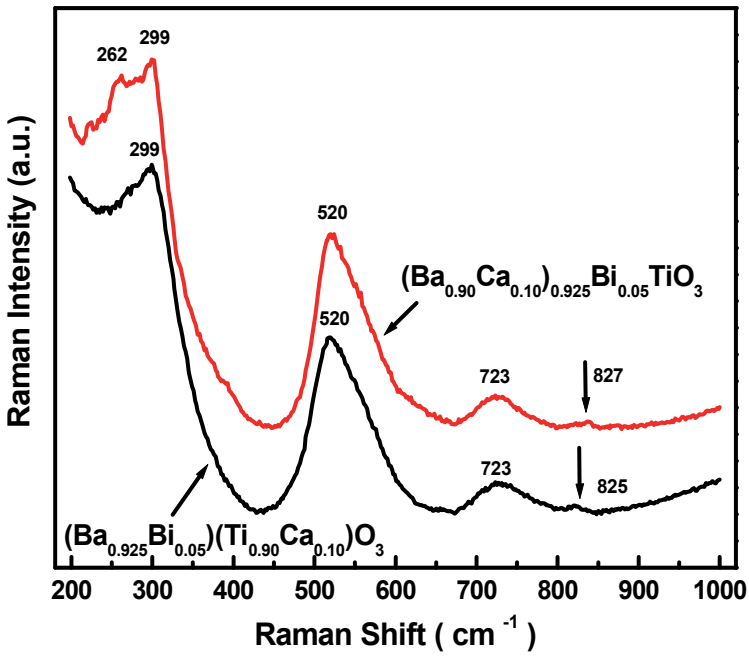

Fig. 9. Raman spectra of the Bi-BCT and Bi-BTC ceramics at room temperature.

3.6 Origin of double-like P-E loops in Bi-BCT and Bi-BSCT

As mentioned above, there are two kinds of vacancy, A-site vacancies and oxygen vacancies, around an acceptor Ca^{2+} ion. Considering the mobility of oxygen vacancies and the immobility of cation vacancies at ordinary temperatures, the observation of double ***P-E*** loops in Fig. 8 can be explained by a special aging effect related to the defect symmetry defined as the conditional probability of finding O^{2-} vacancies at site i (i=1–6) of an ABO_3 single cell (Ren, 2004; Zhang & Ren, 2005, 2006; Liu et al., 2006; Zhang et al., 2004; Feng & Ren, 2007, 2008). Fig. 10 depicts how the double ***P-E*** loops are produced in a single-crystal grain of the aged Bi-BCT sample. The high-temperature sintering gives the oxygen and cation vacancies sufficient mobility. Thus, in the paraelectric phase, the probability of

finding an O^{2-} vacancy and a A-site vacancy around an acceptor Ca^{2+} ion will adopt a cubic symmetry, according to the SC-SRO mechanism of point defects [Fig. 10(d)] (Ren, 2004).

For the de-aged tetragonal samples, which are formed by immediately cooling from the paraelectric state at 470 K down to 300 K, the SRO distribution of point defects retains the same cubic symmetry as that in the cubic paraelectric phase because the diffusionless paraeletric-ferroelectric transition cannot alter the original cubic SRO symmetry of point defects (Ren, 2004). As a result, the de-aged ferroelectric state has tetragonal crystal symmetry, but cubic defect symmetry; thus the two symmetries do not match [see Fig. 10(a)]. According to the SC-SRO mechanism (Ren, 2004; Zhang & Ren, 2005, 2006; Liu et al., 2006; Zhang et al., 2004; Feng & Ren, 2007, 2008), such a state [Fig. 10(a)] is unstable due to the mismatch between the defect symmetry and the crystal symmetry. After aging for a long time, the defect symmetry in each domain follows the polar tetragonal crystal symmetry and exhibits a defect dipole moment following the polarization direction of the residing domain. Every domain is in its stable state, as shown in Fig. 10(b). The SRO symmetry of O^{2-} vacancies around the Ca^{2+} ion can be gradually changed into a polar tetragonal symmetry (which produces a defect dipole $\boldsymbol{P_D}$) [see Fig. 10(b) and 10(e)] by the migration of mobile O^{2-} vacancies, which is the same process as for the acceptor-doped case (Ren, 2004; Zhang & Ren, 2005, 2006; Liu et al., 2006; Zhang et al., 2004; Feng & Ren, 2007, 2008). However, the SRO symmetry of A-site vacancies around Ca^{2+} the ion still remains cubic because the cation vacancies are immobile at such temperatures (Tan et al., 1999) [Fig. 10(b) and 10(f)]. When an electric field is applied to the naturally aged tetragonal Bi-BCT sample, $\boldsymbol{P_S}$ is switched to the field $\boldsymbol{E}$ direction while $\boldsymbol{P_D}$ keeps its original direction during such a sudden process [Fig. 10(b) to 10(c)]. Therefore, after removing the electric field [Fig. 10(c) to 10(b)], the unchanged defect symmetry and the associated $\boldsymbol{P_D}$ cause reversible domain switching. As a consequence, the original domain pattern is restored [Fig. 10(b)] so that the defect symmetry and dipole moment follow the crystal symmetry in every domain. An interesting double hysteresis loop in the ***P-E*** relation for Bi-BCT is expected to accompany this reversible domain switching, as observed in Fig. 8. Clearly, the explanation is the same as that for acceptor-doped ABO_3 ferroelectrics (Ren, 2004; Zhang & Ren, 2005, 2006), since aging originates from the mismatch between the defect symmetry and the crystal symmetry after a structural transition. Comparing the double ***P-E*** loop "2" with "3" in Fig. 8, it can be seen that the naturally aging-induced double loop is obvious if the Bi-BCT samples are given a longer period of aging (33 months), which indicates that a longer time was required to establish an equilibrium defect state at room temperature (300 K).

When the measurement temperature is reduced to 280 K from 300 K, the double ***P-E*** loop becomes a normal one. The change of shape of the ***P-E*** loops in Fig. 5 and Fig. 6 can be explained as follows: normally, the coercive field increases with decreasing temperature, especially in some lead-based ceramic samples (Chu et al., 1993; Sakata, et al., 1992). When the samples were measured at low temperature, the coercive field may become higher than the driving force for reversible domain switching. As a result, the $\boldsymbol{P_D}$ creating the driving force is not enough to switch a reversible domain and thus result in a single ***P-E*** loop observation at low temperature for Bi-BCT. A similar change from double to single ***P-E*** loops with temperature has been observed in specially aged $KNbO_3$-based ceramics (Feng & Ren, 2007).

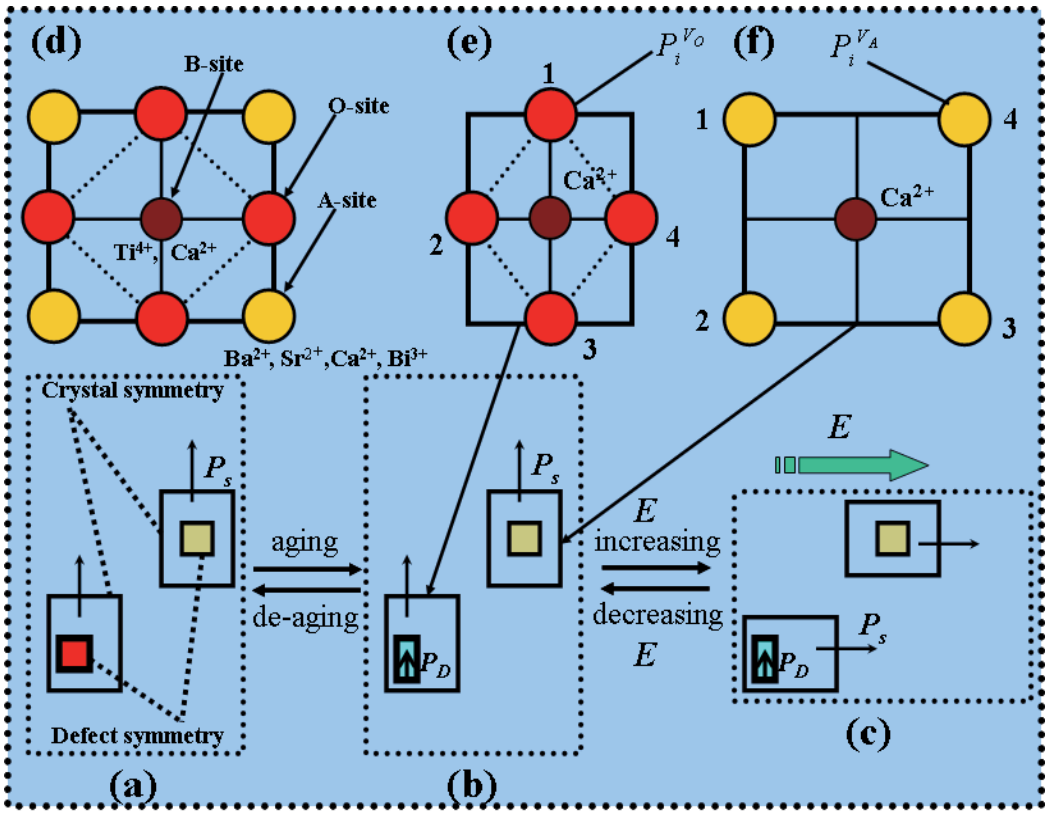

Fig. 10. Microscopic explanation for double-like ***P-E*** loops in bismuth doped BCT ceramics based on the SC-SRO principles. (a) When samples were cooled down below T_C after deaging, the crystal changes to the ferroelectric state with a spontaneous polarization P_S due to the relative displacement of positive and negative ions. The defect symmetry is cubic while the crystal symmetry is tetragonal. (b) After aging, the defect symmetry around an acceptor ion (Ca^{2+}) adopts a polar tetragonal symmetry with a defect dipole P_D, and the defect symmetry of cation vacancies still keeps cubic. (c) On increasing electric field, P_S rotates but P_D keeps the original orientation; this unswitched P_D provides a driving force for the reversible domain switching to (b). (d) When samples was de-aged above the phase transition point T_C, the SRO distribution of point defects keeps the cubic symmetry, oxygen vacancies keep $P_1^{V_O} = P_2^{V_O} = P_3^{V_O} = P_4^{V_O}$ and cation vacancies keep $P_1^{V_A} = P_2^{V_A} = P_3^{V_A} = P_4^{V_A}$, the crystal is in the paraelectric state and has a cubic symmetry. (e)-(f) After natural aging to establish an equilibrium defect state, the redistribution of oxygen vacancies makes $P_1^{V_O} > P_2^{V_O} = P_4^{V_O} > P_3^{V_O}$ [see (e)] while cation vacancies keep $P_1^{V_A} = P_2^{V_A} = P_3^{V_A} = P_4^{V_A}$ because of their immobility (see (f)]. Large rectangle represents crystal symmetry while the small black rectangle represents an oxygen SRO symmetry around an acceptor defect; the gray square represents the SRO of A-site vacancy around an acceptor defect. P_S refers to spontaneous polarization and P_D refers to defect polarization. $P_i^{V_O}$ is the conditional probability of oxygen vacancy occupying O^{2-} site i (i=1–4) next to a given Ca^{2+} and Sr^{2+}, and $P_i^{V_A}$ is the conditional probability of finding a cation vacancy (A-site vacancy) at site i (i=1–4) around Ca^{2+} and Sr^{2+}.

The above results describing the natural aging effect in $(Ba_{1-x}Ca_x)_{0.925}Bi_{0.05}TiO_3$ ferroelectrics are very similar to the special aging effect in acceptor-doped $BaTiO_3$ materials (Ren, 2004; Liu et al., 2006; Zhang et al., 2004; Feng & Ren, 2007; Yuan et al., 2007). The interesting double ***P-E*** loop behavior between the natural aging effect of ABO_3 compound with A-site substitution and the special aging effect of ABO_3 compound with B-site substitution can be explained by the SC-SRO mechanism of point defects. As discussed above, such a mechanism relies essentially on symmetry, not on the crystal structure or ionic species. The key idea of the SC-SRO mechanism is that an equilibrium defect state tends to adopt a match between the defect symmetry and the crystal symmetry in every domain. This tendency does not depend on the crystal structure or ionic species (Ren, 2004; Liu et al., 2006; Zhang et al., 2004; Feng & Ren, 2007, 2008; Yuan et al., 2007).

It seems from the change of shape of hysteresis loops that these two ceramic samples undergo a ferroelectric-antiferroelectric-paraelectric (***FE-AFE-PE***) transition, similar to that observed in $(Na_{0.5}Bi_{0.5})TiO_3$-based ceramics (Takenaka, 1991; Sakata & Masuda, 1974; Tu et al., 1994; Sakata et al., 1992). Some researchers thought that an intermediate phase with double hysteresis loops is as proof of an additional antiferroelectric transition (Sakata & Masuda, 1974; Tu et al., 1994; Balashova & Tagantsev, 1993). Indeed, heterophase fluctuations proposed between the paraelectric and the ferroelectric phase are unreasonable because of energy considerations, but it is possible that at a higher temperature there occurs an extra local phase transition to a nonpolar state. The energy gap between this phase and the ferroelectric phase is relatively small, and therefore heterophase fluctuations between the two phases can take place (Uchino & Nomura, 1978). Inhomogeneities due to chemical disorder cause nonuniformity in the free energy of the two states throughout the material, increasing the probability of heterophase fluctuations. For the selected samples Bi-BSCT, disordering in the Ba, Sr, Ca and Bi cations distributed in A-sites will be favorable for increasing the fluctuation probability, and resulting in an intermediate phase with double hysteresis loops between the paraelectric and the ferroelectric phase. However, it has not been confirmed by other experimental measurements whether the intermediate phase exists in Bi-BSCT. Further experiments on Bi-BCT and Bi-BSCT with TEM for observing the intermediate phase transition need to be carried out.

Here, we need to mention that $BaTiO_3$ ferroelectric systems with dielectric relaxation behavior can usually be formed by doping point defects (impurity or doping) into a normal ferroelectric system. Bi-doped BCST is in such case. These random point defects distort the surrounding crystal lattice and thus generate random local fields. The random distribution of local fields brings about significant effects: the long-range ordering of electric dipoles is prohibited or destroyed while the local short-range ordering is retained. In simpler language, the random point defects will crush the macro-size domains into nano-size domains. Thus, only the local ordered polar nano-domain exists in Bi-doped BCT and BCST. The nearly linear ***P-E*** response (see also Fig. 5 and Fig. 6) is due to the random local field, stemming from the lattice defects by dopants, which has a strong frustration to the nano-domains. This has contributed significantly to our understanding of the contradictions between high dielectric constant and dielectric linearity in the most relaxors. In addition, the linear dielectric response in solid solutions with the dielectric relaxation behavior may provide possibilities for applications.

It is clear that an aging effect exists in Bi-BCT ceramics in the present report, so does it in the more complicated compositions Bi-BSCT ceramics. Based on the SC-SRO mechanism, the diffusional age-induced effect is the main reason causing the double hysteresis loops

observed in Bi-BCT. Similarly, the double hysteresis loops observed between the paraelectric and the ferroelectric states for Bi-BSCT ceramics can be also explained by a point-defect-mediated reversible domain switching mechanism. However, talking about the complexity of ceramic compositions, it is unclear whether the aging effect is only reason resulting in the observed double hysteresis loops for Bi-BCT and Bi-BSCT ceramics according to the suggestion mentioned above, which needs to be confirmed by further experimental evidence.

4. Conclusion

$(Ba_{1-x}Ca_x)_{1-1.5y}Bi_yTiO_3$ (Bi-BCT, x =0.10, 0.20 and 0.30, y=0.05), $(Ba_{1-x}Ca_{x/2}Sr_{x/2})_{1-1.5y}Bi_yTiO_3$ (Bi-BCST, x=0.10, 0.20 and 0.40, y=0 and 0.05) and $(Ba_{0.925}Bi_{0.05})(Ti_{0.90}Ca_{0.10})O_3$ (Bi-BTC) perovskite ceramics were prepared through solid-state reaction technique. The structural, dielectric and ferroelectric properties and ferroelectric aging effect of Bi-BCT and Bi-BSCT ceramics were investigated.

5 at. % of Bi doping can be fully incorporated into the perovskite lattice of Bi-BCT and Bi-BSCT ceramics. The crystalline symmetry of Bi-BCT and Bi-BCST ceramics is a rhombohedral phase for x=0.40 while it is the tetragonal phase for x=0.30, and the crystalline symmetry of ceramics samples tends appreciably towards the coexistence of the tetragonal and rhombohedral phases for Bi-BCT (Bi-BCST) with the compositions of x=0.10 and x=0.20. XRD patterns at elevated temperature has demonstrated that the (002)/(200) refection of Bi-BCT can keep spliting throughout the whole temperature range from 280 K up to 320 K while that of Bi-BSCT can keep spliting throughout the whole temperature range from 280 K up to 300 K.

A typical relaxor behavior, a similar behavior to lead-based relaxor ferroelectrics, has been observed in Bi-BCT and Bi-BSCT ceramics. A random electric field is suggested to be responsible for the relaxor behavior observations. The dielectric peak corresponding to the ferroelectric-antiferroelectric transition cannot be found in the dielectric spectrum within the temperature range 198 K to 430 K for Bi-BCT and Bi-BSCT.

The ***P-E*** relationship at elevated temperature shows that an abnormal double-like ***P-E*** loop was observed for Bi-BCT and Bi-BSCT. The de-aging experiment has shown that there is a diffusional aging effect in Bi-BCT ceramics. The change from the single ***P-E*** loops in the de-aged sample to the double ***P-E*** loops in the aged sample excludes the existence of ferroelectric-antiferroelectric transition in Bi-BCT. Raman scattering gives critical evidence for the formation of O^{2-} vacancies in Bi-BCT. A point-defect-mediated reversible domain switching mechanism is suggested to be responsible for the double hysteresis loops observed between the paraelectric and the ferroelectric states for Bi-BCT ceramics. It is expected that the abnormal ferroelectric behavior of Bi-BSCT ceramics can be explained using a point-defect-mediated reversible domain switching mechanism. The striking similarity of the aging effect between nonequivalence substitution for A-site ions and B-site ions of ABO_3 systems indicates a common physical origin of aging.

5. Acknowledgment

The author acknowledges the financial support of the Scientific Research Program Funded by Shaanxi Provincial Education Department (Program No.2010JK655). This work was also

supported by the PUNAI Education Scholarship through PuYang Refractory Group Co., Ltd. (PRCO).

6. References

Kittel, C. (1951). Theory of Antiferroelectric Crystals. *Physical Review,* Vol.82, No.5, (June 1951), pp. 729–732

Shirane, G.; Sawaguchi, E. & Takagi, Y. (1951). Dielectric Properties of Lead Zirconate. *Physical Review,* Vol.84, No.3, (June 1951), pp. 476–481

Shirane, G. (1952). Ferroelectricity and Antiferroelectricity in Ceramics $PbZrO_3$ Containing Ba or Sr. *Physical Review,* Vol.86, No.2, (June 1952), pp. 219-227

Sawaguchi, E. (1953). Ferroelectricity versus Antiferroelectricity in the Solid Solutions of $PbZrO_3$ and $PbTiO_3$. *Journal of the Physical Society of Japan,* Vol.8, No.5, (September 1953), pp. 615-629

Berlincourt, D.; Jaffe, H.; Krueger, H. H. A.; & Jaffe, B. (1963). Release of Electric Energy in $PbNb(Zr,Ti,Sn)O_3$ by Temperature and by Pressure-enforced Phase Transitions. *Applied Physics Letters*, Vol.3, No.5, (September 1963), pp. 90-92

Berlincourt, D.; Krueger, H. H. A.; & Jaffe, B. (1964). Stability of Phases in Modified Lead Zirconate with Variation in Pressure, Electric Field, Temperature and Composition. *Journal of Physics and Chemistry of Solids,*Vol.25, No.7, (July 1964), pp. 659-674

Biggers, J. V. & Schulze, W. A. (1974). Direct Current Bias of Antiferroelectric PLZT Ceramics. *American Ceramic Society Bulletin,* Vol.53, No.11, (July 1974), pp. 809-812

Gttrttritja, T. R.; Kumarakrishuau, S. & Subbarao, E. C. (1980). Modified PLZT High Voltage Dielectrics. *Ferroelectrics*, Vol.27, No.1, (January 1980), pp. 277-280

Shebanov, L.; Kusnetsov, M. & Sternberg, A. (1994). Electric Field-Induced Antiferroelectric-to-Ferroelectric Phase Transition in Lead Zirconate Titanate Stannate ceramics Modified wtih Lanthanum. *Journal of Applied Physics*, Vol.76, No.7, (October 1994), pp. 4301-4304

Merz, W. J. (1953). Double Hysteresis Loop of $BaTiO_3$ at the Curie Point. *Physical Review,* Vol.91, No.3, (August 1953), pp. 513-517

Ren, X. (2004). Large Electric-Field-Induced Strain In Ferroelectric Crystals by Point-Defect mediated Reversible Domain Switching. *Nature Materials*, Vol.3, (Feburary 2004), pp. 91–94

Zhang, L. & Ren, X. (2005). In Situ Observation of Reversible Domain Switching in Aged Mn-Doped $BaTiO_3$ Single Crystals. *Physical Review B*, Vol.71, No.17, (May 2005), pp. 174108

Zhang, L. & Ren, X. (2006). Aging Behavior in Single-Domain Mn-Doped $BaTiO_3$ Crystals: Implication for A Unified Microscopic Explanation of Ferroelectric Aging. *Physical Revuew B*, Vol.73, No.9, (March 2006), pp. 094121

Liu, W.; Chen, W.; Yang, L.; Zhang, L.; Wang, Y.; Zhou, C.; Li, S. & Ren, X. (2006). Ferroelectric Aging Effect in Hybrid-doped $BaTiO_3$ Ceramics and the Associated Large Recoverable Electrostrain. *Applied Physics Letters*, Vol.89, No.17, (October 2006), pp. 172908

Takenaka, E.; Maruyama, K. I. & Sakata, K. (1991). $(Bi_{1/2}Na_{1/2})TiO_3$-$BaTiO_3$ System for Lead-free Piezoelectric Ceramics. *Japanese Journal of Applied Physics*, Vol.30, No.9B, (September 1991), pp. 2236-2239

Sakata, K. & Masuda, Y. (1974). Ferroelectric and Antiferroelectric Properties of $(Bi_{1/2}Na_{1/2})TiO_3$-$SrTiO_3$ Solid Solution Ceramics. *Ferroelectrics*, Vol.7, No.1, (January 1974), pp. 347-349

Tu, C. S.; Siny, I. G. & Schmidt, V. H. (1994) Sequence of Dielectric Anomalies and High-Temperature Relaxation Behavior in $Na_{1/2}Bi_{1/2}TiO_3$. *Physical Revuew B*, Vol.49, No.13, (April 1994), pp. 11550.

Sakata, K.; Takenaka, T. & Naitou, Y. (1992). Phase Relations, Dielectric and Piezoelectric Properties of Ceramics in the System $Na_{1/2}Bi_{1/2}TiO_3$–$PbTiO_3$. *Ferroelectrics*, Vol.7, No.1, (January 1992), pp. 219-349

Zhang, L.; Chen, W. & Ren, X. (2004). Large Recoverable Electrostrain in Mn-doped (Ba, Sr)TiO_3 Ceramics. *Applied Physics Letters*, Vol.85, No.23, (October 2004), pp. 5658-5660

Feng, Z. & Ren, X. (2007). Aging Effect and Large Recoverable Electrostrain in Mn-doped $KNbO_3$-based Ferroelectrics. *Applied Physics Letters*, Vol.91, No.3, (July 2007), pp. 032904

Feng, Z. & Ren, X. (2008). Striking Similarity of Ferroelectric Aging Effect in Tetragonal, Orthorhombic and Rhombohedral Crystal Structures. *Physical Revuew B*, Vol.77, No.13, (April 2008), pp. 134115

Yuen, G. L.; Yang, Y. & Or, S. W. (2007). Aging-Induced Double Ferroelectric Hysteresis Loops in $BiFeO_3$ Multiferroic Ceramic. *Applied Physics Letters*, Vol.91, No.12, (September 2007), pp. 122907

Yasuda, N. & Konda, J. (1993). Successive Paraelectric-Antiferroelectric-Ferroelectric Phase Transitions in Highly Ordered Perovskite Lead Ytterbium Tantalite. *Applied Physics Letters*, Vol.62, No.5, (Feburary 1993), pp. 535-537

Uchino, K. & Nomura, S. (1978). Dielectric and Magnetic Properties in the Solid Solution System $Pb(Fe_{2/3}W_{1/3})O_3$-$Pb(Co_{1/2}W_{1/2})O_3$. *Ferroelectrics*, Vol.17, No.1, (January 1978), pp. 505-510

Chu, F.; Setter, N. & Tagantsev, A. K. (1993). The Spontaneous Relaxor-Ferroelectric Transition of $Pb(Sc_{0.5}Ta_{0.5})O_3$. *Journal of Applied Physics*, Vol.74, No.8, (October 1993), pp. 5129-5134

Hachiga, T.; Fujimoto, S. & Yasuda, N. (1986). Temperature and Pressure Dependence of the Dielectric Properties of $Pb(Co_{1/2}W_{1/2})O_3$. *Journal of Physics D: Applied Physics*, Vol.19, No.2, (Feburary 1986), pp. 291-298

Srivastava, N. & Weng, G. J. (2006). A Theroy of Double Hysteresis for Ferroelectric Crystals. *Journal of Applied Physics*, Vol.99, No.5, (March 2006), pp. 054103

Zhou, L.; Vilarinho, P. M. & Baptista, J. L. (1999). Solubility of Bismuth Oxide in Barium Titanate. *Journal of the American Ceramic Society,* Vol.82, No.4, (April 1999), pp. 1062-1066

Zhou, L.; Vilarinho, P. M. & Baptista, J. L. (2000). Relaxor Behavior of $(Sr_{0.8}Ba_{0.2})TiO_3$ Ceramic Solid Solution Doped with Bismuth. *Journal of Electroceramic,* Vol.5, No.3, (May 2000), pp. 191-199

Zhou, L.; Vilarinho, P. M. & Baptista, J. L. (2001). Dielectric Properties of Bismuth Doped $Ba_{1-x}Sr_xTiO_3$ Ceramics. *Journal of the European Ceramic Society,* Vol.21, No.4, (April 2001), pp. 531-534

Ang, C.; Yu, Z.; Vilarinho, P. M. & Baptista, J. L. (1998). Bi:$SrTiO_3$: A Quantum Ferroelectric and a Relaxor. *Physical Revuew B*, Vol.57, No.13, (April 1998), pp. 7403-7406

Bednorz, J. G. & Müller, K. A. (1984). $Sr_{1-x}Ca_xTiO_3$: An XY Quantum Ferroelectric with Transition to Randomness. *Physics Review Letters*, Vol.52, No.25, (June 1984), pp. 2289-2292

Toulouse, J.; Vugmeister, B. E. & Pattnaik. (1994).Collective Dynamics of Off-Center Ions in $K_{1-x}Li_xTaO_3$: A Model of Relaxor Behavior. *Physics Review Letters*, Vol.73, No.25, (December 1994), pp. 3467-3470

Bokov, A. A. & Ye, Z. G. (2006). Recent Progress in Relaxor Ferroelectrics with Perovskite Structure. *Journal of Materials Science,* Vol.41, No.1, (January 2006), pp. 31-52

Han, Y. H.; Appleby, J. B. & Smyth, D. M. (1987). Calcium As An Acceptor Impurity in $BaTiO_3$. *Journal of the American Ceramic Society,* Vol.70, No.2, (Feburary 1987), pp. 96-100

Zhuang, Z. Q.; Harmer, M. P.; Smyth, D. M. & Newnham, R. E. (1987). The Effect of Octahedrally-Coordinated Calcium on the Ferroelectric Transition of $BaTiO_3$. *Materials Research Bulletin,* Vol.22, No.10, (October 1987), pp. 1329-1335

Mitsui, T. & Westphal, W. B. (1961). Dielectric and X-ray Studies of $Ca_xBa_{1-x}TiO_3$ and $Ca_xSr_{1-x}TiO_3$. *Physical Review,* Vol.124, No.5, (July 1961), pp. 1354-1359

Baskara, N. & Chang, H. (2003).Thermo-Raman and Dielectric Constant Studies of $Ca_xBa_{1-x}TiO_3$ Ceramics. *Materials Chemistry and Physics,* Vol.77, No.3, (January 2003), pp. 889-894

Karl, K & Hardtl, K. H. (1978). Electrical After-Effects in Pb(Ti, Zr)TiO_3 Ceramics. *Ferroelectrics*, Vol.17, No.1, (January 1978), pp. 473-486

Postnikov, V. S.; Pavlov, V. S. & Turkov, S. K. (1970). Internal Friction in Ferroelectrics Due to Interaction of Domain Boundaries and Point Defects. *Journal of Physics and Chemistry of Solids,* Vol.31, No.8, (August 1970), pp. 1785-1791

Lambeck, P. V. & Jonker, G. H. (1986). The Nature of Domain Stabilization in Ferroelectric Perovskites. *Journal of Physics and Chemistry of Solids,* Vol.47, No.5, (September 1986), pp. 453-461

Krishna, P. S. R.; Pandey, D.; Tiwari, V. S.; Chakravarthy, R. & Dasannachary, B. A. (1993). Effect of Powder Synthesis Procedure on Calcium Site Occupancies in Barium Calcium Titanate: A Rietveld analysis. *Applied Physics Letters*, Vol.62, No.3, (January 1993), pp. 231-233

Chang, M. C. & Yu, S. C. (2000). Raman study for $(Ba_{1-x}Ca_x)TiO_3$ and $Ba(Ti_{1-y}Ca_y)O_3$ crystalline ceramics. *Journal of Materials Science Letters,* Vol.19, No.15, (August 2000), pp. 1323-1325

Park, J. G.; Oh, T. S. & Kim, Y. H. (1992). Dielectric Properties and Microstructural Behaviour of B-Site Calcium-Doped Barium Titanate Ceramics. *Journal of Materials Science,* Vol.27, No.21, (November 1992), pp. 5713-5719

Burns, G. (1974). Lattice Modes In Ferroelectric Perovskites. II. $Pb_{1-x}Ba_xTiO_3$ Including $BaTiO_3$. *Physical Revuew B*, Vol.10, No.5, (September 1974), pp. 1951-1959

Begg, B. D.; Finnie, K. S. & Vance, E. R. (1996). Raman Study of the Relationship between Room-Temperature Tetragonality and the Curie Point of Barium Titanate. *Journal of the American Ceramic Society,* Vol.79, No.10, (October 1996), pp. 2666-2672

Tan, Q.; Li, J. & Viehland, D. (1999). Role of Lower Valent Substituent-Oxygen Vacancy Complexes in Polarization Pinning in Potassium-Modified Lead Zirconate Titanate. *Applied Physics Letters*, Vol.75, No.3, (May 1999), pp. 418-420

Balashova, E. V. & Tagantsev, A. K. (1993). Polarization Response of Crystals with Structural and Ferroelectric Instabilities. *Physical Revuew B*, Vol.48, No.14, (October 1993), pp. 9979-9986

14

The Ferroelectric Dependent Magnetoelectricity in Composites

L. R. Naik and B. K. Bammannavar
Department of Studies in Physics, Karnatak University, Dharwad-580003
India

1. Introduction

Ferroelectric materials (dielectric materials) attracted the attention of many researchers because of their important applications in the field of science and technology. Ferroelectrics are stable materials having spontaneous polarization and can be switched hysteretically by an electric field; but antiferroelectric materials possess ordered dipole moments that cancel each other completely within each crystallographic unit cell. (The stable ferromagnetic materials possess a spontaneous magnetization and can be switched hysteretically by an applied magnetic field but antiferromagnetic materials possess ordered magnetic moments that cancel each other completely within each magnetic unit cell). Ferroelectrics are similar to ferromagnetic materials but ferromagnetic materials exhibit a permanent magnetic moment. In 1921, J. Valasek discovered the phenomenon of ferroelectricity during the study of the anomalous dielectric properties of Rochelle salt ($NaKC_4H_4O_6.\ 4H_2O$) and in 1935 a second ferroelectric material (KH_2PO_4) was investigated followed by some of its isomorphs. In 1944, the third major substance ($BaTiO_3$) was reported by A. Van Orippel, since then his small group suggested many more mixed crystal systems. The dielectric materials are sub divided into 32 crystal classes/ point groups [1] and they get polarized under the influence of an electric field. Out of these 32 classes, 20 classes are piezoelectric, in which a charge can be induced upon the application of mechanical stress. However, out of twenty piezoelectric classes ten exhibits a finite and permanent polarization known as spontaneous polarization in the presence or absence of an applied electric field or stress and such piezoelectrics are known as polar materials. Polar materials possess domain structure and show Curie-Weiss behavior near their phase transition temperature/ Curie temperature. An important and interesting features of the ferroelectrics are the anomalous dielectric properties, non-linearities, reversible polarization and disappearance of ferroelectricity above a certain temperature called transition temperature/ Curie temperature (T_C). At the transition temperature/ Curie temperature the permittivity increases sharply to a very high peak value where as the dielectric constant becomes maximum near the transition temperature. Some general features of ferroelectric materials are as follows

- Ferroelectrics exhibits transition at certain temperature called Curie temperature and lead to high symmetrical structure. At Curie temperature the ferroelectric phase transitions are associated either with anomalous behavior of specific heat or the latent heat.

- Ferroelectric crystal possesses domain structure but at the transition temperature there is a sudden appearance of surface charge and below Curie temperature these materials show piezoelectric and pyroelectric properties.
- Ferroelectrics possess high dielectric constant [2] along the polarization axes as a function of temperature and it reaches to a peak value at the Curie temperature.

$BaTiO_3$ is an important ferroelectric material widely used in ceramic technology. Ferroelectric materials possesses polycrystalline structure with perovskite crystal structure (tetragonal/rhombohedral structure very close to cubic) and has general formula A^{2+} B^{4+} O_3^{2-} in which A denotes divalent or trivalent ion such as barium or lead and B denotes a tetravalent or pentavalent metal ion such as zirconium or titanium.

These crystallites exhibit simple cubic symmetry above the Curie temperature. The crystal structure is centro symmetric with coincidence of positive and negative charge sites as there are no dipoles present in the materials (as it exhibits paraelectric behavior) however, below Curie temperature, the crystallites have tetragonal symmetry in which the positive and negative charge sites no longer coincide.

Lead zirconate titanate (PZT) [3] and barium lead zirconate titanate (BPZT) ferroelectrics are the members of pervoskite family. These ferroelectrics are most widely used in various materials applications. PZT has the cubic pervoskite structure (paraelectric) at high temperature and on cooling below the Curie point the structure undergoes phase transition to form a ferroelectric tetragonal structure. For specific requirements (for certain applications), piezoelectric ceramics are modified by doping them with ions which have a valency, different from that of ions in the lattice. Depending on the doping process, PZT's, are classified into soft PZT's and hard PZT's. The soft PZT's have higher piezoelectric coefficient and are easy to pole and depole, compared to hard PZT's. Barium doped PZT's show good piezoelectric properties, dielectric properties and better ME properties, while lead and zirconium doped $BaTiO_3$ (BPZT) is used to enhance the piezoelectric and mechanical properties. Barium lead zirconate titanate (BPZT - $Ba_{0.8}Pb_{0.2}Zr_{0.8}Ti_{0.2}O_3$) and lead zirconate titanate (PZT- $PbZr_{0.8}Ti_{0.2}O_3$) are chosen as the ferroelectric phases. BPZT is an important piezoelectric material having high dielectric permeability, high dielectric constant and good piezoelectric effect. The induced piezoelectric properties are maintained to obtain maximum piezoelectric conversion factor. Also the PZT has high piezoelectric coefficient, dielectric constant, permittivity and better coupling factor.

2. Methods of preparation

In ceramic technology several methods have been used for the preparation of magnetoelectric composites. The standard double sintering solid state reaction method is one among them (ceramic method) and has been extensively used to study the properties of resulting materials [4, 5]. Magnetoelectric effect is a structure dependent property [6], and at the same time the presence of impurity or intermediate phases in the composite will affect the ME signal [7]. However, the preparation of the ME composites without impurity is a challenging task, as the microstructural mismatching between two phases results in energy loss. Thus care has been taken to prepare the composites to reduce the energy loss. The said method is easier and much cheaper compared to other methods and offers several advantages over the choice of mole fraction of constituent phases, control of grain size and sintering temperature etc. The microstructural aspects such as grain size, pore concentration and grain shapes depend on the purity of the starting materials, mixing condition, sintering temperature, sintering time etc., [8, 9].

In the present work standard double sintering ceramic method is used for the preparation of homogeneous ferrite /ferroelectric phases and their composites of fine particles. In this method it is possible to maintain the stoichiometry of the final product even at large scale production. The method involves the following steps,

1. High purity oxides/ carbonates are mixed together (stoichiometry is maintained) in acetone medium by constant milling for longer period in an agate mortar to form homogenous mixture.
2. In the second stage "Presintering" (heating of the homogenous mixture) process is used to decompose carbonates and higher oxides from the raw materials to remove absorbed gases, moistures and to make oxides to react partially.
3. In the intermediate stage, presintered powder is ground to fine powder to reduce the particle size, which helps for the mixing of unreacted oxides if any. Later on fine powder is mixed with binder and pressed by using a die and a hydraulic press to get the desired shapes.
4. The "Final sintering" (final stage) increases the density of pellets by reducing the porosity. Infact sintering temperature and time affect the microstructure, oxygen content and cation distribution. In this stage uniform grain size, granular grains and other requirements are to be achieved.

The electric and magnetic phases such as ferroelectric and ferrites were prepared separately and then their proper molar proportions are mixed together to form a composites.

3. Structural characterization by XRD measurements

X-ray diffraction (XRD) technique is used for materials characterization (ferrites, ferroelectrics and composites etc) as it provides important information about the internal structure of matter such as grain size (crystallite size), nature of the solid sample (amorphous or crystalline) and crystal structure.

3.1 Ferroelectric phase

The XRD patterns of the ferroelectric systems $Ba_{0.8}Pb_{0.2}\,Zr_{0.8}\,Ti_{0.2}O_3$ and $Pb\,Zr_{0.8}\,Ti_{0.2}O_3$ (fig 1 & 2) with well defined peaks and highest intensity line (101/110) without intermediate phase

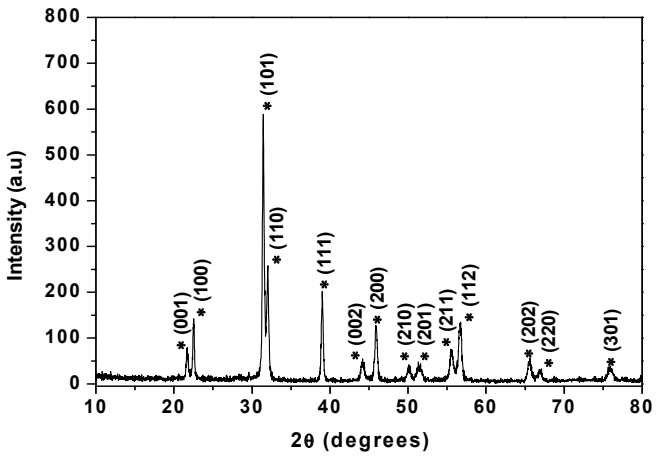

Fig. 1. XRD pattern of $Ba_{0.8}Pb_{0.2}\,Zr_{0.8}\,Ti_{0.2}O_3$ ferroelectric phase

formation confirms the tetragonal perovskite structure. The prominent peaks are indexed with the help of JCPDs data. The observed and calculated 'd' values are good agreement with each other. The lattice parameters of $Ba_{0.8}Pb_{0.2}Zr_{0.8}Ti_{0.2}O_3$ (a = 4.031 Å and c = 4.032 Å) and $PbZr_{0.8}Ti_{0.2}O_3$ (a = 4.128 Å and c = 4.129 Å) are in good agreement with the earlier reports[10].

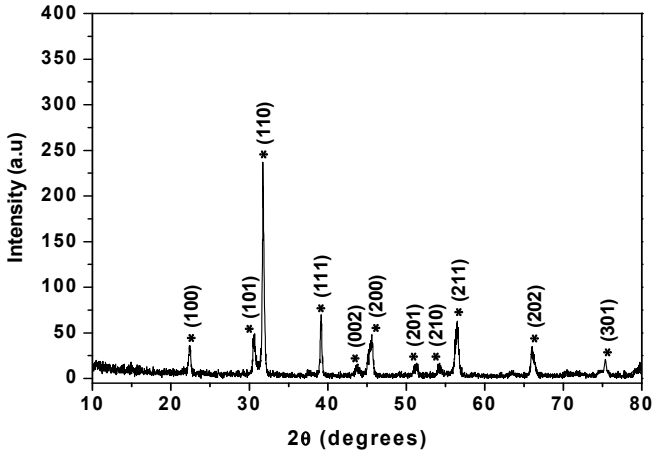

Fig. 2. XRD pattern of $PbZr_{0.8}Ti_{0.2}O_3$ ferroelectric phase

The scanning electron micrographs of two ferroelectric systems are shown in figs (3 & 4). The average grain diameter for each phase is calculated and is well with experimental results. The ferroelectric systems show fine grains with larger grain diameters than ferrite systems. In ceramics the dependence of grain growth mechanism was explained by Paulus [11] with particle size, composition and sintering temperature. However, the small grain size is important in domain geometry for the study of magnetic properties as well as ME properties.

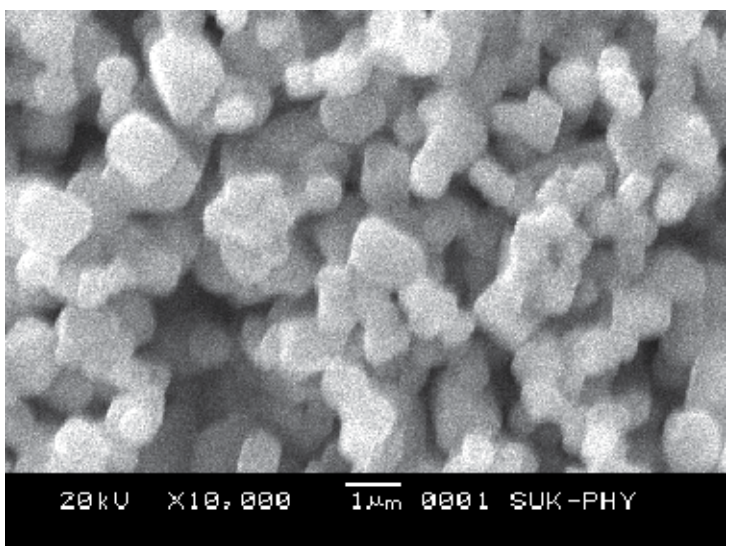

Fig. 3. SEM micrograph of $Ba_{0.8}Pb_{0.2}Zr_{0.8}Ti_{0.2}O_3$ ferroelectric phase

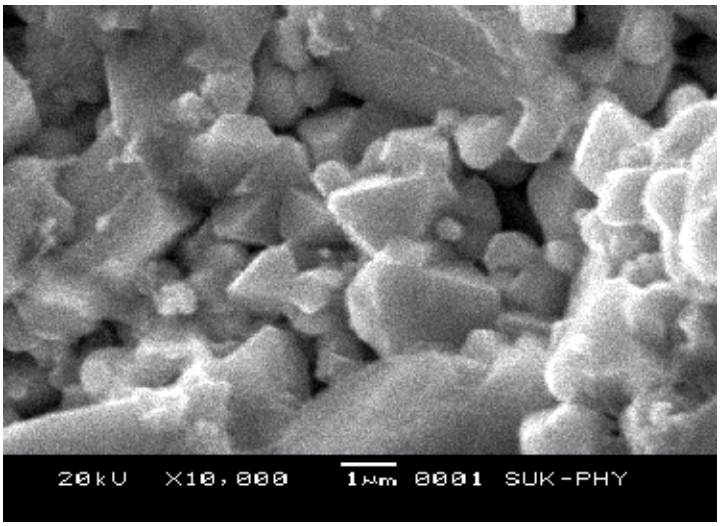

Fig. 4. SEM micrograph of $Pb\,Zr_{0.8}\,Ti_{0.2}O_3$ ferroelectric phase

5. DC electrical resistivity

The DC electrical resistivity of the samples are measured by two probe method. For good electrical contacts, the polished surfaces of pellets are silver coated on both sides and mounted in the sample holder. Afterwords it is placed in the digital temperature controlled muffle furnace and a constant voltage about 5 volts is applied using stabilized power supply unit and the current at different temperature is measured using digital nano ammeter. The resistivity of all the samples ρ_{DC} (ohm-cm) was estimated by measuring the current at the fixed voltage (ohm's law).

$$\rho_{DC} = \frac{R r^2 \pi}{t} \tag{1}$$

Where t - thickness of the pellet (cm), r - radius of the pellet (cm) and R- resistance (ohm). The variation of DC resistivity with temperature for (x) $Ni_{0.2}\,Co_{0.8}\,Fe_2O_4$ + (1-x) $Ba_{0.8}Pb_{0.2}\,Zr_{0.8}\,Ti_{0.2}O_3$ composites (with x = 0.0, 0.15, 0.30, 0.45 and 1.0) are presented elsewhere [12]. The first region among the two regions of conductivity, observed at lower temperature is attributed to ordered states of the ferroelectric phase and the second region observed at higher temperature due to polaron hopping is attributed to the disordered para electric states of the composites. However, the impurities present in the system are almost minimized at higher temperature. Polaron hopping is valid in ferroelectrics as well as in composites containing ferrite and ferroelectrics [13]. According to hopping conduction mechanism the resistivity of composites are found to decrease with increase in ferrite content (due to its low resistivity compared to ferroelectric phase). The ferrite particles disperse throughout the composites and make connected chains with the ferroelectric particles which reduces resistivity significantly. Good dispersion of the ferrite particles are required to obtain high electrical conductivity in the composites. The electrical conductivity in ferrites are explained on the basis of Verwey de Boer mechanism, as it involves the electron exchange between ions of same element which are already present in more than one

valance state and distributed randomly over the crystallographic equivalent lattice sites. The resistivity of the composite is the sum of the resistivities of their constituents [14] and the decrease in resistivity with increase in temperature is attributed to the increase in drift mobility of charge carriers. During the process of preparation, the formation of Fe^{2+} and Fe^{3+} ions depends on the sintering condition. But large drop in resistivity is observed on the addition of a ferrite phase to the composites, it is due to the partial reduction of Fe^{2+} and Fe^{3+} ions at elevated firing temperatures. While preparing the mixtures of two phases to get high ME response in the composites the control of the resistivity of the ferrite phase is necessary compared to ferroelectric phase. Similar results have been identified in the temperature dependent resistivity plot for the (x) $Ni_{0.2}$ $Co_{0.8}$ Fe_2O_4 + (1-x) Pb $Zr_{0.8}$ $Ti_{0.2}O_3$ composites with x = 0.0, 0.15, 0.30, 0.45 and 1.0 [15].

The variation of DC electrical resistivity with temperature for (x) $Ni_{0.5}$ $Zn_{0.5}$ Fe_2O_4 + (1-x) $Ba_{0.8}Pb_{0.2}$ $Zr_{0.8}$ $Ti_{0.2}O_3$ composites with x = 0.0, 0.15, 0.30, 0.45 and 1.0 is also presented earlier [16]. The resistivity of the composites decreases with increase in ferrite content and the increase in resistivity with temperature is due to the increase in drift mobility of the charge carriers. However, the conduction in ferrite may be due to the hopping of electron from Fe^{2+} and Fe^{3+} ions. The number of such ion pairs depends upon the sintering conditions and which accounts for the reduction of Fe^{3+} to Fe^{2+}at elevated temperatures. That is the resistivity of ferrite is controlled by the Fe^{2+} concentration on the B-site. In Ni-ferrite, Ni ions enter the lattice in combination with Fe^{3+} ions resulting in a lower concentration of Fe^{2+} ions with higher resistivity and which is one of the prime requirements for getting higher values of ME output. According to theoretical predictions the plots of ferroelectric phase and composites show two regions of conductivity and the change in slope is due to the transition of the sample from the ferroelectric state to para electric state. However, the regions observed above and below the Curie temperature may be due to the impurities and small polaron hopping mechanism.

The mobility is temperature dependent quantity and can be characterized by the activation energy. But at the grain boundaries, the highly disturbed crystal lattice may cause a drastic decrease in the activation energy. The activation energy in the present case is obtained by fitting the DC resistivity data with the Arrhenius relation $\rho = \rho_o \exp(\Delta E/KT)$, where ΔE is the activation energy and K is Boltzmann constant. It is well known that the electron and hole hopping between $Fe^{2+}/Fe^{3+}$and Zn^{2+}/Zn^{3+}, Ni^{2+}/Ni^{3+}, Ba^{2+}/Ba^{3+}, Ti^{3+}/Ti^{4+} ions is responsible for electrical conduction in the composites. The estimated activation energies for the composites in the higher and lower temperature regions suggest temperature dependent charge mobility and activation energy of paraelectric region greater than 0.2 eV (above Tc), reveals polaron hoping in composites. Similar behavior is observed for (x) $Ni_{0.5}$ $Zn_{0.5}$ Fe_2O_4 + (1-x) $PbZr_{0.8}Ti_{0.2}O_3$ composites (with x = 0.0, 0.15, 0.30, 0.45 and 1.0). In case of composites, the temperature dependent variation of resistivity is very important for the measurements of ME conversion factor, because the conduction in composites being thermally activated mechanism, alters the polarization of the ferroelectric phase as temperature increases. Thus the ME measurements are carried out only at the room temperature [17].

6. Dielectric properties and AC conductivity

6.1 AC conductivity measurements

The temperature dependent AC conductivity (σ_{AC}) are related to the dielectric relaxation caused by the localized electric charge carriers. And the frequency dependent AC conductivity is estimated from dielectric constant and loss tangent (tanδ) using the relation

$$\sigma_{AC} = \varepsilon' \varepsilon_o 2\pi f \tan \delta \quad (2)$$

Where, ε′ is real dielectric constant, ε_o is the permittivity of free space, tanδ is the loss tangent at real ε′ (at dielectric constant) and f is the frequency of applied field. However, the conduction mechanism in composites are obtained from the plots of frequency response of the dielectric behavior and AC conductivity.

6.2 Variation of dielectric constant (ε´) and loss tangent (tanδ)

The variation of dielectric constant with frequency at room temperature for the four composite systems shows good response and are reported elsewere [12]. The dielectric constant decreases with increase in test frequency indicating dispersion in certain frequency region and then reaches a constant value. The high values of dielectric constant at lower frequency region and low values at higher frequency region indicate large dispersion due to Maxwell-Wagner [18, 19] type of interfacial polarization in accordance with Koop's theory. At lower frequencies the dielectric constants of ferrites, ferroelectrics and their composites vary randomly. It is due to the mismatching of grains of ferrites and ferroelectrics in the composites and hence it is difficult to estimate the effective values of dielectric constant of composites.

The decrease in dielectric constant with increase in frequency indicating dielectric dispersion due to dielectric polarization. Dielectric polarization is due to the changes in the valence states of cations and space charge polarization mechanism. At higher frequencies, the dielectric constant is independent of frequency due to the inability of the electric dipoles to follow up the fast variation of the applied alternating electric field and increase in friction between the dipoles. However, at lower frequencies the higher values of the dielectric constant are due to heterogeneous conduction; some times it is because of polaron hopping mechanism resulted in electronic polarization contributing to low frequency dispersion. In composites due to the friction, the dipoles dissipate energy in the form of heat which affects internal viscosity of the system and results in decrease of the dielectric constant; this frequency independent parameter is known as static dielectric constant. The dielectric behavior in composites can also be explained on the basis of polarization mechanism in ferrites because conduction beyond phase percolation limit is due to ferrite. In ferrites, the rotational displacement of $Fe^{3+} \leftrightarrow Fe^{2+}$ dipoles results in orientation polarization that may be visualized as an exchange of electrons between the ions and alignment of dipoles themselves with the alternating field. In the present ferrites, the presence of Ni^{2+}/Ni^{3+}, Co^{2+}/Co^{3+} and Zn^{2+}/Zn^{3+} ions give rise to p-type carriers and also their displacement in the external electric field direction contributes to the net polarization in addition to that of n-type carriers. Since the mobility of p-type carriers is smaller than that of n-type carriers, their contribution to the polarization decreases more rapidly even at lower frequency. As a result, the net polarization increases initially and then decreases with increase in frequency. The transport properties such as electrical conductivity and dielectric dispersion of ferrites are mainly due to the exchange mechanism of charges among the ions situated at crystallographic equivalent sites [20]. Iwauchi [21] and Rezlescu et al have established inverse relation between conduction mechanism and dielectric behavior based on the local displacement of electrons in the direction of applied field.

The variation of dielectric loss factor (tanδ) with frequency was also explained. At lower frequencies loss factor is large and it goes on decreasing with increase in frequency. The loss factor is the energy dissipation in the dielectric system, which is proportional to the imaginary part of the dielectric constant (ε″). At higher frequencies, the losses are reduced due to serial arrangements of dipoles of grains which contribute to the polarization. The losses can also be explained in terms of relaxation time and the period of applied field.

When loss is minimum, then relaxation time is greater than period of applied field and it is maximum when relaxation time is smaller than the period of applied field.

6.3 Ferroelectric phase

The variations of dielectric constant with temperature for two ferroelectric systems (BPZT and PZT) are shown in figs (5 & 6). The dielectric constant increases with increase in temperature and becomes maximum at Curie temperature (T_c) and there after it decreases. For BPZT and PZT ferroelectrics, the observed T_c are nearly 160 ^oC and 410 ^oC, slightly greater than the reported values and can be attributed to constrained grains. Hiroshima et al [22] have reported a close relation between the Curie temperature and internal stresses developed in the constrained grains at the phase transition temperature. The internal stress can shift T_c to higher temperature sides in case of larger grains (diameter greater than 1 μm).

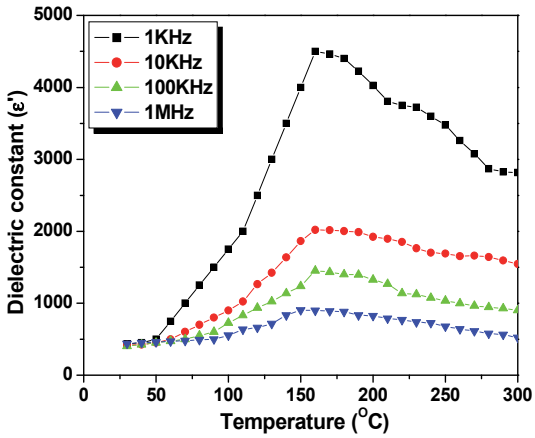

Fig. 5. Variation of dielectric constant with temperature for $Ba_{0.8}Pb_{0.2}\,Zr_{0.8}\,Ti_{0.2}O_3$ ferroelectric phase

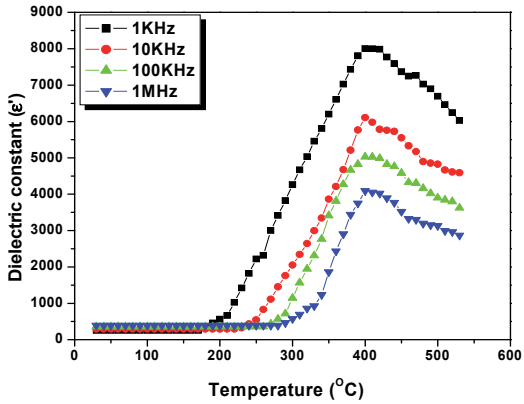

Fig. 6. Variation of dielectric constant with temperature for $Pb\,Zr_{0.8}\,Ti_{0.2}O_3$ ferroelectric phase

The larger grained structure and changes in internal stresses are expected in the pellets due to higher sintering temperature. The large grained ferroelectrics have considerable internal

stress concentration which is enough to form micro cracks at the grain boundaries and hence induced internal stresses are relieved. But in small grain sized ceramics, increased grain boundaries form less micro cracks which reduce the internal stress concentration. Usually the ferroelectric materials have high dielectric constant compared to ferrite; hence dielectric property is enhanced with the increase in ferroelectric content, which is very important in the study of ME output [12]. The nature of variation of dielectric loss tangent with temperature for all the series of composites and their constituent phases shown in figures (7 & 8), almost the same as that of the variation of dielectric constant with temperature. The observed dispersion behavior of the loss tangent is attributed to higher domain mobility near the Curie temperature.

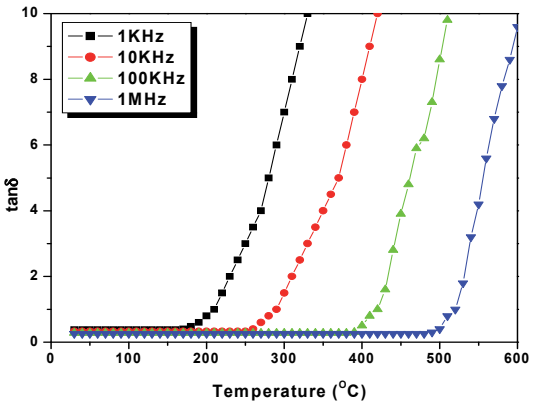

Fig. 7. Variation of dielectric loss tangent with temperature for $Ba_{0.8}\,Pb_{0.2}\,Zr_{0.8}\,Ti_{0.2}O_3$ ferroelectric phase

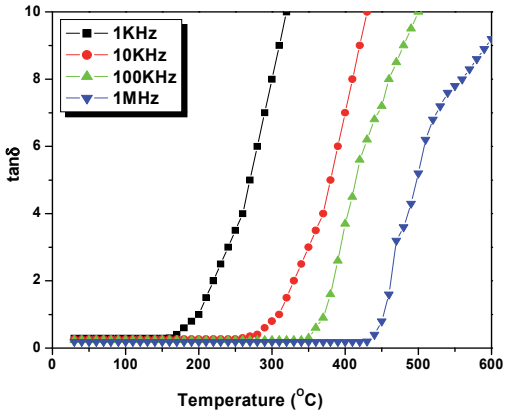

Fig. 8. Variation of dielectric loss tangent with temperature for $Pb\,Zr_{0.8}\,Ti_{0.2}O_3$ ferroelectric phase

6.4 Variation of AC conductivity with frequency at room temperature

The variation of AC conductivity (σ_{AC}) as a function of frequency was presented in figures (9 - 12). From AC conductivity one can retrieve at the behaviour of thermally activated conduction mechanism and the type of polarons responsible for the conduction mechanism.

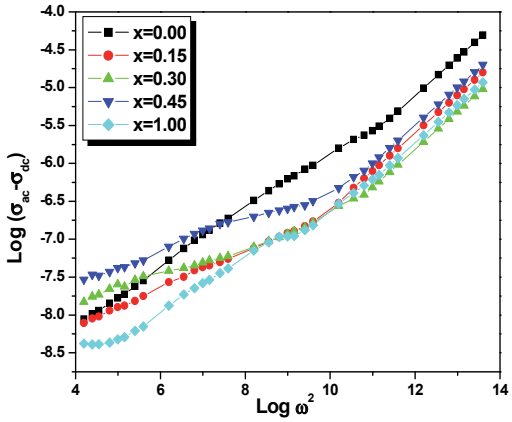

Fig. 9. Variation of AC conductivity with frequency for (x) $Ni_{0.2}Co_{0.8}Fe_2O_4$+ (1-x) $Ba_{0.8}Pb_{0.2}Zr_{0.8}Ti_{0.2}O_3$ composites

Infact the polaron type of conduction was reported by Austin and Mott [23] and Appel et al. According to Alder and Feinleib [24] the direct frequency dependence conduction due to small polarons is given by the relation

$$\sigma_{AC} - \sigma_{DC} = \frac{\omega^2 \tau^2}{\left(1 - \omega^2 \tau^2\right)} \tag{3}$$

Where ω is the angular frequency and τ is the staying time (10^{-10} s), for all the ceramics $\omega^2 \tau^2 < 1$. The plots of log (σ_{AC} -σ_{DC}) against Log ω^2 are linear in nature indicating small polaron type of conduction. However, a slight decrease in the conductivity at a certain frequency is attributed to mixed polaron (small/large) type of conduction and similar results are reported by various workers. In the present case, the AC conductivity of the composites caused by small polarons is responsible for the good ME response.

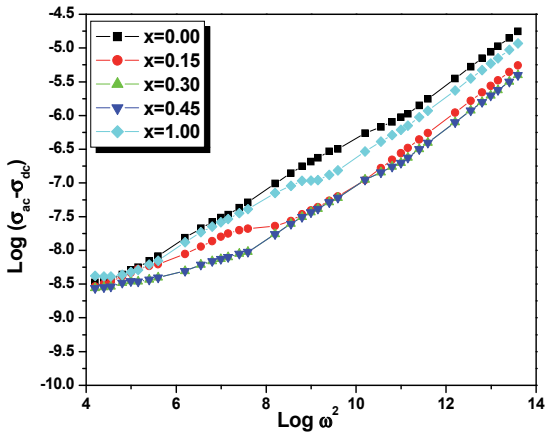

Fig. 10. Variation of AC conductivity with frequency for (x) $Ni_{0.2}Co_{0.8}Fe_2O_4$+ (1-x) $PbZr_{0.8}Ti_{0.2}O_3$ composites

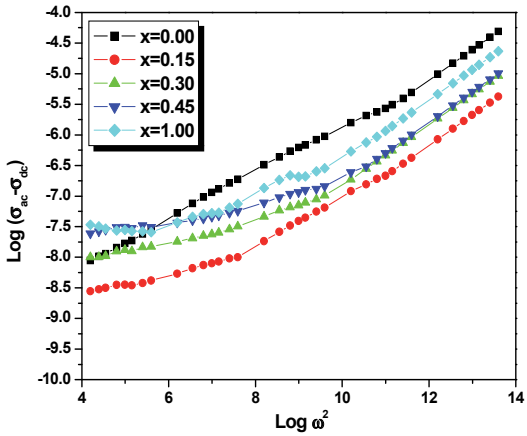

Fig. 11. Variation of AC conductivity with frequency for (x) $Ni_{0.5}$ $Zn_{0.5}$ Fe_2O_4+ (1-x) $Ba_{0.8}Pb_{0.2}$ $Zr_{0.8}$ $Ti_{0.2}O_3$ composites

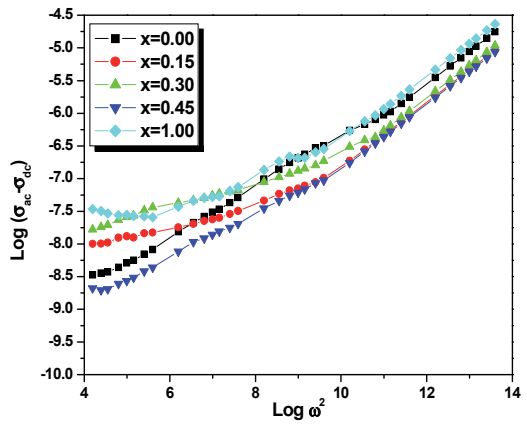

Fig. 12. Variation of AC conductivity with frequency for (x) $Ni_{0.5}$ $Zn_{0.5}$ Fe_2O_4+ (1-x) Pb $Zr_{0.8}$ $Ti_{0.2}O_3$ composites

7. Magnetoelectric effect- A product property

Magnetoelectricity, the product property, requires biphasic surrounding to exhibit the complex behaviour. The primary magnetoelectric (ME) materials can be magnetized by placing them in electric field and can be electrically polarized by placing them in magnetic field [25]. The magnetoelectric effect in the composites having ferrite and ferroelectric phases depends on the applied magnetic field, electrical resistivity, mole percentage of the constituent phases and mechanical coupling between the two phases. The resistivity of the composites is a temperature dependent property which decreases in high temperature region, making the polarization of the samples more difficult. In the present studies the ME voltage coefficient is measured at room temperature. The ME coupling can be obtained by electromechanical conversion in the ferrite and ferroelectric phases by the transfer of stress through the interface between these two phases. Infact magneto mechanical resonance in the ferrite phase and electromechanical resonance in ferroelectric phase are responsible for the origins of ME peaks.

For the composite systems (x) $Ni_{0.2}Co_{0.8}Fe_2O_4$ + (1-x) $Ba_{0.8}Pb_{0.2}Zr_{0.8}Ti_{0.2}O_3$ (with x = 0.15, 0.30 and 0.45) the variation of static magnetoelectric conversion factor with applied DC magnetic field is shown in fig. 13. From the figure it is clear that magnetoelectric voltage coefficient $(dE/dH)_H$ increases slowly with applied magnetic field and after attaining a maximum value again it decreases. The constant value of $(dE/dH)_H$ indicates that the magnetostriction reaches its saturation value at the time of magnetic poling and produces constant electric field in the ferroelectric phase. The static ME conversion factor depends on mole % of ferrite and ferroelectric phases in the composites, however with further increase in mole fraction of ferrite phase, the maganetoelectric voltage coefficient $(dE/dH)_H$ decreases. The lower values of static ME output are due to low resistivity of ferrite phase compared to that of ferroelectric phase. At the time of poling, charges are developed in the ferroelectric grains through the surrounding of low resistivity ferrite grain and leakage of such charges is responsible for low static ME output. However, the static magnetoelectric voltage coefficient $(dE/dH)_H$ decreases with increase in grain size of the ferrite and ferroelectric phases in the composites. The large grains are (polydomain) less effective in inducing piezomagnetic and piezoelectric coefficients than that of the smaller ones [26]. Motagi and Hiskins reported the variation of piezoelectric property of ferroelectric phase with grain size. Infact the ME conversion factor also depends on porosity and grain size. In the present experimental investigation it is found that small grains with low porosity are important for getting high ME out put in the composites. A maximum static ME coefficient of 536 µV/cm Oe is observed in the composite containing 15 % $Ni_{0.2}Co_{0.8}Fe_2O_4$ + 85 % BPZT (table. 1). The observed results for the composite system (x) $Ni_{0.2}Co_{0.8}Fe_2O_4$ + (1-x) Pb $Zr_{0.8}Ti_{0.2}O_3$ (with x = 0.15, 0.30 and 0.45) are shown figure. 14. The high ME out put of 828 µV/cm Oe is observed for the composite containing 15 % $Ni_{0.2}Co_{0.8}Fe_2O_4$ + 85 % Pb $Zr_{0.8}Ti_{0.2}O_3$ (table 1). High magnetostriction coefficient and piezoelectric coefficient of the ferrite and ferroelectric phases are responsible for high ME out put in these composites.

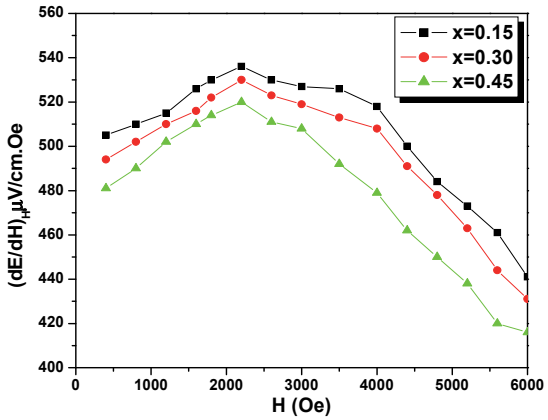

Fig. 13. Magnetic field dependent variation of ME voltage coefficient at room temperature for (x) $Ni_{0.2}Co_{0.8}Fe_2O_4$ + (1-x) $Ba_{0.8}Pb_{0.2}Zr_{0.8}Ti_{0.2}O_3$ ME composites.

From the investigation it is observed that increase in ferrite content in the composites leads to the enhancement of elastic interaction. But there is a limit to the addition of ferrite in the composite because further increase in ferrite content in the composites leads to the decrease in the resistivity of composites. Therefore the additions of ferrites in the composites are restricted to only 0.15, 0.30 and 0.45, because at these values there is a resistivity matching

between ferrite and ferroelectric phases. Many workers studied Ni, Co and Zn ferrite with $BaTiO_3$ ferroelectric by ceramic method and reported very weak ME response inspite of high resistivity of the ferrites. But in the present composites better ME voltage coefficients are obtained, which may be due to the presence of cobalt ions (Co^{+2}) in ferrites, as it causes large lattice distortion in the ferrite lattice and induces more mechanical coupling between the ferrite and ferroelectric phases, leading to the polarization in the piezoelectric phases. Similarly substitution of Zn in nickel also enhances the magnetostriction coefficient and hence shows good ME response.

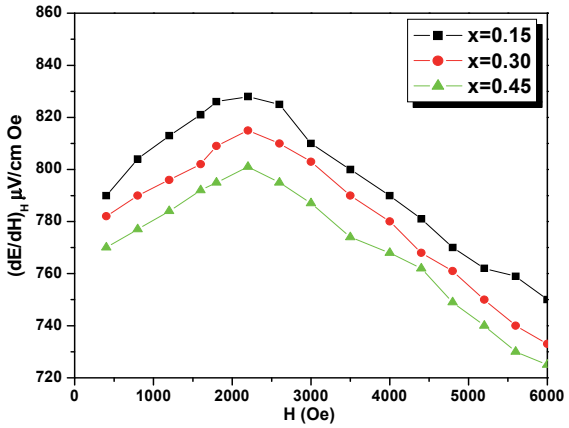

Fig. 14. Magnetic field dependent variation of ME voltage coefficient at room temperature for (x) $Ni_{0.2}Co_{0.8}Fe_2O_4$ + (1-x) Pb $Zr_{0.8}$ $Ti_{0.2}O_3$ ME composites.

The magnetic field dependent variation of the ME voltage coefficient with magnetic field for the composite system (x) $Ni_{0.5}Zn_{0.5}Fe_2O_4$ + (1-x) $Ba_{0.8}Pb_{0.2}Zr_{0.8}Ti_{0.2}O_3$ is shown in fig 15. The ME coefficient increases linearly with applied magnetic filed (< 1.0 K Oe) and after acquiring a maximum value decreases linearly. The initial rise in ME output is attributed to the enhancement in the elastic interaction, which is confirmed by the hysteresis measurements.

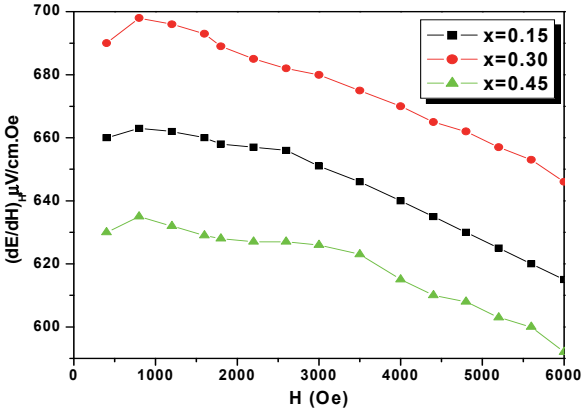

Fig. 15. Magnetic field dependent variation of ME voltage coefficient at room temperature for (x) $Ni_{0.5}Zn_{0.5}Fe_2O_4$ + (1-x) $Ba_{0.8}$ $Pb_{0.2}$ $Zr_{0.8}$ $Ti_{0.2}O_3$ ME composites.

The intensity of the magnetostriction reaches saturation value above 1.0 K Oe and hence, the magnetization and associated strain produce a constant electric field in the ferroelectric phase beyond the saturation limit. The maximum ME voltage coefficient of 698 μV/cm Oe is observed for the composites containing 30 % $Ni_{0.5}Zn_{0.5}Fe_2O_4$ + 70 % $Ba_{0.8}Pb_{0.2}$ $Zr_{0.8}Ti_{0.2}O_3$ (table. 1). It is well known that the ME response of the composites depends on the piezoelectricity of the ferroelectric phase and the magnetostriction of the ferrite phase. The composites prepared with a lower content of the ferrite or ferroelectric phase results in the reduction of piezoelectricity or magnetostriction respectively, leading to a decrease in the static ME voltage coefficient as predicted theoretically. The increase in ME output at x = 0.30 (table. 1) may be attributed to the uniform distribution of small grains in both the phases. However, the uneven particle size of the phases reduces the mechanical coupling between them and causes significant current loss in the sample [27]. The similar results have been observed for the composite system (x) $Ni_{0.5}$ $Zn_{0.5}$ Fe_2O_4 + (1-x) Pb $Zr_{0.8}$ $Ti_{0.2}O_3$ (with x = 0.15, 0.30 and 0.45) shown in fig. 16.

Composition (x)	**ME Voltage Coefficient $(dE/dH)_H$ (μV/cm Oe)**
(x) $Ni_{0.2}$ $Co_{0.8}$ Fe_2O_4 + (1-x) $Ba_{0.8}Pb_{0.2}$ $Zr_{0.8}$ $Ti_{0.2}O_3$	
0.15	536
0.30	530
0.45	520
(x) $Ni_{0.2}$ $Co_{0.8}$ Fe_2O_4 + (1-x) Pb $Zr_{0.8}$ $Ti_{0.2}O_3$	
0.15	828
0.30	815
0.45	801
(x) $Ni_{0.5}$ $Zn_{0.5}$ Fe_2O_4 + (1-x) $Ba_{0.8}Pb_{0.2}$ $Zr_{0.8}$ $Ti_{0.2}O_3$	
0.15	663
0.30	698
0.45	635
(x) $Ni_{0.5}$ $Zn_{0.5}$ Fe_2O_4 + (1-x) Pb $Zr_{0.8}$ $Ti_{0.2}O_3$	
0.15	839
0.30	808
0.45	783

Table. 1. Variation of ME Voltage Coefficient with composition

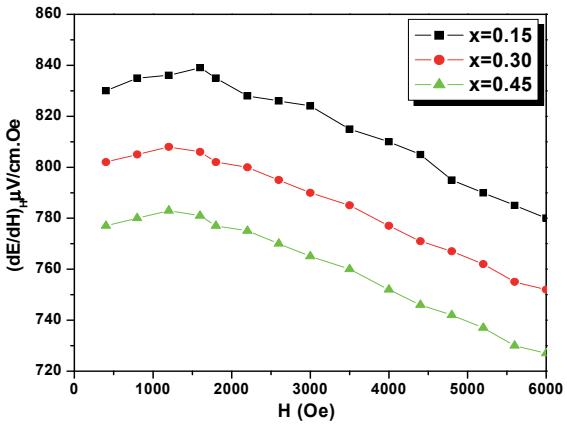

Fig. 16. Magnetic field dependent variation of ME voltage coefficient at room temperature for (x) $Ni_{0.5}Zn_{0.5}Fe_2O_4$ + (1-x) Pb $Zr_{0.8}$ $Ti_{0.2}O_3$ ME composites

8. Conclusion

In the study of ME effect, initially ME voltage coefficient $(dE/dH)_H$ increases with the increase in applied DC magnetic field and thereafter decreases linearly. It is attributed to the increase in elastic interaction caused by magnetostriction and piezoelectric effect aswell as low leakage of currents and high degree of polarization.

1. ME output depends on the resistivity and mole percentage of ferrite/ferroelectric phases and maximum ME output is observed for high resistivity composites. The decrease in dielectric constant with frequency shows the dielectric dispersion at lower frequency region.
2. ME output increases with decrease in the grain size of the individual phases. However, large particles are less effective in inducing piezoelectric and piezomagnetic effect compared to smaller grains. The composites having high porosity exhibit better ME response, because the pores provides resistance to the electrons.
3. The present ME composites having large ME response vary linearly with DC electric field in the low and high magnetic field regions and are attractive for technological applications for ME devices.

The content of ferroelectric is very important for getting high ME voltage coefficient. But in order to obtain still better ME response, one can use layered (bilayer layer and multilayer) composites of two phases (ferrites and ferroelectrics) and it requires minimum deficiencies with particles of nano size.

9. Acknowledgement

The authors are thankful to Prof. B K Chougule, former head Department of Physics, Shivaji University, Kolhapur and Dr. R B Pujar, former, Principal, S S Arts and T P Science Institute Sankeshwar for fruitful discussions.

10. References

[1] Pawar. D. V. (1995). *Bull. Mater. Sci*. 18 141
[2] Srinivasan. G, Rasmussen. E. T, Levin. B. J & Hayes. R. (2003). *Phy. Rev. B*. 65 134402

[3] Hummel. R. E, (2004). *Electronic Properties of Materials*, III edition, Spinger Publication
[4] Kanai. T, Ohkoshi. S. I, Nakajima. A, Wajanabe. T & Hashimoto. K. (2001). *Adv. Mater.* 13 487
[5] Suryanarayana. S. V. (1994). *Bull. Mater. Sci.* 17 (7) 1259
[6] Boomagaard. J. V & Born. R. A. J. (1978). *J. Mater. Sci.* 13 1538
[7] Takada. T & Kiyama. M. (1970). *Ferrite. Proceed. Internl. Conf.* Japan 69
[8] Sato. T, Kuroda. C & Sato. M. (1970). *Ferrite. Proceed. Internl. Conf.* Japan 72
[9] Bragg. W. L. (1915). Nature. (London) 95 561
[10] Goodenough. J. B. (1963). *Magnetism and Chemical Bond.* Interscience, New York
[11] Paulus. M. (1962). *Phys. Stat. Solidi (a).* 2 1181
[12] Bammannavar. B. K, Naik. L. R & Chougule. B. K. (2008). J. Appl. Phys. 104 064123.
[13] Choudharey. R. N. P, Shannigrahi. S. R & Singh. A. K. (1999). *Bull. Mater. Sci.* 22 (6) 75
[14] Boomgaard. J. V &Born. R. A. J. (1978). *J. Mater. Sci.* 13 1538
[15] Bammannavar. B. K, Chavan. G. N, Naik. L .R & Chougule. B. K. (2009). *Matt. Chem. Phys.* 11 746
[16] Bammannavar. B. K & Naik. L. R. (2009). *Smart. Mater. Struct.* 18 085013
[17] Devan. R. S, Kanamadi. C. M, Lokare. S. A & Chougule. B. K. (2006). *Smart. Mater. Struct.* 15 1877
[18] Maxwell. J. C. (1973). *Electricity and Magnetism.* Oxford University Press, London
[19] Wagner. K. W. (1913). *Ann. Physik.* 40 817
[20] Vishwanathan. B & Murthy. V. R. K. (1990). *Ferrite Materials: Science and Technology* .(New Delhi; Narosa Publishing House)
[21] Iwauchi. K. (1971). *Japn. J. Appl. Phys.* 10 152
[22] Hiroshima. T, Tanaka. K & Kimura. T. (1996). *J. Am. Ceram. Soc.* 79 3235
[23] Austin. I. G & Mott. N. F. (1996). *Adv. Phys.* 18 411
[24] Alder. D & Feinleib. J. (1970). *Phys. Rev. B.* 2 3112
[25] Ryu. J, Priya. S, Uchino. K & Kim. H. (2002). *J. Electroceram.* 8 107
[26] Devan. R. S, Lokare. S. A, Patil. D. R, Chougule. S. S, Kolekar. Y. D & Chougule. B. K. (2006). *J. Phys. Chem. Solids.* 67 1524
[27] Bammannavar. B. K & Naik. L. R. (2009). *J. Magn. Magn, Mater.* 321 382

15

Characterization of Ferroelectric Materials by Photopyroelectric Method

Dadarlat Dorin[1], Longuemart Stéphane[2] and Hadj Sahraoui Abdelhak[2]
[1]*National R&D Institute for Isotopic and Molecular Technologies Cluj-Napoca,*
[2]*University Lille Nord de France, ULCO, Dunkerque,*
[1]*Romania*
[2]*France*

1. Introduction

During last decades, the photothermal techniques have been largely applied to the study of thermal and optical properties of condensed matter. Photothermal techniques are based on the same physical principle: the optical energy, absorbed by given material, is partially converted into heat; depending on the way used to measure the quantity of heat and to follow its propagation through the material, several photothermal techniques have been developed (photoacoustic calorimetry, photothermal radiometry, photothermal deflection, thermal lensing, photopyroelectric method) (Tam, 1986). In this chapter we will focus on the simplest one, the photopyroelectric calorimetry and its applications concerning the investigation of some thermal and electrical properties of ferroelectric materials.
The photopyroelectric (PPE) detection was introduced in 1984, as a powerful tool for high-resolution measurement of thermal properties of materials (Coufal, 1984; Mandelis, 1984). The pyroelectric effect consists in the induction of spontaneous polarization in a noncentrosymmetric, piezoelectric crystal, as a result of temperature change in the crystal. Single crystals as $LiTaO_3$ and TGS, ceramics as PZT or polymers as PVDF were used as pyroelectric sensors, for the main purpose of measuring temperature variations. In principle, in the PPE method, the temperature variation of a sample exposed to a modulated radiation is measured with a pyroelectric sensor, situated in intimate thermal contact with the sample (Mandelis & Zver, 1985; Chirtoc & Mihailescu, 1989). The main advantages of this technique were found to be its simplicity, high sensitivity, non-destructive character and adaptability to practical restrictions imposed by the experimental requirements.
From theoretical point of view, in the most general case, the complex PPE signal depends on all optical and thermal parameters of the different layers of the detection cell. A large effort was dedicated in the last decades to simplify the mathematical expression of the PPE signal. As a final result, several particular cases were obtained, in which the information is contained both in the amplitude and phase of the PPE signal (Mandelis & Zver, 1985; Chirtoc & Mihailescu, 1989); the amplitude and phase depend in these cases on one or, in a simple way, on two of the sample's related thermal parameters.
The thermal parameters resulting directly from PPE measurements are usually the thermal diffusivity and effusivity. It is well known that the four thermal parameters, the static volume specific heat, C, and the dynamic thermal diffusivity, α, conductivity, k, and effusivity, e, are

connected by two relationships, $k=C\alpha$ and $e=(Ck)^{1/2}$; in conclusion, only two are independent. It is important to note that the PPE calorimetry is (at the authors knowledge) the only technique able to give *in one measurement* the value of two (in fact all four) thermal parameters.
Consequently, it is obvious that the PPE method is suitable not only to characterize from thermal point of view a large class of solids and liquids, but also to study processes associated with the change of the thermal parameters as a function of temperature (phase transitions, for example), composition (chemical reactions), time (hygroscopicity), etc.
A particular application of the PPE calorimetry is the characterization of the ferroelectric materials. The application is particular in this case because many ferroelectric materials are in the same time pyroelectric materials. Consequently the investigated ferroelectric specimen can be inserted in the PPE detection cell, both as sample or (sometimes) as pyroelectric sensor, offering additional possibilities for thermal characterization.
This chapter makes a brief summary of the theoretical and experimental possibilities offered by the PPE calorimetry in thermal characterization of some ferroelectric materials; the advantages and the limitations of the technique, as well as a comparison with other techniques are presented.

2. Development of the PPE theoretical aspects concerning the thermal characterization of ferroelectric materials

From theoretical point of view, there are two PPE detection configurations, "back" and "front", mainly applied for calorimetric purposes. In the back (BPPE) configuration, a modulated light impinges on the front surface of a sample, and a pyroelectric sensor, situated in good thermal contact with the sample's rear side, measures the heat developed in the sample due to the absorption of radiation. In the front (FPPE) configuration, the radiation impinges on the front surface of the sensor, and the sample, in good thermal contact with its rear side, acts as a heat sink (Mandelis & Zver, 1985; Chirtoc & Mihailescu, 1989). The geometry of the BPPE and FPPE configurations is presented in Fig.2.1.

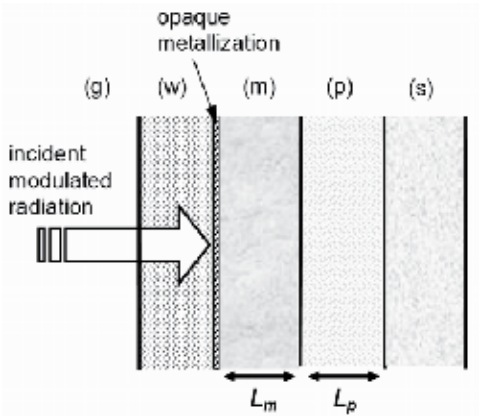

Fig. 2.1 Schematic diagram of the PPE detection cell: (g) – air, (w) – window, (m) – material, (p) – pyroelectric sensor, (s) – substrate.

In the BPPE configuration the ferroelectric sample is represented by the "material" (m) layer; in the FPPE configuration, the "material" layer is missing, and the investigated material is the pyroelectric sensor itself.

2.1 Ferroelectric material inserted as sample in the detection cell ("back" detection configuration)

With the additional simplifying assumptions that the window and substrate are thermally thick, the air and window are optically transparent and the incident radiation is absorbed only at the window-material interface (by a thin opaque layer), the PPE voltage is given by (Delenclos et al., 2002):

$$V = \frac{2V_0 \exp(-\sigma_m L_m)}{(b_{wm}+1)(b_{mp}+1)} \times \frac{\exp(-\sigma_p L_p) + R_{sp}\exp(-\sigma_p L_p) - (1+R_{sp})}{\exp(-\sigma_p L_p) - R_{sp}R_{mp}\exp(-\sigma_p L_p) + (R_{mp}\exp(\sigma_p L_p) - R_{sp}\exp(-\sigma_p L_p))R_{wm}(-2\sigma_m L_m)} \tag{2.1}$$

where

$$R_{jk} = (b_{jk}-1)/(b_{jk}+1)\,; \quad b_{jk} = e_j / e_k\,; \quad \sigma_j = (1+i)a_j\,; \quad \mu = (2\alpha/\omega)^{1/2} \tag{2.2}$$

In Eq. (2.1), V_0 is an instrumental factor, R_{jk} represents the reflection coefficient of the thermal wave at the '*jk*' interface, ω is the angular chopping frequency and σ and a are the complex thermal diffusion coefficient and the reciprocal of the thermal diffusion length ($a = 1/\mu$), respectively. In order to eliminate V_0, a normalization of the signal is necessary, the best reference signal being obtained by the direct illumination of the empty sensor. The obtained normalized signal is:

$$V_n(f) = \frac{2(b_{gp}+1)}{(b_{wm}+1)(b_{mp}+1)}\exp(-\sigma_m L_m)P(f) \tag{2.3}$$

where

$$P(f) = \frac{1 - R_{sp}R_{gp}\exp(-2\sigma_p L_p)}{1 - R_{sp}R_{mp}\exp(-2\sigma_p L_p) + [R_{mp} - R_{sp}\exp(-2\sigma_p L_p)]R_{wm}\exp(-2\sigma_m L_m)} \tag{2.4}$$

If we work in the thermally thick regime for the sensor ($L_p >> \mu_p$) and we extract the phase and the amplitude from Eq. (2.3), we get for the phase:

$$\Theta = -\arctan\left(\frac{\tan(a_m L_m)[1 + R\exp(-2a_m L_m)]}{1 - R\exp(-2a_m L_m)}\right) \tag{2.5}$$

with $R = R_{mw}R_{mp}$, and for the amplitude:

$$\ln V_n = \ln\frac{2(b_{gp}+1)}{(b_{wm}+1)(b_{mp}+1)}) - a_m L_m \tag{2.6}$$

An analysis of Eq. (2.5) indicates that the sample's thermal diffusivity (contained in a_m) can be directly measured by performing a frequency scan of the phase of the PPE signal. The most suitable particular case seems to be the thermally thick regime for the sample, ($L_m >> \mu_m$), when Eqs. (2.5) and (2.6) reduce to:

$$V_n = V_0 \frac{\exp\left[-L_m(\omega/2\alpha_m)^{1/2}\right]}{e_p + e_m}; \tag{2.7}$$

$$\Theta = \Theta_0 - L_m\left(\frac{\omega}{2\alpha_m}\right)^{1/2}. \tag{2.8}$$

Inserting the value of the thermal diffusivity from Eq. (2.8) in Eq. (2.7) we obtain the value of the thermal effusivity, and, using then the well known relationships between the thermal parameters, we get the values of the remaining two thermal parameters, volume specific heat and thermal conductivity.

2.2 Ferroelectric material inserted as sensor in the detection cell ("front" detection configuration)

In the previous paragraph, a pyroelectric sensor was placed in thermal contact with the studied ferroelectric sample. However, as mentioned before, it is possible to extract information on the pyroelectric material itself. The configuration is in this case simpler, being reduced to a three layers model: front medium-air, pyro(ferro)electric material (p) with opaque electrodes, and a substrate (s) in good thermal contact with the pyroelectric sensor (Fig. 2.2.).

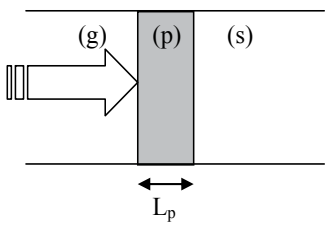

Fig. 2.2 Schematic diagram of the PPE detection cell: (g) – air, (p) – pyroelectric sample, (s) – substrate

If we consider the front medium (g) and the substrate (s) as semi-infinite ($L_g >> \mu_g$ and $L_s >> \mu_s$) the PPE voltage is given by :

$$V = \frac{V_0}{b_{gp}+1} \frac{1-\exp(-\sigma_p L_p) + R_{sp}[\exp(-2\sigma_p L_p) - \exp(-\sigma_p L_p)]}{1 - R_{gp}R_{sp}\exp(-2\sigma_p L_p)}. \tag{2.9}$$

Considering frequencies for which the quantity $\exp(-2\sigma_p L_p)$ can be neglected, the signal expression reduces to:

$$V = \frac{V_0}{b_{gp}+1}[1-(1+R_{sp})\exp(-\sigma_p L_p)]. \tag{2.10}$$

The signal can be normalized by the one obtained with empty sensor, leading to:

$$V_n = 1-(1+R_{sp})\exp(-\sigma_p L_p). \tag{2.11}$$

The amplitude and the phase of the normalized complex signal are then expressed as:

$$\Theta = \arctan \frac{(1+R_{sp})\exp(-a_p L_p)\sin(a_p L_p)}{1-(1+R_{sp})\exp(-a_p L_p)\cos(a_p L_p)}; \tag{2.12}$$

$$|V_n| = \sqrt{[(1+R_{sp})\exp(-a_p L_p)\sin(a_p L_p)]^2 + [1-(1+R_{sp})\exp(-a_p L_p)\cos(a_p L_p)]^2}\ . \tag{2.13}$$

In conclusion to this sub-section, the thermal diffusivity of the ferroelectric layer can be extracted carrying out a frequency scan of the complex PPE signal. Concerning the normalized phase (Eq. (2.12)), it has an oscillating behaviour with zero crossing at frequencies for which a_pL_p is a multiple of π. The values of these frequencies allow a direct determination of the thermal diffusivity of the ferroelectric material, providing its thickness is known and independently on the type of substrate. The value of the thermal diffusivity can be then used in the equation of the normalized amplitude or phase in order to obtain the thermal effusivity of the pyro(ferro)electric layer (providing the effusivity of the substrate is known). In addition to the thermal parameters, it is also possible to extract the temperature dependence of the pyroelectric coefficient γ of the pyroelectric from the instrumental factor V_0. In current mode, it is expressed as:

$$V_0 = -\frac{\gamma I_0 Z_f}{2L_p C_p}, \tag{2.14}$$

with I_0 the intensity of the modulated light source and Z_f the feedback complex impedance of the current preamplifier. The normalized signal amplitude's variation with temperature is then proportional to γ/C_p.

3. Instrumentation

3.1 Experimental set-up

The experimental set-up for PPE calorimetry contains some typical components (Fig. 3.1).

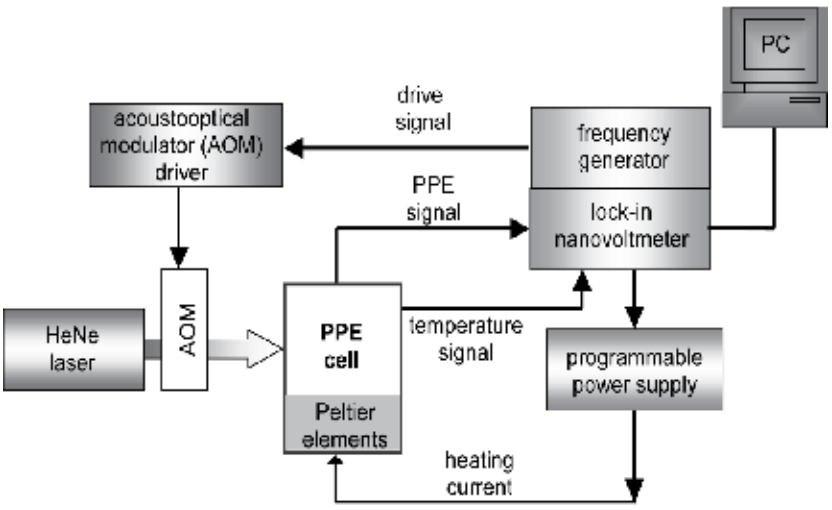

Fig. 3.1 Typical experimental set-up for PPE calorimetry.

The radiation source, usually a laser, is modulated by an acousto-optical modulator or an electro-mechanical chopper. The PPE signal is processed with a lock-in amplifier. A computer with adequate software is used for data acquisition. When performing temperature scans (phase transition investigations, for example), a thermostat, provided with Peltier elements (Jalink et al., 1996), or "cold finger" refrigerator systems (Chirtoc et al., 2009) with additional equipment (programmable power supply, electronic thermometer, etc.) for temperature control, is included in the set-up.

3.2 Detection cells

In the following we will describe some typical detection cells used for PPE calorimetry of ferroelectric materials. All presented cells can operate at room temperature or can be used for temperature scans.

3.2.1 Cold-finger cell

The cold-finger concept (Fig. 3.2) allows investigations at temperatures both below and above the ambient. The cell is provided with two windows, for investigations in both BPPE and FPPE configurations. In principle, the copper bar transmits the temperature to the sample – one extremity of the bar can be cooled down by using liquid nitrogen, or heated up electrically, with a resistive coil. The role of the 0.1 mm thick steel cylinder is to keep the cell (excepting the copper bar) at room temperature. Depending on the operating temperature, one can make vacuum inside the cell or introduce dry atmosphere. The temperature of the sample is measured with a diode, glued with silicon grease to the cell finger, in the vicinity of the sample.

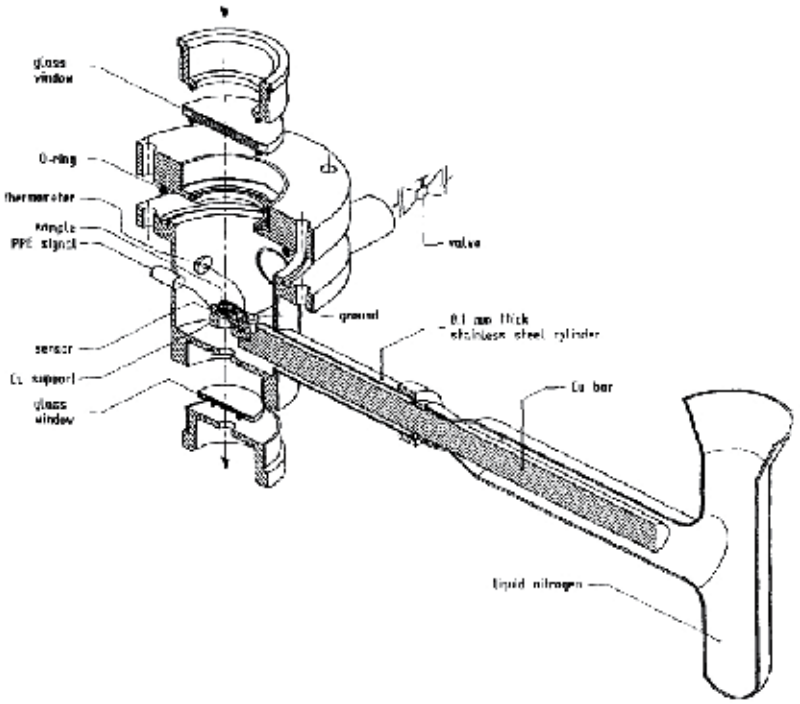

Fig. 3.2 Cold finger refrigerator system

3.2.2 Detection cell provided with Peltier elements

The design of the PPE detection cell equipped with Peltier elements is presented in Fig. 3.3. One face of one of the two Peltier elements (electrically connected in parallel) is thermally connected to a thermostat (liquid flux from a thermostatic bath). The opposite face of the second Peltier element is in thermal contact with an inside-chamber that accommodates the sample-sensor assembly. Temperature feed-back is achieved with a thermistor placed close to the sensor. Computer-controlled temperature scans with positive/negative rates (heating/cooling) are possible.

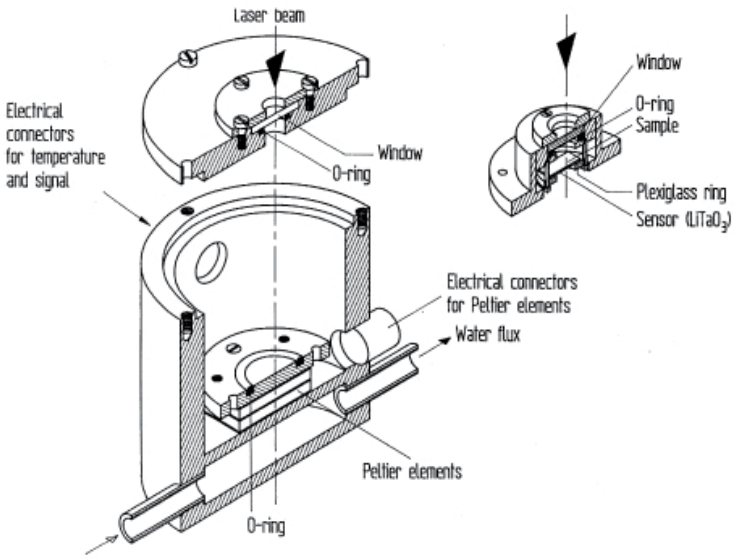

Fig. 3.3 PPE detection cell provided with Peltier elements

3.2.3 Application of an electric field to the sample

The electrical and thermal properties of a ferroelectric material usually depend on an external electric field. The investigation of these properties under external electric field requires some adaptation of the detection cell. Basically, as mentioned above, two cases must be considered: either the ferroelectric sample is in thermal contact with a pyroelectric sensor, either the sample is the sensor itself.

In the first case, in order to avoid the influence of the electric field on the pyroelectric signal, a special attention must be paid for the ground of the signal: the best alternative is to use one electrode of the sensor as a common ground for both the pyroelectric signal and the external applied voltage (Fig. 3.4).

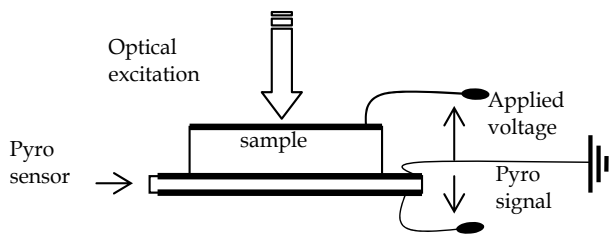

Fig. 3.4 Electrical connections for PPE measurement under electric field.

When the investigated sample is the sensor itself, it is not possible to use the same set-up, because the lock-in amplifier doesn't accept high input voltage. The sample, having usually high impedance, can be inserted in serial inside a circuit constituted of the bias voltage power supply and the lock-in amplifier. In such a way, the input of the lock-in amplifier is not affected by the relative high (tens of volts) applied bias voltage to the sample (Fig. 3.5).

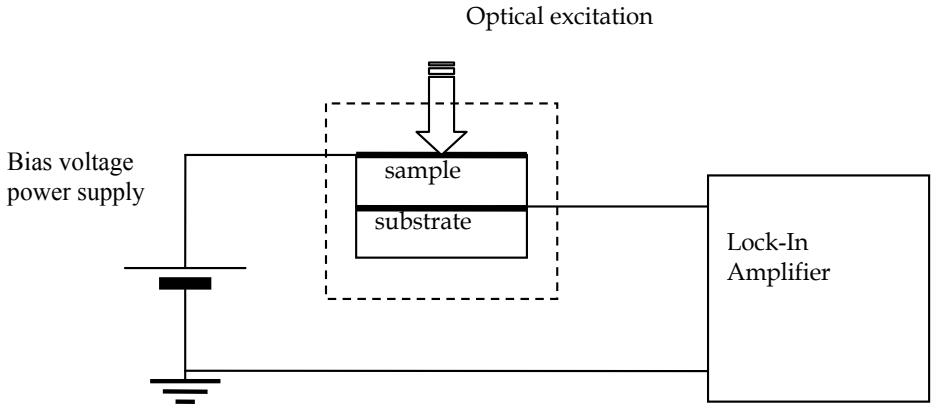

Fig. 3.5 Electrical arrangement for PPE measurement, when applying electric field to the material acting as sensor.

4. Applications

4.1 Investigation of thermal parameters of ferroelectric thin films

For most of the applications concerning the ferroelectric materials, the knowledge of their thermal parameters is necessary because they are relevant for evaluating the figure of merit of a IR sensor (Whatmore, 1986), or a pyroelectric accelerator (Fullem and Danon, 2009) for instance. When used as a sensor in a PPE experiment, the knowledge of these parameters is crucial, because all other measured properties depend of these values (Bentefour et al., 2003). Moreover, it has been shown (Nakamura et al., 2010) that these parameters have slightly different values as a function of the composition/purity of the ferroelectric material.

In the following we consider an opaque ferroelectric material with electrodes perpendicular to the spontaneous polarization, placed in thermal contact with a substrate, the normalized pyroelectric voltage phase and amplitude, resulting from the periodic heating of the material, in the front configuration, is given by the equation (2.12) and (2.13). In practice, several approaches are possible for extracting the thermal parameters of the pyroelectric sensor from the experimental data. We will present here the results obtained on a largely used pyro(ferro)electric sensor: $LiTaO_3$ single crystal.

4.1.1 Thermal parameters extracted from the phase and amplitude, at a given temperature

The behaviour of the normalized phase and amplitude of the PPE signal, as a function of frequency, obtained for a 510μm thick $LiTaO_3$ single crystal is plotted in Fig.4.1.

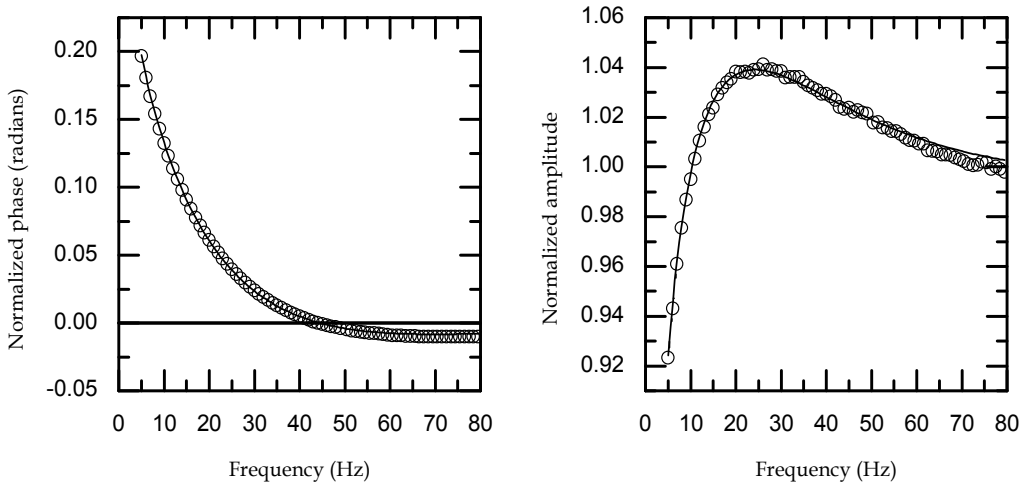

Fig. 4.1 Normalized signal's phase and amplitude obtained with a 510µm thick $LiTaO_3$ film and water as substrate (open circles: experimental data, solid line: best fit).

The phase and amplitude of the signal contain both information about the thermal diffusivity and effusivity of the ferroelectric material. From analytical point of view, the phase goes to zero for a frequency f_0 which verifies the relationship:

$$\frac{L_p\sqrt{f_0}}{\sqrt{\alpha_p}} = \sqrt{\pi}\,. \tag{4.1}$$

In the experiment described before, f_0 = 44.2 Hz leading to a thermal diffusivity of 1.53 10^{-6} $m^2.s^{-1}$ for $LiTaO_3$. This value can be then introduced in equation (2.12) to extract R_{sp} values and finally the thermal effusivity of $LiTaO_3$:

$$e_p = e_s\left(\frac{1-R_{sp}}{1+R_{sp}}\right) \tag{4.2}$$

Knowing the thermal effusivity of water used as substrate (e_s =1580 $W.s^{1/2}.m^{-2}.K^{-1}$), the average value of the calculated thermal effusivity is e_p = 3603 $W.s^{1/2}.m^{-2}.K^{-1}$. A similar procedure can be adopted to extract the thermal parameters from the amplitude of the signal. The frequency f_1 corresponding to the maximum of the amplitude should verify the relationship (see Eq. 2.13):

$$\frac{L_p\sqrt{f_1}}{\sqrt{\alpha_p}} = \frac{3\sqrt{\pi}}{4} \tag{4.3}$$

Fig. 4.1 indicates that the amplitude has a maximum for a frequency f_1=25.3Hz, corresponding to a value of 1.56 10^{-6} $m^2.s^{-1}$ for the thermal effusivity of $LiTaO_3$. By inserting this value in Eq. (2.13) one can extract the value of R_{sp} and, using Eq. (4.2), calculate the thermal effusivity of the ferroelectric sample. From data of Fig. 4.1, one finds e_p = 3821 $W.s^{1/2}.m^{-2}.K^{-1}$.

A simple comparison of Eqs. (4.1) and (4.3) indicates that f_1 is theoretically proportional to f_0 by a ratio 16/9. This criterion can be used to estimate the accuracy of the experimental results. For example, in the experiment described before, one finds a ratio of 1.74 between f_1 and f_0, to be compared to the theoretical value of 16/9 (≈ 1.78) . Another way to check for the validity of the experimental results is to combine the phase and the amplitude of the signal. Considering the model described by Eq. (2.11), a plot of the modulus of the complex quantity (1-V_n) as a function of the square root of frequency should display a line whose slope gives the value of the thermal diffusivity of the sample; the extrapolation of the curve to zero frequency leads to the value of the thermal effusivity. Such a calculation has been performed for the experimental data shown in Fig. 4.1 and the result is represented in Fig. 4.2.

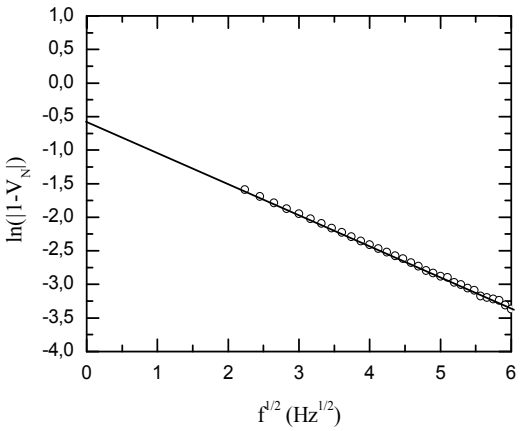

Fig. 4.2 Plot of the logarithm of |1-V_n| as a function of square root of frequency, for data of Fig. 4.1.

Fig. 4.1 indicates that the model is valid for high enough frequencies. The linear fit of the data leads to values of thermal parameters in agreement with previous calculated ones, as reported in table 4.I.

Procedure	Thermal diffusivity ($x10^{-6}.m^2.s^{-1}$)	Thermal effusivity ($W.s^{1/2}.m^{-2}.K^{-1}$)
Zero crossing (phase)	1.53	3821
Maximum (amplitude)	1.56	3603
Combination of amplitude and phase (linear fit)	1.58	3886
Non linear fit		
Phase	1.54	3688
Amplitude	1.53	3718

Table 4.I Comparison of values of thermal diffusivity and effusivity, obtained with various procedures, for a 510µm thick $LiTaO_3$ single crystal.

The previous results show that the proposed model allows the determination of the thermal parameters from a frequency scan of the PPE signal generated by the ferroelectric sample

itself. There are several approaches giving similar results (3% to 5% maximum difference for values of thermal diffusivity and effusivity, respectively). However, it should be pointed out that the results obtained with the phase as source of information are often more reliable due to the fact that the amplitude of the signal can be affected by light source's intensity stability as well as by the optical quality of the irradiated surface. Additionally, the frequency dependence of the amplitude around maximum is rather smooth, and the maximum value difficult to be located exactly.

At the end of this section, we have to mention that the theoretical results have been obtained without any hypothesis on the nature of the ferroelectric material used as pyroelectric sensor. The experimental results were obtained on $LiTaO_3$ crystals, but a similar procedure can be carried out for any type of ferroelectric material, as PZT ceramics, polymer films (PVDF, PVDF-TrFE) and even liquid crystal in S_C* ferroelectric phase. In the next section this last particular case will be described.

4.1.2 Thermal parameters of a liquid crystal in Sc* ferroelectric phase.

In this subsection the procedure described in the previous section has been extended to the study of a ferroelectric liquid crystal (FLC). In chiral smectic S_C* phase of FLCs, molecules are randomly packed in layers and tilted from the layer normal. Each smectic layer possess an in plane spontaneous polarization which is oriented perpendicularly to the molecular tilt. The direction of the tilt plane precesses around an axis perpendicular to the layer planes so that a helicoidal structure of the S_C* is formed. In this helicoidal structure, the S_C* phase doesn't possess a macroscopic polarization. When it is confined in thin film between two substrates, which are treated so that a planar alignment is imposed on the molecules at the surfaces, as used in surface stabilized FLC (SSFLC) devices (Clark & Lagerwall, 1980; Lagerwall, 1999), the smectic layers stand perpendicular to the surfaces and the helix can be suppressed if the LC film is sufficiently thin. This results in two possible states where the orientation of the molecules in the cell is uniform. The polarization vector in these two states is perpendicular to the substrates but oriented in the opposite direction. In both configurations the S_C* film develops a macroscopic polarization, and consequently, a pyroelectric effect of the film can be obtained when it is submitted to a temperature variation. We used the LC film as a pyroelectric sensor and we carried out the procedure described in section 4.1.1 to determine the thermal diffusivity and effusivity of the S_C* mesophase.

The ferroelectric liquid crystal (FLC) used in this study was a mixture FELIX 017/000 from Clariant Inc. (Germany). Its phase sequences and transition temperatures (in°C) are: Crystal -26 S_C* 70 S_A* 75 N* 84.5 I. The sample cell was prepared using a pair of parallel glass substrates. One of the substrates was metallised with gold. It acts as a light absorber and generates a heat wave penetrating into the sample. The other substrate was coated with a transparent electrode of indium-tin oxide in order to control the alignment of the FLC by means of polarized optical microscopy. The gap of the cell was set by a 13 μm thick spacers of PET, and the electrode area was 5 $\times$ 5mm^2. The two plates were spin-coated with PolyVinylAlcohol (PVA) and then rubbed in parallel directions for the FLC alignment. The FLC was inserted by capillary action in the cell in its isotropic phase, then slowly cooled into S_A* and S_C* in the presence of an AC electric field to achieve uniform alignment of the smectic layers. The sample cell was then observed at room temperature by means of polarized optical microscope. It was found that the LC cell exhibits a uniform texture, and we have not observed any "up" and "down" polarization domains coexistence.

In the previous section, the studied pyroelectric sample was a solid material and the normalizing signal was obtained by using air as substrate. Here, the studied material is fluid (this is the case of the liquid crystal material), the normalizing signal is then obtained using another solid pyroelectric material with air as substrate. In this case the normalized signal is given by:

$$V_n = \frac{K_0}{K_1}(1-(1+R_{sp})\exp(-\sigma_p L_p)) \tag{4.4}$$

K_0/K_1 is a real factor independent of the modulation frequency and represents the limit value of the normalized amplitude at high frequency. This factor does not affect the analysis carried out on Eq. (2.11) for the determination of the thermal parameters. The frequency of the zero crossing of the normalized phase (Eq. 3.1) or the frequency corresponding to the normalized amplitude maximum (Eq. 3.3) allows the determination of the absolute value of the thermal diffusivity of the sample. The thermal effusivity can also be calculated from the normalized amplitude once α_p is obtained and the quantity K_0/K_1 is determined from the value of the normalized amplitude at high frequency. The frequency behaviour of the normalized phase of the PPE signal is shown in Fig. 4.3.a

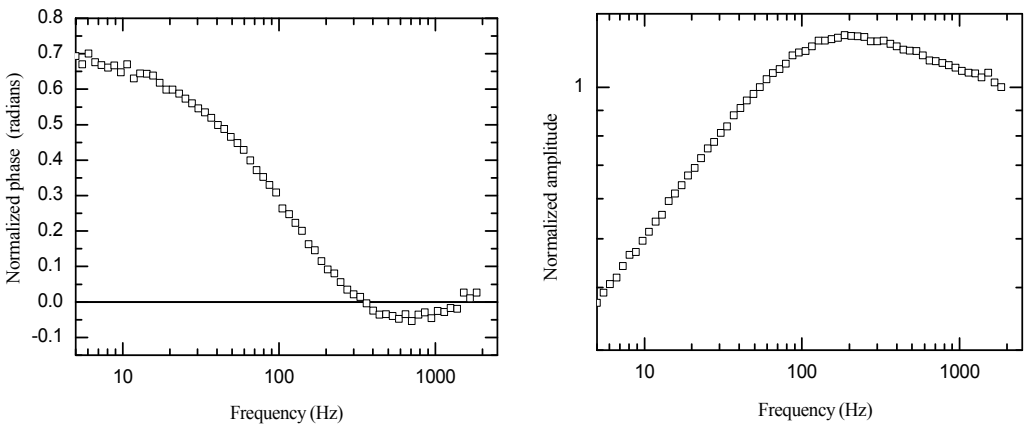

(a) (b)

Fig. 4.3 Experimental frequency behaviour of the normalized phase (a) and the normalized amplitude (b) obtained for the liquid crystal at room temperature, in the S_C^* phase.

As expected from the theory, the phase goes to zero, for a frequency f_0 = 354 Hz. Once f_0 is determined, equation 4.1 is used to obtain the thermal diffusivity of the ferroelectric liquid-crystal sample. A value of $\alpha_p = 1.90\ 10^{-8}$ m^2 s^{-1} was found.

The normalized amplitude of the PPE signal (Fig. 4.3.b) shows a maximum for the frequency f_1 = 191 Hz. The value of α_p calculated by using Eq. (4.3) is $\alpha_p = 1.82\ 10^{-8}$ m^2 s^{-1}, denoting that the values of the thermal diffusivity obtained independently from phase and amplitude are in good agreement.

The effusivity e_p is calculated from the signal phase by using Eqs. (2.12) and (4.2) and taking from the literature the value of the thermal effusivity of glass (e_s = 1503 Ws$^{1/2}$ m^{-2} K^{-1}). The

mean value of e_p is then calculated in a range of frequencies for which the sample is thermally thick; e_p is found to be 340W $s^{1/2}$ m^{-2} K^{-1}.
The same procedure carried out for different temperatures allows for example the investigation on the temperature dependence of the thermal parameters of the smectic S_C* phase and near the S_C*-S_A* transition of FLC materials. However, the use of frequency scans together with temperature scanning procedures can be time consuming when working in the vicinity of critical regions. In the next section, we will introduce a procedure avoiding such frequency scans.

4.1.3 The temperature dependence of the thermal parameters

In the previous section, it has been shown that a frequency scan of the amplitude and/or the phase of the photopyroelectric signal allows the direct measurement of the room temperature values of thermal diffusivity and effusivity of a ferroelectric material and consequently, the calculation of its heat capacity and thermal conductivity. In the following we will describe a procedure useful to study the temperature evolution of these thermal parameters without involving any frequency scan.
Considering the modulus A and the argument ϕ of the complex quantity 1-V_n, and using Eq. (2.11), one has:

$$A = (1 + R_{sp})\exp(-a_p L_p) \text{ and } \phi = a_p L_p$$

The expression for the thermal diffusivity and thermal effusivity is obtained as a function of A and ϕ as:

$$\alpha_p = \frac{L_p^{\,2}\pi f}{\phi^2} \tag{4.5}$$

$$R_{sp} = \frac{A}{\exp(-\phi)} - 1 \tag{4.6}$$

A and ϕ are calculated from the phase Θ and the amplitude $|V_n|$ of the PPE signal, using the relationship:

$$A = \sqrt{|V_n|^2 + 1 - 2|V_n|\cos\Theta} \tag{4.7}$$

$$\phi = \arctan\left[\frac{|V_n|\sin\Theta}{1 - |V_n|\cos\Theta}\right] \tag{4.8}$$

We have applied this procedure to find the temperature dependence of thermal parameters of a 510µm thick $LiTaO_3$ single crystal, provided with opaque electrodes and using ethylene glycol as substrate. The temperature range was 25°C-70°C. During the experiment, the modulation frequency was 7.2Hz. The signal of the $LiTaO_3$ alone (without substrate) was recorded in the same conditions for normalization purposes. The normalized amplitude and phase are represented in Fig. 4.4. The thermal diffusivity and thermal effusivity, calculated from these data, are displayed in Fig. 4.5.

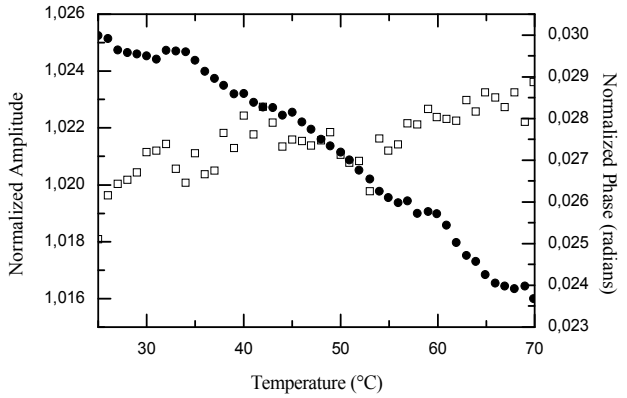

Fig. 4.4 Temperature evolution of the normalized amplitude (empty square) and phase (full circle) of the PPE signal at 7.2Hz of a 510µm thick $LiTaO_3$ single crystal using ethylene glycol as substrate.

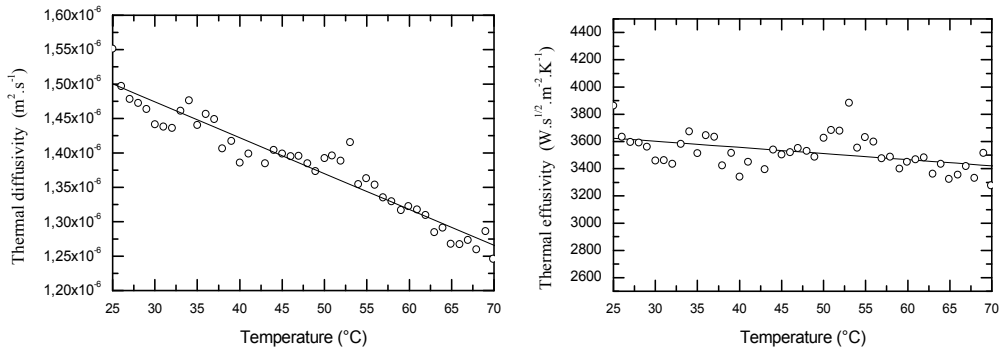

Fig. 4.5 Temperature dependence of the thermal diffusivity and effusivity of $LiTaO_3$ as a function of temperature, calculated from data of Fig. 4.3.

The two others thermal parameters, the volumic heat capacity C_p and the thermal conductivity k_p can then be deduced. The knowledge of C_p allows to extract the temperature dependence of the pyroelectric coefficient γ, from the amplitude of the signal of the sample alone, which is equivalent to the instrumental factor V_0. In the expression of V_0 (Eq. 2.14), only the ration γ/C_p is temperature dependent, thus, multiplying V_0 by the values of C_p and scaling the result to a known value of γ at a given temperature, it is possible to obtain the absolute value of the pyroelectric coefficient as a function of temperature. The results obtained for $LiTaO_3$ are shown in Fig. 4.6 (the value of γ at 25°C was taken from Landolt-Börnstein database (Bhalla and Liu, 1993)).

This subsection was dedicated to experiments in which the combination amplitude-phase of the PPE signal gave information about the room temperature values and temperature dependence of thermal parameters and pyroelectric properties of a ferroelectric material (in position of pyroelectric sensor). Unfortunately, the use of the amplitude of the signal makes the results rather noisy. Such a disadvantage can be avoided by using, when possible, only data from the phase of the signal. In section 4.3.2, a procedure using the signal's phase at two frequencies will be presented, for studies of phase transitions.

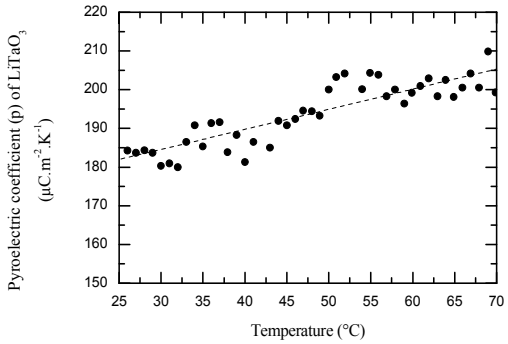

Fig. 4.6 Temperature dependence of the pyroelectric coefficient of $LiTaO_3$ obtained from PPE signal's amplitude.

4.2 PPE detection of phase transitions in ferroelectric materials

As it is well known, phase transitions are processes associated with a breaking of the symmetry of the system. In the case of ferroelectric materials, the ferro-paraelectric phase transition has the polarization as order parameter and, theoretically, it is considered a second order phase transition. Practically, sometimes it was found to be slightly first order (a few amount of latent heat is developed in the process) (del Cerro et al., 1987). For both type of phase transitions (I-st and II-nd order), the second derivatives of some appropriate thermodynamic potential have anomaly at the transition temperature (Curie point for ferroelectric materials). On the other hand, as presented in the theoretical section, the amplitude and phase of the complex PPE signal depend on two (or sometimes one) sample's related thermal parameters. Consequently, it is expected that the PPE technique is suitable to detect both first and second order phase transitions, by measuring the critical anomalies of the thermal parameters.

In time, the PPE technique was applied to detect first (Mandelis et al., 1985) or second (Marinelli et al.,1992) order phase transitions. For second order phase transitions the PPE results were used to calculate the critical exponents of the thermal parameters and to validate the existing theories (Marinelli et al., 1992, Chirtoc and al., 2009). Due to the fact that the PPE technique uses for phase transition investigations the thermal parameters, a wide range of materials belonging to condensed matter, can be listed as investigated specimens: ordinary liquids and liquid mixtures, liquid crystals, liquid, pasty or solid foodstuffs, ferroelectric and magnetic materials, high T_c superconductors, plastics, etc

One of the most important points in making high-temperature-resolution measurements of thermal parameters in the critical region of a phase transition is that the thermal gradients in the investigated sample must be as small as possible. Often, at a phase transition, a strong temperature dependence of the thermal parameters is present when approaching the critical temperature. Thermal gradients tend to smear out this temperature dependence and, sometimes, the phase transition is difficult to be detected. To avoid this effect, it is important to keep the sample in quasi-thermal equilibrium. The measuring techniques, that in most cases are based on the detection of a sample temperature rise, as a response to a heat input, are additional sources of temperature gradients, especially for ac techniques. Accordingly, the techniques involving periodic heating of the sample are preferred, and the PPE technique is among them.

Concerning the ferroelectric materials, Mandelis et al. used for the first time the PPE method for detecting the ferro-paraelectric phase transition in Seignette salt (Mandelis et al., 1985). In the following we will present an application of the PPE technique in detecting the ferroelectric-paraelectric phase transition in a well known ferroelectric crystal, TGS.

4.2.1 TGS as a sample

When inserting a TGS crystal as sample in a PPE detection cell, one has to use the back (BPPE) configuration, with the TGS crystal in the front position (directly irradiated), in intimate thermal contact (through a thin coupling fluid) with a pyroelectric sensor ($LiTaO_3$ or PZT). In experimental conditions of opaque and thermally thick sample and thermally thick sensor, the amplitude, V, and phase, Θ, of the PPE signal are given by the Eqs. (2.7) and (2.8).

An inspection of Eqs.(2.7)-(2.8) leads to the conclusion that it is possible to obtain the temperature behaviour of all four thermal parameters, from one measurement, if we have an isolated value of one thermal parameter (other than thermal diffusivity), to calibrate the amplitude measurement. Consequently, we can obtain the critical behaviour of all static and dynamic thermal parameters around the Curie temperature of a ferroelectric material.

Some important features of Eq. (2.7) should be also stressed:

- The amplitude of the PPE signal is attenuated by an exponential factor as $a_m L_m$ increases;
- The sensitivity of the signal amplitude to the changes in the thermal diffusivity is given by the ratio:

$$\frac{dV}{V} / \frac{d\alpha_m}{\alpha_m} = -\frac{a_m L_m}{2} \tag{4.9}$$

  showing that for $a_m L_m > 2$, a given anomaly in the thermal diffusivity, produces an enhanced signal anomaly;
- For a given sample, the exponent in Eq. (2.7) can be adjusted by changing the modulation frequency and/or sample's thickness, in order to achieve an optimum trade-off between sensitivity and signal-to-noise ratio.

Based on these theoretical predictions, one can start investigating the ferroelectric-paraelectric phase transition of TGS crystal, by performing a room temperature frequency scan of the phase of the PPE signal, in order to obtain the room temperature value of the thermal diffusivity. A typical result is presented in Fig. 4.7.

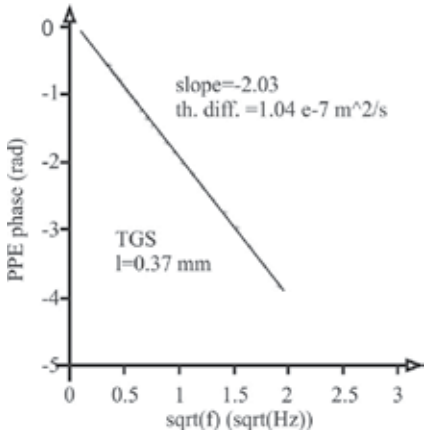

Fig. 4.7 Room temperature frequency scan for the phase of the PPE signal

Typical temperature scans of the amplitude and phase of the PPE signal, in a temperature range including the Curie point of TGS are displayed in Fig.4.8

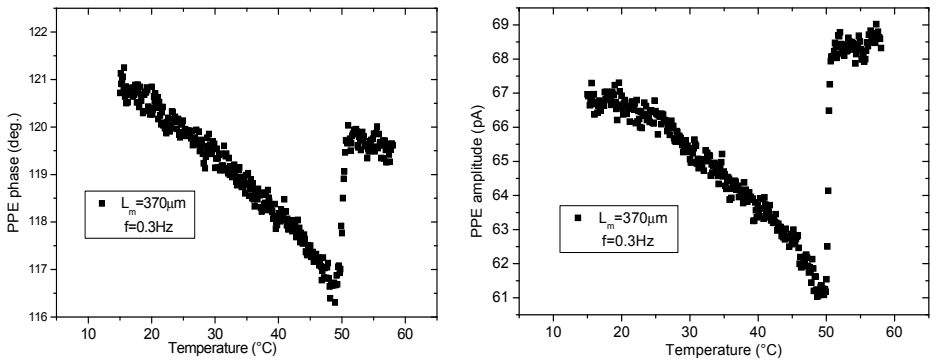

Fig. 4.8 Temperature scan for the phase and the amplitude of the PPE signal

Using Eqs. (2.7)-(2.8), the value of the thermal diffusivity obtained from the slope of the curve in Fig.4.7, and the value of the thermal conductivity from del Cerro et al., 1987, one gets the critical behaviour of all four thermal parameters (Fig.4.9)

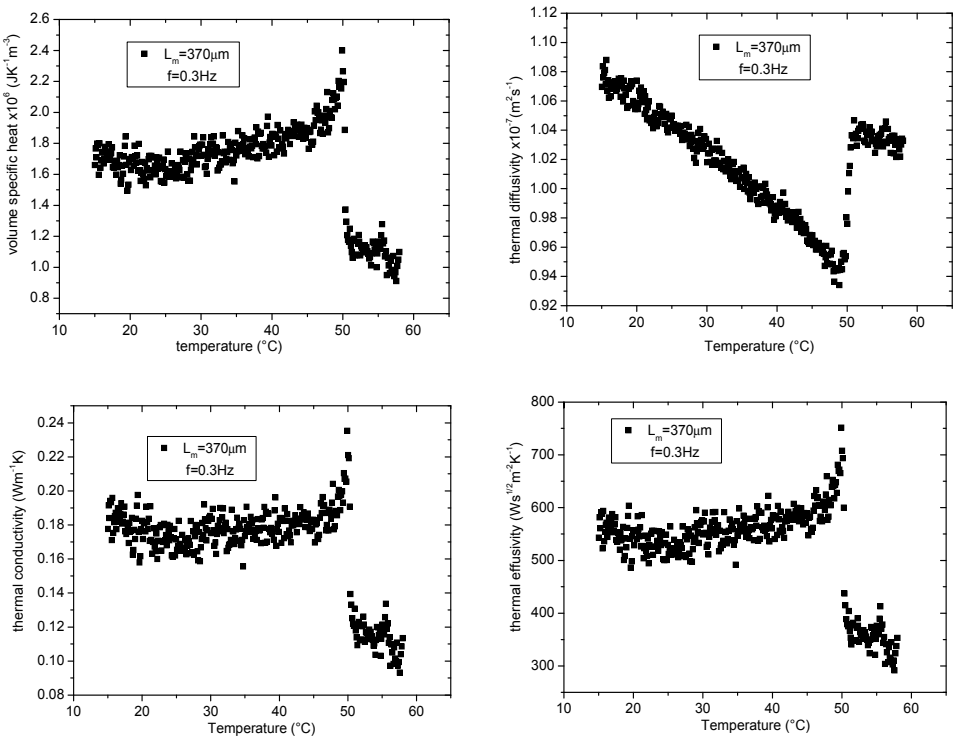

Fig. 4.9 Temperature behaviour of the volume specific heat, thermal diffusivity, conductivity and effusivity of TGS around the Curie point

Some technical details concerning the experiment are: TGS single crystal, 370μm thick, pyroelectric sensor $LiTaO_3$, 300μm thick, chopping frequency for the temperature scan f = 0.3 Hz.
As mentioned above, one of the most important features concerning Eq. (2.7) is the possibility of enhancing the critical anomaly of the thermal diffusivity, by a proper handling of the chopping frequency and sample's thickness.
Such an example, for a TGS crystal with two different thicknesses (230 μm and 500 μm), investigated at different frequencies (6Hz and 25Hz) is displayed in Fig. 4.10. In this experiment, the pyroelectric sensor was a 1mm thick PZT ceramic.

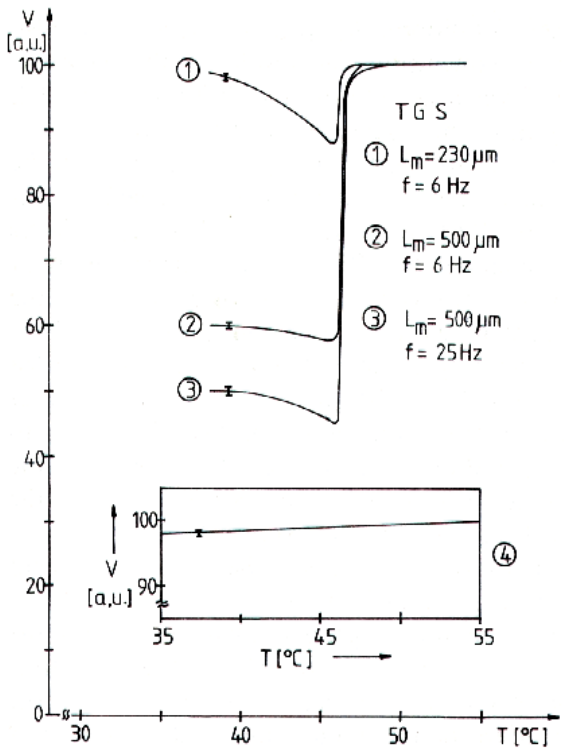

Fig. 4.10 Normalized PPE amplitude as a function of temperature for two TGS single crystals and for two different chopping frequencies (different thermal diffusion length)

Fig. 4.10. indicates that the critical anomaly of the PPE amplitude, ΔV/V, increases from 0.14 up to 1.22 with increasing exponent in Eq. (2.7), for the same critical anomaly (about 0.2 jump in the specific heat – (del Cerro et al., 1987)). This fact supports the suitability of the method for investigations of phase transitions with small critical anomalies of the thermal parameters.

4.2.2 TGS as a pyroelectric sensor

This configuration is based on the information contained in the phase of the FPPE signal and collected from a ferroelectric material, used as pyroelectric sensor in the PPE detection cell.

As presented in the theoretical section, the normalized phase of the FPPE signal, for a detection cell composed by three layers - air, pyroelectric sensor and substrate - is given by:

$$\Theta = \arctan \frac{(1+R_{sp})\exp(-a_p L_p)\sin(a_p L_p)}{1-(1+R_{sp})\exp(-a_p L_p)\cos(a_p L_p)} \tag{4.10}$$

Eq. (4.10) is valid for opaque pyroelectric sensor and for thermally thick substrate. The normalization signal was obtained with empty, directly irradiated sensor. When performing measurements at two different chopping frequencies we obtain:

$$\frac{\tan(\Theta_1)}{\tan(\Theta_2)} = \frac{\exp(-L_p a_{p1})[\cos(L_p a_{p1}) + \sin(L_p a_{p1})\tan(\Theta_1)]}{\exp(-L_p a_{p2})[\cos(L_p a_{p2}) + \sin(L_p a_{p2})\tan(\Theta_2)]} \tag{4.11}$$

with $a_{p1,2} = (\pi f_{1,2}/a_p)^{1/2}$. Eq. (4.11) indicates that one can obtain the thermal diffusivity of the pyroelectric material, used as sensor in the detection cell, by performing two measurements at two different chopping frequencies, providing the geometrical thickness of the sensor is known.

Typical results, obtained for the phase of the PPE signal for a 500 μm thick TGS single crystal, with silicon oil as substrate (together with the normalization signal - directly irradiated empty sensor) are displayed in Fig. (4.11). An external electric field of 6 kV/m was additionally applied.

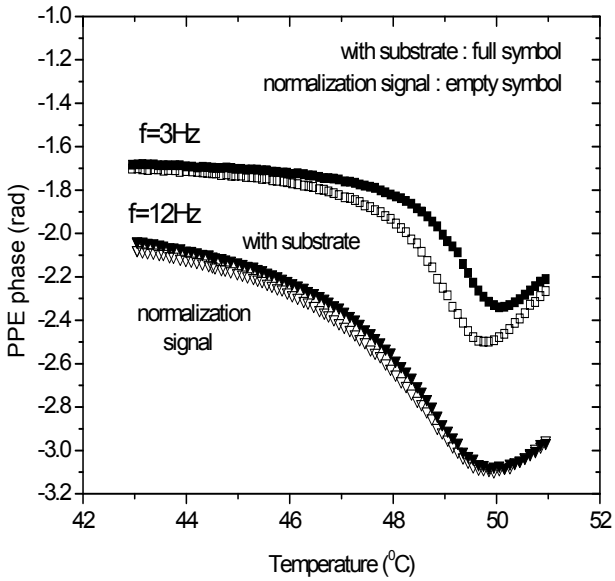

Fig. 4.11 Temperature scans of the phase of the PPE signal, for a 500μm thick TGS single crystal, around the ferroelectric Curie temperature, for 3Hz and 12Hz chopping frequencies, and an external electric field of 6kV/m.

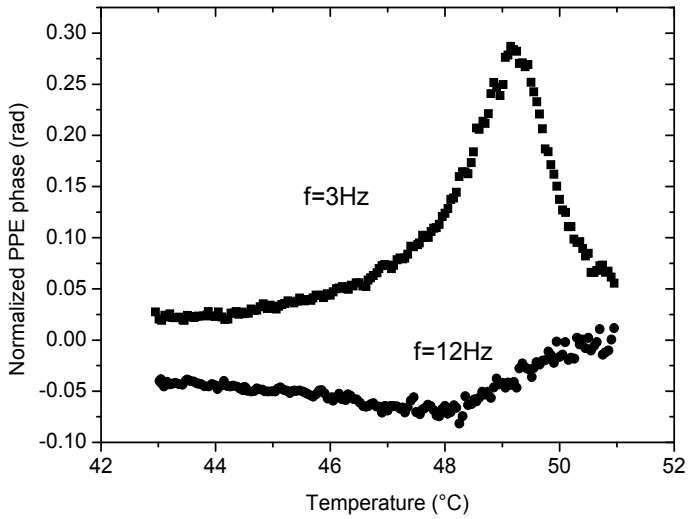

Fig.4.12 Same as Fig.4.11, but for the normalized phase.

Fig. 4.12 presents the normalized phases of the PPE signal for the two frequencies. The critical behaviour of the thermal diffusivity for three values of the external electric field, as obtained from Eq.(4.11), is displayed in Fig. 4.13.

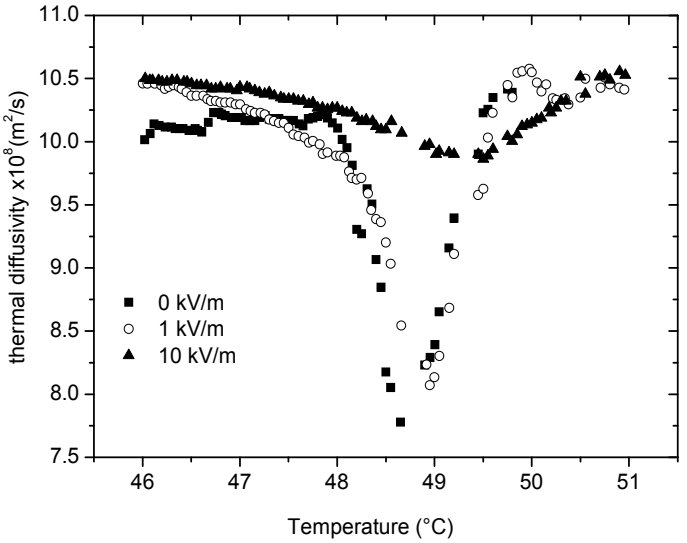

Fig. 4.13 Critical behaviour of the thermal diffusivity of TGS for 0 kV/m (squares); 1 kV/m (circles) and 10 kV/m (triangles).

Fig. 4.13 displays a typical behavior (critical slowing down) of thermal diffusivity for a second order phase transition. The external electric field has the well known influence on the phase transition: it increases the Curie temperature and enlarges the critical region. The

values of the Curie points are in good agreement with those obtained from the direct measurement of the PPE amplitude (Fig. 4.14).

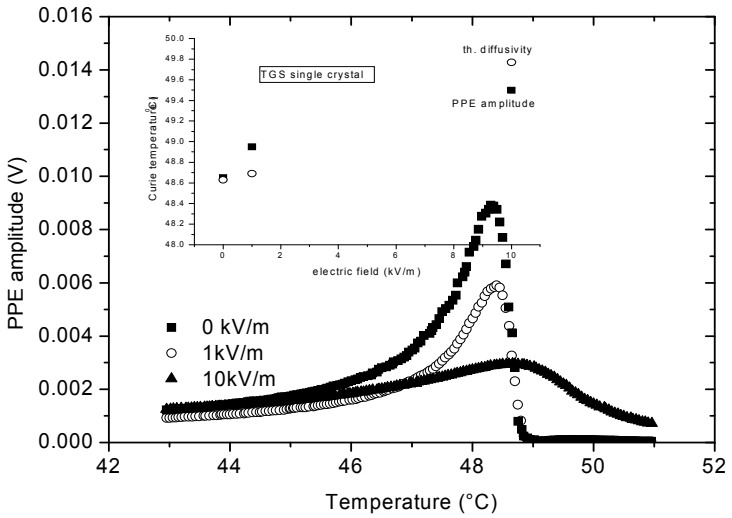

Fig. 4.14 Typical behaviour of the amplitude of the PPE signal for empty TGS sensor and for three values of the external electric field. Insertion: The Curie temperature vs. electric field, as obtained from thermal diffusivity and PPE amplitude (inflection point).

In conclusion to this sub-section, the PPE calorimetry, in the "front" detection configuration, was used to measure the critical behaviour of the thermal diffusivity of TGS single crystal.
In a standard PPE experiment (section 4.3.1) the information on the sample's properties is collected and processed. In this approach, we collect the information on the thermal properties of the pyroelectric sensor itself.
We selected the phase of the PPE signal (and not the amplitude) as source of information due to the well known advantages: the phase is independent on the fluctuations of the incident radiation and the signal to noise ratio is higher than in the case of using the amplitude of the signal. Measurements at two different chopping frequencies and calibration procedures were necessary in order to eliminate the instrumental factors and to obtain a mathematical equation depending on solely one thermal parameter, which is the thermal diffusivity.
The applied external electric field has a typical influence on the critical region of the para-ferroelectric phase transition of TGS: both the Curie temperature and the thickness of the critical region slightly increase with increasing value of the electric field.
The results obtained for the value of the thermal diffusivity of TGS and for the value of the Curie temperatures are in good agreement with data reported in the literature and obtained by other techniques (del Cerro et al., 1987).
Finally, we must emphasize that this configuration speculates the fact that the investigated ferroelectric material is pyroelectric as well. The method was used on a classical TGS crystal, but it appears to be a suitable alternative in studying the thermal properties of the ferroelectric liquid crystals, when the ferroelectric state is imposed by a given layered geometry.

5. Discussions and conclusions

5.1 Comparison with other techniques

It is not possible to perform an exhaustive analysis and comparison of the PPE calorimetry with other types of calorimetry, but some particular advantages of this technique can be mentioned. First of all, due to the fact that the pyroelectric sensor "feels" the temperature variation (and not the temperature), no special thermostatic precautions are requested. This is an advantage compared with adiabatic types of calorimetry, for example. If we compare PPE with differential scanning calorimetry (DSC), PPE is more accurate in detecting the critical temperature (Curie point for ferroelectrics), due to the possibility of scanning very slow (few mK/min – see for example Marinelli et al., 1992) the temperature of the detection cell. In the case of DSC, it is known that the sensitivity increases with increasing temperature variation rate (decreasing the accuracy in measuring the critical temperature).

We cannot overtake two general features that make the PPE calorimetry "unique": (i) it is the only calorimetric technique able to give in one measurement the value of two (in fact all four) thermal parameters; (ii) it is the only technique which, in the critical region of a phase transition, for a given anomaly in the thermal parameters, produces an enhanced signal anomaly.

Finally, some comparison with other PT techniques is welcome. Marinelli et al., 1992 tried to compare the performances of the PPE technique in detecting phase transitions, with another photothermal technique largely used for phase transitions investigations: the photoacoustic (PA) method.

If we follow only the phase channels, they are given in the standard configuration, with optically opaque and thermally thick sample by the equations (Zammit et al., 1988; Marinelli et al., 1992):

$$\Theta_{PA} = \tan^{-1}\left(-1-2/p\right); p = \beta_s \left(2\alpha_s / \omega\right)^{1/2} \tag{5.1}$$

for PA phase, and

$$\Theta_{PPE} = -\tan^{-1}\left(\omega\tau_e\right) - 1/q\,; \quad q = \left(1/L_s\right)\left(2\alpha_s / \omega\right)^{1/2} \tag{5.2}$$

for PPE phase.

The sensitivity of the two techniques to changes in p and q, respectively, are:

$$\left(\frac{d\Theta}{dp}\right)_{PA} = \left(p^2 + p + 2\right)^{-1} \tag{5.3.a}$$

$$\left(\frac{d\Theta}{dq}\right)_{PPE} = q^{-2} \tag{5.3.b}$$

An analysis of Eqs. (5.3.a,b) leads to the conclusion that the maximum sensitivity of the PA technique is reached when p=0 and has the value ½. In the mean time the sensitivity of the PPE technique can go (at least theoretically) to infinity, denoting once again the suitability of this technique for phase transitions detection.

5.2 General features of the PPE calorimetry

PPE technique is a sensitive and accurate calorimetry for thermal inspection of solid state matter. Concerning ferroelectric materials, the main feature of the method is that two detection configurations can be separately or together used for thermal characterization; the ferroelectric material under investigation can be sample or sensor in the PPE detection cell. All four static (specific heat) and dynamic (thermal conductivity, diffusivity and effusivity) thermal parameters can be measured by this technique, and phenomena associated with changes in time, composition or temperature (phase transitions-for example) can be studied. The sensitivity of the method and the accuracy of the results, when investigating ferroelectric materials, depend on various experimental parameters. The possibility of selecting and adjusting these experimental parameters can lead to an optimization of the performances of the method.

The performances of the method depend practically on: the sensor's detectivity, the precision in monitoring the main experimental parameters (chopping frequency, sample's thickness control, temperature, etc), the quality of the sensor-sample thermal contact, the way of performing the acquisition and processing of experimental data. Some typical experimental data are: the detectivity of the pyroelectric $LiTaO_3$ sensors is higher than 10^8 cm $Hz^{1/2}W^{-1}$; minimum detectable temperature variation: 1 μK; minimum controllable temperature variation rate: 10 mK; frequency stability: 10^{-4} Hz.

The main limitations of the technique concerning ferroelectric materials are imposed by the Curie temperature of the pyroelectric sensor, by the properties of the coupling fluid (always necessary when inserting the ferroelectric material as a sample) and by the geometry of the investigated sample (it must be a disk of tens-hundreds of micrometers thick, with polished surfaces).

6. References

Bentefour E.H., Glorieux C., Chirtoc M. &Thoen J. (2003). Characterization of pyroelectric detectors between 170 and 300 K using the photopyroelectric technique, *Review of Scientific Instruments*, Vol. 74, No. 1,(January 2003), pp. 811-813, ISSN 0034-6748

Bhalla A. S. , Liu S. T. (1993). 4.2.3 Pyroelectric coefficients of ferroelectric pyroelectrics, In *: Electrical Properties - Low Frequency Properties of Dielectric Crystals - Piezoelectric, Pyroelectric, and Related Constants , The Landolt-Börnstein Database* , D.F. Nelson (Ed.), Vol. 29b, Springer Verlag, ISBN 978-3-540-55065-5.

Chirtoc, M., Glorieux, C. & Thoen, J.(2009). Thermophysical Properties and Critical Phenomena Studied by Photopyroelectric (PPE) Method, In: *Thermal Wave Physics and Related Photothermal Techniques: Basic Principles and Recent Developments,* E. M. Moraes, (Ed), 125-159, Transworld Research Network, ISBN 978-81-7895-401-1, Kerala, India

Chirtoc, M. & Mihailescu, G.(1989). Theory of Photopyroelectric Method for Investigation of Optical and Thermal Materials Properties. *Physical Review*, Vol. B40, No. 14, (November 1989), pp. 9606-9617, ISSN 1098-0121

Clark N. and Lagerwall S. T.(1980). Submicrosecond Bistable Electro-Optic Switching in Liquid Crystals. *Applied Physic. Letters.* 36 (1980) pp899-901, ISSN 0003-6951

Coufal, H. (1984). Photothermal Spectroscopy Using a Pyroelectric Thin-Film Detector. *Applied Physics. Letters*, Vol. 44, No. 1, (January 1984), pp.59- 61, ISSN 0003-6951

del Cerro, J., Ramos, S. & Sanchez-Laulhe, J. M. (1987). Flux Calorimeter for Measuring Thermo-physical Properties of Solids: Study of TGS. *Journal of Physics E: Scientific Instruments,* Vol. 20, No. 6, (June 1987), pp. 612-615, ISSN 0957-0233

Delenclos, S., Chirtoc, M., Hadj Sahraoui, A., Kolinsky, C. & Buisine, J. M. (2002). Assessement of Calibration Procedures for Accurate Determination of Thermal Parameters of Liquids and their Temperature Dependence Using the Photopyroelectric Method. *Review of Scientific Instruments*, Vol. 73, No.7, (July 2002), pp.2773-2780, ISSN 0034- 6748

Fullem, T. Z., and Y. Danon, Electrostatics of pyroelectric accelerators. *Journal of Applied Physics* Vol. 106, No 7, (October 2009), ISSN 0021-8979

Jalink, H., Frandas, A., van der Schoor, R. & Bicanic, D. (1996). New Photothermal Cell Equiped with Peltier Elements for Phase Transition Studies. *Review of Scientific Instruments*, Vol. 67, No. 11, (November 1996), pp.3990-3993, ISSN 0034- 6748

Lagerwall S. T., *Ferroelectric and Antiferroelectric Liquid Crystals.* (1999). Wiley-VCH, ISBN 978-3527298310, New York

Mandelis, A. (1984). Frequency Domain Photopyroelectric Spectroscopy of Condensed Phases: A New, Simple and Powerful Spectroscopic Technique. *Chemical Physics Letters*, Vol. 108, No. 4, (July 1984), pp. 388-392, ISSN 0009-2614

Mandelis, A. & Zver, M. M. (1985) J. Theory of Photopyroelectric Effect in Solids. *Journal of Applied Physics,* Vol. 57, No. 9, (May 1985), pp. 4421-4430, ISSN 0021-8979

Mandelis, A., Care, F., Chan, K. K. & Miranda, L. C. M. (1985). Photopyroelectric Detection of Phase Transitions in Solids. *Applied Physics A,* Vol. 38, No. 2, (October 1985), pp. 117-122, ISSN 0947-8396

Marinelli, M., Zammit, U., Mercuri, F. & Pizzoferrato, R.(1992). High Resolution Simultaneous Photothermal Measurements of Thermal Parameters at a Phase Transition with the Photopyroelectric Technique. *Journal of Applied Physics*, Vol. 72, No. 3, (August 1992), pp.1096-1100, ISSN 0021-8979

Nakamura M., Takekawa S & Kitamura K, Anisotropy of thermal conductivities in non- and Mg-doped near-stoichiometric LiTaO3 crystals, *Optical Materials*, Vol. 32, No 11, (September 2010), pp. 1410-1412, ISSN 0925-3467

Tam, A. C. (1986). Applications of Photoacoustic Sensing Techniques. *Review of Modern Physics*, Vol. 58, No. 2, (February 1986), pp. 381-431, ISSN 0034-6861

Zammit, U., Marinelli, M., Mercuri, F.,Pizzoferrato, R., Scudieri, F. & Martelucci, S. Photoacoustics as a Technique for Simultaneous measurement of Thermal Conductivity and Heat Capacity. *Journal of Physics E-Scientific Instruments*, Vol. 21, No. 10, (October 1988), pp.935-941, ISSN 0957-0233

Whatmore R.W., Pyroelectric Devices and Materials, *Reports on Progress in Physics*, Vol. 49 (December 1986), pp1335-1386, ISSN 0034-4885

16

Valence Band Offsets of $ZnO/SrTiO_3$, $ZnO/BaTiO_3$, $InN/SrTiO_3$, and $InN/BaTiO_3$ Heterojunctions Measured by X-Ray Photoelectron Spectroscopy

Caihong Jia[1,2], Yonghai Chen[1], Xianglin Liu[1], Shaoyan Yang[1] and ZhanguoWang[1]
[1]*Key Laboratory of Semiconductor Material Science, Institute of Semiconductors, Chinese Academy of Science, Beijing*
[2]*Key Laboratory of PhotovoltaicMaterials of Henan Province and School of Physics Electronics, Henan University, Kaifeng*
China

1. Introduction

The heterostructures of wurtzite semiconductors and perovskite ferroelectric oxide integrate the rich properties of perovskites together with the superior optical and electronic properties of wurtzites, thus providing a powerful method of new multifunctional devices. The electrical and optical properties of the heterostructures are strongly influenced by the interface band offset, which dictates the degree of charge carrier separation and localization. It is very important to determine the valence band offset (VBO) of semiconductor/ferroelectric oxides in order to understand the electrical and optical properties of the heterostructures and to design novel devices. In this chapter, by using X-ray photoelectron spectroscopy (XPS), we determine the VBO as well as the conduction band offset (CBO) values of the typical semiconductor/ferroelectric oxide heterojunctions, such as $ZnO/SrTiO_3$, $ZnO/BaTiO_3$, $InN/SrTiO_3$ and $InN/BaTiO_3$, that are grown by metal-organic chemical vapor deposition. Based on the values of VBO and CBO, it has been found that type-II band alignments form at the $ZnO/SrTiO_3$ and $ZnO/BaTiO_3$ interfaces, while type-I band alignments form at $InN/SrTiO_3$ and $InN/BaTiO_3$ interfaces.

For many years, heterojunctions have been one of the fundamental research areas of solid state science. The interest in this topic is stimulated by the wide applications of heterojunction in microelectronics. Devices such as heterojunction bipolar transistors, quantum well lasers and heterojunction field effect transistors (FET), already have a significant technological impact. The semiconductor-ferroelectric heterostructures have attracted much attention due to their large potential for electronic and optoelectronic device applications (Lorentz et al., 2007; Losego et al., 2009; Mbenkum et al., 2005; Voora et al., 2009; 2010). The ferroelectric constituent possesses switchable dielectric polarization, which can be exploited for modificating the electronic and optical properties of a semiconductor heterostructure. Hysteresis properties of the ferroelectric polarization allows for bistable interface polarization configuration and potentially for bistable heterostructure operation modes. Therefore, the

heterostructures of wurtzite semiconductors and perovskite ferroelectric oxides integrate the rich properties of perovskites together with the superior optical and electronic properties of wurtzites, providing a powerful method of new multifunctional devices (Peruzzi et al., 2004; Wei et al., 2007; Wu et al., 2008). It is well known that the electrical and optical properties of the heterostructures are strongly influenced by the interface band offset, which determines the barrier for hole or electron transport across the interface, and acts as a boundary condition in calculating the band bending and interface electrostatics. Therefore, it is very important to determine the valence band offset (VBO) of semiconductor/ferroelectric oxides in order to understand the electrical and optical properties of the heterostructures and to design novel devices.

Zinc oxide (ZnO) is a direct wide bandgap semiconductor with large exciton binding energy (60 meV) at room temperature, which makes it promising in the field of low threshold current, short-wavelength light-emitting diodes (LED) and laser diodes (Ozgur et al., 2005). It also has a growing application in microelectronics such as thin film transistors (TFT) and transparent conductive electrodes because of high transparency and large mobility. Indium nitride (InN), with a narrow direct band gap and a high mobility, is attractive for the near infrared light emission and high-speed/high-frequency electronic devices (Losurdo et al., 2007; Takahashi et al., 2004). Generally, ZnO and InN films are grown on foreign substrates such as *c*-plane and *r*-plane sapphire, SiC (Losurdo et al., 2007; Song et al., 2008), (111) Si and GaAs (Kryliouk et al., 2007; Murakami et al., 2008). $SrTiO_3$ (STO) single crystal is widely used as a substrate for growing ferroelectric, magnetic and superconductor thin films. Meanwhile, STO is one of the important oxide materials from both fundamental physics viewpoint and potential device applications (Yasuda et al., 2008). The electron density and hence conductivity of STO can be controlled by chemical substitution or annealing in a reducing atmosphere. Furthermore, a high-density, two-dimensional electron (hole) gas will lead to tailorable current-voltage characteristics at interfaces between ZnO or InN and STO (Singh et al., 2003). In addition, the lattice polarity of ZnO and InN (anion-polarity or cation-polarity) is expected to be controlled by the substrate polarity considering the atomic configuration of STO surface, which is also important to obtain a high-quality ZnO or InN epitaxial layer (Murakami et al., 2008). Thus, it is interesting to grow high quality wurtzite ZnO and InN films on perovskite STO substrates, and it is useful to determine the valence band offset (VBO) of these heterojunctions.

The heterojunction of semiconductor-ZnO or InN/ferroelectric-$BaTiO_3$ (BTO) provides an interesting optoelectronic application due to the anticipated strong polarization coupling between the fixed semiconductor dipole and the switchable ferroelectric dipole (Lorentz et al., 2007; Losego et al., 2009; Mbenkum et al., 2005; Voora et al., 2009; 2010). ZnO TFT, highly attractive for display applications due to transparency in the visible and low growth temperatures, are limited by large threshold and operating voltages (Kim et al., 2005). BTO, as a remarkable ferroelectric material with a high relative permittivity, can be used as the gate dielectric to reduce the operating voltages of TFT for portable applications (Kang et al., 2007; Siddiqui et al., 2006), and as an attractive candidate as an epitaxial gate oxide for field effect transistor. In addition, the free carrier concentration in the ZnO channel can be controlled by the ferroelectric polarization of BTO dielectric in the ZnO/BTO heterostructure field-effect-transistors, thus demonstrating nonvolatile memory elements (Brandt et al., 2009). In order to fully exploit the advantages of semiconductor-ferroelectric heterostructures, other combinations such as InN/BTO should be explored. As a remarkable ferroelectric material with a high relative permittivity, BTO can be used as a gate dielectric for InN based field

effect transistor. More importantly, InN/BTO heterojunction is promising for fabricating optical and electrical devices since oxidation treatment is found to reduce the surface electron accumulation of InN film (Cimalla et al., 2007). Therefore, it is important to determine the VBO of these semiconductor/ferroelectric heterojunctions to design and analyze the performance of devices.

In this chapter, we will first present several methods to determine the energy discontinuities. Then, by using x-ray photoelectron spectroscopy (XPS), we determine the VBO as well as the conduction band offset (CBO) values of the typical semiconductor/ferroelectric oxide heterojunctions, such as ZnO/STO, ZnO/BTO, InN/STO, and InN/BTO, that are grown by metal-organic chemical vapor deposition. Based on the values of VBO and CBO, it has been found that type-II band alignments form at the ZnO/STO and ZnO/BTO interfaces, while type-I band alignments form at the InN/STO and InN/BTO interfaces.

2. Measurement methods

The energy band edge discontinuities at heterostructures can be determined by applying a large variety of experimental techniques, such as electrical transport measurements including capacitance-voltage (C-V) and current-voltage (I-V), optical measurement, photoemission measurement (Capasso et al., 1987). For many years, analysis of the capacitance-voltage and current-voltage of heterojunctions have proven to be important probes for determining the energy barriers of pn junction, Schottky barriers and heterojunctions. The energy discontinuities can be determined by C-V measurement, since the C(V) function has the form of:

$$C = \frac{2(\epsilon_1 N_1 + \epsilon_2 N_2)}{q\epsilon_1\epsilon_2 N_1 N_2}(V_D - V)^{-1/2}, \tag{1}$$

where ϵ_1 and ϵ_2 are the dielectric constants of materials 1 and 2, N_1 and N_2 are the dopant concentrations of materials 1 and 2, V_D is the diffusion potential, while q is the electronic charge. Therefore, the plot of C^{-2} versus V gives a straight line, intercepting the V-axis exactly at $V=V_D$. Based on this quantity, the conduction band discontinuity energy, ΔE_c, can be obtained to be

$$\Delta E_c = qV_D + \delta_2 - (E_{g1} - \delta_1), \tag{2}$$

for anisotype pN heterojunctions; and

$$\Delta E_c = qV_D + \delta_2 - \delta_1, \tag{3}$$

for isotype nN heterojunctions. Where δ_1 and δ_2 refer to the position of the Fermi energies relative to the conduction band minimum (or valence band maximum) in n (or p)-type materials 1 and 2, respectively. That is,

$$\delta_i = kTln(\frac{N_{ci}}{N_i}), i = 1, 2. \tag{4}$$

Here, kT is the Boltzmann energy at the temperature T, N_{ci} is the effective conduction band density of states,

$$N_c = \frac{2(2\pi m^* kT)^{\frac{3}{2}}}{h^3}, \tag{5}$$

which is a function of the reduced effective mass of the electron (m^*) and of temperature (T). Therefore, the difference in the Fermi energies between materials 1 and 2 can be simplified to give

$$\delta_2 - \delta_1 = kTln(\frac{N_{D1}}{N_{D2}}) + \frac{3}{2}kTln(\frac{m_2^*}{m_1^*}), \tag{6}$$

for an nN heterojunction. Thus once the diffusion potential V_D is determined, it is relatively straightforward to obtain the conduction band discontinuity. Indeed, as can be seen from the equation above, it is not necessary to have a highly precise measurement of any of the material parameters such as the bulk free carrier concentration or the effective density of states, since ΔE_c depends only logarithmically on these parameters. On the other hand, the dependence of ΔE_c on V_D is linear, and, therefore, it is important that the measurement of the diffusion potential be as accurate as possible.
The current density is given simply by

$$J = A^*T^2exp(-\frac{q\phi_B}{kT}), \tag{7}$$

where ϕ_B is the barrier height, from which the energy band offset can be determined. The transport measurements have the advantage of being a relatively understanding means of acquiring data using simple structures, but the accuracy of these techniques has never been considered to be particularly high, basically due to the existence of parasitic phenomena giving rise to excess stray capacitances or dark currents, which introduces variables cannot be easily treated in the overall analysis and confuse the measurements.
The optical measurement techniques are based on the study of the optical properties of alternating thin layers of two semiconductors. The quantized energy levels associated with each well depend on the corresponding discontinuity, on the width of the well and on the effective mass. The processes involving the localized quantum well states will introduce series of peaks both in the absorption and photoluminescence spectra. From the position in energy of the peaks in each series, it is possible to retrieve the parameters of the well and in particular the value of ΔE_C and ΔE_V. However, this approach requires the fabrication of high-quality multilayer structures with molecular beam epitaxy, and can only be applied to nearly ideal interface with excellent crystal quality.
For x-ray photoelectron spectroscopy (XPS), it is well established that the kinetic energy, E_K, of electrons emitted from a semiconductor depends on the position of the Fermi level, E_F, within the semiconductor band gap. This aspect of XPS makes it possible to determine E_F relative to the valence band maximum, E_V, in the region of the semiconductor from which the photoelectron originate. Therefore, besides analyzing the interface elemental and chemical composition, XPS can also be used as a contactless nondestructive and direct access to measure interface potential related quantities such as heterojunction band discontinuites. This technique was pioneered by Grant ea al (Grant et al., 1978). Since the escape depths of the respective photoelectrons are in the order of 2 nm only, one of the two semiconductors has to be sufficiently thin. This condition may be easily met when heterostructures are grown by molecular beam epitaxy (MBE) or metal-organic chemical vapor deposition (MOCVD). The XPS method for determining VBO is explained by the schematic band diagram displayed in Fig. 1, in which an idealized flat band was assumed. Based on the measured values of ΔE_{CL}, the core level to E_V binding energy difference in bulk semiconductors A and B, (E^A_{CL}-E^A_V) and

(E_{CL}^B-E_V^B), respectively. By inspection of Fig. 1, it can be seen that

$$\Delta E_V(B-A) = (E_{CL}^B - E_V^B) - (E_{CL}^A - E_V^A) + \Delta E_{CL}(A-B). \quad (8)$$

Thus, to apply XPS for ΔE_V measurements, it is essential to determine the bulk semiconductor material parameters (E_{CL}-E_V) for those semiconductors forming the heterojunctions. A primary difficulty with measuring (E_{CL}-E_V) is the accurate determination of the E_V position in photoemission spectra. The most frequently employed method involves extrapolation of a tangent line to the leading edge of the valence band spectrum to the energy axis, this intercept is defined as E_V. Substituting these values to Eq. 8, the VBO of heterojunction A/B can be obtained.

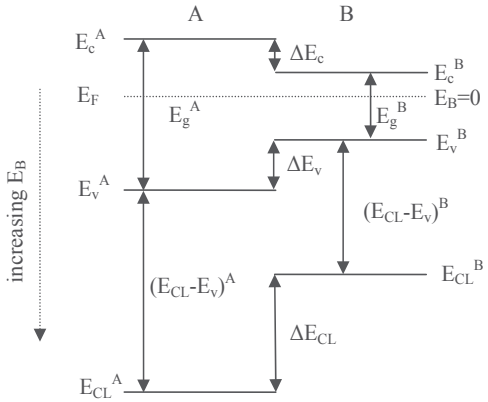

Fig. 1. Schematic energy band diagram illustrating the measurement of VBO by XPS.

3. Experimental

Several samples, bulk commercial (001) STO, (111) STO and (001) BTO substrates, thick (several hundred nanometers) and thin (about 5 nm) ZnO and InN layers grown on the commercial STO and BTO substrates were studied in this work. To get a clean interface, the STO and BTO substrates were cleaned with organic solvents and rinsed with de-ionized water sequentially before loading into the reactor. The thick and thin heterostructures of ZnO/STO, ZnO/BTO, InN/STO and InN/BTO were deposited by MOCVD. More growth condition details of the ZnO and InN layers can be found in our previous reports (Jia et al., 2008; 2009a;b; 2010a;b; 2011; Li et al., 2011).

XPSs were performed on ThermoFisher ESCALAB 250, PHI Quantera SXM, and VG MKII XPS instruments with AlKα (hν=1486.6 eV) as the x-ray radiation source, which had been carefully calibrated on work function and Fermi energy level (E_F). Because all the samples were exposed to air, there must be some impurities (e.g., oxygen and carbon) existing in the sample surface, which may prevent the precise determination of the positions of the valence band maximum (VBM). To reduce the undesirable effects of surface contamination, all the samples were cleaned by Ar^+ bombardment at a low sputtering rate to avoid damage to the samples. After the bombardment, peaks related to impurities were greatly reduced, and no new peaks appeared. Because a large amount of electrons are excited and emitted from the sample, the sample is always positively charged and the electric field caused by the charge can affect the measured kinetic energy of photoelectron. Charge neutralization was performed

with an electron flood gun and all XPS spectra were calibrated by the C 1s peak at 284.8 eV from contamination to compensate the charge effect. Since only the relative energy position in each sample is needed to determine the VBO, the absolute energy calibration for a sample has no effect on the ultimate result. The surfaces of samples were examined initially by low-resolution survey scans to determine which elements were present. Very high-resolution spectra were acquired to determine the binding energy of core level (CL) and the valence band maximum energy in the survey spectra. All the CL spectra were fitted to Voigt (mixed Lorentz-Gaussian) line shape with a Shirley background. Since considerable accordance of the fitted line to the original measured data has been obtained, the uncertainty of the CL position should be less than 0.03 eV, as evaluated by numerous fittings with different parameters. The VBM positions in the valence band (VB) spectra were determined by linear extrapolation of the leading edge of the VB spectra recorded on bulk substrates and thick films to the base lines in order to account for instrument resolution induced tail (Zhang et al., 2007), which has already been widely used to determine the VBM of semiconductors. Evidently, the VBM value is sensitive to the choice of points on the leading edge used to obtain the regression line (Chambers et al., 2001). Thus, several different sets of points were selected over the linear region of the leading edge to perform regressions, and the uncertainty of VBO is found to be less than 0.06 eV in the present work.

4. VBO for ZnO/STO heterojunction

Figure 2 (a) shows the x-ray θ-2θ diffraction patterns of thick ZnO films on (111) STO substrates. The diffractogram indicates only a single phase ZnO with a hexagonal wurtzite structure. Only peaks of ZnO (0002) and (0004) reflection and no other ZnO related peaks are observed, implying a complete *c*-axis oriented growth of the ZnO layer. The highly oriented ZnO films on STO substrate strongly suggest that the nucleation and crystal growth is initiated near the substrate surface. The full width at half maximum (FWHM) of symmetric (0002) scan is about 0.85° along ω-axis, as shown in the inset of Fig. 2(a). X-ray off-axis ϕ scans are performed to identify the in-plane orientation relationships between the film and substrate. The number of peaks in a ϕ scan corresponds to the number of planes for a particular family that possesses the same angle with the film surface. Figure 2 (b) shows the results of x-ray ϕ scans performed using the $\{11\bar{2}2\}$ reflection of ZnO (2θ=67.95°, χ=58.03°) and the $\{110\}$ reflection of STO (2θ=32.4°, χ=35.26°). Only six peaks separated by 60° are observed for the ZnO $\{112\}$ family, which has six crystal planes with the same angle with the growth plane (χ=58.03°), as shown in Fig. 2 (b), indicating a single domain. From the relative position of ZnO $\{112\}$ and STO $\{110\}$ families, the in-plane relationships can be determined to be $[11\bar{2}0]$ZnO$\|[0\bar{1}1]$STO. The atomic arrangement in the (0001) basal plane of ZnO is shown in Fig. 2 (c). The growth in this direction shows a large lattice mismatch of about 17.7% ($\frac{2a_{ZnO}-\sqrt{2}a_{STO}}{\sqrt{2}a_{STO}}\times 100\%$) along the direction of $<11\bar{2}0>_{ZnO}$, although it shows a much smaller lattice mismatch of 1.91% ($\frac{\sqrt{3}a_{ZnO}-\sqrt{2}a_{STO}}{\sqrt{2}a_{STO}}\times 100\%$) along the direction of $<1\bar{1}00>_{ZnO}$ when ZnO rotated 30° in plane.

For ZnO/STO heterojunction, the VBO (ΔE_V) can be calculated from the formula

$$\Delta E_V = \Delta E_{CL} + (E^{ZnO}_{Zn2p} - E^{ZnO}_{VBM}) - (E^{STO}_{Ti2p} - E^{STO}_{VBM}), \tag{9}$$

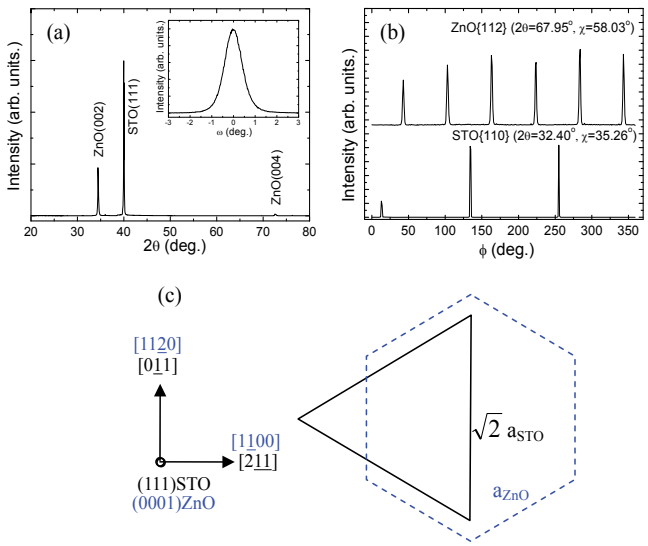

Fig. 2. X-ray θ-2θ (a), ω (inset of (a)), and ϕ (b) scans and atomic arrangement (c) of ZnO films on (111) STO substrate.

where ΔE_{CL}=($E_{Ti2p}^{ZnO/STO}$-$E_{Zn2p}^{ZnO/STO}$) is the energy difference between Zn 2p and Ti 2p CLs measured in the thin ZnO/STO heterojunction sample, and (E_{Ti2p}^{STO}-E_{VBM}^{STO}) and (E_{Zn2p}^{ZnO}-E_{VBM}^{ZnO}) are the VBM energies with reference to the CL positions of bulk STO and thick ZnO film, respectively, which are obtained by XPS measurement from the respective STO substrate and thick ZnO film.

Figure 3 shows the XPS Ti 2p and Zn 2p CL narrow scans and the valence band spectra from the STO substrate and the thick ZnO/STO samples, respectively. As shown in Fig. 3(a), the Zn 2p CL peak locates at 1021.69±0.03 eV. Fig. 3(e) shows the VB spectra of the thick ZnO sample, and the VBM position is determined to be 1.06±0.06 eV by a linear fitting depicted above. As a result, the energy difference of Zn 2p to ZnO VBM (E_{Zn2p}^{ZnO}-E_{VBM}^{ZnO}) can be determined to be 1020.63±0.03 eV. Using the same Voigt fitting and linear extrapolation methods mentioned above, the energy difference of Ti2p to STO VBM (E_{Ti2p}^{STO}-E_{VBM}^{STO}) can be determined to be 457.32±0.06 eV. The CL spectrum of Zn 2p and Ti 2p in thick ZnO film and bulk STO are quite symmetric indicating the uniform bonding state and the only peaks correspond to Zn-O and Ti-O bonds, respectively. The measurement of ΔE_{CL} for the Ti 2p and Zn 2p CLs recorded in the thin ZnO/STO junction is illustrated in Fig. 3(c) and (d). After substraction of the background, the spectra of Ti 2p and Zn 2p CLs were well Voigt fitted and the energy difference of Ti 2p and Zn 2p CLs (ΔE_{CL}) can be determined to be 562.69±0.03 eV. It is noteworthy that the Ti 2p peak is not symmetric and consists of two components by careful Voigt fitting. The prominent one located at 459.22 eV is attributed to the Ti emitters within the STO substrate which have six bonds to oxygen atoms, and the other one shifting by ∼2 eV to a lower binding energy indicates the presence of an interfacial oxide layer. This phenomenon is similar to that observed in the interface of $LaAlO_3$/$SrTiO_3$, and the shoulder at lower binding energy is attributed to TiO_x suboxides, which is expected on account of the TiO_x-terminated STO initial surface (Kazzi et al., 2006). The fair double-peak fitting shown

in Fig. 3(d) confirms the presence of TiO_x suboxides. Substituting the above (E^{STO}_{Ti2p}-E^{STO}_{VBM}), (E^{ZnO}_{Zn2p}-E^{ZnO}_{VBM}) and ΔE_{CL} into Eq. 9, the resulting VBO value is calculated to be 0.62$\pm$0.09 eV.

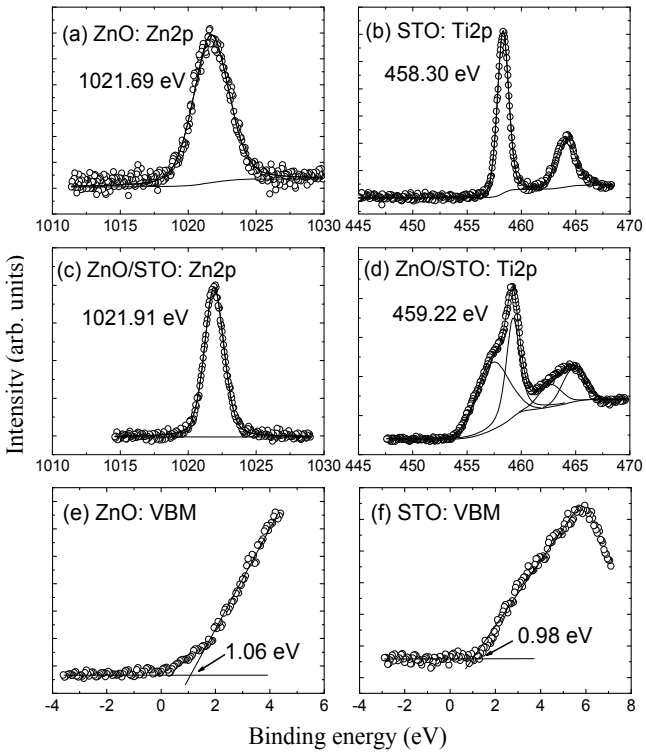

Fig. 3. Zn 2p spectra recorded on ZnO (a) and ZnO/STO (c), Ti 2p spectra on STO (b) and ZnO/STO (d), and VB spectra for ZnO (e) and STO (f). All peaks have been fitted to Voigt line shapes using Shirley background, and the VBM values are determined by linear extrapolation of the leading edge to the base line. The errors in the peak positions and VBM are $\pm$0.03 and $\pm$0.06 eV, respectively.

The reliability of the measured result is analyzed by considering several possible factors that could impact the experiment results. The lattice mismatch between ZnO and STO is about $\sim$17.7%, which will induce a much smaller critical thickness than 5-10 nm, compared with the lattice mismatch of $BaTiO_3$ grown on STO (2.2%) and a critical thickness of 5-10 nm (Sun et al., 2004). Meanwhile, the ZnO epitaxial layer grown on STO substrate by MOCVD is characterized by columnar growth mode, which provides strain relief mechanism (Fan et al., 2008). Thus, the ZnO overlayer in the heterojunction is almost completely strained and the strain-induced piezoelectric field effect can also be neglected. In addition, the error induced by band bending is checked to be much smaller than the average standard deviation of $\pm$0.09 eV given above (Yang et al., 2009). Since the factors that can affect the ultimate result can be excluded from the measured result, the experimental obtained VBO value is reliable.

To further confirm our result, it would be very useful to compare our experimental results with a theoretical model proposed by M$\ddot{o}$nch (Monch et al., 2005). The VBOs of ZnO heterojunctions are predicted based on the difference of the respective interface-induced gap

states (IFIGS) branch-point energies and electric dipole terms. That is

$$\Delta E_V = E_{vl}(\Gamma) - E_{vr}(\Gamma) = \phi^p_{bpr} - \phi^p_{bpl} + D_X(X_{sr} - X_{sl}), \tag{10}$$

where the p-type branch-point energy $\phi^p_{bp}(\Gamma) = E_{bp} - E_V(\Gamma)$ is the energy distance from the valence band maximum to the branch point of the IFIGS and X_s is the electronegativity of the respective semiconductor. The subscripts r and l stand for the right and left side, respectively, of the heterostructure. The dipole parameter D_X is determined by the density of states and extension of the IFIGS at their branch point. This dipole term can also be neglected, just like the common semiconductor heterojunctions, since the electronegativities of the atoms constituting ZnO/STO heterojunction differ by up to 10% only. Through analysis of the VBO values reported for ZnO heterostructure (Monch et al., 2005), the dependence of VBO on the p-type branch-point energy is obtained to be

$$\Delta E_V = \varphi_{vbo}[\phi^p_{bp}(ZnO) - \phi^p_{bp}(semi)]. \tag{11}$$

With the p-type branch-point energies of ZnO (3.04 eV) (Monch et al., 2005) and STO (2.5 eV) (Monch et al., 2004), and the slope parameters φ_{vbo} for insulator heterostructures of 1.14∼1.23, a VBO of 0.64±0.21 eV would be calculated, which is in good agreement with the experimentally determined value of 0.62±0.09 eV. It implies that the IFIGS theory is not only widely used to the group-IV elemental semiconductors, SiC, and the III-V, II-VI, and I-III-VI_2 compound semiconductors and their alloys (Monch et al., 2005), but also applicable to the semiconductor/insulator heterostructures. In addition, the resulting ΔE_V is a sufficiently large value for device applications in which strong carrier confinement is needed, such as light emitters or heterostructure field effect transistors. For instance, the valence band offset in the $Zn_{0.95}Cd_{0.05}O/ZnO$ system is only 0.17 eV (Chen et al., 2005), which is less than that of ZnO/STO.

Finally, the CBO (ΔE_C) can be estimated by the formula $\Delta E_C = \Delta E_V + E_g^{ZnO} - E_g^{STO}$. By substituting the band gap values (E_g^{ZnO}=3.37 eV (Su et al., 2008) and E_g^{STO}=3.2 eV (Baer et al., 1967)), ΔE_C is calculated to be 0.79±0.09 eV. It would be interesting to compare our experimental values with the electrical transport results by Wu et al (Wu et al., 2008). They have investigated the temperature dependent current-voltage characteristic of $ZnO/Nb:SrTiO_3$ junction, and found that the effective barrier height (ϕ_{eff}) is 0.73 eV, which is directly considered to be the CBO in n-N heterojunctions (Alivov et al., 2006). It can be seen that the effective barrier height in Wu's work is consistent with our CBO value. Accordingly, a type-II band alignment forms at the heterojunction interface, in which the conduction and valence bands of the ZnO film are concomitantly higher than those of the STO substrate, as shown in Fig. 4.

5. VBO for ZnO/BTO heterojunction

In x-ray θ-2θ diffraction measurements, as shown in Fig. 5 (a), the ZnO/BTO sample presented the only peak of ZnO (0002) reflection and no other ZnO related peaks were observed, implying a complete c-axis oriented growth of the ZnO layer. From the pole figure of ZnO $\{10\bar{1}1\}$ family, shown in Fig. 5 (b), twelve peaks separated by 30° are present, although ZnO has a sixfold symmetry about the [0001] axis, indicating that the ZnO film is twinned in the growth plane by a 30° in-plane rotation. The relative intensities of the two sets of peaks is

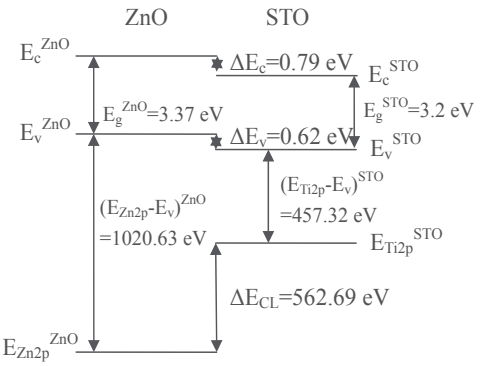

Fig. 4. Energy band diagram of ZnO/STO heterojunction.

related to the proportion of the two domains, indicating that the two domains are almost equal in amount.

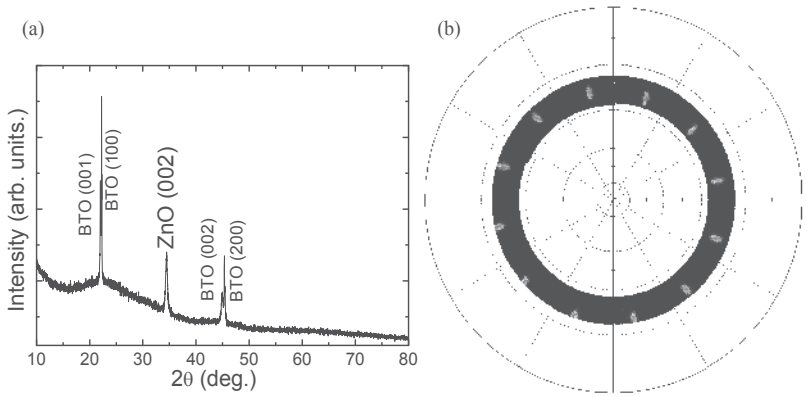

Fig. 5. X-ray θ-2θ diffraction pattern (a) and pole figure (b) of the thick ZnO films on BTO substrates.

For ZnO/BTO heterojunction, the VBO (ΔE_V) can be calculated from the formula

$$\Delta E_V = \Delta E_{CL} + (E_{Zn2p}^{ZnO} - E_{VBM}^{ZnO}) - (E_{Ti2p}^{BTO} - E_{VBM}^{BTO}), \quad (12)$$

where ΔE_{CL}=($E_{Ti2p}^{ZnO/BTO}$-$E_{Zn2p}^{ZnO/BTO}$) is the energy difference between Zn 2p and Ti 2p CLs measured in the thin ZnO/BTO heterojunction, while (E_{Ti2p}^{BTO}-E_{VBM}^{BTO}) and (E_{Zn2p}^{ZnO}-E_{VBM}^{ZnO}) are the VBM energies with reference to the CL positions of bulk BTO and thick ZnO film, respectively. Figure 6 shows the XPS Ti 2p and Zn 2p CL narrow scans and the valence band spectra from the bulk BTO, thick and thin ZnO/BTO samples, respectively. For the thick ZnO film, the Zn 2p CL peak locates at 1022.04±0.03 eV, and the VBM position is determined to be 2.44±0.06 eV by a linear fitting described above, as shown in Fig. 6(a) and (e). The energy difference between Zn 2p and VBM of thick ZnO film (E_{Zn2p3}^{ZnO}-E_{VBM}^{ZnO}) is deduced to be 1019.60±0.09 eV, which is well consistent with our previous reports (Zhang et al., 2007). It can also be clearly seen from Fig. 6 that the CL spectra of Zn 2p and Ti 2p in the thick ZnO film and thin ZnO/BTO heterojunction are quite symmetric, indicating a uniform bonding state and

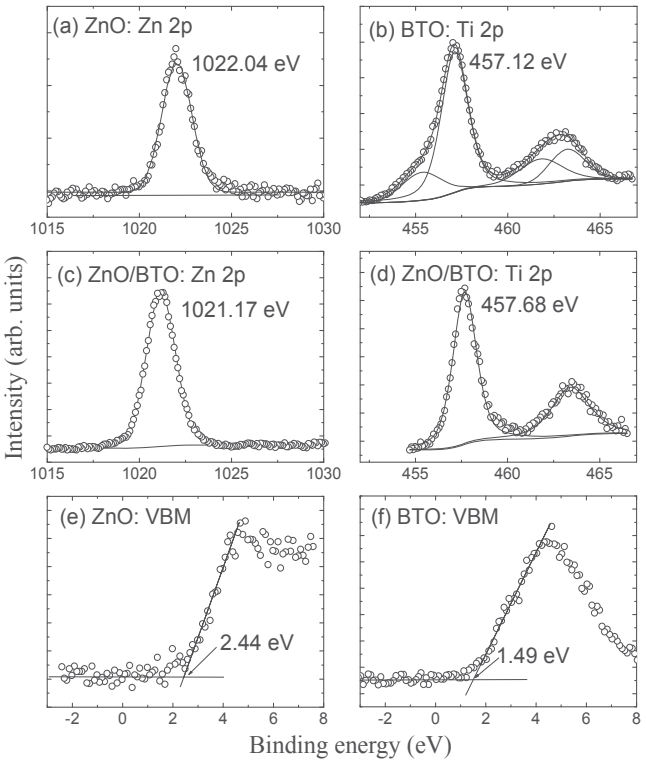

Fig. 6. Zn 2p spectra recorded on ZnO (a) and ZnO/BTO (c), Ti 2p spectra on BTO (b) and ZnO/BTO (d), and VB spectra for ZnO (e) and BTO (f). All peaks have been fitted to Voigt line shapes using Shirley background, and the VBM values are determined by linear extrapolation of the leading edge to the base line. The errors in the peak positions and VBM are ± 0.03 and ± 0.06 eV, respectively.

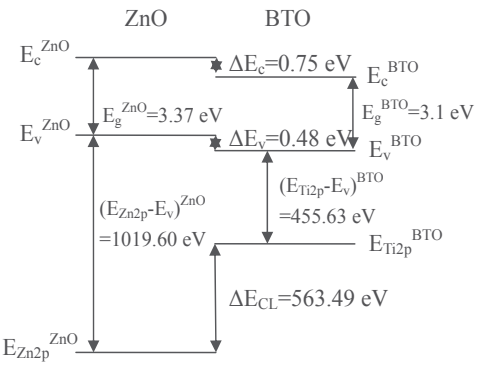

Fig. 7. Energy band diagram of ZnO/BTO heterojunction.

the only peaks correspond to Zn-O and Ti-O bonds, respectively. However, the Ti 2p peak in the bulk BTO is not symmetric and consists of two components by careful Voigt fitting. The prominent one located at 457.12 ± 0.03 eV is attributed to the Ti emitters within the BTO substrate, which have six bonds to oxygen atoms. The other one shifting by ~ 2 eV to a lower

binding energy is attributed to TiO_x suboxides on account of the TiO-terminated BTO initial surface (Kazzi et al., 2006). It is interesting that the Ti 2p peaks transform from asymmetry in bulk BTO to symmetry in the thin ZnO/BTO sample, implying that the TiO_x suboxides in the BTO surface is oxidized completely to the highest valence of Ti^{4+}. The VBM value of bulk BTO is determined to be 1.49±0.06 eV using the linear method. The Fermi level of an insulator is expected to be located in the middle of the forbidden energy gap, so the VBM will be one-half of the band gap of insulators (You et al., 2009). For BTO, the VBM should be 1.55 eV calculated from the band gap of 3.1 eV (Boggess et al., 1990), which is in good agreement with the measured value (1.49±0.06 eV) in the present work. Using the same fitting methods mentioned above, the energy values of CL for the thin ZnO/BTO heterojunction can be determined, as shown in Fig. 6. Substituting the above values into Eq. 12, the resulting VBO value is calculated to be 0.48±0.09 eV.

A small lattice mismatch is present between the BTO[$0\bar{1}1$] direction and the hexagonal apothem of ZnO, which is only about 0.8% ($\frac{\sqrt{3}a_{ZnO}-\sqrt{2}a_{BTO}}{\sqrt{2}a_{BTO}}\times 100\%$) (Wei et al., 2007). This lattice mismatch is so small that the strain-induced piezoelectric field effect can be neglected in this work (Su et al., 2008). In ZnO/MgO heterostructure, the 8.3% mismatch brings a shift of 0.22 eV on VBO (Li et al., 2008). By linear extrapolation method, the strain induced shift in ZnO/BTO is less than 0.02 eV, which is much smaller than the aforementioned deviation of 0.09 eV. The error induced by band bending is checked to be much smaller than the average standard deviation of 0.09 eV given above (Yang et al., 2009). So the experimental obtained VBO value is reliable.

To further confirm the reliability of the experimental values, it would be useful to compare our VBO value with other results deduced by transitive property. For heterojunctions formed between all pairs of three materials (A, B, and C), ΔE_V(A-C) can be deduced from the difference between ΔE_V(A-B) and ΔE_V(C-B) neglecting the interface effects (Foulon et al., 1992). The reported VBO values for some heterojunctions are ΔE_V(ZnO-STO)=0.62 eV (Jia et al., 2009b), ΔE_V(Si-STO)=2.38 or 2.64 eV, and ΔE_V(Si-BTO)=2.35 or 2.66 eV (Amy et al., 2004), respectively. Then the ΔE_V(ZnO-BTO) is deduced to be 0.59, 0.64, 0.9 or 0.33 eV, which is comparable to our measured value 0.48±0.09 eV. Since the samples were prepared under different growth conditions, the different interfaces are responsible for the difference between our measured value and the results from the transitivity. In addition, the resulting ΔE_V is a sufficiently large value for device applications which require strong carrier confinement, such as light emitters or heterostructure field effect transistors (Chen et al., 2005).

Finally, the CBO (ΔE_C) can be estimated by the formula $\Delta E_C=\Delta E_V+E_g^{ZnO}-E_g^{BTO}$. By substituting the band gap values at room temperature (E_g^{ZnO}=3.37 eV (Su et al., 2008) and E_g^{BTO}=3.1 eV (Boggess et al., 1990)), ΔE_C is calculated to be 0.75±0.09 eV. Accordingly, a type-II band alignment forms at the heterojunction interface, in which the conduction and valence bands of the ZnO film are concomitantly higher than those of the BTO substrate, as shown in Fig. 7.

6. VBO for InN/STO heterojunction

Figure 8 (a) shows the typical XRD θ-2θ patterns of InN thin films deposited on (001) STO substrates. InN crystals shows an intense diffraction line at 2θ=31.28° assigned to the (0002) diffraction of InN with hexagonal wurtzite structure, implying that the *c*-axis of InN films is perpendicular to the substrate surface. Figure 8 (b) shows the results of x-ray off-axis

ϕ scans performed using the $\{10\bar{1}1\}$ reflection of InN (2θ=33.49°, χ=61.86°) and the $\{111\}$ reflection of STO (2θ=39.96°, χ=54.74°) to determine the in-plane orientation of the InN film relative to STO. Although InN has a sixfold symmetry about the [0001] axis, the presence of twelve peaks separated by 30° for $\{11\bar{2}2\}$ reflections indicates that the InN films is twinned in the growth plane by a 30° in-plane rotation. The relative intensities of the two sets of peaks is related to the proportion of the two domains, indicating almost the same amount for the two domains. Comparing the locations in ϕ-space of the InN$\{10\bar{1}1\}$ with STO$\{111\}$ families, the two-dimensional epitaxial relationships for the two domains can be derived to be $[1\bar{1}00]$InN$\|$[110]STO for one domain and $[11\bar{2}0]$InN$\|$[110]STO for the other. The atomic arrangements for the two domains are illustrated in the schematic drawings of Fig. 8(c).

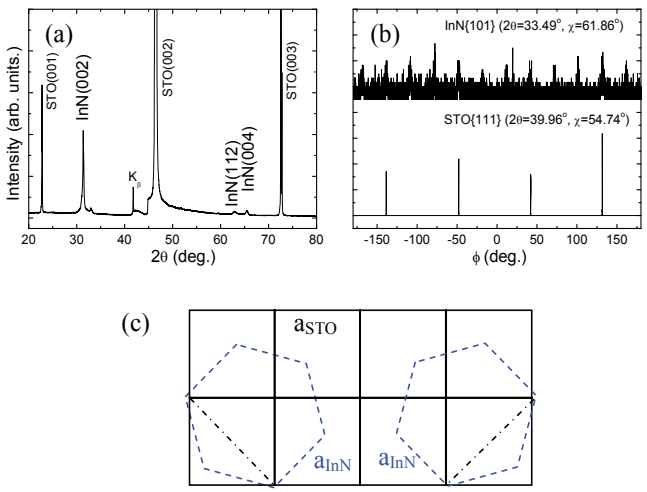

Fig. 8. X-ray θ-2θ (a) and ϕ (b) scanning patterns, and atomic arrangement (c) of the thick InN films on (001)STO substrates.

For InN/STO heterojunction, the VBO (ΔE_V) can be calculated from the formula

$$\Delta E_V = \Delta E_{CL} + (E^{InN}_{In3d} - E^{InN}_{VBM}) - (E^{STO}_{Ti2p} - E^{STO}_{VBM}), \tag{13}$$

where ΔE_{CL}=($E^{InN/STO}_{Ti2p}$-$E^{InN/STO}_{In3d}$) is the energy difference between In 3d and Ti 2p CLs measured in the thin InN/STO heterojunction, while (E^{STO}_{Ti2p}-E^{STO}_{VBM}) and (E^{InN}_{In3d}-E^{InN}_{VBM}) are the VBM energies with reference to the CL positions of bulk STO and thick InN film, respectively. Fig. 9 shows In 3d, Ti 2p CL narrow scans and valence band spectra recorded on thick InN, bulk STO and thin InN/STO heterojunction samples, respectively. The In 3d spectra in thick InN films include two peaks of $3d_{5/2}$ (443.50±0.03 eV) and $3d_{3/2}$ (451.09±0.03 eV), which are separated by the spin-orbit interaction with a splitting energy of around 7.57 eV. Both peaks are found out to consist of two components by careful Voigt fitting. The first In $3d_{5/2}$ component located at 443.50±0.03 eV is attributed to the In-N bonding, and the second, at 444.52±0.03 eV, is identified to be due to surface contamination. This two-peak profile of the In $3d_{5/2}$ spectra in InN is typical and have been demonstrated by other researchers (King et al., 2008; Piper et al., 2005; Yang et al., 2009). Comparison of their binding energy separation with previous results, we suggest that the second peak at 444.52±0.03 eV to the In-O bonding is due to contamination by oxygen during the growth process. The ratio of In-N peak intensity to

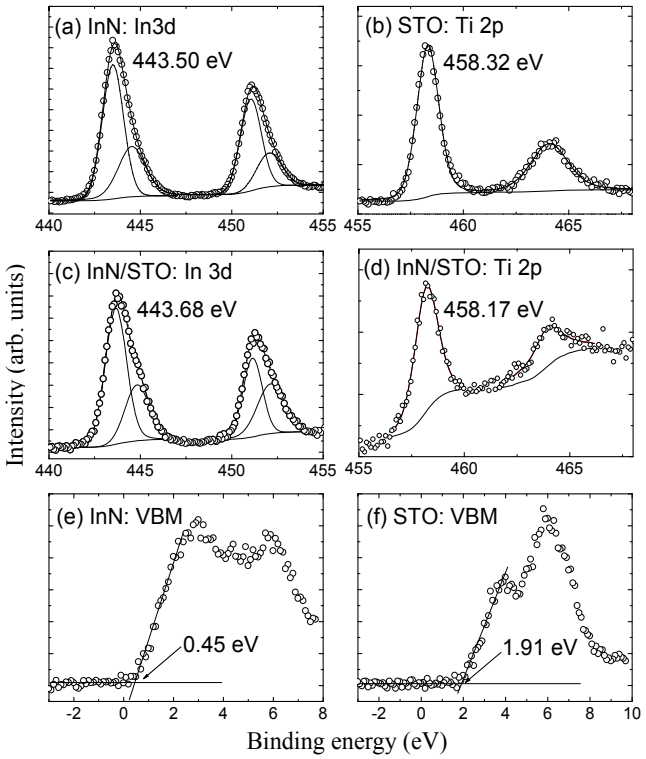

Fig. 9. In 3d spectra recorded on InN (a) and InN/STO (c), Ti 2p spectra on STO (b) and InN/STO (d), and VB spectra for InN (e) and STO (f). All peaks have been fitted to Voigt line shapes using Shirley background, and the VBM values are determined by linear extrapolation of the leading edge to the base line. The errors in the peak positions and VBM are ± 0.03 and ± 0.06 eV, respectively.

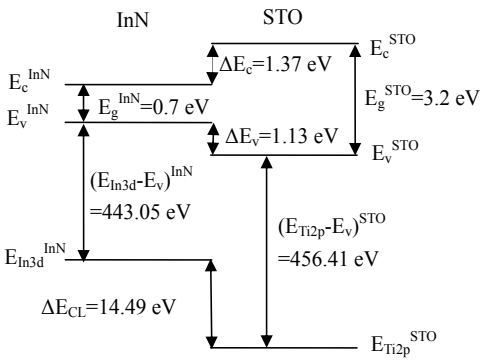

Fig. 10. Energy band diagram of InN/STO heterojunction.

the oxygen related peaks indicates that only a small quantity of oxygen contamination exists in our samples. Both the Ti 2p spectra in bulk STO and thin InN/STO heterojunction are quite symmetric, indicating a uniform bonding state. Using the linear extrapolation method mentioned above, the VBM of InN and STO are 0.45 ± 0.06 eV and 1.91 ± 0.06 eV respectively.

Compared with the spectra recorded on the InN and STO samples, the In 3d core level shifts to 443.68±0.03 eV and Ti 2p shifts to 458.17±0.03 eV in thin InN/STO heterojunction. The VBO value is calculated to be 1.13±0.09 eV by substituting those values into Eq. 13.
Reliability of the analysis of the measured results is provided by considering possible factors that could impact the experimental results. InN is a kind of piezoelectric crystal, so the strain existing in the InN overlayer of the heterojunction will induce piezoelectric field and affect the results. The lattice mismatch between InN and STO is larger than 9.8% ($\frac{\sqrt{3}a_{InN}-\sqrt{2}a_{STO}}{\sqrt{2}a_{STO}} \times 100\%$), so the InN layer can be approximately treated as completely relaxed and this approximation should not introduce much error in our result. In addition, the energy band bends downward at the surface of InN film and there is an electron accumulation layer (Mahboob et al., 2004), so the energy separation between VBM and Fermi level can be changed at the InN surface, which could impact the measured VBO values of the heterojunctions. However, both the CL emissions of In 3d and Ti 2p at the InN/STO heterojunction are collected from the same surface (InN surface), thus, the surface band bending effects can be canceled out for the measurement of ΔE_{CL}, as was the measurement of the band offset of the InN/AlN heterojunction by others (King et al., 2007; Wu et al., 2006). Since the factors that can affect the results can be excluded from the measured results, the experimental obtained VBO value is reliable.
Making use of the band gap of InN (0.7 eV) (Yang et al., 2009) and $SrTiO_3$ (3.2 eV) (Baer et al., 1967), the CBO (ΔE_C) is calculated to be 1.37 eV and the ratio of $\Delta E_C/\Delta E_V$ is close to 1:1. As shown in Fig. 10, a type-I heterojunction is seen to be formed in the straddling configuration. So STO can be utilized as the gate oxide for InN based metal-oxide semiconductor, the gate leakage is expected to be negligible, which is different from the Si based devices (Chambers et al., 2000).

7. VBO for InN/BTO heterojunction

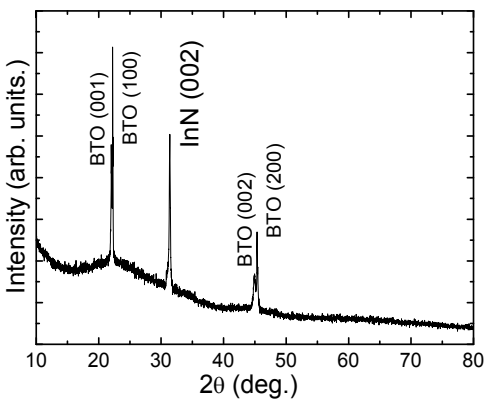

Fig. 11. X-ray θ-2θ scanning patterns of the thick InN films on BTO substrates.

In x-ray θ-2θ diffraction measurements, as shown in Fig. 11, the thick InN/BTO sample presented the only peak of InN (0002) reflection and no other InN related peaks were observed, implying a complete *c*-axis oriented growth of the InN layer. For InN/BTO heterojunction, the VBO (ΔE_V) can be calculated from the formula

$$\Delta E_V = \Delta E_{CL} + (E^{InN}_{In3d} - E^{InN}_{VBM}) - (E^{BTO}_{Ti2p} - E^{BTO}_{VBM}), \quad (14)$$

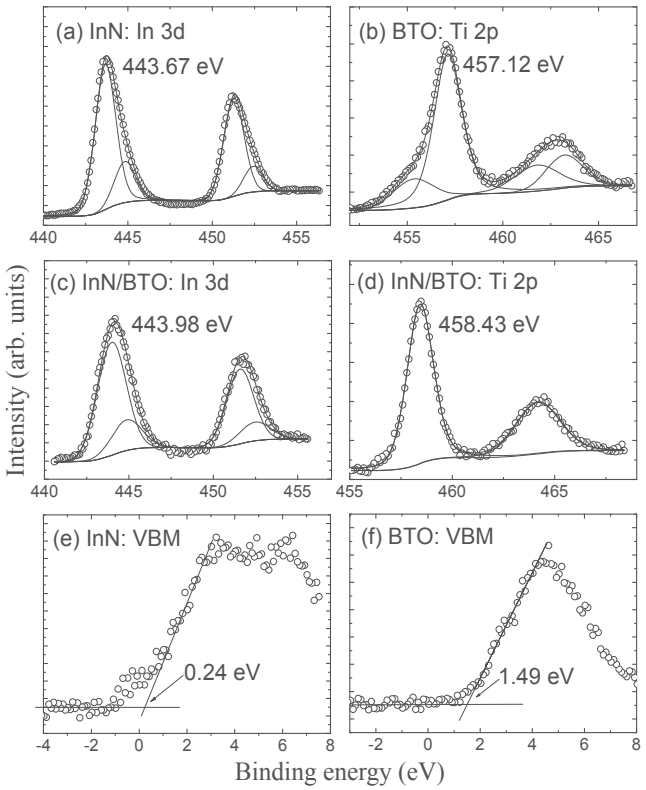

Fig. 12. In 3d spectra recorded on InN (a) and InN/BTO (c), Ti 2p spectra on BTO (b) and InN/BTO (d), and VB spectra for InN (e) and BTO (f). All peaks have been fitted to Voigt line shapes using Shirley background, and the VBM values are determined by linear extrapolation of the leading edge to the base line. The errors in the peak positions and VBM are $\pm$0.03 and $\pm$0.06 eV, respectively.

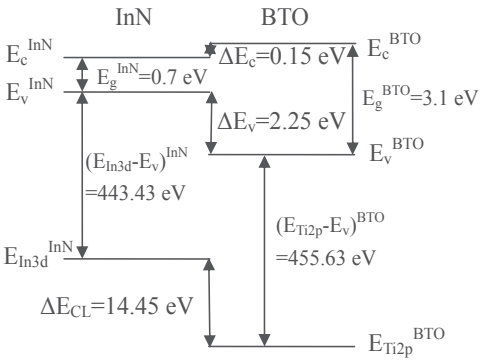

Fig. 13. Energy band diagram of InN/BTO heterojunction.

where $\Delta E_{CL}=(E_{Ti2p}^{InN/BTO}-E_{In3d}^{InN/BTO})$ is the energy difference between In 3d and Ti 2p CLs measured in the thin heterojunction InN/BTO, while $(E_{Ti2p}^{BTO}-E_{VBM}^{BTO})$ and $(E_{In3d}^{InN}-E_{VBM}^{InN})$ are the VBM energies with reference to the CL positions of bulk BTO and thick InN film, respectively.

Figure 12 shows the XPS Ti 2p and In 3d CL narrow scans and the valence band spectra from the bulk BTO, thick InN and thin InN/BTO samples, respectively. For the In 3d spectra of both the InN and thin InN/BTO samples, additional low intensity higher-binding-energy components were required. These extra components are attributed to In-O bonding due to oxide contamination when InN is present at the surface (Piper et al., 2005), as shown in Fig. 12(a). In the thin InN/BTO sample shown in Fig. 12(c), they are attributed to In-O bonding at the InN/BTO interfaces, and/or inelastic losses to free carriers in the InN layer (King et al., 2008). The CL peak attributed to In-N bonding locates at 443.67±0.03 eV and 443.98±0.03 eV for thick InN and thin InN/BTO, respectively, as shown in Fig. 12(a) and (c). It is interesting that the Ti 2p peaks transform from asymmetry in bulk BTO to symmetry in the thin InN/BTO sample, as observed in the thin ZnO/BTO heterostructure (Jia et al., 2010b). Using the same fitting methods mentioned above, the VBM value for the bulk BTO and thick InN films can be determined, as shown in Fig. 12 (e)and (f). Substituting the above values into Eq. 14, the resulting VBO value is calculated to be 2.25±0.09 eV.

The reliability of the measured result is analyzed by considering several possible factors that could impact the experiment results. Both the CL emissions of In 3d and Ti 2p at the InN/BTO heterojunction are collected from the same surface (InN surface), so the surface band bending effects can be canceled out for the measurement of ΔE_{CL}. Another factor which may affect the precision of the VBO value is the strain-induced piezoelectric field in the overlayer of the heterojunction (Martin et al., 1996). There is a large lattice mismatch of about 7.1% ($\frac{\sqrt{3}a_{InN}-\sqrt{2}a_{BTO}}{\sqrt{2}a_{BTO}}\times 100\%$) between the hexagonal apothem of InN and the BTO[$0\bar{1}1$] direction. It is comparable with that of the InN/ZnO heterojunction (7.7%), and the InN thin film of 5 nm is approximately treated as completely relaxed (Zhang et al., 2007). So the strain-induced piezoelectric field effect can be neglected in our experiment. Thus, the experimental obtained VBO value is reliable.

To further confirm the reliability of the experimental values, it would be useful to compare our VBO value with other results deduced by transitive property. The reported VBO values for ZnO/BTO and InN/ZnO heterojunctions are ΔE_V(ZnO-BTO)=0.48 eV (Jia et al., 2010b), and ΔE_V(InN-ZnO)=1.76 eV (Yang et al., 2009), respectively. Then the ΔE_V(InN-BTO) is deduced to be 2.24 eV, which is well consistent with our measured value 2.25±0.09 eV.

Finally, the CBO (ΔE_C) can be estimated by the formula $\Delta E_C = E_g^{BTO} - E_g^{InN} - \Delta E_V$. By substituting the band gap values at room temperature (E_g^{InN}=0.7 eV (Yang et al., 2009) and E_g^{BTO}=3.1 eV (Boggess et al., 1990)), ΔE_C is calculated to be 0.15±0.09 eV. Accordingly, a type-I band alignment forms at the heterojunction interface, as shown in Fig. 13.

8. Conclusions

In summary, XPS was used to measure the VBO of the ZnO(or InN)/STO(or BTO) heterojunctions. A type-II band alignment with VBO of 0.62±0.09 eV and CBO of 0.79±0.09 eV is obtained for ZnO/STO heterojunction. A type-II band alignment with VBO of 0.48±0.09 eV and CBO of 0.75±0.09 eV is obtained for ZnO/BTO heterojunction. A type-I band alignment with VBO of 1.13±0.09 eV and CBO of 1.37±0.09 eV is obtained for InN/STO heterojunction. A type-I band alignment with VBO of 2.25±0.09 eV and CBO of 0.15±0.09 eV is obtained for InN/BTO heterojuncion. The accurately determined result is important for the design and application of these semiconductor/ferroelectric heterostructures based devices.

9. Acknowledgements

This work was supported by the 973 program (2006CB604908, 2006CB921607), and the National Natural Science Foundation of China (60625402, 60990313).

10. References

Alivov Y. I.; Xiao B.; Fan Q.; Morkoc H. & Johnstone D. (2006). *Appl. Phys. Lett.*, Vol. 89, 152115

Amy F.; Wan A. S.; Kahn A.; Walker F. J. & Mckee R. A. (2004). *J. Appl. Phys.*, Vol. 96, 1635

Baer W. S. (1967). *J. Phys. Chem. Solids*, Vol. 28, 677

Boggess T. F.; White J. O. & Valley G. C. (1990). *J. Opt. Soc. Am. B.*, Vol. 7, 2255

Brandt M.; Frenzel H.; Hochmuth H.; Lorentz M.; Grundmann M. & Schubert J. (2009). *J. Vac. Sci. Technol. B*, Vol. 27, 1789

Capasso F. & Margaritondo G. (1987). *Heterojunction band discontinuities: Physics and device applications*, (115-377), Elsevier, 0444870601, North-Holland, Amsterdam Oxford New York Tokyo

Chambers S. A.; Liang Y.; Yu Z.; Droopad R.; Ramdani J & Eisenbeiser (2000). *Appl. Phys. Lett*, Vol. 77, 1662

Chambers S. A.; Liang Y.; Yu Z.; Droopad R. & Ramdani J (2001). *J. Vac. Sci. Technol. A*, Vol. 19, 934

Chen J. J.; Ren F.; Li Y. J.; Norton D. P.; Pearton S. J.; Osinsky A.; Dong J. W.; Chow P. P. & Weaver J. F. (2005). *Appl. Phys. Lett.*, Vol. 87, 192106

Cimalla V.; Lebedev V.; Wang C. Y.; Ali M.; Cke G. E.; Polyakov V. M.; Schwierz F.; Ambacher O.; Lu H. & Schaff W. J. (2007). *Appl. Phys. Lett.*, Vol. 90, 152106

Fan H. B.; Sun, G. S.; Yang S. Y.; Zhang P. F.; Zhang R. Q.; Wei H. Y.; Jiao C. M.; Liu X. L.; ChenY. H.; Zhu Q. S. & Wang Z. G. (2008). *Appl. Phys. Lett.*, Vol. 92, 192107

Foulon Y. & Priester C. (1992). *Phys. Rev. B*, Vol. 45, 6259

Grant R. W.; Waldrop J. R. & Kraut E. A. (1978). *Phys. Rev. Lett.*, Vol. 40, 656

Jia C. H.; Chen Y. H.; Liu G. H.; Liu X. L.; Yang S. Y. & Wang Z. G. (2008). *J. Crystal Growth*, Vol. 311, 200-204

Jia C. H.; Chen Y. H.; Liu G. H.; Liu X. L.; Yang S. Y. & Wang Z. G. (2009). *J. Phys. D: Appl. Phys.*, Vol. 42, 015415

Jia C. H.; Chen Y. H.; Zhou X. L.; Yang A. L; Zheng G. L.; Liu X. L.; Yang S. Y. & Wang Z. G. (2009). *J. Phys. D: Appl. Phys.*, Vol. 42, 095305

Jia C. H.; Chen Y. H.; Zhou X. L.; Liu G. H.; Guo Y.; Liu X. L.; Yang S. Y. & Wang Z. G. (2010). *J. Crystal Growth*, Vol. 312, 373-377

Jia C. H.; Chen Y. H.; Zhou X. L.; Yang A. L.; Zheng G. L.; Liu X. L.; Yang S. Y. & Wang Z. G. (2010). *Appl. Phys. A*, Vol. 99, 511

Jia C. H.; Chen Y. H.; Liu X. L.; Yang S. Y. & Wang Z. G. (2011). *Nano. Res. Lett*, Vol. 6, 316

Kang K. T.; Lim M. H.; Kim H. G.; Kim I. D. & Hong J. M. (2007). *Appl. Phys. Lett.*, Vol. 90, 043502

Kazzi M. E.; Merckling C.; Delhaye G.; Arzel L.; Grenet G.; Bergignat E. & Hollinger G. (2006). *Mater. Sci. Semi. Proc.*, Vol. 9, 954

Kim D.; Choi Y. W. & Tuller H. L., (2005). *Appl. Phys. Lett.*, Vol. 87, 042509

King P. D. C.; Veal T. D.; Jefferson P. H.; Mcconville C. F.; Wang T.; Parbrook P. J.; Lu H. & W.J. Schaff (2007). *Appl. Phys. Lett.*, Vol. 90, 132105

King P. D. C.; Veal T. D.; Lu H.; Hatfield S. A.; Schaff W. J. & Mcconville C.F. (2008). *Surf. Sci.*, Vol. 602, 871

Kryliouk O.; Park H. J.; Won Y. S.; Anderson T.; Davydov A.; Levin I.; Kim J.H. & Freitas Jr. J. A. (2007). *Nanotechnology*, Vol. 18, 135606

Li Y. F.; Yao B.; Lu Y. M.; Li B. H.; Gai Y. Q.; Cong C. X.; Zhang Z. Z.; Zhao D. X.; Zhang J. Y.; Shen D. Z. & Fan X. W. (2008). *Appl. Phys. Lett.*, Vol. 92, 192116

Li Z. W.; Zhang B.; Wang J.; Liu J. M.; Liu X. L.; Yang S. Y.; Zhu Q. S. & Wang Z. G. (2011). *Nano. Res. Lett*, Vol. 6, 193

Lorentz M.; Brandi M.; Schubert J.; Hochmuth H., Wenckstern H. v; Schubert M. & Grundmann M. (2007). *Procc. of SPIE*, Vol. 6474, 64741S

Losurdo M.; Giangregorio M. M.; Bruno G.; Kim T. H.; Wu P.; Choi S.; Brown A.; Masia F.; Capizzi M. & Polimeni A. (2007). *Appl. Phys. Lett.*, Vol. 90, 011910

Losego M. D.; Kourkoutis L. F.; Mita S.; Craft H. S.; Muller D. A.; Collazo R.; Sitar Z. & Maria J. P. (2009). *J. Crystal Growth*, Vol. 311, 1106

Mahboob I.; Veal T. D.; Mcconville C.F.; Lu H. & Schaff W. J. (2004). *Phys. Rev. Lett.*, Vol. 92, 036804

Martin G.; Botchkarev A.; Rockett A. & Morkoc H. (1996). *Appl. Phys. Lett.*, Vol. 68, 2541

Mbenkum B. N.; Ashkenov N.; Schubert M.; Lorentz M.; Hochmuth H.; Michel D.; Grundmann M. & Wagner G. (2005). *Appl. Phys. Lett.*, Vol. 86, 091904

Mönch W. (2004). *Electronic properties of Semiconductor Interfaces*, Springer, Berlin, 176

Mönch W. (2005). *Appl. Phys. Lett.*, Vol. 86, 162101

Murakami H.; Eriguchi K. I.; Torri J. I.; Cho H. C.; Kumagai Y. & Koukitu A. (2008). *J. Crystal Growth*, Vol. 310, 1602

Ozgur U.; Alivov Y. I.; Liu C.; Teke A.; Reshchikov M. A.; Dogan S.; Avrutin V.; Cho S. J. & Morkoc H. (2005). *J. Appl. Phys.*, Vol. 98, 041301

Peruzzi M.; Pedarni J. D.; Bauerle D.; Schwinger W. & Schaffler F. (2004). *Appl. Phys. A.*, Vol. 79, 1873

Piper L. F. J.; Veal T. D.; Walker M.; Mahboob I.; Mcconville C.F., Lu H. & Schaff W. J. (2005). *J. Vac. Sci. Technol. A*, Vol. 23, 617

Siddiqui J.; Cagin E.; D. Chen & Phillips J. D. (2006). *Appl. Phys. Lett.*, Vol. 88, 212903

Singh M.; Wu Y. R. & J. Singh (2003). *Solid State Electron.*, Vol. 47, 2155

Song D. Y.; Holtz M. E.; Chandolu A.; Bernussi A.; Nikishin S. A.; Holtz M. W. & Gherasoiu I. (2008). *Appl. Phys. Lett.*, Vol. 92, 121913

Su S. C.; Lu Y. M.; Zhang Z. Z.; Shan C. X.; Li B. H.; Shen D. Z.; Yao B.; Zhang J. Y.; Zhao D. X. & Fan X. W. (2008). *Appl. Phys. Lett.*, Vol. 93, 082108

Sun H. P.; Tian W.; Pan X. Q.; Haeni J. H. & Schlom D. G. (2004). *Appl. Phys. Lett.*, Vol. 84, 3298

Takahashi N.; Niwa A. & Nakamura T. (2004). *J. Phys. Chem. Solid.*, Vol. 65, 1259

Voora V. M.; Hofmann T.; Schubert M., Brandt M., Lorenz M., Grundmann M., Ashkenov N. & Schubert M. (2009). *Appl. Phys. Lett.*, Vol. 94, 142904

Voora V. M; Hofmann T.; Brandt M.; Lorenz M.; Grundmann M; Ashkenov N.; Schmidt H; Ianno N. & Schubert M. (2010). *Phys. Rev. B*, Vol. 81, No. 19, 195307

Wei X. H.; Li Y. R.; Jie W. J.; Tang J. L.; Zeng H. Z.; Huang W.; Zhang Y. & Zhu J. (2007). *J. Phys. D: Appl. Phys.*, Vol. 40, 7502

Wu C.L.; Shen C. H. & Gwo S. (2006). *Appl. Phys. Lett.*, Vol. 88, 032105

Wu Y. L.; Zhang L. W.; Xie G. L.; Zhu J. L. & Chen Y. H. (2008). *Appl. Phys. Lett.*, Vol. 92, 012115

Yang A. L.; Song H. P.; Liu X. L.; Wei H. Y.; Guo Y.; Zheng G. L.; Jiao C. M.; Yang S. Y.; Zhu Q. S. & Wang Z. G. (2009). *Appl. Phys. Lett.*, Vol. 94, 052101

Yasuda H. & Kanemitsu Y. (2008). *Phys. Rev. B.*, Vol. 77, 193202
You J. B.; Zhang X. W.; Song H. P.; Ying J.; Guo Y.; Yang A. L.; Yin Z. G.; Chen N. F. & Zhu Q. S. (2009). *J. Appl. Phys.*, Vol. 106, 043709
Zhang R. Q.; Zhang P. F.; Kang T. T.; Fan H. B.; Liu X. L.; Yang S. Y.; Wei H. Y.; Zhu Q. S. & Wang Z. G. (2007). *Appl. Phys. Lett.*, Vol. 91, 162104

Part 4

Modeling: Phenomenological Analysis

17

Self-Consistent Anharmonic Theory and Its Application to $BaTiO_3$ Crystal

Yutaka Aikawa
Taiyo Yuden Co, Ltd.
Japan

1. Introduction

Because phase transition is important in solid state physics, numerous attempts have thus far been made to study the nature of phase transitions in magnets, superconductors, ferroelectrics, and so on. For ferroelectrics, both phenomenological and microscopic approaches have been adopted to study phase transitions. Generally, it is considered that at high temperatures, the general phenomenological theory and first-principles calculations appears to be almost mutually exclusive.

It is well known that the phenomenological Landau theory of phase transitions can provide a qualitatively correct interpretation of the soft mode of ferroelectrics at the Curie temperature (L.D.Landau & E.M.Lifshitz, 1958); however, this theory cannot explain the mechanism of ferroelectric phase transition. Furthermore, the coefficients of the expansion terms of the Gibbs potential cannot be explained by the essential parameters derived by first-principles calculations. The first principles calculations were performed to determine the adiabatic potential surface of atoms, and the potential parameters were determined to recreate the original adiabatic potential surface. This procedure ensures a highly systematic study of ferroelectric properties without any reference to the experimental values.

In order to study the phase transition, Gillis et al. discussed first the instability phenomena in crystals, on the basis of a self-consistent Einstein model (N. S. Gills et al., 1968, 1971). In this model each atom is assumed to perform harmonic oscillation with the frequency which is self-consistently determined from the knowledge of interatomic potential in crystal and the averaged motions of all atoms. The effect of anharmonicity comes in through the self-consistent equations. T. Matsubara et al. applied this method to a simple one-dimensional model to discuss anharmonic lattice vibration, which is enhanced on and near the surface than in the interior (T. Matsubara & K. Kamiya,1977).

On the other hand, the combination of the results derived from first-principles calculations with the effective Hamiltonian method implemented by means of a Monte Carlo simulation (W. Zhong et al.,1995), seems to successfully explain the lattice strain change in $BaTiO_3$ at high temperatures. However, the abovementioned approach cannot explain the behavior of the dielectric property of materials at high temperatures during the phase transitions in the soft mode.

To discuss such high temperature transitions, K. Fujii et al. have proposed a self-consistent anharmonic model (K. Fujii et al., 2001), and the author has extended it to derive the ferroelectric properties of $BaTiO_3$ (Y.AIkawa et al., 2007, 2009), in other words, it has been shown that the ferroelectric properties of materials can be described by the interatomic potential, which is derived from first-principles calculations. In the present study we applied a theoretical method, namely, the self-consistent anharmonic theory, to study the cubic-to-tetragonal phase transition in practical applications. The author shows that the transition occurs in the soft mode, and that the relationship between the transition behavior in the high temperature region and the essential parameters at absolute zero temperature which can be derived using first-principles calculations.

In the previous study, the author introduces the anharmonicity not only into crystal potential but also into trial one in order to extend the self-consistent Einstein model, and succeeded to derive the soft mode frequency of $BaTiO_3$ crystal near the transition temperature, and showed that the softening phenomena never take place when harmonic oscillator is adopted as trial potential (Y. Aikawa & K. Fujii, 2010). Furthermore, it becomes possible to explain the relation between the dielectric property in high temperature and atomic potential at absolute zero temperature derived from first principles calculations (Y.Aikawa et al., 2009), and also to explain the isotope effect (Y.Aikawa et al., 2010a), surface effect (Y.Aikawa et al., 2010b; T. Hoshina et al., 2008), and so on.

2. Theoretical analysis

Landau constructed a phenomenological theory for the second order phase transition by considering only the symmetry change of a system (L. D. Landau & E. M. Lifshitz, 1958). Gibbs free energy is expanded by an order parameter σ in the vicinity of transition temperature as

$$G = G_0 + B(T_C - T)\sigma^2 + A\sigma^4 + \cdots$$

It is difficult to reflect microscopic information such as interactions between atoms in the expansion coefficients A, B and the transition temperature T_C.

K. Fujii et.al showed theoretically a softening mechanism from the variational principle at finite temperature (K. Fujii et al., 2001, 2003). In that work, the coefficients of the second and fourth order terms in a trial potential represented by an anharmonic oscillator system were expressed by the characteristic constants of interatomic potentials in a crystal. The author found that the temperature dependence of the coefficient of the second order term in the trial potential shows the same behavior as the Landau expansion. The softening phenomena are discussed on the basis of the temperature- and wave vector-dependence of the expansion coefficient near the instability temperature, and the soft mode is identified by introducing normal coordinates instead of direct atomic displacements.

It is considered a crystal system consisting of N atoms. Let $\boldsymbol{x}_n$ be coordinate of the n-th atom whose mass is m_n. The Hamiltonian of this system is given by

$$H = \frac{1}{2}\sum_n m_n \dot{\boldsymbol{x}}_n^2 + \sum_{nn'} V\left(\left|\boldsymbol{x}_n - \boldsymbol{x}_{n'}\right|\right) \quad , \tag{1}$$

where V are interatomic pair potentials. An interatomic distance between atoms n and n' is given by

$$\boldsymbol{X}_n - \boldsymbol{X}_{n'} = \boldsymbol{a}_{nn'} + \boldsymbol{u}_n - \boldsymbol{u}_{n'} \quad , \tag{2}$$

where $\boldsymbol{a}_{nn'}$ means the interatomic distance in equilibrium state and $\boldsymbol{u}_n$ denotes an atomic displacement from the equilibrium position. The displacement $u_{n,\alpha}$ in the α direction is expanded by using the eigenfunctions $e_{n,\alpha}^{(S)}$ of a dynamical matrix as

$$u_{n,\alpha} = \sum_S m_n^{-1/2} e_{n,\alpha}^{(S)} Q_S \qquad (S = 1, 2, \cdots, 3N) \quad , \tag{3}$$

where Q_S are the normal coordinates. The interatomic distance is represented by

$$\left|\boldsymbol{X}_n - \boldsymbol{X}_{n'}\right| = \left|\boldsymbol{a}_{nn'}\right| + \sum_S c_S^{(nn')} Q_S \quad , \tag{4}$$

where $c_S^{(nn')}$ are defined by using the the direction cosine, $\ell_{nn',\alpha}$, of the interatomic distance vector as (α =x,y,z)

$$c_S^{(nn')} = \sum_\alpha \ell_{nn',\alpha} \left(m_n^{-1/2} e_S^{(n\alpha)} - m_{n'}^{-1/2} e_S^{(n'\alpha)} \right) \quad . \tag{5}$$

Then, Hamiltonian is rewritten in terms of the normal coordinates Q_S as (Y. Aikawa & K. Fujii, 1993)

$$H = \frac{1}{2} \sum_S \dot{Q}_S^2 + \sum_{n,n'} V\left(\left|\boldsymbol{a}_{nn'}\right| + \sum_S c_S^{(nn')} Q_S \right) \quad , \tag{6}$$

The variational principle at finite temperature is applied to obtain thermal properties of the crystal. In this method, an anharmonic oscillator with the fourth order term is adopted as a trial Hamiltonian H_{tr}, (Y. Aikawa & K. Fujii, 2009)

$$H_{tr} = \frac{1}{2} \sum_S \dot{Q}_S^2 + \sum_S A_S Q_S^4 + \sum_S B_S Q_S^2 \quad . \tag{7}$$

The thermal average of a physical quantity $X\left(\dot{Q}_S, Q_S\right)$ is given by

$$\begin{aligned} \left\langle X\left(\dot{Q}_S, Q_S\right) \right\rangle &= \mathrm{Tr}\left[\rho X\left(\dot{Q}_S, Q_S\right) \right] \\ &= \frac{\int_{-\infty}^{\infty} X\left(\dot{Q}_S, Q_S\right) \exp\left(-H_{tr}/\mathrm{k_B}T\right) \prod_S \mathrm{d}\dot{Q}_S \mathrm{d}Q_S}{\int_{-\infty}^{\infty} \exp\left(-H_{tr}/\mathrm{k_B}T\right) \prod_S \mathrm{d}\dot{Q}_S \mathrm{d}Q_S} \end{aligned} \tag{8}$$

The free energy of the crystal is given by

$$\begin{aligned} F &= \left\langle H \right\rangle - \left\langle H_{tr} \right\rangle + F_{tr} \\ &= \left\langle \sum_{n,n'} V\left(\left|\boldsymbol{a}_{nn'}\right| + \sum_S c_S^{(nn')} Q_S \right) \right\rangle - \sum_S A_S \left\langle Q_S^4 \right\rangle - \sum_S B_S \left\langle Q_S^2 \right\rangle + F_{tr} \quad . \end{aligned} \tag{9}$$

The free energy F_{tr} of the trial system is also calculated by using the relation $F_{tr} = -\mathrm{k_B}T \ln Z_{tr}$. The partition function Z_{tr} is represented by using the variables $y_S^4 \equiv A_S Q_S^4 / \mathrm{k_B}T$ and $p_S \equiv \sqrt{1/4 A_S \, \mathrm{k_B}T} \; B_S$ as:

$$
\begin{aligned}
Z_{tr} &= \frac{1}{\mathrm{h}^{6N}} \int_{-\infty}^{\infty} \exp\left(-H_{tr}/\mathrm{k_B}T\right) \prod_S \mathrm{d}\dot{Q}_S \mathrm{d}Q_S \\
&= \frac{1}{\mathrm{h}^{6N}} \left(\sqrt{2\pi \mathrm{k_B}T}\right)^{3N} \prod_S \sqrt{\frac{\mathrm{k_B}T}{A_S}} \int_{-\infty}^{\infty} \exp\left(-y_S^2 - 2p_S y_S^2\right) \mathrm{d}y_S \\
&\equiv \frac{1}{\mathrm{h}^{6N}} \left(\sqrt{2\pi \mathrm{k_B}T}\right)^{3N} \prod_S \sqrt{\frac{\mathrm{k_B}T}{A_S}} z(p_S) \quad ,
\end{aligned}
\tag{10}
$$

where $z(p_S)$ satisfies a differential equation (Y. Onodera,1970):

$$
\frac{\mathrm{d}^2 z(p_S)}{\mathrm{d}p_S^2} - 2p_S \frac{\mathrm{d}z(p_S)}{\mathrm{d}p_S} - z(p_S) = 0 \quad . \tag{11}
$$

The solution $z(p_S)$ is expressed later by the confluent hyper geometric function. The thermal averages of y_S^2 and y_S^4 are easily obtained as

$$
\begin{aligned}
\left\langle y_S^2 \right\rangle &= -\frac{1}{2} \frac{\mathrm{d}}{\mathrm{d}p} \ln z(p_S) \\
\left\langle y_S^4 \right\rangle &= -p \left\langle y_S^2 \right\rangle + \frac{1}{4} \quad .
\end{aligned}
\tag{12}
$$

Thus,

$$
\left\langle Q_S^4 \right\rangle = -\frac{B_S}{2A_S} \left\langle Q_S^2 \right\rangle + \frac{1}{4\beta A_S} \quad . \tag{13}
$$

The free energy given by eq. (9) is rewritten as

$$
\begin{aligned}
F = &\sum_{nn'} \sum_S \int \mathrm{d}q V_q \exp\left[\mathrm{i}q \left| \boldsymbol{a}_{nn'} \right| + \sum_{\ell=1}^{\infty} \frac{(\mathrm{i}q)^\ell}{\ell!} \left(\sum_S 1 \right)^{\ell/2-1} c_S^{(nn')\ell} \left\langle Q_S^\ell \right\rangle_C \right] \\
&- \frac{1}{2} \sum_S B_S \left\langle Q_S^2 \right\rangle - \mathrm{k_B}T \sum_S \ln \frac{\mathrm{e}^{1/4} \left(\mathrm{k_B}T\right)^{3/4} z(P_S)}{(2\pi)^{3/2} \hbar^2 A_S^{1/4}} \quad .
\end{aligned}
\tag{14}
$$

where the potential is decomposed into the Fourier component. The notation $\left\langle \cdots \right\rangle_C$ denotes the cumulant as defined by

$$
\sum_{\ell=0}^{\infty} \frac{\phi^\ell}{\ell!} \left\langle x^\ell \right\rangle = \exp\left(\sum_{\ell=1}^{\infty} \frac{\phi^\ell}{\ell!} \left\langle x^\ell \right\rangle_{\mathrm{C}} \right) \quad , \tag{15}
$$

It is evident from the formula of the trial Hamiltonian that

$$
\left\langle Q_S^n \right\rangle_0 = \begin{cases} 0 & n : odd \\ \left\langle Q_S^n \right\rangle_0 & n : even \end{cases} \quad ,
$$

thus the cumulant expansions are as follows:

$$\begin{aligned}\left\langle Q_S^2\right\rangle_C &= \left\langle Q_S^2\right\rangle \\ \left\langle Q_S^4\right\rangle_C &= \left\langle Q_S^4\right\rangle_0 - 3\left\langle Q_S^2\right\rangle^2 \\ &= -\frac{B_S}{2A_S}\left\langle Q_S^2\right\rangle + \frac{\mathrm{k_B}T}{4A_S} - 3\left\langle Q_S^2\right\rangle^2 \\ &\cdots\end{aligned} \tag{16}$$

From the variation of the free energy with the interatomic distance $\left|\boldsymbol{a}_{nn'}\right|$, we have the equation

$$\frac{\partial\langle V\rangle}{\partial\left|\boldsymbol{a}_{nn'}\right|} = 0 \quad . \tag{17}$$

From the optimum condition $\partial F/\partial A_S = 0$ gives the relation

$$\begin{aligned}&\sum_{nn'}\int \mathrm{d}q V_q \exp\left[\mathrm{i}q\left|\boldsymbol{a}_{nn'}\right| + \sum_{\ell=1}^{\infty}\frac{(\mathrm{i}q)^\ell}{\ell!}\left(\sum_S 1\right)^{\ell/2-1} c_S^{(nn')\ell}\left\langle Q_S^\ell\right\rangle_{\mathrm{C}}\right]\sum_{\ell=1}^{\infty}\frac{(\mathrm{i}q)^\ell}{\ell!}\left(\sum_{\mathrm{S}} 1\right)^{\ell/2-1} c_S^{(nn')\ell}\frac{\partial\left\langle Q_S^\ell\right\rangle_{\mathrm{C}}}{\partial A_S} \\ &-\frac{1}{2}B_S\frac{\partial\left\langle Q_S^\ell\right\rangle_0}{\partial A_S} - \frac{B_S}{2A_S}\left\langle Q_S^\ell\right\rangle_0 + \frac{\mathrm{k_B}T}{4A_S} = 0 \quad .\end{aligned} \tag{18}$$

The optimum condition $\partial F/\partial B_S = 0$ gives the relation

$$\begin{aligned}&\sum_{nn'}\int \mathrm{d}q V_q \exp\left[\mathrm{i}q\left|\boldsymbol{a}_{nn'}\right| + \sum_{\ell=1}^{\infty}\frac{(\mathrm{i}q)^\ell}{\ell!}\left(\sum_S 1\right)^{\ell/2-1} c_S^{(nn')\ell}\left\langle Q_S^\ell\right\rangle_{\mathrm{C}}\right]\sum_{\ell=1}^{\infty}\frac{(\mathrm{i}q)^\ell}{\ell!}\left(\sum_S 1\right)^{\ell/2-1} c_S^{(nn')\ell}\frac{\partial\left\langle Q_S^\ell\right\rangle_{\mathrm{C}}}{\partial B_S} \\ &-\frac{1}{2}B_S\frac{\partial\left\langle Q_S^\ell\right\rangle_0}{\partial B_S} + \frac{1}{2}\left\langle Q_S^\ell\right\rangle_0 = 0 \quad .\end{aligned} \tag{19}$$

From eq. (18) and eq. (19), an equation to be satisfied in the thermal equilibrium state is obtained as

$$\left[\frac{B_S}{A_S} - \frac{1}{2A_S}\sum_{nn'} c_S^{(nn')2}\frac{\partial^2\langle V_S\rangle}{\partial\left|\boldsymbol{a}_{nn'}\right|^2} + 6\left\langle Q_S^2\right\rangle_0\right]\left[\left\langle Q_S^2\right\rangle_0\frac{\partial\left\langle Q_S^2\right\rangle_0}{\partial A_S} + \frac{1}{A_S}\left(B_S\left\langle Q_S^2\right\rangle_0 - \frac{1}{2}\mathrm{k_B}T\right)\frac{\partial\left\langle Q_S^2\right\rangle_0}{\partial B_S}\right] = 0 \,. \tag{20}$$

It is obtained the solution for the anharmonic system as follows:

$$\frac{B_S}{A_S} - \frac{1}{2A_S}\sum_{nn'} c_S^{(nn')2}\frac{\partial^2\langle V_S\rangle}{\partial\left|\boldsymbol{a}_{nn'}\right|^2} + 6\left\langle Q_S^2\right\rangle_0 = 0 \quad . \tag{21}$$

Substituting eq. (21) into eq. (19), an important equation to determine the equilibrium condition for the free energy is obtained as

$$1 - \frac{1}{24A_S}\sum_{nn'} c_S^{(nn')4}\sum_S 1\,\frac{\partial^4\langle V_S\rangle}{\partial\left|\boldsymbol{a}_{nn'}\right|^4} = 0 \,. \tag{22}$$

In high temperature region ($p \ll 1$), the solution for eq. (11) is given by

$$\begin{aligned} z(p) &= \tfrac{1}{2}\Gamma\left(\tfrac{1}{4}\right) \mathrm{F}\left(\tfrac{1}{4}, \tfrac{1}{2}; p^2\right) - \Gamma\left(\tfrac{3}{4}\right) p \mathrm{F}\left(\tfrac{3}{4}, \tfrac{3}{2}; p^2\right) \\ &= \tfrac{1}{2}\Gamma\left(\tfrac{1}{4}\right)\left[1 - 2\delta p + \tfrac{1}{2} p^2 - \delta p^3 + \tfrac{5}{24} p^4 - \tfrac{7}{20} p^5 + \cdots\right] \quad , \end{aligned} \tag{23}$$

where $\delta \equiv \Gamma\left(\tfrac{3}{4}\right) / \Gamma\left(\tfrac{1}{4}\right) \cong 0.338$ and F is the confluent hyper geometric function defined as

$$\mathrm{F}(\alpha, \gamma; z) = 1 + \frac{\alpha}{\gamma} \frac{z}{1!} + \frac{\alpha(\alpha+1)}{\gamma(\gamma+1)} \frac{z^2}{2!} + \cdots \quad , \tag{24}$$

As a result, the average of $Q_S{}^2$ is determined as

$$\left\langle Q_S^2 \right\rangle = \sqrt{\frac{\mathrm{k_B} T}{A_S}} \left[\delta - \tfrac{1}{2}\left(1 - 4\delta^2\right) p_S + 4\delta^3 p_S^2 + \cdots \right] \tag{25}$$

In high temperature approximation, the equation for A_S to satisfy eqs. (21) and (25) is obtained as

$$A_S \cong \frac{\mathrm{k_B} T}{4 f^2} \left(\delta^2 + \frac{2\mathrm{C} f}{\nu_S} \right) \quad , \tag{26}$$

where $\mathrm{C} = \delta^2 - 1/2$ and

$$\nu_S \equiv \frac{\mathrm{k_B} T}{2 B_S} \quad , \tag{27}$$

$$f \equiv \frac{\sum_{nn'} c_S^{(nn')2} \dfrac{\partial^2 \langle V_S \rangle}{\partial \left| \boldsymbol{a}_{nn'} \right|^2}}{\sum_{nn'} c_S^{(nn')4} \dfrac{\partial^4 \langle V_S \rangle}{\partial \left| \boldsymbol{a}_{nn'} \right|^4} \sum_S 1} \quad . \tag{28}$$

To substitute eq. (26) into eq.(22), the equation for determining the instability phenomena in the crystal is obtained as

$$\frac{\mathrm{k_B} T}{f^{(2)}} = \frac{f}{6\left(\delta^2 + \dfrac{2\mathrm{C} f}{\nu_S} \right)} \quad , \tag{29}$$

where

$$f^{(2)} \equiv \sum_{nn'} c_S^{(nn')2} \frac{\partial^2 \langle V_S \rangle}{\partial \left| \boldsymbol{a}_{nn'} \right|^2} \quad . \tag{30}$$

3. Soft mode

The aim of this section is as follows: the author derives equations to determine the soft mode which minimizes the ***k***-dependent part of the second order term in the trial potential,

and apply the result to the transition from cubic to tetragonal phase in a ferroelectric crystal $BaTiO_3$. The force constants between atoms are estimated by comparing the theoretical result for dispersion relations derived from a dynamical matrix with that of a neutron diffraction experiment (G. Shirane et.al., 1967; B. Jannet et al., 1984). The author applies the result to determination equations, and verify that the lowest frequency mode at Γ point corresponds to a mode causing the ferroelectric phase transition of $BaTiO_3$.

3.1 Determination equations for the soft mode

It is considered that the crystal instability takes place when the coefficient of the second order term in the trial potential becomes infinitesimal as temperature approaches to the transition point. Namely, the parameter ν_S increases to an unlimited extent. This type of phase transition accompanied by the symmetry change is suggested as the softening in the crystals (W. Cochran, 1959). The instability temperature T_C is defined by the temperature where $\nu_S \to \infty$ in eq.(29) as

$$\frac{k_B T_C}{f_\infty^{(2)}} = \frac{f_\infty}{6\delta^2} \quad . \tag{31}$$

where f_∞ and $f_\infty^{(2)}$ mean the values of f and $f^{(2)}$ under $\nu_S \to \infty$. In the vicinity of the instability temperature, the parameter ν_S can be represented from eqs.(29) and (31) as:

$$\frac{1}{\nu_S} \cong \frac{3\delta^4}{C f_\infty^2 f_\infty^{(2)}} k_B (T_C - T) \quad , \tag{32}$$

where the instability temperature is obtained as

$$T_C = \frac{k_B}{6\delta^2} \frac{\left(\sum_{nn'} c_S^{(nn')2} \left. \frac{\partial^2 \langle V_S \rangle}{\partial |\boldsymbol{a}_{nn'}|^2} \right|_{\nu_S \to \infty} \right)^2}{\sum_{nn'} c_S^{(nn')4} \sum_S 1 \left. \frac{\partial^4 \langle V_S \rangle}{\partial |\boldsymbol{a}_{nn'}|^4} \right|_{\nu_S \to \infty}} \quad . \tag{33}$$

Consequently, the variational parameter of the second order term is given as

$$B_S = \frac{\delta^2}{4C} \frac{\sum_{nn'} c_S^{(nn')4} \sum_S 1 \left. \frac{\partial^4 \langle V_S \rangle}{\partial |\boldsymbol{a}_{nn'}|^4} \right|_{\nu_S \to \infty}}{\sum_{nn'} c_S^{(nn')2} \left. \frac{\partial^2 \langle V_S \rangle}{\partial |\boldsymbol{a}_{nn'}|^2} \right|_{\nu_S \to \infty}} k_B (T_C - T) \quad , \tag{34}$$

and the variational parameter of the forth order term is also calculated as:

$$A_S = \frac{1}{24} \sum_{nn'} c_S^{(nn')4} \sum_S 1 \left. \frac{\partial^4 \langle V_S \rangle}{\partial |\boldsymbol{a}_{nn'}|^4} \right|_{\nu_S \to \infty} \quad . \tag{35}$$

Near the instability temperature, the optimum value of the trial potential is represented as

$$\left\langle V_{R,\boldsymbol{k}} \right\rangle = B_R(\boldsymbol{k})(T_{\mathrm{C}} - T)\left\langle Q_{R,\boldsymbol{k}}^2 \right\rangle + A_{R,\boldsymbol{k}} \left\langle Q_{R,\boldsymbol{k}}^4 \right\rangle \quad , \tag{36}$$

where the degree of freedom of the system, $S = 3N$, is replaced by the branch and the wave vector $(R, \boldsymbol{k})$. In order that the softening may actually occur, it is necessary that $B_R(\boldsymbol{k})$ becomes minimum at the definite $\boldsymbol{k}$ vector which is written as

$$B_R(\boldsymbol{k}) = \frac{\delta^2 \mathrm{k_B}}{4\mathrm{C}} \frac{\sum_{nn'} c_{R,\boldsymbol{k}}^{(nn')4} \sum_{R,\boldsymbol{k}} 1 \dfrac{\partial^4 \langle V \rangle}{\partial \left| \boldsymbol{a}_{nn'} \right|^4} \Bigg|_{v_{\boldsymbol{k}} \to \infty}}{\sum_{nn'} c_{R,\boldsymbol{k}}^{(nn')2} \dfrac{\partial^2 \langle V \rangle}{\partial \left| \boldsymbol{a}_{nn'} \right|^2} \Bigg|_{v_{\boldsymbol{k}} \to \infty}} \propto \gamma_R(\boldsymbol{k}) \quad , \tag{37}$$

where $\gamma_R(\boldsymbol{k})$ is the $\boldsymbol{k}$-dependent part in $B_R(\boldsymbol{k})$ as

$$\gamma_R(\boldsymbol{k}) \equiv \frac{\sum_{nn'} c_{R,\boldsymbol{k}}^{(nn')4} \sum_{R,\boldsymbol{k}} 1}{\sum_{nn'} c_{R,\boldsymbol{k}}^{(nn')2}} \quad , \tag{38}$$

$$c_{R,\boldsymbol{k}}^{(nn')} = \sum_{\alpha} \ell_{nn',\alpha} \left(m_n^{-1/2} e_{R,\boldsymbol{k}}^{(n,\alpha)} - m_{n'}^{-1/2} e_{R,\boldsymbol{k}}^{(n'\alpha)} \right) \quad . \tag{39}$$

Here, the eigenfunctions $e_{R,\boldsymbol{k}}^{(n,\alpha)}$ of the dynamical matrix given approximately in Appendix can be easily derived. Consequently, determination equations for the soft mode identified by $(R, \boldsymbol{k})$ are given by

$$\mathrm{grad}\, \gamma_R(\boldsymbol{k}) = 0, \qquad \nabla^2 \gamma_R(\boldsymbol{k}) > 0 \quad . \tag{40}$$

First, whether or not the crystal instability takes place is decided by the temperature dependence of the second order term in the trial potential as shown in eq. (36). Next, the soft mode is identified by the determination equations formalized by eq.(40). To apply the equations, the eigenfunctions included in eq. (39) are necessary which are obtained through the eigenvalue problem of the dynamical matrix. Landau theory presents that only one irreducible representation takes part in the phase transition accompanied by the symmetry change. When more than two modes belong to the same irreducible representation, it is unknown which mode corresponds to the soft mode with the lowest frequency. In this section, the author shows that one can solve this difficulty by using eq.(40) as the determination equations for the soft mode.

3.2 Application to the ferroelectric crystal $BaTiO_3$

The author constructs a formalism to specify the atomic displacement pattern in softening of the $BaTiO_3$ crystal. The Bravais lattice of this crystal above the transition temperature is a cubic lattice whose unit cell and Brillouin zone are shown in Fig.1.

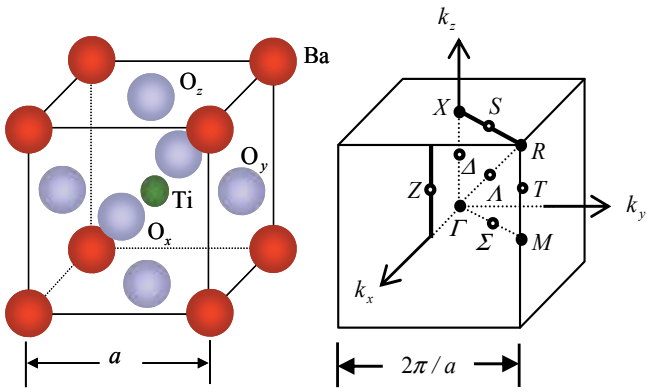

Fig. 1. Cubic structure and Brillouin zone of $BaTiO_3$ at high temperature. (a)The atoms in a unit cell are arranged at the original (n_x, n_y, n_z) for Ti, the corner (n_x+1/2, n_y+1/2, n_z+1/2) for Ba and the face center (n_x+1/2, n_y, n_z) for O, respectively. The atomic masses are defined as M_B, M_T and M_O for Ba, Ti and O, respectively. (b) The optical modes discussed in this work are restricted within the neighborhood of Γ point along the k_Z axis limits.

When the temperature decreases just below the transition temperature, a freezing of the mode that Ti and O ions vibrate reversely along the <001> direction of the crystal causes the structural phase transition from cubic to tetragonal symmetry under softening.

The atomic displacement patterns for vibrational modes at Γ point belonging to the irreducible representation of space group O_h^1 are derived by using the method of projection operator as (G. Burns, 1977)

$$4T_{1u} + T_{2u} \quad , \tag{41}$$

These modes are three-fold degenerate in accordance with the three-dimensional irreducible representation T. There are five branches which consist of one acoustical branch and four optical branches, named A, O_1, O_2, O_3 and O_4. The Slater(S), Last (L), Bending (B) modes and so on can be constructed by a combination of atomic displacements which form the basis functions of T_{1u}. However, one is not able to decide from the group theory which mode appears actually.

The dispersion relations $\omega^2_{R,\boldsymbol{k}}$ depend upon the force constants, shown in Fig. 2 , which are derived from the second-order derivative of the interatomic potential with respect to the interatomic distance, and defined as

$$\alpha = \kappa_{\mathrm{Ti-O}}, \quad \beta = \kappa_{\mathrm{Ba-O}}, \quad \eta = \kappa_{\mathrm{O-O}}, \quad \gamma = \kappa_{\mathrm{Ba-Ti}} \quad , \tag{42}$$

where

$$\kappa_{nn'} = \left. \frac{\partial^2 \left\langle V\left(\left|\boldsymbol{a}_{nn'}\right| + \sum_S c_S^{(nn')} Q_S \right) \right\rangle}{\partial \left(\left|\boldsymbol{a}_{nn'}\right| + \sum_S c_S^{(nn')} Q_S \right)^2} \right|_{\left|\boldsymbol{a}_{nn'}\right|} .$$

It is, however, difficult to estimate the force constants because the various interactions between atoms exist. The author attempt to decide them so as not to contradict the results by the neutron diffraction experiment (G.Shirane et al., 1967; B. Jannet et al.,1984).

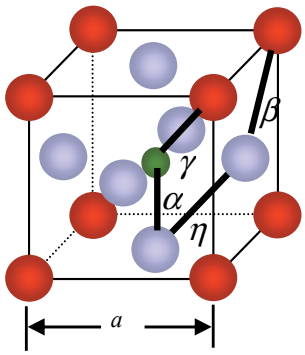

Fig. 2. Definition of the force constants between atoms: α, β, γ and η for Ti-O, Ba-O, Ti-Ba and O-O, respectively.

All the six optical modes which are capable of appearing under the various force constants are obtained by solving the dynamical matrix. In the low frequency region of the dispersion

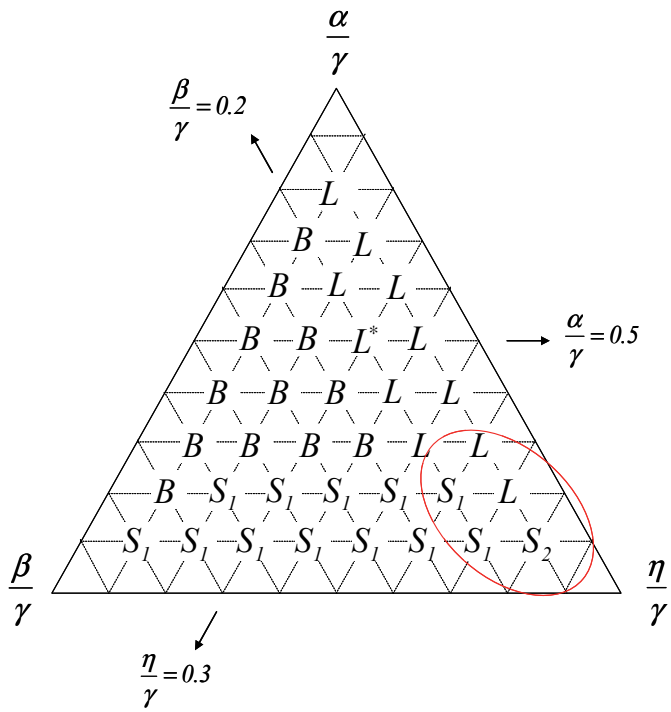

Fig. 3. Triangular diagram composed of the relative force constants $(\alpha/\gamma,\ \beta/\gamma,\ \eta/\gamma)$. The notation L* means that the Last mode corresponds to the lowest frequency mode at the coordinates $(\alpha/\gamma = 0.5,\ \beta/\gamma = 0.2,\ \eta/\gamma = 0.3)$.

curves, only two modes always appear within the set of four modes L, B, S_1 and S_2. The other two modes T_{2u} and *Plane* appear constantly in the high frequency region. It is well-known that the Slater mode is considered to be an optical lattice vibration in which Ti-sublattice vibrates in the reverse direction to O-octahedron. Until now, it has been sufficient to treat the displacements for only Ti and O ions, to explain qualitatively the appearance of an electric polarization. Though the motion of Ba-sublattice has been neglected in the past, the displacements for Ba ions must be considered in the case that the dispersion relations are compared between the theory proposed here and the experiment by the neutron diffraction. There are two kinds of the Slater mode: S_1 in which Ti-sublattice vibrates in the reverse direction to Ba-sublattice and O-octahedrons, and S_2 in which Ba-sublattice and Ti-sublattice vibrate in the reverse direction to O-octahedrons.

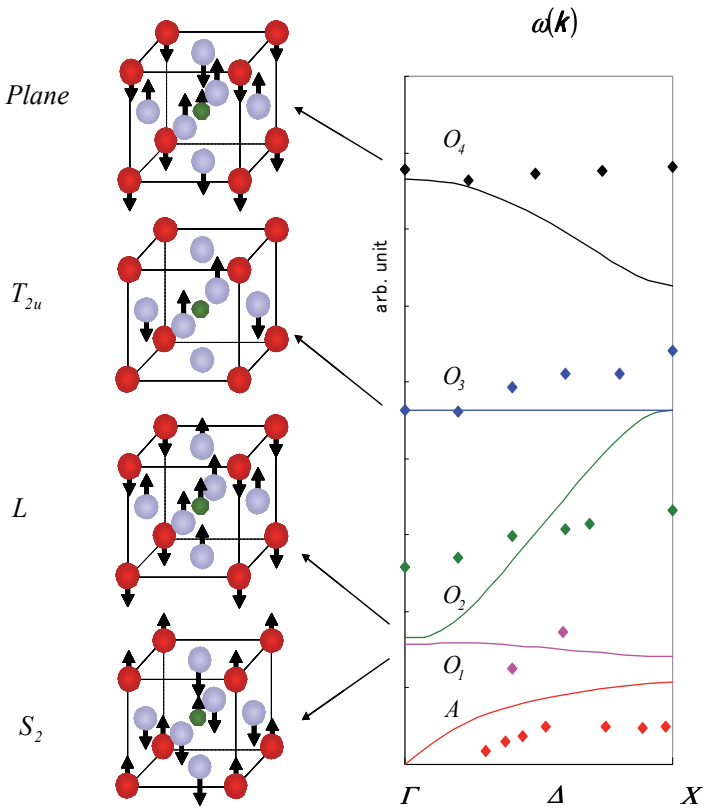

Fig. 4. Dispersion curves with the force constants (α / γ =0.1, β / γ =0.09, η / γ =0.81) of $BaTiO_3$. (a) The lowest frequency mode at Γ point for each branch is shown with the atomic displacement patten. (b) The solid curves represent the theoretical values for the dispersion relations derived from eq. A-1. Small rectangles correspond to the experimental results. (Y.Aikawa & K.Fujii, 2011 to be published in Ferrolelectrics)

The triangular coordinates are introduced whose three axes mean the ratio of α, β and η normalized by γ, namely, α / γ, β / γ, η / γ. The triangular diagram in Fig.3 shows

which mode corresponds to the lowest frequency mode for the given coordinates at Γ point in the Brilloin zone. The dispersion relations within the region enclosed with an ellipse are in agreement with the results obtained by the neutron diffraction experiment. The lowest frequency mode is S_2 mode at the coordinates (α/γ =0.1, β/γ =0.09, η/γ =0.81) in the enclosed region.

The dispersion curves with the force constants $(\alpha/\gamma=0.1,\beta/\gamma=0.09,\eta/\gamma=0.81)$ of $BaTiO_3$ and the experimental values obtained by the neutron diffraction are shown in Fig. 4. Conversely, the author can estimate the relative force constants of the $BaTiO_3$ crystal by the above coordinates.

The (R, $\boldsymbol{k}$)-dependent part, $\gamma_R(\boldsymbol{k})$, for the coefficient $B_R(\boldsymbol{k})(T_C-T)$ of the second order term in the trial potential is given by

$$\gamma_R(\boldsymbol{k})=\frac{\left(c_{R,\boldsymbol{k}}^{(\mathrm{Ti-O})4}+c_{R,\boldsymbol{k}}^{(\mathrm{Ba-O})4}+c_{R,\boldsymbol{k}}^{(\mathrm{O-O})4}+c_{R,\boldsymbol{k}}^{(\mathrm{Ti-Ba})4}\right)\sum_{\boldsymbol{k}}1}{c_{R,\boldsymbol{k}}^{(\mathrm{Ti-O})2}+c_{R,\boldsymbol{k}}^{(\mathrm{Ba-O})2}+c_{R,\boldsymbol{k}}^{(\mathrm{O-O})2}+c_{R,\boldsymbol{k}}^{(\mathrm{Ti-Ba})2}}\quad , \tag{43}$$

It is to be noted that the functions $c_{R,\boldsymbol{k}}^{(nn')}$ are given by the eigenfunctions of the dynamical matrix which is dependent on the force constants. The author has found that the O_1 branch corresponding to the S_2 mode at Γ point tends to decrease in approaching to Γ point and satisfies with the condition given by eq.(40) as shown in Fig. 5.

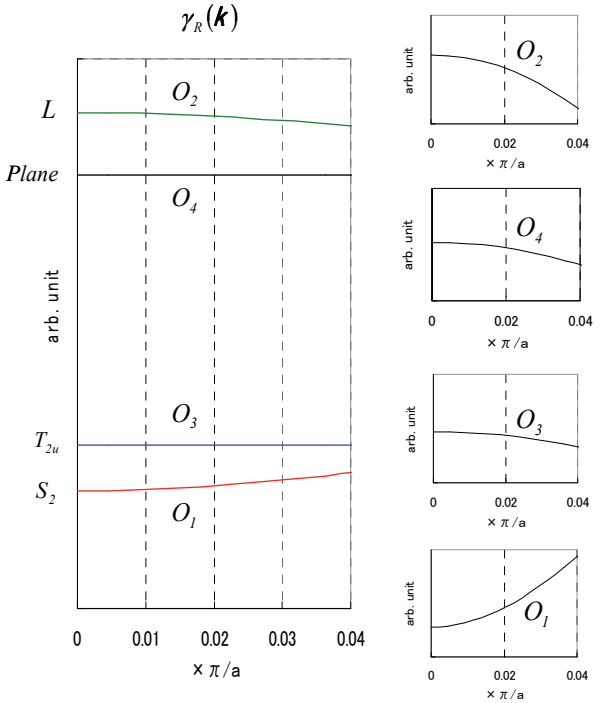

Fig. 5. The function $\gamma_R(\boldsymbol{k})$ for the optical branches near Γ point. (a) The $\boldsymbol{k}$-dependence of $\gamma_R(\boldsymbol{k})$ for the optical branches derived from eq. (43) shows the softening of O_1 branch at Γ point. (b) The details obtained by magnifying the figure (a).

When the S_2 mode freezes, the $BaTiO_3$ crystal undergoes the structural phase transition from cubic to tetragonal symmetry and brings about the ferroelectricity. As a result, the author has been able to show that eq.(40) can provide the justifiable equations to determine the soft mode.

Appendix

The $BaTiO_3$ crystal with the perovskite-type structure has a property that the alloy of Ba-Ti bonding takes in the octahedron of O-O bonding by Ti-O bonding and Ba-O bonding, since the crystal is composed of three components, Ba-cubic lattice, Ti-cubic lattice and O-octahedron. As far as the author take notice of the soft mode at Γ point for the phase transition of $BaTiO_3$ at high temperature region, it is sufficient to discuss within the atomic displacements of one direction.
The equations of motion for atoms in a unit cell can be solved by applying the running wave solutions. The dynamical matrix is obtained as

$$\boldsymbol{D} = \begin{pmatrix} \frac{8\beta+8\gamma}{M_B} & -\frac{8\gamma\cos\frac{a}{2}k_x\cos\frac{a}{2}k_y\cos\frac{a}{2}k_z}{\sqrt{M_BM_T}} & -\frac{4\beta\cos\frac{a}{2}k_y\cos\frac{a}{2}k_z}{\sqrt{M_BM_O}} & -\frac{4\beta\cos\frac{a}{2}k_x\cos\frac{a}{2}k_z}{\sqrt{M_BM_O}} & 0 \\ -\frac{8\gamma\cos\frac{a}{2}k_x\cos\frac{a}{2}k_y\cos\frac{a}{2}k_z}{\sqrt{M_BM_T}} & \frac{2\alpha+8\gamma}{M_T} & 0 & 0 & -\frac{2\alpha\cos\frac{a}{2}k_z}{\sqrt{M_TM_O}} \\ -\frac{4\beta\cos\frac{a}{2}k_y\cos\frac{a}{2}k_z}{\sqrt{M_BM_O}} & 0 & \frac{4\beta+4\eta}{M_O} & 0 & -\frac{4\eta\cos\frac{a}{2}k_x\cos\frac{a}{2}k_z}{M_O} \\ -\frac{4\beta\cos\frac{a}{2}k_x\cos\frac{a}{2}k_z}{\sqrt{M_BM_O}} & 0 & 0 & \frac{4\beta+4\eta}{M_O} & -\frac{4\eta\cos\frac{a}{2}k_y\cos\frac{a}{2}k_z}{M_O} \\ 0 & -\frac{2\alpha\cos\frac{a}{2}k_z}{\sqrt{M_TM_O}} & -\frac{4\eta\cos\frac{a}{2}k_x\cos\frac{a}{2}k_z}{M_O} & -\frac{4\eta\cos\frac{a}{2}k_y\cos\frac{a}{2}k_z}{M_O} & \frac{2\alpha+8\eta}{M_O} \end{pmatrix} \quad \text{A - 1}$$

where the masses of atoms are defined in Fig.1, and the force constants are represented in Fig. 2.

4. Dielectric property

It becomes to shown the relationship between the behavior of the dielectric property at high temperature region and the essential parameter at absolute zero temperature derived from the first principles calculations.

4.1 Interatomic potential

Considering that the ferroelectricity of $BaTiO_3$ mainly depends on the potential between Ti and O atoms, the author introduced the crystal potential at the nth Ti atom along the x-axis as follows (Y. Aikawa, et al., 2009):

$$\begin{aligned} V_n = {} & 2D\left[\exp\left(-2\alpha\Delta r\right)\cosh 2\alpha\left(x_n - < x_n >\right)\right. \\ & \left. -2\exp\left(-\alpha\Delta r\right)\cosh\alpha\left(x_n - < x_n >\right)\right] \\ & + C_F\left(x_n - < x_n >\right) \quad , \end{aligned} \tag{44}$$

where x_n is the coordinate of the nth atom and $\langle x_n \rangle$ is the averaged equilibrium position of the n-site Ti atom along the x –axis, as shown in Fig.1, Δr is the distance between $\langle x_n \rangle$ and the minimum position, D is potential depth, $2D\alpha^2$ is the classical spring constant in the harmonic approximation, and C_F is the coefficient of the long-range order interaction.
Replacing the interatomic distance $|a_{nn'}|$ with the atomic position x_n is expected to result in a good approximation of the nearest interaction in the neighbourhood. Then, Eqs.(17) and (29) are rewritten as follows:

$$\partial \langle V_n \rangle / \partial x_n = 0 \quad , \tag{45}$$

$$\frac{k_B T}{f^{(2)}} = \frac{f}{6\left(\delta^2 + \frac{2Cf}{\nu_S}\right)} \quad , \tag{46}$$

where,

$$f^{(2)} \equiv \sum_{nn'} c_S^{(nn')2} \frac{\partial^2 \langle V_n \rangle}{\partial x_n^2} \quad .$$

$$f \equiv \frac{\sum_{nn'} c_S^{(nn')2} \frac{\partial^2 \langle V_n \rangle}{\partial x_n^2}}{\sum_{nn'} c_S^{(nn')4} \frac{\partial^4 \langle V_n \rangle}{\partial x_n^4} \sum_S 1} \quad .$$

The thermal average of V_n is calculated as

$$\begin{aligned} \langle V_n \rangle = {} & 2D\exp(a_{nn'})\left[\exp(-2\alpha b_{nn'})\cosh 2\alpha\left(x - \langle x_n \rangle\right) - 2\exp(-\alpha b_{nn'})\cosh\alpha\left(x - \langle x_n \rangle\right)\right] \\ & - C_F\left(x - \langle x_n \rangle - \sum_S c_S^{(n)} \langle Q_S \rangle\right) \quad , \end{aligned} \tag{47}$$

$$\begin{aligned} a^{(nn')} &\equiv -\alpha^2 \sum_S c_S^{(nn')2} \langle Q_S^2 \rangle_C - \frac{7}{12}\alpha^4 \sum_S c_S^{(nn')4} \langle Q_S^4 \rangle_C \sum_S 1 \\ b^{(nn')} &\equiv \Delta r - \frac{3}{2}\alpha \sum_S c_S^{(nn')2} \langle Q_S^2 \rangle_C - \frac{5}{8}\alpha^3 \sum_S c_S^{(nn')4} \langle Q_S^4 \rangle_C \sum_S 1 \end{aligned}$$

thus the condition of eq. (45) is

$$y^4 - e^{\alpha b_{nn'}} y^3 + \frac{C_F}{2D\alpha\exp(a_{nn'} - 2\alpha b_{nn'})} y^2 + e^{\alpha b_{nn'}} y - 1 = 0 \quad , \tag{48}$$

here

$$y \equiv \exp(\alpha x) \quad .$$

By using the solution of eq. (48), the equilibrium condition eq.(46) is as follows:

$$\frac{k_B T}{D} = \frac{2\zeta\, g(y)}{3\left(\delta^2 + \frac{2Cf(y)}{\lambda_S \gamma}\right)} \exp(a_{nn'}) \tag{49}$$

Here

$$\lambda_S \equiv \frac{\alpha^2 \mathrm{k_B} T}{2B_S}$$

$$\zeta \equiv \frac{\left(\sum_S c_S^{(nn')2}\right)^2}{\sum_S c_S^{(nn')4} \sum_S 1} \quad ,$$

$$\gamma \equiv \frac{\sum_S c_S^{(nn')4} \sum_S 1}{\sum_S c_S^{(nn')2}} \quad ,$$

$$f(y) \equiv \frac{e^{-\alpha b_{nn'}\left(y^2+y^{-2}\right)-\frac{1}{2}\left(y+y^{-1}\right)}}{4e^{-\alpha b_{nn'}\left(y^2+y^{-2}\right)-\frac{1}{2}\left(y+y^{-1}\right)}} \quad ,$$

$$g(y) \equiv \frac{\left[e^{-\alpha b_{nn'}\left(y^2+y^{-2}\right)-\frac{1}{2}\left(y+y^{-1}\right)}\right]^2}{4e^{-\alpha b_{nn'}\left(y^2+y^{-2}\right)-\frac{1}{2}\left(y+y^{-1}\right)}} e^{-\alpha b_{nn'}} \quad ,$$

The potential parameters D, α, Δr, and C_F listed in Table1 were determined with reference to the results of the first-principles calculations within the density functionl theory.

	Ferro	*Para*
C_F	1.2	0
$D[eV]$	0.094	0.2255
$\alpha[A^{-1}]$	25	25
$\Delta r[A]$	0.02833	0.02833
$C(in\ Eq.42)$	4.8×10^5	4.8×10^5

Table 1. (Y. Aikawa et al., 2009, Ferroelectrics 378)

Ultrasoft pseudopotentials (D. Vanderbilt, 1990) were used to reduce the size of the plane-wave basis. Exchange-correlation energy was treated with a generalized gradient approximation (GGA-PBE96). Y. Iwazaki evaluated the total energy differences for a number of different positions of Ti atoms positions along the *x*-axis (Fig.6) with all other atoms fixed at the original equilibrium positions, which are denoted by open circles in Fig.7. The solid lines in these figures indicate the theoretical values obtained using Eq.(44) with the fitting parameters listed in Table1.

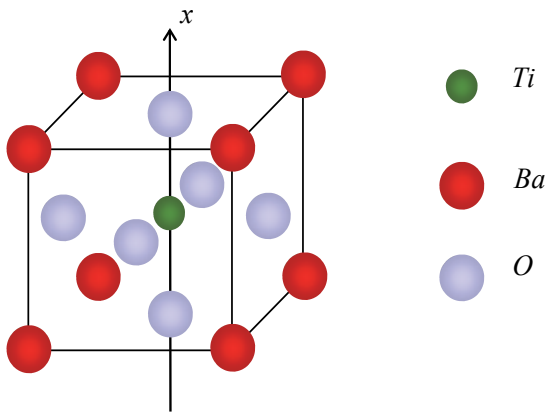

Fig. 6. Perovskite crystal structure of $BaTiO_3$

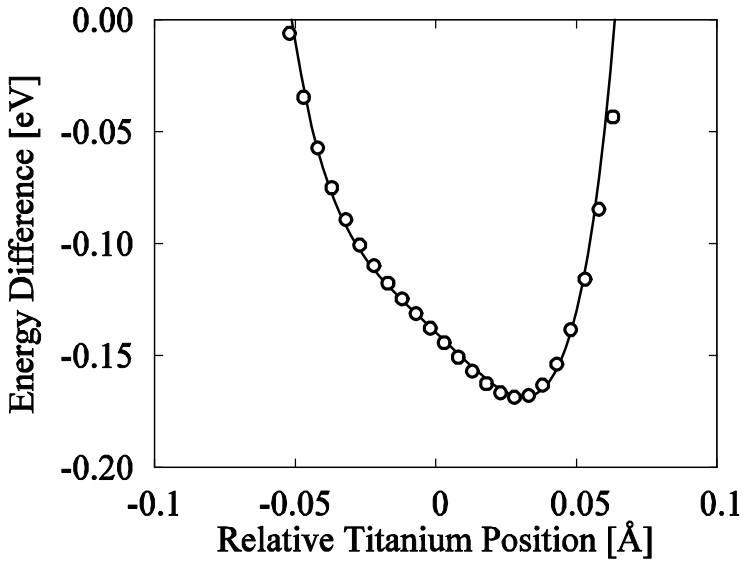

Fig. 7. Atomic potential of Ti in ferroelectric phase of $BaTiO_3$ denoted by open circles were obtained by first principles calculations, the solid line indicate theoretical values given by eq.(44) (Y. Aikawa et al., 2009, Ferroelectrics 378)

4.2 Ferroelectricity of barium titanate

When the softening occurs close to the Curie point, the solution λ_S increases rapidly. This increase implies that the second-order variational parameter B_S tends to zero, the square of the angular frequency Ω_S^2 also tends to zero because the variational parameter $2B_S$ corresponds to $M\Omega_S^2$. Thus,

$$\lambda_S \propto \frac{T}{\Omega_S^2} \quad . \tag{50}$$

The instability of the ferroelectrics in terms of the oscillator model can be explained as follows: as the temperature approaches the Curie temperature Tc, Ω_S^2 changes to zero from a positive value according to displacive ferroelectrics (B>0); Ω_S^2 changes to zero from a negative value according to the order-disorder model (B<0). The former is termed the propagation soft mode, and the latter, the non-propagation soft mode.
The relation between the dielectric constant and the frequency of an optical mode as expressed by Lyddane, Sachs and Teller (R.H.Lyddane et al.,1941) is

$$\varepsilon \propto \frac{1}{\Omega_t^2} \quad , \tag{51}$$

where Ω_t denotes the frequency of transverse optic modes. From eqs. (50) and (51), the relation between ε and λ_S is given by:

$$\frac{\varepsilon}{\varepsilon_0} = \frac{C}{T}\lambda_S \quad , \tag{52}$$

where C is a constant. The temperature dependence of λ_S is calculated by Eq.(49). Fig.8 shows the dielectric constant along the c axis measured as a function of temperature for a single crystal (W. J. Merz, 1953). The solid line in Fig.8 is fitted according to the theoretical calculation performed using Eq.(52) and the potential parameters listed in Table1.

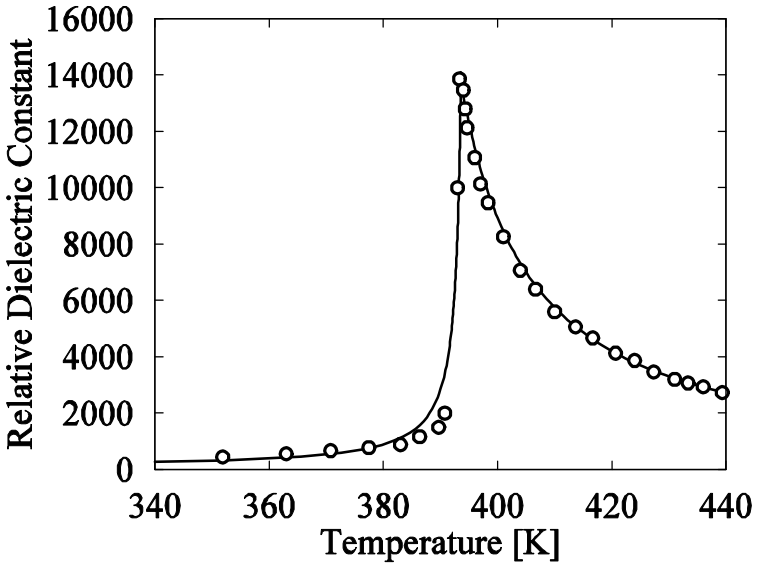

Fig. 8. Temperature dependence of the dielectric constant of single crystal of $BaTiO_3$ along the c axis. The solid line is calculated by Eq. (52), and the open circles are experimental values. (Y. Aikawa et al., 2009, Ferroelectrics 378)

5. Isotope effect

There have been some reports of the isotope effects on displacive-type phase transition, as determined experimentally (T. Hidaka & K. Oka, 1987). In classical approximation (A. D. B. Woods et al., 1960; W. Cochran, 1960), T_C is expected to shift to a higher temperature in

heavy-isotope-rich materials and vice versa. However, the experimental results are completely opposite to the expected results. It has been long considered that the origin of these phenomena in $BaTiO_3$ may be related to the quantum mechanical electron-phonon interaction (T. Hidaka, 1978, 1979).
However, it seems to be problematic to introduce the quantum mechanical electron-phonon interaction to interpret the ferroelectric phase transition in $BaTiO_3$, because the phase transition is a phenomenon in the high-temperature region in which there is scarcely any quantum effect. In order to discuss such a phenomenon in the high-temperature region, K. Fujii et al. have proposed a self-consistent anharmonic model that is applied to the phase transition (K. Fujii et al., 2001), and the author has extended it to derive the ferroelectric properties of $BaTiO_3$ (Y. Aikawa et al., 2009). In this section the isotope effect of T_C is explained through this theory, and the theoretical result is compared with experimental data.

5.1 Theory

Postulating that atomic potential is independent of atomic mass, eq. (33) is rewritten as

$$T_C = \frac{\mathrm{k_B}}{6\delta^2} \frac{\left(\left. \frac{\partial^2 \langle V \rangle}{\partial |\boldsymbol{a}_{nn'}|^2} \right|_{\nu_S \to \infty} \right)^2}{\left. \frac{\partial^4 \langle V \rangle}{\partial |\boldsymbol{a}_{nn'}|^4} \right|_{\nu_S \to \infty}} \zeta \quad , \tag{53}$$

where ζ is the mass-dependent part in T_C as

$$\zeta \equiv \frac{\left(\sum_{nn'} c_S^{(nn')2} \right)^2}{\sum_{nn'} c_S^{(nn')4} \sum_S 1} \quad . \tag{54}$$

In order to calculate eq. (54), it is necessary to obtain the eigen function $e_S^{(n)}$ in eq.(5) by solving the dynamical matrix, which consisted of atomic mass and force constants, as shown in Fig.2. The force constants shown in Fig.2 are derived from the second-order derivative of interatomic potential with respect to interatomic distance.
It is, however, difficult to estimate the force constants because estimate various interactions between atoms exist. The author did attempt to estimate them so as not to contradict the results of neutron diffraction experiments; as (α/γ, β/γ, η/γ) = (0.1, 0.09, 0.81) as derived in 3.2.

5.2 Numerical calculation and comparison with experiments

It was also shown that the soft mode is the Slater mode, which is the lowest frequency optic mode at $\boldsymbol{k}$ = 0 under this condition. Using this force constants, the ratio of T_C (^{y}Ba ^{x}Ti O_3 that is replaced with isotope elements) to T_C (natural $^{137.33}$Ba $^{47.88}$Ti $^{16}O_3$) is obtained by calculating eq.(54) using x = 46-50, y =134-138 as parameters. The results are shown in Fig. 9.

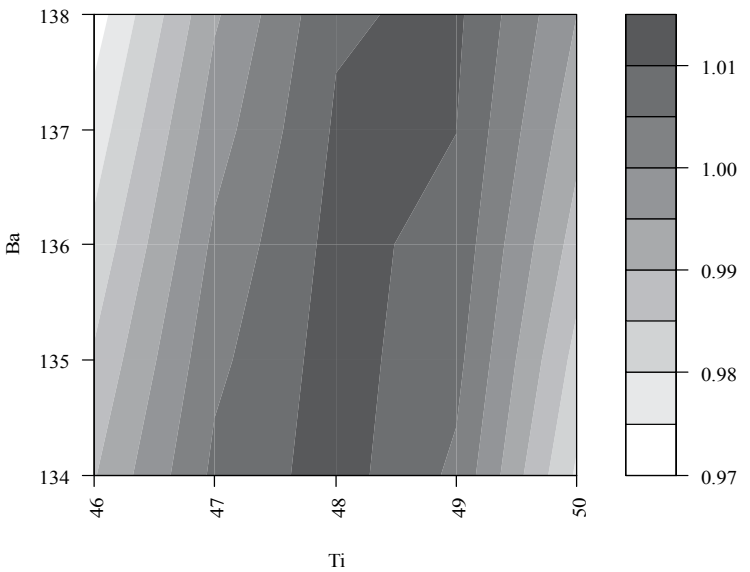

Fig. 9. x-y phase diagrams of the ratio of Tc ($^{y}Ba\ ^{x}Ti\ O_3$) to Tc ($^{137.33}Ba\ ^{47.88}Ti\ ^{16}O_3$) (Y.Aikawa et al., 2010 Jpn. J. Appl. Phys. 49 09ME11)

In Fig.10, the solid curve shows the theoretical values of the transition temperature for the isotope effects of Ti calculated using eq. (54), and the experimental values are represented by open circles. It appears that the theoretical values in the solid curved line are roughly in agreement with the experimental values represented by the open circles as shown in the figure.

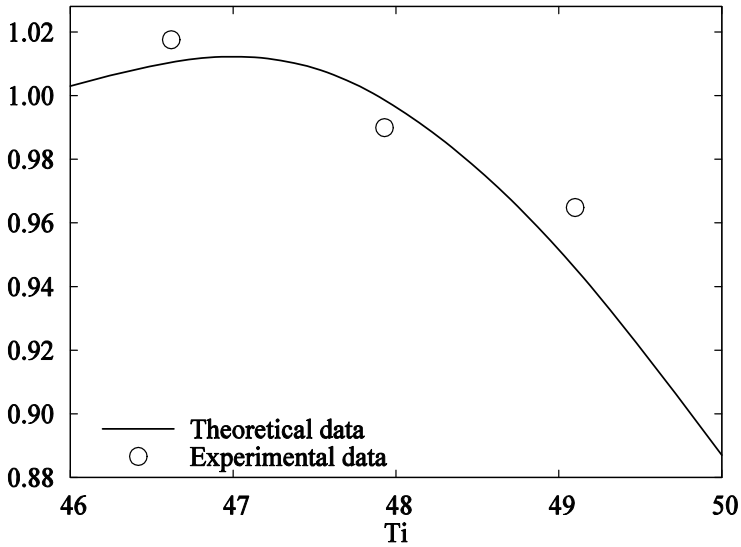

Fig. 10. Comparison between the theoretical and experimental values in terms of x-dependence of the ratio of Tc ($^{137.33}\ Ba\ ^{x}Ti\ ^{16}O_3$) to Tc ($^{137.33}Ba\ ^{47.88}Ti\ ^{16}O_3$). (Y.Aikawa et al., 2010 Jpn. J. Appl. Phys. 49 09ME11)

In the case of harmonic approximation, as the heavy Ti isotope is introduced, the Curie temperature rises, and vice versa for the light Ti isotope (T. Hidaka & K. Oka, 1987), because only the coefficient $c_S^{(nn')2}$ of the harmonic term $\langle Q_S^2 \rangle$ is considered. It is known that anharmonicity promotes the instability in the crystal (K.Fujii et al., 2001), as a result, the instability undergoes the structural phase transition in the crystal systems with a strong anharmonicity. In eq.(54) the effect of the coefficient $c_S^{(nn')4}$ of the fourth-order term $\langle Q_S^4 \rangle$ is to sift T_C to the lower-temperature region, whereas that of the coefficient $c_S^{(nn')2}$ of the quadratic term $\langle Q_S^2 \rangle$ is to shift T_C to the higher-temperature region. In the higher-temperature region, the effect of $\langle Q_S^4 \rangle$ is more important. Therefore, the self-consistent anharmonic theory in the high-temperature region enables the explanation of the tendency that T_C is expect to shift to the lower temperature in the heavier Ti isotope.

The instability temperature or the transition temperature for the trial potential represented by an anharmonic oscillator has been derived from the variational method at finite temperature where the normal coordinates were introduced in this work to reflect the crystal symmetry in the softening phenomenon. The result obtained here has been applied to the isotope effect of the ferroelectric crystal $BaTiO_3$. The transition temperature T_C given by eq. (53) has been applied after substituting the actual values obtained for the force constants into ζ given by eq.(54). As a result, the author has been able to probe that the transition temperature T_C of barium titanate consisting of heavy-isotope Ti is lower than that of barium titanate consisting of light-isotope Ti.

6. Conclusion

The instability temperature or the transition temperature for the trial potential represented by an anharmonic oscillator has been derived from the variational method at finite temperature where the normal coordinates were introduced in this work to reflect the crystal symmetry in the softening phenomenon.

1. Though the expression obtained here has the same form as the Landau expansion, the transition temperature and the expansion coefficients can be represented by the characteristic constants of the potentials between atoms. From the fact that the coefficient of the second order term in the trial potential is expressed by the form such as $B_R(\boldsymbol{k})(T_C - T)$, the author has proposed the equations to determine the soft mode by imposing the condition that its $\boldsymbol{k}$ -dependent part takes the minimum value. The result obtained here has been applied to the structural phase transition of the ferroelectric crystal $BaTiO_3$. The dispersion relations derived from the dynamical matrix has been compared with that from the neutron diffraction experiment. The force constants between atoms have been fitted so as to reproduce the experimental results for the dispersion relations. The determination equations given by eq.(40) has been applied after substituted the actual values obtained for the force constants into $\gamma_R(\mathbf{k})$ given by eq.(38). As a result, the author has been able to probe that the lowest frequency mode at Γ point corresponded to the S_2 mode causing the structural phase transition in the $BaTiO_3$ crystal.
2. The author has shown that the ferroelectric properties of $BaTiO_3$ result from the equilibrium condition of free energy by using the anharmonic oscillation model and the elemental parameters derived using first-principles calculations.

3. The result obtained here has been applied to the isotope effect of the ferroelectric crystal $BaTiO_3$. The transition temperature T_C given by eq. (53) has been applied after substituting the actual values obtained for the force constants into ζ given by eq. (54). As a result, the author has been able to probe that the transition temperature T_C of barium titanate consisting of heavy-isotope Ti is lower than that of barium titanate consisting of light-isotope Ti.

7. References

Aikawa, Y. & Fujii, K. (1993). Theory of Instability Phenomena in Crystals, *J. Phys. Soc. Jpn.* 62, pp.163-169

Aikawa, Y. & Fujii, K. (1998). Theory of instability phenomena and order-disorder transition in CsCl type crystal, *Phys. Rev. B* 57, pp. 2767-2770

Aikawa, Y.; Sakashita, T.; Suzuki, T. & Chazono, H. (2007). Theoretical consideration of size effect for barium titanate, *Ferroelectrics,* 348, pp. 1-7

Aikawa, Y. & Fujii, K. (2009). Theory of instability phenomena and its application to melting in cubic metals, *Mater. Trans.* 50, pp. 249-253

Aikawa, Y.; Iwazaki, Y.; Sakashita,T. & Suzuki, T. (2009). Self-consistent anharmonic theory and its application to ferroelectric crystal, *Ferroelectrics,* 378, pp.8-15

Aikawa, Y.; Sakashita, T. & Suzuki, T. (2010). Self-consistent anharmonic theory and its application to the isotope effect on ferroelectric phase transition in $BaTiO_3$ crystal, *Jpn. J. Appl. Phys.* 49, pp. 09ME11-1～09ME11-5

Aikawa, Y.; Iwazaki, Y. & Suzuki, T. (2010). Theoretical analysis of surface effect of crystal and its application to $BaTiO_3$ fine particle, *J. Ceram. Soc. Jpn* 118, pp. 1057-1061

Akdogan, E. K. & Safari, A. (2002). Phenomenological theory of size effects on the cubic-tetragonal phase transition in $BaTiO_3$ nanocrystals, *Jpn. J. Appl. Phys.* 41, pp.7170-7175

Arlt, G.; Hennings, D. & de With, G. (1985). Dielectric properties of fine-grained barium titanate ceramics, *J. Appl. Phys.* 58, pp.1619-1625

Burns, G. (1977). Introduction to group theory with applications, *Academic Press* pp.91-93 Cochran, W. (1959). Crystal stability and the theory of ferroelectricity, *Phys.Rev.Lett.*3, pp.412-414

Cochran, W. (1960). Crystal stability and the theory of ferroelectricity *Adv. Phys.* 9, pp.387 -423

Fujii, K.; Aikawa,Y. & Ohoka, K. (2001). Structural phase transition and anharmonic effects in crystal, *Phy. Rev. B*63, pp.104107-1～104107-4

Fujii, K. ; Aikawa,Y. & Shimazutsu,Y.(2003). Instability of the order-disorder ferroelectrics, J. Phys. Soc. Jpn. 72, pp.727-729

Gillis, N. S.; Werthamer, N. R. & Koehler, T. R. (1968). Properties of crystalline argon and neon in the self-consistent phonon approximation, *Phys. Rev.*165 pp.951-959

Gills, N. S.; & Koehler, T. R. (1971). Self-consistent treatment of the frequency spectrum of a model paraelectric, *Phys. Rev. B*4, pp.3971-3982

Harada, J. & Honjo, G. (1967). X-ray studies of the lattice vibration in tetragonal barium titanate, *J. Phys. Soc. Jpn* 22, pp.45-57

Hidaka,T. (1978). Theory of a structural phase transition of $SrTiO_3$ at 110K, *Phys. Rev. B* 17, pp. 4363-4367

Hidaka, T. (1979). Electronic instability of the Γ_{15} phonon in $BaTiO_3$, *Phys. Rev. B* 20, pp.2769-2773

Hidaka, T. & Oka, K. (1987). Isotope effect on BaTiO3 ferroelectric phase transitions, *Phys. Rev. B* 35, pp.8502-8508

Hoshina,T.; Takizawa, K.; Li, J.; Kasama,T.; Kakemoto, H. & Tsurumi,T. (2008). Domain size effect on dielectric properties of barium titanate ceramics, *Jpn. J. Appl. Phys.* 47, pp.7607-7611

Hoshina,T.; Wada, S.; Kuroiwa, Y. & Tsurumi, T. (2008). Composite structure and size effect of barium titanate nanoparticles, *Appl. Phys. Lett.* 93, pp.192914-1～192914-3

Jannot, B.; Escribe-Filippini C. & Bouillot, J. (1984). Lattice dynamics of pure barium titanate and barium strontium titanate solid solutions, *J. Phys. C, Solid State Phys.*17, pp.1329-1338

Junquera, J. & Ghosez,P. (2003). Critical thickness for ferroelectricity in perovskite ultrathin films, *Nature* 422, pp.506-509.

Kishi, H.; Mizuno Y. & Chazono,H. (2003). Base metal electrode multilayer ceramic capacitors: past, present and future perspectives, *Jpn. J. Appl. Phys.* 42, pp.1-15

Landau, L. D. & Lifshitz, E. M. (1958). Statistical Physics, *Pergamon,* London Lyddane, R. H.; Sachs, R. G. & Teller, E. (1941). On the polar vibrations of Alkali halides, *Phys. Rev.*59, pp.673-676

Matsubara, T. & Kamiya, K. (1977). Self-consistent Einstein model and Theory of anharmonic surface vibration. I , *Prog. Theor. Phys.* 58, pp.767-776 Merz, W. J. (1953). Double hysteresis loop of $BaTiO_3$ at the Curie point, *Phys. Rev.* 91, pp.513-517

Ohno,T.; Suzuki, D.; Suzuki, H. & Ida, T. (2004). Size Effect for Barium Titanate Nano-particles, *KONA* 22, pp.195-201

Onodera, Y. (1970). Dynamic Susceptibility of Classical Anharmonic Oscillator, *Prog. Theor. Phys.* 44, pp.1477-1499

Perebeinos,V.; Chan, S. W. & Zhang, F. (2002). 'Madelung model' prediction for dependence of lattice parameter on nano crystal size, *Sol. State. Comm.* 123, pp.295-297

Shih, W. Y.; Shih, W. H. & Askey, I. A. (1994). Size dependence of the ferroelectric transition of small $BaTiO_3$ particles: Effect of depolarization, *Phys. Rev. B* 50, pp.15575-15585 Shirane, G.; Frazer, B. C.; Minkiewicz,V. J. & Leake, J. A. (1967). Soft optic modes in barium titanate, *Phys.Rev.Lett.*19, pp.234-235

Vanderbilt,D. (1990). Soft self consistent pseudopotentials in a generalized eigenvalue formalism, *Phys. Rev. B* 41, pp.7892-7895

Woods, A. D. B.; Cocran,W. & Brockhouse, B. N.(1960).Lattice dynamics of alkali halide crystals,*Phys. Rev.* 119, pp.980-999

Wada, S.; Yasuno, H.; Hoshina,T.; Nam, S. M.; Kakemoto, H. & Tsurumi,T. (2003). Preparation of nm-sized barium titanate fine particles and their powder dielectric properties, *Jpn. J. Appl. Phys.* 42, pp. 6188-6195

Zhong, W. L.; Wang,Y. G.; Zhang, P. L. & Qu, B. D. (1994). Phenomenological study of the size effect on phase transition in ferroelectric particles, *Phys. Rev. B*50, pp. 698-703 Zhong, W.; Vanderbilt, D. & Rabe, K. M. (1995). First principles theory of ferroelectric phase transitions for perovskites: the case of $BaTiO_3$, *Phys. Rev. B*52, pp. 6301-6312

18

Switching Properties of Finite-Sized Ferroelectrics

L.-H. Ong[1] and K.-H. Chew[2]
[1]*School of Physics, Universiti Sains Malaysia, Minden, Penang,*
[2]*Department of Physics, University of Malaya, Kuala Lumpur, Malaysia*

1. Introduction

The characteristic property of ferroelectric materials, which is the reversal of polarization by an external electric field, is of technological importance in device applications, particularly in nonvolatile ferroelectric random access memories (NV-FeRAMs). These binary coded NV-FeRAMs can be fabricated by using ferroelectric materials in which the polarization direction can be switched between two stable states when a minimum electric field is applied. To fabricate good quality NV-FeRAMs to meet the demands of the current market, the ability to achieve low coercive field E_c (the minimum external field required to reverse the direction of remnant polarization), short switching time t_s and high packing density (Scott, 2000; Dawber *et al.*, 2005) in the memory chips are great challenges. These challenging factors are closely knitted with the underlying physics on the switching properties of ferroelectric materials. Though the subject of interest has been elucidated both theoretically and experimentally over the past sixty years and the achievements are enormous, but the challenging factors mentioned are still current. Auciello, Scott and Ramesh (1998) have explicitly outlined four main problems in NV-FeRAMs fabrication which are related to basic physics. Firstly, what is the ultimate polarization switching speed? Secondly, what is the thinnest ferroelectric layer which sustains stable polarization? Thirdly, how do switching parameters, such as coercive field, depend on frequency? Lastly, how small can a ferroelectric capacitor be and still maintain in ferroelectric phase? These are fundamental problems which should be tackled through continuous experimental and theoretical efforts.

From the theoretical perspective on this area of studies, a few models (Duiker and Beale, 1990; Orihara *et al.*, 1994; Hashimoto *et al.*, 1994; Shur *et al.*, 1998) were proposed to study the switching properties of ferroelectric thin film based on the Kolmogorov-Avrami theory of crystallization kinetics (Avrami, 1939, 1940 and 1941). In these models, the authors focused on statistics of domain coalescence. Tagantsev *et al.* (2002) proposed another model based on the experimental work of a few groups (Lohse *et al.* 2001; Colla *et al.*, 1998a; Ganpule *et al.*, 2000). Their model also focuses on statistics of domains nucleation. Another approach, which is different from the classical nucleation reversal mechanism, is based on the Landau-type-free energy for inhomogeneous ferroelectric system as discrete lattices of electric

dipoles (Ishibashi, 1990). However, all these models neglect the surface effect, which is shown to have influence on phase transitions of ferroelectric films, and as the films get thinner the surface effect becomes more significant.

The continuum Landau free energy for a ferroelectric film, extended by Tilley and Zeks (Tilley and Zeks, 1984), incorporates the surface parameter δ (extrapolation length). Positive δ models a decrease in local polarization at surface, and negative δ an increase, with a smaller absolute value of δ giving a stronger surface effect. This model has been used to elucidate phase transition and dielectric properties of FE thin films with great success (Wang C. L. *et al*., 1993; Zhong *et al*., 1994; Wang Y. G. *et al*., 1994; Wang C. L. and Smith, 1995; Ishibashi *et al*., 1998; Tan *et al*., 2000; Ong *et al*., 2001; Ishibashi *et al*., 2007) and the results of phase transition and dielectric properties of ferroelectric thin films obtained are well accepted. In this chapter, we outline the progress of theoretical and experimental work on switching phenomena of ferroelectric thin films, and the main focus is on the results of switching properties of ferroelectric thin film obtained from the Tilley – Zeks continuum Landau free energy and Landau-Khalatnikov (LK) dynamic equation (Ahmad *et al*., 2009; Ong and Ahmad, 2009; Ahmad and Ong, 2009; 2011a; 2011b). The surface effects, represented by $\pm\delta$, on properties of polarization reversal, namely, coercive field E_c and switching time t_s will be discussed (Ahmad *et al*., 2009). For positive δ, E_c and t_S decrease with decreasing $|\delta|$ while for negative δ, E_c and t_s increase with decreasing $|\delta|$. Strong surface effects represented by smaller $|\delta|$ are more profound in thin ferroelectric films. As the film size increases, the delay in switching at the centre relative to switching near the edges is more remarkable for systems of zero or small polarization at the edges ($\delta \cong 0$). It is found that the dipole moments at the centre and near the edges switch almost together in small-sized systems of any magnitudes of δ. (Ong *et al*., 2008a; 2008b). We also elucidated the phenomena of polarization reversal of second-order ferroelectric films, particularly the characteristics of hysteresis loops by an applied sinusoidal field. It is shown that at a constant temperature, the size of hysteresis loops increases with increasing film thickness for $\delta > 0$ and the reverse is true for $\delta < 0$. For a film of fixed thickness, the size of hysteresis loop decreases with increasing temperature for cases of $\delta > 0$ and $\delta < 0$. We have demonstrated that the effect of magnitude of the applied field on the hysteresis loops is similar to the experimental results (Ong and Ahmad, 2009). Our numerical data also show that switching time t_S is an exponential function of the applied field and the function implies that there is a definite coercive field in switching for various thicknesses of FE films (Ahmad and Ong, 2011b). Lastly, since in reality, ferroelectric thin films are fabricated on conductive materials (such as $SrRuO_3$) as electrodes, hence, we shall include the effects of misfit strain on switching phenomenon of epitaxial film of $BaTiO_3$ (Ahmad and Ong, 2010a) and conclude with some remarks.

2. Ferroelectric thin film and Tilley-Zeks model

The behaviour of ferroelectric thin films is significantly different from that of the bulk. The arrangement of atoms or molecules at the surface is different from that of the bulk material. Due to the process of surface assuming a different structure than that of the bulk, which is known as surface reconstruction, polarization at the surface is not the same as that in the bulk; and it affects the properties of the material. This so called surface effect may have little influence on the properties of material if the material is thick enough. However, when the

material becomes thinner, the surface effect becomes significant. The demand by current technological applicants on material thickness of ferroelectric thin film is now in the range of nano-scale. Hence, surface effect in ferroelectric thin film is a significant phenomenon and how it can affect switching must be understood.

The Landau free energy for a ferroelectric film, extended by Tilley and Zeks (Tilley and Zeks, 1984), incorporates the surface parameter δ (also named the extrapolation length) and for convenient, we named it TZ model. Positive δ models a decrease in local polarization at the surface, and negative δ an increase; with a smaller absolute value of δ giving a stronger surface effect. This is important since both forms of behavior have been observed in experiments on different materials. With this surface parameter δ, the inherent material properties at the surfaces of a ferroelectric film which can be either of the two cases are explained. This Landau free energy is given by

$$\frac{F}{S} = \int_{-L/2}^{L/2} \left[\frac{\alpha}{2\varepsilon_0} P^2 + \frac{\beta}{4\varepsilon_0^2} P^4 + \frac{\kappa}{2\varepsilon_0} \left(\frac{dP}{dz} \right)^2 \right] dz + \frac{\kappa}{2\varepsilon_0 \delta} \left(P_+^2 + P_-^2 \right), \tag{1}$$

where S is the area of the film with plane surfaces at $z = \pm L/2$ and $P_{\pm} = P(\pm L/2)$. α is temperature dependent, taken in the form $\alpha = \alpha_0 (T - T_{C0})$ with T_{C0} the critical temperature of the bulk material and the constants α_0, β and κ are positive. ε_0 is the dielectric permittivity of the material and the κ term inside the integral in Eq. (1), represents the additional free energy due to spatial variation of P. Whereas the κ term outside the integral in Eq. (1), represents the free energy due to the surface ordering.

3. Phase transition in ferroelectric thin film

We (Ong *et al.*, 2000; 2001) reinvestigated the TZ model and obtained much simpler expressions, compared with previous work (Tilley and Zeks, 1984), for the polarization profiles of ferroelectric thin films in Jacobian elliptic functions for both positive and negative δ. Variation of Eq. (1) about the equilibrium form $P(z)$ shows that this satisfies the Euler-Lagrange equation (Ong *et al.*, 2001)

$$\frac{\alpha}{\varepsilon_0} P + \frac{\beta}{\varepsilon_0^2} P^3 - \frac{\kappa}{\varepsilon_0} \frac{d^2 P}{dz^2} = 0, \tag{2}$$

with the following boundary conditions:

$$\frac{dP}{dz} = \pm \frac{P}{\delta} \quad \text{at} \quad z = \pm L/2. \tag{3}$$

It follows from Eq. (3) that if the extrapolation length δ is positive, $P(z)$ decreases near the surface, and if it is negative, $P(z)$ increases. In consequence, the critical temperature T_C of the film is reduced below T_{C0} for positive δ and increased for negative δ. The first integration of Eq. (2) leads to

$$\frac{dP}{dz} = \pm \left(\frac{\beta}{2\kappa} \right)^{\frac{1}{2}} \left(\frac{1}{\varepsilon_0^2} P^4 + \frac{2\alpha}{\varepsilon_0 \beta} P^2 + \frac{4G}{\beta} \right)^{\frac{1}{2}}, \tag{4}$$

where G is the constant of integration. The extremum of $P(z)$ is at $z = 0$ so that the central value $P(0)$ is a solution of the quadratic equation corresponding to $dP/dz = 0$:

$$P^4 + \frac{2\varepsilon_0\alpha}{\beta}P^2 + \frac{4\varepsilon_0^2 G}{\beta} = \left(p^2 - p_1^2\right)\left(p^2 - p_2^2\right) = 0\,, \tag{5}$$

where the roots P_1 and P_2 are introduced for later use; and the roots are such that $P_2^2 > P_1^2$. It follows from Eq. (5) that the product $P_2^2.P_1^2$ has the same sign as G and it will be seen that while P_2^2 is always positive for both signs of δ, in the case of $\delta > 0$, there is a temperature interval in which G and therefore P_1^2 are negative.

The P integral resulting from Eq. (4) can be expressed by inverse elliptic functions so that ultimately $P(z)$ is expressed in terms of an elliptic function. The detailed forms depend on the sign of δ.

In the case of $\delta > 0$, it can be shown that $0 < G < \alpha_0^2 / 4\beta$ so that, P_1^2 and P_2^2 are both positive. Since positive δ leads to a decrease of $P(z)$ at the surface of the film we have the inequalities $0 < P(z) < P_1 < P_2$. The central value $P(0)$ is the maximum value of $P(z)$ and is in fact equal to P_1. The expression for $P(z)$ is

$$P(z) = P_1 sn(K - z/\xi, \lambda)\,, \tag{6}$$

in standard notation for elliptic functions. The modulus λ is given by $\lambda = P_1 / P_2$; $K = K(\lambda)$ is the complete elliptical modulus and the scale length ξ is

$$\xi = \sqrt{2\varepsilon_0^2\kappa / (\beta^{1/2}P_2^2)}\,. \tag{7}$$

In the case of $\delta < 0$, the analytical work is complicated because the expression for polarization profile depends on temperature range. In the temperature interval $T_0 \le T \le T_C$ in which $G < 0$ and $P_1^2 \le 0 \le P_2^2 \le P^2(z)$. In the interval where G is negative, $P(z)$ takes the form,

$$P(z) = \frac{P_2}{cn(z/\zeta, \lambda_1)} \tag{8}$$

where $\lambda_1 = -P_1^2 / (P_2^2 - P_1^2)$ is the modulus, and the scaling length is given by

$$\zeta^2 = \frac{2\varepsilon_0^2\kappa}{\beta(P_2^2 - P_1^2)}\,. \tag{9}$$

While for the temperature interval $T < T_0$, the parameters satisfy the inequalities $G > 0$, $0 < P_1^2 < P_2^2 < P^2(z)$ 0, and the polarization profile is found to be

$$P(z) = \frac{P_2}{sn(K - z/\xi, \lambda)}\,. \tag{10}$$

Similarly, the modulus λ is given by $\lambda = P_1 / P_2$; $K = K(\lambda)$ is the complete elliptical modulus. These simpler analytical expressions, describing the polarization profile of a

ferroelectric film with either positive or negative δ, are important in helping the study of switching properties of ferroelectric film as well as size and surface effects on properties of phase transition. In the case of negative δ, there is no size induced phase transition; but for positive δ, we have found an expression for the minimum thickness L_C of ferroelectric film to maintain ferroelectric properties. This minimum thickness is a function of δ and temperature T as shown below:

$$L_C(T) = 2\xi_C \tan^{-1}\left(\frac{\xi_C}{\delta}\right). \tag{11}$$

ξ_C is the correlation length at critical temperature given by $\xi_C = \xi_0 / \sqrt{T_{C0} - T_C}$ and ξ_0 is the zero temperature of correlation length. T_C and T_{C0} are the critical temperatures of the film and bulk, respectively. Eq. (11) provides hints to the experimentalists that minimum thickness of ferroelectric film is dependent on the critical temperature, as well as δ; hence these values are material dependent.

We have also presented new thermodynamic functions, the entropy and specific heat capacity, for ferroelectric films with both cases of $\pm\delta$. These thermodynamic functions provide useful information that the phase transitions in both cases of $\pm\delta$ are stable (Ong *et al.*, 2001). The reports in the literature on the claims of possible surface state in the case of negative δ (Tilley and Zeks, 1984) and film transition can be first order even if its bulk is second order (Qu *et al.*, 1997) had caught our attentions and after careful investigation, we found that there is no surface state in the negative δ case and the film transition is always second order as in the bulk transition.

4. Formalism for switching in ferroelectric thin films

Theoretical and experimental work on switching phenomena of bulk ferroelectric began about half a century ago. The interest in this research area has further been extended to ferroelectric thin films; and the interest has not waned even up to these days because of the advancement in thin film fabrication technology, where higher quality and more reliable ferroelectric thin films can be fabricated; thus making the applications of ferroelectric thin films in microelectronic devices and memories (Uchida *et al.*, 1977; Ganpule *et al.*, 2000) more reliable. Current theoretical and experimental researches in polarization reversal in ferroelectric thin films are focused on phenomena related to effects of size and surface in thin films on switching time and coercive field (Ishibashi and Orihara, 1992; Wang and Smith, 1996; Chew *et al.*, 2003).

From the literature, several theoretical models based on a Landau-typed phase transition have given good explanations on switching behaviours of mesoscopic ferroelectric structures (Ishibashi and Orihara, 1992; Wang and Smith, 1996); and some of the predictions concerning size on switching behaviours by Landau-typed models agree well with experimental observations. However, the detailed understanding of surface effect on ferroelectric films under the applied electric field is still inadequate, but understanding of surface effect is important for the overall understanding on the switching behaviours of ferroelectric films. Thus, we extended the TZ model for ferroelectric thin films given in Eq. (1) by adding in the energy expression a term due to electric field ($-EP$)

$$\frac{F}{S} = \int_{-L/2}^{L/2} \left[\frac{\alpha}{2\varepsilon_0} P^2 + \frac{\beta}{4\varepsilon_0^2} P^4 + \frac{\kappa}{2\varepsilon_0} \left(\frac{dP}{dz} \right)^2 - EP \right] dz + \frac{\kappa}{2\varepsilon_0 \delta} \left(P_+^2 + P_-^2 \right) \tag{12}$$

and minimization of Eq. (12) by variational method shows that the polarization satisfies the Euler Lagrange (EL) equation

$$\frac{\alpha}{\varepsilon_0} P + \frac{\beta}{\varepsilon_0^2} P^3 - E - \frac{\kappa}{\varepsilon_0} \frac{d^2 P}{dz^2} = 0 , \tag{13}$$

with the following boundary conditions:

$$\frac{dP}{dz} = \pm \frac{P}{\delta} \quad \text{at} \quad z = \pm L/2 . \tag{14}$$

The Landau-Khalatnikov dynamic equation is used to study switching behaviours in ferroelectric thin films (Ahmad *et al*., 2009; Ong *et al*., 2008a; 2008b; 2009; Ahmad and Ong, 2011b), and it is simplified to the form as follow:

$$\gamma \frac{\partial P}{\partial \tau} = -\frac{\delta (F/S)}{\delta P} = -\frac{\alpha_0 (T - T_{C0})}{\varepsilon_0} P - \frac{\beta}{\varepsilon_0^2} P^3 + \frac{\kappa}{\varepsilon_0} \frac{d^2 P}{dz^2} + E , \tag{15}$$

where γ is the coefficient of viscosity which causes a delay in domain motion and τ is the time. In this equation, the kinetic energy term $m\partial^2 P / \partial \tau^2$ is ignored, since it only contributes to phenomenon in the higher frequency range. The applied electric field E can be a static step field or a dynamic field. We obtained the equilibrium polarization profile $P(z)$ from the elliptic function derived Eq. (1), and this profile is symmetric about the film centre z = 0.0. The initial polarization profile of the ferroelectric film at e = 0.0 is obtained from solving Eq. (4) for the elliptic functions derived by Ong *et al*. (2001). In all our simulations, the initial polarization in the film is switched from its negative value. By solving Eq. (15) using the Runge-Kutta integration by finite difference technique, we obtained the reversal of polarization. The reversal of polarization is studied by applying a stepped electric field and the hysteresis loops are obtained by sinusoidal field respectively, as these fields are usually used in experiments. The applied stepped field is of the form

$$E = E_0 f(\tau) , \tag{16}$$

where $f(\tau)$ is a usual step-function defined as

$$f(\tau) = \begin{cases} 1 & \text{for } 0 \le \tau < \tau_0 \\ 0 & \text{for } \tau_0 \end{cases} . \tag{17}$$

τ_0 is the time taken when the field is switched off and E_0 is the maximum applied electric field. The sinusoidal field in the reduced form is

$$e = e_0 \sin(\omega \tau_r) \,, \tag{18}$$

where e_0 is the amplitude and ω is the angular frequency. The dimensionless formulations used in the calculations are obtained by scaling Eqs. (12) to (16) according to the way discussed in our articles. All parameters listed in the equations above are scaled to dimensionless quantities. We let $\zeta = z / \xi_0$ with $\xi_0{}^2 = \kappa / \alpha_0 T_{C0}$ and ξ_0 corresponds to the characteristic length of the material. Normally, ξ_0 is comparable to the thickness of a domain wall. l is the dimensionless form of thickness L scaled to ξ_0. We have temperature T scaled as $t = T / T_{C0}$, $p = P / P_0$ with $P_0^2 = \varepsilon_0 A T_C / B$ and $e = E / E_C$ with $E_C^2 = 4\alpha_0^3 T_{C0}^3 / (27\varepsilon_0 \beta)$. The global order parameter is the average polarization of the film defined as

$$\overline{p} = \frac{1}{l} \int_{-l/2}^{l/2} p(\zeta)\, d\zeta \,. \tag{19}$$

5. Polarization evolution in ferroelectric films

Surface condition due to δ and size of ferroelectric films affect the switching profiles of ferroelectric films. A ferroelectric film with zero δ means the surface polarization is zero at both surfaces of the film. When a positive electric field E is applied on ferroelectric films with zero and non-zero δ, various stages of switching profiles are shown in Fig. 1 and Fig. 2, respectively, for temperature $T = 0.6 T_{C0}$. The starting equilibrium polarization profile is set at negative at time t = 0; and the profile is switched over to positive state by the applied electric field E until it is completely saturated. In a thin ferroelectric film (Fig. 1), switching at the surface and at the centre is almost the same irrespective of either zero or non-zero δ.

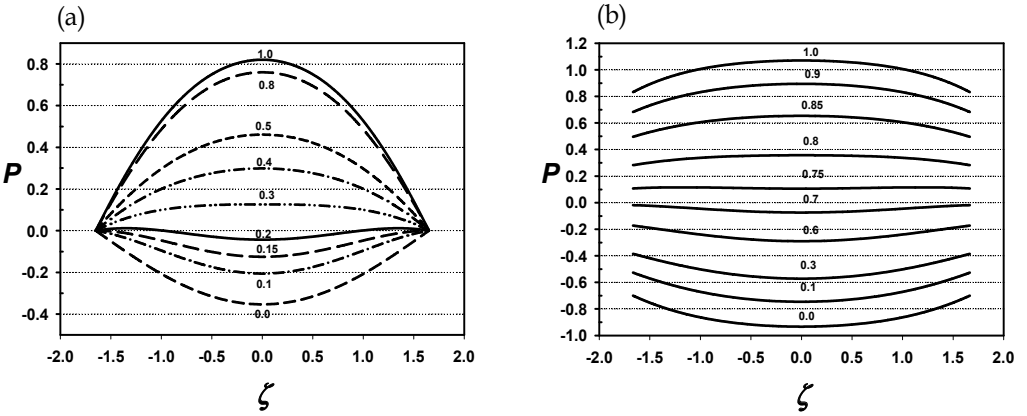

Fig. 1. Polarization profiles during switching, at various time in term of fraction of the total time τ_S'' to reversed the profile, at temperature $T = 0.6 T_{C0}$, applied field $E = 0.83 E_C$, for thickness ζ = 3.3: (a) δ = 0; (b) δ = 2.0. The number at each curve represents time taken to reach the stage in term of fraction of τ_S''. (Ong *et al*., 2008b)

For thick films, surface switching takes place relatively faster than the interior of the films (Fig. 2); the reversal of polarization begins near the surfaces first, and then goes on to the

centre, as shown in Figs. 2(a) and (b). This indicates that the domain wall is formed near the surfaces, followed by a domain wall movement towards the centre. Hence, when the film becomes thicker, the delay in switching at the centre of the film is more distinct compared with the delay nearer the film surfaces. In term of domain wall movement in the film, it obviously takes a longer time for a domain wall to move from the surface to the centre for a thick film than a thin film. However, the delay in switching at the centre is more remarkable in the zero-δ film as the film thickness increases. (Ong *et al.*, 2008a; 2008b).

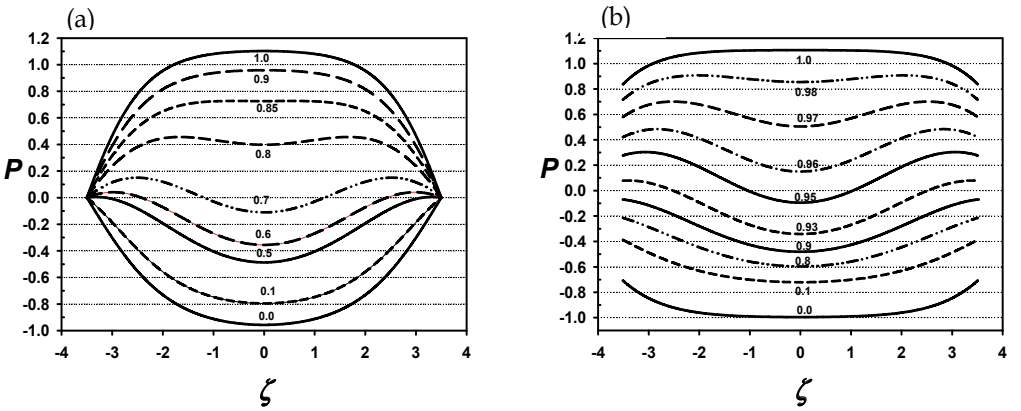

Fig. 2. Polarization profiles during switching, at various time in term of fraction of the total time $\tau_S^{''}$ to reversed the profile, at temperature $T = 0.6T_{C0}$, applied field $E = 0.83E_C$, thickness $\zeta = 7.0$ for (a) $\delta = 0$; (b) $\delta = 2.0$. The number at each curve represents time taken to reach the stage in term of fraction of $\tau_S^{''}$. (Ong *et al.*, 2008b)

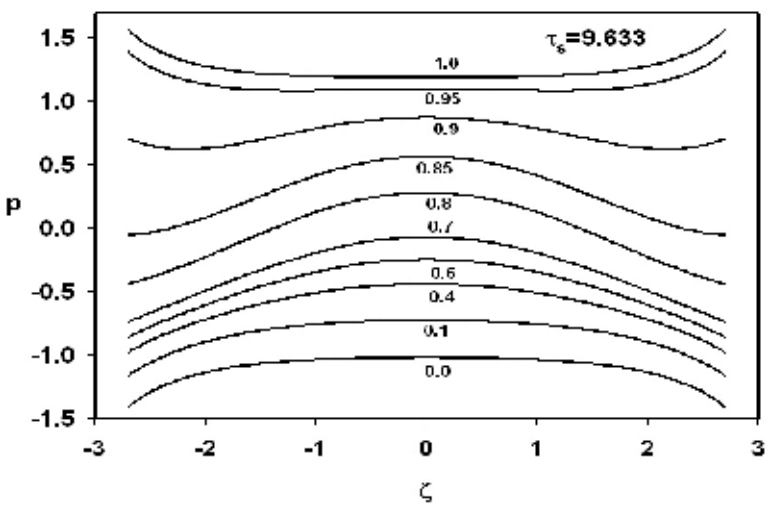

Fig. 3. Polarization profile during switching at various time in term of fraction of the total time $\tau_S^{''}$ to reversed the profile, for film thickness $\zeta = 5.4$, $\delta = -2$, $E = 1.50E_C$, $T = 0.0$. The number at each curve represents time taken to reach the stage in term of fraction of $\tau_S^{''}$.

The general trend in polarization reversal of a film, irrespective of value of δ, shows clearly that total time $\tau_S^{"}$ to reverse the profile is longer as the film gets thicker. In the case of negative δ for thick film, switching of dipole moments at the film centre takes place before that at the film surface, which is obviously shown in Fig. 3. This phenomenon is contrary to what we observed in a ferroelectric film with positive δ (Fig. 1 and Fig. 2); that is switching happens at surface before the film centre. For a ferroelectric film with negative δ, the polarization at the surfaces are greater than that at the centre.

6. Coercive field and switching time in ferroelectric films

The basic understanding of properties of thickness and surface dependence of switching time and coercive field in switching of ferroelectric materials is of great importance to the application of FE thin-films in non-volatile memories, for example the ferroelectric random access memory (FERAM). From the results of earlier work on switching behaviour of single crystal barium titanate (BaTiO3) (Merz, 1954; 1956; Miller and Savage, 1958; Stadler, 1958; Fatuzzo, 1962), a few empirical formulations which illustrate the dependence of switching time on applied electric field in switching of ferroelectric crystals are cited. For instant, in 1954 Merz reported that switching time τ_S is proportional to $1/(E-E_C)$ where E is an applied electric field and E_C is the coercive field strength. A couple of years later, Merz (1956) showed that switching time τ_S versus applied electric field E for low electric field (<10 kV/cm) in single crystal $BaTiO_3$ is an exponential function $\tau_S = \tau_\infty \exp(\alpha / E)$, where τ_∞ is the switching time for an infinite field strength and α is the activation field. This empirical formulation does not imply a definite coercive field in the switching of a single crystal $BaTiO_3$.

A similar empirical formulation for domain wall velocity as an exponential function of applied electric field E was proposed by Miller and Savage (1958); and their formulation also does not imply a definite coercive field in the switching of ferroelectric crystals. From their formulations, we can deduced that when an electric field E, however small is applied to a sample, it is just a matter of time; the dipole moments in the sample will ultimately be switched. Around the same period of time, Stadler (1958) extended Merz's work on a single crystal $BaTiO_3$ for high applied field, ranging from 10 kV/cm to 100 kV/cm; and he found that switching time τ_S is related to an applied electric field E according to a power law: $\tau_S = kE^{-n}$, where k is a constant and n is equal to about 1.5. Later, Fatuzzo (1962) proposed a combination of the power law and the exponential relation between switching time and applied electric field in his analytical calculations based on the assumption of sideway movement of the domain wall. Again, this new formulation shows that there is no definite coercive field in the switching of FE materials. Lately, Kliem and Tadros-Morgane (2005) have shown that their experimental data on extrinsic switching time τ_{ex} (time taken when the polarization has reached 90% of its maximum value) versus applied electric field E for various thicknesses of ultra-thin PVDF Langmuir-Blodgett films do not fit the formula $\tau_S = \tau_\infty \exp(\alpha / E)$ or the intrinsic switching formula $1/\tau_{in} = (E/E_C - 1)^{\frac{1}{2}}[1-(T-T_0)/(T_1-T_0)]^{\frac{1}{2}}$ derived by Vizdrik *et al*. (2003). In the later formula, t_{in} is the switching time, T_0 is the phase transition temperature and $T_1 = T_0 + 3B^3/(4\gamma A)$, where B, γ and A are the Landau parameters. This formula indicates

that there is a definite coercive field for PVDF material in the intrinsic homogeneous switching. Finally Kliem and Tadros-Morgane (2005) showed a best fit of their experimental data by a formulation $\tau_{ex} = \tau_{ex0} \exp(-\eta E / E_C)$ with τ_{ex0} and η depending on sample thickness and E_C, the coercive field obtained from the hysteresis loop.

On the other hand, evidence of a definite coercive field in the switching of FE materials are reported from experimental results, for example in sodium nobate ($NaNbO_3$) (Pulvari, 1960; . Miller *et al*., 1962). Another example is from Fousek and Brezina (1960; 1964), who reported that when the applied voltage on $BaTiO_3$ is below a certain threshold value, no domain wall movement has been observed; but when the applied field is above a threshold field, domain wall movement is detected to be out of phase with the applied voltage. Further more, Fang and Fatuzzo (1962) also reported the occurrence of coercive field on bismuth titanate (Bi_4TiO_{12}). In later measurements on good single crystals by Pulvari (1962, 1964 cited in Fatuzzo and Merz, 1967) also indicated there was definite coercive field in the switching and it was confirmed by Cummins (1965). More recent evidence of definite coercive field observed experimentally was reported in the switching kinetics of ferroelectric Langmuir-Blodgett films of 70% vinylidenefluoride and 30% trifluoroethylene copolymer with thickness up to 15 nm (Vizdrik *et al*., 2003).

There are a couple of theoretical models proposed to study the switching behaviours of FE films; the Kolmogorov-Avrami-Ishibashi theory (Ishibashi and Orihara, 1992a; 1992b; Ishibashi, 1993) which is originated from a model of crystal growth (Kolmogorov, 1937; Avrami, 1939, 1940, 1941) and the Landau-typed model (Ishibashi, 1990; 1992; Wang and Smith, 1996). In the later model, one of the authors (Ishibashi, 1992) fitted his numerical data by the formula $\tau_S = \tau_\infty \exp(\alpha / E)$. While the other authors (Ishibashi, 1990; Nagaya and Ishibashi, 1991) fitted their numerical data by the empirical formulations of Merz (1954, 1956) and Stadler (1958) mentioned above. However, they have not mentioned which formulation gives the best fit. With these developments in the area of research in switching phenomena of FE materials especially in FE thin films, we are motivated to use Landau Devonshire (L-D) free energy of a FE film proposed by Tilley and Zeks (T-Z) (1984) and Landau Khalatnikov equation of motion to look into the dependence of switching time on applied electric field. We have also investigated the effects of thickness on coercive field and switching time and made comparisons with some experimental findings. From the literature, some experimental results (Hase and Shiosaki, 1991; Fujisawa *et al*., 1999) show that coercive field increases with decreasing film thickness while others (Wang *et al*., 2002; Yanase *et al*., 1999) claim the reversed; and these contradictions are explained by the effects of negative and positive values of extrapolation length, δ in the TZ model (Tilley and Zeks, 1984; Ong et al., 2001; Ahmad and Ong, 2009).

There are several definitions of switching time in the literature (Fatuzzo and Merz, 1967; Ishibashi, 1990; 1992; Nagaya and Ishibashi, 1991; Omura and Ishibashi, 1992; Katayama *et al*., 1993); however, in our case, the switching time τ_S is taken as the time taken when the current has reached 10% of its maximum value (Ahmad and Ong, 2009, Omura and Ishibashi, 1992; Katayama *et al*., 1993) similar to what we have done in our previous work[32]. The variation of switching time τ_S in a film of thickness l = 2.0 and extrapolation length $\delta = 3.0$ at temperature t = 0.0, with applied field e is shown in Fig. 4. The triangular markers indicated in Fig. 4 represent the numerical data obtained from our calculations. To investigate whether coercive field truly exists in ferroelectric thin films, curves based on

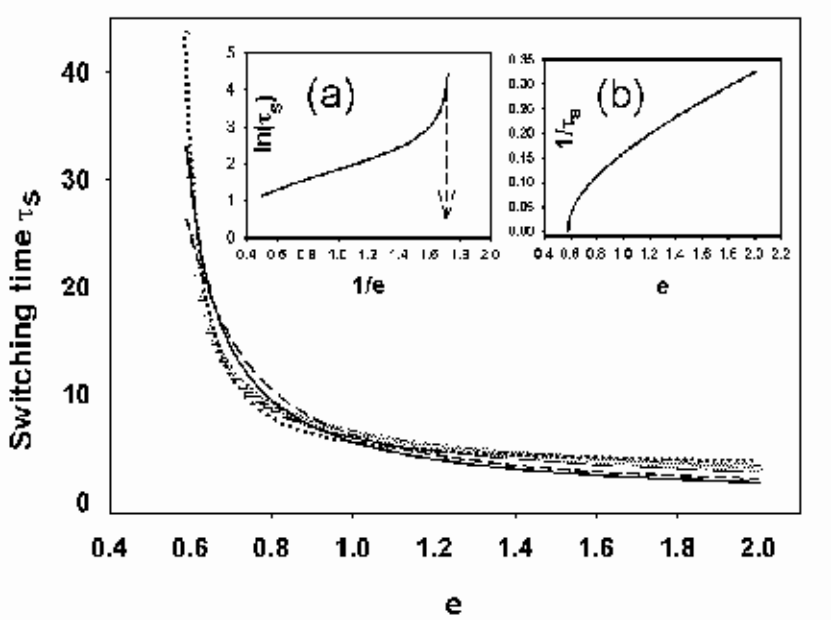

Fig. 4. Switching time τ_S versus applied electric field e for film thickness $l = 2.0$, extrapolation length, $\delta = 3$, and temperature $T = 0.0$. Triangular markings represent the numerical data. The data are fitted by the following functions: dotted line is for $\tau_S = \tau_0 \exp[a/(e-b)]$, solid line is for $\tau_S = k/(e-\alpha)$, and dashed line is for $\tau_S = \tau_0 \exp(\beta/e)$. The inset (a) shows that $\ln(\tau_S)$ vs. $1/e$, and the arrow indicates the coercive field b in the function $\tau_S = \tau_0 \exp[a/(e-b)]$. The inset (b) shows the reciprocal switching time versus e. (Ahmad and Ong, 2011b)

three chosen formulations are drawn to fit the data. The solid-line is drawn based on the formulation by Merz (1954)

$$\tau_S = k/(e-\alpha), \tag{20}$$

where e is the applied field and k and α are constants. From this solid-line curve, the switching time diverges at $e = \alpha$ where α is the sort of coercive field; and the FE film can not be switched for field lower than the coercive field α. Secondly, we have used the empirical formulation (Merz, 1956; Miller and Savage, 1958),

$$\tau_S = \tau_0 \exp(\beta/e) \tag{21}$$

where τ_0 and β are constants, to fit our calculated data; and the dashed line in Fig. 4 represents this formulation. Finally, we fit our data by the following formulation:

$$\tau_S = \tau_0 \exp[a/(e-b)] \tag{22}$$

where τ_0, a and b are constants. The dotted-line curve in Fig. 4 is drawn from Eq. (22) and it shows that switching time τ_S diverges when the applied electric field e approaches b. In order to determine the best fit to our calculated data among the three formulations plotted in Fig. 4, a regression analysis, tabulated in Table 1, was carried out for each fitting.

Formulations	Regression factor, $\boldsymbol{R}$	$\sqrt{R}$	Standard error	Values of coefficients
$\tau_S = k/(e-\alpha)$	0.9550	0.9119	1.5573	$k = 0.433$ $\alpha = 0.579$
$\tau_S = \tau_0 \exp[a/(e-b)]$	0.9891	0.9783	0.7753	$\tau_0 = 6.278$ $a = 0.014$ $b = 0.577$
$\tau_S = \tau_0 \exp(\beta/e)$	0.9305	0.8658	1.9225	$\tau_0 = 0.793$ $\beta = 2.067$

Table 1. Regression analysis of curve fittings for the numerical data shown in Fig. 4

Based on the regression factors obtained, we find that our simulated data are best fitted by Eq. (22) with the highest regression factor of 0.99. To ascertain this fact, a plot of $\ln\tau_S$ versus $1/e$ from our data is shown as the inset (a) of Fig. 4, where τ_S diverges at the value corresponds to b in the equation which is the presumed coercive field. While inset (b) of Fig. 4, which is also plotted from our data, shows the reciprocal switching time $1/\tau_S$ versus electric field e, where the reciprocal switching time decreases precipitously towards zero when the field decreases towards the presumed coercive field b. The same trend of $1/\tau_S$ versus electric field e for PVDF Langmuir-Blodgett films is shown by Vizdrik *et al*. (2003).

Figs. 5 (a), (b) and (c) show the plots of calculated data for switching time τ_S versus applied field e in triangular markers when the film has negative extrapolation length δ. In each of these plots, a lined curve is drawn to represent the three formulations we have discussed in the previous paragraph, respectively. The electric field dependence of switching time is analyzed statistically and the regression factors for the curves to fit the data are compared as shown in Table 2. From the analysis, it has again shown that switching time versus applied field for a film with negative extrapolation length δ follows the same formulation given by Eq. (22). Other than the two examples given in Figs. 4 and 5 and Tables 1 and 2, we have also fitted other calculated data for various thicknesses and values of δ by the formulations mentioned above; and we have found that the formulation given in Eq. (22) gives consistently the highest regression factor for various film thicknesses and extrapolation lengths compared with the other two formulations. Hence, a thin ferroelectric film has a definite coercive field and the switching time is an exponential function of electric field e, which may be in the form suggested by Eq. (22).

In order to illustrate how switching time τ_S of a ferroelectric film depends on film thickness and surface order parameter more explicitly, graphs of τ_S versus thicknesses l for films with positive δ and negative δ are plotted respectively in Figs. 6 and 7. Fig. 6 shows that switching time increases monotonically with increasing film thickness for films with positive δ's. The increased in switching time from thickness closed to critical thickness is steep and as the film becomes thicker, the increased in switching time becomes gradual. Indication of critical thickness in Fig. 6 corresponds with the fact that a ferroelectric film of positive δ surface property, ceases to behave as ferroelectric when the film thickness falls below the critical thickness. For thin films, Fig. 6 also shows that surface parameter

significantly increases with increasing positive δ, but this increasing trend becomes less significant when film becomes thick; and it approaches the limit of a bulk case when the film is thick enough.

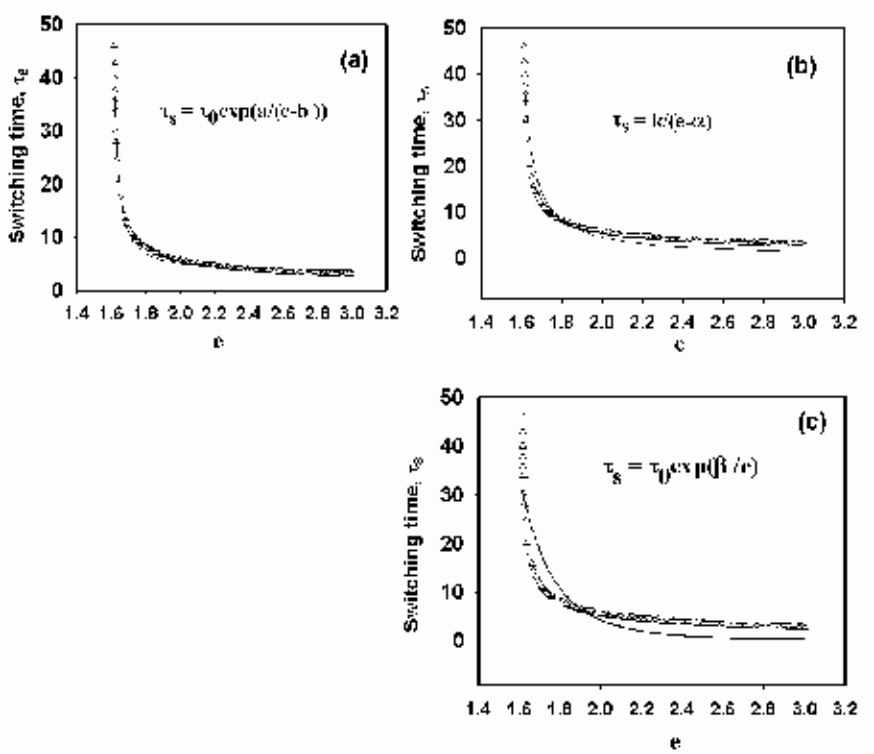

Fig. 5. Switching time τ_S versus applied electric field e for film thickness $l = 2.0$, extrapolation length $\delta = -3$, and $t = 0.0$. The triangular markings in (a), (b), and (c) represent the numerical date. The data are fitted by $\tau_S = \tau_0 \exp[a/(e-b)]$ in (a), $\tau_S = k/(e-\alpha)$ in (b) and $\tau_S = \tau_0 \exp(\beta/e)$ in (c). (Ahmad and Ong, 2011b)

Formulations	Regression factor, ***R***	$\sqrt{R}$	Standard error	Values of coefficients
$\tau_S = k/(e-\alpha)$	0.9711	0.9430	1.9225	k = 1.9439; $\alpha = 1.5643$
$\tau_S = \tau_0 \exp[a/(e-b)]$	0.9931	0.9863	0.9458	$\tau_0 = 3.3300$ a =0.1883 b =1.5405
$\tau_S = \tau_0 \exp(\beta/e)$	0.8947	0.8005	3.5973	$\tau_0 = 0.0011$ $\beta = 16.5115$

Table 2. Regression analysis of curve fittings for the numerical data shown in Fig. 5

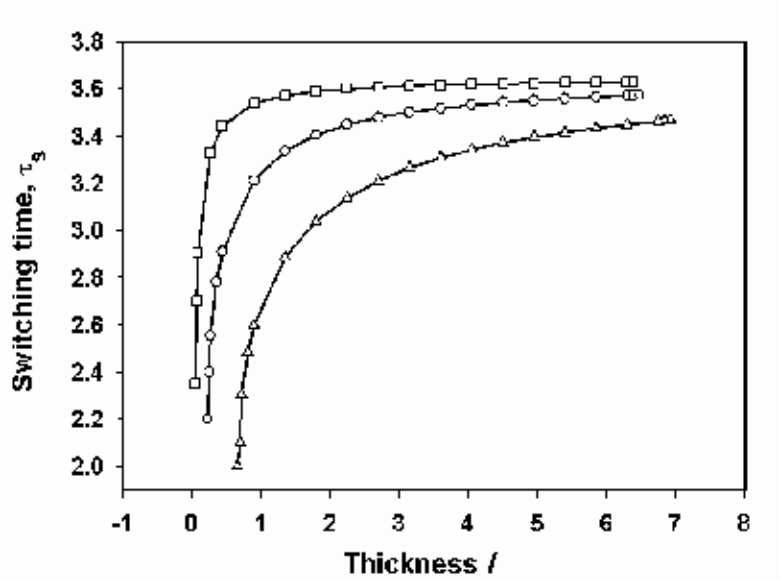

Fig. 6. Switching time τ_S versus film thickness l for various positive δ, applied electric field e = 2.0, and temperature t = 0.0. Symbols: Triangle for $\delta = 3.0$, circle for $\delta = 10.0$ and square for $\delta = 50.0$. (Ahmad and Ong, 2011b)

In negative δ case, Fig. 7 shows that τ_S becomes infinitely large for ultra-thin films. Switching time decreases significantly as film thickness increases from ultra-thin state; subsequently, the decrease in τ_S becomes gradual and approaches the limiting value when the film thickness reaches the bulk thickness. In general, a strong surface effect in film with positive of negative δ corresponds to small magnitude of surface parameter $|\delta|$. Hence, in the case of negative δ, switching time decreases with increasing magnitude of surface parameter $|\delta|$ (Fig. 7) and this surface effect in film with negative δ on switching time tones down when film becomes thick.

Figs. 8 and 9 show the thickness dependence of coercive field for positive δ and negative δ respectively. In Fig. 8 we find that for positive δ, the coercive field decreases with decreasing film thickness; and it is consistent with the experimental results of Wang *et al.* (2002). Deduction from Eq. (13) and Eq. (14) shows that the initial remnant polarization decreases with decreasing thickness when the extrapolation length δ is positive; and this phenomenon agrees with the results obtained from the lattice model (Ricinschi *et al*., 1998).

While for negative δ (Fig. 9), coercive field e_{CF} increases with decreasing film thickness and the values of e_{CF} are above e_C of the bulk. This result is also consistent with the experimental results reported (Hase and Shiosaki, 1991; Fujisawa *et al*., 1999). The semi-empirical scaling law of Janovec-Kay-Dunn (JKD) on the thickness dependence of coercive field E_C predicts that $E_C(d) \propto d^{-2/3}$, where d is the film thickness (Dawber *et al*., 2003). This implies that the negative δ case of our theoretical prediction, where coercive field increases with decreasing thickness, follows the same trend as the JKD law. However, our data on coercive field versus thickness follow the exponential relationship rather than the negative power law.

It is worth giving some comments on Figs. 8 and 9. For positive δ given in Fig. 8, it is interesting to see that the coercive field has finite size behaviour similar to that of the Curie temperature (Zhong, 1994; Wang et al., 1994; Wang and Smith, 1995; Mitoseriu *et al*., 1996) where FE phase vanishes at certain critical thickness (Ishibashi *et al*., 1998). Extrapolating the three curves in Fig. 8 to meet the horizontal axis gives the critical thickness of 0.68, 0.24 and 0.04 for $\delta = 3.0$, 10.0 and 50.0 respectively. While for negative δ (Fig. 9), it is clear that there is no size-driven phase transition. For a film of given thickness, increasing value of positive δ , increases the coercive field of the film. From Fig. 8, it is obvious that for a FE film of large values of positive δ and l (thicker film), the coercive field approaches 1 ($e_{CF} \to e_C = 1$), where $e_C = 1$ is the dimensionless coercive field of the bulk at temperature t = 0.0.

In contrary to a film with surface effect of positive δ , it is clearly shown in Fig. 9 that in a thin film of small l with surface effect of negative δ, the coercive field of the film increases with increasing surface effect (smaller $|\delta|$). However, the influence of surface effect becomes weaker as the film becomes thicker as illustrated in Fig. 9, where the coercive fields of thick films, irrespective of magnitudes of negative δ, approach the bulk coercive field. It is interesting to see that surface effect, which is parameterized by the extrapolation length $\pm\delta$ in this model, is more significant for thin films (small values of l); but for thick films, surface effect is weak and less significant.

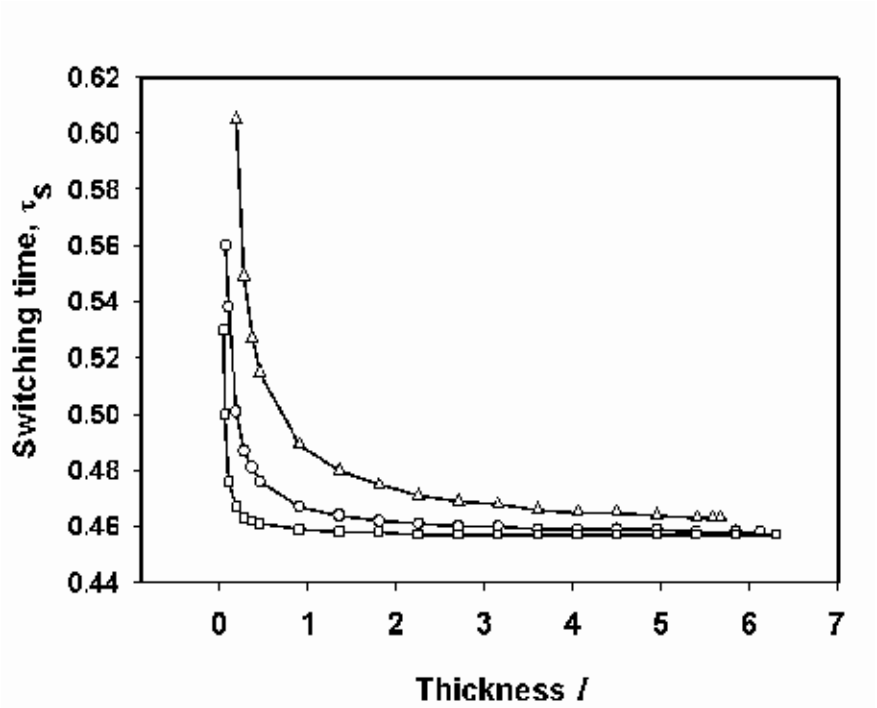

Fig. 7. Switching time τ_S versus film thickness l for various negative δ , applied electric field e = 25.0, and temperature t = 0.0.. Symbols: Triangle for $\delta = -3.0$, circle for $\delta = -10.0$ and square for $\delta = -50.0$. (Ahmad and Ong, 2011b)

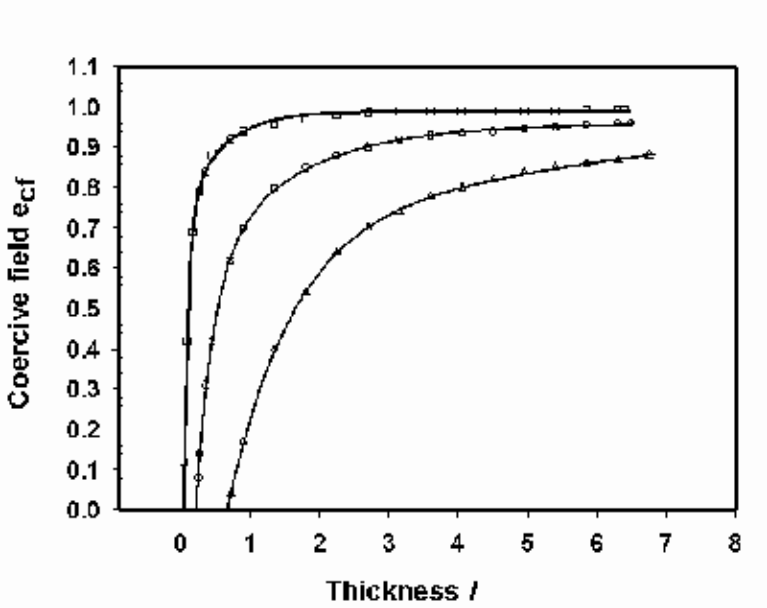

Fig. 8. Coercive field e_{CF} versus film thickness l for various positive δ, and temperature t = 0.0. Symbols: Triangle for $\delta = 3$, circle for $\delta = 10$ and square for $\delta = 50$.
(Ahmad and Ong, 2011b)

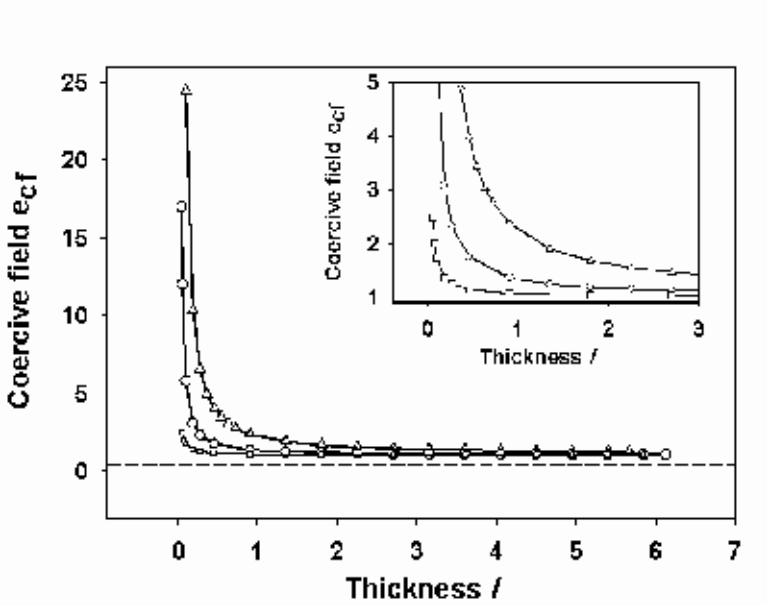

Fig. 9. Coercive field e_{CF} versus film thickness l for various negative δ, and temperature t = 0.0. Symbols: Triangle for $\delta = -3$, circle for $\delta = -10$ and square for $\delta = -50$. The dashed line is bulk coercive field $e_c = 1.0$. The inset shows the zoom in view for $l \le 3$.
(Ahmad and Ong, 2011b)

7. Hysteresis loops of ferroelectric films

Another experimental method in the elucidation of switching behaviours of a ferroelectric film is by applying a sinusoidal electric field to the film and observing the hysteresis loops. From the hysteresis loop obtained, one can find out the coercive field and the remnant polarization; hence the switching characteristics of the film. We use the TZ model, which is described in Section 2, to simulate the hysteresis loops of a ferroelectric film in the application of sinusoidal electric field. The influence of the sinusoidal electric field strength e_0 on the ferroelectric hysteresis loop for a ferroelectric thin film with positive δ, at constant temperature, shows that the average remnant polarization $\overline{p}_r$ and coercive field increase with increasing e_0 (Fig. 10 (a)); but for thick film, only the coercive field is increased (Fig. 10(b)). This result is consistent with the experimental result (Tokumitsu et al., 1994) and the theoretical result of lattice model given by Omura et al. (1991).

The effect of the temperature t on the hysteresis loop for positive and negative δ's can be observed from the curves in Figs. 11 (a) and (b). It can be seen that the system at higher temperature needs lower applied electric field e to switch; and the average polarization $\overline{p}_r$ is lower at higher temperature as the system is at a state which is nearer to the phase transition. These results are consistent with experimental results given by Yuan et al. (2005); and from their studies on strontium Bismuth Titanate $Sr_2BiTi_3O_{12}$(SBT) which has lower density of oxygen vacancies, so the pinning of domain wall is weak. However our result is not consistent with the experimental results given by Zhang et al. (2004) on $\overline{p}_r$ where they used $Ba_{3.25}La_{0.75}Ti_3O_{12}$ (BLT) that has high density of oxygen vacancies which tends to be trapped at the domain boundaries. The oxygen vacancies formed the domain walls pinning centres and hence reduce the number of switchable dipoles. Nevertheless, our study is consistent with the theoretical results of lattice model reported by Tura et al. (1997). Similar features of decreasing size of hysteresis loops with increasing temperature for both positive and negative signs of δ given in their results are found in Figs. 11 (a) and (b).

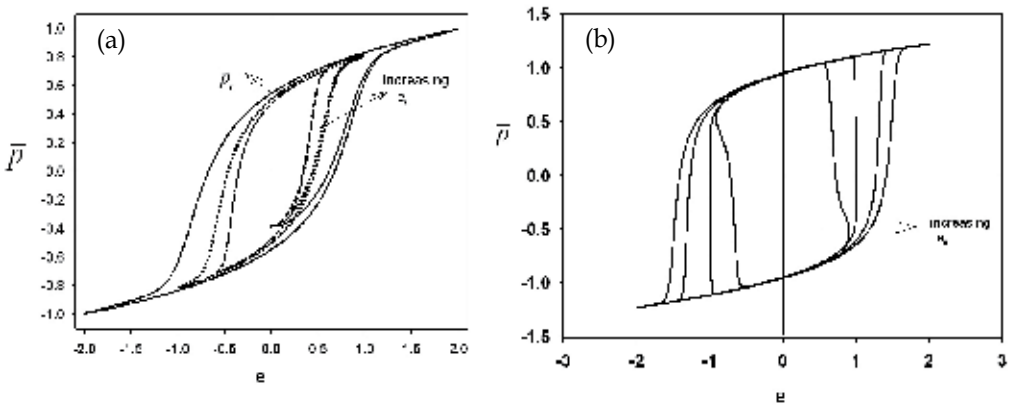

Fig. 10. Hysteresis loops at t = 0.0, $\delta = 3$, $\omega = 0.08$ for various values of field strength e_0 : (a) 0.6, 1.0, 2.0 and l = 1.35; (b) 0.91, 1.0, 1.5, 2.0 and l = 5.0. (Ong and Ahmad, 2009)

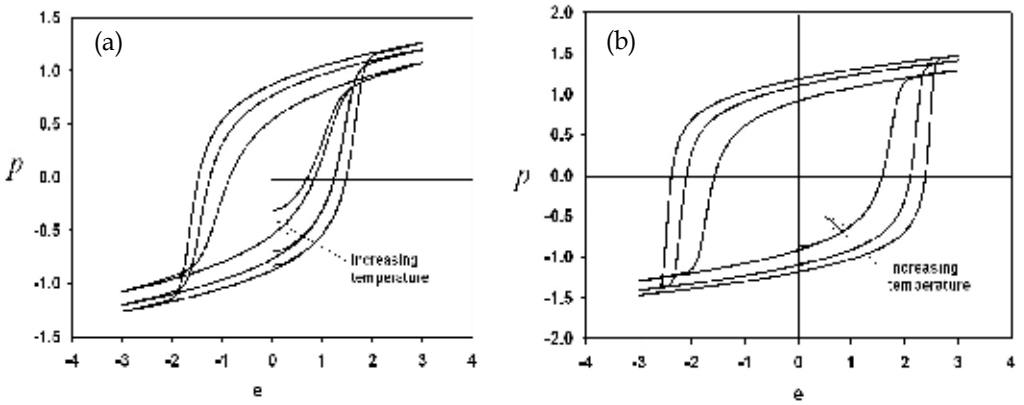

Fig. 11. Hysteresis loops for various values of temperature t: 0.0, 0.2, 0.6.; l = 2.00, e_0 = 3.0, ω = 0.1. and (a) δ = 3.0; (b) δ = −3.0. (Ong and Ahmad, 2009)

The effects of thickness l on hysteresis loops are illustrated in Figs. 12 (a) and (b) for positive and negative δ, respectively. Fig. 12 (a) reveals that for a given positive δ, coercive field e_{CF} and remnant polarization $\overline{p}_r$ increases with increasing thickness and it is consistent with the experimental results by Wang *et al.* (2002) and Yanase *et al*. (1999), and also in agreement with the results obtained from the lattice model (Ricinschi *et al*., 1998)). On the contrary, Hase *et al*. (1991) and Fujisawa *et al*. (1999) in their hysteresis loops measurements found that e_{CF} decreases with increasing film thickness; and this trend of thickness dependence of e_{CF} is found in Fig. 12 (b). In Fig. 12 (b), it reveals that for negative δ, both e_{CF} and $\overline{p}_r$ decrease with increasing thickness and these values of e_{CF} are above e_{C0} of the bulk. However, $\overline{p}_r$ is reported to increase with increasing thickness by Hase *et al*. (1991); but Fujisawa *et al*. (1999) reported that $\overline{p}_r$ is almost unchanged with thickness.

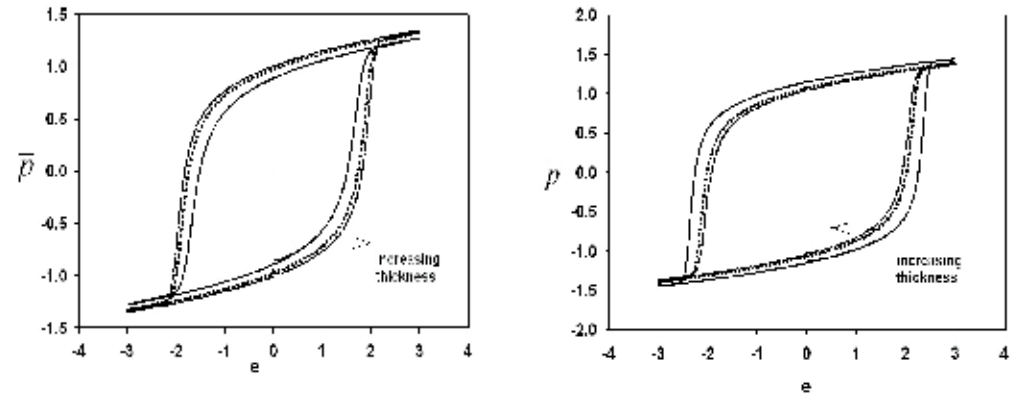

Fig. 12. Hysteresis loops for various values of thickness l: 0.72, 2.0, 5.0; t= 0.00, e_0 = 3.0, ω = 0.1. and (a) δ = 10.0; (b) δ = −10.0. (Ong and Ahmad, 2009)

Surface effects of FE films are represented via the effects of positive and negative extrapolation lengths on hysteresis loop are shown in Figs. 13 (a) and (b) for positive and negative δ, respectively. Both values of e_{CF} and $\overline{p}_r$ increase with increasing values of positive δ (Fig. 13 (a)). This effect can be explained by the increase of initial polarization profile with increasing values of positive δ. It is obvious from Fig. 13 (b) that increasing $|\delta|$, which leads to decreasing surface polarization, tends to decrease e_{CF} and $\overline{p}_r$.

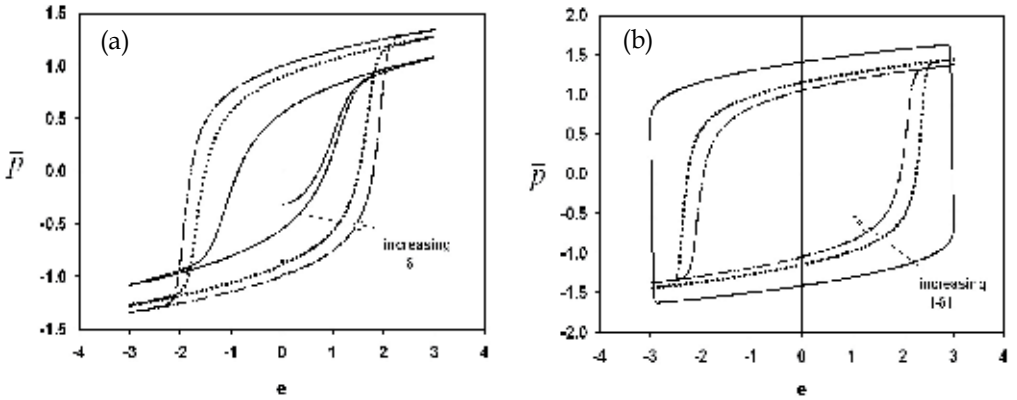

Fig. 13. Hysteresis loops for various values of δ: (a) δ =3.0, 10.0 and 50.0; (b) δ = −3.0, −10.0 and −50.0; for t = 0.0, e_0 = 3.0, and ω = 0.1. (Ong and Ahmad, 2009)

8. Summary and future work

From the analytical calculations using the TZ model for ferroelectric films, we discovered that the minimum thickness of a ferroelectric film is dependent on critical temperature and surface parameter δ; and these parameters are material dependent. In our study of the intrinsic switching phenomena of a ferroelectric film, an exponential function, proposed in Eq. (22), for switching time dependence of applied electric field reveals that a ferroelectric film has an intrinsic coercive field e_{CF}; and this may provide a technical reference to device designers. We have also found that by increasing the film thickness, switching time τ_S and coercive field e_{CF} of a film will increase for film with positive δ; but these intrinsic values will decrease for film with negative δ. The surface effect ($\pm\delta$) on switching time and coercive field of a film is more spectacular for thinner films. The dependence of coercive field and switching time on surface parameter δ, discovered from our theory, indicates that when negative-δ materials are used in fabricating memory devices, switching time τ_S and coercive field e_{CF} will increase when film thicknesses are reduced. Since nano-sized ferroelectric film is currently used in fabricating ferroelectric RAMs, the use of this type of materials, interpreted by theory as negative-δ material, in memory fabrication will be problematic. Hence, we should avoid using materials with negative δ, such as triglycine sulfate (Hadni *et al*., 1983) and potassium nitrate (Scott *et al*., 1988). Ferroelectric materials with position δ are favourable for finite-sized memory device applications; and an example of such materials is lead zirconium titanate.

On the whole, surface parameter δ is a crucial parameter to consider when making the choice of material for thin film fabrication in memory devices. However, it is beyond the scope of a phenomenological model to predict the value of δ from material properties; the type of surface parameter δ in a material could be determined theoretically, for example, by comparison of the film critical temperature with the bulk value. When the film critical temperature is lower than the bulk critical temperature, then the material is said to be of positive-δ material; and for the negative-δ material, the opposite is true.
In our current work, we have restricted attention to materials in which the bulk phase transition is second order and the extension of our analysis to first-order materials is straightforward. The model presented here is concerned with single domain switching, as might occur in a sample of small lateral dimension. Lastly, since in reality, ferroelectric thin films are fabricated on conductive materials (such as $SrRuO_3$) as electrodes, we have included the effects of misfit strain in the study of phase transition of epitaxial film of $BaTiO_3$ (Ahmad and Ong, 2011a). The results showed that the order of transition is modified and the transition temperature has also been increased when the misfit strain is high. The extension of the model to the study of strain effect on switching phenomena is in our immediate plan and we anticipate the results from this study will provide more hints to resolve the current problems in memory device application.

9. Acknowledgments

The work is funded by the FRGS grant, Malaysian Ministry of Higher Learning (Grant No.: 305/PFIZIK/613605).

10. Keywords

ferroelectric, thin films, surface effect, switching properties

11. References

Ahmad M., Ong L. H., and Tilley D. R., Effects of Extrapolation Length delta on Switching Time and Coercive Field, *Journal of Applied Physics*, Vol. 105, 061602 (March 2009) pp.1 – 6, ISSN: 1089-7550

Ahmad M. and Ong L. H., Phase Transitions of Strained Barium Titanate Epitaxial Films, unpublished (2011a)

Ahmad M. and Ong L. H., Switching Time and Coercive Field in Ferroelectric Thin Films, *Journal of Applied Physics*, (in press), (2011b).

Auciello O., Scott J. F. and Ramesh R., The Physics of Ferroelectric Memories, *Physics Today*, Vol 51 issue 7 (July 1998), pp. 22 – 27

Avrami M., Kinetics of Phase Change. I General Theory, *Journal of Chemical Physics*, Vol 7, (1939) pp. 1103-12, ISSN: 1089-7690

Avrami M., Kinetics of Phase Change. II Transformation-Time Relations for Random Distribution of Nuclei, *Journal of Chemical Physics*, Vol 8, (1940) pp. 212-24, ISSN: 1089-7690

Avrami M., Granulation, Phase Change, and Microstructure Kinetics of Phase Change. III, *Journal of Chemical Physics*, Vol 9, (1941) pp. 177-84, ISSN: 1089-7690

Colla E. L., Hong S., Taylor D. V., Tagantsev A. K., Setter N., and No K, Direct observation of region by region suppression of the switchable polarization (fatigue) in Pb(Zr,Ti)O_3 thin film capacitors with Pt electrodes, *Applied Physics Letter*, Vol 72, (1998) pp. 2763-5, ISSN: 1077-3118

Cummins S. E., Switching Behavior of Ferroelectric $Bi_4Ti_3O_{12}$, *Journal of Applied Physics*, Vol 36, (1965) pp. 1958-1962, ISSN: 1089-7550

Dawber M., Chandra P., Littlewood P. B. and Scott J. F., Depolarization Corrections to the Coercive Field in Thin-film Ferroelectrics, *Journal of Physics: Condensed Matter*, Vol 15, (2003) pp. L393-L398, ISSN: 1361-648X

Dawber M., Rabe K.M. and Scott J. F., Physics of thin-film ferroelectric oxides, *Review of Modern Physics*, Vol. 77, No.17, (2005), pp. 1083, ISSN: 1539-0756

Duiker H. M., and Beale P. D., Grain-size effects in ferroelectric switching, *Physical Review B* Vol 41 (1990) pp. 490-5 , ISSN: 1550-235x

Fang P. H. and Fatuzzo E., Switching Properties in Ferroelectrics of the Family $Bi_4Ba_{m-2}Ti_{m+1}O_{3(m+2)}$, *Journal of the Physical Society Japan*, Vol 17, (1962) pp. 238-238, ISSN: 1347-4073

Fatuzzo E., Theoretical Considerations on the Switching Transient in Ferroelectrics, *Physical Review*, Vol 127, (1962) pp. 1999-2005, ISSN: 1536-6065

Fousek J. and Brezina B., The Movement of Single 90° Domain Walls of $BaTiO_3$ in an Alternating Electric Field, *Czechoslovak Journal of Physics*, Vol 10, (1960) pp. 511-528; and The Motion of 90° Wedge Domains in $BaTiO_3$ in an Alternating Electric Field, *Czechoslovak Journal of Physics*, Vol 11, (1961) pp. 344-359, ISSN: 1572-9486

Fousek J. and Brezina B., Relaxation of 90° Domain Walls of $BaTiO_3$ and their Equation of Motion, *Journal of the Physical Society Japan*, Vol 19, (1964) pp. 830-838, ISSN: 1347-4073

Fatuzzo E. and Merz W. J., *Ferroelectricity* (Amsterdam: North-Holland, 1967).

Fujisawa H., Nakashima S., Kaibara K., Shimizu M. and Niu H., Size Effects of Epitaxial and Polycrystalline Pb(Zr, Ti)O_3 Thin Films Grown by Metalorganic Chemical Vapor Deposition, *Japanese Journal of Applied Physics*, Vol 38, (1999) pp. 5392-5396, ISSN: 1347-4065

Ganpule C. S., Nagarajan V., Li H., Ogale A. S., Steinhauer D. E., Aggarwal S., Williams E., Ramesh R. and De Wolf P., Role of 90^0 domains in lead zirconate titanate thin films, *Applied Physics Letters*, Vol 77 (2000) pp. 292-4, ISSN: 1077-3118

Hadni A., Thomas R., Ungar S., and Gerbaux X., Drastic modifications of electrical properties of ferroelectric crystal plates withthickness, the case of triglycine sulphate, *Ferroelectrics*, Vol 47, (1983). pp.201, ISSN: 0015-0193

Hase T. and Shiosaki T., Preparation and Switching Kinetics of Pb(Zr, Ti)O_3 Thin Films Deposited by Reactive Sputtering, *Japanese Journal of Applied Physics*, Vol 30, (1991) pp. 2159-2162, ISSN: 1347-4065

Hashimoto S., Orihara H., and Ishibashi Y., D-E Hysteresis Loop of TGS Based on the Avrami-Type Model, *Journal of Physical Society Japan*, Vol 63 (1994) pp. 1601-10, ISSN: 1347-4073

Ishibashi Y., Theory of Polarization Reversals in Ferroelectrics Based on Landau-Type Free Energy, *Japanese Journal of Applied Physics*, Vol 31, (1992) pp. 2822-2824, ISSN: 1347-4065

Ishibashi Y., A Model of Polarization Reversal in Ferroelectrics, *Journal of the Physical Society Japan*, Vol 59, (1990) pp. 4148-4154, ISSN: 1347-4073

Ishibashi Y., A Theory of Polarization Reversals in Finite Systems, *Integrated Ferroelectrics*, Vol 3, (1993) pp. 351-354, ISSN: 1607-8489

Ishibashi Y., A Model of Polarization Reversal in Ferroelectrics, *Journal of Physical Society Japan*, 59 (1990) pp. 4148-54, ISSN: 1347-4073

Ishibashi Y., Orihara H. and Tilley D. R., 1998 Thickness Transitions of Ferroelectricity in Thin Films, *Journal of Physical Society Japan*, Vol 67 (1998) pp. 3292-7, ISSN: 1347-4073

Ishibashi Y. and Orihara H., Size Effect in Ferroelectric Switching, *Journal of the Physical Society Japan*, Vol 61, (1992) pp. 4650-4656, and A Statistical Theory of Nucleation and Growth in Finite Systems, *Journal of the Physical Society Japan*, Vol 61, (1992) pp. 1919-1925, ISSN: 1347-4073

Ishibashi Y., Iwata M. and Musleh A. M. A., Exact Expressions for Some Dielectric Properties of Ferroelectric Thin Films Based on the Tilley–Zeks Model, *Journal of Physical Society Japan*, Vol 76 (2007) pp. 104702, ISSN: 1347-4073

Katayama T., Shimizu M. and Shiosaki T., Switching Kinetics of Pb(Zr, Ti)O_3 Thin Films Grown by Chemical Vapor Deposition, *Japan Journal of Applied Physics*, Vol 32, (1993) pp. 3943-3949, ISSN: 1347-4065

Kliem H. and Tadros-Morgane R., Extrinsic Versus Intrinsic Ferroelectric Switching: Experimental Investigations Using Ultra-thin PVDF Langmuir–Blodgett Films, *Journal of Physics D: Applied Physics*, Vol 38, (2005) pp. 1860-1868, ISSN: 1361-6463

Kolmogorov A. N., Izv. Akad. Nauk SSSR, Ser. Mat. 3, 355 (1937).

Lohse O., Grossmann, Boettger U., Bolten D., and Waser R., Relaxation mechanism of ferroelectric switching in Pb(Zr,Ti)O_3 thin films, *Journal of Applied Physics*, Vol 89 (2001) pp. 2332-6, ISSN: 1089-7550

Merz W. J., Domain Formation and Domain Wall Motions in Ferroelectric $BaTiO_3$ Single Crystals, *Physical Review*, Vol 95, (1954) pp. 690-698, ISSN: 1536-6065

Merz W. J., Switching Time in Ferroelectric $BaTiO_3$ and Its Dependence on Crystal Thickness, *Journal of Applied Physics*, Vol 27, (1956) pp. 938-943, ISSN: 1089-7550

Miller R. C. and Savage A., Velocity of Sidewise 180° Domain-Wall Motion in $BaTiO_3$ as a Function of the Applied Electric Field, *Physical Review*, Vol 112, (1958) pp. 755-762, ISSN: 1536-6065

Miller R. C., Wood E. A., Remeika J. P. and Savage A., Na($Nb_{1-x}V_x$)O_3 System and ``Ferrielectricity'', *Journal of Applied Physics*, Vol 33, (1962) pp. 1623-1630, ISSN: 1089-7550

Nagaya T. and Ishibashi Y., A Model of Polarization Reversal in Ferroelectrics. II, *Journal of Physical Society Japan*, Vol 60, (1991) pp. 4331-4336, ISSN: 1347-4073

Omura M., Adachi H., and Ishibashi Y.; Simulations of Ferroelectric Characteristics Using a One-Dimensional Lattice Model, *Japanese Journal of Applied Physics*, Vol 30, (1991) pp. 2384 -*2387* , ISSN: 1347-4065

Omura M. and Ishibashi Y., Simulations of Polarization Reversals by a Two-Dimensional Lattice Model, *Japanese Journal of Applied Physics*, Vol 31, (1992) pp. 3238-3240, ISSN: 1347-4065

Ong L. H., Osman J., and Tilley D. R., Landau theory of second-order phase transitions in ferroelectric films, *Physical Review B*, Vol 63, 144109 (2001), ISSN: 1550-235x

Ong L. H., Ahmad M. and Osman J., Switching Behaviours of Ferroelectric Systems of Finite Size, *Ferroelectrics*, Vol. 375, (2008a), pp. 115–121, ISSN: 0015-0193

Ong L. H., Ahmad M. and Osman J., *Jurnal Fizik Malaysia*, Vol 29, (2008b) pp. 11–14, ISSN: 0128-0333

Ong L. H. and Ahmad M., Tilley-Zeks Model in Switching Phenomena of Ferroelectric Films, *Ferroelectrics*, Vol. 380, (2009), pp. 150–159, ISSN: 0015-0193

Orihara H., Hashimoto S., and Ishibashi Y., A Theory of D-E Hysteresis Loop Based on the Avrami Model, *Journal of Physical Society Japan*, Vol 63 (1994) pp. 1031-5, ISSN: 1347-4073

Orihara H. and Ishibashi Y., A Statistical Theory of Nucleation and Growth in Finite Systems, *Journal of the Physical Society Japan*, Vol 61, (1992) pp. 1919-1925, ISSN: 1347-4073

Pulvari C. F., Ferrielectricity, *Physical Review*, Vol 120, (1960) pp. 1670-1673, ISSN: 1536-6065

Ricinschi D., Harangea C., Papusoi C., Mitoseriu L., Tura V. and Okuyama M., Analysis of Ferroelectric Switching in Finite Media as a Landau-type Phase Transition, *Journal of Physics: Condensed Matter*, Vol 10, (1998) pp. 477-492, ISSN: 1361-648X

Scott J. F., Duiker H. D., Beale P. D., Pouligny B., Dimmler K., Parris M., Butler D., and Athems A. S., Properties of ceramic KNO_3 thin film memories, *Physica B & C,* Vol 150, (1988), p.160, ISSN: 0921-4526

Scott J. F., Ferroelectric Memories, Springer, Berlin, (2000), ISBN: 3-540-66387-8

Shur V., Rumyantsev E. and Makarov S., Kinetics of phase transformations in real finite systems: Application to switching in ferroelectrics *Journal of Applied Physics*, Vol 84 (1998) pp. 445-51, ISSN: 1089-7550

Stadler H. L., Ferroelectric Switching Time of $BaTiO_3$ Crystals at High Voltages, *Journal of Applied Physics*, Vol 29, (1958) pp. 1485-1487, ISSN: 1089-7550

Tagantsev A. K., Stolichnov I., Setter N., Cross J. S. and Tsukada M., Non-Kolmogorov-Avrami switching kinetics in ferroelectric thin films, *Physical Review B* Vol 66, 214109 (2002), ISSN: 1550-235x

Tan E. K., Osman J., and Tilley D. R., First-Order Phase Transitions in Ferroelectric Films, *Solid State Communication*, Vol 117, (2000) pp. 61-5, ISSN: 0038-1098

Tilley D. R., and Zeks B., Landau theory of phase transitions in thick films, *Solid State Communication*, Vol 49, (1984) pp. 823-7, ISSN: 0038-1098

Tokumitsu E., Tanisake N., and Ishiwara H.; Partial Switching Kinetics of Ferroelectric $PbZr_xTi_{1-x}O_3$ Thin Films Prepared by Sol-Gel Technique, *Japanese Journal of Applied Physics,* Vol 33, (1994), p. 5201-5206, ISSN: 1347-4065

Tura V., Ricinschi D., Mitoseriu L., Harnagea C., Ando S., Tsukamoto T., and Okuyama M.; Simulation of Switching Properties of Ferroelectrics on the Basis of Dipole Lattice Model, *Japanese Journal of Applied Physics,* Vol 36, (1997), p. 2183-2191, ISSN: 1347-4065

Vizdrik G., Ducharme S., Fridkin V. M. and Yudin S. G., Kinetics of ferroelectric switching in ultrathin films, *Physical Review B*, Vol 68, 094113 (2003) pp. 1-6, ISSN: 1550-235X

Wang C. L., Qu B. D., Zhang P. L., and Zhong W L 1993 The Stability of Ferroelctric Phase Near Critical Size, *Solid State Communication*, Vol 88 (1993) pp. 735-7, ISSN: 0038-1098

Wang C. L. and Smith S. R. B., Landau Theory of the Size-driven Phase Transition in Ferroelectrics, *Journal of Physics: Condensed Matter,* Vol 7 (1995) pp. 7163, ISSN: 1361-648x

Wang C. L. and Smith S. R. P., The Size Effect on the Switching Properties of Ferroelectric Films: A One-dimensional Lattice Model, *Journal of Physics: Condensed Matter*, Vol 8, (1996) pp. 4813-4822, ISSN: 1361-648X

Wang M. C., Hsiao F. Y., His C. S. and Wu N. C., Crystal Structure and Ferroelectricity of Nanocrystalline Barium Titanate Thin Films, *Journal of Crystal Growth*, Vol 246, (2002) pp. 78-84, ISSN: 0022-0248

Wang Y. G., Zhong W. L. and Zhang P. L., Size Driven Phase Transition in Ferroelectric Particles, *Solid State Communication*, Vol 90 (1994) pp. 329-32, ISSN: 0038-1098

Wang Y. G., Zhong W. L. and Zhang P. L., Size Effects on the Curie-Temperature of Ferroelectric Particles, *Solid State Communication,* Vol 92 No. 6, (1994) pp. 519, ISSN: 0038-1098

Yanase N., Abe K., Fukushima N. and Kawakuko T., Thickness Dependence of Ferroelectricity in Heteroepitaxial $BaTiO_3$ Thin Film Capacitors, *Japanese Journal of Applied Physics*, Vol 38, (1999) pp. 5305-5308, ISSN: 1347-4065

Yuan G. L., Liu J. M., Baba-Kishi K., Chan H. L. W., Choy C. L. and Wu D., Switching Fatigue of Ferroelectric Layered-Perovskite Thin Films: Temperature Effect, *Materials Science and Engineering B* Vol 118, (2005) p. 225

Zhang S.-T., Yuan G.-L., Wang J., Chen Y.-F., Cheng G.-X., and Liu Z.-G., Temperature-Dependent Effect of Oxygen Vacancy on Polarization Switching of Ferroelectric $Bi_{3.25}La_{0.75}Ti_3O_{12}$ Thin Films, *Solid State Communication,* Vol 132, (2004), P. 315 ISSN: 0038-1098

Zhong W. L., Qu B. D., Zhang P. L. and Wang Y. G., Thickness dependence of the dielectric susceptibility of ferroelectric thin films, *Physical Review B*, Vol 50 (1994) pp. 12375-80; ISSN: 1550-235x

Zhong W. L., Wang Y. G. and Zhang P.L., Size Effects on Phase-Transitions in Ferroelectric-Films, *Physica Letters A*, Vol 189, (1994) pp. 121, ISSN: 0375-9601

19

Intrinsic Interface Coupling in Ferroelectric Heterostructures and Superlattices

K.-H. Chew[1], L.-H. Ong[2] and M. Iwata[3]
[1]*Department of Physics, University of Malaya, 50603 Kuala Lumpur,*
[2]*School of Physics, Universiti Sains Malaysia, 11800 Minden, Penang,*
[3]*Department of Engineering Physics, Electronics and Mechanics,*
Graduate School of Engineering, Nagoya Institute of Technology, Nagoya,
[1,2]*Malaysia*
[3]*Japan*

1. Introduction

Ferroelectric superlattices comprising two or more different layers have received immense attention due to their potential applications, as well as their striking new or enhanced behaviors (Nakagawara et al., 2000; Dawber et al., 2005). In those structures, the coupling at the interface between the two constituents has been demonstrated to play an important role in governing their properties (Bousquet et al., 2005). Theoretical study of interface coupling in ferroelectric superlattices was initially performed based on the Landau-like formulation by taking the continuum limit of the transverse Ising model (Qu et al., 1997). In their model, the extrapolation lengths describe the inhomogeneity of polarizations near the surfaces and an interface-related parameter gives the strength of the coupling at the interface. We have recently proposed a thermodynamic model with only one unknown parameter to study the effect of interface on polarization behaviours at the interface region between two bulk ferroelectrics (Chew et al., 2003; Tsang et al., 2004). The intrinsic ferroelectric coupling at the interface leads to variation of polarization across the interface of the heterostructures.

In this contribution, we discuss some fundamental properties of the physics of interfaces in ferroelectric heterostructures and superlattices using the Landau-Ginzburg theory. The key issue that will be addressed is how the intrinsic ferroelectric coupling at the interface affects the physical properties of the hybrid structures such as phase transitions, polarization modulation profiles and dielectric susceptibilities. We begin with a discussion for heterostructure of interfaces between a bulk ferroelectrics and dielectrics, in which the influence of thickness is not significant. Explicit expressions describe the spatial profile of polarization at the interface region of the heterostructure are obtained (Chew et al., 2003). The influence of the intrinsic interface coupling on the inhomogeneity and discontinuity or continuity of polarization at the interface is illustrated.

Since ferroelectric superlattice is an interesting system to study the interface effect, the influence of thickness on the polarization profiles of the superlattice is investigated. Analytical expressions of the polarization profile for superlattices are derived and discussed in detailed (Ishibashi et al., 2007; Chew et al., 2009). Explicit expressions for dielectric

susceptibilities in the paraelectric phase of the superlattice are also obtained (Chew et al., 2008). Finally, we apply the model to epitaxial $PbTiO_3/SrTiO_3$ by incorporating the depolarization field and lattice strain in the free energy functional. Some calculated results are discussed with experimental data. We conclude the chapter with some remarks.

2. Model of ferroelectric/dielectric heterostructure interfaces

In this section, the essential details for deriving the formalism of the ferroelectric/dielectric heterostructure interface are presented (Chew et al., 2003). We assume a one-dimensional problem in which the polarizations and related physical quantities vary along the *x*-direction perpendicular to the interface of the heterostructure. The total energy associates with the heterostructure can be expressed as

$$F = F_1 + F_2 + F_i, \tag{1}$$

where F_1 and F_2 are the total free energy density of the ferroelectric constituent *A* and dielectric constituent *B*, respectively. F_i is the coupling energy at the interface between the two constituents.

The total free energy density of the ferroelectric constituent *A* and dielectric constituent *B* are given by

$$\begin{cases} F_1 = \int \left(f_1 - f_1^{'} \right) dx, \\ F_2 = \int \left(f_2 - f_2^{'} \right) dx, \end{cases} \tag{2}$$

which extend from $x \to -\infty$ to $x = 0$ and $x = 0$ to $x \to \infty$, respectively. f_j denotes the Landau-Ginzburg free energy densities of consituent layer j, whereas $f_j^{'}$ gives the energy density in the single domain state of constituent *j*.

In the present study, the coupling energy F_i between the polarizations at the interface is described as

$$F_i = \frac{\lambda}{2}\left(p_i - q_i\right)^2, \tag{3}$$

where p_i and q_i are the interface polarizations at $x = 0$. λ is the coupling constant describing the strength of the interaction.

The free energy density of the ferroelectric constituent *A* with $p^2 = p_b^2 = -\alpha_1/\beta_1$ in the bulk $(x \to -\infty)$ is given by

$$f_1 - f_1^{'} = \frac{\alpha_1}{2}p^2 + \frac{\beta_1}{4}p^4 + \frac{\kappa_1}{2}\left(\frac{dp}{dx}\right)^2 - \left(\frac{\alpha_1}{2}p_b^2 + \frac{\beta_1}{4}p_b^4\right). \tag{4}$$

For the dielectric constituent *B*, we have $q = q_b = 0$ at $x \to \infty$, and the free energy density contribution from the dielectric constituent (with the higher order $\beta_2 q^4 / 4$ term truncated) is

$$f_2 - f_2^{'} = \frac{\alpha_2}{2}q^2 + \frac{\kappa_2}{2}\left(\frac{dq}{dx}\right)^2, \tag{5}$$

because $f_2^{'} = 0$ for a non-polar dielectric. p and q are the order parameters of the ferroelectric and dielectric consituents, respectively. α_1 is a temperature-dependent parameter

$$\alpha_1 = \alpha_{10}\left(T - T_0\right), \tag{6}$$

where $\alpha_{10} > 0$ is a temperarature-independent parameter. $\alpha_2 > 0$, $\beta_1 > 0$, $\kappa_1 > 0$ and $\kappa_1 > 0$ are all temperature-independent coefficients.

The equilibrium states of the heterostructures correspond to the minima of F with respect to variations of p and q. These are given by solving the Euler-Lagrange equations for p and q:

$$\begin{cases} \dfrac{\partial F}{\partial p} - \dfrac{\partial}{\partial x}\left(\dfrac{\partial F}{\partial p'}\right) = 0, \\ \dfrac{\partial F}{\partial q} - \dfrac{\partial}{\partial x}\left(\dfrac{\partial F}{\partial q'}\right) = 0, \end{cases} \tag{7}$$

with the boundary conditions

$$\begin{cases} p = p_i \\ q = q_i \end{cases} \text{ at } x = 0, \tag{8a}$$

and

$$\begin{cases} p = p_b \text{ and } \dfrac{dp}{dx} = 0 \quad \text{at } x \to -\infty, \\ q = q_b \text{ and } \dfrac{dq}{dx} = 0 \quad \text{at } x \to +\infty, \end{cases} \tag{8b}$$

where p_b and q_b are the bulk polarization of the ferroelectric constituent A (at x = -∞) and the dielectric constituent B (at $x = \infty$), respectively.

For the present study of ferroelectric/dielectric heterostructure of interface, it turns out that the free energy F of eq. (1) can be rewritten in terms of the interface polarizations p_i and q_i as order parameters. This gives F as a function of p_i and q_i without the usual integral form. Solving eqs. (1) and (7) simultaneously with the boundary conditions (i.e. eqs. (8a) and (8b)) imposed, and integrating once, the Euler-Lagrange equations becomes,

$$\frac{\alpha_1}{2}(p^2 - p_b^2) + \frac{\beta_1}{4}(p^2 - p_b^4) = \frac{\kappa_1}{2}\left(\frac{dp}{dx}\right)^2, \tag{9}$$

and

$$\frac{\alpha_2}{2}q^2 = \frac{\kappa_2}{2}\left(\frac{dq}{dx}\right)^2. \tag{10}$$

By solving eq. (9), the polarization of the ferroelectric constituent A becomes

$$p = p_b \tanh \frac{K_1}{\sqrt{2}}(x_i - x), \tag{11}$$

where

$$K_1 = \sqrt{-\frac{\alpha_1}{\kappa_1}}. \tag{12}$$

For the dielectric constituent *B*, the solution of eq. (10) gives

$$q = q_i \exp(-K_2 x), \tag{13}$$

with

$$K_2 = \sqrt{\frac{\alpha_2}{\kappa_2}}. \tag{14}$$

If p_i is determined, x_i can be obtained from eq. (11). In eqs. (11) and (13), the magnitude of the interface polarizations p_i and q_i are determined by the interface coupling parameter λ. The total energy, eq. (1), of the heterostructure can be written in terms of p_i and q_i as

$$F = \frac{1}{3}\sqrt{\frac{\beta_1 \kappa_1}{2}}(p_i^3 - 3p_i p_b^2 + 2p_b^3) + \frac{\sqrt{\alpha_2 \kappa_2}}{2} q_i^2 + \frac{\lambda}{2}(p_i - q_i)^2. \tag{15}$$

The equilibrium structure can be found from

$$\frac{\partial F}{\partial p_i} = \sqrt{\frac{\beta_1 \kappa_1}{2}}(p_i^2 - p_b^2) + \lambda(p_i - q_i) = 0, \tag{16}$$

and

$$\frac{\partial F}{\partial q_i} = \sqrt{\alpha_2 \kappa_2} q_i - \lambda(p_i - q_i) = 0. \tag{17}$$

Let us examine the variation of polarization across the interface and the total energy F of the heterostructure for the particular conditions of $\lambda = 0$ and $\lambda \to \infty$. The variation of polarization across the interface can be examined by looking into the continuity or discontinuity in interface polarizations $p_i - q_i$. Without interface coupling ($\lambda = 0$), we find that $p_i = p_b$ and $q_i = 0$. Thus, the mismatch of interface polarizations and the total energy of the heterostructure are found to be

$$p_i - q_i = p_b, \tag{18}$$

and

$$F = 0, \tag{19}$$

respectively.

For a strong interface coupling, i.e., $\lambda \to \infty$, we have $p_i = q_i$, implying that the polarization is continuos across the interface. In order to find $p_i = q_i$, it is convenient to write eq. (15) in term of only p_i as

$$F = \frac{1}{3}\sqrt{\frac{\beta_1 \kappa_1}{2}}(p_i^3 - 3p_i p_b^2 + 2p_b^3) + \frac{\sqrt{\alpha_2 \kappa_2}}{2} p_i^2 , \tag{20}$$

and by minimizing it, we obtain

$$p_i = q_i = p_b \left\{ \sqrt{1 + \frac{1}{2}\left(-\frac{\alpha_2}{\alpha_1}\right)\left(\frac{\kappa_2}{\kappa_1}\right)} - \sqrt{\frac{1}{2}\left(-\frac{\alpha_2}{\alpha_1}\right)\left(\frac{\kappa_2}{\kappa_1}\right)} \right\}, \tag{21}$$

which clearly indicates that the polarizations at the interface are determined by the intermixed properties of two constituents.

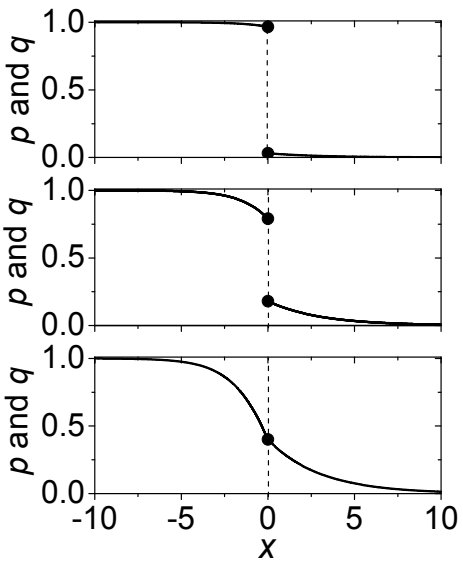

Fig. 1. Spatial dependence of polarization at the interface region of ferroelectric/dielectric heterostructures with $\lambda^{-1} = 10$ (top), 1 (middle) and 0 (bottom). In the curves, the parameters are: $\alpha_1 = -1$, $\alpha_2 = 1$, $\beta_1 = 1$, $\kappa_1 = 4$ and $\kappa_2 = 9$. Solid circles denote the polarization at interface.

Figure 1 shows a typical example of a ferroelectric/dielectric heterostrucutre of interface with different strength of interface coupling λ. It is seen that the mismatch in the polarization across the interface is notable for a loose coupling at the interface $\lambda^{-1} = 10$. The mismatch in the interface polarization becomes smaller with increasing coupling strength. It is interesting to see that the coupling at the interface induces polarization in the dielectric consituent. This may be called the interface-induced polarization, and it extends into the bulk over a distance governed by the characteristic length of the material K_2^{-1}, which is governed by α_2 and κ_2.

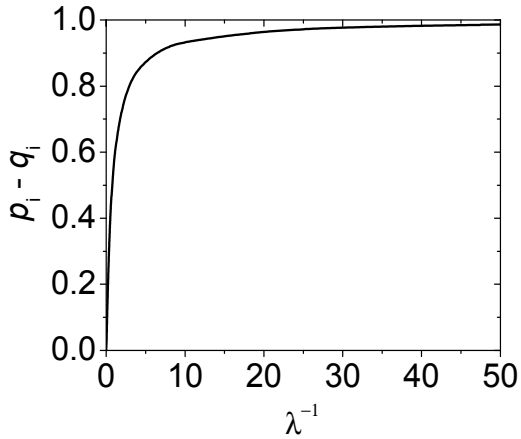

Fig. 2. Mismatch in the polarization at the interface of ferroelectric/dielectric heterostructures as a function of λ^{-1}. Other parameters are the same as for Fig. 1.

In Fig. 2, the mismatch in polarizations across the interface is examined under various strengths of interfacial coupling. The results clearly show that the mismatch in the interface polarizations is decreased with increasing interface coupling strength.

3. Model of ferroelectric/dielectric superlattices

We now consider a periodic superlattice composed of alternating ferroelectric layer and dielectric layer (ferroelectric/dielectic suprelattices), as shown in Fig. 3. Some key points are repeated here for clarity of discussion. Similarly, we assume that all spatial variation of polarization takes place along the x-direction. The thickness of ferroelectric layer and dielectric layer are L_1 and L_2, respectively. L is the periodic thickness of the superlattice. The two layers are coupled with each other across the interface. Periodic boudary conditions are used for describing the superlattices.

By symmetry, the average energy density of the ferroelectric/dielectric superlattice F is (Ishibashi & Iwata, 2007; Chew et al., 2008; Chew et al., 2009)

$$F = \frac{2}{L}\left(F_1 + F_2 + F_i\right). \tag{22}$$

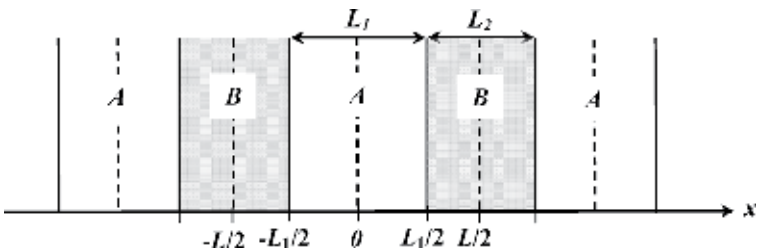

Fig. 3. Schematic illustration of a periodic ferroelectric superlattice composed of a ferroelectric and dielectric layers. The thickness of ferroelectric layer A and dielectric layer B are L_1 and L_2, respectively. $L = L_1 + L_2$ is the periodic thickness of the superlattice.

In eq. (22), the total free energy density of the ferroelectric layer F_1 is given by

$$F_1 = \int_0^{L_1/2} \left(\frac{\alpha_1}{2} p^2 + \frac{\beta_1}{4} p^4 + \frac{\kappa_1}{2} \left(\frac{\mathrm{d}p}{\mathrm{d}x} \right)^2 - pE \right) dx \,, \tag{23}$$

whereas the total free energy densities of the paraelectric layer f_2 is

$$F_2 = \int_{L_1/2}^{L/2} \left[\frac{\alpha_2}{2} q^2 + \frac{\kappa_2}{2} \left(\frac{\mathrm{d}q}{\mathrm{d}x} \right)^2 - qE \right] \mathrm{d}x \,, \tag{24}$$

respectively. In eqs. (23) and (24), p and q are the order parameters of the ferroelectric layer and paraelectric layer, respectively. E denotes the external electric field.
The coupling energy at the interface between the ferroelectric- and dielectric-layers is as shown in eq. (3). In this case, the boundary conditions at the interface (x = $L_1/2$) are described by

$$\begin{cases} \dfrac{\mathrm{d}p}{\mathrm{d}x} = -\dfrac{\lambda}{\kappa_1} (p_\mathrm{i} - q_\mathrm{i}), \\ \dfrac{\mathrm{d}q}{\mathrm{d}x} = \dfrac{\lambda}{\kappa_2} (p_\mathrm{i} - q_\mathrm{i}). \end{cases} \tag{25}$$

3.1 Polarization modulation profiles

We first look at the polarization modulation profiles of the ferroelectric/dielectric superlattice under the absence of an external electric field $E = 0$ (Chew et al., 2009). The polarization profiles of p and q for the ferroelectric and dielectric layers, respectively, can be obtained using the Euler-Lagrange equation. For the dielectric layer, the Euler-Lagrange equation is

$$\kappa_2 \frac{\mathrm{d}^2 q}{\mathrm{d}x^2} = \alpha_2 q \,, \tag{26}$$

and $q(x)$ can be obtained as

$$q(x) = q_\mathrm{c} \cosh K_2 \left(x - \frac{L}{2} \right), \tag{27}$$

and at the interface, we have

$$q_i = q_\mathrm{c} \cosh \frac{K_2 L_2}{2} \,, \tag{28}$$

where q_c is the q value at $\mathrm{d}q / \mathrm{d}x = 0$.
By integrating once, the Euler-Lagrange equation of the ferroelectric layer is

$$\frac{\kappa_1}{2} \left(\frac{\mathrm{d}p}{\mathrm{d}x} \right)^2 = \frac{\alpha_1}{2} \left(p^2 - p_\mathrm{c}^2 \right) + \frac{\beta_1}{4} \left(p^4 - p_\mathrm{c}^4 \right), \tag{29}$$

where p_c is the p value at $dp/dx = 0$. In this case, p_c is the maximum value of p at $x = 0$. Using $p(x) = p_c \sin\theta(x)$ and $p_b^2 = -\alpha_1 / \beta_1$, eq. (29) becomes

$$\sqrt{\frac{-\alpha_1}{\kappa_1(1+k^2)}} \int_{-L_1/2}^{x} dx = \int_{\theta_i}^{\theta} \frac{d\theta}{\sqrt{1-k^2\sin^2\theta}}, \tag{30}$$

where $F(\theta,k)$ and $F(\theta_i,k)$ are the elliptic integral of the first kind with the elliptic modulus k given by

$$k^2 = \frac{p_c^2}{2p_b^2 - p_c^2}. \tag{31}$$

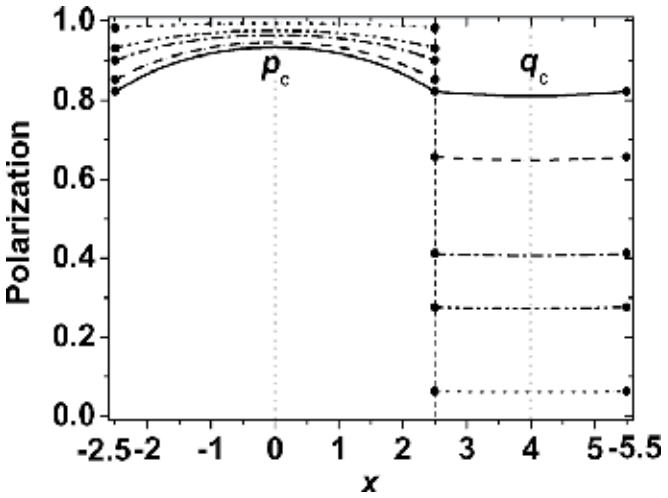

Fig. 4. Spatial dependence of polarization for a superlattice with $L_1 = 5$ and $L_2 = 3$ for various λ^{-1}. The parameters adopted for the calculation are: $\alpha_1 = -1$, $\alpha_2 = 0.1$, $\beta_1 = 1$, $\beta_2 = 1$, $\kappa_1 = 4$ and $\kappa_2 = 9$. In the curves, the values for λ^{-1} are: 100 (dot), 16 (dash-dot-dot), 8 (dash-dot), 2 (dash), and 0 (solid). Dotted circles represent the interface polarizations (Chew et al., 2009).

Let us discuss the polarization modulation profiles in a ferroelectric/dielectric superlattice using the explicit expressions. The characteristic lengths of polarization modulations in the ferroelectric layer near the transition point and the dielectric layer are given by $K_1^{-1} = \sqrt{-\kappa_1 / \alpha_1}$ and $K_2^{-1} = \sqrt{\kappa_2 / \alpha_2}$, respectively. Figure 4 illustrates an example of λ^{-1} dependence of polarization modulation profiles. It is seen that the modulation of the polarization is obvious in the ferroelectric layer, but not in the dielectric layer. This is because $L_1 / 2 > \sqrt{-\kappa_1 / \alpha_1} = 2$ and $L_2 / 2 < \sqrt{\kappa_2 / \alpha_2} \approx 0.95$. For a loosely coupled superlattice of $\lambda^{-1} = 100$ (dot lines), only a weak polarization is induced in the dielectric layer. As the strength of the interface coupling λ increases, the polarization near the interface of the ferroelectric layer is slightly suppressed, whereas the induced-polarization of the soft dielectric layer increases.

3.2 Phase transitions

Using the explicit expressions (as obtained in Sect. 3.1), the average energy density of the superlattice F (eq. (22)) can be written in terms of p_c and q_c as (Chew et al., 2009)

$$F = \frac{2}{L}\left[\sqrt{\frac{-\alpha_1\kappa_1}{1+k^2}}Jp_c^2 + \left(\frac{\alpha_1}{2}p_c^2 + \frac{\beta_1}{4}p_c^4\right)\frac{L_1}{2} + \frac{\lambda}{2}p_c^2\sin^2\theta_i - Cp_cq_c + \frac{D}{2}q_c^2\right], \tag{32}$$

where

$$\begin{cases} C = \lambda\cosh\left(\dfrac{K_2L_2}{2}\right)\cdot\sin\theta_i, \\ D = \dfrac{\sqrt{\alpha_2\kappa_2}}{2}\sinh\left(K_2L_2\right) + \lambda\cosh^2\left(\dfrac{K_2L_2}{2}\right), \\ J = \int_{\pi/2}^{\theta_i}\cos^2\theta\sqrt{1-k^2\sin^2\theta}\;d\theta, \end{cases} \tag{33}$$

with $\theta_i = \sin^{-1}\left(p_i / p_c\right)$. By utilizing $k^2 \approx p_c^2 / \left(2p_b^2\right)$ and K_1 (see eq. (12)) near the transition point, F becomes

$$F = \frac{2}{L}\left[\frac{A}{2}p_c^2 + O\left(p_c^4\right) - Cp_cq_c + \frac{D}{2}q_c^2\right], \tag{34}$$

where

$$A = -\frac{\sqrt{-\alpha_1\kappa_1}}{2}\sin K_1L_1 + \lambda\cos^2\frac{K_1L_1}{2}\ , \tag{35}$$

and $O(p_c^4)$ indicates the higher order terms of p_c^4.

From the equilibrium condition for q_c, $\mathrm{d}F/\mathrm{d}q_c = 0$, the condition of the transition point can be obtained as $A - C^2/D = 0$, i.e.,

$$-\frac{\sqrt{-\alpha_1\kappa_1}}{2}\sin K_1L_1 + R\cos^2\frac{K_1L_1}{2} = 0\,, \tag{36}$$

where

$$R = \frac{\lambda r}{\lambda + r}, \quad r = \sqrt{\alpha_2\kappa_2}\tanh\frac{K_2L_2}{2}\,. \tag{37}$$

In Fig. 5, we show the dependence of p_c and q_c on λ^{-1} for different dielectric stiffness α_2. For a superlattice with a soft dielectric layer $\alpha_2 = 0.1$ and 1, p_c remains almost the same as the bulk polarization $p_c \sim p_b$ for all λ^{-1}. For the case with $\alpha_2 = 5$, p_c is suppressed near the strong coupling regime $\lambda^{-1} \sim 0$. If the dielectric layer is very rigid (α_2 = 10 and 50), we found that p_c is strongly suppressed with increasing interface coupling and q_c remains very weak. It is seen that the polarizations of the superlattices with rigid dielectric layers are completely disappeared at $\lambda^{-1} \approx$ 0.0514 and 0.1189, respectively. These transition points can be obtained using eq. (36).

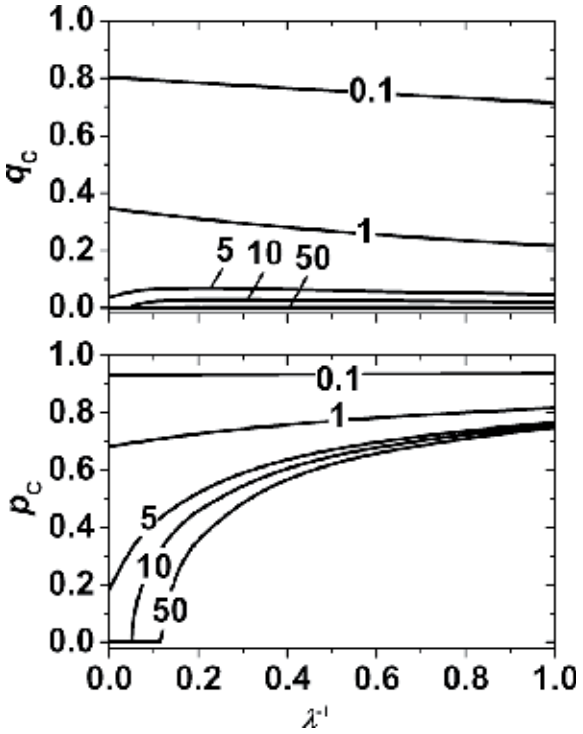

Fig. 5. p_c and q_c as a function of λ^{-1} for various α_2, where α_2 is 0.1, 1, 5, 10, and 50. The other parameters are the same as Fig. 4 (Chew et al., 2009).

As the temperature increases, the ferroelectric layer can be in the ferroelectric state or in the paraelectric state. Phase transition may or may not take place, depending on the model parameters. Let us examine the stability of superlattice in the paraelectric state by taking into account the polarization profile to appear in the ferroelectric state. Instead of the exact solutions obtained from the Euler-Lagrange equations, which are in term of the Jacobi Elliptic Functions, we use (Ishibashi & Iwata, 2007)

$$p = p_c \cos K_1 x \,, \tag{38}$$

thus p_i becomes

$$p_i = p_c \cos \frac{K_1 L_1}{2} \,. \tag{39}$$

The Euler-Lagrange equation for q is given by eq. (26), which gives $q(x)$ as expressed in eq. (27). Substitution of eqs. (27) and (38) into eq. (22), F becomes

$$F = \frac{2}{L}\left[\frac{a_1}{2}p_c^2 + \frac{b_1}{4}p_c^4 + \frac{a_2}{2}q_c^2 - cp_c q_c\right], \tag{40}$$

where

$$\begin{cases} a_1 = \dfrac{1}{4}\left[\left(\alpha_1 + \kappa_1 K_1^2\right)L_1 + \dfrac{\alpha_1 - \kappa_1 K_1^2}{K_1}\sin K_1 L_1\right] + \lambda\cos^2\left(\dfrac{K_1 L_1}{2}\right), \\ b_1 = \dfrac{\beta_1}{4}\left(\dfrac{3L_1}{4} + \dfrac{\sin K_1 L_1}{K_1} + \dfrac{\sin 2K_1 L_1}{8K_1}\right), \\ a_2 = \dfrac{\alpha_2}{K_2}\sinh\dfrac{K_2 L_2}{2}\cosh\dfrac{K_2 L_2}{2} + \lambda\cosh^2\dfrac{K_2 L_2}{2}, \\ c = \lambda\cos\dfrac{K_1 L_1}{2}\cosh\dfrac{K_2 L_2}{2}. \end{cases} \tag{41}$$

Similarly, from the equilibrium condition for q_c, $\mathrm{d}F/\mathrm{d}q_c = 0$, we find eq. (40) can be reduced to a more simple form as

$$F = \frac{2}{L}\left[\frac{a_1^*}{2}p_c^2 + \frac{b_1}{4}p_c^4\right], \tag{42}$$

where

$$a_1^* = \frac{L_1}{4}\left[\alpha_1 + \kappa_1 K_1^2 + \frac{\alpha_1 - \kappa_1 K_1^2}{K_1 L_1}\sin K_1 L_1\right] + R\cos^2\frac{K_1 L_1}{2}, \tag{43}$$

where $R(\lambda, r)$ is given by eq. (37). r is a function of α_2, κ_2 and L_2. The transitions of the superlattice from a paraelectric phase to a ferroelectric state occurs when $a_1^* = 0$. Note here that a_1^* consists of the physical parameters from both the ferroelectric and dielectric layers. It is seen that the influence of the dielectric layer via λ becomes stronger with increasing α_2, κ_2 and L_2. However, the influence is limited at most to $r_{\max} = \sqrt{\alpha_2\kappa_2}$. Let us look at a_1^* in more detail. By taking $\left.\dfrac{\partial a_1^*}{\partial K_1}\right|_{K_1=k} = 0$, we obtain the wave number k. It is qualitatively

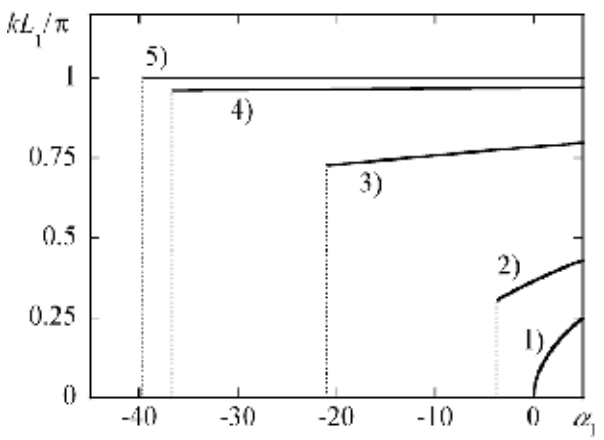

Fig. 6. The dependence of the wave number k for various R/L_1 when $\kappa_1 = 1$ and $L_1 = 1/2$. The curves show the cases 1) $R/L_1 = 0$, 2) $R/L_1 = 2$, 3) $R/L_1 = 20$, 4) $R/L_1 = 200$ and 5) $R/L_1 = \infty$. Dotted lines denote the transition point of each case (Ishibashi & Iwata, 2007).

obvious that k is small, implying a flat polarization profile, when the contribution from the dielectric layer R, is small, while kL_2 approaches π, implying a very weak interface polarization in the ferroelectric layer, when R is extremely large. The dependence of the wave number k on α_1 for various R / L_1 is illustrated in Fig. 6.

3.3 Dielectric susceptibilities

In this section, we will discuss the dielectric susceptibility of the superlattice in the paraelectric phase (Chew et al., 2008). Since $p(x) = q(x) = 0$ in the paraelectric phase (if $E = 0$), the modulated polarizations, $p(x)$ and $q(x)$, are the polarizations induced by the electric field E. The contribution from the higher-order term $\beta_1 p^4 / 4$ is neglected because we consider only the paraelectric phase. By solving the Euler-Lagrange equations, we found

$$\begin{cases} \alpha_1 p - \kappa_1 \dfrac{\mathrm{d}^2 p}{\mathrm{d}x^2} = E, \\ \alpha_2 q - \kappa_2 \dfrac{\mathrm{d}^2 q}{\mathrm{d}x^2} = E, \end{cases} \tag{44}$$

with the condition that F (eq. (22)) including the interface energy (eq. (3)) takes the minimum value. Note that in the present system, the ferroelectric transition point α_c is negative. Thus, one must consider both cases $\alpha_1 \geq 0$ and $\alpha_1 < 0$ in the study of the dielectric susceptibility even in the paraelectric phase. In the present system, the dielectric susceptibility χ is defined as

$$\chi = \frac{2}{LE}\left[\int_0^{L_1/2} p\,\mathrm{d}x + \int_{L_1/2}^{L/2} q\,\mathrm{d}x\right]. \tag{45}$$

3.3.1 Case $\alpha_1 \geq 0$

For the case of $\alpha_1 \geq 0$, the exact solutions are

$$\begin{cases} p = p_c E \cosh K_1 x + \dfrac{E}{\alpha_1}, \\ q = q_c E \cosh K_2 \left(x - \dfrac{L}{2}\right) + \dfrac{E}{\alpha_2}, \end{cases} \tag{46}$$

and

$$\begin{cases} p_i = p_c E \cosh \dfrac{K_1 L_1}{2} + \dfrac{E}{\alpha_1}, \\ q_i = q_c E \cosh \dfrac{K_2 L_2}{2} + \dfrac{E}{\alpha_2}. \end{cases} \tag{47}$$

In this case, $K_1 = \sqrt{\alpha_1 / \kappa_1}$ and K_2 is given by eq. (14). By utilizing eqs. (46) and (47), we can express F in terms of p_c and q_c as

$$F = \frac{2}{L}\left(\frac{a_1}{2}p_c^2 + \frac{a_2}{2}q_c^2 - cp_cq_c - d_1p_c - d_2q_c\right)E^2, \tag{48}$$

where

$$\begin{cases} a_1 = \dfrac{\alpha_1}{2K_1}\sinh K_1L_1 + \lambda\cosh^2\dfrac{K_1L_1}{2}, \\ a_2 = \dfrac{\alpha_2}{2K_2}\sinh K_2L_2 + \lambda\cosh^2\dfrac{K_2L2}{2}, \\ c = \lambda\cosh\dfrac{K_1L_1}{2}\cosh\dfrac{K_2L_2}{2}, \\ d_1 = -\lambda\cosh\dfrac{K_1L_1}{2}\left(\dfrac{1}{\alpha_1} - \dfrac{1}{\alpha_2}\right), \\ d_2 = \lambda\cosh\dfrac{K_2L_2}{2}\left(\dfrac{1}{\alpha_1} - \dfrac{1}{\alpha_2}\right). \end{cases} \tag{49}$$

Using the equilibrium conditions $\partial F / \partial p_c = \partial F / \partial q_c = 0$, we find

$$p_c = \frac{-\lambda}{a_2A}\left(\frac{\alpha_2}{2K_2}\cosh\frac{K_1L_1}{2}\sinh K_2L_2\right)\left(\frac{1}{\alpha_1} - \frac{1}{\alpha_2}\right), \tag{50}$$

and

$$q_c = \frac{\lambda}{a_2A}\left(\frac{\alpha_1}{2K_1}\cosh\frac{K_2L_2}{2}\sinh K_1L_1\right)\left(\frac{1}{\alpha_1} - \frac{1}{\alpha_2}\right), \tag{51}$$

where

$$A = a_1 - \frac{c^2}{a_2}. \tag{52}$$

Based on eq. (45), the dielectric susceptibility for the present case is

$$\chi = \frac{2p_c}{K_1L}\sinh\frac{K_1L_1}{2} + \frac{L_1}{L\alpha_1} + \frac{2q_c}{K_2L}\sinh\frac{K_2L_2}{2} + \frac{L_2}{L\alpha_2}. \tag{53}$$

3.3.2 Case $\alpha_1 < 0$

In this case, the exact solutions of eq. (44) are

$$\begin{cases} p = p_cE\cos K_1x + \dfrac{E}{\alpha_1}, \\ q = q_cE\cosh K_2\left(x - \dfrac{L}{2}\right) + \dfrac{E}{\alpha_2}, \end{cases} \tag{54}$$

where K_1 and K_2 are given by eq. (12) and (14), respectively. Thus, we have

$$\begin{cases} p_{\mathrm{i}} = p_{\mathrm{c}} E \cos\dfrac{K_1 L_1}{2} + \dfrac{E}{\alpha_1}, \\ q_{\mathrm{i}} = q_{\mathrm{c}} E \cosh\dfrac{K_2 L_2}{2} + \dfrac{E}{\alpha_2}. \end{cases} \tag{55}$$

Similarly, we find

$$F = \frac{2}{L}\left(\frac{a_1}{2}p_{\mathrm{c}}^2 + \frac{a_2}{2}q_{\mathrm{c}}^2 - c p_{\mathrm{c}} q_{\mathrm{c}} - d_1 p_{\mathrm{c}} - d_2 q_{\mathrm{c}}\right)E^2, \tag{56}$$

where

$$\begin{aligned} a_1 &= \frac{\alpha_1}{2K_1}\sin K_1 L_1 + \lambda\cos^2\frac{K_1 L_1}{2}, \\ a_2 &= \frac{\alpha_2}{2K_2}\sinh K_2 L_2 + \lambda\cosh^2\frac{K_2 L_2}{2}, \\ c &= \lambda\cos\frac{K_1 L_1}{2}\cosh\frac{K_2 L_2}{2}, \\ d_1 &= -\lambda\cos\frac{K_1 L_1}{2}\left(\frac{1}{\alpha_1} - \frac{1}{\alpha_2}\right), \\ d_2 &= \lambda\cosh\frac{K_2 L_2}{2}\left(\frac{1}{\alpha_1} - \frac{1}{\alpha_2}\right), \end{aligned} \tag{57}$$

and the the values of p_{c} and q_{c} become

$$p_{\mathrm{c}} = \frac{-\lambda}{a_2 A}\left(\frac{\alpha_2}{2K_2}\cos\frac{K_1 L_1}{2}\sinh K_2 L_2\right)\left(\frac{1}{\alpha_1} - \frac{1}{\alpha_2}\right), \tag{58}$$

and

$$q_{\mathrm{c}} = \frac{\lambda}{a_2 A}\left(\frac{\alpha_1}{2K_1}\cosh\frac{K_2 L_2}{2}\sin K_1 L_1\right)\left(\frac{1}{\alpha_1} - \frac{1}{\alpha_2}\right), \tag{59}$$

with

$$A = a_1 - \frac{c^2}{a_2}. \tag{60}$$

Using eqs. (45), the dielectric susceptibility χ for the present case of $\alpha_1 < 0$ is

$$\chi = \frac{2p_{\mathrm{c}}}{K_1 L}\sin\frac{K_1 L_1}{2} + \frac{L_1}{L\alpha_1} + \frac{2q_{\mathrm{c}}}{K_2 L}\sinh\frac{K_2 L_2}{2} + \frac{L_2}{L\alpha_2}, \tag{61}$$

where the phase transition point is given by $A = a_1 - c^2 / a_2 = 0$. Using $A = a_1 - c^2 / a_2 = 0$, the condition of the transition point is

$$\frac{\alpha_1}{2K_1}\sin K_1 L_1 + \frac{\lambda\dfrac{\alpha_2}{2K_2}\sin K_2 L_2}{\dfrac{\alpha_2}{2K_2}\sin K_2 L_2 + \lambda\cosh^2\dfrac{K_2 L_2}{2}}\cos^2\frac{K_1 L_1}{2} = 0. \tag{62}$$

It is interesting to note here that the transition temperature α_1 can be determined using eq. (62), which is exactly the same as eq. (43) (Ishibashi & Iwata, 2007).

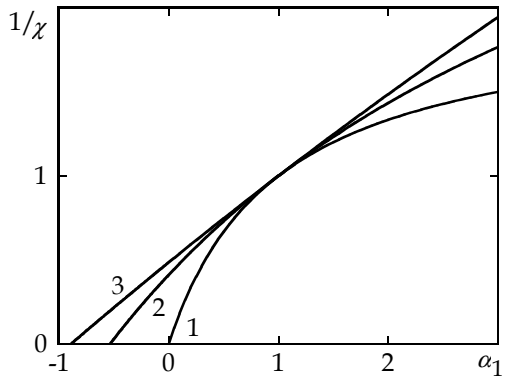

Fig. 7. Reciprocal susceptibility as a function of α_2. The parameter values are adopted as $L = 1$, $L_1 = L_2 = 1/2$, $\kappa_1 = \kappa_2 = 1$, $\alpha_2 = 1$, for cases of: (1) $\lambda = 0$, (2) $\lambda = 0.3$, (3) $\lambda = 3$ (Chew et al., 2008).

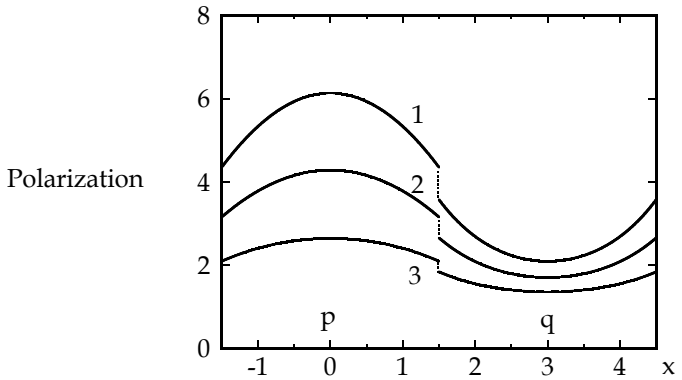

Fig. 8. Spatial dependence of polarization for a superlattice with $L_1 = L_2 = 3$. The parameters adopted for the calculation are: $\kappa_1 = \kappa_2 = 1$, $\alpha_2 = 1$, $\lambda = 3$, for cases of (1) $\alpha_1 = -0.1$, (2) $\alpha_1 = 0$, (3) $\alpha_1 = 0.2$ (Chew et al., 2008).

In Fig. 7, we show the reciprocal susceptibility $1/\chi$ in various parameter values. It is found that the average susceptibility diverges at the transition temperature obtained from eq. (62).

The result indicates that the second-order phase transition is possible in our model of the superlattice structure. It is seen that the susceptibility is continuous at $\alpha_1 = 0$, though the susceptibility is divided into two different functions at $\alpha_1 = 0$. Taking the limit of $\alpha_1 = \pm 0$ from both the positive and negative sides, the explicit expression for the susceptibility at $\alpha_1 = 0$ is

$$\chi = \frac{1}{2L}\left[\frac{2L_1 + L_2}{\alpha_2} + \frac{L_1^2}{2\lambda} + \frac{L_1^3}{12\kappa_1} + \frac{L_1^2 K_2}{\alpha_2}\frac{\cosh^2\frac{K_2 L_2}{2}}{\sinh K_2 L_2}\right], \tag{63}$$

implying that the susceptibility is always continuous at $\alpha_1 = 0$. It is worthwhile to look at the field-induced polarization profile at $\alpha_1 = 0$ because K_1 becomes zero at $\alpha_1 = 0$. By taking the limit of $\alpha_1 = \pm 0$ from both the positive and negative sides for the polarization *p*, the expressions for the polarization profiles in $p(x)$ and $q(x)$ can be explicitly expressed as

$$p(x) = \frac{E}{8\kappa_1}\left(L_1^2 - 4x^2\right) + \frac{EL_1}{2\lambda} + \frac{EK_2 L_1}{\alpha_2}\frac{\cosh^2\frac{K_2 L_2}{2}}{\sinh K_2 L_2} + \frac{E}{\alpha_2}, \tag{64}$$

and

$$q(x) = \frac{EK_2 L_1 \cosh\frac{K_2 L_2}{2}}{\alpha_2 \sinh K_2 L_2}\cosh\left[K_2\left(x - \frac{L}{2}\right)\right] + \frac{E}{\alpha_2} \tag{65}$$

Equation (64) depicts the polarization profile $p(x)$ that exhibits a parabolic modulation at $\alpha_1 = 0$, as shown in Fig. 8. The polarization profile obtained near the transition point may coincide with the polarization modulation pattern of the ferroelectric soft mode in the paraelectric phase.

3.4 Application of model to epitaxial $PbTiO_3/SrTiO_3$ superlattices

Let us extend the model to study the ferroelectric polarization of epitaxial $PbTiO_3/SrTiO_3$ (PT/ST) superlattices grown on ST substrate and under a short-circuit condition, as schematically shown in Fig. 9. Some key points from the previous sections are repeated here for clarity of discussion.

In this study, we need to include the effects of interface, depolarization field and substrate-induced strain in the model. By assuming that all spatial variation of polarization takes place along the *z*-direction, the Landau-Ginzburg free energy per unit area for one period of the PT/ST superlattice can be expressed as (Chew et al., *unpublished*)

$$F = F_{PT} + F_{ST} + F_I, \tag{66}$$

where the free energy per unit area for the PT layer with thickness L_{PT} is

$$F_{PT} = \int_{-L_{PT}}^{0}\left[\frac{\alpha_{PT}^*}{2}p^2 + \frac{\beta_{PT}^*}{4}p^4 + \frac{\gamma_{PT}}{6}p^6 + \frac{\kappa_{PT}}{2}\left(\frac{dp}{dz}\right)^2 + \frac{u_{m,PT}^2}{s_{11,PT} + s_{12,PT}} - \frac{1}{2}e_{d,PT}p\right]dz, \tag{67}$$

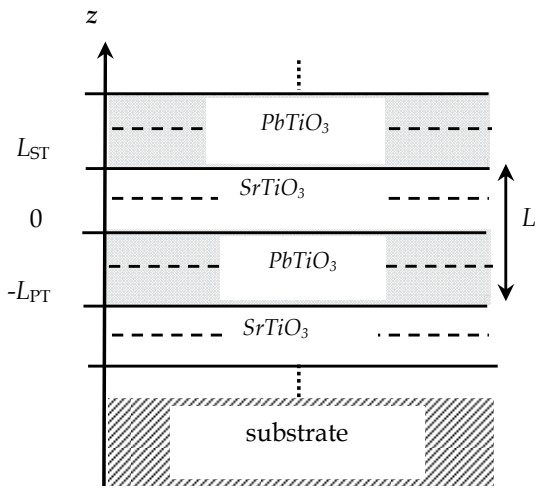

Fig. 9. Schematic illustration of a periodic superlattice composed of a ferroelectric and a paraelectric layers. The thicknesses of $PbTiO_3$ (PT) and $SrTiO_3$ (ST) layers are L_{PT} and L_{ST}, respectively. L denotes the periodic thickness of the PT/ST superlattice.

and the free energy per unit area for the ST layer with thickness L_{ST} is

$$F_{ST} = \int_0^{L_{ST}} \left[\frac{\alpha_{ST}^*}{2} q^2 + \frac{\beta_{ST}^*}{4} q^4 + \frac{\gamma_{ST}}{6} q^6 + \frac{\kappa_{ST}}{2} \left(\frac{dq}{dz} \right)^2 + \frac{u_{m,ST}^2}{s_{11,ST} + s_{12,ST}} - \frac{1}{2} e_{d,ST} q \right] dz. \tag{68}$$

where p and q corresponds to the polarization of PT and ST layers, respectively. For the superlattices with the polarizations perpendicular to the layer's surfaces/interfaces, the inhomogeneity of polarization means that the depolarization field effect is essential. In eqs. (67) and (68), α_j^* and β_j^* are expressed as

$$\left. \begin{aligned} \alpha_j^* &= \alpha_j - \frac{4Q_{12,j}}{s_{11,j} + s_{12,j}} u_{m,j}, \\ \beta_j^* &= \beta_j + \frac{4Q_{12,j}^2}{s_{11,j} + s_{12,j}}, \end{aligned} \right\} \tag{69}$$

where α_j, β_j and γ_j are the Landau coefficients of layer j (j : PT or ST), as usual. $s_{11,j}$ and $s_{12,j}$ are the elastic compliance coefficients, whereas $Q_{12,j}$ is the electrostrictive constant. $u_{m,j} = \left(a_S - a_j \right) / a_S$ denotes the in-plane misfit strain induced by the substrate due to the lattice mismatch. a_j is the unconstrained equivalent cubic cell lattice constants of layer j and a_S is the lattice parameter of the substrate. κ_j is the gradient coefficient, determining the energy cost due to the inhomogeneity of polarization.

With the assumption that the ferroelectric layers are insulators with no space charges, the depolarization field $e_{d,j}$ in the PT and ST layers can be expressed by

$$\begin{cases} e_{d,PT}(z) = -\dfrac{1}{\varepsilon_0}\big(p(z) - P\big), \\ e_{d,ST}(z) = -\dfrac{1}{\varepsilon_0}\big(q(z) - P\big), \end{cases} \tag{70}$$

respectively. In eq. (70), ε_0 denotes the dielectric permittivity in vacuum. The second term describes the mean polarization of one-period superlattice

$$P = \frac{1}{L}\left(\int_{-L_{PT}}^{0} p dz + \int_{0}^{L_{ST}} q dz \right), \tag{71}$$

with the periodic thickness $L = L_{PT} + L_{ST}$. It is important to note here that $e_{d,j}$ acts as the depolarization field, if its direction is opposite to the direction of ferroelectric polarization. If $e_{d,j}$ inclines in the same direction of polarization, it cannot be regarded as the depolarization field; thus, we denote $e_{d,j}$ as "the internal electric field". Hence, the average internal electric field of one-period superlattice is defined as

$$E_d = \frac{1}{L}\left[\int_{-L_{PT}}^{0} e_{d,PT}(z) dz + \int_{0}^{L_{ST}} e_{d,ST}(z) dz \right]. \tag{72}$$

The intrinsic coupling energy between the polarizations at the interfaces $z = 0$ of the two layers is described as

$$F_I = \frac{\lambda}{2}(p_i - q_i)^2, \tag{73}$$

where p_i and q_i are the interface polarizations at $z = 0$ for the PT and ST layers, respectively. In eq. (73), the parameter λ describes the strength of intrinsic interface coupling and it can be conveniently related to the dielectric permittivity in vacuum ε_0 as

$$\lambda = \frac{\lambda_0}{\varepsilon_0}, \tag{74}$$

where λ_0 denote the temperature-independent interface coupling constant. In this case, the existence of the interface coupling $\lambda \neq 0$ leads to the inhomogeneity of polarization near the interfaces, besides the effect of the depolarization field.

In the calculations, it is assumed that 1 *unit cell* (*u.c.*) ≈ 0.4 *nm* and the thickness of ST layer is maintained at $L_{ST} \approx 3$ *u.c.* The lattice constants in the paraelectric state are a_A = 3.969 Å and a_B = 3.905 Å for PT and ST layers, respectively. Based on the lattice constants, the lattice strains are obtained as $u_{m,PT}$ = −0.0164 and $u_{m,ST}$ = 0.

In Fig. 10, we show the average polarization P and internal electric fields E_d of PT/ST superlattices as a function of thickness ratio L_{PT}/L_{ST} for different strength of interface coupling λ_0 . It is seen that P and E_d decrease with increasing λ_0 . As λ_0 increases, the

critical thickness ratio (at which P vanishes) shifts to a higher value. It is seen that there is a good agreement between the calculated and measured polarizations. The calculated polarizations using $\lambda_0 = 10$ (black line) agree reasonably well with most of the experimental measurements for $L_{PT}/L_{ST} > 0.4$, implying that the strength of interface coupling at this regime is strong. At the $L_{PT}/L_{ST} \leq 0.4$ region, the predicted polarizations with $\lambda_0 = 0.2$ (red line) and 0.05 (blue line) agree well with some of the experimental measurements. The E_d versus L_{PT}/L_{ST} curves show a trend similar to P versus L_{PT}/L_{ST}, e.g. E_d disappears at a critical thickness ratio. For each λ_0, the critical thickness ratio of E_d coincides with that of P. It is remarkable to see that for $E_d > 0$, internal electric field is parallel to the direction of the ferroelectric polarization in PT layer, which enhances the polarization of the superlattice.

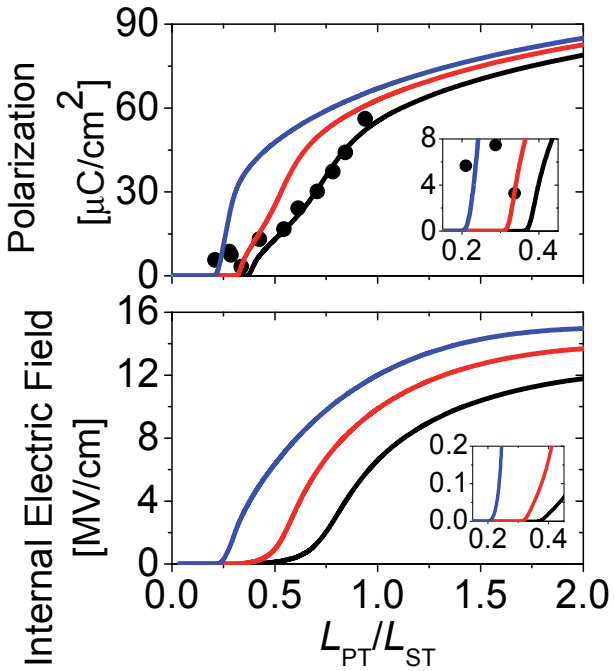

Fig. 10. Polarization and internal electric field as a function of thickness ratio L_{PT}/L_{ST} of PT/ST superlattices at T = 300K. The values of λ_0 are: 10 (—), 0.2 (—) and 0.05 (—). Solid dots (•) represent experimental results from Dawber et al (Dawber et al., 2007). The insets in each figure show the corresponding curves in smaller scale (Chew et al., *unpublished*).

4. Conclusion

We have proposed a model to study the intrinsic interface coupling in ferroelectric heterostructure and superlattices. The layered structure is described using the Landau-Ginzburg theory by incorporating the effect of coupling at the interface between the two constituents. Explicit analytical expressions describing the polarization at the interface

between bulk ferroelectrics and bulk dielectrics were derived and discussed. Here, we mainly discussed only cases where the transition of the ferroelectric constituent is of second order (Chew et al., 2003), though cases of heterostructure at the interfaces involving first-order phase transition were also reported (Tsang et al., 2004).

We further extend the model to investigate the ferroelectricity of superlattice by incorporating the thickness effect. Using the explicit expressions derived from the model, the polarization modulation profiles, phase transitions and dielectric susceptibilities of a superlattice are presented and discussed in detail (Ishibashi & Iwata, 2007; Chew et al., 2008; Chew et al., 2009). The effort to obtain the explicit analytical solutions using the continuum model of Landau-Ginzburg theory is worthwhile. This is because those expressions allow us to gain general insight on how the intrinsic polarization coupling at the interface influences the physical properties of those hybrid structures. Note that the effect of an applied electric field on the polarization behaviors of heterostructure at the interfaces (Chew et al., 2005; Chew et al., 2006) and superlattices (Chew et al., 2011; Chew et al., *unpublished*) is also very important. However, those studies were not discussed. We have also constructed a one-dimensional model on the basis of the Landau-Ginzburg theory to investigate the polarization and dielectric behaviors (Chew et al., 2006; Chew et al., 2007), as well as the switching characteristics (Chew et al., *unpublished*).

At the end of the discussion, we show how the present model can be applied to study the ferroelectric polarization of epitaxial PT/ST superlattices with the polarizations perpendicular to the surfaces/interfaces of the constituent layers (Chew et al., *unpublished*). The effects of interface, depolarization field and substrate-induced strain are required to include in the model. Our calculated polarizations (Chew et al., *unpublished*) agree reasonably well with recent experimental measurements (Dawber et al., 2007). From our study, it suggests that the recent experimental observation on the unusual recovery of ferroelectricity at thickness ratio of $L_{PT}/L_{ST} < 0.5$ (Dawber et al., 2005) may be related to a weakening of ferroelectric coupling at the interface. It is certainly interesting to look at the dielectric susceptibilities and polarization reversals of the superlattices, which will be reported elsewhere.

5. Acknowlegement

This work is supported by the University of Malaya Research Grant (No: RG170-11AFR). L. H. Ong acknowledges the support from FRGS Grant (No: 203/PFIZIK/6711144) by the Ministry of Higher Education, Malaysia.

6. References

Nakagawara, O.; Shimuta, T.; Makino, T.; Arai, S.; Tabata, H. & Kawai, T. (2000). Epitaxial Growth and Dielectric Properties of (111) Oriented $BaTiO_3/SrTiO_3$ Superlattices by Pulsed-laser Deposition, Applied Physics Letter, Vol. 77, No. 20, (November 2000), pp. 3257-3259, ISSN 0003-6951

Dawber, M.; Lichtensteiger, C.; Cantoni, M.; Veithen, M.; Ghosez, P.; Johnston, K.; Rabe, K. M.; & Triscone, J. M. (2005). Unusual Behavior of the Ferroelectric Polarization in

$PbTiO_3/SrTiO_3$ Superlattices, *Physical Review Letters*, Vol. 95, No.17, (October 2005), pp. 177601, ISSN 0031-9007

Bousquet, E.; Dawber, M.; Stucki, N.; Lichtensteiger, C.; Hermet, P.; Gariglio, S.; Triscone, J. M. & Ghosez, P. (2008). Improper Ferroelectricity in Perovskite Oxide Artificial Superlattices, *Nature*, Vol. 452, No. 7188, (April 2008), pp. 732-U4, ISSN 0028 - 0836

Qu, B. D.; Zhong, W. L.; & Prince, R. H. (1997) Interfacial Coupling in Ferroelectric Superlattices, *Physical Review B*, Vol. 55, No. 17, (May 1997), pp. 11218-11224, ISSN 0163-1829

Chew, K.-H.; Ishibashi, Y. ; Shin F. G. & Chan, H. L. W. (2003). Theory of Interface Structure in Double-Layer Ferroelectrics, *Journal of the Physical Society of Japan*, Vol. 72, No.9, (September 2003), pp. 3158-3165, ISSN 0031-9015

Tsang, C. H.; Chew, K.-H.; Ishibashi, Y. & Shin F. G. (2004). Structure of Interfaces in Layered Ferroelectrics of First and/or Second Order Transition, *Journal of the Physical Society of Japan*, Vol. 73, No.11, (November 2004), pp. 3158-3165, ISSN 0031-9015

Ishibashi, Y. & Iwata, M. (2007). Landau-Ginzburg Theory of Phase Transition of Ferroelectric Superlattices, *Ferroelectrics*, Vol. 354, (2007), pp. 8-12, ISSN 0015 - 0193

Chew, K.-H.; Iwata, M.; Ishibashi, Y. & Shin F. G. (2009). Polarization Modulation Profiles in Ferroelectric Superlattices, *Ferroelectrics Letters Section*, Vol. 36, No.1-2, (2009), pp. 12-19, ISSN 0731-5171

Chew, K.-H.; Iwata, M.; & Shin F. G. & Ishibashi Y. (2008). Exact Expressions for Dielectric Susceptibilities in the Paraelectric Phase of Ferroelectric Superlattices Based on Ginzburg-Landau Theory, *Integrated Ferroelectrics*, Vol. 100, No.1, (2008), pp. 79-87, ISSN 1058-4587

Dawber, M.; Stucki, N.; Lichtensteiger C.; Gariglio, S.; Ghosez, P. & Triscone J. M. (2007). Tailoring the Properties of Artificially Layered Ferroelectric Superlattices, *Advanced Materials*, Vol. 19, No. 23, (December 2007), pp. 4153-4159, ISSN 0935-9648

Chew, K.-H.; Ong, L.-H. & Iwata, M. Interface-induced Sign Change of Local Internal Electric Field in Nanoscale Ferroelectric Superlattices, (*unpublished*)

Chew, K.-H.; Ishibashi Y. & Shin F. G. (2005). Ferroelectric Hysteresis Loops as the Manifestation of Interfacial-aided Polarization Reversals in Ferroelectric Heterostructures, *J. Phys. Soc. Jpn.* Vol. 74, No. 8, (August 2005), pp. 2338-2346, ISSN 0031-9015

Chew, K.-H.; Ishibashi Y. & Shin F. G. (2006). Intrinsic Ferroelectric Hysteresis Behaviors for Heterostructures, *Physica Status Solidi A–Applications and Materials Science*. Vol. 203, No. 9, (July 2006) pp. 2205-2208, ISSN 0031-8965

Chew, K.-H.; Ong, L.-H. & Iwata, M. (2011). Switching Dynamics in Ferroelectric Superlattices, *Current Applied Physics*, Vol. 11, No.3, (May 2011), pp. 755-761, ISSN 15671739

Chew, K.-H.; Ong, L.-H. & Iwata, M. Influence of Dielectric Stiffness, Interface and Layer Thickness on Hysteresis Loops of Ferroelectric Superlattices, (*unpublished*)

Chew, K.-H.; Ishibashi, Y. & Shin F. G. (2006). A Lattice Model for Ferroelectric Superlattices, *Journal of the Physical Society of Japan*, Vol. 75, No.6, (June 2006), pp. 064712, ISSN 0031-9015

Chew, K.-H.; Ishibashi, Y. & Shin F.G. (2007). Competition between the Thickness Effects of Each Constituent Layer in Ferroelectric Superlattices, *Ferroelectrics*, Vol. 357, No.6, (2007), pp. 697-701, ISSN 0015-0193

Chew, K.-H., Ong L.-H. & Iwata M. A One-Dimensional Lattice Model of Switching Characteristics in Ferroelectric Superlattices, (*unpublished*)

20

First-Principles Study of ABO_3: Role of the B–O Coulomb Repulsions for Ferroelectricity and Piezoelectricity

Kaoru Miura
Corporate R&D Headquarters, Canon Inc., Shimomaruko, Ohta, Tokyo
Japan

1. Introduction

Since Cohen (Cohen & Krakauer, 1990; Cohen, 1992) proposed an origin for ferroelectricity in perovskite oxides, investigations of ferroelectric materials using first-principles calculations have been extensively studied (Ahart et al., 2008; Bévillon et al., 2007; Bousquet et al., 2006; Chen et al., 2004; Diéguez et al., 2005; Furuta & Miura, 2010; Khenata et al., 2005; Kornev et al., 2005; Miura & Tanaka, 1998; Miura, 2002; Miura et al., 2009; 2010a;b; Miura & Furuta, 2010; Miura et al., 2011; Oguchi et al., 2009; Ricinschi et al., 2006; Uratani et al., 2008; Vanderbilt, 2000; Z. Wu et al., 2005). Currently, using the pseudopotential (PP) methods, most of the crystal structures in ferroelectric perovskite oxides (ABO_3) as well as perovskite-related oxides can be precisely predicted. However, it is also known that the most stable structures of ABO_3 optimized by the first-principles PP methods are sometimes inconsistent with the experimental results.

$BaTiO_3$ is a well-known ferroelectric ABO_3, and shows the tetragonal structure at room temperature. However, even in this well-known material, the optimized structure by the PP methods of first-principles calculations is strongly dependent on the choice of the Ti PPs, i.e., preparation for Ti 3s and 3p semicore states in addition to Ti 3d and 4s valence states is essential to the appearance of the tetragonal structure. This is an important problem for ferroelectricity, but it has been generally recognized for a long time that this problem is within an empirical framework of the calculational technics (Gonze et al., 2005).

It is known that ferroelectric state appears when the long-range forces due to the dipole-dipole interaction overcome the short-range forces due to the Coulomb repulsions. Cohen (Cohen & Krakauer, 1990; Cohen, 1992) proposed that the hybridization between Ti 3d state and O 2p state (Ti 3d–O 2p) in $BaTiO_3$ and $PbTiO_3$, which weakens the short-range force of the Coulomb repulsions between Ti and O ions, is origin of ferroelectricity. However, it seems to be difficult to consider explicitly whether the long-range force due to the dipole-dipole interaction can or cannot overcome the short-range force only with the Ti 3d–O 2p hybridization. Investigations about the relationship between the Ti–O Coulomb repulsions and the appearance of ferroelectricity were separately reported. Theoretically, we previouly investigated (Miura & Tanaka, 1998) the influence of the Ti–O_z Coulomb repulsions on Ti ion displacement in tetragonal $BaTiO_3$ and $PbTiO_3$, where O_z denotes the O atom to the z-axis (Ti is displaced to the z-axis). Whereas the hybridization between Ti 3d state and O_z $2p_z$ state stabilize Ti ion displacement, the strong Coulomb repulsions between Ti 3s and $3p_z$

states and O $2p_z$ states do not favourably cause Ti ion displacement. Experimentally, on the other hand, Kuroiwa *et al.* (Kuroiwa et al., 2001) showed that the appearance of ferroelectric state is closely related to the total charge density of Ti–O bondings in $BaTiO_3$. As discussed above, investigation about a role of Ti 3s and 3p states is important in the appearance of the ferroelectric state in tetragonal $BaTiO_3$.
It has been generally known (Miura & Furuta, 2010) that the most stable structure of ABO_3 is closely related to the tolerance factor t,

$$t \equiv \frac{r_A + r_O}{\sqrt{2}\,(r_B + r_O)} \quad , \tag{1}$$

where r_A, r_B, and r_O denote the ionic radii of A, B, and O ions, respectively. Generally, the most stable structure is tetragonal for $t \gtrsim 1$, cubic for $t \approx 1$, and rhombohedral or orthorhombic for $t \lesssim 1$. In fact, $BaTiO_3$ (t = 1.062) and $SrTiO_3$ (t = 1.002) show tetragonal and cubic structures in room temperature, respectively. However, under external pressure, e.g., hydrostatic or in-plane pressure (Ahart et al., 2008; Fujii et al., 1987; Haeni et al., 2004), the most stable structures of ABO_3 generally change; e.g., $SrTiO_3$ shows the tetragonal and ferroelectric structure even in room temperature when the a lattice parameter along the [100] axis (and also the [010] axis) is smaller than the bulk lattice parameter with compressive stress (Haeni et al., 2004). Theoretical investigations of ferroelectric ABO_3 under hydrostatic or in-plane pressure by first-principles calculations have been reported (Bévillon et al., 2007; Diéguez et al., 2005; Furuta & Miura, 2010; Khenata et al., 2005; Kornev et al., 2005; Miura et al., 2010a; Ricinschi et al., 2006; Uratani et al., 2008; Z. Wu et al., 2005), and their calculated results are consistent with the experimental results. However, even in $BaTiO_3$, which are a well-known lead-free ferroelectric and piezoelectric ABO_3, few theoretical papers about the piezoelectric properties with in-plane compressive stress have been reported.
Recently, we investigated the roles of the Ti–O Coulombrepulsions in the appearance of a ferroelectric states in tetragonal $BaTiO_3$ by the analysis of a first-principles PP method (Miura et al., 2010a). We investigated the structural properties of tetragonal and rhombohedral $BaTiO_3$ with two kind of Ti PPs, and propose the role of Ti 3s and 3p states for ferroelectricity. Moreover, we also investigated the structural, ferroelectric, and piezoelectric properties of tetragonal $BaTiO_3$ and $SrTiO_3$ with in-plane compressive structures (Furuta & Miura, 2010). We discussed the difference in the piezoelectric mechanisms between $BaTiO_3$ and $SrTiO_3$ with in-plane compressive structures, which would be important for piezoelectric material design. In this chapter, based on our previous reports (Furuta & Miura, 2010; Miura et al., 2010a), the author discusses a general role of B–O Coulomb repulsions for ferroelectricity and piezoelectricity in ABO_3, especially in $BaTiO_3$ and $SrTiO_3$.

2. Calculations

Calculations of $BaTiO_3$ and $SrTiO_3$ were performed using the ABINIT package code (Gonze et al., 2002), which is one of the norm-conserving PP (NCPP) methods. Electron-electron interaction was treated in the local-density approximation (LDA) (Perdew & Wang, 1992). Pseudopotentials were generated using the OPIUM code (Rappe, 2004):

(i) In order to investigate the role of Ti 3s and 3p states for $BaTiO_3$, two kinds of Ti PPs were prepared: one is the Ti PP with 3s, 3p, 3d and 4s electrons treated as semicore or valence electrons (Ti3spd4s PP), and the other is the Ti PP with only 3d and 4s electrons treated as valence electrons (Ti3d4s PP). The above seudopotentials were generated using the OPIUM

code (Rappe, 2004), and the differences between the calculated result and the experimental one are within 1.5 % of the lattice parameter and within 10 % of the bulk modulus in the optimized calculation of bulk Ti in both PPs. Moreover, Ba PP with 5s, 5p and 6s electrons treated as semicore or valence electrons, and O PP with 2s and 2p electrons treated as semicore or valence electrons, were also prepared. The cutoff energy for plane-wave basis functions was set to be 50 Hartree (Hr). A 6×6×6 Monkhorst-Pack k-point mesh was set in the Brillouin zone of the unit cell. The number of atoms in the unit cell was set to be five, and positions of all the atoms were optimized within the framework of the tetragonal ($P4mm$) or rhombohedral ($R3m$) structure.

(ii) The ferroelectric and piezoelectric properties of $SrTiO_3$ and $BaTiO_3$ with compressive tetragonal structures are investigated. Pseudopotentials were generated using the OPIUM code (Rappe, 2004); 4s (5s), 4p (5p) and 5s (6s) electrons for Sr (Ba), 3s, 3p, 3d and 4s electrons for Ti, and 2s and 2p electrons for O were treated as semicore or valence electrons. The cutoff energy fo the plane wave basis functions was set to be 50 Hr. A 6×6×6 Monkhorst-Pack k-point mesh was set in the Brillouin zone of the unit cell. The number of atoms in the ABO_3 unit cell was set to be five, and the coordinations of all the atoms were optimized within a framework of the tetragonal ($P4mm$) structure. An $6 \times 6 \times 6$ Monkhorst-Pack k-point sampling was set in Brillouin zone of the unit cell.
In the present calculations, spontaneous polarizations and piezoelectric constants were also evaluated, due to the Born effective charges (Resta, 1994) and density-functional perturbation theory (Hamann et al., 2005; X. Wu et al., 2005). The spontaneous polarization of tetragonal structures along the [001] axis, P_3, is defined as,

$$P_3 \equiv \sum_k \frac{ec}{\Omega} Z^*_{33}(k) u_3(k) \,, \tag{2}$$

where e, c, and Ω denote the charge unit, the lattice parameter of the unit cell along the [001] axis, and the volume of the unit cell, respectively. $u_3(k)$ denotes the displacement along the [001] axis of the kth atom, and $Z^*_{33}(k)$ denotes the Born effective charges (Resta, 1994) which contributes to the P_3 from the $u_3(k)$. The piezoelectric e constants, on the other hand, are defined as

$$e_{\alpha\beta} \equiv \left(\frac{\partial P_\alpha}{\partial \eta_\beta} \right)_u + \sum_k \left(\frac{\partial P_\alpha}{\partial u_\alpha(k)} \right)_\eta \frac{\partial u_\alpha(k)}{\partial \eta_\beta} \,, \tag{3}$$

where P, η, and $u(k)$ denote the spontaneous polarization, the strain, and the displacement of the kth atom, respectively. α and β denote the direction-indexes of the axis, i.e., 1 along the [100] axis, 2 along the [010] axis, and 3 along the [001] axis, respectively. In eq. (3), the first term of the right hand denotes the clamped term evaluated at vanishing internal strain, and the second term denotes the relaxed term that is due to the relative displacements. According to the eqs. (2) and (3), therefore, e_{33} or e_{31} can be especially written as,

$$e_{3\beta} = \left(\frac{\partial P_3}{\partial \eta_\beta} \right)_u + \sum_k \frac{ec}{\Omega} Z^*_{33}(k) \frac{\partial u_3(k)}{\partial \eta_\beta} \qquad (\beta = 3, 1) \,. \tag{4}$$

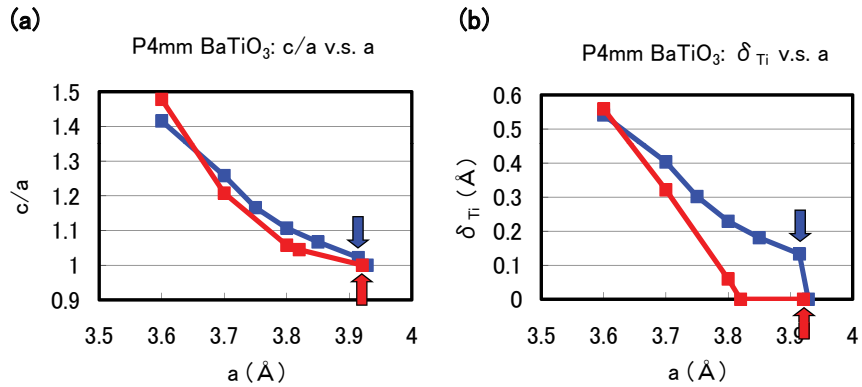

Fig. 1. Optimized calculated results as a function of a lattice parameters in tetragonal $BaTiO_3$: (a) c/a ratio and (b) δ_{Ti} to the [001] axis. Blue lines correspond to the results with the Ti3spd4s PP, and red lines correspond to those with the Ti3d4s PP. Results with arrows are the fully optimized results, and the other results are those with c and all the inner coordinations optimized for fixed a (Miura et al., 2010a).

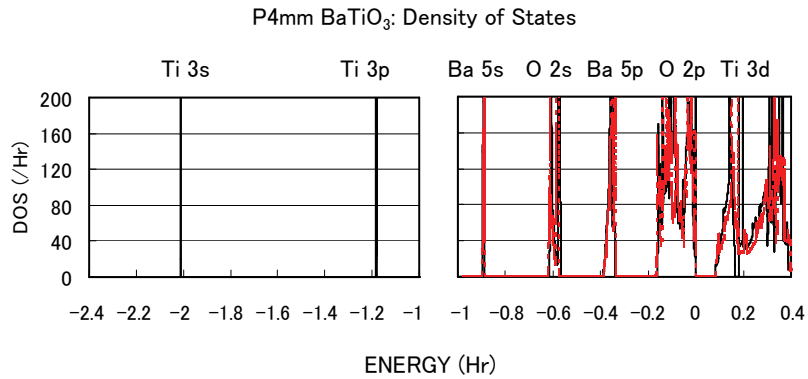

Fig. 2. Total density of states (DOS) of fully optimized tetragonal $BaTiO_3$ with the Ti3spd4s PP (solid line) and cubic $BaTiO_3$ with the Ti3d4s PP (red dashed line) (Miura et al., 2010a).

3. Results and discussion

3.1 $BaTiO_3$: Role of Ti 3s and 3p states for ferroelectricity

In this subsection, the author discusses the role of Ti 3s and 3p states for ferroelectricity for ferroelectricity in tetragonal $BaTiO_3$.

Figures 1(a) and 1(b) show the optimized results for the ratio c/a of the lattice parameters and the value of the Ti ion displacement (δ_{Ti}) as a function of the a lattice parameters in tetragonal $BaTiO_3$, respectively. Results with arrows are the fully optimized results, and the others results are those with the c lattice parameters and all the inner coordinations optimized for fixed

a. Note that the fully optimized sturucture of $BaTiO_3$ is tetragonal with the Ti3spd4s PP, whereas it is cubic ($Pm\bar{3}m$) with the Ti3d4s PP. As shown in Fig. 1(a) and 1(b), c/a and δ_{Ti} show significantly different results for $a \gtrsim 3.7$ whereas they show almost the same results for $a \lesssim 3.7$, for both Ti PPs. This result suggests that the optimized results of ABO_3 with smaller lattice parameters, e.g., under high pressure (Bévillon et al., 2007), are almost independent of the choice of PP.

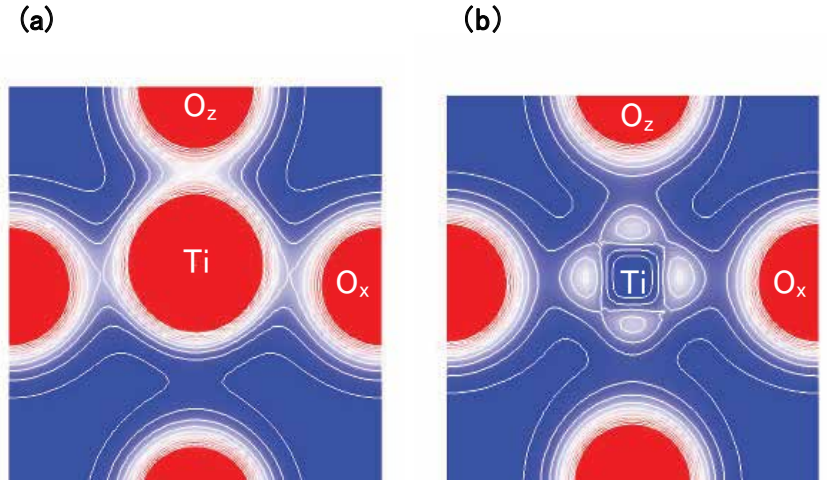

Fig. 3. Two-dimentional electron-density contour map on the xz-plane for tetragonal $BaTiO_3$: (a) with the Ti3spd4s PP, and (b) with the Ti3d4s PP. The optimized calculated results with a fixed to be 3.8 are shown in both figures. The electron density increases as color changes from blue to red via white. Contour curves are drawn from 0.4 to 2.0 $e/^3$ with increments of 0.2 $e/^3$ (Miura et al., 2010a).

The calculated results shown in Fig. 1 suggest that the explicit treatment of Ti 3s and 3p semicore states is essential to the appearance of ferroelectric states in $BaTiO_3$. In the following, the author investigates the role of Ti 3s and 3p states for ferroelectricity from two viewpoints. One viwpoint concerns hybridizations between Ti 3s and 3p states and other states. Figure 2 shows the total density of states (DOS) of tetragonal $BaTiO_3$ with two Ti PPs. Both results are in good agreement with previous calculated results (Chen et al., 2004; Khenata et al., 2005) by the full-potential linear augmented plane wave (FLAPW) method. In the DOS with the Ti3spd4s PP, the energy "levels", not bands, of Ti 3s and 3p states, are located at -2.0 Hr and -1.2 Hr, respectively. This result suggests that the Ti 3s and 3p orbitals do not make any hybridizations but only give Coulomb repulsions with the O orbitals as well as the Ba orbitals. In the DOS with the Ti3d4s PP, on the other hand, the energy levels of Ti 3s and 3p states are not shown because Ti 3s and 3p states were treated as the core charges. This result means that the Ti 3s and 3p orbitals cannot even give Coulomb repulsions with the O orbitals as well as the Ba orbitals.
Another viwpoint is about the Coulomb repulsions between Ti 3s and $3p_{x\,(y)}$ states and $O_{x\,(y)}$ 2s and $2p_{x\,(y)}$ states in tetragonal $BaTiO_3$. Figures 3(a) and 3(b) show two-dimentional electron-density contour map on the xz-plane for tetragonal $BaTiO_3$ with the Ti3spd4s PP, and that with the Ti3d4s PP, respectively. These are the optimized calculated results with a fixed

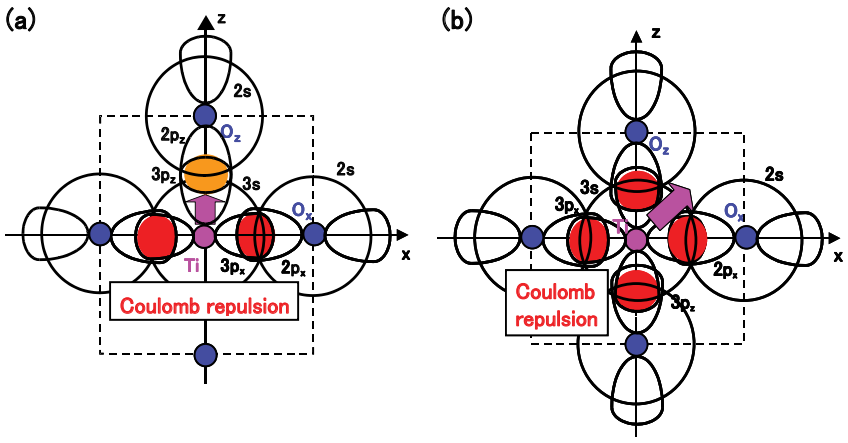

Fig. 4. Illustrations of the proposed mechanisms for the Coulomb repulsions between Ti 3s and 3p states and O 2s and 2p states in $BaTiO_3$: (a) anisotropic Coulomb repulsions between Ti 3s and $3p_{x\,(y)}$ states and $O_{x\,(y)}$ 2s and $2p_{x\,(y)}$ states, and between Ti 3s and $3p_z$ states and O_z 2s and $2p_z$ states, in the tetragonal structure. (b) isotropic Coulomb repulsions between Ti 3s and $3p_{x\,(y)\,(z)}$ states and $O_{x\,(y)\,(z)}$ 2s and $2p_{x\,(y)\,(z)}$ states, in the rhombohedral structure (Miura et al., 2010a).

to be 3.8 , and the electron density in Fig. 3(a) is quantitatively in good agreement with the experimental result (Kuroiwa et al., 2001). The electron density between Ti and O_x ions in Fig. 3(a) is larger than that in Fig. 3(b), which suggests that Ti ion displacement is closely related to the Coulomb repulsions between Ti 3s and 3p states and O 2s and 2p states along the [001] axis (the z-axis in this case).

The present discussion of the Coulomb repulsions is consistent with the previous reports. A recent soft mode investigation (Oguchi et al., 2009) of $BaTiO_3$ shows that Ba ions contribute little to the appearance of Ti ion displacement along the [001] axis. This result suggests that Ti ion displacement is closely related to the structural distortion of TiO_6 octahedra. In the present calculations, on the other hand, the only difference between $BaTiO_3$ with the Ti3spd4s PP and with the Ti3d4s PP is the difference in the expression for the Ti 3s and 3p states, i.e., the explicit treatment and including core charges. However, our previous calculation (Miura & Tanaka, 1998) shows that the strong Coulomb repulsions between Ti 3s and $3p_z$ states and O_z 2s and $2p_z$ states do not favour Ti ion displacement along the [001] axis. This result suggests that the Coulomb repulsions between Ti 3s and $3p_{x\,(y)}$ states and $O_{x\,(y)}$ 2s and $2p_{x\,(y)}$ states would contribute to Ti ion displacement along the [001] axis, and the suggestion is consistent with a recent calculation (Uratani et al., 2008) for $PbTiO_3$ indicating that the tetragonal and ferroelectric structure appears more favourable as the a lattice parameter decreases.

Considering the above investigations, the author proposes the mechanism of Ti ion displacement as follows: Ti ion displacement along the z-axis appears when the Coulomb repulsions between Ti 3s and $3p_{x\,(y)}$ states and $O_{x\,(y)}$ 2s and $2p_{x\,(y)}$ states, in addition to the dipole-dipole interaction, overcome the Coulomb repulsions between Ti 3s and $3p_z$ states and O_z 2s and $2p_z$ states (Miura & Tanaka, 1998). An illustration of the Coulomb repulsions is shown in Fig. 4(a). In fully optimized $BaTiO_3$ with the Ti3spd4s PP, the Ti ion can be displaced due to the above mechanism. In fully optimized $BaTiO_3$ with the Ti3d4s PP, on the other

hand, the Ti ion cannot be displaced due to the weaker Coulomb repulsions between Ti and $O_{x(y)}$ ions. However, since the Coulomb repulsion between Ti and O_z ions in $BaTiO_3$ with the Ti3d4s PP is also weaker than that in $BaTiO_3$ with the Ti3spd4s PP, the Coulomb repulsions between between Ti and $O_{x(y)}$ ions in addition to the log-range force become comparable to the Coulomb repulsions between Ti and O_z ions both in Ti PPs, as the lattice parameter a becomes smaller. The above discussion suggests that the hybridization between Ti 3d and O_z 2s and $2p_z$ stabilizes Ti ion displacement, but contribute little to a driving force for the appearance of Ti ion displacement.
It seems that the above proposed mechanism for tetragonal $BaTiO_3$ can be applied to the mechanism of Ti ion displacement in rhombohedral $BaTiO_3$, as illustrated in Fig. 4(b). The strong isotropic Coulomb repulsions between Ti 3s and $3p_{x(y)(z)}$ states and $O_{x(y)(z)}$ 2s and $2p_{x(y)(z)}$ states yield Ti ion displacement along the [111] axis. On the other hand, when the isotropic Coulomb repulsions are weaker or stronger, the Ti ion cannot be displaced and therefore it is favoured for the crystal structure to be cubic.

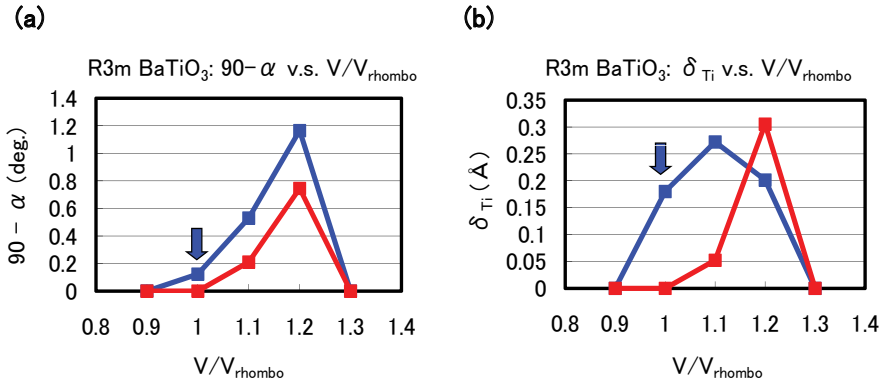

Fig. 5. Optimized calculated results as a function of the fixed volumes of the unit cells in rhombohedral $BaTiO_3$: (a) $90-\alpha$ degree and (b) δ_{Ti} to the [111] axis. Blue lines correspond to the results with the Ti3spd4s PP, and red lines correspond to those with the Ti3d4s PP. V_{rhombo} denote the volume of the fully optimized unit cell with the Ti 3spd4s PP. Results with arrows are the fully optimized results, and the other results are those with all the inner coordinations optimized for fixed volumes of the unit cells (Miura et al., 2010a).

Let us investigate the structural properties of rhombohedral $BaTiO_3$. Figures 5(a) and 5(b) show the optimized results of the $90-\alpha$ degree and δ_{Ti} as a function of fixed volumes of the unit cells in rhombohedral $BaTiO_3$, respectively, where α denotes the angle between two lattice vectors. In these figures, α denotes the angle between two crystal axes of rhombohedral $BaTiO_3$, and δ_{Ti} denotes the value of the Ti ion displacement along the [111] axis. Results with arrows are the fully optimized results; V_{rhombo} denote the volume of the fully optimized unit cell with the Ti 3spd4s PP. The other results are those with all the inner coordinations optimized with fixed volumes of the unit cells. The proposal mechanisms about the Coulomb repulsions seem to be consistent with the calculated results shown in Fig. 5: For $V/V_{rhombo} \lesssim 0.9$ or $\gtrsim 1.3$, the isotropic Coulomb repulsions are weaker or stronger, and the Ti ion cannot be displaced along the [111] axis and therefore the crystal structure is cubic for both Ti PPs. For $0.9 \lesssim V/V_{rhombo} \lesssim 1.3$, on the other hand, the isotropic Coulomb repulsions

are strong enough to yield Ti ion displacement for both Ti PPs. However, since the magnitude of the isotropic Coulomb repulsion is different in the two Ti PPs, the properties of the $90-\alpha$ degree and δ_{Ti} are different quantitatively.

3.2 Role of the Ti–O Coulomb repulsions for piezoelectric $SrTiO_3$ and $BaTiO_3$

As discussed in the previous subsection, the Coulomb repulsions between Ti 3s and $3p_{x(y)}$ states and $O_{x(y)}$ 2s and $2p_{x(y)}$ states have an important role in the appearance of the ferroelectric state in tetragonal $BaTiO_3$. In this subsection, the author discusses the role of the Ti–O Coulomb repulsions for piezoelectric $SrTiO_3$ and $BaTiO_3$.

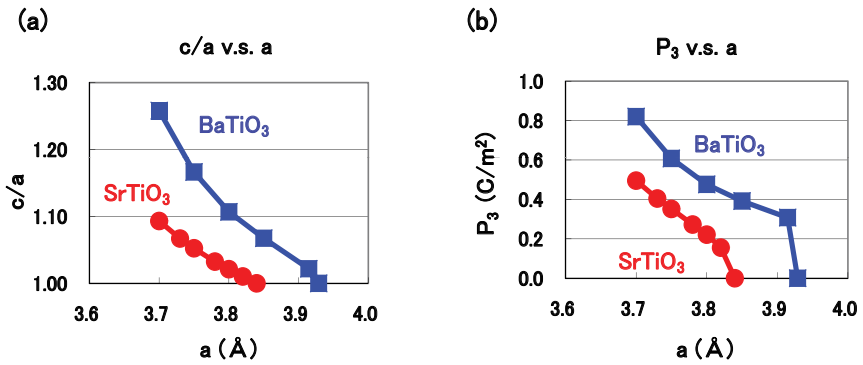

Fig. 6. Optimized calculated results as a function of a lattice parameters in compressive tetragonal $SrTiO_3$ and $BaTiO_3$: (a) c/a ratio and (b) P_3, i.e., spontaneous polarization along the [001] axis (Furuta & Miura, 2010).

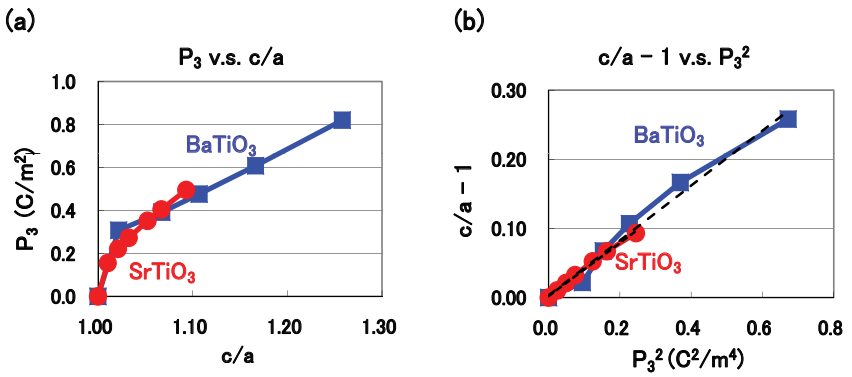

Fig. 7. (a) P_3 as a function of c/a ratios, and (b) c/a ratio as a function of P_3^2. These values are derived from the calculated results as shown in Figs. 6(a) and (b). Dotted and dashed lines in Fig. 7(b) serve as visual guides for $SrTiO_3$ and $BaTiO_3$, respectively (Furuta & Miura, 2010).

Figures 6(a) shows the optimized results for the ratio c/a as a function of the a lattice parameters in tetragonal $SrTiO_3$ and $BaTiO_3$. These results are the fully optimized results and the results with the c lattice parameters and all the inner coordinations optimized for

fixed a. The fully optimized parameters of $SrTiO_3$ (a = 3.84 : cubic) and $BaTiO_3$ (a = 3.91 and c = 4.00 : tetragonal) are within 2.0% in agreement with the experimental results in room temperature. Figures 6(b) shows the evaluated results for P_3 as a function of the a lattice parameters in tetragonal $SrTiO_3$ and $BaTiO_3$, where P_3, which is evaluated by eq. (2), denotes the spontaneous polarization along the [001] axis. Note that the tetragonal and ferroelectric structures appear even in $SrTiO_3$ when the fixed a lattice parameter is compressed to be smaller than the fully-optimized a lattice parameter. As shown in Figs. 6(a) and 6(b), the tetragonal and ferroelectric structure appear more favorable as the fixed a lattice parameter decreases, which is consistent with previous calculated results (Miura et al., 2010a; Ricinschi et al., 2006; Uratani et al., 2008). The results would be due to the suggestion discussed in the previous section that the large Coulomb repulsion of Ti–O bondings along the [100] axis (and the [010] axis) is a driving force of the displacement of Ti ions along the [001] axis, i.e., the large Coulomb repulsion along the [100] axis (and the [010] axis) is essential for the appearance of the tetragonal structure. Figure 7(a) shows the relationship between P_3 and the ratio c/a, where P_3 and c/a are derived from the calculated results shown in Figs. 6(a) and 6(b). The property of $BaTiO_3$ in Fig. 7(a) is in qualitatively agreement with a previous calculational result (Ricinschi et al., 2006). Figure 7(b) shows the relationship between the ratio c/a and P_3^2. Note that $c/a - 1$ is proportional to P_3^2 with alomost the same coefficients in both $SrTiO_3$ and $BaTiO_3$. Clearly, the ratio c/a is a good parameter in both tetragonal $SrTiO_3$ and $BaTiO_3$ with in-plane compressive stress. Therefore, in the following, the author uses the ratio c/a as a parameter for the investigations of the piezoelectric properties.

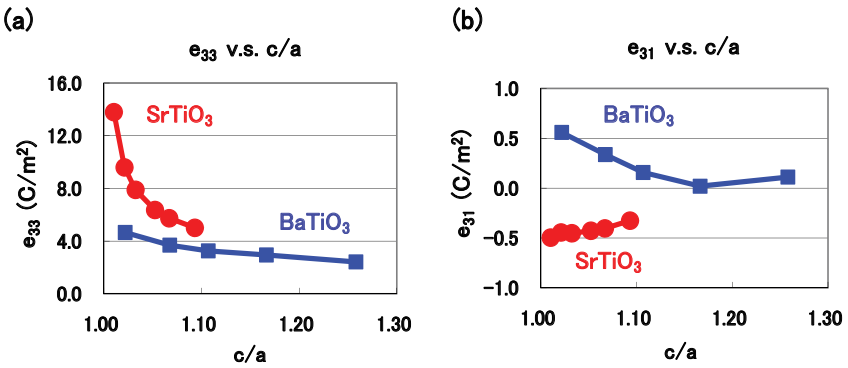

Fig. 8. Evaluated piezoelectric constants as a function of c/a ratios in optimized tetragonal $SrTiO_3$ and $BaTiO_3$: (a) e_{33} and (b) e_{31} (Furuta & Miura, 2010).

Figures 8(a) and 8(b) shows the piezoelectric properties of e_{33} and e_{31} as a function of the ratio c/a in tetragonal $SrTiO_3$ and $BaTiO_3$. The ratio c/a is optimized value as shown in Fig. 6(a) and e_{33} and e_{31} are evaluated values in their optimized structures. Note that e_{33} become larger at $c/a \approx 1$, especially in $SrTiO_3$. These properties seem to be similar to the properties arond the Curie temperatures in piezoelectric ABO_3; Damjanovic emphasized the importance of the polarization extension as a mechanism of larger piezoelectric constants in a recent paper (Damjanovic, 2010). Contrary to e_{33}, on the other hand, the changes in e_{31} are much smaller than the changes in e_{33}, but note that e_{31} shows negative in $SrTiO_3$ while positive in $BaTiO_3$.

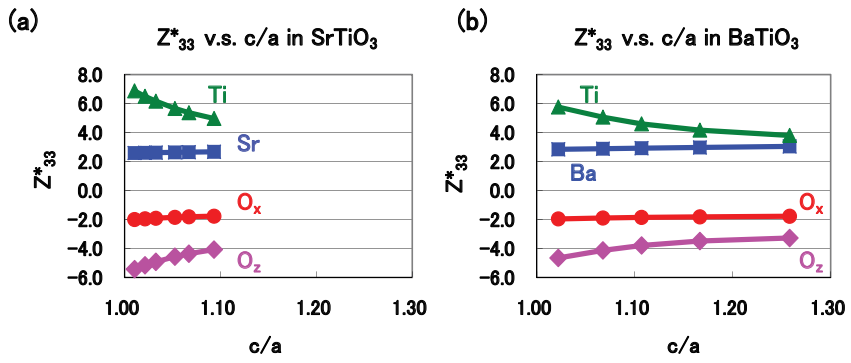

Fig. 9. Evaluated Born effective charges $Z^*_{33}(k)$ as a function of c/a ratios: (a) $SrTiO_3$ and (b) $BaTiO_3$. O_x and O_z denote oxygen atoms along the [100] axis and the [001] axis, respectively (Furuta & Miura, 2010).

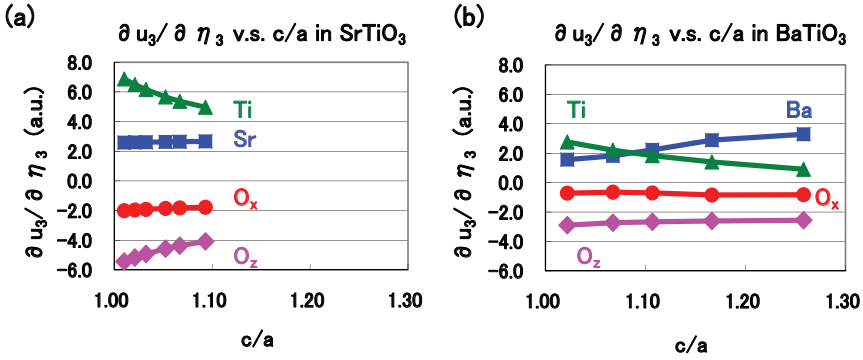

Fig. 10. Evaluated values of $\partial u_3(k)/\partial\eta_3$ as a function of c/a ratios: (a) $SrTiO_3$ and (b) $BaTiO_3$. "a.u." denotes the atomic unit (≈ 0.53) (Furuta & Miura, 2010).

As expressed in eq. (4), e_{3j} is the sum of the contributions from the clamped term and the relaxed term. However, it has been generally known that the contribution to e_{3j} from the clamped term is much smaller than that from the relaxed term; in fact, the absolute values of the e_{33} clamped terms are less than 1 C/m^2 in both $SrTiO_3$ and $BaTiO_3$. The author therefore investigates the contributions to the relaxed term of e_{33} and e_{31} in detail. As expressed in eq. (4), the relaxed terms of e_{3j} are proportional to the sum of the products between the $Z^*_{33}(k)$ and $\partial u_3(k)/\partial\eta_j$ (j = 3 or 1) values. Let us show the evaluated results of $Z^*_{33}(k)$, $\partial u_3(k)/\partial\eta_3$, and $\partial u_3(k)/\partial\eta_1$ in the following. Figures 9(a) and 9(b) show the $Z^*_{33}(k)$ values in $SrTiO_3$ and $BaTiO_3$, respectively. Properties of the $Z^*_{33}(k)$ values are quantitatively similar in both $SrTiO_3$ and $BaTiO_3$. Therefore, the difference in the properties of e_{33} and e_{31} between $SrTiO_3$ and $BaTiO_3$ must be due to the difference in the properties of $\partial u_3(k)/\partial\eta_j$. Figures 10(a) and 10(b) show the $\partial u_3(k)/\partial\eta_3$ values in $SrTiO_3$ and $BaTiO_3$, respectively. In these figures, O_x and O_z denote oxygen atoms along the [100] and [001] axes, respectively, and η_3 is defined as $\eta_3 \equiv (c - c_0)/c_0$, where c_0 denotes the c lattice parameter with fully optimized structure. Clearly, the absolute values of $\partial u_3(k)/\partial\eta_3$ are different in between $SrTiO_3$ and $BaTiO_3$. On

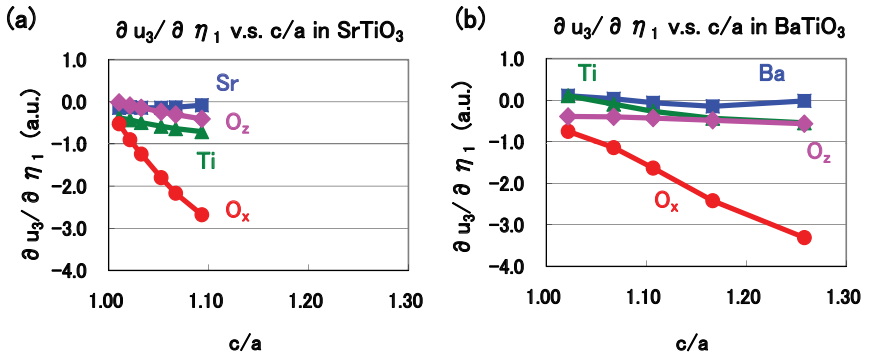

Fig. 11. Evaluated values of $\partial u_3(k)/\partial\eta_1$ as a function of c/a ratios: (a) $SrTiO_3$ and (b) $BaTiO_3$ (Furuta & Miura, 2010).

the other hand, Figs. 11(a) and 11(b) show the $\partial u_3(k)/\partial\eta_1$ values in $SrTiO_3$ and $BaTiO_3$, respectively; η_1 is defined as $\eta_1 \equiv (a - a_0)/a_0$, where a_0 denotes the a lattice parameter with fully optimized structure. The absolute values of $\partial u_3(k)/\partial\eta_1$, especially for Ti, O_x, and O_z, are different in between $SrTiO_3$ and $BaTiO_3$. As a result, the quantitative differences in e_{33} and e_{31} in between $SrTiO_3$ and $BaTiO_3$ are due to the differences in the contribution of the $\partial u_3(k)/\partial\eta_j$ values. In the following, the author would like to discuss the reasons of the quantitative differences in e_{33} and e_{31} in between $SrTiO_3$ and $BaTiO_3$.

Figure 12(a) shows the difference between the A–O_x distance (R_{A-O_x}) and the sum of r_A and r_{O_x} ($r_A + r_{O_x}$) on the (100) plane as a function of the ratio c/a, where the values of the ionic radii are defined as Shannon's ones (Shannon, 1976). Note that R_{A-O_x} is smaller than $r_A + r_{O_x}$ in both $SrTiO_3$ and $BaTiO_3$. However, the difference in absolute value between R_{A-O_x} and $r_A + r_{O_x}$ in $SrTiO_3$ is much smaller than the difference in $BaTiO_3$ for $1.00 \lesssim c/a \lesssim 1.10$. This result suggests that the Sr–O_x Coulomb repulsion on the (100) plane in $SrTiO_3$ is much smaller than the Ba–O_x Coulomb repulsion in $BaTiO_3$ and that therefore Sr and O_x ions of $SrTiO_3$ can be displaced more easily along the [001] axis than Ba and O_x ions of $BaTiO_3$. This would be a reason why the absolute values of $\partial u_3(k)/\partial\eta_3$ of Sr and O_x ions in $SrTiO_3$ are larger than those of Ba and O_x ions in $BaTiO_3$. Figure 12(b) shows the difference between the Ti–O_z distance (R_{Ti-O_z}) and $r_{Ti} + r_{O_z}$ along the [001] axis as a function of the ratio c/a. Note that R_{Ti-O_z} is smaller than $r_{Ti} + r_{O_z}$ in both $SrTiO_3$ and $BaTiO_3$. However, the difference in absolute value between R_{Ti-O_z} and $r_{Ti} + r_{O_z}$ in $SrTiO_3$ is smaller than the difference in $BaTiO_3$ for $1.00 \lesssim c/a \lesssim 1.10$. This result suggests that the Ti–O_z Coulomb repulsion along the [001] axis in $SrTiO_3$ is smaller than that in $BaTiO_3$ and that therefore the Ti ion of $SrTiO_3$ can be displaced more easily along the [001] axis than that of $BaTiO_3$. This would be a reason why the absolute values of $\partial u_3(k)/\partial\eta_3$ of Ti and O_z ions in $SrTiO_3$ are larger than that in $BaTiO_3$.

In the following, the author discusses the relationship between $\partial u_3(Ti)/\partial\eta_3$ and the ratio c/a in detail. Figure 13(a) shows the properties of the diffrences in the total energy (ΔE_{total}) as a function of u_{Ti}. In this figure, the properties of $SrTiO_3$ with c/a = 1.021 (η = 0.011), $SrTiO_3$ with c/a = 1.093 (η = 0.053) and $BaTiO_3$ with c/a = 1.022 as a reference, are shown. Calculations of E_{total} were performed with the fixed crystal structures of previously optimized structures except Ti ions. Figure 13(b) shows illustrations of ΔE_{total} curves with deviations at the minimum points of the ΔE_{total} values, corresponding to the ΔE_{total} curves of $SrTiO_3$ in Fig. 13(a). Clearly, as η_3 becomes smaller, the deviated value at the minimum point of the

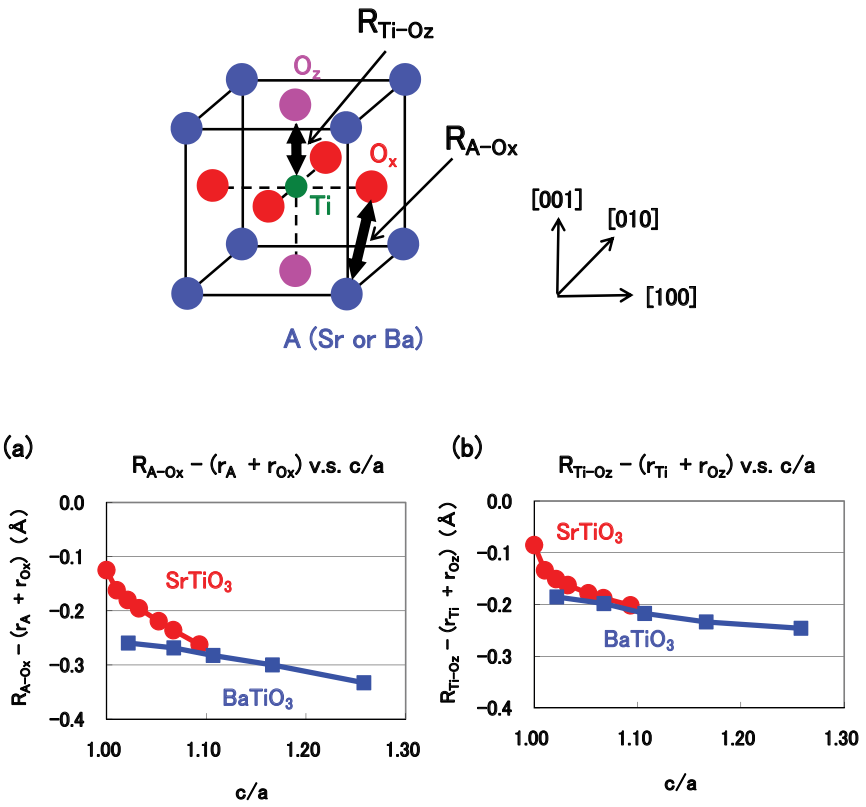

Fig. 12. Evaluated values as a function of c/a ratios in optimized tetragonal $SrTiO_3$ and $BaTiO_3$: (a) difference between the A–O_x distance (R_{A-O_x}) and $r_A + r_{O_x}$, and (b) difference between the Ti–O_z distance (R_{Ti-O_z}) and $r_{Ti} + r_{O_z}$, as a function of the ratio c/a. R_{A-O_x} and R_{Ti-O_z} in $ATiO_3$ are also illustrated; all the ionic radii are much larger, and A and Ti ions are displaced along the [001] axis in real $ATiO_3$ (Furuta & Miura, 2010).

ΔE_{total} values becomes smaller, i.e., the Ti ion can be displaced more favourably. On the other hand, as shown in Fig. 10(a), the absolute value of $\partial u_3(Ti)/\partial \eta_3$ becomes larger as η_3 becomes smaller. Therefore, the Ti ion can be displaced more favourably as the deviated value at the minimum point of the ΔE_{total} values becomes smaller.

Next, let us discuss quantitative properties of e_{31}, especially the reason why e_{31} in $SrTiO_3$ shows negative while positive in $BaTiO_3$. Figure 14(a) shows the difference between the Ti–O_x distance (R_{Ti-O_x}) and $r_{Ti} + r_{O_x}$ along the [100] axis as a function of the ratio c/a. Note that R_{Ti-O_x} is smaller than $r_{Ti} + r_{O_x}$ in both $SrTiO_3$ and $BaTiO_3$. However, the difference in absolute value between R_{Ti-O_x} and $r_{Ti} + r_{O_x}$ in $SrTiO_3$ is larger than that in $BaTiO_3$, i.e., R_{Ti-O_x} in $SrTiO_3$ is smaller than R_{Ti-O_x} in $BaTiO_3$. This result suggests that the Ti–O_x Coulomb repulsion along the [100] axis in $SrTiO_3$ is larger than that in $BaTiO_3$ and that therefore Ti and O_x ions of $SrTiO_3$ can be displaced along the [001] axis more easily than those of $BaTiO_3$, as discussed in previous subsection. This would be a reason why the absolute values of $\partial u_3(k)/\partial \eta_1$ of Ti and O_x ions in $SrTiO_3$ are larger than those in $BaTiO_3$. Therefore, each

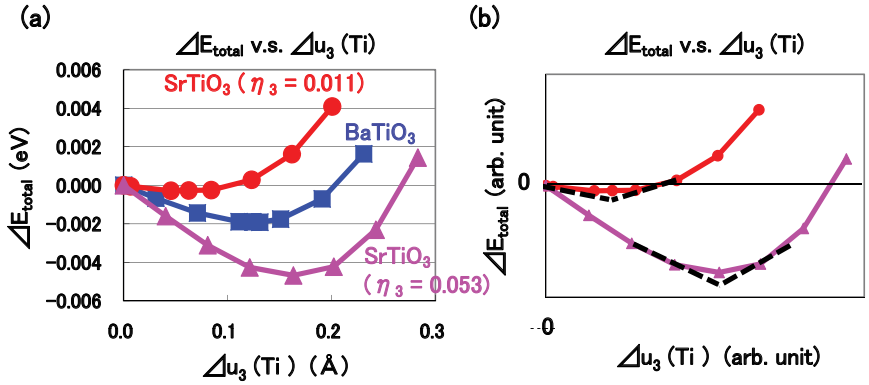

Fig. 13. (a) ΔE_{total} as a function of u_{Ti} in tetragonal $SrTiO_3$ and $BaTiO_3$. (b) Illustration of the ΔE_{total} curves in tetragonal $SrTiO_3$ ($\eta = 0.011$) and $SrTiO_3$ ($\eta = 0.053$) with deviations at the minimum point of ΔE_{total}.

absolute value of $Z^*_{\text{Ti}} \times \partial u_3(\text{Ti})/\partial\eta_1$ (< 0) and $Z^*_{\text{O}_x} \times \partial u_3(\text{O}_x)/\partial\eta_1$ (> 0) in $SrTiO_3$ is larger than that in $BaTiO_3$. Figure 14(b) shows the difference between the A–O_z distance ($R_{A-\text{O}_z}$) and $r_A + r_{\text{O}_z}$ on the (001) plane as a function of the ratio c/a. Note that $R_{A-\text{O}_z}$ is smaller than $r_A + r_{\text{O}_z}$ in both $SrTiO_3$ and $BaTiO_3$. However, the difference in absolute value between $R_{A-\text{O}_z}$ and $r_A + r_{\text{O}_z}$ in $BaTiO_3$ is larger than that in $SrTiO_3$. This result suggests that the Ba–O_z Coulomb repulsion on the (001) plane in $BaTiO_3$ is larger than that in $SrTiO_3$ and that therefore O_z ion of $BaTiO_3$ can be displaced along the [001] axis more easily than that of $SrTiO_3$, as discussed in previous subsection. This would be a reason why the absolute value of $\partial u_3(k)/\partial\eta_1$ of O_z ion in $BaTiO_3$ is larger than that in $SrTiO_3$. Therefore, the absolute value of $Z^*_{\text{O}_z} \times \partial u_3(\text{O}_z)/\partial\eta_1$ (> 0) in $BaTiO_3$ is larger than that in $SrTiO_3$. Finally, as a result, the above investigations suggest that the signature of e_{31} in $SrTiO_3$ or $BaTiO_3$ is closely related to the difference in absolute values between $Z^*_{\text{Ti}} \times \partial u_3(\text{Ti})/\partial\eta_1$ and the sum of $Z^*_{\text{O}_x} \times \partial u_3(\text{O}_x)/\partial\eta_1$ and $Z^*_{\text{O}_z} \times \partial u_3(\text{O}_z)/\partial\eta_1$.

4. Summary

Using a first-principles calculation with optimized structures, the author has investigated the role of the Coulomb repulsions between Ti 3s and 3p states and O 2s and 2p states in ferroelectric $BaTiO_3$. It has been found that the Coulomb repulsions between Ti 3s and $3p_{x(y)}$ states and $O_{x(y)}$ 2s and $2p_{x(y)}$ states are closely related to the appearance of Ti ion displacement in tetragonal $BaTiO_3$. This mechanism seems to be consistent with the appearance of Ti ion displacement in rhombohedral $BaTiO_3$. The present investigation suggests that the Coulomb repulsions between Ti 3s and 3p states and O 2p states have an important role in ferroelectricity. In addition to this suggestion, the author believes that the present investigation will show a guideline for the choice of PPs when first-principles calculations with PP methods are performed. The author has also investigated the ferroelectric and piezoelectric properties of $SrTiO_3$ and $BaTiO_3$ with in-plane compressive tetragonal structures using a first-principles calculation. It has been found that the ferroelectric structure even in $SrTiO_3$ appears with in-plane compressive structures. The piezoelectric constant e_{33} drastically increases in $SrTiO_3$ rather than that in $BaTiO_3$ as the tetragonal ratio c/a (> 1) is

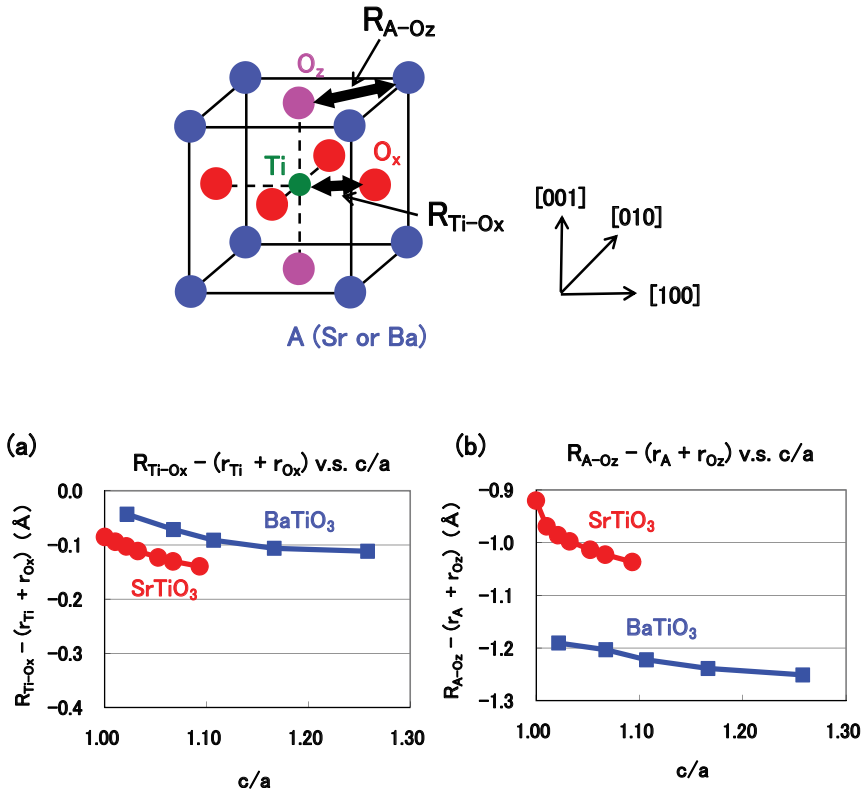

Fig. 14. Evaluated values as a function of c/a ratios in optimized tetragonal $SrTiO_3$ and $BaTiO_3$: (a) difference between the Ti–O_x distance (R_{Ti-O_x}) and $r_{Ti} + r_{O_x}$, as a function of the ratio c/a, and (b) difference between the A–O_z distance (R_{A-O_z}) and $r_A + r_{O_z}$. R_{Ti-O_x} and R_{A-O_z} in $ATiO_3$ are also illustrated (Furuta & Miura, 2010).

close to 1. On the other hand, e_{31} shows negative in $SrTiO_3$ while positive in $BaTiO_3$, although the changes in their absolute values are very small. The author has found that these properties of e_{33} and e_{31} in $SrTiO_3$ and $BaTiO_3$ are closely related to the ionic distances.

5. Acknowledgements

The author thanks Professor H. Funakubo, Professor M. Azuma, M. Kubota and T. Furuta for useful discussion. The present work was partly supported by the Elements Science and Technology Project from the Ministry of Education, Culture, Sports, Science and Technology, Japan. Calculations for the present work were partly performed by the supercomputing grid cluster machine “TSUBAME" in Tokyo Institute of Technology.

6. References

Ahart, M., Somayazulu, M., Cohen, R. E., Ganesh, P., Dera, P., Mao, H., Hemley, R., Ren, Y., Liermann, P. & Wu, Z. (2008). Origin of morphotropic phase boundaries in

ferroelectrics. *Nature*, Vol. 451, No. 7178, pp. 545-549.

Bévillon, É. & Geneste, G. (2007). Unstable polar mode and minimum of the dielectric constant in cubic $BaSnO_3$ under hydrostatic pressure. *Phys. Rev. B*, Vol. 75, No. 21, p. 214106 (5 pages).

Bousquet, E. & Ghosez, P. (2006). First-principles study of barium titanate under hydrostatic pressure. *Phys. Rev. B*, Vol. 74, No. 18, p. 180101(R) (4 pages).

Chen, X., Lu, W. & Shen, S. C. (2004). First-principles study of photoconductivity in $BaTiO_3$ with oxygen vacancies. *Solid State Commun.*, Vol. 130, No. 10, pp. 641-645.

Cohen, R. E & Krakauer, H. (1990). Lattice dynamics and origin of ferroelectricity in $BaTiO_3$: Linearized-augmented-plane-wave total-energy calculations. *Phys. Rev. B*, Vol. 42, No. 10, pp. 6416-6423.

Cohen, R. E. (1992). Origin of ferroelectricity in perovskite oxides. *Nature*, Vol. 358, No. 6382, pp. 136-138.

Damjanovic, D. (2010). A morphotropic phase boundary system based on polarization rotation and polarization extension. *Appl. Phys. Lett.*, Vol. 97, No. 6, p. 062906 (3 pages).

Diéguez, O., Rabe, K. M., & Vanderbilt, D. (2005). First-principles study of epitaxial strain in perovskites. *Phys. Rev. B*, Vol. 72, No. 14, p. 144101 (9 pages), and references therein.

Fujii, Y., Uwe, H. & Sakudo, T. (1987). Stress-Induced Quantum Ferroelectricity in $SrTiO_3$. *J. Phys. Soc. Jpn.*, Vol. 56, No. 6, pp. 1940-1942.

Furuta, T & Miura, K. (2010). First-principles study of ferroelectric and piezoelectric properties of tetragonal $SrTiO_3$ and $BaTiO_3$ with in-plane compressive structures. *Solid State Commun.*, Vol. 150, No. 47-48, pp. 2350-2353.

Gonze, X., Beuken, J.-M., Caracas, R., Detraux, F., Fuchs, M., Rignanese, G.-M., Sindic, L., Verstraete, M., Zerah, G., Jollet, F., Torrent, M., Roy, A., Mikami, M., Ghosez, Ph., Raty,J.-Y. & Allan, D. C. (2002). First-principles computation of material properties: the ABINIT software project. *Comput. Mater. Sci.*, Vol. 25, No. 3, pp. 478-492.

Gonze., X. et al. (2005). Informations on the Troullier-Martins pseudopotentials.
URL: *http://www.abinit.org/downloads/psp-links/lda_tm_psp1_data*

Haeni, J. H., Irvin, P., Chang, W., Uecker, R., Reiche, P., Li, Y. L., Choudhury, S., Tian, W., Hawley, M. E., Craigo, B., Tagantsev, A. K., Pan, X. Q., Streiffer, K., Chen, L. Q., Kirchoefer, S. W., Levy, J. & Schlom, D. G. (2004). Room-temperature ferroelectricity in strained $SrTiO_3$. *Nature*, Vol. 430, No. 7001, pp. 758-761.

Hamann, D. R., Wu, X., Rabe, K. M. & Vanderbilt, D. (2005). Metric tensor formulation of strain in density-functional perturbation theory. *Phys. Rev. B*, Vol. 71, No. 3, p. 035117 (13 pages).

Khenata, R., Sahnoun, M., Baltache, H., Rérat, M., Rashek, A. H., Illes, N. & Bouhafs, B. (2005). First-principle calculations of structural, electronic and optical properties of $BaTiO_3$ and $BaZrO_3$ under hydrostatic pressure. *Solid State Commun.*, Vol. 136, No. 2, pp. 120-125.

Kornev, I. G., Bellaiche, L., Bouvier, P., Janolin, P.-E., Dkhil, B. & Kreisel, J. (2005). Ferroelectricity of Perovskites under Pressure. *Phys. Rev. Lett.*, Vol. 95, No. 19, p. 196804 (4 pages).

Kuroiwa, Y., Aoyagi, S., Sawada, A., Harada, J., Nishibori, E., Tanaka, M. & Sakata, M. (2001). Evidence for Pb-O Covalency in Tetragonal $PbTiO_3$. *Phys. Rev. Lett.*, Vol. 87, No. 21 p. 217601 (4 pages).

Miura, K. & Tanaka, M. (1998). Electronic structures of $PbTiO_3$: I. Covalent interaction between Ti and O ions. *Jpn. J. Appl. Phys.*, Vol. 37, No. 12A, pp. 6451-6459.

Miura, K. (2002). Electronic properties of ferroelectric $SrBi_2Ta_2O_9$, $SrBi_2Nb_2O_9$, and $PbBi_2Nb_2O_9$ with optimized structures. *Appl. Phys. Lett.*, Vol. 80, No. 16, pp. 2967-2969.

Miura, K., Kubota, M., Azuma, M. & Funakubo, H. (2009). Electronic and structural properties of $BiZn_{0.5}Ti_{0.5}O_3$ *Jpn. J. Appl. Phys.*, Vol. 48, No.9, p. 09KF05 (4 pages).

Miura, K., Furuta, T. & Funakubo, H. (2010a). Electronic and structural properties of $BaTiO_3$: A proposal about the role of Ti 3s and 3p states for ferroelectricity. *Solid State Commun.*, Vol. 150, No 3-4, pp. 205-208.

Miura, K., Kubota, M., Azuma, M. & Funakubo, H. (2010b). Electronic, structural, and piezoelectric properties of $BiFe_{1-x}Co_xO_3$. *Jpn. J. Appl. Phys.*, Vol. 49, No.9, p. 09ME07 (4 pages).

Miura, K. & Furuta, T. (2010). First-principles study of structural trend of BiMO$_3$ and BaMO$_3$: Relationship between tetragonal and rhombohedral structure and the tolerance factors. *Jpn. J. Appl. Phys.*, Vol. 49, No. 3, p. 031501 (6 pages), and references therein.

Miura, K., Azuma, M. & Funakubo, H. (2011). [Review] Electronic and structural properties of ABO_3: Role of the *B*–O Coulomb repulsions for ferroelectricity. *Materials*, Vol. 4, No 1, pp. 260-273.

Oguchi, T, Ishii, F. & Uratani, Y. (2009). New method for calculating physical properties from first principles–piezoelectric and multiferroics. *Butsuri*, Vol. 64, No. 4, pp. 270-276 (in Japanese).

Perdew, J. P. & Wang, Y. (1992). Accurate and simple analytic representation of the electron-gas correlation energy *Phys. Rev. B*, Vol. 45, No. 23, pp. 13244-13249.

Rappe, A. M. (2004). Opium–pseudopotential generation project.
URL: *http://opium.sourceforge.net/index.html*

Resta, R. (1994). Macroscopic polarization in crystalline dielectrics: the geometric phase approach. *Rev. Mod. Phys.*, Vol. 66, No. 3, pp. 899-915.

Ricinschi, D., Kanashima, T. & Okuyama, M. (2006). First-principles study of tetragonality ratio and unit-cell volume influence on spontaneous polarization of $BaTiO_3$ and $PbTiO_3$. *J. Soc. Mater. Sci. Jpn.*, Vol. 55, No. 2, pp. 169-172 (in Japanese).

Shannon, R. D. (1976). Revised effective ionic radii and systematic studies of interatomic distances in halides and chalcogenides. *Acta Crystallogr., Sect. A*, Vol. 32, No. 5, pp. 751-767.

Uratani, Y., Shishidou, T. & Oguchi T. (2008). First-principles calculations of colossal piezoelectric response in thin film $PbTiO_3$. *Ext. Abst. Jpn. Soc. Appl. Phys.*, Vol. 55, No. 2, p. 566 (in Japanese).

Vanderbilt, D. (2000). Berry-phase theory of proper piezoelectric response. *J. Phys. Chem. Solids*, Vol. 61, No. 2, pp. 147-150, and references therein.

Wu X., Vanderbilt, D. & Hamann, D. R. (2005). Systematic treatment of displacements, strains, and electric fields in density-functional perturbation theory. *Phys. Rev. B*, Vol. 72, No. 3, p. 035105 (13 pages).

Wu, Z. & Cohen, R. E. (2005). Pressure-induced anomalous phase transitions and colossal enhancement of piezoelectricity in $PbTiO_3$. *Phys. Rev. Lett.*, Vol. 95, No. 3, p. 037601 (4 pages).

21

Ab Initio Studies of H-Bonded Systems: The Cases of Ferroelectric KH_2PO_4 and Antiferroelectric $NH_4H_2PO_4$

S. Koval[1], J. Lasave[1], R. L. Migoni[1], J. Kohanoff[2] and N. S. Dalal[3]
[1]*Instituto de Física Rosario, Universidad Nacional de Rosario, CONICET*
[2]*Atomistic Simulation Group, The Queen's University, Belfast*
[3]*Department of Chemistry and NHMFL, Florida State University*
[1]*Argentina*
[2]*United Kingdom*
[3]*USA*

1. Introduction

A wide variety of molecular compounds are bound by Hydrogen bridges between the molecular units. In these compounds cooperative proton tunneling along the bridges plays an important role.(1) However, it is apparent that not only the proton behavior is relevant but also that of their associated matrix, leading to a wide range of possible behaviors. We are thus faced with the consideration of two in principle coupled subsystems: the proton tunneling subunit and the host lattice. Ubbelhode noted, in 1939,(2) that the nature of the H-bond changes upon substitution of Deuterium (D) for H. In addition, many H-bonded compounds show structural transitions that are strongly affected by deuteration.(3) The common assumption that proton tunneling completely dominates the transitional physics, in a chemically and structurally unchanged host, is an oversimplified model. Since the 1980's, a number of authors have noted in pressure studies that the changes in transition temperatures correlate well with the H-bond parameters.(4) Thus, the proton's (deuteron's) dynamics and the host are mutually determined. The host-and-tunneling system is not separable, and the physics of the proton-tunneling systems must be revised.(5)

Typical examples are KH_2PO_4 (KDP) and its analogs.(6) They were discovered as a novel family of ferroelectric (FE) compounds in the late 1930's by Busch and Scherer.(7) It was shown that KDP undergoes a paraelectric (PE) to FE transition at a critical temperature of ≈ 123 K. It was also found that upon substitution of Ammonium for Potassium the resulting $NH_4H_2PO_4$ (ADP) becomes antiferroelectric (AFE) below $T_c = 148$ K,(8) although chemically the NH_4^+ ion usually behaves similarly to the alkali metal ions, in particular K^+ and Rb^+. The structures of the AFE phase of ADP and the FE phase of KDP are depicted schematically from a top view in Fig. 1(a) and Fig. 1(c), respectively. Both materials exhibit strong H $\rightarrow$ D isotope effects on their transition temperatures. In subsequent years KDP and ADP have found extensive applications in electro-optical and laser spectroscopy. Nowadays, they are widely used in controlling and modulating the frequency of laser radiation in optoelectronic

devices, amongst other uses such as TV screens, electro-optic deflector prisms, interdigital electrodes, light deflectors, and adjustable light filters.(6) Besides the technological interest in these materials, they were also extensively studied from a fundamental point of view. KDP is considered the prototype FE crystal for the wide family of the H-bonded ferroelectric materials, while ADP is the analogous prototype for the AFE crystals belonging to this family. What makes these materials particularly interesting is the possibility of growing quite large, high-quality single crystals from solution, thus making them very suitable for experimental studies. Indeed, a large wealth of experimental data has been accumulated during second half of the past century. (4; 6; 9–13)

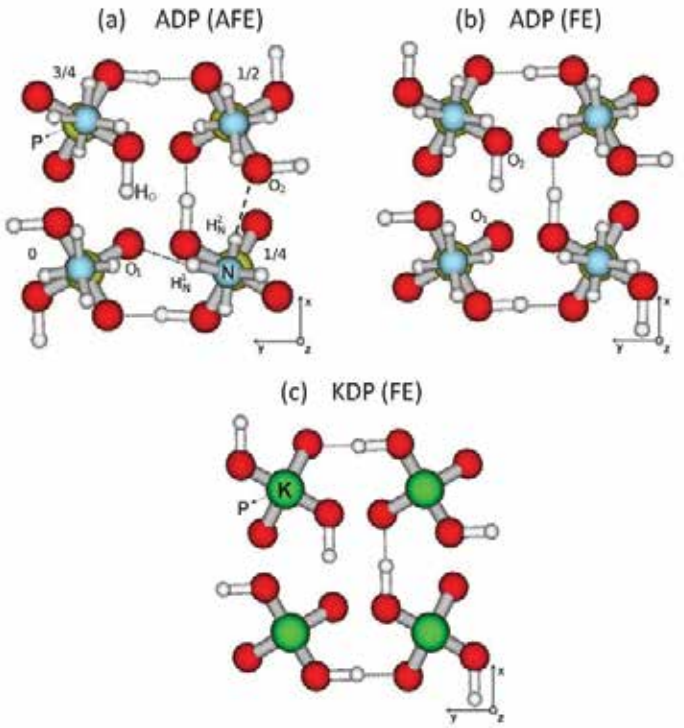

Fig. 1. Schematic representation of (a) AFE phase of ADP, (b) hypothetical FE phase in ADP, and (c) FE phase of KDP. The structures are shown from a top (z-axis) view. Acid H-bonds are shown by dotted lines while in case (a) short and long N-H$\cdots$O bonds are represented by short-dashed and long-dashed lines, respectively. Fractional z coordinates of the phosphate units are also indicated in (a).

The phosphates in KDP and ADP are linked through approximately planar H-bonds forming a three-dimensional network. In the PE phase at high temperature, hydrogens occupy with equal probability two symmetrical positions along the H-bond separated a distance δ (Fig. 2), characterizing the so-called disordered phase. Below the critical temperature in both compounds, hydrogens fall into one of the symmetric sites, leading to the ordered FE phase in KDP (see Fig. 2 and Fig. 1(c)), or the AFE phase in ADP (Fig. 1(a)). In KDP the spontaneous polarization P_s appears perpendicular to the proton ordering plane (see Fig. 2), the PO_4 tetrahedra becoming distorted. In ADP, there is an ordered AFE phase with dipoles pointing

in alternating directions along chains in the basal plane (Fig. 1(a)). In both cases, each PO_4 unit has two covalently bonded and two H-bonded hydrogens, in accordance with the well-known ice rules. The oxygen atoms that bind covalently to the acid H are called donors (O_2 in Figs. 1 and 2), and those H-bonded are called acceptors (O_1 in Figs. 1 and 2).
The proton configurations found around each phosphate in the AFE and FE phases of ADP and KDP, respectively, are essentially different, as depicted in Fig. 1(a) and Fig. 1(c). The low-temperature FE phase of KDP is characterized by local proton configurations around phosphates called *polar*, with electric dipoles and a net spontaneous polarization pointing along the z direction (Fig. 1(c)). There are two possible polar configurations which are built with protons attached to the bottom or the top oxygens in the phosphate, and differ in the sign of the corresponding dipoles along z. These are the lowest-energy configurations realized in the FE phase of KDP. On the other hand, the low-temperature AFE phase of ADP has local proton arrangements in the phosphates called *lateral*. In fact, these configurations have two protons laterally attached to two oxygens, one at the top and the other at the bottom of the phosphate units (Fig. 1(a)). There are four possible lateral configurations, which yields four different orientations of the local dipoles along the basal plane. Another important feature of the ADP structure is the existence of short and long N-H$\cdots$O bonds in the AFE phase, which link the ammonium with different neighboring phosphates (Fig. 1(a)).

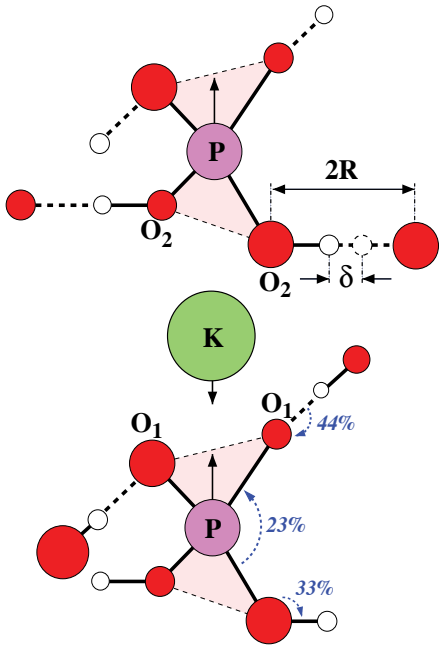

Fig. 2. Schematic lateral view of the atomic motions (solid arrows) happening upon off-centering of the H-atoms which correspond to the FE mode pattern in KDP. Also shown are the concomitant electronic charge redistributions (dotted curved arrows) and the percentages of the total charge redistributed between different orbitals and atoms.

Although considerable progress has been made during the last century, a complete understanding of the FE and AFE transition mechanisms in KDP and ADP is still lacking. The six possible proton configurations obeying the ice rules observed in the low-temperature

phases of KDP and ADP, polar and lateral arrangements respectively, were considered earlier by Slater to develop an order-disorder local model for the phase transition in KDP. (14) Slater assigned energies 0 and $\epsilon_s > 0$ to the polar and lateral configurations respectively in his model for KDP, and predicted a sharp first-order FE transition. But because it is a static model in its original form, it is difficult to use it for understanding, in particular, dynamic properties, such as electric transport and related protonic hopping in the low temperature FE phase. (15) Takagi improved the theory by including the possibility of configurations with one or three protons attached to the phosphate (Takagi configurations) with energy ϵ_t per phosphate, which is well above those of the polar and lateral configurations. (16) These configurations violate the ice rules and arise, e.g., when a proton from a H-bond common to two polar states moves to the other bond side. This leads to the formation of a Takagi-pair defect in two neighboring phosphates that finally remain with one and three protons. (17) The Takagi defects, which are the basic elements of domain walls between regions of opposite polarization, may propagate throughout the lattice and are relevant for the dynamic behavior of the system. (15)

On the other hand, a modification of the original order-disorder Slater model,(14) with a negative Slater energy $\epsilon_s < 0$ proposed by Nagamiya, was the first explanation of antiferroelectricity in ADP. (18) This model favors the AFE ordering of lateral protonic configurations in the O-H$\cdots$O bridges, with dipoles along the basal plane, over the FE ordering of polar configurations with dipoles oriented in the z direction in ADP (see the schematic representation of the hypothetical FE state in ADP, Fig. 1(b)). However, this alone is insufficient to explain antiferroelectricity in ADP. Actually, FE states polarized in the basal plane, not observed experimentally, have energies comparable to the AFE one.(19–21) Ishibashi *et al*. introduced dipolar interactions in a four-sublattice version of the Slater model to rule them out and predicted the observed first-order AFE transition.(19; 20) Although the general characteristics of the AFE transition are well explained by their theory, the transversal and longitudinal dielectric properties are not consistently determined. Using an extended pseudospin model that takes into account the transverse polarization induced by the proton displacements along the H-bonds, Havlin *et al.* were able to explain successfully the dielectric-constant data.(22) The above model explanation of the AFE proton ordering in the low-temperature phase of ADP (Fig. 1(a)) was confirmed by neutron diffraction measurements.(23) Based on that structural data, Schmidt proposed an effective interaction of acid protons across the NH_4^+ ion providing the needed dipolar coupling that leads to the AFE ordering. Although there is no clear microscopic justification for that specific interaction, this model led to successful mean field simulations for ADP and the proton glass $Rb_{1-x}(NH_4)_xH_2PO_4$.(15; 24)

Strong experimental evidence for the coexistence of the FE and AFE domains as T approaches the AFE transition from above has been obtained in EPR studies on ADP using the $(AsO_4)^{4-}$ radical as probe.(25; 26) This suggests that the FE state (Fig. 1(b)) is very close to the AFE ground state (Fig. 1(a)), but there has been no further theoretical justification. Within a model view, a delicate balance between the bare Slater energy and the dipolar interactions would favor one of them.(20)

The strong H $\rightarrow$ D isotope effects exhibited by these materials on their FE or AFE transition temperatures (the critical temperature T_c nearly doubles in the deuterated compounds)(6) are still being debated. This giant effect was first explained by the quantum tunneling model proposed in the early sixties. (27) Within the assumption of interacting, single-proton double wells, this model proposes that individual protons tunnel between the two wells. Protons

have a larger tunnel splitting and are more delocalized than deuterons, thus favoring the onset of the disordered PE phase at a lower T_c. Improvements of the above model to explain the phase transition in KDP include coupling between the proton and the K-PO_4 dynamics. (28–33) These models have been validated *a posteriori* on the basis of their predictions, although there is no direct experimental evidence of tunneling. Only very recent neutron Compton scattering experiments seem to indicate the presence of tunneling.(34) However, the connection between tunneling and isotope effect remains unclear, in spite of recent careful experiments.(35)

On the other hand, a series of experiments carried out since the late eighties (4; 36–40) provided increasing experimental evidence that the geometrical modification of the H-bonds and the lattice parameters upon deuteration (Ubbelohde effect (2)) is intimately connected to the mechanism of the phase transition. The distance δ between the two collective equilibrium positions of the protons (see Fig. 2) was shown to be remarkably correlated with T_c.(4) Therefore, it seems that proton and host cage are connected in a non-trivial way, and are not separable.(5) These findings stimulated new theoretical work where virtually the same phenomenology could be explained without invoking tunneling. (41–45) However, these theories were developed at a rather phenomenological level.

Because of the fundamental importance of the FE and AFE phenomena, as well as from the materials-engineering point of view, it was desirable to carry out quantum mechanical calculations at the first principles (ab initio) level to understand the transition mechanism as well as the isotope effects on the various properties of these materials. These approaches have the advantage of allowing for a confident and parameter-free analysis of the microscopic changes affecting the different phases in these H-bonded FE and AFE compounds. Such an enterprise has recently been possible via the availability of efficient algorithms and large-scale computational facilities. Thus we have carried out ab-initio quantum-theoretical calculations on KDP, (17; 46–48) with particular emphasis on the H $\rightarrow$ D isotope effect in the ferroelectric transition temperature T_c, that shifts from 123 K in KDP to 224 K on deuteration.(6) It was found that the T_c-enhancement can be ascribed to tunneling, but with an additional feed-back effect on the O-H$\cdots$O potential wells.(47; 48)

Encouraged by the KDP results, we undertook a similar study on ADP, (21) because ADP and its analogous AFE compounds such as $NH_4H_2AsO_4$ (ADA) and their deuterated analogues have received much less attention than KDP.(6; 15) Thus how the presence of the NH_4^+ units renders antiferroectricity to ADP and ADA has not been well understood.(15; 18–20) Our *ab initio* results showed that the optimization of the N-H$\cdots$O bonds and the accompanying NH_4^+ distortions lead to the stabilization of the AFE phase over the FE one in ADP.(21)

The purpose of the present contribution is to review and discuss the fundamental behavior of the FE and AFE H-bonded materials KDP and ADP, as explained by our recent first-principles calculations. The following questions are addressed: (i) What is the microscopic mechanism leading to ferroelectricity in KDP and antiferroelectricity in ADP?, (ii) What is the quantum mechanical explanation of the double-site distribution observed in the PE phases of KDP and ADP?, (iii) How does deuteration produce geometrical effects?, (iv) What is the main cause of the giant isotope effect: tunneling, the geometrical modification of the H-bonds, or both?

In the next Section 2 we provide details of the methodology and approximations used. Section 3 is devoted to the ab initio results. In Subsection 3.1 we present and compare the structural results with the available experimental data for both KDP and ADP. In Subsection 3.2 we describe the electronic charge flows involved in the instabilities of the systems. The question,

why ADP turns out to be antiferroelectric, in contrast to KDP, is analyzed in Subsection 3.3. Subsection 3.4 is devoted to the study of the energetics of several local polar configurations embedded in the PE phase in both compounds. In Subsections 3.5 and 3.6 we present a thorough study of quantum fluctuations, and the controversial problem of the isotope effects. In particular, in Subsection 3.5 we analyze the geometrical effects and the issue of tunneling at fixed potential and discuss important consequences for these compounds. We also provide in Subsection 3.6 an explanation for the giant isotope effect observed in KDP by means of a self-consistent quantum mechanical model based on the ab initio data. Similar implications for ADP and other compounds of the H-bonded ferroelectrics family are also discussed. In Subsection 3.7 we review additional ab initio results obtained for KDP: pressure effects, structure and energetics of Slater and Takagi defects and the development of an atomistic model. Finally, in Section 4 we discuss the above issues and present our conclusions.

2. *Ab initio* method and computational details

The first-principles calculations have been carried out within the framework of the density functional theory (DFT), (49; 50) using the SIESTA program. (51; 52) This is a fully self-consistent DFT method that employs a linear combination of pseudoatomic orbitals (LCAO) of the Sankey-Niklewsky type as basis functions (53). These orbitals are strictly confined in real space, what is achieved by imposing the boundary condition that they vanish at a certain cutoff radius in the pseudoatomic problem (i.e. the atomic problem where the Coulomb potential was replaced by the same pseudopotential that will be used in the solid state). With this confinement condition, the solutions are slightly different from the free atom case and have somewhat higher energy. In this approximation, the relevant parameter is precisely the orbital confinement energy E_c which is defined as the difference in energy between the eigenvalues of the confined and the free orbitals. We set in our calculations a value of E_c=50 meV. By decreasing this value further we have checked that we obtain total energies and geometries with sufficient accuracy. In the representation of the valence electrons, we used double-zeta bases with polarization functions (DZP), i.e. two sets of orbitals for the angular momenta occupied in the isolated atom, and one set more for the first nonoccupied angular momentum (polarization orbitals). With this choice, we again obtain enough accuracy in our calculations.(47; 48)

The interaction between ionic cores and valence electrons is represented by nonlocal, norm-conserving pseudopotentials of the Troullier-Martins type.(54) The exchange-correlation energy functional was computed using the gradient-corrected Perdew-Burke-Ernzerhof (PBE) approximation.(55) This functional gives excellent results for the equilibrium volume and bulk modulus of H-bonded ice Ih when compared to other approximations.(56) On the other hand, the BLYP functional,(57; 58) which gives very good results for molecular H-bonded systems,(59) yields results of quality inferior to PBE when used in the solid state.(48) The real-space grid used to compute the Coulomb and exchange-correlation numerical integrals corresponded to an equivalent energy cutoff of 125 Ry. These approximations, especially those related to the confinement of the pseudoatomic orbitals, were also tested against results from standard pseudopotential plane-wave calculations. (48)

The PE phases of KDP and ADP have a body-centered tetragonal (*bct*) structure with 2 formula units (f.u.) per lattice site (16 atoms in KDP and 24 atoms in ADP). For the calculations

that describe homogeneous distortions in KDP, we used the conventional *bct* cell (4 f.u.), but doubled along the tetragonal *c* axis. This supercell comprises 8 f.u. (64 atoms). A larger supercell is required to describe local distortions. To this end, we used the equivalent conventional fct cell (containing 8 f.u., and axes rotated through 45 degrees with respect to the conventional *bct* cell), also doubled along the *c*-axis (128 atoms). For the different phases studied for ADP (FE, AFE, PE), we used the equivalent conventional fct cell. In the following, and unless we state the contrary, the calculations were conducted using a Γ-point sampling of the Brillouin zone (BZ), which proved to be a good approximation due to the large supercells used.(48) The calculations of local distortions in ADP were performed in a 16 f.u. supercell using a 6 k-points BZ sampling, which proved sufficient for convergence.(60)

3. *Ab initio* results

3.1 Characterization of the structures of KDP and ADP

We have performed different computational experiments with the aim of characterizing all phases of KDP and ADP. First, we optimized the PE phase structure of KDP. To this end, we fixed the lattice parameters to the experimental values at T_c+5 K in the conventional *bct* cell,(61) and constrained the H-atoms to remain centered in the O-H$\cdots$O bonds. The full-atom relaxation in these conditions leads to what we call the centered tetragonal (CT) structure, which can be interpreted as an average structure (H_O's centered in the H-bonds) of the true PE phase.(48) Actually, neutron diffraction experiments have shown that the hydrogens in this phase occupy with equal probability two equivalent positions along the H-bond distant $\delta/2$ from the center (Fig. 2).(4; 62) The results of the relaxations with the above constraint for the H to maintain the PE phase show a satisfactory agreement of the structural parameters compared to the experiment, except for the d_{OO} distance which turns out to be too short (see Table 1).

We also relaxed all the internal degrees of freedom, but now fixing the simulation cell to the experimental orthorhombic structure at $T_c - 10\ K$ in the conventional fct cell. (61) The calculated geometrical parameters are shown in Table 1 compared to experimental data. In general the agreement is quite reasonable, again with the exception of the O-O distance.

A detailed analysis revealed that the underestimation in the O-O bond length originates from the approximate character of the exchange-correlation functional, although in the case of the PE phase, it is due in part to the constraint imposed.(48) In fact, it is found in GGA gas-phase calculations of $H_3O_2^-$ an underestimation in d_{OO} of ≈ 0.06 Å when compared to quantum chemical calculations.(63) Moreover, first-principles test calculations indicate a similar underestimation for the water dimer O-O distance compared to the experimental values.(48; 64) On the other hand, the potential for protons or deuterons in the H-bond is very sensitive to the O-O distance.(48) Thus, in order to avoid effects derived from this feature in the following calculations, the O-O distances are fixed to the experimental values observed in the PE phase, unless we state the contrary.

Using a similar procedure, we calculated the PE structure of ADP.(60) We found that the agreement is good compared to the experimental data, as is shown in Table 1.(65; 66) In a second step, we relaxed all atom positions but now fixing the lattice parameters to the orthorhombic experimental cell of ADP.(65) In this case, we have also allowed the O-O distance to relax, since we were interested in the overall structure. The relaxation in the orthorhombic structure leads to an AFE phase in fair agreement with the experiment (see

Table 1). Although the calculated P-O bonds are somewhat longer than the experimental values, the degree of tetrahedra distortion measured by the difference between d(P-O_2) and d(P-O_1) is well reproduced by the calculations. The calculated O-O distance is now underestimated only by 1.5% in comparison to the experimental value, which is again due to the approximation of the exchange-correlation functional as explained above. Although the N-H$\cdots$O distance is in general well reproduced, the calculated geometry of NH_4^+ turns out to be a little expanded respect to the experiment. This could be ascribed to an underestimation in the degree of covalency of the N-H bond due to the orbital-confinement approximation in the first principles calculation with the SIESTA code. On the other hand, the proton shift $\delta/2$ from the H-bond center turns out to be about half the value of that from the x-ray experiment (see Table 1). However, high resolution neutron diffraction results of δ for ADP lie close to the corresponding value for the isomorphic compound KDP,(62) which is ≈ 0.34 Å at atmospheric pressure, in fair agreement with the present calculations. Moreover, our calculated value of δ is close to that found in ab initio calculations for KDP, (48) which is reasonable since the H-bond geometry is expected to depend mostly on the local environment which is similar for both compounds. Therefore, we conclude that the experimental value of δ in the AFE phase of ADP, as is shown in Table 1, may be overestimated because of the low resolution of x-rays to determine proton positions.(65)

In the calculated AFE structure arising from the all-atom relaxation (see the schematic plot for the pattern of atom distortions in Fig. 3 (c)), the ammonium ion displaces laterally about $u_N^{min} = 0.09$ Å producing a dipole that reinforces that determined by the lateral arrangement of acid protons in the phosphate. On the other hand, if we allow the system to relax following the FE pattern in ADP as shown in Fig. 3(b), the relaxed structure is that plotted schematically in Fig. 1 (b) with an energy slightly higher than that for the AFE minimum. (21) In this calculated FE phase of ADP, the ammonium ion displaces along z about 0.05 Å reinforcing the z dipoles produced by the arrangement of acid protons in the phosphates, which is analogous to the behavior of the K^+ ion in KDP (see FE mode in KDP as plotted in Fig. 2). (47; 48)

3.2 Charge redistributions associated with the instabilities in KDP and ADP

We have analyzed the charge redistributions produced by the ordered proton off-centering in KDP (48) and ADP (60). To this aim, we computed the changes in the Mulliken orbital and bond-overlap populations in going from the PE phases to the FE and AFE phases of KDP and ADP, respectively. We have also performed the analysis of the charge redistributions in the non-observed FE phase of ADP. The ordered phases for both compounds were calculated in a hypothetical tetragonal structure in order to be able to compute charge differences related to the PE phase. (46; 48) Mulliken populations depend strongly on the choice of the basis set. Differences, however, are much less sensitive. The results are shown in Table 2 for the atoms and bonds pertaining to the O-H$\cdots$O bridges and the phosphates in both materials (also shown is the K atom population for KDP).

As a common feature for both compounds, we observe an increase of the charge localized around O_1 with the main contribution provided by a decrease in the O_2 charge. This is followed by an increase in the acid hydrogen population for ADP and minor charge redistributions in the remaining atoms for both compounds. The significant enhancement of the population of the O_1 atom is also accompanied by an increase in the bond overlap population of the O_2-H, and O_1-P bonds and a decrease of this magnitude in the $O_1\cdots$H and O_2-P bonds. The trends observed in Table 2 are confirmed by charge density difference plots

Structural parameters	PE ADP AI	PE ADP Exp	PE KDP AI	PE KDP Exp[c]	AFE(ADP) AI	AFE(ADP) Exp[a]	FE(KDP) AI	FE(KDP) Exp[c]
a	-	7.473 [a]	-	7.426	-	7.503	-	10.546
b	-	7.473 [a]	-	7.426	-	7.512	-	10.466
c	-	7.542 [a]	-	6.931	-	7.488	-	6.926
d(O-O)	-	2.481 [a]	2.407	2.483	2.462	2.50	2.446	2.497
$d(O_2\text{-}H_O)$	1.240	1.049 [b]	1.204	1.071	1.093	0.90	1.108	1.056
δ	0	0.377 [b]	0	0.341	0.277	0.70	0.230	0.385
$d(P\text{-}O_1)$	1.541	1.538 [b]	1.592	1.543	1.572	1.522	1.572	1.516
$d(P\text{-}O_2)$	1.541	1.538 [b]	1.592	1.543	1.618	1.566	1.618	1.579
$<O_1\text{-}P\text{-}O_1$	108.6	108.6 [b]	108.6	110.6	111.7	112.5	114.5	114.6
$<O_2\text{-}P\text{-}O_2$	108.6	108.6 [b]	108.6	110.6	104.6	104.7	107.6	106.7
$<O_1 \cdots H\text{-}O_2$	180.0	177.1 [b]	176.6	178.2	175.3	-	176.8	179.4
$d(N\text{-}H_N^1)$	1.048	1.002 [b]	-	-	1.052	0.90	-	-
$d(N\text{-}H_N^2)$	1.048	1.002 [b]	-	-	1.042	0.83	-	-
$d(N\text{-}O_1)$	3.170	3.172 [b]	-	-	3.139	3.152	-	-
$d(N\text{-}O_2)$	3.170	3.172 [b]	-	-	3.182	3.152	-	-
$d(N\text{-}H_N^1 ... O_1)$	2.895	-	-	-	2.779	-	-	-
$d(N\text{-}H_N^2 ... O_2)$	2.895	-	-	-	2.923	-	-	-

Table 1. Comparison of the *ab initio* (AI) calculated internal structure parameters of KDP and ADP (Ref.(60)) with experimental data for the PE, AFE(ADP) and FE(KDP) phases considered in the text. Distances in Å and angles in degrees.
[a] Ref. (65); [b] Ref. (66); [c] Ref. (61)

in these systems. (21; 46; 48) Thus, when the protons displace off-center and approach the O_2 atom, the charge localizes mostly in the O_1 atom and to a lesser extent in the O_1-P orbitals. This is accompanied by a weakening of the $O_1 \cdots H$ bond and a strengthening of the O_1-P bond, which shortens (see Table 1). On the other hand, the charge flows away from the O_2 atom and the O_2-P bond and localizes mostly in the O_2-H bond which strengthens. Then, the PO_4 tetrahedron distortion as observed in Table 1 is a consequence of the strengthening and weakening of the O_1-P and O_2-P bonds respectively, as the protons displace off-center in the H-bonds. The overall effect of the acid H's off-centering in the PO_4 + acid H-bond subsystem of ADP and KDP can be summarized as a flow of electronic charge from the O_2 side of the phosphate tetrahedron towards the O_1 side with a concomitant modification of its internal geometry. Thus, the charge redistributions results for the acid H-bonds shown in Table 2 enable us to conclude that the behavior for these bonds in both compounds are very similar. (21; 46; 48) A schematic view of the displacements of the atoms along the FE mode in KDP and the accompanying electronic charge redistributions produced upon off-centering of the H-atoms is shown in Fig. 2.

We have also compared in ADP the behavior of the N-H$\cdots$O bonds between oxygen and ammonium in the AFE phase with that in the hypothetical FE one (See the schematic lateral view in Fig. 3(b)).(60) To this aim, we computed the changes in the Mulliken orbital and bond-overlap populations for these bonds in going from the PE to the AFE and FE configurations. The results are shown in Table 3. When the acid H's are displaced with the FE pattern of Fig. 3 (b), all H_N's remain equivalent and the O$\cdots$$H_N$ bonds weaken. This

Phase	O_1	O_2	P	H	O_1-P	O_2-P	$O_1 \cdots$ H	O_2-H	K
FE(KDP)	+82	-58	-8	-17	+46	-44	-91	+70	-3
AFE(ADP)	+100	-151	+5	+35	+44	-33	-98	+91	-
FE(ADP)	+93	-151	+2	+36	+52	-43	-91	+86	-

Table 2. Changes $\Delta q = q(x) - q(PE)$ (x = AFE,FE for ADP or FE for KDP) in the Mulliken orbital and bond overlap populations in going from the PE to the AFE and FE phases in ADP (60) or to the FE phase in KDP (48). Shown are populations of the atoms and bonds belonging to the phosphates and the O-H$\cdots$O bridges in both compounds. Also reported is the result for the K atom in KDP. Units in e/1000.

Phase	N	H^2_N	H^1_N	N-H^1_N	N-H^2_N	$O_1 \cdots H^1_N$	$O_2 \cdots H^2_N$
AFE	+7	+7	-9	-4	+4	+16	-14
FE	+1	+1	+1	+3	+3	-7	-7

Table 3. Changes $\Delta q = q(x) - q(PE)$ (x = AFE or FE) in the Mulliken orbital and bond overlap populations in going from the PE to the AFE and FE phases in ADP (60). Shown are populations of the atoms and bonds belonging to the NH_4^+ ions and the N-H$\cdots$O bridges . Units in e/1000.

behavior is compatible with the decrease in the bond overlap population for this bond in Table 3. On the contrary, with the AFE distortion (see Fig. 3(c)), the arising short and long N-H$\cdots$O bonds behave in an opposite way. In fact, the long N-$H^2_N \cdots O_2$ bond suffers a decrease in the $O_2 \cdots H^2_N$ bond overlap population and a weakening of the bond while the corresponding magnitude of the short N-$H^1_N \cdots O_1$ bond increases and the bond strengthens. The charge variations are observed to be nearly twice the corresponding value for the analogue magnitude in the FE phase. Similarly, in the AFE phase the N-H^2_N bond strengthens with a slight increment in the bond overlap population and the N-H^1_N bond weakens with a decrease in the localized charge. These charge redistributions in the ammonium tetrahedron give rise to its distortion (see Table 1). As a consequence, we observe a charge flow from the long to the short N-H$\cdots$O bonds which is concomitant to the ammonium distortion, absent in the FE phase.(60) This behavior is also observed in charge density difference plots for ADP.(21) In the next Section we discuss how the charge flow inside ammonium and its distortion are related to the stabilization of the AFE phase over the FE one in ADP.(21)

3.3 Origin of antiferroelectricity in ADP

With the aim of studying the AFE and FE instabilities and their relative importance in ADP, we have performed different calculations.(21) First we consider the joint displacement of N and acid H_O protons from their centered positions in the PE phase, denoted by u_N and u_{H_O} respectively. These are performed in two cases: (i) following the AFE pattern of distortion (see Fig. 3(c)), and (ii) following the FE pattern (see Fig. 3(b)). The H_N's of the ammonium and P's are allowed to relax (this is always the case unless we state the contrary), while the O's remain fixed for the reasons explained in Subsection 3.1. The ab-initio total-energy curve is plotted in Fig. 3(a) as a function of u_{H_O}, for the concerted motion of H_O and N corresponding to each pattern. We observe that the calculated minimum-energy AFE state is only slightly more stable than the FE counterpart, with a small energy difference of 3.6 meV/f.u. (f.u. = formula unit). With the O's relaxations the AFE state remains 1.25 meV/f.u. below the FE one. If we additionally relax the lattice parameters according to the symmetries of each phase, this difference grows to $\approx$ 3.8 meV/f.u. We have also determined recently the closeness in energy to the AFE state of two other possible ordered phases with translational symmetry and xy-polarized PO_4 tetrahedra.(21) Thus, we confirm the closeness between the AFE and FE

states in ADP, a fact that suports Ishibashi's model (19; 20) and also provides an explanation for the coexistence of AFE and FE microregions near the AFE transition.(25; 26)

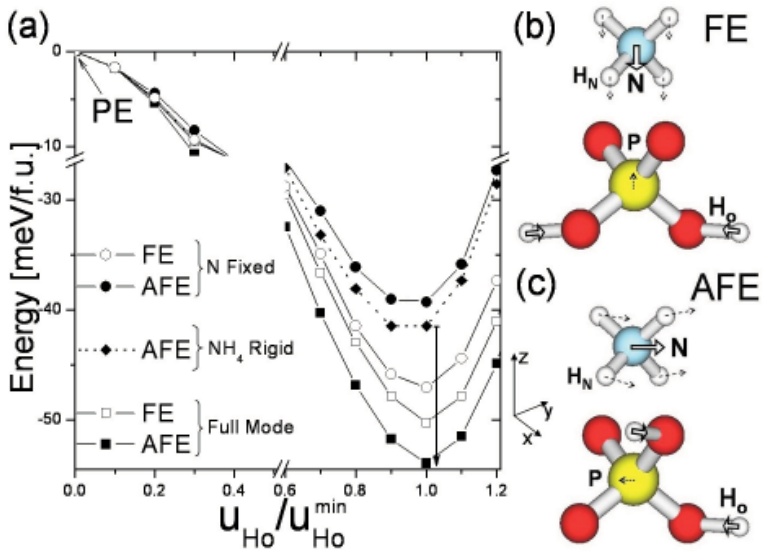

Fig. 3. (a) Energy as a function of the acid H displacement u_{H_O} for different patterns of atomic displacements corresponding to the FE and AFE distortions depicted in Figs. 3(b) and 3(c) respectively. $u_{H_O}^{min}$ denotes the H_O displacement at the corresponding energy minimum. In addition to the full FE or AFE modes, other curves show the effect of imposing different constraints while performing the FE or AFE modes: N fixed or NH_4^+ moved rigid as in the PE phase. Lateral views of the ADP formula unit indicate the atomic displacements in the (b) FE and (c) AFE modes. White arrows correspond to displacements imposed according to each mode, dashed arrows to accompanying relaxations.

In order to determine the mechanism for the stabilization of the AFE vs FE state, we also considered the energy contribution of the N and H_O motion separately.(21) If we set $u_{H_O} = 0$, a finite displacement u_N along z (see Fig. 3(b)) does not contribute to any energy instability in the FE case. Moreover, the N displacement along the xy-plane in the AFE case (see Fig. 3(c)) produces a very tiny instability (less than 1 meV/f.u.). Alternatively, we move the acid H_O's and set $u_N = 0$, i.e. N's are fixed to their positions in the PE phase (see Figs. 3(b) and 3(c)). We observe in this case a larger energy decrease for the FE pattern compared to the AFE one (see circles in Fig. 3(a)). It is worth mentioning that here the H_N's relaxations in the ammonium are very small in contrast with the case where both N and H_O's are allowed to displace. In the FE case, a further energy decrease of less than 10% of the total instability is achieved when the N's are allowed to move together with the H_O's (see open circles and squares at the energy minima in Fig. 3(a)). The fact that the FE-pattern relaxation with $u_{H_O} = 0$ does not produce any instability prompts us to conclude that the source of the FE instability in ADP is the acid proton off-centering ($u_{H_O} \neq 0$), similar to what is found in KDP.(48) The proton off-centering also produces the AFE instability, but this motion alone is insufficient to explain antiferroelectricity in ADP.(21)

Finally, we have considered the displacements of all atoms following the pattern of the AFE mode, with the only constraint that the structure of the NH_4^+ groups is kept rigidly symmetric

as in the PE phase.(21) The energies obtained in this case are shown by solid diamonds in Fig. 3(a), which have to be compared to those corresponding to the full relaxation of the FE phase by open squares (in the last case H_N relaxations in the NH_4^+ groups are negligible). We observe that the FE state is more stable than the AFE one as long as the NH_4^+ tetrahedra are not allowed to deform by relaxing their H_N's. Notice that by not allowing the relaxation of the ammonium, this ion behaves in the same way as the K^+ ion in KDP, where the FE phase is more stable than the AFE distortions.(48; 67) If we allow for the optimization of the N-H$\cdots$O bridges by relaxing the NH_4^+, the stabilization of the AFE state against the FE one is achieved. This energy decrease is visualized in Fig. 3(a) by the arrow between full diamonds and squares at $u_{H_O}/u_{H_O}^{min} = 1$. Therefore, the origin of antiferroelectricity in ADP is ascribed to the optimal formation of N-H$\cdots$O bridges.(21) This conclusion is further supported by a study of the energy variation produced by a global rigid rotation of the NH_4^+ molecules around the z-axis.(21)

3.4 Local instabilities and the nature of the PE phases of KDP and ADP

The observed proton double-occupancy in the PE phases of KDP and ADP,(38; 61; 62) is an indication of the order-disorder character of the observed transitions. The origin of this phenomenon can be ascribed either to static or thermally activated dynamic disorder, or to tunneling between the two sites. The physics behind these scenarios is intimately connected to the instabilities of the system with respect to correlated but localized H motions in the PE phase, including also the possibility of heavy-ions relaxation.

We have analyzed localized distortions by considering increasingly larger clusters embedded in a host PE matrix of KDP (47; 48) and ADP (60). For the reasons exposed above, the host is modeled by protons centered between oxygens, and the experimental structural parameters (including the O-O distances) of KDP and ADP in their PE phases.(61; 65) In order to assess the effect of the volume increase observed upon deuteration, we also analyzed the analogous case of D in DKDP by expanding the host structural parameters to the corresponding experimental values.(47; 48; 61) We also compared qualitatively the effect of volume expansion in ADP by considering a larger equilibrium O-O distance in the lattice.(60) The trends are compared qualitatively to the case of KDP, although we have to bear in mind that the instabilites in both systems have a different character (FE in KDP and AFE in ADP).

First, we considered distortions for clusters comprising N hydrogens (deuteriums) in KDP: (a) N=1 H(D) atom, (b) N=4 H(D) atoms which connect a PO_4 group to the host, (c) N=7 H(D) atoms localized around two PO_4 groups, and (d) N=10 H(D) atoms localized around three PO_4 groups. The correlated motions follow the pattern for the FE mode shown in Fig. 2.

We represented the correlated pattern with a single collective coordinate x whose value coincides with the H(D) off-center displacement $\delta/2$ (see Fig. 2). Notice that this coordinate is equivalent to that defined above as u_{H_O} for the proton off-centering. For the sake of simplicity, we considered equal displacements along the direction of the O-O bonds for all the hydrogen atoms in the cluster. Two cases were considered: (i) first, we imposed displacements only on H atoms, maintaining all other atoms fixed, (ii) second, we also allowed for the relaxation of the heavy ions K and P, which follow the ferroelectric mode pattern as expected (Fig. 2). In a next step, we quantized the cluster motion in the corresponding effective potential to determine the importance of tunneling in the disordered phase of KDP. Although, rigorously speaking, the size dependence should be studied for larger clusters than those mentioned here, short-range

quantum fluctuations in the PE phase are sufficiently revealing, especially far away from the critical point.

We show in Fig. 4(a) and Fig. 4(b) the total *ab initio* energy as a function of the collective coordinate x for the clusters considered in KDP and DKDP, respectively.(47; 48) In the case of KDP, all the clusters considered are stable if only hydrogens are displaced. Actually, the largest cluster calculated (N=10) is very stable, as indicated by the open circles in Fig. 4(a). In the expanded lattice of DKDP, results indicate a small barrier of $\sim$ 6 meV for the N=7 move, and a larger value of $\approx$ 25 meV for the N=10 cluster (see open squares and circles respectively in Fig. 4(b)).

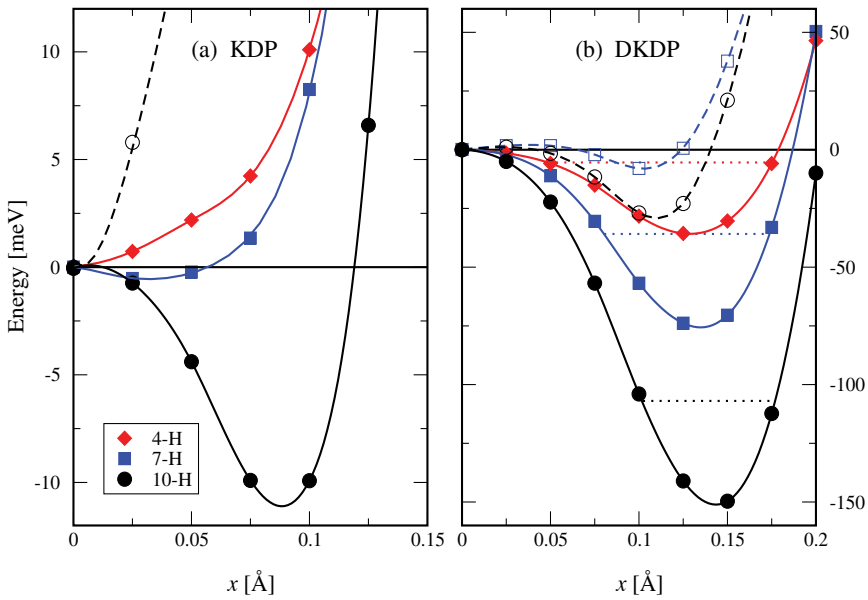

Fig. 4. Energy profiles for correlated local distortions in (a) KDP and (b) DKDP. Reported are clusters of: 4 H(D) (diamonds), 7 H(D) (squares), and 10 H(D) (circles). Empty symbols and dashed lines indicate that only the H(D) atoms move. Motions that involve also heavy atoms (P and K) are represented by filled symbols and solid lines. Negative GS energies signaling tunneling, are shown by dotted lines. Lines are guide to the eye only.

The energy profiles vary drastically when we allow the heavy atoms relaxations for the above correlated motions in KDP.(47; 48) Now, clusters involving two or more PO_4 units exhibit instabilities in both KDP and DKDP. In the case of the N=10 cluster, the barrier in DKDP is of the order of 150 meV. The appearance of these instabilities provides a measure of the FE correlation length in the system. In the expanded DKDP lattice, the instabilities are much stronger, and the correlation length is accordingly shorter than in KDP.

In the next step, we solved the Schrödinger equation for the collective coordinate x for each cluster in the corresponding effective potentials of Fig. 4.(47; 48) To this aim, we calculated the effective mass for the local collective motion of the cluster as $\mu = \sum_i m_i a_i^2$, where i runs over

the displacing atoms and m_i are their corresponding atomic masses. In this equation, a_i is the i-atom displacement at the minimum from its position in the PE phase, relative to the H(D) displacement.

In the cases where only the N deuteriums are displaced in the unstable clusters of DKDP (see Fig. 4(b)), all by the same amount, the calculated ground states (GS) energies lie above the barriers. Thus, tunneling of H (D) alone seems to be precluded as an explanation of the double site occupancy observed in the PE phases of KDP and DKDP, at least for clusters of up to 10 hydrogens (deuteriums).(47; 48)

When the heavier atoms are allowed to relax, the effective masses per H(D) calculated for these correlated motions in different clusters are about $\mu_H \approx 2.3$ ($\mu_D \approx 3.0$) proton masses (m_p) in KDP (DKDP), respectively. The resulting GS energy levels are quantized below the barrier for all clusters including the heavy atoms motion in DKDP (see dotted lines in Fig. 4(b)). Thus, there is a clear sign of tunneling for the correlated D motions involving also the heavy ions.(47; 48) These collective motions can be understood as a local distortion reminiscent of the global FE mode. (68) On the other hand, even the largest cluster considered (N=10) in KDP, has the GS level quantized above the barrier. The critical cluster size where the onset of tunneling is observed provides a rough indication of the correlation volume: it comprises more than 10 hydrogens in KDP, but no more than 4 deuteriums in DKDP. Thus, the dynamics of the order-disorder transition would involve fairly large H(D)-clusters together with heavy-atom (P and K) displacements. The observed proton double-occupancy is explained in our calculations by the tunneling of large and *heavy* clusters.(47; 48) This is confirmed by the double-site distribution determined experimentally for the P atoms. (69; 70)

In the case of ADP, we have analyzed local cluster distortions embedded in its PE phase.(60) We considered the experimental lattice in this phase,(65) and in order to vary the O-O distance, the PO_4 tetrahedra were rotated rigidly. We also let the ammonium relax to optimize the N-H$\cdots$O bridges. We considered displacements of N=1 proton, and also clusters of N=4 and N=7 simultaneously displaced acid protons from their centered positions in the H-bonds while keeping fixed the rest of the atoms. In the cases of N=4 and N=7 protons the displacement patterns correspond to the AFE mode (see Fig. 1(a) and Fig. 3(c)). We calculated the total energy for each configuration. We plot in Fig. 5 the resulting potential profiles for the protons along the bridges as a function of their off-center displacements u_{H_O} from the middle of the H-bonds. We observe that the off-centering of a single proton leads to an energy minimum, at variance with the case of KDP.(48; 67) This behavior in ADP has to be ascribed to the energy contributions of N-H$\cdots$O bridges, which compensate the energy increase due to the formation of Takagi pair defects. The variation of the O-O distance does not affect this energy minimum, as well as the one observed at lower displacements for the N=4 and N=7 proton movements, thus confirming that it can be related to the N-H$\cdots$O bridges in the three cases.(60) On the other hand, we observe that the second minimum at larger distances is strongly dependent on the O-O distance. In fact, this minimum is incipient at d_{OO}=2.48 Å and is clearly seen at d_{OO}=2.52 Å for the N=4 and N=7 proton displacements. This instability is therefore ascribed to favorable lateral Slater configurations related to the O-H$\cdots$O bonds.(17; 60) The same bonds favor the formation of local polar configurations in KDP at a similar H off-centering distance $\delta/2$ (see Fig. 4).(47; 48) This minimum becomes deeper for larger proton clusters and is located at a H off-centering distance which approaches the one corresponding to the global ordered phases in both compounds.(21; 47)

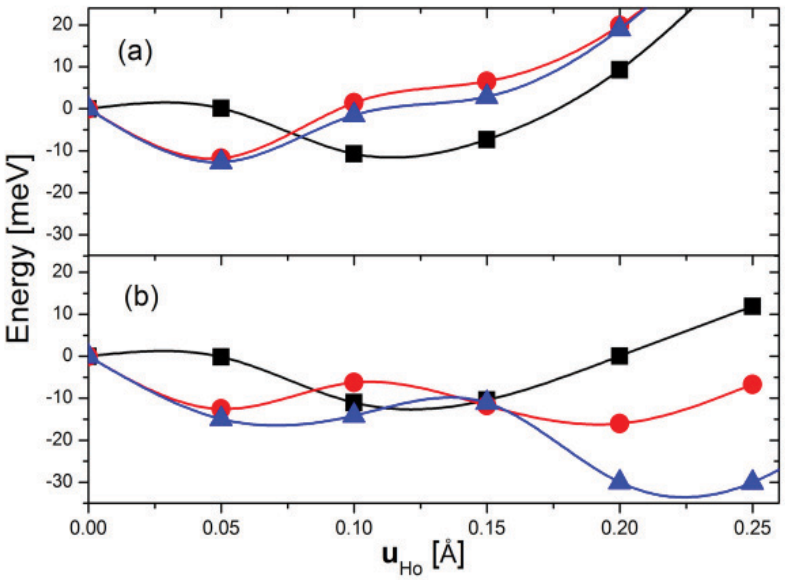

Fig. 5. Energy profiles for correlated proton distortions along the acid H-bonds as a function of the acid proton displacement u_{H_O} in ADP. The results are shown for different O-O distances in the crystal: a) d_{OO}=2.48 Å and b) d_{OO}=2.52 Å. Reported are clusters of N=1 H (squares), N=4 H (circles), and N=7 H (triangles).

3.5 Geometrical effect vs tunneling

Let us now address the origin of the huge isotope effect on T_c, observed in KDP and its family. After the pioneering work of Blinc,(27) the central issue in KDP has been whether tunneling is or is not at the root of the large isotope effect. However, this fact was never rigorously confirmed, in spite of the large efforts made in this direction. Recently, a crucial set of experiments done by Nelmes and coworkers indicated that the tunneling picture, at least in its crude version, does not apply. Actually, by applying pressure and tuning conveniently the D-shift parameter δ, they brought T_c^{DKDP} almost in coincidence with T_c^{KDP}, in spite of the mass difference between D and H in both systems. (4; 38; 62) This indicates that the modification of the H-bond geometry by deuteration – the *geometrical effect* – is the preponderant mechanism that accounts for the isotope effects in the transition.

The tunnel splitting Ω tends to vanish as the cluster size grows ($N \to \infty$).(47; 48) On the other hand, it is expected that for the nearly second-order FE transition in these systems,(71) only the large clusters are relevant. For large tunneling clusters, the potential barriers are large enough and the GS levels are sufficiently deep (see Fig. 4) that the relation $\hbar\Omega_{H(D)} \ll K_B T_c$ is fulfilled so much for D as for H. The above relation implies, according to the tunneling model, that a simple change of mass upon deuteration at fixed potential could not explain the near doubling of T_c. Let us consider the largest cluster (N=10) in Fig. 4 for DKDP, which is larger than the crossover length in this system. In this case, the GS level amounts to E_{GS} = -107 meV (calculated with a total effective mass of $\mu_D = 35.4\ m_p$). This value is well below the central barrier. The corresponding tunneling splitting is of the order of $\hbar\Omega_D = 0.34$ K. If we maintain

the potential fixed, and change the cluster effective mass to that for the non-deuterated case ($\mu_H = 25.3\ m_p$), the calculated tunnel splitting is now only slightly larger $\hbar\Omega_H = 1.74$ K. As $T_c^{DKDP} \approx 229K$, the relation $\hbar\Omega_{H(D)} \ll K_B T_c$ is clearly satisfied. As a consequence, a small change in T_c should be expected by the sole change of Ω at fixed potential. This conclusion agrees with the neutron diffraction results at high pressure,(4; 38; 62) where the isotope effect in T_c appears to be very small at fixed structural conditions.

We plot in Fig. 6 (a) the calculated proton and deuteron wave functions (WF) in the DKDP fixed potential for the N=7 cluster. The plot shows very slight differences between both WF. Moreover, the distance between peaks as a function of the effective mass at fixed potential remains almost unchanged, as can be seen by the square symbols in Fig. 6 (c). We conclude that the geometric effect in the H-bond at fixed potential is very small.(47; 48)

In constrast to the case of DKDP, the proton WF for the N=7 cluster in the KDP potential exhibits a broad single peak, as shown in Fig. 6 (a). Now, this question emerges: How can we explain such a big geometric change in going from DKDP to KDP? After this question, the first observation comes from what is apparent in Fig. 4: energy barriers in DKDP are much larger than those in KDP, implying that quantum effects are significantly reduced in the expanded DKDP lattice. On the other hand, we observe in Fig. 6(a) that the proton WF in KDP has more weight around the middle of the H-bond ($\delta_c \approx 0$, where δ_c is the collective coordinate) than in DKDP. In other words, due to quantum delocalization effects the proton is more likely to be found at the H-centered position between oxygens than the deuteron. Consequently, as the proton is pushed to the H-bond center due to zero-point motion the covalency of the bond becomes stronger. The mixed effect of quantum delocalization and gain in covalency leads to a geometric change of the O-H$\cdots$O bridge, which in turn affects the crystal cohesion. In fact, the increased probability of the proton to be midway between oxygens, strengthens the O-H$\cdots$O covalent grip and pulls the oxygens together, causing a small shrinking of the lattice. The effect of this shrinking is to decrease the potential depth, making the proton even more delocalized. This produces again an increase in the covalency of the O-H$\cdots$O bond, pulling effectively the oxygens together, an so on in a self-consistent way. We have identified this self-consistent phenomenon as the one that shrinks the lattice from the larger classical value to the smaller value found for KDP.(47; 48) Thus, the large geometrical effect in these systems is attained by this self-consistent phenomenon, which in turn is triggered by tunneling. The overall effect is eventually much larger than the deuteration effect obtained at fixed potential. The upper limit to the effect described above was evaluated with additional classical electronic calculations by looking at the effects of H-centering in the FE phase of KDP.(47; 48) It was found that the lattice volume shrinks about 2.3 % upon centering the H's. Moreover, at the equilibrium volume, the proton centering creates an equivalent pressure of $\approx$ 20 kbar. However, the protons are equally distributed on both sides of the bond in the true high-temperature PE phase, thus reducing the magnitude of the effect.

3.6 The nonlinear self-consistent phenomenon and the isotope effects

The large geometric effect observed due to deuteration may be explained, as discussed in the previous subsection, by a self-consistent mechanism combining quantum delocalization, the modification of the covalency in the bond, and the effect over the lattice parameters. The mechanism is also capable of explaining, at least qualitatively, the increase in the order parameter and T_c with deuteration. The origin of the self-consistent phenomenon is the

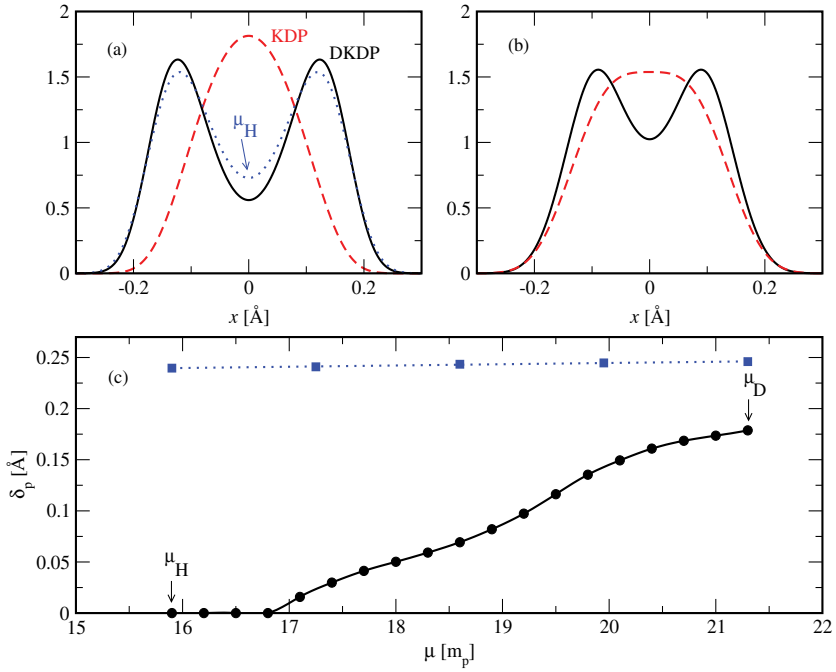

Fig. 6. WF for the 7-H(D) cluster potential for (a) *ab initio* and (b) self-consistent model calculations. Solid (dashed) lines are for D (H). Dotted line is for H in the DKDP potential. (c) WF peak separation δ_p as a function of the cluster effective mass μ (given in units of the proton mass) for the self-consistent model (circles) and for fixed DKDP potential (squares). Lines are guides to the eye.

difference in tunneling induced by different masses, but is strongly amplified through the geometric modification of the lengths and energy scales.

We have constructed a simple model which accounts for the non-linear self-consistent behavior described above.(47; 48) To this aim, we considered the Schrödinger equation for the clusters by adding to the underlying hydrogen potential a quadratic WF-dependent term. The effective potential now reads:

$$V_{\text{eff}}(x) = V_0(x) - k|\Psi(x)|^2, \tag{1}$$

where $x = \delta_c/2$ and $V_0(x)$ is a quartic double-well similar to those of Fig. 4. The quadratic term $|\Psi(x)|^2$ produces the non-linear feedback in the model. In fact, the enhancement of the proton delocalization relative to the deuteron leads to an increase of $|\Psi(x)|^2$ at the center (increased probability to be found at the middle of the H-bond), which in turn produces a decrease in the barrier for the effective potential, which further delocalizes the proton, and so on until self-consistency is achieved. The bare potential is written as follows:

$$V_0(x) = E_b^0 \left[-2 \left(\frac{2x}{\delta_{min}^0} \right)^2 + \left(\frac{2x}{\delta_{min}^0} \right)^4 \right], \tag{2}$$

in terms of its energy barrier E_b^0 and minima separation δ_{min}^0. We have chosen the parameters values k = 20.2 meV Å, E_b^0 = 35 meV and δ_{min}^0 = 0.24 Å to qualitatively reproduce the WF profiles in the cases of KDP (broad single peak) and DKDP (double peak), for the same cluster size.(47; 48) The WF self-consistent solutions depend only on the effective mass μ, once these parameters are fixed. We show in Fig. 6 (b) the WF corresponding to μ_D (solid line) and μ_H (dashed line), which are similar to those calculated from the ab initio potentials for the N=7 cluster (Fig. 6 (a)). Also shown in Fig. 6 (c) is the distance between peaks δ_p in the WF as a function of μ. Starting from the finite value for μ_D (DKDP), Fig. 6 (c) shows how δ_p decreases remarkably towards lower μ values for the self-consistent solution. This happens until it vanishes near μ_H (KDP) (see circles in Fig. 6(c)). This behavior is in striking contrast with the very weak dependence obtained at fixed DKDP potential and geometry (square symbols in Fig. 6(c)). The amplification in the self-consistent geometrical modification of the H-bond, as is evidenced by the large mass dependence of the WF in Fig. 6(c), can now explain satisfactorily the large isotope effect found in KDP.(47; 48)

We have shown in Subsection 3.5 that the energy barriers for proton transfer in clusters of different sizes embedded in the PE phase of ADP, are strongly dependent on the O-O distance and the cluster sizes (Fig. 5). This behavior is similar to that found in KDP (see Fig. 4).(47; 48) As in that case, it is expected that the H $\rightarrow$ D substitution in ADP, which implies an increase of the D localization near the potential minimum along the O-O bond, will lead to its weakening and a lattice expansion. The consequent barrier-height increase would couple selfconsistently with tunneling in the way described above leading to the large isotope effect observed in ADP.(62) This mechanism is expected to be universal for the family of H-bonded ferroelectrics exhibiting large isotope effects.

3.7 Additional ab initio results for KDP

3.7.1 Pressure effects

Neutron diffraction experiments under pressure revealed in the late eighties the importance of structural modifications due to deuteration.(4; 62) A remarkable correlation was found between T_c and the separation δ between the two equivalent positions along the H-bond, observed to be occupied by the H(D) atoms. Moreover, the critical temperature T_c of KDP could be almost perfectly reproduced by compressing DKDP in such a way as to bring the value of δ to that of KDP at ambient pressure. Furthermore, T_c appears to be linearly proportional to δ for different H-bonded ferroelectric materials, deuterated or not, all of them ending at a universal point $\delta_0 \approx 0.2$ Å as T_c goes to zero and the FE phase is no longer possible.(62) The experiments then suggest that the effects of deuteration can be reverted by applying pressure. This prompted us to explore the connection between pressure and isotope effects by means of first-principles calculations and the above described phenomenological model. Deuterons, being heavier, have less probability than H to be found near the bond center, where a collective double-well barrier exist (see Fig. 4). Thus they localize farther than H from the bond center (larger δ). One might expect that by applying pressure to DKDP, thus lowering the energy barrier at the bond center, the latter will be approached by the peak of the D probability distribution. For the pressure at which the peak separation δ for DKDP coincides with that of KDP, both would have the same T_c according to the observed phenomenology.(62) Moreover, this T_c equality is observed for any pressure applied to KDP and correspondingly higher pressure applied to DKDP such that their δ's are brought in coincidence. However the δ coincidence at the high pressures used in the experiments is achieved in our calculations only

by taking into account the mutual self-consistent arrangement between D(H) distribution and host structure (the geometrical effect), modeled as explained in Subsection 3.6 at the different imposed pressures. More details on this analysis are given in Refs.(48; 72). These results give further support to our self-consistent model explanation of the geometrical isotope effects.

3.7.2 Structure and energetics of Slater and Takagi defects

The observation by magnetic resonance experiments of deuterons jumping along the bridges in the FE phase of DKDP,(73) allows for the appearance of phosphates with 2 latteral attached D (called Slater defects) or a pair of neighboring phosphates, one with only 1 and the other with 3 attached D's (called Takagi defects, which violate the Ice rules). Slater and Takagi defects have been accounted for in the modeling of domain-walls motion near the transition in KDP and DKDP.(74; 75) The energies of these defects have been estimated from model calculations in several compounds of the KDP-family.(76–79) By means of *ab initio* calculations we had obtained the structure and stability of the Slater and Takagi defects in the FE phase of KDP.(17) We showed that the Slater defects are stabilized only in form of defect chains. In contrast, the Takagi defects are not stable. Our result for the energy necessary to form a Takagi-pair defect is $\approx$ 54 meV, in fair good agreement with previous phenomenological estimations.(76–79) For the determination of the Slater defect energy we had followed two procedures. One of them was just to calculate the energy per phosphate for the meta-stable configuration of the Slater defect chain. We called this the *correlated* Slater defect energy, and it has a value of 5 meV, in good agreement with the phenomenological estimations. The other procedure was to displace the two hydrogens connecting three neighboring phosphates, in such a way to leave two phosphates in Takagi configurations connected to an intermediate phosphate in lateral Slater configuration. This allowed us to obtain an *uncorrelated* Slater defect energy of $\approx$ 17 meV. These results suggest that the phenomenological estimation involve correlations between configurations of different H_2PO_4 groups. We observed that the formation of the Slater defect chains is accompanied by phosphate rotations, and a concomitant lattice contraction in the basal plane. This allowed us to suggest that a lattice contraction observed in the neighborhood of the phase transition (80; 81) can be ascribed to an increase of the Slater defect population.

3.7.3 Developement of an atomistic model

The possibility of studying the FE-PE phase transition at a first-principles level requires the formation of clusters of enough size to enable tunneling, as described in Section 3.4. This is precluded by the required sizes of the simulation supercells, which leads to exceedingly demanding computations. Even more demanding is the consideration of the proton (deuterium) quantum dynamics. Therefore, in order to address these issues we developed an extended shell model of KDP capable of describing reasonably well the physical properties of the system in its different phases.(67; 82) We paid particular attention to those properties that are relevant to the FE-PE phase transition. Fairly good agreement with first-principles and experimental results was achieved for the structural parameters, Γ-phonon frequencies in both the PE and FE phases,(83) and the underlying potential energy for a single H moving along the H-bond in the FE phase.(67) The total energies as a function of global displacements with the FE mode pattern and as a function of local distortions in the PE phase for the various cluster sizes analyzed in Section 3.4 in both KDP and DKDP, are also well reproduced.(82)

4. Discussion and conclusions

The described ab-initio calculations of the PE and ordered equilibrium phases of ADP and KDP lead to structural parameters in good agreement with the experimental data obtained by x-ray and neutron diffraction. The systematic underestimation of the O-O distances compared to experiments in both compounds should be ascribed to the approximation in the exchange-correlation functional. On the other hand, the apparent underestimation of the acid hydrogen off-center distance $\delta/2$ in the calculation for ADP could be ascribed to the unreliability of the x-ray measurements of the proton position. The N-O distance in the N-H$\cdots$O bridges of ADP is very close to the usual value ≈ 2.8 Å for this kind of bonds.(84–86) In addition, a somewhat overestimated N-H distance was found in our calculation when compared to the neutron diffraction measurements. This could be ascribed to the local orbital approximation for the valence electrons used in the SIESTA code. We have observed similar discrepancies between SIESTA and plane wave pseudopotential calculations for KDP in the calculation of the O-H distance in the O-H$\cdots$O bridges.(48)

The FE transition and the nature of the instability that leads to the onset of the spontaneous polarization P_s in KDP have been extensively discussed in the past.(28; 87; 88) It was originally assumed that P_s, which is oriented along the c-axis, was due to the displacements of K^+ and P^- ions along this axis, although the H(D) ordering, nearly parallel to the basal plane, is undoubtedly correlated with the transition.(28) Within this model, the observed value of P_s can only be explained if very large charges for the phosphorus ion are assumed.(87) Another mechanism was that of Bystrov and Popova (87) who proposed that the source of P_s could be the electron density shift in the P-O and P-O-H bonds in the polar direction, which occurs when the protons order almost perpendicularly. However, model calculations cannot determine this assumption for it is originated in the complex electronic interactions in the system.(88)

We were able to overcome this model limitation by means of *ab initio* calculations. Actually, we have shown that the FE instability in KDP has its origin on an electronic charge reorganization within the internal P-O and P-O-H bonds of the phosphates, as the H-atoms order off-center in the H-bonds. The overall effect produced by the H-ordering is an *electronic charge flow* from the O2 side to the O1 side of the PO_4 tetrahedron. This comes with a distortion of the phosphates.(46; 48) The mechanism found agrees with the explanation given in Ref. (87), and is also in accordance with the results obtained by another recent first-principles calculation.(89)

We have found that the charge redistributions in the the acid proton bridges and phosphates associated with the instabilities in ADP and KDP are very similar. In fact, as it happens in KDP, the flow of charge from the O2 side to the O1 side of the PO_4 tetrahedron is also verified in ADP. However, this alone is insufficient to produce antiferroelectricity in ADP, as is shown in an energy analysis of different possible distortions.(21) On the other hand, a differentiation between two types of N-H$\cdots$O bridges, long and short, also occurs concomitant with the ammonium tetrahedra distortions as the AFE instability takes place in ADP. We have also verified by a Mulliken charge analysis the existence of an electronic charge flow from the long to the short N-H$\cdots$O bridges which occurs simultaneously with the ammonium distortion. This charge flow is absent in the hypothetical FE phase of ADP.(60) The above features found in ADP are also confirmed by charge density difference plots.(21)

We have shown that the optimization of the N-H$\cdots$O bridges leads to the stabilization of the AFE phase in ADP. This is consistent with the proposition of Schmidt that an effective

acid-protons interaction mediated by the ammonium through the N-H$\cdots$O bonds plays an important role.(15; 21) Actually, the strengthening of N-H$\cdots$O bonds which generates the energy imbalance in favor of the AFE phase, also distorts the NH_4^+ ion, repels the acid H that is close to the stronger N-H$\cdots$O bond, involves significant charge transfers, and thus creates dipole moments in the plane of the O-H$\cdots$O bonds, in full agreement with the neutron data (23) and Schmidt's conjecture (15).

There is a long controversy regarding the character of the FE transition in KDP. The coupled proton-phonon model displaying essentially a displacive-like transition is supported by some experimental facts.(90) The importance of the order-disorder character of the transition originated in the H_2PO_4 unit dipoles is highlighted by other experiments, e.g. Raman studies.(91; 92) Moreover, electron-nuclear double-resonance (ENDOR) measurements (93) indicate that not only the H_2PO_4 group, but also the K atoms, are disordered over at least two configurations in the paraelectric phase. Neutron scattering experiments show that the P atom is distributed over at least two sites in DKDP. (69; 70) It is clear that, in spite of the still unresolved character of the transition, local instabilities arising from the coupling of light and heavy ions are very important in this system. This should be the case, irrespective of the correlation length scale associated with the transition.

Our calculations in the PE phase of KDP showed that local proton distortions with the FE mode pattern (Fig. 2) need to be accompanied by heavy ion relaxations in the PO_4-K group in order to produce significant instabilities,(47; 48) a fact which is in agreement with experiments.(69; 70; 91–93) The correlation length associated with the FE instability is much larger in KDP than in DKDP, suggesting that DKDP will behave more as an order-disorder ferroelectric than KDP. We have also demonstrated the relevance of proton correlations and the acid H-bond geometry in the energy scale of the local AFE instabilities inherent to the PE phase of ADP.(60) This fact is found to be similar to that observed in KDP.

Undoubtedly, the huge isotope effect in the critical temperature and the order parameter of the transition is the most striking feature not yet satisfactorily understood in these compounds. As we have already mentioned, the first explanation was that proposed by the tunneling model and later modifications.(27; 28) However, the vast set of experiments later carried out by Nelmes and co-workers, (4; 10; 38; 62; 69; 70) and the comprehensive structural compilation done by Ichikawa *et al.*, (3; 36; 40) showed the importance of the so-called geometrical effect as an alternative explanation. An overall and consistent explanation of the phenomenon became more elusive when other experiments (34; 35; 91; 92; 94) and models (29; 30; 32; 33; 41; 43; 95) favored one or the other vision, or even both. Still unanswered questions like: if tunneling occurs, what are the main units that tunnel?, what is the connection between tunneling and geometrical effects?, and what is the true microscopic origin of the latter?, are possibly some of the reasons why a full explanation of the isotope effect is not yet available. In the present review, we showed how the *ab initio* scheme have also helped to shed light onto the underlying microscopic mechanism for the isotope effect.

We demonstrated in KDP that protons alone are not able to tunnel. In fact, distortions involving only the light atoms display tiny double wells, and the particles are broadly delocalized around the center of the H-bonds. We concluded that the simplified version of the tunneling model, i.e. that of a tunneling proton, or even a collective proton soft-mode alone, is not supported by our calculations.

Due to the correlation with heavier ions, we observe "tunneling clusters" with an effective mass much larger than that of a single, or even several, protons (deuterons). The different sizes

of these clusters correspond to different lengths and energy scales whose magnitudes differ between KDP and DKDP and which compete in their PE phases. This view agrees with recent neutron Compton scattering experiments where it is concluded that there is a mass-dependent quantum coherence lenght in these compounds.(94) We found that the smallest tunneling unit in DKDP is the KD_2PO_4 group. This is in accordance with the idea developed by Blinc and Žekš of a tunneling model for the whole H_2PO_4 unit,(96) which helped to describe the typical order-disorder phenomena observed in some experimental trends.(90) However, as we reviewed in this work, the explanation for the isotope effect is even more complex than the concept of an atom or molecular unit that is able to tunnel alone as its main cause.

It is clear that the larger clusters will prevail as the transition approaches, in spite of the complex scenario existing in the PE phase due to the appearance of different length scales. We showed that tunnel splittings in these clusters at fixed potential are much smaller than the thermal energy at the critical temperature. Thus, if the potential remains fixed, tunneling alone is not able to account for the large isotope effect in the system. However, the main effect of replacing deuterons by protons is an enhancement of the quantum delocalization at the bond center, which affects the chemical properties of the O-H$\cdots$O bond. This in turn shrinks the lattice which further delocalizes the proton, and so on in a nonlinear loop.

We have shown with a simple model based on our *ab initio* results, how this feedback effect strongly amplifies the geometrical modifications in the H(D)-bridge. The selfconsistent phenomenon is triggered by tunneling, but, in the end, the geometrical effect dominates the scenario and accounts for the huge isotope effect, in agreement with neutron scattering experiments. (4; 62) Therefore, these aspects, which were largely debated in the past, here appear as complementary and deeply connected to each other. (29; 30; 47; 48; 88)

The existence of tunneling units has been found in a large variety of molecular compounds and biomolecules. Moreover, the importance of both, tunneling and structural changes, has been well established in the reaction mechanisms of enzymes (97) and other biological processes. It is clear that the nonlinear feedback between tunneling and structural modifications, as discussed in this review, is a phenomenon of wider implications. As one of the numerous examples where these features are observed, one can mention the FE transition in $CaAl_2Si_2O_7(OH)_2H_2O$ (lawsonite), which was recently shown to be related to the proton mobility.(98) Actually, the much smaller isotope effect observed for this compound in comparison with that for KDP seems to be related with the absence of strong correlations with the host, which are essential for the nonlinear mechanism discussed above.(47; 48; 98) Therefore, our results for the H-bonded ferroelectrics support the conclusion that the general theories of host-and-tunneling systems must be revised. (5)

We would now like to extend our methodology to different systems like the subset of systems known as the 'proton glasses' in which an alloy is made by mixing a ferroelectric compound with an isomorphic antiferroelectric compound.(99; 100) These materials show the slow dynamics of a glassy system, even though they are single crystals, and exhibit the H-D isotope effect.(99; 100) Other interesting systems are those where the transitions could be classified either of 'order-disorder' or 'displacive' type or where the order-disorder and the displacive behaviors coexist.(33) In recent studies of the hydrogen-bonding properties of the NH_4^+ cation, ferroelectricity was discovered in a new class of magnetic compounds $M_{3-x}(NH_4)_xCrO_8$ (M = Na, K, Rb, Cs).(101) It was found that the transition is of the order-disorder type, with a critical temperature depending linearly on the composition variable x. This suggests that the N-H$\cdots$O bond plays the central role in the FE instability of these new compounds, with a

net effect reminiscent of the mechanism found in ADP,(21) although in the latter the AFE ordering is favored. Ferroelectric properties were also recently found in a related novel ammonium-based compound, Diammonium Hypodiphosphate $(NH_4)_2H_2P_2O_6$, although there is not yet a theoretical microscopic explanation of this phenomenom.(102) Therefore, it would be also desirable to extend our first-principles calculations to the study and dessign of new FE and AFE materials based on the H-bonding properties of the NH_4^+ cation.
On the other hand, a promising perspective arises from the recently developed atomistic model for KDP,(67) which was briefly described in subsection 3.7.3. As mentioned above, it was fitted to reproduce first-principles structural, dynamical and energetic properties of various stable and metastable structures to a very good extent.(67) This model will be useful to study, in large systems, the nuclear quantum-dynamical and thermal fluctuations responsible for the FE-PE phase transition and the isotope effects observed in KDP.
In summary, it has been shown that the H off-centering controls the instability proccess in KDP. This ordering leads to an electronic charge redistribution and ionic displacements that originate the spontaneous polarization of the FE phase. On the other hand, the origin of antiferroelectricity in ADP is ascribed to the optimization of the N-H$\cdots$O bonds. The closeness in energy found between the AFE and the hypothetical FE phases in ADP is in accordance with the experimental observation of coexistence of AFE and FE microdomains near the vicinity of the transition. The dynamics of protons alone in the PE phases of KDP and ADP cannot explain the observed double-peaked proton distribution in the bridges. By contrast, the importance of the correlations between protons and heavier ions displacements within clusters has been demonstrated. Recent evidence of tunneling obtained from Compton scattering measurements supports our conclusions regarding the existence of tunneling clusters. We have also shown that the huge isotope effect observed in KDP cannot be explained by the quantum effects of a mass change obtained in a system at fixed geometry and potential. We found that as a consequence of the modification of the covalency in the bridges, structural changes arise producing a feedback effect on the tunneling that strongly enhances the phenomenon. The resulting amplification in this nonlinear feedback of the geometrical effect is in agreement with experimental data from neutron scattering.

5. Acknowledgements

We thank E. Tosatti, G. Colizzi, and A. Bussmann-Holder for helpful discussions. S. K., J. L., and R. L. M. acknowledge support from Consejo Nacional de Investigaciones Científicas y Técnicas (CONICET), Argentina.

6. References

[1] *Proton Transfer in Hydrogen-Bonded Systems*; NATO ASI Series B: Physics, Vol. 291; Ed. T. Bountis; Plenum Press (1992); ISBN 0-306-44216-7.
[2] J.M. Robertson and A.R. Ubbelohde, Proc. R. Soc. London A 170, 222 (1939).
[3] M. Ichikawa, Chem. Phys. Lett. 79, 583 (1981).
[4] M.I. McMahon, R.J. Nelmes, W.F. Kuhs, R. Dorwarth, R.O. Piltz, and Z. Tun, Nature (London) 348, 317 (1990).
[5] J.A. Krumhansl, Nature (London) 348, 285 (1990).
[6] M. E. Lines and A. M. Glass, *Principles and Applications of Ferroelectric and Related Materials* (Clarendon Press, Oxford, 1977).

[7] G. Busch and P. Scherrer, Naturwiss. 23, 737 (1935).
[8] G. Busch, Helv. Phys. Acta 11, 269 (1938).
[9] R. Blinc and B. Žekš, in *Soft Modes in Ferroelectrics and Antiferroelectrics*, edited by E. P. Wohlfarth (North-Holland, Amsterdam, 1974).
[10] R. J. Nelmes, Ferroelectrics 71, 87 (1987).
[11] Y. Takagi, Ferroelectrics 72, 67 (1987).
[12] F. Gervais and P. Simon, Ferroelectrics 72, 77 (1987).
[13] G. Samara, Ferroelectrics 71, 161 (1987).
[14] J. C. Slater, J. Chem. Phys. 9, 16 (1941).
[15] V. H. Schmidt, Ferroelectrics 72, 157 (1987).
[16] Y. Takagi, J. Phys. Soc. Jpn. 3, 273 (1948).
[17] J. Lasave, S. Koval, N. S. Dalal, and R. Migoni, Phys. Rev. B 72, 104104 (2005).
[18] T. Nagamiya, Progr. Theor. Phys. 7, 275 (1952).
[19] Y. Ishibashi, S. Ohya, and Y. Takagi, J. Phys. Soc. Jpn. 33, 1545 (1972).
[20] Y. Ishibashi, S. Ohya, and Y. Takagi, J. Phys. Soc. Jpn. 37, 1035 (1974).
[21] J. Lasave, S. Koval, N.S. Dalal, and R.L. Migoni, Phys. Rev. Lett. 98, 267601 (2007).
[22] S. Havlin, E. Litov, and H. Sompolinsky, Phys. Rev. B 14, 1297 (1976).
[23] A. W. Hewat, Nature 246, 90 (1973).
[24] V. H. Schmidt, J. T. Wang, and P. Schnackenberg, Jpn. J. Appl. Phys. 24, Suppl. 24-2, 944 (1985).
[25] B. Lamotte, J. Gaillard and O. Constantinescu, J. Chem. Phys. 57, 3319 (1972).
[26] N.S. Dalal, J.A. Hebden, D.E. Kennedy and C.A. McDowell, J. Chem. Phys. 66, 4425 (1977).
[27] R. Blinc, J. Phys. Chem. Solids 13, 204 (1960).
[28] K. Kobayashi, J. Phys. Soc. Jpn. 24, 497 (1968).
[29] E. Matsushita and T. Matsubara, Prog. Theor. Phys. 67, 1 (1982).
[30] T. Matsubara and E. Matsushita , Prog. Theor. Phys. 71, 209 (1984).
[31] M. Kojyo and Y. Onodera, J. Phys. Soc. Jpn. 57, 4391 (1988).
[32] A. Bussmann-Holder and K. H. Michel, Phys. Rev. Lett. 80, 2173 (1998).
[33] N. Dalal, A. Klymachyov and A. Bussmmann-Holder, Phys. Rev. Lett. 81, 5924 (1998).
[34] G.F. Reiter, J. Mayer and P. Platzman, Phys. Rev. Lett. 89, 135505 (2002).
[35] S. Ikeda, Y. Noda, H. Sugimoto and Y. Yamada, J. Phys. Soc. Jpn. 63, 1001 (1994).
[36] M. Ichikawa, K. Motida and N. Yamada, Phys. Rev. B 36, R874 (1987).
[37] Z. Tun, R.J. Nelmes, W.F. Kuhs and R.D.F. Stansfield, J. Phys. C 21, 245 (1988).
[38] R.J. Nelmes, J. Phys. C 21, L881 (1988).
[39] J. Seliger and V. Žagar, Phys. Rev. B 59, 13505 (1999).
[40] M. Ichikawa, D. Amasaki, T. Gustafsson and I. Olovsson, Phys. Rev. B 64, R100101 (2001).
[41] H. Sugimoto and S. Ikeda, Phys. Rev. Lett. 67, 1306 (1991).
[42] H. Sugimoto and S. Ikeda, J. Phys.: Condens. Matter 8, 603 (1996).
[43] D. Merunka and B. Rakvin, Phys. Rev. B 66, 174101 (2002).
[44] D. Merunka and B. Rakvin, Solid State Commun. 129, 375 (2004).
[45] D. Merunka and B. Rakvin, Chem. Phys. Lett. 393, 558 (2004).
[46] S. Koval, J. Kohanoff, R. L. Migoni, and A. Bussmann-Holder, Comput. Mater. Sci. 22, 87 (2001).
[47] S. Koval, J. Kohanoff, R. L. Migoni and E. Tosatti, Phys. Rev. Lett. 89, 187602 (2002).

[48] S. Koval, J. Kohanoff, J. Lasave, G. Colizzi, and R.L. Migoni, Phys. Rev. B 71, 184102 (2005).
[49] P. Hohenberg and W. Kohn, Phys. Rev. 136, B864 (1964).
[50] W. Kohn and L. J. Sham, Phys. Rev. 140, A1133 (1965).
[51] P. Ordejón, E. Artacho and J.M. Soler, Phys. Rev. B 53, R10441 (1996).
[52] D. Sánchez-Portal, P. Ordejón, E. Artacho and J.M. Soler, Int. J. Quantum Chem. 65, 453 (1997).
[53] O.F. Sankey and D.J. Niklewski, Phys. Rev. B 40, 3979 (1989).
[54] N. Troullier and J.L. Martins, Phys. Rev. B 43, 1993 (1991).
[55] J.P. Perdew, K. Burke and M. Ernzerhof, Phys. Rev. Lett. 77, 3865 (1996).
[56] D. R. Hamann, Phys. Rev. B 55, R10157 (1997).
[57] A. D. Becke, Phys. Rev. A 38, 3098 (1988).
[58] C. Lee, W. Yang, and R. Parr, Phys. Rev. B 37, 785 (1988).
[59] M. Tuckerman, D. Marx and M. Parrinello, Nature 417, 925 (2002).
[60] J. Lasave, S. Koval, R. L. Migoni, and N. S. Dalal, unpublished.
[61] R.J. Nelmes, Z. Tun and W.F. Kuhs, Ferroelectrics 71, 125 (1987).
[62] R. J. Nelmes, M. I. McMahon, R. O. Piltz and N. G. Wright, Ferroelectrics 124, 355 (1991).
[63] A. R. Grimm, G. B. Bacskay and A. D. J. Haymet, Mol. Phys. 86, 369 (1995).
[64] T. R. Dyke, K. R. Mack and J. S. Muenter, J. Chem. Phys. 66, 498 (1977).
[65] T. Fukami, S. Akahoshi, K. Hukuda, and T. Yagi, J. Phys. Soc. Jpn. 56, 2223 (1987).
[66] N. Pérès, M. Souhassou, B. Wyncke, G. Gavoille, A. Cousson, and W. Paulus, J. Phys.: Condens. Matter 9, 6555 (1997).
[67] J. Lasave, J. Kohanoff, R. L. Migoni, and S. Koval, Physica B 404, 2736 (2009).
[68] G. Colizzi, PhD Thesis (Queen's University Belfast, 2005).
[69] M. I. McMahon, R. J. Nelmes, R. O. Piltz and W. F. Kuhs, Europhys. Lett. 13, 143 (1990).
[70] M. I. McMahon, R. J. Nelmes, R. O. Piltz, W. F. Kuhs and N. G. Wright, Ferroelectrics 124, 351 (1991).
[71] G. A. Samara, Ferroelectrics 5, 25 (1973).
[72] G. Colizzi, J. Kohanoff, J. Lasave, S. Koval and R.L. Migoni, Ferroelectrics 301, 61 (2004).
[73] V.H. Schmidt and E.A. Uehling, Phys. Rev. 126, 447 (1962).
[74] V.H. Schmidt, Phys. Rev. 164, 749 (1967).
[75] V.H. Schmidt, G. Bohannan, D. Arbogast and G. Tuthill, J. Phys. Chem. Solids 61, 283 (2000).
[76] H.B. Silsbee, E.A. Uehling, and V.H. Schmidt, Phys. Rev. 133, A165 (1964).
[77] R. Blinc and S. Svetina, Phys. Rev. 147, 430 (1966).
[78] W. Reese, Phys. Rev. 181, 905 (1969).
[79] C.W. Fairall and W. Reese, Phys. Rev. B 11, 2066 (1975).
[80] J. Kobayashi, Y. Mesu, I. Mizutani, and Y. Enomoto, Phys. Status Solidi A 3, 63 (1970).
[81] A. Katrusiak, Phys. Rev. B 48, 2992 (1993).
[82] S. Koval, J. Lasave, J. Kohanoff and R. Migoni, Ferroelectrics 401, 103 (2010).
[83] G. Colizzi, J. Kohanoff, J. Lasave, and R. L. Migoni, Ferroelectrics 401, 200 (2010).
[84] A. E. Mirsky and L. Pauling, Proc. Nat. Acad. Sci. 22, 439 (1936).
[85] S. Scheiner in *Proton Transfer in Hydrogen-Bonded Systems*, NATO ASI Series B: Physics, Vol. 291, Ed. T. Bountis, p. 29 (Plenum, 1992).
[86] L. Pacios in *Hydrogen Bonding - New Insights*, Ed. S. J. Grabowski, p. 109 (Springer, 2006).
[87] D. S. Bystrov and E. A. Popova, Ferroelectrics 72, 147 (1987).

[88] R. Blinc and B. Žekš, Ferroelectrics 72, 193 (1987).
[89] Q. Zhang, F. Chen, N. Kioussis, S. G. Demos and H. B. Radousky, Phys. Rev. B 65, 024108 (2001).
[90] See for instance, M. Tokunaga and T. Matsubara, Ferroelectrics 72, 175 (1987); and references therein.
[91] Y. Tominaga, M. Kasahara, H. Urabe and I. Tatsuzaki, Solid State Commun. 47, 835 (1983).
[92] Y. Tominaga, H. Urabe and M. Tokunaga, Solid State Commun. 48, 265 (1983).
[93] B. Rakvin and N. S. Dalal, Phys. Rev. B 44, R892 (1991).
[94] G. Reiter, A. Shukla, P. M. Platzman and J. Mayers, New J. Phys. 10, 013016 (2008).
[95] S. E. Mkam Tchouobiap and H. Mashiyama, Phys. Rev. B 76, 014101 (2007).
[96] R. Blinc and B. Žekš, J. Phys. C15, 4661 (1982).
[97] A. Kohen, R. Cannio, S. Bartolucci and J. P. Klinman, Nature 399, 496 (1999).
[98] E. K. H. Salje and M. A. Carpenter, J. Phys.: Condens. Matter 23, 112208 (2011).
[99] N.S. Dalal and A. Bussmann-Holder, Structure and Bonding, 24, 1 (2006).
[100] Z. Trybulla, J. Stankowski, L. Szczepanska, R. Blinc, A. I. Weiss, and N.S. Dalal, Physica B 153, 143 (1988).
[101] R. Samantaray, R. J. Clark, E. S. Choi, H. Zhou, and N. S. Dalal, J. Am. Chem. Soc. 133, 3792 (2011).
[102] P. Szklarz, M. Chański, K. Ślepokura and T. Lis, Chem. Mater. 23, 1082 (2011).

22

Temperature Dependence of the Dielectric Constant Calculated Using a Mean Field Model Close to the Smectic A - Isotropic Liquid Transition

H. Yurtseven[1] and E. Kilit[1,2]
[1]*Department of Physics, Middle East Technical University, Ankara*
[2]*Department of Physics, Van Yuzuncu Yil University, Van*
Turkey

1. Introduction

Various transitions among the phases of isotropic liquid (I), nematic (N) and smectic (SmA, SmC and SmC*) in liquid crystals have been studied extensively. The nematic-smectic A (NA) and the smectic A- smectic C (AC) or the smectic A-smectic C* (AC*) transitions are usually continuous and they are considered to belong to the three-dimensional XY universality class for the critical fluctuations (de Gennes, 1973). Experimentally, this requires a wide range of the nematic phase (Garland & Nounesis, 1994) for the NA transition, whereas at the AC transition the critical fluctuations are very large (Safinya et al., 1980).
Ferroelectric liquid crystals exhibiting transitions from the isotropic liquid (I) to the nematic (N), smectic A and the smectic C or smectic C* (with optically active molecules), have also been studied extensively, in particular, those with high spontaneous polarization such as 4-(3-methyl-2-chlorobutanoyloxy)- 4′ -heptyloxybiphenyl (A7). Experimental studies on the ferroelectric liquid crystals with high spontaneous polarization (Bahr & Heppke, 1986- Mercuri et al., 2003) have been reported in the literature. The AC (or AC*) transitions in the ferroelectric liquid crystals (Bahr & Heppke, 1990- Denolf et al., 2006) and in the antiferroelectric liquid crystals (Ema,, et al., 1996) have also been studied experimentally. Theoretical studies on the AC and AC* transitions have been reported in the literature (Musevic et al.,. 1983- Mukherjee, 2009). We have also studied the AC and AC* transitions in the ferroelectric liquid crystals (A7 and C7) theoretically by using the mean field models in our previous works (Salihoğlu et al., 1998- Yurtseven 2011).
Among the various physical properties of the ferroelectric liquid crystals, the dielectric properties have been studied extensively close to the AC (or AC*) transitions (Bahr et al., 1987, Musevic et al., 1983, Yurtseven & Kilit, 2008, Kilit & Yurtseven, 2008, Benguigui, 1984). In an another ferroelectric liquid crystal known as DOBAMBC which shows a second order transition (Zeks, 1984, Indenbom et al., 1976, Carlsson & Dahl, 1983), the AC* transition is associated with an increase in the dielectric constant $\varepsilon_{\perp}$ with decreasing temperature, as observed experimentally (Bahr et al., 1987). This increase in the $\varepsilon_{\perp}$ has been attributed to the contributions from a soft mode and also a Goldstone mode of this ferroelectric material with

low spontaneous polarization. It has been observed experimentally that the ferroelectric liquid crystal 4-(3-methyl-2-chlorobutanoyloxy)- 4′ -heptyloxybiphenyl exhibits similar to the DOBAMBC an increase in the dielectric constant $\varepsilon_\perp$ with decreasing temperature from SmA to SmC* at different voltages (Bahr et al., 1987). This increase in $\varepsilon_\perp$ also occurs for the pure optically active compound, the 50% optically active mixture and the racemate at the SmA-I transition of 4-(3-methyl-2-chlorobutanoyloxy)- 4′ -heptyloxybiphenyl (Bahr et al., 1987).
A first order or second order character of the phase transitions in the ferroelectric liquid crystals can be characterized by the critical behaviour of the order parameters which occurs as the temperature decreases from the isotropic liquid to the nematic and smectic phases. There is no order parameter in the isotropic liquid phase, whereas in the nematic and smectic phases there occur orientational order parameter ψ (in the nematic and smectic phases). In the smectic phases of a ferroelectric liquid crystal, in addition to the orientational order parameter ψ, the spontaneous polarization P occurs. P can couple with ψ since the symmetry is reduced as the temperature decreases in the smectic phase. This coupling between the spontaneous polarization P and the orientational order parameter ψ can also occur in the crystal which contains optically active molecules such as 4-(3-methyl-2-chlorobutanoyloxy)- 4′ -heptyloxybiphenyl (A7). In this ferroelectric liquid crystal, in particular, the optically active molecules can induce the phase transition which changes towards a second order (continuous) as the temperature decreases from the isotropic liquid to the smectic phase, whereas the racemic A7 can exhibit a first order (discontinuous) transition.
In this study, a first order transition of the racemic A7 and the second order transition of the 50% optically active compound are investigated by calculating the temperature dependence of the dielectric constant $\varepsilon_\perp$ on the basis of the experimental results (Bahr et al., 1987). For this calculation, our mean field model which we have studied for the AC* transition ($P^2\theta^2$ coupling, θ is the tilt angle in the C* phase) previously (Salihoğlu et al., 1998), is used with the biquadratic $P^2\psi^2$ coupling between the spontaneous polarization P and the orientational order parameter ψ. For both 50% optically active compound and the racemic A7, the isotropic liquid-smectic A transition is studied by expanding the free energy in terms of the order parameters P and ψ according to the Landau phenomenological model. With the $P^2\psi^2$ coupling, our mean field model considers quadrupolar interactions for the 50% optically active compound and for the racemic A7 differently from the bilinear $P\theta$ coupling which considers the dipole-dipole interactions as studied in a previous study (Bahr et al., 1988). The mean field models with the $P^2\theta^2$ coupling have also been treated in some earlier theoretical studies (Zeks, 1984- Blinc, 1992).
In section 2, we describe our mean field model for the SmA-I transition. Section 3 gives our calculations and results which are discussed in section 4. Finally, conclusions are given in section 5.

2. Theory

Close to the smectic A-isotropic liquid transition can be investigated by a mean field model. In the smectic A phase, the order parameters are the orientational order parameter ψ and the spontaneous polarization P. So, the free energy in this phase can be expanded in terms of ψ and P as given below:

$$g = \frac{1}{2}\alpha\psi^2 + \frac{1}{4}b\psi^4 + \frac{1}{6}c\psi^6 + \frac{1}{2\chi_0\varepsilon_0}P^2 - DP^2\psi^2 + \frac{1}{4}eP^4 \tag{1}$$

This expansion of the free energy has already been introduced in our earlier study (Salihoğlu et al., 1998). In Eq.(1) the coefficient α is taken as the temperature dependent given by

$$\alpha = a(T - T_o) \tag{2}$$

where a is constant and T_o is the transition temperature. When the smectic A-isotropic liquid (SmA-I) transition is considered as a first order, then b is negative in Eq.(1) with the additional ψ^6 term and the coefficients c, D and e are taken as positive. In Eq.(1) the other constants, ε_0 is the vacuum permittivity and χ_0 describes the susceptibility at $\psi = \psi_0$. We consider a quadratic coupling $P^2\psi^2$ in our mean field model to describe the quadrupolar interactions in the liquid crystalline system studied here. The last term to the power P^4 in Eq.(1) stabilizes the system thermodynamically. Since there is no ordering in the isotropic liquid (order parameter is zero), we have

$$F_l = 0 \tag{3}$$

The free energy g (Eq.1) can be minimized with respect to the orientational order parameter ψ and the spontaneous polarization P, which gives

$$\alpha\psi + b\psi^3 + c\psi^5 - 2DP^2\psi = 0 \tag{4}$$

and

$$\frac{1}{\chi_o\varepsilon_o}P - 2DP\psi^2 + eP^3 = 0 \tag{5}$$

Eq.(5) then gives

$$P^2 = \frac{1}{e}\left(2D\psi^2 - \frac{1}{\chi_o\varepsilon_o}\right) \tag{6}$$

By substituting this expression into Eq.(4), one gets

$$c\psi^4 + b^*\psi^2 + d^* = 0 \tag{7}$$

with the definitions of the coefficients

$$b^* = b - \frac{4D^2}{e} \tag{8}$$

and

$$d^* = a(T - T_o) + \frac{2D}{e\chi_o\varepsilon_o} \tag{9}$$

When we substitute the spontaneous polarization P (Eq.6) into the free energy g (Eq.1), we then get

$$g = \frac{1}{2}\alpha'\psi^2 + \frac{1}{4}b'\psi^4 + \frac{1}{6}c'\psi^6 \tag{10}$$

where

$$\alpha' = \alpha + \frac{2D}{e\chi_o\varepsilon_o} \tag{11}$$

$$b' = b - \frac{4D^2}{e} \tag{12}$$

and

$$c' = c \tag{13}$$

In order to describe the SmA-I transition, the condition for a first order transition can be obtained according to the relation among the coefficients (Salihoğlu et al., 1998)

$$\frac{\alpha' c'}{b'^2} = \frac{3}{16} \tag{14}$$

For a first order transition, a difference occurs between the transition temperature T_o and the observed T_c, which can be given in Eq.(2) as

$$\alpha = a(T_o - T_c) \tag{15}$$

at $T=T_c$. As we have already derived in our previous study (Salihoğlu et al., 1998), this temperature difference can be obtained using Eqs.(11-14) as

$$T_c = T_o + \frac{3}{16}\frac{b'^2}{ac} - \frac{2D}{ea\chi_o\varepsilon_o} \tag{16}$$

The inverse susceptibility χ^{-1} can be derived from the free energy g (Eq. 10) according to the definition

$$\chi_\psi^{-1} = \partial^2 g / \partial\psi^2 \tag{17}$$

This second derivative then gives

$$\chi^{-1} = \alpha' + 3b'\psi^2 + 5c'\psi^4 \tag{18}$$

In Eq.(18) the coefficient α' depends on the temperature through Eq.(11) by using Eq.(2). The coefficients b' and c' are taken as constants, as before.
Since we expressed the inverse susceptibility χ^{-1} to the powers of the orientational order parameter ψ in Eq.(18), it will be determined by the temperature dependence of ψ. From the molecular field theory (Matsushita, 1976), the order parameter ψ depends on the temperature according to the relation

$$\psi = [3(1-\frac{T}{T_c})]^{1/2}, \qquad 0<(T_c - T)<<T_c \tag{19}$$

with the critical exponent $\beta = 1/2$. By using this temperature dependence of ψ (Eq.19) in Eq.(18), we obtain the inverse susceptibility χ^{-1} or the dielectric constant ($\chi = \varepsilon - 1$) as a function of temperature for the smectic A-isotropic liquid transition in our mean field model studied here.

3. Calculations and results

The inverse susceptibility χ^{-1} was calculated here as a function of temperature according to Eq.(18) on the basis of the temperature dependence of the orientational order parameter ψ (Eq.19) for the ferroelectric phase of A7. We first calculated the temperature dependence of ψ below T_c for the smectic A-isotropic liquid transition of A7. It was calculated (Eq.19) for the 50% optically active mixture (T_c=81.9°C) and for the racemate (T_c=82°C) at the smectic A-isotropic liquid transition.

In order to calculate the inverse susceptibility χ^{-1} from the orientational order parameter ψ as a function of temperature, we determined the coefficients α', b' and c' in Eq.(18). For this determination, the experimental data for the dielectric constant $\varepsilon_\perp$ (Bahr et al., 1987) was used ($\chi = \varepsilon_\perp - 1$). In Eq.(18), the expression for α' (Eq.11) through α (Eq.15) can be used and the inverse susceptibility becomes

$$\chi^{-1} = a(T - T_o) + \frac{2D}{e\chi_o\varepsilon_o} + a_1\psi^2 + a_2\psi^4 \tag{20}$$

where the coefficients are $a_1 = 3b'$ and $a_2 = 5c'$. The second term as a constant in Eq.(20) can be computed from the value of the inverse susceptibility at the transition temperature ($T=T_o$) where the order parameter is zero (Figs. 1 and 2). This gives

$$\chi^{-1}\Big|_{T=T_o} = \frac{2D}{e\chi_o\varepsilon_o} \tag{21}$$

Values of this constant term were obtained from the experimental values of $\varepsilon_\perp$ at $T=T_c$ for the smectic A-isotropic liquid transition of the 50% mixture and the racemic A7 compound, as given in Table 1.

A7	T_c (°C)	a x 10^{-2} (°C^{-1})	a_1	a_2	$\varepsilon_\perp$	χ^{-1}	$\alpha' c' / b'^2$
50% mixture	81.9	5.88	1.224	3.63	5.21	0.238	1.88
Racemic	82.0	0.48	0.152	-0.312	5.07	0.246	-11.97

Table 1. Values of the coefficients a, a_1 and a_2 which were obtained by fitting Eq.(20) to the experimental data for the dielectric constant $\varepsilon_\perp$ of the 50% mixture and the racemic A7 (Bahr et al., 1987) for the smectic A phase ($T<T_c$) close to the SmA-I transition. The experimental values of $\varepsilon_\perp$ (or χ^{-1}) at the transition temperature T_c (Bahr et al., 1987) are given here. Values of the transition temperature T_o calculated from Eq.(16) are indicated for both compounds. The temperature difference ΔT is also given here.

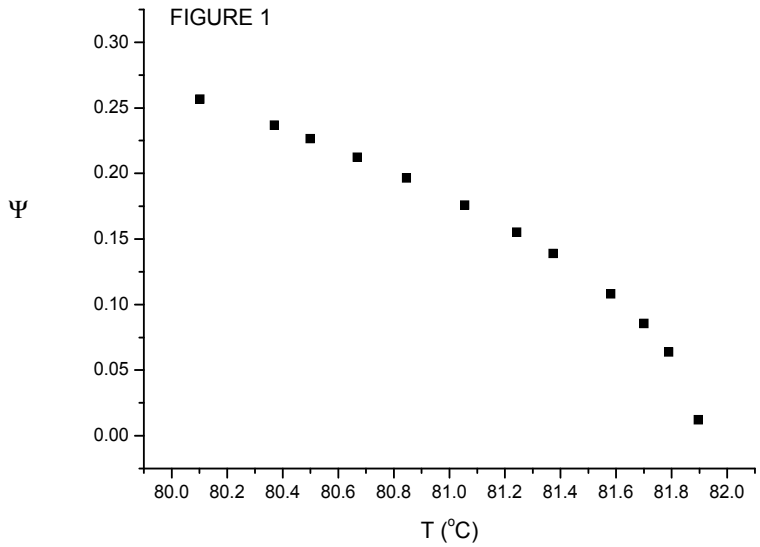

Fig. 1. The orientational order parameter ψ calculated from the mean field theory (Eq.19) as a function of temperature for the smectic A phase of the 50% optically active mixture of A7 (T_c=81.9°C).

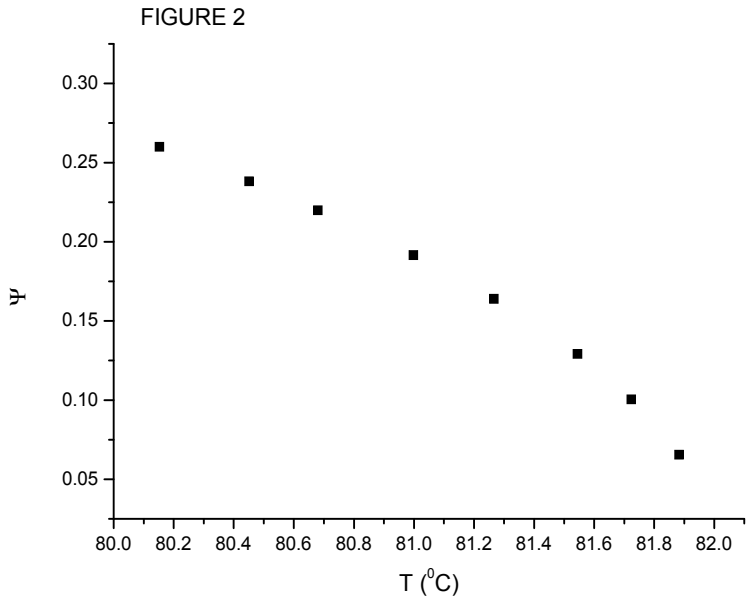

Fig. 2. The orientational order parameter ψ calculated from the mean field theory (Eq.19) as a function of temperature for the smectic A phase of the racemic A7 (T_c=82 °C).

Finally, the coefficients a, a_1 and a_2 given in Eq.(20) were determined from the temperature dependence of the orientational order parameter ψ (Eq.19) as we plotted in Figs. 1 and 2 for the 50% mixture and racemic A7, respectively. For this determination of the coefficients a, a_1 and a_2, we also used the experimental data for the dielectric constant $\varepsilon_\perp$ of the 50% mixture and the racemic A7 (Bahr et al., 1987) in Eq.(20). By fitting Eq.(20) to the experimental data for $\varepsilon_\perp$ (or χ^{-1}), the coefficients a, a_1 and a_2 were obtained for both compounds (50% mixture and racemic A7), as given in Table 1. Figs. 3 and 4 give the dielectric constant $\varepsilon_\perp$ calculated (Eq.18) with the experimental data (Bahr et al., 1987) for the 50% mixture and the racemic A7, respectively, for the smectic A-isotropic liquid transition.

The temperature dependence of the dielectric constant $\varepsilon_\perp$ was also calculated in the isotropic liquid phase for the 50% mixture and the racemic A7 according to Eq.(20) where the orientational order parameter is zero (ψ =0). Eq.(20) then becomes

$$\chi^{-1} = a(T - T_c) + \frac{2D}{e\chi_0\varepsilon_0} \tag{22}$$

for the inverse susceptibility (or the dielectric constant) in the isotropic liquid phase of A7. We first calculated the inverse susceptibility χ^{-1} for the 50% mixture of A7 as a function of temperature by using in Eq.(22) the same value of the coefficient a (=5.88x10^{-2} ^{o}C $^{-1}$) which we determined for the smectic A phase (Table 1). We also used in Eq.(22) our value of $\chi^{-1}\big|_{T=T_o}$ (Eq.21) as given in Table 1. Our calculated values of $\varepsilon_\perp$ are plotted in Fig.3 for the 50% mixture in the isotropic phase at various temperatures.

As we performed for the SmA phase, this time we followed the same procedure by fitting Eq.(22) to the experimental data for the 50% mixture in the isotropic liquid. We then determined the coefficient a for the isotropic liquid phase by keeping the value of $\chi^{-1}\big|_{T=T_o}$ the same as before (Table 1). Table 2 gives the a value determined for the 50% mixture of A7. By means of this a value (Table 2), the dielectric constant $\varepsilon_\perp$ was obtained (Eq.22), as plotted as a function of temperature for the isotropic liquid phase in Fig.3.

A7	T_c (^{o}C)	a x 10^{-2} (^{o}C^{-1})	χ^{-1}	T_c (^{o}C)	$\Delta T = T_0 - T_c$ (^{o}C)	$\alpha' c' / b'^2$
50% mixture	81.9	7.9	0.238	84.4	2.5	1.9
Racemic	82.0	4.2	0.234	87.7	5.7	-11.3

Table 2. Values of the coefficients a and $\chi^{-1}\big|_{T=T_0}$ (Eq.21), which were obtained by fitting (Eq.(22) to the experimental data for the dielectric constant $\varepsilon_\perp$ of the 50% mixture and the racemic A7 for the isotropic liquid phase ($T>T_c$) close to the SmA-I transition. The temperature difference ΔT and the ratio $\alpha' c' / b'^2$ (Eq. 14) obtained for both compounds are given.

For the racemic A7, we were unable to predict the observed $\varepsilon_\perp$ data for the isotropic liquid phase from Eq.(22) by using the same values of the coefficient a and $\chi^{-1}\big|_{T=T_o}$, which we determined for the SmA phase (Table 1). Instead, we fitted Eq.(22) to the experimental data (Bahr et al., 1987) for the isotropic liquid phase and determined the values of the coefficient a

and $\chi^{-1}\big|_{T=T_o}$, as given in Table 2. We plot the $\varepsilon_\perp$ values obtained in Fig. 4 as a function of temperature for the racemic A7 in the isotropic liquid phase.

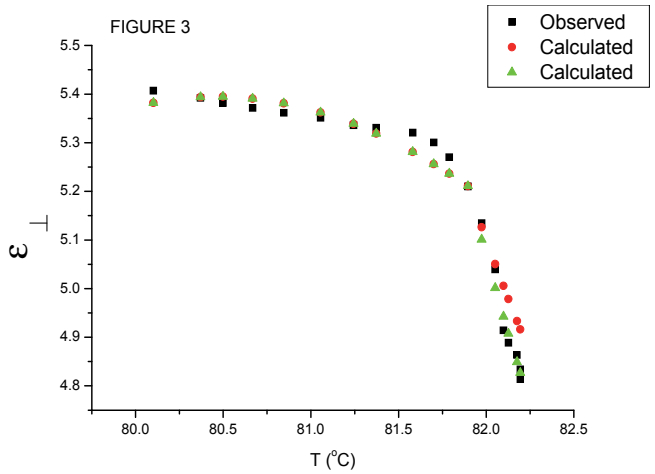

Fig. 3. Values calculated from Eqs. (20) and (22) for the smectic A and the isotropic liquid phases, respectively, for the 50% mixture of A7. The ψ values used in Eq.(20) were calculated from the mean field theory (Eq. 19). Calculated values (■) were obtained from fitting the Eq.(20) (SmA) and Eq.(22) (I) to the experimental data (Bahr et al., 1987) for the $\varepsilon_\perp$. Calculated values (▲) in the isotropic liquid phase were obtained by using the coefficients of the smectic A phase (Table 1) in Eq.(22). The observed data (Bahr et al., 1987) is also plotted here (T_c=81.9 °C).

The transition temperature T_o can also be calculated from the experimental transition temperature T_c for the 50% mixture and the racemic A7. The T_o values were calculated by using the values of the coefficients a and $\chi^{-1}\big|_{T=T_C}$ (Table 2), b' (or a_1) and c (or a_2) (Table 1) for the 50% mixture and the racemic A7, which we give in Table 2 for both compounds. The temperature range $\Delta T(=T_0-T_c)$ was determined for the 50% and the racemic A7, as tabulated in Table 2. We also obtained the ratio $\alpha' c'/b'^2$ for both compounds, as given in Tables 1 and 2. We computed this ratio for the smectic A phase (Table 1) and for the isotropic liquid (Table 2) by using the coefficients for both the 50% mixture and the racemic A7. Finally, the slope ratio from the plots of the dielectric constant $\varepsilon_\perp$ vs. temperature for the smectic A and isotropic liquid phases (SmA/I) was calculated for both the 50% mixture and the racemic A7. The slope ratio of SmA/I was computed close to the transition temperature for the 50% mixture (Fig.3) and for the racemic A7 (Fig. 4) in the temperature ranges, as given in Table 3.

A7	T_c (°C)	Slope ratio(SmA/I)	Temperature range (SmA)	Temperature range(I)
50% mixture	81.9	0.4 (≈ 1/2)	81.7 < T < 81.974	82.051 < T < 82.195
Racemic	82.0	13.8 (≈ 14)	80.451 < T < 81.724	82.27<T<82.622

Table 3. The slope ratio (SmA/I) for the calculated $\varepsilon_\perp$ vs. T plots of the 50% mixture (Fig.3) and of the racemic A7 (Fig.4) within the temperature interval indicated.

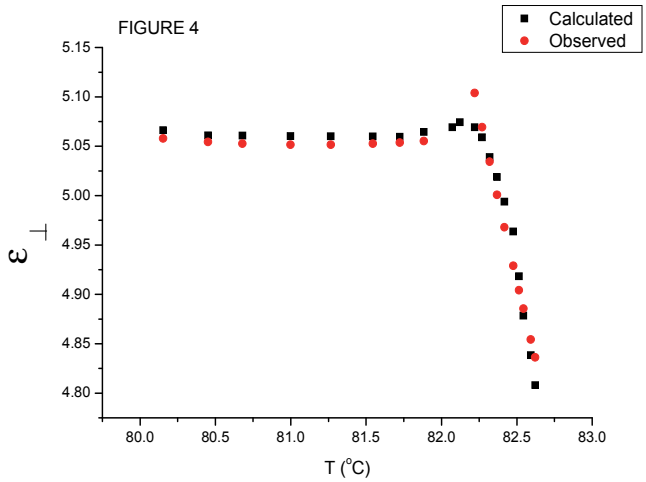

Fig. 4. Values calculated from Eqs. (20) and (22) for the smectic A and the isotropic liquid phases, respectively, for the racemic A7. The ψ values used in Eq.(20) were calculated from the mean field theory (Eq. 19). Calculated values were obtained from the fitting Eq.(20) (SmA) and Eq.(22) (I) to the experimental data (Bahr et al., 1987) for the $\varepsilon_\perp$. The observed data (Bahr et al., 1987) is also plotted here (T_c=82°C).

4. Discussion

The temperature dependence of the dielectric constant $\varepsilon_\perp$ was calculated here using our mean field model with the biquadratic coupling $P^2\psi^2$, as given by Eq.(1). For this calculation of $\varepsilon_\perp$ or the inverse dielectric susceptibility χ^{-1} (Eq.20), the orientational order parameter ψ was first calculated as a function of temperature from the mean field theory (Eq.19), as plotted in Figs.1 and 2 for the 50% optically active compound and the racemic 4-(3-methyl-2-chlorobutanoyloxy)- 4′ -heptyloxybiphenyl, respectively. The temperature dependence of the spontaneous polarization P can also be calculated from Eq.(6) which gives similar critical behaviour as the orientational order parameter ψ. It decreases smoothly with increasing temperature in the SmA phase as the smectic A- isotropic liquid (SmA-I) transition temperature (Table 1) is approached for the 50% mixture and the racemic A7.

By using the temperature dependence of the order parameter for the 50% optically active (Fig.1) and the racemic A7 (Fig.2), the dielectric constant $\varepsilon_\perp$ was calculated in these compounds, as plotted in Figs. 3 and 4, respectively. This calculation was carried out for the smectic A phase ($\psi \neq 0$) and for the isotropic liquid ($\psi = 0$) according to Eqs. (20) and (22), respectively, as stated above. Eqs. (20) and (22) were both fitted to the experimental data for the smectic A and the isotropic liquid phases with the coefficients given in Tables 1 and 2. We also calculated the dielectric constant $\varepsilon_\perp$ of the 50% mixture in the isotropic liquid by using the same values of a and the $\chi^{-1}\big|_{T=T_C}$ extracted for the smectic A phase (Table 1). Those calculated $\varepsilon_\perp$ values are also in good agreement with the experimental data in the isotropic phase of the 50% mixture, as plotted in Fig.3. As seen from Fig.3, variation of the dielectric constant $\varepsilon_\perp$ is continuous with the temperature so that the $\varepsilon_\perp$ decreases continuously as the

temperature increases from the smectic A to the isotropic liquid phase for the 50% optically active A7. This continuous change in the dielectric constant $\varepsilon_\perp$ indicates a second order transition between the smectic A and the isotropic liquid of the 50% mixture. In regard to the variation of the $\varepsilon_\perp$ with the temperature for the racemic A7 (Fig.4),the smectic A-isotropic liquid transition in this compound is more likely closer to the first order transition. In the smectic A phase, the dielectric constant $\varepsilon_\perp$ varies slightly within the temperature interval of nearly 2K (from about 80.5 to 82K) and then there occurs a kink just above 82K (at around 82.25K) prior to the isotropic liquid (Fig. 4). When Eqs.(20) and (22) were fitted to the experimental data (Bahr et al., 1987) for the smectic A and the isotropic liquid phases, respectively, this kink that occurs in the racemic A7 was not studied in particular, which might be the pretransitional effect. As shown in Fig.4, Eqs. (20) and (22) are adequate to describe the observed behaviour of the smectic A and the isotropic liquid phases of the racemic A7, respectively. Above T_c in the isotropic liquid phase of the racemic A7, the dielectric constant $\varepsilon_\perp$ exhibits closely a discontinuous behaviour. It drops more rapidly in a small temperature interval, as shown in Fig. 4. In fact, this first order behaviour is supported by a very large value of ≈-11 or -12 for the ratio $\alpha' c' / b'^2$ extracted (Eq.14) by using the coefficients (Table 1 and 2) for the racemic A7 in comparison with the value of 1.9 for the 50% mixture. The first order character of the smectic A- isotropic liquid transition can also be seen from the temperature difference ($\Delta T = T_0 - T_c$) which is nearly 6K for the racemic A7 compared to the value of 2.5 K for the 50% mixture (Table 2). Another comparison for the first order (racemic A7) and the second order (50% mixture) character of the smectic A- isotropic liquid transition in both compounds can be made in terms of the slope ratio of the SmA/I, as given in Table 3. Again, a very large value of ≈14 for the racemic A7 also indicates a first order SmA-I transition in this compound in comparison to the value of $\sim 1/2$ for the 50% mixture which can be considered to exhibit a second order SmA-I transition within the temperature intervals studied. This slope ratio can be used as a criterion to describe a first or second order transition exhibited by the ferroelectric liquid crystals, which was used in particular for the smectic A-smectic C* (AC*) phase transition in A7 (Bahr et al., 1987), and also in general for the ferroelectrics and related materials (Lines & Glass, 1979).

The dielectric constant $\varepsilon_\perp$ was calculated using the temperature dependence of the orientational order parameter ψ (Eq.19) from the mean field theory in Eq.(18), as stated above. According to the minimization condition, by taking the derivative of the free energy g (Eq.10) with respect to the ψ ($\partial g / \partial \psi = 0$), a quadratic equation obtained in ψ^2 can be solved, which also gives a similar functional form of the temperature dependence of ψ with the critical exponent of $\beta = 1/2$ from the mean field theory, as given by Eq.(19). This quadratic solution in ψ^2 can also be used to calculate the temperature dependence of the spontaneous polarization P (Eq.6) and of the dielectric constant $\varepsilon_\perp$ (or χ^{-1}) (Eq.18). The calculated $\varepsilon_\perp$ can then be compared with the experimental data (Bahr et al., 1987) for the SmA-I transition of 4-(3-methyl-2-chlorobutanoyloxy)- 4′ -heptyloxybiphenyl below T_c.

As shown in Figs. (3) and (4), the observed behaviour of the dielectric constant $\varepsilon_\perp$ is described satisfactorily by our mean field model with the $P^2\theta^2$ coupling which considers quadrupolar interactions in the 50% mixture and the racemic A7. Our results for the dielectric constant $\varepsilon_\perp$ (Figs. 3 and 4) indicate that the quadrupolar interaction ($P^2\psi^2$ coupling) is the dominant mechanism for the first order (or a weak first order) transition in the racemic A7 and the second order (or close to a second order) transition in the 50% mixture.

5. Conclusions

The dielectric constant $\varepsilon_{\perp}$ of the ferroelectric 50% optically active and the racemic compounds of 4-(3-methyl-2-chlorobutanoyloxy)- 4′ -heptyloxybiphenyl was calculated as a function of temperature for the smectic A-isotropic liquid (SmA-I) transition. A mean field model with the biquadratic coupling $P^2\psi^2$ between the spontaneous polarization P and the orientational order parameter ψ of the smectic A (SmA) phase was used to calculate $\varepsilon_{\perp}$ through the temperature dependence of the order parameter ψ.
Our mean field model describes adequately the observed behaviour of $\varepsilon_{\perp}$ for this liquid crystal with high spontaneous polarization close to the smectic A –isotropic liquid transition. It is indicated here that the 50% mixture exhibits a second order (or close to a second order) and that the racemic A7 exhibits a first order (or a weak first order) smectic A-isotropic liquid transition.

6. References

Bahr Ch. & Heppke, G. (1986). Ferroelectric liquid-crystals with high spontaneous polarization. *Mol. Cryst. Liq. Cryst. Lett.*, Vol. 4, No.2, pp. 31-37 .

Bahr, Ch., Heppke G. & Sharma, N.K. (1987). Dielectric studies of the smectic-C-]-smectic A transition of a ferroelectric liquid-crystal with high spontaneous polarization. *Ferroelectrics,* Vol. 76, No. 1-2, pp. 151-157.

Bahr, Ch., Heppke, G. & Sabaschus, B. (1988). Chiral-racemic phase-diagram of a ferroelectric liquid-crystal with high spontaneous polarization. *Ferroelectrics,* Vol. 84, pp. 103-118.

Bahr, Ch. & Heppke, (1990). Influence of electric-field on a 1st-order smectic-A ferroelectric-smectic-C liquid-crystal phase-transition - a field-induced critical-point. G. *Phys. Rev. A*, Vol. 41, No. 8, pp. 4335-4342.

Bahr, Ch. & Heppke, G. (1991). Critical exponents of the electric-field-induced smectic-alpha ferroelectric-smectic-C liquid-crystal critical-point. *Phys. Rev. A*, Vol. 44, No. 6, pp 3669-3672.

Benguigui, L. (1984). Dielectric-properties and dipole ordering in liquid-crystals. *Ferroelectrics,* Vol. 58, No. 1-4, pp. 269-281.

Blinc, R. (1992). Models for phase transitions in ferroelectric liquid crystals: Theory and experimental results, In: *Phase Transitions in Liquid Crystals,* Martellucci, S. & Chester , A.N.,. Plenum Press, New York

Carlsson, T. & Dahl, I. (1983). Dependence of the tilt angle on external forces for smectic-C and chiral smectic-C liquid-crystals - measurement of the heat-capacity of DOBAMBC. *Mol. Cryst. Liq. Cryst.*, Vol. 95, No. 3-4, pp. 373-400.

Carlsson, T., Zeks, B., Levstik, A., Filipic, C., Levstik, I. & Blinc, R. (1987). Generalized landau model of ferroelectric liquid-crystals. *Phys. Rev*. A, Vol. 36, No. 3, pp. 1484-1487.

de Gennes, P. G. (1973) *The physics of liquid crystals*. Clarendon Press. ISBN: 0 19 851285 6, Oxford

Denolf, K., Van Roie, B., Pitsi, G. & Thoen, (2006). Investigation of the smectic-A-smectic-C* transition in liquid crystals by adiabatic scanning calorimetry. *J. Mol. Cryst. Liq. Cryst.*, Vol. 449, pp. 47-55.

Dumrongrattana, S. & Huang, C.C. (1986). Polarization and tilt-angle measurements near the smectic-A-chiral-smectic-C transition of p-(n-decyloxybenzylidene)-p-amino-(2-methyl-butyl)cinnamate (DOBAMBC). *Phys. Rev. Lett.*, Vol. 56, No. 5, pp. 464-467.

Ema, K., Yao, H., Fukuda, A., Takanishi, Y. & Takezoe, H. (1996). Non-Landau critical behavior of heat capacity at the smectic-A-smectic-C-alpha(*) transition of the

antiferroelectric liquid crystal methylheptyloxycarbonylphenyl octyloxycarbonylbiphenyl carboxylate. Phys. Rev. E, Vol. 54, No. 4, pp. 4450-4453.

Garland, C.W. & Nounesis, G. (1994). Critical-behavior at nematic smectic-A phase-transitions. *Phys. Rev. E,* Vol. 49, No. 4, pp. 2964 -2971.

Indenbom, V. L., Pikin, S. A. & Loginov, E. B. (1976). Phase-transitions and ferroelectric structures in liquid-crystals. *Kristallografiya,* Vol. 21, No. 6, pp. 1093-1100.

Johnson, P.M., Olson, D.A., Pankratz, S., Bahr, Ch., Goodby, J.W. & Huang, C.C. (2000). Ellipsometric studies of synclinic and anticlinic arrangements in liquid crystal film. *Phys. Rev. E,* Vol. 62, No. 6, pp. 8106-8113.

Kilit, E. & Yurtseven, H. (2008). Calculation of the dielectric constant as a function of temperature near the smectic AC* phase transition in ferroelectric liquid crystals. *Ferroelectrics*, Vol. 365, pp.130-138.

Lines M. E. & Glass, A. M. (1979). *Principles and Applications on Ferroelectrics and Related Materials*, Oxford University Press, pp. 71-81, Oxford

Matsushita, M. (1976). Anomalous temperature dependence of the frequency and damping constant of phonons near T_λ in ammonium halides. *J. Chem. Phys.,* Vol. 65, p. 23.

Mercuri, F., Marinelli, M., Zammit, U., Huang, C.C. & Finotello, D. (2003). Critical behavior of thermal parameters at the smectic-A-hexatic-B and smectic-A-smectic-C phase transitions in liquid crystals. *Phys. Rev. E,* Vol. 68, No. 5, Article Number 051705.

Mukherjee, P. K. (2009). Tricritical behavior of the smectic-A to smectic-C-* transition. *J. Chem. Phys.*, Vol. 131, No. 7, Article Number 074902.

Musevic, I., Zeks, B., Blinc, R., Rasing, Th. & Wyder, P. (1983). Dielectric study of the modulated smectic-C star uniform smectic-C transition in a magnetic-field. *Phys. Stat. Sol. (b),* Vol.119, No. 2, pp. 727-733.

Safinya, C.R., Kaplan, M., Als-Nielsen, J., Birgeneau, R. J., Davidov, D., Litster, J. D., Johnson, D. L. & Neubert, M. (1980). High-resolution x-ray study of a smectic-A-smectic-C phase-transition. *Phys. Rev. B,* Vol. 21 No. 9, pp. 4149-4153.

Salihoğlu, S., Yurtseven, H. & Bumin, B. (1998). Concentration dependence of polarization for the AC* phase transition in a binary mixture of liquid crystals. *Int J. Mod. Phys. B*, Vol. 12, No. 20, pp. 2083-2090.

Salihoğlu, S., Yurtseven, H., Giz, A., Kayışoğlu, D. & Konu, A. (1998). The mean field model with P-2 theta(2) coupling for the smectic A-smectic C* phase transition in liquid crystals. *Phase Trans.,* Vol. 66, No. 1-4, pp. 259-270.

Yurtseven, H. & Kilit, E. (2008). Temperature dependence of the polarization and tilt angle under an electric field close to the smectic AC* phase transition in a ferroelectric liquid crystal. *Ferroelectrics*, Vol. 365, pp. 122-129.

Yurtseven, H. & Kurt, M. (in press) (2011). Tilt angle and the temperature shifts calculated as a function of concentration for the AC* phase transition in a binary mixture of liquid crystals, *Int. J. Mod. Phys. B*

Zeks, B. (1984). Landau free-energy expansion for chiral ferroelectric smectic liquid-crystals. *Mol. Cryst. Liq. Cryst*., Vol. 114, No. 1-3, pp. 259-270.

23

Mesoscopic Modeling of Ferroelectric and Multiferroic Systems

Thomas Bose and Steffen Trimper
Martin-Luther-University Halle, Institute of Physics
Germany

1. Introduction

Motivated by the progress of a multi-scale approach in magnetic materials the dynamics of the Ising model in a transverse field introduced by de Gennes (1963) as a basic model for a ferroelectric order-disorder phase transition is reformulated in terms of a mesoscopic model and inherent microscopic parameters. The statical and dynamical behavior of the Ising model in a transverse field is considered as classical field theory with fields obeying Poisson bracket relations. The related classical Hamiltonian is formulated in such a manner that the quantum equations of motion are reproduced. In contrast to the isotropic magnetic system, see Tserkovnyak et al. (2005), the ferroelectric one reveals no rotational invariance in the spin space and consequently, the driving field becomes anisotropic. A further conclusion is that the resulting excitation spectrum is characterized by a soft-mode behavior, studied by Blinc & Zeks (1974) instead of a Goldstone mode which appears when a continuous symmetry is broken, compare Tserkovnyak et al. (2005). Otherwise the underlying spin operators are characterized by a Lie algebra where the total antisymmetric tensor plays the role of the structural constants. Using symmetry arguments of the underlying spin fields and expanding the driving field in terms of spin operators and including terms which break the time reversal symmetry we are able to derive a generalized evolution equation for the moments. This equation is similar to the Landau Lifshitz equation suggested by Landau & Lifshitz (1935) with Gilbert damping, see Gilbert (2004). Alternatively, such dissipative effects can be included also in the Lagrangian written in terms of the spin moments and bath variables Bose & Trimper (2011). Due to the time reversal symmetry breaking coupling the resulting equation includes under these circumstances a dissipative equation of motion relevant for ferroelectric material. The deterministic equation is extended by stochastic fields analyzed by Trimper et al. (2007). The averaged time dependent polarization offers three modes below the phase transition temperature. The two transverse excitation energies are complex, where the real part corresponds to a propagating soft mode and the imaginary part is interpreted as the wave vector and temperature dependent damping. Further there exists a longitudinal diffusive mode. All modes are influenced by the noise strength. The solution offers scaling properties below and above the phase transition. The results are preferable and applicable for ferroelectric order-disorder systems.
A further extension of the approach is achieved by a symmetry allowed coupling of the polarization to the magnetization. The coupling is related to a combined space-time symmetry due to the fact that the magnetization is an axial vector with $\vec{m}(\vec{x},-t) = -\vec{m}(\vec{x},t)$ whereas

the polarization is represented by a polar vector $\vec{p}(-\vec{x},t) = -\vec{p}(\vec{x},t)$. Multiferroic materials are characterized by breaking the combined space-time symmetry. Possible couplings are considered. Introducing a representation of spin fields without fixed axis one can incorporate spiral structures. Different to the previous system the ground state is in that case an inhomogeneous one. The resulting spectrum is characterized by the conventional wave vector **q** and a special vector **Q** characterizing the spiral structure.
Our studies can be grouped into the long-standing effort in understanding phase transitions in ferroelectric and related materials, for a comprehensive review see Lines & Glass (2004). To model such systems the well accepted discrimination in ferroelectricity of order-disorder and displacive type is useful as discussed by Cano & Levanyuk (2004). Both cases are characterized by a local double-well potential the depth of which is assumed to be V_0. Furthermore, the coupling between atoms or molecules at neighboring positions is denoted by J_0. The displacive limit is identified by the condition $V_0 \ll J_0$, i.e. the atoms are not forced to occupy one of the minimum. Instead of that the atoms or molecular groups perform vibrations around the minimum. The double-well structure becomes more important when the system is cooled down. The particle spend more time in one of the minimum. Below the critical temperature T_c the displacement of all atoms tends preferentially into the same direction giving rise to elementary dipole moments, the average of which is the polarization. The opposite limit $V_0 \gg J_0$ means the occurrence of high barriers between the double-well structure, i.e. the particles will reside preferentially in one of the minimum. Above the critical temperature the atoms will randomly occupy the minimum whereas in the low temperature phase $T < T_c$ one of the minimum is selected. The situation is sketched in Fig. 1. Following de Gennes (1963) the double-well structure can be modeled by a conventional Ising model where the eigenvalues of the pseudo-spin operator S^z specify the minima of the double-well potential. The dynamics of the system is described by the kinetic energy of the particles which leads to an operator S^x. Due to de Gennes (1963) and Blinc & Zeks (1972; 1974) the situation is described by the model Hamiltonian (TIM)

$$H = -\frac{1}{2}\sum_{<ij>} J_{ij} S_i^z S_j^z - \sum_i \Omega S_i^x \,, \tag{1}$$

where S^x and S^z are components of spin-$\frac{1}{2}$ operators. Notice that these operators have no relation to the spins of the material such as KH_2P0_4 (KDP). Therefore they are denoted as pseudo-spin operators which are introduced to map the order-disorder limit onto a tractable Hamiltonian. The coupling strength between nearest neighbors J_{ij} is assumed to be positive and is restricted to nearest neighbor interactions denoted by the symbol $< ij >$. The transverse field is likewise supposed as positive $\Omega > 0$. Alternatively the transverse field can be interpreted as tunneling frequency. In natural units the time for the tunneling between both local minimums is $\tau_t = \Omega^{-1}$ whereas the transport time between different lattice sites is given by $\tau_i = (\hbar J)^{-1}$. The high temperature limit is determined by $\tau_t < \tau_i$ or $\Omega > \hbar J$. The tunnel frequency is high and the behavior of the system is dominated by tunneling processes. With other words, the kinetic energy is large which prevents the localization of the particles within a certain minimum. The low temperature limit is characterized by a long or a slow tunneling frequency or a long tunneling time $\tau_t > \tau_i$. The behavior is dominated by the coupling strength J.
Since already the mean-field theory of the model Eq. (1), see Stinchcombe (1973) and also Blinc & Zeks (1972), yields a qualitative agreement with experimental data, the model was increasingly considered as one of the basic models for ferroelectricity of order-disorder type

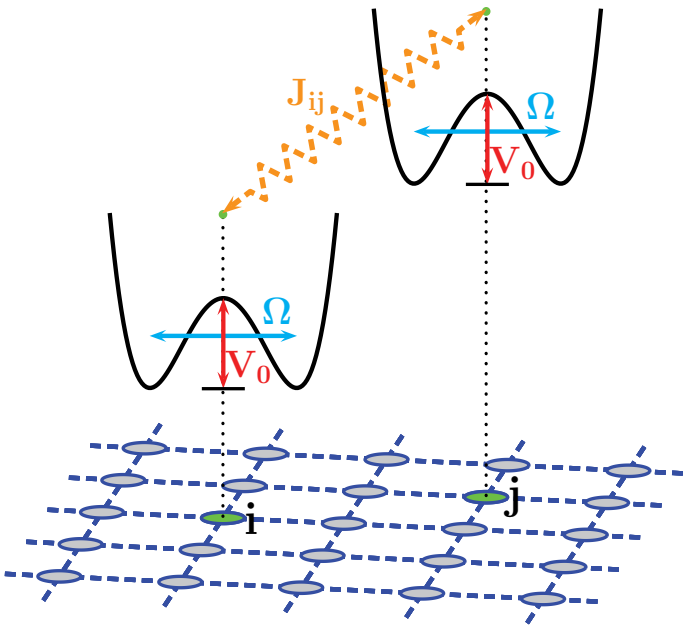

Fig. 1. Schematical representation of the physical situation in ferroelectric material. J_{ij} is the interaction between the atoms in the double-well potential at lattice site i and j, Ω is the tunneling frequency and V_0 the height of the barrier.

as analyzed by Lines & Glass (2004); Strukov & Levnyuk (1998). Whereas the displacive type of ferroelectricity offers a mainly phonon-like dynamics, a relaxation dynamics is attributed to the order-disorder type by Cano & Levanyuk (2004). The Ising model in a transverse field allows several applications in solid state physics. Thus a magnetic system with a singlet crystal field ground state discussed by Wang & Cooper (1968) is described by Eq. (1), where Ω plays the role of the crystal field. The model had been extensively studied with different methods by Elliot & Wood (1971); Gaunt & Domb (1970); Pfeuty & Elliot (1971), especially a Green's function technique was used by Stinchcombe (1971). It offers a finite excitation energy and a phase transition. A more refined study using special decoupling procedures for the Green's function investigated by Kühnel et al. (1977) allows also to calculate the damping of the transverse and longitudinal excitations as demonstrated by Wesselinowa (1984). Very recently Michael et al. (2006) have applied successfully the TIM to get the polarization and the hysteresis of ferroelectric nanoparticles and also the excitation and damping of such nanoparticles, compare Michael et al. (2007) and also the review article by Wesselinowa et al. (2010).

Despite the great progress in explaining ferroelectric properties based on the microscopic model defined by Eq. (1), the ferroelectric behavior should be also discussed using classical models. Especially, the progress achieved in magnetic systems, see Landau et al. (1980) and for a recent review Tserkovnyak et al. (2005), has encouraged us to analyze the TIM in its classical version capturing all the inherent quantum properties of the spin operators. The classical spin is introduced formally by replacing $\vec{S} \rightarrow \vec{S}/(\hbar S(S+1))$ in the limit $\hbar \rightarrow 0$

and $S \to \infty$. Stimulated by the recent progress in studying ferromagnets reviewed by Tserkovnyak et al. (2005), we are interested in damping effects, too. In the magnetic case the classical magnetic moments obey the Landau-Lifshitz equation, see Landau et al. (1980). It describes the precession of spins around a self-organized internal field, which can be traced back to the interaction of the spins. The reversible evolution equation can be extended by introducing dissipation which is phenomenologically proposed by Landau & Lifshitz (1935) or alternatively the so called Gilbert-damping is introduced by Gilbert (2004). Usadel (2006) has studied the temperature-dependent dynamical behavior of ferromagnetic nanoparticles within a classical spin model, while a nonlinear magnetization in ferromagnetic nanowires with spin current is discussed by He & Liu (2005). Even the magnetization of nanoparticles in a rotating magnetic field is analyzed by Denisov et al. (2006) based on the Landau-Lifshitz equation. The dynamics of a domain-wall driven by a mesoscopic current is inspected by Ohe & Kramer (2006) as well as the thermally assisted current-driven domain-wall was considered recently by Duine et al. (2007).
In the present chapter we follow the line offered by magnetic materials to extend the analysis to ferroelectricity accordingly. The main difference as already mentioned above is that in ferroelectric system the internal field is an anisotropic one and therefore, both the reversible precession and the irreversible damping are changed.

2. Model

In this section the model and the basic equation will be discussed. Especially the differences between isotropic magnets and anisotropic ferrolectrics are analyzed.

2.1 Hamiltonian

In this section we propose a classical Hamiltonian which is dynamical equivalent to the quantum case introduced in Eq. (1). The Hamiltonian is constructed in such a manner that it leads to the same evolution equations for the spins. The most general form is given by

$$H = \int d^d x \left(-\Omega_\mu S_\mu + \frac{1}{2} J_{\mu\nu\kappa\delta} \frac{\partial S_\mu}{\partial_\kappa} \frac{\partial S_\nu}{\partial_\delta} + \frac{1}{2} \Gamma_{\mu\nu} S_\mu S_\nu \right) . \tag{2}$$

Here summation over repeated indices is assumed. If the system is symmetric in spin space the coupling tensor J is diagonal in the spin indices $J_{\mu\nu\kappa\delta} = \delta_{\mu\nu} \tilde{J}_{\kappa\delta}$ In case that spin and configuration space are independent one concludes the separation $J_{\mu\nu\kappa\delta} = \hat{J}_{\mu\nu} \tilde{J}_{\kappa\delta}$. The anisotropic TIM is obtained by assuming $\vec{\Omega} = (0, 0, \Omega)$, $\hat{J}_{\mu\nu} = J\delta_{\mu z}\delta_{\nu z}$, $\tilde{J}_{\kappa\delta} = \delta_{\kappa\delta}$, and $\Gamma_{\mu\nu} = Jz\delta_{\mu z}\delta_{\nu z}$ Here z is the coordination number. The Hamiltonian reads now

$$H_f = \int d^d x \left(-\Omega S^x + \frac{J}{2} (\nabla S^z)^2 - JzS_z^2 \right) . \tag{3}$$

The last equation represents the TIM on a mesoscopic level, i. e. the spin variables are spatiotemporal fields $\vec{S}(\vec{x}, t)$. The Hamiltonian Eq.(3) offers no continuous symmetry as the corresponding magnetic one. For that case the magnetic Hamiltonian is written in terms of spin fields $\vec{\sigma}(\vec{x}, t)$ as Tserkovnyak et al. (2005)

$$H_m = \frac{K}{2} \int d^d x (\nabla \vec{\sigma})^2 . \tag{4}$$

Here K designates the exchange coupling. The last Hamiltonian is invariant under spin-rotation. A further difference between the ferroelectric and the magnetic case is the form of the internal field and the underlying dynamics which obeys the mesoscopic equation of motion, compare Hohenberg & Halperin (1977):

$$\frac{\partial S_\alpha}{\partial t} = \{H, S_\alpha\}\,. \tag{5}$$

This equation will be discussed in the following subsection.

2.2 Poisson brackets

Because the Hamiltonian Eq. (2) is given in terms of classical fields the dynamics of the system has to be formulated using Poisson brackets. They are defined for two arbitrary functionals of an arbitrary field ϕ by

$$\{A(\phi), B(\phi')\} = \int d^d x\, d^d x' \frac{\delta A}{\delta \phi_\alpha(x)} \{\phi_\alpha(x), \phi_\beta(x')\} \frac{\delta B}{\delta \phi_\beta(x')}\,.$$

In case that the arbitrary field ϕ is realized by the components of spin fields we get due to Mazenko (2003)

$$\{A(S), B(S)\} = \int d^d x\, \epsilon_{\alpha\beta\gamma} S_\alpha(\vec{x}) \frac{\delta A}{\delta S_\beta(\vec{x})} \frac{\delta B}{\delta S_\gamma(\vec{x})}\,. \tag{6}$$

Here we have applied the Poisson brackets for angular momentum fields

$$\{S_\alpha(\vec{x}, t), S_\beta(\vec{x}', t)\} = \epsilon_{\alpha\beta\gamma} S_\gamma(\vec{x}, t)\, \delta(\vec{x} - \vec{x}')\,.$$

According to Eq. (6) the spin field satisfies the evolution equation

$$\frac{\partial \vec{S}}{\partial t} = \vec{B} \times \vec{S}\,, \tag{7}$$

where the effective internal field $\vec{B}$ is introduced by

$$B_\alpha(\vec{x}, t) = -\frac{\delta H_f}{\delta S_\alpha(\vec{x}, t)}\,. \tag{8}$$

Using the Hamiltonian Eq. (3) the vector of the internal field is given by

$$\vec{B} = (\Omega, 0, [Jz + J\nabla^2] S^z)\,. \tag{9}$$

Eqs. (7)-(8) coincide with the quantum mechanical approach based on the Heisenberg equation of motions

$$i\hbar \frac{\partial S_r^\alpha}{\partial t} = [H,\, S_r^\alpha\,]\,,$$

and the quantum model defined in Eq. (1), compare also the article by Trimper et al. (2007). Because the quantum model is formulated on a lattice we have performed the continuum limit. Eq. (7) describes the precession of the spin around the internal field $\vec{B}$ defined in Eq. (8). Notice that the Hamiltonian should be invariant against time reversal. From here we conclude that the tunneling frequency Ω or alternatively the transverse field is changed to $-\Omega$ in case of $t \to -t$. As a consequence the self-organized internal field $\vec{B}$ is antisymmetric under time

reversal. In the magnetic case, represented by the Hamiltonian in Eq. (4), the internal field is isotropic and is defined by

$$\vec{B}^{(m)} = K\nabla^2\vec{\sigma}\,. \tag{10}$$

Directly from Eq. (7) it follows that the spin length $\vec{\sigma}^2$ or even $\vec{S}^2$ is conserved which is reflected in the quantum language by the conservation of the total spin $[H, \vec{S}^2]_- = 0$. Vice versa one concludes from the conservation of any vector, that $\dot{\vec{S}} \cdot \vec{S} = 0$, i.e. the time derivative of the vector is perpendicular to the vector itself which is simply fulfilled by assuming $\dot{\vec{S}} \propto \vec{A} \times \vec{S}$ for an arbitrary vector field $\vec{A}$. Insofar Eq. (7) is a consequence of the spin conservation. The same is valid for the spin field $\vec{\sigma}$.

2.3 Dissipation

Eq. (7) is a reversible equation, i.e. it is invariant against time reversal. As demonstrated in the next section Eq. (7) allows pseudo-spin-wave solutions. However, the excitation does not tend to restore a continuous symmetry, i.e. the Goldstone theorem, for details see Mazenko (2003), is not valid. Instead of that a soft mode behavior is observed. Normally, the excitation modes are damped. It is the aim of the present section to extend the evolution equation by including damping effects. From a microscopic point of view the damping can be traced back to scattering processes of spin-wave excitations with different wave vectors emphasized by Wesselinowa (1984) in second order of the interaction J. In principle this interaction effects are included in the microscopic Hamiltonian. Recently, Wesselinowa et al. (2005) have studied the influence of layer defects to the damping of the elementary modes in ferroelectric thin films. Likewise the analysis can be generalized for ferroelectric nanoparticles, where the interaction of those can also lead to finite life-times of the excitation modes as performed by Michael et al. (2007). Otherwise, the damping of pseudo-spin-waves can be originated by a coupling to lattice vibrations. Due to the coupling of the TIM to phonons the spin excitations can be damped as detected by Wesselinowa & Kovachev (2007). Generally one expects that due to attenuation the spin length is not conserved. On a mesoscopic level the inclusion of damping effects are achieved by a generalized evolution in the form

$$\frac{\partial\vec{S}(\vec{x},t)}{\partial t} = \vec{B}(\vec{x},t) \times \vec{S}(\vec{x},t) + \vec{D}(\vec{S})\,. \tag{11}$$

The origin of the damping term $\vec{D}$ is a pure dynamic one, i.e. all possible static parts should be subtracted. From Eq. (11) one finds

$$\frac{\partial\vec{S}^2}{\partial t} = \vec{D} \cdot \vec{S} < 0\,.$$

A non-trivial damping part is oriented into the direction of the effective field $\vec{B}$. Following Hohenberg & Halperin (1977) and using the approach discussed by Trimper et al. (2007) we make the ansatz

$$D_\alpha = -\Lambda_{\alpha\beta}(\vec{S})B_\beta\,. \tag{12}$$

In case the coefficient matrix $\Lambda_{\alpha\beta}(\vec{S})$ is positive and independent of the spin field Eq. (11) corresponds to a pure relaxation dynamics for a non-conserved order parameter field. This fact reflects another difference to the magnetic case, where the internal field is defined in Eq. (10). The evolution equation for the Heisenberg spins $\vec{\sigma}$ reads

$$\frac{\partial \vec{\sigma}(\vec{x},t)}{\partial t} = \vec{B}^{(m)}(\vec{x},t) \times \vec{\sigma}(\vec{x},t) + \Lambda_{\alpha\beta} K \nabla^2 \vec{\sigma}\,.$$

Provided the coefficient matrix $\Lambda_{\alpha\beta}$ is independent on $\vec{\sigma}$ the damping effects are realized by spin diffusion and hence the order parameter is conserved according to the classification introduced by Hohenberg & Halperin (1977).
To proceed further in the ferroelectric model with non-conserved order parameter let us expand the coefficient matrix $\Lambda_{\alpha\beta}(\vec{S})$ in terms of the spin field $\vec{S}$, where only terms are included which break the time reversal symmetry. Denoting the field independent part as $\Lambda^{(0)}_{\alpha\beta}$ we get up to second order in $\vec{S}$

$$\Lambda_{\alpha\beta}(\vec{S}) = \Lambda^{(0)}_{\alpha\beta} + \Lambda^{(1)}_{\alpha\beta\gamma\delta} S_\gamma S_\delta + O(\vec{S}^4)\,. \tag{13}$$

Due to the spin algebra the tensor structure of the coefficients Λ are given in terms of the structure constant of the underlying Lie-group, i.e. the complete antisymmetric tensor $\epsilon_{\alpha\beta\gamma}$ and unit tensor $\delta_{\alpha\beta}$. The zeroth order term is

$$\Lambda^{(0)}_{\alpha\beta} \propto \epsilon_{\alpha\mu\nu}\epsilon_{\beta\mu\nu}\,.$$

From here we define

$$\Lambda^{(0)}_{\alpha\beta} = \frac{1}{\tau_1}\delta_{\alpha\beta}\,, \tag{14}$$

where τ_1 plays the role of a relaxation time. Because the damping should be pointed to the direction of the effective field and consequently the vector $\vec{D}$ is perpendicular to the propagating part $\vec{B} \times \vec{S}$. Summarizing these conditions we make the ansatz

$$\Lambda^{(2)}_{\alpha\beta\gamma\delta} = \frac{1}{2\tau_2}\left[\,\epsilon_{\alpha\beta\rho}\,\epsilon_{\rho\gamma\delta} + \epsilon_{\alpha\gamma\rho}\,\epsilon_{\rho\beta\delta} + \epsilon_{\alpha\delta\rho}\,\epsilon_{\rho\beta\gamma}\right]. \tag{15}$$

In the conventional vector notation the complete equation of motion reads now

$$\frac{\partial \vec{S}}{\partial t} = \vec{B} \times \vec{S} - \frac{1}{\tau_1}\vec{B} - \frac{1}{\tau_2}\vec{S} \times (\vec{S} \times \vec{B})\,. \tag{16}$$

There appear two damping terms characterized by the relaxation times τ_1 and τ_2, the determination of those is beyond the scope of a mesoscopic approach. They could reflect the coupling to other degrees of freedom and become of the order of microscopic spin-flip-processes. Eq. (16) reminds of the Landau-Lifshitz-Gilbert equation discussed in the ferromagnetic case, see Tserkovnyak et al. (2005). The differences to the magnetic case are the form of the internal field $\vec{B}$ and the underlying symmetry. The consequences will be discussed in the next section.

3. Excitation spectrum

In this section we investigate the spectrum of collective pseudo-spin-wave excitations and their damping. The starting point is Eq. (16). Firstly we study the reversible precession part.

3.1 Soft mode

Because no continuous symmetry is broken one expects a soft mode behavior, see Blinc & Zeks (1974); Lines & Glass (2004), which is characterized by the temperature dependent excitation energy $\varepsilon(\vec{q}, T)$ offering the following behavior

$$\lim_{T \to T_c} \varepsilon(\vec{q} = 0, T) = 0\,. \tag{17}$$

The situation is sketched schematically in Fig. 2 To compute the dispersion relation we insert

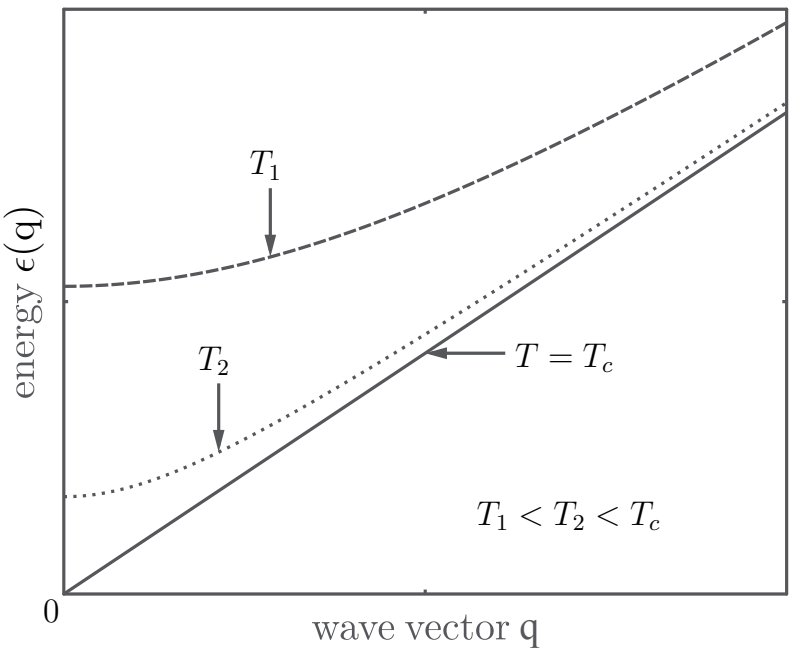

Fig. 2. Soft mode behavior: There is a gap for wave vector $\vec{q} = 0$, which tends to zero for $T \to T_c$, compare Eq. (17) .

the internal field $\vec{B}$ defined in Eq. (9) into Eq. (7). In the frame of linear spin-wave theory the spin field $\vec{S}(\vec{x}, t)$ is splitted into a static and a dynamic part according to

$$\vec{S}(\vec{x}, t) = \vec{p}(\vec{x}) + \vec{\varphi}(\vec{x}, t)\,, \tag{18}$$

where $\vec{p}(\vec{x}) = (p_x, 0, p_z)$ is a time-independent but temperature-dependent vector in the $x - z$ plane as suggested in Eq. (1). In case that $\vec{p}$ is independent of the coordinates it describes the homogeneous polarization whereas for multiferroic material, for a review compare Wang et al. (2009), one finds a spiral structure of the form

$$\vec{p}(\vec{x}) = p_0[\cos(\vec{Q} \cdot \vec{x})\vec{e}_x + \sin(\vec{Q} \cdot \vec{x})\vec{e}_y\,] + p_z\vec{e}_z\,. \tag{19}$$

Here $\vec{Q}$ characterizes the spiral structure.
Inserting the ansatz made in Eq. (18) into Eq. (7) the field $\vec{\varphi}$ obeys in spin-wave approximation

$$\dot{\vec{\varphi}} = \vec{B}_1 \times \vec{p} + \vec{B}_0 \times \vec{\varphi}\,,$$

with $\vec{B}_0 = (\Omega, 0, Jzp_z)$, and $\vec{B}_1 = (0, 0, J(\nabla^2 + z)\varphi_z)$. The direction of the homogeneous polarization is given by $\vec{p} \times \vec{B}_0 = 0$. The last relation has two solutions

$$\begin{aligned} (i)\ p_z(T) \neq 0\,, \quad p_x = \frac{\Omega}{Jz} \quad \text{if} \quad T \leq T_c \\ (ii)\ p_z = 0 \quad , \quad p_x(T) \neq \frac{\Omega}{Jz} \quad \text{if} \quad T > T_c\,. \end{aligned} \tag{20}$$

Here the phase transition temperature is obtained by $p_z(T = T_c) = 0$. Moreover, the relation $p_x(T_c) = \Omega/Jz$ should be fulfilled, i.e. p_x remains fixed and is temperature-independent below T_c. In a quantum language it means that the quantization axis is oriented within the $x - z$-plane in accordance with microscopic investigations, see for instance de Gennes (1963); Kühnel et al. (1977). In the frame of a multi scale approach the temperature dependence of p_x and p_z is calculated based upon the microscopic model Eq. (1). In the high temperature regime p_x decreases with increasing temperature which can be estimated to be $p_x \propto \Omega/T$, compare the book by Lines & Glass (2004). The quantity p_z offers a behavior like $p_z \propto (-\tau)^\beta$ where $\tau = (T - T_c)/T_c$ is the relative distance to the phase transition temperature and $\beta \leq 1/2$ is the critical exponent of the polarization. The results are shown in Fig. 3. The subsequent analysis

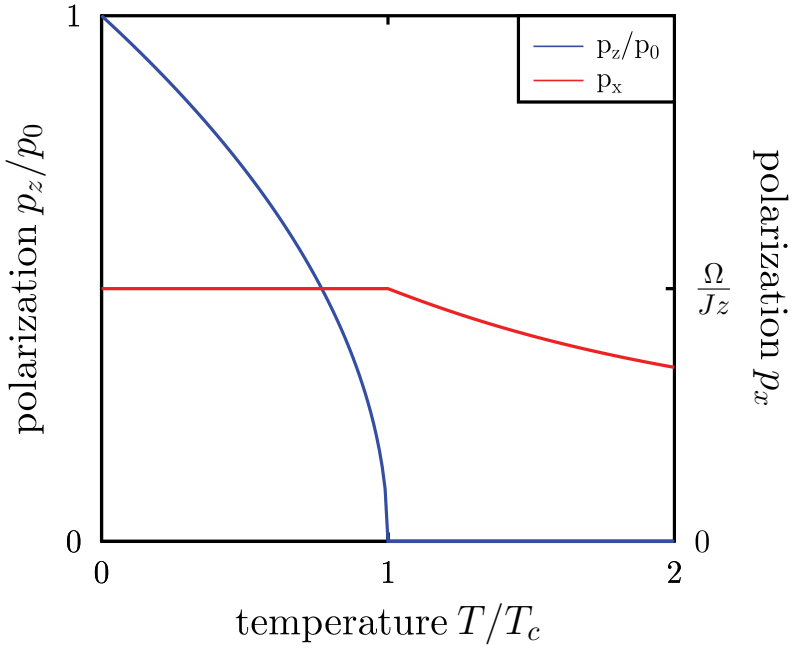

Fig. 3. Static polarization $p_z(T)$ (blue line) and $p_x(T)$ (red line) versus the ratio T/T_c. Whereas p_z vanishes at T_c according to a power law $\propto (-\tau)^\beta$, p_x remains temperature independent for $T < T_c$.

is performed for the low and the high temperature phase separately. For $T < T_c$, i. e. $p_z \neq 0$ one finds after Fourier transformation

$$\begin{aligned} \dot{\varphi}_x(\vec{q}, t) &= -Jzp_z\varphi_y(\vec{q}, t)\,, \quad \dot{\varphi}_z(\vec{q}, t) = \Omega\varphi_y(\vec{q}, t) \\ \dot{\varphi}_y(\vec{q}, t) &= Jzp_z\varphi_x(\vec{q}, t) - [\,\Omega - p_x J\kappa(\vec{q})\,]\varphi_z(\vec{q}, t)\,. \end{aligned} \tag{21}$$

Here we have used the abbreviation $\kappa(\vec{q}) = z - q^2$. Notice that the lattice constant a is set to unity and the approach is valid in the long wave length limit $qa \ll 1$. Notice that we set $a = 1$. A non-trivial solution of Eqs. (21) is given by $\varphi_\alpha \propto \exp[i\varepsilon(\vec{q})t]$. The eigenvalue of the coefficient matrix leads to the excitation energy $\varepsilon_l(\vec{q})$, which is in the low temperature phase dominated by the coupling J as pointed out already in the introduction. It results

$$\varepsilon_l(\vec{q}, T) = Jz\sqrt{p_z^2 + p_x^2 \frac{\vec{q}^2}{z}}\,. \tag{22}$$

This dispersion relation reveals the typical soft mode behavior characterized by Eq. (17) and depicted in Fig. 2. Such a behavior is in accordance to the microscopic behavior, see Kühnel et al. (1977); Stinchcombe (1973). The excitation field is found to be

$$\vec{\varphi}(\vec{q}, t) = \Phi_l(\vec{q}) \left(\frac{Jzp_z e^{i\pi/2}}{\varepsilon_l(\vec{q})}, 1, \frac{\Omega e^{-i\pi/2}}{\varepsilon_l(\vec{q})} \right) \exp[i\varepsilon_l(\vec{q})t]\,, \tag{23}$$

where $\Phi_l(\vec{q})$ is the amplitude of the excitation mode determined by the initial condition.
The high temperature phase is characterized by $p_z = 0$. For that case one gets a similar dispersion relation as for $T < T_c$ which can be written as

$$\varepsilon_h(\vec{q}, T) = \Omega\sqrt{\frac{p_x(T)}{p_x(T_c)} \frac{\vec{q}^2}{z} + \frac{p_x(T_c) - p_x(T)}{p_x(T_c)}}\,. \tag{24}$$

Above the critical temperature the excitation energy is dominated by the tunneling field Ω. This result corresponds to the discussion in the introduction concerning the relevance of the different time scales. The dispersion relation Eq. (24) offers likewise a soft mode behavior due to $p_x(T = T_c) = \frac{\Omega}{Jz}$ according to Eq. (20). Furthermore, the relation $p_x(T)/p_x(T_c) < 1$ is fulfilled as one can observe also in Fig. 2. Making a Taylor-expansion of the second term in Eq. (24) the zero-wave vector mode satisfies in the vicinity of T_c the relation

$$\varepsilon_h(\vec{q} = 0) = \sqrt{\frac{Jz\Omega^2}{T_c^2} \left[1 - \left(\frac{\Omega}{zJ} \right)^2 \right]} (T - T_c)^{1/2}\,, \tag{25}$$

provided $\Omega < Jz$. In the opposite case a phase transition is suppressed at finite temperatures. The prefactor in front of the q^2 term in the dispersion relation, Eq. (22) and (24), sometimes called as stiffness parameter remains finite at T_c. This result is also different to the magnetic case, where the stiffness constant tends to zero for $T \to T_c$. The spin wave field $\vec{\varphi}(\vec{q})$ exhibits in the high temperature phase a similar form as for $T < T_c$, but one has to set $p_z = 0$ and ε_l has to be replaced by ε_h. As expected the field $\vec{\varphi}$ is continuous at T_c.

3.2 Dynamic scaling

In the vicinity of a second order phase transition a system is usually characterized by critical exponents and scaling relations, see Hohenberg & Halperin (1977). Especially there exist characteristic energies (propagating and relaxation modes) which fulfill

$$\varepsilon_c(\vec{q}, T) = q_c^z f_1(q\xi) \equiv \xi^{-z_c} f_2(q\xi)\,. \tag{26}$$

Here z_c means the dynamic scaling exponent, ξ is the correlation length which behaves near to T_c as $\xi \propto (\tau)^{-\nu}$ with the critical exponent ν and $\tau = (T - T_c)/T_c$. As well f_1 and f_2 are

scaling functions which depend only on the combination $q\xi$. The domain of wave vector and relative distance to the critical temperature τ is due to Hohenberg & Halperin (1977) shown in Fig. 4. The critical regime denoted as region I is characterized by $q\xi >> 1$ which is relevant

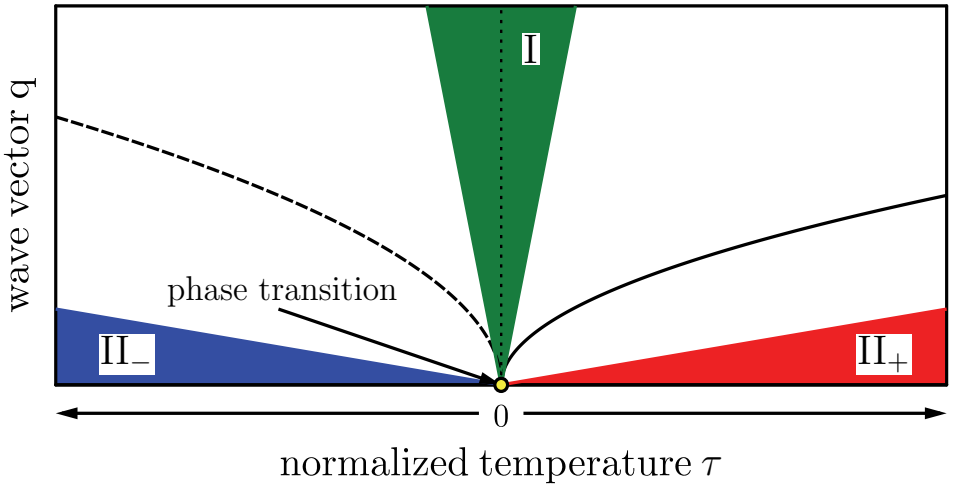

Fig. 4. Domain of wave vector versus $\tau = (T - T_c)/T_c$, I is the critical regime (green), $II_\pm$ are the hydrodynamic regimes above (red) and below T_c (blue). The bold and the dashed line indicate the cross-over between the regimes.

for $T \approx T_c$. The two other regimes II_+ and II_- are the hydrodynamic regimes relevant for $T > T_c$ and $T < T_c$, respectively. Our model exhibits propagating modes denoted as ε_l, Eq. (22), and ε_h, Eq. (24). They play the role of the characteristic energy and obey the scaling form of Eq. (26). So we get in the low temperature phase

$$\varepsilon_l(\vec{q}, T) = q p_x(T) J \sqrt{z(1 + (q\xi_l)^{-2})}. \tag{27}$$

From here we conclude the dynamical exponent $z_c = 1$, the correlation length below the phase transition $\xi_l^{-2} = z p_z^2 / p_x^2$ and the scaling function $f_l(x) \propto \sqrt{1 + x^{-2}}$. The critical exponents fulfill the relation $\nu = \beta$, which is in accordance with the scaling law $z_c = \beta/\nu$. A similar expression is found above T_c with the same dynamic exponent, but a different correlation length $\xi_h^{-2} = z(p_x(T_c) - p_x(T))/p_x(T)$.

3.3 Damping effect

For the complete Eq. (16) with damping we make the same ansatz as in Eq. (18) to find the complex dispersion relation $\omega(\vec{q}, T)$. In the low temperature phase $T \leq T_c$ the system reveals three complex modes

$$\begin{aligned} \omega_{1,2}(\vec{q}, T) &= \pm\varepsilon_l(\vec{q}, T) - i\frac{\Gamma_{1l}(\vec{q}, T)}{2\tau_1} - i\frac{\Gamma_{2l}(\vec{q}, T)}{2\tau_2}, \\ \omega_3(\vec{q}, T) &= -i\frac{(Jzp_z)^2 J\,\kappa(\vec{q})}{\varepsilon_l^2(\vec{q}, T)\tau_1} \equiv -i\omega_d(\vec{q}, T). \end{aligned} \tag{28}$$

The spin-wave field $\vec{\varphi}(\vec{q},t)$ introduced in Eq. (18) behaves as

$$\vec{\varphi}_{1,2}(\vec{q},t) \propto \exp\left[\left(\pm i\varepsilon_l - \left[\frac{\Gamma_{1l}}{2\tau_1} + \frac{\Gamma_{2l}}{2\tau_2}\right]\right) t\right], \quad \varphi_3(\vec{q},T) \propto \exp(-\omega_d(\vec{q},T)\, t)\,.$$

Whereas the modes $\omega_{1,2}$ describe the propagation of pseudo-spin waves and their damping, the mode $\omega_3 = -i\omega_d(\vec{q},T)$ is a pure imaginary one, influenced only by τ_1. Such a situation is also known for magnets, see Hohenberg & Halperin (1977) with two complex transverse modes and one diffusive longitudinal mode. Due to the different physical situation the pure imaginary mode ω_3 offers here a dispersion relation different to diffusion. The results in Eq. (28) are valid in the long wave length limit $q \ll 1$ and in first order in $\tau_{1,2}^{-1}$. In this approximation the propagating part $\varepsilon_l(\vec{q},T)$ remains unchanged in Eq. (22). Higher order terms give rise to a slightly changed behavior. The finite life-time of the excitation is related to the temperature and wave vector dependent damping terms which read

$$\begin{aligned}\Gamma_{1l}(\vec{q},T) &= \frac{J\kappa(\vec{q})\Omega^2}{z\,\varepsilon_l^2(\vec{q},T)}q^2,\\ \Gamma_{2l}(\vec{q},T) &= \frac{\varepsilon_l^2(\vec{q},T) + (Jzp_z(T))^2 + \Omega^2}{Jz} \quad \text{with} \quad \kappa(\vec{q}) = z - q^2\,.\end{aligned} \tag{29}$$

At the critical point the damping is continuously as demonstrated in Trimper et al. (2007). While the life-time in the high temperature phase is only weakly temperature dependent, it depends on T in the low temperature regime via p_z which disappears at T_c according to $p_z(T) \propto (-\tau)^\beta$ with a critical exponent $\beta \leq 1/2$. The temperature dependence of the excitation energy and the relevant life-time $(\Gamma_{2l})^{-1}$ of the soft mode at $\vec{q} = 0$ are depicted in Trimper et al. (2007). The damping function can be written in scaling form using the results obtained in subsection (3.2). For simplicity we assume $\tau_1 \simeq \tau_2 \equiv \tau_0$. Defining $\gamma_{1l} = \Gamma_{1l}/2\tau_o$ and $\gamma_{2l} = \Gamma_{1l}/2\tau_o$. In the long wave length limit it results

$$\frac{2\tau_o\gamma_{1l}}{Jz} = (\,q\xi_l\,)^2 \qquad \frac{2\tau_o\gamma_{2l}}{Jzp_x^2} = 1 + \frac{q^2}{z}\left[1 + 2(\,q\xi_l)^{-2}\right] \tag{30}$$

Whereas the excitation energy ε_l is dominated by a linear q-term, see Eq. (27), and disappears for $T \to T_c$ at $\vec{q} = 0$, the damping is quadratic in q. In our case the life time remains fixed at T_c. Apparently one finds the total damping $\gamma_l = \gamma_{1l} + \gamma_{2l}$ satisfies in the vicinity of the critical temperature

$$\gamma_l^{-1}(\vec{q},T_c) < \gamma_l^{-1}(\vec{q},T \leq T_c)\,.$$

When the system is approaching the phase transition temperature, the elementary excitation decays more rapidly for wave vector $\vec{q} \neq 0$.

The corresponding damping parameters Γ_{1h} and Γ_{2h} can be also found in the high temperature limit characterized by $p_z = 0$ and $p_x \to 0$, compare Fig. 3. The analytical expressions are presented in Trimper et al. (2007). In that case we obtain $\varepsilon_h(\vec{q},T \to \infty) = \Omega$, i.e the mode is frozen in. A corresponding analysis for the damping shows that the system is overdamped with $\varepsilon_h \ll \Gamma_{1h}$.

The analysis can be performed likewise on a microscopic level using Eq. (1), cf. Michael et al. (2006). In that case a more refined Green's function technique enables us to calculate both the excitation energy and its damping. The temperature dependence of both quantities is in accordance to the present analysis and also in qualitative agreement with experimental results as shown by Michael et al. (2007).

4. Stochastic equation

The model defined by Eq. (16) can be extended by introducing stochastic forces. To that aim we have two possibilities:

(i) All the residual degrees of freedom, which are not taken into account so far, will be incorporated into the model as an additive noise. If this stochastic force is denoted as $\vec{\eta}(\vec{x},t)$ the evolution equation reads now

$$\frac{\partial \vec{S}}{\partial t} = \vec{B}\times\vec{S} - \frac{1}{\tau_1}\vec{B} - \frac{1}{\tau_2}\vec{S}\times(\vec{S}\times\vec{B}) + \vec{\eta}(\vec{x},t)\,,$$
$$\left\langle \eta_\alpha(\vec{x},t)\eta_\beta(\vec{x}',t')\right\rangle = 2T\delta_{\alpha\beta}\delta(\vec{x}-\vec{x}')\delta(t-t')\,, \tag{31}$$

where for simplicity a Gaussian white noise is supposed.

(ii) A second realization is given by assuming that the effective field $\vec{B}$, see Eq. (8), is extended by a stochastic force, i.e. $\vec{B}(\vec{x},t) \to \vec{B}(\vec{x},t) + \vec{\eta}(\vec{x},t)$. Such a situation leads to a multiplicative noise and is already discussed for a magnet in Usadel (2006) studying ferromagnetic resonance, and in Bose & Trimper (2010) including also colored noise.

Here we are interested in the model defined by Eqs. (31). The spin-wave fields obey in the low temperature phase the relation

$$\frac{\partial \varphi_\alpha(\vec{q},t)}{\partial t} = W_{\alpha\beta}(\vec{q})\,\varphi_\beta(\vec{q},t) + \eta_\alpha(\vec{q},t)\,. \tag{32}$$

Here $\mathbf{W}$ is a 3×3 matrix

$$W_{\alpha\beta} = \begin{pmatrix} -\frac{m_z A_l}{\tau_2} & -A_l & \frac{m_z B_l q^2}{\Omega\tau_2} \\ A_l & -\frac{\Omega^2+A_l^2}{Jz\tau_2} & -\frac{B_l q^2}{\Omega} \\ \frac{m_z\Omega}{\tau_2} & \Omega & -\frac{J\kappa(\vec{q})}{\tau_1} - \frac{B_l q^2}{Jz\tau_2} \end{pmatrix}$$

with the coefficients $A_l = Jzp_z$ and $B_l = \Omega^2/z$. Eq. (32) is solved by the Green's function defined by

$$G_{\alpha\beta}(t-t') = \Theta(t-t')\left\langle \frac{\delta\varphi_\alpha(t)}{\delta\,\eta_\beta(t')}\right\rangle .$$

Here $\Theta(t)$ is the Heavyside function. After Fourier transformation the Green's function is written in lowest order in $\tau_{1,2}^{-1}$ as

$$G_{\alpha\beta}(\vec{q},\omega) = \frac{g_{\alpha\beta}(\vec{q}\,,\omega)}{[\omega-\omega_1(\vec{q},T)][\omega-\omega_2(\vec{q},T)][i\omega+\omega_d(\vec{q},T)]}\,, \tag{33}$$

where the excitation energies in the low temperature phase $\omega_{1,2}$ and ω_d are already introduced in Eqs. (28). The elements of the matrix $g_{\alpha\beta}(\vec{q}\,,\omega)$ are given by

$$g_{11} = -\omega^2 - i\omega\left[\frac{\Omega+\varepsilon_l^2}{Jz\tau_2} + \frac{J\kappa(\vec{q})}{\tau_1}\right] + B_l q^2\,,\quad g_{22} = -\omega^2 - i\omega\left[\frac{\varepsilon_l^2}{Jz\tau_2} + \frac{J\kappa(\vec{q})}{\tau_1}\right],$$
$$g_{33} = -\omega^2 - i\omega\frac{2A_l^2+\Omega^2}{Jz\tau_2} + A_l^2\,,\quad g_{12} = A_l[i\omega - \frac{J\kappa}{\tau_1}] = -g_{21}\,,$$
$$g_{23} = \frac{i\omega B_l q^2}{\Omega} = -\frac{B_l q^2 g_{32}}{\Omega^2}\,,\quad g_{13} = \frac{B_l q^2}{\Omega}\left[A_l - \frac{i\omega p_z}{\tau_2}\right] = \frac{B_l q^2 g_{31}}{\Omega^2}\,. \tag{34}$$

The real correlation function is defined conventionally by

$$\left\langle \varphi_\alpha(\vec{q},\omega)\varphi^\dagger(\vec{q},\omega)\right\rangle = C_{\alpha\beta}(\vec{q},\omega)(2\pi)^{d+1}\,.$$

Using the solution for φ in terms of Green's function in Eq. (33) and the relation for the excitation energy $\omega_{1,2}^* = -\omega_{2,1}$ the correlation function reads

$$\begin{aligned} C_{\alpha\beta}(\vec{q},\omega) &= \frac{2Tc_{\alpha\beta}(\vec{q},\omega)}{(\omega^2-\omega_1^2)(\omega^2-\omega_2^2)((\omega^2+\omega_d^2)} \\ c_{\alpha\beta}(\vec{q},\omega) &= g_{\alpha\mu}(\vec{q},\omega)g^*_{\mu\beta}(\vec{q},\omega) \end{aligned} \tag{35}$$

The coefficents of the correlation function $c_{\alpha\beta}$ are obtained from the corresponding expressions in Eq. (34). A direct calculation shows that the fluctuation-dissipation theorem is fulfilled

$$C_{\alpha\beta}(\vec{q},\omega) = \frac{2T}{\omega}\Im\, G_{\alpha\beta}(\vec{q},\omega)\,.$$

In the context of the linear spin-wave approximation the stochastic equations with additive noise term do not give more information as the conventional equations. The poles of the Green's function determine the excitation energy like in the microscopic case. The situation is different for a multiplicative noise where the effective field $\vec{B}$ is supplemented by a stochastic force. This behavior is discussed for magnets by Bose & Trimper (2010).

5. Multiferroics

As already remarked there is a new class of materials, called multiferroics, see Eerenstein et al. (2006); Fiebig (2005); Van den Brink & Khomskii (2008), which are classified as materials possessing at least two ferroic orders such as ferromagnetic and ferroelectric order in a single phase. For a recent review consult Wang et al. (2009). In this section we present a mesoscopic model where the ferroelectric properties are described by the Hamiltonian Eq. (3) and the magnetic part by non-linear sigma model defined in Eq. (4). The total Hamiltonian for such a multiferroic system reads

$$H = H_f + H_m + H_{fm} \tag{36}$$

The coupling term should be invariant against time reversal symmetry and space inversion. Due to Mostovoy (2006) we use

$$H_{fm} = \int d^dx\, \lambda_{\alpha\beta\gamma\delta} S_\alpha \sigma_\beta \frac{\partial \sigma_\delta}{\partial x_\gamma}\,, \tag{37}$$

where the symmetry allowed coupling constant is

$$\lambda_{\alpha\beta\gamma\delta} = \lambda_1 \epsilon_{\alpha\beta\mu}\epsilon_{\mu\gamma\delta} + \lambda_2 \delta_{\alpha\beta}\delta_{\gamma\delta}.$$

In case the magnetization field $\vec{\sigma}$ fulfills $\nabla\cdot\vec{\sigma} = 0$, see Landau & Lifshitz (1935), the coupling is

$$H_{fm} = \lambda_1 \int d^dx\, \vec{S}\cdot[\vec{\sigma}\times(\nabla\times\vec{\sigma})] \tag{38}$$

Using the same procedure as before, i.e. defining the effective fields for the magnetic and for the ferroelectric case, then the equations for the magnetic spin field $\vec{\sigma}$ and the ferroelectric pseudo-spin field $\vec{S}$ are given by the following expressions

$$\begin{aligned}\frac{\partial \sigma_\alpha}{\partial t} &= K(\nabla^2 \vec{\sigma})_\alpha + \lambda_1 \epsilon_{\alpha\beta\gamma}\sigma_\beta \left(\sigma_\mu \frac{\partial S_\gamma}{\partial x_\mu} - S_\mu \frac{\partial \sigma_\gamma}{\partial x_\mu}\right) \\ \frac{\partial S_\alpha}{\partial t} &= (\vec{B}\times\vec{S})_\alpha + \lambda_1 \left(\vec{S}\times(\vec{\sigma}\times\nabla\times\vec{\sigma})\right)_\alpha . \end{aligned} \tag{39}$$

The internal field for the ferroelectric subsystem is defined in Eq. (9). Now let us discuss the excitation energies for the magnetic and the ferroelectric system which are coupled mutually due to the multiferroic effect. To this aim we set according to Eq. (18)

$$\vec{S}(\vec{x},t) = \vec{p}(\vec{x}) + \vec{\varphi}(\vec{x},t)\,, \quad \vec{\sigma}(\vec{x},t) = \vec{m}(\vec{x}) + \vec{\Phi}(\vec{x},t)\,.$$

For simplicity we consider excitations around a homogeneous ground state, i.e $\vec{p} = (p_x, 0, p_z)$ and $\vec{m} = (0,0,m_z)$. The magnetization $\vec{m}$ points in the z-direction. Here we consider the experimentally realized situation, compare the review article by Wang et al. (2009), that lowering the temperature the system undergoes firstly at T_c a phase transition into a ferroelectric phase characterized by $p_z \neq 0\,, p_x = \Omega/(Jz)$ as well as $m_z = 0$. This phase is observable in the temperature regime $T_m \leq T < T_c$, where T_m is the magnetic phase transition temperature. A further reducing of the temperature leads at $T = T_m < T_c$ to a transition into the magnetic phase, characterized by $m_z \neq 0$. In the low temperature regime one observes the multiferroic phase with $m_z \neq 0$, $p_z \neq 0$ and $p_x = \Omega/Jz$. In this regime the excitation energy offers a dispersion relation which depends on the parameters of the ferroelectric subsystem $(J,\, \omega)$, the coupling strength of the magnetic system K as well as the mutual coupling constant λ_1 between both systems. A tedious but straightforward calculation shows that the excitation energy of the ferroelectric system $\varepsilon_l(\vec{q},T)$ remains unchanged in first order expansion with respect to the coupling λ_1, i.e. in the interval $T_m < T \leq T_c$ the system reveals a soft mode behavior characterized by the dispersion relation presented in Eq. (18). In the low temperature phase $T < T_m$ we get in lowest order in λ_1 an excitation energy of the multiferroic system in the following form

$$\varepsilon_{fm}^2(\vec{q},T) = (Km_z(T)q)^2 \left[\,(\,q_x^2 + (q_y+Q)^2 + q_z^2 - Q^2\,\right]\,. \tag{40}$$

Here the parameter Q is defined by

$$Q = \frac{\lambda_1 \Omega}{2JKz}\,.$$

This parameter reflects the influence of the ferroelectricity in the multiferroic phase. In absence of a multiferroic coupling the dispersion relation yields the well known Goldstone mode of the magnetic system $\varepsilon_m = Km_z q^2$. The multiferroic mode ε_{fm} remains a Goldstone mode, i. e. $\varepsilon_{fm}(\vec{q}=0) = 0$, because at the magnetic transition a continuous symmetry is broken. The wave vector Q indicates (probably) the presence of spiral structures, compare Tokura & Seki (2010). Notice that we have considered only excitations with respect to the homogeneous ground state characterized by $\vec{p} = \text{const}$. The result is altered in case one studies an inhomogeneous static state given by Eq. (19) for instance. This point deserves further studies.

6. Conclusions

In this chapter we have discussed a mesoscopic modeling of ferroelectric materials. There exists two limiting cases denoted as displacive and order-disorder ones. The last category is often discussed in terms of an Ising model in a transverse field. Such a quantum model can be studied using different techniques, especially Green's function methods. Otherwise ferroelectric systems offer a phase transition at finite temperatures. In this region the quantum effects are not relevant and therefore, a mesoscopic description should be adequate. The mesoscopic limit of the underlying quantum model is constructed in such a manner that the evolution equations coincides, namely those based on the Heisenberg equation of motion and on the Poisson bracket relations, respectively. The main effort in this region came from the analysis of magnetic materials. Motivated by several theoretical activities in that field, we have studied the basic model for describing the order-disorder transition in ferroelectrics. To that aim we have brought forward the concept of mesoscopic evolution equations with damping terms to one of the standard models for ferroelectricity. In doing so we followed our paper, see Trimper et al. (2007), which is modified and extended accordingly. Whereas the previous discussion was primarily focused on isotropic magnetic systems, we are able to derive the mesoscopic evolution equation for a ferroelectric system under quite general conditions as the behavior of the spin moments, a self-organized effective field and its behavior under time reversal symmetry as well as the underlying Lie group properties of the moments. In particular, we have demonstrated that the form of the damping terms is rather universal, although the realization of the effective field in ferroelectric systems is distinct from that of the ferromagnet ones. The reason consists of the different symmetry of the ferroelectric system. While the classical Heisenberg model reflects the isotropic symmetry, the Ising model in a transverse field is anisotropic. The differences are clearly indicated. Consequently the differences lead to a totally different dynamic behavior which is observed in both the reversible propagating part and its damping. Thus the ferroelectric mode becomes a massive one and the life-time of the elementary excitation offers another temperature dependence. In terms of a multi-scale approach the relevant incoming static quantities as the polarization are calculated using the microscopic model. Our approach allows the investigation of both the low and the high temperature phase. They are discussed within dynamic scaling theory. As a further step we are interested in systems where magnetic and polarization behavior is coupled leading to a new class of systems known as multiferroicity reviewed recently by Wang et al. (2009). Such systems are characterized by the occurrence of spiral structures manifested in an inhomogeneous ground state as shown in Eq. (19). In the quantum model this phenomena can be described by spin operators without fixed quantization direction, as studied by Michael & Trimper (2011). In this chapter we studied a simple model allowing a sequence of phases, namely for $T > T_c$ the system is paraelectric as well as paramagnetic. Reducing the temperature the system offers a phase transition at T_c into a ferroelectric but paramagnetic phase. When the temperature is lowered further there is at T_m a transition into the magnetic phase which is due to the multiferroic coupling simultaneously characterized by the parameters of the ferroelectric and the magnetic system. The multiferroic dispersion relation suggests the occurrence of incommensurable structures which can be also interpreted as spiral structure. A related more detailed approach using the mesoscopic formulation is under progress.

7. References

Blinc, R. & Zeks, B. (1972). Dynamics of order-disorder-type ferroelectrics and anti-ferroelectrics, *Adv. Phys.* 21: 693.

Blinc, R. & Zeks, B. (1974). *Soft modes in ferroelectrics and antiferroelectrics*, North-Holland, Amsterdam.

Bose, T. & Trimper, S. (2010). Correlation effects in the stochastic Landau-Lifshitz-Gilbert equation, *Phys. Rev. B* 81(10): 104413.

Bose, T. & Trimper, S. (2011). Lagrangian formulation of a dissipative magnetic system on a mesoscopic scale, *Euro. Phys. Lett. submitted* .

Cano, A. & Levanyuk, A. P. (2004). Low-temperature structural phase transitions: Phonon-like and relaxation order-parameter dynamics, *Phys. Rev. B* 70: 064104.

de Gennes, P. G. (1963). Collective motions of hydrogen bonds, *Solid State Communications* 1: 37.

Denisov, S. I., Lyutyy, T. V. & Hänggi, P. (2006). Magnetization of nanoparticle systems in a rotating magnetic field, *Phys. Rev. Lett.* 97: 227202.

Duine, R. A., Núñez, A. S. & MacDonald, A. H. (2007). Thermally assisted current-driven domain-wall motion, *Phys. Rev. Lett.* 98: 056605.

Eerenstein, W., Mathur, N. D. & Scot, t, J. (2006). Multiferroic and magnetoelectric materials, *Nature* 442: 759.

Elliot, R. J. & Wood, C. (1971). The Ising model with a transverse field. i. high temperature expansion, *J.Phys. C: Solid State Phys.* 4: 2359.

Fiebig, M. (2005). Revival of the magnetoelectric effect, *J.Phys.D: Appl.Phys.* 38: R123.

Gaunt, D. S. & Domb, C. (1970). Equation of state of the Ising model near the critical point, *J. Phys. C: Solid State Phys.* 3: 1442.

Gilbert, T. L. (2004). A phenomenological theory of damping in ferromagnetic materials, *IEEE Trans. Magn* 40: 3343.

He, P.-B. & Liu, W. M. (2005). Nonlinear magnetization dynamics in a ferromagnetic nanowire with spin current, *Phys. Rev. B* 72: 064410.

Hohenberg, P. C. & Halperin, B. I. (1977). Theory of dynamic critical phenomena, *Rev. Mod. Phys.* 49: 435–479.

Kühnel, A., Wendt, S. & Wesselinowa, J. (1977). Dynamic behaviour of the Ising model in a transverse field, *physica status solidi (b)* 84: 653.

Landau, L. D. & Lifshitz, E. M. (1935). On the theory of the dispersion of magnetic permeability in ferromagnetic bodies, *Zeitschr. d. Sowjet.* 8: 153.

Landau, L. D., Lifshitz, E. M. & Pitaevski, L. P. (1980). *Statistical Physics, Part 2*, Pergamon, Oxford.

Lines, M. E. & Glass, A. (2004). *Principles and Applications of Ferroelectrics and Related Materials*, Clarendon Press, Oxford.

Mazenko, G. F. (2003). *Fluctuations, order, and defects*, John Wiley & Sons. Inc Hoboken, New jersey.

Michael, T. & Trimper, S. (2011). The excitation spectrum of multiferroics at finite temperatures, *Phys. Rev. B accepted* .

Michael, T., Trimper, S. & Wesselinowa, J. M. (2006). Size and doping effects on the coercive field of ferroelectric nanoparticles: A microscopic model, *Phys. Rev. B* 74: 214113.

Michael, T., Trimper, S. & Wesselinowa, J. M. (2007). Size effects on static and dynamic properties of ferroelectric nanoparticles, *Phys. Rev. B* 76: 094107.

Mostovoy, M. (2006). Ferroelectricity in spiral magnets, *Phys. Rev. Lett.* 96: 067601.

Ohe, J.-i. & Kramer, B. (2006). Dynamics of a domain wall and spin-wave excitations driven by a mesoscopic current, *Phys. Rev. Lett.* 96: 027204.

Pfeuty, P. & Elliot, R. J. (1971). The Ising model with a transverse field. ii. ground state properties, *J. Phys. C: Solid State Phys.* 4: 2370.

Stinchcombe, R. B. (1971). Ising model in a transverse field. ii. spectral functions and damping, *J. Phys. C: Solid State Phys.* 6: 2484, 2507.

Stinchcombe, R. B. (1973). Ising model in a transverse field, *J. Phys. C: Solid State Phys.* 6: 2459.

Strukov, B. A. & Levnyuk, A. P. (1998). *Ferroelectric Phenomena in Crystals*, Springer, Berlin.

Tokura, Y. & Seki, S. (2010). Multiferroics with spiral spin order, *Adv. Mater.* 22: 1554.

Trimper, S., Michael, T. & Wesselinowa, J. M. (2007). Ferroelectric soft modes and Gilbert damping, *Phys. Rev. B* 76: 094108.

Tserkovnyak, Y., Brataas, A., Bauer, G. E. W. & Halperin, B. I. (2005). Nonlocal magnetization dynamics in ferromagnetic heterostructures, *Rev. Mod. Phys.* 77: 1375–1421.

Usadel, K. D. (2006). Temperature-dependent dynamical behavior of nanoparticles as probed by ferromagnetic resonance using Landau-Lifshitz-Gilbert dynamics in a classical spin model, *Phys. Rev. B* 73: 212405.

Van den Brink, J. & Khomskii, D. (2008). Multiferroicity due to charge ordering, *J. Phys.: Condens. Matter 20 (2008) 434217 (12pp)* 20: 434217.

Wang, K. F., Liu, J. M. & Ren, Z. F. (2009). Multiferroicity: the coupling between magnetic and polarization order, *Adv. Phys.* 58: 321.

Wang, Y.-L. & Cooper, B. R. (1968). Collective excitations and magnetic ordering in materials with singlet crystal-field ground state, *Phys. Rev.* 172: 539–551.

Wesselinowa, J. M. (1984). Damping of the transverse and longitudional excitations of the IIsng model in a transverse field, *physica status solidi (b)* 121: 317.

Wesselinowa, J. M. & Kovachev, S. (2007). Hardening and softening of soft phonon modes in ferroelectric thin films, *Phys. Rev. B* 75: 045411.

Wesselinowa, J. M., Michael, T. & Trimper, S. (2010). *Handbook of Nanophysics Vol.4*, Taylor & Francis, London, Editor: Klaus Sattler.

Wesselinowa, J. M., Trimper, S. & Zabrocki, K. (2005). Impact of layer defects in ferroelectric thin films, *J. Phys.: Cond. Mat* 17: 4687.

24

A General Conductivity Expression for Space-Charge-Limited Conduction in Ferroelectrics and Other Solid Dielectrics

Ho-Kei Chan[1,2]
[1]*School of Physics, Trinity College Dublin, College Green, Dublin 2,*
[2]*Department of Applied Physics, Hong Kong Polytechnic University, Kowloon,*
[1]*Ireland*
[2]*Hong Kong, China*

1. Introduction

For a current density J and an applied voltage V, the experimentally observable Mott-Gurney law $J \sim V^2$ (Carbone et al., 2005; Coelho, 1979; Laha & Krupanidhi, 2002; Pope & Swemberg, 1998; Suh et al., 2000) for steady-state trap-free space-charge-limited conduction (SCLC) inside a plane-parallel dielectric capacitor is derived from three independent assumptions - (i) the presence of a single free-carrier type (i.e. injection of only *p*-type or *n*-type free charge-carriers into the dielectric), (ii) the absence of an intrinsic (Ohmic) conductivity, and (iii) the existence of a constant dielectric permittivity ε (i.e. the material being a linear dielectric). Due to the limited applicability of the Mott-Gurney law, there has been the need to derive a more general SCLC formula that applies to cases (i) with the simultaneous presence of *p*-type and *n*-type free charge-carriers, (ii) with the presence of a small but finite intrinsic conductivity σ_{in}, as well as (iii) with any possible field dependence of the dielectric permittivity ε. In 2003, while we were searching for a theoretical explanation to the well-known experimental observation of polarization offsets (Schubring et al., 1992) in compositionally graded ferroelectric films, we employed the law of mass action to derive a general local conductivity expression for double-carrier-type SCLC in solid dielectrics and showed numerically that SCLC is a possible origin of the observation of polarization offsets in those graded ferroelectric films (Chan et al., 2004). In those graded films, there exist gradients of electric displacements and therefore, according to Gauss' law, a corresponding presence of free space-charge. The local electrical conductivity is influenced, or even limited, by the presence of free space-charge and consequently becomes non-Ohmic. An important conclusion from this general local conductivity expression is the *necessary* dominance of a single free-carrier type at the limit of zero intrinsic conductivity, which links two of the three independent assumptions in the original derivation of the Mott-Gurney law. In a later study (Zhou et al., 2005a), we have employed this new conductivity expression to understand the origin of imprint effect in homogeneous ferroelectric films. In this Book Chapter, we will (i) review the original derivation of the Mott-Gurney law (Coelho, 1979; Pope & Swemberg,

e-mail: epkeiyeah@yahoo.com.hk

1998), (ii) review the original problem of polarization offsets in compositionally graded ferroelectric films (Schubring et al., 1992) and explain why such a new local conductivity expression was needed in our theoretical investigation, (iii) review our original derivation of this general local conductivity expression (Chan et al., 2004), (iv) review our study on the limiting case of zero intrinsic conductivity (Chan et al., 2007; Zhou et al., 2005a), (v) supply the derivation of a general expression, via the mass-action approximation, for the corresponding local diffusion-current density (Chan, unpublished), which incorporates the Einstein relations and takes into account the possible presence of a temperature gradient, (vi) present an alternative derivation of this local conductivity expression (Chan, unpublished) with a detailed theoretical justification of the mass-action approximation, and (vii) discuss, in the concluding section, possible future work as to a better understanding of the mechanism of charge flow in a compositionally graded ferroelectric film as well as of the scope of applicability of the general local conductivity expression.

2. Derivation of the Mott-Gurney law

Space-charge-limited conduction (SCLC) in a solid dielectric occurs when free charge-carriers are injected into the dielectric sample at relatively large electric fields (Carbone et al., 2005; Coelho, 1979; Laha & Krupanidhi, 2002; Pope & Swemberg, 1998; Suh et al., 2000). For the case of SCLC in a trap-free plane-parallel dielectric capacitor (Fig. 1), the current density J and the applied voltage V follow a scaling relation

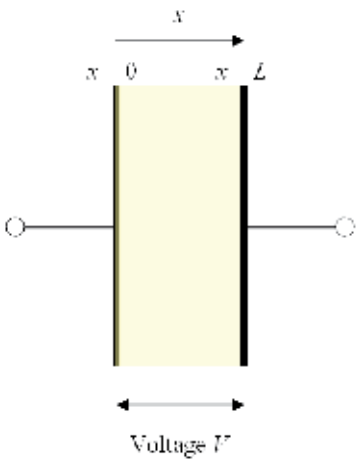

Fig. 1. Schematic diagram of a plane-parallel dielectric capacitor. V is the applied voltage, and x is the position from the electrode where the electric current flows into the dielectric sample. The positive direction of x is the flow direction of the electric current.

$$J \sim V^2 \tag{1}$$

which can be observed experimentally (Carbone et al., 2005; Laha & Krupanidhi, 2002; Suh et al., 2000), and can be derived theoretically (Coelho, 1979) as follows: Consider the case of SCLC by only p-type free charge-carriers, and let this case be denoted by a subscript p in each of the quantities involved. Let the charge mobility $\mu_p > 0$ and the dielectric permittivity

$\varepsilon > 0$ be both independent of the position x from the electrode where the electric current flows into the dielectric sample. The flow direction of the electric current is then given by the positive direction of x. According to Gauss' law, the free-charge density is given by

$$\rho_p(x) = \varepsilon \frac{dE_p(x)}{dx} \geq 0 \tag{2}$$

where $E_p(x)$ is the electric field along the positive direction of x. At steady states, the continuity equation

$$\vec{\nabla} \cdot \vec{J}_p = 0 \tag{3}$$

implies that the current density J_p is independent of the position x. At the absence of both intrinsic (Ohmic) conductivity and diffusion currents, this current density is given by

$$J_p = \mu_p \rho_p(x) E_p(x) = \frac{\mu_p \varepsilon}{2} \frac{dE_p(x)^2}{dx} \tag{4}$$

A spatial integration of Eq. (4) from 0 to x using the boundary condition $E_p(0) = 0$ yields

$$J_p = \frac{\mu_p \varepsilon}{2x} E_p(x)^2 \geq 0 \tag{5}$$

or equivalently

$$E_p(x) = \sqrt{\frac{2J_p x}{\mu_p \varepsilon}} \geq 0 \tag{6}$$

The present justification for the boundary condition $E_p(0) = 0$ is that, at the boundary $x = 0$, any electric field along the positive direction of x, if it ever exists, would be `neutralized' by an electric field in the opposite direction as generated by the injected p-type free carriers (Coelho, 1979). Here we provide a "quantitative explanation" for this: At $x = 0$, the electric field satisfies the inequality $E_p(0) \geq 0$. But since, at this boundary, there is a step change of the free-charge density from zero to some finite positive value, the inequality $E_p(0) \leq 0$ is also satisfied as any finite local electric field is also expected to be pointing along the negative direction of x. The simultaneous inequalities $E_p(0) \geq 0$ and $E_p(0) \leq 0$ together imply $E_p(0) = 0$. Using Kirchoff's loop law (i.e. Kirchoff's voltage law) and Eq. (6), we obtain

$$V = \int_0^L E_p(x) dx = \left(\frac{8J_p}{9\mu_p \varepsilon} \right)^{1/2} L^{3/2} \tag{7}$$

Hence,

$$J_p = \left(\frac{9\mu_p \varepsilon}{8L^3} \right) V^2 \sim V^2 \tag{8}$$

If *n*-type instead of *p*-type free carriers are injected into the dielectric sample, Eqs. (2) and (4) should be replaced by

$$\rho_n(x) = \varepsilon \frac{dE_n(x)}{dx} \leq 0 \tag{9}$$

and

$$J_n = -\mu_n \rho_n(x) E_n(x) = -\frac{\mu_n \varepsilon}{2} \frac{dE_n(x)^2}{dx} \tag{10}$$

respectively, where $\mu_n > 0$, and the subscript n denotes the case of SCLC by only n-type free carriers. Following a derivation similar to that for the case of p-type SCLC but with a consideration of the boundary condition $E_n(L) = 0$, we obtain

$$J_n = \left(\frac{9\mu_n \varepsilon}{8L^3} \right) V^2 \sim V^2 \tag{11}$$

It follows that the scaling relation $J \sim V^2$ holds regardless of whether the injected free carriers are *p*-type or *n*-type.

3. Polarization offsets in graded ferroelectrics and the need for a general local conductivity expression

Our theoretical investigation of SCLC began with a study of the well-known phenomenon of polarization offsets in compositionally graded ferroelectric films (Bao et al. 2000a, 2000b, 2000c, 2001a, 2001b; Bouregba et al., 2003; Brazier et al., 1998; Chen et al., 1999; Mantese et al., 1997; Matsuzaki & Funakubo, 1999; Schubring et al., 1992). Ferroelectric materials are materials that generally exhibit nonlinear, hysteretic *D-E* or *P-E* relations, where *D* is the electric displacement, *P* is the polarization and *E* is the electric field. In contrast to the "normal" hysteresis loops, i.e. loops that are centred at the origin of the *D-E* or *P-E* plot, as observed for homogeneous ferroelectric films, it was first reported in *Physical Review Letters* (Schubring et al., 1992) that compositionally graded ferroelectric films can exhibit vertical displacements of their hysteresis loops along the polarization axis, i.e. polarization offsets, when driven by an alternating applied electric field and placed inside a Sawyer-Tower circuit (Chan et al., 2004; Sawyer & Tower, 1930) for typical *D-E* measurements of ferroelectric materials. This intriguing phenomenon, believed to have potential device applications in infrared detection, actuation and energy storage (Mantese & Alpay, 2005), has triggered much subsequent research in the ferroelectrics community into a theoretical understanding of its origin (Alpay et al., 2003; Bouregba et al., 2003; Brazier et al., 1999; Chan et al., 2004; Fellberg et al., 2001; Mantese & Alpay, 2005; Mantese et al., 1997; Okatan et al., 2010; Poullain et al., 2002).

Such a phenomenon of polarization offsets in compositionally graded ferroelectric films is characterized by three key experimental observations: (i) The shift magnitude exhibits a strong dependence on electric field and temperature (Schubring et al., 1992). In particular, it typically exhibits a power 3 to 5 dependence on the magnitude of the applied electric field (Bao et al., 2000a, 2000b, 2000c, 2001b; Bouregba et al., 2003; Brazier et al., 1998; Mantese et al., 1997); (ii) The vertical hysteresis shift changes from upward to downward, or vice versa,

when the compositional gradient is inverted (Bouregba et al., 2003; Brazier et al., 1998; Mantese et al., 1997). (iii) A vertical polarization offset typically develops like the charging up of a capacitor, where the "time constant" is of the order of magnitude as the product of the capacitance and input impedance of the reference capacitor in the Sawyer-Tower circuit.
In the past two decades, various theoretical ideas and models have been proposed to account for the origin of this phenomenon: Originally, the vertical hysteresis shift, or "polarization offset", was thought of as a static polarization developed across the graded ferroelectric film (Mantese et al., 1997), upon excitation by an alternating applied electric field. However, the experimental values of those "offsets" are at least an order of magnitude larger than the typical spontaneous polarization of the ferroelectric material, and therefore such a large static polarization component is deemed unlikely, if not impossible (Brazier et al., 1999). Other theoretical considerations include an interpretation of the vertical hysteresis shift as the result of a static voltage developed across the ferroelectric film (Brazier et al., 1999), as a result of asymmetric electrical conduction by leakage currents in the film (Bouregba et al., 2003), and as an effect of space charge in a perfectly insulating ferroelectric film (Okatan et al., 2010).
In our theoretical investigation where all of the key experimental observations mentioned above were reproduced theoretically (Chan et al., 2004), we proposed that the observation of polarization offsets in a compositionally graded ferroelectric film is a result of "time-dependent" space-charge-limited conduction inside the graded film, where the term "time-dependent" was used because the ferroelectric film was excited by an alternating applied electric field, in contrast to the abovementioned case of steady-state SCLC, in the absence of displacement currents, as described by the Mott-Gurney law. This central assumption was based on the following considerations: A similar phenomenon of polarization offsets was observed for homogeneous ferroelectric films in the presence of a temperature gradient (Fellberg et al., 2001), where the vertical hysteresis shift disappeared when the applied temperature gradient was removed. This suggests that, for this particular case, the shift is a result of thermally induced gradients in the polarization P (Alpay et al., 2003; Fellberg et al., 2001), or more generally in the electric displacement D, where the latter implies the presence of free space-charge according to Gauss' law. If the vertical hysteresis shifts that arise from compositional and thermal gradients are of the same origin, the observation of polarization offsets in compositionally graded ferroelectric films might be mainly a result of electrical conduction by free space-charge, i.e. SCLC. Here, we have deliberately aborted the assumption of a perfectly insulating ferroelectric film, as adopted by some other schools of thought (Alpay et al., 2003; Mantese & Alpay, 2005; Okatan et al., 2010), because experimental observations of small but finite leakage currents, as well as of SCLC currents, have been widely reported in the literature for ferroelectrics and other solid dielectrics (Bouregba et al., 2003; Carbone et al., 2005; Coelho, 1979; Laha & Krupanidhi, 2002; Pope & Swemberg, 1998; Poullain et al., 2002; Suh et al., 2000) and they form a subject of their own (Pope & Swemberg, 1998).
For our consideration of SCLC in compositionally graded ferroelectric films, the Mott-Gurney law $J \sim V^2$ does not apply, due to the following reasons: (i) In the case of a time-varying applied voltage, there is also the presence of displacement currents so that the conduction current J , which now does not necessarily equal the total current, could be varying with position, i.e. Eq. (3) no longer holds. (ii) In many ferroelectric and dielectric materials, there exist two opposite types of free charge-carriers, p-type and n-type, with

the system behaving like a wide bandgap semiconductor. Such double-carrier cases are not considered by the Mott-Gurney law. (iii) The Mott-Gurney law offers no way to take into account any small but finite intrinsic conductivity of a ferroelectric or dielectric material. (iv) For non-linear dielectric materials, the dielectric permittivity ε is not a constant, usually field-dependent, and for ferroelectrics it is even time- or history-dependent. And for inhomogeneous materials, e.g. compositionally graded ferroelectrics, ε typically exhibits a spatial variation. In view of these limitations, we have derived a new local conductivity expression (Chan et al., 2004) that is applicable to cases with the presence of both *p*-type and *n*-type free carriers, with a small but finite local conductivity, and with any possible dependence of the local dielectric permittivity ε on the system parameters. It is worth pointing out that a corresponding global conductivity expression, e.g. the Mott-Gurney law, must be obtained via the continuity condition in Eq. (3) and can only be derived with knowledge of the relation of ε with other system parameters. For example, in the derivation of the Mott-Gurney law, ε is a known quantity – it is taken as a constant, independent of any system parameter. In the following Section, we will review our original derivation (Chan et al., 2004) of this local conductivity expression, where the law of mass action was employed as an *ad hoc* approximation to describe the interactions between the two opposite types of free charge-carriers. A detailed justification of this mass-action approximation is provided in subsequent Sections.

4. Original derivation of the general local conductivity expression

For a time-varying applied voltage $V(t)$, the local conduction-current density $J_c(x,t)$, the local electric field $E(x,t)$ as well as the local electric displacement $D(x,t)$ are generally functions of the position x and the time t. The local conduction-current density is related to the local electric field via a generally time-dependent local conductivity $\sigma(x,t)$:

$$J_c(x,t) = \sigma(x,t)E(x,t) \tag{12}$$

Consider the simultaneous presence of *p*-type and *n*-type free charge-carriers with the position-dependent mobilities $\mu_p(x)$ and $-\mu_n(x)$, and of electric charges q and $-q$, respectively. Here we have chosen $\mu_p(x)$, $\mu_n(x)$ and q to all be positive quantities. Due to charge neutrality, the intrinsic number concentrations of the two opposite types of free carriers are equal, and they are here both denoted by the symbol $C_{in}(x)$. The time-dependent conductivity can then be expressed as

$$\begin{aligned}\sigma(x,t) = {} & q\mu_p(x)[C_{in}(x) + \Delta p(x,t)] \\ & + [-q][-\mu_n(x)][C_{in}(x) + \Delta n(x,t)]\end{aligned} \tag{13}$$

where $\Delta p(x,t)$ and $\Delta n(x,t)$ are respectively the differences between the intrinsic and total number concentrations for each type of free carriers. Here we define a generally position-dependent local intrinsic conductivity

$$\sigma_{in}(x) \equiv q[\mu_p(x) + \mu_n(x)]C_{in}(x) \tag{14}$$

such that the time-dependent conductivity in Eq. (13) can be expressed as

$$\sigma(x,t) = \sigma_{in}(x) + q[\mu_p(x)\Delta p(x,t) + \mu_n(x)\Delta n(x,t)] \tag{15}$$

According to Gauss' law, the density of free space-charge is given by

$$\begin{aligned}\frac{\partial D(x,t)}{\partial x} &= q[C_{in}(x)+\Delta p(x,t)]+[-q][C_{in}(x)+\Delta n(x,t)] \\ &= q[\Delta p(x,t)-\Delta n(x,t)]\end{aligned} \tag{16}$$

Since there generally exist interactions, i.e. generation and recombination, between the two opposite types of free charge-carriers, the free-carrier concentrations $C_{in}(x)+\Delta p(x,t)$ and $C_{in}(x)+\Delta n(x,t)$ are *not* independent of each other, and should be described by an additional physical constraint

$$F[\Delta p(x,t),\Delta n(x,t)]=0 \tag{17}$$

As an *ah hoc* approximation, we regard any ferroelectric or dielectric material as a wide bandgap semiconductor and then employ the equilibrium law of mass action to be this additional physical constraint:

$$C_{in}(x)^2=[C_{in}(x)+\Delta p(x,t)][C_{in}(x)+\Delta n(x,t)] \tag{18}$$

The physics described by Eq. (18) is as follows (Chan et al., 2007): In a wide bandgap semiconductor, there are the endothermic generation and exothermic recombination of free charge-carriers. If the energy released by free-carrier recombination is immediately used for free-carrier generation, i.e. a "heat balance" condition, the rates of these endothermic and exothermic processes must be equal, and there would not be any net production of heat nor any net generation of free carriers. On the other hand, the rate of each of these processes can be assumed, as a first approximation, to be proportional to the product of the reactants' concentrations, i.e. *the number of ways per unit volume the different types of reactants can combine to undergo the process*. Since, for a dielectric insulator, the concentration of the source particles for free-carrier generation (e.g. valence electrons or molecules) is by definition orders of magnitude larger than the concentrations of the free carriers, the concentration of source particles, and hence the rate of free-carrier generation, should only have an insignificant time fluctuation and should practically be a material-pertaining property. It follows that any rate of free-carrier recombination, which we have here assumed to be proportional to the product of the concentrations of *p*-type and *n*-type free carriers, can all be taken as equal to the same approximately time-invariant rate of free-carrier generation, hence Eq. (18).
Upon rewriting Eqs. (16) and (18) as

$$\Delta p(x,t)=\frac{1}{q}\frac{\partial D(x,t)}{\partial x}+\Delta n(x,t) \tag{19}$$

and

$$C_{in}(x)[\Delta p(x,t)+\Delta n(x,t)]+\Delta p(x,t)\Delta n(x,t)=0 \tag{20}$$

respectively, it can be seen that two quadratic equations, for $\Delta p(x,t)$ and $\Delta n(x,t)$ respectively, can be obtained:

$$\Delta p(x,t)^2 + B_p(x,t)\Delta p(x,t) + C_p(x,t) = 0 \tag{21}$$

and

$$\Delta n(x,t)^2 + B_n(x,t)\Delta n(x,t) + C_n(x,t) = 0 \tag{22}$$

where

$$B_p(x,t) \equiv -\frac{1}{q}\frac{\partial D(x,t)}{\partial x} + 2C_{in}(x) \tag{23}$$

$$C_p(x,t) \equiv -\frac{C_{in}(x)}{q}\frac{\partial D(x,t)}{\partial x} \tag{24}$$

$$B_n(x,t) \equiv \frac{1}{q}\frac{\partial D(x,t)}{\partial x} + 2C_{in}(x) \tag{25}$$

and

$$C_n(x,t) \equiv \frac{C_{in}(x)}{q}\frac{\partial D(x,t)}{\partial x} \tag{26}$$

It follows that

$$\begin{aligned} & q[\mu_p(x)\Delta p(x,t) + \mu_n(x)\Delta n(x,t)] \\ &= \frac{q}{2}\{\mu_p(x)[-B_p(x,t) \pm \sqrt{B_p(x,t)^2 - 4C_p(x,t)}] \\ &\quad + \mu_n(x)[-B_n(x,t) \pm \sqrt{B_n(x,t)^2 - 4C_n(x,t)}]\} \end{aligned} \tag{27}$$

Using the definitions of the quadratic coefficients $B_p(x,t)$, $C_p(x,t)$, $B_n(x,t)$ and $C_n(x,t)$, as well as the definition of $\sigma_{in}(x)$ in Eq. (14), the following relations can be obtained:

$$\begin{aligned} & -\frac{q}{2}[\mu_p(x)B_p(x,t) + \mu_n(x)B_n(x,t)] \\ &\quad = \frac{[\mu_p(x) - \mu_n(x)]}{2}\frac{\partial D(x,t)}{\partial x} - \sigma_{in}(x) \end{aligned} \tag{28}$$

and

$$\begin{aligned} \frac{q}{2}\sqrt{B_p(x,t)^2 - 4C_p(x,t)} &= \frac{q}{2}\sqrt{B_n(x,t)^2 - 4C_n(x,t)} \\ &= \frac{1}{2}\sqrt{\left[\frac{\partial D(x,t)}{\partial x}\right]^2 + \frac{4\sigma_{in}(x)^2}{[\mu_p(x) + \mu_n(x)]^2}} \end{aligned} \tag{29}$$

Using Eqs. (15), (28) and (29), Eq. (27) can be rewritten as

$$
\begin{aligned}
& q[\mu_p(x)\Delta p(x,t) + \mu_n(x)\Delta n(x,t)] \\
& = \frac{[\mu_p(x) - \mu_n(x)]}{2}\frac{\partial D(x,t)}{\partial x} - \sigma_{in}(x) \\
& \quad + \frac{[\pm\mu_p(x) \pm \mu_n(x)]}{2}\sqrt{\left[\frac{\partial D(x,t)}{\partial x}\right]^2 + \frac{4\sigma_{in}(x)^2}{[\mu_p(x) + \mu_n(x)]^2}} \\
& = \sigma(x,t) - \sigma_{in}(x)
\end{aligned}
\tag{30}
$$

so that an expression for the time-dependent local conductivity $\sigma(x,t)$ can be obtained:

$$
\begin{aligned}
\sigma(x,t) = & \frac{[\mu_p(x) - \mu_n(x)]}{2}\frac{\partial D(x,t)}{\partial x} \\
& + \sqrt{\left\{\frac{[\pm\mu_p(x) \pm \mu_n(x)]}{2}\frac{\partial D(x,t)}{\partial x}\right\}^2 + \frac{[\pm\mu_p(x) \pm \mu_n(x)]^2\sigma_{in}(x)^2}{[\mu_p(x) + \mu_n(x)]^2}}
\end{aligned}
\tag{31}
$$

According to Eqs. (15), (16) and (31), for the case of $\Delta p(x,t) = \Delta n(x,t) = 0$, we have

$$
\frac{\partial D(x,t)}{\partial x} = 0 \tag{32}
$$

and

$$
\sigma(x,t) = \sigma_{in}(x) = \frac{[\pm\mu_p(x) \pm \mu_n(x)]}{[\mu_p(x) + \mu_n(x)]}\sigma_{in}(x) \tag{33}
$$

where the latter implies that only the root of all upper positive signs in Eq. (31) is valid. Therefore, the correct expression for the time-dependent conductivity should be:

$$
\begin{aligned}
\sigma(x,t) = & \frac{[\mu_p(x) - \mu_n(x)]}{2}\frac{\partial D(x,t)}{\partial x} \\
& + \sqrt{\left\{\frac{[\mu_p(x) + \mu_n(x)]}{2}\frac{\partial D(x,t)}{\partial x}\right\}^2 + \sigma_{in}(x)^2}
\end{aligned}
\tag{34}
$$

which describes a nonlinear relation between the space-charge density and the overall local conductivity in the presence of a non-zero intrinsic conductivity.

5. Limiting case of zero intrinsic conductivity

Consider a case where $\sigma_{in}(x) \rightarrow 0$ but $\sigma(x,t)$ remains finite. According to Eq. (15), either $\mu_p(x)$ or $\mu_n(x)$ has to be non-zero for $\sigma(x,t)$ to remain finite. From the definition of the intrinsic conductivity in Eq. (14), for $\sigma_{in}(x) \rightarrow 0$ we must have $C_{in}(x) \rightarrow 0$, because the mobility sum $[\mu_p(x) + \mu_n(x)]$ is finite. For $C_{in}(x) \rightarrow 0$, Eq. (20) becomes

$$\Delta p(x,t)\Delta n(x,t) \approx 0 \tag{35}$$

Multiplying both sides of Eq. (19) by $\Delta p(x,t)$ or $\Delta n(x,t)$ and then applying Eq. (35), we obtain

$$\Delta p(x,t)\left[\Delta p(x,t) - \frac{1}{q}\frac{\partial D(x,t)}{\partial x}\right] \approx 0 \tag{36}$$

and

$$\Delta n(x,t)\left[\Delta n(x,t) + \frac{1}{q}\frac{\partial D(x,t)}{\partial x}\right] \approx 0 \tag{37}$$

The solutions to Eqs. (36) and (37) are

$$\Delta p(x,t) \approx 0, \quad \Delta p(x,t) \approx \frac{1}{q}\frac{\partial D(x,t)}{\partial x} \tag{38}$$

and

$$\Delta n(x,t) \approx 0, \quad \Delta n(x,t) \approx -\frac{1}{q}\frac{\partial D(x,t)}{\partial x} \tag{39}$$

respectively. According to Eq. (19), however, only the following combinations of solutions are allowed.

$$\Delta p(x,t) \approx 0 \quad and \quad \Delta n(x,t) \approx -\frac{1}{q}\frac{\partial D(x,t)}{\partial x} \tag{40}$$

and

$$\Delta n(x,t) \approx 0 \quad and \quad \Delta p(x,t) \approx \frac{1}{q}\frac{\partial D(x,t)}{\partial x} \tag{41}$$

Since $C_{in}(x) \rightarrow 0$, the quantities $\Delta p(x,t)$ and $\Delta n(x,t)$ effectively become the total free-carrier concentrations and must therefore be non-negative. Eqs. (40) and (41) thus lead to an important conclusion: *At the limit of zero intrinsic conductivity, either p-type or n-type free charge-carriers become dominant*, with the cases of

$$\frac{\partial D(x,t)}{\partial x} > 0 \tag{42}$$

and

$$\frac{\partial D(x,t)}{\partial x} < 0 \tag{43}$$

corresponding to the dominance of *p*-type and *n*-type free charge-carriers, respectively. This conclusion provides a linkage between two of the three independent assumptions, i.e. the absence of an intrinsic conductivity and the presence of only a single type of free charge-

carriers, in the original derivation of the Mott-Gurney law: Although Eqs. (40) and (41) only conclude that the simultaneous presence of *p*-type and *n*-type free carriers is *locally* forbidden, this conclusion also holds *globally* across a dielectric sample for the case of a plane-parallel dielectric capacitor as described by the Mott-Gurney law. In the absence of diffusion currents, the total-current density J is equal to the conduction-current density J_c, and they are both spatially continuous; For any non-zero total-current density J, the space-charge density must be non-zero everywhere, otherwise there would be the case of $J = J_c = 0$ somewhere in the sample. Globally, regions of positive space-charge density and regions of negative space-charge density cannot be present simultaneously in the dielectric sample, otherwise there would exist inter-regional boundaries of zero space-charge density at which $J = J_c = 0$. It follows that the space-charge density must be of the same sign across the dielectric sample as well, which implies that the simultaneous presence of *p*-type and *n*-type free charge-carriers is also globally forbidden.
For $\sigma_{in}(x) \rightarrow 0$, Eq. (34) becomes

$$\begin{aligned}\sigma(x,t) &\approx \frac{[\mu_p(x)-\mu_n(x)]}{2}\frac{\partial D(x,t)}{\partial x} \\ &+ \frac{[\mu_p(x)+\mu_n(x)]}{2}\left|\frac{\partial D(x,t)}{\partial x}\right|\end{aligned} \tag{44}$$

If Eq. (42) holds, we have

$$\begin{aligned}\sigma(x,t) &\approx \frac{[\mu_p(x)-\mu_n(x)]}{2}\frac{\partial D(x,t)}{\partial x} \\ &+ \frac{[\mu_p(x)+\mu_n(x)]}{2}\frac{\partial D(x,t)}{\partial x} \\ &\approx \mu_p(x)\frac{\partial D(x,t)}{\partial x}\end{aligned} \tag{45}$$

Else if Eq. (43) holds, we have

$$\begin{aligned}\sigma(x,t) &\approx \frac{[\mu_p(x)-\mu_n(x)]}{2}\frac{\partial D(x,t)}{\partial x} \\ &+ \frac{[\mu_p(x)+\mu_n(x)]}{2}\left[-\frac{\partial D(x,t)}{\partial x}\right] \\ &\approx -\mu_n(x)\frac{\partial D(x,t)}{\partial x}\end{aligned} \tag{46}$$

Eqs. (45) and (46) together verify that, in the case of $\sigma_{in}(x) \rightarrow 0$, the charge mobility in the expression for the generally time-dependent local conductivity $\sigma(x,t)$ is correctly equal to that of the dominant type of free carriers.

6. Derivation of a general expression for the local diffusion-current density

Apart from electrical conduction, i.e. the electric-field-driven flow of free charge-carriers, there also exists the possibility of charge diffusion due to the presence of a charge-density

gradient or a temperature gradient, where the latter is often being referred to as the thermoelectric effect. For any bulk dielectric sample, consider the i^{th} infinitesimal volume with dimensions Δx, Δy and Δz. Along the x-direction, for example, the net force acting on the p-type free carriers within this infinitesimal volume is given by

$$F_{p,i} = (P_{p,i-1} - P_{p,i+1})\Delta y \Delta z \tag{47}$$

where P and the subscript p denote the local pressure and p-type free charge-carriers, respectively. The total amount of charge carried by the p-type free carriers in this infinitesimal volume is

$$Q_{p,i} = qC_p \Delta x \Delta y \Delta z \tag{48}$$

where

$$C_p \equiv C_{in} + \Delta p \tag{49}$$

is the total concentration of p-type free carriers for this infinitesimal volume. The corresponding force per unit charge, i.e. the mechanical counterpart of the electric field, is then given by

$$\tilde{E}_{p,i} \equiv \frac{F_{p,i}}{Q_{p,i}} = -\frac{(P_{p,i+1} - P_{p,i-1})}{qC_p \Delta x} \tag{50}$$

And for the case of conduction by n-type free carriers, we have

$$\tilde{E}_{n,i} \equiv \frac{F_{n,i}}{Q_{n,i}} = -\frac{(P_{n,i+1} - P_{n,i-1})}{(-qC_n)\Delta x} \tag{51}$$

where

$$C_n \equiv C_{in} + \Delta n \tag{52}$$

is the total concentration of n-type free carriers. In the continuum limit, Eqs. (50) and (51) can be replaced by

$$\tilde{E}_p(x,t) = -\frac{1}{qC_p(x,t)} \frac{\partial P_p(x,t)}{\partial x} \tag{53}$$

and

$$\tilde{E}_n(x,t) = -\frac{1}{[-qC_n(x,t)]} \frac{\partial P_n(x,t)}{\partial x} \tag{54}$$

respectively. The diffusion-current density is then given by

$$\begin{aligned} J_d(x,t) &= q[\mu_p(x) C_p(x,t) \tilde{E}_p(x,t) \\ &\quad + \mu_n(x) C_n(x,t) \tilde{E}_n(x,t)] \\ &= -\left[\mu_p(x) \frac{\partial P_p(x,t)}{\partial x} + [-\mu_n(x)] \frac{\partial P_n(x,t)}{\partial x} \right] \end{aligned} \tag{55}$$

Using an ideal-gas approximation for each of the two types of free charge-carriers, i.e.

$$P_p(x,t) = k_B T(x,t) C_p(x,t) \tag{56}$$

and

$$P_n(x,t) = k_B T(x,t) C_n(x,t) \tag{57}$$

where k_B is the Boltzmann constant and $T(x,t)$ is a generally position- and time-dependent local temperature, the diffusion-current density can be expressed as

$$\begin{aligned} J_d(x,t) = -k_B T(x,t) & \left[\begin{array}{l} \mu_p(x) \dfrac{\partial C_p(x,t)}{\partial x} \\ +[-\mu_n(x)] \dfrac{\partial C_n(x,t)}{\partial x} \end{array} \right] \\ & - k_B \frac{\partial T(x,t)}{\partial x} \Big[\mu_p(x) C_p(x,t) + [-\mu_n(x)] C_n(x,t) \Big] \end{aligned} \tag{58}$$

where

$$D_{o,p}(x,t) \equiv \frac{\mu_p(x) k_B T(x,t)}{q} \tag{59}$$

and

$$D_{o,n}(x,t) \equiv \frac{[-\mu_n(x)] k_B T(x,t)}{(-q)} \tag{60}$$

are the Einstein relations for the local diffusion coefficients of *p*-type and *n*-type free charge-carriers, respectively. Using the definitions in Eqs. (49) and (52), Eq. (58) can be rewritten as

$$\begin{aligned} J_d(x,t) = -k_B T(x,t) & \left[\begin{array}{l} [\mu_p(x) - \mu_n(x)] \dfrac{dC_{in}(x)}{dx} \\ +\mu_p(x) \dfrac{\partial \Delta p(x,t)}{\partial x} - \mu_n(x) \dfrac{\partial \Delta n(x,t)}{\partial x} \end{array} \right] \\ & - k_B \frac{\partial T(x,t)}{\partial x} \left[\begin{array}{l} [\mu_p(x) - \mu_n(x)] C_{in}(x) \\ +\mu_p(x) \Delta p(x,t) - \mu_n(x) \Delta n(x,t) \end{array} \right] \end{aligned} \tag{61}$$

From Eqs. (21) and (22), we obtain

$$\begin{aligned} \Delta p(x,t) = & \frac{1}{2q} \frac{\partial D(x,t)}{\partial x} - C_{in}(x) \\ & + \sqrt{\left[\frac{1}{2q} \frac{\partial D(x,t)}{\partial x} \right]^2 + C_{in}(x)^2} \end{aligned} \tag{62}$$

and

$$\Delta n(x,t) = -\frac{1}{2q}\frac{\partial D(x,t)}{\partial x} - C_{in}(x) + \sqrt{\left[\frac{1}{2q}\frac{\partial D(x,t)}{\partial x}\right]^2 + C_{in}(x)^2} \tag{63}$$

Differentiating Eqs. (62) and (63) with respect to x yields

$$\frac{\partial \Delta p(x,t)}{\partial x} = \frac{1}{2q}\frac{\partial^2 D(x,t)}{\partial x^2} - \frac{dC_{in}(x)}{dx} + \left\{\sqrt{\left[\frac{1}{2q}\frac{\partial D(x,t)}{\partial x}\right]^2 + C_{in}(x)^2}\right\}^{-1} \times\left[\frac{1}{4q^2}\frac{\partial D(x,t)}{\partial x}\frac{\partial^2 D(x,t)}{\partial x^2} + C_{in}(x)\frac{dC_{in}(x)}{dx}\right] \tag{64}$$

and

$$\frac{\partial \Delta n(x,t)}{\partial x} = -\frac{1}{2q}\frac{\partial^2 D(x,t)}{\partial x^2} - \frac{dC_{in}(x)}{dx} + \left\{\sqrt{\left[\frac{1}{2q}\frac{\partial D(x,t)}{\partial x}\right]^2 + C_{in}(x)^2}\right\}^{-1} \times\left[\frac{1}{4q^2}\frac{\partial D(x,t)}{\partial x}\frac{\partial^2 D(x,t)}{\partial x^2} + C_{in}(x)\frac{dC_{in}(x)}{dx}\right] \tag{65}$$

respectively. Putting Eqs. (62) to (65) into Eq. (61), we obtain a general expression for the local diffusion-current density:

$$J_d(x,t) = J_{d1}(x,t) + J_{d2}(x,t) \tag{66}$$

where

$$J_{d1}(x,t) \equiv -\frac{k_B T(x,t)[\mu_p(x) + \mu_n(x)]}{2q}\frac{\partial^2 D(x,t)}{\partial x^2} - [\mu_p(x) - \mu_n(x)]k_B T(x,t) \times\left\{\sqrt{\left[\frac{1}{2q}\frac{\partial D(x,t)}{\partial x}\right]^2 + C_{in}(x)^2}\right\}^{-1} \times\left[\frac{1}{4q^2}\frac{\partial D(x,t)}{\partial x}\frac{\partial^2 D(x,t)}{\partial x^2} + C_{in}(x)\frac{dC_{in}(x)}{dx}\right] \tag{67}$$

and

$$J_{d2}(x,t) \equiv -k_B \frac{\partial T(x,t)}{\partial x} \left[\begin{array}{l} \dfrac{[\mu_p(x)+\mu_n(x)]}{2q} \dfrac{\partial D(x,t)}{\partial x} \\ +[\mu_p(x)-\mu_n(x)] \\ \times \sqrt{\left[\dfrac{1}{2q}\dfrac{\partial D(x,t)}{\partial x}\right]^2 + C_{in}(x)^2} \end{array} \right] \tag{68}$$

Eq. (67) denotes a contribution to the diffusion current from the presence of a gradient in the space-charge density or in the intrinsic free-carrier concentration, while Eq. (68) denotes a contribution from the presence of a temperature gradient. At the limit of zero intrinsic conductivity, we have $C_{in}(x) \rightarrow 0$ as explained in the beginning of the previous section. Eqs. (67) and (68) are then reduced to

$$\begin{aligned} J_{d1}(x,t) \approx & -\frac{[\mu_p(x)+\mu_n(x)]k_B T(x,t)}{2q} \frac{\partial^2 D(x,t)}{\partial x^2} \\ & -\frac{[\mu_p(x)-\mu_n(x)]k_B T(x,t)}{2q} \frac{\dfrac{\partial D(x,t)}{\partial x}\dfrac{\partial^2 D(x,t)}{\partial x^2}}{\left|\dfrac{\partial D(x,t)}{\partial x}\right|} \end{aligned} \tag{69}$$

and

$$J_{d2}(x,t) \approx -k_B \frac{\partial T(x,t)}{\partial x} \left[\begin{array}{l} \dfrac{[\mu_p(x)+\mu_n(x)]}{2q} \dfrac{\partial D(x,t)}{\partial x} \\ +\dfrac{[\mu_p(x)-\mu_n(x)]}{2q} \left|\dfrac{\partial D(x,t)}{\partial x}\right| \end{array} \right] \tag{70}$$

respectively. Similar to the case of Eq. (44), for Eqs. (69) and (70) we can also verify that in the case of $\sigma_{in}(x) \rightarrow 0$ the charge mobility is correctly equal to that of the dominant type of free carriers. Following Eqs. (69) and (70), if Eq. (42) is satisfied, we have

$$\begin{aligned} J_{d1}(x,t) \approx & -\frac{[\mu_p(x)+\mu_n(x)]k_B T(x,t)}{2q} \frac{\partial^2 D(x,t)}{\partial x^2} \\ & -\frac{[\mu_p(x)-\mu_n(x)]k_B T(x,t)}{2q} \frac{\dfrac{\partial D(x,t)}{\partial x}\dfrac{\partial^2 D(x,t)}{\partial x^2}}{\left[+\dfrac{\partial D(x,t)}{\partial x}\right]} \\ \approx & -\frac{\mu_p(x) k_B T(x,t)}{q} \frac{\partial^2 D(x,t)}{\partial x^2} \end{aligned} \tag{71}$$

and

$$J_{d2}(x,t) \approx -k_B \frac{\partial T(x,t)}{\partial x} \left[\begin{array}{l} \dfrac{[\mu_p(x)+\mu_n(x)]}{2q} \dfrac{\partial D(x,t)}{\partial x} \\ + \dfrac{[\mu_p(x)-\mu_n(x)]}{2q} \left[+ \dfrac{\partial D(x,t)}{\partial x} \right] \end{array} \right] \approx -\frac{\mu_p(x) k_B}{q} \frac{\partial D(x,t)}{\partial x} \frac{\partial T(x,t)}{\partial x} \tag{72}$$

Else if Eq. (43) is satisfied, we have

$$J_{d1}(x,t) \approx -\frac{[\mu_p(x)+\mu_n(x)]k_B T(x,t)}{2q} \frac{\partial^2 D(x,t)}{\partial x^2} - \frac{[\mu_p(x)-\mu_n(x)]k_B T(x,t)}{2q} \frac{\dfrac{\partial D(x,t)}{\partial x} \dfrac{\partial^2 D(x,t)}{\partial x^2}}{\left[-\dfrac{\partial D(x,t)}{\partial x} \right]} \approx -\frac{\mu_n(x) k_B T(x,t)}{q} \frac{\partial^2 D(x,t)}{\partial x^2} \tag{73}$$

and

$$J_{d2}(x,t) \approx -k_B \frac{\partial T(x,t)}{\partial x} \left[\begin{array}{l} \dfrac{[\mu_p(x)+\mu_n(x)]}{2q} \dfrac{\partial D(x,t)}{\partial x} \\ + \dfrac{[\mu_p(x)-\mu_n(x)]}{2q} \left[- \dfrac{\partial D(x,t)}{\partial x} \right] \end{array} \right] \approx -\frac{\mu_n(x) k_B}{q} \frac{\partial D(x,t)}{\partial x} \frac{\partial T(x,t)}{\partial x} \tag{74}$$

7. Alternative derivation of the general local conductivity expression

We begin our alternative derivation of the general local conductivity expression in Eq. (34) by identifying the following quantities that appear in the conductivity expression:

$$\mu'(x) \equiv \frac{\mu_p(x)-\mu_n(x)}{2} \tag{75}$$

and

$$\mu''(x) \equiv \frac{\mu_p(x)+\mu_n(x)}{2} \tag{76}$$

The drift velocities of *p*-type and *n*-type free carriers can then be expressed as

$$v_p(x,t) = \mu_p(x)E(x,t) = \mu'(x)E(x,t) + \mu''(x)E(x,t) \tag{77}$$

and

$$v_n(x,t) = -\mu_n(x)E(x,t) = \mu'(x)E(x,t) - \mu''(x)E(x,t) \tag{78}$$

where

$$\mu''(x) \geq \left|\mu'(x)\right| \geq 0 \tag{79}$$

and $\mu'(x)$ can be positive or negative. In this description, both *p*-type and *n*-type free carriers share the same velocity component $\mu'(x)E(x,t)$, with the presence of the additional velocity components $\mu''(x)E(x,t)$ and $-\mu''(x)E(x,t)$ for *p*-type and *n*-type free carriers, respectively. The generally time-dependent local electrical conductivity can then be expressed as a sum of contributions from the velocity components $\mu'(x)E(x,t)$ and $\pm\mu''(x)E(x,t)$:

$$\begin{aligned}\sigma(x,t) = {} & q\mu'(x)[C_p(x,t) - C_n(x,t)] \\ & + q\mu''(x)[C_p(x,t) + C_n(x,t)]\end{aligned} \tag{80}$$

According to Gauss' law, the density of free space-charge is given by

$$\rho_q(x,t) = \frac{\partial D(x,t)}{\partial x} = q[C_p(x,t) - C_n(x,t)] \tag{81}$$

In the absence of free space-charge, i.e. $\rho_q(x,t) = 0$, both $C_p(x,t)$ and $C_n(x,t)$ are by definition equal to the intrinsic free-carrier concentration $C_{in}(x)$, and the electrical conductivity $\sigma(x,t)$ would then be equal to the intrinsic conductivity

$$\sigma_{in}(x) \equiv 2q\mu''(x)C_{in}(x) \tag{82}$$

according to Eq. (80).
Consider the reversible generation and recombination of *p*-type and *n*-type free carriers:

1 source particle ←→ 1 *p*-type free carrier + 1 *n*-type free carrier

As described right below Eq. (18), the rate of free-carrier generation is assumed to be equal to the rate of free-carrier recombination due to a "heat balance" condition, and the rate of each of these processes is assumed to be proportional to the product of the "reactants". Following these, for $C_s(x,t)$ being the concentration of the source particles for free-carrier generation (e.g. valence electrons or molecules) we have

$$K_g C_s(x,t) = K_r C_p(x,t) C_n(x,t) \tag{83}$$

where K_g and K_r are, respectively, the rate constants for the generation and recombination of free carriers. If the conditions

$$C_p(x,t) << C_s(x,t) \tag{84}$$

and

$$C_n(x,t) << C_s(x,t) \tag{85}$$

hold for a dielectric insulator such that

$$C_s(x,t) \approx C_s(x) \tag{86}$$

i.e. the concentration of source particles for free-carrier generation has an insignificant fluctuation with time and is practically a material-pertaining property, we have

$$K_g C_s(x) \approx K_r C_p(x,t) C_n(x,t) \approx K_r C_{in}(x)^2 \tag{87}$$

which implies

$$C_p(x,t) C_n(x,t) \approx C_{in}(x)^2 \tag{88}$$

As an example, we show that this mass-action approximation is valid for a dielectric insulator which has holes and free electrons as its *p*-type and *n*-type free charge-carriers, respectively, and which has valence electrons as its source particles: A hole is by definition equivalent to a missing valence electron. At anywhere inside the dielectric sample, the generation and annihilation of a hole correspond, by definition, to the annihilation and generation of a valence electron, respectively, and the flow-in and flow-out of a hole are, respectively, by definition equivalent to the flow-out and flow-in of a valence electron in the opposite directions. Therefore,

$$\frac{\partial C_p(x,t)}{\partial t} = -\frac{\partial C_s(x,t)}{\partial t} \tag{89}$$

so that the total concentration of holes and valence electrons is given by

$$C_{p+s}(x) \equiv C_p(x,t) + C_s(x,t) \tag{90}$$

Eq. (83) can then be written as

$$K_g[C_{p+s}(x) - C_p(x,t)] = K_r C_p(x,t) C_n(x,t) \tag{91}$$

For the case of zero space charge where $C_p(x,t) = C_n(x,t) = C_{in}(x)$, we have

$$K_g[C_{p+s}(x) - C_{in}(x)] = K_r C_{in}(x)^2 \tag{92}$$

Define a material paramter

$$\alpha(x) \equiv \frac{C_{in}(x)}{C_{p+s}(x)} \le 1 \tag{93}$$

and consider the limit of $\alpha(x) \rightarrow 0$ for the case of a dielectric insulator. Combining Eqs. (91) to (93), we obtain the mass-action relation in Eq. (88):

$$\begin{aligned} & C_p(x,t) C_n(x,t) \\ & = \lim_{\alpha(x)\to 0} \frac{C_{in}(x)[C_{in}(x) - \alpha(x) C_p(x,t)]}{[1-\alpha(x)]} = C_{in}(x)^2 \end{aligned} \tag{94}$$

Going back to our derivation of the conductivity expression, we notice that Eqs. (81) and (88) together imply

$$C_p(x,t)^2 - \frac{\rho_q(x,t)}{q} C_p(x,t) - C_{in}(x)^2 \approx 0 \tag{95}$$

and

$$C_n(x,t)^2 + \frac{\rho_q(x,t)}{q} C_n(x,t) - C_{in}(x)^2 \approx 0 \tag{96}$$

from which we obtain

$$C_p(x,t) \approx \frac{1}{2}\left[\frac{\rho_q(x,t)}{q} + \sqrt{\left[\frac{\rho_q(x,t)}{q} \right]^2 + 4C_{in}(x)^2} \right] \geq 0 \tag{97}$$

$$C_n(x,t) \approx \frac{1}{2}\left[-\frac{\rho_q(x,t)}{q} + \sqrt{\left[\frac{\rho_q(x,t)}{q} \right]^2 + 4C_{in}(x)^2} \right] \geq 0 \tag{98}$$

and

$$C_p(x,t) + C_n(x,t) \approx \sqrt{\left[\frac{\rho_q(x,t)}{q} \right]^2 + 4C_{in}(x)^2} \tag{99}$$

Using Eqs. (80) to (82) as well as Eq. (99), we obtain the following expression for the generally time-dependent local electrical conductivity:

$$\sigma(x,t) \approx \mu'(x)\rho_q(x,t) + \sqrt{[\mu''(x)\rho_q(x,t)]^2 + \sigma_{in}(x)^2} \tag{100}$$

By defining the reduced paramters

$$\sigma^*(x,t) \equiv \frac{\sigma(x,t)}{\sigma_{in}(x)} \tag{101}$$

$$\mu^*(x) \equiv \frac{\mu'(x)}{\mu''(x)} \in \{-1,+1\} \tag{102}$$

and

$$\rho_q^*(x,t) \equiv \frac{\rho_q(x,t)}{2qC_{in}(x)} \tag{103}$$

Eq. (100) can be expressed in a simpler form:

$$\sigma^*(x,t) \approx \mu^*(x)\rho_q^*(x,t) + \sqrt{[\rho_q^*(x,t)]^2 + 1} \tag{104}$$

For the limiting case of zero intrinsic conductivity with $C_{in}(x) \rightarrow 0$, Eqs. (97) and (98) can be rewritten as

$$C_p(x,t) \approx \frac{1}{2}\left[\frac{\rho_q(x,t)}{q} + \left|\frac{\rho_q(x,t)}{q}\right|\right] \tag{105}$$

and

$$C_n(x,t) \approx \frac{1}{2}\left[-\frac{\rho_q(x,t)}{q} + \left|\frac{\rho_q(x,t)}{q}\right|\right] \tag{106}$$

respectively, which imply the dominance of either type of free carriers: If $\rho_q(x,t) > 0$, we have

$$C_p(x,t) \approx \frac{\rho_q(x,t)}{q} \quad and \quad C_n(x,t) \approx 0 \tag{107}$$

Else if $\rho_q(x,t) < 0$, we have

$$C_p(x,t) \approx 0 \quad and \quad C_n(x,t) \approx -\frac{\rho_q(x,t)}{q} \tag{108}$$

8. Conclusions and future work

In this Chapter, a generalized theory for space-charge-limited conduction (SCLC) in ferroelectrics and other solid dielectrics, which we have originally developed to account for the peculiar observation of polarization offsets in compositionally graded ferroelectric films, is presented in full. The theory is a generalization of the conventional *steady-state* trap-free SCLC model, as described by the Mott-Gurney law, to include (i) the presence of two opposite types of free carriers: *p*-type and *n*-type, (ii) the presence of a finite intrinsic (Ohmic) conductivity, (iii) any possible field- and time-dependence of the dielectric permittivity, and (iv) any possible time dependence of the dielectric system under study. Expressions for the local conductivity as well as for the local diffusion-current density were derived through a mass-action approximation for which a detailed theoretical justification is provided in this Chapter. It was found that, in the presence of a finite intrinsic conductivity, both the local conductivity and the local diffusion-current density are related to the space-charge density in a nonlinear fashion, as described by Eqs. (34), (66), (67) and (68), where the local diffusion-current density is generally described as a sum of contributions from the presence of a charge-density gradient and of a temperature gradient. At the limit of zero intrinsic conductivity, it was found that either *p*-type or *n*-type free carriers are dominant. This conclusion provides a linkage between the independent assumptions of (i) a single carrier type and (ii) a negligible intrinsic conductivity in the conventional steady-state SCLC model. For any given space-charge density, it was also verified that the expressions we have derived correctly predict the dominant type of free carriers at the limit of zero intrinsic conductivity.

Future work should be carried out along at least three possible directions: (i) As a further application of this general local conductivity expression, further numerical investigations should be carried out on how charge actually flows inside a compositionally graded ferroelectric film. This would provide answers to interesting questions like: Does a graded ferroelectric system exhibit any kind of charge-density waves upon excitation by an

alternating electric field? What are the physical factors (dielectric permittivity, carrier mobility, etc.) that could limit or enhance the degree of asymmetry in the SCLC currents of a graded ferroelectric film? The latter question has been partially answered by ourselves (Zhou et al., 2005b), where we have theoretically found that the observation of polarization offsets, i.e. the onset of asymmetric SCLC, in a compositionally graded ferroelectric film is conditional upon the presence of relatively large gradients in the polarization and in the dielectric permittivity. Certainly, a detailed understanding of the mechanism of asymmetric electrical conduction in such a graded ferroelectric film would also provide insights into the designing of new types of electrical diodes or rectifiers. The recently derived expression for the local diffusion-current density, as first presented in this Book Chapter (Eqs. (66) to (68)), has also opened up a new dimension for further theoretical investigations: Using this expression, the effect of charge diffusion in the presence of a charge-density gradient or a temperature gradient can be taken into account as well, and a whole new range of problems can be studied. For example, it would be interesting to know whether asymmetric electrical conduction would also occur if a compositionally graded ferroelectric film is driven by a sinusoidal applied temperature difference instead of a sinusoidal applied voltage. In this case, one also needs to take into account the temperature dependence of the various system parameters like the remanent polarization and the dielectric permittivity. The theoretical predictions should then be compared against any available experimental results. (ii) Going back to the generalized SCLC theory itself, it would be important to look for possible experimental verifications of the general local conductivity expression, and to establish a set of physical conditions under which the conductivity expression and the corresponding mass-action approximation are valid. Theoretical predictions from the conductivity expression should be made for real experimental systems and then be compared with available experimental results. It would also be worthwhile to generalize the mass-action approximation, and hence the corresponding local conductivity expression, to other cases where the charge of the free carriers, or the stoichiometric ratio between the concentrations of *p*-type and *n*-type free carriers in the generation-recombination processes, is different. (iii) In the derivation of the Mott-Gurney law $J \sim V^2$, the boundary conditions $E_p(0) = 0$ and $E_n(L) = 0$ were employed to describe the cases of conduction by *p*-type and *n*-type free carriers, respectively. If we keep $E_p(0)$ or $E_n(L)$ as a variable throughout the derivation, an expression of J as a function of $E_p(0)$ or $E_n(L)$ can be obtained and it can be shown that both the boundary conditions $E_p(0) = 0$ and $E_n(L) = 0$ correspond to a state of maximum current density. As an example, for the case of conduction by *p*-type free carriers, we have (Fig. 2)

$$j_p \equiv \frac{J_p L^3}{\mu_p \varepsilon V^2} = \left[\frac{9 - 12 e_p(0)^2}{16}\right] + \sqrt{\left[\frac{9 - 12 e_p(0)^2}{16}\right]^2 + \frac{3}{4} e_p(0)^3 [1 - e_p(0)]} \tag{109}$$

where $e_p(0) \equiv E_p(0)L/V$. If we consider our general local conductivity expression which takes into account the presence of a finite intrinsic conductivity and the simultaneous presence of

p-type and *n*-type free carriers, it would be important to know whether this maximum-current principle can be generally applied to obtain the system's boundary conditions.

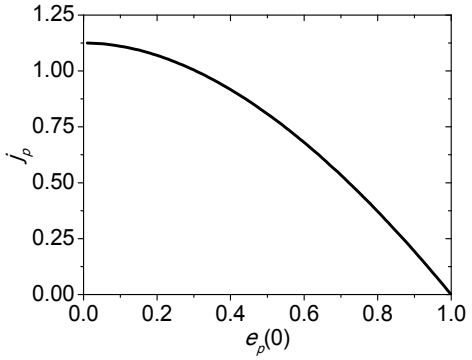

Fig. 2. Plot of j_p against $e_p(0)$, showing a maximum of j_p at $e_p(0) = 0$.

9. Acknowledgments

Stimulating discussions with Prof. Franklin G. Shin, Dr. Chi-Hang Lam and Dr. Yan Zhou are gratefully acknowledged.

10. References

Alpay, S. P.; Ban, Z. G. & Mantese, J. V. (2003). Thermodynamic Analysis of Temperature-graded Ferroelectrics. *Applied Physics Letters*, Vol. 82, pp. 1269 – 1271 (February 2003), ISSN 1077-3118

Bao, D.; Mizutani, N.; Zhang, L. & Yao, X. (2001). Composition Gradient Optimization and Electrical Characterization of (Pb,Ca)TiO_3 Thin Films. *Journal of Applied Physics,* Vol. 89, pp. 801 – 803 (January 2001), ISSN 1089-7550

Bao, D.; Wakiya, N.; Shinozaki, K.; Mizutani, N. & Yao, X. (2001). Abnormal Ferroelectric Properties of Compositionally Graded Pb(Zr,Ti)O_3 Thin Films with $LaNiO_3$ Bottom Electrodes. *Journal of Applied Physics,* Vol. 90, pp. 506 – 508 (July 2001), ISSN 1089-7550

Bao, D.; Mizutani, N.; Yao, X. & Zhang, L. (2000). Structural, Dielectric, and Ferroelectric Properties of Compositionally Graded (Pb,La)TiO_3 Thin Films with Conductive $LaNiO_3$ Bottom Electrodes. *Applied Physics Letters,* Vol. 77, pp. 1041 – 1043 (August 2000), ISSN 1077-3118

Bao, D.; Mizutani, N.; Yao, X. & Zhang, L. (2000). Dielectric and Ferroelectric Properties of Compositionally Graded (Pb,La)TiO_3 Thin Films on Pt/Ti/SiO_2/Si Substrates. *Applied Physics Letters,* Vol. 77, pp. 1203 – 1205 (August 2000), ISSN 1077-3118

Bao, D.; Yao, X. & Zhang, L. (2000). Dielectric Enhancement and Ferroelectric Anomaly of Compositionally Graded (Pb,Ca)TiO_3 Thin Films Derived by a Modified Sol-gel Technique. *Applied Physics Letters,* Vol. 76, pp. 2779 – 2781 (May 2000), ISSN 1077-3118

Bouregba, R.; Poullain, G.; Vilquin, B. & Le Rhun, G. (2003). Asymmetrical Leakage Currents as a Possible Origin of the Polarization Offsets Observed in Compositionally Graded Ferroelectric Films. *Journal of Applied Physics,* Vol. 93, pp. 5583 – 5591 (May 2003), ISSN 1089-7550

Brazier, M.; McElfresh, M. & Mansour, S. (1998). Unconventional Hysteresis Behavior in Compositionally Graded Pb(Zr,Ti)O_3 Thin Films. *Applied Physics Letters,* Vol. 72, pp. 1121 – 1123 (March 1998) , ISSN 1077-3118

Brazier, M.; McElfresh, M. & Mansour, S. (1999). Origin of Anomalous Polarization Offsets in Compositionally Graded Pb(Zr,Ti)O_3 Thin Films. *Applied Physics Letters,* Vol. 74, pp. 299 – 301 (January 1999), ISSN 1077-3118

Carbone, A.; Kotowska, B. K. & Kotowski, D. (2005). Space-Charge-Limited Current Fluctuations in Organic Semiconductors. *Physical Review Letters,* Vol. 95, No. 236601 (December 2005), ISSN 1079-7114

Chan, H. K.; Lam, C. H. & Shin, F. G. (2004). Time-dependent Space-charge-limited Conduction as a Possible Origin of the Polarization Offsets Observed in Compositionally Graded Ferroelectric Films. *Journal of Applied Physics,* Vol. 95, pp. 2665 – 2671 (March 2004), ISSN 1089-7550 [The currently valid email address of the corresponding author Ho-Kei Chan is "epkeiyeah@yahoo.com.hk"]

Chan, H. K.; Zhou, Y.; Lam, C. H. & Shin, F. G. (2007). Theory of Time-dependent Space-charge-limited Conduction, *Proceedings of IEEE 2007 9th International Conference on Solid Dielectrics,* pp. 35 - 38, ISBN 1-4244-0751-6, Winchester, United Kingdom, July 8-13, 2007 [Typo in the paper: Eq. (5) should be referred to as the Mott-Gurney law]

Chen, Z.; Arita, K.; Lim, M. & Paz De Araujo, C. A. (1999). Graded PZT Thin Film Capacitors with Stoichimetric Variation by MOD Technique. *Integrated Ferroelectrics,* Vol. 24, pp. 181 – 188 (August 1999), ISSN 1607-8489

Coelho, R. (1979). *Physics of Dielectrics for the Engineer,* Elsevier Scientific, ISBN 0444417559, New York, United States of America

Fellberg, W.; Mantese, J. V.; Schubring, N. W. & Micheli, A. L. (2001). Origin of the "up", "down" Hysteresis Offsets Observed from Polarization-graded Ferroelectric Materials. *Applied Physics Letters,* Vol. 78, pp. 524 – 526 (January 2001), ISSN 1077-3118

Laha, A. & Krupanidhi, S. B. (2002). Leakage Current Conduction of Pulsed Excimer Laser Ablated $BaBi_2Nb_2O_9$ Thin Films. *Journal of Applied Physics,* Vol. 92, pp. 415 – 420 (July 2002), ISSN 1089-7550

Mantese, J. V. & Alpay, S. P. (2005). *Graded Ferroelectrics, Transpacitors and Transponents,* Springer, ISBN 0387233113, New York, United States of America

Mantese, J. V. ; Schubring, N. W.; Micheli, A. L.; Catalan, A. B.; Mohammed, M. S.; Naik, R. & Auner, G. W. (1997). Slater Model Applied to Polarization Graded Ferroelectrics. *Applied Physics Letters,* Vol. 71, pp. 2047 – 2049 (October 1997), ISSN 1077-3118

Matsuzaki, T. & Funakubo, H. (1999). Preparation and Characterization of Pb(Nb,Ti)O_3 Thin Films by Metalorganic Chemical Vapor Deposition. *Journal of Applied Physics,* Vol. 86, pp. 4559 – 4564 (October 1999), ISSN 1089-7550

Okatan, M. B.; Mantese, J. V. & Alpay, S. P. (2010). Effect of Space Charge on the Polarization Hysteresis Characteristics of Monolithic and Compositionally Graded Ferroelectrics Acta Materialia, Vol. 58, pp. 39 – 48 (January 2010), ISSN 1359-6454

Pope, M. & Swemberg, C. E. (1998). *Electronic Processes in Organic Crystals and Polymers,* Oxford University Press, ISBN 0195129636, Oxford, United Kingdom

Poullain, G.; Bouregba, R.; Vilquin, B.; Le Rhun, G. & Murray, H. (2002). Graded Ferroelectric Thin Films: Possible Origin of the Shift Along the Polarization Axis. *Applied Physics Letters,* Vol. 81, pp. 5015 – 5017 (December 2002), ISSN 1077-3118

Sawyer, C. B. & Tower, C. H. (1930). Rochelle Salt as a Dielectric. *Physical Review,* Vol. 35, pp. 269 – 273 (February 1930), ISSN 0031-899X

Schubring, N. W.; Mantese, J. V.; Micheli, A. L.; Catalan, A. B. & Lopez, R. J. (1992). Charge Pumping and Pseudo-pyroelectric Effect in Active Ferroelectric Relaxor-type Films. *Physical Review Letters,* Vol. 68, pp. 1778 – 1781 (March 1992), ISSN 1079-7114

Suh, K. S.; Kim, J. E.; Oh, W. J.; Yoon, H. G. & Takada, T. (2000). Charge Distribution and Conduction Characteristics of 2-vinylpyridine-grafted Polyethylenes. *Journal of Applied Physics,* Vol. 87, pp. 7333 – 7337 (May 2000), ISSN 1089-7550

Zhou, Y.; Chan, H. K.; Lam, C. H. & Shin, F. G. (2005). Mechanisms of Imprint Effect on Ferroelectric Thin Films. *Journal of Applied Physics,* Vol. 98, No. 024111 (July 2005), ISSN 1089-7550

Zhou, Y.; Chan, H. K.; Lam, C. H. & Shin, F. G. (2005). Effects of Polarization and Permittivity Gradients and Other Parameters on the Anomalous Vertical Shift Behavior of Graded Ferroelectric Thin Films. *Journal of Applied Physics,* Vol. 98, No. 034105 (August 2005), ISSN 1089-7550

Part 5

Modeling: Nonlinearities

25

Nonlinearity and Scaling Behavior in a Ferroelectric Materials

Abdelowahed Hajjaji[1], Mohamed Rguiti[2], Daniel Guyomar[3],
Yahia Boughaleb[4] and Christan Courtois[2]
[1]*Ecole Nationale des Sciences Appliquees d'El Jadida,Université d'el Jadida, EL Jadida,*
[2]*Laboratoire des Materiaux et Procedes, Universite de Lille Nord de France, Maubeuge,*
[3]*Laboratoire de Genie Electrique et Ferroelectricite (LGEF),*
Villeurbanne Cedex,Université de Lyon,
[4]*Departement de Physique, Faculte des Sciences,*
Laboratoire de Physique de la Matiere Condensee (LPMC), El Jadida
[1,4]*Morocco*
[2,3]*France*

1. Introduction

Due to their electromechanical properties, piezoelectric materials are widely used as sensors and actuators [1-3]. Under low driving levels, their behavior remains linear and can be described by means of linear constitutive equations. A majority of the transducers is used on these levels. Increasing the levels of electric field or stress leads to a depoling that results in the degradation of the dielectric and piezoelectric performances. This latter phenomenon is usually considered to be due to the irreversible motion of the domain walls [4-11]. The resulting nonlinear and hysteretic nature of piezoelectric materials induces a power limitation for heavy duty transducers or a lack of controllability for positioners. Consequently, a nonlinear modeling including a hysteresis appears to be a key issue in order to obtain a good understanding of transducer behavior and to determine the boundary conditions of use.
Several models have been proposed in the literature found understanding the hysteretic behavior of various materials.12–14. However, a majority of these phenomenological models is purely eclectic, and it is consequently difficult to interpret the results as a function of other parameters (stress and temperature) in order to obtain a clear physical understanding.

2. Stress/electrical scaling in ferroelectrics

2.1 Presentation of the scaling law

In order to determine a scaling law between the electric field and the stress, one should start by following piezoelectric constitutive equations restricting them in one dimension.
These equations can be formulated with stress and electric field as independent variables, thus giving

$$dS = s_{33}^{E}(E,T)dT + d_{33}(E,T)dE \tag{1}$$

where E, T, and S represent the electric field, the mechanical stress, and the strain, respectively. The constants ε_{33}^{T}, s_{33}^{E}, and d_{33} correspond to the dielectric permittivity, the elastic compliance, and the piezoelectric constant, respectively. Here, the superscripts signify the variable that is held constant, and the subscript 3 indicates the poling direction.
The coefficients are defined as

$$\frac{dS(E,T=0)}{dE} = d_{33} \tag{2}$$

$$\frac{dD(E=0,T)}{dT} = \frac{dP(E=0,T)}{dT} = d_{33} \tag{3}$$

From a given P:

$$\frac{dS(E,T=0)}{dE} = \frac{dP(E=0,T)}{dT} \tag{4}$$

It can also be descried as following;

$$\frac{dS(E,T=0)}{dP(E,T=0)}\frac{dP(E,T=0)}{dE} = \frac{dP(E=0,T)}{dT} \tag{5}$$

The interrelation between the strain (S) and the spontaneous polarization (P) is estimated using a global electrostrictive relationship, i.e., the strain is an even function of the polarization of the polarization,

$$S = \sum_{i=0}^{i=2n} \alpha_i P^i(E,T=0) \quad \text{with } n \in N^+ \tag{6}$$

Here, n is the polynomial order and α_x is the electrostrictive coefficient of order x.
The derivatives of the strain are

$$\frac{dS}{dP(E,T=0)} = \sum_{i=1}^{i=2n} i.\alpha_i P^{i-1}(E,T=0) = h(P(E,T=0)) \tag{7}$$

Introducing the attest relationship in the previous calculations leads to:

$$h(P(E,T=0)).\frac{dP(E,T=0)}{dE} = \frac{dP(E=0,T)}{dT} \tag{8}$$

$$\frac{dP(E,T=0)}{dE} = \frac{dP(E=0,T)}{h(P(E,T=0))dT} \tag{9}$$

$$\frac{dP(E,T=0)}{dE} = \frac{dP(E=0,T)}{d\left(h(P(E,T=0))T\right)} \tag{10}$$

Thus,

$$\Delta E \equiv h(P(E,T=0))\Delta T \text{ and } \Delta T \equiv \frac{\Delta E}{h(P(E,T=0))} \tag{11}$$

Thus, we consider that the term h(P)T plays the same role to the electric field *E*. This statement is fraught with consequence because this equivalence must be preserved for all cycles (*P, S* or coefficients). According to the equation (7), the function h(P) must be odd, so that the effect of "electric field" equivalent reversed with the sign of polarization. Moreover, we know experimentally that the polarization tends to zero when the compressive stress tends to infinity. Moreover, h(P) to zero when the stress tends to infinity for not polarised ceramics in the opposite direction. Precisely, the equivalence implies that the couple $\begin{pmatrix} E = Ec \\ P = 0 \end{pmatrix}$ is equivalent to the couple $\begin{pmatrix} T = \infty \\ P = 0 \end{pmatrix}$. Hence;

$\lim_{T\to\infty} h(P)T = Ec$ => $\lim_{T\to\infty} h(P) = \frac{Ec}{T}$.

As illustrated in the figure 1, the scaling law (1) can be used to derive the stress polarization P behavior from the $P = f(E)$ cycle or reciprocally to drive the polarization behavior versus the electrical field once the $P = g(T)$ cycle is known. As it can be seen of figure in the $P = g(T)$ can be obtained from the $P = f(E)$ cycle by streching the x axis.

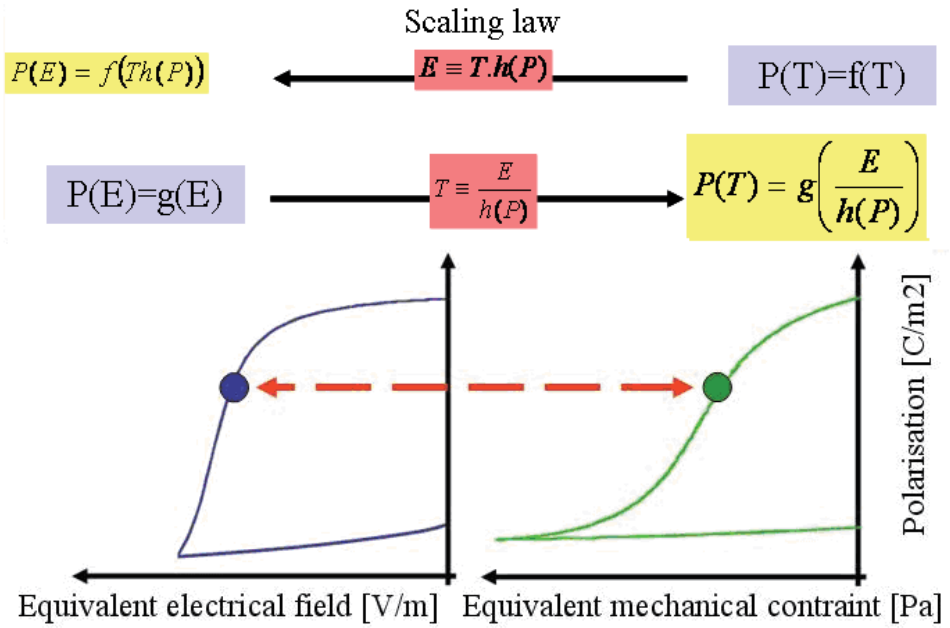

Fig. 1. Schematic illustration of the law scaling (1).

2.2 Determination of the parameters of the scaling law

Considering physical symmetries in the materials, a similar polarization behavior (P) can be observed during variation of an electric field (E) or the mechanical stress (T). Both of these external disturbances are caused by the depoling of the sample. An explication concerning how to apply the scaling law is here given based on the equations developed in Sec. II.

Starting from Eq. (7), the entire derivation of strain by polarization can be calculated based on experimental data, $\frac{dS}{dP(E,T=0)} = h(P(E,T=0))$. In order to determine the right-hand term of Eq. (8) i.e(h(P(E,T=0)), the strain was plotted as a function of the polarization with a variation in electric field. The famous strain—polarization hysteresis loop, shaped as a butterfly—was obtained. It can be approximated by the square of the polarization variation, and neglecting only a small amount of the hysteresis, quadratic electrostriction is obtained, as shown in Fig. 2. A model based on this assumption provides a simplified constitutive law that presents all of the switching behavior in the polarization relation.

Table 1 shows the expression of h(P(E,T=0)) for various structure of ceramics. It is noticeable that the polynomials of h(P(E,T=0)) depend on the structure. The switching of domains and the variation in angles based on the structure (i.e., 90° and 180° for a tetragonal material and 71° and 109° for a rhombohedral material) were believed to be the cause of the variation in the polynomials. Micromechanics models determine domain switching possibilities with an electromechanical energy criterion with an electrical and a mechanical parameter.12,17 These parameters must be greater than the product of the coercive electric field and the critical value of the spontaneous polarization. The 180°, 71°, and 90° domains play different roles in minimizing the free energy.

Material	Structure	Function h(P(E,T=0))
PMN-25PT	Rhomohedral (R)	$0.0589P^3 - 0.0019P^2 + 0.0017P + 0.0001$
PMN-40PT	Tetragonal (T)	$0.2933P^3 - 0.0056P^2 + 0.0392P + 0.0006$
P188	MPB (R+T)	$0.056P$

Table 1.

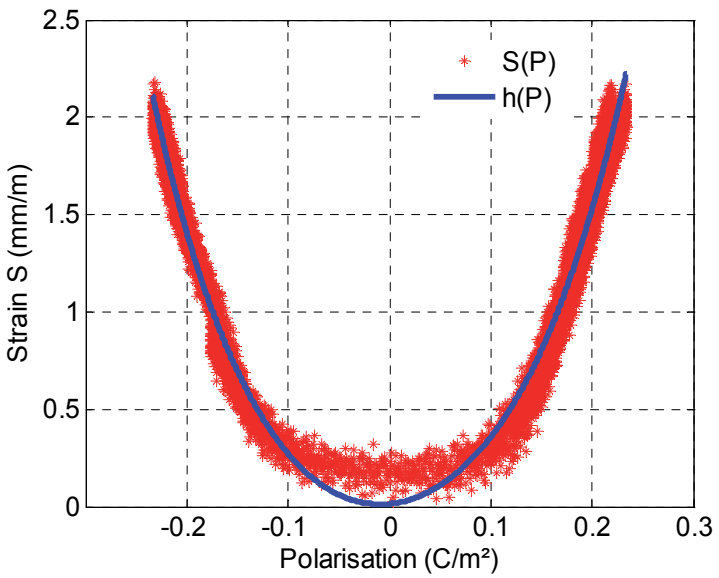

Fig. 2. Strain-electric-displacement hysteresis loops during electric-field loading at zero stress for ferroelectric material.

2.3 Verification of the scaling law

The viability of the proposed scaling law was explored using two distinct experiments on soft PZT. Starting from the experimental depoling under stress P=f(T), the depoling was plotted as a function of h[P(E=0,T)]T] giving $(P = g\{h[P(E=0,T)T]\})$ and was compared to the direct measurement of P=g(E). The electric field dependence of polarizations P=g(E), was plotted as a function of $E/\{h[P(E,T=0)]\}$ (giving $P = g(E/\{h[P(E,T=0)]\}$ and compared to the direct measurement of P= f(T). This is portrayed in Fig. 1. The second comparison was helpful in determining the appropriateness of the scaling law for fields close to the coercive field (Ec). In this area, a small portion of the curve P(E) produced a wide range of constraints on the line P(T) due to $T \to \infty$ when $E \to Ec$. These results are presented in Fig. 3

In a general manner, the experimental and reconstructed cycles demonstrated reasonable agreements, with regard to both increasing and decreasing paths, for the soft PZT.

This good agreement for both P(E) and P(T) cycles thus confirmed the viability of the scaling law for soft PZT. Only one parameter ruled the "scale" of the strain and the scale of the stress effect. This ease of conversion between P(E) and P(T) cycles by such a simple law gives numerous opportunities regarding the use of piezoelectric materials. It is possible to predict the depoling behavior over the entire stress cycle (compressive or tensile)/field plane. These results are important to the design and performance of actuators and sonar transducers.

The proposed scaling law can be used for several electrical models in order to understand the hysteretic behaviour of piezoelectric materials [12-14]. This scaling law is interesting in order to introduce the stress as an equivalent electric field; the behavior of ferroelectric materials under a combined electric field (E) and stress (T) can thus be determined. It is also interesting to note that for practical use, the maximum stress can be determined from this scaling law. This result is presented in Fig. 3. The small variations of polarization were observed for applied electric field lower than E_M (here, 0.7 kV/mm). Therefore polarizations undergo a rapid change in polarization. Based on this E_M value, the equivalent stress (T_M) can be directly obtained (40 MPa). As a consequence, the maximum stress for application can be obtained without stress experiment.

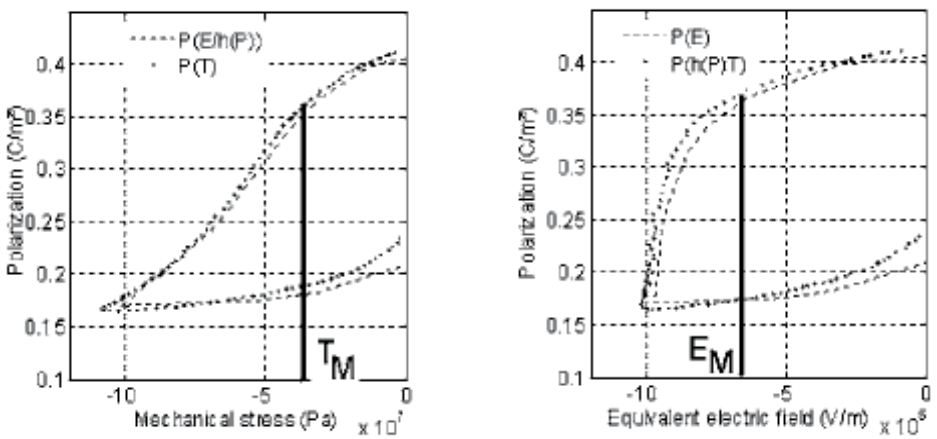

Fig. 3. Experimental validation of the scaling law for soft PZT

3. Temperature/electric field scaling in ferroelectrics

3.1 Presentation of the scaling law

In order to determine a scaling law between the electric field and the temperature, one should start by following the piezoelectric constrictive equations, restricting them in one dimension.

These equations can be formulated with the temperature and the electric field as independent variables; thus, giving

$$d\Gamma = c.\frac{d\theta}{\theta}.d\theta + p.dE \text{ and } dD = \varepsilon_{33}^{T} dE + pd\theta \tag{12}$$

$$D = \varepsilon_0 E + P \tag{13}$$

D, P, E, θ *and* Γ and G represent the electric displacement, the polarization, the electric field, the temperature and the entropy, respectively, and where c and p, respectively, correspond to the heat capacity and the pyroelectric coefficient. Here, the superscripts signify the variable that is held constant, and the subscript 3 indicates the poling direction. Since the polarization is large enough compared to $\varepsilon_0 E$, $P >> \varepsilon_0 E$, then $D \approx P$.

The coefficients are defined as:

$$\frac{d\Gamma(E,\theta_0)}{dE} = p \tag{14}$$

$$\frac{dD(E_0,\theta)}{d\theta} = \frac{dP(E_0,\theta)}{d\theta} = p \tag{15}$$

For a given P:

$$\frac{d\Gamma(E,\theta_0)}{dE} = \frac{dP(E_0,\theta)}{d\theta} = p \tag{16}$$

which can also expressed as:

$$\frac{d\Gamma(E,\theta_0)}{dP(E,\theta_0)}\frac{dP(E,\theta_0)}{dE} = \frac{dP(E_0,\theta)}{d\theta} = p \tag{17}$$

Here, θ_0 and E_0 correspond to room temperature (298 K) and the initial electric field (0 kV/mm), respectively.

From a physical point of view, the entropy cannot depend on the polarization orientation in the ferroelectrics material. It means that the entropy must be an even function of polarization. Limiting the entropy expansion to the second order and ensuring

$$\Gamma = \alpha P + \beta.P^2 \tag{18}$$

Here, α and β are a two constant.

The derivatives of the strain can be written as:

$$\frac{d\Gamma}{dP(E,\theta_0)} = \alpha + 2\beta.P(E,\theta_0) \tag{19}$$

Introducing Eq. (19) in the previous calculations leads to:

$$\alpha + 2.\beta.P(E,\theta_0).\frac{dP(E,\theta_0)}{dE} = \frac{dP(E_0,\theta)}{d\theta} = p \tag{20}$$

$$\frac{dP(E,\theta_0)}{dE} = \frac{dP(E_0,\theta)}{(\alpha + 2.\beta.P(E,\theta_0))d\theta} = p \tag{21}$$

The function $\alpha + 2.\beta.P(E,\theta_0)$ does not depend on temperature.
Thus, Eq. 21 can be written as

$$\frac{dP(E,\theta_0)}{dE} = \frac{dP(E_0,\theta)}{d\left(\alpha + 2.\beta.P(E,\theta_0).\theta\right)} = p \tag{22}$$

According to Fig. 4, for a given value of polarization (P), we can write the following equality $P = dP(E,\theta_0) = dP(E_0,\theta)$
Thus,

$$\Delta E \equiv \alpha + 2.\beta.P(E,\theta_0)).\Delta\theta \text{ and } \Delta\theta \equiv \frac{\Delta E}{\alpha + 2.\beta.P(E,\theta_0))} \tag{23}$$

With; $\Delta E \equiv E - E_0 = E$ and $\Delta\theta = \theta - \theta_0$
The term $\alpha + 2.\beta.P(E,\theta_0)).\Delta\theta$ can thereby be considered to play an equivalent role as that of the electric field (ΔE). Such a statement is fraught with a consequence, since this equivalence must be preserved for all cycles (P, Γ or coefficients). Moreover, $(\alpha + 2.\beta.P(E,\theta_0)).\Delta\theta$ is equal to $\alpha.\Delta\theta_C$ $(\alpha \times \Delta\theta_C = E_C, P = 0)$ when the temperature tends to Curie temperature (θ_C).
The equivalence thus precisely implies that the couple $\begin{pmatrix} E = Ec \\ P = 0 \end{pmatrix}$ is equivalent to the couple $\begin{pmatrix} \theta = \theta_C \\ P = 0 \end{pmatrix}$. Hence;

$$\lim_{\theta \to \theta_C} (\alpha + 2.\beta.P(E,\theta_0)).\Delta\theta) = E_C \Rightarrow \lim_{\theta \to \theta_C} (\alpha + 2.\beta.P(E,\theta_0)) = \frac{E_C}{\Delta\theta_C} = \alpha \tag{24}$$

As illustrated in Fig. 4, the scaling law can be used to derive the behavior of the polarization as a function of the temperature P(θ) from P(E) cycle, or reciprocally to drive the polarization behavior versus the electrical field, once the P(E) cycle is known.

3.2 Verification of the scaling law

The effects of various electric fields and temperatures on the polarization profile are illustrated in Figure 5, where Figure 5(a) represents the polarization variation as a function of the temperature for an electric field E=0 V/mm. It was shown by Hajjaji et al [15] that the depolarization as a function of the temperature was mainly due to the decrease in the dipole moment and the fact that the variation in this dipole moment was reversible. In the vicinity of the ferroelectric to paraelectric transition, the temperature depolarization of the ceramics

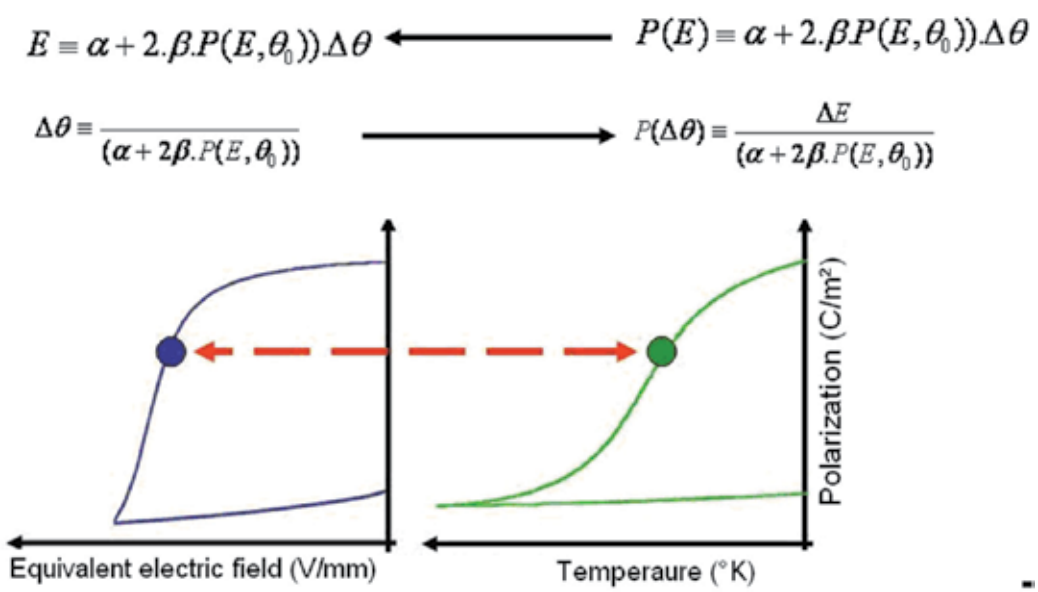

Fig. 4. Schematic illustration of the temperature/electric field scaling law

was the result of a 0–90° domain switching, whereas a 0–180° domain switching did not occur with temperature. The effects were thus quite obvious. At a fixed θ (cf. Fig. 2(b)), the polarization variation was minor for low applied electric fields. It then began to increase as E increased gradually from 350 V/mm (a value close to Ec). For the electric field, the depolarization of the ceramic was governed by the domain wall motion. As demonstrated by Pruvost et al.[27], the depolarization process under an electric field was more complicated than its counterpart under a compressed stress or temperature in the sense that the electric field depolarization involved more than one mechanism. For electric tetragonal ceramics; there existed three possibilities for domain switching: 0–90°, 90–180°, and 0–180°. It should be pointed out that the focus of the present study was to investigate the characteristics of the polarization variation when the sample was in a stable state. For this, the employed fields (E) were below 450 V/mm (E<Ec) and the temperature dependence took place below 373 K.

Despite the difference between the mechanisms of depolarization as a function of electric field and temperature, we have try determining a law that links the two (electric field E and temperature θ) and to identify one from another.

In order to obtain a suitable scaling relation for the ceramic, one can first follow the suggested scaling law given in Eq. (23). This enables a direct determination of the proportionality coefficients α and β from the experimental data. The coefficient α can be determined from the following equation (24) ($\frac{E_C}{\Delta\theta_C} = \alpha = 4300$) . According to Fig 5(a and b), a plot of the eclectic field (ΔE) as a function of Δθ renders it possible to obtain the coefficient β (β=3000). Based on the plot in Figure 3, it was revealed that the experimental data could be fitted (with R^2=0.99), within the measured uncertainty, by: $\Delta E = (\alpha + 2.\beta.P(E,\theta_0)).\Delta\theta$.

In addition, the viability of the proposed scaling law was explored by way of two distinct experiments on soft PZT. Starting from the experimental depoling under temperature $P(\theta)$,

the depoling was plotted as a function of $(\alpha+2.\beta.P(E_0,\theta)\times\Delta\theta)$ (giving $P(\alpha+2.\beta P(E_0,\theta)\times\Delta\theta)$ and was compared to the direct measurement of *P(E)*. The experimental result under an electric field, *P(E)*, was plotted as a function of $\frac{E}{(\alpha+2.\beta.P(E,\theta_0))}$ (giving $P(\frac{E}{\alpha+2.\beta.P(E,\theta_0)})$) and was compared to the direct measurement of P(θ). This is depicted in Figure4.

The second comparison was helpful in determining the appropriateness of the scaling law for fields close to the coercive field *(E_c)*. In this area, a small portion of the curve *P(E)* produced a wide range of temperatures on the line *P(θ)*, due to $\theta\rightarrow\theta_C$ when $E\rightarrow Ec$ (cf. Figures 6 and 7). In a general manner, the experimental and reconstructed cycles were in reasonably good agreement, with regard to both increasing and decreasing paths. This decent correlation for both the *P(E)* and *P(θ)* cycles thus confirmed the viability of the scaling law.

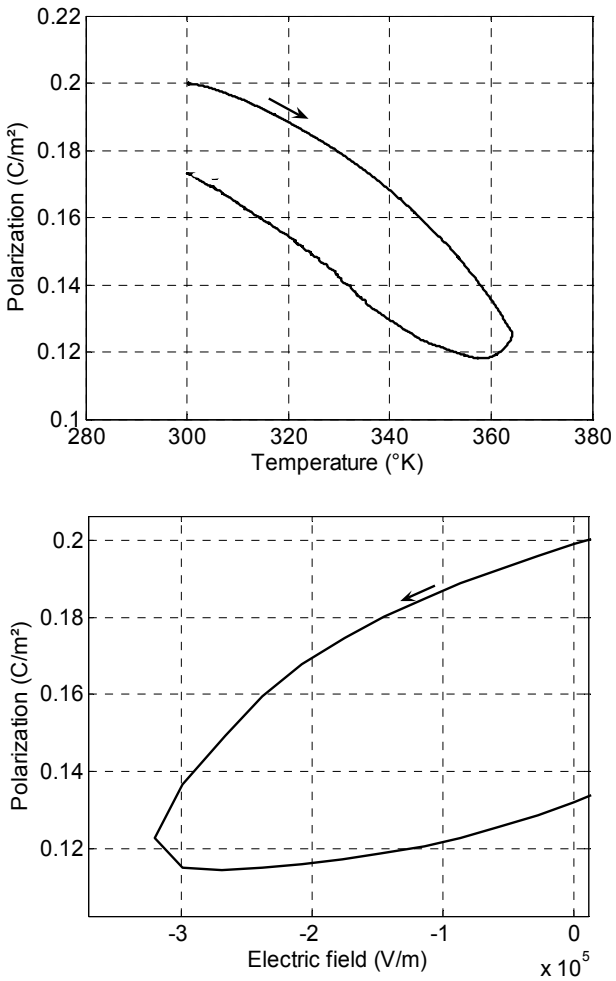

Fig. 5. (a) Polarization versus electric field on $Pb(Mg_{1/3}Nb_{2/3})_{0.75}Ti_{0.25}O_3$ ceramic. (b) Polarization versus temperature on $Pb(Mg_{1/3}Nb_{2/3})_{0.75}Ti_{0.25}O_3$ ceramic

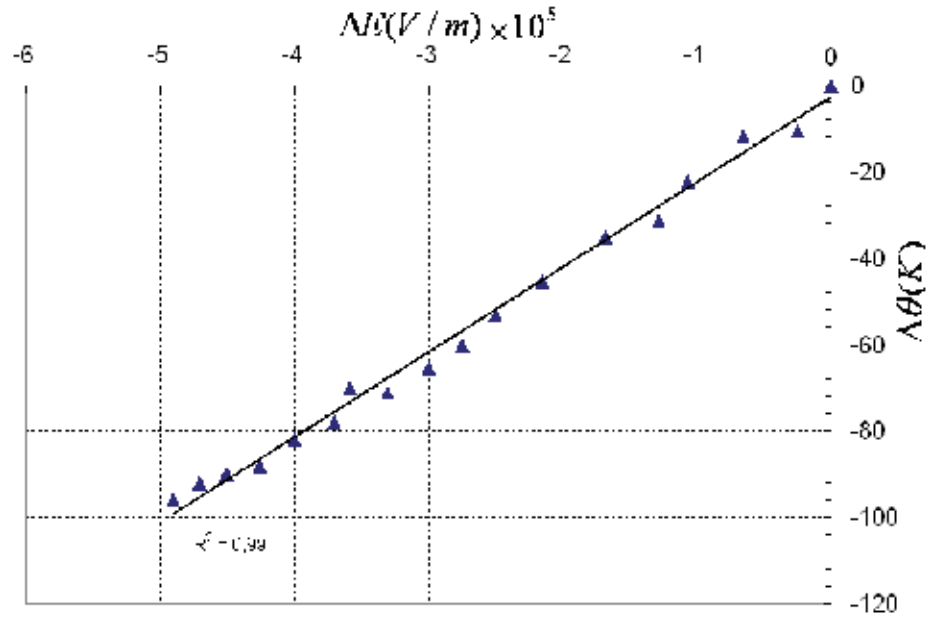

Fig. 6. Scaling of electric field against (Δθ) for $Pb(Mg_{1/3}Nb_{2/3})_{0.75}Ti_{0.25}O_3$ ceramic

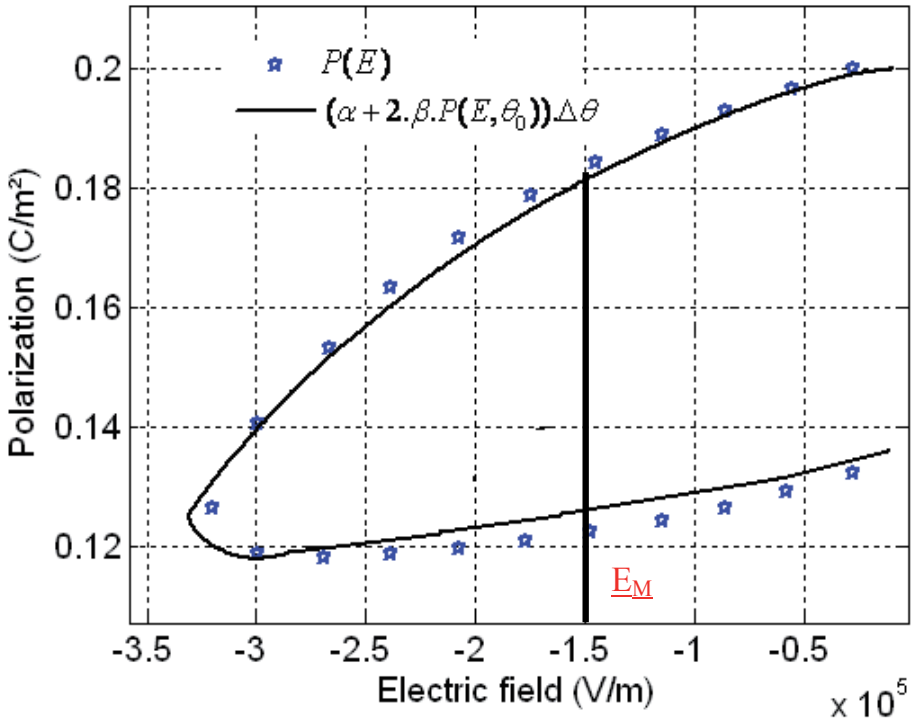

Fig. 7. Experimental validation of the scaling law for PMN-25PT ceramic

It is interesting to note that for purely electrical measurements, the presented law rendered it possible to determine the maximum temperature for practical use (cf. Figure 7). Small variations in polarization were observed for an applied electric field lower than E_M (here, 150 V/mm), leading to the conclusion that the polarizations underwent a rapid change. Based on the obtained E_M value, one can determine the equivalent temperature (θ_M) corresponding to the maximum temperature used.

The relationship $\Delta\theta = \frac{E}{\alpha + 2.\beta.P(E,\theta_0)}$ leads to both a negative, i.e., $\Delta\theta_{\min} = \frac{E_{\min}}{\alpha + 2.\beta.P(E_{\min},\theta_0)}$, and a positive, i.e., $\Delta\theta_{\max} = \frac{E_{\max}}{\alpha + 2.\beta.P(E_{\max},\theta_0)}$, bound. The absolute value of $\Delta\theta_{min}$ can thus be considered to be much larger than $\Delta\theta_{max}$. Consequently, a symmetric electrical field cycle would give rise to a dissymmetric cycle in terms of temperature. Reciprocally, a symmetric temperature cycle would result in an asymmetric cycle in terms of the electrical field.

4. Temperature/stress scaling in ferroelectrics

4.1 Presentation of the scaling law

In order to determine the general laws between the mechanical stress, electrical field, and the temperature, we are based on previous studies of Guyomar et al [7]. These studies were proposed a scaling effect between electric field and a term composed by the polarization multiplied by the stress:

$$\Delta E \equiv \alpha \Delta T \times P(E,T_0) \tag{25}$$

Where α is the proportionality constant between ΔE and ΔT. Both ΔE and ΔT represent the electric field and the mechanical stress variation. $P(E,T_0)$ is the polarization at zero stress(T_0=0MPa).

In the other study Hajjaji et al proposed a scaling law between the electrical field and the temperature [16]. This law is expressed by the following expression.

$$\Delta E \equiv (\chi + 2\beta \times P(E,\theta_0)) \times \Delta\theta \tag{26}$$

Here, χ and β are a two constant. $P(E, \theta_0)$ is the polarization at room temperature (θ_0=298K) and Δθ is the temperature variation.

In most cases the coefficient χ is negligible compared to $2\beta \times P(E,\theta_0)$. Thus, the expression (26) becomes:

$$\Delta E \equiv (2\beta \times P(E,\theta_0)) \times \Delta\theta \text{ and } \Delta\theta \equiv \frac{\Delta E}{(2 \times \beta.P(E,\theta_0))} \tag{27}$$

With; $\Delta E \equiv E - E_0 = E$ and $\Delta\theta = \theta - \theta_0$

According to equations (25) and (27) we find the following expression:

$$\Delta E \equiv \alpha \Delta T \times P(E,T_0) \equiv 2\beta \times P(E,\theta_0) \tag{28}$$

$$P(E,T_0) = P(E,\theta_0)$$

$$\alpha\Delta T \equiv 2\beta\Delta\theta \tag{29}$$

With; $\Delta E \equiv T - T_0 = T$ and $\Delta\theta = \theta - \theta_0$ $\quad (\theta_0 = 298K)$

Thus

$$T \equiv \delta \times \Delta\theta \tag{30}$$

As illustrated in figure 8, we determine P(T) and P(θ) from P(E) (steps 1 and 3), P(E) and P(θ) from P(T) (steps 1 and 2), and at the end we can determine P(E) and P(T) from P(θ) (steps 2 and 3),.

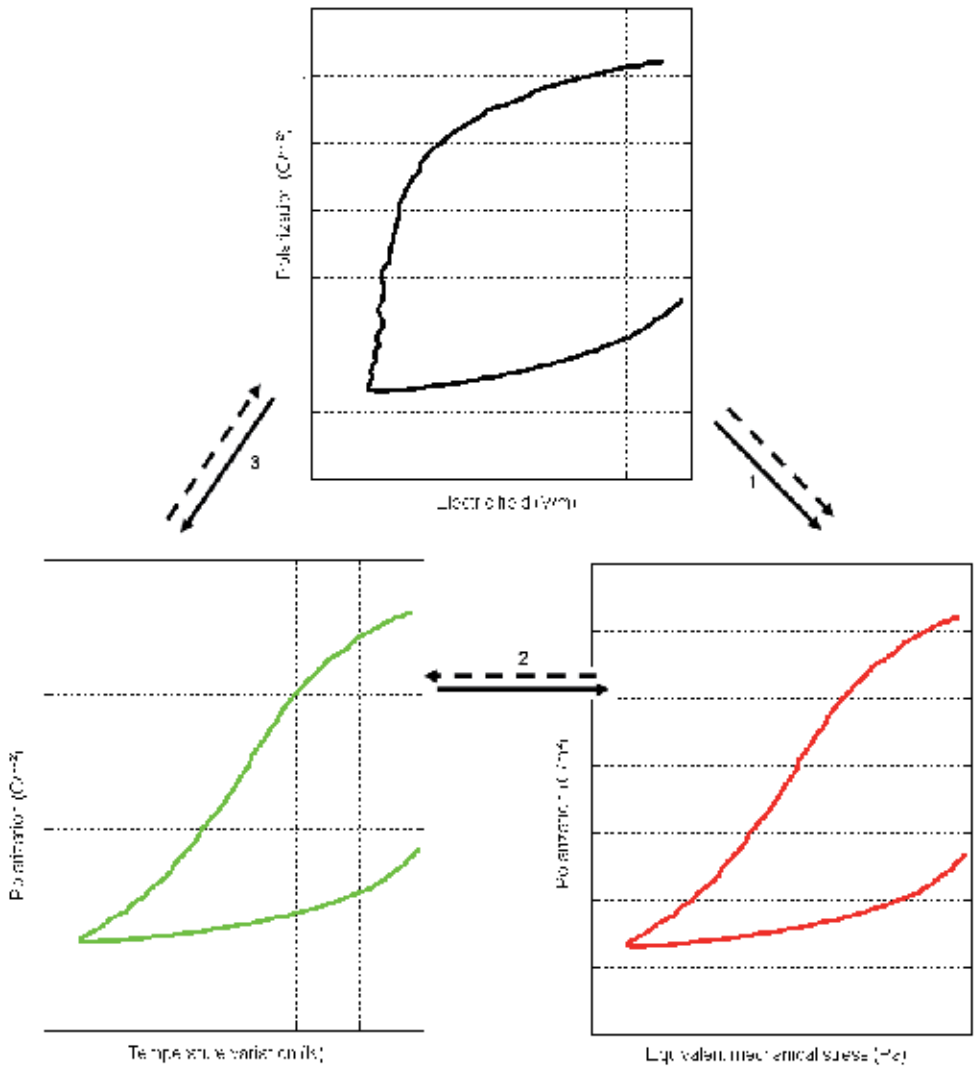

Fig. 8. Schematic illustration of the scaling laws

4.2 Verification of the scaling law

Figure 9 shows the relation between ΔT and $\frac{\Delta E}{P(E,T_0)}$ where good linear fits are apparent (R close to 1). This implies a power-law relation between the mechanical stress and electric field, i.e., ($\Delta E \equiv \alpha \Delta T \times P(E,T_0)$, the exponent α can be extracted from the slope, i.e. $\alpha = \frac{d(\frac{(\Delta E)}{P(E,T_0)})}{d(\Delta T)}$.

The expression (25) allows expressing the mechanical stress as an equivalent electric field and the electric field as an equivalent stress. Thus, a good agreement between electrical field and mechanical stress proved that the proposed scaling law allows predicting the depoling behavior under stress using only purely electrical measurements. Reciprocally, the predictions of the depoling behaviour under an electrical field were permitted using only purely mechanical measurements. It was found that such an approach permitted the prediction of the maximal stress application from purely electrical measurements (i.e., measurements of S(E) and P(E)). The maximal stress for application is the stress that can be applied to materials without they lose their piezoelectric properties.

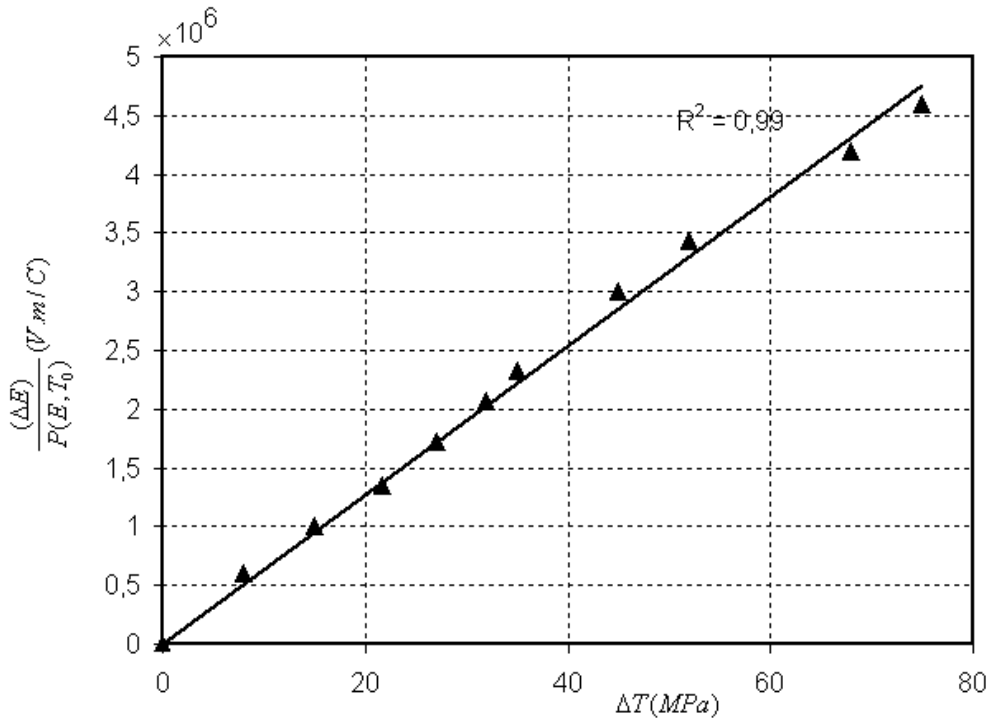

Fig. 9. Experimental validation of the scaling law between electrical field and mechanical stress for PZT ceramic

In the other study we proposed a scaling law between the electrical field and the temperature [16]. This law is expressed by the expression (25) ($\Delta E \equiv (2\beta \times P(E,\theta_0)).\Delta\theta$).

Figure 10 shows the relation between $\frac{\Delta E}{P(E,\theta_0)}$ and $\Delta\theta$ where good linear fits are apparent (R close to 1). This implies a power-law relation between the temperature and electric field, i.e., $(\Delta E \equiv (2\beta \times P(E,\theta_0)).\Delta\theta)$, the exponent β can be extracted from the slope, i.e. $2\beta = \frac{d(\frac{\Delta E}{P(E,\theta_0)})}{d(\Delta\theta)}$.

According to this law, it is possible to determine the behavior of the polarization in function of temperature from the electrical measurements. Reciprocally, it is possible to determine the behavior of the polarization in function of the electric field from thermal measurements. It is interesting to note that for purely electrical measurements, the presented law rendered it possible to determine the maximum temperature for practical use. Small variations in polarization were observed for an applied electric field lower than E_M (here, 150 V/mm), leading to the conclusion that the polarizations underwent a rapid change. Based on the obtained E_M value, one can determine the equivalent temperature (θ_M) corresponding to the maximum temperature used.

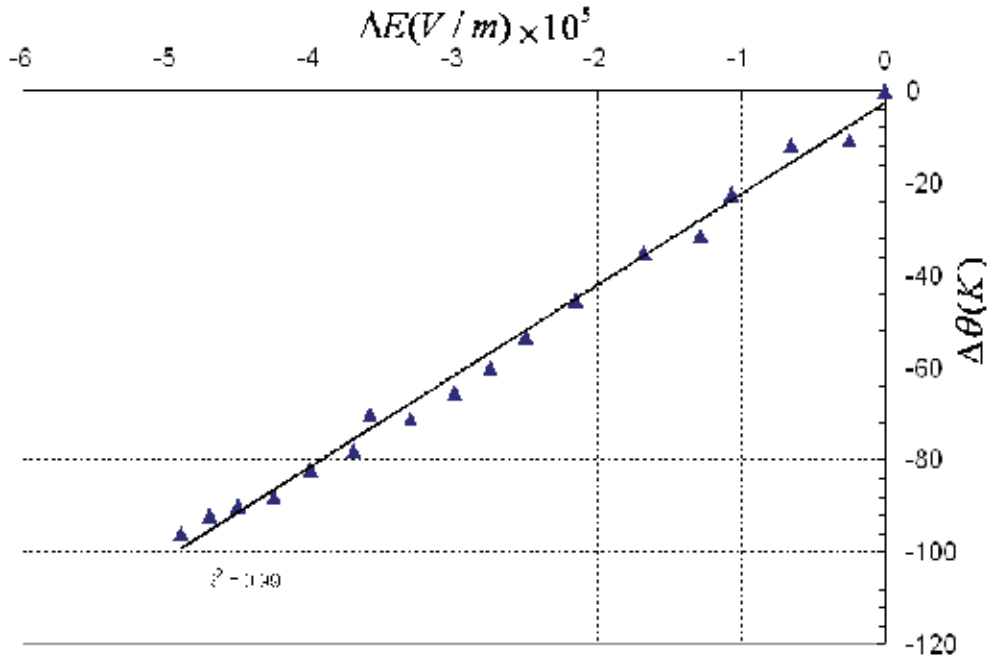

Fig. 10. Experimental validation of the scaling law between electrical temperature variations for PZT ceramic

Considering physical symmetries, similar behaviors can be observed under stress or temperature. Indeed both external disturbances may result in depling of the sample. We consider here a scaling effect that is described with (equation 30): $T \equiv \delta \times \Delta\theta$.

Where T is the mechanical stress, $\Delta\theta$ the temperature variation, and δ the scaling parameter. We therefore explore the viability of this assumption using two distinct

experiments on the same PZT material. We record first the depoling under mechanical stress. In a second time, we record the depoling under temperature. We try to obtain the same depoling values under mechanical stress or temperature in order to compare therefore the scaling effect. Starting from the experimental depoling under mechanical stress P(T), we plot the depoling as a function of "$\frac{T}{\delta}$" P($\frac{T}{\delta}$) and is compared to direct measurement $P(\Delta\theta)$. In the same manner the the experimental result under stress P($\Delta\theta$) is plotted as a function of $\delta\times\Delta\theta$ (giving P($\delta\times\Delta\theta$)) and compared to the direct measurement P(T). In figure 4 are shown these results. The agreement is outstanding considering the different natures of mechanical stress and temperature. The two external disturbances acts very differently on the domain configurations [8-11], but at the macroscopic scale, over an important averaging, it is shown here that a very sharp scaling law can be considered. It is important to note the consequences of such a scaling once it has been demonstrated experimentally. It is possible to predict the poling behavior over the entire stress/temperature plane as shown on figure 11.

In order to confirm these results, we plotted the mechanical stress as a function to the temperature variation. Figure 12 shows the relation between Δθ and *T*, where good linear fits are apparent (*R*2 close to 1). This implies a power-law relation between the stress and temperature, i.e., ($T \equiv \delta\times\Delta\theta$), the exponent δ can be extracted from the slope, i.e. $\delta = \frac{d(T)}{d(\Delta\theta)}$. According to figure 12, the coefficient δ is equal to 0.35×10^6.

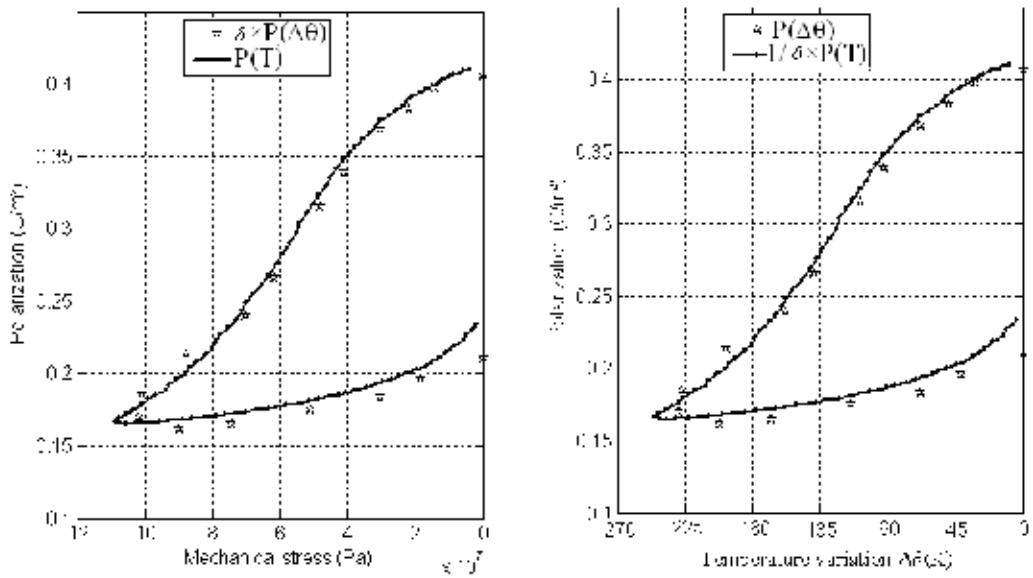

Fig. 11. Experimental validation of the scaling law for soft PZT ceramic.

In the literature, a majority of these phenomenological models are purely electric, mechanic, or thermal [19-22]. Consequently, it is difficult to interpret the results as a function of the combined to two or three excitations (mechanical stress and temperature for example).

The proposed scaling law can be used for several models have been proposed in the literature for comprehending the hysteretic behavior of various materials, which renders it interesting for introducing the temperature as an equivalent to the mechanical stress, or reciprocally to introducing the mechanical stress as an equivalent to the temperature.
The behavior of ferroelectric materials under a combined mechanical stress (T) and temperature (θ) can thus be determined, which will help in the identification and understanding of the effect of the simultaneous action of temperature and mechanical stress on ceramics.
According to this law, it is possible to determine the behavior of the polarization in function of temperature from the mechanical measurements. Reciprocally, it is possible to determine the behavior of the polarization in function of the mechanical stress from thermal measurements. It is interesting to note that for purely mechanical measurements, the presented law rendered it possible to determine the maximum temperature for practical use, and reciprocally it is possible to determine the maximum stress for practical use from purely thermal measurements.

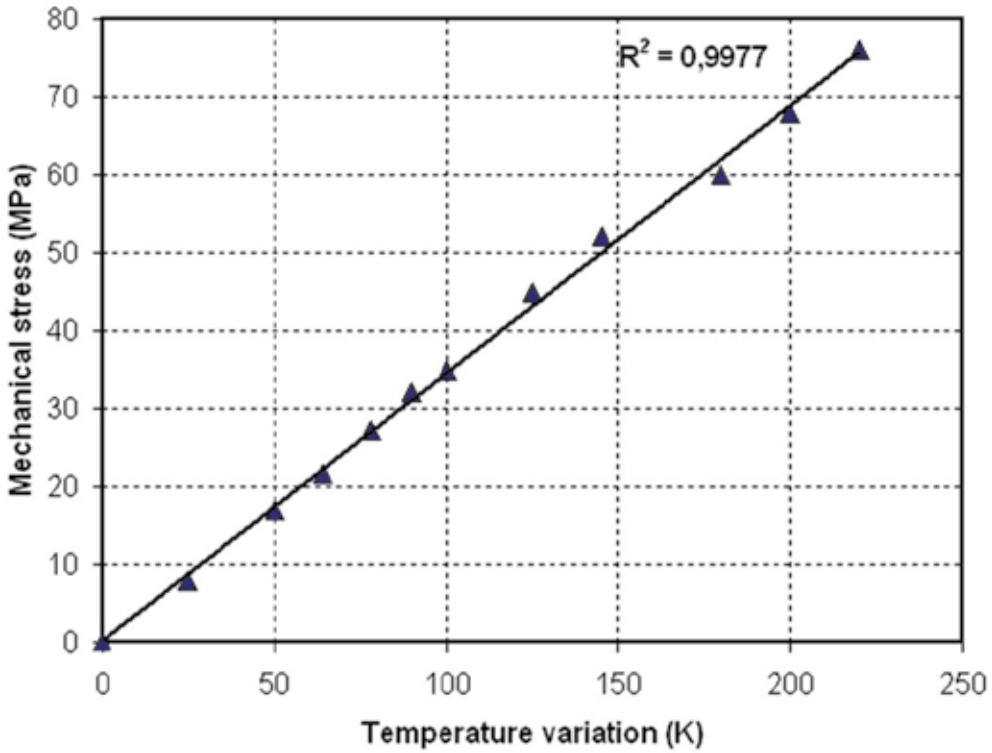

Fig. 12. Experimental validation of the scaling law between mechanical stress and temperature variation for PZT ceramic

5. Predictions of material behavior

Due to their electromechanical properties, piezoelectric materials are widely employed as sensors and actuators [16-17]. Most of these piezoelectric materials are utilized under

different conditions (stress, electrical field, and temperature).It would thus be interesting to predict their behaviors under a variety of excitations without having to perform too much experimental work, i.e., just carrying out a single experiment and providing the other experimental values. For example, from a simple measurement of the polarization as a function of the electric field, one could predict the behavior of the polarization as a function of temperature negative and positive(step 2) and stress (compressive and tensile stress) (step 1). In conclusion, we could determine P(T) and P(θ) from P(E) (steps 1 and 3),P(E) and P(θ) from P(T) (steps 1 and 2), and finally P(E) and P(T) from P(θ) (steps 2 and 3),.

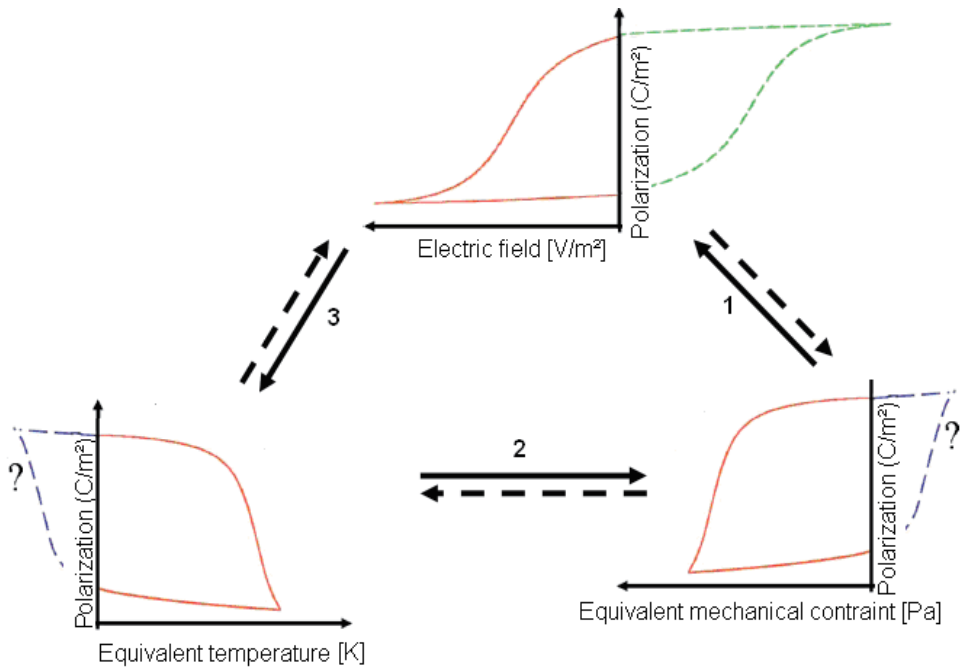

Fig. 13. Schematic illustration of the material behavior under excitations.

6. Relationship between the coefficients d_{33} and ε_{33}

The proposed scaling law can also be applied to the minor cycles. This fact provides a great advantage for the problem of the relation between ε_{33} and d_{33} according to

$$\varepsilon_{33} = \frac{\partial P}{\partial E} \tag{2}$$

$$d_{33} = \frac{\partial P}{\partial T} \tag{3}$$

It is quite difficult to experimentally obtain a real d33 corresponding to an exact ε_{33}. During the experiment, the electrical field (E) was stopped at a certain level to obtain a value of the polarization (P), and the permittivity (ε_{33}) could thus be defined. When E was stopped, d_{33} was calculated based on the obtained$_{33}$ and did consequently not correspond to thereal d_{33}.

As illustrated in Fig. 14, the measuring point for P was not on the main cycle but slightly beside, on the minor cycle. This result was due to the difference of $E_0+\Delta E$ from ε, not corresponding to that of $T_0+\Delta T$ from d_{33}. Resultantly, the calculation of d_{33} could not be based on an exact value. By using the proposed simple scaling law, on the other hand, it was possible to obtain an exact value for d_{33},

$$\frac{\partial P}{\partial T} = -h(P)\frac{\partial P}{\partial E} \tag{4}$$

thus,

$$d_{33} = -h(P)P\varepsilon_{33}\,. \tag{5}$$

Figure 15 depicts the prediction of the piezoelectric constant (d_{33}) under a compressive stress. In this case, d_{33} was calculated from the function h[P(E,T=0)] and compared with experimental values. It could be observed that the experimental and calculated piezoelectric constants displayed a similar variation with the compressive stress. Such a good agreement between simulation and experiment proved that the proposed law scaling rendered it possible to predict the piezoelectric constant (d_{33}) under stress using only purely electrical measurements. Reciprocally, predictions of the dielectric constant (ε_{33}) under an electrical field were permitted using only purely mechanical measurements.

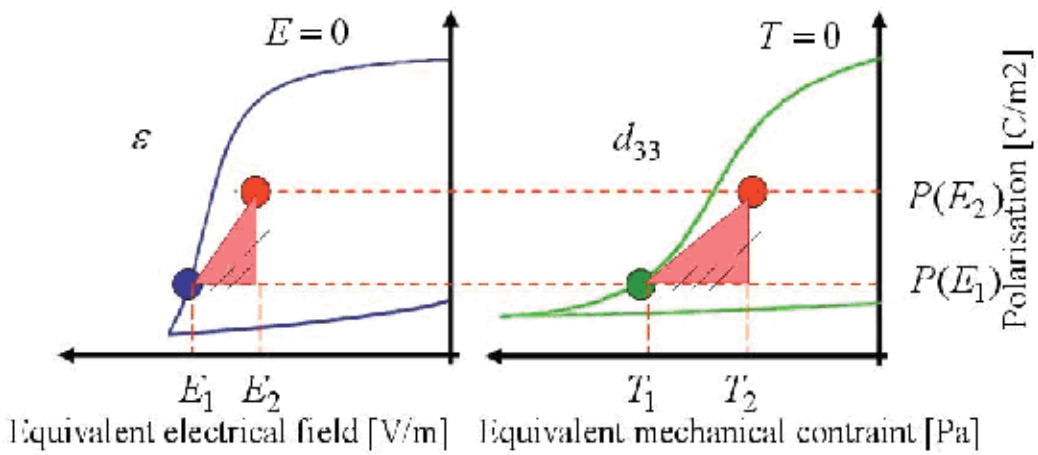

Fig. 14. relation between ε_{33} et d_{33}

7. Conclusion

The present chapter proposes a three simple scaling laws taking into account the electrical field, the stress, temperature, and the polarization of ferroelectric materials in the form of $\Delta E \equiv \alpha\Delta T \times P(E,T_0)$, $\Delta E \equiv (2\beta \times P(E,\theta_0)).\Delta\theta$ and $\Delta T \equiv \delta \times \Delta\theta$. The nonlinear behavior was considered and compared to that predicted by a linear reversible constitutive law in order to demonstrate the range of validity of the linear assumptions.

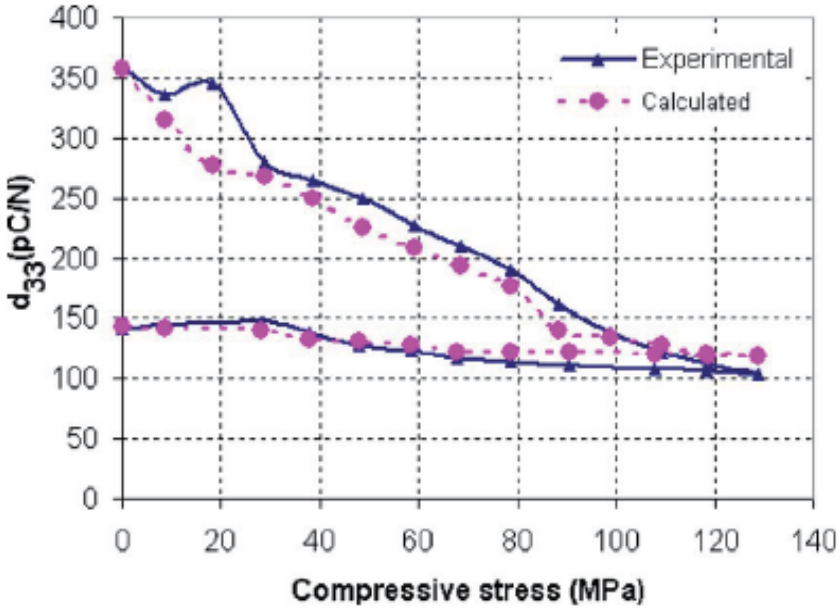

Fig. 15. (Color online) Evolution of the piezoelectric coefficient under compressive stress

The proposed scaling laws can be used for several models have been proposed in the literature for comprehending the hysteretic behavior of various materials, which renders it interesting to interpret the results as a function of the combined to two or three excitations (mechanical stress and temperature for example).The ease of conversion between P(E), P(θ) and P(T) cycles by such a simple laws gives numerous opportunities regarding the use of piezoelectric materials. It was possible to predict the depoling behavior over the entire stress cycle (compressive or tensile), or to predict the depoling behavior over the entire temperature cycle (negative or positive) from to the hysteresis cycle. Thus, one should note that applying a symmetric electrical field cycle leads to a dissymmetric cycle under stress and temperature. Consequently, the polarization behaves differently as a function of compressive as opposed to tensile stresses. Moreover, the polarization behaves also differently as a function of positive and negative temperature.

8. References

[1] L. E. Cross, Ferroelectrics 76,241 (1987).
[2] G. H. Haertling, J. Am. Ceram. Soc. 82, 797 (1999).
[3] S. E. Park and T. R. Shrout, IEEE Trans. Ultrason. Ferroelectr. Freq.
[4] B. Jaffe, W. R. Cook, and H. Jaffe, Piezoelectric Ceramics Academic, London, (1971)
[5] C. Bedoya, C. H. Muller, J.-L. Baudour, V. Madigou, M. Anne, and M. Roubin, Mater. Sci. Eng., B 75,43 (2000).
[6] E. C. Subbarao, M. C. McQuarrie, and W. R. Buessem, J. Appl. Phys. 28, 1194 (1957).
[7] A. Hajjaji, S. Pruvost, G. Sebald, L. Lebrun, D. Guyomar, and K. Benkhouja, Solid State Sci. 10, 1020 (2008).
[8] S. Pruvost, G. Sebald, L. Lebrun, D. Guyomar, and L. Severat, Acta Mater. 56, 215 (2008).

[9] vA. E. Glazounov and M. J. Hoffmann, J. Eur. Ceram. Soc. 21, 1417 (2001).
[10] D. Berlincourt, H. Helmut, and H. A. Krueger, J. Appl. Phys. 30, 1804 (1959).
[11] A. Hajjaji, S. Pruvost, G. Sebald, L. Lebrun, D. Guyomar, and K. Benkhouja, Acta Mater. 57, 2243 (2009).
[12] S. C. Hwang, J. E. Huber, R. M. McMeeking, and N. A. Fleck, J. Appl. Phys. 84, 1530 (1998).
[13] T. Steinkopff, J. Eur. Ceram. Soc. 19,1247 (1999).
[14] B. Ducharne, D. Guyomar, and G. Sebald, J. Phys. D 40,551 (2007).
[15] A Hajjaji, S Pruvost, G Sebald, L Lebrun, D Guyomar, K Benkhouja, Acta Mater. 57 (2009) 2243.
[16] A. Hajjaji, D. Guyomar, S. Pruvost, S. Touhtouh, K. Yuse, and Y. Boughaleb, Physica B (2010).
[17] G. H. Haertling, J. Am. Ceram. Soc. 82, 797 (1999).
[18] S.-E. Park and T. R. Shrout, IEEE Trans. Ultrason. Ferroelectr. Freq. Control 44, 1140 (1997).
[19] S. C. Hwang, J. E. Huber, R. M. McMeeking, and N. A. Fleck, J. Appl.Phys. 84, 1530 (1998).
[20] T. Steinkopff, J. Eur. Ceram. Soc. 19,1247 (1999).
[21] B. Ducharne, D. Guyomar, and G. Sebald, J. Phys. D: Appl. Phys. 40,551 (2007).
[22] G. Sebald, S. Pruvost, L. Seveyrat, L. Lebrun, and D. Guyomar, J. Eur. Ceram. Soc. 27, 4021 (2007).

26

Harmonic Generation in Nanoscale Ferroelectric Films

Jeffrey F. Webb
Swinburne University of Technology, Sarawak Campus
Malaysia

1. Introduction

The presence of surfaces or interfaces causes the behavior of ferroelectric materials to differ from that of the bulk, in a way analogous to that for magnetic and superconducting materials(Tilley, 1993; 1996). Here we will be concerned with a theoretical model that takes into account the influence of surfaces on a ferroelectric film. There is also experimental evidence that indicates that size effects in ferroelectrics are observable (Gerbaux & Hadni, 1989; Gerbaux et al., 1989; Höchli & Rohrer, 1982; Kulkarni et al., 1988; Marquardt & Gleiter, 1982; Mishina et al., 2003; Scott & Araujo, 1989) ;more recently, the strong influence of boundaries on ferroelectric behaviour has been demonstrated (Li et al., 1996; 1997).Due to the advent of ferroelectric random access memories (Scott, 1998) size effects in ferroelectric thin films are of increasing importance.
This chapter shows how the Landau-Devonshire theory of ferroelectrics can be applied to thin films and how the dynamic response to incident electromagnetic radiation can be calculated. One aim is to show how harmonic generation components that occur because of the nonlinear response of the ferroelectric can found and in particular how they are reflected from the film. This is done because it relates to reflection measurements that could be carried out on the film to investigate the theoretical proposals experimentally. Since ferroelectrics are responsive in the terahertz region, terahertz wave measurements, especially in the far infrared region would be the most relevant. Another aim is to present a general theory that serves as a foundation for other calculations involving ferroelectric films.
To begin with, the Landau-Devonshire theory for calculating the static polarization is developed starting with a bulk ferroelectric and progressing from a semi-infinite film to one of finite thickness. It is then shown how dynamical equations can be incorporated together with a Maxwell wave equation in order to calculate the dynamic response. This in general is a nonlinear problem and using a standard perturbation expansion technique it is shown how the harmonic components can be isolated and calculated. Finally a specific example of second harmonic generation for a ferroelectric film on a metal substrate is given in which the reflection coefficient is calculated exactly under simplified boundary conditions.

2. Landau-Devonshire theory

The starting point of the Landau-Devonshire theory is the Gibbs free energy expressed as a series expansion in powers of components of the polarization vector $\mathbf{P}$. The equilibrium

polarization is found from the minimum of the free energy function; the temperature dependence is such that below the Curie temperature the minimum corresponds to a non-zero polarization but above this temperature it is zero, thus representing one of the basic properties of a ferroelectric. Also the property that the spontaneous polarization can be reversed by the application of an external electric field is manifest in the theory by more than one minimum in the free energy so that the polarization can be switched between different possible equilibrium polarizations. We will need a free energy expression for a ferroelectric film. Here we first develop the ideas for a bulk ferroelectric and a semi-infinite ferroelectric as this is an instructive way to lead up to the thin film case.

2.1 Bulk ferroelectrics

For a bulk ferroelectric a Gibbs free energy of the following form is often used (Lines & Glass, 1977)

$$F = \frac{1}{2}AP^2 + \frac{1}{4}BP^4 + \frac{1}{6}CP^6, \tag{1}$$

where

$$A = a(T - T_{C0}) \tag{2}$$

and

$$P^2 = P_x^2 + P_y^2 + P_z^2. \tag{3}$$

The equilibrium polarization for the bulk ferroelectric is given by the minimum of the free energy, found by solving

$$\frac{\partial F}{\partial P} = 0 \rightarrow AP_B + BP_B^3 + CP_B^5 = 0. \tag{4}$$

For first order transitions, which are discontinuous, $B < 0$ and $C > 0$. But for second order transitions, where the magnitude of the polarization changes continuously from P_B to zero as the temperature is raised through T_{C0}, the term in P^6 can be dropped ($C = 0$) and $B > 0$. a is always a positive constant. The theory is phenomenological so that the parameters described take values that can be found from experiment, or which, in some cases, can be calculated using first-principles methods based on microscopic models of ferroelectrics (Iniguez et al., 2001).

Figure 1 illustrates the behaviour for the second-order case $C = 0$; for $T > T_{C0}$ the minimum of F is at $P = 0$, corresponding to no spontaneous polarization above T_{C0}, the paraelectric phase; and for $T < T_{C0}$ minima occur at $P = \pm P_B$, where

$$P_B = \frac{|A|}{B}. \tag{5}$$

This represents the switchable spontaneous polarization that occurs in the ferroelectric phase.

The free energy in Landau theory is invariant under the symmetry transformations of the symmetry group of the paraelectric phase. The expression in Equation (1) is therefore, in general, only an approximation to the actual free energy. For example, for a cubic ferroelectric such as barium titanate, the paraelectric phase has cubic symmetry and the terms $P_x^4 + P_y^4 + P_z^4$ and $P_x^2P_y^2 + P_y^2P_z^2 + P_z^2P_x^2$ are separately invariant and would need to be included in the free energy. However, as brought out by Strukov & Lenanyuk (1998), for the simplest transition of

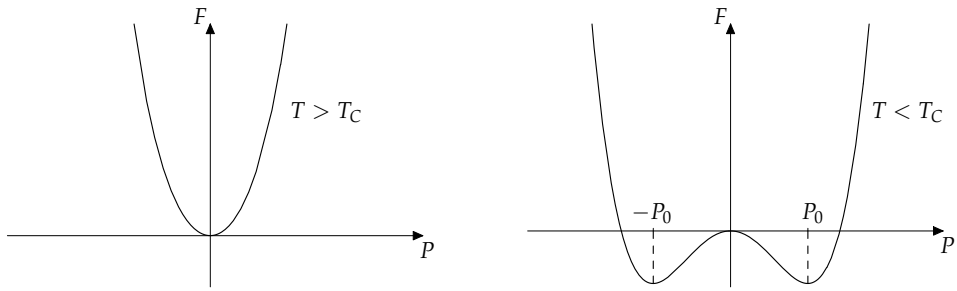

Fig. 1. Landau Free energy above and below T_{C0}.

a perovskite ferroelectric from its cubic paraelectric phase to a tetragonal ferroelectric phase Equation (1) has appropriate symmetry.

2.2 A semi-infinite film

We take the film surface to be in the xy plane of a Cartesian coordinate system, and assume that the spontaneous polarization is in-plane so that depolarization effects (Tilley, 1996) do not need to be taken into account. The spontaneous polarization due to the influence of the surface, unlike in the bulk, may not be constant when the surface is approached. Hence we now have $\mathbf{P} = \mathbf{P}(z)$, and this implies that a term in $|dP/dz|^2$ is present in the free energy expansion together with a surface term (Chandra & Littlewood, 2007; Cottam et al., 1984), and the free energy becomes

$$F = \iint dxdy \int_0^\infty dz \left[\frac{1}{2}AP^2 + \frac{1}{4}BP^4 + \frac{1}{6}CP^6 + \frac{1}{2}D\left(\frac{dP}{dz}\right)^2 \right] + \frac{1}{2}D \iint dx\, dy\, P^2(0)\delta^{-1}, \quad (6)$$

so that the free energy per unit area where S is the surface area of the film is

$$\frac{F}{S} = \int_0^\infty dz \left[\frac{1}{2}AP^2 + \frac{1}{4}BP^4 + \frac{1}{6}CP^6 + \frac{1}{2}D\left(\frac{dP}{dz}\right)^2 \right] + \frac{1}{2}DP^2(0)\delta^{-1}. \quad (7)$$

The surface term includes a length δ which will appear in a boundary condition required when the free energy is minimized to find the equilibrium polarization. In fact, finding the minimum, due to the integral over the free energy expansion, is now the problem of minimizing a functional. The well know Euler-Lagrange technique can be used which results in the following differential equation

$$D\frac{d^2P}{dz^2} - AP - BP^3 - CP^5, \quad (8)$$

with boundary condition

$$\frac{dP}{dz} - \frac{1}{\delta}P = 0, \quad \text{at } z = 0. \quad (9)$$

The solution of the Euler-Lagrange equation with this boundary condition gives the equilibrium polarization $P_0(z)$. It can be seen from Equation (9) that δ is an extrapolation length and that for $\delta < 0$ the polarization increases at the surface and for $\delta > 0$ it decreases at the surface, as is illustrated in Figure 2.

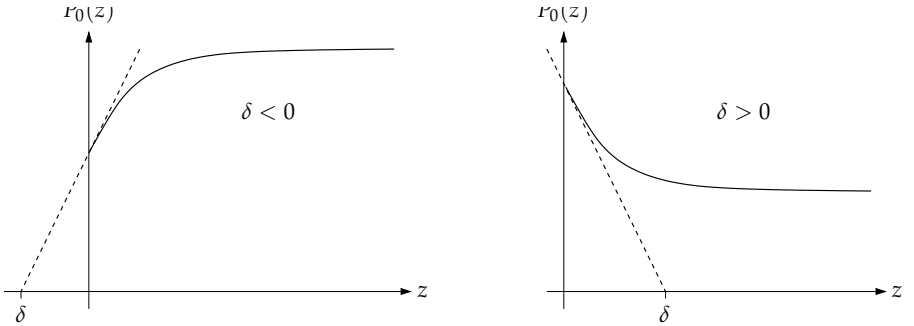

Fig. 2. Extrapolation length δ. For $\delta < 0$ the polarization increases at the surface and for $\delta > 0$ it decreases at the surface. The dotted lines have slopes given by $[dP_0/dz]_{z=0}$.

For first order transitions with $C \neq 0$ the solution to Equation (9) must be obtained numerically (Gerbaux & Hadni, 1990). However for second order transitions ($C = 0$) an analytical solution can be found as will now be outlined. The equation to solve in this case, subject to Equation (9), is

$$D\frac{d^2P}{dz^2} - AP - BP^3. \tag{10}$$

The first integral is

$$\frac{1}{2}D\left(\frac{dP}{dz}\right)^2 - \frac{1}{2}AP^2 - \frac{1}{4}BP^4 = G, \tag{11}$$

and since as $z \to \infty$, P tends to its bulk value P_B while $dP/dz \to 0$,

$$G = (1/2)AP_{\text{bulk}}^2 - (1/4)BP_{\text{bulk}}^4. \tag{12}$$

For $T < T_{C0}$, we take $P_{\text{bulk}} = P_B$, where P_B is given by Equation (5) and $G = A^2/4B$. Following Cottam et al. (1984), integration of Equation (11) then gives

$$P_0(z) = P_B \coth[(z + z_0)/\sqrt{2}\xi], \quad \text{for } \delta < 0, \tag{13}$$

$$P_0(z) = P_B \tanh[(z + z_0)/\sqrt{2}\xi], \quad \text{for } \delta > 0, \tag{14}$$

where ξ is a coherence length given by

$$\xi^2 = \frac{D}{|A|}. \tag{15}$$

Application of the boundary condition, Equation (9), gives

$$z_0 = (\xi\sqrt{2}\sinh^{-1}(\sqrt{2}|\delta|/\xi). \tag{16}$$

Plots of Equations (13) and (14) are given by Cottam et al. (1984).
For the $\delta < 0$ case in which the polarization increases at the surface it can be shown (Cottam et al., 1984; Tilley, 1996), as would be expected, that the phase transition at the surface occurs at a higher temperature than the bulk; there is a surface state in the temperature range $T_{C0} < T < T_C$. For $\delta > 0$, the polarization turns down at the surface and it is expected that the critical temperature T_C at which the film ceases to become ferroelectric is lower than T_{C0}, as has been brought out by Tilley (1996) and Cottam et al. (1984).

2.3 A finite thickness film

Next a finite film is considered. The thickness can be on the nanoscale, where it is expected that the size effects would be more pronounced. The theory is also suitable for thicker films; then it is more likely that in the film the polarization will reach its bulk value.
The free energy per unit area of a film normal to the z axis of thickness L, and with in-plane polarization again assumed, can be expressed as

$$\frac{F}{S} = \int_{-L}^{0} dz \left[\frac{1}{2}AP^2 + \frac{1}{4}BP^4 + \frac{1}{6}CP^6 + \frac{1}{2}D\left(\frac{dP}{dz}\right)^2 \right] + \frac{1}{2}D\left[P^2(-L)\delta_1^{-1} + P^2(0)\delta_2^{-1}\right], \quad (17)$$

which is an extension of the free energy expression in Equation (7) to include the extra surface. Two different extrapolation lengths are introduced since the interfaces at $z = -L$ and $z = 0$ might be different—in the example below in Section 5.2 one interface is air-ferroelectric, the other ferroelectric-metal. The Euler-Lagrange equation for finding the equilibrium polarization is still given by Equation (8) and the boundary conditions are

$$\frac{dP}{dz} - \frac{1}{\delta_1}P = 0, \quad \text{at } z = -L, \quad (18)$$

$$\frac{dP}{dz} + \frac{1}{\delta_2}P = 0, \quad \text{at } z = 0. \quad (19)$$

With the boundary conditions written in this way it follows that if $\delta_1, \delta_2 < 0$ the polarization turns up at the surfaces and for $\delta_1, \delta_2 > 0$, it turns down. When the signs of δ_1 and δ_2 differ, at one surface the polarization will turn up; at the other it will turn down.
Solution of the Euler-Lagrange equation subject to Equations (18) and (19) has to be done numerically(Gerbaux & Hadni, 1990; Tan et al., 2000) for first order transitions. Second order transitions where $C = 0$, as for the semi-infinite case, can be found analytically, this time in terms of elliptic functions (Chew et al., 2001; Tilley & Zeks, 1984; Webb, 2006). Again the first integral is given by Equation (11). But now the second integral is carried out from one boundary to the point at which $(dP/dz) = 0$, and then on to the next boundary, and, as will be shown below, G is no longer given by Equation (12) . The elliptic function solutions that result are different according to the signs of the extrapolation lengths. There are four permutations of the signs and we propose that the critical temperature, based on the previous results for the semi-infinite film, will obey the following:

$$\delta_1, \delta_2 > 0 \Rightarrow T_C < T_{C0} \quad (P \text{ increases at both surfaces}), \quad (20)$$

$$\delta_1, \delta_2 < 0 \Rightarrow T_C < T_{C0} \quad (P \text{ decreases at both surfaces}), \quad (21)$$

$$\delta_1 > 0, \delta_2 < 0, |\delta_2| \lesseqgtr |\delta_1| \Rightarrow T_C \lesseqgtr T_{C0} \quad (P \text{ decreases at } z = -L, \text{ increases at } z = 0\,), \quad (22)$$

$$\delta_1 < 0, \delta_2 > 0, |\delta_1| \lesseqgtr |\delta_2| \Rightarrow T_C \lesseqgtr T_{C0} \quad (P \text{ increases at } z = -L, \text{ decreases at } z = 0\,). \quad (23)$$

There will be surface states, each similar to that described for the semi-infinite film, for any surfaces for which P increases provided that $T_C > T_{C0}$.
The solutions for the two cases $\delta_1 = \delta_2 = \delta < 0$ and $\delta_1 = \delta_2 = \delta > 0$ will be given first because they contain all of the essential functions; dealing with the other cases will be discussed after that. Some example plots of the solutions can be found in Tilley & Zeks (1984) and Tilley (1996).

2.3.1 Solution for $\delta_1 = \delta_2 = \delta > 0$

Based on the work of Chew et al. (2001), after correcting some errors made in that work, the solution to Equation (10) with boundary conditions (19) and (20) for the coordinate system implied by Equation (17) is

$$P_0(z) = P_1 \,\mathrm{sn}\left[K(\lambda) - \frac{z + L_2}{\zeta}, \lambda\right], \tag{24}$$

where $0 < L_2 < L$[1] and the position in the film at which $dP/dz = 0$ is given by $z = -L_2$ (for a fixed L, the value of L_2 uniquely defined by the boundary conditions); λ is the modulus of the Jacobian elliptic function sn and $K(\lambda)$ is the complete elliptic integral of the first kind (Abramowitz & Stegun, 1972). Also,

$$P_1^2 = -\frac{A}{B} - \sqrt{\frac{A^2}{B^2} - \frac{4G}{B}}, \tag{25}$$

$$P_2^2 = -\frac{A}{B} + \sqrt{\frac{A^2}{B^2} - \frac{4G}{B}}, \tag{26}$$

$$\lambda = \frac{P_1}{P_2}, \quad \text{and} \quad \zeta = \frac{1}{P_2}\sqrt{\frac{2D}{B}}. \tag{27}$$

Although this is an analytic solution, the constant of integration G is found by substituting it into the boundary conditions; this leads to a transcendental equation which must be solved numerically for G.

2.3.2 Solution for $\delta_1 = \delta_2 = \delta < 0$

The equations in this section are also based on the work of Chew et al. (2001), with some errors corrected.

In this case there is a surface state, discussed above when $T_{C0} \leqslant T \leqslant T_C$ and for $T < T_{C0}$ the whole of the film is in a ferroelectric state. In each of these temperature regions the solution to Equation (10) is different.

For the surface state,

$$P_0(z) = \frac{P_2}{\mathrm{cn}\left[\dfrac{z + L_2}{\zeta_1}, \lambda_1\right]}, \quad T_{C0} \leqslant T \leqslant T_C, \tag{28}$$

where

$$\lambda_1 = \left[1 - \left(\frac{P_2}{P_1}\right)^2\right]^{-1}, \quad \zeta_1 = \frac{\lambda}{Q}\sqrt{\frac{2D}{B}}, \quad \text{and} \quad Q^2 = -P_1^2, \tag{29}$$

with P_1, P_2 and L_2 as defined above. G (implicit in P_1 and P_2) has to be recalculated for the solution in Equation (28) and again this leads to a transcendental equation that must be solved numerically.

[1] The reason for the notation L_2, rather than say L_1 is a matter of convenience in the description that follows of how to apply the boundary conditions to find the integration constant G that appear via Equations (25) and (26).

When the whole film is in a ferroelectric state

$$P_0(z) = \frac{P_2}{\mathrm{sn}\left[K(\lambda) - \dfrac{z+L_2}{\zeta}, \lambda\right]}, \quad T < T_C, \tag{30}$$

where K, λ and ζ are as defined above, and G is found by substituting this solution into the boundary conditions and solving the resulting transcendental equation numerically.

2.3.3 Dealing with the more general case $\delta_1 \neq \delta_2$

One or more of the above forms of the solutions is sufficient for this more general case. The main issue is satisfying the boundary conditions. To illustrate the procedure consider the case $\delta_1, \delta_2 > 0$. The polarization will turn down at both surfaces and it will reach a maximum value somewhere on the interval $-L < z < 0$ at the point $z = -L_2$; for $\delta_1 \neq \delta_2$ this maximum will not occur when $L_2 = L/2$ (it would for the δ case considered in Section 2.3.2).

The main task is to find the value of G that satisfies the boundary conditions for a given value of film thickness L. For this it is convenient to make the transformation $z \to z - L_2$. The maximum of P_0 will then be at $z = 0$ and the film will occupy the region $-L_1 \leqslant L \leqslant L_2$, where $L_1 + L_2 = L$. Now the polarization is given by

$$P_0(z) = P_1 \,\mathrm{sn}\left[K(\lambda) - \frac{z}{\zeta}, \lambda\right]. \tag{31}$$

Transforming the boundary conditions, Equations (18) and (19), to this frame and applying them to Equation (31) to the case under consideration ($\delta_1, \delta_2 > 0$) leads to

$$\frac{\delta_1}{\zeta(G)} \,\mathrm{cn}\left[K(\lambda(G)) + \frac{L_1}{\zeta(G)}, \lambda\right] \mathrm{dn}\left[K(\lambda(G)) + \frac{L_1}{\zeta(G)}, \lambda\right] = -\,\mathrm{sn}\left[K(\lambda(G)) + \frac{L_1}{\zeta(G)}, \lambda\right] \quad \text{(bc1)}$$

and

$$\frac{\delta_2}{\zeta(G)} \,\mathrm{cn}\left[K(\lambda(G)) - \frac{L_2}{\zeta(G)}, \lambda\right] \mathrm{dn}\left[K(\lambda(G)) - \frac{L_2}{\zeta(G)}, \lambda\right] = \mathrm{sn}\left[K(\lambda(G)) - \frac{L_2}{\zeta(G)}, \lambda\right]. \quad \text{(bc2)}$$

Here the G dependence of some of the parameters has been indicated explicitly since G is the unknown that must be found from these boundary equations. It is clear that in term of finding G the equations are transcendental and must be solved numerically. A two-stage approach that has been successfully used by Webb (2006) will now be described (in that work the results were used but the method was not explained).

The idea is to calculate G numerically from one of the boundary equations and then make sure that the film thickness is correctly determined from a numerical calculation using the remaining equation. For example, if we start with (bc1), G can be determined by any suitable numerical method; however the calculation will depend not only on the value of δ_1 but also on L_1 such that $G = G(\delta_1, L_1)$. To find the value of L_1 for a given L that is consistent with $L = L_1 + L_2$, (bc2) is invoked: here we require $G = G(\delta_2, L_2) = G(\delta_2, L - L_1) = G(\delta_1, L_1)$, and the value of L_1 to be used in $G(\delta_1, L_1)$ is that which satisfies (bc2). In invoking (bc2) the calculation—which is also numerical of course—will involve replacing L_2 by $L - L_1 = L - L_1[\delta_2, G(\delta_1, L_1)]$. The numerical procedure is two-step in the sense that the (bc1) numerical calculation to find $G(\delta_1, L_1)$ is used in the numerical procedure for calculating L_1 from (bc2)

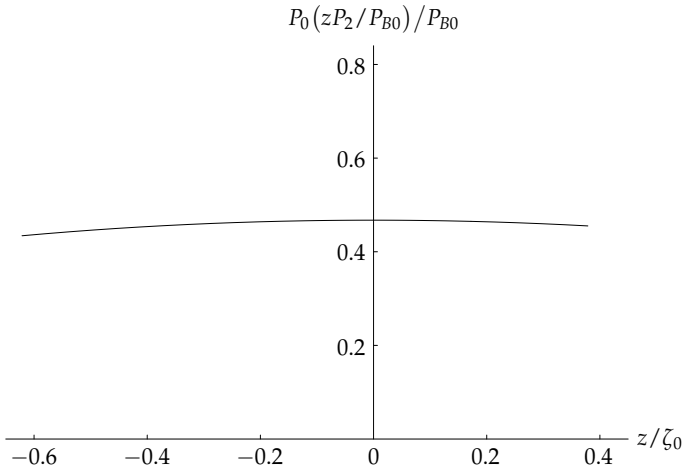

Fig. 3. Polarization versus distance for a film of thickness L according to Equation (31) with boundary conditions (bc1) and (bc2). The following dimensionless variables and parameter values have been used: $P_{B0} = (aT_{C0}/B)^{1/2}$, $\zeta_0 = [2D/(aT_C)]^{1/2}$, $\Delta T' = (T - T_{C0})/T_{C0} = -0.4$, $L' = L/\zeta_0 = 1$, $\delta_1' = 4L'$, $\delta_2' = 7L'$, $G' = 4GB/(a/T_{C0})^2 = 0.127$, $L_1' = L_1/\zeta_0 = 0.621$, $L_1' = L_2/\zeta_0 = 0.379$.

(in which L_2 is written as $L - L_1$). In this way the required L_1 is calculated from (bc2) and L_2 is calculated from $L_2 = L - L_2$. Hence G, L_1 and L_2 have been determined for given values of δ_1, δ_2 and L.
It is worth pointing out that once G has been determined in this way it can be used in the $P_0(z)$ in Equation (24) since the inverse transformation $z \to z + L_2$ back to the coordinate system in which this $P(z)$ is expressed does not imply any change in G.
Figure 3 shows an example plot of $P_0(z)$ for the case just considered using values and dimensionless variables defined in the figure caption.
A similar procedure can be used for other sign permutations of δ_1 and δ_2 provided that the appropriate solution forms are chosen according to the following:

1. $\delta_1, \delta_2 < 0$: use the transformed ($z \to z - L_2$) version of Equation (28) for $T_{C0} \leqslant T \leqslant T_C$, or the transformed version of Equation (30) for $T < T_C$.
2. $\delta_1 > 0, \delta_2 < 0$: for $-L_1 \leqslant L < 0$ use Equation (31); for $0 \leqslant L \leqslant L_2$ follow 1.
3. $\delta_1 < 0, \delta_2 > 0$: for $-L_1 \leqslant L < 0$ follow 1; for $0 \leqslant L \leqslant L_2$ use Equation (31).

3. Dynamical response

In this section the response of a ferroelectric film of finite thickness to an externally applied electric field **E** is considered. Since we are interested in time varying fields from an incident electromagnetic wave it is necessary to introduce equations of motion. It is the electric part of the wave that interacts with the ferroelectric primarily since the magnetic permeability is usually close to its free space value, so that in the film $\mu = \mu_0$ and we can consider the electric field vector **E** independently.

An applied electric field is accounted for in the free energy by adding a term $-\mathbf{P}\cdot\mathbf{E}$ to the expansion in the integrand of the free energy density in Equation (17) yielding

$$\frac{F_E}{S}=\int_{-L}^{0}dz\left[\frac{1}{2}AP^2+\frac{1}{4}BP^4+\frac{1}{6}CP^6+\frac{1}{2}D\left(\frac{dP}{dz}\right)^2-\mathbf{P}\cdot\mathbf{E}\right]+\frac{1}{2}D\left[P^2(-L)\delta_1^{-1}+P^2(0)\delta_2^{-1}\right]. \tag{32}$$

In order to find the dynamical response of the film to incident electromagnetic radiation Landau-Khalatnikov equations of motion (Ginzburg et al., 1980; Landau & Khalatnikov, 1954) of the form

$$m\frac{\partial^2\mathbf{P}}{\partial t^2}+\gamma\frac{\partial\mathbf{P}}{\partial t}=-\boldsymbol{\nabla}_\delta F_E=-\left(D\frac{\partial^2\mathbf{P}}{\partial z^2}-A\mathbf{P}-B\mathbf{P}^3-C\mathbf{P}^5\right)+\mathbf{E}, \tag{33}$$

are used. Here m is a damping parameter and γ a mass parameter;

$$\boldsymbol{\nabla}_\delta=\hat{\mathbf{x}}\frac{\delta}{\delta P_x}+\hat{\mathbf{y}}\frac{\delta}{\delta P_y}+\hat{\mathbf{z}}\frac{\delta}{\delta P_z}, \tag{34}$$

which involves variational derivatives, and we introduce the term variational gradient-operator for it, noting that $\hat{\mathbf{x}}$, $\hat{\mathbf{y}}$ and $\hat{\mathbf{z}}$ are unit vectors in the positive directions of x, y and z, respectively. These equations of motion are analogous to those for a damped mass-spring system undergoing forced vibrations. However here it is the electric field $\mathbf{E}$ that provides the driving impetus for $\mathbf{P}$ rather than a force explicitly. Also, the potential term $\boldsymbol{\nabla}_\delta F_E|_{\mathbf{E}=0}$ is analogous to a nonlinear force-field (through the terms nonlinear in P) rather than the linear Hook's law force commonly employed to model a spring-mass system. The variational derivatives are given by

$$\frac{\delta F}{\delta P_x}=\left(A+3BP_0^2\right)Q_x+B\left(2P_0Q_x^2+P_0Q^2+Q^2Q_x\right)-D\frac{\partial^2Q_x}{\partial z^2}-E_x \tag{35}$$

and

$$\frac{\delta F}{\delta P_\alpha}=\left(A+BP_0^2\right)Q_\alpha+B\left(2P_0Q_xQ_\alpha+Q^2Q_\alpha\right)-D\frac{\partial^2Q_\alpha}{\partial z^2}-E_\alpha,\quad \alpha=y\text{ or }z, \tag{36}$$

where $Q^2=Q_x^2+Q_y^2+Q_z^2$, and $\mathbf{P}$ has been written as a sum of static and dynamic parts,

$$\begin{aligned}P_x(z,t)&=P_0(z)+Q_x(z,t),\\ P_y(z,t)&=0+Q_y(z,t)=Q_y(z,t),\\ P_z(z,t)&=0+Q_z(z,t)=Q_z(z,t).\end{aligned} \tag{37}$$

In doing this we have assumed in-plane polarization $\mathbf{P}_0(z)=(P_0(z),0,0)$ aligned along the x axis. This is done to simplify the problem so that we can focus on the essential features of the response of the ferroelectric film to an incident field. It should be noted that if $\mathbf{P}_0(z)$ had a z component, depolarization effects would need to be taken in to account in the free energy; a theory for doing this has been presented by Tilley (1993). The in-plane orientation avoids this complication. The Landau Khalatnikov equations in Equation (33) are appropriate

for displacive ferroelectrics that are typically used to fabricate thin films (Lines & Glass, 1977; Scott, 1998) with $BaTiO_4$ being a common example.
The equations of motion describe the dynamic response of the polarization to the applied field. Also the polarization and electric field must satisfy the inhomogeneous wave equation derived from Maxwell's equations. The wave equation is given by

$$\frac{\partial^2 E_\alpha}{\partial x^2} - \frac{\epsilon_\infty}{c^2}\frac{\partial^2 E_\alpha}{\partial t^2} = \frac{1}{c^2\epsilon_0}\frac{\partial Q_\alpha}{\partial t^2}, \quad \alpha = x, y, \text{or } z. \tag{38}$$

where, c is the speed of light in vacuum, ϵ_0 is the permittivity of free space, and ϵ_∞ is the contribution of high frequency resonances to the dielectric response. The reason for including it is as follows. Displacive ferroelectrics, in which it is the lattice vibrations that respond to the electric field, are resonant in the far infrared and terahertz wave regions of the electromagnetic spectrum and that is where the dielectric response calculated from the theory here will have resonances. There are higher frequency resonances that are far from this and involve the response of the electrons to the electric field. Since these resonances are far from the ferroelectric ones of interest here they can be accounted for by the constant ϵ_∞ (Mills, 1998).
Solving Equations (35) to (38) for a given driving field **E** will give the relationship between **P** and **E**, and the way that the resulting electromagnetic waves propagate above, below, and in the film can be found explicitly. However to solve the equations it is necessary to postulate a constitutive relationship between **P** and **E**, as this is not given by any of Maxwell's equations (Jackson, 1998). Therefore next we consider the constitutive relation

4. Constitutive relations between P and E

4.1 Time-domain: Response functions

In the perturbation-expansion approach (Butcher & Cotter, 1990) that will be used here the constitutive relation takes the form

$$\mathbf{Q} = \mathbf{P} - \mathbf{P}_0 = \mathbf{Q}^{(1)}(t) + \mathbf{Q}^{(2)}(t) + \ldots + \mathbf{Q}^{(n)}(t) + \ldots, \tag{39}$$

where $\mathbf{Q}^{(1)}(t)$ is linear with respect to the input field, $\mathbf{Q}^{(2)}(t)$ is quadratic, and so on for higher order terms. The way in which the electric field enters is through time integrals and response function tensors as follows (Butcher & Cotter, 1990):

$$\mathbf{Q}^{(1)}(t) = \epsilon_0 \int_{-\infty}^{+\infty} d\tau\, \mathbf{R}^{(1)}(\tau) \cdot \mathbf{E}(t-\tau) \tag{40}$$

$$\mathbf{Q}^{(2)}(t) = \epsilon_0 \int_{-\infty}^{+\infty} d\tau_1 \int_{-\infty}^{+\infty} d\tau_2\, \mathbf{R}^{(2)}(\tau_1, \tau_2) : \mathbf{E}(t-\tau_1)\mathbf{E}(t-\tau_2), \tag{41}$$

and the general term, denoting an nth-order tensor contraction by $\overset{(n)}{|}$, is

$$\mathbf{Q}^{(n)}(t) = \epsilon_0 \int_{-\infty}^{+\infty} d\tau_1 \cdots \int_{-\infty}^{+\infty} d\tau_n\, \mathbf{R}^{(n)}(\tau_1, \ldots, \tau_n) \overset{(n)}{|} \mathbf{E}(t-\tau_1) \cdots \mathbf{E}(t-\tau_n), \tag{42}$$

which in component form, using the summation convention, is given by

$$Q_{\alpha}^{(n)}(t) = \epsilon_0 \int_{-\infty}^{+\infty} d\tau_1 \cdots \int_{-\infty}^{+\infty} d\tau_n \, R^{(n)}_{\alpha\mu_1\cdots\mu_n}(\tau_1,\ldots,\tau_n) E_{\mu_1}(t-\tau_1)\cdots E_{\mu_n}(t-\tau_n), \tag{43}$$

where α and μ take the values x, y and z. The response function $\mathbf{R}^{(n)}(\tau_1,\ldots,\tau_n)$ is real and an nth-order tensor of rank $n+1$. It vanishes when any one of the τ_i time variables is negative, and is invariant under any of the $n!$ permutations of the n pairs $(\mu_1,\tau_1),(\mu_2,\tau_2),\ldots,(\mu_n,\tau_n)$. Time integrals appear because in general the response is not instantaneous; at any given time it also depends on the field at earlier times: there is temporal dispersion. Analogous to this there is spatial dispersion which would require integrals over space. However this is often negligible and is not a strong influence on the thin film calculations that we are considering. For an in-depth discussion see Mills (1998) and Butcher & Cotter (1990).

4.2 Frequency-domain: Susceptibility tensors

Sometimes the frequency domain is more convenient to work in. However with complex quantities appearing, it is perhaps a more abstract representation than the time domain. Also, in the literature it is common that physically many problems start out being discussed in the time domain and the frequency domain is introduced without really showing the relationship between the two. The choice of which is appropriate though, depends on the circumstances (Butcher & Cotter, 1990); for example if the incident field is monochromatic or can conveniently be described by a superposition of such fields the frequency domain is appropriate, whereas for very short pulses of the order of femtoseconds it is better to use the time domain approach.

The type of analysis of ferroelectric films being proposed here is suited to a monochromatic wave or a superposition of them and so the frequency domain and how it is derived from the time domain will be discussed in this section. Instead of the tensor response functions we deal with susceptibility tensors that arise when the electric field $\mathbf{E}(t)$ is expressed in terms of its Fourier transform $\mathbf{E}(\omega)$ via

$$\mathbf{E}(t) = \int_{-\infty}^{+\infty} d\omega \, \mathbf{E}(\omega) \exp(-i\omega t), \tag{44}$$

$$\tag{45}$$

where

$$\mathbf{E}(\omega) = \frac{1}{2\pi} \int_{-\infty}^{+\infty} d\tau \, \mathbf{E}(\tau) \exp(i\omega\tau). \tag{46}$$

Equation (44) can be applied to the time domain forms above. The nth-order term in Equation (42) then becomes,

$$\mathbf{Q}^{(n)}(t) = \epsilon_0 \int_{-\infty}^{+\infty} d\omega_1 \cdots \int_{-\infty}^{+\infty} d\omega_n \, \boldsymbol{\chi}^{(n)}(-\omega_\sigma;\omega_1,\ldots,\omega_n) \,\vdots^{(n)}\, \mathbf{E}(\omega_1)\cdots\mathbf{E}(\omega_n)\exp(-i\omega_\sigma t), \tag{47}$$

where

$$\boldsymbol{\chi}^{(n)}(-\omega_\sigma;\omega_1,\ldots,\omega_n) = \int_{-\infty}^{+\infty} d\tau_1 \cdots \int_{-\infty}^{+\infty} d\tau_n \, \mathbf{R}^{(n)}(\tau_1,\ldots,\tau_n) \exp\left[i \sum_{j=1}^{n} \omega_j \tau_j \right], \tag{48}$$

which is called the nth-order susceptibility tensor, and, following the notation of Butcher & Cotter (1990),

$$\omega_\sigma = \omega_1 + \omega_2 + \cdots + \omega_n. \tag{49}$$

As explained by Butcher & Cotter (1990) intrinsic permutation symmetry implies that the components of the susceptibility tensor are such that $\chi^{(n)}_{\alpha\mu_1\cdots\mu_n}(-\omega_\sigma;\omega_1,\ldots,\omega_n)$ is invariant under the $n!$ permutations of the n pairs (μ_1,ω_1), $(\mu_2,\omega_2),\ldots,(\mu_n,\omega_n)$.
The susceptibility tensors are useful when dealing with a superposition of monochromatic waves. The Fourier transform of the field then involves delta functions, and the evaluation of the integrals in Equation (47) is straightforward with the polarization determined by the values of the susceptibility tensors at the frequencies involved. Hence, by expanding $\mathbf{Q}(t)$ in the frequency domain,

$$\mathbf{Q}^{(n)}(t) = \int_{-\infty}^{+\infty} d\omega \, \mathbf{Q}^{(n)}(\omega) \exp(-i\omega t), \tag{50}$$

where

$$\mathbf{Q}^{(n)}(\omega) = \frac{1}{2\pi} \int_{-\infty}^{+\infty} d\tau \, \mathbf{Q}^{(n)}(\tau) \exp(i\omega\tau), \tag{51}$$

one may obtain, from Equation (47),

$$\mathbf{Q}^{(n)}(\omega) = \epsilon_0 \int_{-\infty}^{+\infty} d\omega_1 \cdots \int_{-\infty}^{+\infty} d\omega_n \, \boldsymbol{\chi}^{(n)}(-\omega_\sigma;\omega_1,\ldots,\omega_n) \overset{(n)}{\mid} \mathbf{E}(\omega_1)\cdots\mathbf{E}(\omega_n)\delta(\omega-\omega_\sigma), \tag{52}$$

where we have used the identity (Butcher & Cotter, 1990)

$$\frac{1}{2\pi} \int_{-\infty}^{+\infty} d\omega \, \exp[i\omega(\tau - t)] = \delta(\tau - t), \tag{53}$$

in which δ is the Dirac delta function (not to be confused with an extrapolation length). We have expanded the Fourier component of the polarization $\mathbf{Q}$ at the frequency ω_σ as a power series, so

$$\mathbf{Q}(\omega) = \sum_{r}^{\infty} \mathbf{Q}^{(r)}(\omega). \tag{54}$$

The component form of Equation (52) is

$$\left[Q^{(n)}(\omega)\right]_\alpha = \epsilon_0 \int_{-\infty}^{+\infty} d\omega_1 \cdots \int_{-\infty}^{+\infty} d\omega_n \, \chi^{(n)}_{\alpha\mu_1\cdots\mu_n}(-\omega;\omega_1,\ldots,\omega_n) \times \left[E(\omega_1)\right]_{\mu_1} \cdots \left[E(\omega_n)\right]_{\mu_n} \delta(\omega-\omega_\sigma). \tag{55}$$

Again the summation convention is used so that repeated Cartesian-coordinate subscripts $\mu_1 \cdots \mu_n$ are to be summed over x, y and z.
Next the evaluation of the integrals in Equation (52) is considered for a superposition of monochromatic waves given by

$$\mathbf{E}(t) = \frac{1}{2} \sum_{\omega' \geqslant 0} \left[\mathbf{E}_{\omega'} \exp(-i\omega' t) + \mathbf{E}_{-\omega'} \exp(i\omega' t) \right] \tag{56}$$

Here, since $\mathbf{E}(t)$ is real, $\mathbf{E}_{-\omega'} = \mathbf{E}^*_{\omega'}$. The Fourier transform of $\mathbf{E}(t)$ from Equation (44) is given by

$$\mathbf{E}(\omega) = \frac{1}{2} \sum_{\omega' \geqslant 0} \left[\mathbf{E}_{\omega'} \delta(\omega - \omega') + \mathbf{E}_{-\omega'} \delta(\omega + \omega') \right]. \tag{57}$$

With $\mathbf{E}(t)$ given by Equation (56), the n-th order polarization term in Equation (47) can be rewritten as

$$\mathbf{Q}^{(n)}(t) = \frac{1}{2} \sum_{\omega' \geqslant 0} \left[\mathbf{Q}^{(n)}_{\omega} \exp(-i\omega t) + \mathbf{Q}^{(n)}_{-\omega} \exp(i\omega t) \right], \tag{58}$$

where $\mathbf{Q}^{(n)}_{-\omega} = \left(\mathbf{Q}^{(n)}_{\omega} \right)^*$ because $\mathbf{Q}^{(n)}(t)$ is real.

By substituting Equation (57) into Equation (52) an expression for $\mathbf{Q}^{(n)}_{\omega}$ can be obtained. The Cartesian μ-component following the notation of Ward (1969) and invoking intrinsic permutation symmetry (Butcher & Cotter, 1990) can be shown to be given by

$$\left(Q^{(n)}_{\omega_\sigma} \right)_\alpha = \epsilon_0 \sum_{\omega} K(-\omega_\sigma; \omega_1, \ldots, \omega_n) \chi^{(n)}_{\alpha \mu_1 \cdots \mu_n}(-\omega_\sigma; \omega_1, \ldots, \omega_n) (E_{\omega_1})_{\mu_1} \cdots (E_{\omega_n})_{\mu_n}, \tag{59}$$

which in vector notation is

$$\mathbf{Q}^{(n)}_{\omega_\sigma} = \epsilon_0 \sum_{\omega} K(-\omega_\sigma; \omega_1, \ldots, \omega_n) \boldsymbol{\chi}^{(n)}(-\omega_\sigma; \omega_1, \ldots, \omega_n) \stackrel{(n)}{|} \mathbf{E}_{\omega_1} \cdots \mathbf{E}_{\omega_n}. \tag{60}$$

As with Equation (55), the summation convention is implied; the $\sum_\omega$ summation indicates that it is necessary to sum over all distinct sets of $\omega_1, \ldots, \omega_n$. Although in practice, experiments can be designed to avoid this ambiguity in which case there would be only one set and no such summation. K is a numerical factor defined by

$$K(-\omega_\sigma; \omega_1, \ldots, \omega_n) = 2^{l+m-n} p, \tag{61}$$

where p is the number of distinct permutations of $\omega_1, \ldots, \omega_n$, n is the order of nonlinearity, m is the number of frequencies in the set $\omega_1, \ldots, \omega_n$ that are zero (that is, they are d.c. fields) and $l = 1$ if $\omega_\sigma \neq 0$, otherwise $l = 0$.
Equation (59) describes a catalogue of nonlinear phenomena (Butcher & Cotter, 1990; Mills, 1998). For harmonic generation of interest in this chapter, $K = 2^{1-n}$ corresponding to n-th order generation and $-\omega_\sigma; \omega_1, \ldots, \omega_n \rightarrow -n\omega; \omega, \ldots, \omega$. For example second-harmonic generation is described by $K = 1/2$ and $-\omega_\sigma; \omega_1, \ldots, \omega_n \rightarrow -2\omega; \omega, \omega$.

5. Harmonic generation calculations

The general scheme for dealing with harmonic generation based on the application of the theory discussed so far will be outlined and then the essential principles will be demonstrated by looking at a specific example of second harmonic generation.

5.1 General considerations

The constitutive relations discussed in the previous section show how the polarization can be expressed as a power series in terms of the electric field. The tensors appear because of the anisotropy of ferroelectric crystals. However depending on the symmetry group some of the tensor elements may vanish (Murgan et al., 2002; Osman et al., 1998). The tensor components appear as unknowns in the constitutive relations. The Landau-Devonshire theory approach provides a way of calculating the susceptibilities as expressions in terms of the ferroelectric parameters and expressions that arise from the theory. The general problem for a ferroelectric film is to solve the equations of motion in Equation (33) for a given equilibrium polarization profile in the film together with the Maxwell wave equation, Equation (38), by using a perturbation expansion approach where the expansion to be used is given by the constitutive relations and the tensor elements that appear are the unknowns that are found when the equations are solved. Terms that have like electric field components will separate out so that there will be equations for each order of nonlinearity and type of nonlinear process. Starting from the lowest order these equations can be solved one after the other as the order is increased. However for orders higher than three the algebraic complexity in the general case can become rather unwieldy. For nth-order harmonic generation, as pointed out in the previous section, $\omega_\sigma = n\omega$ corresponding to the the terms in Equation (59) given by

$$\left(Q^{(n)}_{n\omega}\right)_\alpha = \epsilon_0 K(-n\omega;\omega,\ldots,\omega)\chi^{(n)}_{\alpha\mu_1\cdots\mu_n}(-n\omega;\omega,\ldots,\omega)(E_\omega)_{\mu_1}\cdots(E_\omega)_{\mu_n}, \tag{62}$$

where the sum over distinct set of frequencies has been omitted but remains implied if it is needed. For calculations involving harmonic generation only the terms in Equation (62) need to be dealt with.

The equations of course can only be solved if the boundary conditions are specified and for the polarization and it is assumed that equations of the form given above in Equation (9) will hold at each boundary. Electromagnetic boundary conditions are also required and these are given by continuity E and H at the boundaries, as demonstrated in the example that follows.

5.2 Second harmonic generation: an example

Here we consider an example of second harmonic generation and choose a simple geometry and polarization profile that allows the essence of harmonic generation calculations in ferroelectric films to be demonstrated whilst at the same time the mathematical complexity is reduced. The solution that results will be applied to finding a reflection coefficient for second harmonic waves generated in the film. This is of practical use because such reflections from ferroelectric films can be measured. Since the main resonances in ferroelectrics are in the far infrared region second harmonic reflections will be in the far infrared or terahertz region. Such reflection measurements will give insight into the film properties, including the size effects that in the Landau-Devonshire theory are modelled by the D term in the free energy expressions and by the extrapolation lengths in the polarization boundary conditions. We will consider a finite thickness film with a free energy given by Equation (17) and polarization

boundary conditions given in Equations (18) and (19), but for the simplest possible case in which the extrapolation lengths approach infinity which implies a constant equilibrium polarization. We consider the ferroelectric film to be on a metal substrate. Assuming that the metal has infinite electrical conductivity then allows a simple electromagnetic boundary conditions to be employed consistent with $\mathbf{E} = 0$ at the ferroelectric-metal interface. The presence of the metal substrate has the advantage that the reflected waves of interest in reflection measurements are greater that for a free standing film since there is no wave transmitted to the metal substrate and more of the electromagnetic energy is reflected at the metal interface compared to a free standing film that transmits some of the energy. The film thickness chosen for the calculations is 40 nm in order to represent the behaviour of nanoscale films.

Note that the focus is on calculating a reflection coefficient for the second harmonic waves reflected from the film. The tensor components do not appear explicitly as we are dealing with ratios of the wave amplitudes for the electric field. However the equations solved provide expressions for the electric field and polarization and from the expressions for the polarization the tensor components can be extracted if desired by comparison with the constitutive relations. There are only a few tensor components in this example because of the simplified geometry and symmetry chosen, as will be evident in the next section.

5.2.1 Some simplifications and an overview of the problem

The incident field is taken to be a plane wave of frequency ω with a wave number above the film of magnitude $q_0 = \omega/c$, since the region above the film behaves like a vacuum in which all frequencies propagate at c. We only consider normal incidence and note that the field is traveling in the negative z direction in the coordinate system used here in which the top of the film is in the plane $z = 0$, the bottom in the plane $z = -L$. Therefore $\mathbf{q}_0 = q_0(-\hat{\mathbf{z}})$ and the incident field can be represented by

$$\frac{1}{2}\left[\mathbf{E}_0 e^{iq_0(-\hat{\mathbf{z}})\cdot z\hat{\mathbf{z}}} e^{-i\omega t} + \mathbf{E}_0^* e^{iq_0(\hat{\mathbf{z}})\cdot z\hat{\mathbf{z}}} e^{i\omega t}\right] = \frac{1}{2}\left[\mathbf{E}_0 e^{-iq_0 z} e^{-i\omega t} + \mathbf{E}_0^* e^{iq_0 z} e^{i\omega t}\right], \tag{63}$$

where

$$\mathbf{E}_0 = E_0[(E_{0x}/|E_0|)\hat{\mathbf{x}} + (E_{0y}/|E_0|)\hat{\mathbf{y}}], \tag{64}$$

written in this way because in general E_0 is a complex amplitude. However, we will take it to be real, so that other phases are measured relative to the incident wave, which, physically, is no loss of generality.

Two further simplifications that will be used are: (i) The spontaneous polarization P_0 will be assumed to be constant throughout the film, corresponding to the limit as δ_1 and δ_2 approach infinity in the boundary conditions of Equations (18) and (19). The equilibrium polarization of the film is then the same as for the bulk described in Section 2.1, and considering a single direction for the polarization, we take

$$P_0(z) = P_0 = \begin{cases} P_B & \text{if } T < T_C, \\ 0 & \text{if } T > T_C, \end{cases} \tag{65}$$

where P_B is given by Equation (5) and $T_C = T_{C0}$. The coupled equations, Equations (35), (36) and (38), can then be solved analytically. Insights into the overall behavior can still be achieved, despite this simplification, and the more general case when $P_0 = P_0(z)$, which

implies a numerical solution, will be dealt with in future work. (ii) Only an x polarized incident field will be considered ($E_{0y} = 0$ in Equation (64)) and the symmetry of the film's crystal structure will be assumed to be uniaxial with the axis aligned with $\mathbf{P}_0 = P_0\hat{\mathbf{x}}$. Under these circumstances $E_\alpha = Q_\alpha = 0$, $\alpha = y,\ z$, meaning that the equations that need to be solved are reduced to Equations (35), and (38) for $\alpha = z$.
The problem can now be solved analytically. From Equations (39) to (41) it can be seen that, for the single frequency applied field, there will be linear terms corresponding to frequency w and, through $\mathbf{Q}^{(2)}$ in Equation (41), there will be nonlinear terms coming from products of the field components (only those involving E_x^2 for the case we are considering), each involving a frequency 2ω—these are the second harmonic generation terms. It is natural to split the problem in to two parts now: one for the linear terms at ω, the other for the second harmonic generation terms at 2ω. Since we are primarily interested in second harmonic generation it may seem that the linear terms do not need to be considered. However, the way that the second harmonics are generated is through the nonlinear response of the polarization to the linear applied field terms. This is expressed by the constitutive relation in Equation (39), from which it is clear that products of the linear terms express the second harmonic generation, which implies that the linear problem must be solved before the second harmonic generation terms can be calculated. This will be much more apparent in the equations below. In view of this we will deal with the problem in two parts one for the linear terms, the other for the second harmonic generation terms. Also, since we have a harmonic incident field (Equation (63)) the problem will be solved in the frequency domain.

5.2.2 Frequency domain form of the problem for the inear terms

For the linear terms at frequency ω, we seek the solution to the coupled differential equations, Equations (35) and (38) with constitutive relations given by Equations (40) and (41), and a P_0 given by Equation (69). This is expressed in the frequency domain through Fourier transform given in Equations (65) and (66).
The resulting coupled differential equations are

$$D\frac{d^2Q^\omega}{dz^2} + M(\omega)Q^\omega + E^\omega = 0, \tag{66}$$

$$\frac{d^2E^\omega}{dz^2} + \frac{\omega^2\epsilon_\infty}{c^2}E^\omega + \frac{\omega^2}{\epsilon_0 c^2}Q^\omega = 0, \tag{67}$$

for $-L \leqslant z \leqslant 0$, where,

$$M(\omega) = m\omega^2 + i\omega\gamma - 2BP_0^2. \tag{68}$$

Taking the ansatz e^{iqz} for the form of the $Q^\omega$and E^ωsolutions, non trivial solutions (which are the physically meaningful ones) are obtained providing that the determinant of the coefficient matrix—generated by substituting the ansatz into Equations (66) and (67)—satisfies

$$\begin{vmatrix} 1 & -Dq^2 + M(\omega) \\ -q^2 + \frac{\omega^2\epsilon_\infty}{c^2} & \frac{\omega^2}{\epsilon_0 c^2} \end{vmatrix} = 0. \tag{69}$$

This leads to a quadratic equation in q^2 whose solution is

$$(q_j^\omega)^2 = \frac{g_1(\omega)(-1)^{j+1}\sqrt{g_2(\omega)}}{2D}, \quad j = 1, 2, \tag{70}$$

where

$$g_1(\omega) = \frac{D\omega^2\epsilon_\infty}{c^2} + M(\omega), \tag{71}$$

$$g_2(\omega) = g_1^2(\omega) - \frac{4D\omega^2}{\epsilon_0 c^2}\left[\epsilon_\infty\epsilon_0 M(\omega) - 1\right], \tag{72}$$

and the ω dependence of the q solutions has been made explicit with the superscript. The general solution of the coupled equations, Equations (66) and (67) for the electric field is therefore,

$$E^\omega(z) = a_1 E_0 e^{-iq_1^\omega z} + a_2 E_0 e^{iq_1^\omega z} + a_3 e^{-iq_2^\omega z} + a_4 e^{iq_2^\omega z} \tag{73}$$

$$= E_0 \sum_{j=1}^{4} a_j e^{(-1)^j i q_{n_j}^\omega z}, \tag{74}$$

where $n_j = \lceil j/2 \rceil$. It is convenient to include the incident amplitude E_0 as a factor when expressing the constants as this will cancel when the boundary conditions are applied so that the a_1 to a_4 amplitudes are the wave amplitudes of these four waves in the film relative to the incident amplitude. The first term on the right side of Equation (73) is a transmitted wave traveling through the film towards the metal boundary (in the direction of $-z$ in our coordinate system), the second is the wave reflected from the metal boundary and traveling back towards the top of the film corresponding to the wave vectors $-q_1^\omega$ and q_1^ω, respectively; a similar pattern follows for the $\pm q_2^\omega$ modes of the last two terms. It is interesting to note that the presence of both $\pm q_1^\omega$ and $\pm q_2^\omega$ modes is a direct result of the D term in the free energy that is introduced to account for variations in the polarization. In this sense our calculation, despite using a constant P_0 value, is still incorporating the effects of varying polarization (the full effects, as discussed above, involve numerical calculations which will be done in future work). If there was no D term then only the $\pm q_1^\omega$ modes would be present and the character of the solution would be different.

Above the film, alongside the incident wave there is a reflected wave. Thus we have

$$E_{\mathrm{I}}^\omega(z) = E_0 e^{-iq_0 z} + rE_0 e^{iq_0 z}, \quad z > 0 \tag{75}$$

where r is the linear reflection coefficient (there will also be a wave from second harmonic generation which is considered in the next section).

To complete the solution of the linear problem it remains to calculate the a_j and r amplitudes (five in total) by applying boundary conditions. The boundary conditions are the usual electromagnetic boundary conditions of continuity of the electric and magnetic fields, and here, we will express the continuity of the magnetic field as the continuity of $d\mathbf{E}/dz$; this follows from the electromagnetic induction Maxwell equation, $\boldsymbol{\nabla} \times \mathbf{E} = -\partial\mathbf{B}/\partial t$ (since the film is nonmagnetic $\mathbf{B} = \mu_0\mathbf{H}$ not only above the film but also in the film). The boundary conditions on $\mathbf{P}$ in Equations (18) and (19) will also be used, in the limiting case of infinite

extrapolation lengths. In fact, as discussed by Chandra & Littlewood (2007), an infinite extrapolation length for the metal boundary may well be a value consistent with experimental results on films with metal electrodes attached.
In view of the forgoing the required boundary conditions are:

$$E_{\mathrm{I}}^{\omega}(0) = E^{\omega}(0), \ \left.\frac{dE_{\mathrm{I}}^{\omega}}{dz}\right|_{z=0} = \left.\frac{dE^{\omega}}{dz}\right|_{z=0}, \ \left.\frac{dQ^{\omega}}{dz}\right|_{z=0} = 0, \tag{76}$$

for the top surface, and

$$E^{\omega}(-L) = 0, \ \left.\frac{dQ^{\omega}}{dz}\right|_{z=-L} = 0, \tag{77}$$

for the film-metal interface at the bottom. Note that the electric field boundary condition at the bottom implies that the metal conductivity is infinite so that no electric field penetrates the metal. This is a common approximation for metal boundaries and should be sufficient for our purposes since the conductivity of the ferroelectric film is much smaller than for the metal (Webb, 2006). Also the continuity of the magnetic field is not used at the bottom; it is not required because, with five unknowns, five boundary conditions are sufficient to find them.
Applying the boundary conditions leads to a set of simultaneous equations, the solution of which yields expressions for r and the a_j in terms of the other parameters, and hence solves the linear problem. These equations may be expressed in matrix form as

$$\mathsf{M}(\omega)\mathsf{a}_{\mathrm{lin}} = \mathsf{b}_{\mathrm{lin}}, \tag{78}$$

where

$$\mathsf{M}(\omega) = \begin{pmatrix} 1 & 1 & 1 & 1 & -1 \\ q_1^{\omega} & -q_1^{\omega} & q_2^{\omega} & -q_2^{\omega} & q_0 \\ \kappa_1^{\omega} & \kappa_2^{\omega} & \kappa_3^{\omega} & \kappa_4^{\omega} & 0 \\ \Delta_1^{\omega} & \Delta_2^{\omega} & \Delta_3^{\omega} & \Delta_4^{\omega} & 0 \\ \kappa_1^{\omega}\Delta_1^{\omega} & \kappa_2^{\omega}\Delta_2^{\omega} & \kappa_3^{\omega}\Delta_3^{\omega} & \kappa_4^{\omega}\Delta_4^{\omega} & 0 \end{pmatrix}, \tag{79}$$

$$\mathsf{a}_{\mathrm{lin}} = \left(a_1, a_2, a_3, a_4, r\right)^{\mathsf{T}}, \tag{80}$$

$$\mathsf{b}_{\mathrm{lin}} = \left(1, q_0, 0, 0, r\right)^{\mathsf{T}}, \tag{81}$$

and we define

$$\kappa_j^{\omega} = (-1)^j q_{n_j}^{\omega}\left[(q_{n_j}^{\omega})^2 - \epsilon_{\infty} q_0^2\right], \quad \Delta_j^{\omega} = e^{(-1)^{j+1} i q_{n_j} L}. \tag{82}$$

The resulting symbolic solution is rather complicated and will not be given here explicitly. It is easily obtained, however, with a computer algebra program such as Maxima or Mathematica. A more efficient approach for numerical plots is to compute numerical values of all known quantities before solving the matrix equation, which is then reduced to a problem involving the five unknowns multiplied by numerical constants.

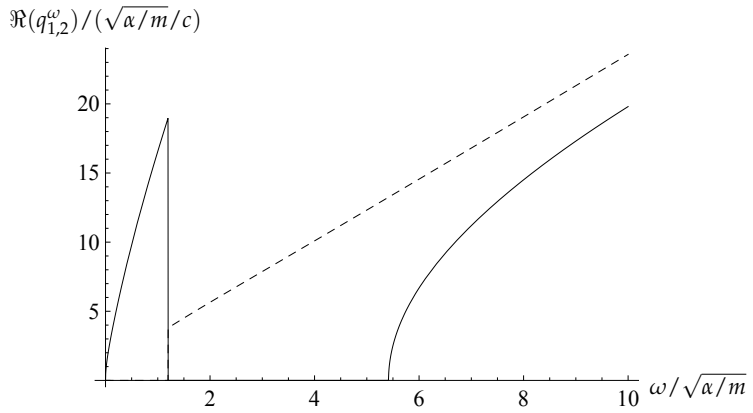

Fig. 4. Dimensionless plot of $\Re(q_1^{\omega})$ and $\Re(q_2^{\omega})$ (dotted line) versus frequency for $a = 6.8 \times 10^5\,\mathrm{V\,K^{-1}A^{-1}s^{-1}}$, $D = 2.7 \times 10^{-21}\,\mathrm{A\,Kg^{-1}m^{-1}}$, $m = 6.4 \times 10^{-21}\,\mathrm{kg\,m^3A^{-1}s^{-2}}$, $L = 40\,\mathrm{nm}$, $T/T_c = 0.5$, $\gamma = 1.3 \times 10^{-9}\,\mathrm{A^{-1}V^{-1}m^{-3}}$, and $\epsilon_\infty = 3.0$. These values are for $BaTiO_4$, and follow Chew et al. (2001).

The real parts of the dispersion relations in Equation (70) are plotted in Figure 4 for the q_1^{ω} and q_2^{ω} modes. The q_1^{ω} mode is the usual mode found in dielectrics and the frequency region, known as the reststrahl region, in which it is zero is where there are no propagating waves for that mode. However, it is clear from the plot that the real part of the q_2^{ω} mode is not zero in this region and so there will be propagation leading to a different reflection coefficient than what would be observed otherwise. This is due to the effect of the D term.
In Figure 5 the magnitude of the reflection coefficient r—available from the solution to the linear problem—is plotted against frequency. With no D term the reflection coefficient would take the value 1 in the reststrahl region. It is clear from the plot that there is structure in this region that is caused by the q_2^{ω} mode. So reflection measurements are a way of investigating the varying polarization modeled through the D term. The plot is for a film thickness of 40 nm. So our model predicts that these effects will be significant for nanoscale films. It is also expected that structure in this region will be found for the second harmonic generation reflection, the calculation of which which we now turn to.

5.2.3 Frequency domain form of the problem for the nonlinear second harmonic generation terms

The second harmonic generation terms come from the second order nonlinear terms, at frequency 2ω and the coupled differential equations that need to be solved for these terms are

$$D\frac{d^2Q^{2\omega}}{dz^2} + M(2\omega)Q^{2\omega} + E^{2\omega} = 3BP_0^2[Q^{\omega}]^2, \tag{83}$$

$$\frac{d^2E^{2\omega}}{dz^2} + \frac{(2\omega)^2\epsilon_\infty}{c^2}E^{2\omega} + \frac{(2\omega)^2}{\epsilon_0 c^2}Q^{2\omega} = 0, \tag{84}$$

$$\text{for } -L \leqslant z \leqslant 0.$$

It can be seen from this that there will be a homogeneous solution analogous to the linear solution but now at frequency 2ω and in addition, due to the term involving $[Q^{\omega}]^2$ in

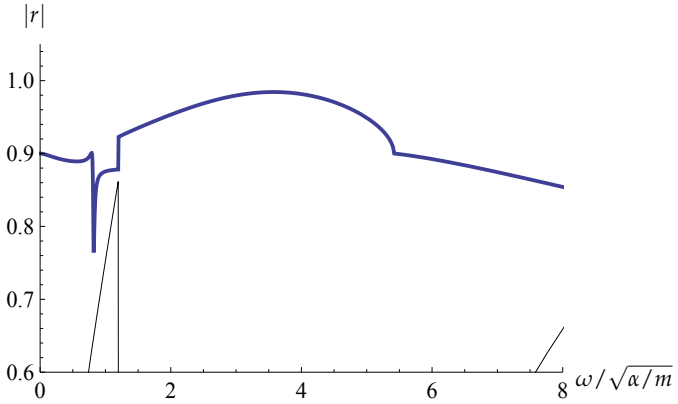

Fig. 5. Magnitude of linear reflection coefficient r versus dimensionless frequency. The lower curve is a scaled down plot of the dispersion curve for q_1^{ω} showing the reststrahl region. Parameter values as in Figure 4.

Equation (83), there will be particular solutions. $[Q^{\omega}]^2$ can be found from the solution to the linear problem for E^{ω} substituted into Equation (67), and thus the particular solutions to Equations (83) and (84) can be determined. In this way the general solution can be shown to be given by

$$E_0^2 \Lambda \sum_{j=1}^{4} \phi_j e^{(-1)^j i q_{n_j}^{2\omega} z} + E_0^2 \sum_{j=1}^{4} \sum_{k=1}^{4} W_{jk} e^{iB_{jk} z}, \tag{85}$$

together with,

$$W_{jk} = \frac{12 B P_0^2 A_{jk}}{\epsilon_0 \left[4 q_0^2 \epsilon_\infty - B_{jk}^2\right] \left[D B_{jk}^2 - M(2\omega)\right]}, \tag{86}$$

$$A_{jk} = S_{n_j} S_{n_k} a_j a_k, \tag{87}$$

$$s_j = (q_j^{\omega})^2 - \epsilon_\infty \omega / c^2, \tag{88}$$

$$B_{jk} = (-1)^j q_{n_j}^{\omega} + (-1)^k q_{n_k}^{\omega}. \tag{89}$$

It is convenient to include the factor E_0^2 in Equation (85) since it will cancel out later when the boundary conditions are applied. The factor Λ has been included to make the ϕ_j amplitudes dimensionless so that they are on the same footing as the a_j amplitudes in the linear problem. Due to the second harmonic generation terms in the film there will also be a second harmonic generation field transmitted from the film to the air above, but since this ultimately exists because of the incident field the second harmonic generation wave above the film is a reflected wave caused by the incident field. It is expressed by

$$E_{\mathrm{I}}^{2\omega}(z) = E_0^2 \Lambda \rho e^{2 i q_0 z}, \quad z > 0, \tag{90}$$

where ρ is the second harmonic generation reflection coefficient.
Again there are five unknowns: ρ and the ϕ_j, which are also found by applying the boundary conditions. The particular solutions make the problem more complex algebraically, but in principle the solution method is the same as for the linear case. Applying the conditions in

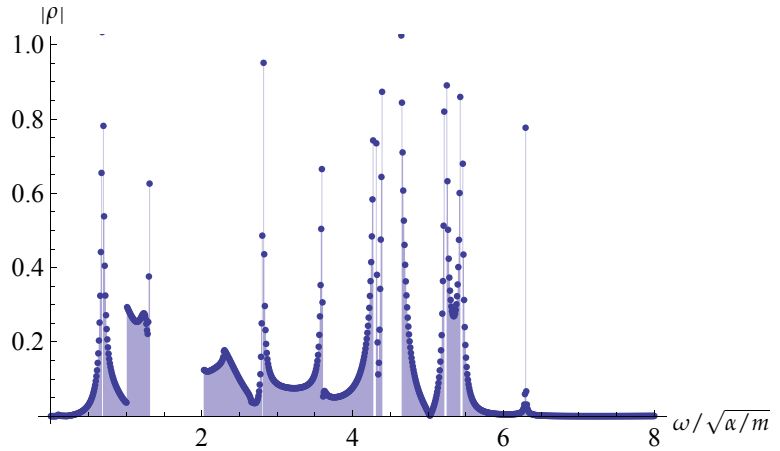

Fig. 6. Second harmonic generation reflection coefficient ρ versus dimensionless frequency. Parameter values are as in Figure 4.

Equations (76) and (77) leads to five simultaneous equations that can be expressed as

$$\mathsf{M}(2\omega)\mathsf{a}_{\mathrm{SHG}} = \mathsf{b}_{\mathrm{SHG}}, \tag{91}$$

where

$$\mathsf{a}_{\mathrm{SHG}} = \left(\phi_1, \phi_2, \phi_3, \phi_4, \rho\right)^{\mathsf{T}}, \tag{92}$$

$$\mathsf{b}_{\mathrm{SHG}} = \left(\mathcal{P}_1, \mathcal{P}_2, \mathcal{P}_3, \mathcal{P}_4, \mathcal{P}_5\right)^{\mathsf{T}}, \tag{93}$$

with

$$\left.\begin{aligned} \mathcal{P}_1 = -(1/\Lambda)\sum_{jk} W_{jk},\ \mathcal{P}_2 = (1/\Lambda)\sum_{jk} W_{jk}B_{jk}, \\ \mathcal{P}_3 = (1/\Lambda)\sum_{jk} W_{jk}O_{jk},\ \mathcal{P}_4 = -(1/\Lambda)\sum_{jk} W_{jk}\delta_{jk}, \\ \mathcal{P}_5 = (1/\Lambda)\sum_{jk} W_{jk}O_{jk}\delta_{jk}, \end{aligned}\right\} \tag{94}$$

and

$$O_{jk} = B_{jk}\left(4\epsilon_\infty q_0^2 - B_{jk}^2\right), \quad \delta_{jk} = e^{-iB_{jk}L}. \tag{95}$$

Now the unknowns for the second harmonic generation problem can be found by solving Equation (91), in a similar way to what was done for the linear problem, and from this the second harmonic generation reflection coefficient ρ can be found.

A plot of $|\rho|$ versus frequency is given in Figure 6. A dramatic structure is evident and, as with the linear reflection, is also present in the reststrahl region. So second harmonic generation reflection measurements are expected to be a sensitive probe of size effects in nanoscale ferroelectric thin films according to the model presented here.

The numerical values calculated for the second harmonic generation reflection coefficient are much smaller than for the linear one. This is to be expected since second harmonic generation is a second-order nonlinear effect. This numerical result is consistent with that found by Murgan et al. (2004), but their work did not include the mode due to the D term. Also the general features of the second harmonic generation reflection coefficient are similar to a brief second harmonic generation study that was done by Stamps & Tilley (1999) for a free standing film. However the effect of the metal substrate considered here has made the second harmonic generation reflection features more pronounced.
It is also of interest to compare the numerical values here with experimental studies. Many second harmonic generation reflection experimental studies have covered optical frequencies higher than the far-infrared frequencies that are relevant to the work in this paper. It is hoped that our work will stimulate more experimental work in the far-infrared region. Detailed numerical work that is now in progress can then be compared with such experiments.

6. Conclusion

This chapter has considered how Landau-Devonshire theory together with Landau-Khalatnikov equations of motion can be used to model a ferroelectric film. A fairly general theory encompassing size effect that cause the equilibrium polarization to be influenced by surfaces together with the nonlinear dynamical response to incident electromagnetic waves has been given. Then, a specific example of second harmonic generation in ferroelectric films was presented with an emphasis on calculating the reflection coefficient that is relevant to far infrared reflection measurements. It has been shown how the theory suggests that such reflection measurements would enable the ferroelectric properties of the film such as the size effects to be probed.
Some of the more general aspects of the theory are not really needed for this specific example but an aim of presenting the more general formulae is to provide a foundation for the many other calculations that could be done, both linear and nonlinear. A large number of different nonlinear effects could be studied. Also the incorporation of a space varying equilibrium polarization profile of the sort given in Sections 2.2 and 2.3 into the dynamical calculations would be provide a more detailed study than the example given here. Also it would be of use to find a general set of formula that expresses the set of equations that need to be solved for the reflection problem due to general nth-order second harmonic generation. Currently the set of equations for each order has to be derived for each case since no general formulae of for this seems to exist in the literature. The generalization is not entirely trivial, but some progress along those lines as been made by (Webb, 2003; 2009; Webb & Osman, 2003), but quite a lot more needs to be done to produce the set of equations for the nth-order reflection problem.

7. References

Abramowitz, M. & Stegun, I. A. (eds) (1972). *Handbook of Mathematical Functions*, Dover, New York.

Butcher, P. N. & Cotter, D. (1990). *The Elements of Nonlinear Optics*, Cambridge University Press, Cambridge, UK.

Chandra, P. & Littlewood, P. B. (2007). A landau primer for ferroelectrics, *in* K. Rabe, C. H. Ahn & J. M. Triscone (eds), *Physics of Ferroelectrics*, Vol. 105 of *Topics in Applied Physics*, Springer, Heidelberg, p. 69.

Chew, K. H., Ong, L. H., Osman, J. & Tilley, D. R. (2001). Theory of far-infrared reflection and transmission by ferroelectric thin films, *J. Opt. Soc. Am B* 18: 1512.

Cottam, M. G., Tilley, D. R. & Zeks, B. (1984). Theory of surface modes in ferroelectrics, *J. Phys C* 17: 1793–1823.

Gerbaux, X. & Hadni, A. (1989). Far infrared and phase transitions in ferroelectric materials, *Phase Transitions* 14: 117.

Gerbaux, X. & Hadni, A. (1990). *Static and dynamic properties of ferroelectric thin film memories*, PhD thesis, University of Colorado.

Gerbaux, X., Hadni, A. & Kitade, A. (1989). Far ir spectra of ferroelectric Rochelle Salt and sodium ammonium tartrate, *Phys. Stat. Sol. (a)* 115: 587.

Ginzburg, V. L., Levanyuk, A. P. & Sobyanin, A. A. (1980). Light scattering near phase transition points in solids, *Phys. Rep.* 57: 151.

Höchli, U. T. & Rohrer, H. (1982). Separation of the D_{4h} and O_h phases near the surface of $SrTiO_3$, *Phys. Rev Lett.* 48: 188.

Iniguez, J., Ivantchev, S. & Perez-Mato, J. M. (2001). Landau free energy of $BaTiO_3$ from first principles, *Phys. Rev. B* 63: 144103.

Jackson, J. D. (1998). *Classical Electrodynamics*, 3rd edn, Wiley, New York.

Kulkarni, A., Rohrer, G., Narayan, S. & McMillan, L. (1988). Electrical properties of ferroelectric thin film KNO_3 memory devices, *Thin Solid Films* 164: 339.

Landau, L. D. & Khalatnikov, I. M. (1954). On the anomalous absorption of sound near a second-order phase transition point, *Dok. Akad. Navk SSSR* 96: 469.

Li, S., Eastman, J. A., Li, Z., Foster, C. M., Newnham, R. E. & Cross, L. E. (1996). Size effects in nanostructured ferroelectrics, *Phys. Lett.* 212: 341.

Li, S., Eastman, J. A., Vetrone, J. M., Foster, C. M., Newnham, R. E. & Cross, L. E. (1997). Dimension and size effects in ferroelectrics, *Jap. J. Appl. Phys.* 36: 5169.

Lines, M. E. & Glass, A. M. (1977). *Principles and Applications of Ferroelectrics and Related Materials*, Clarendon, Oxford, UK.

Marquardt, P. & Gleiter, H. (1982). Ferroelectric phase transition in microcrystals, *Phys. Rev. Lett.* 48: 1423.

Mills, D. L. (1998). *Nonlinear Optics*, second edn, Springer, Berlin.

Mishina, E. D., Sherstyuk, N. E., Barsky, D., Sigov, A. S., Golovko, Y. I., Mukhorotov, V. M., Santo, M. D. & Rasing, T. (2003). Domain orientation in ultrathin (Ba,Sr)TiO_3 films measured by optical second harmonic generation, *J. Appl. Phys* 93: 6216.

Murgan, R., Razak, F., Tilley, D. R., Tan, T. Y., Osman, J. & Halif, M. N. A. (2004). Second harmonic generation from a ferroelectric film, *Comp. Mat. Sci* 30: 468.

Murgan, R., Tilley, D. R., Ishibashi, Y., Webb, J. F. & Osman, J. (2002). Calculation of nonlinear susceptibility tensor components in ferroelectrics: Cubic, tetragonal, and rhombohedral symmetries, *J. Opt. Soc. Am. B* 19: 2007.

Osman, J., Ishibashi, Y. & Tilley, D. R. (1998). Calculation of nonlinear susceptibility tensor components in ferroelectrics, *Jpn. J. Appl. Phys* 37: 4887.

Scott, J. F. (1998). The physics of ferroelectric ceramic thin films for memory applications, *Ferroelectr. Rev.* 1: 1.

Scott, J. F. & Araujo, C. (1989). Ferroelectric memories, *Science* 246: 1400.

Stamps, R. L. & Tilley, D. R. (1999). Possible far infrared probes of ferroelectric size effects, *Ferroelectrics* 230: 221.

Strukov, B. A. & Lenanyuk, A. P. (1998). *Ferroelectric Phenomena in Crystals*, Springer, Berlin.

Tan, E. K., Osman, J. & Tilley, D. R. (2000). First-order phase transitions in ferroelectric films, *Solid State Communications* 116: 61–65.

Tilley, D. R. (1993). Phase transitions in thin films, *in* N. Setter & E. L. Colla (eds), *Ferroelectric Ceramics*, Birkhäuser Verlag, Berlin, p. 163.

Tilley, D. R. (1996). Finite-size effects on phase transitions in ferroelectrics, *in* C. P. de Araujo, J. F. Scott & G. W. Taylor (eds), *Ferroelectric Thin Films: Synthesis and Basic Properties*, Integrated Ferroelectric Devices and Technologies, Gordon and Breach, Amsterdam, p. 11.

Tilley, D. R. & Zeks, B. (1984). Landau theory of phase transtions in thick films, *Solid State Commun.* 49: 823.

Ward, J. F. (1969). Optical third harmonic generation in gases by a focused laser beam, *Phys. Rev.* 185: 57.

Webb, J. F. (2003). A general approach to perturbation theoretic analysis in nonlinear optics and its application to ferroelectrics and antiferroelectrics, *Int. J. Mod. Phys. B* 17: 4355.

Webb, J. F. (2006). Theory of size effects in ferroelectric ceramic thin films on metal substrates, *J. Electroceram.* 16: 463.

Webb, J. F. (2009). A definitive algorithm for selecting perturbation expansion terms applicable to the nonlinear dynamics of ferroelectrics and cad-modeling, *Proceedings of the International Conference on Computational Design in Engineering (CODE 2009)*, Seoul, Korea.

Webb, J. F. & Osman, J. (2003). Derivation of nonlinear susceptibility coefficients in antiferroelectrics, *Microelectronic Engineering* 66: 584.

27

Nonlinear Hysteretic Response of Piezoelectric Ceramics

Amir Sohrabi and Anastasia Muliana
Department of Mechanical Engineering
Texas A&M University, College Station,
USA

1. Introduction

Ferroelectric materials, such as lead zirconate titanate (PZT), have been widely used in sensor, actuator, and energy conversion devices. In this paper, we are primarily interested in the electro-mechanical response of polarized ferroelectric ceramics subject to cyclic electric fields at various magnitudes and frequencies. There have been experimental studies on understanding the effect of electric fields and loading rates on the overall electro-mechanical response of PZT (see for examples Crawley and Anderson 1990, Zhou and Kamlah 2006). The electrical and mechanical responses of PZT are also shown to be time-dependent, especially under high electric field (Fett and Thun 1998; Cao and Evans 1993; Schaufele and Hardtl, 1996). Ben Atitallah et al. (2010) studied the hysteretic response of PZT5A and active PZT fiber composite at several frequencies and isothermal temperatures. They show the nonlinear and time-dependent piezoelectric constants of the PZTs and PZT fiber composites. In a review of nonlinear response of piezoelectric ceramics, Hall (2001) discussed experimental studies that show strong time-dependent and nonlinear behavior in the electro-mechanical response of ferroelectric ceramics. The time-dependent effect becomes more prominent at electric fields close to the coercive electric field of the ferroelectric ceramics and under high magnitude of electric fields a ferroelectric ceramics exhibits nonlinear electro-mechanical response. Furthermore, high mechanical stresses could result in nonlinear mechanical, electrical, and electro-mechanical responses of the ferroelectric materials. Within a context of a purely mechanical loading in viscoelastic materials, time-dependent response is shown by a stress relaxation (or a creep strain). This results in stress-strain hysteretic response when a viscoelastic material is subjected to a cyclic mechanical loading. There are different types of viscoelastic materials, such as polymers, biological tissues, asphalts, and geological materials. It is understood that these materials possess different microstructural characteristics at several length scales; however the macroscopic (overall)[1] mechanical response of these materials, i.e. stress relaxation and hysteretic response, especially for a linear response, follows similar trends. Experimental studies have shown that there are similarities with regards to the macroscopic time-dependent (or

[1] In this context, by observing the macroscopic response of materials we treat the bodies as continuous and homogeneous with respect to their mechanical response although there is no clear cut as at which length scale the bodies can be considered continuous and homogeneous.

frequency dependent) response of piezoelectric ceramics, i.e. electro-mechanical coupling, dielectric constant, and mechanical stress-strain relation, to the macroscopic time-dependent and hysteretic behaviors of viscoelastic materials although it is obvious that the microstructural morphologies of piezoelectric ceramics are completely different from the ones of viscoelastic materials mentioned above.

The macroscopic response of materials depends upon their microstructural changes when these materials are subjected to various histories of external stimuli such as mechanical load and/or electric field. Several constitutive models have been developed to examine the effect of electric field and mechanical stress on the overall hysteretic response of ferroelectric materials. These constitutive models can be classified as purely phenomenological models derived based on classical mechanics and thermodynamics framework and micromechanics based models that incorporate changes in the polycrystalline (micro) structure of ferroelectric ceramics with external stimuli. In the phenomenological models, changes in the microstructures of materials due to external stimuli are not explicitly modeled; however the effects of microstructural changes on the macroscopic response of materials can be incorporated by allowing the material parameters to vary with the external stimuli. It is also noted that any changes in micro- and macroscopic responses of materials occur in some finite period and in most cases these changes also depend upon how fast or slow the external stimuli are prescribed to the bodies, leading to what so called 'rate-dependent response'. Changes in the microstructures of materials with external stimuli are rather complicated. It might not be possible to incorporate detailed mechanisms that trigger these changes in developing constitutive models, mainly due to the complexity of these microstructural changes that occur at various scales and it is not well understood how the interactions among different field variables at the microscopic scale affects the macroscopic response. Several micromechanics based models are derived with a motivation to incorporate some aspects of the microstructural characteristics in predicting macroscopic response of materials. These micromechanics models are of course based on some assumptions and hypotheses. For examples: Smith et al. (2003, 2006) developed a constitutive model for hysteretic polarization switching response based on free-energy of a single crystal structure. It is assumed that the free energy is related to dipole reorientation in each crystal structure. A stochastic homogenization approach is used to obtain macroscopic hysteretic response of polycrystal structures. Chan and Hagood (1994) modeled a polarization reversal behavior of a single-crystal piezoceramic by assuming that the single crystal can be polarized to six possible directions and the overall responses of the piezoceramics are obtained either by averaging the crystallite responses in a global coordinate system or by taking into account internal alignment of the crystallites. Chen and Lynch (1998) incorporated the effects of grain orientations and crystal structures, i.e. tetragonal and rhombohedral, on the macroscopic hysteretic response of piezoelectric ceramics. These various microstructural-based models that require different material parameters are shown capable of simulating nonlinear hysteretic macroscopic response of piezoelectric ceramics. In most cases, these material parameters are characterized from the macroscopic response of the materials. An attempt of using molecular dynamics simulations in predicting macroscopic nonlinear hysteretic response of ferroelectric materials has also been considered. Such studies can be found in Uludogan et al. (2008) and Fang and Sang (2009). All of the above models that to some extents include microstructural aspects of piezoelectric ceramics are derived with a motivation to explain and improve understanding

on the nonlinear hysteretic response; however it might be difficult if not possible to perform experiments that can trace detailed microstructural changes at various microscopic scales during the hysteretic response, not to mention incorporating the rate of these changes as well. A discussion on the development of constitutive models of ferroelectric materials can be found in Smith (2005) and Lines and Glass (2009).

Bassiouny et al. (1988a and b, 1989) formulated a phenomenological model for predicting electromechanical hysteretic response of piezoelectric ceramics. They defined a thermodynamic potential in terms of reversible and irreversible parts of the polarization. The irreversible part is the energy associated with the residual electric polarization. This constitutive model leads to rate-independent equations for the electro-mechanical coupling in piezoelectric ceramics (in analogy to the flow rule plasticity model). Huang and Tiersten (1998a and b) used a phenomenological based model for describing electro-mechanical hysteretic behavior in ferroelectric ceramics. Their model can capture the overall nonlinear hysteretic response, but it does not incorporate the effect of frequencies on the overall hysteretic response. Another example of phenomenological models of nonlinear rate-independent hysteretic response of piezoelectric ceramics is by Kamlah and Tsakmakis (1999). The nonlinearity is due to polarization switching when the piezoelectric ceramics are subjected to high electric field and compressive stress. Similar to the crystal plasticity model of Bassiouny et al. (1988a and b) Landis (2002) developed a phenomenological model for predicting polarization switching in ferroelectric materials. They used an idea of rate-independent plasticity model and discussed an extension of the constitutive model to include a rate-dependent response. Tiersten (1971, 1993) developed a nonlinear electro-elastic model for predicting response of polarized piezoelectric ceramics undergoing large electric driving fields and small strains. The constitutive model includes higher order terms of electric fields. Crawley and Anderson (1990) suggested that the nonlinear electric field can be incorporated by taking a linear piezoelectric constant to depend on the electric field. Massalas et al. (1994) and Chen (2009) presented nonlinear thermo-electro-mechanical constitutive equations for elastic materials with memory-dependent (viz. viscoelastic materials) that incorporate the effect of heat generation due to the dissipation of energy on the nonlinear thermo-electro-mechanical response of conductive materials. The advantages of the phenomenological models are in their relatively simple forms in which the material parameters can be easily characterized from macroscopic experiments, which are beneficial for designing structures consisting of piezoelectric ceramics.

The electro-mechanical response of ferroelectric ceramics is shown to be time- (or rate-) dependent within a context of dielectric- and piezoelectric relaxation; however limited studies have been done on predicting time-dependent response of ferroelectric ceramics. We extend the concepts of response of viscoelastic solids to evaluate the nonlinear time-dependent electro-mechanical (macroscopic) response of polarized ferroelectric materials, i.e. piezoelectric ceramics. General time-integral electro-mechanical phenomenological constitutive models based on multiple integral and nonlinear single integral forms are used. We assume that the dielectric and piezoelectric constants of the materials change with electric field and the rate of time-dependent polarization and strain responses can also change with the magnitude of the electric field. This manuscript is organized as follows. Section two discusses a nonlinear time-dependent constitutive model based on integral formulations for electro-mechanical response of piezoelectric ceramics, followed by numerical implementation and verification of the models in section three. Section four

presents analyses of piezoelectric bimorph actuators having time-dependent material properties. The last section is dedicated to a conclusion and a discussion of the proposed nonlinear time-integral models.

2. Nonlinear time-dependent constitutive model for piezoelectric ceramics

2.1 Nonlinear electro-elastic constitutive model

A phenomenological constitutive model[2] for polarized ferroelectric ceramics at an isothermal condition is described in terms of the following field variables: stress $\boldsymbol{\sigma}$, strain $\boldsymbol{\varepsilon}$, electric field $\mathbf{E}$, electric flux (displacement) $\mathbf{D}$. It is assumed that loading is within a quasi-static condition such that the effect of inertia on the electro-mechanical response can be neglected. The constitutive model for polarized ferroelectric ceramics can be obtained by defining a thermodynamic potential $\psi_e(\boldsymbol{\varepsilon},\mathbf{E})$ (see Bassiouny et al. 1988a; Tiersten, 1993; Huang and Tiersten, 1998). The relations between the different field variables are obtained from:

$$\sigma_{ij} = \left.\frac{\partial \psi_e}{\partial \varepsilon_{ij}}\right|_{\mathbf{E}} \qquad D_i = -\left.\frac{\partial \psi_e}{\partial E_i}\right|_{\boldsymbol{\sigma}} \tag{2.1}$$

The components of the electric field and strain are expresses as $E_i = -\varphi_{,i}$ and $\varepsilon_{ij} = \frac{1}{2}\left(u_{i,j} + u_{j,i}\right)$, respectively; where φ and u_i are the electric potential and scalar component of the displacement, respectively. This study focuses on understanding response of piezoelectric ceramics undergoing large electric fields and the brittle nature of piezoelectric ceramics limits their deformation to small strains. The thermodynamic potential includes up to second order strain tensor and higher order electric field. Tiersten (1993) suggested the following free energy function at an isothermal condition:

$$\psi_e = \frac{1}{2}C_{ijkl}\varepsilon_{ij}\varepsilon_{kl} - e_{ijk}\varepsilon_{jk}E_i - \frac{1}{2}\kappa_{ij}E_iE_j - \frac{1}{2}b_{ijkl}E_iE_j\varepsilon_{kl} - \frac{1}{6}\chi_{ijk}E_iE_jE_k + H.O.T \tag{2.2}$$

where C_{ijkl}, e_{ijk}, κ_{ij}, b_{ijkl}, and χ_{ijk} are the fourth-order elasticity tensor, third-order electro-mechanical tensor (piezoelectric constant), second-order electric permeability (dielectric constant), fourth-order electro-mechanical tensor, and third-order electric permeability tensor, respectively. The above elasticity constants are measured at constant or zero electric field, while the electrical properties are measured at constant or zero strains. The stress and electric displacement are:

$$\begin{aligned} \sigma_{ij} &= C_{ijkl}\varepsilon_{kl} - e_{kij}E_k - \frac{1}{2}\hat{b}_{klij}E_kE_l \\ D_i &= e_{ijk}\varepsilon_{jk} + \hat{\kappa}_{ij}E_j + \frac{1}{2}\chi_{ijk}E_jE_k \end{aligned} \tag{2.3}$$

[2] We deal with a constitutive model for a continuous and homogeneous body, suitable for simulating response of a piezoelectric ceramic below its coercive electric field.

where

$$\hat{b}_{ijkl} = b_{ijkl} - 2\kappa_o\left(\delta_{ki}\delta_{lj} - \frac{1}{2}\delta_{ij}\delta_{kl}\right)$$
$$\hat{\kappa}_{ij} = \kappa_{ij}^{\varepsilon} = \kappa_o\delta_{ij} + \kappa_{ij} \tag{2.4}$$

Here κ_o is the permittivity constant at free space and δ_{ij} is the delta Kronecker. Tiersten (1993) also discussed an alternative expression of the constitutive model with nonlinear electric field and small strain when stress, electric field, and temperature are taken as the independent field variables:

$$\varepsilon_{ij} = S_{ijkl}\sigma_{kl} + d_{kij}E_k + \frac{1}{2}f_{klij}E_kE_l$$
$$D_i = d_{ijk}\sigma_{jk} + \kappa_{ik}^{\sigma}E_k + \frac{1}{2}\chi_{ijk}^{\sigma}E_jE_k \tag{2.5}$$

The elastic compliances, S_{ijkl}, piezoelectric constant, d_{ijk}, and nonlinear electroelastic constants, f_{ijkl}, are:

$$S_{ijkl} = C_{ijkl}^{-1}$$
$$d_{ijk} = e_{imn}S_{mnjk} \tag{2.6}$$
$$f_{ijkl} = \hat{b}_{ijmn}S_{mnkl}$$

The second- and third-order electric permeability constants are measured at zero or constant stresses:

$$\kappa_{ij}^{\sigma} = \hat{\kappa}_{ij} + e_{imn}d_{jmn}$$
$$\chi_{ijk}^{\sigma} = \chi_{ijk} + e_{imn}f_{jkmn} \tag{2.7}$$

2.2 Nonlinear time-dependent constitutive model

In analogy to the time-dependent deformation of viscoelastic materials, we extend the nonlinear electro-elastic model developed by Tiersten (1993) to include time-dependent material parameters. There have been several integral models developed to describe nonlinear viscoelastic behavior: modified superposition principle (Findley and Lai, 1967), multiple integral model (Green and Rivlin 1957), finite strain integral models (Pipkins and Rogers 1968; Rajagopal and Wineman 2010), single integral models (Pipkins and Rogers 1968; Schapery 1969), and quasi-linear viscoelastic model (Fung 1981). The work by Green and Rivlin (1957) provides the fundamental framework for nonlinear viscoelastic response using the principles of continuum mechanics. It is assumed that small changes in the input field variables cause only small changes in the corresponding output field variables; this can be approximated by using continuous functions by polynomials. For a nonlinear viscoelastic material, Green and Rivlin (1957) formed a sum of multiple integrals of the polynomial functions to incorporate history of input variables in predicting output at current time. The constitutive equations (2.3) and (2.5) are expressed in the polynomial functions of independent field variables. In analogy to the correspondence between elastic and viscoelastic materials, we extend the nonlinear electro-elastic equations of Tiersten (1993) to include the time-dependent effect (for non-aging materials):

$$\varepsilon_{ij}(t) = \int_{0^-}^{t} S_{ijkl}(t-s)\frac{d\sigma_{kl}(s)}{ds}ds + \int_{0^-}^{t} d_{kij}(t-s)\frac{dE_k(s)}{ds}ds + \frac{1}{2}\int_{0^-}^{t}\int_{0^-}^{t} f_{klij}(t-s_1,t-s_2)\frac{dE_k(s_1)}{ds_1}\frac{dE_l(s_2)}{ds_2}ds_1ds_2$$
$$D_i(t) = \int_{0^-}^{t} d_{ijk}(t-2)\frac{d\sigma_{jk}(s)}{ds}ds + \int_{0^-}^{t} \kappa_{ik}^{\sigma}(t-s)\frac{dE_k(s)}{ds}ds + \frac{1}{2}\int_{0^-}^{t}\int_{0^-}^{t} \chi_{ijk}^{\sigma}(t-s_1,t-s_2)\frac{dE_j(s_1)}{ds_1}\frac{dE_k(s_2)}{ds_2}ds_1ds_2 \quad (2.8)$$

It is also possible to include higher order terms of the electric field. In order to graphically visualize the linear and nonlinear kernel functions of time, let us consider a one-dimensional multiple integral forms (up to the second order):

$$R(t) = \int_{0^-}^{t} \varphi_1(t-s)\frac{dI(s)}{ds}ds + \int_{0^-}^{t}\int_{0^-}^{t} \varphi_2(t-s_1,t-s_2)\frac{dI(s_1)}{ds_1}\frac{dI(s_2)}{ds_2}ds_1ds_2 \quad (2.9)$$

where $R(t)$ is the corresponding output at current time t, $I(s)$ is the input history prescribed at $0^- \le s \le t$, $\varphi_1(t)$ and $\varphi_2(t,t)$ are the two kernel functions. When the kernels are assumed to increase with time, Fig. 2.1 illustrates the linear and second order kernel functions of time (see Findley et al. (1976) for a detailed explanation). It is also assumed that the material response is unaltered by an arbitrary shift of the time scale, so that $\varphi_2(t,t-s_1) = \varphi_2(t-s_1,t)$. The following functions can be used for the two kernels in Eq. (2.9):

$$\varphi_1(t-s) = A_0 + A_1(1.-e^{-(t-s)/\tau_1})$$
$$\varphi_2(t-s_1,t-s_2) = B_0 + B_1(2.-e^{-(t-s_1)/\lambda_1} - e^{-(t-s_2)/\lambda_1}) + B_2(1.-e^{-(t-s_1)/\lambda_2})(1.-e^{-(t-s_2)/\lambda_2}) \quad (2.10)$$

where A_0, A_1, B_0, B_1, B_2, τ_1, λ_1, λ_2 are the material parameters that need to be determined from experiments. A set of experiments may be performed by applying the input variables at different times, say at t=0 and t=s_1. The main disadvantage of the multiple integral forms is in characterizing material parameters from experiments, even when only up to the second order kernel function is considered. The characterization of material parameters becomes even more complicated for the anisotropic and nonlinear time-dependent case, which is the case for piezoelectric ceramics.

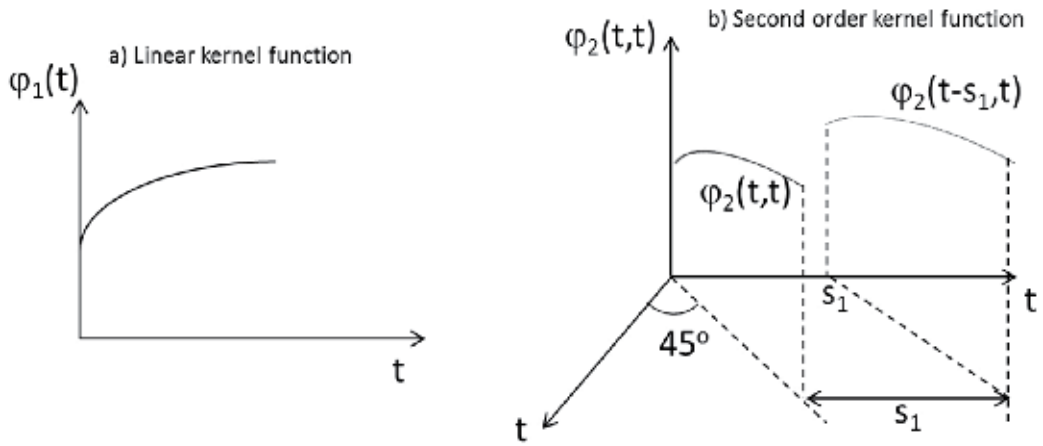

Fig. 2.1. Time-dependent kernel functions (see Findley et al., 1976)

It is also possible to include higher order terms of the electric field. In case of the third order term is included, the following third order kernel function can be considered:

$$\begin{aligned}&\varphi_3(t-s_1,t-s_2,t-s_3)=C_0+C_1(3.-e^{-(t-s_1)/\eta_1}-e^{-(t-s_2)/\eta_1}-e^{-(t-s_3)/\eta_1})+\\&C_2(1.-e^{-(t-s_1)/\eta_2})(1.-e^{-(t-s_2)/\eta_2})(1.-e^{-(t-s_3)/\eta_2})\end{aligned} \tag{2.11}$$

It is also necessary that $\varphi_3(t,t,t-s_1)=\varphi_3(t-s_1,t,t)=\varphi_3(t,t-s_1,t)$.

To reduce complexity in analyzing nonlinear viscoelastic behavior and characterizing material properties a single integral with nonlinear integrand has been used and found capable of approximating nonlinear responses in viscoelastic materials. Such models are discussed in Findley and Lay (1966), Pipkins and Rogers (1968), and Schapery (1969). Chen (2009) derived a nonlinear thermo-electro-viscoelastic constitutive equation that incorporates heat generation due to the dissipation of energy[3] and damage. The Gibbs free energy is defined in terms of a functional of the histories of stress, temperature, temperature gradient and electric field in the reference configuration and damage is introduced as an internal state variable. This constitutive model is based on a single integral form that includes hysteresis, aging, and damage in the electro-active materials, written as:

$$\begin{aligned}\frac{1}{2}C_{ij}(t)&=L^0_{ij}+\int_{-\infty}^{t}J_{ijkl}(0,t-s,\mathbf{d})\frac{d\Sigma_{kl}(s)}{ds}ds+\int_{-\infty}^{t}\alpha_{ij}(0,t-s,\mathbf{d})\frac{dT(s)}{ds}ds+\\&\quad\int_{-\infty}^{t}f_{ijk}(0,t-s,\mathbf{d})\frac{dE_k(s)}{ds}ds\\\rho_o s(t)&=M^0+\int_{-\infty}^{t}\alpha_{ij}(t-x,0,\mathbf{d})\frac{d\Sigma_{ij}(x)}{dx}dx+\frac{1}{T_0}\int_{-\infty}^{t}C_g(t-x,0,\mathbf{d})\frac{dT(x)}{dx}dx+\\&\quad\int_{-\infty}^{t}\eta_i(t-x,0,\mathbf{d})\frac{dE_i(x)}{dx}dx\\D_i(t)&=N^0_i+\int_{-\infty}^{t}f_{ijk}(t-x,0,\mathbf{d})\frac{d\Sigma_{jk}(x)}{dx}dx+\int_{-\infty}^{t}\eta_i(0,t-s,\mathbf{d})\frac{dT(s)}{ds}ds+\\&\quad\int_{-\infty}^{t}\kappa_{ij}(0,t-s,\mathbf{d})\frac{dE_j(s)}{ds}ds\end{aligned} \tag{2.12}$$

where $\mathbf{C},\boldsymbol{\Sigma},\mathbf{D},\mathbf{E},T,s$ are the right Cauchy-Green stretch tensor, second Piola-Kirchoff stress tensor, electric displacement vector, electric field vector, temperature, and entropy, respectively; ρ_0 is the mass density at a reference state; $\mathbf{L}^0,\mathbf{M}^0,\mathbf{N}$ are the right Cauchy-Green stretch tensor, product of the entropy and mass density, and electric displacement tensor at a reference state; $\mathbf{J},\boldsymbol{\alpha},\mathbf{f},\boldsymbol{\eta},\boldsymbol{\kappa},C_g$ are the compliance, thermal expansion, piezoelectric constant, pyroelectric constant, dielectric, and heat capacity, respectively; T_0 is the reference temperature; and $\mathbf{d}$ is the damage tensor. It is also necessary that each kernel in Eq. (2.12) satisfy the following condition: $\varphi(t-x,t-s,\mathbf{d})=\varphi(t-s,t-x,\mathbf{d})$. Chen (2009) also discussed

[3] Viscoelastic materials are known to dissipate significant amount of energy during cyclic loading; an electric current flows through a piezoelectric materials also dissipate energy which is converted to heat. Thus, it is necessary to account for this heat generation in predicting time-dependent response of piezoelectric materials.

the time-dependent forms for each material property in Eq. (2.12) in order to incorporate aging and damage.

If we follow an approach suggested by Crawley and Anderson (1990) in which the nonlinear electric field can be incorporated by taking a linear piezoelectric constant to depend on the electric field, a single integral model with nonlinear integrand as the first approximation for modeling the time-dependent electro-mechanical response with nonlinearity due to high electric field is expressed[4] as:

$$\begin{aligned}\varepsilon_{ij}(t) &= \int_{0^-}^{t} S_{ijkl}(t-s)\frac{d\sigma_{kl}(s)}{ds}ds + \int_{0^-}^{t}\frac{\partial R_{ij}}{\partial E_k}(t-s)\frac{dE_k(s)}{ds}ds \\ D_i(t) &= \int_{0^-}^{t} d_{ijk}(t-s)\frac{d\sigma_{jk}(s)}{ds}ds + \int_{0^-}^{t}\frac{\partial F_i}{\partial E_k}(t-s)\frac{dE_k(s)}{ds}ds\end{aligned} \tag{2.13}$$

where $R_{ij}\left[E_k(t-s),t\right]$ and $F_i\left[E_k(t-s),t\right]$ are the scalar components of the time-dependent strain and electric displacement, respectively, at current time $t \geq 0$ due to an input history of $E_k(s)$. It is assumed that $R_{ij}\left[0,t\right] = F_i\left[0,t\right] = 0$ and $R_{ij}\left[E_k(t),t\right] = F_i\left[E_k(t),t\right] = 0 \quad \forall t < 0.0$. The following kernels can be used for the material parameters in the constitutive models in Eq. (2.13):

$$\begin{aligned}S_{ijkl}(t) &= S^{(0)}_{ijkl} + S^{(1)}_{ijkl}\left[1. - e^{-t/\tau^{(1)}_{S_{ijkl}}}\right] \\ d_{ijk}(t) &= d^{(0)}_{ijk} + d^{(1)}_{ijk}\left[1. - e^{-t/\tau^{(1)}_{d_{ijk}}}\right] \\ R_{ij}(E_k(0),t) &= R^{(0)}_{ij}(E_k(0)) + R^{(1)}_{ij}(E_k(0))\left[1. - e^{-t/\tau^{(1)}_{R_{ij}}}\right] \\ F_i(E_k(0),t) &= F^{(0)}_{i}(E_k(0)) + F^{(1)}_{i}(E_k(0))\left[1. - e^{-t/\tau^{(1)}_{F_i}}\right]\end{aligned} \tag{2.14}$$

It can be seen that the above kernels reduce to time-independent functions by eliminating the second term from the material parameters. By choosing $R^{(0)}_{ij}(E_k(0)), R^{(1)}_{ij}(E_k(0)), F^{(0)}_{i}(E_k(0)), F^{(1)}_{i}(E_k(0))$ to vary linearly with the electric field, the above equation reduces to a linear time-dependent electro-mechanical coupling model. It is also possible to include more than one term for the time-dependent parts in Eq. (2.14). The time-dependent compliance $S_{ijkl}(t)$ and piezoelectric constants $d_{ijk}(t)$ in Eq. (2.14) can be characterized from creep test by applying constant stresses or from hysteretic response due to cyclic stress inputs at different frequencies. The components of strain $R_{ij}(t)$ and electric displacement $F_i(t)$ can be determined from the hysteretic response due to sinusoidal electric field inputs at different amplitudes and frequencies. If the experimental setup permits for

[4] This approach yields to a nonlinear single integral model of Pipkins and Rogers (1968).

applying a fixed electric field, then the time-dependent strain and electric displacement can also be determined from this test. It is noted that for a piezoelectric ceramic such as a polarized PZT (let x_3 be the poling axis), only some of the components of the material parameters are nonzero, reducing the experimental effort in calibrating these parameters.

2.3 Time-integration methods

We present a numerical algorithm for determining time-dependent response of strain and electric displacement due to arbitrary stress and electric field inputs. We start with a numerical algorithm for one-dimensional single integral model with a nonlinear integrand and followed by an algorithm for multiple integral representations.

Let $R[I(t-s),t]$ be the time-dependent response at current time $t \geq 0$ due to an input history $I^s \equiv I(s)$. A general single integral representation for the response is:

$$R^t \equiv R[I^s,t] = R[I^0,t] + \int_{0+}^{t} \frac{\partial R}{\partial I}[I^s,t-s]\frac{dI^s}{ds}ds \qquad t \geq 0 \tag{2.15}$$

where

$$R[I^0,t] = R_0(I^0) + R_1(I^0)\left(1. - \exp\left[-\frac{t}{\tau_1}\right]\right) \tag{2.16}$$

$$\frac{\partial R}{\partial I}[I^s,t-s] = \frac{\partial R_0(I^s)}{\partial I} + \frac{\partial R_1(I^s)}{\partial I}\left(1. - \exp\left[-\frac{t-s}{\tau_1}\right]\right) \tag{2.17}$$

Here we use a superscript to denote the time-dependent variables. A recursive method is used for solving the above integral form. Substituting Eqs. (2.16) and (2.17) into Eq. (2.15) yields:

$$R^t = R_0(I^t) + R_1(I^t) - R_1(I^0)\exp\left[-\frac{t}{\tau_1}\right] - q^t \tag{2.18}$$

where

$$q^t = \int_{0^+}^{t} \frac{\partial R_1(I^s)}{\partial I}\exp\left[-\frac{t-s}{\tau_1}\right]\frac{dI^s}{ds}ds \tag{2.19}$$

is the history variable, which can be approximated as:

$$q^t \approx \exp\left[-\frac{\Delta t}{\tau_1}\right]q^{t-\Delta t} + \left[\frac{\partial R_1(I^t)}{\partial I}\frac{dI}{ds}\bigg|_t + \exp\left[-\frac{\Delta t}{\tau_1}\right]\frac{\partial R_1(I^{t-\Delta t})}{\partial I}\frac{dI}{ds}\bigg|_{t-\Delta t}\right]\frac{\Delta t}{2} \qquad t > 0.0 \tag{2.20}$$

The superscript $t-\Delta t$ denotes the previous time history. At initial time, $q^t = q^0 = 0.0$ and $R^0 = R_0(I^0)$. Equations (2.18) and (2.19) give the corresponding output due to an arbitrary input *I(s)*. For the multi-axial constitutive relation, the approximate solution in Eq. (2.18) can be applied independently to each scalar component in Eq. (2.13).

The numerical algorithm for the multiple integral models (one-dimensional representation) in Eq. (2.9) with the kernels defined in Eq. (2.10) can be approximated by applying the recursive method as discussed above. The linear kernel is approximated as:

$$\int_{0^-}^{t} \varphi_1(t-s)\frac{dI(s)}{ds}ds \approx \left[A_0 + A_1\right]I(t) - A_1 I(0^+)\exp\left[-\frac{t}{\tau_1}\right] - q_1^t \tag{2.21}$$

$$q_1^t \approx \exp\left[-\frac{\Delta t}{\tau_1}\right]q_1^{t-\Delta t} + A_1\frac{\Delta t}{2}\left[\left.\frac{dI}{ds}\right|_t + \exp\left[-\frac{\Delta t}{\tau_1}\right]\left.\frac{dI}{ds}\right|_{t-\Delta t}\right] \qquad t > 0.0 \tag{2.22}$$

The second order kernel is rewritten as:

$$\begin{aligned}
&\int_{0^-}^{t}\int_{0^-}^{t} \varphi_2(t-s_1,t-s_2)\frac{dI(s_1)}{ds_1}\frac{dI(s_2)}{ds_2}ds_1 ds_2 = \\
&\left[B_0 + B_1(2.-e^{-t/\lambda_1}-e^{-t/\lambda_1}) + B_2(1.-e^{-t/\lambda_2})(1.-e^{-t/\lambda_2})\right]I(0^+)I(0^+) + \\
&\int_{0^+}^{t}\int_{0^+}^{t}\left[B_0 + B_1(2.-e^{-(t-s_1)/\lambda_1}-e^{-(t-s_2)/\lambda_1}) + B_2(1.-e^{-(t-s_1)/\lambda_2})(1.-e^{-(t-s_2)/\lambda_2})\right]\frac{dI(s_1)}{ds_1}\frac{dI(s_2)}{ds_2}ds_1 ds_2
\end{aligned} \tag{2.23}$$

and it can be approximated by:

$$\begin{aligned}
&\int_{0^-}^{t}\int_{0^-}^{t} \varphi_2(t-s_1,t-s_2)\frac{dI(s_1)}{ds_1}\frac{dI(s_2)}{ds_2}ds_1 ds_2 \approx \\
&\left[B_0 + B_1(2.-e^{-t/\lambda_1}-e^{-t/\lambda_1}) + B_2(1.-e^{-t/\lambda_2})(1.-e^{-t/\lambda_2})\right]I(0^+)I(0^+) + \\
&\left(B_0 + 2B_1\right)\left(I(t)-I(0^+)\right)^2 - B_1\left(I(t)-I(0^+)\right)\left(f_1^t + g_1^t\right) + \\
&B_2\left[\left(I(t)-I(0^+)\right)^2 - f_2^t\left(I(t)-I(0^+)\right) - g_2^t\left(I(t)-I(0^+)\right) + f_2^t g_2^t\right]
\end{aligned} \tag{2.24}$$

where the history variables $f_1^t, f_2^t, g_1^t, g_2^t$ at $t > 0.0$ are given as:

$$\begin{aligned}
f_1^t &\approx \exp\left[-\frac{\Delta t}{\lambda_1}\right]f_1^{t-\Delta t} + \frac{\Delta t}{2}\left[\left.\frac{dI}{ds_1}\right|_t + \exp\left[-\frac{\Delta t}{\lambda_1}\right]\left.\frac{dI}{ds_1}\right|_{t-\Delta t}\right] \\
g_1^t &\approx \exp\left[-\frac{\Delta t}{\lambda_1}\right]g_1^{t-\Delta t} + \frac{\Delta t}{2}\left[\left.\frac{dI}{ds_2}\right|_t + \exp\left[-\frac{\Delta t}{\lambda_1}\right]\left.\frac{dI}{ds_2}\right|_{t-\Delta t}\right] \\
f_2^t &\approx \exp\left[-\frac{\Delta t}{\lambda_2}\right]f_2^{t-\Delta t} + \frac{\Delta t}{2}\left[\left.\frac{dI}{ds_1}\right|_t + \exp\left[-\frac{\Delta t}{\lambda_2}\right]\left.\frac{dI}{ds_1}\right|_{t-\Delta t}\right] \\
g_2^t &\approx \exp\left[-\frac{\Delta t}{\lambda_2}\right]g_2^{t-\Delta t} + \frac{\Delta t}{2}\left[\left.\frac{dI}{ds_2}\right|_t + \exp\left[-\frac{\Delta t}{\lambda_2}\right]\left.\frac{dI}{ds_2}\right|_{t-\Delta t}\right]
\end{aligned} \tag{2.25}$$

At initial time, $f_1^0 = f_2^0 = g_1^0 = g_2^0 = 0.0$ and $R(0) = A_0 I(0^+) + B_0 I(0^+)I(0^+)$. Thus, the corresponding response due to an arbitrary input obtained from the multiple integral model is approximated as:

$$
\begin{aligned}
&R(t) \approx \left[A_0 + A_1\right] I(t) - A_1 \exp\left[-\frac{t}{\tau_1}\right] - q_1^t + \\
&\left[B_0 + B_1(2. - e^{-t/\lambda_1} - e^{-t/\lambda_1}) + B_2(1. - e^{-t/\lambda_2})(1. - e^{-t/\lambda_2})\right] I(0^+) I(0^+) + \\
&\left(B_0 + 2B_1\right)\left(I(t) - I(0^+)\right)^2 - B_1\left(I(t) - I(0^+)\right)\left(f_1^t + g_1^t\right) + \\
&B_2\left[\left(I(t) - I(0^+)\right)^2 - f_2^t\left(I(t) - I(0^+)\right) - g_2^t\left(I(t) - I(0^+)\right) + f_2^t g_2^t\right]
\end{aligned}
\tag{2.26}
$$

For the multi-axial constitutive relation, the approximate solution in Eq. (2.26) can be applied independently to each scalar component in Eq. (2.8).

3. Numerical implementation and parametricstudies

We present a numerical implementation of the above time-dependent constitutive models. We include parametric studies on understanding the effects of different material parameters and input histories on the overall time-dependent response of polarized ferroelectric materials. Both nonlinear single integral and multiple integral models will be discussed.

3.1 Single integral model

This section deals with using a single integral model to simulate hysteretic response of a polarized ferroelectric, which focuses on PZTs, subject to a sinusoidal electric field input. Let x_3 be the poling axis of the PZT and an electric field input $E_3(s) = E_{\max} \sin \omega t$ is applied along the poling axis. We consider several case studies: linear time-dependent response at a stress free condition, nonlinear time-dependent response at a stress free condition, and response under a combine mechanical stress and electric field. The following material parameters are considered for the linear time-dependent electro-mechanical coupling and dielectric constant:

$$
\begin{aligned}
&d_{333}(t) = \left[380 + 150(1. - e^{-t/5})\right] \cdot 10^{-12} C / N(m / V) \\
&d_{311}(t) = d_{322}(t) = \left[-200 - 100(1. - e^{-t/2})\right] \cdot 10^{-12} C / N(m / V) \\
&d_{113} = d_{223} = 437 \cdot 10^{-12} C / N(m / V) \\
&\kappa_{33}^{\sigma}(t) = \left[23 + 2.3e^{-t/10}\right] \cdot 10^{-9} F / m \\
&\kappa_{11}^{\sigma} = \kappa_{22}^{\sigma} = 30 \cdot 10^{-9} F / m
\end{aligned}
\tag{3.1}
$$

The first case considers sinusoidal electric field inputs at three different frequencies: 0.01, 0.1, and 1 Hz and two amplitudes: 0.25 and 0.75 MV/m. Figure 3.1 illustrates the electric-field and transverse strain (E_3-ε_{11}) response during the first quarter cycle. It is seen that the electric-field and strain curves show nonlinear behavior which is due to the delay (time-dependent) response of the material. The nonlinearity is more pronounced as the frequency decreases. At the frequency 1Hz the curve shows almost a linear behavior as the electric field is applied relatively fast with regards to the characteristics time of the materials and thus only a little time is given for the material to experience a time-dependent (or relaxation) effect. From Eq. (3.1), the characteristics time of the electro-mechanical coupling d_{311} is 2 seconds. Thus, one should be very careful when interpreting an experimental data that involves nonlinear phenomena. As shown in Fig. 3.1, the response seems to suggest the

nonlinear relation between the electric field and transverse strain which can be attributed to the electric field (or strain) dependent material properties, but instead this nonlinearity is due to the linear time-dependent effect. Figure 3.2 shows a hysteretic response of a PZT material at frequency 0.1 Hz and maximum applied electric field of 0.25 MV/m. Experimental data are obtained from Crawley and Anderson (1990). The single integral model with time-dependent material parameter in Eq. (3.1) is shown to be capable of simulating the hysteretic response.

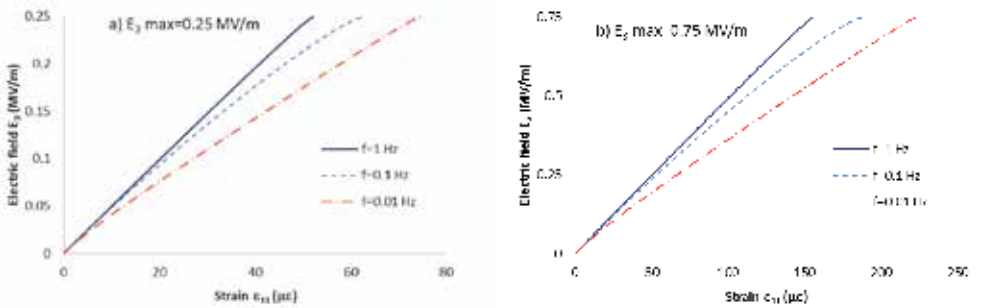

Fig. 3.1. Transverse strain responses during the first quarter cycle of the sinusoidal input

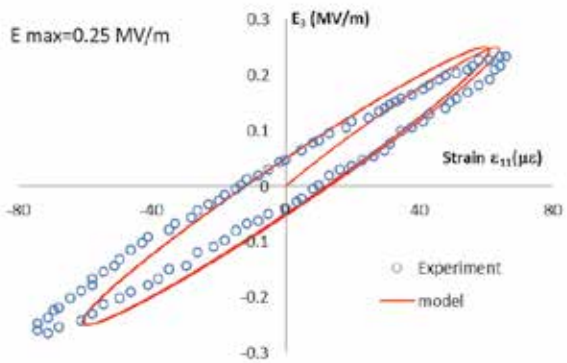

Fig. 3.2. Linear hysteretic response of a PZT at f=0.1 Hz

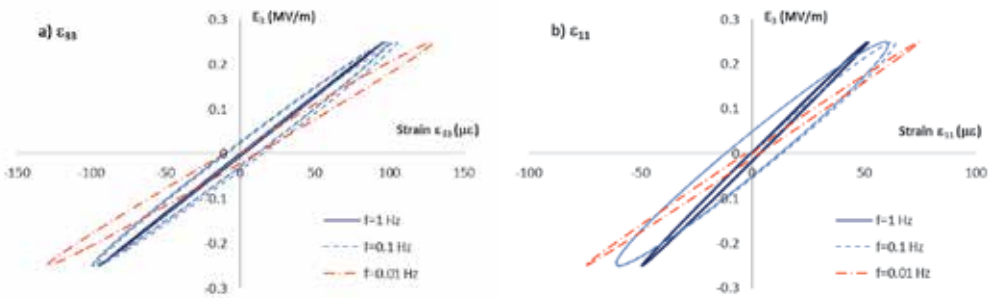

Fig. 3.3. Linear hysteretic response of the axial and transverse strains

The effect of frequencies on the hysteretic response of the linear single integral model is illustrated in Fig. 3.3. It is noted that the strain along the poling axis is a compressive strain since the electric field is applied opposite to the poling direction to create elongation in the in-plane (transverse) direction. From Eq. (3.1) it can be seen that the characteristics time in d_{311} is smaller than the one in d_{333}; thus, the transverse strain exhibits faster relaxation when subjected to an electric field along the poling axis. When the rate of loading is comparable to the characteristics time, the effect of time-dependent material properties on the hysteretic response becomes significant, as shown by the response with a frequency of 0.1 Hz. When the rate of loading is relatively fast (or slow) with regards to the characteristics time, i.e. f=0.01 and 1 Hz, insignificant (less pronounced) time-dependent effect is shown, indicated by narrow ellipsoidal shapes. This is because under a relatively fast loading, the material does not have enough time to experience delay changes at the microstructures[5]; while under a relatively slow loading these delay changes at the microstructures are (nearly) complete. The creep functions in the electro-mechanical coupling results in a smaller slope of the electric field-strain curve when a lower frequency is considered. Figure 3.4 depicts the linear response at different magnitudes of electric fields, which show a perfect elliptical shape when saturated condition is reached.

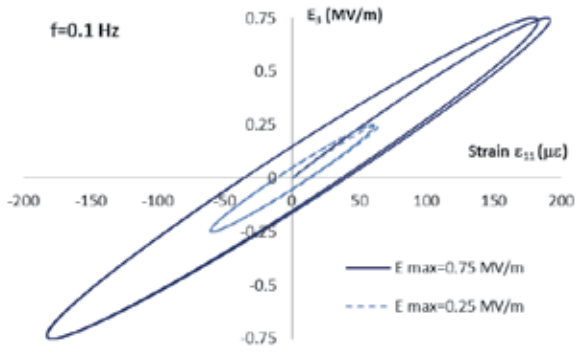

Fig. 3.4. The effect of the amplitude of the electric field on the linear hysteretic response (f=0.1 Hz)

We use a single integral model with nonlinear integrands to illustrate the hysteretic response of a polarized PZT. The following nonlinear functions of the integral model in Eq. (2.13) are chosen for the electro-mechanical coupling E_3-ε_{11}:

$$\varepsilon_{11}(t) = -200\left(1+\alpha|E_3|\right)E_3 - 100\left(1+\beta|E_3|\right)E_3\left(1.-e^{-t/2}\right) \quad \left(10^{-12}C/N\right) \tag{3.2}$$

Figure 3.5 illustrates the effect of different nonlinear parameters on the hysteretic electro-mechanical response. We use nonlinear functions that vary linearly with electric field; it is also possible to pick different functions. We assume that the electro-mechanical coupling properties increase with increasing the magnitude of the electric field and we also assume

[5] It is noted that we measure these time-dependent changes with respect to the laboratory (experimental) time at the macroscopic level.

that the material relaxes faster with increase in the magnitude of the electric field. The following material constants are used in the numerical simulations: $\alpha = \beta = 0.5m/MV$ and the characteristics time varies with the magnitude of electric field as: $(1+\gamma|E_3|)2; \gamma = -0.75$. In this case, we are interested in the response of piezoceramics below the coercive electric field such that the piezoceramics does not experience polarization switching. We also assume that applying electric fields along and opposite to the poling axis cause similar changes in the corresponding strains[6]. The nonlinear parameters show distortion in the hysteretic response from an ellipsoidal shape. As in the linear case, we also show the effect of the amplitude of the electric field on the nonlinear hysteretic response. All of the above nonlinear material parameters are incorporated in the numerical simulations. Figure 3.6 shows the hysteretic response obtained from the nonlinear single integral model. The deviation from the ellipsoidal shape is more pronounced for the hysteretic response under the highest magnitude of the electric field, which is expected. Under relatively small amplitude of the electric field, the hysteretic response shows almost a perfect ellipse as the nonlinearity is less pronounced.

In the third case study, we apply a constant stress input together with a sinusoidal electric field input:

$$\sigma_{33}(t) = -20H(t)MPa \qquad E_3(t) = \pm 0.75 \sin \omega t MV/m \tag{3.3}$$

where *H(t)* is the Heaviside unit step input. The following time-dependent compliance and linear electro-mechanical coupling constant are considered[7]:

$$\begin{aligned} S_{3333}(t) &= 0.0122\left(1.5 - 0.5e^{-t/50}\right) GPa^{-1} \\ d_{333}(t) &= \left[380 + 150(1. - e^{-t/5})\right] \cdot 10^{-12} C/N(m/V) \end{aligned} \tag{3.4}$$

The above compliance corresponds to the elastic (instantaneous) modulus E_{33} of 82 GPa. In the linear model the strain output due to the applied compressive stress can be superposed with the strain output due to the applied electric field. Under a relatively high compressive stress applied along the poling axis depoling of the PZT could occur, leading to nonlinear response. The scope of this manuscript is not on simulating a polarization reversal behavior and we assume that the superposition condition is applicable for the time-dependent strain outputs due to stress and electric field inputs. We allow the polarized PZT to experience creep when it is subjected to a stress. The creep response is described by the compliance in Eq. (3.4). A sinusoidal electric field with amplitude of 0.75 MV/m and frequency of 0.1 Hz is applied. Two cases regarding the history of the electric field input are considered: The first case starts with applying the electric field in the opposite direction to the poling axis, $E_3(0^+) < 0.0$. The second case starts with the electric field input in the direction of the

[6] It is noted that the corresponding strain response in a polarized ferroelectric ceramics when the electric field is applied along the poling axis need not be the same as the strain output when the electric field is applied opposite to the poling axis. In most cases they are not the same, especially under a relative high magnitude of electric field as the process of polarization switching might occur even before it reaches the coercive electric field.

[7] The PZT is modeled as a viscoelastic solid with regards to its mechanical response. The creep deformation in a viscoelastic solid will reach an asymptotic value at steady state (saturated condition).

poling axis, $E_3(0^+) > 0.0$. When an electric field is applied opposite to the current poling axis, the PZT experiences contraction in the poling direction, indicated by a compressive strain. When the polarized PZT is subjected to an electric field in the poling direction, it experiences elongation in that direction.

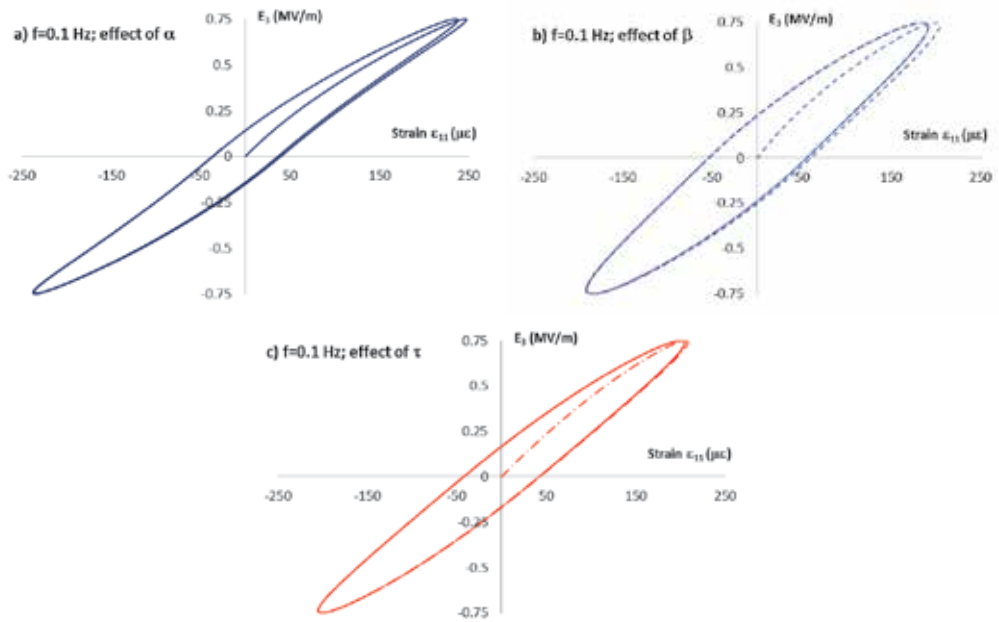

Fig. 3.5. The effect of nonlinear parameters on the hysteretic response

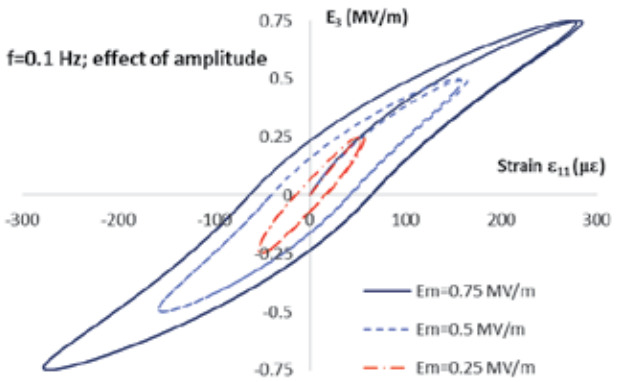

Fig. 3.6. The effect of the amplitude of the electric field on the nonlinear hysteretic response (f=0.1 Hz)

We examine the effect of the electric field input history on the corresponding strain output when the PZT undergoes creep deformation. Figure 3.7 illustrates the hysteretic response under the input field variables in Eq. 3.3. As expected, the creep deformation in the PZT due

to the compressive stress continuously shifts the hysteretic response to the left of the strain axis (higher values of the compressive strains) until steady state is reached for the creep deformation. At steady state, the hysteretic response should form an ellipsoidal shape. It is also seen that different hysteretic response is shown under the two histories of electric fields discussed above. When the electric field is first applied opposite to the poling axis, the first loading cycle forms a nearly elliptical hysteretic response. This is not the case when the electric field is first applied in the poling direction (Fig. 3.7b). The hysteretic response under a frequency of 1 Hz is also illustrated in Figs. 3.7c and d, which show an insignificant time-dependent effect. This is due to the fact that the rate of loading under f=1 Hz is much faster as compared to the creep and time-dependent response of the material. It is also seen that under frequency 1 Hz, the strain- and electric field response is almost linear. Thus, under such condition it is possible to characterize the linear piezoelectric constants of materials, i.e. $d_{311}, d_{322}, d_{333}, d_{113}, d_{223}$ from the electric field-strain curves. At this frequency of 1 Hz, the slope in the strain-electric field curves (Figs. 3.7c and d) remains almost unaltered with the history of the applied electric field. This study can be useful for designing an experiment and interpreting data in order to characterize the piezoelectric properties of a piezoelectric ceramics.

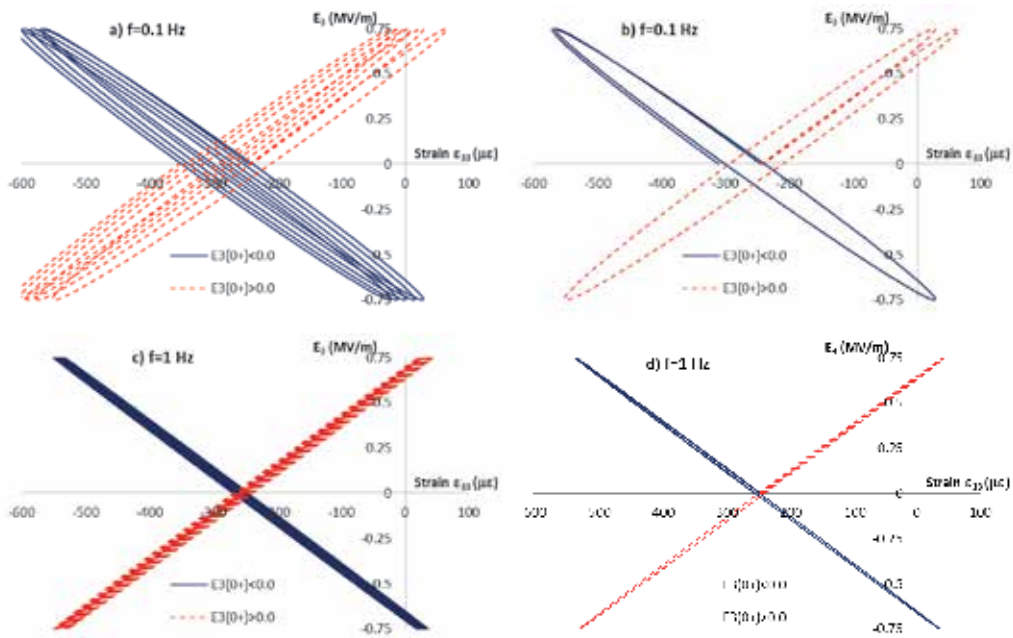

Fig. 3.7. The corresponding hysteretic response under coupled mechanical and electric field inputs

3.2 Multiple integral model

This section presents a multiple integral model to simulate hysteretic response of a piezoelectric ceramics subject to a sinusoidal electric field. We consider up to the third order kernel function and we examine the effect of these kernel functions on the overall nonlinear hysteretic curve. The following material parameters are used for the simulation:

$$
\begin{aligned}
&A_0 = 200 \cdot 10^{-12} m / V; A_1 = 100 \cdot 10^{-12} m / V \\
&\tau_1 = 2\,\text{sec} \\
&B_0 = B_1 = B_2 = 20 \cdot 10^{-18} m^2 / V^2 \\
&\lambda_1 = 2\,\text{sec}; \lambda_2 = 5\,\text{sec} \\
&C_0 = C_1 = C_2 = 50 \cdot 10^{-24} m^3 / V^3 \\
&\eta_1 = 2\,\text{sec}; \eta_2 = 5\,\text{sec}
\end{aligned}
\tag{3.5}
$$

When only the first and third kernel functions are considered, the nonlinear hysteretic response at steady state under positive and negative electric fields is identical as shown by an anti-symmetric hysteretic curve in Fig. 3.8a. The hysteretic response under the amplitude of electric field of 0.25 MV/m shows nearly linear response. Including the second order kernel function allows for different response under positive and negative electric fields as seen in Fig. 3.8b. At low amplitude of applied electric field, nearly linear response is shown; however this hysteretic response does not show an anti-symmetric shape with respect to the strain and electric field axes. The contribution of each order of the kernel function depends on the material parameters. For example the material parameters in Eq. (3.5) yield to more pronounced contribution of the first order kernel function; while the contributions of the second and third order kernel functions are comparable.

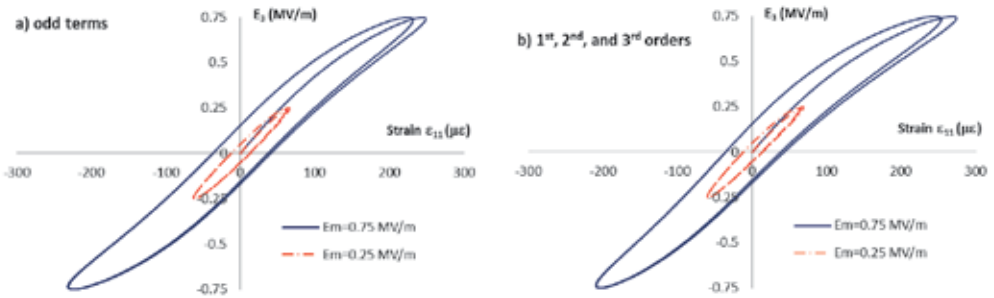

Fig. 3.8. The effect of the higher order terms on the hysteretic response (f=0.1 Hz)

Intuitively, the corresponding strain response of a piezoelectric ceramics when an electric field is applied in the poling direction (positive electric field) need not be the same as when an electric field is applied opposite to the poling direction (negative electric field), especially for nonlinear response due to high electric fields. Depoling could occur in the piezoelectric ceramics when a negative electric field with a magnitude greater than the coercive electric field is considered. Thus, to incorporate the possibility of the depoling process, the even order kernel functions can be incorporated in the multiple time-integral model. In order to numerically simulate the depolarization in the piezoelectric ceramics we apply a sinusoidal electric field input with amplitude of 1.5 MV/m. We consider the first and second order kernel functions and use the following material parameters so that the contributions of the first and second order kernel functions on the strain response are comparable:

$$
\begin{aligned}
&A_0 = 200 \cdot 10^{-12} m / V; A_1 = 100 \cdot 10^{-12} m / V \\
&\tau_1 = 2\,\text{sec} \\
&B_0 = B_1 = B_2 = 100 \cdot 10^{-18} m^2 / V^2 \\
&\lambda_1 = 2\,\text{sec}; \lambda_2 = 5\,\text{sec}
\end{aligned}
\tag{3.6}
$$

Figure 3.9 illustrates the corresponding strain response from the multiple integral model having the first and second kernel functions. The response shows an un-symmetric butterfly-like shape. The un-symmetric butterfly-like strain-electric field response is expected for polarized ferroelectric materials undergoing high amplitude of sinusoidal electric field input. The nonlinear response due to the positive electric field is caused by different microstructural changes than the microstructural changes due to polarization switching under a negative electric field.

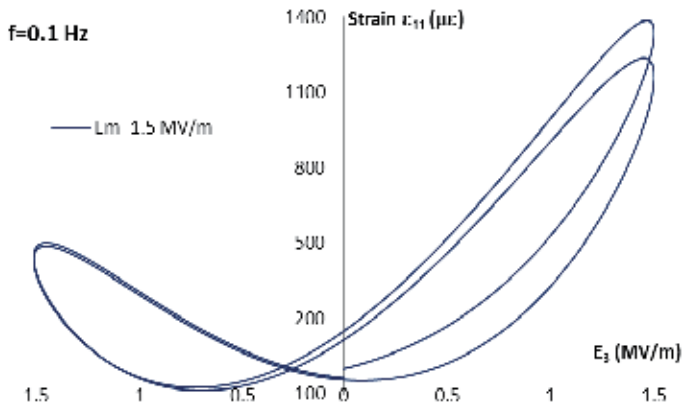

Fig. 3.9. The butterfly-like shape of the electro-mechanical coupling response

4. Analyses of piezoelectric beam bending actuators

Stack actuators have been used in several applications that involve displacement controlling, such as fuel injection valves and optical positioning (see Ballas 2007 for a detailed discussion). They comprise of layers of polarized piezoelectric ceramics arranged in a certain way with regards to the poling axis of an individual piezoceramic layer in order to produce a desire deformation. In conventional bending actuators, a single layer piezoceramic requires a typical of operating voltage of 200 V or more. By forming a multi-layer piezoceramic actuator, it is possible to reduce the operating voltage to less than 50 V. In this section, we examine the effect of time-dependent electro-mechanical properties of the piezoelectric ceramics on the bending deflections of an actuator comprising of two piezoelectric layers, known as a bimorph system.

Consider a two dimensional bimorph beam consisting of two layers of polarized piezoelectric ceramics and an elastic layer, as shown in Fig. 4.1. In order to produce a bending deflection in the beam, the two piezoelectric layers should undergo opposite tensile and compressive strains. This can be achieved by stacking the two piezoelectric layers with the poling axis in the same direction and applying a voltage that produces opposite electric fields in the two layers or by placing the two piezoelectric layers with poling axis in the opposite direction and applying a voltage that produces electric fields in the same direction. The beam is fixed at one end and the other end is left free; the top and bottom surfaces are under a traction free condition. A potential is applied at the top and bottom surfaces of the beam and the corresponding displacement is monitored. We prescribe the following boundary conditions to the bimorph beam:

$$
\begin{aligned}
&u_1(0,x_2,t)=u_2(0,x_2,t)=\frac{\partial u_2}{\partial x_1}(0,x_2,t)=0 \qquad -\frac{h}{2}\le x_2\le\frac{h}{2},t\ge 0\\
&\sigma_{22}\left(x_1,\frac{h}{2},t\right)=\sigma_{22}\left(x_1,-\frac{h}{2},t\right)=0 \qquad 0\le x_1\le L,t\ge 0\\
&\sigma_{12}(L,x_2,t)=0 \qquad -\frac{h}{2}\le x_2\le\frac{h}{2},t\ge 0;\sigma_{12}\left(x_1,\frac{h}{2},t\right)=\sigma_{12}\left(x_1,-\frac{h}{2},t\right)=0 \qquad 0\le x_1\le L,t\ge 0 \quad (4.1)\\
&\varphi\left(x_1,\frac{h_s}{2},t\right)=\varphi\left(x_1,-\frac{h_s}{2},t\right)=0 \qquad 0\le x_1\le L,t\ge 0\\
&\varphi\left(x_1,\frac{h}{2},t\right)=\varphi\left(x_1,-\frac{h}{2},t\right)=V_h(t) \qquad 0\le x_1\le L,t\ge 0
\end{aligned}
$$

where u_1 and u_2 are the displacements in the x_1 and x_2 directions, respectively. The bonding between the different layers in the bimorph beam is assumed perfect; thus the traction and displacement continuity conditions are imposed at the interface layers. The beam has a length L of 100mm, width b of 1mm and the thickness of each piezoelectric layer is 1mm. Let us consider a bimorph beam without an elastic layer placed in between these piezoelectric layers. We assume that the beam is relatively slender so that it is sensible to adopt Euler-Bernoulli's beam theory in finding the corresponding displacement of the bimorph beam; the calculated displacements are at the neutral axis of the beam and we shall eliminate the dependence of the displacements on the x_2 axis, $u_1(x_1,t)$ and $u_2(x_1,t)$. The kinematics concerning the deformations of the Euler-Bernoulli beam, with the displacements measured at the neutral axis of the beam is:

$$
\varepsilon_{11}(x_1,x_2,t)=\frac{\partial u_1}{\partial x_1}(x_1,t)-x_2\frac{\partial^2 u_2}{\partial x_1^2}(x_1,t) \tag{4.2}
$$

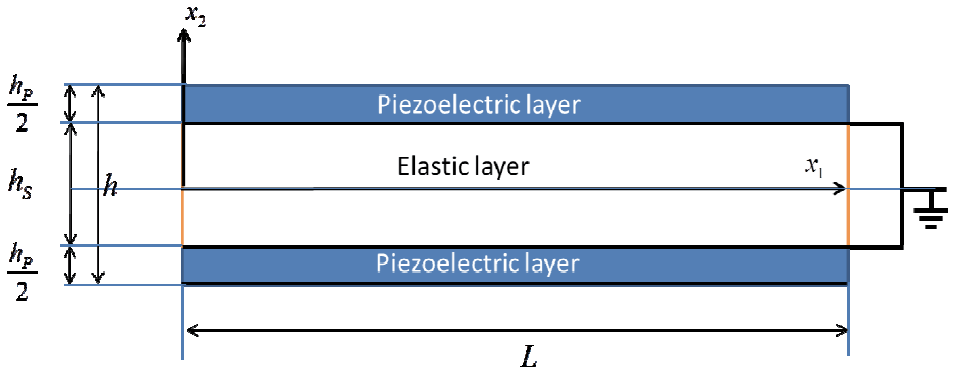

Fig. 4.1. A bimorph beam

Since we only prescribe a uniform voltage on the top and bottom surfaces of the beam, the problem reduces to a pure bending problem[8]: the internal bending moment depends only on

[8] We shall only consider the longitudinal stress- and strain and the transverse displacement measured at the neutral axis of the beam.

time, $M_3(t)=M(t)$ and the longitudinal stress is independent on the x_1, $\sigma_{11}(x_2,t)$. At each time t, the following equilibrium conditions must be satisfied:

$$\begin{aligned} &\int_A \sigma_{11}(x_2,t)\,dA = 0 \\ &M(t) = -\int_A x_2\sigma_{11}(x_2,t)\,dA \end{aligned} \tag{4.3}$$

As a consequence, the first term of the axial strain in Eq. (4.2) is zero and the curvature of the beam depends only on time. The constitutive relations for the piezoelectric layers are:

$$\begin{aligned} \sigma_{11}(x_2,t) &= \int_{0^-}^{t} \frac{\partial C_{1111}}{\partial s}(x_2,t-s)\varepsilon_{11}(x_2,s)ds - \int_{0^-}^{t} \frac{\partial e_{211}}{\partial s}(x_2,t-s)E_2(x_2,s)ds \\ D_2(x_2,t) &= \int_{0^-}^{t} \frac{\partial e_{211}}{\partial s}(x_2,t-s)\varepsilon_{11}(x_2,s)ds + \int_{0^-}^{t} \frac{\partial \kappa_{22}}{\partial s}(x_2,t-s)E_2(x_2,s)ds \end{aligned} \tag{4.4}$$

where the electric field at the piezoelectric layer with the thickness $h_p/2$ is assumed uniform $E_2(x_2,t) = -\dfrac{V_h(t)}{h_p/2}$ for $0 \le x_2 \le \dfrac{h_p}{2}$ and $E_2(x_2,t) = \dfrac{V_h(t)}{h_p/2}$ for $-\dfrac{h_p}{2} \le x_2 \le 0$. The poling axes of the two piezoelectric layers are in the same direction. The axial stress becomes (h_s=0):

$$\sigma_{11}(x_2,t) = -\begin{cases} -\dfrac{2}{h_p}\displaystyle\int_{0^-}^{t} \frac{\partial e_{211}}{\partial s}(t-s)V_h(s)ds & 0 \le x_2 \le \dfrac{h_p}{2} \\ \dfrac{2}{h_p}\displaystyle\int_{0^-}^{t} \frac{\partial e_{211}}{\partial s}(t-s)V_h(s)ds & -\dfrac{h_p}{2} \le x_2 \le 0 \end{cases} \tag{4.5}$$

Substituting the stress in Eq. (4.5) to the internal bending moment in Eq. (4.3) yields to:

$$M(t) = b\frac{h_p}{2}\int_{0^-}^{t} \frac{\partial e_{211}}{\partial s}(t-s)V_h(s)ds \tag{4.6}$$

Finally, the equation that governs the bending of the bimorph beam (pure bending condition) subject to a time varying electric potential is:

$$\frac{\partial^2 u_2}{\partial x_1^2} = \frac{1}{I}\int_{0^-}^{t} \frac{\partial S_{1111}}{\partial s}(t-s)M(s)ds = \frac{b}{I}\frac{h_p}{2}\int_{0^-}^{t} \frac{\partial S_{1111}}{\partial s}(t-s)\int_{0^-}^{s} \frac{\partial e_{211}}{\partial s}(s-\zeta)V_h(\zeta)d\zeta ds = \Phi(t) \tag{4.7}$$

where I is the second moment of an area w.r.t. the neutral axis of the beam. Integrating Eq. (4.7) with respect to the x_1 axis and using BCs in Eq. 4.1, the deflection of the beam is:

$$u_2(x_1,t) = \frac{1}{2}\Phi(t)x_1^2 \tag{4.8}$$

The following time-dependent properties of PZT-5A are used for the bending analyses of stack actuators:

$$C_{1111}(t) = \left[90 + 30e^{-t/50}\right] GPa$$
$$e_{211}(t) = -\left[5.35 + 1.34e^{-t/5}\right] C/m^2 \tag{4.9}$$

A sinusoidal input of an electric potential with various frequencies are applied. Figure 4.2 illustrates hysteresis response of the bending of the bimorph beam. The displacements are measured at the free end (x_1=100mm). As discussed in Section 3.1, when the rate of loading is comparable to the characteristics time, the effect of time-dependent material properties on the hysteretic response becomes significant, as shown by the response with frequencies of 0.05 Hz and 0.1 Hz. When the rate of loading is relatively fast (or slow) with regards to the characteristics time, i.e. f=0.01 Hz and 1 Hz, insignificant (less pronounced) time-dependent effect is shown, indicated by narrow ellipsoidal shapes.

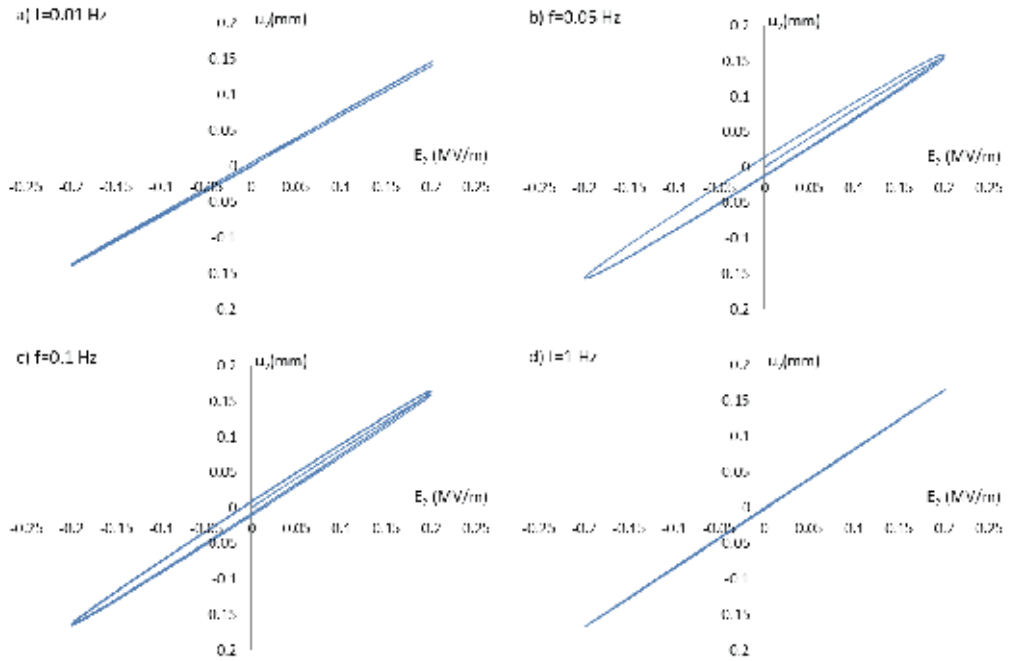

Fig. 4.2. The effect of input frequencies on the tip displacements of the bimorph beam

5. Conclusions

We have studied the nonlinear and time-dependent electro-mechanical hysteretic response of polarized ferroelectric ceramics. The time-dependent electro-mechanical response is described by nonlinear single integral and multiple integral models. We first examine the effect of frequency (loading rate) on the overall hysteretic response of a linear time-dependent electro-mechanical response. The strain-electric field response shows a nonlinear relation when the time-dependent effect is prominent which should not be confused with the nonlinearity due to the magnitude of electric fields. We also study the effect of the magnitude of electric fields on the overall hysteretic response using both nonlinear single integral and multiple integral models. As expected, the nonlinearity due to the electric field

results in a distortion of the ellipsoidal hysteretic curve. We have extended the time-dependent constitutive model for analyzing bending in a stack actuator due to an input electric potential at various frequencies. The presented study will be useful when designing an experiment and interpreting data that a nonlinear electro-mechanical response exhibits. This study is also useful in choosing a proper nonlinear time-dependent constitutive model for piezoelectric ceramics.

6. Acknowledgment

This research is sponsored by the Air Force Office of Scientific Research (AFOSR) under grant FA 9550-10-1-0002.

7. References

[1] Ballas, RG (2007) Piezoelectric Multilayer Beam Bending Actuators, Springer-Verlag Berlin

[2] Bassiouny, E., Ghaleb, AF, and Maugin GA (1988a), "Thermodynamical Formulation for Coupled Electromechanical Hysteresis Effects-I. Basic Equations," Int. J. Engrg Sci., 26, pp. 1279-1295

[3] Bassiouny, E., Ghaleb, AF, and Maugin GA (1988b), "Thermodynamical Formulation for Coupled Electromechanical Hysteresis Effects-I. Poling of Ceramics," Int. J. Engrg Sci., 26, pp. 975-987

[4] Ben Atitallah, H, Ounaies, Z, and Muliana A, "Temperature and Time Effects in the Electro-mechanical Coupling Behavior of Active Fiber Composites", 16th US National Congress on Theoretical and Applied Mechanics, June 27 - July 2, 2010, State College, Pennsylvania, USA

[5] Cao, H. and Evans, A.G. (1993), "Nonlinear Deformation of Ferroelectric Ceramics" J. Amer. Ceramic Soc., 76, pp. 890-896

[6] Chan, K.H. and Hagood, N.W. (1994), "Modeling of Nonlinear Piezoceramics for Structural Actuation," Proc. of SPIE's Symp. on Smart Structures and Materials, 2190, pp. 194-205

[7] Chen, W. and Lynch, C.S. (1998), "A Micro-electro-mechanical Model for Polarization Switching of Ferroelectric Materials," Acta Materialia, 46, pp. 5303-5311

[8] Chen, X. (2009), "Nonlinear Electro-thermo-viscoelasticity," Acta Mechanica, in press

[9] Crawley, E.F. and Anderson, E.H. (1990), "Detailed Models of Piezoceramic Actuation of Beams" J. Intell. Mater. Syst. Struct., 1, pp. 4-25

[10] Fett, T. and Thun, G. (1998), "Determination of Room-temperature Tensile Creep of PZT," J. Materials Science Letter, 17, pp. 1929-1931

[11] Green, AE and Rivlin, RS (1957), "The Mechanics of Nonlinear Materials with Memory, Part I," Archive for Rational Mechanics and Analysis, 1, pp. 1

[12] Fang, D. and Sang Y. (2009), "The polarization properties in ferroelectric nanofilms investigated by molecular dynamics simulation, "Journal of Computational and Theoretical Nanoscience, 6, pp. 142-147

[13] Findley, W. and Lai., J (1967), "A Modified Superposition Principle Applied to Creep of Nonlinear Viscoelastic Material Under Abrupt Changes in State of Combined Stress" Trans. Soc. Rheol., 11, pp. 361

[14] Findley, WN, Lai, JS, Onaran, K (1976), "Creep and Relaxation of Nonlinear Viscoelastic Materials," Dover Publication, New York
[15] Fung, Y.C (1981) Biomechanics: Mechanical Properties of Living Tissues, Springer, New York
[16] Hall, D.A. (2001), "Review Nonlinearity in Piezoelectric Ceramics," J. Materials Sci, 36, pp. 4575-4601
[17] Huang L and Tiersten HF (1998), "Electroelastic equations describing slow hysteresis in polarized ferroelectric ceramic plates," J. App. Physics, 83, pp. 6126-6139
[18] Huang L and Tiersten HF (1998), "An Analytical Description of Slow Hysteresis in Polarized Ferroelectric Ceramic Actuators," J. Intel. Mater. Syst. and Struct., 9, pp. 417-426
[19] Kamlah, M. and Tsakmakis, C (1999), "Phenomenological Modeling of the Nonlinear Electro-mechanical Coupling in Ferroelectrics," Int. J. Solids and Structures, 36, pp. 669-695
[20] Landis, C. (2002), "A phenomenological multiaxial constitutive law for switching in polycrystalline ferrorlectric ceramics," J. Mech. Phys. Solids, vol. 50, pp. 127–152
[21] Li J. and Weng GJ (2001), "A Micromechanics-Based Hysteresis Model for Ferroelectric Ceramics," J. Intel. Material Systems and Structures, 12, pp. 79-91
[22] Lines, M.E. and Glass, A. E. (2009) Principles and Applications of Ferroelectrics and Related Materials, Oxford University Press, New York
[23] Massalas, C.V., Foutsitzi, G., Kalpakidis, V.K. (1994), "Thermoelectroelasticity Theory for Materials with Memory," Int. J. Engng. Sci., 7, pp. 1075-1084
[24] Pipkin, A.C. and Rogers, T.G. (1968), "A nonlinear integral representation for viscoelastic behavior," J. Mech. Phys. Solids, 16, pp. 69-72
[25] Rajagopal, K. R. and Wineman, A. S. (2010), "Application to Viscoelastic Clock Models in Biomechanics," Acta Mechanica, 213, pp. 255–266
[26] Schaeufele, A. and Haerdtl, K.H. (1996), "Ferroelastic Properties of Lead Zirconate Titanate Ceramics" J. Amer. Ceramic Soc., 79, pp. 2637-2640
[27] Schapery, R. A. (1969), "On the Characterization of Nonlinear Viscoelastic Materials," Polymer Engineering and Science, Vol. 9, No. 4, pp. 295-310
[28] Smith, R.C., Seelecke, S., Ounaies, Z., and Smith, J. (2003), "A Free Energy Model for Hysteresis in Ferroelectric Materials," J. Intel. Mater. Syst. and Structures, 14, pp. 719-739
[29] Smith, R.C., Seelecke, S., Dapino, M., Ounaies, Z. (2006), "A unified framework for modeling hysteresis in ferroic materials," J. Mech. Phys. Solids, 54, pp. 46-85
[30] Smith, RC (2005), Smart Material Systems: Model Development. Philadelphia, PA: SIAM
[31] Tiersten, H.F. (1971), "On the Nonlinear Equations of Thermo-electroelasticity," Int. J. Engr. Sci, Vol. 9, pp. 587-604
[32] Tiersten, H.F. (1993), "Electroelastic Equations for Electroded Thin Plates Subject to Large Driving Voltages" J. Applied Physics, 74, pp. 3389-3393
[33] Uludogan M, Guarin, DP, Gomez, ZE, Cagin, T, and Goddard III, WA (2008), "DFT studies on ferroelectric ceramics and their alloys: BaTiO3, PbTiO3, SrTiO3, AgNbO3, AgTaO3, PbxBa1-xTiO3 and SrxBa 1-xTiO3", Computer Modeling in Engineering and Sciences, 24, pp. 215-238

[34] Zhou, D. and Kamlah, M. (2006), "Room-temperature Creep of Soft PZT under Static Electrical and Compressive Stress Loading," Acta Materialia, 54, pp. 1389-1396

28

Modeling and Numerical Simulation of Ferroelectric Material Behavior Using Hysteresis Operators

Manfred Kaltenbacher and Barbara Kaltenbacher
Alps-Adriatic University Klagenfurt
Austria

1. Introduction

The piezoelectric effect is a coupling between electrical and mechanical fields within certain materials that has numerous applications ranging from ultrasound generation in medical imaging and therapy via acceleration sensors and injection valves in automotive industry to high precision positioning systems. Driven by the increasing demand for devices operating at high field intensities especially in actuator applications, the field of hysteresis modeling for piezoelectric materials is currently one of highly active research. The approaches that have been considered so far can be divided into four categories:

(1) *Thermodynamically consistent models* being based on a macroscopic view to describe microscopical phenomena in such a way that the second law of thermodynamics is satisfied, see e.g., Bassiouny & Ghaleb (1989); Kamlah & Böhle (2001); Landis (2004); Linnemann et al. (2009); Schröder & Romanowski (2005); Su & Landis (2007).

(2) *Micromechanical models* that consider the material on the level of single grains, see, e.g., Belov & Kreher (2006); Delibas et al. (2005); Fröhlich (2001); Huber (2006); Huber & Fleck (2001); McMeeking et al. (2007).

(3) *Phase field models* that describe the transition between phases (corresponding to the motion of walls between domains with different polarization orientation) using the Ginzburg Landau equation for some order parameter, see e.g., Wang et al. (2010); Xu et al. (2010).

(4) *Phenomenological models using hysteresis operators* partly originating from the input-output description of piezoelectric devices for control purposes, see e.g., Ball et al. (2007); Cimaa et al. (2002); Hughes & Wen (1995); Kuhnen (2001); Pasco & Berry (2004); Smith et al. (2003).

Also multiscale coupling between macro- and microscopic as well as phase field models partly even down to atomistic simulations have been investigated, see e.g., Schröder & Keip (2010); Zäh et al. (2010).

Whereas most of the so far existing models are designed for the simulation of polarization, depolarization or cycling along the main hysteresis loop, the simulation of actuators requires the accurate simulation of *minor loops* as well.

Moreover, the physical behavior can so far be reproduced only qualitatively, whereas the use of models in actuator simulation (possibly also aiming at simulation based optimization) needs to *fit measurements* precisely.
Simulation of a piezoelectric device with a possibly complex geometry requires not only an input-output model but needs to resolve the spatial distribution of the crucial electric and mechanical field quantities, which leads to partial differential equations (PDEs). Therewith, the question of *numerical efficiency* becomes important.
Preisach operators are phenomenological models for rate independent hysteresis that are capable of reproducing minor loops and can be very well fitted to measurements, see e.g., Brokate & Sprekels (1996); Krasnoselskii & Pokrovskii (1989); Krejčí (1996); Mayergoyz (1991); Visintin (1994). Moreover, they allow for a highly efficient evaluation by the application of certain memory deletion rules and the use of so-called Everett or shape functions.
In the following, we will first describe the piezoelectric material behavior both on a microscopic and macroscopic view. Then we will provide a discussion on the Preisach hysteresis operator, its properties and its fast evaluation followed by a description of our piezoelectric model for large signal excitation. In Sec. 4 we discuss the steps to incorporate this model into the system of partial differential equations, and in Sec. 5 the derivation of a quasi Newton method, in which the hysteresis operators are included into the system via incremental material tensors. For this set of partial differential equations we then derive the weak (variational) formulation and perform space and time discretization. The fitting of the model parameters based on relatively simple measurements is performed directly on the piezoelectric actuators in Section 6. The applicability of our developed numerical scheme will be demonstrated in Sec. 7, where we present a comparison of measured and simulated physical quantities. Finally, we summarize our contribution and provide an outlook on further improvements of our model to achieve a multi-axial ferroelectric and ferroelastic loading model.

2. Piezoelectric and ferroelectric material behavior

Piezoelectric materials can be subdivided into the following three categories

1. *Single crystals*, like quartz
2. *Piezoelectric ceramics* like barium titanate ($BaTiO_3$) or lead zirconate titanate (PZT)
3. *Polymers* like PVDF (polyvinylidenfluoride).

Since categories 1 and 3 typically show a weak piezoelectric effect, these materials are mainly used in sensor applications (e.g., force, torque or acceleration sensor). For piezoelectric ceramics the electromechanical coupling is large, thus making them attractive for actuator applications. These materials exhibit a polycrystalline structure and the key physical property of these materials is ferroelectricity. In order to provide some physical understanding of the piezoelectric effect, we will consider the microscopic structure of piezoceramics, partly following the exposition in Kamlah (2001).
A piezoelectric ceramic material is subdivided into grains consisting of unit cells with different orientation of the crystal lattice. The unit cells consist of positively and negatively charged ions, and their charge center position relative to each other is of major importance for the electromechanical properties. We will call the material *polarizable*, if an external load, e.g., an electric field can shift these centers with respect to each other. Let us consider $BaTiO_3$ or PZT, which have a polycrystalline structure with grains having different crystal lattice.

Above the Curie temperature T_c – for $BaTiO_3$ $T_c \approx 120\,^oC$ - $130\,^oC$ and for PZT $T_c \approx 250\,^oC$ - $350\,^oC$, these materials have the perovskite structure. The cube shape of a unit cell has a side length of a_0 and the centers of positive and negative charges coincide (see Fig. 1). However, below T_c the unit cell deforms to a tetragonal structure as displayed in Fig. 1, e.g.,

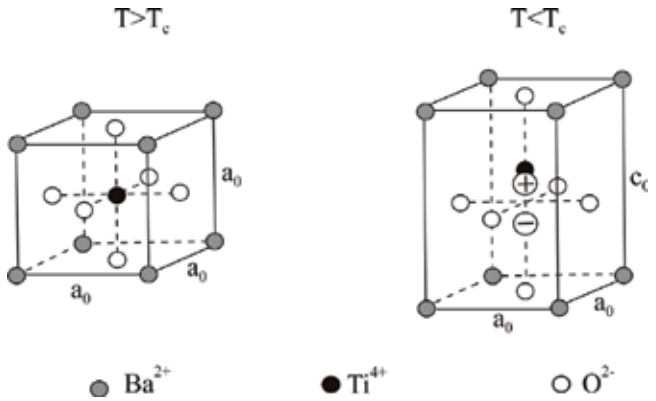

Fig. 1. Unit cell of $BaTiO_3$ above and below the Curie temperature T_c.

$BaTiO_3$ at room temperature changes its dimension by $(c_0 - a_0)/a_0 \approx 1\,\%$. In this ferroelectric

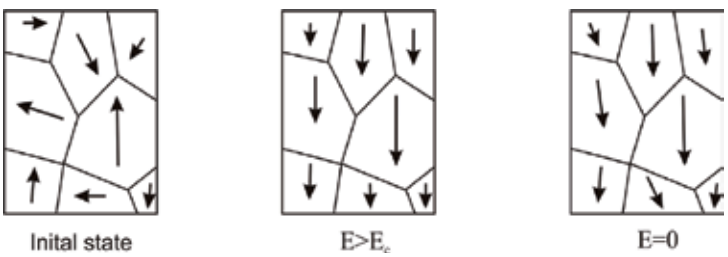

Fig. 2. Orientation of the polarization of the unit cells at initial state, due to a strong external electric field and after switching it off.

phase, the centers of positive and negative charges differ and a dipole is formed, hence the unit cell posses a spontaneous polarization. Since the single dipoles are randomly oriented, the overall polarization vanishes due to mutual cancellations and we call this the thermally depoled state or virgin state. This state can be modified by an electric or mechanical loading with significant amplitude. In practice, a strong electric field $E \approx 2\,\mathrm{kV/mm}$ will switch the unit cells such that the spontaneous polarization will be more or less oriented towards the direction of the externally applied electric field as displayed in Fig. 2. Now, when we switch off the external electric field the ceramic will still exhibit a non-vanishing residual polarization in the macroscopic mean (see Fig. 2). We call this the *irreversible* or *remanent polarization* and the just described process is termed as *poling*.

The *piezoelectric effect* can be easily understood on the unit cell level (see Fig. 1), where it just corresponds to an electrically or mechanically induced coupled elongation or contraction of both the c-axes and the dipole. Macroscopic piezoelectricity results from a superposition of this effect within the individual cells.

Ferroelectricity is not only relevant during the above mentioned poling process. To see this, let us consider a mechanically unclamped piezoceramic disc at virgin state and load the

electrodes by an increasing electric voltage. Initially, the orientation of the polarization within the unit cells is randomly distributed as shown in Fig. 3 (state 1). The switching of the domains

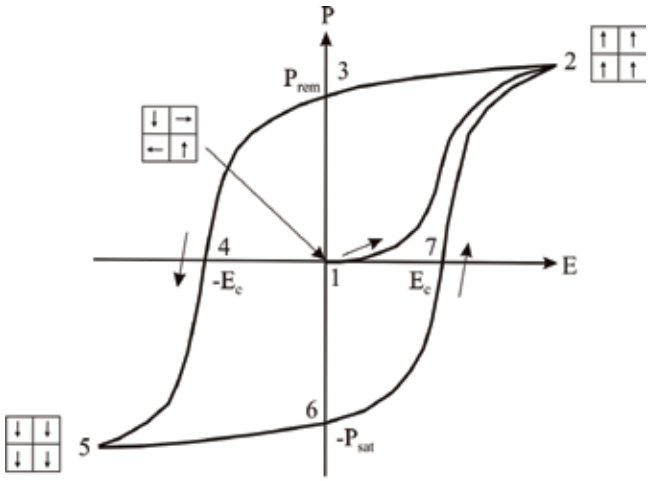

Fig. 3. Polarization P as a function of the electric field intensity E.

starts when the applied electric field reaches the so-called coercitive intensity E_c[1]. At this state, the increase of the polarization is much faster, until all domains are switched (see state 2 in Fig. 3). A further increase of the external electric loading would result in an increase of the polarization with only a relatively small slope and the occurring micromechanical process remains reversible. Reducing the applied voltage to zero will preserve the poled domain structure even at vanishing external electric field, and we call the resulting macroscopic polarization the remanent polarization P_{rem}. Loading the piezoceramic disc by a negative voltage of an amplitude larger than E_c will initiate the switching process again until we arrive at a random polarization of the domains (see state 4 in Fig. 3). A further increase will orient the domain polarization in the new direction of the external applied electric field (see state 5 in Fig. 3).

Measuring the mechanical strain during such a loading cycle as described above for the electric polarization, results in the so-called *butterfly curve* depicted in Fig. 4, which is basically a direct translation of the changes of dipoles (resulting in the total polarization shown in Fig. 3) to the c-axes on a unit cell level. Here we also observe that an applied electric field intensity $E > E_c$ is required in order to obtain a measurable mechanical strain. The observed strong increase between state 1 and 2 (or 7 and 2, respectively) is again a superposition of two effects: Firstly, we achieve an increase of the strain due to a reorientation of the c-axes into direction of the external electric field, which often takes place in two steps (90 degree and 180 degree switching). Secondly, the orientation of the domain polarization leads to the macroscopic piezoelectric effect yielding the reversible part of the strain. As soon as all domains are switched (see state 2 in Fig. 4), a further increase of the strain just results from the macroscopic piezoelectric effect. A separation of the switching (irreversible) and the piezoelectric (reversible) strain can best be seen by decreasing the external electric load to zero.

[1] It has to be noted that in literature E_c often denotes the electric field intensity at zero polarization. According to Kamlah & Böhle (2001) we define E_c as the electric field intensity at which domain switching occurs.

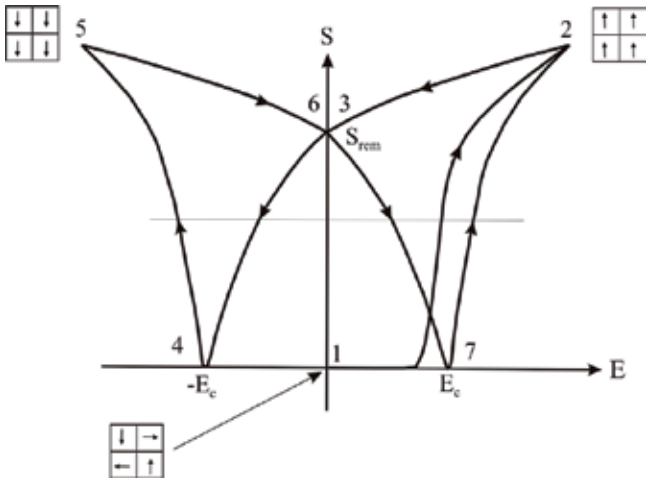

Fig. 4. Mechanical strain S as a function of the electric field intensity E.

Alternatively or additionally to this electric loading, one can perform a mechanical loading, which will also result in switching processes. For a detailed discussion on the occurring so-called ferroelastic effects we refer to Kamlah & Böhle (2001).

3. Preisach hysteresis operators

Hysteresis is a memory effect, which is characterized by a lag behind in time of some output in dependence of the input history. Figure 3, e.g., shows the curve describing the polarization P of some ferroelectric material in dependence of the applied electric field E: As E increases from zero to its maximal positive value E_{sat} at state 2 (virgin curve), the polarization also shows a growing behavior, that lags behind E, though. Then E decreases, and again P follows with some delay. As a consequence, there is a positive remanent polarization P_{rem} for vanishing E, that can only be completely removed by further decreasing E until a critical negative value is reached at state 4. After passing this threshold, a polarization in negative direction — so with the same orientation as E — is generated, until a minimal negative value is reached. The returning branch of the hysteresis curve ends at the same point $(E_{\text{sat}}, P_{\text{sat}})$ at state 2, where the outgoing branch had reversed but takes a different path, which results in a gap between these two branches and the typical closed main hysteresis loop. We write

$$P(t) = \mathcal{H}[E](t)$$

with some hysteresis operator $\mathcal{H}$. Normalizing input and output by their saturation values, e.g., $p(t) = P(t)/P_{\text{sat}}$ and $e(t) = E(t)/E_{\text{sat}}$, results in

$$p(t) = \mathcal{H}[e](t)\,.$$

In the remainder of this section we assume that both the input e and the output p are normalized so that their values lie within the interval $[-1, 1]$, and give a short overview on hysteresis operators following mainly the exposition in Brokate & Sprekels (1996) (see also Krejčí (1996) as well as Krasnoselskii & Pokrovskii (1989); Mayergoyz (1991); Visintin (1994)).

Probably the most simple example of hysteresis is the behavior of a switch or *relay* (see Fig. 5), that is characterized by two threshold values $\alpha > \beta$. The output value p is either -1 or $+1$ and changes only if the input value e crosses one of the switching thresholds α, β: If, at some time instance t, $e(t)$ increases from below to above α, the relay will switch up to $+1$, if e decreases from above to below β, it will switch down to -1, in all other cases it will keep its value — either plus or minus one, depending on the preceding history. Therefore, we just formally define the relay operator $\mathcal{R}_{\beta,\alpha}$ by

$$\mathcal{R}_{\beta,\alpha}[e] = p$$

according to the description above.

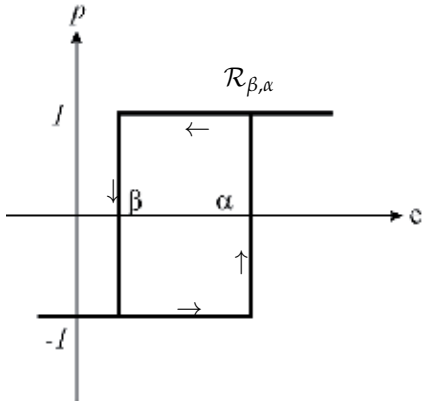

Fig. 5. Hysteresis of an elementary relay.

A practically important phenomenological hysteresis model that was originally introduced in the context of magnetism but plays a role also in many other hysteretic processes, is given by the *Preisach operator*

$$\mathcal{H}[e](t) = \iint_{\beta \le \alpha} \wp(\beta,\alpha)\mathcal{R}_{\beta,\alpha}[e](t)\, d(\alpha,\beta)\,, \tag{1}$$

which is a weighted superposition of elementary relays. The initial values of the relays $\mathcal{R}_{\beta,\alpha}$ (assigned to some "pre-initial" state e_{-1}) are set to

$$\mathcal{R}_{\beta,\alpha}[e_{-1}] = \begin{cases} -1 \text{ if } \alpha > -\beta \\ +1 \text{ else.} \end{cases} \tag{2}$$

Determining $\mathcal{H}$ obviously amounts to determining the weight function $\wp$ in Equation (1). The domain $\{(\beta,\alpha) \mid \beta \le \alpha\}$ of $\wp$ is called the *Preisach plane*. Assuming that $\wp$ is compactly supported and by a possible rescaling, we can restrict our attention to the Preisach unit triangle $\{(\beta,\alpha) \mid -1 \le \beta \le \alpha \le 1\}$ within the Preisach plane (see Fig. 6), which shows the Preisach unit triangle with the sets S^+, S^- of up- and down-switched relays at the initial state according to Equation (2).

We would now like to start with pointing out three characteristic features of hysteresis operators in general, and especially of Preisach operators (see Equation (1)), that will play a role in the following:

Firstly, the output $p(t)$ at some time t depends on the present as well as past states of the input $e(t)$, but not on the future (Volterra property).

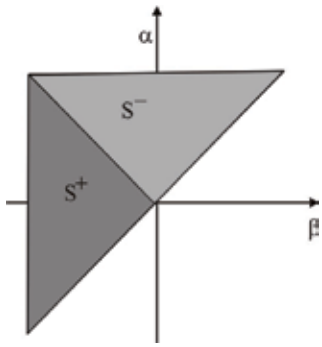

Fig. 6. Preisach plane at the initial state according to Equation (2).

Secondly, it is rate independent, i.e., the values that the output attains are independent of the speed of the input in the sense that for any continuous monotonically increasing transformation κ of the time interval $[0,T]$ with $\kappa(0)=0$, $\kappa(T)=T$, and all input functions e, there holds

$$\mathcal{H}[e\circ\kappa]=\mathcal{H}[e]\circ\kappa\,. \tag{3}$$

As a consequence, given a piecewise monotone continuous input e, the output is (up to the speed in which it is traversed) uniquely determined by the local extrema of the input only, i.e.,the values of e at instances where e changes its monotonicity behavior from decreasing to increasing or vice versa.
The third important characteristic of hysteresis is that it typically does not keep the whole input history in mind but forgets certain passages in the past. I.e., there is a certain deletion in memory and it is quite important to take this into account also when doing computations: in a finite element simulation of a system with hysteresis, each element has its own history, so in order to keep memory consumption in an admissible range it is essential to delete past values that are not required any more.
Deletion, i.e., the way in which hysteresis operators forget, can be described by appropriate orderings on the set S of strings containing local extrema of the input, together with the above mentioned correspondence to piecewise monotone input functions.

Definition 1. *(Definition 2.7.1 in Brokate & Sprekels (1996))*
Let $\preceq$ be an ordering (i.e., a reflexive, antisymmetric, and transitive relation) on S. We say that a hysteresis operator forgets according to $\preceq$, if

$$s'\preceq s\ \Rightarrow \mathcal{H}(s)=\mathcal{H}(s')\quad \forall s,s'\in S$$

Due to this implication, strings can be reduced according to certain rules. With the notation

$$[[e,e']]:=[\min\{e,e'\},\max\{e,e'\}]$$

the relevant deletion rules for Preisach operators with neutral initial state Equation (2) can be written as follows (for an illustration see Fig. 7):

- *Monotone deletion rule:* only the local maxima and minima of the input are relevant.

$$\begin{aligned}&(e_0,\dots,e_N)\mapsto(e_0,\dots,e_{i-1},e_{i+1},\dots,e_N)\\ &\text{if } e_i\in[[e_{i-1},e_{i+1}]]\end{aligned} \tag{4}$$

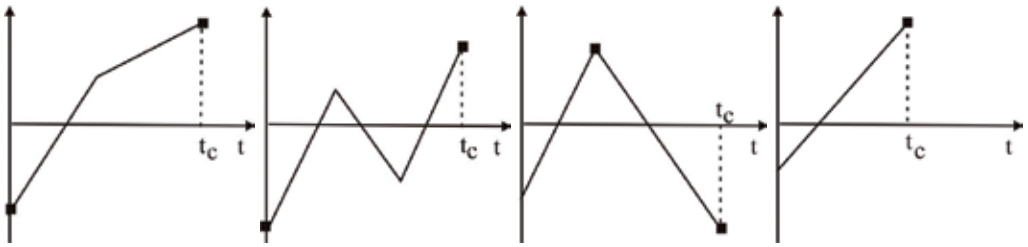

Fig. 7. Illustration of deletion rules according to Equation (4) - Equation (7). Here the filled boxes mark the dominant input values, i.e., those sufficing to compute output values after time t_c.

- *Madelung rule:* Inner minor loops are forgotten.

$$\begin{aligned}&(e_0,\ldots,e_N)\mapsto(e_0,\ldots,e_{i-1},e_{i+2},\ldots,e_N)\\&\text{if } [[e_i,e_{i+1}]]\subset[[e_{i-1},e_{i+2}]]\wedge e_i\notin[[e_{i-1},e_{i+1}]]\wedge e_{i+1}\notin[[e_i,e_{i+2}]]\end{aligned}\tag{5}$$

- *Wipe out:* previous absolutely smaller local maxima (minima) are erased from memory by subsequent absolutely larger local maxima (minima).

$$\begin{aligned}&(e_0,\ldots,e_N)\mapsto(e_1,\ldots,e_N)\\&\text{if } e_0\in[[e_1,e_2]]\end{aligned}\tag{6}$$

- *Initial deletion:* a maximum (minimum) is also forgotten if it is followed by an minimum (maximum) with sufficiently large modulus.

$$(e_0,\ldots,e_N)\mapsto(e_1,\ldots,e_N)\quad\text{if } |e_0|\le|e_1|\tag{7}$$

It can be shown that irreducible strings for this Preisach ordering with neutral initial state are given by the set

$$S_0=\{s\in S\mid s=(e_0,\ldots,e_N)\text{ is fading and }|e_0|>|e_1|\}$$

where

$$\begin{aligned}&s=(e_0,\ldots,e_N)\text{ is fading}\quad\Leftrightarrow\\&\Big(s\in S_A\text{ and }|e_0-e_1|>|e_1-e_2|>|e_2-e_3|>\ldots>|e_{N-1}-e_N|\Big)\,.\end{aligned}$$

Considering an arbitrary input string, the rules above have to be applied repeatedly to generate an irreducible string with the same output value, which could lead to a considerable computational effort. However, when computing the hysteretic evolution of some output function by a time stepping scheme, we update the input string and apply deletion in each time step and fortunately in that situation reduction can be done at low computational cost. Namely, only one iteration per time step is required and there is no need to recursively apply rules Equation (4)–Equation (7), see Lemma 3.3 in Kaltenbacher & Kaltenbacher (2006). After achieving an irreducible string $(e_0,\ldots,e_N)$, the hysteresis operator can be applied very

efficiently by just evaluation of a sum over the string entries

$$\mathcal{H}(s) = h(-e_0, e_0) + \sum_{k=1}^{N} h(e_{k-1}, e_k) \qquad \forall s = (e_0, \ldots, e_N) \tag{8}$$

instead of computing the integrals in Equation (1). In Equation (8) h is the so-called *shape function* or *Everett function* (cf. Everett (1955)), which can be precomputed according to

$$h(e_{N-1}, e_N) = 2\,\mathrm{sign}(e_N - e_{N-1}) \iint_{\Delta(e_{N-1}, e_N)} \wp(\beta, \alpha)\, d(\alpha, \beta)\,. \tag{9}$$

4. Piezoelectric model

We follow the basic ideas discussed in Kamlah & Böhle (2001) and decompose the physical quantities into a reversible and an irreversible part. For this purpose, we introduce the reversible part $\mathbf{D}^{\mathrm{r}}$ and the irreversible part $\mathbf{D}^{\mathrm{i}}$ of the dielectric displacement according to

$$\mathbf{D} = \mathbf{D}^{\mathrm{r}} + \mathbf{D}^{\mathrm{i}}\,. \tag{10}$$

In our case, using the general relation between dielectric displacement $\mathbf{D}$, electric field intensity $\mathbf{E}$, and polarization $\mathbf{P}$ we set $\mathbf{D}^{\mathrm{i}} = \mathbf{P}^{\mathrm{i}}$ (irreversible part of the electric polarization). Analogously to Equation (10), the mechanical strain $\mathbf{S}$ is also decomposed into a reversible part $\mathbf{S}^{\mathrm{r}}$ and an irreversible part $\mathbf{S}^{\mathrm{i}}$

$$\mathbf{S} = \mathbf{S}^{\mathrm{r}} + \mathbf{S}^{\mathrm{i}}\,. \tag{11}$$

The decomposition of the strain $\mathbf{S}$ is done in compliance with the theory of elastic-plastic solids under the assumption that the deformations are very small Bassiouny & Ghaleb (1989). That assumption is generally valid for piezoceramic materials with maximum strains below 0.2 %.

The reversible parts of mechanical strain $\mathbf{S}^{\mathrm{r}}$ and dielectric displacement $\mathbf{D}^{\mathrm{r}}$ are described by the linear piezoelectric constitutive law.

Now, in contrast to the thermodynamically motivated approaches in, e.g., Bassiouny & Ghaleb (1989); Kamlah & Böhle (2001); Landis (2004), we compute the polarization from the history of the driving electric field $\mathbf{E}$ by a scalar Preisach hysteresis operator $\mathcal{H}$

$$\mathbf{P}^{\mathrm{i}} = \mathcal{H}[\mathbf{E}]\ \mathbf{e}_P\,, \tag{12}$$

with the unit vector of the polarization $\mathbf{e}_P$, set equal to the direction of the applied electric field. Taking this into consideration, we currently restrict our model to uni-axially loaded actuators.

The butterfly curve for the mechanical strain could be modeled by an enhanced hysteresis operator as well. The use of an additional hysteresis operator for the strain can be avoided based on the following observation, though. As seen in Fig. 8, the mechanical strain S_{33} appears to be proportional to the squared dielectric polarization P_3, i.e., the relation $S^{\mathrm{i}} = \beta \cdot (\mathcal{H}[\mathbf{E}])^2$, with a model parameter β, seems obvious. To keep the model more general, we choose the ansatz

$$S^{\mathrm{i}} = \beta_1 \cdot \mathcal{H}[\mathbf{E}] + \beta_2 \cdot (\mathcal{H}[\mathbf{E}])^2 + \ldots + \beta_l \cdot (\mathcal{H}[\mathbf{E}])^l\,. \tag{13}$$

Similarly to Kamlah & Böhle (2001) we define the tensor of irreversible strains as follows

$$[\mathbf{S}^{\mathrm{i}}] = \tfrac{3}{2}\left(\beta_1 \cdot \mathcal{H}[\mathbf{E}] + \beta_2 \cdot (\mathcal{H}[\mathbf{E}])^2 + \cdots + \beta_l \cdot (\mathcal{H}[\mathbf{E}])^l\right)\left(\mathbf{e}_P\, \mathbf{e}_P{}^T - \tfrac{1}{3}\,[\mathbf{I}]\right). \tag{14}$$

The parameters $\beta_1 \ldots \beta_n$ need to be fitted to measured data.

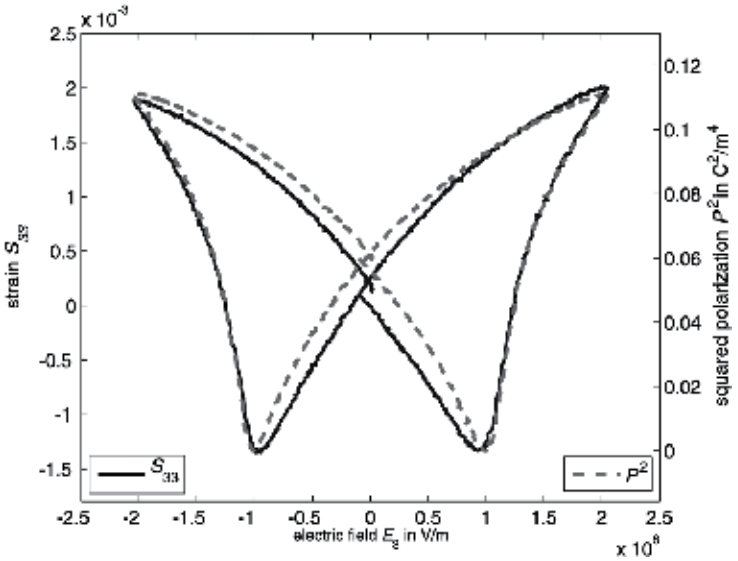

Fig. 8. Measured mechanical strain S_{33} and squared irreversible polarization P_3^{i} of a piezoceramic actuator on different axis.

Moreover, the entries of the tensor of piezoelectric moduli are now assumed to be a function of the irreversible electric polarization $\mathbf{P}^{\mathrm{i}}$. Here the underlying idea is that the piezoelectric properties of the material only appear once the material is poled. Without any polarization, the domains in the material are not aligned, and therefore coupling between the electric field and the mechanical field does not occur. If the polarization is increased, the coupling also increases. Hence, we define the following relation

$$[\mathbf{e}(\mathbf{P})] = \frac{|\mathbf{P}^{\mathrm{i}}|}{P^{\mathrm{i}}_{\mathrm{sat}}}\,[\mathbf{e}]\,. \tag{15}$$

Herein, $P^{\mathrm{i}}_{\mathrm{sat}}$ denotes the irreversible part of the saturation polarization $P_{\mathrm{sat}} = P^{\mathrm{r}}_{\mathrm{sat}} + P^{\mathrm{i}}_{\mathrm{sat}}$ (see state 2 in Fig. 3), $[\mathbf{e}]$ the tensor of constant piezoelectric moduli and $[\mathbf{e}(\mathbf{P}^{\mathrm{i}})]$ the tensor of variable piezoelectric moduli. Therewith, we model a uni-axial electric loading along a fixed polarization axis.
Finally, the constitutive relations for the electromechanical coupling can be established and written in e-form

$$\mathbf{S} = \mathbf{S}^{\mathrm{r}} + \mathbf{S}^{\mathrm{i}}\,;\;\; \mathbf{P}^{\mathrm{i}} = \mathcal{H}[\mathbf{E}]\mathbf{e}_P \tag{16}$$

$$\sigma = [\mathbf{c}^{\mathrm{E}}]\,\mathbf{S}^{\mathrm{r}} - [\mathbf{e}(\mathbf{P}^{\mathrm{i}})]^t\mathbf{E} \tag{17}$$

$$\mathbf{D} = [\mathbf{e}(\mathbf{P}^{\mathrm{i}})]\,\mathbf{S}^{\mathrm{r}} + [\varepsilon^{\mathrm{S}}]\,\mathbf{E} + \mathbf{P}^{\mathrm{i}} \tag{18}$$

or equivalently in d-form

$$\mathbf{S} = \mathbf{S}^{\mathrm{r}} + \mathbf{S}^{\mathrm{i}}\,;\;\; \mathbf{P}^{\mathrm{i}} = \mathcal{H}[\mathbf{E}]\mathbf{e}_P \tag{19}$$

$$\mathbf{S} = [\mathbf{s}^{\mathrm{E}}]\,\boldsymbol{\sigma} + [\mathbf{d}(\mathbf{P}^{\mathrm{i}})]^t\mathbf{E} + \mathbf{S}^{\mathrm{i}} \tag{20}$$

$$\mathbf{D} = [\mathbf{d}(\mathbf{P}^{\mathrm{i}})]\,\boldsymbol{\sigma} + [\boldsymbol{\varepsilon}^{\sigma}]\,\mathbf{E} + \mathbf{P}^{\mathrm{i}}\,. \tag{21}$$

Due to the symmetry of the mechanical tensors, we use Voigt notation and write the mechanical stress tensor $[\boldsymbol{\sigma}]$ as well as strain tensors $[\mathbf{S}]$ as six-component vectors (e.g., $\boldsymbol{\sigma} = (\sigma_{xx}\,\sigma_{yy}\,\sigma_{zz}\,\sigma_{yz}\,\sigma_{xz}\,\sigma_{xy})^t = (\sigma_1\,\sigma_2\,\sigma_3\,\sigma_4\,\sigma_5\,\sigma_6)^t$). The relations between the different material tensors are as follows

$$[\mathbf{s}^{\mathrm{E}}] = [\mathbf{c}^{\mathrm{E}}]^{-1}\,;\;\; [\mathbf{d}]^t = [\mathbf{c}^{\mathrm{E}}]^{-1}[\mathbf{e}]^t\,;\;\; [\boldsymbol{\varepsilon}^{\sigma}] = [\boldsymbol{\varepsilon}^{\mathrm{S}}] + [\mathbf{d}]^t[\mathbf{e}]\,.$$

The governing equations for the mechanical and electrostatic fields are given by

$$\rho\ddot{\mathbf{u}} - \mathcal{B}^t\boldsymbol{\sigma} - \mathbf{f} = 0\,;\;\; \boldsymbol{\nabla}\cdot\mathbf{D} = 0\,;\;\; \boldsymbol{\nabla}\times\mathbf{E} = 0\,, \tag{22}$$

see, e.g., Kaltenbacher (2007). In Equation (22) ρ denotes the mass density, $\mathbf{f}$ some prescribed mechanical volume force and $\ddot{\mathbf{u}} = \partial^2\mathbf{u}/\partial t^2$ the mechanical acceleration. Furthermore, the differential operator $\mathcal{B}$ is explicitely written as

$$\mathcal{B} = \begin{pmatrix} \frac{\partial}{\partial x} & 0 & 0 & 0 & \frac{\partial}{\partial z} & \frac{\partial}{\partial y} \\ 0 & \frac{\partial}{\partial y} & 0 & \frac{\partial}{\partial z} & 0 & \frac{\partial}{\partial x} \\ 0 & 0 & \frac{\partial}{\partial z} & \frac{\partial}{\partial y} & \frac{\partial}{\partial x} & 0 \end{pmatrix}^t . \tag{23}$$

With the same differential operator, we can express the mechanical strain - displacement relation

$$\mathbf{S} = \mathcal{B}\mathbf{u}\,. \tag{24}$$

Since the curl of the electric field intensity vanishes in the electrostatic case, we can fully describe this vector by the scalar electric potential φ, and write

$$\mathbf{E} = -\boldsymbol{\nabla}\varphi\,. \tag{25}$$

Combining the constitutive relations Equation (16) - (18) with the governing equations as given in Equation (22) together with Equation (24) and (25), we arrive at the following non-linear coupled system of PDEs

$$\rho\ddot{\mathbf{u}} - \mathcal{B}^T\left(\,[\mathbf{c}^E]\left(\mathcal{B}\mathbf{u} - \mathbf{S}^{\mathrm{i}}\right) + [\mathbf{e}(\mathbf{P}^{\mathrm{i}})]^t\boldsymbol{\nabla}\varphi\right) = 0 \tag{26}$$

$$\boldsymbol{\nabla}\cdot\left(\,[\mathbf{e}(\mathbf{P}^{\mathrm{i}})]\left(\mathcal{B}\mathbf{u} - \mathbf{S}^{\mathrm{i}}\right) - [\boldsymbol{\varepsilon}^S]\boldsymbol{\nabla}\varphi + \mathbf{P}^{\mathrm{i}}\right) = 0 \tag{27}$$

with

$$\mathbf{P}^{\mathrm{i}} = \mathcal{H}[-\boldsymbol{\nabla}\varphi]\mathbf{e}_P \tag{28}$$

$$[\mathbf{S}^{\mathrm{i}}] = \left(\frac{3}{2}\sum_{i=0}^{l}\beta_i\left(\mathcal{H}[-\boldsymbol{\nabla}\varphi]\right)^i\right)\left(\mathbf{e}_P\,\mathbf{e}_P^T - \frac{1}{3}\mathbf{I}\right). \tag{29}$$

5. FE formulation

A straight forward procedure to solve Equation (26) and (27) is to put the hysteresis dependent terms (irreversible electric polarization and irreversible strain) to the right hand side and apply the FE method. Therewith, one arrives at a fixed-point method for the nonlinear system of equations. However, convergence can only be guaranteed if very small incremental steps are made within the nonlinear iteration process. A direct application of Newton's method is not possible, due to the lack of differentiability of the hysteresis operator. Therefore, we apply the so-called *incremental material parameter* method, which corresponds to a quasi Newton scheme applying a secant like linearization at each time step. For this purpose, we decompose the dielectric displacement $\mathbf{D}$ and the mechanical stress σ at time step t_{n+1} as follows

$$\mathbf{D}_{n+1} = \mathbf{D}_n + \Delta\mathbf{D}; \qquad \sigma_{n+1} = \sigma_n + \Delta\sigma\,. \tag{30}$$

Since we can assume, that $\mathbf{D}_n$ and σ_n have fulfilled their corresponding PDEs (the first two equations in Equation (22)) at time step t_n, we have to solve

$$\rho\Delta\ddot{\mathbf{u}} - \mathcal{B}^t\Delta\sigma - \Delta\mathbf{f} = 0 \qquad \boldsymbol{\nabla}\cdot\Delta\mathbf{D} = 0\,. \tag{31}$$

Now, we perform this decomposition also for our constitutive equations as given in Equation (20) and (21)

$$\mathbf{S}_n + \Delta\mathbf{S} = [\mathbf{s}^{\mathrm{E}}]\,(\sigma_n + \Delta\sigma) + \mathbf{S}^{\mathrm{i}}_n + \Delta\mathbf{S}^{\mathrm{i}} + \left([\mathbf{d}_n]^t + [\Delta\mathbf{d}]^t\right)(\mathbf{E}_n + \Delta\mathbf{E}) \tag{32}$$

$$\mathbf{D}_n + \Delta\mathbf{D} = \left([\mathbf{d}_n] + [\Delta\mathbf{d}]\right)(\sigma_n + \Delta\sigma) + [\varepsilon^{\sigma}]\,(\mathbf{E}_n + \Delta\mathbf{E}) + \mathbf{P}^{\mathrm{i}}_n + \Delta\mathbf{P}^{\mathrm{i}}\,. \tag{33}$$

Again assuming equilibrium at time step t_n, we arrive at the equations for the increments

$$\Delta\mathbf{S} = [\mathbf{s}^{\mathrm{E}}]\,\Delta\sigma + [\mathbf{d}_{n+1}]^t\Delta\mathbf{E} + \Delta\mathbf{S}^{\mathrm{i}} + [\Delta\mathbf{d}]^t\mathbf{E}_n \tag{34}$$

$$\Delta\mathbf{D} = [\mathbf{d}_{n+1}]\Delta\sigma + [\varepsilon^{\sigma}]\,\Delta\mathbf{E} + \Delta\mathbf{P}^{\mathrm{i}} + [\Delta\mathbf{d}]\sigma_n\,. \tag{35}$$

Now, we rewrite the two equations above as

$$\Delta\mathbf{S} = [\mathbf{s}^{\mathrm{E}}]\,\Delta\sigma + [\tilde{\mathbf{d}}_{n+1}]^t\Delta\mathbf{E} + [\Delta\mathbf{d}]^t\mathbf{E}_n \tag{36}$$

$$\Delta\mathbf{D} = [\mathbf{d}_{n+1}]\Delta\sigma + [\tilde{\varepsilon}]\,\Delta\mathbf{E} + [\Delta\mathbf{d}]\sigma_n\,, \tag{37}$$

thus incorporating the hysteretic quantities in the material tensors. The coefficients of the newly introduced effective material tensors compute as follows

$$\tilde{\varepsilon}_{jj} = \varepsilon^{\sigma}_{jj} + \frac{\Delta P^{\mathrm{i}}_j}{\Delta E_j} \quad j = 1,2,3 \tag{38}$$

$$\left(\tilde{d}_{31}\right)_{n+1} = (d_{31})_{n+1} + \frac{\Delta S^{\mathrm{i}}_1}{\Delta E_z}\,; \quad \left(\tilde{d}_{32}\right)_{n+1} = (d_{32})_{n+1} + \frac{\Delta S^{\mathrm{i}}_2}{\Delta E_z} \tag{39}$$

$$\left(\tilde{d}_{33}\right)_{n+1} = (d_{33})_{n+1} + \frac{\Delta S^{\mathrm{i}}_3}{\Delta E_z}\,; \quad \left(\tilde{d}_{15}\right)_{n+1} = (d_{15})_{n+1}\,. \tag{40}$$

Since we need expressions for σ and $\mathbf{D}$ in order to solve Equation (31), we rewrite Equation (36) and (37) and obtain

$$\Delta\sigma = [\mathbf{c}^{\mathrm{E}}]\Delta\mathbf{S} - [\mathbf{c}^{\mathrm{E}}][\tilde{\mathbf{d}}_{n+1}]^t\Delta\mathbf{E} - [\mathbf{c}^{\mathrm{E}}][\Delta\mathbf{d}]^t\mathbf{E}_n \tag{41}$$

$$\Delta\mathbf{D} = [\mathbf{d}_{n+1}][\mathbf{c}^{\mathrm{E}}]\Delta\mathbf{S} + \left([\tilde{\varepsilon}] - [\mathbf{d}_{n+1}][\mathbf{c}^{\mathrm{E}}][\tilde{\mathbf{d}}_{n+1}]^t\right)\Delta\mathbf{E} - [\mathbf{d}_{n+1}][\mathbf{c}^{\mathrm{E}}][\Delta\mathbf{d}]^t\mathbf{E}_n + [\Delta\mathbf{d}]\sigma_n\,. \tag{42}$$

To simplify the notation, we make the following substitutions

$$[\mathbf{e}_{n+1}]^t = [\mathbf{c}^{\mathrm{E}}][\mathbf{d}_{n+1}]^t\,;\quad [\tilde{\mathbf{e}}_{n+1}]^t = [\mathbf{c}^{\mathrm{E}}][\tilde{\mathbf{d}}_{n+1}]^t$$
$$[\Delta\mathbf{e}]^t = [\mathbf{c}^{\mathrm{E}}][\Delta\mathbf{d}]^t\,;\quad [\tilde{\tilde{\varepsilon}}] = [\tilde{\varepsilon}] - [\mathbf{d}_{n+1}][\mathbf{c}^{\mathrm{E}}][\tilde{\mathbf{d}}_{n+1}]^t\,.$$

Substituting Equation (41) and (42) into Equation (31) results in

$$\rho\Delta\ddot{\mathbf{u}} - \mathcal{B}^t[\mathbf{c}^{\mathrm{E}}]\mathcal{B}\Delta\mathbf{u} - \mathcal{B}^t[\tilde{\mathbf{e}}_{n+1}]^t\tilde{\mathcal{B}}\Delta\varphi = \Delta\mathbf{f} + \mathcal{B}^t[\Delta\mathbf{e}]^t\boldsymbol{\nabla}\varphi_n \tag{43}$$

$$\boldsymbol{\nabla}\cdot[\mathbf{e}_{n+1}]\mathcal{B}\Delta\mathbf{u} - \boldsymbol{\nabla}\cdot[\tilde{\tilde{\varepsilon}}]\boldsymbol{\nabla}\Delta\varphi = -\boldsymbol{\nabla}\cdot[\mathbf{d}_{n+1}][\Delta\mathbf{e}]^t\boldsymbol{\nabla}\varphi_n - \boldsymbol{\nabla}\cdot[\Delta\mathbf{d}]\sigma_n\,. \tag{44}$$

This coupled system of PDEs with appropriate boundary conditions for $\mathbf{u}$ and φ defines the strong formulation for our problem. We now introduce the test functions $\mathbf{v}$ and ψ, multiply our coupled system of PDEs by these test functions and integrate over the whole computational domain Ω. Furthermore, by applying integration by parts[2], we arrive at the weak (variational) formulation: Find $\mathbf{u} \in (H_0^1)^3$ and $\varphi \in H_0^1$ such that[3]

$$\int_\Omega \rho\,\mathbf{v}\cdot\Delta\ddot{\mathbf{u}}\;\mathrm{d}\Omega + \int_\Omega (\mathcal{B}\mathbf{v})^t[\mathbf{c}^{\mathrm{E}}]\mathcal{B}\Delta\mathbf{u}\,\mathrm{d}\Omega + \int_\Omega (\mathcal{B}\mathbf{v})^t[\tilde{\mathbf{e}}_{n+1}]^t\boldsymbol{\nabla}\Delta\varphi\,\mathrm{d}\Omega \tag{45}$$
$$= \int_\Omega \mathbf{v}\cdot\Delta\mathbf{f}\,\mathrm{d}\Omega - \int_\Omega (\mathcal{B}\mathbf{v})^t[\Delta\mathbf{e}]\boldsymbol{\nabla}\varphi_n\,\mathrm{d}\Omega$$

$$\int_\Omega (\boldsymbol{\nabla}\psi)^t[\mathbf{e}_{n+1}]\mathcal{B}\Delta\mathbf{u}\,\mathrm{d}\Omega - \int_\Omega (\boldsymbol{\nabla}\psi)^t[\tilde{\tilde{\varepsilon}}]\boldsymbol{\nabla}\Delta\varphi\,\mathrm{d}\Omega \tag{46}$$
$$= -\int_\Omega (\boldsymbol{\nabla}\psi)^t[\mathbf{d}_{n+1}][\Delta\mathbf{e}]^t\boldsymbol{\nabla}\varphi_n\,\mathrm{d}\Omega$$
$$-\int_\Omega (\boldsymbol{\nabla}\psi)^t[\Delta\mathbf{d}]\sigma_n\;\mathrm{d}\Omega$$

for all test functions $\mathbf{v} \in (H_0^1)^3$ and $\psi \in H_0^1$. Now, using standard Lagrangian (nodal) finite elements for the mechanical displacement $\mathbf{u}$ and the electric scalar potential φ (n_{n} denotes the number of nodes with unknown displacement and unknown electric potential)

$$\Delta\mathbf{u} \approx \Delta\mathbf{u}^h = \sum_{i=1}^{d}\sum_{a=1}^{n_{\mathrm{n}}} N_a\Delta u_{ia}\mathbf{e}_i = \sum_{a=1}^{n_{\mathrm{n}}} \mathbf{N}_a\Delta\mathbf{u}_a\,;\quad \mathbf{N}_a = \begin{pmatrix} N_a & 0 & 0\\ 0 & N_a & 0\\ 0 & 0 & N_a\end{pmatrix} \tag{47}$$

[2] For simplicity we assume a zero mechanical stress condition on the boundary.

[3] H_0^1 is the space of functions, which are square integrable along with their first derivatives in a weak sense, Adams (1975).

$$\Delta\varphi \approx \Delta\varphi^h = \sum_{a=1}^{n_\mathrm{n}} N_a \Delta\varphi_a \tag{48}$$

as well as for the test functions $\mathbf{v}$ and φ, we obtain the spatially discrete formulation

$$\begin{pmatrix} \mathbf{M}_{uu} & 0 \\ 0 & 0 \end{pmatrix} \begin{pmatrix} \Delta\underline{\ddot{\mathbf{u}}} \\ \Delta\underline{\ddot{\varphi}} \end{pmatrix} + \begin{pmatrix} \mathbf{K}_{uu} & \tilde{\mathbf{K}}_{u\varphi} \\ \mathbf{K}_{\varphi u} & -\tilde{\tilde{\mathbf{K}}}_{\varphi\varphi} \end{pmatrix} \begin{pmatrix} \Delta\underline{\mathbf{u}} \\ \Delta\underline{\varphi} \end{pmatrix} = \begin{pmatrix} \underline{f}_u \\ \underline{f}_\varphi \end{pmatrix} . \tag{49}$$

In Equation (49) the vectors $\Delta\underline{\mathbf{u}}$ and $\Delta\underline{\varphi}$ contain all the unknown mechanical displacements and electric scalar potentials at the finite element nodes. The FE matrices and right hand sides compute as follows

$$\mathbf{K}_{uu} = \bigwedge_{e=1}^{n_\mathrm{e}} \mathbf{k}_{uu}^e \;;\; \mathbf{k}_{uu}^e = [\mathbf{k}_{pq}] \;;\; \mathbf{k}_{pq} = \int_{\Omega^e} \mathcal{B}_p^t [\mathbf{c}^\mathrm{E}] \mathcal{B}_q \, \mathrm{d}\Omega \tag{50}$$

$$\tilde{\mathbf{K}}_{u\varphi} = \bigwedge_{e=1}^{n_\mathrm{e}} \tilde{\mathbf{k}}_{u\varphi}^e \;;\; \tilde{\mathbf{k}}_{u\varphi}^e = [\tilde{\mathbf{k}}_{pq}] \;;\; \tilde{\mathbf{k}}_{pq} = \int_{\Omega^e} \mathcal{B}_p^t [\tilde{\mathbf{e}}_{n+1}]^t \hat{\mathcal{B}}_q \, \mathrm{d}\Omega \tag{51}$$

$$\mathbf{K}_{\varphi u} = \bigwedge_{e=1}^{n_\mathrm{e}} \mathbf{k}_{\varphi u}^e \;;\; \mathbf{k}_{\varphi u}^e = [\mathbf{k}_{pq}] \;;\; \mathbf{k}_{pq} = \int_{\Omega^e} \hat{\mathcal{B}}_p^t [\mathbf{e}_{n+1}] \mathcal{B}_q \, \mathrm{d}\Omega \tag{52}$$

$$\tilde{\tilde{\mathbf{K}}}_{\varphi\varphi} = \bigwedge_{e=1}^{n_\mathrm{e}} \tilde{\tilde{\mathbf{k}}}_{\varphi\varphi}^e \;;\; \tilde{\tilde{\mathbf{k}}}_{\varphi\varphi}^e = [\tilde{\tilde{\mathbf{k}}}_{pq}] \;;\; \tilde{\tilde{\mathbf{k}}}_{pq} = \int_{\Omega^e} \hat{\mathcal{B}}_p^t [\tilde{\tilde{\varepsilon}}] \hat{\mathcal{B}}_q \, \mathrm{d}\Omega \tag{53}$$

$$\underline{f}_u = \bigwedge_{e=1}^{n_\mathrm{e}} \underline{f}_u^e \;;\; \underline{f}_u^e = [\underline{f}_p] \tag{54}$$

$$\underline{f}_p = \int_{\Omega^e} \mathbf{N}_p \Delta\mathbf{f} \, \mathrm{d}\Omega - \int_{\Omega^e} \mathcal{B}_p^t [\Delta\mathbf{e}_{n+1}] \hat{\mathcal{B}} \psi_n \, \mathrm{d}\Omega$$

$$\underline{f}_\varphi = \bigwedge_{e=1}^{n_\mathrm{e}} \underline{f}_\varphi^e \;;\; \underline{f}_\varphi^e = [\underline{f}_p] \tag{55}$$

$$\underline{f}_p = -\int_{\Omega^e} \mathcal{B}_p^t [\mathbf{d}_{n+1}] [\Delta\mathbf{e}]^t \hat{\mathcal{B}} \varphi_n \, \mathrm{d}\Omega - \int_{\Omega^e} \hat{\mathcal{B}}_p^t [\Delta\mathbf{d}] \sigma_n \, \mathrm{d}\Omega \, .$$

In Equation (50) - (55) n_e denotes the number of finite elements, $\bigwedge$ the FE assembly operator (assembly of element matrices to global system matrices) and $\mathcal{B}_p$, $\hat{\mathcal{B}}_p$ compute as

$$\mathcal{B}_p = \begin{pmatrix} \frac{\partial N_p}{\partial x} & 0 & 0 & 0 & \frac{\partial N_p}{\partial z} & \frac{\partial N_p}{\partial y} \\ 0 & \frac{\partial N_p}{\partial y} & 0 & \frac{\partial N_p}{\partial z} & 0 & \frac{\partial N_p}{\partial x} \\ 0 & 0 & \frac{\partial N_p}{\partial z} & \frac{\partial N_p}{\partial y} & \frac{\partial N_p}{\partial x} & 0 \end{pmatrix}^t$$

$$\hat{\mathcal{B}}_p = \left(\partial N_p/\partial x, \, \partial N_p/\partial y, \, \partial N_p/\partial z\right)^t .$$

Time discretization is performed by the Newmark scheme choosing respectively the values 0.25 and 0.5 for the two integration parameters β and γ to achieve 2nd order accuracy Hughes (1987). Therewith, we arrive at a predictor-corrector scheme that involves solution of a nonlinear system of algebraic equations of the form

$$\begin{pmatrix} \mathbf{K}^*_{uu} & \tilde{\mathbf{K}}_{u\varphi}(\Delta\underline{\mathbf{u}}, \Delta\underline{\varphi}) \\ \mathbf{K}_{\varphi u} & -\tilde{\tilde{\mathbf{K}}}^*_{\varphi\varphi}(\Delta\underline{\mathbf{u}}, \Delta\underline{\varphi}) \end{pmatrix} \begin{pmatrix} \Delta\underline{\mathbf{u}} \\ \Delta\underline{\varphi} \end{pmatrix} = \begin{pmatrix} \underline{g}_u(\Delta\underline{\mathbf{u}}, \Delta\underline{\varphi}) \\ \underline{g}_\varphi(\Delta\underline{\mathbf{u}}, \Delta\underline{\varphi}) \end{pmatrix}$$

with $\mathbf{K}^*_{uu}$, $\tilde{\tilde{\mathbf{K}}}^*_{\varphi\varphi}$ the effective stiffness matrices. The solution for each time step $(n+1)$ is obtained by solving this fully discrete nonlinear system of equations of the form $A(z)z = b(z)$ by the iteration $A(z_k)z_{k+1} = b(z_k)$ (often denoted as linearization by freezing the coefficients) until the following incremental stopping criterion is fulfilled

$$\frac{||\Delta\underline{\mathbf{u}}^{n+1}_{k+1} - \Delta\underline{\mathbf{u}}^{n+1}_{k}||_2}{||\Delta\underline{\mathbf{u}}^{n+1}_{k+1}||_2} + \frac{||\Delta\underline{\varphi}^{n+1}_{k+1} - \Delta\underline{\varphi}^{n+1}_{k}||_2}{||\Delta\underline{\varphi}^{n+1}_{k+1}||_2} < \delta_{\text{rel}} \tag{56}$$

with k the iteration counter. In our practical computations (see Sec. 7) we have set δ_{rel} to 10^{-4}. For further details we refer to Kaltenbacher et al. (2010).

6. Fitting of material parameters

The determination of all material parameters for our nonlinear piezoelectric model is a quite challenging task. Since we currently restrict ourselves to the uni-axial case, two experimental setups suffice to obtain the necessary measurement data for the fitting procedure.
According to our ansatz (decomposition into a reversible and an irreversible part of the dielectric displacement and mechanical strain) we have to determine the following parameters:

- entries of the constant material tensors $[\mathbf{s}^{\mathrm{E}}]$, $[\mathbf{d}]$, $[\boldsymbol{\varepsilon}^{\sigma}]$ (see Equation (20) and Equation (21));
- weight function $\wp$ of the hysteresis operator (see Equation (1),
- polynomial coefficients $\beta_1, \dots \beta_l$ for the irreversible strain (see Equation (13)).

The determination of the linear material parameters is performed by our enhanced inverse scheme, Kaltenbacher et al. (2006); Lahmer et al. (2008). To do so, we carry out electric impedance measurements on the actuator and fit the entries of the material tensors by full 3d simulations in combination with the inverse scheme. Figure 9 displays the experimental setup, where it can be seen that we electrically pre-load the piezoelectric actuator with a DC voltage. The amplitude of the DC voltage source is chosen in such a way that the piezoelectric material is driven into saturation. The reason for this pre-loading is the fact, that the irreversible physical quantities show saturation and a further increase beyond saturation is just given by the reversible physical quantities. These reversible quantities however, are modeled by the linear piezoelectric equations using the corresponding material tensors.
The data for fitting the hysteresis operator and for determination of the polynomial coefficients for the irreversible strain are collected by a second experimental setup as displayed in Fig. 10. A signal generator drives a power amplifier to generate the necessary input voltage. Thereby, we use a voltage driving sequence as shown in Fig. 10 to provide appropriate data for identifying the hysteretic behavior Mayergoyz (1991). The first peak

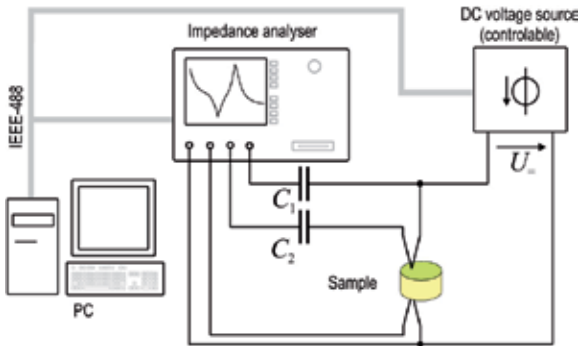

Fig. 9. Experimental setup for measuring the electric impedance at saturation of piezoelectric actuators.

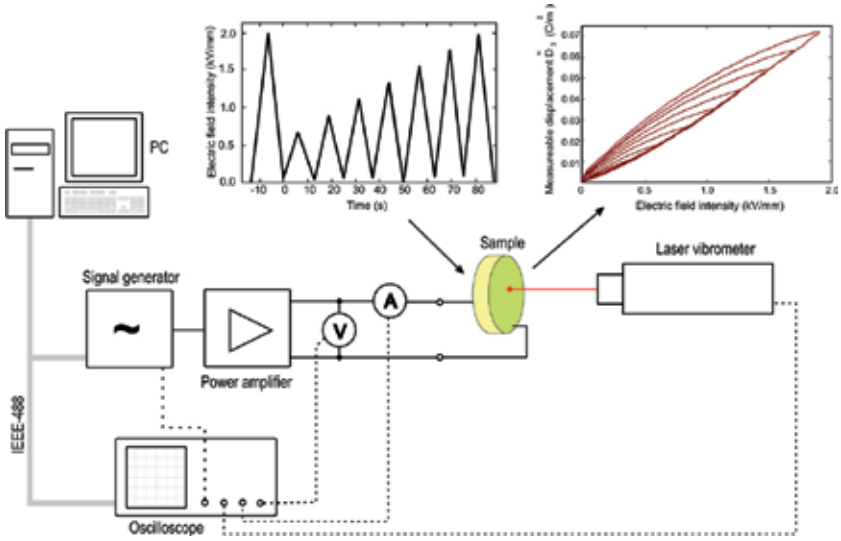

Fig. 10. Principle experimental setup for measuring the hysteresis curves of piezoelectric actuators.

within the excitation signal guarantees the same initial polarization for every measurement. The electric current $i(t)$ to the actuator is measured by an ampere-meter, the electric voltage $u(t)$ at the actuator by a voltmeter and the mechanical displacement $x(t)$ by a laser vibrometer. Now in the first step, we can compute the total electric displacement D_3 by

$$D_3(t) = P_{\mathrm{rem}}^{\mathrm{i}} + \frac{1}{A}\int_0^t i(\tau)\,\mathrm{d}\tau = P_{\mathrm{rem}}^{\mathrm{i}} + D_3^{\mathrm{m}}(t)\,. \tag{57}$$

In Equation (57) A denotes the surface of the electrode, D_3^{m} the measurable electric displacement and $P_{\mathrm{rem}}^{\mathrm{i}}$ accounts for the fact, that for unipolar excitations the dielectric displacement does not return to zero for zero electric field (instead it returns to the remanent polarization, which cannot be determined by the current measurement but has to be measured separately). Furthermore, we compute the electric field intensity E_3 just by dividing the

applied electric voltage u by the distance between the actuator's electrodes. With the linear material parameters d_{33} and $\varepsilon_{33}^{\sigma}$ we can now compute a first guess for the irreversible polarization

$$P_{3,\text{init}}^{\text{i}}(t) = D_3(t) - d_{33}\sigma_3(t) - \varepsilon_{33}^{\sigma}E_3(t)\,. \tag{58}$$

Here σ_3 accounts for any mechanical preloading as in the case of the stack actuator or is set to zero as in the case of the disc actuator (stress-free boundary conditions). In the case of a clamped actuator, one will need an additional force sensor to determine σ_3.
By simply iterating between the following two equations

$$d_{33}(P_3) = \frac{P_3^{\text{i}}}{P_{\text{sat}}^{\text{i}}}\, d_{33} \tag{59}$$

$$P_3^{\text{i}} = D_3 - d_{33}(P_3^{\text{i}})\sigma_3 - \varepsilon_{33}^{\sigma}E_3 \tag{60}$$

for each time instance t, we achieve at $P_3^{\text{i}}(t)$ and $d_{33}(P_3^{\text{i}}(t))$. Using Equation (20) we obtain the irreversible strain

$$S_3^{\text{i}}(t) = S_3(t) - s_{33}^{\text{E}}\sigma_3(t) - d_{33}(P_3^{\text{i}}(t))E_3(t)\,, \tag{61}$$

where $S_3(t)$ has been computed from the measured displacement x and the geometric dimension of the actuator. Since S_3^{i} is now a known quantity, we solve a least squares problem to obtain the coefficients β_i according to our relation for the irreversible strain (see Equation (13))

$$\min_{(\beta_1\ldots\beta_l)} \sum_{i=1}^{n_T} \left(\sum_{j=1}^{l} \beta_j \left(P_3^{\text{i}}(t_i) \right)^j - S_3(t_i) \right)^2 \tag{62}$$

collocated to n_T discrete time instances t_i. Once the input $E_3(t)$ and the output $P_3(t)$ of the Preisach operator $\mathcal{H}$ are directly available, the problem of identifying the weight function $\wp$ amounts to a linear integral equation of the first kind

$$\int_S \wp(\alpha,\beta)\mathcal{R}_{\beta,\alpha}[E_3](t)\, d\alpha\, d\beta = P_3(t) \qquad t \in \left[0, \bar{t}\right]. \tag{63}$$

Using a discretization of the Preisach operator as a linear combination of elementary hysteresis operators $\mathcal{H}_\lambda$

$$\mathcal{H} = \sum_{\lambda\in\Lambda} a_\lambda \mathcal{H}_\lambda \tag{64}$$

and evaluating the output at n_T discrete time instances $0 \le t_1 < t_2 < \cdots < t_{n_T} \le \bar{t}$, we approximate the solution of Equation (63) by solving a linear least squares problem for the coefficients $\mathbf{a} = (a_\lambda)_{\lambda\in\Lambda}$

$$\min_{\mathbf{a}} \sum_{i=1}^{n_T} \left(\sum_{\lambda\in\Lambda} a_\lambda \mathcal{H}_\lambda[E_3](t_i) - P_3(t_i) \right)^2. \tag{65}$$

In Equation (64), $\mathcal{H}_\lambda$ may be chosen as simple relays,

$$\mathcal{H}_\lambda = \mathcal{R}_{\beta_j,\alpha_i}\,,$$

see Section 3. The solution of Equation (65) provides the coefficients a_λ (see Fig. 11), which corresponds to a piecewise constant approximation of the weight function. In that case,

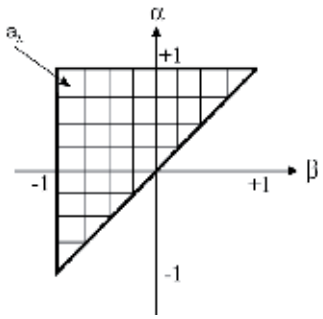

Fig. 11. Discretization of the Preisach plane by piecewise constants a_λ within each element.

obviously the set Λ consists of index pairs $\lambda = (i, j)$ corresponding to different up- and down-switching thresholds α_i, β_j and the array λ is supposed to be reordered in a column vector to yield a reformulation of Equation (65) in standard matrix form.
For further details of the fitting procedure, we refer to Hegewald (2008); Hegewald et al. (2008); Kaltenbacher & Kaltenbacher (2006); Rupitsch & Lerch. (2009).

7. Application

7.1 Piezoelectric disc actuator

In our first example we consider a simple disc actuator made of SP53 (CeramTec material) with a diameter of 35 mm and a thickness of 0.5 mm (see Fig. 12(a)).

Fig. 12. Geometric setup and axisymmetric geometry used for FE simulation: (a) Geometric setup of the disc actuator; (b) FE model exploiting rotational symmetry as well as axial symmetry (for display reasons not true to scale).

We exploit both rotational and axial symmetry and end up with a two-dimensional axi-symmetric FE model (see Fig. 12(b)). Along the z-axis we set the radial and along the r-axis the axial displacement to zero. Furthermore, we set the electric potential to zero along the r-axis and apply half the measured electric voltage along the top electrode (since we model the disc actuator just by its half thickness).
First we perform an impedance measurement of the piezoelectric disc with an electric preloading (see Fig. 9) and apply our inverse scheme to obtain the entries of the material tensors, Lahmer et al. (2008). Second, we do measurements according the experimental setup in Fig. 10 and apply the fitting procedure as described in Sec. 6. The results for the constant

s_{11} (m^2/N)	s_{33} (m^2/N)	s_{12} (m^2/N)	s_{13} (m^2/N)	s_{66} (m^2/N)
$1,82 \cdot 10^{-11}$	$2,04 \cdot 10^{-11}$	$-4,85 \cdot 10^{-12}$	$-5,71 \cdot 10^{-12}$	$6,33 \cdot 10^{-11}$

d_{31} (C/N)	d_{33} (C/N)	d_{15} (C/N)	ε_{11} (F/m)	ε_{33} (F/m)
$-1,74 \cdot 10^{-10}$	$4,30 \cdot 10^{-10}$	$4,87 \cdot 10^{-10}$	$7,39 \cdot 10^{-9}$	$1,68 \cdot 10^{-8}$

(a)

ν	β_ν / $(m^2 \cdot C^{-1})^\nu$
1	$1,13 \cdot 10^{-2}$
2	$2,33 \cdot 10^{-1}$
3	$8,70 \cdot 10^{0}$
4	$7,06 \cdot 10^{1}$

(b)

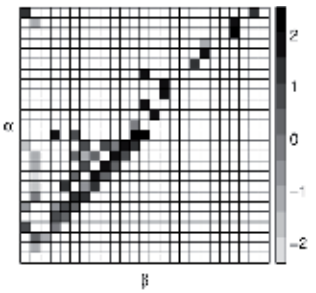

Table 1. Model parameters for the single disc actuator: (a) Material parameters and polynomial coefficients for the irreversible mechanical strain; (b) Logarithmic values of the Preisach weight function for $M = 25$.

material parameters, the polynomial coefficients for approximating the irreversible strain and the Preisach weight function are listed in Tab. 1.[4]

A FE simulation is performed with these fitted data, using the above described boundary conditions and a triangular excitation voltage different from the one used for the fitting procedure. The average number of nonlinear iterations within each time step to achieve the stopping criterion of (56) with an accuracy of $\delta_{\text{rel}} = 10^{-4}$ was only about two and no restriction on the time step size had to be imposed.

Figure 13 displays in detail the comparison of the measured and FE simulated data. This example clearly demonstrates, that using the fitted model parameters our FE scheme reproduces quite accurately the measured data in the experiment.

7.2 Piezoelectric revolving drive

The second practical example concerns a piezoelectric revolving motor as displayed in Fig. 14 Kappel et al. (2006). This drive operates in a large frequency range, and its main advantage is the compact construction and the high moment of torque. The rotary motion of the drive displayed in Fig. 14 results due to a sine-excitation of the two stack actuators with a 90 degree phase shift. The construction of the drive guarantees that shaft and clutch driving ring have a permanently contact at each revolving position.

[4] M, the discretization parameter for the Preisach plane, defines the number of discrete Preisach weights as $M(M+1)/2$.

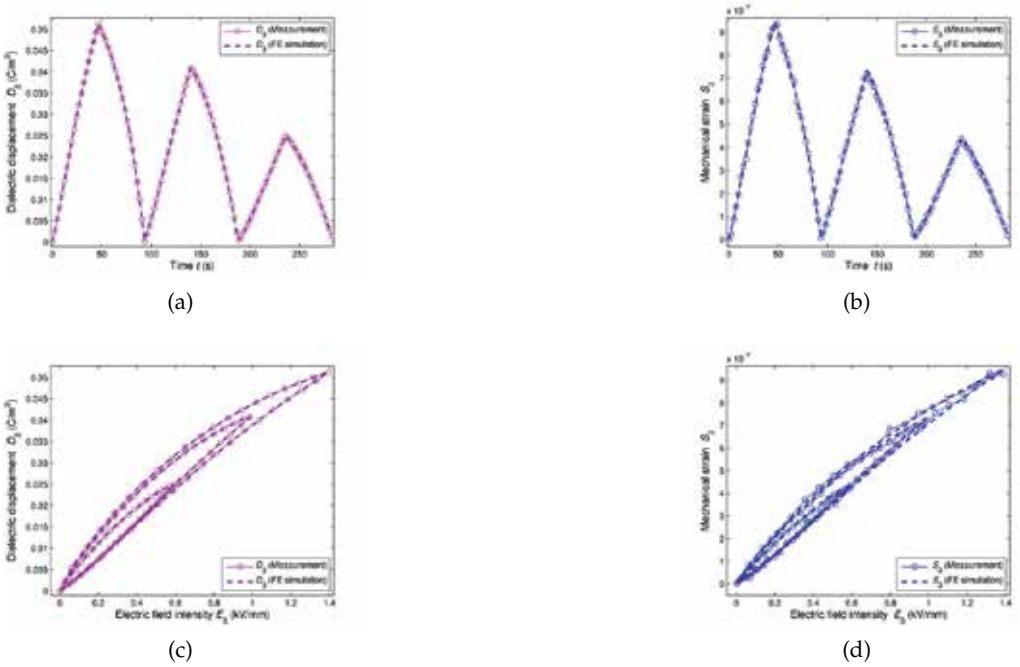

Fig. 13. Comparison of the measured and FE simulated data for the piezoelectric disc actuator: (a) Dielectric displacement over time; (b) Mechanical strain over time; (c) Dielectric displacement over electric field intensity; (d) Mechanical strain over electric field intensity.

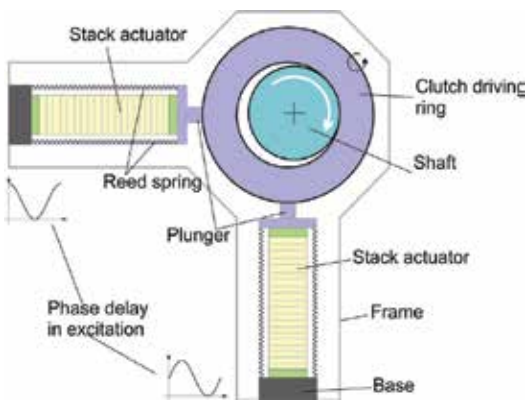

Fig. 14. Princple setup of the piezoelectric revolving drive Kappel et al. (2006)

The two stack actuators are of the same type, and their principle setup is displayed in Fig. 15(a). These stacks consists of 360 layers, each having a thickness of 80 μm and cross section of $6.8 \times 6.8\,\mathrm{mm}^2$. The overall length of the stack actuator is 30 mm and it exhibits a maximal stroke of 40 μm.

For the FE simulation we choose the full 3d setup and model the whole stack as one homogenized block. Since we currently restrict ourselves to the uni-axial electric load case, it makes no sense to fully resolve the inter-digital structure of the electrodes. Furthermore, we

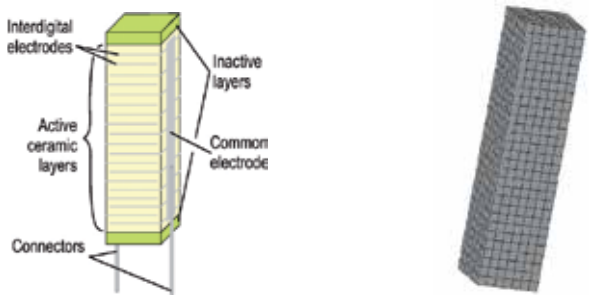

(a) (b)

Fig. 15. Geometric setup and FE model of stack actuator: (a) Geometric setup of the stack actuator; (b) Computational grid.

set the electric potential at the top surface to the measured voltage multiplied by the number of layers, since we do not resolve the layered structure.
Again, we do an impedance measurement at the electrically preloaded stack actuator and use our inverse scheme to get all entries of the material tensors. Next we use our measurement setup according to Fig. 10 and excite the stack actuator with a triangular signal. The material tensor entries as well as the polynomial coefficients for the irreversible strain and the Preisach weight function for the hysteresis operator are provided in Tab. 2.
Now in a second step, we use the fitted material parameters for our advanced piezoelectric material model and set up a FE model for the piezoelectric revolving drive as displayed in Fig. 16(a). For the clutch driving ring and plunger we apply standard material parameters of steel,

(a) (b)

Fig. 16. Piezoelectric revolving drive: (a) FE grid; (b) Strongly scaled (factor of about 150) mechanical deformation for a characteristic time step, when the left actuator is at maximal load.

and we do not model the shaft and its contact to the clutch driving ring. For the excitation we apply DC-shifted cosine- and sine-signals. The DC-shift guarantees, that the stack actuators are in an unipolar operating mode. The maximal achieved electric field intensity is about 2 kV/mm. In addition to the simulation, an experimental lab setup has been designed, where

s_{11} (m^2/N)	s_{33} (m^2/N)	s_{12} (m^2/N)	s_{13} (m^2/N)	s_{66} (m^2/N)
$1,29 \cdot 10^{-11}$	$2,54 \cdot 10^{-11}$	$-3.72 \cdot 10^{-12}$	$-5,85 \cdot 10^{-12}$	$3,39 \cdot 10^{-11}$

d_{31} (C/N)	d_{33} (C/N)	d_{15} (C/N)	ε_{11} (F/m)	ε_{33} (F/m)
$-8,09 \cdot 10^{-11}$	$2,83 \cdot 10^{-10}$	$2,52 \cdot 10^{-10}$	$5,82 \cdot 10^{-9}$	$0,81 \cdot 10^{-8}$

(a)

ν	β_ν / $(m^2 \cdot C^{-1})^\nu$
1	$1,79 \cdot 10^{-2}$
2	$6,60 \cdot 10^{-2}$
3	$8,13 \cdot 10^{-1}$
4	$1,91 \cdot 10^{1}$

(b)

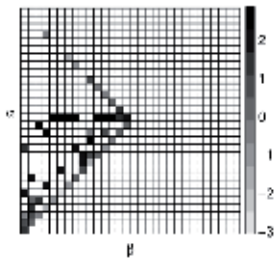

Table 2. Model parameters for the stack actuator: (a) Material parameters and polynomial coefficients for the irreversible mechanical strain; (b) Logarithmic values of the Preisach weight function for $M = 30$.

the shaft has also been neglected, Hegewald (2008). The displacements in x- and y-direction have been measured with a laser vibrometer.
In Fig. 16(b) we show the mechanical deformation of the whole considered setup for a characteristic time step, when the left stack actuator is at maximal stroke. A comparison between measured and simulated displacements both in x- and y-direction is displayed in Fig. 17. The fit for the displacement in x-direction is almost perfect; in y-direction there is some small difference.
Furthermore, in Fig. 18 we show the trajectory of one point on the ring. One observes that the resulting trajectory differs from a perfect circle. We also performed a simulation with a linear piezoelectric material model and obtained a perfect circle for the trajectory. Hence, the deviation from a perfect circle is clearly a result of the nonlinear (hysteretic) behavior of the stack actuators.

8. Summary and outlook

We have discussed a nonlinear piezoelectric model based on Preisach hysteresis operators and explained in detail the efficient solution of the governing partial differential equations by a quasi Newton scheme within the FE method. Moreover, we have described a procedure for determining the model parameters from measurements. Practical applications have

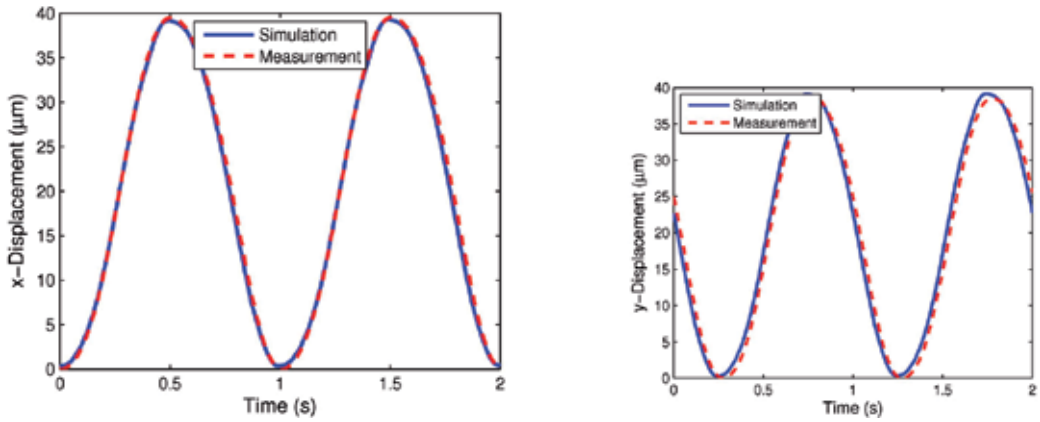

(a) (b)

Fig. 17. Comparison between measurement and simulation: (a) displacement in x-direction; (b) displacement in y-direction.

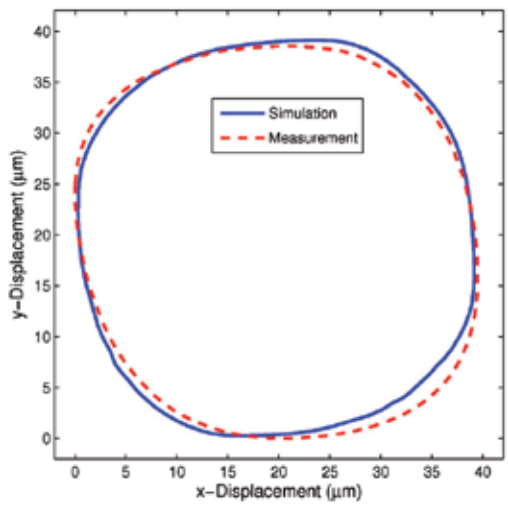

Fig. 18. Trajectory of one point of the ring obtained from measurements and simulation.

demonstrated, that the model is very well capable to provide qualitatively and quantitatively correct simulations.

Currently, we are investigating the extension of our model to also take ferroelastic loading into account. Such an approach can, e.g., be found in Ball et al. (2007). A very interesting option for modelling both ferroelectricity and ferroelasticity in a thermodynamically consistent manner is enabled by so-called hysteresis potentials, see Krejčí (2010).

Referring to Equation (28), Equation (29), we finally describe a possible extension to a multi-axial piezoelectric model. First of all, we have to apply a vector Preisach hysteresis model (see, e.g Mayergoyz (1991)), which for each electric field intensity vector $\mathbf{E}$ provides a

vector for the irreversible polarization $\mathbf{P}^{\mathrm{i}}$

$$\mathbf{P}^{\mathrm{i}} = \boldsymbol{\mathcal{H}}(\mathbf{E})\,. \tag{66}$$

Furthermore, we compute the coupling tensor $[\mathbf{e}(\mathbf{P}^{\mathrm{i}})]$ as in Equation (15) and rotate it in the direction of the irreversible polarization $\mathbf{P}^{\mathrm{i}}$. Similarly as in the scalar case, we define the irreversible strains by

$$[\mathbf{S}^{\mathrm{i}}] = \tfrac{3}{2}\left(\beta_1 \cdot |\boldsymbol{\mathcal{H}}[\mathbf{E}]| + \beta_2 \cdot |\boldsymbol{\mathcal{H}}[\mathbf{E}]|^2 + \cdots + \beta_n \cdot |\boldsymbol{\mathcal{H}}[\mathbf{E}]|^n\right)\left(\mathbf{e}_P\,\mathbf{e}_P{}^T - \tfrac{1}{3}\,[\mathbf{I}]\right) \tag{67}$$

with the unit vector of the irreversible polarization defined by $\mathbf{e}_P = \mathbf{P}^{\mathrm{i}}/|\mathbf{P}^{\mathrm{i}}|$.

9. References

Adams, R. A. (1975). *Sobolev Spaces*, Pure and Applied Mathematics, Academic Press.

Ball, B. L., Smith, R. C., Kim, S. J. & Seelecke, S. (2007). A stress-dependent hysteresis model for ferroelectric materials, *Journal of Intelligent Material Systems and Structures* 18: 69–88.

Bassiouny, E. & Ghaleb, A. F. (1989). Thermodynamical formulation for coupled electromechanical hysteresis effects: Combined electromechanical loading, *International Journal of Engineering Science* 27(8): 989–1000.

Belov, A. Y. & Kreher, W. S. (2006). Simulation of microstructure evolution in polycrystalline ferroelectrics ferroelastics, *Acta Materialia* 54: 3463 3469.

Brokate, M. & Sprekels, J. (1996). *Hysteresis and Phase Transitions*, Springer, New York.

Cimaa, L., Laboure, E. & Muralt, P. (2002). Characterization and model of ferroelectrics based on experimental preisach density, *Review of Scientific Instruments* 73(10).

Delibas, B., Arockiarajan, A. & Seemann, W. (2005). A nonlinear model of piezoelectric polycrystalline ceramics under quasi-static electromechanical loading, *Journal of Materials Science: Materials in Electronics* 16: 507–515.

Everett, D. (1955). A general approach to hysteresis, *Trans. Faraday Soc.* 51: 1551–1557.

Fröhlich, A. (2001). *Mikromechanisches Modell zur Ermittlung effektiver Materialeigenschaften von piezoelektrischen Polykristallen*, Dissertation, Universität Karlsruhe (TH), Forschungszentrum Karlsruhe.

Hegewald, T. (2008). *Modellierung des nichtlinearen Verhaltens piezokeramischer Aktoren*, PhD thesis, Universität Erlangen-Nürnberg, URL: http://www.opus.ub.uni-erlangen.de/ opus/volltexte/2008/875/, URN: urn:nbn:de:bvb:29-opus-8758.

Hegewald, T., Kaltenbacher, B., Kaltenbacher, M. & Lerch, R. (2008). Efficient modeling of ferroelectric behavior for the analysis of piezoceramic actuators, *Journal of Intelligent Material Systems and Structures* 19(10): 1117–1129.

Huber, J. E. (2006). Micromechanical modelling of ferroelectrics, *Current Opinion in Solid State and Materials Science* 9: 100–106.

Huber, J. E. & Fleck, N. A. (2001). Multi-axial electrical switching of a ferroelectric: theory versus experiment, *Journal of the Mechanics and Physics of Solids* 49: 785 811.

Hughes, D. C. & Wen, J. T. (1995). Preisach modeling and compensation for smart material hysteresis, *Proceedings: Active Materials and Smart Structures*, Vol. 2427, pp. 50–64.

Hughes, T. J. R. (1987). *The Finite Element Method*, 1 edn, Prentice-Hall, New Jersey.

Kaltenbacher, B. & Kaltenbacher, M. (2006). Modelling and iterative identification of hysteresis via Preisach operators in PDEs, *in* J. Kraus & U. Langer (eds), *Lectures on*

Advanced Computational Methods in Mechanics, de Gruyter, chapter 1, pp. 1–45. ISBN 978-3-11-019556-9.

Kaltenbacher, B., Lahmer, T., Mohr, M. & Kaltenbacher, M. (2006). PDE based determination of piezoelectric material tensors, *European Journal of Applied Mathematics* 17: 383–416.

Kaltenbacher, M. (2007). *Numerical Simulation of Mechatronic Sensors and Actuators*, 2. edn, Springer, Berlin. ISBN: 978-3-540-71359-3.

Kaltenbacher, M., Kaltenbacher, B., Hegewald, T. & Lerch, R. (2010). Finite element formulation for ferroelectric hysteresis of piezoelectric materials, *Journal of Intelligent Material Systems and Structures* 21: 773–785.

Kamlah, M. (2001). Feroelectric and ferroelastic piezoceramics - modeling of electromechanical hysteresis phenomena, *Continuum Mech. Thermodyn.* 13: 219–268.

Kamlah, M. & Böhle, U. (2001). Finite element analysis of piezoceramic components taking into account ferroelectric hysteresis behavior, *International Journal of Solids and Structures* 38: 605–633.

Kappel, A., Gottlieb, B., Schwebel, T., Wallenhauer, C. & Liess, H. (2006). Pad - piezoelectric actuator drive, *Proceedings of the 10th International Conference on New Actuators, ACTUATOR 2006*, Bremen, Germany, pp. 457–460.

Krasnoselskii, M. & Pokrovskii, A. (1989). *Systems with Hysteresis*, Springer, Heidelberg.

Krejčí, P. (1996). *Hysteresis, Convexity, and Dissipation in Hyperbolic Equations*, Gakkotosho, Tokyo.

Krejčí, P. (2010). An energetic model for magnetostrictive butterfly hysteresis, *5th International Workshop on MULTI-RATE PROCESSES & HYSTERESIS in Mathematics, Physics, Engineering and Information Sciences*. Pécs, Hungary.

Kuhnen, K. (2001). *Inverse Steuerung piezoelektrischer Aktoren mit Hysterese-, Kriech- und Superpositionsoperatoren*, Dissertation, Universität des Saarlandes, Saarbrücken.

Lahmer, T., Kaltenbacher, M., Kaltenbacher, B. & Lerch, R. (2008). FEM-Based Determination of Real and Complex Elastic, Dielectric and Piezoelectric Moduli in Piezoceramic Materials, *IEEE Transactions on Ultrasonics, Ferroelectrics, and Frequency Control* 55(2): 465–475.

Landis, C. M. (2004). Non-linear constitutive modeling of ferroelectrics, *Current Opinion in Solid State and Materials Science* 8: 59–69.

Linnemann, K., Klinkel, S. & Wagner, W. (2009). A constitutive model for magnetostrictive and piezoelectric materials, *International Journal of Solids and Structures* 46: 1149 1166.

Mayergoyz, I. D. (1991). *Mathematical Models of Hysteresis*, Springer-Verlag New York.

McMeeking, R. M., Landis, C. M. & Jimeneza, M. A. (2007). A principle of virtual work for combined electrostatic and mechanical loading of materials, *International Journal of Non-Linear Mechanics* 42(6): 831–838.

Pasco, Y. & Berry, A. (2004). A hybrid analytical/numerical model of piezoelectric stack actuators using a macroscopic nonlinear theory of ferroelectricity and a preisach model of hysteresis, *Journal of Intelligent Material Systems and Structures* 15: 375–386.

Rupitsch, S. J. & Lerch., R. (2009). Inverse method to estimate material parameters for piezoceramic disc actuators, *Applied Physics A* 97(4): :735–740.

Schröder, J. & Keip, M.-A. (2010). Multiscale modeling of electro–mechanically coupled materials: homogenization procedure and computation of overall moduli, *Proceedings of the IUTAM conference on multiscale modeling of fatigue, damage and fracture in smart materials*, Springer, Heidelberg.

Schröder, J. & Romanowski, H. (2005). A thermodynamically consistent mesoscopic model for transversely isotropic ferroelectric ceramics in a coordinate-invariant setting, *Archive of Applied Mechanics* 74: 863–877.

Smith, R. C., Seelecke, S., Ounaies, Z. & Smith, J. (2003). A free energy model for hysteresis in ferroelectric materials, *Journal of Intelligent Material Systems and Structures* 14: 719–737.

Su, Y. & Landis, C. M. (2007). Continuum thermodynamics of ferroelectric domain evolution: Theory, fnite element implementation and application to domain wall pinning, *Journal of the Mechanics and Physics of Solids* 55: 280 305.

Visintin, A. (1994). *Differential Models of Hysteresis*, Springer, Berlin.

Wang, J., Kamlah, M. & Zhang, T.-Y. (2010). Phase field simulations of low dimensional ferroelectrics, *Acta Mechanica* . (to appear).

Xu, B.-X., Schrade, D., Müller, R., Gross, D., Granzow, T. & Rödel, J. (2010). Phase field simulation and experimental investigation of the electro-mechanical behavior of ferroelectrics, *Z. Angew. Math. Mech.* 90: 623–632.

Zäh, D., Kiefer, B., Rosato, D. & Miehe, C. (2010). A variational homogenization approach to electro-mechanical hystereses, talk at the 3rd GAMM Seminar on Multiscale Material Modeling, Bochum.

Edited by Mickaël Lallart

Ferroelectric materials have been and still are widely used in many applications, that have moved from sonar towards breakthrough technologies such as memories or optical devices. This book is a part of a four volume collection (covering material aspects, physical effects, characterization and modeling, and applications) and focuses on the characterization of ferroelectric materials, including structural, electrical and multiphysic aspects, as well as innovative techniques for modeling and predicting the performance of these devices using phenomenological approaches and nonlinear methods. Hence, the aim of this book is to provide an up-to-date review of recent scientific findings and recent advances in the field of ferroelectric system characterization and modeling, allowing a deep understanding of ferroelectricity.

ISBN 978-953-51-4455-7

Photo by VladKyselov / iStock

IntechOpen